

Solid Freeform Fabrication Proceedings

August 1999

Solid Freeform Fabrication as an important and totally integrated approach to design, materials processing and manufacturing research results related to it is contained in this proceedings of the SFF Symposium held in Austin, Texas on August 9-11, 1999

SFF Topics covered in the Symposium include:

Machine Design
Computer Sectioning
Reverse Engineering
Materials Processing
Applications

David L. Bourell , Joseph J. Beaman,
Richard H. Crawford, Harris L. Marcus,
and Joel W. Barlow, Editors

© 1999 The University of Texas at Austin

All rights of reproduction in any form are protected by U.S. Copyright Laws.
Permission to copy all or portions of the proceedings contents must be obtained
from the authors and The University of Texas at Austin.

Library of Congress ISSN 1053-2153

DISTRIBUTION STATEMENT A
Approved for Public Release
Distribution Unlimited

20000505 101

DTIC QUALITY INSPECTED 1

End of Fiscal Year Letter - ONR Grant N00014-99-1-0849
Solid Freeform Fabrication Symposium -1999
David L. Bourell, PI

A. Description of the Technical Research or Development Goals: This grant helped to underwrite the publication expenses associated with the Ninth Solid Freeform Fabrication (SFF) Symposium. The symposium took place on August 9-11, 1999 in Austin, Texas at the University of Texas.

It included papers on computer interfaces with SFF, materials processing and properties associated with SFF and machine design and requirements for SFF.

B. Significant Research or Development Results During the Past Year: The Ninth Solid Freeform Fabrication Symposium, held at The University of Texas in Austin on August 9-11, 1999, was attended by over 150 national and international researchers. Papers addressed SFF issues in computer software, machine design, materials synthesis and processing, and integrated manufacturing. A total of 117 presentations were made, 83 oral presentations and 34 poster presentations. This represents the most presentations ever given at the SFF Symposium and reflects 15 percent growth in the oral presentations compared to last year, indicative of our attempt to provide "stand-up" opportunities for as many research presenters as possible. The diverse domestic and foreign attendees represented industrial users, SFF machine manufacturers, universities, and government. The excitement generated at the Symposium reflects the participants' total involvement in SFF and the future technical health of this growing technology. The Symposium organizers look forward to its being a continuing forum for technical exchange among the expanding body of researchers involved in SFF.

The Symposium was again organized in a manner to allow the multi-disciplinary nature of the SFF research to be presented coherently, with various sessions emphasizing computer issues, machine topics, and the variety of materials aspects of SFF. This year, the three-day event was completely composed of individual oral presentations (no panel discussions/presentations) to accommodate the demand for this dissemination format. Once again, the afternoon parallel sessions were increased to three sessions. We believe that documenting the constantly changing state of SFF art as represented by these Proceedings will serve both the people presently involved in this fruitful technical area as well as the large flux of new researchers and users entering the field.

We are pleased to report that the SFF Symposium attracted a large number of young scientists this year. We had 66 students attend this year, approximately 37% of the entire meeting. Participants represented 51 universities (19 international universities), 26 industries (5 international) and 8 national labs and government agencies. The Organizing Committee has always valued the role of technical meetings as a venue for graduate students in research. We strive to make the conference affordable and therefore accessible to students. The 1999 meeting registration cost of \$100 for students reflected this. Non-student cost was \$350.

Information on the SFF Symposium was made available through the worldwide web at <http://lff.me.utexas.edu/>. On-line registration forms, hotel information, general information brochure, proceedings order forms, maps, and previous years' talk titles are all available. The symposium email address is sffsymp@uts.cc.utexas.edu.

C. Plans for Next Year's Research or Development: Plans are currently underway for organization of the Eleventh Solid Freeform Fabrication Symposium. The dates are August 7-9, 2000. The Call for Papers has gone out. We currently have received over 75 abstracts for the 2000 SFF Symposium, representing authors from 15 countries, 44 universities (21 international) and 17 industries/national labs.

REPORT DOCUMENTATION PAGE				Form Approved OMB No. 0704-0188	
Public reporting burden for this collection of information is estimated to average 1 hour per response, including the time for reviewing instructions, searching data sources, gathering and maintaining the data needed, and completing and reviewing the collection of information. Send comments regarding this burden estimate or any other aspect of this collection of information, including suggestions for reducing this burden to Washington Headquarters Service, Directorate for Information Operations and Reports, 1215 Jefferson Davis Highway, Suite 1204, Arlington, VA 22202-4302, and to the Office of Management and Budget, Paperwork Reduction Project (0704-0188) Washington, DC 20503.					
PLEASE DO NOT RETURN YOUR FORM TO THE ABOVE ADDRESS.					
1. REPORT DATE (DD-MM-YYYY) 01-05-2000		2. REPORT DATE		3. DATES COVERED (From - To) 07-01-99 to 10-31-99	
4. TITLE AND SUBTITLE Solid Freeform Fabrication Symposium - 1999 Report and Proceedings				5a. CONTRACT NUMBER	
				5b. GRANT NUMBER N00014-99-1-0849	
				5c. PROGRAM ELEMENT NUMBER	
6. AUTHOR(S) D. L. Bourell and J. J. Beaman, Jr.				5d. PROJECT NUMBER	
				5e. TASK NUMBER	
				5f. WORK UNIT NUMBER	
7. PERFORMING ORGANIZATION NAME(S) AND ADDRESS(ES) The University of Texas at Austin Solid Freeform Fabrication Symposium Department of Mechanical Engineering C2200 Austin, TX 78712-1063				8. PERFORMING ORGANIZATION REPORT NUMBER	
9. SPONSORING/MONITORING AGENCY NAME(S) AND ADDRESS(ES) Ralph F. Wachter ONR 361 Ballston Centre Tower One 800 North Quincy Street Arlington, VA 22217-5660				10. SPONSOR/MONITOR'S ACRONYM(S)	
				11. SPONSORING/MONITORING AGENCY REPORT NUMBER	
12. DISTRIBUTION AVAILABILITY STATEMENT approved for public release					
13. SUPPLEMENTARY NOTES					
14. ABSTRACT The Tenth Solid Freeform Fabrication Symposium, held at The University of Texas in Austin on August 9-11, 1999, was attended by over 170 national and international researchers. Papers addressed SFF issues in computer software, machine design, materials synthesis and processing, and integrated manufacturing. New sessions on ceramic materials and multiple materials SFF were added to this year's program. One hundred seventeen presentations were made, 83 oral presentations and 34 poster presentations. The diverse domestic and foreign attendees included industrial users, SFF machine manufacturers, university researchers and representatives from the government.					
15. SUBJECT TERMS Freeform Fabrication, Symposium, Proceedings					
16. SECURITY CLASSIFICATION OF:			17. LIMITATION OF ABSTRACT		18. NUMBER OF PAGES
a. REPORT unclass- ified	b. ABSTRACT unclass- ified	c. THIS PAGE unclass- ified	UL		910
19a. NAME OF RESPONSIBLE PERSON David L. Bourell					19b. TELEPHONE NUMBER (include area code) (512) 471-3170

Table of Contents

	<u>Page</u>
<i>Preface</i> -----	ix
<i>Organizing/Advisory Committee</i> -----	xi
Modeling	
An Interactive Virtual System for Simulation and Optimization of Rapid Prototyping	
<i>S. H. Choi, S. Samavedam, The University of Hong Kong</i> -----	1
A Knowledge-based Decision Support System for RP&M Process Selection	
<i>F. Xu, Y. S. Wong, H. T. Loh, National University of Singapore</i> -----	9
RP Process Selection for Rapid Tooling in Sand Casting	
<i>Wanlong Wang, James G. Conley, Henry W. Stoll, Rui Jiang, Northwestern University</i> -----	19
Agile Product Testing with Constrained Prototypes	
<i>Uichung Cho, Kristin L. Wood, Richard H. Crawford, The University of Texas</i> -----	29
Knowledge-based System for the Choice of Rapid Prototyping Process	
<i>Alain Bernard, Université Nancy</i> -----	39
A Methodology to Create STL Files from Data Point Clouds Generated with a Coordinate Measuring Machine	
<i>Irene Tyvaert^a, Georges Fadel^b, Emmanuelle Rouhaud^a, ^aUniversité de Technologie de Troyes, ^bClemson University</i> -----	47
Precision LCVD System Design with Real Time Process Control	
<i>Daniel L. Jean, Chad E. Duty, Brian T. Fuhrman, W. Jack Lackey, Georgia Institute of Technology</i> -----	59
Process Planning Based on User Preferences	
<i>Aaron P. West, David W. Rosen, Georgia Institute of Technology</i> -----	67
Volume Modeling for Rapid Prototyping	
<i>Di Ma, Feng Lin, Chee Kai Chua, Nanyang Technological University</i> -----	77
Selective Laser Sintering Process Management Using a Relational Database	
<i>Dongping Shi, Ian Gibson, The University of Hong Kong</i> -----	85
Implementation and Evaluation of Novel Buildstyles in Fused Deposition Modeling (FDM)	
<i>Tobias Wasser, Anshu Dhar Jayal, Christoph Pistor, University of Utah</i> -----	95
Application of Design of Experiments to Extrusion Freeform Fabrication (EFF) of Functional Ceramic Prototypes	
<i>J. Walish^a, M. Sutaria^a, M. Dougherty^a, R. Vaidyanathan^a, S. Kasichainula^b, P. Calvert^b, K. Cooper^c, ^aAdvanced Ceramics Research, ^bUniversity of Arizona, ^cNASA Marshall Space Flight Center</i> -----	103

Automated Layer Decomposition for Additive/Subtractive Solid Freeform Fabrication <i>Y. C. Chang, J. M. Pinilla, J. H. Kao, J. Dong, K. Ramaswami, F. B. Prinz,</i> Stanford University -----	111
Automated Planning for Material Shaping Operations in Additive/Subtractive Solid Freeform Fabrication <i>Jianpeng Dong, Ju-Hsien Kao, Jose M. Pinilla, Yu-Chi Chang, Fritz B. Prinz,</i> Stanford University -----	121
Computer-Aided Process Planning for Automatic Generation of 3D Digitizing Process for Laser Sensors <i>Alain Bernard, Stéphane Davillerd, Benoit Sidot,</i> Université Nancy-----	129
A Mathematical Description of Layered Manufacturing Fabrication <i>Feng Lin^a, Wei Sun^a, Yongnian Yan^b,</i> ^a Drexel University, ^b Tsinghua University -----	139
SALD and SALVI Virtual Laboratory <i>Zbigniew M. Bzymek, David Ferreira, Harris Marcus, Leon L. Shaw,</i> The University of Connecticut at Storrs-----	147
A Memory Efficient Slicing Algorithm for Large STL Files <i>S. H. Choi, K. T. Kwok,</i> The University of Hong Kong-----	155
A Minimum Bounding Box Algorithm and Its Application to Rapid Prototyping <i>C. K. Chan, S. T. Tan,</i> The University of Hong Kong -----	163
Slicing STEP-based CAD Models for CAD/RP Interface <i>Haeseong J. Jee, Byong-Yeol Lee,</i> Hongik University-----	171
Representation and Design of Heterogeneous Components <i>Ashok V. Kumar, Aaron Wood,</i> University of Florida-----	179
Heterogeneous Solids: Possible Representation Schemes <i>Stephane M. Morvan, Georges M. Fadel,</i> Clemson University -----	187
Functionally Gradient Material Design and Modeling Using Hypertexture for Solid Freeform Fabrication <i>Seok-Min Park, Richard H. Crawford, Joseph J. Beaman,</i> The University of Texas at Austin -----	199
Application of Genetic Algorithms in the Design of Multi-Material Structures Manufactured in Rapid Prototyping <i>Oliver König^a, Georges M. Fadel^b,</i> ^a ETH Zurich, ^b Clemson University-----	209
An Ejection Mechanism Design Method for AIM Tools <i>Sundiata K. Jangha, David W. Rosen,</i> Georgia Institute of Technology -----	219
Fractal Growth Modeling of Electrochemical Deposition in Solid Freeform Fabrication <i>Jack G. Zhou, Zongyan He, Jian Guo,</i> Drexel University -----	229
Residual Stresses in Layered Manufacturing <i>A. Nickel, D. Barnett, G. Link, F. Prinz,</i> Stanford University-----	239
Thermal Effects of In-Bed Rapid Prototyping Metastructures <i>Jeffery L. Norrell, Kristin L. Wood, Richard H. Crawford,</i> The University of Texas at Austin -----	247

Materials

Optimization of Powder Layer Density in Selective Laser Sintering <i>N. P. Karapatis, G. Egger, P.-E. Gygax, R. Glardon, Swiss Federal Institute of Technology</i> -----	255
Atmospheric Control during Direct Selective Laser Sintering of Stainless Steel 314S Powder <i>C. Hauser, T. H. C. Childs, K. W. Dalgarno, R. B. Eane, The University of Leeds</i> -----	265
Selective Laser Sintering of Stainless Steel 314S HC Processed Using Room Temperature Powder Beds <i>C. Hauser, T. H. C. Childs, K. W. Dalgarno, The University of Leeds</i> -----	273
Direct Laser Fabrication of High Performance Metal Components via SLS/HIP <i>Martin Wohler, Suman Das, Joseph J. Beaman, David L. Bourell, The University of Texas at Austin</i> -----	281
Si/SiC-Ceramic Prototypes via LS²I-Process (Liquid Silicon Infiltration of Laser Sintered C-SiC Parts) <i>Peter Stierlen, Peter Eyerer, Institute of Polymer Testing and Polymer Science</i> -----	289
Selective Laser Sintering of Zirconia with Micro-Scale Features <i>Nicole Harlan, Seok-Min Park, David L. Bourell, Joseph J. Beaman, The University of Texas at Austin</i> -----	297
Measurement of the Sintering Dynamics of Polymeric Powders at Near SLS Conditions <i>J. Steinberger, K. Manetsberger, J. Shen, J. Müllers, DaimlerChrysler Research Center</i> -----	303
Cryogenic Mechanical Alloying of Poly (ether ether ketone) – Polycarbonate Composite Powders for Selective Laser Sintering <i>J. Schultz, R. Kander, C. Suchicital, Virginia Tech</i> -----	311
Processing, Characterization and Modeling of Non-Random Porous Ceramic Structures <i>Ashwin Hattiangadi, Amit Bandyopadhyay, Washington State University</i> -----	319
Extrusion Freeform Fabrication of Functional Ceramic Prototypes <i>R. Vaidyanathan^a, J. L. Lombard^a, J. Walish^a, S. Kasichainula^b, P. Calvert^b, K. Cooper^c, ^aAdvanced Ceramics Research, Inc., ^bUniversity of Arizona, ^cNASA Marshall Space Flight Center</i> -----	327
Maximizing the Strength of Fused-Deposition ABS Plastic Parts <i>J. F. Rodríguez, J. P. Thomas, J. E. Renaud, University of Notre Dame</i> -----	335
Thermo-mechanical Analysis of Parts Fabricated via Fused Deposition Modeling (FDM) <i>Manish Bharvirkar, Phong Nguyen, Christoph Pistor, University of Utah</i> -----	343
Mechanical and Rheological Properties of Feedstock Material for Fused Deposition of Ceramics and Metals (FDC and FDMet) and Their Relationship to Process Performance <i>N. Venkataraman^a, S. Rangarajan^a, M. J. Matthewson^a, A. Safari^a, S. C. Danforth^a, A. Yardimci^b, S. I. Guceri^c, ^aRutgers University, ^bAdvanced Engineering Design Center, ^cUniversity of Illinois at Chicago</i> -----	351

Novel Ceramics and Metal-Ceramic Composites via Fused Deposition Process <i>Amit Bandyopadhyay, Raj Atisivan, Susmita Bose, Washington State University</i>	361
Process Variable Effects on Laser Deposited Ti-6Al-4V <i>C. A. Brice^a, K. I. Schwendner^a, D. W. Mahaffey^a, E. H. Moore^b, H. L. Fraser^a, ^aThe Ohio State University, ^bAFRL/MLLM Wright-Patterson Air Force Base</i>	369
Microstructure and Property Optimization of LENS Deposited H13 Tool Steel <i>J. Brooks, C. Robino, T. Headley, S. Goods, M. Griffith, Sandia National Laboratories</i>	375
Process Maps for Laser Deposition of Thin-Walled Structures <i>Aditad Vasinonta^a, Jack Beuth^a, Michelle Griffith^b, ^aCarnegie Mellon University, ^bSandia National Laboratories</i>	383
Coated Feedstock for Fabrication of Ceramic Parts by CAM-LEM <i>Zhien Liu, N. Suppakarn, James D. Cawley, Case Western Reserve University</i>	393
Direct Fabrication of Polymer Composite Structures with Curved LOM <i>Donald Klosterman, Richard Chartoff, Mukesh Agarwala, Ira Fiscus, John Murphy, Sean Cullen, Mark Yeazell, University of Dayton</i>	401
Low Shrinkage Metal Skeletons by Three Dimensional Printing <i>Emanuel Sachs^a, Samuel Allen^a, Costas Hadjiloucas^a, Jeannie Yoo^b, Michael Cima^a, Massachusetts Institute of Technology, Imation Enterprises Corporation</i>	411
Fabrication of High Quality Ceramic Parts Using Mold SDM <i>S. Kang^a, A. G. Cooper^a, J. Stampfl^a, F. Prinz^a, J. Lombardi^b, L. Weiss^c, J. Sherbeck^d, ^aStanford University, ^bAdvanced Ceramics Research, ^cCarnegie Mellon University, ^dM-DOT Inc.</i>	427
Net-Form Manufacturing of Aluminum Components: the Dependence of Processing Parameters on Component Quality <i>Melissa Orme^a, Qingbin Liu^a, Robert Smith^a, Charles Huang^a, John Fischer^b, ^aUniversity of California at Irvine, ^bBoeing Commercial Airplane Group</i>	435
Design for Controlled Thermal Expansion Using Anisotropy in Parts Made from Liquid Crystal Stereolithography Resins <i>Richard P. Chartoff^a, Jill S. Ullett^b, John W. Schultz^b, ^aThe University of Dayton, ^bGeorgia Tech Research Institute</i>	443
Comparison of the Curing Process of Epoxy and Acrylate Resins for Stereolithography by Means of Experimental Investigations and FEM-Simulation <i>J. Eschl, T. Blumenstock, P. Eyerer, Institute for Polymer Testing and Polymer Science</i>	453
Rapid Pattern Based Powder Sintering with Room Temperature Polymer Infiltration <i>Zongyan He, Yong S. Kim, Monnappa Kokkengada, Jack G. Zhou, Drexel University</i>	461

Structural Analysis of Silicon Carbide Deposited by Gas-Phase Selective Area Laser Deposition (SALD)	
<i>S. Harrison, H. L. Marcus, The University of Connecticut at Storrs</i>	471
Effect of Hydrogen on Silicon Carbide Deposition from Tetramethylsilane—Raman Scattering Studies	
<i>Lianchao Sun, James E. Crocker, Leon L. Shaw, Harris L. Marcus, The University of Connecticut at Storrs</i>	479
Conceptual Design of a Smart Portable SFF System	
<i>Zbigniew M. Bzymek^a, Chandrasekhar Roychoudhuri^a, Leon L. Shaw^a, Wojciech Marks^b, ^aThe University of Connecticut at Storrs, ^bInstitute of Fundamental Technical Problems of the Polish Academy of Science</i>	487
Processing and Characterization of SALDVI Ceramic Structures	
<i>James E. Crocker, Lianchao Sun, Helene Ansquer, Leon L. Shaw, Harris L. Marcus, The University of Connecticut at Storrs</i>	495
Fabrication of Inorganic Material Models with Local Chemical Reaction Heat by Laser Sintering	
<i>Takayuki Kamitani, Osamu Yamada, Yoji Marutani, Osaka Sangyo University</i>	503
Electrically Stimulated Bilayer Hydrogels as Muscles	
<i>Paul Calvert, Zengshe Liu, University of Arizona</i>	511
 Process Development	
Intelligent Toolpath for Extrusion-based LM Process	
<i>Dan Qiu, Noshir A. Langrana, Stephen C. Danforth, Ahmad Safari, Mohsen Jafari, Rutgers—The State University of New Jersey</i>	519
Solid Freeform Fabrication Using the Wirefeed Process	
<i>M. L. Griffith, M. T. Ens, D. L. Greene, D. E. Reckaway, J. A. Romero, T. B. Crenshaw, L. D. Harwell, T. E. Buchheit, V. Tikare, Sandia National Laboratories</i>	529
A SFF Approach Utilizing Condensed Gas Precursors and Pulsed Laser Deposition	
<i>Erik Geiss, Harris L. Marcus, The University of Connecticut at Storrs</i>	537
The Laser Microchemical Lathe: Rapid Freeform Part Fabrication from the Vapor Phase	
<i>K. Williams, N. Jaikumar, G. Saiprasanna, M. Hegler, J. Maxwell, Louisiana Tech University</i>	543
Cooling Configurations for Rapid Tooling “A Comparison Study”	
<i>Vito Gervasi, Christopher J. Urban, Steven E. Gerritsma, Milwaukee School of Engineering</i>	553
A Vacuum Furnace Process for DTM’s RapidSteel 2.0 Material	
<i>Klas Boivie, Torsten Kjellberg, The Royal Institute of Technology</i>	563
MSOE TetraLattice™ “Applications and Simplified CAD Representation”	
<i>Vito R. Gervasi, Lisa M. Milkowski, James V. Canino, Rebecca J. Zick, Milwaukee School of Engineering</i>	571

Refrigerative Stereolithography for Support-Free and Accurate Fabrication <i>Akiya Kamimura, Tamotsu Murakami, Naomasa Nakajima, The University of Tokyo</i> -----	583
An Experimental and Analytical Study of Ice Part Fabrication with Rapid Freeze Prototyping <i>Wei Zhang, Ming C. Leu, Guanghua Sui, Zhiming Ji, New Jersey Institute of Technology</i> -----	591
Direct Thick Layer Rapid Prototyping from Medical Images <i>Pater B. Chamberlain, Charles L. Thomas, University of Utah</i> -----	599
Rapid Prototyping by Injection Molding <i>Shaun D. Compton, Charles L. Thomas, Vipul Lotke, University of Utah</i> -----	607
Rapid Tooling of Ceramic Parts and Molds Using High-Pressure Slip Casting of Si₃N₄ <i>Rolf Pfeifer^a, Liwu Wang^b, Peter Eyerer^a, ^aInstitute of Polymer Testing and Polymer Science, ^bMax-Planck-Institut für Metallforschung and INAM</i> -----	615
Rapid Tooling of AL₂O₃ Parts Using Temperature Induced Forming <i>Rolf Pfeifer^a, Liwu Wang^b, Peter Eyerer^a, ^aInstitute of Polymer Testing and Polymer Science, ^bMax-Planck-Institut für Metallforschung and INAM</i> -----	623
Fast Ink-Jet Based Process <i>I. Ederer^a, H. Seitz^a, A. Welisch^b, ^aFGB, ^bFORWISS</i> -----	631
Extrusion and Deposition of Semi-Solid Metals <i>Steffi Finke^a, William Wei^b, Frits Feenstra^a, ^aTNO Institute of Industrial Technology, ^bUniversity of Twente/W.E.I. Consulting</i> -----	639
Electrophotographic Powder Deposition for Freeform Fabrication <i>Ashok V. Kumar, Hongxin Zhang, University of Florida</i> -----	647
Direct Generation of Metal Parts and Tools by Selective Laser Powder Remelting (SLPR) <i>W. Meiners, C. Over, K. Wissenbach, R. Poprawe, Fraunhofer Institute for Laser Technology</i> -----	655
Design and Evaluation of a Novel Laser-Cutting Machine for Computer-Aided Manufacturing of Laminated Engineering Materials <i>Sangeun Choi, Wyatt S. Newman, Case Western Reserve University</i> -----	663
Fused Deposition Modeling in Microgravity <i>Robert Crockett^a, Dan Petersen^b, Ken Cooper^c, ^aMilwaukee School of Engineering, ^bNASA Johnson Space Center, ^cNASA George C. Marshall Space Flight Center</i> -----	671
Automated Loading and Unloading of FDM Systems <i>Øivind Brockmeier, Christopher Westcott, Jan Helge Bøhn, Virginia Tech</i> -----	679
Additive/Subtractive Material Processing for Mesoscopic Parts <i>Yih-Lin Cheng, Jurgen Stampfl, Rudolf Leitgeb, Fritz B. Prinz, Stanford University</i> -----	687
The Sand Painter: Two-Dimensional Powder Deposition <i>Joseph Pegna, Stéphane Pattofatto, Raphael Bergé, Carol Bangalan, Henry Herring, Mathias LeSaux, Jason Engler, Concordia University</i> -----	695

Accuracy Study on Laminated Object Manufacturing for the Metallic Functional Parts with Complex Surface <i>Yi Shuping^a, Tamotsu Murakami^b, Naomasa Nakajima^b, ^aChongqing University, ^bThe University of Tokyo</i> -----	711
Spin Casting as a Tool in Rapid Prototyping (Centrifugal Rubber Mould Casting) <i>L. J. Barnard, Technikon Free State</i> -----	719
Reducing Part Deformation by Inducing Phase Transformation <i>Gayle Link, Tonya Huntley, Alex Nickel, Rudolf Leitgeb, Tony Nguyen, Fritz Prinz, Stanford University</i> -----	727
Controlling Heat Input, Spatter and Weld Penetration in GMA Welding for Solid Freeform Fabrication <i>I. Kmecko, D. Hu, R. Kovacevic, Southern Methodist University</i> -----	735
Contour Crafting—State of Development <i>Behrokh Khoshnevis, University of Southern California</i> -----	743
 Applications	
The Maitreya Project: Large Scale Prototyping a Case Study <i>Alair Griffin^a, Charles Thomas^b, ^aJavelin, ^bUniversity of Utah</i> -----	751
Hard Metal Tooling via SFF of Ceramics and Powder Metallurgy <i>Mukesh Agarwala^a, Donald Klosterman^a, Nora Osborne^a, Allan Lightman^a, Robert Dzugan^b, Geoff Rhodes^c, Christian Nelson^d, ^aUniversity of Dayton Research Institute, ^bEMTEC, ^cCrucible Materials Corp., ^dDTM Corp.</i> -----	759
Applications of FFF in the Metal Casting Industry <i>Rui Jiang, Wanlong Wang, James G. Conley, Northwestern University</i> -----	767
Fabrication of Metal Components Using FDMet: Fused Deposition of Metals <i>Guohua Wu, Noshir A. Langrana, Sriram Rangarajan, Ryan McCuiston, Rajendra Sadanji, Stephen Danforth, Ahmad Safari, Rutgers—The State University of New Jersey</i> -----	775
Assessment of Environmental Performance of Rapid Prototyping and Rapid Tooling Processes <i>Yanchun Luo, Ming C. Leu, Zhiming Ji, New Jersey Institute of Technology</i> -----	783
3D Welding and Milling – A Direct Approach for Fabrication of Injection Molds – <i>Yong-Ak Song^a, Sehyung Park^a, Haeseong Jee^b, Doosun Choi^c, Bosung Shin^c, ^aKorea Institute of Science and Technology, ^bHong-Ik University, ^cKorea Institute of Machinery and Metals</i> -----	793
Rapid Tooling by Integrating Electroforming and Solid Freeform Fabrication Techniques <i>Bo Yang, Ming C. Leu, New Jersey Institute of Technology</i> -----	801
Rapid Tooling for Injection Molding of Rubbers <i>J. Eschl, T. Blumenstock, P. Eyerer, Institute for Polymer Testing and Polymer Science</i> -----	809

Investigation of Reinforced Ceramic Molds for Resin Patterns <i>Shirong He, Hiroyuki Yoshiura, Chiaki Mori, Oita Industrial Research Institute</i> -----	817
Direct Manufacture of Spatially Engineered Components for Aerospace Applications by Fused Deposition of Ceramics <i>Charles Gasdaska, Vikram R. Jamalabad, Daniel Dalfonzo, Thomas Paterson, Liang Xue, Lee Poandl, AlliedSignal Research & Technology</i> -----	825
Production Strategies for Production-Quality Parts for Aerospace Applications <i>J. D. Cawley^a, J. E. Best^a, Z. Liu^a, A. J. Eckel^b, B. D. Reed^b, D. S. Fox^b, R. Bhatt^b, ^aCase Western Reserve University, ^bNASA Glenn Research Center at Lewis Field</i> -----	833
Stereolithography Patterns for Investment Casting: Prototyping to Production <i>Curtis Wahlgren, Suresh Jayanthi, DSM Somos</i> -----	841
Manufacturing High Resolution Parts with Stereolithography Method <i>Carsten Tille^a, Ralf Deuke^b, Rico Eidam^c, ^aTechnische Universität München—Feingerätebau, ^bAlphaform GrmbH, ^cSiemens AG</i> -----	849
Application of Solid Freeform Fabrication Technology to NASA Exploration Missions <i>Kevin Watson^a, Dan Petersen^a, Robert Crockett^b, ^aNASA – Johnson Space Center, ^bMilwaukee School of Engineering</i> -----	857
Three-Dimensional Printing, 3DP™, of Electronic Ceramic Components <i>S. Uhland^a, R. Holman^a, B. DeBear^a, P. Saxton^a, M. Cima^a, E. Sachs^a, Y. Enokido^b, H. Tsuchiya^b, ^aMassachusetts Institute of Technology, ^bTDK U.S.A. Corporation</i> -----	865
Rapid Prototyping & Tooling in China <i>Yongnian Yan^a, Wanlong Wang^b, Renji Zhang^a, Lihua Lin^a, ^aTsinghua University, ^bNorthwestern University</i> -----	873
Rapid Prototyping as an Instructional and Recruitment Tool for Attracting Qualified High-School Students to Engineering as a Career Option <i>R. Umashankar^a, C. Choi^a, A. Ortega^a, R. Vaidyanathan^b, G. Artz^b, T. Anderson^b, A. Mulligan^b, ^aUniversity of Arizona, ^bAdvanced Ceramics Research, Inc.</i> -----	883
Author/Attendee List -----	889
Keyword Index -----	907

PREFACE

The Tenth Solid Freeform Fabrication (SFF) Symposium, held at The University of Texas in Austin on August 9-11, 1999, was attended by over 170 national and international researchers. Papers addressed SFF issues in computer software, machine design, materials synthesis and processing, and integrated manufacturing. New sessions on ceramic materials and multiple materials SFF were added to this year's program. The diverse domestic and foreign attendees included industrial users, SFF machine manufacturers, university researchers and representatives from the government. We are pleased once again with the strong showing of university students. The excitement generated at the Symposium reflects the participants' total involvement in SFF and the future technical health of this growing technology. The Symposium organizers look forward to its being a continuing forum for technical exchange among the expanding body of researchers involved in SFF.

The Symposium was again organized in a manner to allow the multi-disciplinary nature of the SFF research to be presented coherently, with various sessions emphasizing computer issues, machine topics, and the variety of materials aspects of SFF. We believe that documenting the changing state of SFF art as represented by these Proceedings will serve both the people presently involved in this fruitful technical area as well as new researchers and users entering the field.

The editors would like to extend a warm "Thank You" to Rosalie Foster for her detailed handling of the logistics of the meeting and the Proceedings, as well as her excellent performance as registrar and problem solver during the meeting. We would like to thank the Organizing Committee, the session chairmen, the attendees for their enthusiastic contributions, and the speakers both for their significant contribution to the meeting and for the relatively prompt delivery of the manuscripts comprising this volume. We look forward to the continued close cooperation of the SFF community in organizing the Symposium. We also want to thank the Office of Naval Research and the National Science Foundation for supporting this meeting financially. The meeting was co-organized by the University of Connecticut at Storrs, and the Mechanical Engineering Department, Laboratory for Freeform Fabrication and the Texas Materials Institute at The University of Texas at Austin.

The editors.

Organizing Committee

Joel Barlow	University of Texas at Austin
Joseph Beaman	University of Texas at Austin
David Bourell	University of Texas at Austin
Richard Crawford	University of Texas at Austin
Harris Marcus	University of Connecticut at Storrs

Advisory Committee

Clint Atwood	Sandia National Labs
Robert Brown	The Gillette Company
Richard Chartoff	University of Dayton
Michael Cima	Massachusetts Institute of Technology
Stephen Danforth	Rutgers-The State University of New Jersey
Steve Fishman	Office of Naval Research
Jim Maxwell	Louisiana Tech University
Kesh Narayanan	National Science Foundation
Thomas Pang	Ciba Specialty Chemicals Corporation
Fritz Prinz	Stanford University
Eli Sachs	Massachusetts Institute of Technology
Ralph Wachter	Office of Naval Research
Lee Weiss	Carnegie Mellon University

An Interactive Virtual System for Simulation and Optimization of Rapid Prototyping

S. H. Choi and S. Samavedam

Department of Industrial and Manufacturing Systems Engineering

The University of Hong Kong, Pokfulam Road, Hong Kong

shchoi@hkucc.hku.hk and srinivas@hkusua.hku.hk

Abstract

The paper describes the development of a computer system for simulation and optimization of rapid prototyping (RP) processes. The system provides a test-bed for virtual prototyping by integrating product design and RP with simulation and realistic visualization techniques. It enhances the dimensional accuracy and reduces the build-time of product prototypes. The virtually fabricated parts may be exported in VRML format over the Internet for effective communication between the manufacturer and the customer. The designer may use the system to *design-build-break* as many parts as required at a relatively low cost and in a short period of time. Therefore, virtual simulation of RP processes facilitates tuning of the control parameters according to the requirements, and hence reduces the number of physical prototypes needed to produce a part.

1.0 Introduction

Innovative products and shorter *time-to-market* cycles are essential for the success of every company. A typical product development cycle (concept->design->evaluation->redesign) consists of several sub-processes, such as prototyping, simulation and optimization. An important way to reduce the product development cycle time is to accelerate the prototyping processes. This is often achieved by using rapid prototyping (RP) techniques. A typical RP process, as shown in Fig. 1, includes pre-processing, physical processing and post processing stages. The pre-processing stage involves creation of 3D CAD models and process planning. The process planning stage generates appropriate laser path signals based on the control parameters specified by the designer. The physical processing stage drives the laser to build the part in layers. The method of achieving this differs amongst various processes. The post-processing comprises a few operations, which include removal of support structure, and curing and cleaning and of the part, as needed for the RP process.

The process planning stage is almost identical to all the RP processes. However, it significantly influences the quality of the part, which can be measured by the accuracy, build-time, efficiency and strength. It involves part orientation, slicing of the CAD model and laser path generation. For liquid-based processes, support structures are required. All these steps affect the part quality. The orientation of an RP part affects its accuracy, build-time and strength. For example, orienting the part with minimum z-height possible will result in fewer slices, and hence a reduction in build-time. Layer thickness affects the accuracy and build-time. The accuracy may be improved when the part is built with a smaller thickness, but the build-time will increase inversely. Hatch spacing refers to the distance between the laser paths. It affects the build-time and strength. Typically, the user has to determine these process planning parameters. Thus the quality of the part depends on the users' experiences, which are often inconsistent. To overcome this problem, several semi- or fully automatic algorithms have been proposed to optimise the process planning to enhance part quality [1-4]. However, most of these methods choose only a single criterion as the objective function, while other

criteria are treated as constraints or ignored altogether. Also these methods do not reconstruct the part for verification before manufacture. A system that provides a convenient means for the designer to tune the control parameters and to visualise the desired part before manufacture will reduce the prototype development time. Virtual reality (VR) addresses this need. It mainly consists of a suite of 3D graphics and real-time simulation software that allow the user to interact with a computer-generated environment. Simulating an RP process in VR may result in accurate determination of the control parameters. The simulated part can be quickly regenerated and easily modified and transported over the Internet. This may reduce the need for physical prototypes to a larger extent.

An integrated virtual system for optimisation of pre-processing parameters is now being developed. Fig. 2 illustrates the main modules of the system. It includes the model generator, the model viewer, and the virtual simulator. The model generator accepts the digitised data of the part and processes it to generate a tessellated CAD model. The model viewer accepts the model created either by the model generator or a CAD model in STL format. It allows the designer to visualise the part in virtual environment and to interact with it. The virtual simulator module orientates the part based on the user-defined criteria and simulates the RP process. This module quantifies the accuracy, build-time and efficiency. It also facilitates visualisation of the desired part before physical fabrication is committed. The integrated virtual system enables the user to design a part in STL format or digitised data. These CAD models can also be used to simulate the RP process to optimise the control parameters. Subsequently, the system helps materialise the final part in digital format for analysis and effective communication. The system was developed on Window NT, WorldToolKit (WTK) and Visual C++, with interfaces with AutoCAD and Solidworks. A semi-immersive virtual reality system with shutter glasses and a 21" monitor are used. The shutter glasses are used to obtain stereoscopic visual effect.

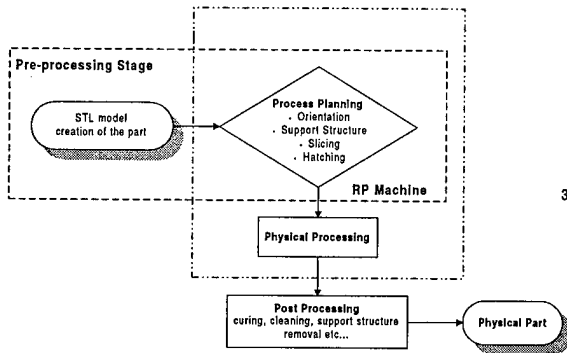


Fig. 1 Rapid Prototyping Process

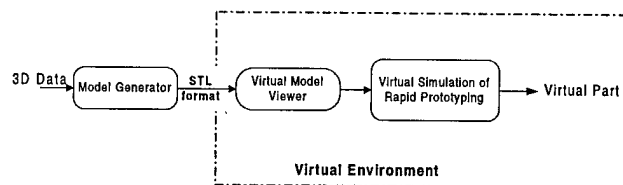


Fig. 2 The Modules of the Virtual System

2.0 Model Generator

This module generates a 3D CAD model from digitised data [5]. It involves digitising the surface data of a part by using a mechanical or laser scanner. The surface data are filtered to eliminate redundant points. The algorithm employed calculates the change of the slopes between successive points and compares it with the user-specified tolerance. If the change of slope falls within the tolerance, the corresponding point is eliminated. Employing this approach, the regions with high curvature are approximated with a large number of points, while flat surfaces with fewer points. The filtered points are considered as control points of

spline curves, which are created both longitudinally and transversely to reconstruct the surface of the part. The designer can also alter the control points to manipulate the geometry locally. These surfaces are approximated with a given tolerance to generate a CAD model in STL format. The model generator can also generate male and female cavities of the part for rapid tooling purposes.

3.0 Model Viewer

This module reads in a product model in STL format, such as the dolphin in Fig. 3, and displays it in the virtual environment. The main element of VR is its stereoscopic presentation, which generates a compelling illusion of the product. The stereo-viewing ability allows the designer to gain '*being there*' feeling. This creates an impression to the designer that he or she is acting upon a real object. The model viewer thus provides a real-time tool for the designer to explore and enhance the features of the part. The ability to view a model from different perspectives helps the designer analyse it by inspecting both the external geometry and the interior structure. For complex prototypes, it may be necessary to analyse the interior of the part for layout, visibility, and accessibility etc. The designer can view and analyse with a realistic feeling the interior of the virtual prototype. Furthermore, the aesthetic evaluation of a product can be performed in VR by mapping a combination of texture and colours to it. Lighting and illumination effects may also be created for better assessment of the part. Thus virtual parts not only represent the geometry but also material properties like colour, texture and reflectivity, which are not completely supported by CAD systems. Indeed, visualisation of STL models in VR interactively may help the designer check its validity [6].

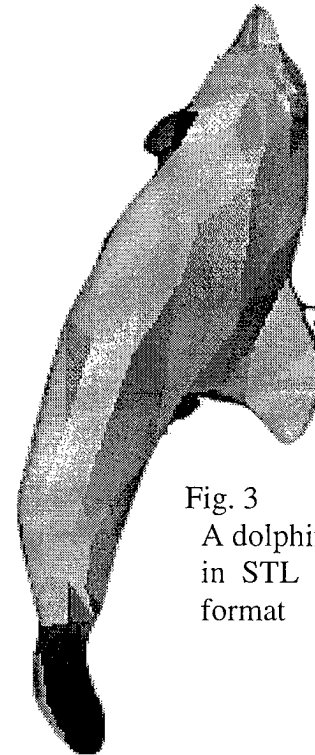


Fig. 3
A dolphin
in STL
format

The module allows the designer to interact naturally with the virtual part with 3D mouse. The designer can view it in stereo, rendered or wireframe mode and navigate around and into the part. Visualisation of the CAD models in a realistic display enhances the designer's imagination upon viewing and manipulation, which facilitates refining the design.

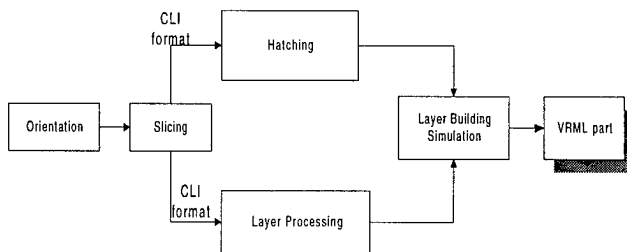


Fig. 4 The flow of Virtual Simulation

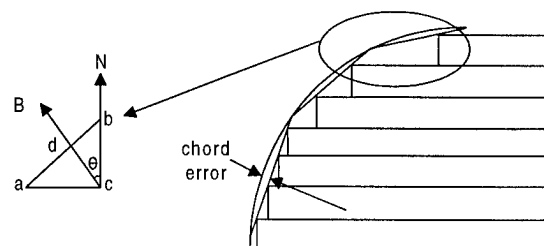


Fig. 5 The stair-step effect of layer thickness

4.0 Virtual Simulation

This module simulates the rapid prototyping process. Fig. 4 illustrates its sub-modules and the detailed structure can be found in [7]. The orientation module determines the optimal orientation. The slicing module employs uniform slicing to slice a part. The layer processing module process the slice data to generate layers, while the hatching module determines the laser paths. The layer building simulation module generates the part. It also calculates the build-time, efficiency and accuracy of the part for a given orientation. The methods used to determine these criteria are discussed below.

Accuracy

Accuracy can be defined as the geometric deviation of the part from the progenitor CAD model. In process planning stage, the loss of accuracy is mainly due to the generation of layers by extrusion of planar contours. This results in stepped approximation of the boundary of the original CAD model. Consequently, all the parts generated by layer manufacturing technique exhibit "stair-step" effect, as shown in Fig. 5. This effect is more significant on slanted and curved surfaces. This error can be quantified by cusp height, which is the distance between the intended and approximated surface at each facet. For each facet, the surface normal indicates the angle that the facet makes with the build direction. If the surface normal is not perpendicular to the build direction, the facet will exhibit some stair-step effect. For a given facet, with a, b, c as vertices in Fig. 5 and the notations at the end of the paper, the error can be evaluated as follows:

$$\text{Cusp height } (h_c) = bc \cos\theta \quad (1)$$

$$\text{Maximum cusp height (MCH)} = \max (h_c) \quad (2)$$

$$\text{Average cusp height (ACH)} = \frac{\sum_{i=1}^{N_f} h_{c,i}}{N_f} \quad (3)$$

The average cusp height represents the mean of the linear deviation of the facets, while the maximum cusp height is the maximum linear deviation among the facets. The cusp height estimation predicts the linear deviation of the surface on geometry. Hence in the present approach, cusp height for measuring the dimensional error is adopted.

Build-Time

Build-time can be defined as the time required to build the part physically. The system aims at developing a generic build-time estimator for RP processes using optical laser heads. It evaluates the time as a function of laser velocity, scan distance and layer thickness. The velocity for SLA can be obtained from literature [8]. For SLS the laser velocity derived from [9] is shown in Eq. 4.

$$\text{Velocity (V)} = \frac{P \times (1 - R)}{\rho \times d_b \times \ell_m \times [C_p (T_m - T_b) + k L_h]} \quad (4)$$

The build-time of a part can be obtained by summing up the time taken for each layer, as shown in Eq. 8, which is derived from Eq. 5. The time taken for a layer can be divided into the scan time and the set-up time. The set-up time can be obtained from the machine manual and it is normally constant for all layers. The time required for scanning a layer varies along the z-axis and can be obtained as a ratio of the scan distance to the scan velocity from Eq. 6.

The total scan distance within a layer can be obtained from the hatch file. The velocity can be estimated based on the process. For example, it can be estimated from Eq. 4 for SLS process. The elements in the set-up time for the SLS process are given in Eq. 7.

$$\text{Build-time of a part} = \sum_{i=1}^{N_\ell} T_{\ell i} + (T_s \times N_\ell) \quad (5)$$

$$\text{Scan time } (T_\ell) = \frac{L_d}{L_v} \quad (6)$$

$$\text{Setup time } (T_s) = t_{pd} + t_m + t_r + t_{pr} + t_d \quad (7)$$

$$\text{Therefore, Build-time of the part} = \frac{h}{\ell_m} T_s + \frac{\sum_{i=1}^{N_\ell} \left(d_{si} \times \frac{\ell}{\ell_m} \right)}{\ell_v} \quad (8)$$

The scanning pattern differs from process to process. The laser scans the layer in horizontal and vertical directions. A hatching algorithm was developed to evaluate the total scan distance of each layer. The laser velocities can be obtained from the power equation of the process involved. The power equation of the RP includes process parameters, such as the laser beam diameter, the slice height for SLS, and the overcure depth for SLA. The present approach allows the user to evaluate build-times for different process parameters. The algorithm developed is mainly targeted at SLS machine, though it may be subsequently modified for other processes. For standard DTM materials, it estimates build-time with approximately 93% accuracy.

Efficiency

Efficiency can be measured by in terms of material utilisation. It can be obtained as a ratio of volume of the parts with the total volume of the workspace. However, in most cases the parts may not be completely filling the build chamber and may contain only a limited part. Hence, the volume of workspace that a part uses is different when compared to the total volume of the workspace. The volume occupied by a part can be obtained as the product of the height of material deposition and the surface area of the work platform. The maximum material height may vary with parts orientation. For example, the volume occupied by a rectangular box when oriented at 45° is more than when it is oriented at 90° or 0° to its base. Thus the volume occupied by a part can be approximated with its bounding box for a given orientation. Even if the parts are packed in the workspace, the packing algorithms usually pack them by building bounding box around each part. The enclosing bounding box to the volume of the workspace in use indicate the maximum material utilised for a given orientation of the part. The relative efficiency is given in Eq. 9.

$$\text{Efficiency } (\eta) = \frac{\sum_{i=1}^{N_p} V_{pi}}{h_m \times A_w} \quad (9)$$

4.1 Orientation

This module orients the STL model in the build direction. The optimal build orientation is determined based on the minimum build-time or the maximum accuracy criterion. For the minimum build-time criterion, the part is enclosed in a bounding box and oriented such that it has the minimum z-height in the build-direction. This reduces the number of layers required and hence the build-time. The build-time is estimated from Eq. 8.

For the accuracy criterion, the part is rotated about the x- and y- axes within a given range at specific intervals. The rotation of the part about the z-axis will not change the angle between the facet normal and the build-direction. For each rotation, the average cusp and the maximum cusp heights are estimated. If the maximum cusp height exceeds the given value, that orientation is not considered. The orientation that gives the minimum average of these values is the preferred orientation of the part for the maximum accuracy criterion. For each rotation the build-time and the relative efficiency indicating the material utilisation are also estimated. From these data the designer may fine tune and subsequently select the preferred set of process parameters.

4.2 Slicing and Layer Processing

Once the part is oriented it has to be sliced. A uniform slicing algorithm is employed to slice the CAD model. All the slice contours have to be processed for displaying the layer in the virtual system and for hatching to generate for build-time estimations. The layer processing module processes the layer data for display purposes. It determines the contour hierarchy within a layer, i.e., to place all the contours within a layer in a tree structure. The contour that surrounds a set of contours is considered as the parent contour. For faster display and rendering purposes, all the contours in a parent contour are joined with imaginary lines to form a closed contour. After arranging the contours, each parent contour is extruded to form a certain portion of a layer or a layer itself. Each parent contour is treated as a child node within the layer node.

4.3 Virtual Simulation

This module simulates the building process of layers in the system. The designer can interactively view the building of a single layer or multiple layers. Once the simulation is completed, the designer can rotate the part to view it or to map surface texture to visualise the physical part that the RP machine will subsequently deliver. Visualisation, in general, is a method of extracting meaningful information from complex data sets through the use of interactive graphics and imaging. It facilitates navigating through the unseen. For example, navigation around a virtually fabricated mould cavity of the logo of the University of Hong Kong in Fig. 6 allows the designer to explore the interior of the mould for design improvements. It also provides mechanisms that facilitate exploring the internal and opaque structures of the part.

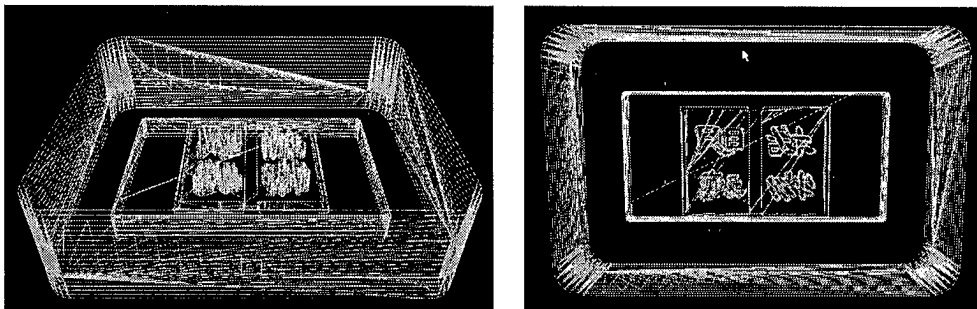


Fig. 6: A set of mould cavities for the University logo

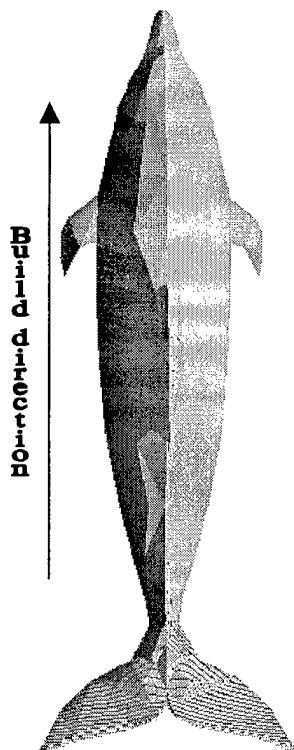


Fig.7A Preferred orientation for maximum accuracy criterion

The system evaluates the accuracy, build-time and relative efficiency based on Eqs. 3, 8, and 9 respectively. Fig. 7 illustrates a virtually fabricated dolphin. It is fabricated using fine nylon on SLS 2000 with a layer thickness and hatch spacing of 0.1mm. The preferred orientation for maximum accuracy is shown Fig. 7A. The maximum cusp height (MCH) and the average cusp height (ACH) were .099mm and .032mm respectively. The ACH for minimum build-time orientation was 0.045mm, which was higher than the ACH of maximum accuracy orientation due to the angle between the facets' normal with the build-direction. The minimum build-time was 2.1 hours with the orientation shown in Fig. 7B. This is because of the minimum z-height and hence the minimum number of layers. The build-time for maximum accuracy criterion is 3.9 hours, since the number of layers required were 534, whereas there were only 184 for minimum build-time criterion. The actual laser-scan times for both cases were the same. However, the variations in the build-times were mainly due to the time required for the machine to prepare for the extra number of layers.

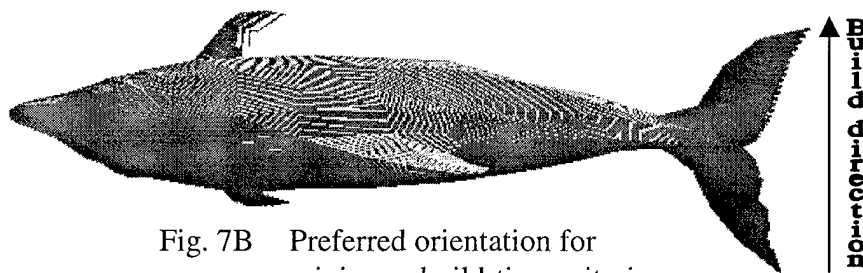


Fig. 7B Preferred orientation for minimum build-time criterion

If the cusp height of a facet is higher than the tolerance level, that layer is marked with a different colour. Visual presentation of the part along with the numerical values of the accuracy gives the designer a better illustration of the stair-step effect. Efforts are also underway to superimpose the actual STL model on the fabricated one. The actual translucent model of the part is superimposed on the virtually fabricated one. This enables the designer to realise the difference between the intended model and the virtually fabricated part. The designer can parametrically modify the virtual part to match the intended model, and thus make qualitative judgement about the product by manipulating the virtual part and viewing its geometric changes. If the RP part is an assembled or a merged part, visualisation facilitates analyse of its fitting. The system can export the virtually fabricated part in VRML format for effective communication between designers at various locations. Thus, virtually fabricating the part helps avoid manufacturing bottlenecks and facilitates tuning the control parameters for physical fabrication. This reduces the manufacturing costs and the development time involved. The responsiveness to customer demands is therefore significantly enhanced.

5.0 Conclusions

A virtual environment for faster prototype development has been developed. It allows the designer to design a part either with STL or digitised data. It facilitates optimisation of the rapid prototyping process parameters. The mathematical models developed predict the

accuracy, build-time and efficiency of a part for a given orientation. It allows the designer to visualise the desired part in a virtual environment before committing to manufacture. Work is now underway to develop a layer format that can incorporate colour information along with the laser path data to facilitate fabrication of multi-coloured parts.

Acknowledgement:

The authors would like to thank the Research Grant Council of the Hong Kong Government and the CRCG of the University of Hong Kong for their financial support for this project. Thanks are also due to Dr. I. Gibson and his colleagues for their help in conducting the experiments on the SLS machine.

References:

1. David C Thomson and Richard H. Cawford, "Computational Quality Measures for Evaluation of Part Orientation in FreeForm Fabrication", *Journal of Manufacturing Systems*, 1997, Vol. 16, No. 4, pp. 273-289.
2. F. Xu, H. T. Loh, Y.S. Wong, "Considerations and selection of optimal orientation for different rapid prototyping systems", *Rapid Prototyping Journal*, Vol. 5, No. 2, 1999 pp. 54-60.
3. Anne L. Marsan, Seth Allen, Prashant Kulkarni, Deba Dutta, "An Integrated Software System for Process Planning for Layered Manufacturing", *Solid Freeform Fabrication*, pp. 661-669, 1997.
4. Frank, Dietmer, and Fadel Georges, "Expert System-based Selection of the Preferred Direction of Build for Rapid Prototyping Processes", *Journal of Intelligent Manufacturing*, Vol. 6, No. 5, pp. 339-345, 1995.
5. SurfCAD, Internal Report, IMSE Dept., The University of Hong Kong.
6. Stephanie M. Morvan and Georges M. Fadel, "IVCES, Interactively Correcting .STL Files in a Virtual Environment", *Proceedings of The 1996 ASME Design Engineering Technical Conference*, Aug, 1996.
7. S. H. Choi and S. Samavedam, "A Virtual System for Rapid Prototyping", *Proceedings of the First Conference on Rapid Prototyping and Manufacturing'98*, Beijing, pp. 475- 481, 1998.
8. Pual F. Jacobs, "Stereolithography and other RP&M technologies : from rapid prototyping to rapid tooling", SME, 1996.
9. Steen, W. M., "Laser material processing", Springer, 1998.

Notations:

P	power (W);	η	relative efficiency;
h_c	cuspl height (mm);	A_w	surface area of workspace (mm^2);
N_f	total number of facets;	V_p	enclosing box volume of a part (mm^3);
N_p	total number of parts;	t_{pd}	time required to move the platform down (s);
N_ℓ	total number of layers;	t_m	time required for material deposition (s);
T_ℓ	scan time of a layer (s);	t_r	roller movement time (s);
T_s	setup time of a layer (s);	t_{pr}	time required for the platform to rise (s);
ℓ	layer thickness (mm);	t_d	time delay between these operations (s);
ℓ_m	machine layer thickness (mm);	ρ	material density (g mm^{-3});
h	total height of the part (mm);	d_b	laser beam diameter (mm);
d_s	scan distance of a layer (mm);	C_p	specific heat ($\text{J g}^{-1}\text{K}^{-1}$);
L_d	laser scan distance (mm);	T_m	melting temperature (K);
L_v	laser scan velocity (mm s^{-1});	T_b	bed temperature (K);
ACH	Average Cuspl Height;	k	sinter factor;
MCH	Maximum Cuspl Height;	L_h	latent heat (J g^{-1});
B	build direction;	R	reflectivity of the mirror;
		h_m	maximum material height (mm);

A Knowledge-based Decision Support System for RP&M Process Selection

F. Xu, Y.S. Wong and H.T. Loh
Department of Mechanical & Production Engineering,
National University of Singapore
10 Kent Ridge Crescent, Singapore 119260

Abstract

Due to the large variety of RP&M material/machines and the strengths/weaknesses associated with different RP&M processes, the decision to select a suitable RP&M system becomes increasingly difficult. This paper presents a knowledge-based approach for the selection of suitable RP&M material/machine to meet specific requirements of RP&M applications. The system receives input data on the CAD model and the user's specifications, and generates outputs that provide the most appropriate combination of RP&M material/machine. Optimal orientations, together with estimated manufacturing time and cost, are considered and given in the final outcome to help the user make the choice.

1. Introduction

In the past decade, the world has seen a rapid growth of RP&M technology: new RP&M processes have been initiated; dimensional accuracy and material properties of RP&M parts have improved; application fields of RP&M parts are expanding. At present there are more than 30 kinds of RP&M machines available in the market. Most of the commercialized RP&M machines can handle more than one kind of materials, with some having four or five choices. For each set of RP&M material and machine, there exists optimal process parameter settings, or optional building styles, for part fabrication. The large variety of RP&M material/machines plus the individual strength/weaknesses with the different RP&M processes make the selection of suitable RP&M system a difficult task (Loh *et al* 1998). Meanwhile, as a group of rapid prototyping facilities, RP&M machines play the role of a bridge between computer-aided design and manufacturing activities. A software tool that enables designers or engineers to select the right RP&M material, machine and optimal orientation for a given RP&M application would thus be essential and useful, helping to shorten the time between design and manufacturing activities further.

The difficulties on the task of selecting suitable RP&M machine for a specific part fabrication have been noticed by other researchers (Grimm 1996, Campbell and Bernie 1996, Phillipson and Henderson, 1997, BIBA WWW, 1998). Grimm outlines a number of guidelines on the choosing between SLS and SLA for a specific part fabrication. Campbell and Bernie proposed the setting up of RP&M machine databases in term of machine capabilities in constructing different types of form features. The evaluations of manufacturing time/cost with a certain RP&M system for a given CAD model are not addressed in the paper. The Phillipson paper describes their RP Advisor that helps the user select RP&M machine. The selection of material was not considered in the software. A software tool called Rapid Prototyping System Selector has been found on the web (BIBA WWW, 1998). Developed on a RDBMS, the RP System Selector find the suitable rapid prototyping system by calculating the degree of fulfilment of each system with respect to the vector of user's requirement. The influence of part

geometry on the building quality was not considered. In this paper, we present a knowledge-based approach in the selection of RP&M process.

2. Knowledge-based RP&M Process Selector

2.1 Information Requirements of RP&M Material/Machine Selector

The selection of RP&M material/machine is a high-level decision-making process, requiring extensive knowledge and expertise on RP&M processes. Factors considered usually include manufacturing time, manufacturing cost, the part geometry, the RP&M material properties, the process capabilities and the user requirements on material properties, surface finish, functional purpose, etc. Basically, the process-related information can be categorized into following fields:

- 1) RP&M material data, including the mechanical, thermal and chemical properties of the material, the cost of material, the physical appearance, etc.;
- 2) RP&M machine data, including the feasible materials, the building style, the controllable process parameters, the machine capabilities, etc.;
- 3) RP&M application data, supplying typical application-related requirements on material property, tolerance, surface finish, etc.;
- 4) Geometric data, providing information such as the part envelope, the part volume, the smallest linear dimensions, the types of form features, etc.;
- 5) Model specification, including application purpose, dimensional tolerance, general surface finish, material properties, etc.

These five fields define the five highest-level clusters of information needed in RP&M process selection. The information achievable can be in the form of facts, experimental data, or numerical models. Based on the information, process-related decisions can be made for the fabrication of the RP&M part, as illustrated in Figure 1.

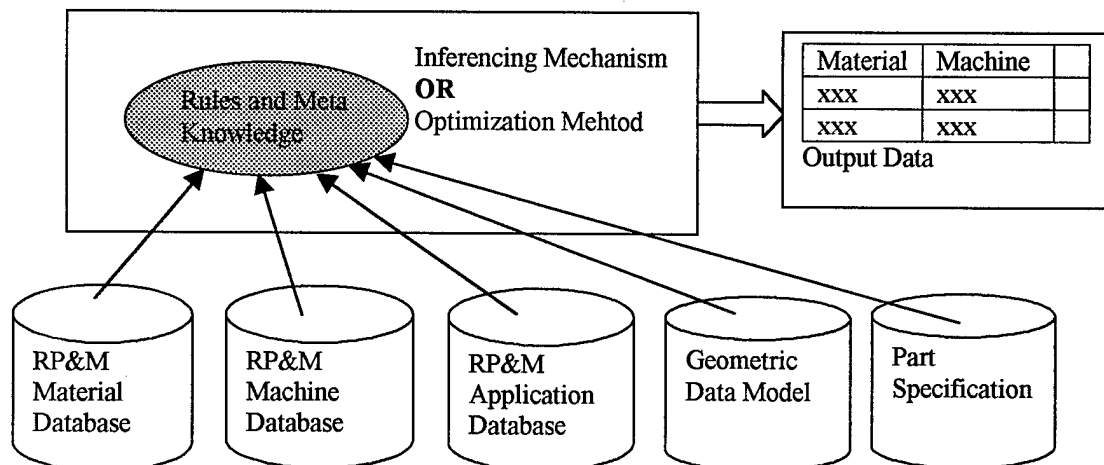


Figure 1 Information Requirements in RP&M Material/Machine Selector

2.2 Feasibility of Knowledge-based RP&M Process Selector

The selection of RP&M material/machine involves large amount of information. Also, to make decisions properly, the prototype requirements or the part specification must be first

refined into low-level goals. Since different objectives required of an RP&M part/prototype may be conflicting when detailed into low-level tasks, meta-knowledge is needed to control the decision flow in the execution of tasks. The interdependent relationships among the manufacturing quality, the manufacturing time/cost and the part geometry, plus the non-procedural characteristic of the selection process suggest the suitability of employing knowledge-based approach in the system. The separation of knowledge from the inference mechanism allows the process-related knowledge to be easily modified and supplemented.

3. Object-oriented Data Organization

As a design approach, object-oriented design encompasses the process of object decomposition and depicts a complex system from the perspectives of classes, attributes and methods (Booch, 1991, Cattell, 1991, Yourdon and Argila, 1996). In the domain of RP&M, a common nature of RP&M machines is using additive methods to construct 3-dimensional solid objects. The hierarchy and similarities among RP&M machines as well as the reoccurrence of application cases, show the feasibility of an object-oriented design in the system.

3.1 RP&M Material Database

The compilation of a comprehensive RP&M material database is useful for the management of the variety in the material domain. In the family of RP&M material, a number of abstractions are defined to facilitate the management and selection of RP&M material. As illustrated in Figure 2, the highest level of abstraction is named as *RP&M material*, which is further inherited by four child abstractions, namely *Ceramic-based*, *Plastic-based*, *Metal-based* and *Fibre-based*. Each specific RP&M material in the material database is declared as an instance of certain class. The class attributes and member functions are shown in Figure 3.

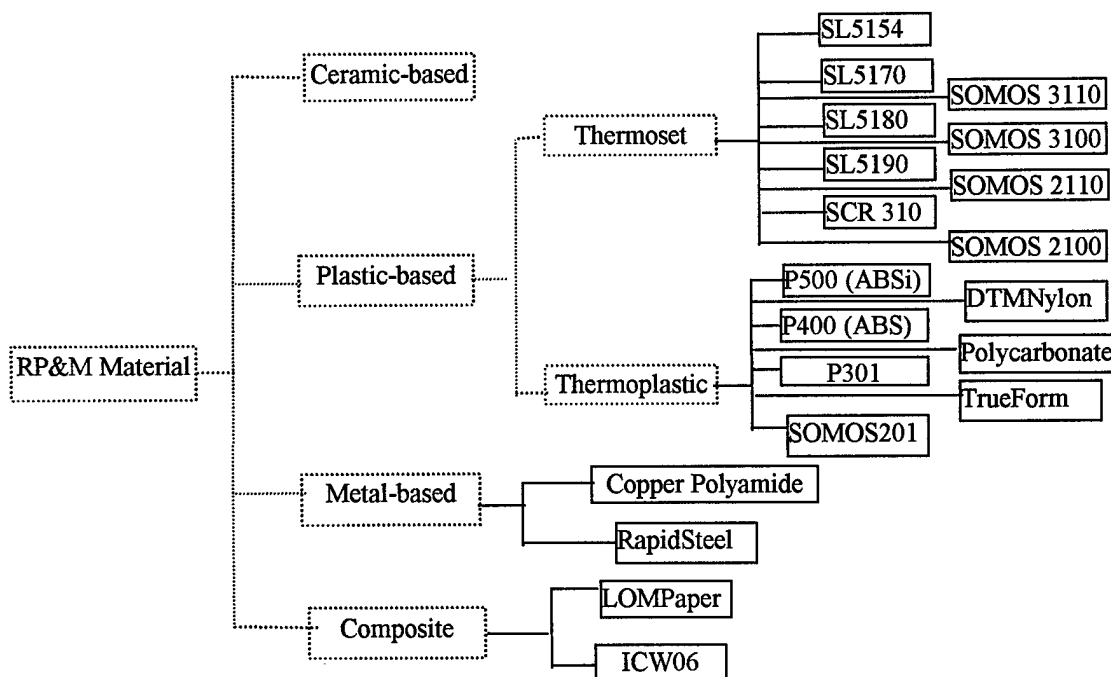


Figure 2 Hierarchy and Abstractions in the Field of RP&M Material

3.3 RP&M Machine Database

The RP&M machine database should give information on the underlying process, the process characteristics, machine parameters, material types feasible on the machine, part building styles and machine capabilities on dimensional accuracy, surface finish, etc. Object-oriented technique is used to organise facts and knowledge inherent to RP&M machines. The hierarchy in the domain of RP&M machine is shown in Figure 3, where the rectangle in dotted line indicates an abstraction while the rectangles in solid line indicate objects, or specific RP&M machines.

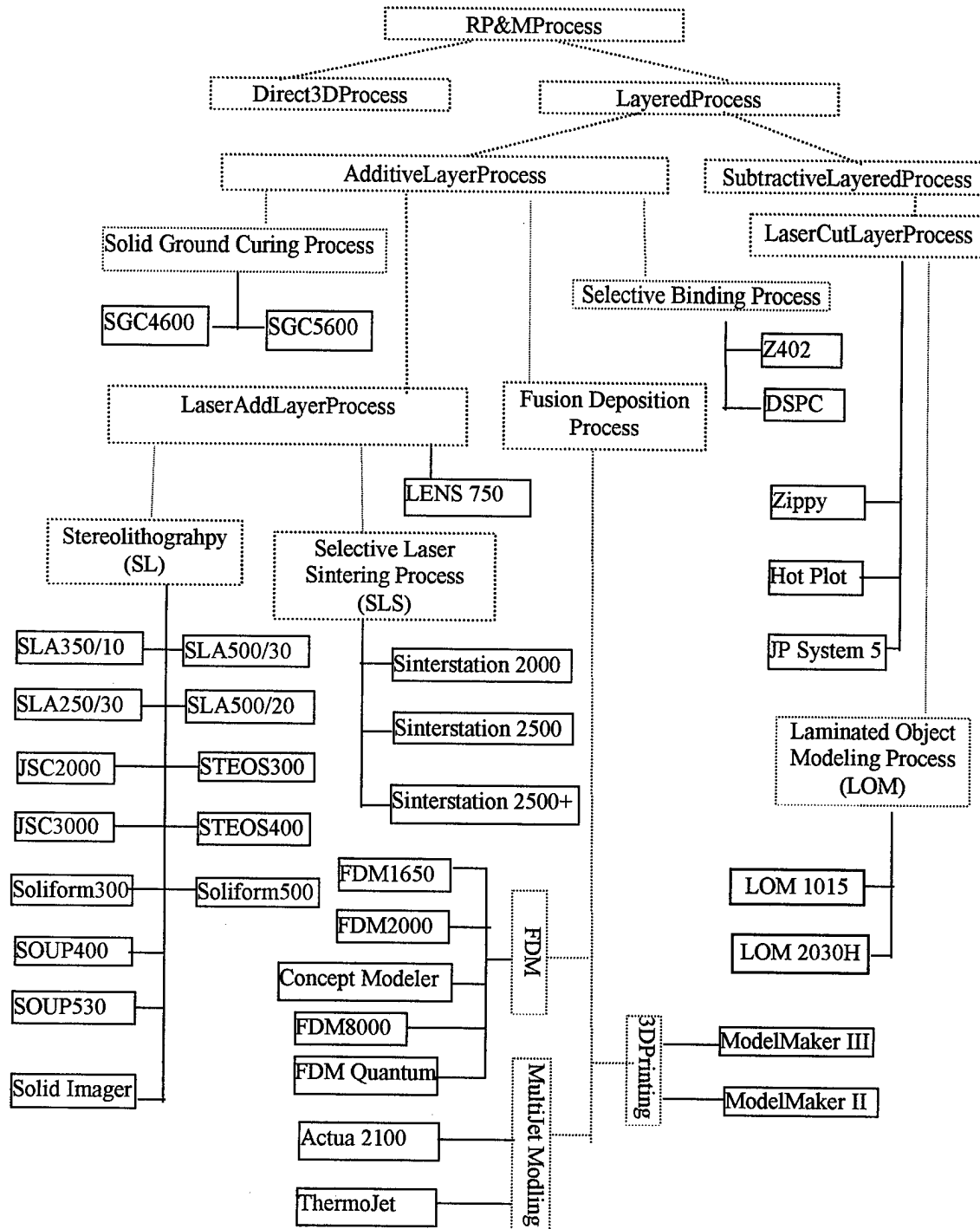


Figure 3 Hierarchy and Abstractions in the Family of RP&M Machines

3.4 RP&M Application Database

The construction of RP&M application database can help users trace the previous RP&M applications and reduce the user's efforts on the definition of part specification. The application of RP&M parts can be classified into three categories: visualization prototype, functional part/prototype and manufacturing tool. For each category applications, the range of the general requirements on the geometric quality, mechanical property or thermal property may be defined. *RP&M Application* is created as the highest-level abstraction in the application domain. Under the base class, three abstractions, namely *VisuModel*, *FunctionPart* and *ManuTool*, are defined to represent the aforementioned three categories of RP&M applications. In the category of *ManuTool*, different applications can be defined based on the follow-up manufacturing processes when a process chain is involved in the tooling process.

3.5 Part Definition

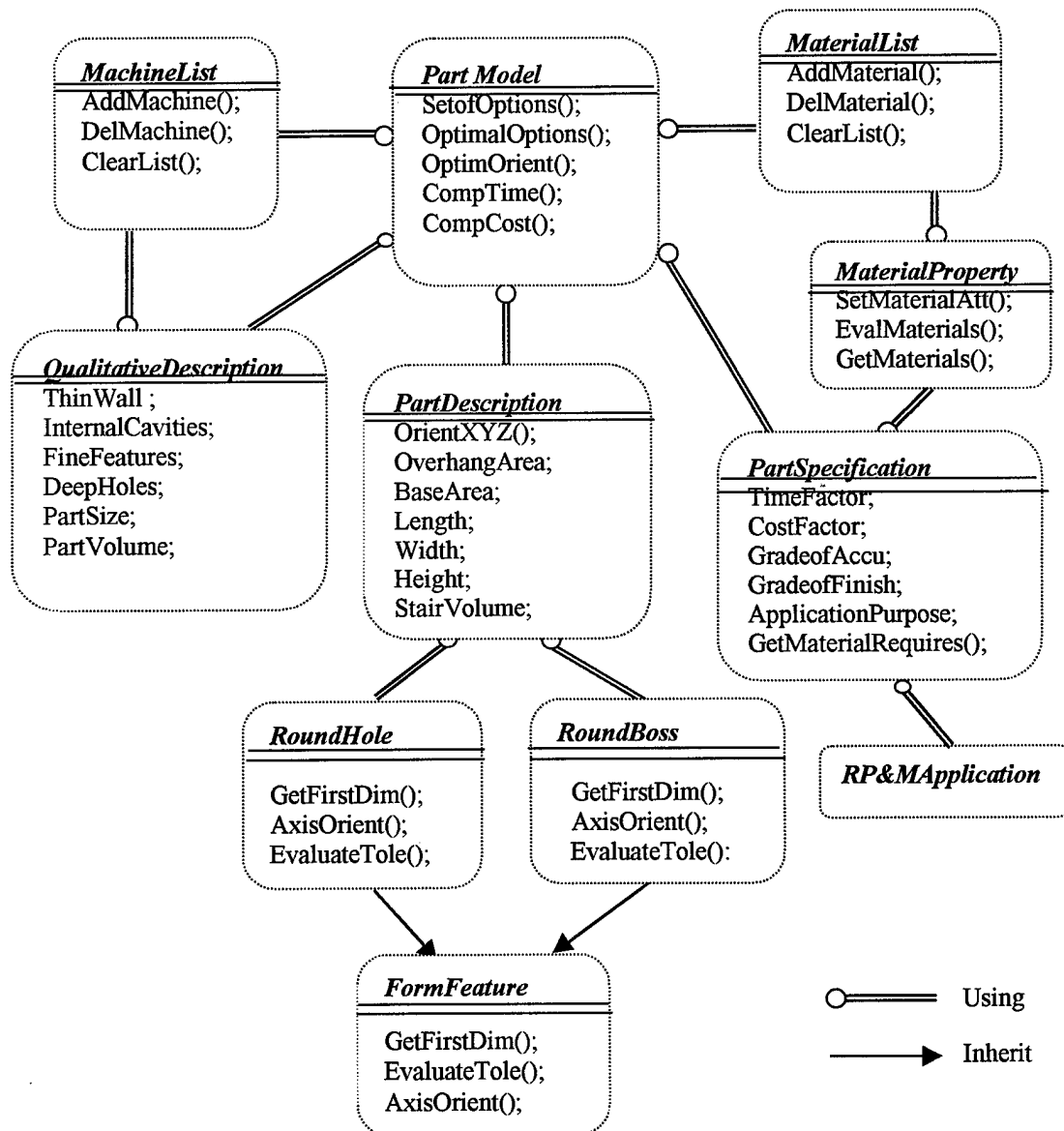


Figure 4 Object-oriented Representation of the Product Model

Development of an object-oriented representation for the product model is an important task in the research. To satisfy the information requirements in the knowledge-based RP&M process selector, the part definition should include both geometric characteristics of the CAD model and the non-geometric aspects. A high-level abstraction called *Part Model* is defined to capture each specific CAD model. The *Part Model* has five internal objects, i.e. *Part Specification*, *Part Description*, *Qualitative Description*, *Machine List*, *Material List*, and has using relationship with objects such as *RP&M Process*, *RP&M Material* and *RP&M Application*, etc. as shown in the diagram in Figure 4. The abstraction of *Part Specification* encapsulates information on material requirements, dimension tolerance, surface finish, application purpose, while the *Part Description* gives information on the geometric attributes of the CAD model in a specific orientation. The abstraction of *Qualitative Description*, on the other hand, encapsulates the general qualitative description of the part shape given by the user.

4 Knowledge-based RP&M Material/Machine Selection

Besides facts and procedural knowledge, empirical knowledge also play important roles in the selection of RP&M material and machine. The factual knowledge related to the selection of RP&M material/machine are stored in the database. The procedural and empirical knowledge, on the other hand, are expressed as method functions or organised into rule sets according to the tasks and the object they work on.

4.1 Knowledge Acquisition and Representation

The selection of RP&M material/machine for a specific part fabrication relies on both numerical evaluation and expertise-based guidelines. The evaluation relates to the examination of material property, the building envelope, the building accuracy of critical features, etc. The guidelines refer to the high-level heuristic knowledge and the controls required in the selection of RP&M process. To acquire knowledge, experiments and interview with experts have been carried on. Mathematical models on computing manufacturing time and cost in RP&M part fabrication are also established.

Evaluations and expertise-based guidelines are expressed in the format of production rules and invoked from the methods of corresponding objects in the system. According to the functionality, the production rules are organised into three rule sets, named as *Material Evaluations*, *Process Guidelines*, and *Machine Evaluations*, respectively. The rule set of *Material Evaluations* includes rules related to the task of material selection or material property evaluation. Rules that summarise experts' experience and reflect the limitations of generic RP&M processes are collected in the rule set of *Process Guidelines*. Rule_1 and Rule_2 are two examples in the rule set of *Material Evaluations*.

```

Rules1a in Material Evaluations {
If:
?application = PartSpecification.ApplicationPurpose; /*get the application purpose */
?user_hardness = PartSpecification.Hardness;
?user_hardness == NULL; /* the user don't specify the requirement on hardness */
Then:
MaterialProperty.Hardness=?application.Hardness; /* the hardness requirement in the
application database is retrieved */
}

```

```

Rule1b in MaterialEvaluations {
If:   ?hardness=MaterialProperty.Hardness; /* Obtain the attribute value */
      ?hardness!=NULL; /*
      PartModel.MaterialList != ` ( ); /*there are material candidates available */
Then: for ?material inlist PartModel.MaterialList /* Check material one by one */
{     if ?material.Hardness< part_hardness;
      then PartModel.MaterialList -= ?material;
      }/* Material whose hardness is lower than that required is removed */
}

```

In the rule set of *Machine Evaluations*, the resolution of the RP&M building system, the dimensional accuracy of critical features and the building envelope of the part are examined. RP&M machines that satisfy both the accuracy requirement of the critical form features and the physical requirements of the fabricating part are found out and chose as the suitable machines.

4.2 Framework of Object-oriented Knowledge-based RP&M Process Selection

The object-oriented knowledge-based RP&M material/machine selector is designed to work with a 3D CAD system. The interface and the working mechanism of the object-oriented knowledge-based RP&M material/machine selector is illustrated in Figure 9.

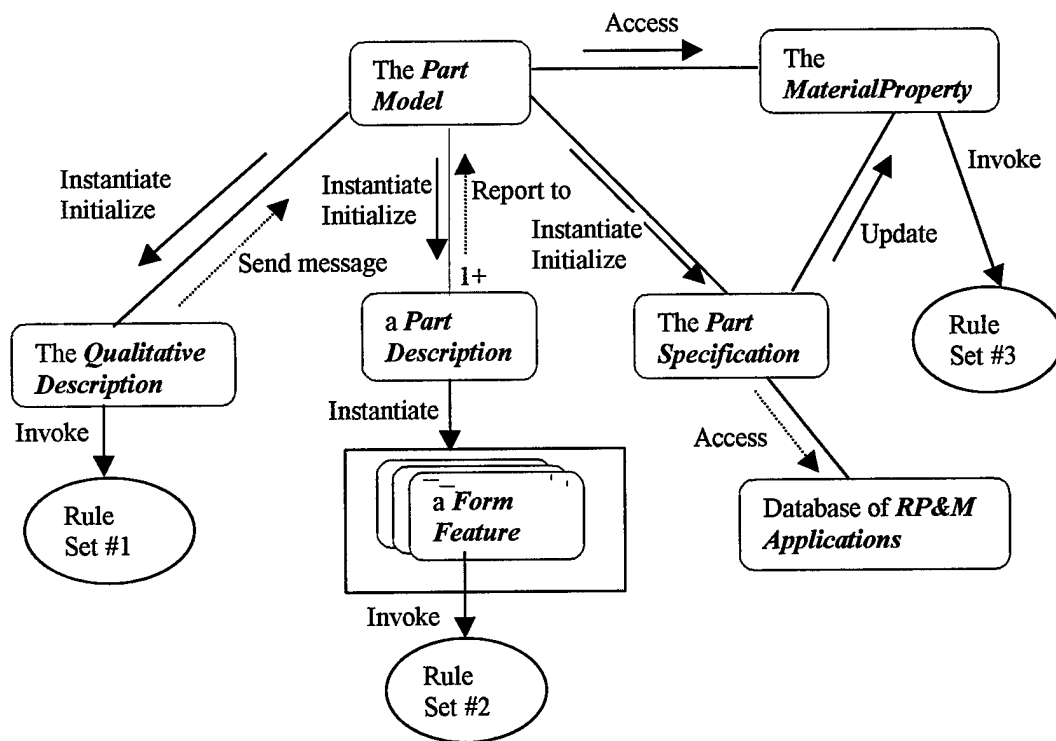


Figure 5 Object Diagram of the Knowledge-based RP&M Material/Machine Selector

Based on a given CAD solid model, a *Part Model* object is first created. The initialization of the *Part Model* object simultaneously instantiates the objects of *Qualitative Description*, *Part Specification* and *Part Description*, *Machine List*, *Material List*, etc., as illustrated in Figure 5. All the RP&M material available in the database is assigned to *Material List* in the initialisation. The material-related rule-sets are activated from the method function of the *Part Specification* object. RP&M materials that do not satisfy the application requirements on material would be

removed from the *Material List* via the firing of rules. Similarly, the chaining in the rule sets of *Process Guidelines* and *Machine Evaluations* would guarantee the selection of RP&M machines that satisfy the application requirements on the building quality and the manufacturing cost. Numerical procedures, such as the computation of manufacturing time, the computation of manufacturing cost, the optimal orientation determination, are implemented in the method functions of the *part model*.

5 Implementation and Case Study

A prototype based on the proposed object-oriented model has been developed using Kappa, a knowledge-based application development platform. The commercial object-oriented developing platform together with its inherent data management functionality reduces the amount of development efforts required. The main screen of the prototype is shown in Figure 6. The implemented RP&M material/machine selector can serve as a software tool assisting the designers in the selection of appropriate RP&M machines in the product development cycle. Geometric data of a CAD model needed in the knowledge-based system is extracted from the CAD model database and passed to the knowledge-based system.

Figure 6 Implementation of the Knowledge-based RP&M Material/Machine Selector

A perfume bottle, shown in Figure 7-(1), is used as a visualisation application case. In order to evaluate the visual appeal of this design, the designer want to build a physical model to show to potential customers for their comments. A number of RP&M machines, namely SLA 250, JSC-2000, SLS 2000, LOM 1013H and Concept Modeler, are assumed to be available to

the designer. Since the prototype is used for visualisation purpose, the designer's requirement on dimensional tolerance is not critical. The surface finish of the prototype, however, should not be too coarse and affect the judgement of customers. Based on the designer's requirements, the application-related inputs are set as the following:

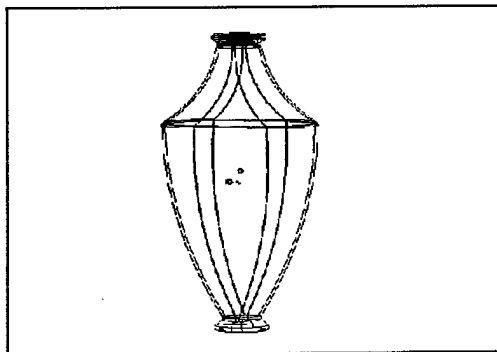
Application Category: <i>Visualisation Model</i>	Minimum Tensile Strength (N/mm ²): <i>30</i>
Application Purpose: <i>Concept Proof</i>	Minimum Tensile Modulus (N/mm): <i>600</i>
Material Type: <i>No Preference</i>	Minimum Material Hardness (Shore D): <i>30</i>
Minimum Flexural Strength (N/mm ²): <i>30</i>	Resistance to Humidity: <i>Normal</i>
Minimum Flexural Modulus (N/mm): <i>600</i>	Resistance to Heat: <i>Normal</i>

The descriptions on the general shape of the product model are set as:

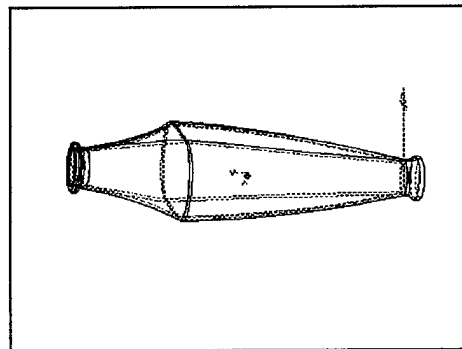
Thin Wall: <i>None</i>	Sculptured Surfaces: <i>Some</i>
Cavities with small opening: <i>Yes</i>	Size of the Part: <i>Medium</i>
Deep Holes (L/D>5): <i>None</i>	Ratio of Volume vs. Size: <i>Small</i>
Fine Features: <i>None</i>	

The operational factors are set as following:

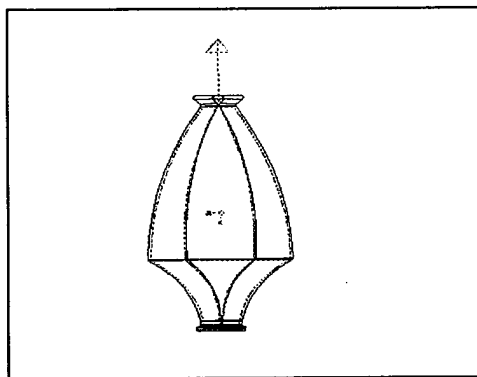
Dimension Tolerance: 0.1mm~0.3mm	Time factor: <i>Normal</i>
Surface finishing: 16<R _a <266 micro	Cost factor: <i>Normal</i>



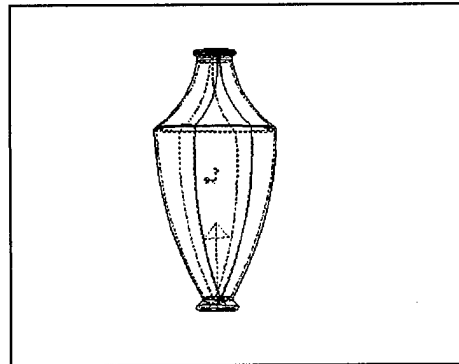
(1) Concept Design of a Perfume Bottle



(2) Orientation with the least building height



(3) Orientation with the Least Staircase Effect



(4) Orientation with the least overhang

Figure 7 Perfume Bottle in Different Orientations

Geometric attributes of the product model in different orientations, as shown in Figure 7, are evaluated in the environment of a CAD system and stored in a flat file. The flat file is then passed to the knowledge-based module for examination. For this application case, all RP&M material included in the material database are found to be suitable. The suitable machines

however do not include LOM. The large internal cavity in the model prevents it from using the LOM process. For the suitable combination of RP&M material, machine and orientations, the manufacturing time and cost are computed. According to the user's considerations on time and cost, the optimal solution is selected, i.e. the combination of P400ABS (material), Concept Modeler (an FDM machine), and the orientation shown in Figure 7-(4). Should the user change the requirements, the selection would be restarted.

6 Conclusion

An object-oriented approach for knowledge-based decision-support in RP&M part fabrication has been introduced in this paper. Based on the approach, an RP&M material/machine selector has been developed to assist the user select the right RP&M material/machine for a specific part fabrication. Using rule-based reasoning and database, the selector first finds the applicable RP&M material/machines. From the list of applicable RP&M systems, the optimal combination of material, machine and part orientation is then found out based on the minimisation of cost.

At present, information about the four RP&M processes, namely SL, SLS, FDM and LOM, are included in the RP&M material/machine database. While the developed software focus on the selection of material and machine in RP&M part fabrication, the object-oriented knowledge-based approach can be extended to handle other tasks arising in the integration of design and prototyping/manufacturing activities. With the compilation of more comprehensive machine databases, the decision-support system is expected to provide a detailed process plan for the fabrication of a specific application with RP&M.

References

- Booch, G. (1991). Object-oriented Design with Applications. the Benjamin/Cummings Publishing Company, California.
- Bremen Institute of Industrial Technology World Wide Web site, 1998. [Http://www.biba.uni-bremen.de/groups/rp/rp_selec.html](http://www.biba.uni-bremen.de/groups/rp/rp_selec.html).
- Campbell, R. I., and Bernie, M.R.N. (1996), "Creating a database of rapid prototyping system capabilities", *Journal of Materials Processing Technology* (61), pp163-167.
- Cattell, R.G. G. (1991). Object Data Management. Addison-Wesley Publishing Company, Mass., United States.
- Frank, D. and Fadel, G. (1995), "Expert System-based Selection of the Preferred Direction of Build for Rapid Prototyping Processes". *Journal of Intelligent Manufacturing*, No.6, pp339-345.
- Grimm, T.A. (1996), "SLS and SLA: different technologies for different applications", *Rapid Prototyping and Manufacturing Conference '96*, SME, Dearborn, MI, p1-11.
- Hopgood, Adrian A. (1993). Knowledge-based Systems for Engineers and Scientists. CRC Press.
- Loh, H.T. Xu, F. and Wong Y.S. (1998), "Optimal Orientation Selection in Different Rapid Prototyping Processes", *Proceeding Of First International Conference on Rapid Prototyping & Manufacturing '98*, Beijing, pp140-148.
- Phillipson, D. K. and Henderson, M. R. (1997), "Rapid Prototyping Machine Selection Programme", *Proceeding of the 7th International Conference on Rapid Prototyping*, pp291-303.
- Yourdon, Edward and Carl Argila (1996), *Case Studies in Object Oriented Analysis and Design*, Prentice-Hall Inc.

RP Process Selection for Rapid Tooling in Sand Casting

Wanlong Wang, James G. Conley, Henry W. Stoll, and Rui Jiang
Department of Mechanical Engineering
Northwestern University
Evanston, IL 60208-3111

ABSTRACT

The significant cycle-time improvements and geometrical capabilities of solid freeform fabrication systems have led to applications in sand casting industry for design verification and tooling. The time and cost effective deployment of rapid tooling processes using rapid prototyping technology has thus becoming an emerging area to be studied. To make full use of the advantages of rapid prototyping processes, the factors influencing the tooling approach must be identified and understood. This understanding is then used to develop a decision-making structure for RP process selection for rapid tooling in sand casting. In this manuscript we review our work in evaluating and building a framework for tooling process selection for sand casting.

Key words: rapid tooling, process selection, tool path selection, sand casting, rapid prototyping

1.0 Introduction

A sand casting is produced by pouring molten metal into a mold cavity. The mold cavity is created by packing sand around a pattern and then withdrawing the pattern. Since the pattern imprint forms the cavity, the pattern creates the external shape of the cast part. If the part has features or regions that are undercut relative to the parting line, these are formed by cores that are placed in the mold cavity. The cores are supported by core prints and chaplets in some cases that allow the molten metal to flow between the core and the mold wall. In addition, cores may be necessary to produce a desired "zero" draft external surface depending on the parting line selected. Figure 1 illustrates the tooling process for sand casting. Generally speaking, sand casting is a low cost approach to creating low volumes of parts with few restrictions on geometric complexity.

Rapid tooling (RT) has evolved from rapid prototyping technology and its applications. It uses the rapid prototyping model as a tooling master to create the patterns and cores through direct or intermediate tooling processes. Rapid prototyping and tooling have found wide spread application in sand casting design verification and tool making in recent years.

In practice, there are three kinds of tooling processes used: traditional manual pattern making, computer numerical control machining, and rapid prototyping. The method selected for making the pattern and cores, which we call "tool path selection", is determined by a series of decisions regarding the fabrication method, material, and tooling approach to be used. There are a number of publications that address a particular rapid tooling process in sand casting [1-5]. To our knowledge, however, studies on tool path selection for sand casting are very few. Related works

include Mensing and Gibson's [6] build time comparison study of large parts using SLA, Sanders, Stratasys, SLS, LOM and milling processes, and Paxton's [7] benchmarking study on rapid tooling processes. These investigations mainly focus on the time or cost comparison of the different processes, but do not address a methodology for decision-making. Stoll, et al [8] have done initial research in this area. Their work discusses decision variables, decision factors, decision structures and a decision process. A complete and integrated method to investigate the tooling path selection is presented. But article focuses on tool path selection at the macro-level, and does not present much detail on the selection of a particular rapid prototyping process.

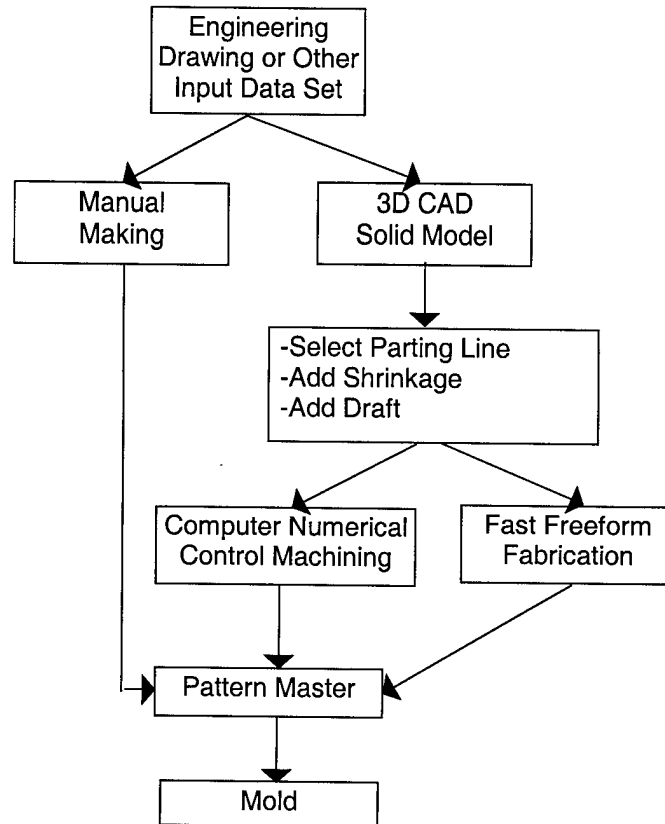


Figure 1. Tooling process for sand casting

In this paper, we first review the process characteristics of RP processes and then discuss the basic principles of tool path selection for sand casting. We then investigate criteria to select a RP process, determine the decision factors, organize the decision structure and develop integrated decision process. The present investigation is limited to tooling master fabrication. As such, we do not address direct tooling processes.

2.0 Review of Rapid Prototyping Processes

There are a number of rapid prototyping processes that find wide spread application in industry. Each process has its own characteristics, advantages and disadvantages. To make a "best" decision of RP process selection, one must have a clear understanding of those processes and their respective advantages and disadvantages.

Stereolithography Apparatus (SLA) involves selective curing of a photo-curable polymer using a laser beam directed by the computer in accordance with the tessellated version (.STL) of the CAD model. This process is generally highly accurate and can provide parts and/or pattern elements with good surface finish. The mechanical properties of the photo-cured polymer do not match most production engineering materials and shrinkage and warpage may occur in the post-processing process. Additionally, pre-building of a support base is needed [9]. This process is especially suitable for complex parts with thin-walls or lug features, small size or high precision requirements.

Laminated Object Manufacturing (LOM) stacks layers of thin sheets of paper to make the prototype. Each layer is cut to match a cross-section of the model. The finished model has the surface finish and consistency of wood. It is especially suitable for complex, large or bulky parts. The strength of the LOM model is above average. This process does not need support generation. Since post-processing is done manually, waste material removal is time consuming. Another disadvantage of this process is that the waste material can not be reused [10].

Fused Deposition Modeling (FDM) uses a spool of filament that feeds into the unit's heated extruding head like wire feeds into an automatic welder. The product has good dimensional accuracy and surface finish, and fast building speed. The material strength is low. Supports are needed in this process. [11]

Selective Laser Sintering (SLS) deposits and sinters a layer of heat-fusible powder to form the cross-section area of a model. An initial cross-section of the object under fabrication is selectively 'drawn' on the layer of powder by a heat generating CO₂ laser. This process achieves average accuracy and has multiple material choices. It can fabricate very strong metal composite inserts or molds used for injection molding. In sand casting, it can directly produce the sand mold using SandForm Zr II (zircon) or Si (silica) sand casting materials. This process does not need support generation thus is easy for post-processing. [12,13]

Solid Ground Curing (SGC) uses a glass photo-mask and an ultra-violet floodlight to build a model slice on a solid environment. This eliminates curling, warping, support structure, and any need for final curing. It is a high precision process. But the building time and cost is above average for the current RP market. [14]

Three Dimensional Printing (3DP) uses a technology similar to the ink-jet printing to spray a binder materials on a thin distribution of powder spread over the surface of a powder bed. The binder material joins particles where the object is to be formed. The accuracy is average, as is the strength. No support generation is needed. [15]

Sanders Prototype (SP) involves a liquid to solid inkjet plotter with a separate z-axis input. The dual inkjet subsystem rides on a precision x/y carriage and deposits both thermoplastic and wax materials on the build substrate under program control, according to the path generated by STL model. These droplets may be placed at any desired location upon the build substrate within 0.00025 inches (0.007 mm) in the x and y directions. The droplets adhere to each other during the liquid-to-solid phase transition to form a uniform mass. The drying process is fast enough to allow milling of the layers immediately following the deposition cycle. This process is claimed

as the most accurate amongst the RP processes. Support materials are required to support overhangs and cavities in the model during the model build sequence. [16]

3.0 Tool Path Selection for Sand Casting

In considering the tool path that selected for a particular sand casting, one must consider the *dimensions of decision space*: fabrication method, tool materials and tooling approach. There are three kinds of fabrication methods: manual, computer numeric control (CNC) machining and rapid prototyping (RP). Regarding the tool materials, there is a variety of materials that can be used, such as mahogany, pine, urethane plastic, synthetic materials, metals, and FFFF materials (e.g. polymers, papers, ABS plastics, and metal powders). For the tooling approach, loose pattern, gated pattern, match-plate pattern and cope & drag tooling are the mainstream methods of the foundry tooling industry.

The second consideration of tool path selection are the decision *factors* and *constraints*. It is a complex mental excise to comprehensively consider each aspect of the tooling process from the engineering drawing to the final foundry production. In this process, a tool engineer or decision maker must consider data status, production volume, state of development, the direct user of the tooling, part geometry, critical features, pattern shop capability, tool cost, lead-time, casting tolerance and accuracy, and tool durability. He must understand what are independent and dependent factors and the relationship or tradeoff among these factors.

For example, the decision-maker must know that each of the tool path selection factors imposes constraints on the selection process by eliminating certain decision variable combination from further consideration. Independent decision factors (e.g. production volume, geometric complexity, no draft allowed) typically impose rigid constraints that must be satisfied. A production quantity of 30 units is a rigid constraint, the tool must be capable of producing 30 acceptable castings. While the dependent factors (e. g. cost, time, accuracy, and durability) are negotiable because of the complex couplings and tradeoffs that exist between these factors. For example, there are many tool path alternatives that are capable of producing 30 castings. The tool path that is eventually selected will typically result in the most desirable tradeoff between cost, time, and quality. This, in turn, is likely to depend on the relative importance of the dependent decision factors.

The third consideration of tool path selection is the *decision structure* and *process*. The decision structure involves how to organize the decision space and factors, how to determine the possible decision options for tool path, and how to evaluate the criteria for optimal decision making. Once sufficient information is available, a rational decision process is necessary to make the final decision for tool path selection. Based on the industry practice, an integrated decision-making process is proposed by Stoll, *et al* [8]. The reader is referred to this paper for a more in-depth discussion on this topic. Figure 2 shows an example flow chart of the decision-making process for tool path selection for sand casting.

4.0 RP Process Selection for Tool Making

Selecting the best RP process for a given application involves a similar decision process. *RP process selection* is defined as the selection of an appropriate commercially available RP process by careful evaluation of the decision factors and customer's requirements.

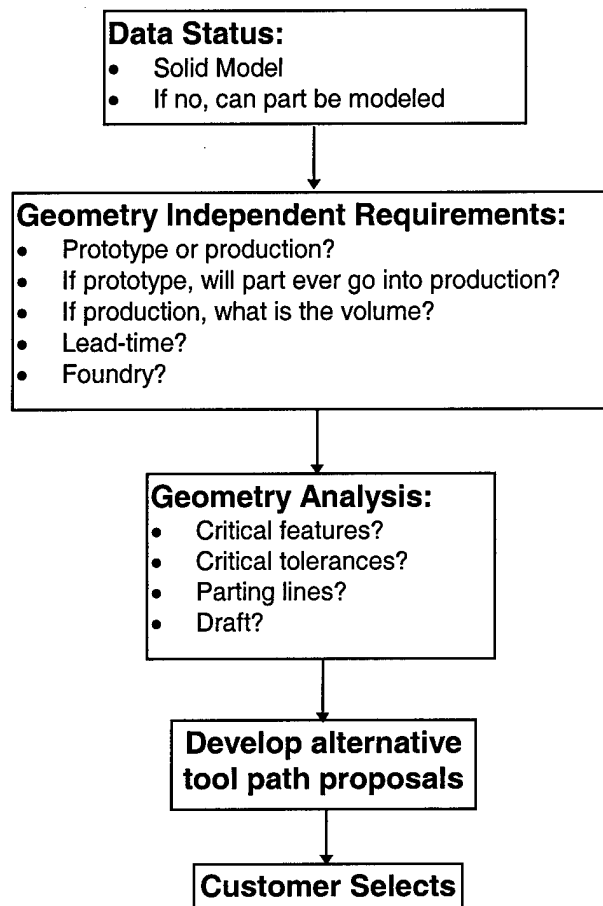


Figure 2. The tool path selection process.

4.1 Decision Factors

The decision factors associated with RP processes include part geometry and critical features, post-processing, building materials (strength and durability), production volume, time, cost and accuracy. There are also some factors that are common to all RP processes such as the data status (generally a 3D CAD model required), building orientation selection, slicing strategy (constant or variable thickness), and so forth.

4.1.1 Part Geometry and Critical Features

Part geometry constrains and underlies the selection of the best RP process. It constrains because only those processes that are capable of generating the desired geometry can be considered. It underlies the decision because each tool path that is favorable for producing the desired geometry will also be more or less suited for producing particular features or aspects of the geometry. Deciding on the right RP process for a given part geometry is therefore very dependent on the decision-maker's experience and judgment. For example, most experienced tool builders can look at a part and immediately determine that SLA is the best fabrication method or that LOM would not work well. The tool builder does this by noting specific features of the part geometry and then mentally filtering the possibilities based on learned experience. This mental evaluation is the "essence" of the tool path selection process.

In making the evaluation, the decision-maker generally considers several aspects of the part geometry. These include:

- Wall thickness
- Aspect ratio
- Special features such as fillets, lugs, small holes, and undercuts
- Surface complexity

Thin walls and severe aspect ratios can be a problem for some RP processes such as LOM. Conversely, a bulky part may be very suitable for the LOM process. Cross-section geometry such as fillets, rounds and transitions between features may be difficult for all RP processes if the angles between the Z-axis direction (layering direction) and the surface normal are bigger than 45° . Small lugs or holes may be suitable for the Sander technique. The tool-maker must understand the critical features of the parts so that an optimal process is chosen based on the part geometry and its application.

4.1.2 Post-processing

Post-processing is necessary for most RP processes. It generally includes two aspects: removing the support structure and finishing the surface. The amount of post-processing work required to achieve a level of surface finish differs widely amongst the processes. For example, it may be very difficult to remove the support materials from an internal cavity of a LOM model, while the same task may be relatively easy for the SLS or 3DP methods.

4.1.3 Building Materials (Strength and Durability)

There are a variety of building materials used in different RP processes such as paper, polymer, ABS plastic, wax, metal or ceramic powders, etc. Since different materials demonstrate different mechanical strength and durability, the building material will eventually affect the tool life and accuracy. To select the appropriate process, the tool-maker needs to know the production volume and how sand ramming of the pattern will influence tool life and tool wear.

4.1.4 Production Volume

The tooling material selected and the tooling approach used depends to a large extent on the *production volume*, which is the number of castings to be produced over the lifetime of the tool. If a large number of castings are to be produced, then the tooling material and approach is likely to differ from that used for a short production run. For example, if only a few castings are to be poured (<10), then many RP processes may be acceptable. If moderate production volumes (10 to 300) are anticipated, then some RP processes cannot be used only because of material strength and durability limitation. For large production volumes (>300), few tool "paths" can be used. For example, the RapidSteel process of SLS can produce highly durable metal molds.

4.1.5 Time, Cost and Accuracy Trade-Off

Time, cost and accuracy are dependent factors that affect the decision-making process. This is particularly true for RP processes because of the nature of layered manufacturing. The decision-maker needs to evaluate the trade-offs between these factors to find the best or most acceptable combination.

4.2 Decision Structure

The decision space must be investigated in making a RP process selection for tool making. More specifically, a tool engineer or decision-maker must understand what set of possible decision combinations are possible and what constitutes a "best" RP process selection.

4.2.1 Decision Space for RP Process Selection

Choosing RP process involves two independent decision variables: RP process and material. Product requirements (time, cost and accuracy) generally determine which combination of RP process and material is best. If we view each of these decision variables as a dimension of the RP process selection process, we can envision a decision table as shown in Table 1.

Table 1 Decision table for RP process selection

	SLA	LOM	SLS	FDM	SGC	3DP	SP
Polymer	X				X		
Paper		X					
Wax			X	X			X
ABS Plastics			X	X		X	
Metal Powder			X			X	
Ceramics		X	X			X	
Sand			X				
Composite		X					

In this table, there are 16 combinations of process and materials. For each material class, there are several options to be considered.

4.2.2 Decision Constraints

Each of the factors discussed in Section 4.1 imposes constraints on the RP process selection by eliminating certain decision variable combinations from further consideration. Independent decision factors typically impose rigid constraints that must be satisfied. These constraints include geometry, production volume, material strength, etc. A large size part with thin walls and many lugs as critical features may not be a good candidate for the LOM process. A very large volume production (>1000) may need RapidSteel to produce the master. For small or medium production volumes, a number of the RP processes can be used to create the elements of the tool.

4.3 Integrated Decision Process

RP process selection is a comprehensive mental exercise that is generally undertaken by an experienced tool builder. In general, the procedure followed by each tool-maker will depend upon both the decision-makers' knowledge and experience and upon the pattern shop facilities available. The general flow of the RP process selection is shown in Fig. 3. It is important to note that, although the process appears to be linear, in reality, it is highly iterative and non-linear and may involve many conversations with the customer. Typically, the final decision emerges as the customer and the tool-maker work together to evolve an acceptable approach.

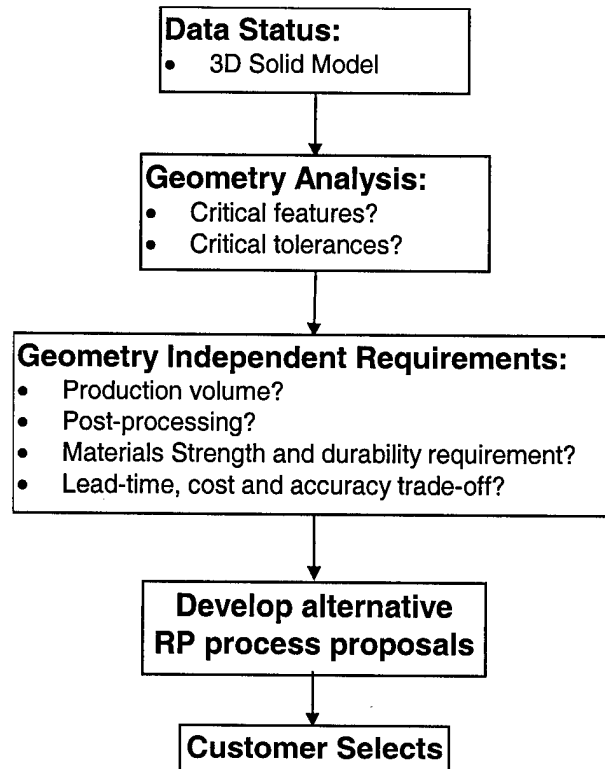


Figure 3 Integrated decision process for RP process selection

5.0 Conclusion

RP process selection for tool making, which involves the selection of a particular RP process and material, is a sub-decision that must be made as part of the tool path selection process. This paper reviews the general RP processes, discussed the tool path selection for sand casting, and investigates the decision factors and decision-making process for RP process selection. This investigation attempts to clarify the factors and their influences on the decision process so that a further optimal decision support system may be developed based upon this understanding.

Acknowledgment

We would like to acknowledge the generous support of the US Defense Logistic Agency (DLA), Clinkenbeard Associates in this research program.

References

1. R. Gustafson, E. Guinn, and D. Tait, (1995) "Rapid Prototyping for Pattern and Foundry Tooling", *Modern Casting*. v 85 n 2 Feb 1995. p 48-50.
2. W. Wang, J. G. Conley and H. W. Stoll. "Rapid tooling for sand casting using laminated object manufacturing". Accepted by *Rapid Prototyping Journal*, November 1998
3. W. Wang, J. G. Conley and H.W. Stoll, "Dimensional Variability Analysis In Post-Processing Of Rapid Tooling", *Proceedings of the 9th Solid Freeform Fabrication Symposium*, University of Texas at Austin, August 10-12, 1998, p 417-426.

4. R. Gustafson (1999) "Rapid Prototyping: A Tool for Casting Design and Verification", *Modern Casting*. V 89 n 3. p 44-47.
5. W. Wang, J. G. Conley and H. W. Stoll, "Rapid Tooling Error Analysis for Sand Casting", *Transactions of the AFS 102nd Casting Congress*, Atlanta, GA, May 10-13, 1998, p 567-571.
6. G. Mensing and I. Gibson, "Build time estimations for large scale modeling", *Proceedings of the 9th Solid Freeform Fabrication Symposium*, University of Texas at Austin, August 10-12, 1998, p 343-350.
7. J. Paxton, "Benchmarking rapid tooling process", *Rapid prototyping and manufacturing '99 - Advanced product development Technologies in Action*, Volume 3, April 20-22, 1999, Rosemont Convention Center, Rosemont, Illinois. p 519-603.
8. H. W. Stoll, J. G. Conley, W. Wang and R. Gustafson, "Tool path selection for sand casting", presented at *AFS 103rd Casting Congress and CastExpo*, America's Center, St. Louis, MO, March 13-16, 1999.
9. 3D Systems, Inc. Homepage: <http://www.3dsystems.com/>
10. Helysis, Inc. Homepage: <http://helisys.com/>
11. Stratasys, Inc. Homepage: <http://www.stratasys.com/>
12. DTM Corp Homepage: <http://www.dtm-corp.com/>
13. DTM Corporation, "The selective laser sintering process -- third generation desktop manufacturing". *Proceedings of National Conference on Rapid Prototyping*, The University of Dayton, June 4-5, 1990, p5-10.
14. Cubital Homepage: <http://www.cubital.com/cubital/>
15. E. Sachs, M. Cima, J. Cornie. "Three dimensional printing: ceramic shells and cores for casting and other applications," *Proceedings of the Second International Conference on Rapid Prototyping*, The University of Dayton, June 23-26, 1991, p39-54.
16. Sanders Prototype, Inc. Homepage: <http://www.sanders-prototype.com/>

Agile Product Testing with Constrained Prototypes

Uichung Cho Kristin L. Wood Richard H. Crawford

Manufacturing and Design Lab.
Department of Mechanical Engineering
The University of Texas at Austin
Austin, Texas 78712

Abstract

The means to acquire reliable functional information is a critical factor that differentiates product development time and cost. Thanks to advances in solid freeform fabrication techniques, industries can produce geometrically complex parts within dramatically reduced time and cost. Even though industries can save significant efforts by performing functional tests rapid prototypes, they still prefer full-scale product tests, especially in later design phases, due to inherent limitations in traditional similarity methods (TSM). This paper describes a new method to perform reliable functional tests with rapid prototypes that cannot be properly handled by the TSM.

1 Introduction

The means to acquire and manage system information, which guides design activities, is influential to the performance of design processes. Our ancestors created primitive devices mainly through natural experiences. Recognizing the need to obtain necessary information with efficiency, people started to perform planned observations (active observations), reflecting on them to exploit specific phenomena. Thanks to such exploits and advances in virtual modeling techniques, contemporary designers are able to obtain necessary functional information far more efficiently. However, there are still needs to obtain reliable functional information in time, as the phenomena that can be described purely by mathematics are still very limited.

Thanks to advances in various rapid prototyping techniques, industries can fabricate geometrically complex parts with dramatically reduced effort (Jacobs, 1992; Aubin, 1994). Considering the significant time and cost spent on product testing to verify or improve final product quality, it is natural to expect various industrial applications of rapid prototypes for function testing. However, industries utilize rapid prototypes mostly in early design phases, and very limited case studies are reported on functional testing with rapid prototypes to verify product performance or tune design parameters (Dornfield, 1995; O'Reilly, 1993), mainly due to material issues (Wall et al., 1991). This paper introduces a new method to correlate distorted systems that cannot be handled by traditional methods, especially when systems are composed of multiple parts.

2 Similarity Methods for Prototype Testing

To predict full-scale product behavior using economic scaled (rapid) prototypes, mainly two types of similarity methods can be applied:

- Dimensional analysis that designs scaled models, and correlates product and scaled model behavior on the basis of dimensions of dominant system parameters, through the Buckingham Π theorem (Bridgman, 1931; Sedov, 1959; Szucs, 1980; Baker et al., 1991).
- Analytical fractional analysis that mathematically correlates the solutions of two known equations, by comparing and manipulating the equations (Sedov, 1959; Kline, 1966).

In dimensional analysis, one should design scaled models so that all of corresponding dimensionless parameters of the scaled model and target system should be identical. Especially when prototyping materials are limited, the chance to fabricate well-scaled models is very low. Besides, one should precisely know system parameters beforehand. Such limitations are clarified in our previous publications (Cho et al. 1998(a)(b)). In comparison to dimensional analysis, analytical fractional analysis can provide more accurate scale testing results (Kline, 1965). However, one should know precise governing equations, material properties, and loading conditions that are not well informed in many circumstances.

In order to overcome such limitations in traditional methods, we introduced a novel empirical similarity method (ESM), in which geometrically simple specimens are utilized as additional information sources. One can refer to (Cho and Wood 1997, Cho et al. 1998(a)(b)) for fundamentals of the method, and this paper will describe the concept through an archery bow example focusing on correlation of systems composed of multiple parts.

3 System Correlation through Relative State Representation

When products are composed of multiple parts, the TSM requires to design scaled models to satisfy the following material proportionality condition:

Proportionality of material properties - The material property ratio of corresponding model and product components should be kept identical, in order to perform scale testing with the TSM.

The proportionality condition is very difficult to be satisfied, when available prototyping materials are limited. If two systems do not satisfy this proportionality, they are defined

to have distorted configurations, and there exists no method to correlate systems with distorted configurations within the authors' knowledge. As an initial attempt, we test the possibility to predict behaviors of systems composed of two materials, utilizing a scaled model fabricated from a single prototyping material.

The product specimen¹, the scaled model, and the product system parameters can be represented in terms of the model specimen² parameters, through the scale and form factors. One should notice that the form factors and the state scale factors should satisfy

$$\lambda_{X1} \cdot \phi_p = \lambda_{X2} \cdot \phi_m, \quad (1)$$

where the state scale factors λ_{X1} and λ_{X2} can be mathematically derived through dimensional analysis, and ϕ_m and ϕ_p are unknown form factors. From the equation, the form factors ϕ_m and ϕ_p , which represent the amplifications of the model and product states under pure geometrical changes, should be identical, if $\lambda_{X1} = \lambda_{X2}$, viz. the model and the model specimen are designed from the same similarity constraints.

In our new approach, each part is designed following the II theorem in order to maintain the identity of the form factors of the model and the product, and the scale factors of the specimen pair and mode-product pair. Through the identical factors, one can represent the lumped model of the product specimen, the scaled model and the product, in terms of the model specimen parameters. As a result, one can represent the product state as a function of the states of the specimens and the model. The step by step procedure of this new approach named as lumped ESM is summarized below.

Procedure of the Lumped ESM:

- (1) Build lumped parameter models: Describe the states of the model pair (the model and the model specimen) and the product pair (the product and the product specimen) as lumped models with unknown effective lumped parameters of each part of the systems.
- (2) Determine the scale factor of each component: Considering the material/loading parameters and size scaling, design scaled models through dimensional analysis, and mathematically derive the scale factors of lumped parameters (the ratio of the product and model parameters) of each component.
- (3) Relatively describe lumped models: Employing the derived scale factors and an unknown form factor (between the model specimen and the model), represent the product specimen, the scaled model, and the product in terms of lumped parameters of the model specimen.
- (4) Represent product states in terms of the model and specimen states: By comparing and manipulating the four lumped models, describe the unknown product states as a function of the measured states of the scaled model and the specimen pair.

In summary, the lumped ESM correlate the states of model and product pairs by implicitly deriving the unknown lumped parameters through the measured states of a scaled model, and a specimen pair.

¹Geometrically simplified version of product

²Geometrically simplified version of scaled model



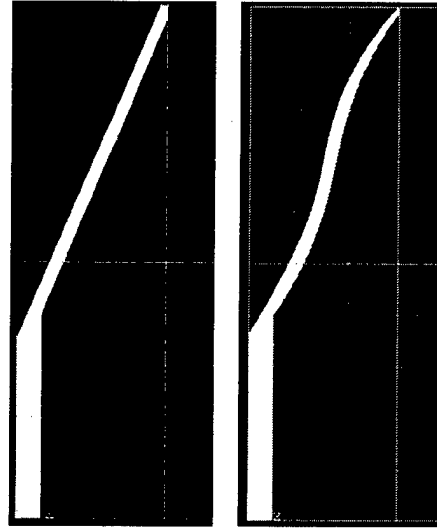
Figure 1: Exemplary Archery Bows

Numerical Archery Bow Example

In designing archery bows, the shooting force, viz. the force required to fully deform a bow to shooting position, is a typical system behavior that draws our attention. One should design bows so that both ergonomic (e.g., required shooting forces) and functional (e.g., arrow speed at a distance) requirements are satisfied.

Virtual bow models may not be accurate enough to design quality bows, mainly due to geometrical and material nonlinearity. Large bow deformation causes significant geometrical nonlinearity, and the stress-strain behavior may not be linear within the wide strain range, considering popular bow materials (e.g., fibers and woods). For these reasons, designers may need to fabricate several test bows to verify or improve product quality. Considering the geometrical complexity of bow frames shown in Figure 1, significant cost and time to fabricate test-bows are expected. We illustrate and validate the lumped ESM to predict the required (or resultant) force of a product bow in an effective manner. As a preliminary study for future physical testing, we test lumped ESM using numerically simulated bow behaviors. In this bow example, the TSM requires the identity of the Young's modulus ratios of the bow frames and strings of models and products. However, the identity of the ratios cannot be satisfied in many cases, as the prototyping material choices to fabricate the string and the frame of model bows are limited.

Shooting forces were simulated with ANSYSTM, and the finite element bow models of the target (product and scale model) and specimen bows of interest are shown in Figure 2. In the finite element models, the string is modeled as a two-dimensional elastic link (Spar element), and the bow frame as triangular solid elements (Plane2). The width of the bow frame is set to 35mm, and the cross section area of the string to 10mm². As shown in Table 1, we use the same bow string for both model and product bows, considering the difficulty in finding proper frame (or string) materials that satisfy the condition required



FE Models (Grid Size=0.1mX0.1m)

(a) Specimen

(b) Target

Figure 2: Symmetric Half of the Specimen and Product Bows

Parameters	Polymer Bows (Models)	Fiber Bows (Products)
Frame E^b (GN/m^2)	7.46 (Mean)	16.0 (Constant)
String E^s (GN/m^2)	5	5
String Pre-Strain	1E-8	1E-8

Table 1: System Parameters of the Bows

by the TSM,

$$\frac{E_p^b}{E_m^b} = \frac{E_p^s}{E_m^s}, \quad (2)$$

where the superscripts b and s denote bow frame and string, and the subscripts m and p denote model and product materials, respectively. In this simulation, we consider full-size models for the purpose of clear comparisons. However, one can reduce the size of the model bows without loss of generality, as long as the model systems are designed from the same scale laws.

To predict shooting forces of the target fiber bow (product) in Figure 2 (b) through the ESM, it is assumed that bows can be modeled as lumped spring systems shown in Figure 4. Then, the shooting force of a model specimen (polymer bow with the simple geometry shown in Figure 2 (a)) can be represented as,

$$F_{ms} = \frac{k_{ms}^b \cdot k^s}{k_{ms}^b + k^s} \cdot \delta, \quad (3)$$

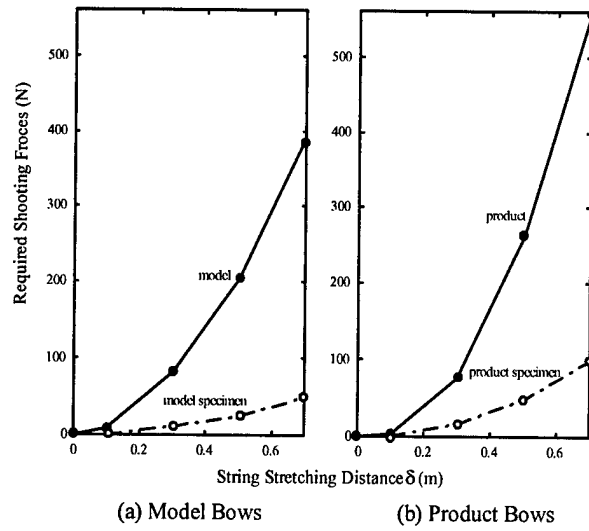


Figure 3: Simulated Shooting Forces of the Bows

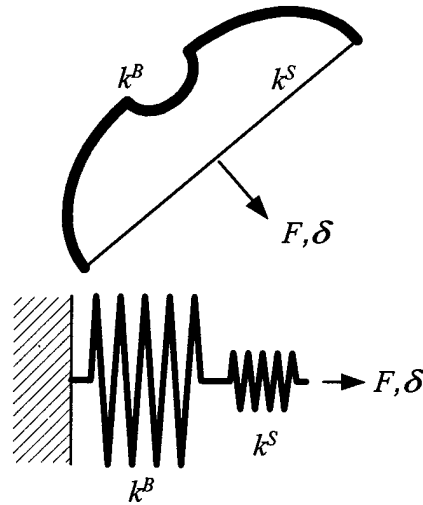


Figure 4: Lumped Model of a Bow

where F is the shooting force (or the force required to deform the bow), δ is the traveling distance of the bow string, and k^b and k^s are unknown effective spring constants of the bow frame and string respectively. By defining a new state variable X , the force equation can be equivalently represented as

$$X_{ms} = \frac{\delta}{F_{ms}} = c_{ms}^b + c^s, \quad (4)$$

where $c^b = \frac{1}{k^b}$ and $c^s = \frac{1}{k^s}$ represent effective compliance of the bow frame and string. Then the states of the scaled model, product specimen, and product bows can be represented as

$$\begin{aligned} X_{ps} &= \lambda_c c_{ms}^b + c^s, \\ X_m &= \phi c_{ms}^b + c^s, \\ X_p &= \lambda_c \phi c_{ms}^b + c^s, \end{aligned} \quad (5)$$

where $\lambda_c = \frac{c_p^b}{c_m^b} = \frac{c_{ps}^b}{c_{ms}^b}$ is the compliance scale factor, and $\phi = \frac{c_p^b}{c_{ps}^b} = \frac{c_m^b}{c_{ms}^b}$ is an unknown form factor of the bow frames.

The remaining task is to express X_p as $X_p = h(X_m, X_{ms}, X_{ps})$, so that we can predict X_p from the measured states, X_m, X_{ms} , and X_{ps} . From Equations (4) and (5), we can derive the following equations without bow string related parameters

$$\begin{aligned} X_p - X_{ps} &= \lambda_c (\phi - 1) c_{ms}^b, \\ X_m - X_{ms} &= (\phi - 1) c_{ms}^b. \end{aligned} \quad (6)$$

By combining the two equations, one can derive the following prediction equation without unknown form factor ϕ ,

$$X_p = \lambda_c (X_m - X_{ms}) - X_{ps}, \quad (7)$$

where

$$\lambda_c = \frac{1}{\lambda_k} = \frac{E_m}{E_p}. \quad (8)$$

As a result, one can determine $X_p(\delta)$ from Equation (7) based on the measured $X(\delta)$ of the specimens and the model, to predict the bow force of the product $F_p(\delta)$ from the definition of the state X .

Figures 5 (a) and (b) show the shooting force predicted through the TSM and ESM. The TSM cannot predict the bow force with accuracy, as

$$\frac{E_p^b}{E_m^b} \neq \frac{E_p^s}{E_m^s}. \quad (9)$$

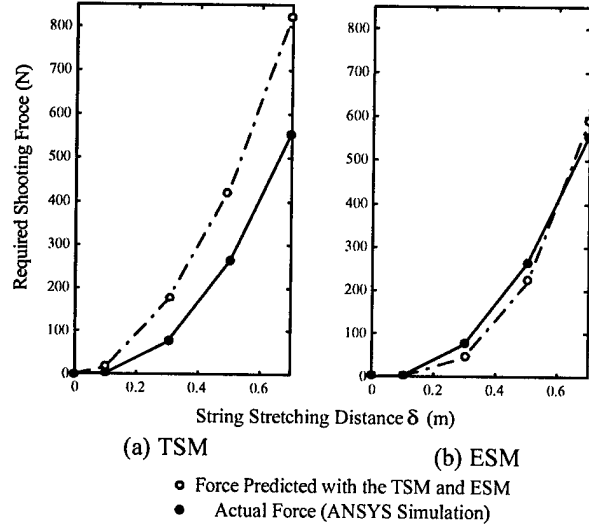


Figure 5: Prediction of the Shooting Force with the TSM and ESM

One way to perform scale testing with the TSM is to assume that the influence of the bow string to the reaction force is relatively small in comparison to the bow frame. In that case, the ratio of the reaction force should be $\frac{F_p}{F_m} = \frac{E_p^b}{E_m^b}$, and it should be equal to $16/7.46 = 2.14$. Figure 5(a) shows the force predicted through the TSM ($F_p = 2.14F_m$), neglecting the effect of the bow strings. As we expected, there exists large discrepancy between the actual and predicted reaction forces of the product bow (Figure 5(a)). In contrast, the bow force predicted through our new lumped ESM (Equation (7)) is plotted in Figure 5(b), and one can notice the remarkably improved prediction accuracy. The ESM results are comparable to the full-scale product testing, and one may save significant effort to fabricate full-scale product bow for testing, especially fabricating scaled models from rapid prototyping processes.

4 Conclusions

Through a simple bow example, the capability of the ESM to correlate systems with distorted configurations has been demonstrated. In general, specimens are used to estimate specific material properties or determine form factors. In contrast, the ESM explicitly estimate neither system parameters or form factors. Instead, the ESM implicitly abstracts the relative influence of system information (e.g., material properties, form factors, boundary conditions) through a specimen pair. By adopting this approach, one can correlate two distorted systems even without knowledge of system parameters.

REFERENCES

Aubin, R.F. 1994. "A World Wide Assessment of Rapid Prototyping Technologies," In *Proceedings of Solid Freeform Fabrication Symposium*, Austin, TX, August, 1994, pp.118-145.

Baker, W.E., Westine, P.S., Dodge, F.T. 1991. *Similarity Methods and Engineering Dynamics: Theory and Practice of Scale Modeling*, Elsevier.

Bridgman, P.W. 1937. *Dimensional Analysis*, Yale University Press, New Haven.

Cho, U. and Wood, K.L. 1997. "Empirical Similitude Method for the Functional Test with Rapid Prototypes," In *Proceedings of the 1997 Solid Freeform Fabrication Symposium*, Austin, TX, pp.559-567.

Cho, U., Wood, K.L., and Crawford, R.H. 1998(a) "Online Functional Test with Rapid Prototypes: A Novel Empirical Similarity Method," *Rapid Prototyping Journal*, Vol. 4, Number 3, pp.128-138.

Cho, U., Wood, K.L., and Crawford, R.H. 1998(b) "Novel Empirical Similarity Method for the Reliable Product Test with Rapid Prototypes," In *Proceedings of the 1998 ASME DETC*, number 98-DETC/DAC-5605, Atlanta, GA. ASME.

Dornfield W.H. 1995. "Direct Dynamic Testing of Scaled Stereolithographic Models," *Sound and Vibration*, August, pp. 12-17.

Szucs, E. 1980. *Similitude and Modeling*, Elsevier Scientific Publishing Company.

Jacobs, P. F. 1992. *Rapid Prototyping and Manufacturing: Fundamentals of Stereolithography*, Society of Manufacturing Engineers, McGraw-Hill Inc.

Kline, S.J. 1965. *Similitude and Approximate Theory*, McGraw-Hill, Inc.

Langhaar, H.L. 1951. *Dimensional Analysis and Theory of Models*, John Wiley and Sons, Inc., New York.

O'Reilly, S.B. 1993. "FFF at Ford Motor Company," In *Proceedings of the 1993 SFF Symposium*, Austin, TX, pp. 168-177.

Sedov, L.I. 1959. *Similarity and Dimensional Methods in Mechanics*, Academic Press, New York.

Wall, M.B. et al. 1991. "Making Sense of Prototyping Technologies for Product Design," In *Proceeding of ASME 3rd International Conference on Design Theory and Methodology*, Vol.31, pp.157-164.

Alain Bernard

CRAN (Research Center for Automatic Control of Nancy)

Université Nancy I - BP 239

54506 Vandoeuvre les Nancy Cedex – France

Tel: +33 3 83 91 27 29. Fax: +33 3 83 91 23 90.

E-mail: alain.bernard@cran.u-nancy.fr

ABSTRACT

This paper introduces a knowledge-based system for the choice of rapid product development processes.

Rapid product development processes are not limited to layer-manufacturing machines, but they also integrate CAD, reverse engineering, indirect methods for metallic and plastic part manufacturing, etc...

Due to short delays, people have no time to test and compare different solutions of rapid product development processes. Even if people have time, tests are time and money consuming. It is also very difficult for somebody to know all about industrial technologies, and to be able to evaluate a multi-criteria choice in a short time.

The aim of the proposed knowledge-based system is to generate, from the specification of parts or tools, different alternatives of rapid product development processes, which can be discriminated and optimized when considering a combination of the different specification criteria (cost, quality, delay, etc...).

Keywords : knowledge-based system, rapid prototyping process, optimization

1. INTRODUCTION

The evolution of layer-manufacturing techniques (Bernard and al, 1998) (AFPR, 1998), during the last ten years, and the development of new applications show that rapid prototyping, and more recently rapid tooling and rapid manufacturing (Wohlers, 1999) (SME, 1999), are new ways for industrial production tools. Nowadays, it is possible to obtain, in a very short time, good quality and low price prototype parts or tools. This is due the development of various kinds of technologies, but also thanks to the different materials transformed on the layer-manufacturing machines. Of course, the development and the integration of numerical environments (systems and interfaces) have favored the efficiency of such processes.

But, due to the large number of possible combinations of technologies (from 3D digitizing and reverse engineering (Bernard, 1999) (Zhang and al, 1995) (Varady and al, 1997) to mass production thanks to metallic tools), industrial companies are not able to capitalize realistic knowledge in order to choose the optimal process for a given specifications, even if they have a long experience in rapid prototyping. More over, the evolution of technologies and their strategic aspect make it important to be able to classify rapid product development processes with regards to real efficiency and reliability.

Life cycle of products is very short. So, companies have to adapt their development and industrialization organization in order to reduce time-to-market, based on numerical information that has become the reference for the product. In fact, new challenges concern the capability to manufacture the just necessary number of products. The main consequence is flexibility for tool manufacturing with low-price and consumable tools, instead of very cost-consuming tools. This is possible because of numerical information, used along the complete development of the product, and due to new materials. But, consequently, it is necessary to validate product and process concepts very early during design stage. Some recent developments in rapid manufacturing allow such possibilities.

These examples show that the dynamic evolution of technologies is not easy to take into account in real time. This is why it is strategic to find the just necessary process for given specifications.

What is proposed in this paper is an approach for knowledge and know-how capitalization, and for computer-aided process planning (CAPP) from given specifications (type of part, material, delay, quality, color, etc...).

In the following paragraphs, the proposed solutions in terms of modeling and process-planning alternatives and choices are developed.

2. RAPID PRODUCT DEVELOPMENT PROCESS

The experience shows that quite all industrial products are concerned by rapid product development technologies. It is mainly due to the variety of technologies and more especially of materials. As said before, there are various fields of applications to favor less time consuming for product development.

The other main evolution is related to the integration of layer-manufacturing technologies with CAD and numeric models. Such CAD systems and environment are not so expensive and are more user-friendly. So, the exploitation of known processes in other application fields is possible for new users. Due to the stability of the technologies, the results are really 3D images of CAD models of parts or tools, more functional and accurate, in many different materials.

In spite of last arguments in favor of the use of rapid product development processes, this domain has a permanent evolution. It is very difficult to appreciate all the real capabilities offered for industrial applications. But it is really more and more interesting to use such means because the number of parts that have to be manufactured at one time seems to be lower and lower. This fact induces a new tendency and favors the development of rapid tooling technologies, in order to obtain some real industrial processes which are alternatives to actual traditional processes. The main originality is to develop materials and technologies that allow obtaining economical and consumable tools which life time is limited. And due to the integration of CAD reference models with these new processes, it is possible to produce as many economical tools as needed, even if this is in one, ten years or more.

In order to be able to decide what is the best process at a time, taking into account the industrial context and the particular specifications of the product, it is strategic to capitalize the knowledge related to all the technologies. If so, it would be possible to distribute this knowledge to all the services which need it (design, manufacturing, industrialization, control, ...). Of course, the volume and the dynamic aspect of this knowledge have to be taken into account when choosing conceptual models for data modeling and data processing. One of the main difficulties is that data will be related to both knowledge and know-how.

All these arguments show the necessity of a computer environment dedicated to CAPP for rapid product development. This system will allow to obtain alternatives of rapid product development processes and also to choose the best one optimized from multi-criteria or based on a particular main criterion.

The interest for a large company to use such environment is to allow all the services having the global technological information at the same time. According to us, it should also be a tool for general knowledge capitalization.

Concerning a small or medium company, this information system has a strategic interest because this environment should be accessed through a Web application ; in particular, that will allow evaluating alternatives of processes based on real means and companies (subcontractors and all their technologies, their capabilities in terms of cost, delay, quality, etc...).

The last aspect is of course that this system will also contribute to help training sessions in order to highlight technologies and the main choice criteria between technologies and more generally between rapid product development processes.

3. PROPOSED SOLUTIONS FOR KNOWLEDGE AND KNOW-HOW CAPITALIZATION

After the analysis of the problem, it has been decided to model a set of generic objects in order to represent the information related to generic knowledge and know-how in rapid product development domain.

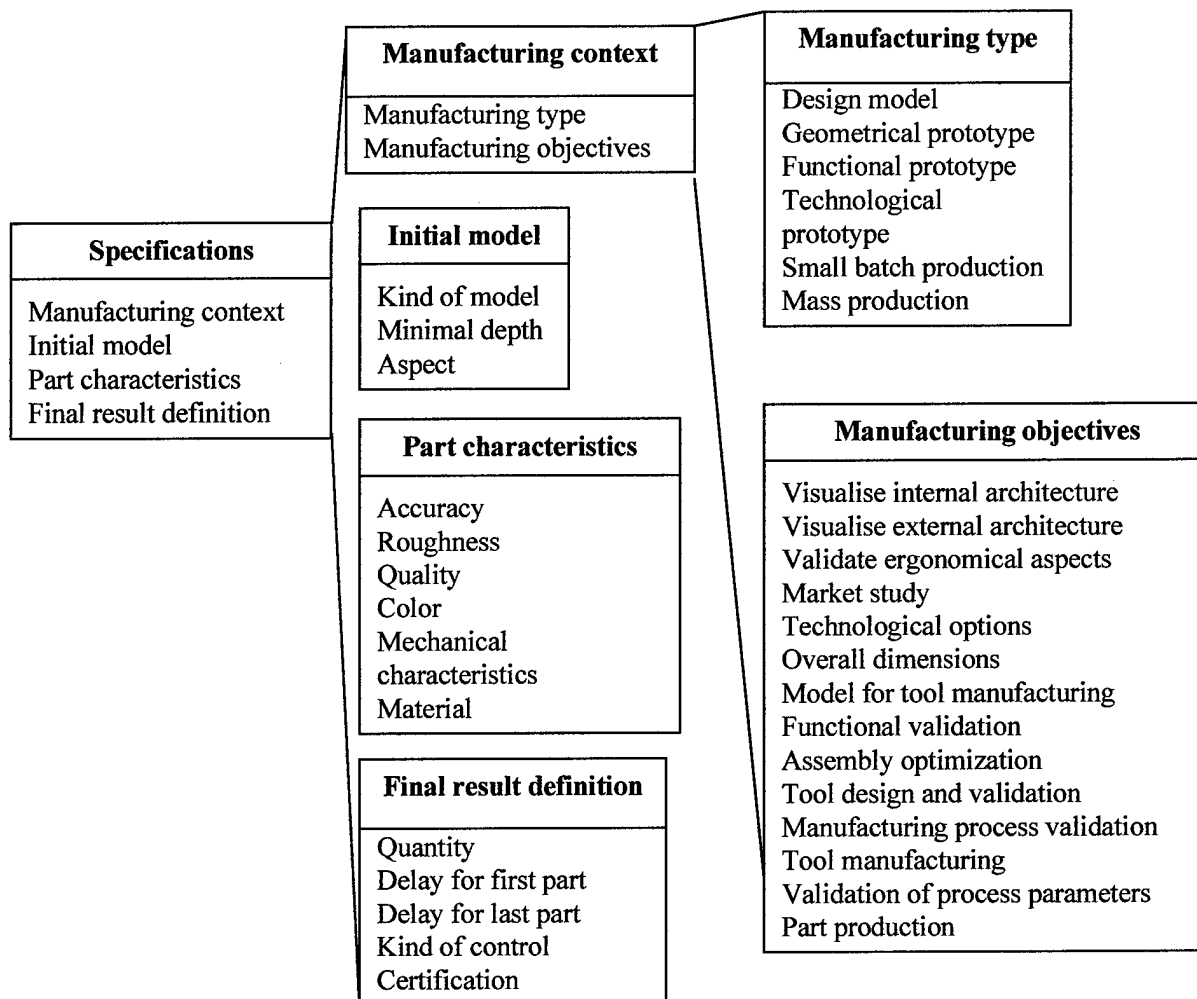


Figure 1. Some elements of specifications decomposition

These objects are classified into six main classes:

- knowledge of the specifications:
this is the starting point of the process, because this is what is given by the client to his subcontractor ;
- knowledge of the different technologies and processes:
it is of course necessary to model all the technologies and the main choice criteria, and the knowledge is obtained from documents, experiences and interviews of experts ;
- knowledge of case studies:
this is necessary because the case studies are the image of what is really feasible (success) or not feasible (failure) ;
- global knowledge of rapid industrialization:
this is related to the different technologies and to all application fields, in order to define precisely the limits of the domain ;
- knowledge related to process choice:
this more especially concerns to the formalization of choice criteria and to their representation ;
- knowledge of computing methods:

the final objective is the final reasoning in order to generate different rapid product development processes, and to choose between these processes in order to find the optimal one.

The entry point of a CAPP system is the definition of the specifications related to the product that has to be manufactured. Figure 1 shows the decomposition of the specifications, which is modeled for each capitalized case study. The main attributes are related to manufacturing context (manufacturing type and context), initial model (more especially STL file, CAD file, physical object, drawings, minimum depth, aspect), final result definition (quantity, delay, certification and control) and part characteristics (material, quality, accuracy, roughness, color, mechanical and physical characteristics).

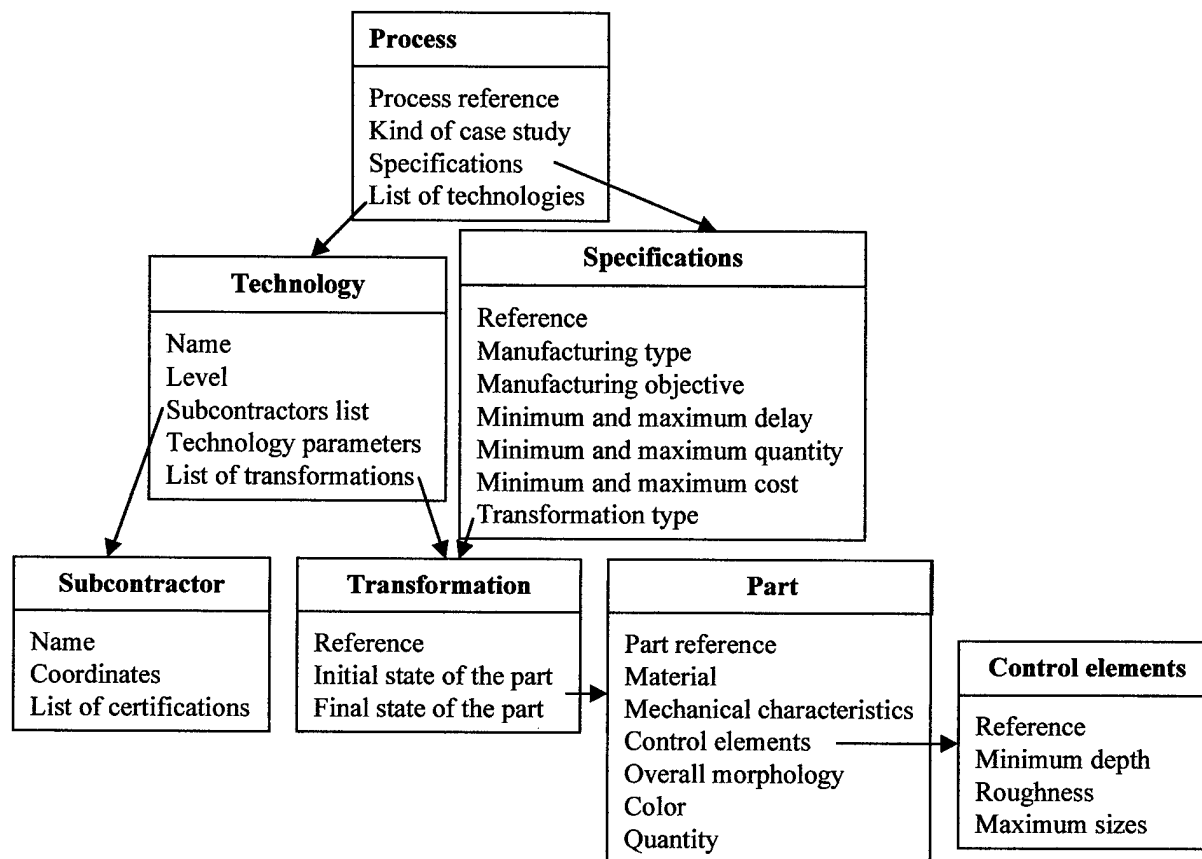


Figure 2. Some elements of semantic net

From a given specification, the system extracts the processes from the knowledge database. This is possible because each technology and each rapid product development process have also been individually modeled, with all their features and fundamentals. Thanks to this structure and based on conceptual models (figure 2), reasoning is computed in order to generate alternatives of rapid product development processes.

Because of the necessity of evolution, the proposed system has different functionalities in order to introduce knowledge elements based on the specifications corresponding to the different alternatives of rapid prototyping processes. Some of these functionalities have been integrated in the user module of the system.

The first one is the capability to specify the specifications of the part that has to be manufactured. This module is necessary in order to help the user to define his needs.

The second one is to select a process from the knowledge database. This is the basic functionality that allows the generation of all the different possible processes.

The third one is to generate all the processes, which correspond to the defined specifications.

The fourth one is necessary for the selection of the best process, with regards to the specifications constraints, as quality, aspect, cost, delay, reliability, etc...

The fifth one is to generate new processes when introducing new technologies. This functionality is based on the state notion. The idea is simple. A technology transforms a part from an initial state to a final state. The introduction of a new given technology consists in finding the other technologies, which deliver final states that correspond to the initial state of this given technology. It is also necessary to identify the technologies that need an initial state, which corresponds to the final state of this given technology. Consequently, the immediate consequence is the existence of new process alternatives.

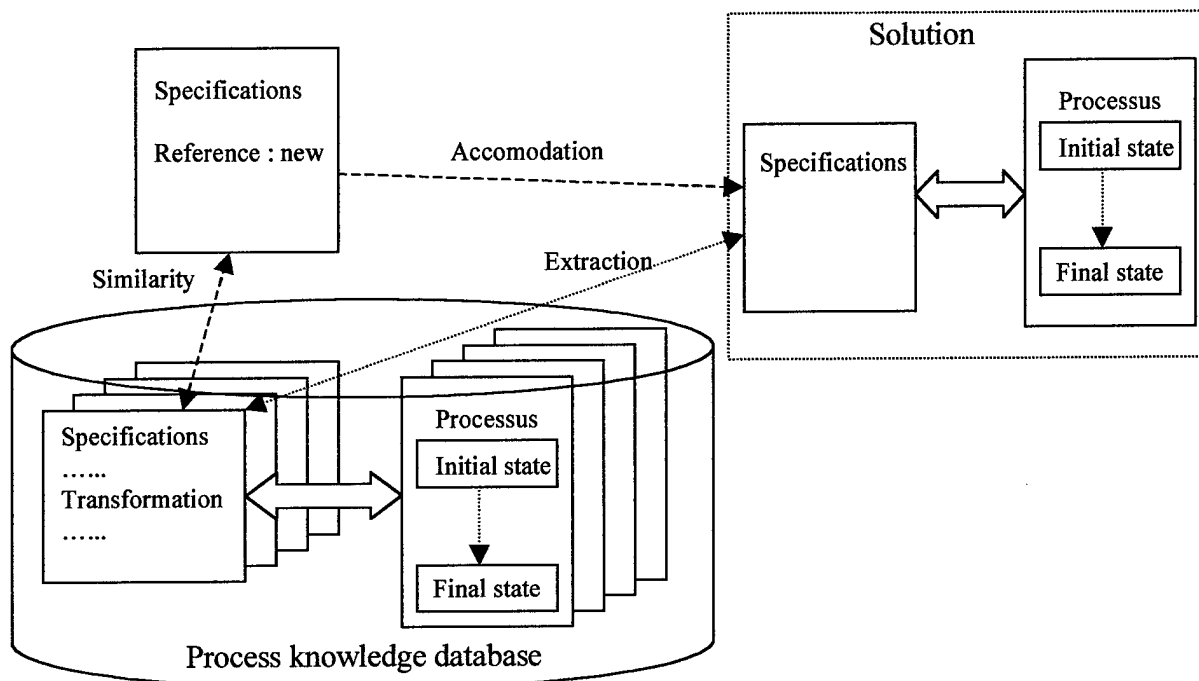


Figure 3. Extraction of a process from the knowledge database

4. EXPERIMENTATION

The experimentation module has been developed from the initial analysis work of A. Deglin (Deglin, 1998). This first approach was oriented to a graph representation of all the processes. Afterwards, V. Trousselard (Trousselard, 1999) tried to generalize this approach and began testing case-based reasoning approach (Pankakosky and al, 1998) instead of graph analysis. He also used a very specific approach specially dedicated to knowledge capitalization, from Kade-Tech company.

The present version of the environment is mainly dedicated to plastic parts. All the technologies and about eighty different processes have been modeled. The chosen compatible database is Oracle. Some industrial specifications have been entered for test in order to verify the efficiency of reasoning rules. The first results are very positive and the next version should take into account many other processes, especially for metallic parts and economical tools.

The current step of the work is the capitalization of all metallic part processes, and some complementary elements on plastic parts. Of course, due to new technologies and new needs, all technology evolutions are memorized and possible processes are extended, more especially for ceramics.

The system will also take into account specifications for tools instead of parts. Of course, tools processes are already integrated in global process generation for parts. In the figure 4, one should understand technology as one single technology (as stereolithography) or as a subprocess (a sequence of technologies, like stereolithography and vacuum casting).

Based on such approach, all the possible processes, which allow obtaining the final part from the initial model (part initial state), are selected and presented to the user. Then, the final step is the selection of the best process by taking into account mono or multi-criteria optimization. It is important to remind that each

technology represented in the database corresponds to an effective machine and company, with actual delays, costs, quality, etc...

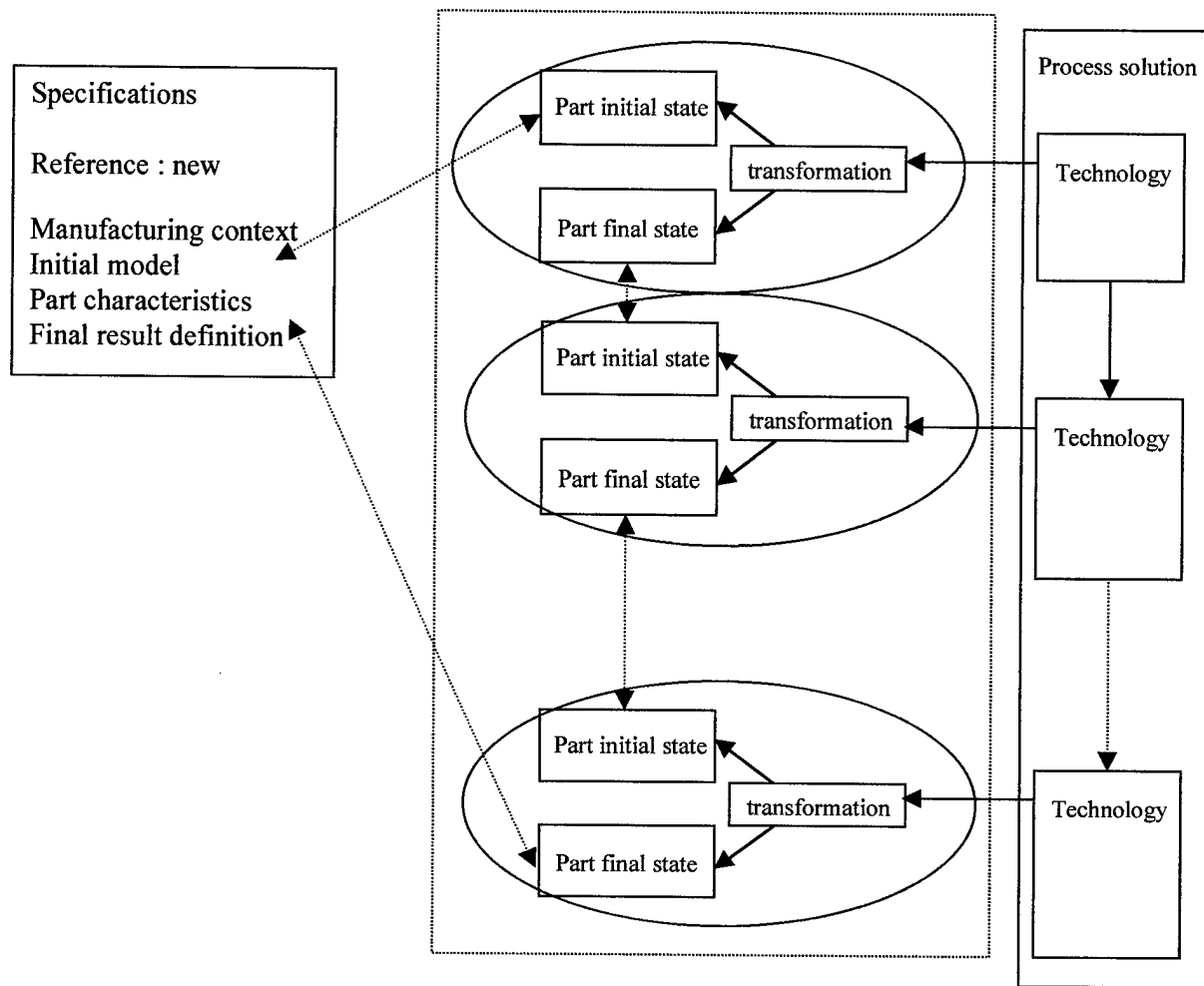


Figure 4. Elements of representation of the chosen process

5. CONCLUSION

The objective of the proposed knowledge-based environment is to capitalize knowledge and know-how on rapid product development processes (Bernard (coordinator), 1998). The first step is to model the state of the art, thanks to bibliography and to interviews of different experts (users, researchers, service bureaus, independent experts, etc...).

As mentioned before, such a system should be generalized for all the technologies used by a company and not only rapid prototyping processes. Before this project, the experience in CRAN laboratory was mainly oriented to computer-aided process planning for milling (2 ½, 3 and 5 axis), and the graph analysis algorithms have already been used. Case-based reasoning is being tested for rapid product development application. It is not sure that it will be the final choice for alternative process generation. During the next months, other approaches will be tested in order to optimize computing time.

Another important aspect will be the possibility to interface web sites of subcontractors and cost evaluation applications for all the modeled technologies, in order to be able to generate realistic costs and delays, for a given specifications. This will be proposed to different companies and service bureaus. The first operational version should be presented on July 2000.

6. ACKNOWLEDGEMENTS

The author would like to acknowledge different persons. T. Fouquerel (from Aérospatiale) for the industrial validation of the idea. The two students who work on this project, A. Deglin and V. Trousselard. The different experts (especially T. Deschamps from Resine Technologie and Y. Seeleuthner from Ateliers Cini) for their availability during the interviews. Finally, Kade-Tech company for their help in Kadviser (Knowledge based system) use.

7. REFERENCES

- (AFPR, 1998) AFPR, *Proceedings of the 7th European Conference on Rapid Prototyping*, November 1998, Paris, France.
- (Bernard and al, 1998) A. Bernard and G. Taillandier. *Le prototypage rapide*, 1998, N° ISBN 2-86601-673-4, Editions Hermès, Paris, France.
- (Bernard (coordinator), 1998) A. Bernard (Coordinator), *Développement rapide de produit*, International Journal of CAD/CAM and computer graphics, Vol. 13, n°4-5-6, December 1998, N° ISSN 0298-0924, Editions Hermès, Paris, France
- (Bernard, 1999) A. Bernard, *State of the art on reverse engineering*, Time-Compression Technology (TCT'99), October 1999, Nottingham, UK (to be published).
- (Deglin, 1998) A. Deglin, *Analysis of needs for CAPP system development in rapid product development field*, internal report, CRAN, October 1998, France.
- (Pankakosky and al, 1998) J. Pankakosky, E. Elranta, M. Luhtala, J. Nikkola, *Applying case-based reasoning to manufacturing systems design*, Internal report, Institute of Industrial Automation, Helsinki University of Technology, 1998, Helsinki, Finland.
- (SME, 1999) SME, *Proceedings of Rapid Prototyping and Manufacturing (RP&M'99)*, April 1999, Chicago, USA.
- (Trousselard, 1999) V. Trousselard, *First version of a CAPP system for rapid product development process generation*, final report, ESIAL, June 1999, France
- (Varady and al, 1997) T. Varady, R. R. Martin and J. Cox, *Reverse engineering of geometric models - an introduction*, Computer Aided design, 1997, vol. 29, n° 4, pp. 255 - 268.
- (Wolhers, 1999) T. Wolhers, *State of Industry report*, 1999
- (Zhang and al, 1995) S. G. Zhang, A. Ajmal and S. Z. Yang, *Reverse engineering and its application in rapid prototyping and computer integrated manufacturing*, Proceedings of Computer Applications in Production and Engineering (CAPE'95), May 1995, Beijing, Chine, pp. 171 - 178.

A Methodology to Create STL Files from Data Point Clouds Generated with a Coordinate Measuring Machine

Irene Tyvaert, Universite de Technologie de Troyes, France

Prof. Georges Fadel, Clemson University

Prof. Emannelle Rouhaud, Universite de Technologie de Troyes, France

Abstract

Industries have always had the need to reproduce objects especially when drawings are no longer or were never available (reverse engineering). Coordinate measurement machines, whether touch- or laser-based, enable users to generate a point cloud representing a surface. The aim of this work is to develop a methodology and its translation into a software program to generate closed STL file models from such data point clouds.

The first step in the research is to develop an algorithm to merge several surfaces (data point clouds) from a real object in exactly the same reference frame. Then, a tessellation program is implemented to create the STL file considering computational costs and minimizing the number of triangles while maintaining the accuracy of the original part.

The implementation is illustrated on two examples and conclusions are drawn.

Keywords: Reverse Engineering, Rapid Prototyping, Tessellation, CMM, and STL

Introduction

Reverse engineering is not a novel idea. It was probably born out of the need to reproduce either virtually or physically some human organs for medical applications. In fact it is difficult to accurately draw bones or organs with CAD software; accurate models from in-situ organs were represented in 2D slices obtained from CAT Scan images [1]. Physicians wanted to be able to test surgical procedures before operating on a patient, and thus needed an accurate three-dimensional representation of the local environment. Reverse engineering was what they hoped for. Mechanical industries also had a vested interest in such a technology because some CAD models were often unavailable or unusable for parts, which had to be duplicated or modified [3]. With the advent of coordinate measuring machines (CMM), the ability to measure a part and obtain a point cloud became reality. That point cloud was and still is mainly used for measurement and validation purposes. However these machines use contact probing digitization of a part's surface and thus cannot work on some fragile parts. Furthermore, they are relatively slow, and require careful programming to accomplish the desired task. Non-contact sensing techniques emerged later, mostly laser based. Those laser techniques rely on a laser beam projected onto the part's surface while optical sensors receive the reflected beam. The digitization is very fast and does not depend on surface contact. Unfortunately, the results are affected by the reflective quality of the surface and shadows or scratches on the surface can have a significant effect on measurement accuracy. Moreover, the price of these machines is important. For these reasons, and because many industries have a CMM in house to control the quality of their production, the CMM is the main source of data considered in this paper for reverse engineering applications.

Rapid prototyping is a technology that has evolved to enable users to produce directly a physical artifact from CAD data. For this research, our goal is to enable a link between a coordinate measuring machine and a rapid prototyping machine, thus realizing in effect a three-dimensional duplication machine (stereo-copy). This technology uses the STL format; its generation is easier than any other standard CAD formats (IGES, STEP). An STL file contains only coordinates of vertices in 3D space that are sorted to form triangles and to express on which side of the triangles the material lies (surface normal).

Coordinates Acquisition with a CMM

Several parameters control the quality of the coordinates acquired in a CMM. In this section, we describe some of the machine characteristics. The CMM machine used in our implementation is a Brown and Sharpe MicroVal PFX with the Micromasure IV version 3.1 control software.

Probe type:

The probe type and geometry are key to the quality of the measurements. The selection of the most appropriate probe is usually based on experience. If the probe tip is too big, namely larger than the radius of curvature of a feature on the part to measure, the result will be inaccurate. Moreover, the point clouds generated if the machine is used to measure absolute point coordinates instead of relative distances may not be accurate since the probe geometry has to be taken into account. CMM manufacturers provide a compensation mode to correct for the probe geometry (Figure 1 [4]).

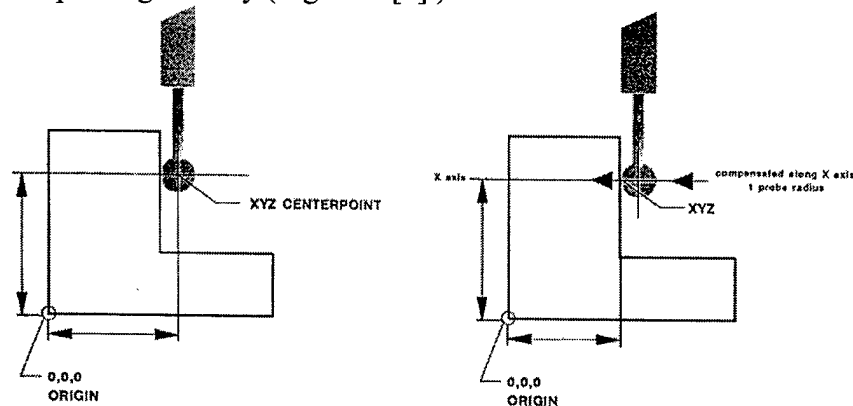


Figure 1: Uncompensated and Compensated Measurements

For the reverse engineering application, absolute data measure is required, and the compensation factor is essential. It is however very difficult to acquire correctly the coordinates of the points touched by the probe because the standard procedure is to use a standard offsetting method with the ball radius along the probing direction. One can see that the results are not always correct and depend on the normal vector angle (Figure 2 [4]). Some errors are not negligible [5](Table 1[4]).

Two other probe parameters are critical. The first one is the rigidity of the stylus. The smaller the probe, the more the stylus is subject to bending. This issue is very important if the fast speed acquisition mode is chosen. The second parameter is related to the geometry of the stylus. Some geometries cannot be used to acquire data if the part geometry interferes

with a feature on the part. Thus, the data acquisition aspect requires experience and know-how in order to generate usable data.

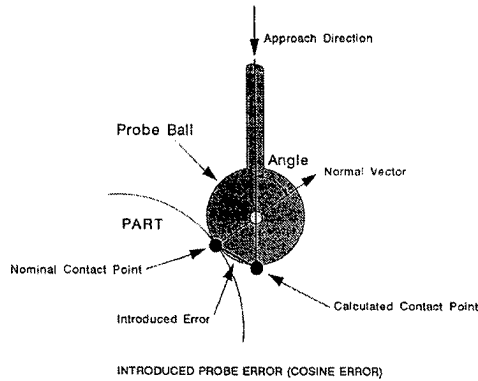


Figure 2: Error from the Compensation Procedure

Probe diameter (mm)	0.50	1.00	2.00	3.00	4.00	6.00
Angle to normal (deg)	Magnitude of error introduced by not probing normal to surface					
1.00	0.0000	0.0001	0.0002	0.0002	0.0003	0.0005
2.00	0.0002	0.0003	0.0006	0.0009	0.0012	0.0018
3.00	0.0003	0.0007	0.0014	0.0021	0.0027	0.0041
4.00	0.0006	0.0012	0.0024	0.0037	0.0049	0.0073
5.00	0.0010	0.0019	0.0038	0.0057	0.0076	0.0115
7.50	0.0022	0.0043	0.0086	0.0129	0.0173	0.0259
10.0	0.0039	0.0077	0.0154	0.0231	0.0309	0.0463
15.0	0.0088	0.0176	0.0353	0.0529	0.0709	0.1058
20.0	0.0160	0.0321	0.0642	0.0963	0.1284	0.1925

Table 1: Values of the Acquisition Error Depending on the Probe Diameter

Measurement procedure

To understand the tessellation algorithm, it is necessary to understand how the CMM proceeds to obtain the data point cloud.

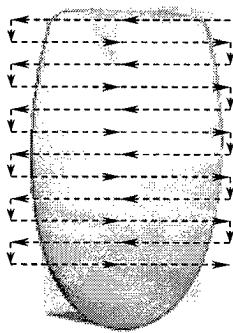


Figure 3: The way of scanning

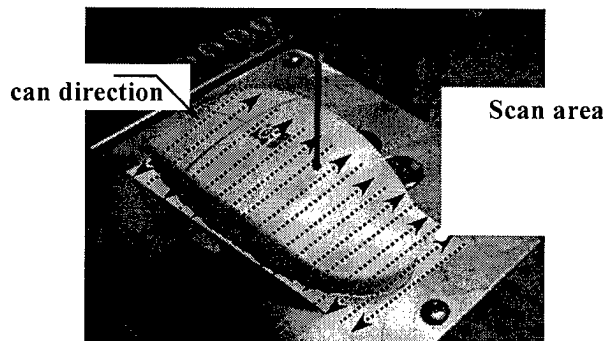


Figure 4: Definition of the parameters for scanning

The MMIV software scans the part through a point grid (Figure 3) and results in a regular point data distribution. The number of points for each line is constant. The process of scanning requires the definition of the limit of the grid and of the number of points per line (Figure 4). The main problem is to define the best measurement procedure to capture all the details without unduly increasing the scan time.

STL file generation

After the digitization of the part is completed, the STL file can be generated from the data point clouds. The STL format, introduced by 3D-Systems©, represents a geometry with a series of triangles. Each triangle has exactly three adjacent triangles (one along each edge) and is assembled in a surface defining a closed volume.

Three main topics are developed in the following paragraphs to explain how the STL file is created from a list of points representing one surface. The resulting algorithm is summarized in the flowchart of Figure 5.

Tessellation

The process of tessellation needs to follow the appropriate rules to generate properly triangular surfaces conform to the STL format.

The tessellation algorithm developed in this paper uses the structure of the CMM data. Indeed, sorting of the data points depends on the grid, and the tessellation works on two lines of data points at a time. (Figure 6). The tessellation algorithm described in the next paragraph for two data lines, is illustrated in the flowchart shown in Figure 7.

In Figure 6, tessellation is performed from the left to the right. The two points located on the left side (A, 1) are initially considered, each of these points being on their respective line. Triangle formation depends on the choice of a third point, which can either be B or 2, both of these points being located immediately to the right of the two points considered. The shortest diagonal dimension (A2 or 1B) will determine the point to be selected. Once all three points are determined, the triangle can be built. The selection sequence starts over and the two initial points to consider are located on different lines and on the outer right side of the last generated triangle (B, 1).

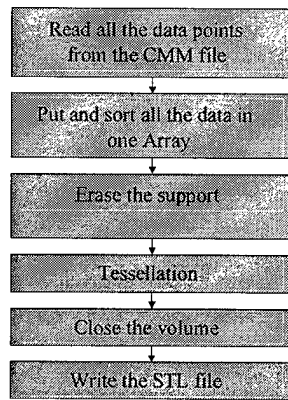


Figure 5: Main algorithm

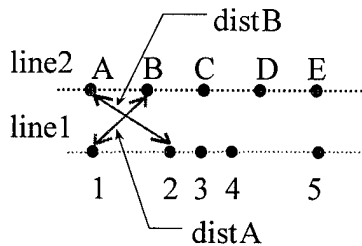


Figure 6: Tessellation with 2 Data Lines

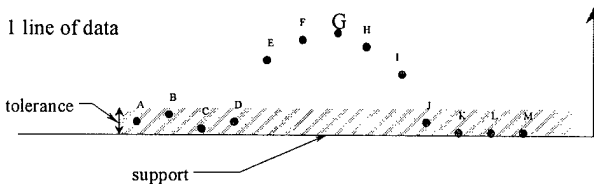


Figure 8: Determining where the Support is.

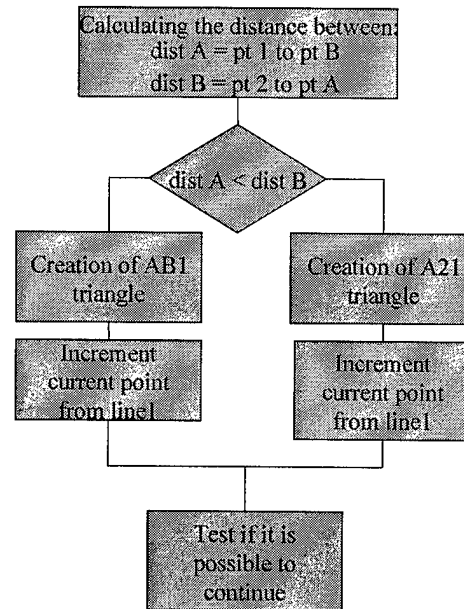


Figure 7: Tessellation Algorithm

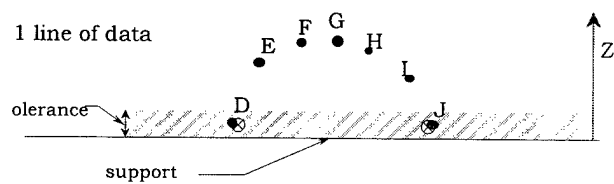


Figure 9: Suppression of the Support

Erasing the ground

When using the CMM, the supporting platform of the part needs to be digitized in order to capture all the required details. Thus, the proposed algorithm consists of defining the points of the part without the support points. Since the support is flat and at the bottom of the part, a custom height is set to delete all the points included within this tolerance, starting from the lowest point (Figure 8). The major constraint is that two points must be kept to represent the ground during the tessellation (Figure 9). The height of the part will not be accurate if this process is not used. Furthermore, the program deletes the complete line of points if they all belong to the support. Therefore, the tessellation is performed only on the points that belong to the part.

Closure of the volume

The result obtained so far represents a surface and not a volume, and the last operation must close the surface to correctly define the STL file. For a convex part, “three” surfaces are ignored at the end of the tessellation since:

- The CMM only scans the top surface (no data about the bottom of the part)
- The tessellation proceeds only slice per slice in the YZ-plane

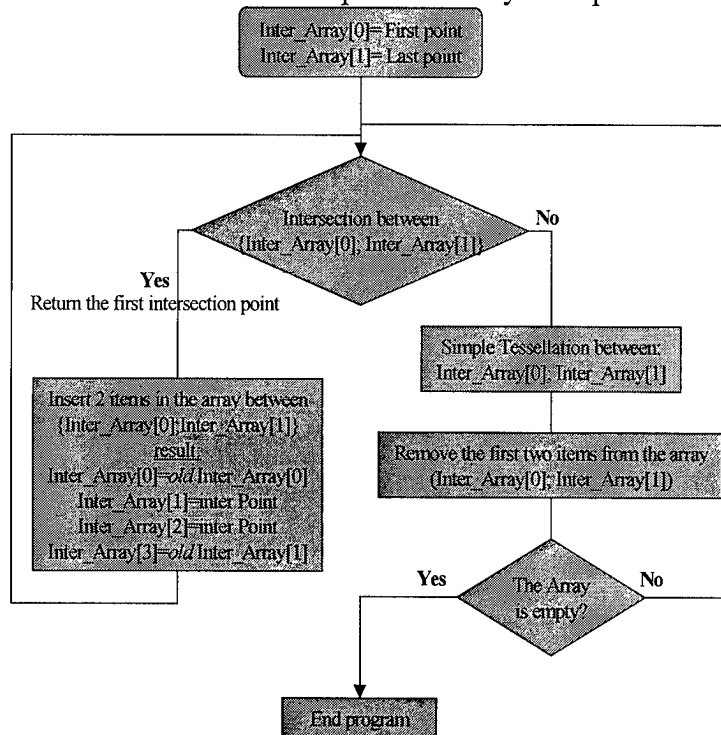


Figure 10: Edges Tessellation Flowchart

Thus, the under-side and two sides (right and left in this case) are not digitized, and without these surfaces, the volume is not closed. Therefore, it is necessary to implement another algorithm, to generate the missing surfaces.

The tessellation for the under surface is simple and proceeds like the previously described procedure (Figure 11). Edge tessellation is more complex. The form of the data points does not follow a set pattern (Figure 12). The algorithm is explained in the flowchart shown in Figure 10.

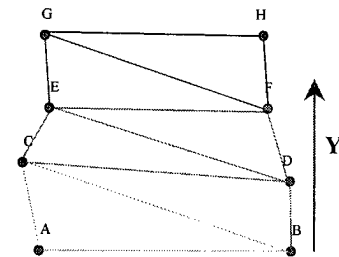


Figure 11: Back Tessellation

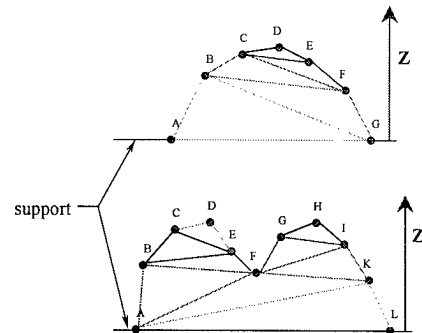


Figure 12: Edges Tessellation

Multiple Faces

Having scanned the required surfaces, a method is needed to merge them.

Common space

The main problem is to find a common space. Each surface acquisition has its own referential. Therefore, merging two surfaces without common referential is very difficult. The idea is to use certain scanning parameters. Indeed, defining the axis and origin, which are needed before the digitization, can be used to correctly orient the surfaces. Upon definition of a referential with the CMM, all rotational degrees of freedom are locked.

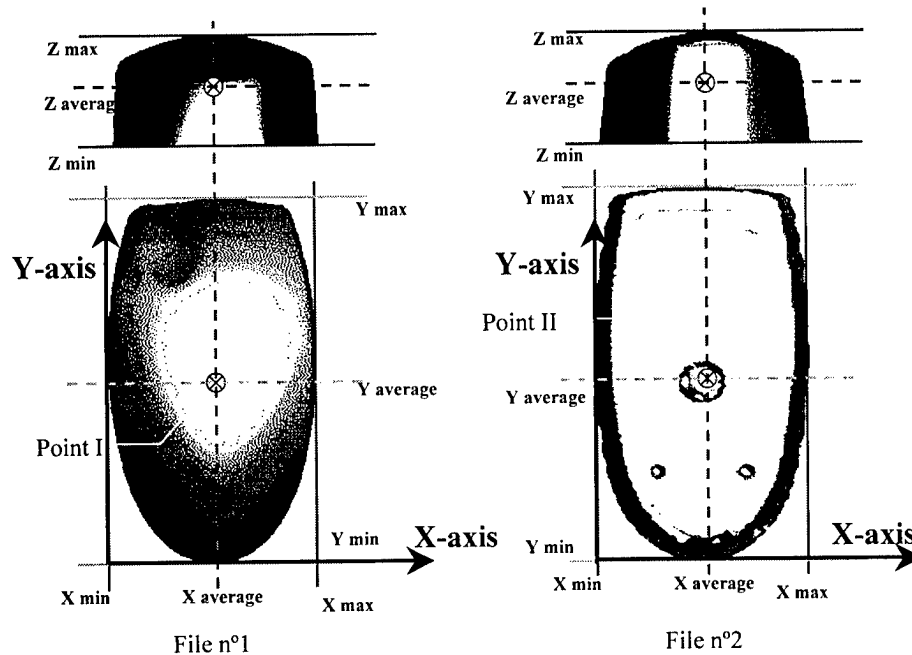


Figure 13: Operations to Obtain the Common Space

In fact, these references determine unique X and Y axes for all digitization. Thus, if the definition is correct, surfaces are well oriented with respect to each other but not yet centered.

The next step is to translate the surface to a same origin. To find a common point (Point I and Point II), it is assumed that the overall dimensions of the part remain unchanged, and the middle of the largest dimensions in X and Y provide the reference point needed (Figure 13).

Merge method

The merging operation depends on the angle of the added surface. The most difficult part of this operation is to correctly sort the data points. In fact, the tessellation algorithm presented in section "*Tessellation*" which sorts the data points, is also used here.

The simplest method is to merge the top and under surfaces. The junction and stitching is indeed straightforward since both surfaces have almost the same area and only a few common points. However, the edge surfaces represent a new view of the part, which makes it difficult to identify common points.

For the back surface (180° rotation), the algorithm matches the points using the Z-axis level (Figure 14). For all other edges, the distances between points from both surfaces (Figure 15) are calculated to determine the order of the points.

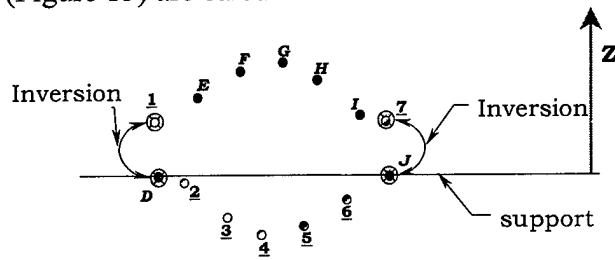


Figure 14: Merging with 180° Surface

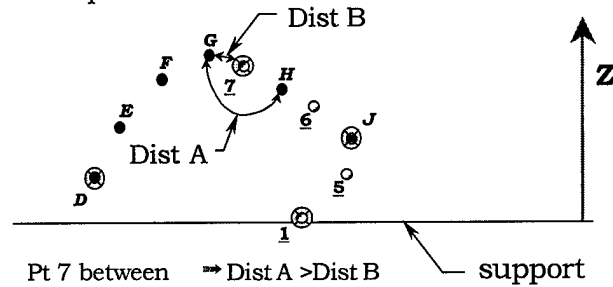


Figure 15: Merging with 90° and -90° Surfaces

Problems:

This algorithm has some limitations. During the merging operation, all the points from the direct part (without the support) are used even if they are inaccurate (point on the support closest to the part and retained by the algorithm). Therefore, some points may be eliminated during the stitching.

The other limitations come from the tessellation, which works only with two lines of data points at a time. Due to this characteristic, the merging of two surfaces can only occur when the same number of lines and thus the same scanning grid for both surfaces are used. This aspect prevents optimizing the scanning time that can result from employing different grid sizes for surfaces with simple geometries.

Improvement of the STL file

The research presented utilizes a CMM machine to digitize a part. In order not to miss any geometrical detail, a large number of measurement points are normally acquired. If all the points are used in the STL file generation, the size of this file can easily become too large. In fact, keeping lots of data points in nearly planar regions is redundant. Removal of data points in these regions would not affect the accuracy for rapid prototyping machines [6]. There are different methods to solve this problem. The first consists of building a decimation algorithm meant to work directly on the STL file. The second is based on decreasing the number of points before the tessellation is performed. This latter alternative being the simplest and the fastest, was retained and is detailed below.

Deleting redundant points

To determine which points are essential, the program uses a user input acceptable tolerance height h between two vectors (EF and EG in Figure 16). The variable h is obtained with the calculated angle β . If the calculated h is less than the prescribed one, the middle point is eliminated.

This method has some limitations. In fact the decimation works only in one direction. Also, the reduction of points is not optimal, and the neighboring lines are not taken into consideration. Nevertheless, with this method, the tessellation algorithm can still be used and the processing remains fast.

It was observed that on average about 80% of the points were eliminated through linear decimation thus contributing to a significant reduction of the STL file size.

Furthermore, the decimation can result in improved accuracy. The use of the tolerance can lead to smoothing out measurement inaccuracies and eliminating minor surface irregularities.

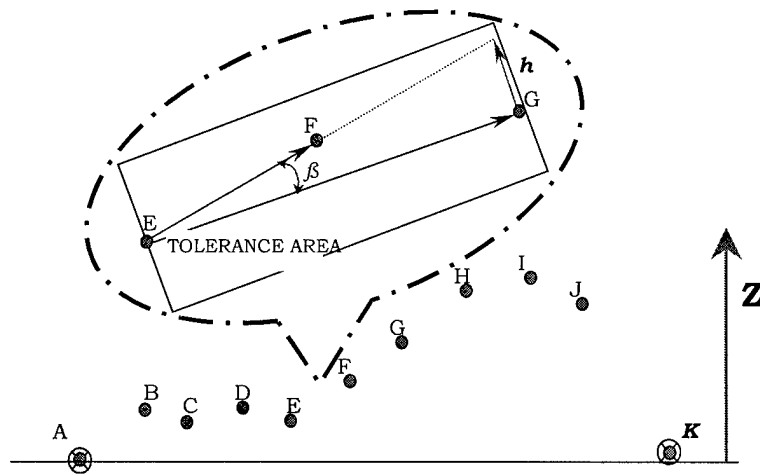


Figure 16: Determination of Unnecessary Points

Applications

A *Test part* was designed in Pro/Engineer and built with a Rapid Prototyping machine (SLA 250). For ease of comparison, simple geometrical shapes were used. The *Test part* was digitized using different grids and decimation was used to reduce the triangle count in the STL file. Measurements compared the built part to the CAD model, however just on the top surface since it was impossible to have very good accuracy along the edges.

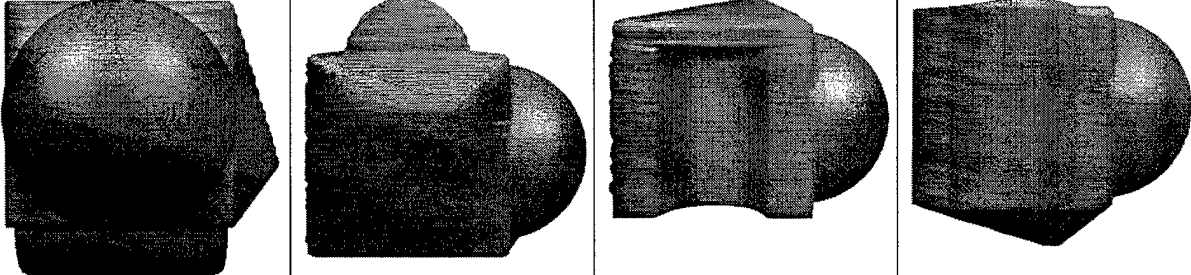
							
Forms	Value (mm)	Grid 71*70		Grid 56*55		Grid 31*30	
Cylinder	30.00	30.02	+ 0.02	30.24	+ 0.24	28.7	- 0.3
Sphere	24.98	24.92	+ 0.08	24.89	+ 0.09	24.879	+ 0.101
Hollow cylinder	30.00	15.01	+ 0.01	~ 14.98	- 0.02	14.92	- 0.08

Table 2 : Errors as a Function of Grid Size

To have the perfect part it is necessary to consider several parameters:

- The scanning grid: The number of points can improve the surface and the accuracy of the copy part. Over sampling the surface generates noise observable on the tessellation. Errors occur when the tip travels along the edges and touches the side of the sphere. Furthermore, the program that computes the compensation due to the stylus geometry does not work very well, so uncontrollable errors were present.

- The decimation method can help to achieve a better accuracy. The decimation reduces the number of points and improves the flat surfaces. Moreover, decimation improves the junction of two surfaces. For example, with too many points, it may be difficult to determine the corners of the part. Using decimation, the corners appear like chamfers or sharp edges.

The problem of good accuracy depends on the user's intention. In fact, the choice of parameters should depend on the surface characteristics. For cylindrical surfaces, it is better to choose a small grid size and a small decimation tolerance. For a plane, the grid needs to be fine only if the contour of the part is important.

An improvement in accuracy (specifically the contour) can be achieved with the merge function. After the merging operation, only points from the part are kept, resulting in a more accurate STL file. Unfortunately, to use this function, some special supports need to be built to maintain the part in position. The example of the golf club head below illustrates the merging function's performance.

The other important observation is that the CMM is not aware of the space spanned by the part for digitization. The user needs to set grid size and limit points to allow the machine to reach the part's edges. Therefore, the contour and the quality of the copy part depend on these parameters. In the cases presented, the grid size was arbitrarily set to keep exactly the same number of points. Therefore, sometimes the results were better with a larger grid size. For the test part, the accuracy obtained was within 0.2 millimeters.

Results with the merge method

For a second example, a golf club head was chosen as a model. Since both sides are relevant, this part is a good application for the merge function.

One scan was applied to each surface. The creation of an assembly was necessary to digitize accurately the opposing surfaces. Furthermore, the setting of the digitization software had to be the same, otherwise the merging would fail. Several tests were performed with different grid sizes and different tips. The best results were obtained with a 70 * 70 points grid and a 3 mm tip. The entire digitizing process took 12 hours per surface. At the end of the process, the part obtained and shown in Figures 17 and 18, can be considered a good copy of the original part. Nevertheless, some problems are present where both surfaces meet each other. Furthermore, due to the height of the part, the digitizing process used a long tip to enable data capture. As a consequence, some details of the groove were lost.

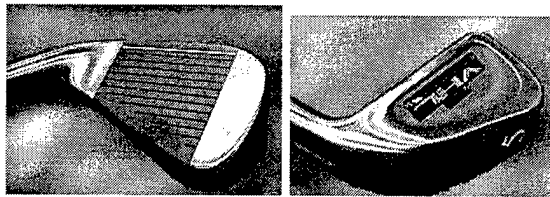


Figure 17: Original part



Figure 18: Copy of the golf club

Conclusion

The work presented in this report is focused on the development of a methodology and program, which allow direct STL files generation from real parts, using CMM for data acquisition.

Explanations are provided on how the software works and which parameters the user needs to set to build a good copy. The research also proposes a method to merge different surfaces. This new approach shows that it is possible to use a CMM to completely digitize a part, although the probe may not be able to acquire all the different surfaces in one sequence.

A decimation algorithm is described to simplify and decrease the size of STL files. Several tests show that it helps to obtain more accurate results.

Nevertheless, reverse engineering smooth surfaces like those of the golf club head is more difficult than simple geometries such as those of the test-part. Furthermore, it is almost impossible with this technique to represent corners or perfect planes with only the points acquired by the CMM. Although the results proved to be satisfactory, inaccuracies between original and computerized models were mainly due to a malfunction of the compensation program of the CMM.

Future work

Future work should be aimed at improving and obtaining a complete reverse engineering procedure using the CMM as a primary data acquisition routine. First of all, a more detailed study needs to be achieved to demonstrate the accuracy of the results when using the compensation program. As mentioned in this report, this function did not work properly in our software version.

The program does not consider hollow areas on the original part. Also, parts with holes are not correctly processed. Furthermore, the decimation program works only in the XZ direction. Further reduction in size of the STL file could be obtained if the decimation was also performed in the YZ direction.

During the tessellation, a method could be proposed to add some points when necessary. For example, if the angle displayed in Figure 16 is too important, a new point resulting from the intersection of lines EF and GH created with the points located before and after the points F and G should be considered. The case of the corners is an example.

These proposed improvements along with the continuous growing interest in reverse engineering would then make it possible and very interesting to propose this new concept to companies without significant financial investments.

References

- [1] Harry Hutchinson, "*Relief for weary bones*", Mechanical Engineering; Vol. 121, No. 6, pp 54-57, June 1999
- [2] Kwan H. Lee and H. Woo; "*Use of reverse engineering method for rapid product development*"; Computers Ind. Engineering Vol. 35 pp. 21-24 1998
- [3] William B. Thompson, Jonathan C. Owen, H. James de St. Germain, Stevan R. Stark and Thomas C. Handerson; "*Feature-Based Reverse Engineering of Mechanical Parts*"; IEEE Transactions on Robotics and Automation, Vol. 15, pp 57-66 1999
- [4] "*MMIV Software Reference, Manual*"; Brown & Sharpe Mfg. Co.; Training Brief #15-2, 1994

[5] C. Menq and F. L. Chen; "*Curve and Surface Approximation from CMM Measurement Data*"; Computer Ind. Engineering; Vol. 30, No. 2, pp 211-225, 1996

[6] Y. H. Chen, C.T. NG and Y.Z. Wang; "*Data Reduction in Integrated Reverse Engineering and Rapid*"; Computer Integrated Manufacturing, Vol. 12, No 2, pp 97-103, 1999

Precision LCVD System Design with Real Time Process Control

Daniel L. Jean, Chad E. Duty, Brian T. Fuhrman, and W. Jack Lackey
Rapid Prototyping and Manufacturing Institute
Woodruff School of Mechanical Engineering
Georgia Institute of Technology
Atlanta, GA 30332

Abstract

A Laser Chemical Vapor Deposition (LCVD) system was designed using a fixed 100 Watt CO₂ laser focused on a moveable substrate. Temperature and height measurement devices monitor the reaction at the point of deposition to provide feedback for controlling the process. The LCVD system will use rapid prototyping technology to directly fabricate fully three-dimensional ceramic, metallic, and composite parts of arbitrary shape. Potential applications include high temperature structures, electronic/photonic devices, and orthopaedic implants.

Introduction

The Laser Chemical Vapor Deposition^{1,2} (LCVD) process consists of using a laser as the heat source for a CVD reaction to selectively deposit one or many materials. The basic mechanism of pyrolytic LCVD is as follows: 1) a chamber is filled with reactive gases, 2) a laser enters the chamber and heats a small spot on a substrate inside the chamber, 3) the gases react at the spot and deposit the desired material, and 4) either the laser or the substrate is moved to "draw" a line of deposition. Many lines can be drawn to create a three-dimensional part. Different materials can be deposited by simply using different reactive gases in the chamber.

Various materials have been deposited using LCVD, including C, B, Si, SiC, Si₃N₄, Al₂O₃, TiN, TiC, Ni, Ag, and various other metals and ceramics.^{3,4} LCVD was originally developed to draw conductive lines on microelectronic circuits, and it has been used to grow fibers, coatings, and objects and structures.^{5,6,7} The structures created include scaffolds and micro-springs.^{8,9}

The LCVD system will be combined with rapid prototyping technology to enable fabrication of precise metal and ceramic parts of arbitrary shape, thus advancing the current state of RP technology. Currently, RP systems are limited by material choice and part accuracy. The ceramic RP systems use a nozzle to deliver a powder or slurry, so the resolution of the system is limited by the nozzle diameter. Both ceramic RP parts and selective laser sintering (SLS) parts require post-processing steps such as high temperature curing to reduce porosity, which also reduces part accuracy. The resulting parts often still contain significant porosity, leading to poor mechanical properties.

The resolution of the LCVD system is limited by the laser spot size, which can be 1 μ m or smaller for finely detailed parts. LCVD is an atom by atom deposition process, so the final

parts approach 100% dense without the need for a sintering step. Since the reactants can be easily changed to deposit different materials, the LCVD system is capable of multi-material deposition within the same part.

Physical Description of System

The LCVD system¹⁰ is designed to produce fast and accurate patterns of deposition. A 100 watt CO₂ laser is focussed onto a graphite substrate to provide the energy for the pyrolytic LCVD reaction. The substrate's position is controlled by three precision stages oriented in the Z, X, and θ directions (figure 1). This X- θ stage orientation enables high speed complete coverage of the substrate (using a spiral pattern) without the high reversal forces associated with an X-Y positioning system (figure 2). The two linear stages have a resolution of 0.1 μm , while the rotational stage has an encoder with 4000 lines per revolution corresponding to a resolution of 0.09 degrees. The limits of the stage travel allow for a cylindrical build envelope 3 cm in diameter by 3 cm high. The stages are housed in a chamber directly below the reaction chamber. The two chambers are separated by a flexible bellows that allows substrate movement without exposing the stages to the corrosive CVD gases (figures 3).

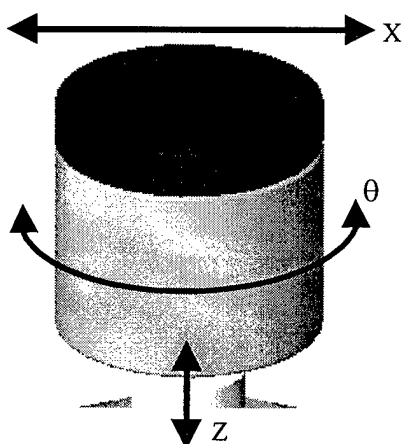


Figure 1. Rotating-translating stage.

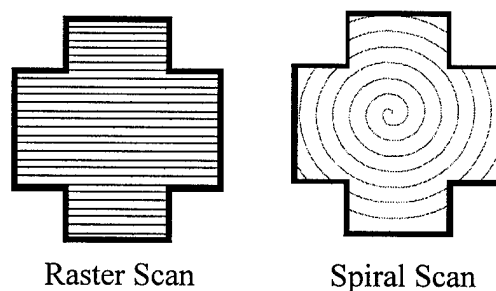


Figure 2. Raster scan and spiral scan for laser paths during deposition.

To increase the reaction rate, the reactive gasses are introduced directly into the reaction zone via a nozzle. The nozzle replenishes the reactants at the reactive zone much faster than conventional diffusion. This increase in available reactants will greatly increase the deposition rates over diffusion alone. Morishige and Kishida reported an increase in deposition rate of over an order of magnitude by using a nozzle to deposit lines of gold¹¹.

To further increase deposition rates, the substrate is heated from two sources. A Kanthal wire resistive heating element globally heats the substrate to a temperature just below the deposition temperature. Additionally, the laser is used to locally heat a small spot on the substrate to the reaction temperature. The global heating will reduce the thermal stress in the

deposit due to a smaller temperature gradient at the laser spot. It will also speed up the process since the laser has to raise the substrate's temperature by only a small portion of the total heating required.

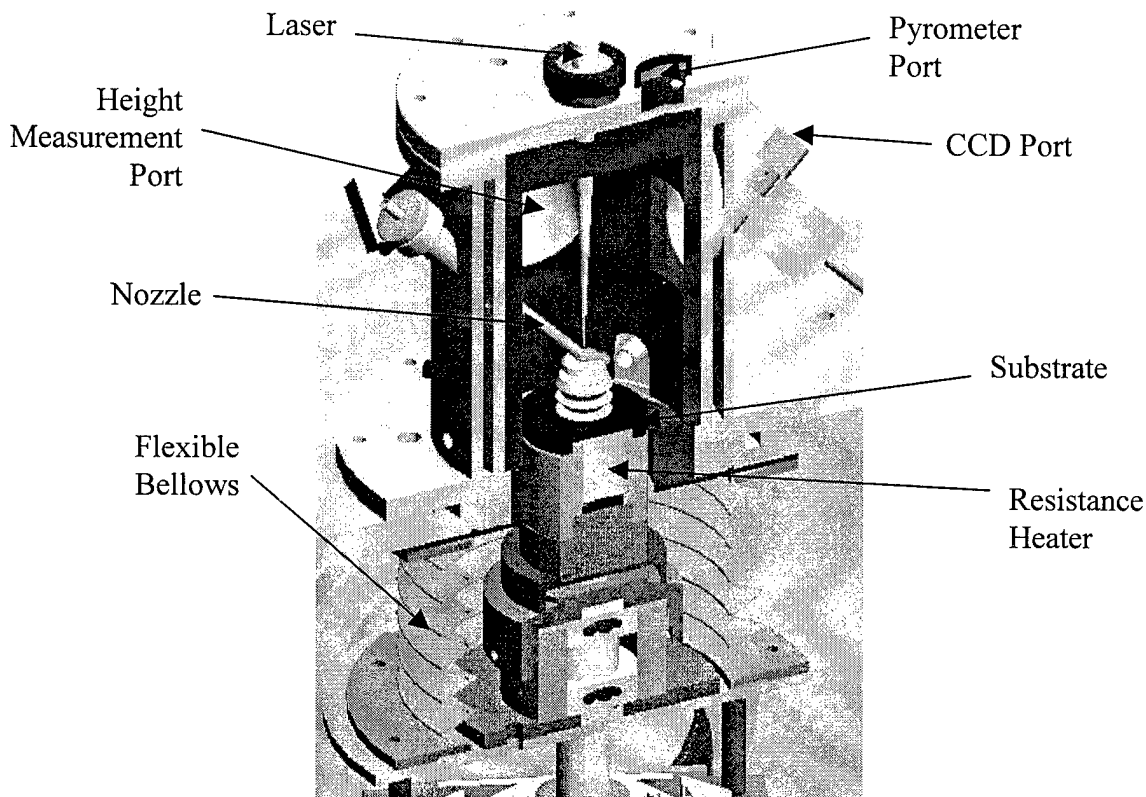


Figure 3. LCVD upper reaction chamber.

Need for Process Control

To create precise parts, the individual lines of deposition must have the same height and width. Process parameters such as temperature and deposition height will be monitored to accomplish the required uniform deposition.

Since deposition rates are highly dependent on temperature, there is a narrow temperature region required for a uniform deposition rate. The deposition temperature varies during processing due to several factors. One possible variation in deposition rate occurs when the deposit is more thermally conductive than the substrate. As a line of deposition is drawn, the new deposit will conduct more heat from the laser spot than the substrate alone, so the laser spot temperature will decrease. The deposition will be smaller with the decrease in temperature, and less heat will be conducted away from the laser spot, resulting in a higher temperature. A delayed feedback loop occurs that results in a periodic deposition, observed by Y. C. Du *et al.* while depositing lines of polycrystalline silicon¹² (figure 4).

The temperature will also vary due to history effects. A line deposited adjacent to a previous deposition may have a higher temperature due to the residual heat from the previous deposition. Changes in reagent product concentration and flow rates will also cause changes in deposition rates. The flow of reagent to the deposition spot will change depending on the surface features of the part being made. Certain regions on the part will have specific features, different from other areas on the part. The gas flow pattern will change depending on the surface features, and so different precursor supply rates will be present during deposition. To account for the changing process parameters, the system will use various sensing components outlined in the next section to determine the deposition temperature and deposition rates in order to control the LCVD process.

Control Techniques

An optical 2-color micro pyrometer is used to measure the temperature at the laser spot. The pyrometer compares the radiation at 2 wavelengths, so the reading is independent of variables that affect the radiation the same at both wavelengths (e.g. dust). The pyrometer can remotely measure temperature independent of the target's emissivity, assuming the target is a gray body (an accurate assumption for a graphite substrate). The pyrometer reading will be used to regulate the temperature at the laser spot by adjusting the laser power.

The global temperature of the substrate will be monitored by a thermocouple placed on the underside of the substrate. This temperature reading will be used to control power to the global resistance heater located below the substrate.

To measure the deposition height, a laser triangulation sensor is used. The deposition height sensor would be extremely useful if it could accurately measure the deposition at the laser spot and thus allow for corrections in the deposition rate. The height sensor must be offset from the substrate by 7 inches due to the geometry of the reaction chamber. Unfortunately, the sensor's maximum resolution is 5 μm at the 7 inch offset, which is much greater than the layer thickness. Therefore the height sensor cannot be used to directly control the process during deposition. If it were able to give instant readings at the deposition spot, the stage speed could be adjusted to account for the varying deposition rates. Instead of controlling the process, the height sensor is used to measure several points on the deposited object after many layers have been deposited. The resulting point cloud will be compared to the original CAD model to determine if and where material needs to be deposited to correct for errors during the deposition process.

A CCD camera is used to observe the morphology of the structure being deposited during operation. The lens on the camera is capable of 200 times magnification at a six-inch offset, so

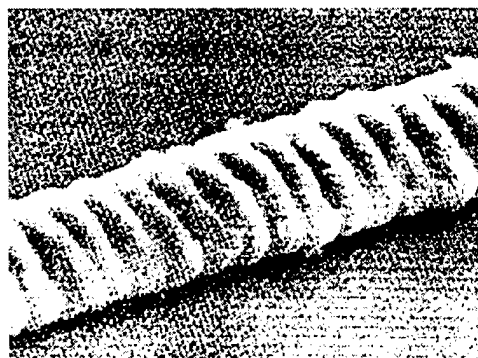


Figure 4. Periodic structure, Y.C. Du *et al.*¹²

great detail can be seen during the deposition process. This allows for *in situ* visual observation of the LCVD deposition process.

Operation

The LCVD system is capable of three modes of operation, depending on the use of the nozzle and the laser (figure 5). In the first mode of operation, the nozzle supplies the reagent, and the laser spot defines the heated reaction zone. The second mode of operation uses the laser without the nozzle, and the entire chamber is filled with the reagent gasses similar to conventional LCVD techniques. These first two modes can be compared to determine the effectiveness of the nozzle. The third mode of operation uses the nozzle but no laser. The substrate is heated to the reaction temperature with the global heater, and the nozzle defines the deposition area by supplying the reactive gas to the desired location. This third mode is similar to CVD since no laser is used, but there is a nozzle to control the selective areas of deposition. In all three modes of operation, the deposition material can be changed by simply changing the reagent gasses giving the system multiple material deposition capability.

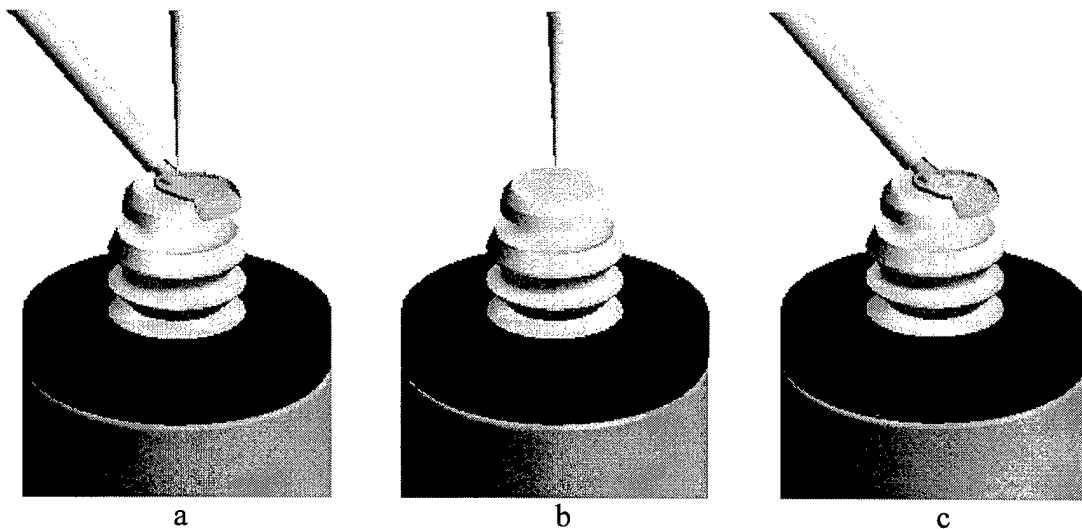


Figure 5. Three modes of operation: a) laser and nozzle, b) laser only, and c) nozzle only.

Potential Applications

The LCVD system is best suited for applications involving precise, 3-dimensional, multiple material parts. Applications include 3-D laminated structures and electro-mechanical devices. The laminated structure can be fabricated with varying orientations of the laminated layers to promote isotropic properties while increasing strength and fracture toughness. Accelerometers can be fabricated with the LCVD system, incorporating 3 axes in one small package without the need for assembly. The LCVD system provides the fully 3-dimensional capability not present in current micro-fabrication processing systems such as surface micro-machining and lithography.

Conclusion

The LCVD system (figure 6) has the versatility and process control to accurately fabricate arbitrarily shaped multi-material objects. The precision stages ensure accurate deposition. The temperature feedback helps to control the processing conditions, while the height measurement device allows for the correction of height differences during processing. The CCD camera allows for detailed visual inspection of the reaction zone during deposition. These feedback systems provide the control needed for accurate deposition.

Several features were incorporated into the design to ensure high deposition rates. A nozzle delivers the reactants to greatly increase their concentration over conventional diffusion. The dual heating of the substrate shortens the time to reach deposition temperature, and the stage design allows for fast, accurate, and complete coverage. These advances give the LCVD system the control needed to fabricate net-shape multiple material parts from the gas phase.

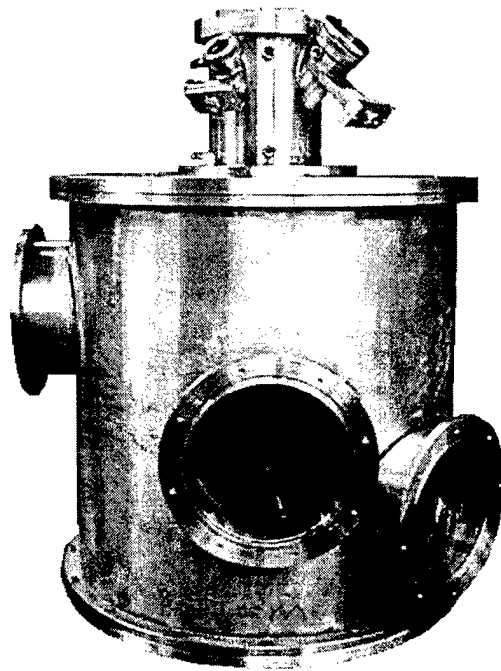


Figure 6. LCVD reaction chamber. The lower chamber is 22 inches in diameter and 22 inches high, and the upper chamber is 5 inches in diameter and 8 inches high.

Acknowledgments

We would like to thank Dr. Harris Marcus, Shay Harris and Jim Crocker for their valuable discussions related to the design of the LCVD system.

References

1. J. Mazumder and A. Kar, Theory and Application of Laser Chemical Vapor Deposition, Plenum Press, New York, 1995.
2. D. Ehrlich and J. Tsao, ed., Laser Microfabrication, Academic Press, Inc., Boston, 1989.
3. L. S. Nelson and N. L. Richardson, "Formation of Thin Rods of Pyrolytic Carbon by Heating with a Focused Carbon Dioxide Laser," *Material Research Bulletin*, 7, 971-976, 1972.
4. D. Bauerle, *Chemical Processing with Lasers*, Springer-Verlag, Berlin, 224, 71-93, 1986.
5. L. O'Conner, "Developing Bigger Micromachines," *Mechanical Engineering*, 82-83, February 1996.
6. J. Maxwell and J. Pegna, "Experimental Developments Toward Multi-Material Micron Scale Rapid Prototyping," *ASME DE*, 82, 1, 227-231, 1995.
9. W. Thissel and H. Marcus, "Design of a Closed Loop Computer Controlled System for Selective Area Laser Deposition. I. Laser Systems, Gasflow, and Substrate Temperature Control," *Materials and Manufacturing Processes*, 2, 4, 673-701, 1996.
8. J. Maxwell, K. Larson, M. Bowman, P. Hooge, K. Williams, and P. Coane. "Rapid Prototyping of Functional Three-Dimensional Microsolenoids and Electromagnets by High Pressure Laser Chemical Vapor Deposition." *Proceedings Solid Freeform Fabrication Symposium*, 529-536, 1998.
9. O. Lehmann and M. Stuke, "Generation of Three-Dimensional Free-Standing Metal Micro-Objects by Laser Chemical Processing," *Applied Physics A*, 53, 343-345, 1991.
10. C. Duty, D. Jean, W.J. Lackey, "Design of a Laser CVD Rapid Prototyping System," Proceedings of the American Ceramics Society Meeting, Cocoa Beach, Florida, Jan. 1999.
11. Y. Morishige and S. Kishida, "Thick Gold-Film Deposition by High-Repetition Visible Pulsed-Laser Chemical Vapor Deposition," *Applied Physics A*, Springer-Verlag, 59, 394-399, 1994.
12. Y.C. Du, U. Kempfer, K. Piglmayer, D. Bauerle, and U.M. Titulaer, "New Types of Periodic Structures in Laser-Induced Chemical Vapor Deposition," *Applied Physics A*, Springer-Verlag, 167-171, 1985.

PROCESS PLANNING BASED ON USER PREFERENCES

Aaron P. West
Graduate Research Assistant

David W. Rosen
Associate Professor

The George W. Woodruff School of Mechanical Engineering
Georgia Institute of Technology
Atlanta, GA 30332-0405
404-894-9668 david.rosen@me.gatech.edu

Keywords: Stereolithography, Process Planning, Adaptive Slicing, Decision-Based Design, Preferences

ABSTRACT

Typical approaches to adaptive slicing in previous literature have typically used surface finish requirements to control the slicing process. As a result, slice schemes improve the part's surface quality, but do not enable explicit trade-offs between finish and build time. The purpose of this article is to present a process planning method that enables the preferences of the user for surface finish, build time, and accuracy to control how trade-offs are made in a process plan. A multi-objective goal formulation is used by this method to evaluate how well user preferences are met by a process plan. This method consists of three modules, for determining part orientation, for slicing the part, and for determining other parameter values. An example with several scenarios representing different user preferences is provided to illustrate the process planning method.

1 INTRODUCTION

The stereolithography (SLA) technology is inherently a very flexible process, with over 20 process variables. This flexibility allows parts and features on those parts to be built very accurately and efficiently. However, the SLA technology is complex enough that even experienced operators may not be able to select appropriate variable values to achieve desired build objectives. Through the use of empirical data, analytical models, and heuristics, methods of process planning may be developed that enable even novice users of stereolithography to achieve efficient and high quality builds. We believe that the methods, if not the specific data, are applicable to other layer-based manufacturing processes.

Stereolithography creates solid objects using a layer based manufacturing approach [1]. Physical prototypes are manufactured by fabricating cross sectional contours or slices one on top of another. These slices are created by tracing with a laser 2D contours of a CAD model in a vat of photopolymer resin. The prototype to be built rests on a platform that is dipped into the vat of resin. After each slice is created, the platform is lowered and the laser traces the next slice of the CAD model. Thus the prototype is built from the bottom up. The creation of the physical prototype requires a number of key steps: input data, part preparation, layer preparation, and finally laser scanning of the two-dimensional cross-sectional slices. The input data consist of a CAD model, a precise mathematical description of the shape of an object. Part preparation is the phase at which operator controlled parameters and machine parameters are entered to control how the prototype is fabricated. Layer preparation is the phase in which the CAD model is divided into a series of slices, as defined by the part preparation phase, and translated by software algorithms into a machine language.

The key area of interest in this research is the part preparation phase. The set of parameters used to build the prototype, called the process plan, has a significant effect on the quality of the resulting

prototype. As such, the purpose of this research is to develop a process planning method for improving the quality of prototypes in stereolithography. This is to be accomplished by assisting the user in setting machine parameters so that characteristics of the fabricated prototype reflect the original intent of the user/designer/customer (we will use the term 'user'). The characteristics under investigation in this paper include build time, geometric tolerances, and surface finish.

2 BACKGROUND

2.1 Process Planning Literature

There has been a good deal of research on process planning of layer based manufacturing technologies such as stereolithography. This literature spans from topics such as build process optimization [2], to inaccuracy prediction and correction [3], and support structure generation [4].

Many researchers have investigated adaptive slicing of parts for layer based fabrication. The objective of adaptive slicing is to develop a slicing scheme, or method of slicing the CAD model, that meets a user-defined tolerance. This tolerance, commonly referred to as a cusp, serves as an indication of the allowable deviation between the true CAD model surface and the physical surface of the prototype. The error associated with this deviation is present in all layer-based manufacturing technologies to one degree or another. Separately, Dolenc and Mäkelä [5] and Tata [6] were some of the first researchers. They adaptively sliced parts that were represented using STL files. Other researchers [7, 8, 9], have presented adaptive slicing methods that slice CAD part models represented by analytical surfaces. All approaches attempt to improve the geometric accuracy of the physical prototype by calculating the appropriate layer thickness based on the local geometry of the CAD model, which will minimize the error associated with the stairstep effect to an acceptable level as defined by the cusp.

Marsan et al. [10] take a broad view of process planning and break it into four steps. The first step involves entering design data into a Solid Builder, used to generate a B-rep solid model. The next step is orienting the solid model in the Orientation Module. Support structures are then automatically generated. Next the oriented solid model is passed on to an Adaptive Slicing Module, where it is adaptively sliced to minimize the error associated with the stairstep effect. The final module is Path Planning which is currently undertaken using commercial software.

Research at Georgia Tech focused on developing methods to facilitate trade-offs among build time, accuracy, and surface finish goals. McClurkin and Rosen [11] developed a computer aided build style selection (CABSS) tool that aids users in making trade-offs among these goals. Only three variables were considered: part orientation (3 choices), layer thickness, and hatch spacing. Lynn [12] extended this work by conducting a detailed study of SLA accuracy, where response surfaces [13] are used to quantify the achievable accuracy for a set of geometric tolerances applied to a variety of surface types. The four build-style variables investigated in that research were fill-overcure, hatch-overcure, sweep period, and z-level wait period. Initial work on integrating the accuracy response surfaces into CABSS was reported in [14].

2.2 Compromise Decision Support Problems

A compromise Decision Support Problem (cDSP) is a hybrid multiobjective problem formulation, incorporating concepts from both traditional mathematical programming and goal programming. The objective is to explore the design space and improve a selected concept based on a set of goals, constraints, and bounds [15]. The cDSP is often used to model decisions consisting of multiple goals that are often in conflict with one another. A satisfactory solution is one that meets both the constraints and bounds and balances the performance of the conflicting goals. In the case of process planning for stereolithography, a part is presented in a "default" build style to serve the purpose of the existing alternative to be improved. This build style is improved by changing the build process variables. The structure of the cDSP is shown below.

Given: A feasible alternative, assumptions, parameter values, and goals.
Find: Values of design and deviation variables.
Satisfy: System constraints, system goals, and bounds on variables.
Minimize: Deviation function that measures distance between goal targets and design point.

System constraints must be met for the design to be feasible and are functions of the system variables. System goals model the design aspirations of the designer. The deviation variables measure how far away the actual achievement levels are from the target levels and are often weighted when used to formulate the deviation functions. The alternative (in this case a build process style) is improved by finding a combination of system variables such that all the system constraints are satisfied while the deviation function is minimized.

The mathematical form of a goal is given in Equation 1 for the i th goal. Each goal, A_i , has two associated deviation variables d_i^+ and d_i^- which indicate the extent of the deviation from the target (G_i). The deviation variables, d_i^+ and d_i^- , are always non-negative, and the product constraint, $d_i^+ \cdot d_i^- = 0$, ensures that at least one of the deviation variables for a particular goal is always zero. In a cDSP, the objective that is minimized is called the deviation function. In this work, the deviation function is a weighted sum of the deviation variables (Equation 2).

$$A_i(X) + d_i^- - d_i^+ = G_i \quad (1)$$

$$Z = \sum W_i (d_i^- + d_i^+) \quad (2)$$

2.3 Adaptive Slicing Method

Layer thickness has a large impact on both the resulting surface finish of the prototype and the time required to build the prototype. The method of selecting the layer thickness depends upon the type of CAD model (analytical or tessellated) and the method of slicing (adaptive or uniform). In this research an analytical CAD model is used with elements of both adaptive and uniform slicing.

There are two primary methods of calculating the layer thickness of analytical surfaces. Surfaces such as planes and cones/cylinders with a vertical feature axis may be treated as uniformly sliced surfaces. Curved surfaces such as spheres, B-splines, and cones/cylinders that do not have a vertical feature axis must be adaptively sliced. In adaptive slicing, the layer thickness is allowed to vary across the extents of the surface and conform to the local geometry. A more complete discussion of the adaptive slicing methodology may be found in references [8, 9].

The adaptive slicing method utilized in this research is in principle very similar to the method proposed in [8]. The key difference however lies in the calculation of layer thickness. In stereolithography, the layer thickness is often a discrete value. While in theory the layer thickness could be considered continuous, in practice this would be quite difficult since each layer thickness value has associated with it a set of preferred build parameters. An acceptable layer thickness in this method would be one in which the calculated cusp is equal to or less than the user-specified cusp. In this manner a slice scheme may be developed using the adaptive slicing method with a set of discrete layer thicknesses.

3 PROCESS PLANNING FORMULATION

3.1 The Overall Approach

Selection of SLA process variable values in many cases depends upon the intended function the user might have in mind for a given prototype. The expectations for a prototype to be used in marketing might be dramatically different than the expectations for functional testing. In such a situation, one would also expect that the process plans to fabricate these prototypes would be different. However, to effectively develop these alternative process plans, there must exist an understanding of the tradeoffs being made when one process plan is compared to the next. By

quantifying attributes such as accuracy, surface finish, and build time, process variable values can be selected quantitatively based on the relative importance of these attributes.

In developing the process planning method, a cDSP word formulation is the first step. This provides a means of organizing the important inputs, variables, constraints, and goals to be dealt with in the development of a process planning method. The word formulation for the process planning method consists of three cDSP's, as shown in Figure 1. The system variables include two part parameters: the slice scheme and the orientation, two layer parameters: hatch and fill overcure, and two recoat parameters: sweep period and z-level wait. Part parameters pertain to the build variables directly associated with the part. Layer parameters pertain to the build variables that control how each layer is solidified in the vat of resin. Recoat parameters pertain to the build variables that control how a new layer of resin is deposited over the previously solidified layer. There are two constraints that are taken into consideration as well, the presence of large horizontal planes and the presence of support structures. The goals in the problem formulation consist of surface finish, accuracy, and build time.

Problem Formulation		
<u>Orientation Module</u>	<u>Slicing Module</u>	<u>Parameter Module</u>
Goals	Goals	Goals
Build Time	Build Time	Build Time
Accuracy	Accuracy	Accuracy
Surface Finish	Surface Finish	Surface Finish
Variables	Variables	Variables
Orientation	Layer Thickness	Sweep Period
		Z-Wait
Constraints	Constraints	Fill Overcure
Support Structures	Horizontal Plane	Hatch Overcure
Horizontal Planes		Constraints

Figure 1 Process Planning Problem Formulations.

Each of the three cDSP's shares the same build goals, however the system variables and constraints differ depending upon the sub-problem of interest. The start of process planning begins with an ACIS based CAD model, and a set of feature tolerances (surface finish and geometric requirements) and goal preferences for the different build goals, which are supplied by the user. These inputs are used to generate and evaluate a set of suitable orientations in the orientation module. Select orientations are sent on to the slicing module where sets of slice schemes are developed for each orientation. Again each of these slice schemes is evaluated. Suitable slice schemes are then sent to the parameter module where build and recoat parameters are evaluated for each of the slice schemes. Next, multiple solutions are presented to the user. At this point in the process planning method it is up to the user to look at the resulting process plans and decide which plan will be the most suitable to fabricate the prototype.

3.2 Constraints

In this work, constraints are issues that must be addressed when developing a process plan, such as the presence of support structures, trapped volumes, large horizontal planes, and small or thin features. In some situations, these issues could result in a crashed build or seriously detract from prototype quality. With this line of thinking, the method of handling constraints in this research is to assess penalties to the build goals if a constraint is present. The constraints taken into consideration in this research are the presence of support structures and large horizontal planes.

Support Structures Support structures help to hold a prototype in position while it is being built, but can have a detrimental effect on the surface quality of the surfaces affected. The presence of support structures usually has the effect of increasing the surface roughness of the affected surface, especially in the localized area of contact. The sum of the areas of the affected facets in a given surface may then be used to assess the degree of support structures present on the surface. The penalty assessed to the surface finish, $SF_Penalty$, for the affected surface can be calculated by $SF_Penalty = SLCoeff * \left(\frac{SPA_{area}}{TL_{area}} \right)$. A ratio of the supported area, SPA_{area} , and the total surface area, TL_{area} , is used to capture the degree of support structure contact. The surface finish coefficient, $SFCoeff$, is developed empirically (see Surface Finish Goal below).

Large Horizontal Planes The presence of large horizontal planes often requires the process plan to be adjusted locally at the vertical location of the horizontal plane. This is done to ensure that the horizontal plane will exhibit a smooth flat surface. To prevent this surface error both the sweep period and the z-level wait are increased for a number of layers above and below the horizontal plane according to this equation:

$BT_Penalty = \sum_{i=start_slice}^{end_slice} (newsweep - sweep[i] + newwait - wait[i])$ where the $start_slice$ and end_slice are the slices a set distance from the horizontal plane and the quantities $(newsweep - sweep[i])$ and $(newwait - wait[i])$ represent the increases in sweep period and z-level wait for slice i .

3.3 Build Goals

The three build goals, surface finish, accuracy, and build time, are used to evaluate the process plan at the three different stages of its development (Orientation, Slicing, and Parameter stages). The objective of both the surface finish and accuracy goals is to minimize the deviation between that which is specified by the user (geometric tolerances and surface finish requirements) and that which is obtainable by the stereolithography process. The objective of the build time goal is to minimize the time necessary to build the prototype.

Surface Finish Goal A composite evaluation of how well each surface finish tolerance may be met serves as the overall evaluation for the surface finish goal. Empirical data are used to develop models that predict the obtainable surface finish for a given layer thickness on a surface at a given orientation. Previous research [16] reported data in which the finish of a planar surface is measured for a series of different orientations. Similar experiments were performed in this work [17], but instead of associating the surface finish with the orientation, the cusp (a function of both layer thickness and orientation) is associated with the surface finish. In this manner the surface finish corresponding to a given cusp and layer thickness can be predicted for all surfaces in a part.

Accuracy Goal As with the surface finish, each geometric tolerance is evaluated separately then combined into an overall composite evaluation of accuracy. The accuracy models used in this work come from the response surface models developed by Lynn et al.[14]. Six types of geometric tolerances were considered in this work: positional, flatness, parallelism, perpendicularity, concentricity, and circularity. A total of thirty-six different response surfaces were developed based on the type of surface, the orientation of that surface, and the type of geometrical tolerance [12]. Given the tolerance type, orientation of the surface to which the tolerance is annotated, and the values of the layer and recoat parameters, predictions of the achievable accuracy for every geometric tolerance can be made.

Composite Evaluation of Goals The concept behind creating a composite evaluation of the surface finish or accuracy goal is to measure how well the overall accuracy or surface finish goal is being met. To develop the composite evaluation, the specified tolerance is divided by the achievable tolerance and then multiplied by a weighting factor for that specific tolerance. This product is summed for each tolerance. The general form for both surface finish and accuracy goals is

$$GOAL = \sum_{n=0}^{n=T} \begin{cases} \frac{SpecTol_n}{AchievTol_n + Penalty} \geq 1 \Rightarrow weight_n * 1 \\ \frac{SpecTol_n}{AchievTol_n + Penalty} \leq 1 \Rightarrow weight_n * \frac{SpecTol_n}{AchievTol_n} \end{cases}$$

In this development T represents the

$$GOAL + d_i^- - d_i^+ = 1$$

number of surface finish or accuracy tolerances, $SpecTol_n$ represents the user defined requirement for either the finish or accuracy tolerance, $AchievTol_n$ represents the predicted value, and d_i^+ and d_i^- represent the deviation from the desired overall finish or accuracy tolerance. If the specified tolerance is greater than the achievable tolerance, the current feature is surpassing the specified tolerance and is not counted against the goal achievement. If the sum of the weights is equal to 1, d_i^+ will always be 0, and d_i^- will always lie in the interval [0,1]. In this manner a single measure for the overall surface finish or accuracy is obtained, where it is always desirable to minimize d_i^- . The *Penalty* for the surface finish goal would be the *SF_Penalty* described earlier.

Build Time Goal Quantification of the build time goal is based upon empirical data collected from a computer based build time estimator for stereolithography. The build time estimator [11] reads the vector (.v) and range (.r) files created by Maestro, 3D Systems's software, and calculates the build time to within roughly 2 percent. Using empirical data, three build time models (response surfaces) are developed that predict the time necessary to trace out the three vector types (hatch, fill, border) for one slice of the prototype. Summing up the time for all of the slices for a given slicing scheme, and adding the recoat time associated with each slice, yields a prediction of the build time for a given process plan. The general form of the build time goal is $\frac{(BuildTime + BT_Penalty) - BuildTime_{min}}{BuildTime_{max} - BuildTime_{min}} + d_{BT}^- - d_{BT}^+ = 0$ where d_{BT}^- is always 0 and d_{BT}^+ will lie on the interval [0,1]. In this manner a measure of build time is obtained where it is always desirable to minimize d_{BT}^+ .

3.4 Deviation Function

Using the deviations of the three build goals, a single aggregate deviation function is created to measure the overall performance of the build goals. The stereolithography user specifies, at the start of process planning, a relative importance or weight for each of the build goals, with the sum of these weights equal to one. The overall deviation is calculated by summing the product of the weight and the deviation for each of the build goals. The general form is presented here:

$Z = SFwt * (d_{SF}^- + d_{SF}^+) + ACwt * (d_{AC}^- + d_{AC}^+) + BTwt * (d_{BT}^- + d_{BT}^+)$, where d_{*}^+ and d_{*}^- represent the deviations from the specified goal. The value of the overall deviation Z will always lie in the interval [0,1]. The build process variables that minimize the individual goal deviations, and thus the overall deviation function, represent a solution that satisfies the operator preferences.

4 RESULTS

4.1 A Sample Problem

To demonstrate the process planning method outlined in this research an example problem is presented. This example is used to step through the process of annotating the model, running the process planning software and selecting the process plan that will best meet the requirements set by the user. The selection is made by examining the goal achievement of each of the three goals as indicated by the deviation values as well as the predicted values for accuracy, surface finish, and build time. In this formulation, the process planning software reads an ACIS based CAD model (.SAT file). The user is first queried for goal preferences. The values of the preferences must sum to one with higher values indicating a stronger preference for a given goal. In this example problem, one set of goal preferences is investigated in depth and the results of several different sets of goal preferences are discussed briefly. The purpose of examining several different scenarios is

to develop a better understanding of the tradeoffs being made in any given process plan based on the user preferences. The set of layer thicknesses used for this example problem is 2, 4, and 8 mils, which are typical values for a SLA-250. The CAD model shown in Figure 2 is a bracket and provides a variety of geometric surfaces.

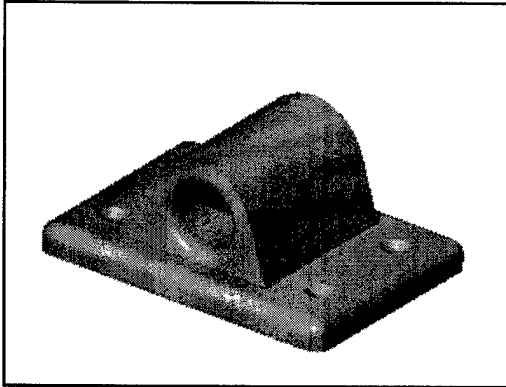


Figure 2 Example Part, Bracket

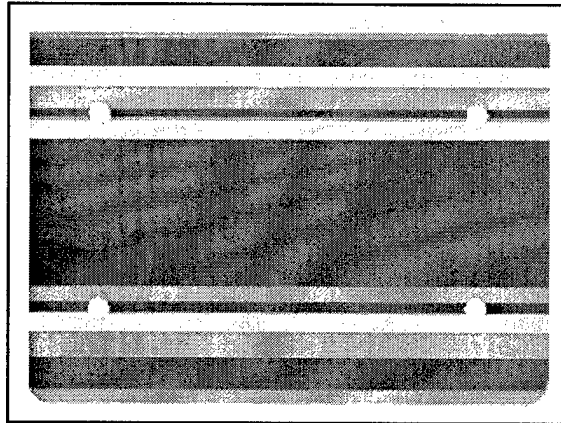


Figure 3 Slice Scheme for Trial 5

4.2 Tolerance and Finish Requirements

After specifying the goal preferences, the user is queried for the surface finish requirements of each surface. Four surfaces of the CAD model in Figure 2 are deemed to be critical. The inner cylindrical surface is to have a 2.5 micron surface finish. The two rounded edges on either side of the cylindrical surface should have a surface finish requirement of 3.8 micron. The down facing planar surface at the base of the bracket is to have a 3.8 micron surface finish. The remaining surfaces are set to a default surface finish of 7.6 micron. Next the user is queried for geometric tolerances. A cylindrical tolerance (0.003 in.) is applied to the inner cylindrical surface. A parallelism tolerance (0.004 in) is applied between the bottom surface and the top up facing planar surface, and a flatness tolerance (0.004 in) is also used on the bottom surface.

4.3 Analyzing the Alternative Solutions

Table 1 provides an overview of the goal preferences and the resulting deviations for each of the different scenarios. The solutions that are shown in the table represent the process plans with the lowest overall deviations for the given goal preferences.

Table 1 Process Planning Results

Trial	Weighting of Goals (AC, SF, BT)	Overall Dev.	Accuracy Dev.	Surface Finish Dev.	Build Time Dev.
1	(0.90, 0.05, 0.05)	0.30	0.31	0.07	0.21
2	(0.05, 0.90, 0.05)	0.04	0.31	0.01	0.32
3	(0.05, 0.05, 0.90)	0.07	0.68	0.36	0.02
4	(0.60, 0.20, 0.20)	0.24	0.31	0.09	0.19
5	(0.20, 0.60, 0.20)	0.13	0.31	0.01	0.30
6	(0.20, 0.20, 0.60)	0.15	0.31	0.23	0.07

As can be seen from the table, the weightings of the build goals have some affect on the resulting deviations. There are significant tradeoffs being made between the surface finish and build time goals, as one would expect. However, the accuracy goal does not appear to be significantly influenced by either of the other goals. Comparison of trial 6 with trial 3 provides the best example of the tradeoffs being made between the build time and surface finish goal. Both trials have a

weighting scheme with the build time goal having the highest goal preference (0.90 for trial 3 and 0.60 for trial 6). The build time deviation is slightly higher for trial 6 yet at the same time the surface finish deviation is also slightly lower. Thus it is evident that there is some degree of tradeoff being made between the build time and surface finish goals.

The accuracy breakdown for solution (1:1) is:

Tol #	Face #	Tol Type	Desired Value (mm)	Actual Value (mm)
0	2	Cylindrical	0.0762	0.0762
1	19	Parallelism	0.1016	0.381
2	33	Flatness	0.1016	0.152

The surface finish breakdown for solution (1:1) is:

Face #	Desired Value (micron)	Actual Value (micron)
0	3.8	5.05
1	7.6	4.34
2	2.5	1.3
3	3.8	2.64
4	7.6	0.13
5	7.6	6.05
...		
32	7.6	1.55
33	3.8	1.24

Figure 4 Results of Trial 5.

The slicing scheme for Trial 5 is shown in Figure 3, where the darkest shading represents areas where the model is to be built with a 0.008 in layer thickness while the lighter shading represents 0.004 and 0.002 in layer thicknesses. As one would expect, the rounded edges on the bracket require the use of a smaller layer thickness to meet the surface finish requirements. Figure 4 shows the output from the process planning software for trial 5. In this printout, all accuracy and surface finish requirements are listed as well as the predicted values. Face 2 represents the inner cylindrical surface, while faces 0 and 3 represent the rounded edges on either side of that cylindrical surface. Thus in this process plan, most of the critical surfaces are meeting the specified surface finish requirements. By looking at the slicing scheme and the surface finish and accuracy predictions a much better understanding of the given process plan may be developed. Armed with this type of information, the user can make much more informed decisions as to which process plan should be ultimately used for the fabrication of the prototype.

5 CONCLUSIONS

A process planning method was developed that allows the use of multiple build goals in setting up a process plan for stereolithography. Surface finish, accuracy, and build time are the three build goals used in this method. The intent of this process planning method is not to develop the optimal process plan for the fabrication of the prototype, but rather, to assist the stereolithography user in the development of a process plan by quantifying the tradeoffs between the three build goals. These tradeoffs have been shown to exist and can be quantified using the methods outlined in this paper. By quantifying these tradeoffs the stereolithography operator is in a much better position to develop the process plan that will be used to achieve the specific goals and characteristics that are desirable in the end prototype.

This process planning method has the potential to significantly aid stereolithography operators in process planning, but it is not without limitations. The dependence upon empirical data for the evaluation of the build goals is a limiting factor. The goal evaluations used in this process planning method have been developed using empirical data for a SLA-250 machine, thus specific predictions

for accuracy, build time, and surface finish are limited to prototypes built with a SLA-250 machine. It has also been observed that the use of a large number of blocks (greater than eight or nine) in the slicing module results in long computational times. Continuing efforts are being made to further define the capabilities and limitations of this process planning method.

ACKNOWLEDGMENTS

We gratefully acknowledge the support from NSF grant DMI-9618039, from the RPMI member companies, and from the George W. Woodruff School of Mechanical Engineering at Georgia Tech.

REFERENCES

1. Jacobs, P. F. (1992). *Rapid Prototyping & Manufacturing, Fundamentals of Stereolithography*, Society of Manufacturing Engineers.
2. Onuh, S. O. and K. K. B. Hon (1997). "Optimizing Build Parameters and Hatch Style for Part Accuracy in Stereolithography." Proceedings from the 1997 Solid Freeform Fabrication Symposium, Austin, Texas.
3. Gervasi, V. R. (1997). "Statistical Process Control for Solid Freeform Fabrication Process." Proceedings from the 1997 Solid Freeform Fabrication Symposium, Austin, Texas.
4. Allen, S. and D. Dutta (1995). "Determination and Evaluation of Support Structures in Layered Manufacturing." *Journal of Design and Manufacturing*, 5: 153-162
5. Dolenc, A. and Mäkelä, I. (1994) "Slicing Procedures for Layered Manufacturing Techniques," *Computer-Aided Design*, 26(2):119-126.
6. Tata, K. (1995) "Efficient Slicing and Realization of Tessellated Objects for Layered Manufacturing," Masters Thesis, Clemson University, Clemson, SC.
7. Sabourin, E, Houser, S A, Bøhn, J H, "Adaptive Slicing using Stepwise Uniform Refinement," *Rapid Prototyping Journal*, 2(4):20-26, 1996.
8. Kulkarni, P. and D. Dutta (1996). "An Accurate Slicing Procedure for Layered Manufacturing." *Computer Aided Design*, 28(9): 683-697.
9. Xu, F., Y. S. Wong, H. T. Loh, F. Y. H. Fuh and T. Miyazawa (1997). "Optimal Orientation with Variable Slicing in Stereolithography." *Rapid Prototyping Journal*, 3(3):76-88.
10. Marsan, A., S. W. Allen, P. Kulkarni, V. Kumar and D. Dutta (1997). "An Integrated Software System for Process Planning for Layered Manufacturing." Proceedings 1997 SFF Symposium, Austin, TX.
11. McClurkin, J. and D. W. Rosen (1998). "Computer-aided Build Style Decision Support for Stereolithography." *Rapid Prototyping Journal*, 4(1): 4-13.
12. Lynn, C.M. (1998) "Accuracy Models for SLA Build Style Decision Support," Masters Thesis, Georgia Institute of Technology.
13. Myers, R.H. and Montgomery, D.C. (1995) *Response Surface Methodology: Process and Product Optimization using Designed Experiments*, John Wiley & Sons, New York.
14. Lynn, C. M., A. West and D. W. Rosen (1998). "A Process Planning Method and Data Format for Achieving Tolerances in Stereolithography," Proceedings 1998 Solid Freeform Fabrication Symposium, Austin, TX.
15. Mistree, F., O. F. Hughes and B. A. Bras (1993). "The Compromise Decision Support Problem and the Adaptive Linear Programming Algorithm." *Structural Optimization: Status and Promise*. Washington, D.C., M. P. K. (Ed.), 247-289.
16. Reeves, P. E. and R. C. Cobb (1997). "Reducing the Surface Deviation of Stereolithography using In-process Techniques." *Rapid Prototyping Journal*, 3(1):20-31.
17. West, A. P. (1999) "A Decision Support System for Fabrication Process Planning in Stereolithography," Masters Thesis, Georgia Institute of Technology.

Volume Modeling for Rapid Prototyping

[†]Di Ma, Feng Lin, Chee Kai Chua

BioMedical Engineering Research Center
Nanyang Technological University
Nanyang Avenue, Singapore 639798
[†]Email: p144846745@ntu.edu.sg

Abstract: The expanding workspace of Rapid Prototyping will draw on the new developments in geometric modeling. Volume modeling has substantial advantages over other modeling schemes to meet the emerging requirements of Rapid Prototyping technology. It provides us with a new approach to design complex geometry and topology. The integration of the volume modeling and Rapid Prototyping technology will help us to fully exploit RP's ability to fabricate objects with complex structures. This paper addresses our research and practice in a volume modeling system toward Rapid Prototyping. Novel techniques in volumetric data manipulation, NURBS volume models and triangular facet generation over solid models are presented. Computer models designed by this system and their corresponding DTM products are also shown at the end of this paper.

1. Introduction

Rapid prototyping (RP), otherwise known as *Solid Freeform Fabrication (SFF)* or *Layer Manufacturing Technology (LMT)*, is among the latest revolutionary technologies in manufacturing which are taking the industry by storm [1]. It represents a range of systems which can fabricate 3D structures from a computer-aided system in a matter of hours. A common feature among these RP systems is that they all apply additive methods in fabrication process, that is, to build a part, prototype, or tool in a gradual, controlled way by laying down material, point by point or layer by layer, until the part is completed. With additive methods the fabrication process is indispensable on the part's complexity. Thus complex objects with arbitrary shapes and microstructures, which, if not impossible, will be very difficult for traditional manufacturing methods, can be fabricated through RP system with the same manner as in fabricating simple geometry objects. The revolutionary development of RP in manufacturing will draw on the new development in geometric modeling.

Applications of computer graphics in the area of CAD/CAM take an important role in the modern manufacturing industry. But existing CAD tools are geared toward the design of parts manufactured by traditional methods, they do not help designers exploit the expanded design space offered by RP technology. In addition, Rapid Prototyping are encountering non-CAD based surface and volume coordinate data increasingly in commercial developing and manufacturing applications [2]. In some areas, such as in medicine, only non-CAD data exists. These data can not be input into current CAD/CAM systems for further modifying and manipulation unless they are converted to geometric representation by fitting or approximating methods.

To overcome these problems, a new modeling scheme – volume modeling is proposed to tackle the emerging requirements of the RP technology. Volume modeling has the ability to

represent arbitrary geometry/topology and supports reverse engineering. The integration of volume modeling and RP will help us to fully exploit RP's ability to fabricate complex structured objects.

2. Volume Modeling

Traditionally, computer graphics studies methods of modeling and rendering geometric objects. Volume graphics [3], as a sub-discipline of computer graphics, focuses on special methods of modeling and rendering complex objects/phenomena with inhomogeneous materials and arbitrary structures in a discrete 3-dimensional space. In volume modeling, objects are stored in a discrete volumetric data set, which is defined by a grid of voxels, figure 1. A voxel is a spatial element which is defined by a unit cube centered at (x, y, z) . Each voxel is associated with its properties such as density, color, opacity, physical size and other user-defined parameters.

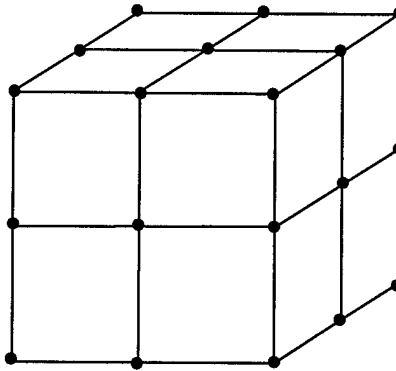


Figure 1: A $3 \times 3 \times 3$ volumetric data set, each solid circle represents a voxel

A volume model is a discrete representation of 3D objects. It has a close correspondence with RP process (layer by layer). The access to a given point in a volume data set is easy. In a linear list, the address of an individual voxel with coordinate (x, y, z) is:

$$Addr = z \times x_{max} \times y_{max} + y \times x_{max} + x$$

where $x_{max} \times y_{max} \times z_{max}$ is the resolution of the 3D data set. This formula can be easily extended to address a layer of voxels. On the other hand, RP process is a “discretized” fabrication process. RP technology decreases the 3-dimensional fabrication process into a 2-dimensional one. In a specific layer, small fabrication primitives, such as drops or layers, are applied over former layer. A volume model is ready to provide corresponding point or layer information with each case.

Compared with the other modeling schemes, volume modeling has the following distinct properties:

- *model complex geometry / topology object*

As there is no constraints put on the voxel description, complex structures can be achieved just by defining voxels either within or outside the modeled object. In addition, Boolean operations can be easily applied on the volume models. CAD tools built using volume models allow arbitrary shape manipulation and sculpting.

- *design inhomogeneous object*

By defining the property of each voxel within it, a volume model can represent inhomogeneous objects (composites), flexible objects and objects that are made of solid, liquid and amorphous materials. Conventional design tools are not oriented to the design of composite objects.

- *easy 3D data acquisition*

3D medical image data obtained from CT/MRI scanners are natural volume models. It is easy to obtain the volume models from these 3D image data set. This is of great value in reverse engineering.

3. Modeling Technology

Due to its discrete property, the control and manipulation over the volume models are not easy. To overcome the drawback of the lack of structural information within a volume model, NURBS-based volume modeling is proposed [4]. NURBS has become the *de facto* standard for the representation, design and data exchange of geometric information processed by computers [5]. An NURBS-based volume modeler will have advantages from both NURBS modeling and volume modeling.

NURBS volume is proposed to represent 3D solid objects. Its Cartesian coordinate form is as follows:

$$v(u, v, t) = \frac{\sum_{i=0}^m \sum_{j=0}^n \sum_{k=0}^l N_{i,p}(u) N_{j,q}(v) N_{k,r}(t) w_{i,j,k} \hat{P}_{i,j,k}}{\sum_{i=0}^m \sum_{j=0}^n \sum_{k=0}^l N_{i,p}(u) N_{j,q}(v) N_{k,r}(t) w_{i,j,k}}$$

where $\hat{P}_{i,j,k} = (x_{i,j,k}, y_{i,j,k}, z_{i,j,k})$ are the Cartesian coordinates of the volume control points. $w_{i,j,k}$ is the weight on the control point $\hat{P}_{i,j,k}$. p, q, r are the order of the volume in the parametric u -direction, v -direction and t -direction respectively. $U = \{u_0, u_1, \dots, u_f\}$, $V = \{v_0, v_1, \dots, v_g\}$ and $T = \{t_0, t_1, \dots, t_h\}$ are knot vectors in the respective directions, $f = m + p$, $g = n + q$, $h = l + r$. $N_{i,p}(u)$, $N_{j,q}(v)$, $N_{k,r}(t)$ are p th-order, q th-order, r th-order B-spline basis functions defined on the knot vectors U , V , T respectively.

A NURBS volume is a continuous model while a volume model is a discrete representation. A NURBS volume can be turned into its corresponding volume model through the process of voxelization [6]. As Boolean operations are difficult to be applied on high order NURBS volumes, the key idea of NURBS based volume modeling is to exploit the flexibility of NURBS modeling and use the voxelized objects as components to construct complex objects.

4. Interfacing Volume Modeling with Rapid Prototyping

The general method to interface 3D discrete data set with Rapid Prototyping is to use contour information as input [7]. It requires the extraction of the contour information from a 3D discrete data set. This step is straightforward. But the major drawback in this approach is the need for interpolation when processing contour data sets [2].

As STL is the *de facto* standard input format for RP, it is logical to generate STL files directly from a volume model. Generation of STL files through volume modeling and iso-surface extraction is proposed. A modified Marching Cubes algorithm is used to generate triangle facets and get the gradient information of each vertex from a volume model. Marching Cubes algorithm is a classic iso-surface extraction algorithm [8]. It is performed on a volumetric data set and generates triangle facets within each unit cube using a divide-and-conquer approach. It retains inter-slice connectivity from the original 3D data. After verifying the consistence of facet normals, then write them into a STL format file. Figure 2 shows an ear STL model.

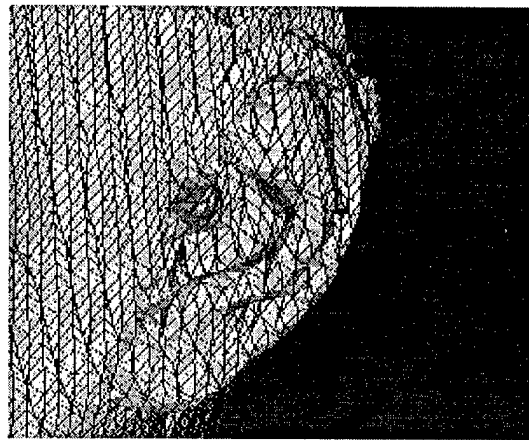


Figure 2: An ear STL model

Volume modelers have advantages over surface and solid modelers in the goal of achieving validity of STL file generation. The seamless representation of a volume model avoids the problems caused by internal walls and structures. The process of Marching Cubes algorithm to produce triangle facet guarantees the final model's shell-closure property. The coherence mechanism makes the final STL free of leaks and overlapping facet. Correct facet-orientation can be obtained by normal verification.

5. Software System Development

An experimental system has been developed for volume modeling and STL generation. Figure 3 gives an overview of the architecture of this geometric modeling system. The system consists three layers: input layer, internal layer and output layer, each layer includes both data and operations.

Research has been started with the fundamental issues such as 3D data acquisition, volumetric data segmentation, voxelization of parametric surface and volume, volume rendering, surface boundary reconstruction, and interface with CAD/CAM systems.

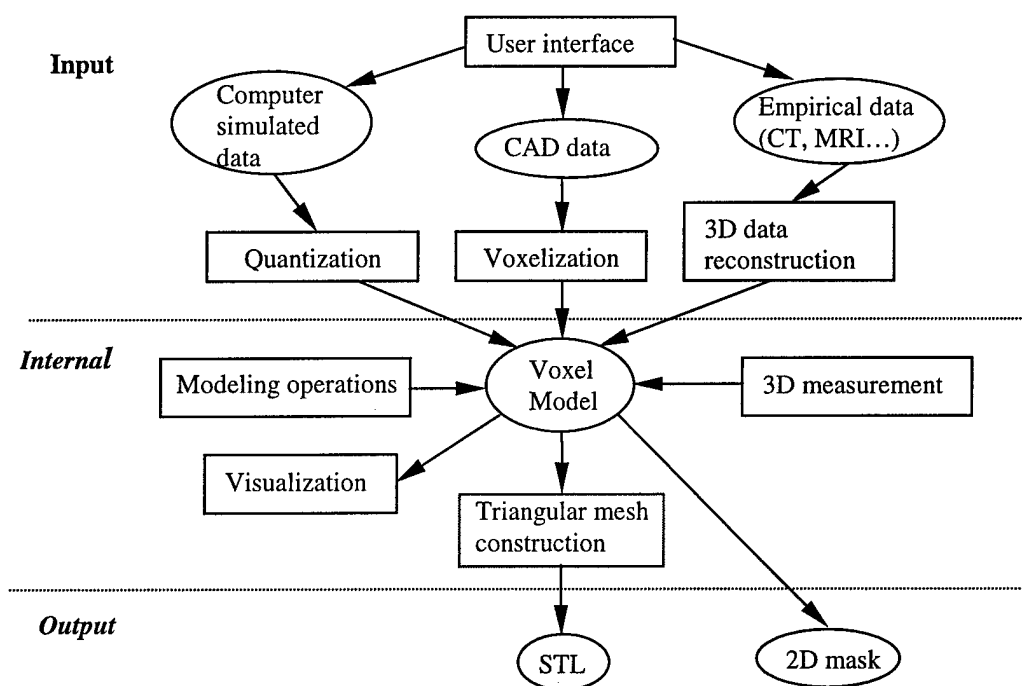


Figure 3: System Architecture

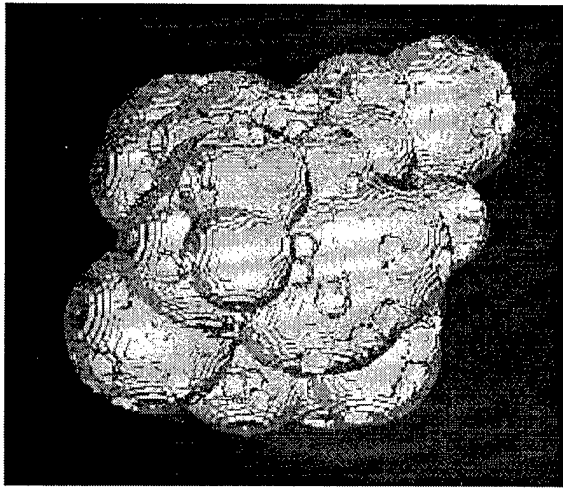
6. Experimental Result

STL models generated from the experimental system were fabricated by DTM Corporation's Sinterstation 2000 system. The SLS (Selective Laser Sintering) process creates three-dimensional objects, layer by layer, from CAD data files in the industry-standard STL file format using powdered materials with heat generated by CO₂ laser within the Sinterstation 2000 System. The interaction of the laser beam with the powder raises the temperature to the glass transition temperature which is below the point of melting, resulting in particle bonding, fusing the particles to themselves and the previous layer to form a solid [9].

Figure 4, 5 show the STL models and their corresponding DTM's products respectively. STL files are displayed by Materialise's Magics View.

Part Por (Figure 4) is a porosity model created by a computer simulation process. The arbitrary shape and inner microstructure of part Por illustrate the ability of volume modeling in complex topology and geometry design.

The original image data of part Halfbrain (figure 5) is obtained from a $128 \times 128 \times 84$ resolution version of UNC chapel Hill brain data, an MRI scan of human head. We only use half part of the brain model.

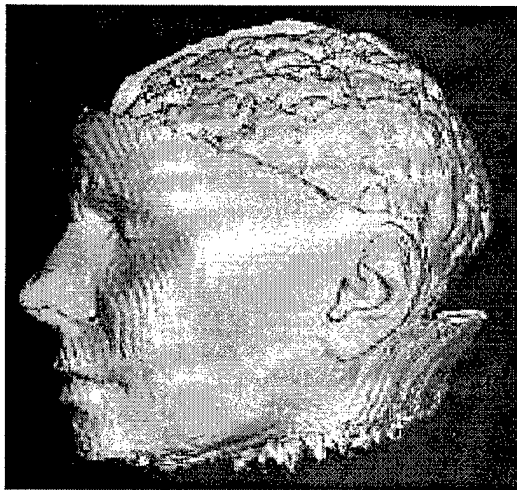


(a) STL model

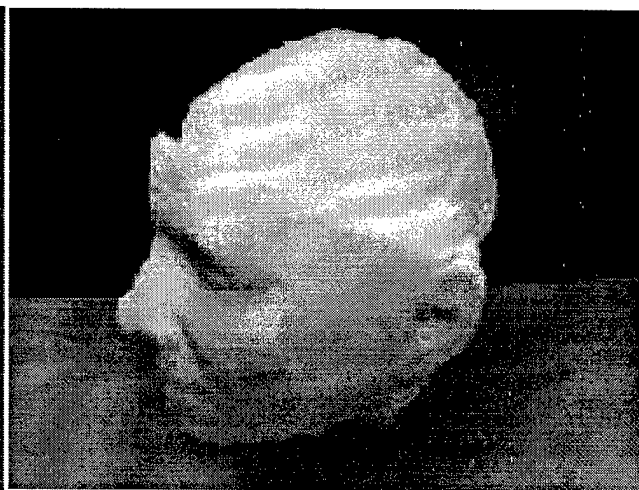


(b) DTM product

Figure 4: Part Por



(a) STL model



(b) DTM product

Figure 5: Part Halfbrain

7. Conclusion

This paper addressed the research and practice in a volume modeling system toward RP. By its close resemblance with the process of RP and its ability to represent natural objects/scenes, volume modeling is proposed as the modeling scheme to tackle the challenges posed by RP technology. As the lack of structural information in a volume model causes the manipulation and control over a volume model difficult, NURBS-based volume modeling is proposed to handle this problem. NURBS-based volume modeling possesses advantages from both NURBS modeling and volume modeling. The issue of interfacing between volume modeling and RP is also addressed. A novel approach is proposed for generating STL file format through volume modeling and iso-surface extraction. This approach guarantees the validity of the final STL files.

References:

1. Chua Chee Kai and Leong Kah Fai, *Rapid Prototyping: Principles and Applications in Manufacturing*, John Wiley & Sons, Inc., 1997
2. Vail, N.K., et al, "Interfacing Reverse Engineering Data to Rapid Prototyping", *Solid Freeform Fabrication Proceedings 1996*, Austin, TX, August, 1996
3. Kaufman, A., Cohen, D., Yagel, R., "Volume Graphics", *IEEE Computer*, pp. 51-64, Vol.26, No.7, 1993
4. Zhongke Wu, Hock Song Seah and Feng Lin, "NURBS-based volume modeling", *Workshop on Volume Graphics '99*, Swansea, UK, March, 1999
5. L. Piegl and W. Tiller, *The NURBS book*. New York: Springer-Verlag, 1997
6. Zhongke Wu, Hock Song Seah and Feng Lin, "Voxelization of NURBS curve, surface and volume", submitted to *IEEE transaction on Visualization and Computer Graphics*.
7. Richard H. Crawford, "Computer Aspects of Solid Free Form Fabrication: Geometry, Process Control, and Design", *Solid Freeform Fabrication Proceedings 1993*, Austin, TX, August, 1993
8. Lorence, W.E. and Cline, H.E., "Marching cubes: a high resolution 3D surface construction algorithm", *Computer Graphics*, pp.163-169, Vol.21, No.4, 1987
9. Chua Chee Kai, et al, "A Study of the State-of-the-Art Rapid Prototyping Technologies", *The International Journal of Advanced Manufacturing Technology*, pp.146-152, Vol.14, 1998

Selective Laser Sintering Process Management Using a Relational Database

Dongping Shi and Ian Gibson

Centre for Advanced Product Development Technologies
Department of Mechanical Engineering
The University of Hong Kong
Pokfulam Road, Hong Kong

ABSTRACT

With more and more materials used in the Selective Laser Sintering (SLS) process, it is becoming necessary to use a database to manage the process efficiently. In this paper, a relational database for the SLS process is described. The database includes powdered material data, sintering parameters, machine characteristics, mechanical properties and surface quality of prototypes. Use of this database will make it is easy to store and retrieve processing information and make decisions for planning the SLS. This paper will go on to describe how the database can be extended to include other RP technologies.

Keywords: Rapid Prototyping (RP), Selective Laser Sintering (SLS), Database Management Systems (DBMS), Process Planning.

INTRODUCTION

With the rapid development of modern science, computer technology plays a more and more important role in manufacturing engineering. Many advanced technologies such as computer-aided design/computer-aided manufacturing (CAD/CAM), computer integrated manufacturing (CIM), robotics, concurrent engineering (CE), and flexible manufacturing systems (FMS) have been applied to manufacturing industry. Time-to-market becomes a key factor to determine the survival of a manufacturing company in the global market. Meanwhile, due to globalization of information technology (IT), CIM is seen as a key competitive strategy for future advanced manufacturing systems in the 21st century.

Being regarded as a major technological breakthrough after NC technology, rapid prototyping (RP) is receiving more and more attention from manufacturers and researchers. Also based on computer technology, RP can produce any complex object in a few hours directly from a computer model without any part-specific tooling or knowledge [1]. Now, a lot of companies are using RP to help speed up their product's time-to-market.

Selective laser sintering (SLS) is a premier RP process with a wide range of materials that can be fabricated into prototypes for conceptual, functional, and tooling applications. With increasing use in the manufacturing chain, it is becoming necessary to use a database to manage the process efficiently. In this paper, a relational database for management of the SLS process is described. Information elements stored in the database include powdered material data, sintering parameters, machine characteristics, prototype's mechanical properties and surface quality. Online exploitation of databases can make it is easy to store and retrieve processing information and make decisions for planning the use of SLS equipment.

FUNDAMENTALS OF RELATIONAL DATABASE

In the simplest sense, a database is a collection of records and files that are organized for a particular purpose [2]. The basic element in the database is called an entity. There are three kinds of relationships between entities: one-to-one, one-to-many, and many-to-many (Figure 1).

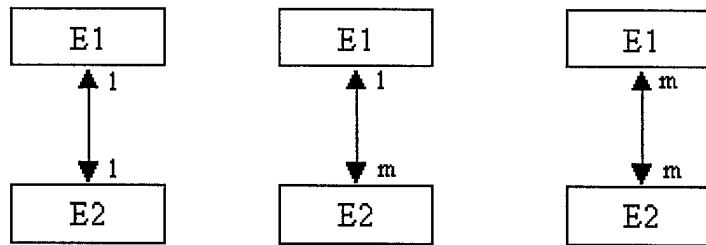


Figure 1 Three kinds of relationships between entities

Nearly all modern database management systems (DBMS) store and handle information using the relational database management model. The term relational stems from the fact that each record in the database contains information related to a single subject and only that subject. Data concerning two classes of information can be manipulated as a single entity based on related data values. This structure is popular among CIM systems because it is relatively easy to design and modify data structures.

A relational database management system (RDBMS) has three main types of capabilities:

- Data definition—to define what data will be stored in the database, the type of data, and how the data is related. In some cases, it is also needed to define how the data should be formatted and how it should be validated.
- Data manipulation—to handle the data in many ways such as to select data fields, to filter the data, and to sort it.
- Data control—to define who is allowed to read, update, or insert data. In many cases, it is also defined how data can be shared and updated by multiple users.

The relational database management systems can be built with many commercial software packages like Oracle, dBASE, FoxPro, and Access. In our research project, the database management system for the selective laser sintering process has been built with Access97.

Within an Access database, the main objects are tables, queries, forms, reports, macros, and modules [3]:

- Table—to store the data for the tasks. It is made up of columns, or fields, each of which contains a specific kind of data, and rows, or records, which collect all the data about a particular object.
- Query—to provide a custom view of data from one or more tables. It can be defined to select, update, insert, or delete data. Access stores every query as a Structured Query Language (SQL) command.
- Form—designed for data input or display or for control of application execution.

- Report—designed for formatting, calculating, printing, and summarizing selected data.
- Macro—a structured definition of one or more actions to perform in response to a defined event.
- Module—custom procedures using the Visual Basic for Application (VBA) language. It can be called from anywhere in the application, or directly associated with a form or a report to respond to events on the associated form or report.

Figure 2 shows the main objects and their relationships in Access.

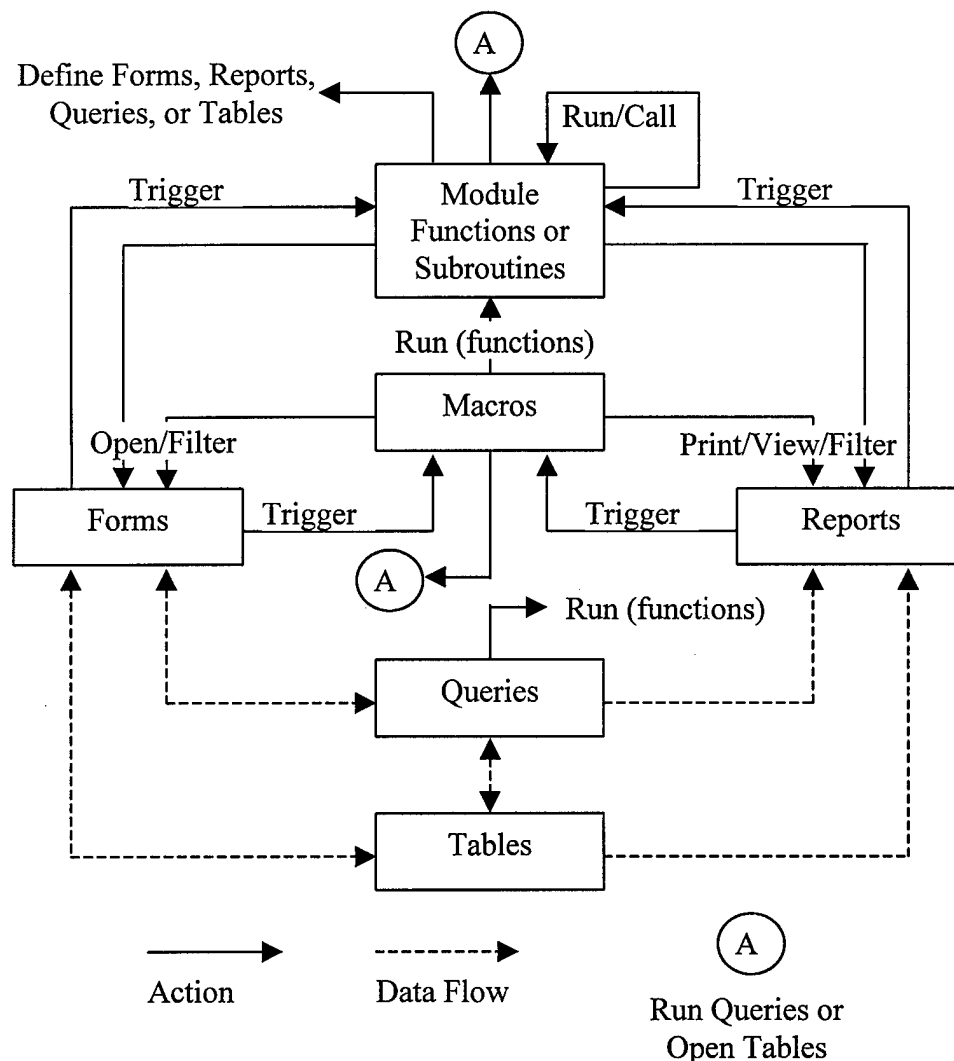


Figure 2 Main objects and their relationships in Access

IMPLEMENTATION

In the SLS process, the main entities are SLS machines, powdered materials, sintered prototypes, and sintering parameters. Some useful data, such as machine vendors, powdered

material properties, prototype's mechanical properties and surface quality, are related with the above four entities. All entities and their relationships are stored in tables.

Table and Query Design

Table design is an important step in building a relational database. It is recommended to design many separated tables for retrieving and storing data more efficiently. Some tables and their relationships in the database are shown in Figure 3 and Figure 4.

Materials

Material ID	Initial Name	Material Name	Material Type ID	Sintering Parameters ID	Applications	Price	Physical ID	Vendor ID
-------------	--------------	---------------	------------------	-------------------------	--------------	-------	-------------	-----------

Machines

Machine ID	Machine Name	Max Laser Power	Build Chamber	Position Accuracy	Max Beam Speed	Vendor ID	Price	Photo
------------	--------------	-----------------	---------------	-------------------	----------------	-----------	-------	-------

Sintering Parameters

Sintering Parameter ID	Fill Laser Power	Fill Scan Speed	Slice Thickness	Fill Scan Spacing	X Scale	Y Scale	Z Scale	X Offset	Y Offset	Z Offset
------------------------	------------------	-----------------	-----------------	-------------------	---------	---------	---------	----------	----------	----------

Mechanical Properties

Mechanical ID	Young Modulus	Poisson Ratio	Tensile Strength	Impact Strength	Hardness	Elongation	Surface Tension
---------------	---------------	---------------	------------------	-----------------	----------	------------	-----------------

Figure 3 Tables defined in the database

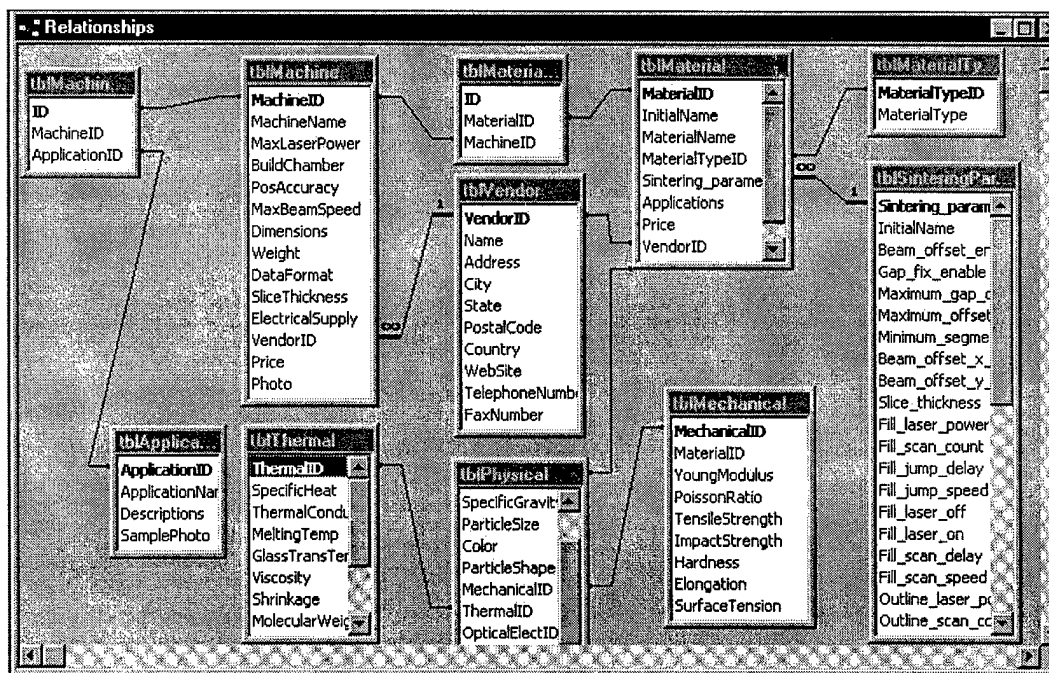


Figure 4 Relationships among tables

Queries provide a custom view of data from one or more tables. In the SLS process, the relationships of machine-to-material, machine-to-application, and material-to-application, belong to the many-to-many relationship. Using queries, it is easy to find useful information from these relationships.

Forms and Reports

Forms are designed to view and change data in the database. There are five important forms designed with respect to the four entities: frmMachines, frmMaterials, frmApplications, frmSinteringParameters, and frmPrototypeQualities. The form frmMachines provides the specifications about SLS machines. This also includes two subforms that list materials and applications available for the machine. The form frmMaterials provides specifications about the powdered materials. The form frmApplications provides the description and samples concerning applications. The form frmSinteringParameters provides sintering parameters for materials in sintering machines. The form frmPrototypeQualities provides the prototype's mechanical properties and surface quality.

Reports are designed to print data as required. Four main reports are built for printing the specifications of machines, specifications of powdered materials, sintering parameters and building profiles, and prototype's mechanical properties and surface quality.

Layout of Database

The layout of the database is shown in Figure 5.

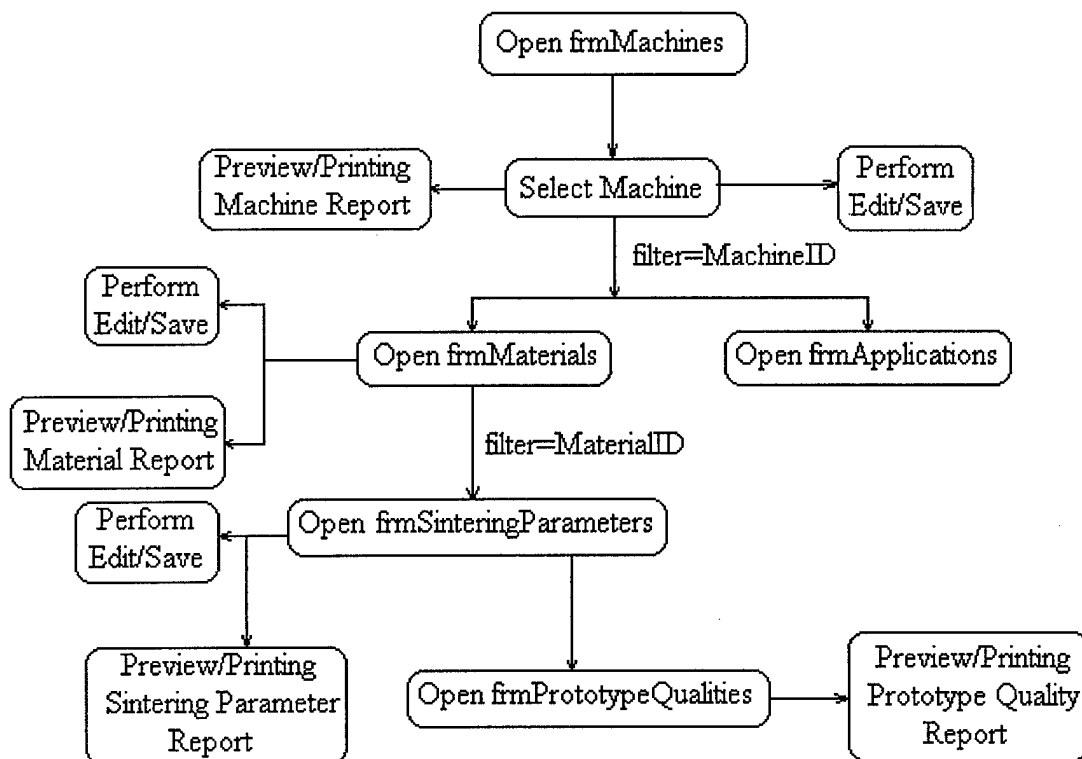


Figure 5 Layout of the database

APPLICATIONS

Currently, there are six kinds of selective laser sintering system available in the market from two vendors. More than ten powdered materials can be fabricated as visualization models, functional models, patterns for casting, and patterns for tooling. In the sintering process, a lot of sintering parameters should be set according to powdered materials. Taking the DTM sinterstation 2000 system for example, there are 31 parameters that should be set in warm-up, build, and cool-down stages, and 6 parameters related to scale and beam offset in X, Y, Z. In our previous research [4], it was found that the prototype's mechanical properties and surface quality are dependent on part orientation, powdered material properties and sintering parameters. This is important since the prototype's mechanical properties and surface quality are important factors in the design-manufacturing cycle. The database provides a convenient way to view, edit, save and print useful information. It assists the user to select machines, materials, and suitable sintering parameters according to application requirements in the design stage. Another useful application is process planning on the SLS [5].

Figure 6 to Figure 9 demonstrate use of the database.

The screenshot displays a software window titled "Sintering Station Systems". It contains several input fields for machine specifications, a photo of a person operating a machine, and two lists for materials and applications. At the bottom, there are buttons for "Preview Report", "Printing Report", "Save", and "Close", along with a record navigation bar.

MachineName: SinterStation2000

MaxLaserPower: 50 W

BuildChamber: 305(D)*381(L)mm

PosAccuracy: 0.1mm

MaxBeamSpeed: 2m/s

DataFormat: STL

SliceThickness: 0.76~.508mm

VendorName: DTM Corp.

VendorAddress: 1611 Headway Circle, Building 2, Austin, Texas, TX 78754, U.S.A, Tel: (1 512) 339-2922, Fax: (1 512) 832-6753, Web Site: www.dtm-corp.com

Photo: [Image of a person operating a machine]

Materials:

InitialName
Polycarbonate
Fine Nylon

Applications:

ApplicationName
Visualization Models

Buttons: Preview Report, Printing Report, Save, Close

Record: 1 of 6

Figure 6 Form of frmMachines showing specifications, materials, and applications related to the machine

frmMaterials

Close Add New Save Cancel

MaterialID: 1 InitialName: Polycarbonate

ParticleSize(micro): ~ 90 (30-175) Color: white

SpecificGravity(g/cm³): 1.2 Price(US\$/kg): \$61.00

Thermal Properties:

Specific Heat(J/g K): 1.206 Conductivity(W/m K): 0.21

Thermal Coefficient(-K): 0.000065 Viscosity(N-sec/m²): 213.6(573K)

Melting Temp(C): 225 Glass Trans Temp(C): 150


Shrinkage: 0.0136 ThermalID: 1

Applications: Visualization models, functional models

Preview Report Printing Report Sintering


Record: 1 of 11

Figure 7 Form frmMaterials showing some physical and thermal properties, and applications of the material

 **Database Management System for the Selective Laser Sintering Process**
Centre for Advanced Product Development Technologies, Department of Mechanical Engineering, The University of Hong Kong, Pokfulam Road, Hong Kong

Specifications of Selective Laser Sintering Systems

MachineID	MachineName	Max Laser Power	BuildChamber
1	SinterStation2000	50 W	305(D)*381(L)mm

Pos Accuracy	0.1mm	Photo 
Max Beam Speed	2m/s	
Data Format	STL	
Slice Thickness	.076~.608mm	
Vendor Name	DTM Corp.	
Vendor Address	1611 Headway Circle, Building 2, Austin, Texas, TX 78754, U.S.A. Tel: (1 612) 339-2922, Fax: (1 512) 832-6753 Web Site: www.dtm-corp.com	

Materials:	Applications:
Polycarbonate	Visualization Models
Wax Compound	Functional Prototypes

Figure 8 Report of machine specifications



Database Management System for the Selective Laser Sintering Process

Centre for Advanced Product Development Technologies, Department of Mechanical Engineering, The University of Hong Kong, Pokfulam Road, Hong Kong

Sintering Parameters and Building Profiles

Sintering_parameters_ID		1		IntraIDName		Polycarbonate	
X_scale	Y_scale	Z_scale	X_offset	Y_offset	Z_offset		
1.014	1.014	1.0025	0.1015mm	0.1015mm	0.0		
Slice_thickness		Fill_laser_power	Fill_scan_speed		Slicer_fill_scan_spacing		
0.1524mm		11-12(w)	1155466		0.1524mm		
Left_feed_heater_setpoint		Right_feed_heater_setpoint		Part_cylinder_heater_setpoint			
88.0		88.0		154.0			
Part_heater_PID_setpoint		Piston_heater_PID_setpoint		Fill_laser_off		Fill_laser_on	
154.0		20.0		1383		1012	
Outline_scan_speed		Outline_laser_power		Outline_scan_count		Outline_jump_speed	
1155466		0.0		0		8812632	
Fill_scan_count	Fill_jump_speed	Fill_scan_delay		Fill_jump_delay		Slicer_fill_first	
1	8812632	50		500		1	
Outline_scan_on		Outline_scan_delay		Outline_jump_delay		Outline_laser_off	
1012		50		500		1383	
Beam_offset_enable		Beam_offset_x_radius		Beam_offset_y_radius		Slicer_winding_fill	
0		0.1015mm		0.1015mm		1	

Figure 9 Report of sintering parameters

CONCLUSIONS

A relational database has been developed for management of the selective laser sintering process. Use of the database makes it is easy to store and retrieve processing information and make decisions for planning the use of SLS equipment. In addition, the database provides an interface to integrate the SLS process with other manufacturing techniques to form part of a CAPP or CIM system. Indeed, this system is aimed at providing a means for effective technology management.

Further research works should be carried out on extending the database to cover all RP processes, incorporating a knowledge base to form an RP planning system. Although using similar data, organized in a similar way, the data interrogation of such a system and the reports would be quite different.

Data collection is important for supporting the database. Further experimental work is ongoing to collect data on materials and prototypes as part of a 'fine-tuning' process. This could also be done with the assistance of other researchers, users and vendors to support this project by providing data concerning their experience in use of the technology.

REFERENCES

1. Terry Wohlers, *Rapid Prototyping: State of the Industry-1997 Worldwide Progress Report*, Wohler Associates, Inc., 1997.
2. Dimitris N. Chorafas, *Manufacturing Databases and Computer Integrated Systems*, CRC Press, Inc., Boca Raton, Florida, 1993.
3. John L. Viescas, *Running Microsoft Access 97*, Microsoft Press, Redmond, Washington, 1997.
4. Ian Gibson and Dongping Shi, "Material Properties and Fabrication Parameters in Selective Laser Sintering Process", *Rapid Prototyping Journal*, Vol. 3, No. 4, 1997, pp. 129-136.
5. Ian Gibson *et al*, "Decision Support Systems for the Selective Laser Sintering Process", *Proceedings of the 7th European Conference on Rapid Prototyping and Manufacturing*, Aache, Germany, 1998, pp. 83-91.

Implementation and Evaluation of Novel Buildstyles in Fused Deposition Modeling (FDM)

Tobias Wasser, Anshu Dhar Jayal, Christoph Pistor

University of Utah, Salt Lake City, 1999

1 Abstract

Previous investigations have shown that the optimization of extrusion dynamics in conjunction with the buildstyle pattern is of paramount importance to increase part quality in Fused Deposition Modeling (FDM). Recently domain decomposition and space filling curves have been introduced for slice generation in FDM [1]. The current work focuses on the implementations of fractal-like buildstyle patterns using Simulated Annealing [2, 3], Lin-Kernighan algorithms [4] and Construction Procedures based on Nearest Neighbor Heuristics [5]. These computational optimization procedures are able to generate filling patterns that allow the continuous deposition of a single road to fill arbitrary shaped domains. The necessary software modules to produce arbitrary three-dimensional artifacts have been developed and are evaluated with respect to part quality and build time.

2 Introduction

Today path generation and optimization problems found in manufacturing processes, such as FDM, typically aim for solutions that results in the shortest possible cycle time. On one hand this necessitates the determination of the shortest path. On the other hand, the manufacturing cycle time will be minimized the higher the speed which can be achieved on the individual path segments. As a result, variations in traveling speed are increased whenever sharp turns are taken, due to the deceleration and acceleration limitations of motion control and the manufacturing equipment. All manufacturing processes are more or less sensitive to these changes in traveling speed but usually require more advanced control capabilities as speed variations increase. Additional examples of processes particularly sensitive to tool traveling speed variations would be the robotic spray painting of car body parts or the automated fluid dispensing onto a surface. Both also benefit from a non-self-intersecting continuous path, which is a must for the FDM process. The simplest solution to the problem is therefore to apply hatch

patterns in Meander-form, which consist of parallel lines only, that fill the desired domain. However, this approach results in a highly oriented final structure, which can only be by changing the Meander-orientation in different slices. Some of the problems caused by this orientation are:

- highly anisotropic parts (Figure 1),
- discontinuous nozzle- or toolpath,
- voids due to minimum curve radii and areas which cannot be reached by Meander-like patterns and
- patterns of the surface structure/roughness (surface- or microstructure).

A solution to this problem is a path with segments of random orientation, which can completely cover the domain to be processed and which does not self-intersect. Space Filling Curves (SFC) such as the Hilbert SFC have been used in the past [1] to build parts with the FDM process. But until now these processes were limited to highly regular shaped objects and not applicable for arbitrary boundaries.

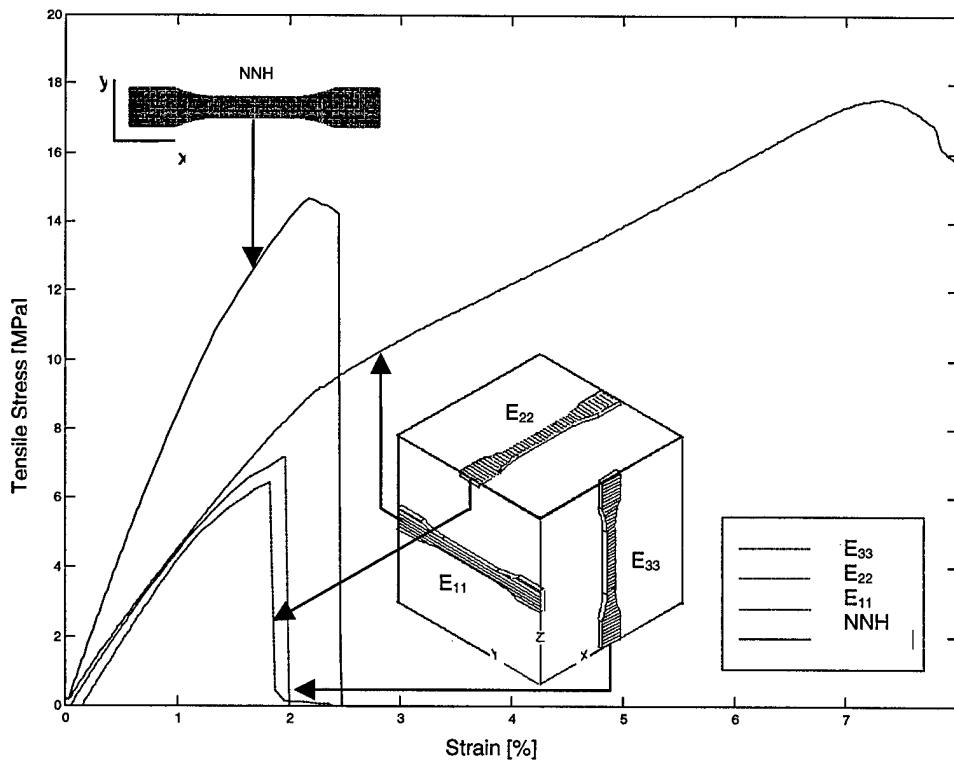


Figure 1: Stress-Strain Diagram for Uni-Directional (E_{11} , E_{22} , E_{33}) and Nearest Neighbor Heuristics (NNH) Tool-Path

With the introduction of underlying equidistant grids that are able to fill arbitrary boundaries, it is possible to get a number of nodes in each plane, which must be visited by the nozzle or tool. The spacing of the grid for the FDM-process is based on the roadwidth of the deposited material. For the Stratasys FDM 1650 a minimum roadwidth of 0.508 mm has been measured. The schedule of the visit must fulfill certain criteria, which are similar to the definitions for Eulerian and Hamiltonian tours in graph theory [5]:

1. all nodes have to be visited,
2. no node must be visited more than once,
3. minimal distance between nodes,
4. shortest possible total path length (sum over distances),
5. there may be no intersecting path elements,
6. only vertical and horizontal moves and
7. only in the nodes at the boundary diagonal moves are allowed.

The computational solutions for the problems with the aforementioned requirements are based on the Traveling Salesman Problem (TSP) [3,5]. The general TSP is not limited to points on equidistant grids but allows weight factors to describe the “distances” between nodes or better criterias. Therefore the TSP is also addressing problems beyond Euclidean planes or even problems where the distance between AB is not the same as the distance from BA (i.e. the distance matrix is not symmetric).

3 Solutions for the Traveling Salesman Problem

State of the art solutions to the Traveling Salesman Problem are based on solutions to optimization problems. After a first random tour that visits all nodes only once and allows intersections, the total length (sum of distances) is optimized, using the fact that a shorter tour always exists when crossings are still present [5]. Very simple optimization algorithms are based on node or edge insertion algorithms. Better quality algorithms are based for example on Simulated Annealing or the Lin-Kernighan algorithm. Instead of using random tours at the beginning of optimization algorithms it is also possible to use heuristics to develop start up solutions. The described Maze algorithm is based on Nearest Neighbor Heuristics and makes use of Rotation Operations.

3.1 Simple Optimization Algorithms

Node insertion algorithms select nodes whose position in the tour schedule is changed. The nodes to be changed and their new position are chosen completely randomly and unguided. Edge insertion functions are similar to the simple node insertion function except, that two nodes get selected. Then the order of all points in between gets reversed. And the new edge is inserted in front of another selected node of the remaining tour. For small problems, this random procedure is able to achieve optimum solutions. But it also can happen that the algorithm becomes trapped in local minima. With an increase in problem size (number of nodes) the improvement in unguided random selection decreases asymptotically. Therefore all of the better algorithms focus on either guiding the solution finding process or on solving the problem of local minima.

3.2 Simulated Annealing

The algorithm starts at a high-energy (cost or initial tour) configuration. Then the simulation chooses random neighboring configurations called Careful Annealing in physical systems and Simulated Annealing in optimization problems. If the neighboring configurations result in an improvement in the Energy State (tour length), then the simulation is updated, in order to achieve the Ground State or the Optimal Solution [2,3]. Until now this procedure matches the simple optimization algorithm. However by introducing a probability factor which judges if a configuration is defined as the new state even if this neighbor is not better than his origin configuration, the algorithm solves the problem of being trapped in local minima. This probability factor is also continuously upgraded during iterations [2,3].

Problematic during the use of Simultaneous Annealing is the number of nodes; even with long running times there is the possibility that the Optimal Solutions intersect, since intersections are not optimized. Laarhoven and Aarts [2] recommended to run the whole algorithm as often as there are nodes, in order to secure an optimal tour safely. This increases the running time by the number of nodes. When the initial configuration is constructed by nearest neighbor heuristics, it is noticed that the annealing process first worsens the configuration and cannot guarantee an optimal solution.

3.3 Lin-Kernighan Algorithm

Lin and Kernighan introduced their improvement heuristic in 1971 [4]. Their objective was to improve the toolpath of a numerically controlled laser used for cutting holes. In order to improve the cycle time, their focus was on the positioning of the laser and not on the cutting process, since the laser was only burning holes with equal diameters. While Simulated Annealing focused on the problems of trapped situations, Lin and Kernighan started with guiding the acquisition of neighboring solutions. The main idea was that since the single distances caused in their sum the total cost or length of each configuration, an optimization algorithm should find better positions for nodes with very long single distances. Therefore

Lin and Kernighan used guiding criteria in order to reach an optimal solution. Throughout the literature the Lin-Kernighan algorithm is recognized as the heuristic with the most promising results. In order to solve the problem of getting trapped in local minima and to achieve better running times, Lin and Kernighan found the best solutions by using five nodes simultaneously in each improve-

ment loop. Similar algorithms are called k-optimization algorithms whereby k is the number of nodes in each loop. The improvement rate or time gain over all other processes is noticed throughout all problem instances, but similar to all discussed heuristics this solution rate is highly asymptotic (Figure 2).

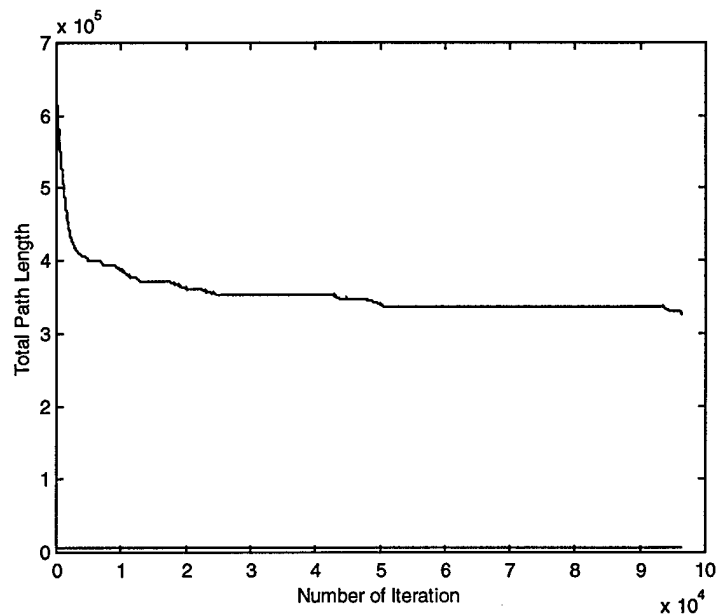


Figure 2: Total path length over the numbers of iteration for a problem with 10597 nodes (tensile-bar).

3.4 Heuristics for initial configurations

Instead of optimizing a complete random initial configuration, heuristics can be used to find better startup solutions. Both Insertion Heuristics and Nearest Neighbor Heuristics

have been implemented and evaluated. Since the implementation of Nearest Neighbor Heuristics fulfill the requirements of non-self intersecting path elements, an algorithm using rotation operations has been designed to create complete toolpaths.

3.4.1 Insertion Heuristics

Starting with an initial randomly chosen tour containing only a small amount of nodes, the final path is obtained by adding new nodes to this tour according to certain criteria.

The starting tour consists of three nodes, which thus had as a Hamiltonian tour the minimal possible total path length. The new nodes were selected either randomly or by the criteria of maximal (Figure 3) or minimal distance to the rest of the already configured nodes. After their selection the nodes were included in the tour such that their position was a minimal addition in the total path length. These heuristics can create very good initial configurations in short time, since the running time is $O(n)$,

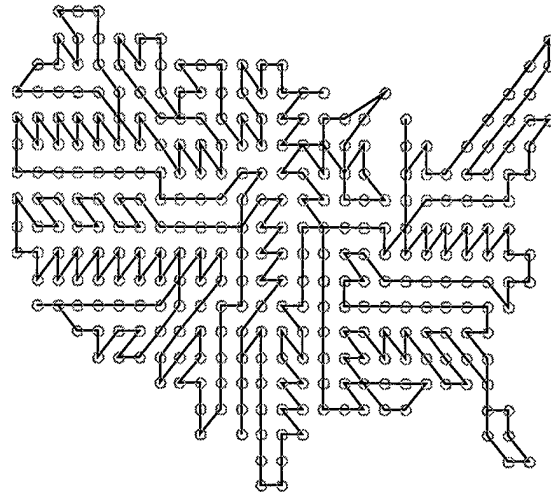


Figure 3: Tour consisting of 325 nodes achieved by Farthest Insertion Heuristic.

and they can create or introduce tour solutions that are similar to meanders (there are long quasi-parallel sections); however intersections still occur.

3.4.2 Nearest Neighbor Heuristics

In these algorithms a single random node is selected and from this starting node, the entire tour is constructed by adding one new node at a time. The objective for each new node is that it has a minimal distance to the current end point of the tour. For the equidistant grid this means that there are theoretically four possible connections. But there are only up to three new possibilities, since the last connection reaching this point cannot be opened or lost. The main problem is that this algorithm gets trapped in areas, where all of the surrounding nodes are already part of the tour configuration.

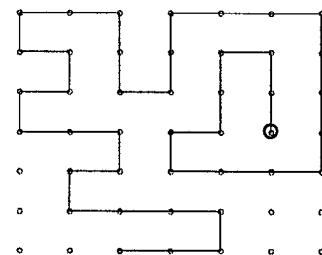


Figure 4: A dead end.

In other words the last node of the tour has reached a dead end (Figure 4).

The solution for this dead end is to allow the algorithm to connect randomly or guided to a free node. But the results are not acceptable as intersections occur in the generated toolpath. However, if this algorithm is to be used for finding a first initial tour that will be optimized by another algorithm, the selection of free nodes in this fashion is tolerable. In fact the quality of the tour configuration is already so good that the subsequently implemented optimization algorithms always lead to longer total path lengths.

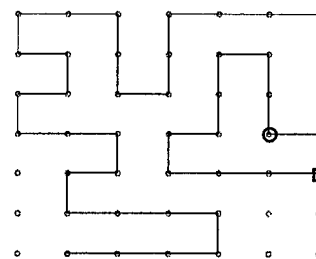


Figure 5: Rotation Operation

Instead of “jumping” in the tour to another free node, it is also possible to rotate the connections. The Operations that changed the configuration shown in Figure 4 to the configuration in Figure 5 were:

1. selecting a node which is already part of the tour configuration,
2. opening its connection with the next node in the tour schedule,
3. turning the scheduled order of points around for those nodes, which were freed from the tour schedule and
4. connecting the trapped node (circle) from before to the selected node.

With these changes a new tour end is achieved and the Nearest Neighbor Heuristic starts again. An example in Figure 6 shows the broad variation in a solution for a 1,300 nodes problem. A simple distance algorithm guides the selection of nodes where the connections are being broken up to the nearest free nodes. And in the final version, the algorithm allows diagonal moves at the boundary. On the Stratasys FDM 1650, several tensile bars were built, in which the toolpath was configured by the Nearest Neighbor

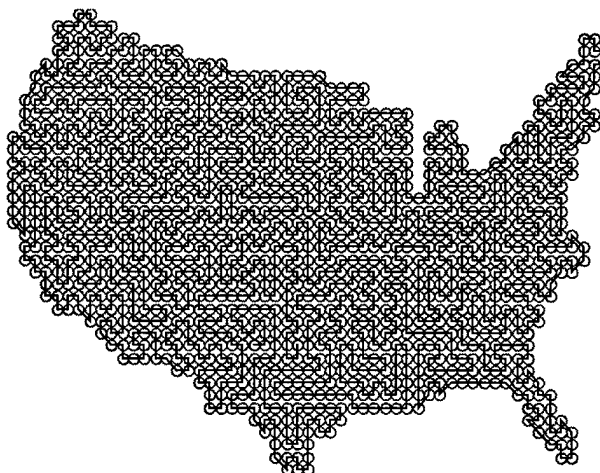


Figure 6: 1,300 node tour achieved through Nearest Neighbor Heuristic.

Heuristic. One slice of a standard tensile bar includes 10,597 nodes. The subsequently

conducted Stress-Strain tests revealed a higher Elastic modulus (Figure 7). The built parts had a higher density and their fracture behavior was close to injection molded ABS parts. The noticeable corner in the graphs is caused by the start of delamination in the bars.

4 Conclusions

The quality achieved with the new toolpaths measurable in density (amount of voids) and Elastic modulus proves the importance of the implementation of the new buildstyle patterns. Figure 8, a representative 1,300 node task, shows the CPU Time involved for the solution finding. CPU Time has such an importance, since for instance in FDM for every slice the TSP has to be solved. This makes the Nearest Neighbor Heuristic approach with the use of rotation operations, as described by Reinelt [5] and Paragraph 3.4.2., the most feasible method for generating a toolpath in Solid Freeform Fabrication (SFF).

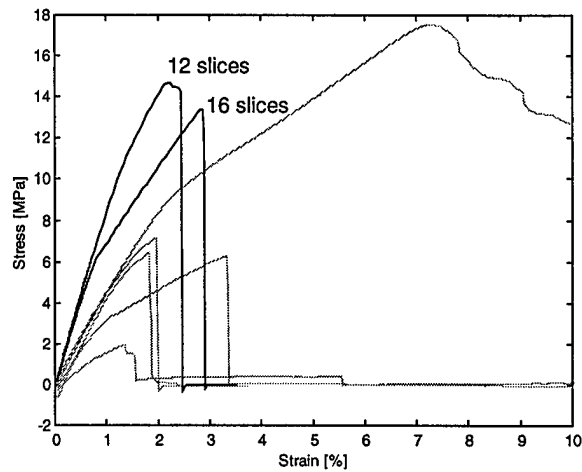


Figure 7: Stress-Strain Tests of bars using Nearest Neighbor Heuristic and unidirectional bars.

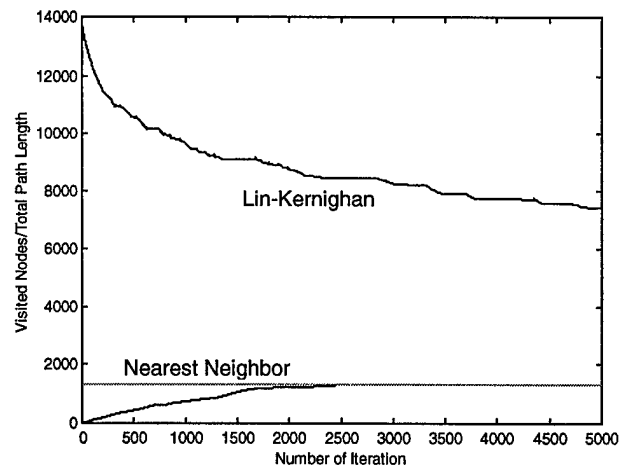


Figure 8: Progress of algorithms over time.

5 References

- [1] M. Bertoldi, M. A. Yardimci, C. M. Pistor, S. I. Güceri, "Domain Decomposition and Space Filling Curves in Toolpath Planning and Generation," University of Illinois at Chicago, 1998.
- [2] P. J. M. van Laarhoven, E. H. L. Aarts, "Simulated Annealing: Theory and Applications," D.Reidel Publishing Company: Dordrecht, 1987.
- [3] Kunwoo Lee, "Principles of CAD/CAM/CAE Systems," Addison-Wesley: Reading, Seoul, 1999.
- [4] S. Lin, B. W. Kernighan, "An Effective Heuristic Algorithm for the Traveling-Salesman Problem," Bell Telephone Laboratories: Murray Hill, 1971.
- [5] Gerhard Reinelt, "The Traveling Salesman: Computational Solutions for TSP Applications," Springer-Verlag: Berlin, Heidelberg, 1994.

Application of Design of Experiments to Extrusion Freeform Fabrication (EFF) of Functional Ceramic Prototypes

J. Walish, M. Sutaria, M. Dougherty, R. Vaidyanathan.
Advanced Ceramics Research, Tucson, AZ 85706

S. Kasichainula, P. Calvert. University of Arizona
Arizona Material Laboratories, Tucson, AZ 85712

K. Cooper. NASA Marshall Space Flight Center, Huntsville, AL 35812

Extrusion Freeform Fabrication (EFF) is an adaptation of the Stratasys Fused Deposition Modeling (FDM™) process for the Solid Freeform Fabrication (SFF) of functional ceramic prototypes. It is a complex process involving many process variables, including parameters that are operation, machine, materials, and geometry specific. A Taguchi factorial Design of Experiments (DOE) technique was utilized to study the effects of machine specific process parameters as well as their interactions based on the mechanical and physical properties of sintered ceramic specimens. Post-processing software was developed to control and modify these parameters. This software interface was designed to mimic the Quickslice™ interface for setting motion parameters based upon the material and the operation. The results of this investigation provided useful information for the experimental analysis of the machine specific process parameters. Suitable parameters were selected for the EFF process for fabricating representative ceramic prototypes. With the optimized parameters, complicated parts were successfully fabricated using both Kyocera SN282 and Starck M-11 silicon nitride powders.

I. Introduction

Extrusion Freeform Fabrication (EFF) is an SFF technique based on the Stratasys FDM™ approach^a for the fabrication of functional ceramic prototypes [1]. More details are given in reference 2. While possessing the benefits of Fused Deposition of Ceramics (FDC™) [1995 Volume from reference 1] and FDM™, EFF has the added advantages that it can handle higher viscosity feed stock materials and higher extrusion temperatures compared to FDC™ and FDM™. Similar to other SFF techniques, EFF also allows the sequential deposition of multiple layers to form a complex ceramic shape. This has been achieved by retrofitting a high-pressure extruder head to a Stratasys FDM™ modeler (figures 1 and 2). The CAD file is processed by the Quickslice™ software and used to control the EFF high-pressure extrusion head [1]. However, the operation parameters that are automatically set by Quickslice, are optimized for polymer filament type of feedstock. These parameters are not necessarily the optimum parameters for the SFF of ceramic parts. To further control process parameters for SFF of ceramic parts, SML Post™, a Visual Basic based post-processing software was developed to modify selected process parameters. SML Post™ could modify the start-delay, preflow, start-flow, start-distance, main-flow, shutoff-distance, roll-back, speed, and acceleration that were originally set by Quickslice™. Presently, the road-width, slice-thickness, and fill-patterns are still set by

^a Stratasys Inc., Eden Prairie, MN

Quickslice. However, SML Post™ could modify these parameters also, if needed.

An examination of the initial ceramic parts that were built using EFF suggested that further optimization was needed to improve the part quality and surface finish of the parts. This was the motivation for the work presented here. The optimization could be performed on both machine and material parameters. Material parameters include the type of ceramic powder used, the particle size distribution of the powder, the type of sintering aides used, and the type of binder system. Machine parameters are items such as extrusion temperature, nozzle diameter, modeling envelope temperature, and percent flow (flow rate). For the work presented here, only machine specific parameters were optimized using the Taguchi method of Design of Experiments (DOE) [3, 4].



Figure 1. Stratasys FDM™ retrofitted
With a high pressure head

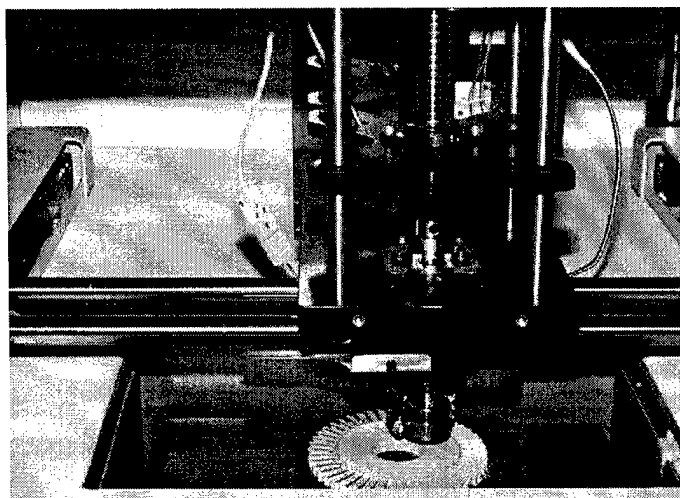


Figure 2. Close up view of the high pressure
head creating a ceramic prototype

II. Experimental Procedure

An optimization of machine parameters was undertaken in order to improve part quality and surface finish. The part features used for optimization were dimensional accuracy, surface finish, and the time taken to build the sample. In order to reduce the number of experiments, the number of variables was reduced to seven. The same .sml file was used for all of the trials to reduce the number of variables. These variables could be changed using the post processing software (SML Post). The start distance and shutoff distance were held constant at values previously determined as optimal. These numbers were obtained by trial and error. Earlier work had produced a binder system that demonstrated favorable extrusion qualities when compounded with the ceramic powder [2]. The same ceramic feed stock was used for the optimization experiments. It is expected that minor modifications of the feedstock would result in similar optimized parameters for the EFF of those feedstocks.

A. Optimization of the Perimeter Operation

The Taguchi method of Design of Experiments (DOE) was used for the statistical experimental design. Within the four types of operations used to deposit the material (perimeter,

contour, raster, and open), the parameters for perimeter were optimized first due to the relative ease and speed at which the experiments could be performed. A two level experiment with seven variables was performed to select and screen the most critical variables. The variables chosen for the screening experiment were start delay, pre-flow, start flow, main flow, rollback, speed, and acceleration. A description of the seven variables is given in table I.

A Taguchi L12 array with three repetitions was chosen. With three repetitions, there was a 95% confidence level that a term identified as being significant truly belongs within the standard deviation as well as a 90% chance of finding a significant term if one actually existed. At this point, the predetermined high and low values of the different variables were entered into a computer program which created and analyzed DOE experiments (see table II). The software is called "Keep it simple statistically or KISS" supplied by Digital Computation. A three-level set of experiments was conducted to optimize the variables.

Cylinders with a diameter of two inches and a wall thickness of one road per layer were fabricated. The cylinders were built to a height of 0.2 inches. An exit distance of 1.25 inches was used in all cases. Twelve samples were made for each repetition.

The parts were analyzed in a number of ways. Thickness measurements from three points on the cylinders were taken for all 36 parts. The thickness before and after the starting point, and exactly opposite the starting point were measured. The standard deviation in part dimensions between the three points on each cylinder was calculated. The average thickness, the average excess (an average of the measured thickness minus the thickness specified in the .sml file), time, and the end thickness minus the beginning thickness were also determined. By analyzing the statistics and graphs returned by the DOE software, the most important factors were found. The DOE software analyzed the measured responses and calculated a factor known as "P(2 tail)". According to the DOE rule of thumb, if the "P(2 tail)" number for a particular variable is below 0.05, then that variable should be considered to belong in the regression model. If the "P(2 tail)" value was between 0.05 and 0.10, then that variable was marginally important. However, this variable would also be included in the three-level set of experiments. A variable with a higher value of "P(2 tail)" would be considered not to belong in the regression model.

A Taguchi L9 matrix was created for the three-level experiments. The variables were chosen based on the screening experiments. The low and high values were retained from the screening experiment, while the middle value was an average of the low and high values. The parameters with a P(2 tail) number above 0.10 were set at values thought of as optimum, based on previous experimental results. The three-level Taguchi L9 matrix is shown in table III. The difference between the start and finish thickness of the parts created was measured and analyzed by the software. The optimized values of the machine parameters for obtaining the smallest difference in start and finish thickness were calculated by the DOE software. Several test parts were made with the optimized parameters.

B. Optimization of the Raster Operation

As with the perimeter optimization, raster optimization was carried out using the Taguchi DOE techniques. The two-level experiment for the raster was done with the same seven

variables as the perimeter two-level experiment plus the road width. The test shape for this set of experiments was a 1"x2" rectangular plate with a rectangular hole cut out of the middle and a uniform wall thickness of 1/8". Thirty-six (36) experiments were conducted. However, some of the parts were irregular and had a poor surface finish. Therefore, a decision was made to judge these parts on a strictly qualitative scale of 0 to 10, 10 being the best. A road width of 0.0030" was used for all the experiments, since this closely matched the optimum road width obtained with the 0.0016" nozzle used.

III. Results and Discussion

For optimizing the parameters for building the perimeter, the time to build the part and the difference in part thickness at the start and finish were used as responses and analyzed by the DOE software. Since the build time yielded only one definite important factor (speed) and one possibly important factor (main flow), the difference in thickness at start and finish was used in constructing the three-level experiment. The effect of the different parameters on the difference in part thickness at the start and finish is shown in figure 3. The slope of the marginal means plot in figure 3 is indicative of the significance of the different build parameters. From figure 3, it was seen that the start-delay, main-flow, rollback, and speed were significant factors for the optimization of the perimeter. The Taguchi L9 matrix created for the three-level experiments based on these results was shown in table III. The difference between the start and finish thickness of the parts created was measured and analyzed by the software. The program returned values for the P(2 tail) which confirmed that all of the variables that were used at this experimental stage were significant in minimizing the difference between the start and finish thickness. The optimized values of the machine parameters for obtaining the smallest difference in start and finish thickness are shown in table IV. These values are for a particular powder/binder system and tip size. Further optimizations will have to be performed in order to obtain the same kind of results for different tip sizes and different feedstock material. In the case of raster, the start-delay, main-flow, roll back, speed and road width parameters were observed to be the most significant.

It was found that when using the optimized parameters, the surface finish of the parts was greatly improved with respect to parts that were built previously without optimization. Four test cylinders were made using the optimized parameters for perimeter. The most dramatic change occurred with the build speed. The build speed suggested by the optimization program was 0.3" per second, compared to 0.8" per second before optimization. The surface finish and the seam where the layer was started and finished showed no pooling of excess material. Figures 4a and 4b shows cylinders that were made with minor changes in the parameters, while figure 4c shows a cylinder that was built with the optimized parameters. Sample parts with good surface finish and part quality was built using the optimized raster parameters. As indicated above, optimum part quality was obtained with a road width of 0.030" when using a tip size of 0.016". Further optimization experiments are in progress with tip sizes of 0.012" and 0.025".

Mechanical testing was completed for Starck silicon nitride samples fabricated with the optimized conditions. Prior tests had shown that post-polishing provided increases in strength. Samples were made with both 0 degree and alternating 0/90 raster directions. The strength values for all test bars can be seen in table V. For samples with a 0 degree raster build, the strength data

was similar for polished and unpolished specimens. The test bars that were made with 0 and 90 degree alternating raster angles showed poor surface finish, compared to 0 degree only, and thus the data shows a difference in strength values for polished and unpolished samples. Because of the geometry of the test bar, a 90 degree raster angle is a poor choice since the road would only be about 0.1 inches long. The smaller the road, the more chances of introducing a defect into the part.

Other silicon nitride powders have been used for EFF with the same binder system and extrusion conditions with favorable results. Two sample parts fabricated using the optimized conditions are shown in figures 5 and 6. In figure 5, green parts made with Kyocera SN282 silicon nitride and Starck M-11 silicon nitride powder are shown. Figure 6 shows a turbine blade that was made with the optimized parameters.

IV. Conclusion

This investigation has established the feasibility of using DOE techniques for the optimization of the EFF process when creating functional ceramic prototypes. For building the perimeter, the parameters that control the EFF process quality are start-delay, main flow, speed and rollback. For the raster, the start-delay, main-flow, roll back, speed and road width parameters were observed to be the most significant. It has been demonstrated here that with the optimized parameters, the overall part quality was improved. Complicated ceramic shapes were built by the EFF process using the optimized parameters. Currently more optimizations are planned for other tip sizes.

V. Acknowledgements

This work has been performed under NASA STTR program contract number NAS8-98025. The authors would like to thank Jiong Peng of the University of Arizona for her help in the preparation and optimization of the EFF samples.

References

1. Proceedings of the Solid Freeform Fabrication Symposium, Vol. 1990-1998, Edited by H.L. Marcus, et al., the University of Texas at Austin, Austin, TX.
2. R. Vaidyanathan, J. L. Lombardi, B. Tennison, S. Kasichainula and P. Calvert, "Rheological properties of ceramic formulations for Extrusion Freeform Fabrication," presented at the 23rd Annual Cocoa Beach Ceramic Society meeting on Ceramics and Composites, Cocoa Beach, FL, Jan. 1999 (in press).
3. Ross, Phillip J., Taguchi Techniques for Quality Engineering, McGraw-Hill: New York, NY, 1996.
4. Schmidt, Stephen R., Launsby, Robert G., Understanding Industrial Designed Experiments, Air Academy Press, 1994.
5. Vaidyanathan, R., et al, "Extrusion Freeform Fabrication of silicon nitride parts," Proceedings of the 10th Solid Freeform Fabrication Symposium, (1999), in print.

Table I: A description of the software controlled (process) parameters.

Parameter	Description
Start delay	The lag time between layers
Pre-flow	Extrusion rate during stops
Start flow	Extrusion rate at the start of the exit distance
Start distance	Distance from start point for main flow to start
Main flow	Extrusion rate over the bulk of the layer
Shutoff distance	The distance from the stop point for main flow to stop
Rollback	The rate the material is pulled back to reduce the flow
Speed	The rate at which the head moves along a set path
Acceleration	The rate at which the extrusion head changes speed

Table II: The Taguchi L12 matrix used in the screening experiment for perimeter optimization.

Factor	A	B	C	D	E	F	G				
Row #	Start Delay	Preflow	Start Flow	Main Flow	Rollback	Speed	Acceleration		Y1	Y2	Y3
1	0	49	51	50	141	200	1				
2	0	49	51	50	141	1000	9				
3	0	49	127	176	255	200	1				
4	0	127	51	176	255	200	9				
5	0	127	127	50	255	1000	1				
6	0	127	127	176	141	1000	9				
7	1	49	127	176	141	200	9				
8	1	49	127	50	255	1000	9				
9	1	49	51	176	255	1000	1				
10	1	127	127	50	141	200	1				
11	1	127	51	176	141	1000	1				
12	1	127	51	50	255	200	9				

Table III: The Taguchi L9 matrix used for the three-level experiments for optimizing perimeter.

Factor	A	B	C	D
Row #	Start Delay	Main Flow	Rollback	Speed
1	0	120	141	200
2	0	148	199	600
3	0	176	255	1000
4	0.5	120	199	1000
5	0.5	148	255	200
6	0.5	176	141	600
7	1	120	255	600
8	1	148	141	1000
9	1	176	199	200

Table IV. The optimized parameters obtained with DOE for EFF

Optimized parameters	
Start delay	0.82 sec
Preflow	79
Start flow	89
Start distance	0.06"
Main flow	128%
Shutoff distance	0.073"
Rollback	229
Speed	0.293"/sec
Acceleration	5

Table V. Flexural strength data for EFF test bars as a function of raster-build direction

Raster-build direction	Surface condition	Flexural strength (MPa)
0°	Unpolished	594 ± 80
0°	Polished	613 ± 12
0°/90° alternating	Unpolished	227 ± 39
0°/90° alternating	Polished	312 ± 71

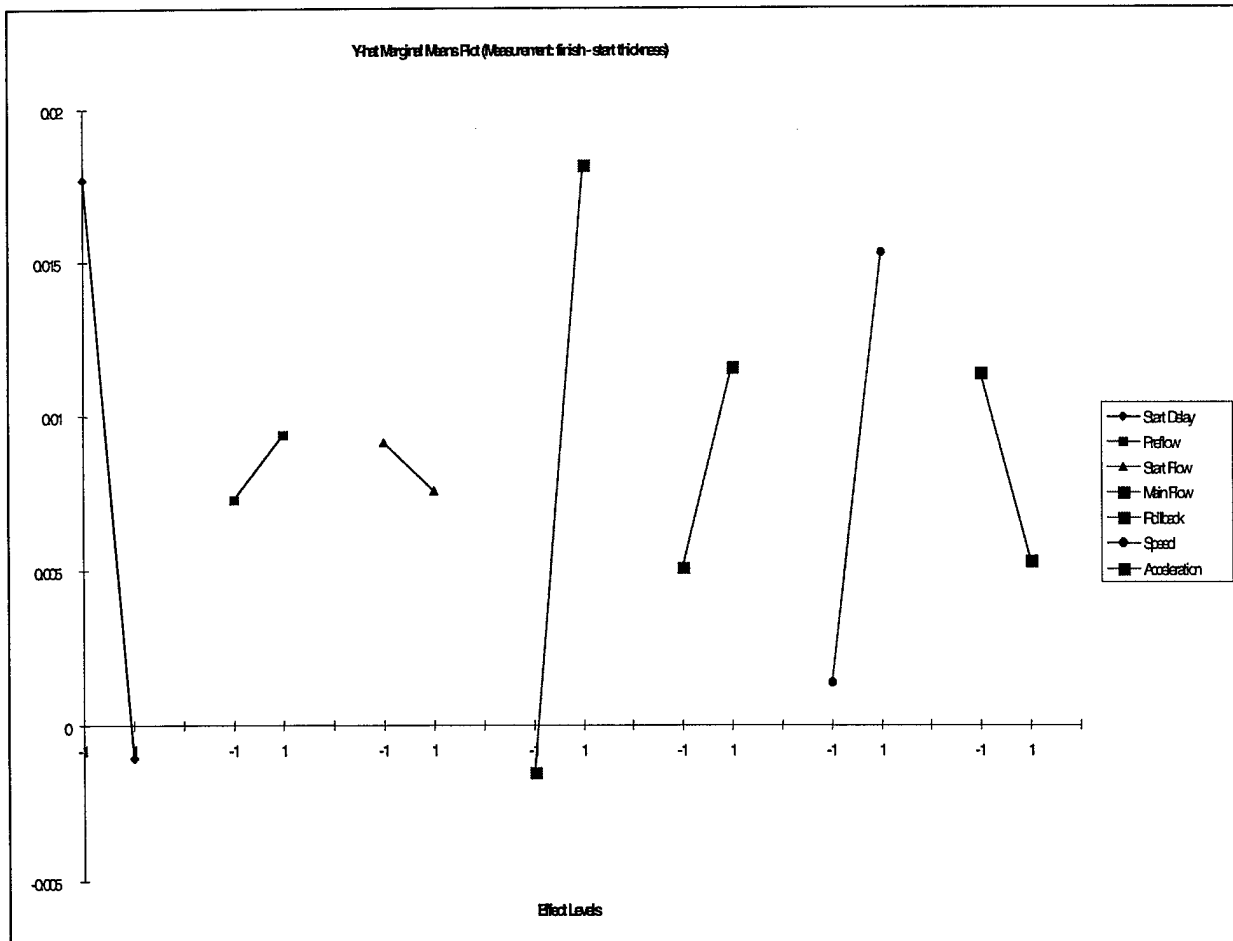


Figure 3: The marginal means plot based on the difference in start and finish thickness.

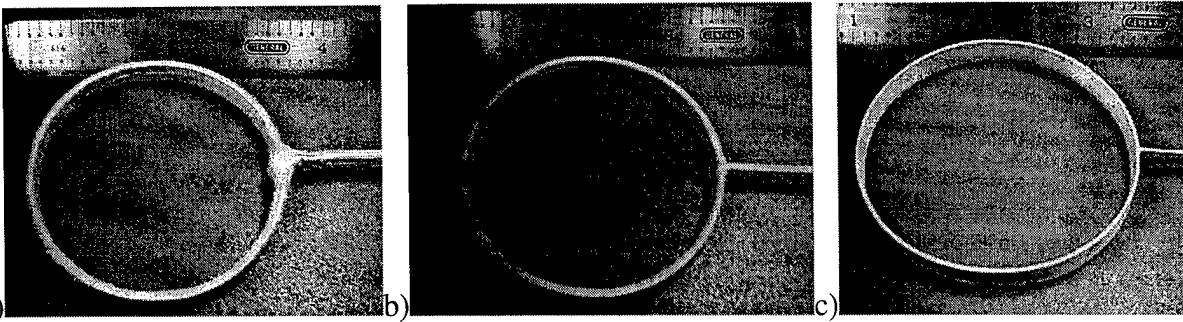


Figure 4: Cylinders a and b were fabricated prior to optimization. Cylinder c was constructed with the optimized parameters.



Figure 5: Impellers made with Kyocera and Starck silicon nitride powders.



Figure 6: A turbine blade made with the new parameters.

Automated Layer Decomposition for Additive/Subtractive Solid Freeform Fabrication

Y. C. Chang, J. M. Pinilla, J. H. Kao, J. Dong, K. Ramaswami, F. B. Prinz

micchang@Stanford.edu, jmp@Stanford.edu, jhkao@Stanford.edu, jdong@Stanford.edu, krishram@Stanford.edu, fbp@Stanford.edu

Department of Mechanical Engineering, Stanford University

Abstract

The new additive/subtractive technology (Shape Deposition Manufacturing) enhances Solid Freeform Fabrication (SFF) capability in producing near net-shape surface finish. This technology also builds parts in fewer layers compared with conventional layered manufacturing technology. However, to decompose a part into freeform layers usually requires expensive geometric computation. Also, to plan build sequences often requires human intervention because of the complicated spatial relationships among the freeform layers. At present decomposition and build sequence planning are both performed by experienced designers/users. In this paper, a novel decomposition approach based on surface splitting is proposed to facilitate computation and planning of the additive/subtractive SFF processes. The results shown in this paper are from models with 3D planar geometry. Continuous effort is devoted into extending and implementing this new approach for models with 3D freeform geometry.

1. Introduction

Traditional layered manufacturing techniques have a shorter cycle time of realizing a part from a CAD model compared with that of typical machine shop practices. Cycle time is shortened mainly because the technology employs a slicing strategy which greatly simplifies the planning task of building a part. Under this strategy, a given solid model is sliced horizontally into a set of planar layers, and these planar layers are then built one at a time from bottom up. In this case, planning the build sequence of a given model is no more than listing the sliced layers along the build direction, which is straightforward and can be automated easily.

On the other hand, certain issues limit the application of this technology. First, parts built by this technology generally show stair steps on the layer-to-layer boundaries. This lack of C2 continuity on the part surfaces is undesirable especially for parts made of ceramic materials, because each stair step can serve as a crack initiation site. In addition, the mechanical properties of parts will be affected by the bonding between layers. Clearly, reducing the number of layers by increasing the slicing interval can improve the mechanical properties. Nonetheless, the surface finish of the built parts may well become worse as the interval becomes larger. As a consequence, a trade-off has to be made case by case.

In contrast to traditional layered manufacturing technology, the new additive/subtractive SFF technology not only builds parts in fewer layers, but also achieves much finer surface finish. Instead of horizontal slicing, this new technology decomposes a solid model along a set of parting lines into freeform layers [3]. However, such decomposition usually requires expensive computation. In addition, the spatial relationship among these freeform layers is much more complicated than that among the planar layers. As a result, the build sequence can not be determined without carefully examining the geometry of each freeform layer. Therefore, the layer build sequence under this new technology is still completed mainly by experienced designers.

As shown later in this paper, a modified approach is developed for the additive/subtractive SFF technology in order to release designers from the time consuming task of decomposing a model and arranging build sequences. This new approach has been implemented successfully for models with 2.5D features. With limited testing results so far, it is shown to be able to work for models with 3D freeform features as well.

2. Surface Splitting

Currently decomposition of a given part is done in a “solid” level. That is, a given solid model is split into smaller manufacturable solid portions. An algorithm has been proposed [3] to automatically decompose a 3D part into a set of freeform layers for Shape Deposition Manufacturing (SDM) processes. In addition, all the feasible build sequences can be generated through a compact graph algorithm [6]. However, performing operations in a “solid” level usually requires expensive geometric computation.

To lower computation load, the feasibility of utilizing surfaces of a solid to partition the solid into manufacturable freeform layers for SDM processes is investigated. Since the shape of any part is represented completely by its surfaces, theoretically we can realize a solid object according to its surfaces. Simply stated, the object can be shaped out of a stock of material by performing machining operations on all surfaces of the object in such a sequence that each surface is machined without damaging any previously built surface. With this concept, each surface on the solid serves as a build unit which “partitions” the whole solid. There is no need for splitting the solid.

However, one critical manufacturing characteristic has to be considered before the concept can be applied to SDM processes. In SDM processes, the build direction of a part is pre-selected and remains unchanged for all machining stages of the part, which means the cutters always access the target machining areas from the top along the build direction. As a result, some surfaces can not be machined in a single step. As it can be seen in Fig. 1, we can not shape area B of surface S together with area A at one step without damaging A. But surface S can be fully shaped if we machine out area B first, deposit more part material on top of B, and then machine out area A. Under this reasoning, all surfaces of a part can be machined along the build direction as long as the surfaces containing both undercut and non-undercut regions are properly split into subsurfaces where each subsurface contains only either undercut or non-undercut region.

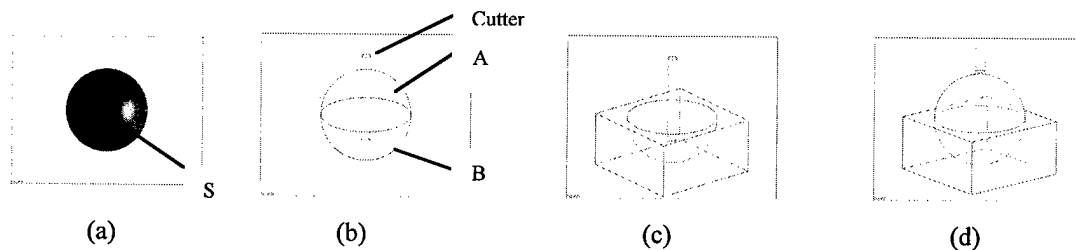


Fig. 1 (a) Sphere S (b) Surfaces A and B on the sphere (c) Machine Surface B (d) Machine Surface A

In the following sections we will first define the terms used in this approach and then describe the procedures for surface splitting.

2.1 Definitions

Undercut, non-undercut, and non-monotonic surface

The type of a surface of a given solid model can be classified into three categories [3] as shown in Fig. 2(a):

Assume that $N(u,v)$ is the normal vector at a point (u,v) on surface S , and b is the selected build direction, then

- S is an undercut surface if $N(u,v) \cdot b < 0$ for all (u,v) in S domain.
- S is a non-undercut surface if $N(u,v) \cdot b \geq 0$ for all (u,v) in S domain.
- S is a non-monotonic surface if it contains both undercut and non-undercut portions.

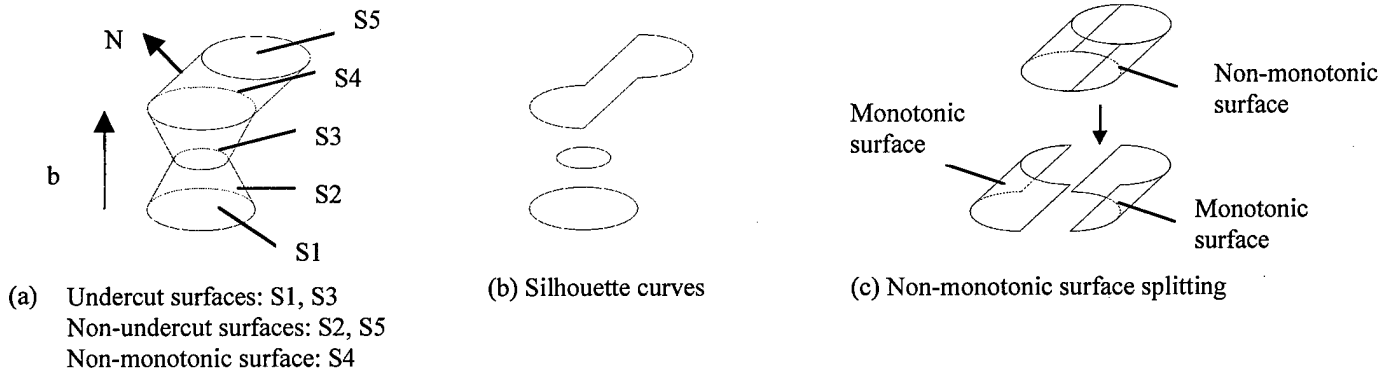


Fig. 2 (a) Three surface types (b) Silhouette curves (c) Non-monotonic surface splitting

Silhouette curve

A silhouette curve is defined as the curve along which $N(u,v) \cdot b = 0$. In other words, silhouette curves serve as the boundary between undercut and non-undercut portions of the surface. Thus one non-monotonic surface can be split into two or more monotonic (undercut or non-undercut) surfaces along the silhouette curves as shown in Fig. 2(c).

Overlapping surfaces

For any two surfaces, if there exist areas where a ray intersects both surfaces along the build direction, these two surfaces are “overlapping” surfaces.

Self-overlapping surface

If a ray intersects a monotonic surface more than once along the build direction, this surface is said to contain self-overlapping features. Fig. 3 illustrates the situation.

2.2 Procedure description

Five steps are taken to split surfaces of a solid model:

- Generate silhouette curves on all the non-monotonic surfaces of the given solid model.
- Split these non-monotonic surfaces into monotonic surfaces through the silhouette curves obtained in the previous step.
- Split self-overlap surfaces, if there exists any, into surfaces without self-overlap features [3].

- Split overlapping surfaces so that each resulting surface is either totally overlapped or totally not overlapped with other surfaces [3], then
 - Mark each resulting surface as either an undercut or a non-undercut surface.
- A simple example is given in Fig. 4.

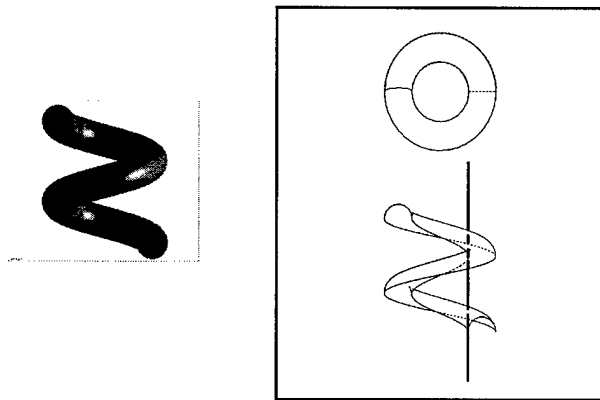


Fig.3 Self-overlapping surface

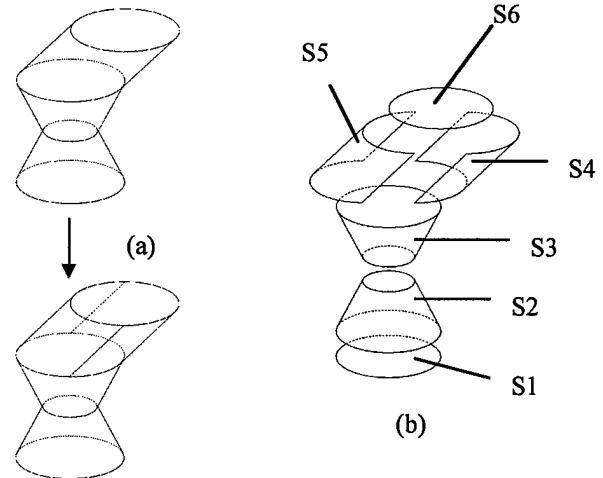


Fig.4 (a) Generate silhouette curves (b) Six surface compacts

After performing the five steps, the surfaces of the solid have been split into subsurfaces which serve as the basic build units.

3. Surface Compact Graph Construction

Up to this stage, all the surfaces of the target solid have been split into smaller subsurfaces such that each subsurface can be processed in one additive/subtractive build cycle. The target solid can now be produced by shaping these subsurfaces in certain build sequences. As mentioned earlier, a feasible build sequence is basically a spatial arrangement of subsurfaces which assures the cutters will not run into the already built subsurfaces while the target subsurface is being machined. In order to identify such sequences, the spatial relationships among all these freeform subsurfaces have to be examined and recorded. A special graph structure named Compact Graph [4] is utilized to record these spatial relationships because it not only offers a concise format of keeping these spatial information, but also provides useful algorithms to explore alternative build sequences afterwards. Finally, a “preliminary surface compact graph” is obtained after the subsurface entities and their spatial relationships are recorded through the Compact Graph structure. Again, the terminology and procedures are stated in the following sections.

3.1 Definitions

Surface compact

A surface compact represents a set of undercut or non-undercut surfaces which can be machined/processed together in one SDM cycle. In its simplest form, a surface compact is either an undercut surface or a non-undercut surface.

Surface compact graph

A graph in which each node represents one surface compact and each edge connecting two nodes indicates certain spatial relationship (either precedence or adjacency) between these two nodes.

Precedence relationship

One surface compact (or node) is "precedent" to another surface compact if there exists a ray which intersects both compacts along the build direction. Thus if surface compact A is "precedent" to surface compact B, compact A has to be built before compact B can be built. In other words, the precedence relationship between two compacts represents the build order between them.

Adjacency relationship

Two surface compacts (or nodes) are "adjacent" if they have common boundary.

3.2 Procedure description

Three steps are taken to construct a preliminary surface compact graph:

- One node is created in correspondence with one surface compact obtained through the surface splitting stage.
- Precedence relationship between each undercut surface compact and each non-undercut surface compact is examined. If there exists a precedence relationship between the two surface compacts, a directed edge is created between their associated nodes.
- The adjacency relationship between any two surface compacts (or nodes) is then examined and an undirected edge is created if there exists adjacency relationship between the two compacts.

After all surface compacts are processed through the three steps above, the spatial relationship among all surface compacts is preserved in the resulting preliminary surface compact graph, as shown in the example below. (Fig. 5)

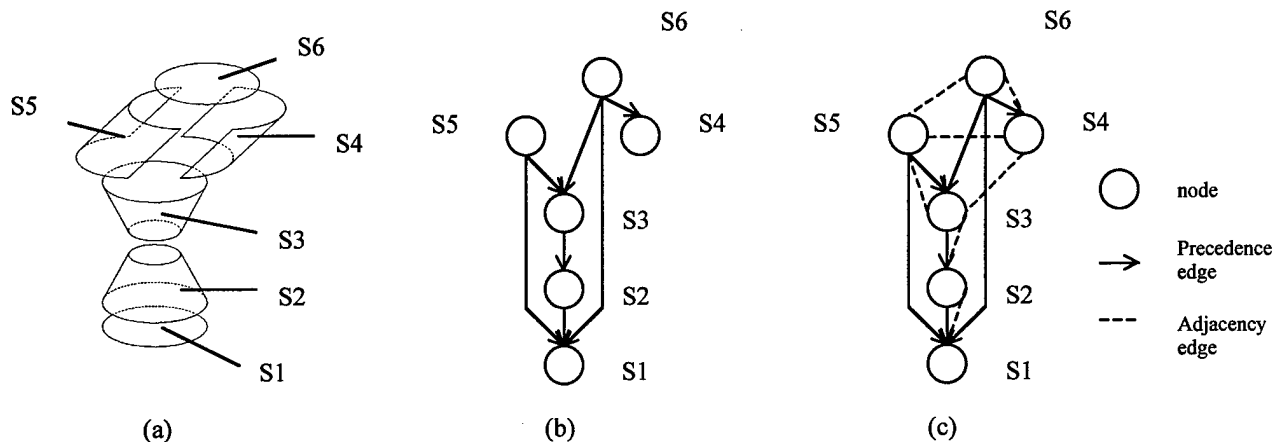


Fig. 5 (a) Surface compacts (b) Surface compact nodes and precedence edges (c) Preliminary surface compact graph

4. Surface Compact Graph Consolidation

The preliminary surface compact graph obtained above represents the spatial relationships between every two surface compacts. However, redundant spatial relationships may well exist in this preliminary graph. Because the computation cost of finding build sequences will be affected by these redundant spatial relationships, an intermediate step to consolidate the preliminary graph is taken before we search for the build sequences. At this stage, the preliminary surface compact graph is consolidated into a minimal surface compact graph.

4.1 Definitions

Redundant precedence edge

If the precedence relationship represented by a precedence edge can be also represented through a combination of other precedence edges, this precedence edge is called a “redundant” edge since it repeatedly expresses an existing precedence relationship.

Minimal surface compact graph

Through the two steps described below, a preliminary surface compact graph can be consolidated into a more concise graph named minimal surface compact graph. This minimal graph contains fewer nodes and edges but still describes the spatial relationship among the surfaces of a given solid model. Formally speaking, a minimal surface compact graph results when the nodes in a given preliminary graph can not be further merged and all the redundant precedence edges are removed. For instance, a solid with six surfaces can be represented by a minimal graph of four nodes and six edges rather than six nodes and thirteen edges as shown in Fig. 6.

4.2 Procedure description

Two steps are required to consolidate a preliminary surface compact graph into a minimal graph:

- Any two adjacent nodes can be merged into a new node if no precedence edge exists between them.
- Locate and remove all redundant precedence edges in the graph with certain checking algorithm [5].

After the adjacent node merge and redundant edge removal steps, a minimal surface compact graph containing the least number of nodes and edges is formed.

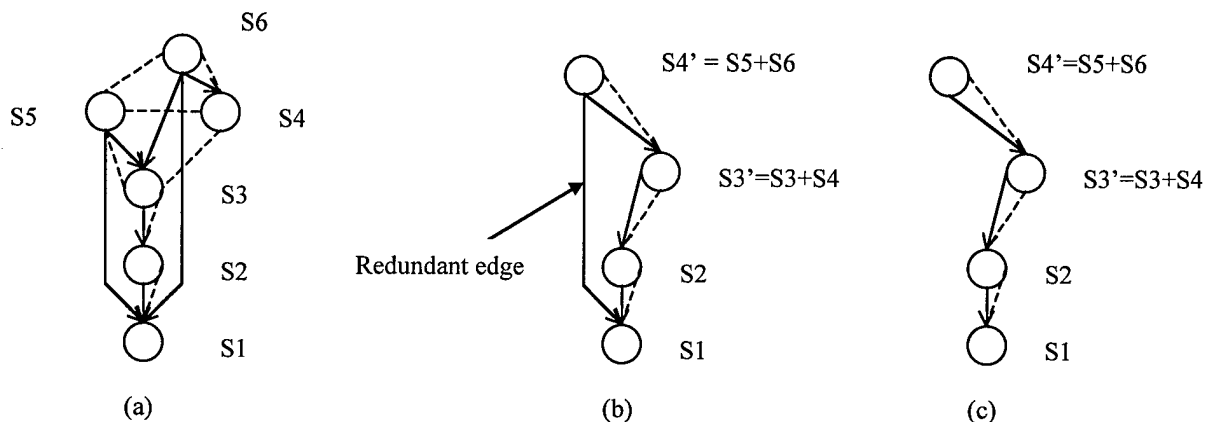


Fig.6 (a)Preliminary graph (b)Node merge and redundant edge removal (c)Minimal graph

5. Build Sequence Generation

As explained above, the minimal surface compact graph records all the build precedence relationships among nodes. Alternative build sequences can be explored by partitioning this minimal graph properly. Because the structure of a minimal surface compact graph is equivalent to that of a Compact Adjacency Graph (CAG) [4], the algorithms developed for CAG [6] can be also applied to a minimal surface compact graph. By employing these algorithms, the build sequence will be extracted automatically from the minimal graph as shown below. (Fig. 7)

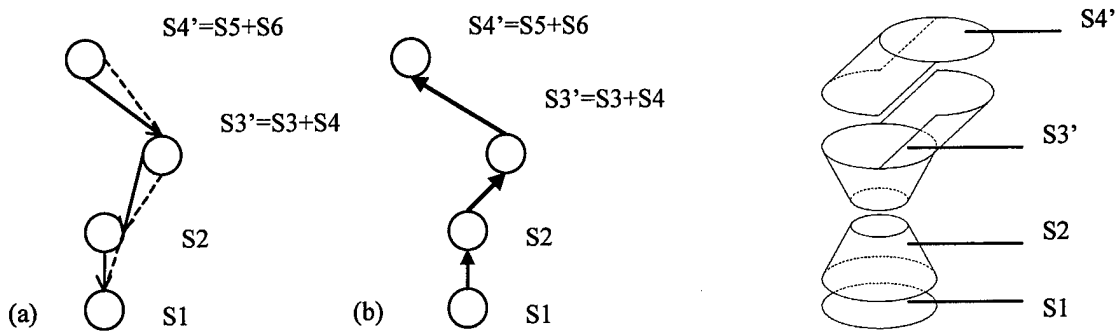


Fig.7 (a) Minimal graph (b) Build sequence: S1 -> S2 -> S3' -> S4'

6. Result

The example part has twenty-four surfaces originally. Ten undercut surfaces and fourteen non-undercut surfaces are identified after performing surface splitting on the part. The preliminary surface compact graph contains twenty-four nodes representing these twenty-four surfaces. After graph consolidation, the resulted minimal surface compact graph contains only four nodes, which suggests this part can be built in four layers as illustrated in Fig. 10. In short, we first deposit support material and machine surface compact S1, then deposit part material and machine S2. More support material is deposited on top of S2 and S3 area is machined. Finally, we deposit part material on top of S3 and machine S4 area.

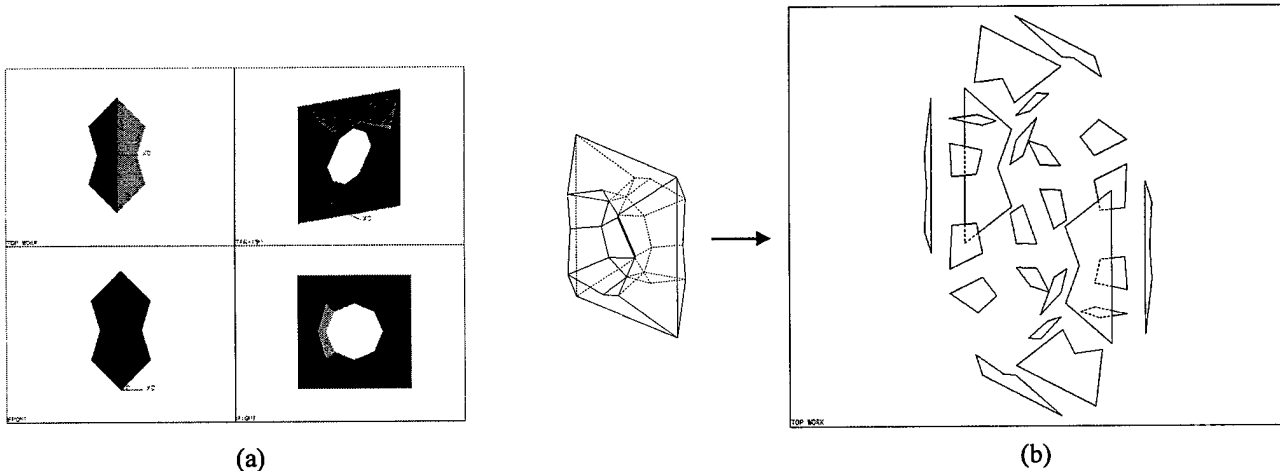


Fig.9 (a) Example part (b) Decomposed surfaces

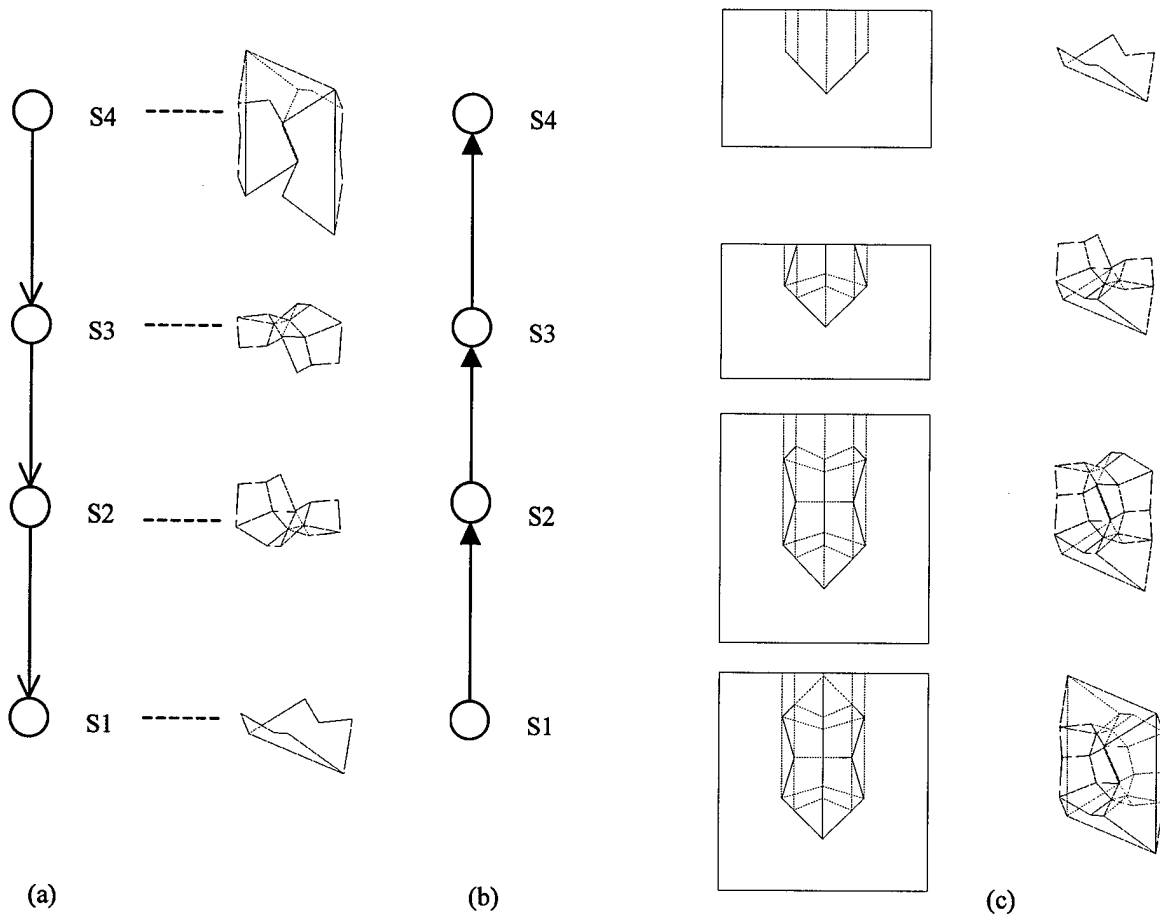


Fig. 10 (a) Minimal surface compact graph (b) Build sequence: S1->S2->S3->S4 (c) Build sequence illustration

7. Conclusions

Instead of decomposing a solid model horizontally, the proposed decomposition strategy splits and distinguishes the surfaces of the given solid into undercut and non-undercut surface compacts. Based on the surface compacts, the compact graph algorithms can then construct build sequences of the given model automatically. Compared with traditional planar slicing approach, this new surface compact approach results in fewer build layers for 2.5D and 3D freeform solid models.

8. Acknowledgement

We wish to acknowledge the financial support of DARPA under the 3D Reasoning project and Prof. C. Sequin of UC Berkeley for providing us the example part.

9. References

1. Harris L. Marcus and David L. Bourell. (1993) Solid Freeform Fabrication. Advanced materials and Processes, 144(3) pp28-35
2. Merz R., Prinz F. B., Ramaswami K., Terk M., and Weiss L. E. (1994) Shape Deposition Manufacturing. SFF symposium '94 Austin, Texas.

3. Ramaswami, K., Y. Yamaguchi, et al. (1997). Spatial Partitioning of Solids for Solid Freeform Fabrication. ACM/SIGGRPAH Symposium on Solid Modeling and Applications.
4. Pinilla, J. M., Kao J. H., et al. (1997). The Compact Graph Format: An Interchange Standard for Solid Freeform Fabrication. NIST workshop on Rapid Prototyping, Maryland, NIST.
5. Pinilla J. M., Kao J. H., Prinz F.B. (1998). Process Planning and Automation for Additive-Subtractive Solid Freeform Fabrication. Process planning and execution for SFF processes, SFF symposium '98 Austin, Texas.
6. Pinilla J. M., Kao J. H., Prinz F.B. (1999). Compact Graph Representation for Solid Freeform Fabrication (SFF). Submitted for publication.

Automated Planning for Material Shaping Operations in Additive/Subtractive Solid Freeform Fabrication

Jianpeng Dong, Ju-Hsien Kao, Jose M. Pinilla, Yu-Chi Chang and Fritz B. Prinz

Stanford University
Department of Mechanical Engineering
Stanford, CA 94305-3030

Abstract

Combining the advantages of layered manufacturing and material removal processes, additive/subtractive solid freeform fabrication (A/S SFF) can build parts with complex shapes without compromising precision requirements. However, preparing material removal operations requires special expertise, which has in fact become one of the bottlenecks of the A/S SFF manufacturing process. To achieve automated planning, a shaping process planner is being developed based on 3D solid representation and a surface classification scheme. This planner can generate numeric control (NC) codes for CNC milling in an automatic fashion on non-undercut features of arbitrary 3D input geometry. Planning approaches are also presented in order to shape parts accurately and efficiently. The proposed shaping planner thus delivers on the promise of fully automated process planning in A/S SFF.

Keywords: CAD, CAM, Solid Freeform Fabrication , CNC Machining, Process Planning, Tool Path Generation, Automation

1. Introduction

In most Solid Freeform Fabrication (SFF) systems, CAD models are first decomposed into 2D layers, and then physical parts are built up layer by layer. Decomposing a 3D model and building a physical part in this fashion, however, can result in stair-steps on freeform surfaces; thus sacrificing surface finish and dimensional accuracy of the resulting parts [2].

Additive/subtractive Solid Freeform Fabrication (A/S SFF) combines the advantages of layered manufacturing and material removal processes, such as CNC milling, so it can build parts with complex shapes without compromising precision requirements. However, integration of material removal operations with material addition operations makes process planning for A/S SFF much more challenging than that for purely additive SFF [1]. In particular, preparing for shaping operations and generating numeric control (NC) codes for CNC milling require special expertise and experience, which have in fact become one of the bottlenecks of the A/S SFF manufacturing process. To make A/S SFF more productive, a process planner for shaping operations is indispensable.

In this paper, A/S SFF process will be examined from a process planning perspective. Then how to automate shaping operations will be considered. Based on a proposed surface classification scheme, strategies are presented to improve machining efficiency and maintain part accuracy. Finally, an example part is analyzed to show the capabilities of the proposed planner.

2. Shaping Process Planner

A/S SFF processes [1-3] involve iteration of material deposition and material removal operations, as can be seen from Figure 1. Starting with build direction selection, it then decomposes a CAD model into 3D layers with variable thickness using a 3D model decomposition technique. This technique can identify parting lines of undercut and non-undercut features of a model, and uses these parting lines to split the model [2, 4]. Part and support structures are thus constructed with extrusion operations in the computer. As a result, undercut features of the model will become non-undercut features of one of the decomposed 3D layers; thus no undercut features of the 3D layers need to be shaped during manufacturing. This model decomposition technique enables us to build 3D layers incrementally. Because these decomposed 3D layers can be shaped accurately with CNC milling machines, A/S SFF is capable of building complex parts with higher dimensional accuracy and better surface finish than purely additive SFF.

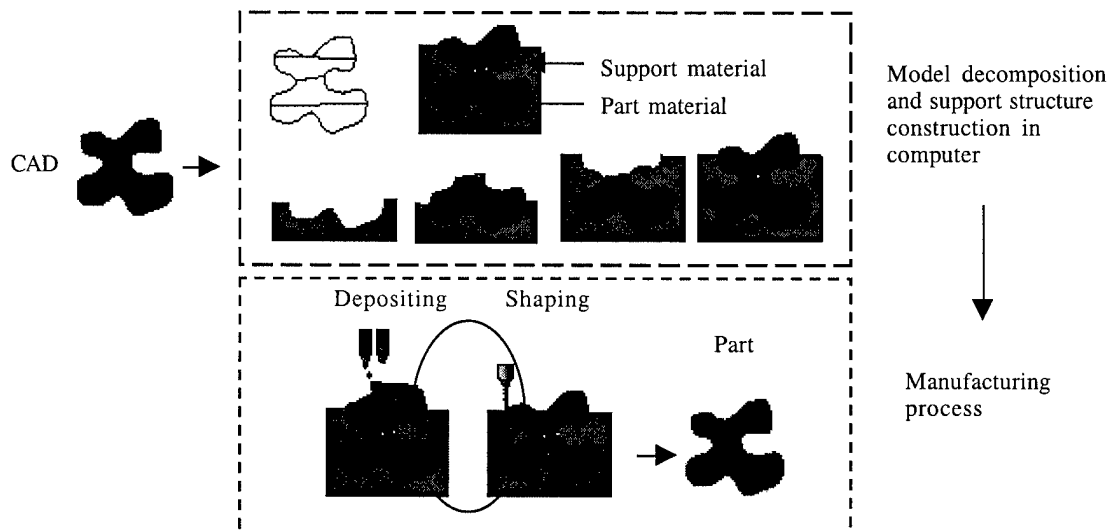


Figure 1. A/S SFF process planning

As discussed above, a distinct characteristic of shaping operations in A/S SFF is that only non-undercut features of the decomposed 3D layers need to be machined during manufacturing. Decomposing CAD models in this way also avoids fixture design for shaping these 3D layers because previously built layers form the natural support structures. In addition, model decomposition takes removal process constraints, such as cutter length, into account; thus making all non-undercut surfaces of each 3D layer accessible by cutters from above. Therefore, shaping process planning becomes easier than conventional CNC machining.

An automated shaping planner has been designed to be capable of generating NC codes for any given 3D layer without human intervention, which is shown in Figure 2. The inputs for this planner are decomposed 3D layers, and the outputs are the NC codes for shaping the layers. It also needs the cutter geometry information before tool paths can be generated and machine information before post-processing can be accomplished. The implementation of this planner lies on top of commercial CAD/CAM packages, Unigraphics, which provides toolkits to access to CAD model database and generate tool paths.

In this paper, the discussion will focus on planning finishing operations on 3-axis CNC milling machines because finishing operations take the majority of the machining time and are crucial to part dimensional accuracy and surface finish.

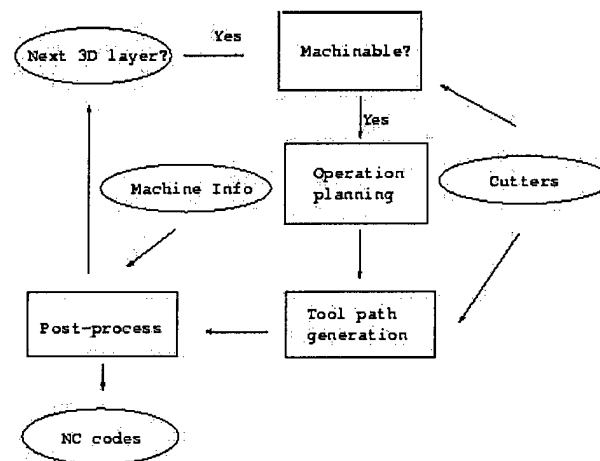


Figure 2. Shaping planner

3. Tool Path Generation

The essential tasks of a shaping process planner are to select and organize different shaping operations and to generate tool cutting paths over the model surfaces to be shaped. These selection and organization decisions are based on what tool path generation methods are available and how tool paths are generated. A variety of tool path generation methods have been developed. Most of recent research work focuses on generating tool paths over freeform surfaces. Usually, a model is a mixture of a variety of surfaces; hence an automated planner should deal with the whole model instead of individual surfaces. But generating tool paths over different types of surfaces is rarely studied. Several non-commercial approaches have been proposed, but they are either impractical or too hard to have a robust implementation [5-7, 10].

In this study, two widely available types of tool paths, layer-based and projection-based, are used. In the case of layer-based methods, a group of parallel planes of constant spacing (which is called the cutting depth) are used to slice the whole model, and intersection curves of these planes with the model are offset with respect to the cutter geometry to form the tool paths. In the case of projection-based methods, a loop of curves are selected as boundary curves. The boundary curves are then recursively offset by a constant distance (which is called the step-over distance). The resulted offset curves are projected onto the up-facing surfaces in order to update the z coordinate of each point of the offset curves. These modified curves are the tool paths.

The most important parameters controlling the machining tolerance are cutting depth (in the case of layer-based tool paths) and step-over distance (in the case of projection-based tool paths). Both of them are required by the CAM packages to be **constant** during tool path generation. Some variations do exist [8,9]. For instance, the whole model can be divided into several blocks. Within each block, the constant constraint is required, but the

values chosen in different blocks may be different. In addition, the number of such blocks are limited. Owing to these constraints, each method may produce longer tool paths than necessary to meet the machining tolerance. If the cusp height of material left over after the model is machined is used as a measurement of the machining tolerance, how the ideal cutting depth or step-over distance changes as the normal of a to-be-shaped surface changes can be shown in Figure 3.

Figure 3 (a) shows an inclined face being shaped with a ball endmill. The relationship between machining tolerance δ , cutter radius r , face inclining angle α , step-over distance s and cutting depth c is given in the follows expressions:

$$c = \sqrt{r^2 - (r - \delta)^2} \sin \alpha \quad (1)$$

$$s = \sqrt{r^2 - (r - \delta)^2} \cos \alpha \quad (2)$$

As can be seen from Figure 3 (b), the ideal cutting depth of layer-based tool paths will have the minimum value when the inclining angle α is equal to 0° , and it will have the maximum value when $\alpha = 90^\circ$; On the other hand, the ideal step-over distance of projection-based tool paths will have the minimum value when $\alpha = 90^\circ$, and the maximum value when $\alpha = 0^\circ$. It can also be seen that when $\alpha = 45^\circ$, the ideal cutting depth and step-over distance have the same value. Owing to the restriction that both cutting depth and step-over distance should be kept constant during tool path generation, the smallest cutting depth or step-over distance value has to be chosen when a freeform surface is to be shaped; otherwise, the machining tolerance can not be guaranteed where the corresponding ideal values are smaller than the specified values. However, this smallest value will lead to longer machining time where the ideal value is greater than the specified one; thus sacrificing machining efficiency in this case. Ways of improving the machining efficiency have to be found.

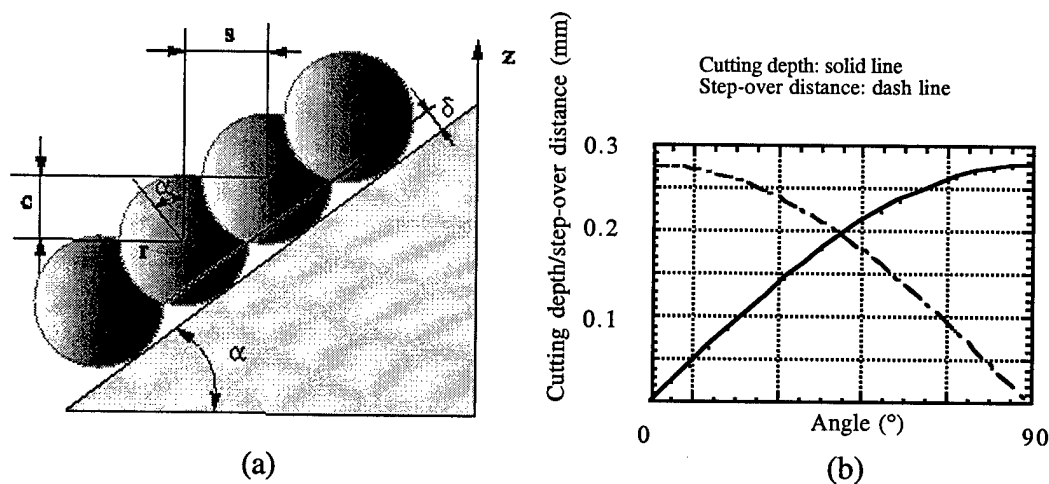


Figure 3. Normal direction effect on cutting depth and step-over distance. Cutter radius is 12.7 mm, and cusp height is 0.003 mm.

4. Surface Classification

Considering the effect of surface steepness, non-undercut surfaces (because in A/S SFF only non-undercut surfaces of a compact are to be shaped) are classified into three categories: (1) vertical walls which have normal perpendicular to the z direction; (2) horizontal faces which have normal parallel to the z direction; (3) freeform surfaces or inclined faces. Furthermore, freeform surfaces and inclined surfaces are identified as flat and steep surfaces. The criterion for distinguishing a flat surface from a steep one is to use a 45° angle between the surface normal and the build direction. If the surface normal forms an angle less than or equal to 45° with the z direction, this surface will be identified as steep surface; otherwise, it is flat. If necessary, a freeform surface will be split into flat and steep portions based on the same criterion.

Different types of surfaces should be shaped differently. For instance, to machine vertical walls or horizontal planar surfaces, flat end-mills are usually used; while ball end-mills are usually used to machine curved freeform surfaces or inclined faces on 3-axis CNC machines. To enhance machining efficiency, freeform surfaces or inclined faces are further categorized based on their surface normal values. The details will be illustrated in Section 5.

5. Machining Strategies

5.1 Hybrid-machining

Machining using either layer-based or projection-based approaches alone is inefficient because the cutting depth or step-over is restricted to be constant. One solution is to apply layer-based and projection-based tool paths one after the other, shaping the whole model. In this case, the smallest ideal step-over distance or cutting depth value does not have to be used. Instead, the corresponding values at a 45° angle are used. The reasons are as follows. If the ideal step-over distance at 45° can achieve the specified machining tolerance, then using the same step-over distance will produce smaller cusp heights over those surfaces with a normal greater than 45° . Similarly, if the cutting depth at 45° can achieve the specified machining tolerance, then using the same cutting depth will produce smaller cusp heights over those surfaces with a normal less than 45° . By applying both tool paths, the whole model is guaranteed to be shaped to the specified machining tolerance.

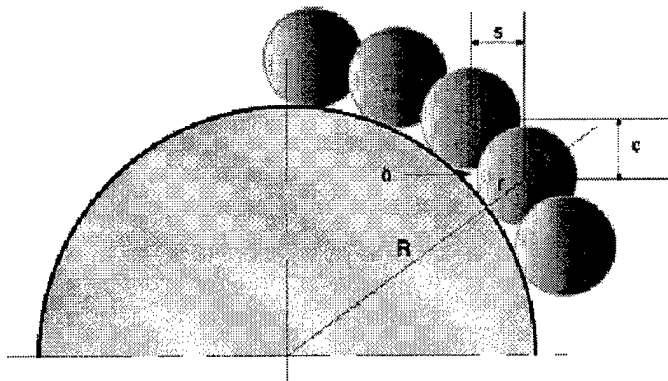


Figure 4. Relationships between different machining approaches

This strategy significantly reduces the machining time even though almost every surface will have to be shaped twice. A simple example is shown in Figure 4. As can be seen, a half-sphere with a radius of 50 mm is being shaped by a ball end cutter with a radius of 12.7 mm. The cutting feed rate is 1000.0 mm/min. No cutter change or tool engage and retract time is considered. If each type of tool paths is applied alone, to shape this model to the specified tolerance, which is assumed to be 0.003 mm, more than 20 hours has to be spent on machining, as can be seen from Table 1. By applying both tool paths, since a greater step-over distance and cutting depth can be used, the machining time is reduced by two orders of magnitude. Obviously, this strategy is still not efficient because almost every surface of the model has been machined twice.

Table 1. Machining efficiency comparison of different tool path generation approaches (Time in minutes).

Approach	Layer-based	Projection-based	Hybrid	Splitting
Machining time	2028	1292	29	20

5.2 Surface-splitting

To avoid machining every surface twice, a surface splitting approach is proposed to distinguish surfaces based on surface normal distribution. First, classify all the surfaces based on the scheme presented above. If necessary, split freeform surfaces and inclined surfaces into flat and steep portions. Generate tool paths on vertical walls or horizontal planar faces using flat end-mills, and generate layer-based tool paths on steep portions and projection-based tool paths on flat portions separately using ball end-mills.

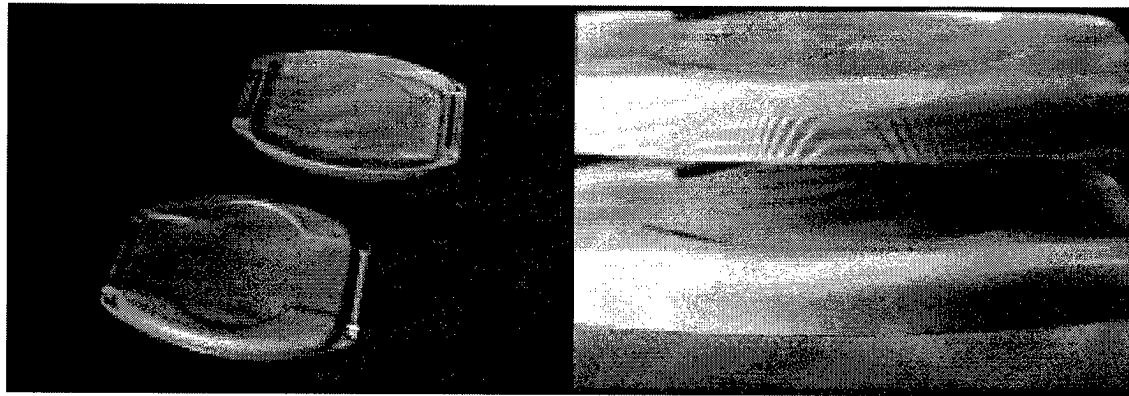
A similar algorithm to model decomposition has been developed in order to find the boundary curves between flat surface portions and steep ones in the model. In this case, instead of finding the parting lines (each point on which has a normal perpendicular to z direction), the splitting curves (each point on which has a normal parallel to a planar face with either a 45° inclination angle) need to be identified. Once the splitting curves are found, they are used to identify which portions of a surface should be machined using layer-based tool paths and which portions should be shaped using projection-based tool paths. Furthermore, same type surfaces can be grouped together; thus reducing the total number of operations.

If this approach is applied to the same model shown in Figure 4, it reduces machining time by about 1/3 compared with the above hybrid-machining method, as can be seen in Table 1.

6. Case Study

The proposed shaping planner can be used to shape non-undercut features of any 3D layers and output the NC codes with few limited manual inputs, such as cutter information (tool number) and machining tolerance. Currently, it also needs to manually identify narrow deep cavities and select different cutters based on the geometry of such cavities. But an automated cutter selection module will be developed as a part of the planner based on a medial axis transform (MAT) representation of the model [11].

Figure 5 shows two sample parts built with this planner. The right photograph shows two parts shaped with different approaches. The above one was shaped only using projection-based tool paths. The bottom one was shaped using hybrid-machining approach. Both of them use the same step-over distance. As can be seen from this photograph, the hybrid-machining approach exhibits better surface quality. Because a greater step-over distance and cutting depth were adopted, the machining efficiency was also enhanced.



(a)

(b)

Figure 5. Sample parts built using different approaches. (a) Sample parts, (b) parts shaped by projection-based tool paths alone (above) and by hybrid-machining approach (bottom)

7. Conclusions

A generic shaping operation planner purely based on model geometry is presented. Using widely available tool path generation methods, its implementation is simple and its performance is robust. Two approaches, hybrid-machining and surface-splitting, are proposed to reduce machining time and enhance efficiency of the material removal operations in A/S SFF. In particular, the proposed surface-splitting approach can reduce machining time by two orders of magnitude. This method splits the surfaces into different portions or distinguish individual surfaces into different types based on surface normal. Tool paths are then generated by alternatively applying layer-based and projection-based methods on different types or portions of surfaces. This planner will not only reduce the planning overhead introduced by the shaping operations in A/S SFF, but it will eventually become part of a fully automated A/S SFF process planner.

Acknowledgments

The authors acknowledge support from the Defense Advanced Research Projects Agency, the Office of Naval Research and Unigraphics Solutions Inc.

References

- [1] J. M. Pinilla, J. Kao and F. B. Prinz, 1998, Process Planning and Automation for Additive-Subtractive Solid Freeform Fabrication, SFF Symposium 1998, Austin, TX
- [2] L. Weiss, R. Merz, et al, 1997, Shape Deposition Manufacturing of Heterogeneous Structures, Journal of Manufacturing Systems, 16 (4), 239-48

- [3] A. G. Cooper, S. Kang, J. W. Kietzman, F. B. Prinz, J. L. Lombardi and L. Weiss, 1998, Automated Fabrication of Complex Molded Parts Using Mold SDM, SFF Symposium 1998, Austin, TX
- [4] Krishnan Ramaswami, Process Planning for Shape Deposition Manufacturing, Ph.D. Dissertation, 1997, Stanford, CA.
- [5] S. Marshall and J. G. Griffiths, 1994, A Survey of Cutter Path Construction Techniques for Milling Machines, INT.J. PROD. RES., 32 (12), 2861-77
- [6] K. Suresh and D. Yang, 1994, Constant Scallop-height Machining of Free-form Surfaces, J. Engineering for Industry, 116 (2), 253-9
- [7] R. Lin and Y. Koren, 1996, Efficient Tool-Path Planning for Machining Free-form Surfaces, J. of Engineering for Industry, 118 (2), 20-8
- [8] P. Kulkarni and D. Dutta, 1996, An Accurate Slicing Procedure for Layered Manufacturing, Computer-Aided Design, 28 (9), 683-97
- [9] A. Dolenc and I. Makela, 1994, Slicing Procedures for Layered Manufacturing Techniques, Computer-Aided Design, 26 (2), 119-26
- [10] B. S. Prabhu and S. S. Pande, 1999, Automatic Extraction of Manufacturable Features from CAPP Models Using Syntactic Pattern Recognition Techniques, 37 (6), 1259-81
- [11] J. Kao, Ph.D. dissertation, 1999, Process Planning for Additive/Subtractive Solid Freeform Fabrication Using Medial Axis Transform, Stanford, CA.

Computer-Aided Process Planning for automatic generation of 3D digitizing process for laser sensors

Alain Bernard, Stéphane Davillerd, Benoit Sidot

CRAN (Research Center for Automatic Control of Nancy)
Université Nancy I - BP 239

54506 Vandoeuvre les Nancy Cedex – France

Tel: +33 3 83 91 27 29. Fax: +33 3 83 91 23 90.

E-mail: alain.bernard@cran.u-nancy.fr

ABSTRACT

This paper introduces some results of a research work carried out on the automation of digitization process of complex parts using a precision 3D-laser sensor.

It will be presented a new way to scan automatically a complex 3-D part in order to measure and to compare the acquired data with the reference CAD model. Due to the fact that rapid prototyping processes do not allow the direct manufacturing of high precision parts, it is very often necessary to measure a first part in order to modify the process parameters.

After introducing the digitization means, based on a CMM machine and a plane laser sensor, the simulation environment will be presented as adapted for simulation and validation of 3D-laser scanning paths. The CAPP (Computer Aided Process Planning) system used for the automatic generation of the laser scanning process will also be introduced.

Keywords: scanning process simulation, inspection, optimization

1 INTRODUCTION

Life cycle of new products needs time compression, from early design stages to industrial production. Rapid prototyping (Bernard & al., 1998) is very often used to produce test parts representative of CAD model. The objective of digitalization consists, starting from a physical object, in acquiring a digital image of the surfaces of the parts on a point cloud form. After a processing to make it coherent, this cloud is exploitable by CAD software for the surface reconstruction of the part, its manufacture or its measurement (Figure 1).

In this project, and due to industrial demands, the main objective is measurement of prototype parts or tools, in order to verify their conformity to the reference CAD model. In this field of application, the efficiency of the first step of the process “scanning – point cloud treatment – surface (or volume) modeling or technological applications (STL, CNC, ...)” (Figure 2) is one of the main important steps of control process because it decides of how the part will be digitize, and mainly of the final result.

The challenge of the presented project is to automatically generate the measuring process of the part in order to be able to characterize the errors compared to the CAD reference model.

This complete goal contains different sub-objectives. The first one is to be able to simulate and to validate a scanning process for a plane laser sensor, and, at last, to automatically generate this scanning process and the corresponding sensor paths. The context is defined as follow:

- the digitalization environment (CMM, sensor) is known and the kinematics parameters are defined,
- the CAD model of the part to be measured is the reference and is numerically defined.

The fact that the CAD model of the part is known involves that this is not reverse engineering objective (Bernard & al., 1998) (Zhang & al., 1995) but the goal is the inspection (or measurement) result and the comparison of point clouds with the CAD model (figure 3).

The main problem is to obtain rapidly digital data from scanning process in order to have an efficient comparison between the reference CAD model and data obtained by digitization (Moron, 1996)(Prieto & al., 1998).

The main application fields of this application are rapid product development, and more especially foundry and plastic injection applications. So, geometry of parts is very complicated and mechanical probes are not well adapted for data acquisition. In order to reduce time consuming and to improve point cloud density, it has been decided to use a plane laser sensor. One of the major improvements of the

complete inspection process using laser sensor is to automate off-line generation, simulation and validation of the laser sensor scanning process.

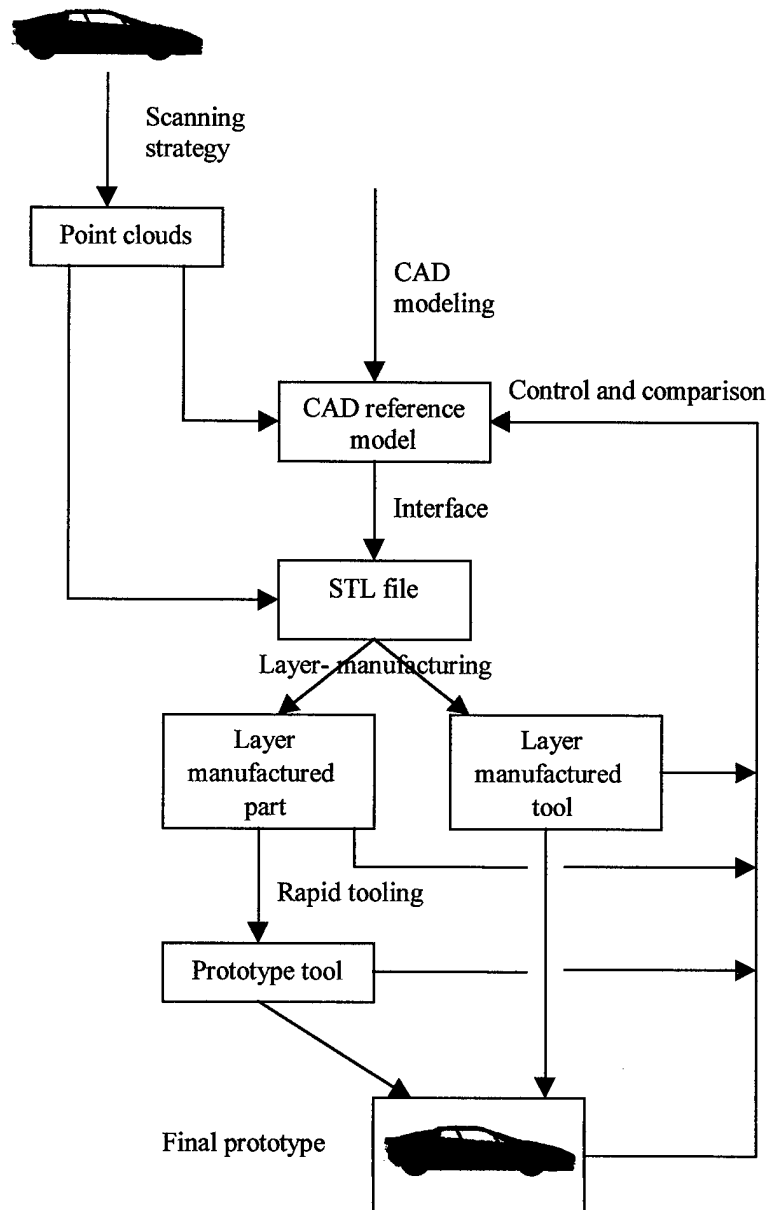


Figure 1. Rapid prototyping process

In order to proceed this project, it was decided to invest in a 3D precision system (laser sensor integrated on a CMM). Then we initiated an analysis of the digitizing process, using such means, with the intention of automating maximum operations of global acquisition process (Varady & al., 1997).

In this paper, it will be presented a brief description of the environment on which was based this research, and more particularly of the integration of the laser sensor. After a brief analysis of the steps of scanning, the proposed simulation and validation of 3D-laser sensor scanning process will be presented. Finally, some elements for the automatic generation of the scanning process (determination of the related positions between part and sensor, trajectory definition) will also be introduced and argued.

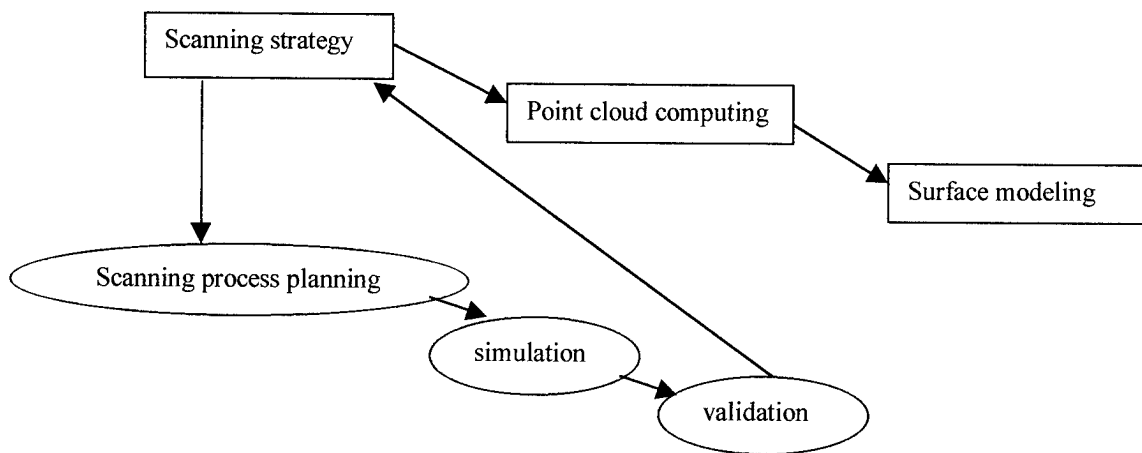


Figure 2. Scanning and modeling process

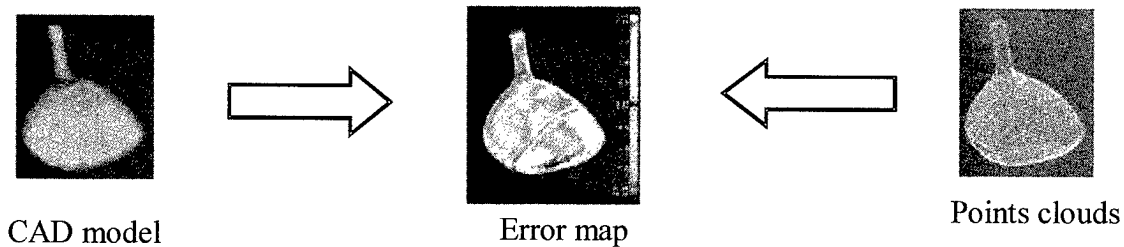


Figure 3. Control objective and environment

2 SCANNING WORKCELL

Laser sensors are materially unable to completely digitize a complex part in only one relative orientation between sensor and part. According to part complexity and according to sensor technical specifications, it remains areas where digitalization is not possible. These areas are the result of shadow or occultation phenomena depending whether the surface part is seen by the camera but non-enlightened, or the surface indeed enlightened but unseen by the camera.

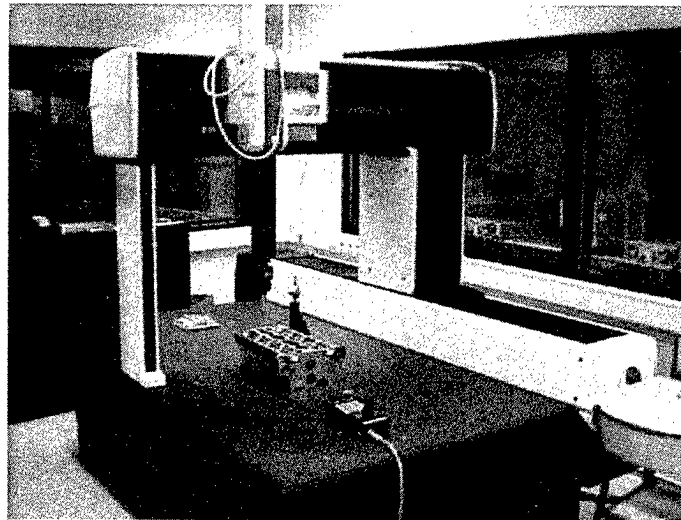


Figure 4. Coordinate measuring machine

The digitization cell is made with a coordinate measuring machine (CMM) GAMMA 1203, from DEA (figure 4) and a laser sensor from Kréon Industrie (Kréon Industrie, 1997). It is made of the 3D plane laser sensor KLS 51 (Figure 5), an Electronic Control Unit (ECU) and the “Kréon Reporter Plus” software. This environment has been detailed in (Davillerd, 1998).

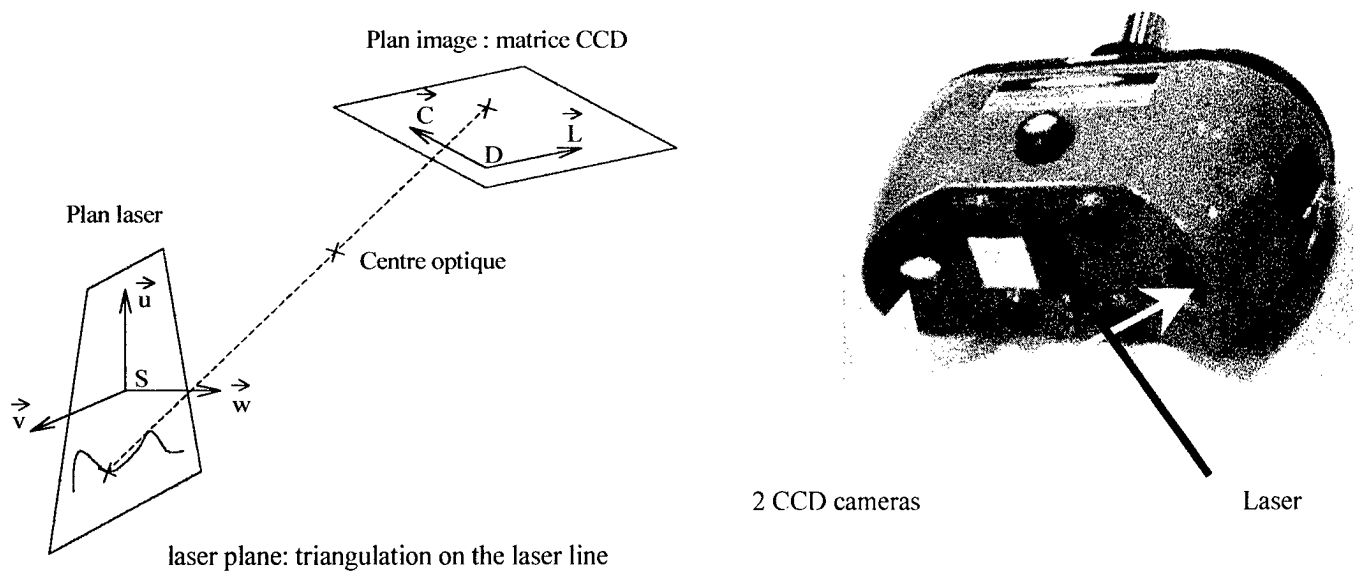


Figure 5. KLS 51 laser plane sensor

Furthermore, it can be noticed that thanks to the software and to the mechanical interface between the CMM and the sensor, the Kréon acquisition system is able to manage 4 positions of sensor, around the Z-axis, imperatively parallel with machine axes.

Based on the active triangulation principle, the sensor uses plane laser technology and is equipped with two CCD (Charge Coupled Device) cameras, placed here and there of the laser plane. The use of two cameras instead of only one allows attenuating the problems involved in the shadow or occultation phenomena on complex parts and increasing the number of points acquired with each digitization.

The Kréon acquisition system has a measurement field of trapezoidal form with a 45-mm depth. This characteristic confers on the user facilities for the creation of trajectories by reducing the movements necessary to place the surface to be scanned in the measurement field.

3 DIGITIZATION IMPROVEMENTS

In this environment, a complete analysis of the digitalization process has been proceeded to find the critical stages, which will be studied and improved. A flow chart describing this process is detailed in (Davillerd, 1998). It has been decomposed into three main steps: scanning process definition, scanning process execution, and data acquisition computing. In the following, each of these three steps will be detailed.

3.1. Scanning process definition.

This step consists in several stages like: digitization strategy definition, machine calibration, sensor calibration, software origin definition, part set-up, and strategy implementation. Only two of them are very critical: digitization strategy definition and strategy implementation.

Digitization strategy definition is the stage in which the user defines part orientations and sensor orientations that needed to digitize the part. Also, he has to define reference features to be able to readjust point clouds in a next stage. These reference features can consist in part features or in features added on the part or in a rotation axis.

Strategy implementation is very time consuming. Indeed, the user has here to define sensor trajectories. So he programs the coordinates of linear movements and indicates to the system the moment along with it has to digitize (Figure 7). He also chooses the acquisition step. In this way, he also implicitly defines the recovery (number of point that will be digitized in more than one position, and that will have to be filtered).

3.2. Acquisition execution.

Starting from the trajectory file defined by the user, the ECU pilots the sensor in the machine reference system and Kréon Reporter Plus software records the acquired points. Everything is automatic and has not to be improved.

3.3. Data acquisition computing.

It consists in two steps. First, point cloud filtering is necessary because the acquisition generates an important quantity of points. Consequently a simplification is necessary and consists in grid application. But the needed quantity and quality of points essentially depends on the using application: for example point machining, surface reconstruction or imaging.

And finally, the readjusting stage is very important because it conditions the final results. Each point cloud is defined in a particular frame then all frames have to be regrouped in a unique one. This operation can be made manually or by using matrices. Then, after the part is digitized according to the defined strategy, the whole numerical information of the part is defined (figure 6).

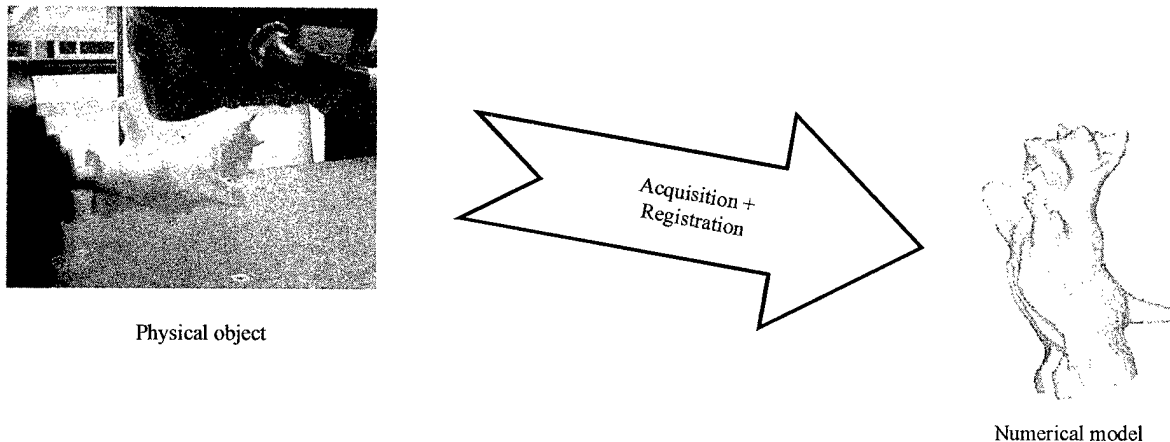


Figure 6. The part on its fixture and the final point cloud.

4 SIMULATION AND VALIDATION

Scanning is a "step by step" process. This means that the CMM moves, then stops its movements, the sensor acquires data and the CMM moves again. Thus, each acquisition is a discrete event. Let us detail this event for the 3D-laser-scanning sensor KLS 51.

The first stage is the part illumination by the laser. A plane laser lights the part up. A beam coming from a laser diode creates this plane. This beam goes through a cylindrical lens in order to create the plane. This plane is about 0.3 mm thick in the middle of the measurement field.

The second stage is the scene acquisition. Each camera takes a gray level image of the scene. Each CCD camera acquires the laser trace on the part and its thickness.

The third and last stage is the image computing. Each image is processed in order to generate 3D coordinates of acquired points. First, image is cut in order to keep interesting information. This treatment defines the trapezoidal sensor measurement field. A numerical treatment called sub-pixel algorithm is then used to reduce thickness to one point. Triangulation calculation allows the system to extract the three dimensional coordinates of 300 points on the trace length (Kréon Industrie, 1997).

The objective of simulation is to visualize CMM movements and each acquisition of the sensor. So, it has been necessary to model the digitization cell in a robotic CAD environment (CIMSTATION INSPECTION from Silma). Several applications exist (Chedmail & al., 1998): spot welding, arc welding, painting and projection are available. Collision between the sensor and the digitization environment can be detected as well.

The analysis of this environment shows that sensor actions could be similar to paint deposition. (Silma, 1998). Indeed, laser beam action is the illumination of part surface and it could be compared with

a paint deposition on the lighting area. In the same way, camera action is the part surface observation and it could be compared with a paint deposition on the viewed area. In this way, the plane laser sensor work has to be adapted in the chosen robotic CAD software from the paint deposition simulation.

So, a solid model of the laser sensor has been adapted on the head of the machine in CIMSTATION ROBOTICS environment. Attachment, 4-positions interface and sensor surface models are reconstructed from IGES CAD files with CIMSTATION functions (Figure 7).



Figure 7. Models of machine, sensor and simulation features.

Original models have been proposed for the laser and each camera, adapted from paint plumes, which have special paint deposition function. Laser plume model has been created from a cone plume. The measurement field restriction treatment has been integrated in this plume; i.e. laser plume paint deposition will only be effective in the measurement field area. Each camera plume model has been created from a cone plume too. Then the intersection of the area painted by the laser plume and the area painted by either camera plume corresponds to the digitized points. Sub-pixel algorithm allows a compromise between laser width, mesh size of the CAD model and a realistic time to execute calculations in order to keep an interactive exploitation of the results.

In conclusion, digitization cell and sensor have been modeled (Davillerd, 1999). It is now possible for each particular 3D part to simulate digitization trajectories that should have been previously created. Based on these elements, off-line simulation allows testing and verifying digitization trajectories efficiency without immobilizing the digitization cell. More over, it is also possible to validate these trajectories by the analysis of the valid points (enlightened and seen by one or two cameras) obtained using the simulation module. The analysis algorithm is under validation.

5 COMPUTER-AIDED PROCESS PLANNING FOR AUTOMATIC GENERATION OF 3D DIGITIZING PROCESS FOR LASER SENSORS

In this paragraph, an analysis is proposed in order to generate an automatic scanning process.

As mentioned earlier, the objective is control. In this field, two configurations are possible. At first, the CAD model of the part is known and it has never been scanned. It is almost necessary to generate all the process to digitize the part. The second hypothesis is that the part has already been scanned manually and the result is not satisfactory (empty areas or too much redundant points). In these cases, the proposed algorithm has to define a new efficient scanning process.

In fact, we think that two stages are necessary to generate an automatic scanning process. The first stage is the determination of the different orientations between the sensor and the part, and the second stage is the definition of the trajectories, for each orientation, which allow digitizing the maximum part surface. In the following, we suggest different concepts to solve these two stages.

5.1 Definition of the relative orientations between the sensor and the part.

For the first stage, we need to know whether the surface element S_i is located in the laser measurement plan and whether one of the two cameras sees the entire or a part of the ray projected by the laser on the surface element S_i . These conditions refer to a visibility concept. It has been studied in

different application fields, like machining (Risacher, 1997)(Chen, & al., 1992), inspection with mechanical probe (Spyridi & al., 1989) and inspection with computer vision (Trucco & al., 1997). Into machining and inspection with a mechanical probe field, the resolution of the visibility is based on spherical geometry. Chen (1992) introduced it for machining and Spyridi (1994) for control. This technique studies the visibility (V_i) of each part surface and the machine visibility (V_j). Both of them are described by a point, a line or a surface onto the Gaussian sphere (Chen, 1992) (figure 8). The orientations of the part and of the tool are computed by intersecting the maximum of part surfaces visibility with the machine visibility. If any surface visibilitys are intersecting with the machine visibility, then all the surfaces can be machined or inspected with only one part and sensor orientation (figure 9).

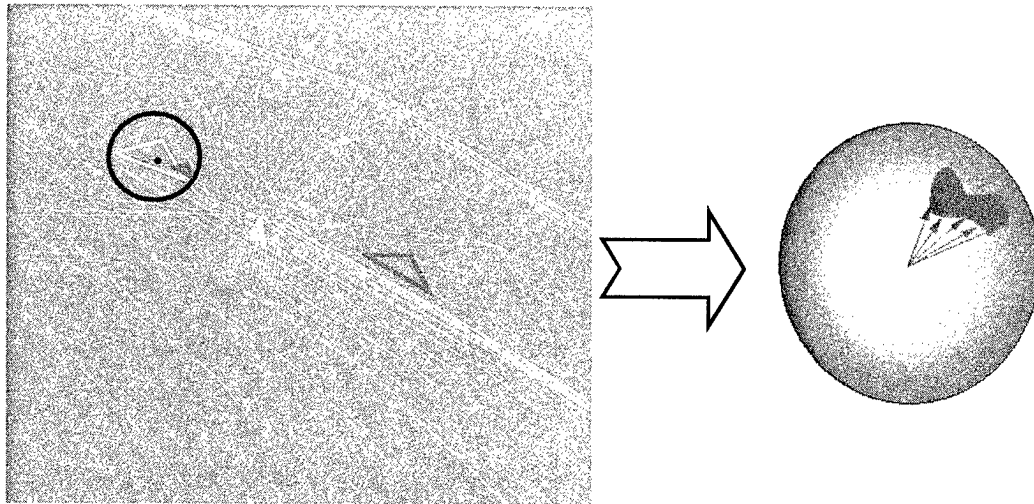


Figure 8. Part STL elements and visibility characteristics.

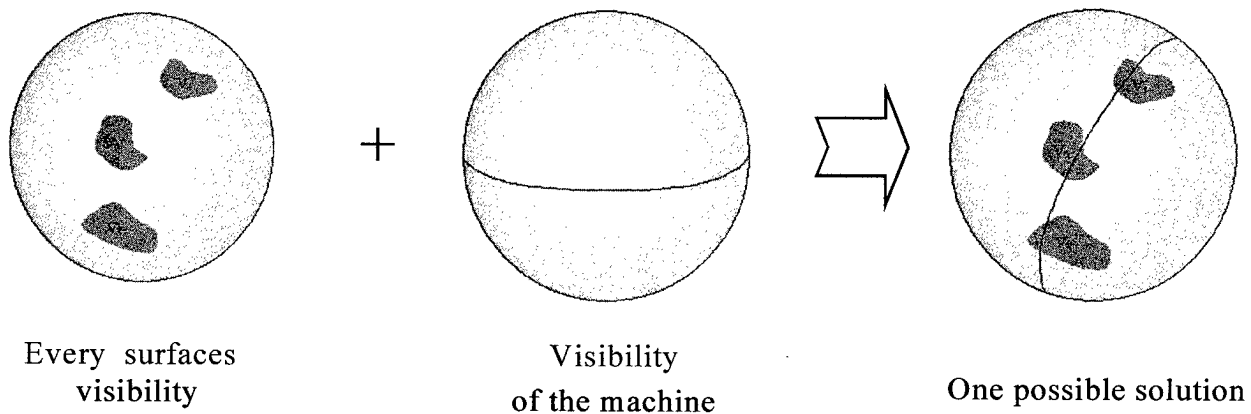


Figure 9. Intersection of part visibility and machine visibility.

5.2 Trajectories definition.

When the part and the sensor have been oriented, the trajectories can be defined. According to the automatic determination of these trajectories, some examples can be found in machining field (Risacher, 1997) and in robotic field. In the first field, Dragomatz (1997) made “a classified bibliography of literature on NC milling path generation”. This paper is useful to seek an introduction to the literature as a whole. It is partitioned into categories and papers to path generation classified according to the topics they cover. In the same way, Chedmail (1998) describes the different methods of path planning in robotics. The goal will be, after adaptation and transformation of these methods, to optimize the trajectories for each related position between the part and the sensor.

5.3 Constraints for the automatic scanning process generation.

Different solutions have been introduced to generate an automatic scanning process. But, there are several constraints that must be taken into account during the algorithm development.

One of these constraints is the recovery, which is not mastered by the user when he defines the process. When the system defines a trajectory, it takes account to the recovery otherwise there may be redundancy or missing of points. This recovery notion (figure 10) is difficult to master because of the laser measurement zone form. The trapezoidal form makes that when the part surface is located at the top end of the measurement zone, the trace projected by the laser is smallest than when the part surface is located at the bottom of the zone.

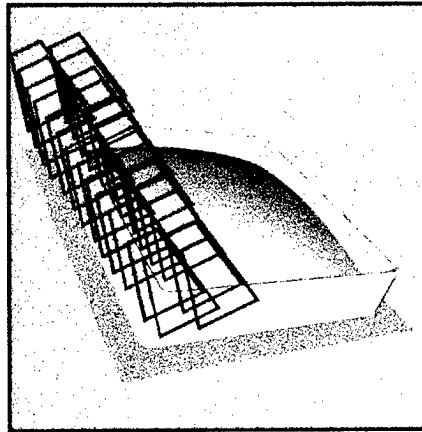


Figure 10. Path recovery.

Concerning the measurement zone, the acquisition is possible in the all weight of the zone, i.e., the sensor can move in the same z-coordinate; the part surface can vary in z, and stay in the measurement zone. The difficulty in this case is to model the “tool”. For example, in machining, the tool works with its end. It is also true with a touch probe. It is more complicated to specify the active part of the laser plane.

Another constraint is the angle between the laser beam and the part surface. Even if the algorithm determines a visibility, it must be verified that the angle does not keep away from the normal of the surface.

6 CONCLUSION AND OUTLINES

Control of complex part needs to be improved in term of scanning efficiency. This contribution is related to “simulation – validation – CAPP for generation of 3D-laser scanning process”.

At this time, the first step has been implemented and the second one is under development. The third one will be achieved in October 1999, based on spherical geometry.

The final complete system will contribute to optimize the development of new products and to accelerate the control phase.

REFERENCES

- Bernard, A., Taillandier, G. (1998) **Le prototypage rapide**, Editions Hermès, Paris, France.
- Chedmail, P., Dombre, E., Wenger, P. (1998) **La CAO en robotique, Outils et méthodologies**, Série études en mécanique des matériaux et des structures, Editions Hermès, Paris, France.
- Chen, L. L., Woo, T. C. (1992) Computational geometry on the sphere with application to automated machining. **Journal of Mechanical Design**, 114, 288-295.
- Davillerd, S., Sidot, B., Bernard, A., Ris, G. (1998) Definition of the fundamentals for the automatic generation of digitalization processes with 3D-laser sensor. **Proceedings of the SPIE, The International Society for Optical Engineering**, 3520.
- Davillerd, S. (1999) Simulation des trajectoires d'un capteur laser numérisant une pièce mécanique complexe. **Engineer Thesis**, Spécialité : production automatisée, Nancy, France.

Dragomatz, R. L., Mann, S. (1997) A classified bibliography of literature on NC milling path generation. **Computer Aided Design**, 29 (3), 239-247.

Kréon Industrie (1997) Présentation technique des produits Kréon. **Kréon Industrie**, Limoges, France.

Moron, V. (1996) Mise en correspondance de données 3D avec un modèle CAO : application à l'inspection automatique. **Ph. D. Thesis**, INSA, Lyon, France.

Prieto, F., Redarce, H. T., Lepage, R., Boulanger, P. (1998) Visual system for the fast and automated inspection of 3D parts. **Proceedings 7^{èmes} Assises Européennes du Prototypage Rapide**, Paris, France.

Risacher, P (1997) Choix de configurations de machines-outils pour l'usinage de surfaces complexes. **Ph. D. Thesis**, Ecole Centrale de Nantes, Spécialité : Génie Mécanique, Nantes, France.

Silma (1998) **CimStation Robotics**, Paint application solution user's guide, Adept Technology.

Spyridi, A. J., Requicha, A. A. G. (1989) Accessibility analysis for the automatic inspection of mechanical parts by CMM. **Technical report**, Computer Science department, University of Southern California.

Spyridi, A. J. (1994) Automatic generation of high-level inspection plans for coordinate measuring machines. **Ph. D. Dissertation**, Computer Science Department, University of Southern California, USA.

Trucco, E., Umasuthan, M., Wallace, A.M. and Roberto, V. (1997) Model-based planning of optimal planing sensor placements for inspection. **IEEE Transactions on Robotics and Automation**, 13 (2), pp. 182-194.

Varady, T., Martin, R. R., Cox, J. (1997) Reverse engineering of geometric models - an introduction. **Computer Aided Design**, 29 (4), 255-268.

Zhang, S. G., Ajmal, A., Yang, S. Z. (1995) Reverse engineering and its application in rapid prototyping and computer integrated manufacturing. **Proceedings Computer Applications in Production and Engineering (CAPE'95)**, Beijing, Chine, pp. 171-178.

A Mathematical Description of Layered Manufacturing Fabrication

Feng Lin and Wei Sun
Department of Mechanical Engineering and Mechanics
Drexel University
Philadelphia, PA 19104

Yongnian Yan
Department of Mechanical Engineering
Tsinghua University
Beijing, P.R. China 100084

Abstract

This study is attempted to use a mathematical definition to describe the principles of Layer Manufacturing Processing. The concept of model decomposition (layered subtraction for 3D model slicing) and material accumulation (layered addition for prototyping fabrication) and the associated sequence function and sequence potential to explain and define the layered manufacturing processing is presented. In the mathematical description, a 3D CAD model is graphically represented by a set of points collected within the bounded surfaces. In addition to its geometric feature, a processing sequence indicator is also assigned to each point as an attribute to associate with its slicing and fabricating sequence. Model decomposition slices the collected points into a series of point sets according to their sequence indicator, and material accumulation processes the layered fabrication by stacking the point sets to form the designed object. A scalar field function is used to express the variation of the sequence indicators for the selected point sets and to define iso-sequence planes. The iso-sequence planes are the processing layers consisting of all points with the same sequence indicator. Material accumulation is conducted in the gradient direction of each iso-sequence plane. Example of using proposed scalar field function and the iso-sequence plane for flat and no-flat layered prototyping processing is also presented.

Keywords: Layered Manufacturing, Rapid Prototyping, Solid Freeform Fabrication

1. Introduction

Layered Manufacturing, or frequently referred as Rapid Prototyping and Manufacturing or Solid Freeform Fabrication, has been proved as an effective tool for product development due to its advantages of shorten product development cycle, time to market and product quality. Different layered manufacturing techniques and systems have been developed and reported^[1-7]. For example, Stereolithography Apparatus (SLA), the earliest layered manufacturing processing, solidifies the liquid resin on the selected region by an ultraviolet laser. When the processing layer is solidified, fresh resin is emerged to form a new layer for processing. 3D solid object is thus built layer by layer through this layered forming processing. Laminated Object Manufacturing (LOM) cuts sections from coated sheet paper and laminates them layer by layer to fabricate 3D solid part. Selective Laser Sintering (SLS) produces the sections by selective sintering the powder plastic, wax, ceramics, or metal through a CO₂ laser beam. In Fuse Deposition Modeling (FDM), material is melted and extruded from a thin nozzle. With the controlled nozzle's movement, the fine molten material is paved in the section layer and fuse together with other layers to form a 3D solid object.

2. The Decomposition-Accumulation Principle of Layered Manufacturing

We divide the processes of layered manufacturing into following two procedures: Model Decomposition and Material Accumulation. Figure 1 presents a flow chart to describe these two procedures.

In the model decomposition processing, a 3D model is sliced into a series of sections. Those sections are the processing layers for later material accumulation. The processing paths are then generated according

to the specific requirement of freeform techniques, such as filling or offsetting. In the material accumulation processing, fabrication tools move along the defined processing paths to add the materials and stack or bind them to the previous layers. The model decomposition slices the CAD model or a continuous volumetric object into the discontinuously discrete layers and generates processing path for the accumulation process, while the material accumulation stacks the discontinuously discrete layers to produce physical prototypes. The principle of layered manufacturing is based on these two procedures. Figure 2 describes a hierarchical structure of the decomposition-accumulation procedures. According to Figure 2, a 3D volume is decomposed along one of the three directional axes to form series discrete surfaces, lines and points. Those discrete entities (surfaces, lines and points) are then stacked and transformed into the physical entities through the material accumulation. The model decomposition procedure has three levels of sub-decompositions: body sub-decomposition, surface sub-decomposition, and line sub-decomposition. The body sub-decomposition slices a 3D volume into 2D sections. The body sub-decomposition is necessary to all kinds of current layered manufacturing processing.

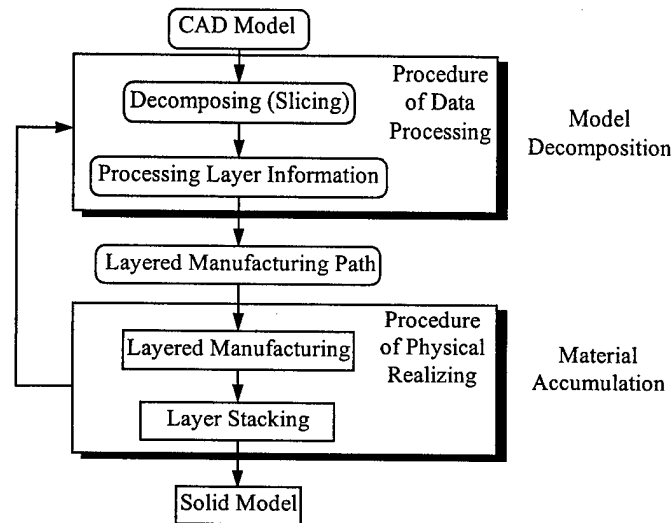


Figure 1 Layered manufacturing processing

After the body sub-decomposition, some layered manufacturing systems require further decomposition to define the processing paths. This is the second level decomposition and is called as the surface sub-decomposition. The third level decomposition is to decompose the section lines into section points. We define this as the line sub-decomposition. It should be pointed that the definitions of section lines and section points are abstract and only serve for the explanation purpose. Processing methods used in the layered manufacturing may be different from one system to another. This will result in different algorithms and process paths for the surface decomposition as well as the line decomposition. However, the principle of the model decomposition and its sub-decomposition for body, surface and line are all alike. For example, Laminate Object Manufacturing only requires the body sub-decomposition while Model Maker of Sanders requires all three level sub-decompositions.

Limitations of material thickness and fabrication efficiency constraints that the processing layers can not be too thin and the resolution density can not be too high during the body sub-decomposition. Usually, the interval of each body sub-decomposition is generally between 0.1mm to 0.25mm and the resolution from 4/mm to 10/mm. This is much lower than that in surface sub-decomposition and line sub-decomposition which the resolution densities are limited only by the material particulate dimension and resolution ratio of the control system movement. For most layered manufacturing systems, the material particulate dimension and the resolution ratio of the control system movement could be in the range of 0.01mm, and their resolutions could be greater than 100/mm. Therefore, out of three level of sub-decompositions, the body sub-decomposition will produce the most error than the other two. For example, the most common

staircase appearance along the prototyping surface is due to the error of the body sub-decomposition. Since the body sub-decomposition is an essential processing for model decomposition in the layered manufacturing, this study is to focus on this discrete process and trying to use a mathematical description to define and to explain the layer manufacturing processing.

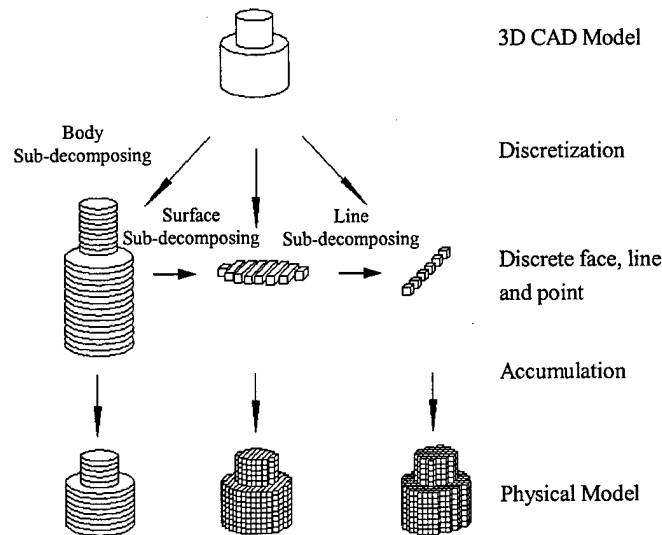


Figure 2. Hierarchy of decomposition-accumulation procedure

3. A Mathematics Description of Layer Manufacturing Processing

3.1 The representation of a 3D shape

In this paper, a 3D volume is represented as a collection of points within the bounded surface defined as: a 3D shape " V ", with an entire exterior closed surface " S ", is the combination of all points within S , " P_i " and on S , " P_b ":

$$V = P_i \cup P_b \quad (1)$$

where, S is assumed to be a continuous, closed and self-non-intersecting surface. For a partitioned surface, S is the union of the partitioned areas " s_i ".

$$S = s_1 \cup s_2 \cup s_3 \cup \dots \cup s_i \quad (2)$$

where, $i = 1, 2, 3, \dots m$, represents the number of the partitioned areas.

For example, the *stl* format, a *de facto* standard graphical interface of layered manufacturing technology, represents the part's surface by a set of triangular facets^[6]. In this case, s_i corresponds to the triangular facet, which is the content in *stl* file, and S corresponds to the join of all the facets, which is the whole surface of part needs to be fabricated.

3.2 Sequence and Sequence Function

In layered manufacturing process, a 3D object is fabricated by decomposing and stacking sequence. Layers, the general forming unit in layered manufacturing process, can be considered as the material group with a certain sequence number. Once the layered manufacturing process is selected and the fabricating orientation is defined, the sequence, which is the order of the material accumulation, is setup and applied onto the 3D shape. Each point belongs to the 3D shape will be assigned with a sequence number to indicate the layer they should belong to. The 3D shape is then separated into layers according to the sequence applied to it. This separating operation is termed as decomposition processing, while fabricating part by stacking the discrete layers one by one following the sequence is termed as the

material accumulation. The decomposition and accumulation should follow the same sequence otherwise the part's shape may be altered from the original CAD model. Fabricating by a specified sequence is another feature for layered manufacturing process.

We consider that the sequence is a number dispersal in 3 dimensional space \mathcal{V} in which the process of layered manufacturing is realized. The sequence function is assumed as a scalar function $\phi(x, y, z)$ defined in \mathcal{V} . To completely describe a point P in \mathcal{V} , we need not only to define its coordinate $p(x, y, z)$ for its spatial position, but also the value of sequence function $\phi(x, y, z)$ to indicate the layer it belongs to and when for the point to be processed with the material accumulation.

The sequence function $\phi(x, y, z) \in [a, b]$, if

$$\exists C = \{c_i; a \leq c_0 < c_1 < \dots < c_{i-1} < c_i < c_{i+1} < \dots < c_n \leq b, i = 1, 2, \dots, n\} \quad (3)$$

where, C is an ordered real number set and c_i represents the i th layer with n layers in total. a and b represents the values of the upper and lower bounds. For a volume defined in the i th layer:

$$v_i = V \cap P_i \quad (4)$$

where, V is the 3D shape, and P_i is the set of points whose sequences are all between c_{i-1} and c_i :

$$\begin{cases} P_i = \{p(x, y, z); c_{i-1} \leq \phi(x, y, z) < c_i\} & i = 1, 2, \dots, n-1 \\ P_n = \{p(x, y, z); c_{n-1} \leq \phi(x, y, z) \leq c_n\} \end{cases} \quad (5)$$

and
$$v_i \cap v_j = \emptyset, \quad i \neq j, i, j = 1, 2, \dots, n \quad (6)$$

$$V = v_1 \cup v_2 \cup \dots \cup v_n \quad (7)$$

The geometric description of the 3D shape V , its boundary S and the sequence function $\phi(x, y, z)$ is presented in Figure 3. In this figure, the sub-volume v_i at the i th layer consists of all points whose sequences are between c_{i-1} and c_i within the 3D shape V .

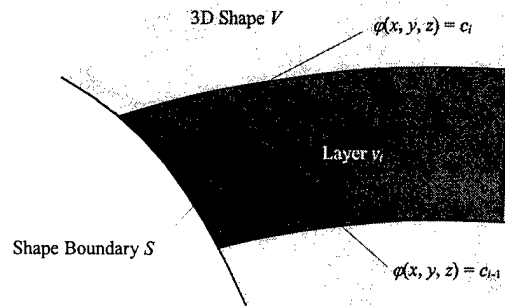


Figure 3 Geometric description of the processing layer

Current layered manufacturing techniques are difficult to produce the exact boundary of S described in Figure 3. The boundary of layer is usually formed in straight with its obliquity normally parallel to the fabrication orientation. The actual boundary of the 3D prototyping part is staircase-like. Therefore, the processing layer v'_i by the layered manufacturing process is not equal to the geometrically defined sequence layer v_i as shown in Figure 4.

The error e_i is the difference between the sequence layer v_i and the processing layer v'_i :

$$e_i = (v_i - v'_i) \cup (v'_i - v_i) \quad (8)$$

Because e_i is produced from the layered manufacturing processing, we call e_i the layered process error of i th layer. For an actual 3D prototyping part, the total layered process error E is:

$$E = e_1 \cup e_2 \cup \dots \cup e_n \quad (9)$$

The layered process error E or e_i is related to the layer's geometric border obliquity and the processing orientation of the material accumulation. The detail analysis and quantity prediction of the layered process error was discussed in somewhere else^[3].

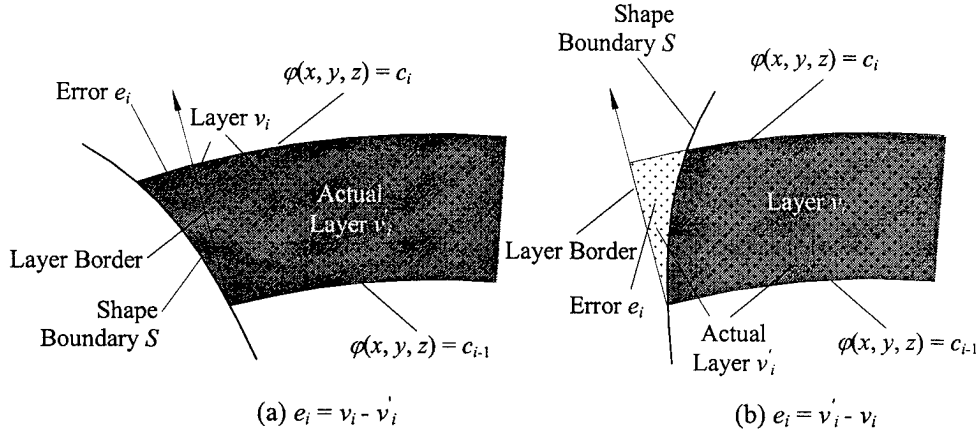


Figure 4. Error between the sequence layer and processing layer

3.3 Iso-sequence Plane and Sequence Potential

According to the field theory, the sequence function $\phi(x, y, z)$ is a scalar function distributed in a 3D space \mathcal{V} . Let's assume a series of iso-sequence planes and $\phi(x, y, z)$ be equal to the ordered set c_i as shown in Figure 5:

$$\phi(x, y, z) = c_i, \quad i = 1, 2, \dots, n \quad (10)$$

The iso-sequence plane consists of all points with the same sequence indicator. In the decomposition processing, these iso-sequence planes are what we use to intersect and slice the designed 3D object. In the accumulation processing, these planes are where the layer is generated. For example, in SLA, the iso-sequence plane is the surface of the resin vat, on which the layer will be solidified from the liquid resin. In LOM, the iso-sequence plane is the top plane of the laminated part, on which new coated paper will be attached and cut into the sections. In SLS, it is the plane in which the fresh powder is spread and sintered. In current layered manufacturing processes, the iso-sequence plane is normally a 2D flat surface parallel to the XY plane.

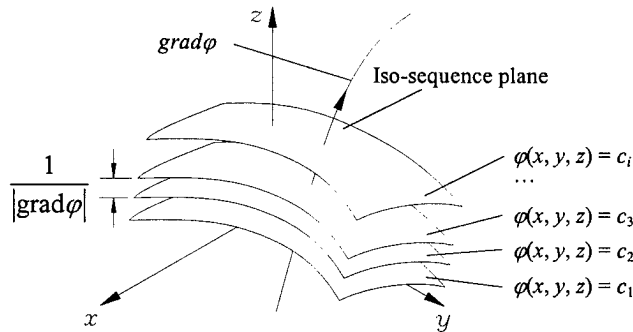


Figure 5. Iso-sequence plane and Sequence function

The gradient of the sequence function is:

$$\mathbf{d}(x, y, z) = \text{grad}\varphi = \frac{\partial\varphi}{\partial x}\mathbf{i} + \frac{\partial\varphi}{\partial y}\mathbf{j} + \frac{\partial\varphi}{\partial z}\mathbf{k} = X(x, y, z)\mathbf{i} + Y(x, y, z)\mathbf{j} + Z(x, y, z)\mathbf{k} \quad (11)$$

where \mathbf{i} , \mathbf{j} and \mathbf{k} are the unit vectors in \mathcal{V} along X , Y , Z axis, respectively. $\mathbf{d}(x, y, z)$ is spatial vector representing the gradient of the sequence function. Since $\mathbf{d}(x, y, z)$ is perpendicular to the iso-sequence plane everywhere, as shown in Figure 5, we can use the vector of $\mathbf{d}(x, y, z)$ to represent the processing orientation, i.e., along the direction of $\mathbf{d}(x, y, z)$, the 3D design model will be dispersed in the decomposition procedure and the material accumulation will be conducted in the material accumulation procedure. To this reason, we define $\mathbf{d}(x, y, z)$ as the sequence potential. Now each point in the space \mathcal{V} will be associated with both sequence indicator $\varphi(x, y, z)$ and sequence potential $\mathbf{d}(x, y, z)$ defined from $\varphi(x, y, z)$.

The sequence function can also be derived from the sequence potential $\mathbf{d}(x, y, z)$ as following:

$$\begin{aligned} \varphi(x, y, z) = \varphi(x_0, y_0, z_0) &+ \int_{x_0}^x X(x, y_0, z_0)dx \\ &+ \int_{y_0}^y Y(x, y, z_0)dy + \int_{z_0}^z Z(x, y, z)dz \end{aligned} \quad (12)$$

where (x_0, y_0, z_0) is the coordinate of initial point and $\varphi(x_0, y_0, z_0)$ is the initial sequence number. As the requirement of iso-sequence plane defined by $\varphi(x, y, z)$, the vortices of $\mathbf{d}(x, y, z)$ must be equal to zero :

$$\frac{\partial X}{\partial y} = \frac{\partial Y}{\partial x}, \quad \frac{\partial Y}{\partial z} = \frac{\partial Z}{\partial y}, \quad \frac{\partial Z}{\partial x} = \frac{\partial X}{\partial z} \quad (13)$$

The module of sequence potential $|\mathbf{d}(x, y, z)|$ represents the maximum change rate of the sequence number $\varphi(x, y, z)$ at point (x, y, z) . It indicates the density of the number of iso-sequence planes within a unit length. If we define the module $|\mathbf{d}(x, y, z)|$ equal to the reciprocal of the slicing interval, h_i , which is the distance between two adjacent iso-sequence planes:

$$|\mathbf{d}(x, y, z)| = \frac{1}{h_i} \quad (14)$$

then $|\mathbf{d}(x, y, z)|$ expresses the layer density which indicates how many layers should be sliced and fabricated within a unit length.

4. Application Examples

4.1 Description of Current Layered Manufacturing Processing

In the current layered manufacturing process, the fabricating direction is usually defined vertically upward and the layer thickness is uniform. Assume that the fabricating orientation is along Z -axis and the fabricating layer is parallel to the XY plane with a uniform thickness h , as shown in Figure 6, the sequence potential \mathbf{d}_c is then defined as:

$$\mathbf{d}_c(x, y, z) = \frac{1}{h}\mathbf{k} \quad (15)$$

The corresponding sequence function $\varphi_c(x, y, z)$ is obtained as:

$$\varphi_c(x, y, z) = \varphi_c(x_0, y_0, z_0) + \int_{z_0}^z \frac{1}{h} dz = \varphi_c(x_0, y_0, z_0) + \frac{1}{h}(z - z_0) \quad (16)$$

where, the subscript c represents the current layered manufacturing processing, and $\varphi_c(x_0, y_0, z_0)$ represents the sequence indicator of the initial layer at z_0 . In most cases, the sequence indicator always starts from zero.

$$\varphi_c(x_0, y_0, z_0) = 0 \quad (17)$$

z_0 is position of the initial layer. If the slicing starts from XY plan, then z_0 is equal to zero. Thus,

$$\varphi_c(x, y, z) = \frac{z}{h} \quad (18)$$

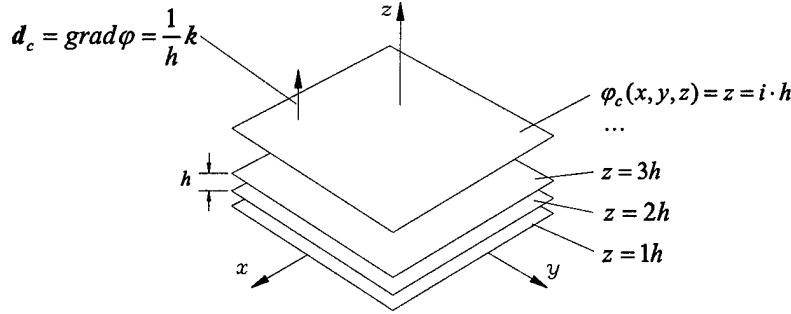


Figure 6. Sequence function and sequence potential for current LM processing

From the z coordinate we can identify which layer a given point should belong to. The iso-sequence planes for current layered manufacturing processes is derived from:

$$\begin{aligned} \varphi_c(x, y, z) = \frac{z}{h} = 1 &\Rightarrow z = h; \\ \varphi_c(x, y, z) = 2 &\Rightarrow z = 2h; \\ \varphi_c(x, y, z) = 3 &\Rightarrow z = 3h; \\ &\dots \\ \varphi_c(x, y, z) = i &\Rightarrow z = i \cdot h. \end{aligned}$$

where the ordered set C is $\{c_i; c_i = 0, 1, 2, \dots\}$ and $z = ih$ represents a series of flat planes parallel to each other and to the XY plane. Those flat planes are well suitable to be used to describe the current layered manufacturing processes because most of them can produce flat surfaces only.

4.2 Description of No-flat Layered Manufacturing

Because of the disadvantage of staircase produced by the flat layered manufacturing, no-flat layered manufacturing becomes a more realistic process for freeform fabrication. For a non-planar 3D object shown in Figure 7, the iso-sequence planes are defined as a set of curved surfaces.

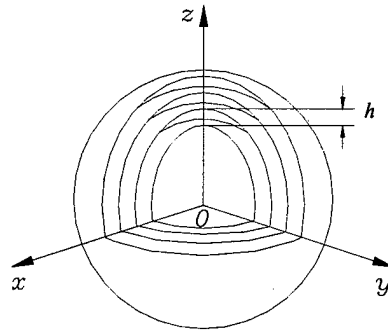


Figure 7. The concentric sphere iso-sequence planes

For instance, suppose a layered manufacturing process with a radial sequence potential, the material will then be added in the radial direction. The sequence potential can be obtained by:

$$d_r = \text{grad} \varphi = \frac{1}{h\sqrt{x^2 + y^2 + z^2}}(xi + yj + zk) \quad (19)$$

Let's assume that the vector module defined here be equal to $1/h$. This means that we assume an isotropic uniform layer thickness, h , across the thickness direction. Let $\varphi(x_0, y_0, z_0)$ be equal to 0, and (x_0, y_0, z_0) equal to $(0,0,0)$, from Equations 11 and 12, we derive the sequence function $\varphi_r(x, y, z)$ as:

$$\varphi_r(x, y, z) = \int_0^x \frac{1}{h\sqrt{x^2}} dx + \int_0^y \frac{1}{h\sqrt{x^2 + y^2}} dy + \int_0^z \frac{1}{h\sqrt{x^2 + y^2 + z^2}} dz = \frac{1}{h} \sqrt{x^2 + y^2 + z^2} \quad (20)$$

then:

$$\varphi(x, y, z) = \frac{1}{h} \sqrt{x^2 + y^2 + z^2} = 1 \Rightarrow \sqrt{x^2 + y^2 + z^2} = h;$$

$$\varphi(x, y, z) = 2 \Rightarrow \sqrt{x^2 + y^2 + z^2} = 2h;$$

...

$$\varphi(x, y, z) = i \Rightarrow \sqrt{x^2 + y^2 + z^2} = i \cdot h.$$

The iso-sequence planes, as showed in Figure 7, are a set of concentric sphere defined by $\sqrt{x^2 + y^2 + z^2} = i \cdot h$ with an interval h .

5. Conclusion

This study uses a mathematical description to explain the principle of layered manufacturing processing through the model decomposition: to decompose a 3D model into a series of sequence layers, and the material accumulation: to accumulate and stack processing layer into physical prototype. The 3D model is a set of points, which are bounded by the surface. Each point is associated with spatial position and sequence indicator. The sequence function $\varphi(x, y, z)$ and sequence potential $d(x, y, z)$ are defined to correlate the iso-sequence planes which consist of the point sets with the same sequence indicator and the orientation of material accumulation. Example of using the derived mathematical formulation to describe the current layered manufacturing processing is also presented.

References:

1. Jacobs, P.F., "Stereolithography and other RP&M Technologies: from Rapid Prototyping to Rapid Tooling," SME publishing, Dearborn, Michigan. 1996.
2. Warner, M., and Hsieh, B., "Let's Cast a LOM part: A case Study of Laminated Object Manufacturing Machine," *Proceedings of the Third International Conference on Rapid Prototyping*. University of Dayton, Dayton, USA, 1992, pp. 287-294.
3. Lin, F., "Research on the Principle of Slicing Solid Manufacturing Process and The system Development," *Ph.D. Dissertation*, Tsinghua University, China, 1997.
4. Chi, C., "Process Insight About LOM Systems," *Proceedings of Solid Freeform Fabrication Symposium*. The University of Texas at Austin. 1996, pp. 515-522.
5. Comb, J. W., Priedeman, W.R. and Turley, P. W., "FDM Technology Process Improvements," *Proceedings of Solid Freeform Fabrication Symposium*, The University of Texas at Austin, 1994, pp. 42-49.
6. Lin, F., "Simultaneously Build the Positive and Negative Prototypes of a Part," *Proceedings of The Chinese First Conference on RP&M*, Beijing, China, 1995, pp. 62-72.
7. Wohlers, T. "Rapid Prototyping and Tooling: State of the Industry, 1999 Worldwide Progress Report," Wohlers Associates, Inc., 1999.

SALD and SALVI Virtual Laboratory

Zbigniew M. Bzymek*), David Ferreira*), Harris Marcus**) and Leon L. Shaw**)

*) Department of Mechanical Engineering, University of Connecticut, Storrs CT

**) Department of Metallurgy and Materials Engineering, University of Connecticut, Storrs CT

Abstract

This paper describes efforts to apply virtual manufacturing techniques to produce machine parts using Solid Freeform Fabrication (SFF). In particular, the work was done to develop a Virtual SFF Laboratory for the Selective Area Laser Deposition (SALD) and Selective Area Laser Deposition Vapor Infiltration (SALDVI) for the manufacture of machine parts and research on their characteristics, as well as for research on development of SALD and SALDVI technologies. It was the goal of the authors to supply the user with a tool to design a part, develop its three dimensional model, render it and observe its shape and dimensions. Except for research, the laboratory is intended to be used for teaching principles of design and manufacturing of machine parts, as well as for demonstrating SALD and SALVI processes to visitors. The Virtual Laboratory was developed on Silicon Graphics workstations. The Virtual Laboratory can create a multi-media, stereoscopic presentations of the SALD and SALVI processes in the Solid Freeform Fabrication Laboratory at the Institute of Material Science (IMS) at the University of Connecticut. The presentations can also be distributed through the Internet.

Introduction

Since 1983, when Myron Krueger conducted research at the University of Connecticut and introduced his concept of "artificial reality" [1], a considerable number of further investigations have been done. The term "artificial reality" is now seldom used and has given way to the term "virtual reality", though both describe projects in which potential, but as yet unrealized systems are developed. One of the first such projects was a virtual engine model created by Pratt and Whitney at the CAD&CAM and ES (Computer-Aided Design & Computer-Aided Modeling and Expert Systems) Laboratory of the University of Connecticut by Krueger and Bowley in the middle of 1980s.

Real-time virtual models, machines, and systems which visualize manufacturing processes present a promising low-cost, highly effective method for improving the quality and efficiency of manufactured durable goods. The computer models numerically and visually demonstrate the physical phenomena of a process, and allow for study and observation of the process and its behavior [2]. Manufacturing researchers and designers studying the dynamic simulation of the process are able to make modifications to the model and its parameters and observe, using the visual output devices, the impact of these modifications on any aspect of the process.

Virtual models, machines, systems, and processes are becoming useful tools in manufacturing and design research, and in the development of products. They provide the ability to investigate the properties of the part prior to building a physical model or prototype. These technologies are used in the design of machining and production processes, and in the design of finished goods. They consist of a group of recently developed techniques and approaches that allow the construction of computer models of parts along with simulation of fabrication processes. What makes this group of manufacturing technologies special is that it allows one to check production parameters before actual prototypes are manufactured.

The use of these virtual manufacturing techniques could result in great savings of both time and money. In general, virtual modeling promises shorter design cycles with more design iterations, leading to an optimal design and better use of resources. The end goal of any virtual manufacturing is to produce a virtual model of a part, set of parts or machine that will "virtually"

make the part from a database file containing the geometrical description of a physical object in terms of pre-defined geometric entities. The actual manufacturing hardware provides the physical means to machine the part, whereas virtual machining mimics the behavior of the hardware and makes the part as a computer model. Special software is employed to bridge the gap between the CAD data and the virtual manufacturing system. Such software should control various parameters, such as the rate at which the positioning system proceeds, the tool path, the thickness of the layer of the material for removal and/or length of the path, the slice length, and other factors. Virtual manufacturing provides a means for refining motion control and simplifying part manipulation for various manufacturing hardware systems. The SALD and SALDVI virtual laboratory was developed taking into consideration all of the advantages of virtual modeling.

Virtual Laboratory

Manufacturing processes, especially closed-chamber processes, are difficult to observe, to study and run for the sole purpose of design and research studies. This is an area in which the Virtual Laboratory is especially useful. It simulates the actual production environment with all its functions, i.e. designing a part, creating STL (STereo Lithography) or VRML (Virtual Reality Modeling Language) files, slicing them, converting into laser path files, and supplying the rendering parameters. This paper reports on the development of such a laboratory and its application to actual research, teaching and the demonstration of problems [3,4,5].

Part Design

For the purpose of rendering using SALD and SALDVI systems, the parts are designed using a software package called I-DEAS [6,7]. I-DEAS Master Series is an advanced Computer Aided Design (CAD) software package that allows users to create very complex and detailed geometries. I-DEAS was used to design parts to be created in a three dimensional space (Figure 1). A special procedure is used for creating a three dimensional model in I-DEAS Master Series and converting that model into an STL file format so the model can be used in Solid Freeform Fabrication (SFF). A VRML format was also examined and it was discovered that format has some advantages in useful in sending files through the Internet [8]. After the geometry of the parts is described, the parts are displayed on the screen in a simulated three dimensional image.

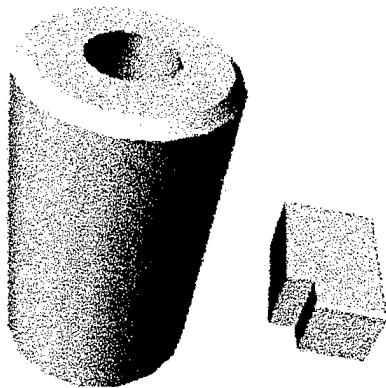


Figure 1. A shaft and a block designed for rendering using SALDVI.

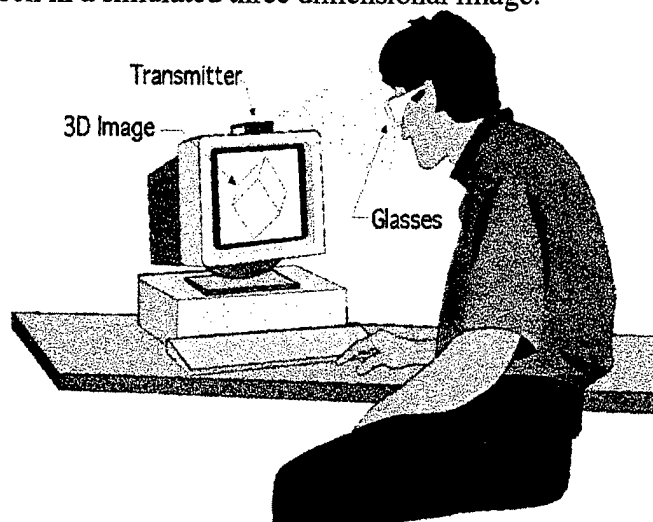


Figure 2. A part examining session using CrystalEyes™ stereo view system [10].

Inventor and Stereoview

It has been proven that objects created in I-DEAS can be readily transferred into Inventor for animation and stereo viewing. This creates an invaluable visualization tool, not only for the researcher, engineer and technician, but also for the people who want to learn more about SFF processes. Inventor is a useful tool for visualizing 3D objects either created in the Inventor program using basic 3D shapes, or complex geometries imported from other programs. Once a model has been brought into Inventor, it can be animated and textured using some basic commands. If a more robust animation sequence is needed, C++ can be used to call various Inventor libraries. Inventor is a good visualization tool because it directly supports the use of stereo viewing. Stereo viewing is a system that incorporates the use of a special set of glasses with LCD lenses. The lenses act like shutters, opening and closing many times a second, the left and right lens alternate shutter cycles, such that only one eye sees the computer screen at any instant in time. Mounted on the computer monitor is an emitter box that sends an infrared signal to the glasses, this signal synchronizes the lenses of the glasses with the images on the screen. The computer screen cycles through two different views of a model in sync with the glasses, resulting in the left eye seeing one view of a model and the right eye seeing another. The images in the left and right eye are combined in the brain and the illusion of a 3D image is created (Figure 2).

Object Examining

Once an object was created in I-DEAS, as in the case under discussion here where a model of the SFF laboratory in IMS was created, it was converted to an Inventor file format and brought into Inventor. Each component of the model was created separately and brought together in the I-DEAS assembly module, this allowed the objects to be manipulated independently, as separate "children" in Inventor. If the different components were constructed in the same drawing and saved as one part, it would exist as one object in Inventor, and the different components could not be manipulated individually.

I-DEAS also supports an additional feature that allows three-dimensional models to be exported in the Inventor format. Inventor files can also be created using an additional application that takes STL or IGES files and translates them into Inventor format. The SGI (Silicon Graphics, Inc.) Irix 6.2 operating system has a built in command that converts STL files into Inventor files. This command is: STLtoINV <filename.stl> <filename.iv>.

Stereo viewing is used for part examination. First, I-DEAS Master Series [6,7] is used to create complex parts. Once created in I-DEAS, the models are converted into Inventor [9,11] and an Inventor file format is generated. Inventor is used to add realistic features to the image of the part designed and is capable of constructing basic three-dimensional geometries. It also fully exploits the stereo-viewing capability by adding sound and animation to the model. The part can be viewed and animated in stereo view (Figure 2). Stereo viewing is a very powerful visualization tool in design. It makes three-dimensional objects appear as if they were suspended before the computer screen, giving the viewer a sense of a true three-dimensional structure from a flat, two-dimensional computer screen. This presents users with a better three-dimensional representation of a modeled object's behavior, so that features and functions can be examined in detail.

The work was conducted using Silicon Graphics Indigo Extreme work stations equipped with Inventor, GL library, C compilers and stereo view systems. The installation of stereo view glasses using a CrystalEyesTM [10] stereo view system allows the viewing of the entire system in three dimensional space. This system will be improved with some C++ programming routines under study that promise to make the animation sequences more robust.

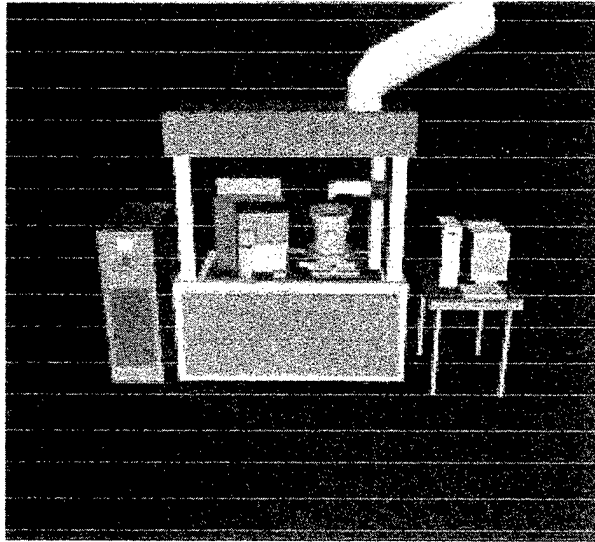


Figure 3. A general view of SALD and SALDVI rendering system.

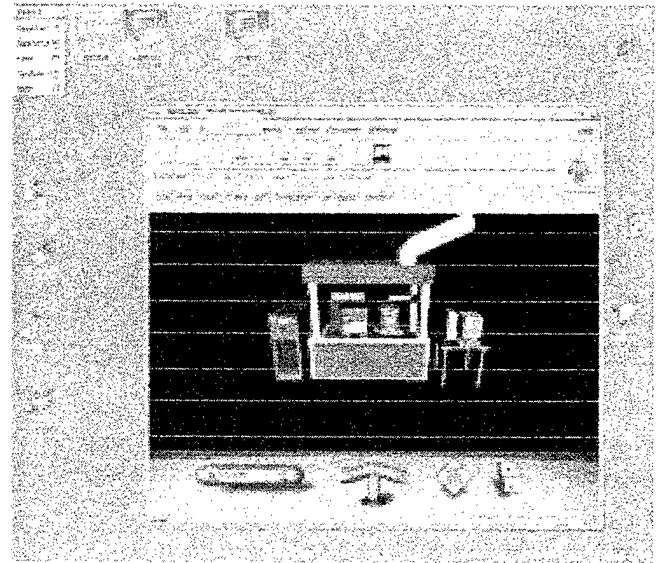


Figure 4. A SALD and SALDVI rendering system - view on the World Wide Web.

Part Rendering

Once part is designed using I-DEAS Master Series, special procedures are used to create a three dimensional model and convert it into STL file format. This file is sliced and a special file to drive the laser is created. Once this is done, the model can be used for SALD and SALDVI rendering. The virtual laboratory is equipped to render parts [3], as well as to simulate joining [4] SiC tubes. All of this is available in the virtual session.

Once a model is created in I-DEAS, it can be easily exported into a STL format. The .stl or stereolithography format is an ASCII or binary file used in the interchange between CAD systems and the rapid prototyping machines. It lists the triangular surfaces that describe a computer-generated solid model. This is the standard input format for most rapid prototyping machines. From this STL file, the object is then processed into a set of coordinates that can then be sent to a laser scanning system for Solid Freeform Fabrication (SFF).

Virtual Laboratory Session

The Virtual Laboratory session can be conducted in In situ or remote modes. The In situ mode takes place in the SFF Laboratory of IMS, where there are SGI systems at the disposal of the users. The SALD and SALDVI system is displayed on the screen (Figure 3). To tour the

laboratory in the remote mode, users can use Netscape to navigate through the system (Figures 4, 5, 6). In this mode, the user can visit two operations. In operation one, a shaft (Figure 1, 5, 6) is rendered. In operation two, the process of joining two pieces of silicon-carbide tube via SALD can be witnessed and studied. The pieces of tube joined by the SALD process are shown as a finished product in Figure 8. Figure 10 is a magnified image of this finished product. The virtual process of joining two pieces of tube via SALD is shown in Figures 9 a,b,c. An added bonus of the virtual laboratory is that the user can “virtually” enter rendering chambers during part generation (Figures 3 and 4) or during the joining operation (Figures 5 and 6). This is impossible to do in the real-world operation.

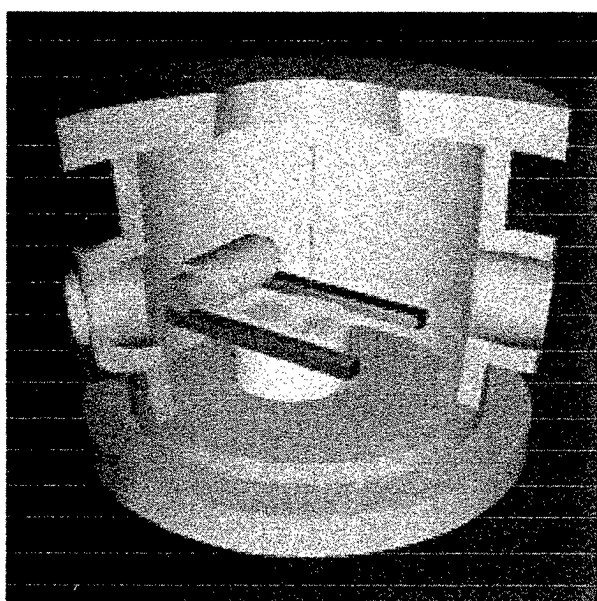


Figure 5. A SALDVI rendering chamber with the powder feeding mechanism and the part support.

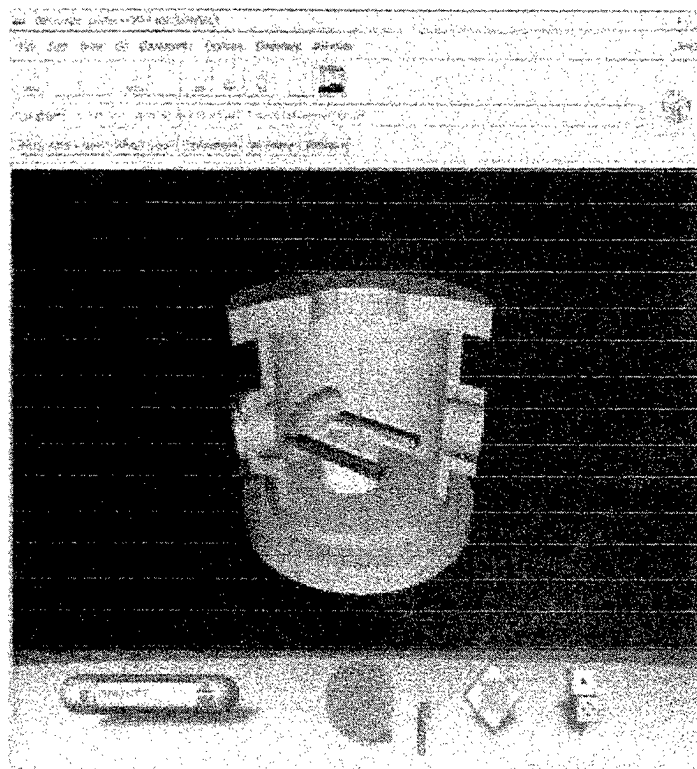


Figure 6. A SALDVI rendering Chamber with the powder feeding. View on the World Wide Web.

Internet Session

The virtual laboratory can be visited on Internet [12,13] where the user can operate it through the WWW. After coming to the IMS page and entering the lab page, a greeting screen appears (Figure 11). The remote mode is enabled automatically and the user can enjoy his/ her visit to the laboratory (Figures 3 to 10). The virtual laboratory is also accessible by the World Wide Web where projects can be examined. It has been used successfully in teaching, design, and technology presentations.

Possible Future Development

At this time, the Virtual Laboratory can be used only to examine designs and processes previously created. In future developments, we anticipate adding the ability to create a part virtually in real time, the ability to examine the part, and the ability to render the part using the SALDVI process. Also, more investigation is being done to study the C++ programming language aspects, so that all the objects in the project will fit together into a single flowing presentation. C++ will also help to make the animation better and add more realism to the process. Future work is suggested to improve the part design and fabrication animation. More features may also be added to the presentation capabilities.

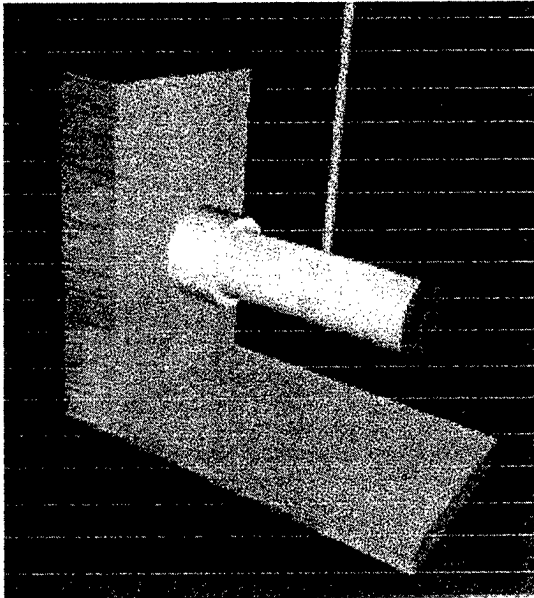


Figure 7. Two pieces of silicon - carbide tube SALD joining process.

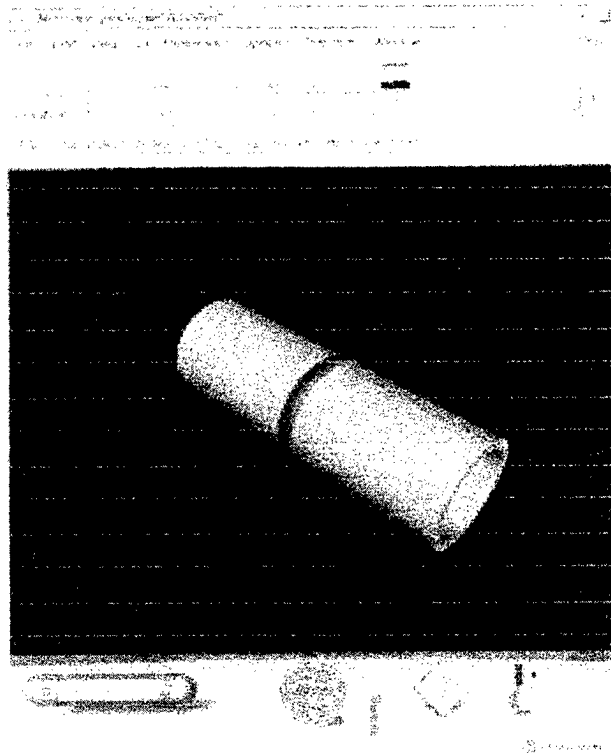


Figure 8. Two pieces of silicon - carbide tube joined by SALD. View on the WWW.

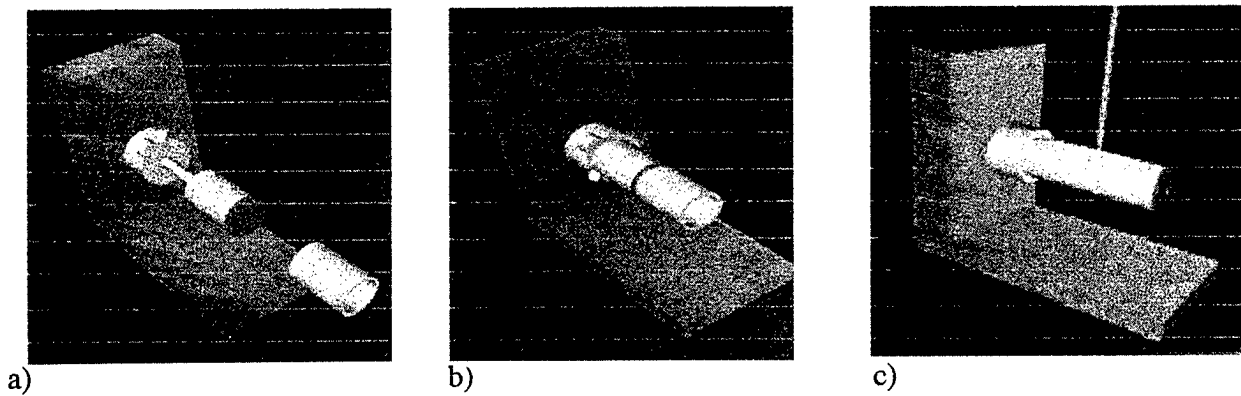


Figure 9. Three frames from the virtual SALD Operation.

a) Two separate pieces, b) The pieces are brought together, c) The pieces are joined.

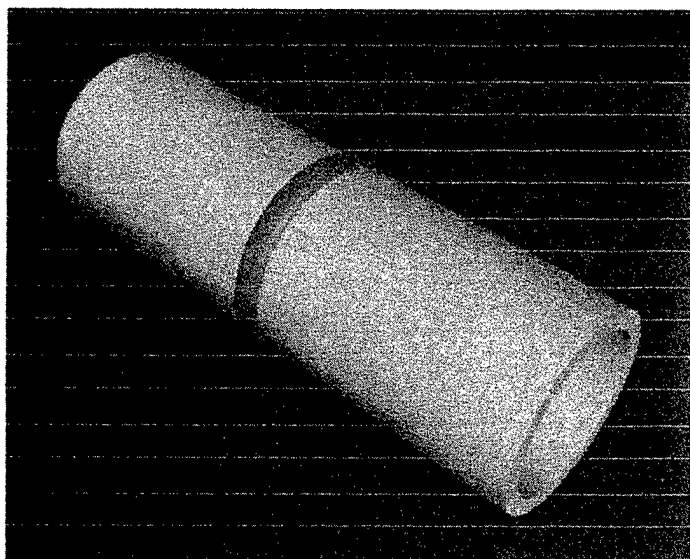


Figure 10. Two pieces of silicon - carbide
Tube joined by SALD.

Welcome To The Virtual Tour

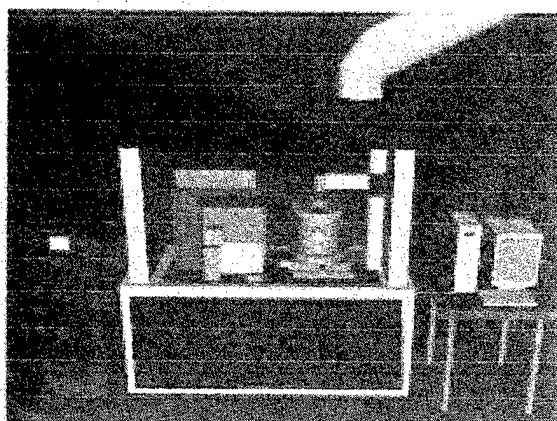


Figure 11. A welcome screen
on Internet [12,13].

Concluding Remarks

This work is still in progress, and at this stage, the user can only study the rendering of the parts that have already been programmed. It is extremely useful for case studies and for presentations to the research team, students and visitors. The virtual laboratory is also accessible by the World Wide Web where its products can be examined and contributions to the general knowledge of SALD and SALDVI processes can be found. It has been used successfully in teaching, design, and technology presentations.

Acknowledgment

This effort was initiated by the Institute of Material Science (IMS). The research was funded in part by the Office of Naval Research, ONR Grant # N00014-95-1-0978. The StereoView system was added thanks to grants from the UConn Teaching Institute and IMS. The authors would like to thank the members of the IMS SFF Seminar for their help and support.

References

- [1] Myron W. Kruger, 1983, "Artificial Reality. Technology and Art. Man-Machine Systems", Addison-Wesley, Reading, Massachusetts;
- [2] Zbigniew M. Bzymek, "Visual Models of Manufacturing Processes", ICCI'96, June 26 - 28, Waterloo University, Canada, ICCI'96 Journal, pp. 1259-1263;
- [3] Crocker J., Sun L., Shaw L. L., Marcus H.: Preparation and Properties of the In-site Devices Using the SALD and SALDVI Techniques, Solid Freeform Symposium 1998, *Proceedings - August 10-12, 1998*, Edited by: David L. Bourell, Joseph J. Beaman, Richard H. Crawford, Harris L. Marcus and Joel W. Barlow, The University of Texas at Austin, pp. 543 - 547;

- [4] Harrison S., Marcus H. L.: Gas -Phase Selective Area Deposition (SALD) Joining of SiC Tubes with SiC Filler Material, Solid Freeform Symposium 1998, *Proceedings - August 10-12, 1998*, Edited by: David L. Bourell, Joseph J. Beaman, Richard H. Crawford, Harris L. Marcus and Joel W., Barlow, The University of Texas at Austin, pp. 537 - 542;
- [5] Sun L., Jakubenas K. J., Crocker J., Harrison S., Shaw L. L., Marcus H. L.: Fabrication of In-situ SiC/C thermocouples by SALD, Solid Freeform Symposium 1997, *Proceedings - August 11-13, 1997*, Edited by: David L. Bourell, Joseph J. Beaman, Richard H. Crawford, Harris L. Marcus and Joel W., Barlow, The University of Texas at Austin, pp. 481 - 488;
- [6] Exploring I-DEASTTM Design, 1993, Structural Dynamics Research Corporation (SDRC), *SDRC I-DEAS Master Series*, SDRC, 2000 Eastman Drive, Milford, Ohio 45150;
- [7] Exploring I-DEASTTM Process Simulation, 1993, Structural Dynamics Research Corporation (SDRC), *SDRC I-DEAS Master Series*, SDRC, 2000 Eastman Drive, Milford, Ohio 45150;
- [8] Wang Y., Computer interface and Virtual Prototyping, Master Thesis, 1997, University of Connecticut;
- [9] Wernecke, Josie: The Inventor Mentor, *Addison Wesley Publishing*, 1994;
- [10] CrystalEyes 2, *Stereo Eyewear User's Manual*, CristalEyes-StereoGraphics Corporation ;
- [11] Inventor, Software Description, *Silicon Graphics WWW page*:, HYPERLINK <http://www.sgi.com>;
- [12] SFF Laboratory, University of Connecticut, *Institute of Materials Science WWW page*: HYPERLINK: <http://www.ims.uconn.edu>; <http://www.ims.uconn.edu>;
- [13] Solid Freeform Fabrication Laboratory web site, HYPERLINK: <http://www.ims.uconn.edu/~hmarcus>;

A Memory Efficient Slicing Algorithm for Large STL Files

S. H. Choi and K. T. Kwok

Department of Industrial and Manufacturing Systems Engineering
The University of Hong Kong, Pokfulam Road, Hong Kong
Email: shchoi@hkucc.hku.hk and ktkwok@hkusua.hku.hk

ABSTRACT

This paper proposes a memory efficient slicing algorithm for Rapid Prototyping (RP) processes. The algorithm is aimed to overcome the constraints of computer memory inherent in the conventional slicing methodologies. It extracts from the Stereolithography (STL) file the facets that intersect with the cutting plane to process the slice data and the topological information. Reading only the facets of the current layer greatly reduces the amount of computer memory required and involves less computationally intensive searching operations. Thus, large STL files of virtually unlimited sizes can be sliced to facilitate the RP process. The algorithm is also relatively fault-tolerant in that inconsistent contour due to defects of the STL file may be more effectively repaired.

The topological information of the layer contours can be subsequently processed by further operations, such as hatching, physical fabrication or virtual simulation. To cater for the variations of RP processes, the Common Layer Interface (CLI) format is adopted as the output interface.

1. INTRODUCTION

Rapid Prototyping (RP) is an additive fabrication process. Contrary to the traditional subtractive machining processes such as milling, RP processes use liquid, powder or sheet materials to form a part layer by layer. These parts are used in various stages of the product development. The role of RP has become more important since it was introduced about 10 years ago.

Fig.1 shows the flow of a typical RP process. The first phase is to validate the 3D CAD model, which is then orientated with the optimal orientation with respect to the build time and the surface quality. Support structures are then generated based on the process requirements. The final model is then sliced with a set of horizontal planes. Each horizontal plane gives a piecewise linear contour, which is then crosshatched to determine the laser paths to control the sintering or solidification process. The process is repeated for the next layer until the model increment to its final shape.

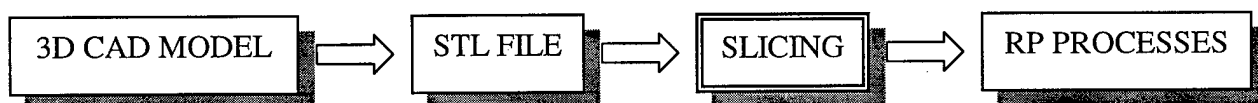


Fig. 1 STL as an interface between CAD and RP

2. SLICING STRATEGIES

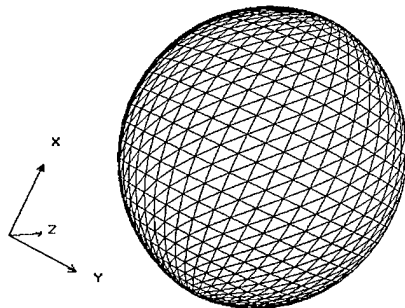


Fig. 2 Sphere in STL format

When creating parts layer by layer, a CAD model of the part is required [1]. Currently, STL format is the *de facto* standard representation of CAD data input. Tessellation is the process that converts a CAD model to a STL file. We consider now only the CAD model as the input, despite there are lots more data input methods such as reverse engineering data and layered data from mathematical programs.

A STL file consists of an unordered list of triangular facets covering the outer surface of the model. Each facet is described by a set of X, Y and Z coordinates for each of the three vertices and a unit normal pointing outside of the solid. An example of STL sphere is shown in Fig. 2. As STL is just an approximation of the surface model, the user needs to define the chordal value, which is the maximum distance from the surface to the vector representing the surface of a facet. STL format offers good geometry approximation of the CAD model if small layer thickness is used. However, the smaller the tolerance, the larger the number of facets required to represent the solid, and hence the bigger the file size. Other cases would also result large STL file sizes, such as complex medical scan data which require high resolution for specific vital purposes (Fig. 6), life-sized models of large objects to be fabricated by RP processes (Figs. 7 and 8) or virtual models developed for different applications (Fig. 9).

The major disadvantage of tessellated or facet models used in most current RP systems is that they are poorly suited for representing highly curved objects. A simple solution to improve the overall surface quality is to increase the number of facets and decrease the slice thickness that results in large STL file. Hitherto, commercially available slicing algorithms usually read the whole STL file into the computer memory to reconstruct the topological relationship of the surface facets. However, a complex or accurate CAD model is often too large to read into the memory. Consequently, slicing cannot take place and thus becomes a bottleneck in the RP process. This bottleneck limits the use of RP technology in certain areas where highly detailed or complex models are required.

2.1 Direct Slicing

Direct slicing has been proposed to alleviate the problem of STL by skipping the facet representation and slice the CAD model directly [2]. It can therefore, solve the big STL file problem if implemented between the CAD system and RP machine. Implementation of direct slicing based on binary representation (B-rep) solid model and constructive solid geometry (CSG) had been proposed. However, similar to sloping surface approach [3], the major disadvantage of direct slicing is that it is machine/CAD dependent. Solid model representation such as B-rep and CSG are fundamentally different, and a generic model format has yet to be devised.

2.2 Adaptive Slicing

Adaptive slicing was proposed to maximize the geometry without affecting the accuracy. In contrast to uniform slicing, adaptive slicing increases the slice density in highly convoluted regions, and reduces it in other regions wherever possible. Adaptive slicing mainly addresses the geometry issues and need a specific RP system to achieve the desired results. However, there are still not RP machines that fully support or able to take full advantages of adaptive slicing. The build thickness for a single layer is usually fixed to a small range between certain upper and lower limits. In case of large model size adaptive slicing offers no compensation. The current RP systems such as Selective Laser Sintering (SLS) and Fused Deposition Modeling (FDM) only fuse a layer of building material having a thickness of less than 0.5 mm in order to have a higher accuracy along the build direction.

Most researchers tend to propose another file format to replace the STL file standard. Jacob [4] proposed a new rapid prototyping interface, which includes facets topological information. However, similar to other proposed formats [5], they failed to provide imperious advantages over STL file as a new standard. Others focus on process parameter optimization [7,8] but less effort has been given to solve the big STL file problem that provides a practicable and economical solution to the existing RP users. Due to the nature of STL file, no sorting or reconstructing algorithm is able to give satisfactory results. Once if the input STL file is too large to fit in the system memory or has minor defects, it will stop the RP process or even 'hang' the machine. It is the purpose of this paper to solve this memory limitation problem.

It can be concluded that STL representation of CAD models is still the most versatile interface for commercially available RP systems. STL format has been a unified input to all downstream processes that are performed in rapid prototyping as well as other layered manufacturing. STL export option has been implemented in most CAD systems that ensures a unified neutral interface between CAD and RP systems. Solving the memory bottleneck provides an economical and practicable option for RP users. A memory efficient slicing algorithm that eliminates the bottleneck has been developed and is discussed in the following sections.

3. THE MEMORY EFFICIENT SLICING ALGORITHM

The memory efficient slicing algorithm adopts a different approach. Instead of storing the whole model into the computer memory, this algorithm reads only the facets that intersect with the cutting plane as shown in Fig. 4. Hence although the number of facets in a STL file depends on the model density, the number of facets read in the computer memory is greatly reduced. The difference is even more observable as the facet density becomes higher.

Fig. 5 shows the overall flowchart of the slicing program. The facet model will be scanned to obtain properties such as maximum and minimum vertices, model name and number of facets. Once the model has been scanned, all the properties will be displayed on the screen. Since a valid STL model should be in the positive Cartesian space, a Model Manipulator module has been developed to handle the case of negative vertices, which may be produced from the CAD to STL conversion or part orientation optimization. The simple Model Manipulator uses the translation

matrix for the calculations of model rotation, model transition and model scaling. With the Model Manipulator, the STL model can be properly orientated before the slicing process.

In the slicing stage, the algorithm mainly involves manipulation of the facet data and comparison of z-coordinates of the facets, and then calculates the line segment that defines the contour for the layer. The line segments are vectors following the anti-clockwise rule, which will be stored in the computer memory for contour construction. The sliced line segments are sorted and joined to form a closed contour by simple head-to-tail searching mechanism with a given tolerance. The tolerance is the maximum distance between the head and the tail of two joining line segments, as shown in Fig. 3. The choice of the tolerance value is critically related to the chordal value of the STL file [10]. In this algorithm, the maximum tolerance is set to equal to the shortest edge in the STL file.

Once the model is sliced in each layer, the topological relationship needs to be sorted. The anti-clockwise nature of the line segments can be used to identify the inner loop and the outer loop. Other topological information such as number of holes and number of surrounding contours should be calculated also. This is done by the ray-crossing or ray-shooting containment test [11], which is implemented in the Contour Sorter Module. The Sorting Module outputs the sorted layer contours for subsequent processes. The Layer Viewer Module is used to view the contour output. The user can view the layer contour to check its validity.

Finally, the sliced data are used to generate a data file in the Common Layer Interface (CLI) format [12]. The CLI data format containing the contour information is independent of the RP machines. CLI is a simple and efficient format for data input to all Layer Manufacturing Technology systems based on a 2.5D layer representation. Moreover, medical scan data is already accommodated in CLI format [13].

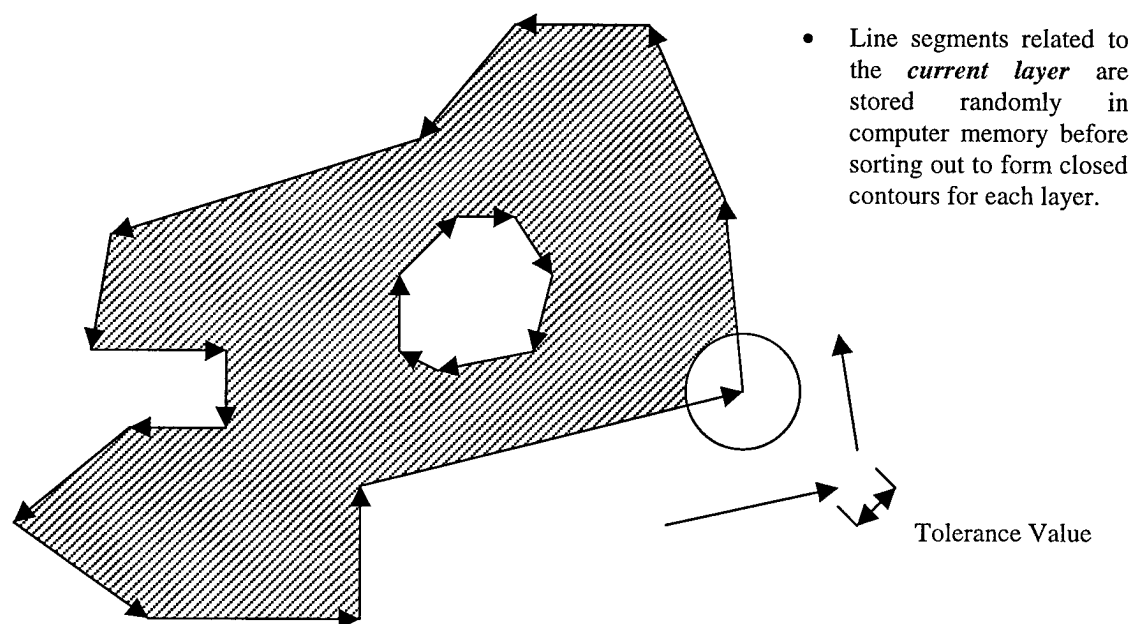


Fig. 3 Sample layer contour following the anti-clockwise rule

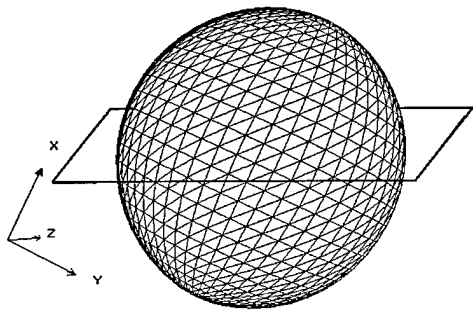


Fig. 4a: Conventional slicing algorithm stores *all facets* in computer memory, which limits the size and complexity of the design and thus leads to breakdown of the rapid prototyping process.

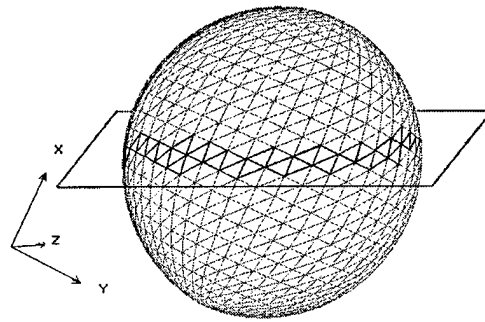


Fig. 4b: The memory efficient slicing algorithm stores only the *facets intersect with the cutting plane*, thus alleviates bottlenecks due to memory limitations and thereby facilitates rapid prototyping of large and complex models.

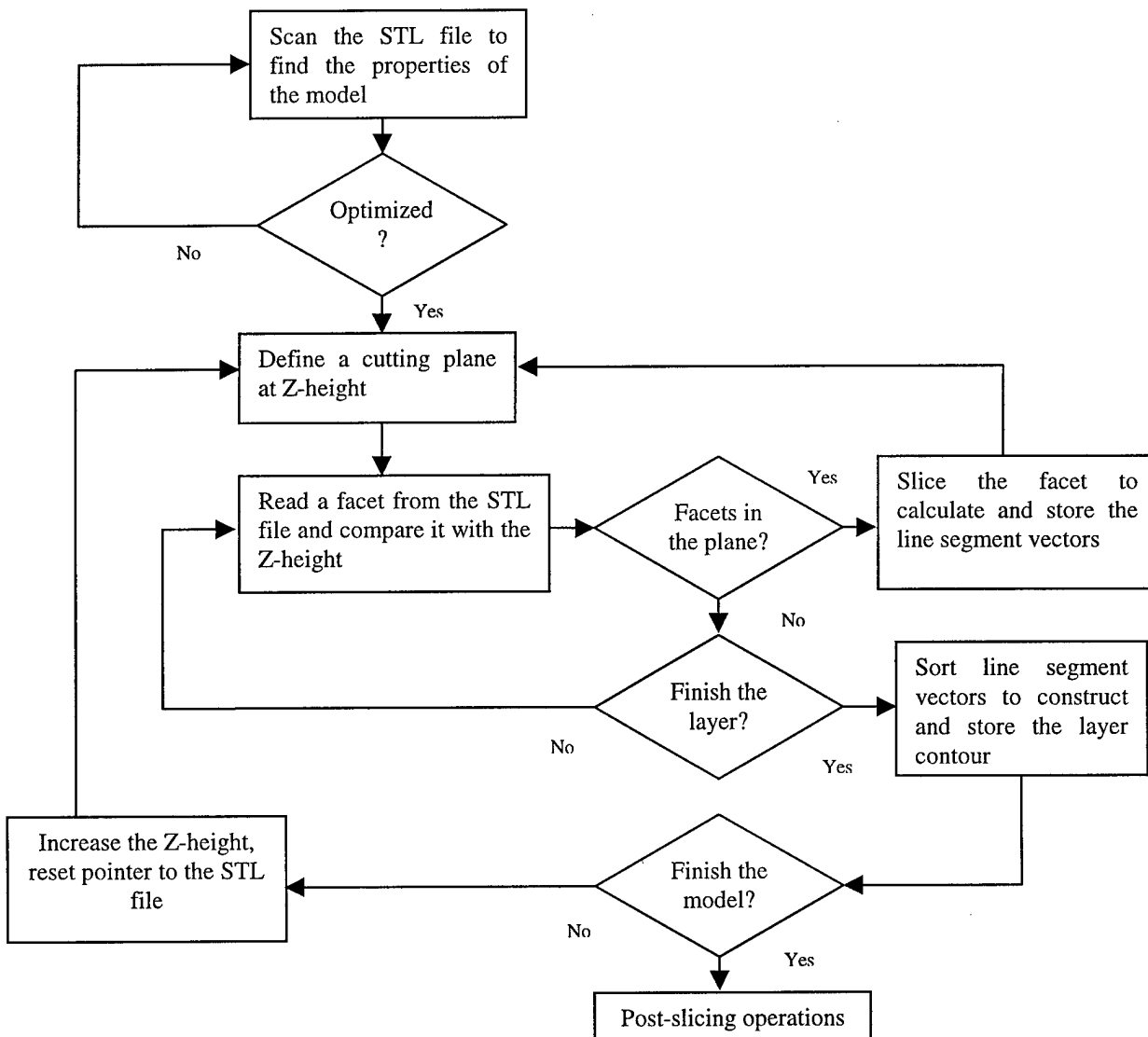


Fig. 5: Flowchart of the memory efficient slicing algorithm

4. EXAMPLES

The algorithm has been developed in Visual C++ and is now being enhanced. Samples STL files of different sizes and shapes have been sliced to test the functionality and stability of the program. The configuration of the computer used is as follows: Intel Pentium 166MHz processor, 64MB Ram, a 4.2GB hard disk with SCSI controller and Microsoft Windows 98. Fig. 6 shows a human skull model, which consists of 767,256 facets. A bell and a car of 426,572 and 151,350 facets are given in Figs. 7 and 8 respectively, while Fig. 9 shows a computer generated virtual model that consists of 74,634 facets. Screen captures of Layer Viewer Module are also shown in Figs. 6 to Fig. 9. Layer Viewer displays contours in different colours for better visualisation and easier error detection. Indeed, most commercially available slicing algorithms will not endure even one fault facet [6], and slicing will not proceed unless all the triangles are perfectly linked together in the STL file. In contrast, the proposed algorithm will slice the STL file even if some edges are missing. The slice can be viewed in Layer Viewer module, and hence the user can manually edit the slice in case of unbound contours.

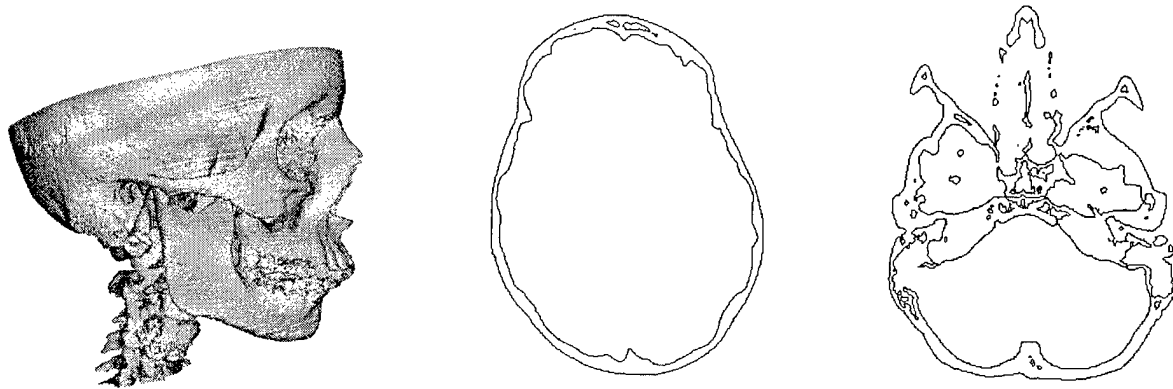


Fig. 6 A Human Skull Model (36MB binary STL file, with two slices at different Z-height generated by the algorithm. Mean processing time per slice is approximately 1 minute)

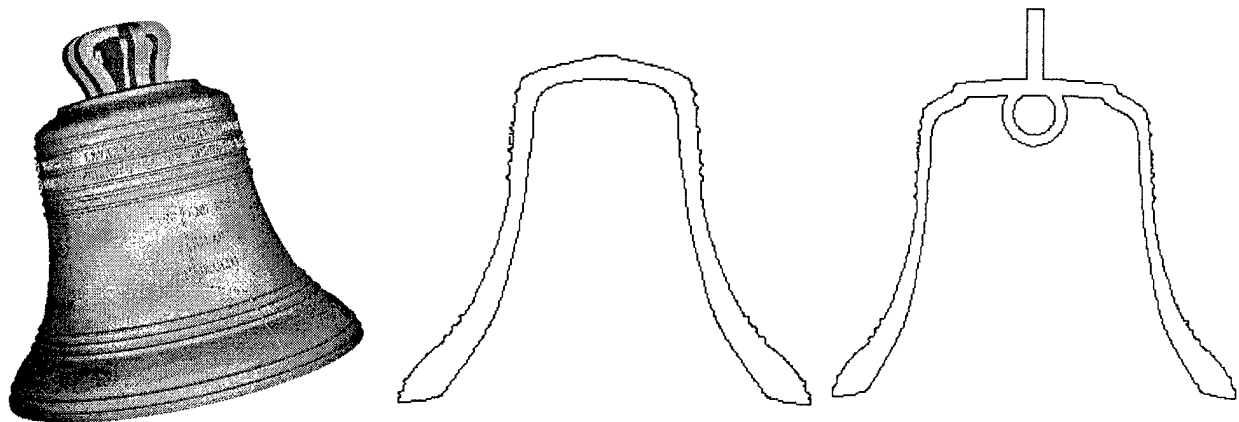


Fig. 7 A Bell Model (21 MB binary STL file, with two slices generated at different Z-height by the algorithm. Mean processing time per slice is approximately 30 seconds)

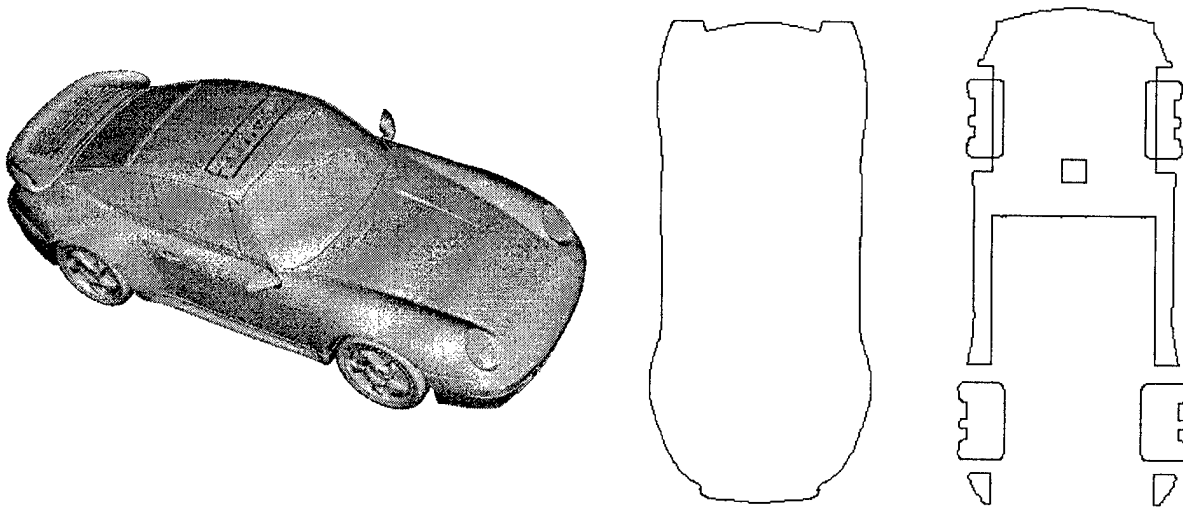


Fig. 8 A Car Model (7.21MB binary STL file, with two slices generated at different Z-height by the algorithm. Mean processing time per slice is approximately 12 seconds)

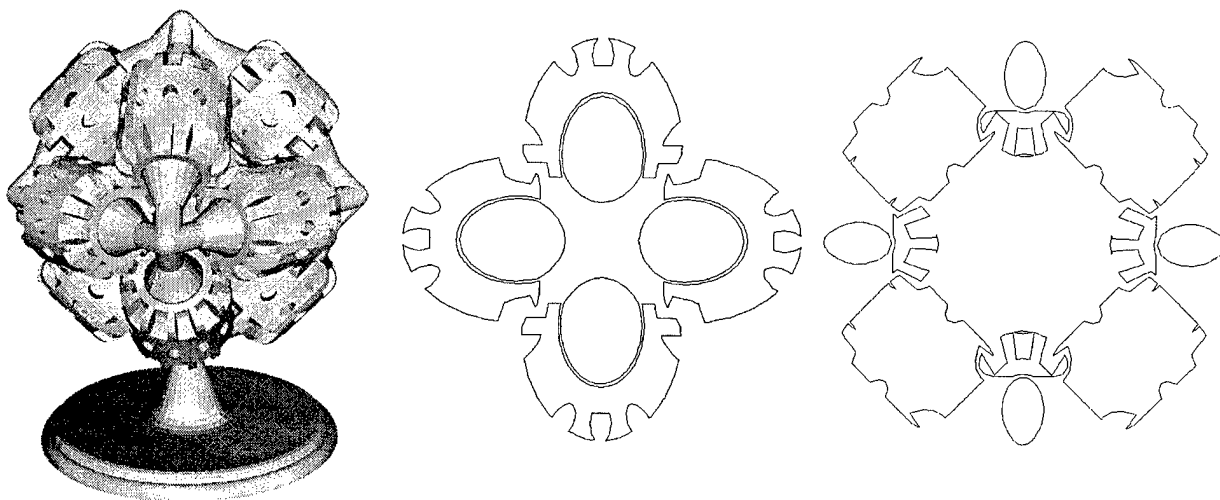


Fig. 9 A Virtual Model (3.55MB binary STL file, with two slices generated at different Z-height by the algorithm. Mean processing time per slice is approximately 5.2 seconds)

5. CONCLUSION

The productivity of layered manufacturing can be improved by using a versatile slicing algorithm, which should be able to slice STL models of any sizes and complexities. Traditional slicing algorithms can only handle relatively small STL models because of the limitation of computer memory. A new memory efficient slicing algorithm has been developed to solve this problem. The advantage of this algorithm is its ability to slice STL models of virtually unlimited sizes. It processes only the facets of a single layer to free up memory. This feature would be essential to make large objects such as a life-sized vehicle, or complex and detailed models used in medical applications.

ACKNOWLEDGEMENT

The authors would like to thank the Research Grant Council of the Hong Kong Government and the CRCG of the University of Hong Kong for their financial support for this project.

REFERENCES

1. Vinod Kumar and Debasish Dutta, "An assessment of data formats for layered manufacturing", *Advances in Engineering Software* vol. 28 (1997), pp. 151-164
2. P. J. de Jager, "A comparison between zero and first order approximation algorithms for layered manufacturing", *Rapid Prototyping Journal*, vol. 3 number 4 1997, pp.144-149
3. Zhiwen Zhao and Luc Laperriere, "Adaptive Direct Slicing of the Solid Model for Rapid Prototyping", <http://ecoleing.uqtr.quebec.ca>
4. Gan G.K. Jacob, "Development of a new rapid prototyping interface", *Computers in industry* vol. 39 (1999), pp. 61-70
5. Anna Kochan, "Rapid prototyping trends", *Rapid Prototyping Journal* vol. 3 number 4, 1997, pp. 150-152
6. K. F. Leong, C. K. Chau and Y. M. Ng, "A study of Stereolithography File Errors and Repair", *The International Journal of Advanced manufacturing Technology* (1996) 12:407-414
7. Zhu Wei-Ming and Yu Kai-Ming, "Pre-processing Technologies for Rapid Prototyping and Rapid Tooling – a Survey", *CIRT International Symposium – Advanced Design and Manufacture in the Global Manufacturing Era*. August 21-22, 1997, Hong Kong, pp. 802-808
8. Minoo Bablani and Amit Bagchi, "Quantification of errors in Rapid Prototyping Processes, and Determination of Preferred Orientation of Parts", *Transaction of the North American Manufacturing Research Institute of the SME*, vol. xxiii, May 1995, pp. 319-324
9. Michael J. Laszlo, "Computational Geometry and Computer Graphics in C++", Prentice Hall, 1996, pp.116-130
10. Joel E. McClurkin and David W. Rosen, "Computer-aided build style decision support for stereolithography", *Rapid Prototyping Journal* vol. 4 number 1, 1998, pp. 4-13
11. R. L. Hope, P.N. and P.A. Jacobs, "Adaptive slicing with sloping layer surfaces", *Rapid Prototyping Journal* vol. 3 number 3, 1997, pp. 89-98
12. <http://www.cranfield.ac.uk>, Cranfield University EARP
13. Common Layer Interface, Version 2.0, pp.19-21

A minimum bounding box algorithm and its application to rapid prototyping

C K Chan and S T Tan

Department of Mechanical Engineering,
The University of Hong Kong, Hong Kong

Email Address: edwinchan@bigfoot.com and sttan@hkucc.hku.hk

ABSTRACT

This paper describes a method for determining the minimum bounding box of an arbitrary solid. The method simplifies the complex three-dimensional problem by projecting the solid onto the three principal planes and makes use of the projected contours for analysis. The orientations of the contours are determined by rotating them within a specific angle range. These orientations are then used to approximate the orientation of the solid so that its bounding box volume is minimised.

Keywords: bounding box, iterative method, minimum

INTRODUCTION

The problem of determining the minimum bounding box occurs in a variety of industrial applications likes packing and optimum layout design. The algorithm can be applied to many other fields, ranging from a straightforward consideration of whether an object will fit into a predetermined container, or whether it can be made from standard sized stock material⁷, to uses in constructing bounding boxes in solid modellers to improve their performance. Freeman and Shapira³ described a method for finding the rectangle of minimum area in which a given arbitrary plane curve can be contained. They proved that the rectangle of minimum area enclosing a convex polygon has a side collinear with one of the edges of the polygon. Also, the rectangle of minimum area enclosing the convex hull of an arbitrary plane curve is the same as the minimum area rectangle encasing the curve. Their method consists of two steps. Firstly, it determines the convex hull that encloses the given curve. Secondly, it rotates the convex hull such that one of its edges is collinear with a specific principal axis, say the X-axis, and then evaluates its bounding box area. This process is applied to all the edges of the curve. Finally, the rectangle of minimum area capable of containing this polygon is determined. Based on the idea of Freeman and Shapira³, Martin and Stephenson¹ described a family of algorithms for solving problems such as whether a given object fits inside a rectangular box and the minimum bounding box for an object, both in two and three dimensions. Martin and Stephenson¹ proposed that the idea of Freeman and Shapira³ could be extended to three-dimensional case. That is, the box of minimum volume enclosing a convex polyhedron has a face collinear with one of the faces of the polyhedron. Also, the box of minimum volume enclosing a convex hull of an arbitrary polyhedron is the same as the minimum volume box encasing the polyhedron. Thus, the object is oriented one at a time with each face of the polyhedron lying on say, the XY plane. The bounding box of the object and its volume are computed for each orientation. The smallest volume and its corresponding orientation are recorded.

In the above algorithm, the computational time is significant if the number of faces of the polyhedron is large because bounding box must be checked for each face. In the STL¹¹ computer model for rapid prototyping, the number of facets ranges from hundreds to millions. Furthermore, the real world is full of objects that are not polyhedron and convex. A

conversion process⁵ of these objects to convex polyhedra is needed. For a complex model, this conversion process is computationally expensive. Moreover, this method is approximate and the accuracy relies on the tolerance setting of the conversion process.

A new algorithm is proposed as an alternative to solve the problem with a simple approach. It simplifies the complicated 3D problem into a 2D problem. The algorithm is described in the following section.

THE ALGORITHM

The algorithm is used to determine the orientation of an arbitrary solid so that its bounding box volume is minimized. Relations between the 3D problem and the projected contours of the solid are introduced. An iterative method is constructed to deal with the projected contours.

Relations between the 3D bounding box and 2D projected contour

Problem: Given an arbitrary solid, how should the solid be positioned so that the volume of the bounding box is minimum? To obtain the minimum volume encasing box for a given arbitrary solid, we shall make use of the following definitions and theorems. Instead of showing the detail proofs of the theorems, an example is illustrated at the end of the theorems. The proofs are described in details in reference¹².

DEFINITION: A bounding box is defined as a box whose body diagonal is delimited by the minimum X, Y, Z values and maximum X, Y, Z values of the given solid.

AXIOM: Given an arbitrary solid model in 3D space, all orientations of the model can be achieved by rotating the model about any point in the 3D space.

THEOREM 1: The areas of three mutually perpendicular faces of a given box are minimized if and only if the volume of the box is minimum. On the contrary, they are maximized if and only if the volume of the box is maximum.

The key issue is how to reorient a model to achieve Theorem 1. A new method is proposed (discussed later) which can be applied to an arbitrary model. During the rotation of a model about a point, its projected areas on the principal planes are inter-related. This means that the three bounding boxes are also inter-related and their relations are revealed in the following theorems.

THEOREM 2: Given an arbitrary 2-D contour, let h and w be the height and width of its bounding box respectively. If the contour is rotated about the bounding box centre, the value of w will lag behind the value of h by $\pi/2$. At the same time, the values of h and w will repeat regularly by a period of π .

THEOREM 3: Given the same arbitrary contour, if the contour is rotated about the bounding box centre, the bounding box area repeats itself by a period of $\pi/2$.

THEOREM 4: Given the same arbitrary contour, if the height of the bounding box is equal to the width and the contour is rotated about the bounding box centre by an angle β , such that its bounding box area is minimum, then both the height and the width is minimum.

Let $A(\theta)$, $w(\theta)$ and $h(\theta)$ be the area, the width and the height functions at angle θ respectively. The theorem is stated as follows:

If $A(\beta) = \{A(\theta)\}_{\min}$ and $h(\beta) = w(\beta)$, then $h(\beta) = \{h(\theta)\}_{\min}$ and $w(\beta) = \{w(\theta)\}_{\min}$.

THEOREM 5: Following from the above theorem, if the contour is rotated about the bounding box centre by an angle β , such that its bounding box area is minimum, either the height or the width or both the height and the width of the bounding box is minimum. Let $A(\theta)$, $w(\theta)$ and $h(\theta)$ be the area, the width and the height functions at angle θ respectively. The reverse is also true. The theorem is stated as follows:

$A(\beta) = \{A(\theta)\}_{\min}$ if and only if $h(\beta) = \{h(\theta)\}_{\min}$ or $w(\beta) = \{w(\theta)\}_{\min}$ or both are true.

THEOREM 6: Given the same contour, the height of the bounding box of a contour will be equal to the width at a certain angle θ during rotation from 0 to $\pi/2$. The theorem is stated as follows:

$$h(\theta) = w(\theta) \text{ for an angle } \theta \text{ where } 0 \leq \theta \leq \pi/2$$

THEOREM 7: Given an arbitrary 2-D contour, let $h(\theta)$ and $w(\theta)$ be the height and width functions of the bounding box respectively, where θ is the angle of rotation of the contour. $h(\theta)$ and $w(\theta)$ must be less than or equal to the length of the diagonal of the bounding box at any orientation. The theorem is stated as follows:

$$h(\theta) \leq \sqrt{h(\lambda)^2 + w(\lambda)^2} \text{ and } w(\theta) \leq \sqrt{h(\lambda)^2 + w(\lambda)^2}$$

where λ is any other angle of rotation of the contour.

THEOREM 8: Following from Theorem 7, if the area of the bounding box of the contour is minimum at angle β ($0 < \beta < \pi/2$ by Theorem 3) and $h(\beta)$ is minimum (see Theorem 5), it remains minimum even though the contour is changed. This is true provided that $w'(\beta) = w(\beta)$ and $\{h'(\theta)\}_{\min} \leq w(\beta)$ where $w'(\theta)$ and $h'(\theta)$ are the width and the height functions of the bounding box of the new contour respectively. The same applies if $w(\beta)$ is minimum instead of $h(\beta)$.

THEOREM 9: Given an arbitrary solid model, let R_x , R_y , R_z be the vectors parallel to the three principal axes X, Y, Z respectively. They also pass through the bounding box center of the arbitrary solid. Let P_{xy} , P_{yz} , P_{zx} be the three principal planes. If the model is first rotated about R_z until its projected bounding box area on the corresponding P_{xy} is minimum, one of the edges of the bounding box (i.e. height or width) will have achieved minimum. Without affecting the value of this edge, the model is further rotated about one of the two remaining vectors (i.e. R_x or R_y) until its projected bounding box area on the corresponding principal plane is minimum. One of the edges of the bounding box (i.e. height or width) will have achieved minimum. The model is further rotated about the vector, which is normal to the two minimum edges, until its projected bounding box area on the corresponding principal plane is minimum. The volume of the bounding box of the model so derived will thus be minimum. The same procedure can be applied if the model is rotated about the other two vectors (i.e. R_x or R_y) first.

Iteration process

A graph of the projected bounding box area of the model in Figure 3 on the XY plane against the angle of rotation is shown in Figure 1. By Theorem 3, the angle range being tested is $\pi/2$. To determine the absolute minimum located within this angle range, the following method is used. Within a small angle, the bounding box of the projected area of an arbitrary contour

does not change much. Thus, the contour can be rotated by a small angle increment (δ), says 5 degree, within the angle range. This value of increment is sufficient for most contour patterns such that there is one minimum point located within the angle range only. Each time the bounding box of the contour and its area are computed, the smallest area and its corresponding angle (θ) are recorded. Thus, the absolute minimum projected area lies in the angle range ($\theta - \delta$) and ($\theta + \delta$). If β is the angle at which the projected bounding box area is minimum, we have

$$\theta - \delta < \beta < \theta + \delta.$$

Within the angle range, an iterative process can be started to determine β . The angle range can be divided into k equal segments at angles $[a_0, a_1, a_2, a_3, \dots, a_{k-1}]$ (see Figure 2). The projected contour is then rotated about its bounding box centre at angles $[a_0, a_1, a_2, a_3, \dots, a_{k-1}]$. The corresponding

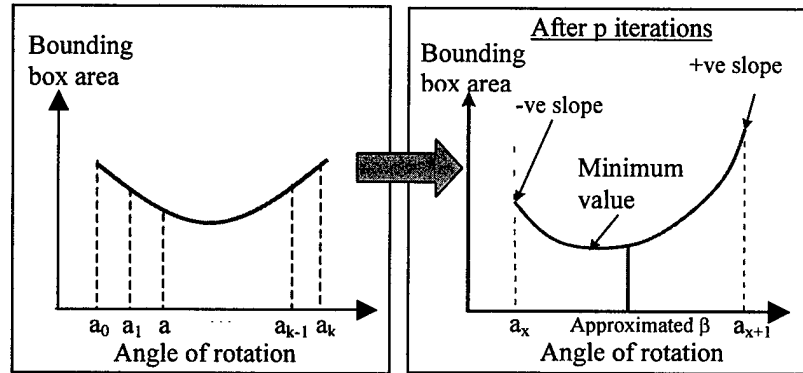


Figure 2. Bounding box area against angle of rotation.

slopes of the projected contour at these angles are recorded for further analysis. If there is a slope change across an angle pair (a_x, a_{x+1}) (see Figure 2), this pair will be used as the range for the next iteration until a predefined number of steps (p) is achieved. The angle (β) required for rotation is approximated by

$$\beta = a_x + 0.5 \times (a_{x+1} - a_x)$$

The accuracy of the iteration process is given by,

$$\text{Accuracy} = \frac{\text{initial iteration range}}{2 \times k^p} = \frac{2 \times \delta}{2 \times k^p} = \frac{\delta}{k^p}$$

For example, if $\delta = 5$, $k = 4$ and $p = 5$,

$$\text{Accuracy} = \frac{5}{4^5} \approx 0.005 \text{ deg}$$

The iteration process is fairly accurate and efficient.

Bounding box area against angle of rotation

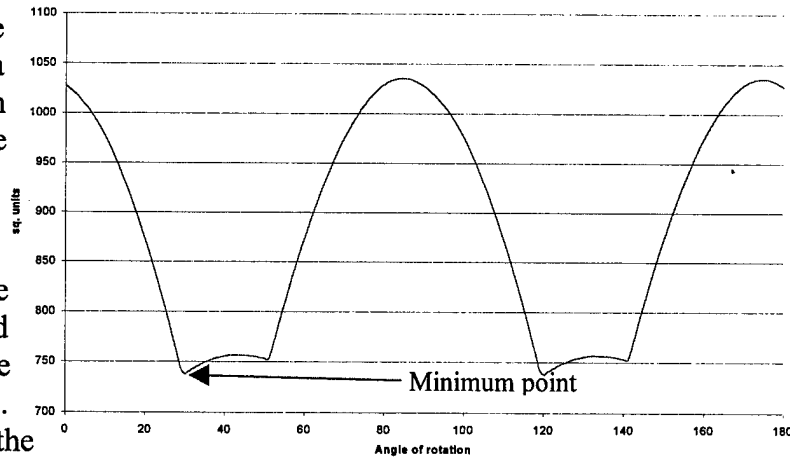
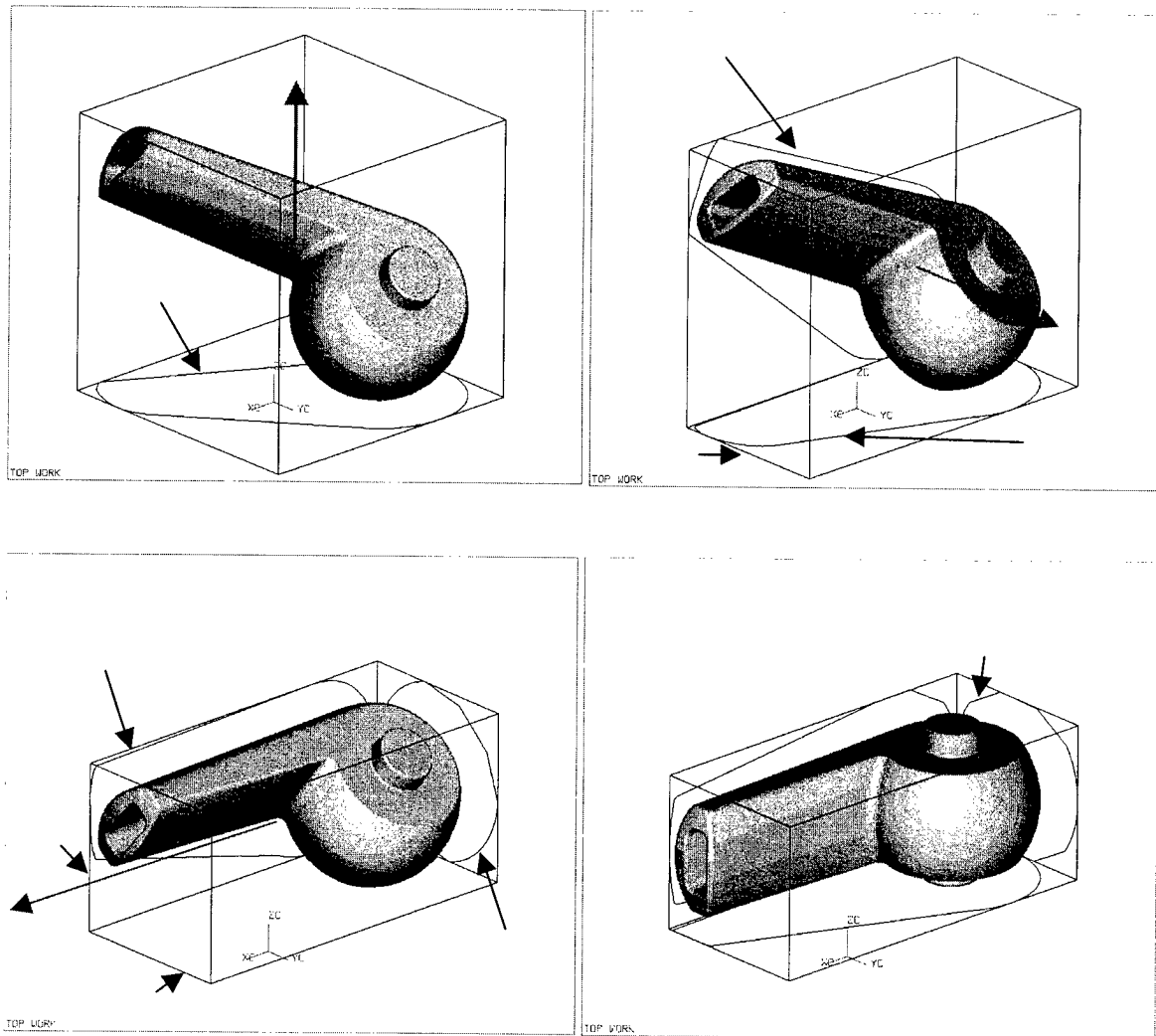


Figure 1. Projected bounding box area against angle of rotation.

Examples



1. Projecting the model on the XY plane to find the 2D bounding box as shown in Figure 3.
2. Constructing an axis R_z normal to the XY plane and passing through the box centre.
3. Rotating the model about R_z until its projected bounding box area on XY plane achieves a minimum by the proposed algorithm (see Figure 3). The resultant model is shown in Figure 4 and we get the so called XY-bounding box with E_y is minimum in this case.
4. Now the bounding box edge that point to positive Y-axis direction is minimum. Therefore the axis R_y is used in next rotation. Repeat step 1, 2 and 3 for the ZX plane (see Figure 5). Hence we get the ZX-bounding box with E_z is minimum in this case.
5. Repeat step 1, 2, 3 for YZ planes which is formed by edge E_y and E_z . (see Figure 6)
6. By Theorem 9, the model is now oriented at a position which gives a minimum bounding box volume. One more example is shown in Figure 7.

	Model	Bounding box size (units)	Volume (cu. Units)	% reduction
Model in Figure 3	Original	38.6×31.6×30.7	31626	57.3
	Resultant	41.6×19.0×17.1	13520	
Model in Figure 7	Original	4.07×4.65×3.59	67.91	77.9
	Resultant	2.01×1.49×5.00	15.02	

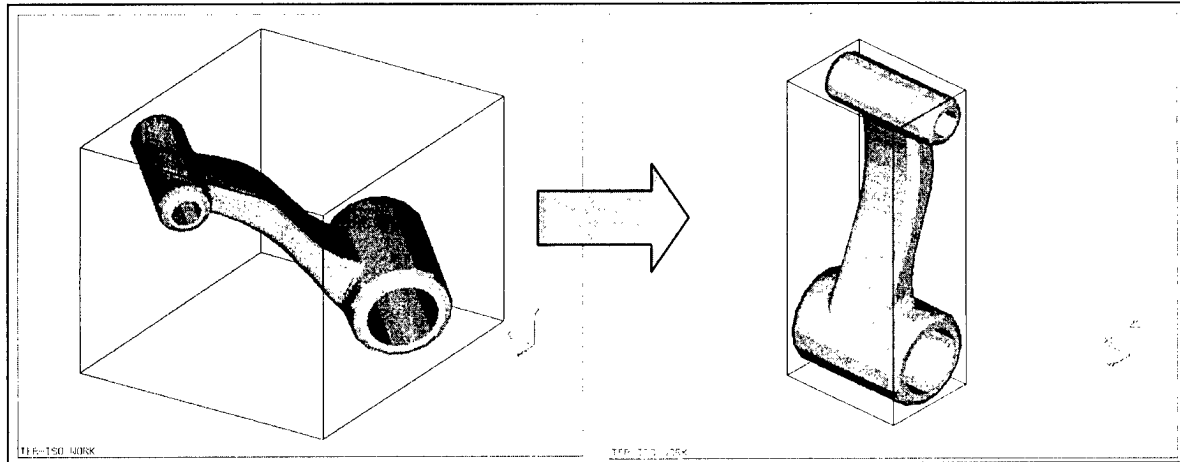


Figure 7. Example illustrating the proposed algorithm.

DISCUSSION

By the use of the above proposed algorithm, the minimum bounding box of an arbitrary model can be determined. The proposed algorithm is independent of model representation method, be it CSG model or B-rep. This is the main advantage over the one proposed by Martin and Stephenson¹.

The algorithm proposed by Martin and Stephenson¹ depends on the number of facets (f) generated from a model and also the number of edges (e) in each facet. The running time is linear $O(f \times e)$ without considering the pre-processing time, that is, the time requires to find the three-dimensional convex polyhedron. In reference (5), the authors showed that the running time for determining the three dimensional convex hull of a polyhedron is $O(n \times \log n)$ where n is the number of vertices. In the proposed algorithm, if a polyhedron is considered, the critical factor is the choice of angle increment (δ), number of iterations (p), and the number of subdivided element (k) in each iteration. The running time is $O[(k \times p) / \delta]$. It is very difficult to compare the functions of running time between the two processes because the parameters involved are different. However, the conversion process from an arbitrary model to a convex polyhedron is computationally expensive if the number of facets is large. On the contrary, the new algorithm can be applied directly to any model. The running time of the new algorithm is considered to be faster than that proposed by Martin and Stephenson¹.

In the case of complex shape solids for example, the one shown in Figure 8, it is rather difficult to determine its minimum bounding box. The data for the example built by SLS is shown in following table.

Model	Bounding box size (mm)	Build time (hrs)	% reduction
Original	65.03×62.89×65.97	4:19	23.9
Resultant	69.47×47.59×53.84	3:17	

Although the difference may not appear to be very significant, however, in certain application such as the rapid prototyping (RP) process, the time taken to slice the object positioned at the minimum box configuration would give rise to a significant saving in build

time. This is particularly so for those RP processes whose build time is build height dependent, e.g. Selective Laser Sintering (SLS). The actual built part is shown in Figure 9.

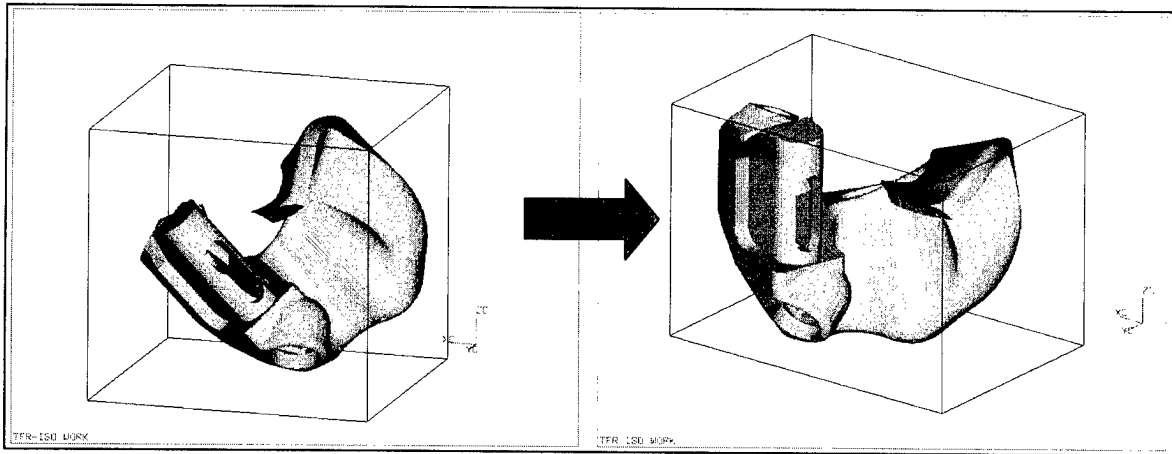


Figure 8. Complex solid from which minimum box can not be determined easily.

In the proposed algorithm, after obtaining the initial angle range using Theorem 3, the angle range for iteration is set by comparing the bounding box area in each rotation. Although this is valid for almost all model shapes, some special cases may be missed. Therefore, two other slightly modified approaches may be used.

Approach 1: The projected contour is rotated by a small angle increment within the initial angle range. After each rotation, its bounding box area and the slope at that point are evaluated. Since the sign of slopes around each turning point changes from positive to negative or vice versa, we can locate all minimum points by checking all the sign change of slopes. Through an iterative process, all minimum points can then be determined. Thus, the absolute minimum area and its corresponding angle can be found.

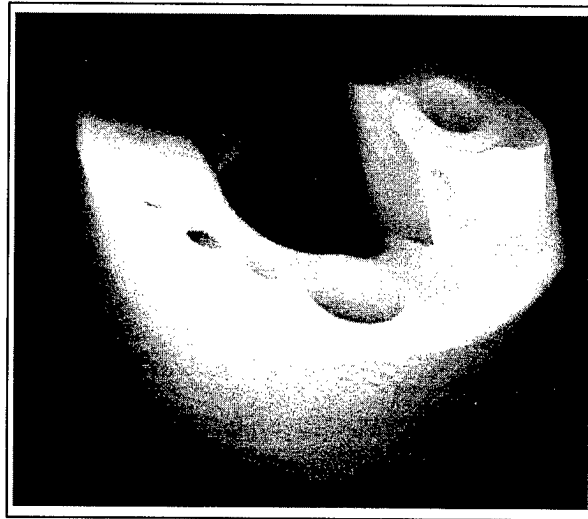


Figure 9. The actual built part by SLS.

Through an iterative process, all minimum points can then be determined. Thus, the absolute minimum area and its corresponding angle can be found.

Approach 2: Instead of checking the sign change of slopes. A cubic spline curve can be fitted into those points and the absolute minimum can be determined from the curve equation.

The first approach is more general because it determines all the minimum points regardless of whether they are local or absolute. However, the running time depends on the number of minimum points. With more number of minimum points, the running time is increased but it does ensure that the derived area is an absolute minimum and its corresponding angle is the correct one. Comparatively, the second approach is faster and the running time depends on the angle increment. Although this method is the fastest, it compromises on the accuracy of the fitted minimum point. Some special contour pattern cases have also been noted. Firstly, if the projected contour is a regular polygon, the minimum bounding box areas of the contour during rotation will repeat regularly many times. Secondly, if the projected contour is a circle, the bounding box area of the contour is a

constant throughout the rotation. Thirdly, if the projected contour is approximately round in shape, the bounding box area of the contour will vary within a very narrow range. All these case can be identified easily. This observation may be useful in further work for feature recognition.

CONCLUSION

In this paper, an alternative method for determining the minimum volume bounding box of an arbitrary solid has been suggested. By the use of the algorithm explained above, the minimum bounding box of any solid can be efficiently determined. The algorithm is also valid for a surface model as long as the bounding box of the projection of the arbitrary model can be determined⁸. The algorithm can be applied to determine the orientation of a model in packing problems, rapid prototyping and parting line determination¹⁰. Another interesting observation is that the reverse of the algorithm is also true. That is, the maximum bounding box of a model can be determined by reversing the algorithm.

ACKNOWLEDGEMENTS

The authors thank the Department of Mechanical Engineering, The University of Hong Kong and the Hong Kong Research Grant Council for providing financial support.

REFERENCE

1. RR Martin and PC Stephenson, 'Putting objects into boxes'. Computer-Aided Design, volume 20 number 9 (1988) pp506-514.
2. B Chazelle, 'The polygon containment problem'. Adv. Comput. Res., Vol 1 (1983) pp 1-33.
3. H Freeman and R Shapira, 'Determining the minimum-area encasing rectangle for and arbitrary closed curve' Comm. ACM, Vol 18 No 7 (1975) pp 409-413.
4. G T Toussaint, 'Solving geometric problems with the "rotating calipers"' Proc. IEEE MELECON '83 (Athens, Greece).
5. M de Berg, M van Kreveld, M Overmars and O Schwarzkopf, 'Convex Hulls'. Computational Geometry, Springer (1997) pp233-239.
6. D F Rogers and J Alan Adams, 'Cubic splines'. Mathematical Elements for Computer Graphics, McGraw-Hill (1990) pp250-267.
7. Leonard, E John and Shah, J Jami, 'Automatic bar stock selection for machining'. American Society of Mechanical Engineers, Design Engineering Division (Publication) DE., Vol 69 No 2 (1994).
8. Yamada, Atsushi and Yamaguchi Fujio, 'Homogeneous bounding boxes as tools for intersection algorithms of rotational bezier curves and surfaces'. Visual Computer, Vol 12 No 4 (1996) pp202-214.
9. Mazzetti Marco and Ciminiera Luigi, 'Computing CSG-tree boundaries as algebraic expressions'. Computer Aided Design Vol 26 No 6 (1994) pp417-425.
10. YH Chen, 'Determining parting direction based on minimum bounding box and fuzzy logics'. International Journal of machine tools & manufacture Vol 37 No 9 pp1189-1199.
11. Georges M. Fadel and Chuck kirschman, 'Accuracy issues in CAD to RP translations'. Rapid prototyping Journal Vol 2 No 2 (1996) pp4-17.
12. C K Chan and S T Tan, 'Determination of the minimum bounding box of an arbitrary solid: An iterative approach'. Internal report CC01-98 Mechanical Engineering Department of University of Hong Kong. (1998) pp3-15.

Slicing STEP-based CAD Models for CAD/RP Interface

Haeseong J. Jee, Byong-Yeol Lee

Dept. of Mechanical Engineering, Hongik University
72-1 Sangsu-Dong, Mapo-Ku, 121-791 Seoul, Korea

ABSTRACT

SFF technologies have an ability of creating a physical part directly from its computer model by adding material on a layer by layer basis. One of the problems lies in their current file format for CAD data exchange. Current method using the *de facto* industry standard STL have at times resulted in problems such as accuracy, redundancy, and integrity in its representing CAD models. In this paper we propose a method of slicing and editing STEP-based RP models for the new data transfer paradigm between CAD systems and RP systems using STEP..

Key words: SFF, CAD, STL, Data Exchange Standard, STEP

1. INTRODUCTION

The major application of Solid Freeform Fabrication (SFF) has been the early verification of product designs and quick production of prototypes for testing. Despite this tremendous progress, many problems remain unsolved including several geometric issues [1] that must be resolved in coming years before this new technology is in common use. These include the issues of model slicing [2] or reverse engineering [3], which is, however, beyond the scope of this paper. We suggest the biggest problem lies in its *de facto* data exchange standard file format STL between CAD systems and SFF processes. In general, drawbacks of STL in its handling geometric information can be summarized as redundancy, accuracy, and integrity. Several research efforts have been far done in order to overcome these drawbacks. Generating topological information from this bucket of Facets [4] or, preferably, generating topological structures for surface models in the stage of pre-STL tessellation [5] has been done in resolving the issue of model redundancy. Repairing the model [6], if necessary, to ensure a well-formed representation is for model integrity, and, for overcoming its model accuracy, several research efforts for improving general polygonal models can be also applicable to an STL model. One among those approaches, for example, is simplifying a polygonal model by reducing the large number of polygons from a given polygonal CAD model. This simplification can be made by two approaches; one is re-tiling polygonal surfaces by positioning newly created vertex points using point repulsion [7] and the other re-triangulating within a distance tolerance from the surface to a plane that approximates the surface near the vertex [8]. Even with all these efforts, however, the biggest problem of STL confronted in future designs for SFF technologies still remains yet unsolved; STL does not carry, except the geometry, any design information at all. In other words, .STL file format does not compatible with any high level design information such as tolerance, mechanical properties, and surface patterns, which will be indispensable for further design applications made by SFF technologies. A next generation data exchange standard replacing

STL is hence required to be incorporated with high level design information for advanced design transformation into SFF technologies. Not surprisingly, the need of new data exchange standard will also steer research efforts toward solutions to a problem of how to handle, in the design stage, those high level design information remains open for those SFF processes. Several current RP research efforts are focused on development of a future alternative data format to address the shortcomings of STL and to enable data transfer for future advanced rapid manufacturing capabilities. This alternative data transfer mechanism is recently referred to as the Solid Interchange Format (SIF).

Since 1984 the International Organization for Standardization (ISO) has been working on the development of a new standard for the exchange of product data between computer-based systems in use for design and manufacturing. This standard, ISO 10303, is informally known as STEP (STandard for the Exchange of Product Data). STEP is coming standard. Many major companies are working with it, and all serious CAD vendors are beaver away generating translators for it. What makes STEP the first solution when other standards have not yet met expectations? In short, STEP has a well-defined internal components that can enable the data exchange easier while a design and engineering data are, in general, becoming increasingly complex. In addition, its open architecture and international acceptance to the world makes it valuable in terms of trade and growth. Carleberg is the first who mentions a STEP model as the input to a SFF system [9], and Gilman and Rock have also proposed a framework (an architecture and methodology) that integrates a heterogeneous environment of CAD and SFF systems using STEP [10]. Since then, developing new capabilities of STEP specifically designed for SFF purposes has been research issues around the world [11, 12, 13, 14] and, finally, an RP Interest Group was first formed within the standards organization developing STEP (ISO TC 184/SC4) to consider the requirements for RP data and the possible applicability of the existing STEP standard in 1998 [15].

In this paper, we propose STEP-Slicer, a model slicing paradigm using STEP standard for SFF processes. A tentative framework of working model based on the STEP for carrying SFF process features with part geometry is proposed for constructing CAD/RP interface, and the STEP-based CAD model is visualized, edited, and finally sliced using its own SFF process features.

2. FRAMEWORK FOR CAD/RP INTERFACE USING STEP

In this paper, as shown in the figure 1, a collaborative virtual environment (www.CyberRP.com) is constructed between various CAD softwares and different SFF processes. This environment can help smooth data transfer from CAD to RP by providing appropriate functional modules including visualization and virtual prototyping. In this paradigm of data transfer, people may exchange product models for fabrication using a tentative working model of AP_SIF (Application Protocol for SIF) using STEP. The AP_SIF can be developed based on integrated resource models such as geometric and topological representation (Part 42). It is now over the existing AP203 (Part203: Configuration controlled 3D designs of mechanical parts and assemblies) and provides information about specific SFF process features with the geometry. SFF process features here can be considered as layer thickness, material, and part orientation generally machine-dependent in relative to any specific SFF machine.

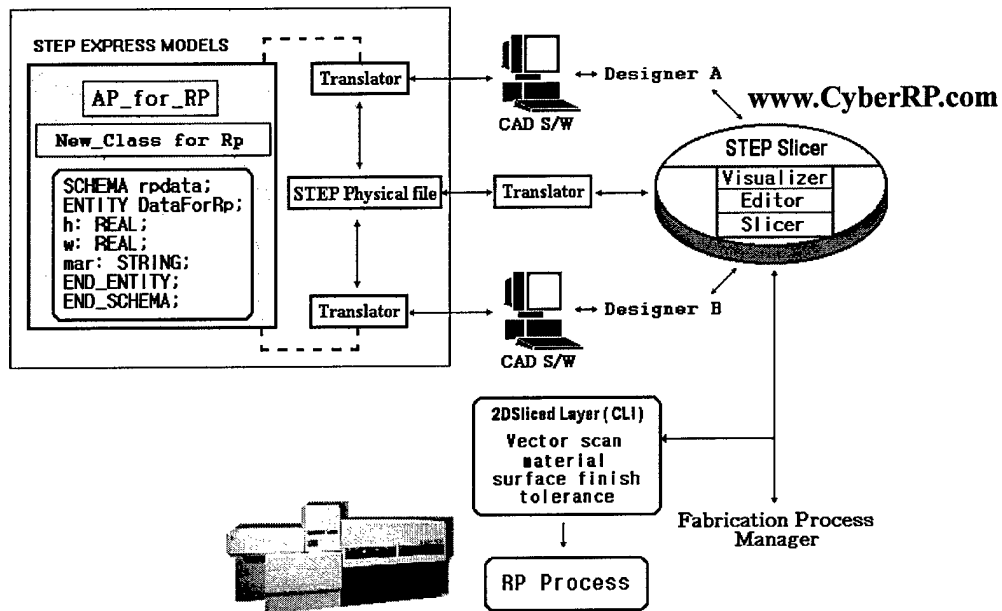


Figure 1. Basic framework for CAD/RP interface using STEP

Since there are many different and distributed SFF machines, these machine-dependent information (called MDI) must be captured by fabricator when the part geometry is translated into appropriate SFF machine process code. In order to do so, CAD softwares must initially assign necessary MDI onto the part geometry before it is translated into AP_SIF for data exchange. Nowadays, there are several different CAD softwares that can create product geometries with different applications. Similarly, most recent SFF processes have quite different capabilities, and most are not even isotropic, so that MDI such as part orientation, position, and size during the fabrication process becomes a crucial issue in integrating a heterogeneous environment of CAD and SFF processes using the data exchange standard. Although all of the SFF processes build one layer at a time, important differences exist among them in the nature of modeling and process planning. One of the most important issues is the layer thickness, which depends on the particular fabrication process. Many SFF processes are executed under a uniform layer thickness and homogeneous material during fabrication so the object geometry is decomposable into uniform sliced layers and, therefore, both the minimum layer thickness and the maximum layer thickness depends on the particular SFF process. In addition, material layer thickness, part orientation, and post process such as curing or unused material removing after the fabrication may also have to be generalized for all possible SFF processes. On the other hand, if the object needs support structures for its layered growth or there are composition variations, a process planning step is necessary to prescribe the orientation of the object and support structure before it is sliced into layers. In this paper, a tentative schema of SFF process features for defining the MDI is proposed as shown in figure 2. This will be compatible with AP_SIF so that they can exchange the information with each other at the time of translation. In the result, the real integration of geometry and the MDI for the fabrication must occur in the stage of 2-D slicing of the geometry (not SIF) after the translation.

As shown in the figure 2, for example, a part name can first be assigned to a part geometry, and the geometry itself can be specified with its dimension, position, orientation, and multiplicity within the physical fabrication space of an SFF process. In the meantime, for practical fabrication, the geometry consists of its own sliced layers (total layer No.) and, similarly, each layer consists of several segments (segment No.). Description of a part geometry will be also compatible with high level design information such as tolerance, surface finish and volume material, and each layer and segment in a part geometry can also be specified with its own SFF process features. Each layer, for example, has its own material index No. different with other layers. Each segment, on the other hand, has its own tolerance depending on its sectional geometry. In addition, depending on each different SFF process, part_support information will be needed in case of SLA process.

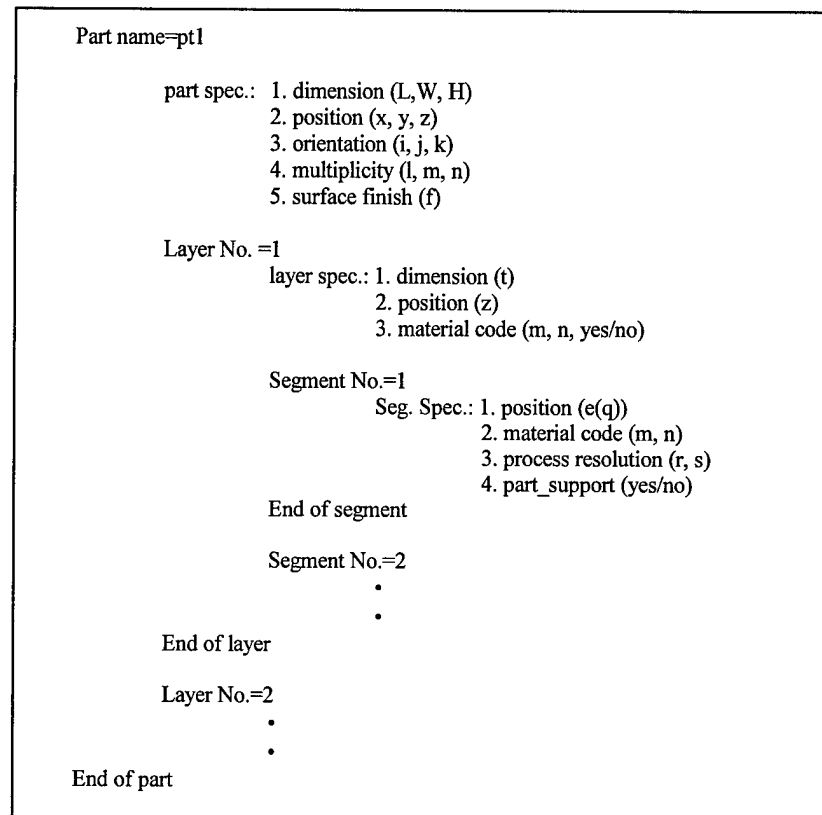


Figure 2. A set of SFF process codes for MDI.

3. SLICING METHOD USING STEP-Slicer

STEP-Slicer is developed using OpenGL in Visual C++6.0 environment supported by ST-Developer Version 7.0, a commercial software product of STEP Tools Inc. The system architecture of STEP-Slicer is shown in figure 3. Its initial version first came out of a simple

visualization module for STEP physical file, which uses AP203 when representing the part geometric data as many previous approaches did. It is now composed of three modules-visualization, editing, and slicing.

Suppose that a designer creates a CAD model using typically existing CAD tools. The geometry from the CAD tool can be converted into a STEP physical file (preferably AP_SIF) using the translator for export. STEP_Slicer then first reads the STEP physical file, generates an intermediate geometric representation, and quickly displays it to users via 3-D visualization. It, as the second module, also enables a users to edit the geometry-add or remove specific portions of the geometry as well as re-define position, orientation, and dimension of the part geometry for part lay-out within the 3D fabrication space. In most cases, not surprisingly, system users are supposed do these works by themselves unless they are original part designer. Many users, as the most important system feature of all, might want to add high level design information, such as minimum layer thickness, material for fabrication, and surface property, to the geometric design. Those high level design information can be also readily exchanged between different designers or fabricators. In fact, the part geometry is supposed to be sliced into a stack of 2-D layers and translated into machine codes for fabrication using the design information carried by itself. STEP_Slicer enables a user to carry out all these works inside the system. Figure 4, 5, 6 show some implementations that STEP files are read, edited, and sliced for SFF processes. Figure 7 shows an example STEP files built upon a mix of faceted boundary representation, cylindrical surface, and B-spline surface.

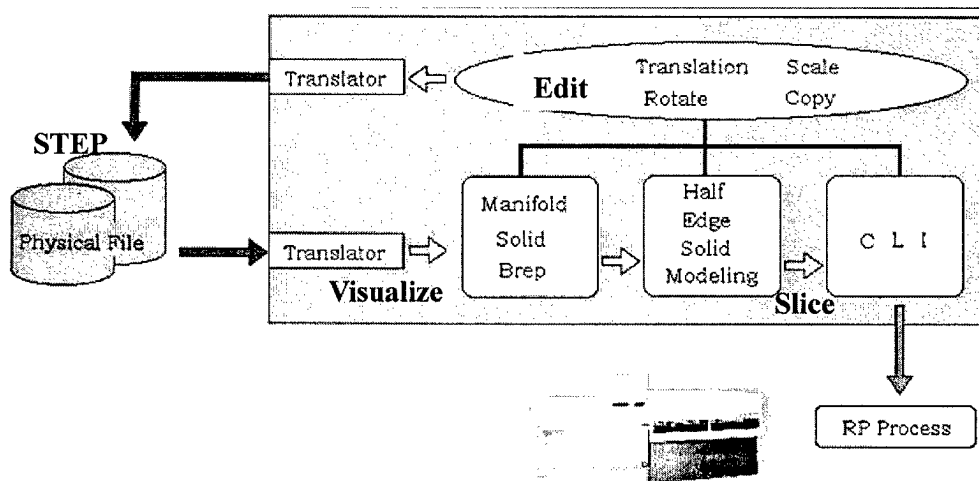


Figure 3. The system configuration of STEP-Slicer

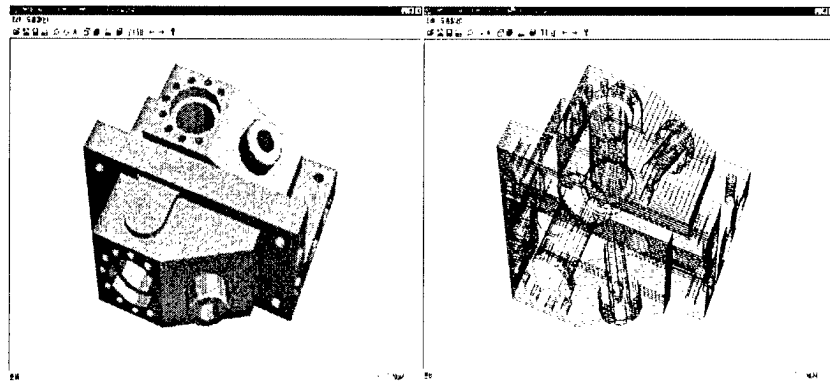


Figure 4. An example of STEP model edition (orientation/ position).

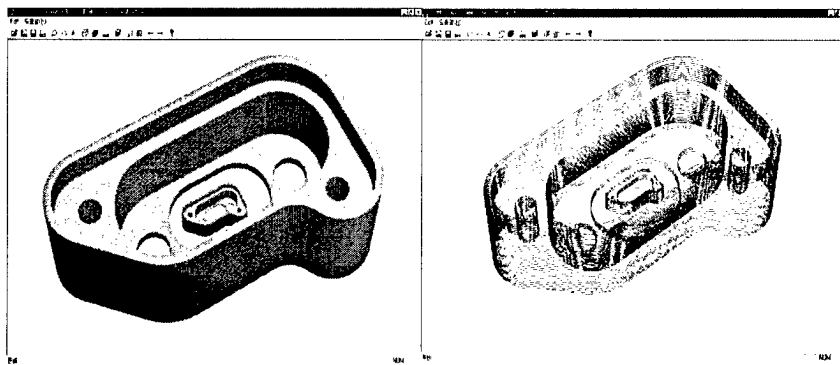


Figure 5. An example of STEP model edition (dimension).

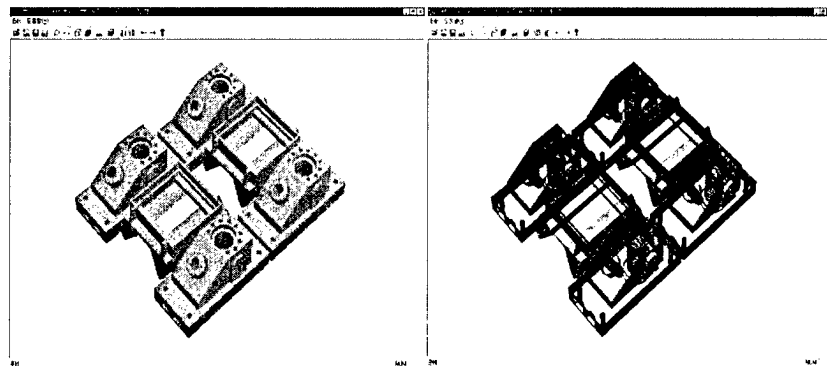


Figure 6. An example of STEP model edition (part layout).

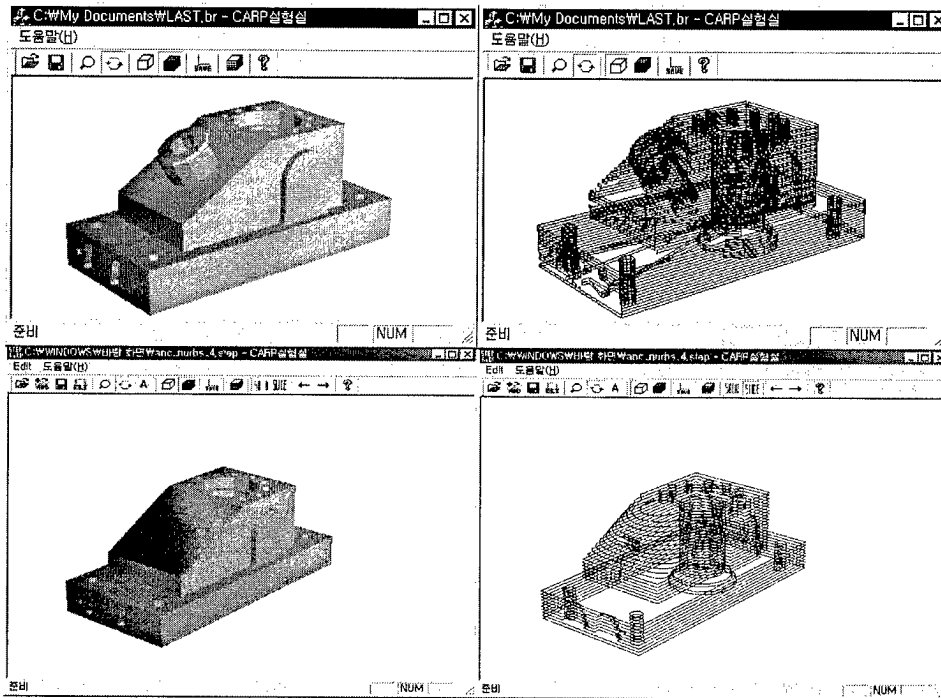


Figure 7. An example of STEP model edition (plane to B-spline surface)

4. CONCLUSION

Solid Freeform Fabrication technologies can create a physical part directly from a computer model. Though STL is current *de facto* industry data exchange standard between CAD models and SFF technologies, it is incomplete in its describing product geometry. STEP is the coming standard. Many major companies are already working with it. This is one of the biggest reason why STEP can be a useful way of exchanging CAD-SFF data. This paper proposes a method of slicing and editing STEP-based RP models for the next generation data transfer paradigm between CAD systems and RP systems using STEP. As the first step for the purpose, this paper propose a basic framework of working model based on STEP with a tentative schema of SFF process features. The new data exchange standard must be compatible with, but independent of, process fabrication features. An implementation of visualizing, editing, and slicing is also proposed based an information for a complete data exchange standard. As for future works, an information model of the schema using a proper modeling language like EXPRESS and AP_SIF, an application protocol for SFF over AP203, will further be developed for the complete new data exchange standard.

5. ACKNOWLEDGEMENTS

This work was supported by grant No. 981-1007-048-2 from the Basic Research program of the KOSEF.

6. REFERENCES

- [1] Crawford, R. H., Solid Freeform Fabrication Technologies and Source of Geometric Data, 3rd SIAM Conference of Geometric Design, Tempo, Arizona, November 1993.
- [2] Suh, Y.S. and Michael J. Wozny, "Adaptive Slicing for Solid Freeform Fabrication Process", SFF Symposium 94, U. of Texas, Austin, August 1994.
- [3] Zollikofer, C.P.E and Marcia S. Ponce de Le, Tools for Rapid Prototyping in the Biosciences, IEEE Computer Graphics and Applications, November 1995.
- [4] Rock, S.J and M.J. Wozny, Generating Topological Information from a Bucket of Facet, Research Doc., Rensselaer Design Research Center, 1992.
- [5] Sheng, X. and R. Meier, Generating Topological Structures for Surface Models, IEEE Computer Graphics and Applications, November 1995.
- [6] Bohn, J.H. and M. Wozny, Automatic CAD Model Repair, 4th IFIP 5.2 Workshop on Geometric Modeling in Computer-Aided Design, RPI, New York, September 1992.
- [7] Turk, Greg, Re-Tiling Polygonal Surfaces, Computer Graphics, Proc. SIGGRAPH, Vol. 26, No. 2, July 1992.
- [8] Schroeder, W.J. et al., Decimation of Triangle Meshes, Computer Graphics, Proc. SIGGRAPH, Vol. 26, No. 2, July 1992.
- [9] Carleberg, C., "Product Model Driven Manufacturing," The SFF Symposium, U. of Texas, 1994, 270-76.
- [10] Gilman, C.R. and Stephen J. Rock, "The Use of STEP to integrate Design and Solid Freeform Fabrication", The SFF Symposium, U. of Texas, 1995. 213-20.
- [11] Pratt, Mike, "The STEP Standard as a Geometry Transfer Medium for SFF", Section 6.11, NSF Workshop on Design Methodologies for Solid Freeform Fabrication, June 5-6, 1995.
- [12] Jee, H. J., Sriram, R.D., and Pratt, M.J., "Workshop Proceedings: STEP-based Solid Interchange Format" November 25, 1996, National Institute of Standards and Technology, 1998 (to be released).
- [13] Jurrens, K.K., "Standards for the Rapid Prototyping Industry", The Future of Rapid Prototyping Internet-based Conference. <http://www.mcb.co.uk/services/conferen/jun98/forp/jurrens.html>, 1988.
- [14] Dutta, D., Kumar, V., Pratt, M.J., and Sriram, R.D. "Towards STEP-based data transfer in layered manufacturing", to appear, Tenth International IFIP WG5.2/5.3 Conference, Prolamat '98, September 9-11, 1988.
- [15] Mak, H., "Minutes for the STEP for Rapid Prototyping meeting in Bad Aibling", ISO TC 184/SC4, June, 1988.

Representation and design of heterogeneous components

Ashok V. Kumar and Aaron Wood

Department of Mechanical Engineering
University of Florida,
Gainesville, FL 32611 USA

Abstract

Recent advances in rapid prototyping techniques enable the fabrication of components whose composition can be controlled and varied in any desired fashion. This presents design engineers with the opportunity and the challenge to design heterogeneous components that optimize some design objective or can provide certain functionality. However, there are no well-established techniques for representing heterogeneous components or design tools to arrive at the appropriate composition distribution. A shape and composition model based on iso-parametric interpolation functions is presented that can be used in conjunction with non-linear programming algorithms to automatically compute optimal composition distribution.

1. Introduction

Limitation of manufacturing processes is one of the reasons why most traditional structural and mechanical components are made of homogeneous materials. Even though in many applications appropriately designed heterogeneous components may be more optimal from a functional point of view, manufacturing considerations have traditionally rendered such designs infeasible. However, with the advent of rapid prototyping or solid freeform fabrication (SFF) processes (Kochan 1993, Ashley 1991) many of the traditional manufacturing constraints are no longer applicable. SFF processes build parts by adding material to the part layer-by-layer. One of the promises of such layered manufacturing methods is that it will be possible to fabricate heterogeneous components or functionally gradient materials for which the material composition within the component can be varied in a desired fashion. While most of the SFF techniques are theoretically capable of composition control within manufactured parts, powder based processes and fused deposition processes appear to be particularly promising. Progress towards composition control of heterogeneous components have been reported recently using SFF processes such as Selective Laser Sintering (SLS) (Jepson et al, 1997), 3D printing (Yoo et al, 1998), Shape Deposition Manufacturing (SDM) (Fessler et al 1997), Direct Light Fabrication (Lewis and Nemme, 1997) and Laser Engineered Net Shaping (LENS) (Griffith et al, 1997) etc. Other specialized processes such as Fused Deposition of Ceramics (Gasdaska et al, 1998) and Direct Metal Deposition (Mazumder et al, 1997) have also been applied to manufacture multi-material components.

Material composition distribution can be thought of as a volumetric property of the solid since it varies within the part and has to be expressed as a function of the spatial coordinates. Most traditional designs do not have volumetric properties and therefore the

need for expressing such properties did not exist. Traditional geometric modeling systems and design tools therefore do not support the ability to model, analyze or design heterogeneous components. Recently, methods for modeling such components have been explored. Kumar V. and Dutta D. (1998) have presented an extension of the traditional solid model representation based on regular sets (r-sets), to define r_m -sets that include material data. They have defined set operations for combining these r_m -sets to define heterogeneous solids. Jackson et al (1998) present an alternate representation where they subdivide a solid model into simpler domains over which composition functions are defined using Bernstein polynomials as basis functions.

In this paper, a representation of material distribution is presented that is based on a finite element mesh generated over the solid or a feasible region. The material composition data at the nodes are interpolated to obtain composition data within each element. The nodal values of composition data can be modified to vary the composition distribution pattern within the solid. In addition, one can also perform finite element analysis using the mesh to determine structural, thermal or dynamic properties of the resultant solid. Finally, by defining the design as an optimization process where material composition at the nodes are treated as the design variables, it is possible to compute the optimal composition distribution that maximize or minimizes the design objective while satisfying the design constraints. Kumar and Gossard (1996) have used a similar representation to model geometry using shape density function.

In section 2, the shape and composition representation is described. Analysis of heterogeneous components using finite element method is described in section 3. A method for designing these components by optimizing the composition distribution is considered in section 4. A few examples are presented in section 5, where the design of a porous component is considered. Finally, conclusions are presented in section 6.

2. Shape and composition representation

Volumetric properties can be expressed as a scalar or vector field defined over the volume of the solid. Therefore, varying density may be defined as a scalar field $\phi = \phi(x, y, z)$, while the directions of anisotropy, fiber orientation of a composite material or material composition of multi-material component may be express as a vector field $\mathbf{v} = \mathbf{v}(x, y, z)$. In order to define such fields, a piece-wise interpolation scheme could be used similar to that used in finite element method. The volume is subdivided into simpler cells (or elements) and the field within each cell is interpolated based on the values at the nodes (see Bathe, 1996 or Carey and Oden, 1981). This requires augmenting boundary representation of solids with a finite element like mesh as well as data on nodal values of the volumetric properties.

In the general case, when the component has 'n' materials, a vector of length n can express the composition at any point. The first n-1 members of the vector represent the volume fraction of the first n-1 materials that make up the composite and the nth member represents the void fraction. For example, if the material is porous so that it is made of one material and void, its composition can be expressed as either the void fraction or the density of the material so that the composition distribution, in this case, can be expressed

using a scalar field. We will illustrate the composition representation, analysis and optimization using this example, where the composition is expressed as a density field $\phi(\mathbf{x})$. Extension to the general case is possible using the methods described here.

Figure 1 illustrates the geometry and composition representation. The inverted L-shaped region shown is the feasible domain within which the geometry is defined. The figure shows contours of the density function corresponding to constant values of densities. The fully dense regions (where $\phi=1$) are shown in white color while the black regions have density equal to zero and are therefore void of material. All other density values are represented using a grayscale color distribution with lighter shades representing higher density than darker shades.

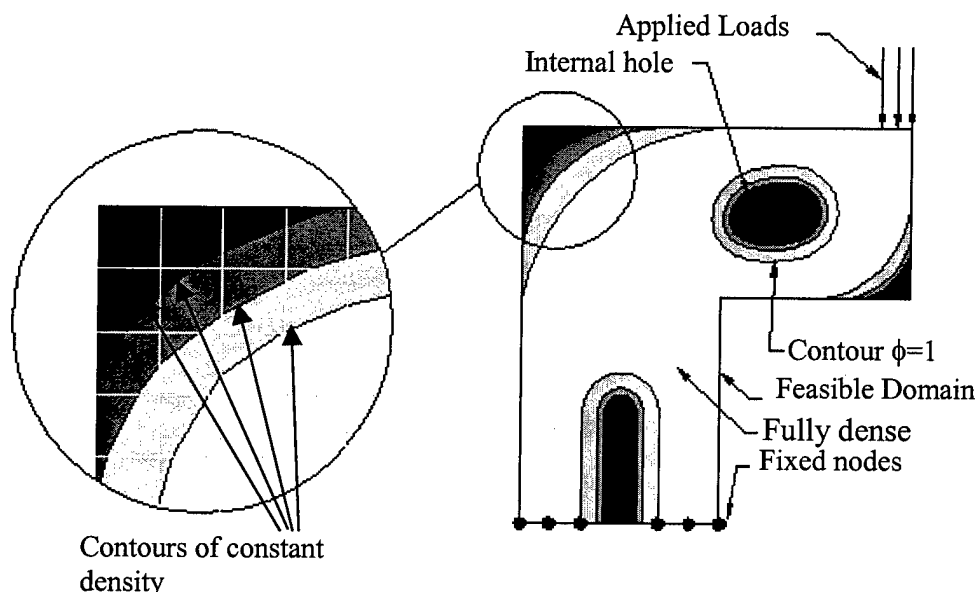


Figure 1: Shape Representation

In order to define the density function within the feasible domain, the domain is divided into a quadrilateral mesh as illustrated in the magnified section of Figure 1 and the nodal values of density are specified. The density function distribution within each element is obtained by interpolating the nodal values. Using four-node quadrilateral elements, the density function within each element can be expressed as,

$$\phi(s, t) = \phi_1 N_1(s, t) + \phi_2 N_2(s, t) + \phi_3 N_3(s, t) + \phi_4 N_4(s, t) \quad (2.1)$$

where, ϕ_i are the nodal density values and $N_i(s, t)$ are the isoparametric shape functions for the four-node quadrilateral element expressed in terms of the parametric coordinates s and t (Bathe, 1996). The shape functions can be expressed as

$$\begin{aligned}
N_1 &= \frac{1}{4}(1+s)(1+t), & N_2 &= \frac{1}{4}(1-s)(1+t); \\
N_3 &= \frac{1}{4}(1-s)(1-t), & N_4 &= \frac{1}{4}(1+s)(1-t)
\end{aligned}
\tag{2.2}$$

For an isoparametric element, the mapping between the parametric space and the real coordinates (x, y) is defined by

$$x = \sum_{i=1}^4 x_i N_i(s, t) \quad \text{and} \quad y = \sum_{i=1}^4 y_i N_i(s, t)
\tag{2.3}$$

The design problem definition consists of specifying the feasible domain, the loads the structure has to carry and the displacement boundary conditions that describe how the structure is supported. In Figure 1, the arrows at the top represent the load supported by the structure. The solid circles represent nodes that are constrained to have zero displacement.

3. Analysis using Finite Element Method

The finite element mesh used to represent the shape and the composition distribution can also be used to perform a finite element analysis to obtain structural and other mechanical properties of the solid. In doing so, firstly, the variation of material properties as a function of composition must be established either experimentally or using appropriate analytical models. In this paper, we assume polynomial material property versus density relation. The real relation depends on the microstructure and may vary if the component is made using different techniques even if the composition is identical.

In constructing the stiffness matrix, we integrate the principle of virtual work, over each element to obtain the element stiffness matrix and then assemble these together to obtain the global stiffness matrix. We have used four-node iso-parametric quadrilateral elements for the analysis. Therefore, the displacements are represented using the same piece-wise bilinear interpolation that was used to represent the composition distribution (equation 2.2) within each element. This representation yields the following strain-displacement relation for the element,

$$\{\epsilon^e\} = [\mathbf{B}] \{u_n^e\}
\tag{3.1}$$

where, $\{u_n^e\}$ is the displacement vector corresponding to the quadrilateral finite element. The governing equations can be expressed in general using the following type of weak form of a variational principal.

$$\int_V \{\delta \mathbf{X}\}^T [\mathbf{B}]^T [\mathbf{D}(\phi)] [\mathbf{B}] \{\mathbf{X}\} dV = \int_S \{\delta \mathbf{X}\}^T \{\mathbf{f}\} dS + \int_V \{\delta \mathbf{X}\}^T \{\mathbf{b}\} dV
\tag{3.2}$$

The above equation represents the weak form applied to an element. V is the volume of the element, S is the surface area of the element that lies on the boundary of the object, $\{\mathbf{f}\}$ is the traction acting on these boundaries and $\{\mathbf{b}\}$ is the body force acting on the

element. The vector $\{X\}$ contains the nodal variables while the $\{\delta X\}$ vector contains the corresponding virtual variables. The $[D(\phi)]$ matrix contains material properties associated with the analysis.

The matrix $[D]$ depends on the material properties and therefore is a function material composition (density in our example). The left-hand side of equation (3.2) needs to be integrated to determine the stiffness matrix. The integration was performed using Gauss quadrature algorithm (Bathe, 1996). In order to determine the correct order of quadrature to use, the degree of the polynomial terms of the $[B]^T[D(\phi)][B]$ matrix must be determined. Since density is a linear function in the parametric coordinates, the terms in the matrix $[B]^T[D][B]$ are polynomials of degree $2+n$ where n is the degree of the polynomial assumed in the material property-composition relation. Gauss quadrature of order m (using $m \times m$ integration points) can integrate a polynomial of degree $2m-1$ accurately. Therefore, if we choose polynomial material property-density relation of degree 4, the terms in $[B]^T[D][B]$ matrix are polynomial of degree 6, which can be integrated using fourth-order Gauss quadrature or 16 integration points.

4. Optimization of composition distribution

Finite element analysis described in the previous section can yield information about the mechanical properties of heterogeneous components. However, from a design perspective one would like to compute the composition distribution that would induce the desired property. For example, one may solve for the optimal density distribution with the objective of minimizing the compliance of the structure subject to a limit on its volume or mass. Minimizing the compliance is the same as maximizing the stiffness of the structure. This is a very common objective function used in structural optimization and has been used extensively in topology optimization research (Bendsoe and Kikuchi, 1988, Kumar and Gossard, 1996). Below we illustrate the process by minimizing compliance of a planar structure. The minimization of compliance may be written as,

$$\text{Minimize } L(u(\phi)) = \int_{\Omega} \mathbf{f} \cdot \mathbf{u}(\phi) d\Omega + \int_{\Gamma_t} \mathbf{t} \cdot \mathbf{u}(\phi) d\Gamma \quad (4.1)$$

subject to,

$$M(\phi) = \int_{\Omega} \phi d\Omega \leq M_0, \quad M_0 = (1 - \alpha)M_i, \quad \text{where } M_i = \int_{\Omega} d\Omega \quad (4.2)$$

$$\int_{\Omega} \{\delta \epsilon\}^T [D(\phi)] \{\epsilon\} d\Omega_0 = L(\delta \mathbf{u}) \quad (4.3)$$

$$0 \leq \phi \leq 1 \quad (4.4)$$

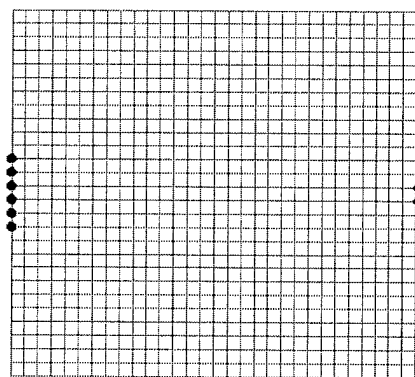
$L(u)$, the mean compliance, is twice the work done by the applied forces (traction \mathbf{t} and body force \mathbf{f}) during the displacement \mathbf{u} . Equation (4.2) describes the constraint that the mass M of the optimal geometry should be less than or equal to M_0 . In order to remove α percentage of mass from the initial mass M_i , we set M_0 to $(1 - \alpha)M_i$. $\{\epsilon\}$ and $\{\delta \epsilon\}$ are the strain and virtual strain in the structure caused by the displacement \mathbf{u} and the virtual displacement $\delta \mathbf{u}$ respectively. $[D(\phi)]$ is the matrix of elasticity constants that relate

stresses and strains for a linear elastic material. We assume that these elasticity constants are functions of the density.

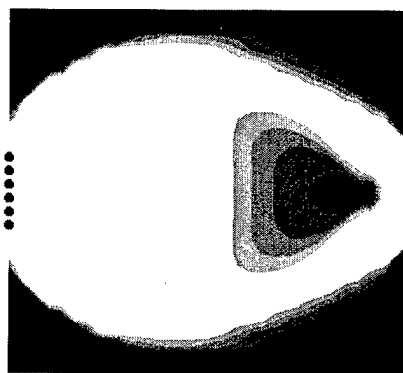
The optimization problem given by the equations (4.1) through (4.4) can be solved using a nonlinear programming algorithm. Each evaluation of the objective function requires a computationally expensive finite element analysis. For this reason, an optimization algorithm that does not require excessive objective function evaluations is desired. Our work uses a variation of sequential linear programming, which is described in Kumar (1993).

5. Examples and Results

Examples of optimizing the density distribution with the objective of minimizing the compliance are presented here. Figure 2 shows a rectangular geometry that is loaded like a cantilever beam so that it can be modeled as a plane stress problem. The rectangle is 10x9 units in dimension and is divided into 810 elements. The nodes on the left marked using solid circles were constrained to have no displacements and two nodes on the right were subjected to loads acting vertically downwards of magnitude 1000 units (shown using solid circles with lines drawn in the direction of the force). The Young's modulus of the fully dense material was assumed to be 3×10^7 units and Poisson's ratio of 0.3. The Young's modulus was assumed to vary linearly with the relative density ϕ . The optimal density distribution is shown in Figure 2 when computed using the constraint that the final mass of the structure should only be 70% of the mass of the fully dense structure.



a) Mesh, Load and Boundary conditions



b) Optimal density distribution

Figure 2: Optimal density distribution for a cantilever

In figure 3, the design of a beam-like structure subjected to three sets of transverse loads is considered. A rectangular geometry, whose dimensions were 300 x 100 units, was divided into a uniform quadrilateral mesh containing 3333 nodes and 3200 elements. Three nodes on the lower two corners were constrained to have zero displacement (shown as solid circles in the figure). Three sets of forces were applied to the lower edge, each set consisting of three point loads (100 units each) applied over three nodes. The

structure was modeled as a plane stress problem. The optimal density distribution that minimizes the compliance was computed subject to the constraint that the final mass of the structure should be only 30% of the mass of the fully dense structure. The Young's modulus, E , of the fully dense material was assumed to be 10,000 units. When it was assumed that Young's modulus varied linearly with relative density ϕ , the result shown in figure 3 (a) was obtained. If the region that is almost black is considered void of material (since the density there is very low) we obtain a structure within which the density is varying gradually from zero to one. However, when a quadratic relation was assumed, we obtained a fully dense (almost homogeneous) structure, as shown in figure 3(b).

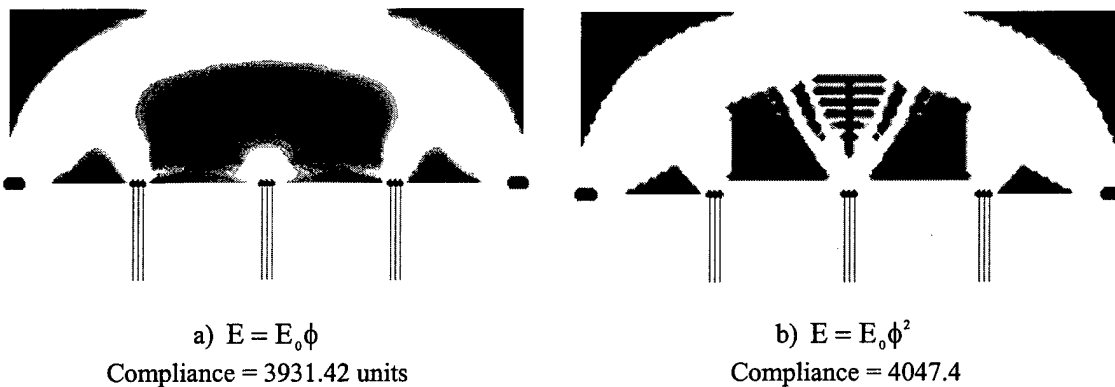


Figure 3: Optimal density distribution for a frame like structure

It is clear that the material property-density relation has a significant influence on the optimal geometry computed. Notice that the heterogeneous design obtained by assuming a linear E vs. ϕ relation has a lower compliance (is more stiff) than the fully dense homogeneous design obtained using a quadratic relation.

6. Conclusion

In this paper, some of the advantages of representing shape and composition distribution using a finite element mesh and its associated interpolation functions are described. Even though only four-node elements were used in this paper, it is possible to use higher order two and three-dimensional elements and their interpolations functions to model arbitrary heterogeneous solids. A material with varying density or void fraction was considered as an example here but future work will focus on using this representation to model multi-material composites. Design of heterogeneous components for other structural and non-structural applications and the associated design objectives and constraints also needs to be studied in the future.

7. Acknowledgements

The authors would like to acknowledge assistance from Mr. Lichao Yu in implementing the finite element analysis software. Partial funding from ONR contract N00014-98-1-0694 is gratefully acknowledged.

8. References

- [1] Ashley, S., 1991, "Rapid Prototyping Systems", Mechanical Engineering, pp. 34-43.
- [2] Bathe K. J., 1996, Finite element Procedures, Prentice Hall.
- [3] Bendsoe, M. P. and Kikuchi, N., 1988, "Generating optimal topologies in structural design using a homogenization method", Computer Methods in Applied Mechanics and Engineering, Vol. 71, pp. 197-224.
- [4] Carey G. F. and Oden J. T., 1981, "Finite elements, An Introduction, vol I and A second course, vol II", Prentice-Hall.
- [5] Fessler J. R., Nickel A. H., Link G. R., Prinz F. B. and Fussell P., 1997, "Functionally Gradient Metallic prototypes through Shape Deposition Manufacturing", Solid Freeform Fabrication Proceedings, Austin, pp. 521-528.
- [6] Gasdaska C, Clancy R. Ortiz M., Jamalabad V., Virkar A., and Popovitch D., 1998, "Functionally optimized Ceramic Structures", Solid Freeform Fabrication Proceedings, Austin, pp. 705-712.
- [7] Griffith M. L., Harwell L. D., Romero J. T., Schlienger E., Atwood C. L., and Smugeresky J. E., 1997, "Multi-material processing by LENS", Solid Freeform Fabrication Proceedings, Austin, pp. 387-394.
- [8] Jackson T. R., Patrikalakis N. M., Sachs E. M., and Cima M. J., "Modeling and designing components with locally controlled composition",
- [9] Jepson, L., Beaman, J. J., Bourell, D. L. and Wood, K. L., 1997, "SLS processing of Functionally Gradient Materials", Proceedings of the Solid Freeform Fabrication symposium, Austin, pp. 67-80.
- [10] Kochan, D., 1993, *Solid Freeform Manufacturing: Advanced Rapid Prototyping*, Manufacturing research and technology, vol. 19, Elsevier.
- [11] Kumar A. V. and Gossard D. C., 1996, "Synthesis Of Optimal Shape And Topology Of Structures", Journal of Mechanical Design, Transactions of the ASME, vol. 118, no. 1, pp. 68.
- [12] Kumar, A. V., 1993, "Shape and Topology Synthesis of Structures using a Sequential Optimization Algorithm", Ph.D. Thesis, Massachusetts Institute of Technology, Cambridge, MA.
- [13] Kumar V. and Dutta D., 1998, "An approach to modeling and representation of heterogeneous objects", Journal of Mechanical Design, Transactions of the ASME, vol. 120, pp. 659-667.
- [14] Lewis G. and Neme R., 1997, "Properties of near-net shape metallic components made by the Direct Light Fabrication process", Solid Freeform Fabrication Proceedings, Austin, pp. 513-520
- [15] Mazumder J., Choi J., Nagarathnam J., Koch J. and Hetzner D., 1997, "Direct Metal Deposition of H13 tool steel for 3.D comonents", Journal of Minerals, vol. 49, no.5, pp. 55-60.
- [16] Yoo, K., Cho, K., Bae, W. S., Chima M. and Suresh S., 1998, "Transformation-toughened Ceramic multi-layers with compositional gradients", Journal of American Ceramic Society, vol. 81, no. 1, pp. 21-32.

Heterogeneous Solids: Possible Representation Schemes

Stephane M. Morvan
smorvan@ces.clemson.edu

Georges M. Fadel
gfadel@ces.clemson.edu

Clemson Research in Engineering Design and Optimization
Dept. of Mechanical Engineering
Clemson University,
Clemson, SC 29634-0921

Abstract

Solid freeform fabrication processes allow parts to be built with accuracy and mechanical integrity, permitting them to be used in tooling or form and fit applications. There is already a need for multi-color parts for surgical applications, which will eventually lead to multi-material RP machines. Whether for on the spot color deposition or for functionally tailored multiple materials parts, RP machines with such capabilities are becoming available. They will eventually lead to the true promise of Solid Freeform Fabrication: a system that can build a functional mechanism without assembly, and from multiple materials. This paper is aimed at understanding the new challenges raised from representing solids whose material distribution is changing gradually from one material to another (HC), and those made of a collection of discrete materials (HD). Several representation schemes are reviewed and critiqued. Techniques borrowed from medical imaging and geoscience modeling are used to better understand the modeling of heterogeneous and gradient solids, from a geometric standpoint.

1 Problem Statement

Current solid modeling technologies model an object using its boundaries, implicitly making the assumption that the interior of the solid is made of a single, homogeneous material. Recent progress in commercial RP solutions [1] will allow parts to be built with localized mechanical properties. Thus, as more efforts are directed towards material optimization techniques [2], [3] there is a need to shift the focus of a solid representation scheme from the geometry to a more abstract attribute-oriented representation scheme. In such a representation, the geometry of an object as it is conventionally known, would become the residual of all the spaces spanned by the attributes under consideration. Example attributes are: thermal properties, mechanical characteristics, electrical conductivity and density.

2 Rapid Prototyping

The enabling technology behind the creation of heterogeneous objects has to be able to output an artifact representing an object designed with a computer. Rapid Prototyping (RP) seems to be the medium of choice in such applications. RP embodies digital designs into physical mockups in a matter of hours. The techniques behind the RP process rely on the ability to add (and/or in some cases remove), material at any arbitrary location in space. There are two general classes of RP processes (even though combinations do exist): additive-based processes and removal-based processes. The distinction between the processes depends on whether the process adds material to reach the final shape of the artifact, or if it removes material from a bulk to reach

that same shape. The following two sections review those two important families of processes. This review is by all means non-exhaustive, and is here only to briefly outline the principles behind them. Further description of RP processes is proposed in [4].

2.1 Additive Processes

Additive processes involve the following or a variation thereof: the object to be manufactured is broken down in layers and the part is built from bottom to top by stacking cross sections of the object. Each layer is manufactured by way of an additive process, one at a time and in a set order, then the object is shifted down to allow the next layer to be added.

Some of the enabling technologies behind additive processes are based on the hardening of a photo-polymer by a laser (SLA) or by ultra-violet floodlights (SGC), or the cutting of an adhesive paper (LOM). Another variation, in powder-based processes, is to sinter a bin of finely grained powder (SLS) [5]. Some processes also rely on a thermoplastic plotting system, akin to an inkjet plotter to deposit the material (FDM, 3Dprinters). Many of those processes require additional support structures to maintain the artifacts' structural integrity throughout the building stage, thus requiring the additional step of part cleanup.

Some RP makers use a color-coded support material whose removal does not risk obliterating a feature from the part. In some other cases, the technological choice of the process prevents from using a secondary material, and the support structures and the part both share the same material, with the exception being that the support structure is attached to the part only temporary by a breakable junction.

2.2 Removal Processes

This class of processes is more on a par with traditional manufacturing technologies. Essentially, it involves milling, grinding or cutting material from a bulk of raw material. Though this technique certainly has more limitations than the additive processes (recessed pockets are one of them), it does provide a valid alternative to obtain mechanical parts with properties and finish that are often unattainable with additive processes.

The bulk material is typically made of a ductile material, which can be cut at a great rate of speed to quicken the process. Example materials are aluminum, steel, Styrofoam and balsa. It is obvious that for manufacturing reasons, the bulk material should be made of a single material, otherwise the rate of cutting will vary from one material to the next, resulting in uneven surfaces, or rips at the interface between the two materials.

3 Solid Modeling Representation Schemes

Traditional mechanical design encompasses several tasks and disciplines. For instance, designing a car's body involves considerations of structural soundness, ergonomics, aerodynamics, vehicle dynamics, aesthetics and after-life disposability. In addition, modern engineering often professes some form of optimality which insures that a designed product responds ideally to a set of constraints, both from the consumers' and from the manufacturer's perspectives.

It is evident that today's design cycles are complex, demanding and expensive, and that the interplay of different disciplines requires rugged tools to assist the designers and to support

collaborative and concurrent work. The widespread use of computers has greatly contributed to reduce the time required to perform the aforementioned activities, leading to a design cycle nearly 100% digital (i.e. performed entirely on computers).

Ideally, the enabling technology behind a digital design cycle is made of tightly integrated software tools revolving around a central application called a CAD (Computer Aided Design) System. Most CAD Systems are mature software products, sometimes resulting from a decade of research or more. Behind all these CAD Systems is the ability to portray a product in a representation allowing the modifications, simulations and variations encountered during the design phase. Since mechanical design has always been concerned with the dimensioning of parts, a natural choice for this representation is based on the geometric features of a product and its dimensions. This is referred to as solid modeling, and the next section will briefly review the representation concepts behind the various modelers found in CAD Systems today.

3.1 Boundary Representation Schemes (B-Rep.)

The B-Rep is a surface boundary representation where solids are defined by a list of their enclosing surface boundaries. This representation originated from the definition of a polyhedra: it is made from polygons, which are made from triangles, which in turn are made from edges and lastly edges are made from vertices. The representation was then further expanded to include arbitrary representations (Beziers patches or NURBS surfaces) for the enclosing surfaces. The surface boundaries are oriented such that given any surface point, the solid interior can be easily determined. For instance, a pyramid with a square base is made of four triangles and a square (Figure 1). This representation is notably good at representing most solids and especially the details embedded in complex shapes, though a known drawback of the B-Rep is the difficulty to verify whether or not a solid is closed or topologically valid.

This difficulty emanates from the task of inferring from the enclosing surfaces (typically surfaces described by two parameters) that a valid, closed 3D entity is defined. A solid is closed when the enclosing boundaries form a closed/fixed volume. A solid is valid if it does not self-intersect. For a more rigorous description of a B-Rep solid topology and its problems, refer to [6].

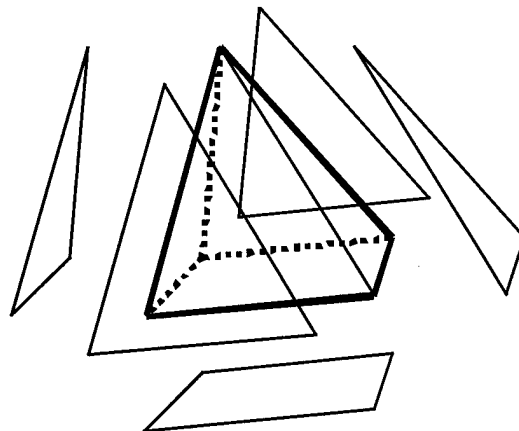


Figure 1: A Boundary Representation for a Pyramid with a Square Base.

3.2 Constructive Solid Geometry (CSG)

The CSG representation [7] defines solids as being made from three-dimensional volumetric primitives (blocks, cylinder, spheres, cones...) associated together using binary operators (intersection, union, subtraction) to form a binary tree (CSG tree) whose end result (the topmost node) is the desired solid. The binary operator requires two arguments to yield a result. A binary tree [8] is defined recursively (up to a sufficient depth) as being constituted by a root node and two binary trees (which in turn are made of two nodes and four binary trees). In the case of a CSG tree, the end leaves are primitive solids and the topmost root node is the desired product, the intermediate nodes being the results of intermediate operations.

Creating complex solids by combining simple primitives is intrinsically appealing when the need to manufacture a product appears, as some operators are homeomorphic to material removal processes: for example, drilling a hole in a block is similar to subtracting a cylinder from that same block.

Inherently, since the operators applied on the primitives are isomorphic, we are generally guaranteed that the resulting solids are both closed and valid. The cost of having a solid defined as being made from other interrelated solids is associated with the complexity required to manage the CSG tree which may need to be entirely recomputed when updates are made to the model. Also, displaying the solid requires it to be converted into simple display primitives such as triangles, a non-trivial operation.

It should be noted that most modern CSG solid modeling packages do rely at some point on a mixed representation of solids (mixed between B-Rep and CSG), as CSG lacks the capability to perform local operations such as fillet, a typical operation in B-Rep based solid modeling packages. Overall, the CSG representation does an excellent job at representing objects, however, as object complexity grows, the traversal of the binary tree becomes increasingly computationally intensive often resulting in long updates for minor changes.

3.3 Set Theory

This mathematical representation principle lies almost entirely in the following consideration: "S is a solid which can be defined as follows, given a boundary B defined by an implicit equation $f(x,y,z) = 0$, $M(x_M, y_M, z_M)$ is a point such that:

- $f(x_M, y_M, z_M) < 0 \Rightarrow$ the point is outside S
- $f(x_M, y_M, z_M) = 0 \Rightarrow$ the point is on the border of S (=B)
- $f(x_M, y_M, z_M) > 0 \Rightarrow$ the point is inside S

The set of all points inside S and on its border defines the solid. Unfortunately, the strict nature of the membership of a point M in the set (it is either in, on or out of the solid) precludes polyphase objects or gas mixtures to be represented accurately. The need to model these objects is now omnipresent: whether it is for the Finite Element analysis of an engine's explosion cycle or for a feature animation film, there is indeed a need to represent objects completely (which then raises the correct definition of an object).

Used initially for manufacturing, this set-based representation for solids has been outgrown by the demands put on it. An example application for this representation is svLis 3.0, a set theoretic based solid modeling kernel [9]. This kernel allows Boolean operations to be performed on solids represented using set theory. Nevertheless, the problem at hand and the advances in modern manufacturing processes are now raising new interest in this representation:

- Ability to have multiple membership for a point (e.g. being part of several materials),
- Allow porous models to be created,
- Allow one (or more) materials to blend gradually
- Allow mechanical/thermal/electrical/... properties to be specified locally

4 Volumetric Representations

4.1 Voxels

Two definitions are commonly found for a voxel, the basic unit of a volumetric representation:

- A voxel, like a pixel, has 0 dimension. Akin to the way that a digital image is represented by an array of pixels, a volumetric dataset is made of voxels laid out on a regular 3D grid. For every voxel in this dataset, a scalar value quantifies the membership of this voxel to a given reference material. Often, such a representation can be termed 'spatial enumeration.'
- A voxel can also be considered to be a cube of small size.

There is no strict definition for a voxel, but we will choose to remain consistent with the definition of a pixel and say that the voxel is a 3D extension of a pixel and thus, has no dimensionality.

4.1.1 Volume Rendering

Thanks to constant increases in the computing power of desktop computers, Volume Rendering, traditionally reserved to medical imaging, is now finding its way in areas such as failure analysis, computational fluid dynamics and meteorology. Though volume rendering [10] merely refers to the act of rendering volumetric data, our primary concern is not with this task, but rather with the underlying representation of the data to be rendered, along with some of the concepts involved in the handling of this data.

Initially, volumetric data was gathered from Magnetic Resonance Imaging (MRI) scanners. These scanners gather data from human organs by measuring the energy received from disrupted atoms as they realign after being subject to an out-of-phase excitation signal. Since tissues of similar composition exhibit similar responses to this out-of-phase, signal consistency is insured in the interpretation of the data. The snapshot of a cross section is developed by using this response as a basis for the computation of the light intensity of the pixels constituting the snapshot. Conceptually, the scanning of the organs is made in all three planes at the same time but a phase shift in the excitation signal (for all three planes) generates a phase shift in the restituting signal, which allows cross section images to be isolated. Without computers, a doctors' attention has to

span several cross sections at a time to correctly interpret the 3D dimensional nature of the organs. Stacking the cross sections in 3D space not only helped minimize errors of interpretation but also provided doctors and surgeons with a 3D image that could be panned, zoomed and rotated to better locate individual details.

The principles of Volume Rendering are similar to those of raytracing: for every pixel on the view plane, a ray of light is cast orthogonal to the view plane and directed toward the objects to be rendered. Each elementary element of volume (termed a voxel) intersecting the ray, is composited (or combined) with other intersecting voxels to provide the final light intensity of the pixel on the view plane. Since this computation is performed repeatedly for every view generated of the volume, a weight can be attributed for voxels of similar absorption to filter out some tissues while emphasizing other. A noteworthy recipient of these techniques is the Visible Human [11], where a man's body was entirely digitized through a similar process, resulting in 1800 cross sections of his body (1000 transverse and coronal MR scans, 1878 transverse scans w/ corresponding photographs).

4.1.2 Voxel Based Representations

Volumetric data sets emanating from human organs are extremely dense, and much of the voxels forming the volume are non-empty. Thus there is little incentive to design space efficient data-structures. The main efforts made to improve the storage of volumetric datasets are aimed at improving the speed of volume rendering algorithms by preprocessing the voxels [12], [13] and skipping empty cells [14]. The use of voxels to represent matter raises an interesting issue when it comes to render the outer surfaces of objects. These surfaces exhibit a shape that is often inappropriately captured by voxels. Nevertheless, these surfaces are rendered as if they were described by a conventional polygonal mesh using a normal estimation algorithm and an interpolation kernel [15]. The improvement over 'naïve' volume rendering is certainly significant, but interpolating the surfaces makes it difficult to use this technique for solid modeling where surfaces are often designed with strict tolerances.

Additionally, since the voxels are a sampling of physical data, the storage requirements for those sets are severe: a model containing a grid made from 512 arrays of 512x512 voxels uses at the very least 128 M-byte of memory (for 1 bit encoding). The data set is usually very large and thus not easily held in main memory without using some form of virtual memory. Another application of a voxel based modeling scheme for solids is also presented in [16], where the aim is to see how a voxel-based modeling fits within an RP enabled manufacturing environment.

It should be noted that the use of voxels for solid modeling does greatly simplify CSG operations on solids [14]: Boolean operations performed on solids are reduced to plain voxel to voxel operations whose outcomes are extremely simple to compute. For instance, an empty voxel intersecting a full voxel is an empty voxel, an empty voxel 'union' a full voxel is a full voxel.

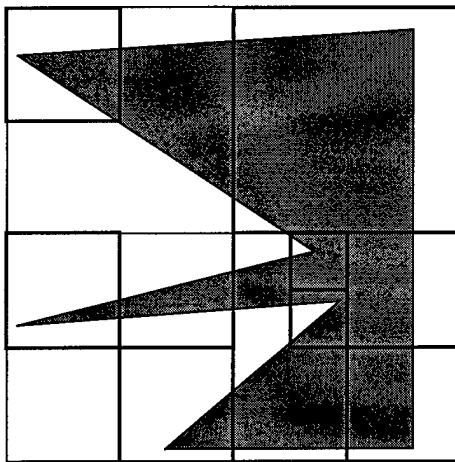
4.1.3 Octrees

Samet [17] proposed to use a hierarchical space-partitioning scheme in order to store volumetric data, specifically the Octree. The principles of an octree are simple: to recursively subdivide a cube into 8 smaller cells $1/8^{\text{th}}$ the size of the original cube, until either the cube is

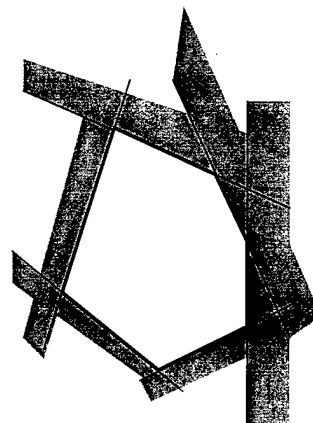
empty or its content is below a set threshold size. Ayala *et al.* [18] then proposed to perform Boolean operations and rigid body motions on octrees. Although the octree encoding has an interesting potential, it is in the termination criteria of the decomposition sequence that the complexity lies. Some example termination criteria, for 3D polyhedra, are:

- A single vertex in the cell,
- A single edge in the cell,
- A single face contained in the cell,
- Several faces sharing the same edge in the cell (which may or may not be in the cell, Fig. 3a).

In the case of its 2D counterpart, the quadtree, it is demonstrated that regardless of the termination criteria used, the number of cells is proportional to the perimeter of the object to be decomposed and to the resolution of the decomposition ([17], Chapter 1). Thus, for complex closed hollow 2D polygons, a quadtree decomposition can yield a large number of cells, which restricts its use.



3a. Sample Termination Criteria for QuadTree
(single edge sharing the same vertex)



3b. Cell Tree Decomposition of a Convex
Polygon

Figure 3a-3b: Sample Termination Criteria for Quadtree & Cell Tree Decomposition

A solid modeling application using an octree based representation scheme is presented in [19]. In this application the termination criteria of the decomposition is to have a single face contained within each cell. Once again, a noteworthy benefit from this volume based decomposition is the simplicity of Boolean operations on solids: though these are slightly more complicated than the operations performed on voxels (cells of different sizes may require additional treatment), their outcome is easily predicted. Equally important, rigid body transformations (rotations, scaling and translations in 3D) are also described without directly applying a transformation matrix to the coordinates of the vertices of the objects and decomposing it (the operation is performed directly on the octree).

4.1.4 The Cell Tree

The Cell Tree [20] is an encoding for general polyhedral point sets of arbitrary dimensions (bounded or unbounded). This encoding represents a polyhedral by the algebraic sum of simpler, convex polyhedra (holes are 'subtracted'). Each convex polyhedral chain is described by the intersection of halfspaces and represented in a vector (Fig. 3b). A halfspace partitions an n -dimensional space in halves, and is a hyperplane of dimension $n-1$. The representation is assumed to be minimal: a halfspace not intersecting any other halfspace (e.g. empty intersection) is removed from the vector. Also, since the description is minimal, a halfspace is a boundary of the convex polyhedral it is describing. To further normalize this representation, the halfspaces used in the description of a polyhedral are listed in a single location. A convex polyhedral is then represented using a list of 1s, -1s and 0s referring to whether or not this polyhedral is respectively using a given halfspace, its opposite or not using it.

Performing Boolean operations on polyhedra is then a slightly more complicated matter than with the previous representation schemes, though it does not necessitate elaborated algorithms. The union of two polyhedra involves merging the two databases of halfspaces and adding more convex polyhedra to the chain. Subtracting a polyhedral is a similar task, since the description allows unbounded polyhedra, the complementary of the polyhedral to be subtracted is created by negating the list of vectors it uses, and then added to the convex polyhedra chain.

It is interesting to note that this representation offers some features that other representation do not: in the case of 3D polyhedra, there is no need to evaluate the vertices or the edges, strictly speaking, the entire shape is represented using only planes. However, a very stringent requirement in this representation is that every 3D solids must have a convex decomposition.

4.1.5 Geoscience Modeling

Geoscience modeling shares some similitude with mechanical CAD, especially in the area of domain (2D or 3D) representation: 2D geographic domains can be represented by way of polygons, and a 3D hill can be represented with a set of 2D elevation maps. The added dimension of attributes such as soil composition, humidity and erosion tends to make this modeling certainly very relevant for the problem at hand. The critical aspects relevant to us in geoscience modeling [21] are those of uncertainty and fuzziness of the boundaries of the objects described.

According to [22] there are two main geographic data models used: the exact model and the continuous field model (Figure 4a-4b resp.). The exact model is made of adjoining polygons tagged with a number of attributes representing a region with set properties (such as soil composition, pollution...). Conversely, the continuous field model, instead of attaching the attributes to a topology, assumes that each attribute is a continuous and smooth varying function over space. In practice, the function is often discretized on a regularly spaced grid and the overlay of all the grids should provide a meaning similar to the one of the exact object model (with the exception of the boundaries). Note that [23] retained an approach resembling the exact field model in his treatment of multiple material solids.

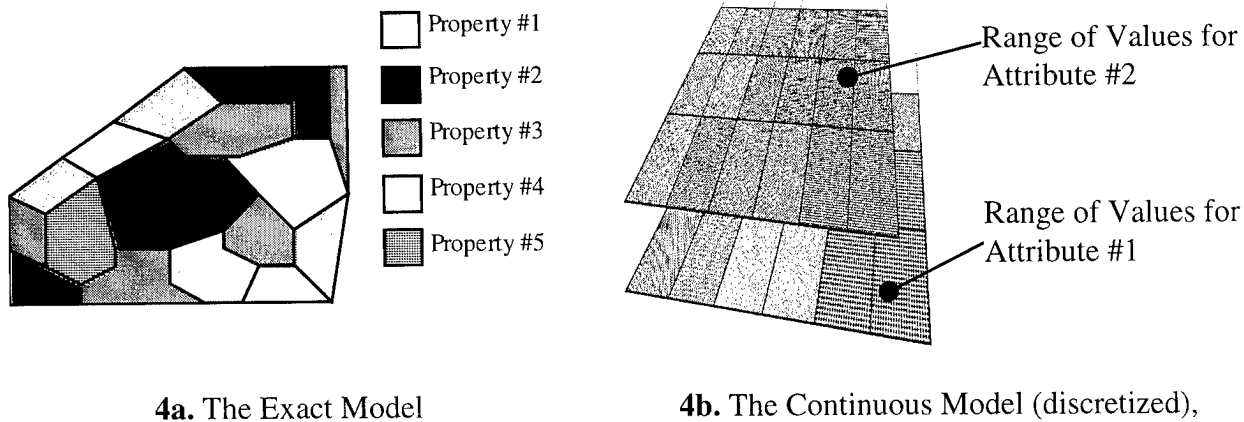


Figure 4a-4b. Geographic Data Models

Strictly speaking, heterogeneous solids do not have any uncertainties associated with their boundary definition. Evidently, the designer of a part knows exactly where a material is and where it isn't. It is interesting to observe how for example a soil boundary is modeled and how the change of a soil (which is often gradual) is treated in terms of fuzziness of the set (the uncertainty, due to measurement errors, is not relevant here). For soils, the "core" region is defined as the region that attains maximal membership in a given attribute, while the boundary is defined as the region attaining between 0 and the maximal membership (the latter interval being open on both ends). The use of fuzzy logic to model the boundary is proposed [24] and a similar approach, pertaining to a gradual change between two materials is certainly an interesting issue. A more elaborate discussion to differentiate a 'Boolean region' from a 'fuzzy region' is presented in [22]. The discussion illustrates why the problem of point membership in a region can not always be a true or false answer in terrain modeling.

5 Heterogeneous Objects Approach at the University of Michigan

Initially, the University of Michigan's efforts were aimed at a theoretical approach to representing heterogeneous solids, [23], [25], [26]. The representation of a solid made from n materials was viewed as an application from the geometrical space to the primary material space [23]. In this context, an n -dimensional vector is associated to every triple (x, y, z) within the solid under consideration. This n -dimensional vector represents the material composition as a combination of the primary materials, such that the sum of all the individual components equals to one. Regularized set operations are then defined on these solids. Furthermore, in another work several blending functions between primary materials are extracted from the literature [28]. Note that no detailed representation structure of the data is proposed to date

It is only recently [27], with the use of a DMD (Direct Material Deposition) apparatus that the attention has shifted to the entire design process: from design to manufacturing while including design homogenization to obtain the ideal microstructure pattern distribution. The material is considered at the microstructure level, which evidently translates into large amounts of data and many variables to consider during the optimization stage. This representation lacks the ability to group together a large number of similar microstructures to reduce the amount of data needed.

6 Conclusion

Several representation schemes have been reviewed. As expected, there is a need to combine the features of traditional mechanical representations with the features of volumetric representations. There is no perfect solution in any of the prevalent representation schemes, and effort must target either the development of novel schemes or the combination of available representations. Furthermore, once the problem of material representation is resolved, these same principles can be applied to other types of attributes such as electrical conductivity or thermal resistance. This will allow heterogeneous solids to be completely and entirely represented.

7 References

- [1]. Swann T.A., Keicher D.M., and Miller W.D. "Laser Engineered Net Shaping (LENSTTM) Technology Commercialization." *Rapid Prototyping and Manufacturing '98*, Dearborn, MI.
- [2]. König O. (1999). "Application of Genetic Algorithms in the Design of Multimaterial Structures Manufactured in Rapid Prototyping," Diploma Thesis, ETH Zurich, Zurich, Switzerland.
- [3]. Huang J., and Fadel G.M. (1999). "Heterogeneous Flywheel Modeling & Optimization." *Journal of Materials & Design*(Special Issue: Rapid Prototyping and Manufacturing).
- [4]. Jacobs P.F. (1996). *Stereolithography and other RP&M Technologies*, ASME Press.
- [5]. Deckard C.R. (1988). "Selective Laser Sintering," Ph.D., University of Texas, Austin, TX.
- [6]. Hoffmann C. M. (1989). *Geometric and Solid Modeling, An Introduction*, Morgan Kaufmann Publisher Inc., San Mateo.
- [7]. Requicha A. A. G., and Voelcker H. B. (1983). "Solid Modeling: Current Status and Research Directions." *IEEE Computer Graphics Applications*(October 1983), 25-37.
- [8]. Wood D. (1993). *Data Structures, Algorithms, and Performance*, Addison-Wesley, New York.
- [9]. Bowyer A., Bayliss G., Berchtold J., Eisenthal D., Martin R., Parry-Barwick S., Pidcock D., Taylor R., Voiculescu I., Wallis A., and Wise K. (1999). "svLis 3.0 - The SvLis Set-theoretic Kernel Geometric Modeller Version 3.0." http://www.bath.ac.uk/~ensab/G_mod/Svlis/.
- [10]. Sabella P. (1988). "A Rendering Algorithm for Visualizing 3D Scalar Fields." *Computer Graphics*, 22(August 1988), 51-59.
- [11]. Various authors. (1996). *The Visible Human Project Conference Proceedings*, National Institutes of Health, William H. Natcher Conference Center, Bethesda, Maryland USA.
- [12]. Freund J., and Sloan K. "Accelerated Volume Rendering Using Homogeneous Region Encoding." *IEEE Visualization*, 191-197.
- [13]. Mueller K., and Yagel R. (1996). "Fast Perspective Volume Rendering with Splatting by Utilizing a Ray-Driven Approach." *IEEE Computer Graphics and Applications*(July 1996), 65-72.
- [14]. Shareef N., and Yagel R. "Rapid Previewing via Volume-Based Solid Modeling." *Third Symposium on Solid Modeling and Applications*, Salt Lake City, 281-291.
- [15]. Möller T., Machiraju R., Mueller K., and Yagel R. "A Comparison of Normal Estimation Schemes." *IEEE Visualization*, 19-26.

- [16]. Chandru V., Manohar S., and Prakash C.E. (1995). "Voxel-Based Modeling for Layered Manufacturing." *IEEE Computer Graphics and Applications*(November 1995), 42-47.
- [17]. Samet H. (1989). *The Design and Analysis of Spatial Data Structures*, Addison-Wesley.
- [18]. Ayala D., Brunet P., Juan R., and Navazo I. (1985). "Object Representation by Means of Nonminimal Division Quadrees and Octrees." *ACM Transactions on Graphics*, 4(1), 41-59.
- [19]. Meagher D. (1982). "Geometric Modeling Using Octree Encoding." *Computer Graphics and Image Processing*, 19, 129-147.
- [20]. Günther O. (1988). *Efficient Structures for Geometric Data Management*, Springer-Verlag.
- [21]. Burrough P.A., and Frank A.U. (1996). *Geographic Objects with Indeterminate Boundaries*, Taylor & Francis.
- [22]. Fisher P. (1996). "Boolean and Fuzzy Region." *Geographic Objects with Indeterminate Boundaries*, Burrough P. A. and Frank A. U., eds., Taylor & Francis, 87-94.
- [23]. Kumar V., and Dutta D. "An Approach to Modeling Multi-Material Objects." *Third Symposium on Solid Modeling and Applications*, Atlanta, GA, 336-343.
- [24]. Usery E. L. (1996). "A Conceptual Framework and Fuzzy Set Implementation for Geographic Features." *Geographic Objects with Indeterminate Boundaries*, Burrough P.A. and Frank A.U., eds., Taylor & Francis, 71-85.
- [25]. Kumar V., and Dutta D. "Solid Model Creation for Materially Graded Objects." *Symposium on Solid Freeform Fabrication*, 613-620.
- [26]. Kumar V., Burns D., Dutta D., and Hoffman C. (1998). "A Framework for Object Modeling." *UM-MEAM-98-07*, CAD/CAM Group, Ann Arbor.
- [27]. Dutta D., Ghosh A.K., Kikuchi N., and Mazumder J. "Design, Representation and Fabrication of Designed Materials." *ASME Energy Sources Technology Conference*, Houston, TX.
- [28]. Bhashyam S., Shin K. H., and Dutta D., "An Integrated CAD System for Design of Heterogeneous Objects." *UM-MEAM-99-08*, CAD/CAM Group, Ann Arbor.

Functionally Gradient Material Design and Modeling Using Hypertexture for Solid Freeform Fabrication

Seok-Min Park, Richard H. Crawford, and Joseph J. Beaman

Laboratory for Freeform Fabrication
The University of Texas at Austin

Abstract

SFF technologies have the potential to become manufacturing process that are capable of producing parts that have not been feasible by other techniques. The fabrication of Functionally Gradient Material (FGM) is one of the possible candidate. It is critical to provide three dimensional material gradient data in the solid model to fabricate FGM. The approach is to model spatially varying material density distribution on implicit solid geometry using a hypertexturing scheme and a procedural volumetric modeling. It is essentially an extension of procedural solid texture synthesis, which has been effectively used to model cloud, gas, and flow stream. It will save the amount of information storage especially when the gradient pattern is repeating. Geometric operation becomes convenient since the material data are linked to the geometry only by the reference surfaces.

1 Introduction

SFF technologies have the potential to become manufacturing process that are capable of producing parts that have not been feasible by other techniques. The fabrication of Functionally Gradient Material (FGM) is one of the possible candidates. An FGM is a non-homogeneous solid which exhibits spatially varying volume fractions of the constituents. It has its micro-elements systematically and continuously distributed and controlled so as to provide functionality suited to the intended service environment. Layer based manufacturing becomes a natural choice when material distribution inside a part varies continuously in three dimensions. To accomplish the fabrication of FGMs, SFF processes must be supported by advanced software. The SFF community is currently experiencing a growing need for including additional information, such as material distributions in the solid model.

For fabricating FGMs, it is critical to provide three dimensional material gradient data in the solid model. The material data should be able to exist in discrete, gradient, or mixed form. Predetermined spatial distribution data must easily be represented in the data format. The modeling tool should support procedural modification of the distribution interactively.

2 Approach

2.1 Hypertexturing

I used a hypertexture scheme to model spatially varying material density distributions. Hypertexture is a technique which is intermediate between shape and texture by using space-filling

applicative functions to modulate density. The model is essentially an extension of procedural solid texture synthesis that is well known in computer graphics, but evaluated throughout a volumetric region using a Density Modulation Function (DMF) [4].

In hypertexture, a continuous characteristic function which is a mapping from $f : R^3 \rightarrow [0, \dots, 1]$ is defined for the solid geometry. All points \vec{x} for which $f(\vec{x})$ is zero are said to be outside the object. All points \vec{x} for which $f(\vec{x})$ is one are said to be strictly inside the object. Finally, all points for which $0 < f(\vec{x}) < 1$ are said to be in the object's fuzzy region. This formulation gives the object surface an appreciable thickness. Finally, the fuzzy shape and the solid become unified once solid texture functions are combined with the function that describes the object's fuzzy region [4].

Procedural texturing or modeling methods can be categorized into two types: explicit and implicit methods. In implicit methods, a texture pattern is defined as a function f of points in the texture space, and the pattern consists of a level set of f , that is, the set of all points at which the function has a particular value. Since implicit models tend to be continuous throughout a region of the modeling space, they are appropriate for continuous density and flow phenomena such as clouds and fog [4]. Thus, the implicit scheme will be chosen to model the material gradient because of their ease of specification and smoothly blending density distributions. The implicit density functions are best defined by summed, weighted, parameterized, primitive implicit surfaces [4].

2.2 Implicit Surfaces

Algebraic implicit formulation was used as a representation scheme for both solid and sliced geometries. Implicit surfaces for solid geometry are two-dimensional, geometric shapes that exist in three dimensional space; they are defined according to a particular mathematical form. Intuitively, an implicit surface consists of those points in three dimensional space that satisfy some particular requirement. The requirement is represented mathematically by a function, generically named f , whose argument is a point \vec{p} . By definition, if $f(\vec{p}) = 0$, then \vec{p} is on the surface. The function f does not explicitly describe the surface, but implies its existence [1].

Compared to parametric surfaces, implicit surfaces are receiving increased attention especially with respect to their accurate yet compact depiction of solid objects and their innate blending properties. That is, implicit surface functions naturally describe the interior of an object, whereas a parametric description of an object usually consists of piecewise surface patches and requires additional information for the interior. Geometric queries, such as point classification to determine whether a point is inside, outside, or on the surface, are simpler with implicit surfaces than with parametric surfaces. The ability to enclose volume and to represent blends of volumes endows implicit surfaces with inherent advantages in geometric design and the corresponding fabrication.

The union of two algebraic surfaces, unlike the union of two solid models, is usually given by the product of the corresponding algebraic functions. Intuitively, if f is zero, then any multiple of f , including multiplication by another function, is zero. It is called the closure property. Unfortunately, the multiplication $f_1 f_2$ confuses the sense of inside and outside. That is, points that are within both spheres as well as points that are beyond both spheres evaluate positively; only points within one and only one sphere evaluate negatively.

Solid modeling emphasizes operations on volumes rather than on surfaces. Accordingly, it typically defines the union of objects f_1 and f_2 by $\min(f_1, f_2)$. Intuitively, if a point is

within any sphere it evaluates negatively, regardless of the number of surrounding sphere. Conversely, $\max(f_1, f_2)$ evaluates positively if a point is outside any sphere, thus representing the intersection of the volumes.

Analytic expressions approximating union and intersection are given as;

$$\begin{aligned} \text{union}_a(f_1, \dots, f_n) &= (f_1^{-a} + \dots + f_n^{-a})^{-\frac{1}{a}} \\ \text{intersect}_a(f_1, \dots, f_n) &= (f_1^a + \dots + f_n^a)^{\frac{1}{a}} \end{aligned}$$

where $a > 0$, $\lim_{a \rightarrow \infty} \text{union}_a(f_1, \dots, f_n) = \min$, and $\lim_{a \rightarrow \infty} \text{intersect}_a(f_1, \dots, f_n) = \max$.

2.3 Density Modulation Functions (DMF)

The geometric gradient information is determined and controlled interactively by a DMF, which is used to modulate an object's density within its material space. It consists of the several procedural functions such as bias, gain, and noise functions which are the base level functions that higher order DMFs are built upon. These functions are used to control some aspect of an object's spatial characteristics. The following briefly introduces these functions.

The bias function, is mainly used to either push up or pull down an object's density around the middle of the fuzzy region. The bias function is typically defined by $t^{\frac{\ln(b)}{\ln(0.5)}}$. The values at three points are fixed such that, $\text{bias}(0) = 0$, $\text{bias}(0.5) = b$ and $\text{bias}(1) = 1$. By decreasing or increasing b , the values in an object's fuzzy region can be biased up or down smoothly [12].

The gain function can be effectively used as an intuitive method to control whether a function spends most of its time near its middle range, or, conversely, near its extremes. As a result, the density distribution can be tweaked to be either flatter or steeper across the fuzzy region. The gain function over the unit interval, for example, can be defined as follows.

$$\begin{aligned} \text{gain}(0) &= 0 \\ \text{gain}(0.25) &= 0.5 - \frac{g}{2} \\ \text{gain}(0.75) &= 0.5 + \frac{g}{2} \\ \text{gain}(1) &= 1 \end{aligned}$$

By controlling the value of g , the rate at which the midrange of an object's fuzzy region goes from 0 to 1, can be increased or decreased [12].

In case that the material information is supplied in a discrete data form, for example, directly from FEM analysis, a polynomial interpolation can be exploited to interconnect the data points in a mathematical form for DMF. For graded compositions, analytic functions must be defined, capable of representing smooth variation over the domain of material subspace. There exists a number of effective polynomial bases for interpolation. One of the most popular bases is the *Bernstein-Bézier* basis. The basic formulations are as follows.

$$\begin{aligned} \text{Tensor} : P(x, y, z) &= \sum_{i=0}^m \sum_{j=0}^n \sum_{k=0}^p W_{ijk} B_i^m(x) B_j^n(y) B_k^p(z) \\ \text{Barycentric} : P(x, y, z) &= \sum_{i=0}^m \sum_{j=0}^{m-i} \sum_{k=0}^{m-i-j} W_{ijk} B_{ijk}^m(x, y, z) \end{aligned}$$

$$B_{ijk}^m(x, y, z) = \binom{m}{ijk} x^i y^j z^k (1 - x - y - z)^{m-i-j-k}$$

The composition at a point can be considered as a blend of the control compositions with their influence determined by the value of their basis functions, analogous to the surface reconstruction with a mesh of control points.

In order to represent objects made of multiple materials using hypertexture, the mathematical space must be modified. The space for the model must now include material subsets apart from the global spatial dimensions that captured the geometry and topology of the object. The material subset also needs to provide its own space for geometry and topology because the hypersurfaces should be in primitive volume and it is convenient to separate homogeneous regions and heterogeneous regions.

3 Results and Discussion

3.1 Discrete Point Data Set

I used a 64 equally spaced discrete point data set in three dimension for demonstration. This data set was scanned into the program to create an implicit polynomial form of continuous DMF by tensor product of trivariate *Bernstein-Bézier* interpolation. It was first mapped onto the pre-determined material subspace domain which contains the graded portion of the secondary material only. If discontinuous or isolated material distribution is needed, more material subspace would be created. One of the surface of the material subspace was mapped onto the surface of the geometry with the prescribed depth. Figure 1 shows an example of material gradient representation on a simple cube and its cross section in z direction.

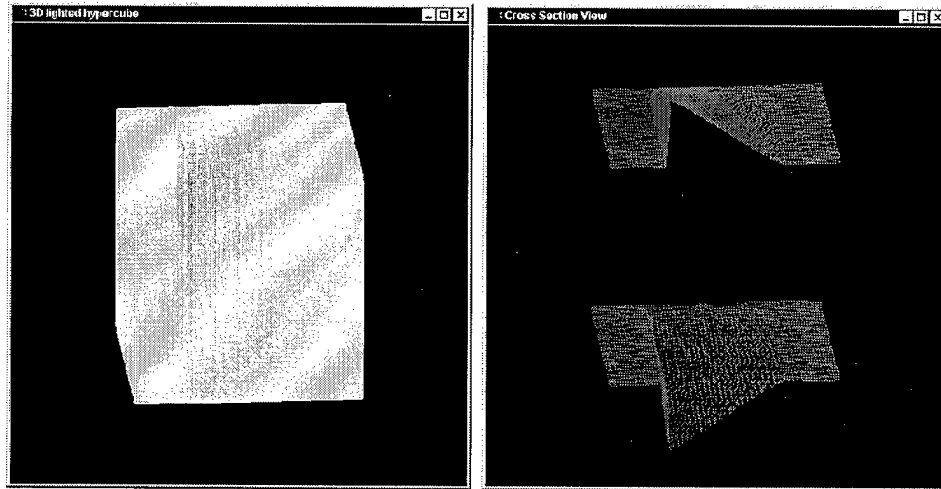


Figure 1: Trivariate *Bernstein-Bézier* interpolation

3.2 Pattern Sketching

When gradient information is based on iterative experiments, designers need to sketch and modify the gradient pattern in the solid model in accordance with the experimental results.

I used the cascaded form of the Bias and Gain functions, which are controlled only by Bias Coefficient, b and Gain Factor, g . The mapping on the material subspace and the solid geometry followed the same procedure as the discrete data set representation. The sketched material gradients with different Bias Coefficient and Gain Factor, are shown in Figure 2

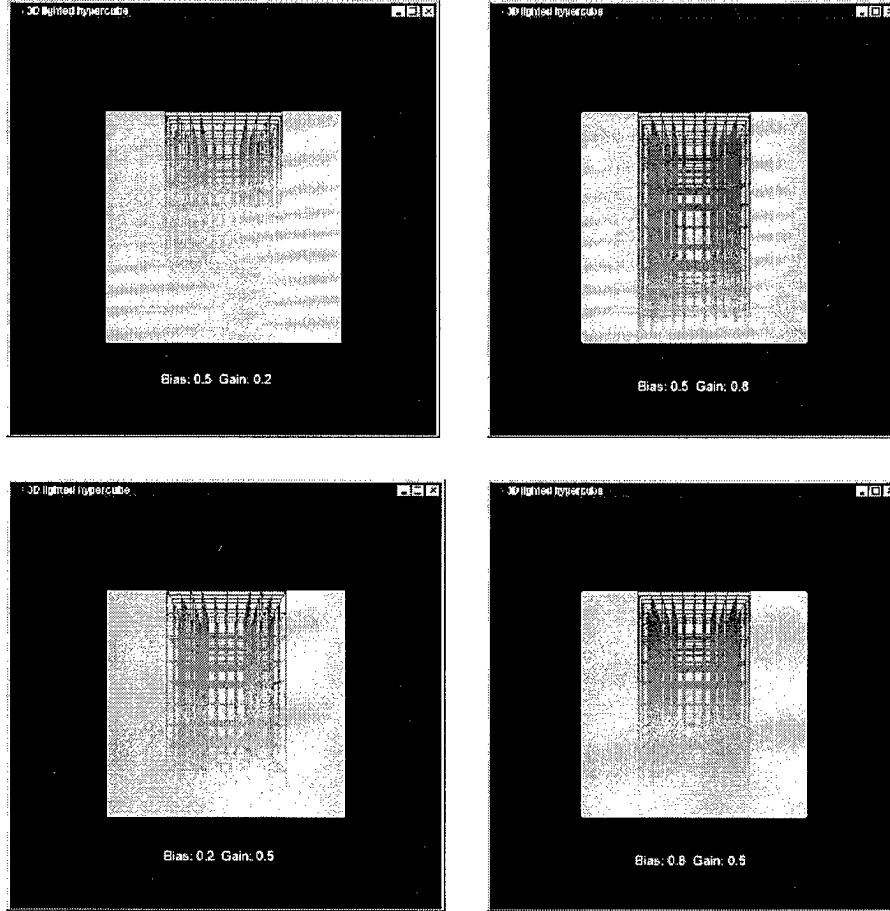


Figure 2: Material Gradient by Bias and Gain Functions

3.3 Applications

The first application chosen for demonstration, is the Wiffle Cube, a rounded cube with a sphere removed. It is defined by $1 - (a^2x^2 + a^2y^2 + a^2z^2)^{-6} - (b^8x^8 + b^8y^8 + b^8z^8)^6 = 0$, with $a = 0.43$ and $b = 0.5$. A sharply edged wedge occurs along each circular opening of the cuboid. As shown in Figure 3, this implicit surface was first polygonized and rendered using the polygonization scheme and the surface normal of each polygon.

The Bias and Gain functions were applied on the material subspace of the spherical coordinates with given range of radius. The highest density at the inner surface of the spherical shell and zero density at the outer surface. Figure 4 shows the material gradient representation and its sliced geometry that were mapped onto the center of the Wiffle Cube. Since both geometry and material data are formulated in implicit algebraic form, they retain the clo-

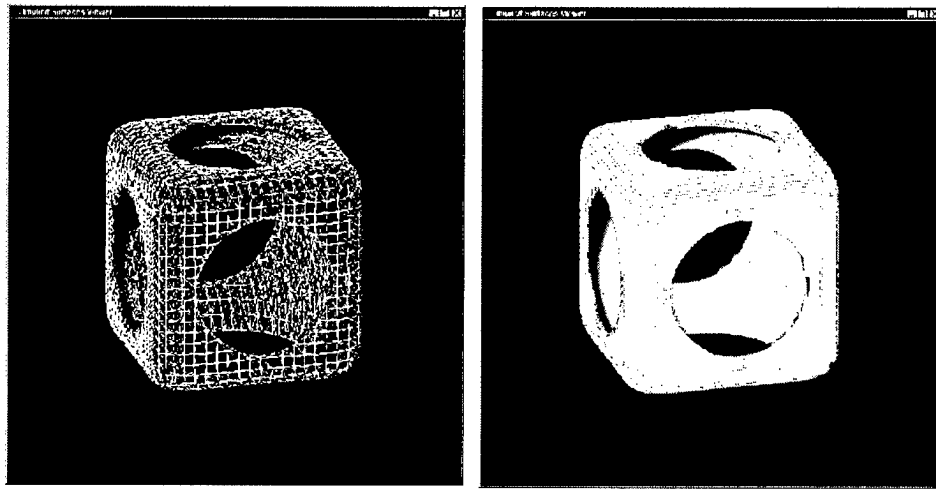


Figure 3: Wiffle Cube

sure property that preserve the implicit of the representation even after geometric operations. Therefore, only by specifying a cutting plane, the slicing of the material and the geometry can be represented in implicit form.

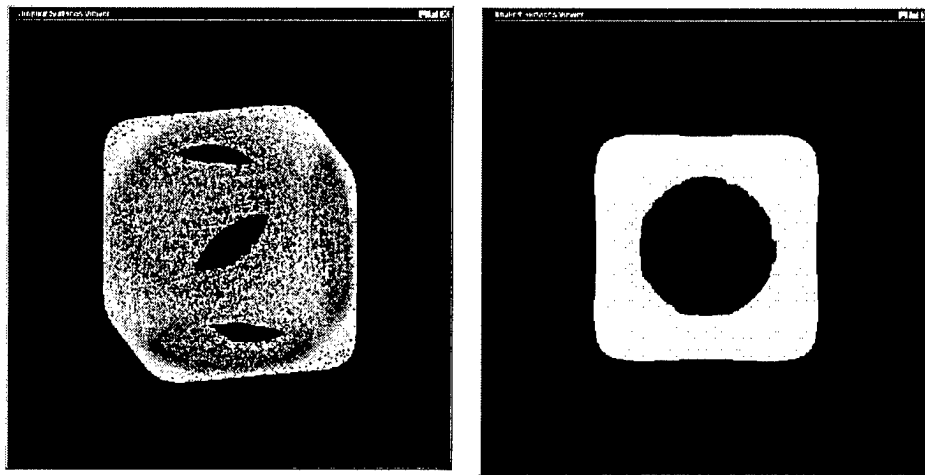


Figure 4: Spherical Material Gradient in Wiffle Cube

FGMs of ceramic and metal can be employed in advanced dental and medical applications, mainly as implants and replacements. As bioceramic materials such as Calcium Phosphate, favorably bioreact with existing bone, they can serve as porous media to support the ingrowth of new bone tissue, which results in permanent bonding with the body. The strength and life of the implants can be even more enhanced by applying biocompatible metal such as titanium for the core of the implant.

A simplified human femur implant for hip socket was created using blending and union of implicit spheres and ellipsoids. The base shape was formulated in the following form. Detailed

features were added by feature based boolean operations. The geometry of the implant is rendered in Figure 5.

```

Implant(x, y, z)
    blend=5.0
    newx=0.5*x*1.414+1-0.5*y
    newy=0.5*x+0.5*(-2+y)*1.414

    tmp= pow(elpipsoid(y,x,z,7.5,0.25,0.25),-blend)
        +pow(elpipsoid(newy, newx, z, 0.6, 0.1,0.1), -blend)
        +pow(pow((y-3.4)*4/3,2)+pow((x-0.6)*4/3,2)+pow((z-0.0)*4/3,2), -blend)

    return pow(tmp,-1/blend)-1.0

elpipsoid(x, y, z, a, b, c)
    result=x*x/a+y*y/b+z*z/c
    return (result < 0.001? 0.001 : result)

```

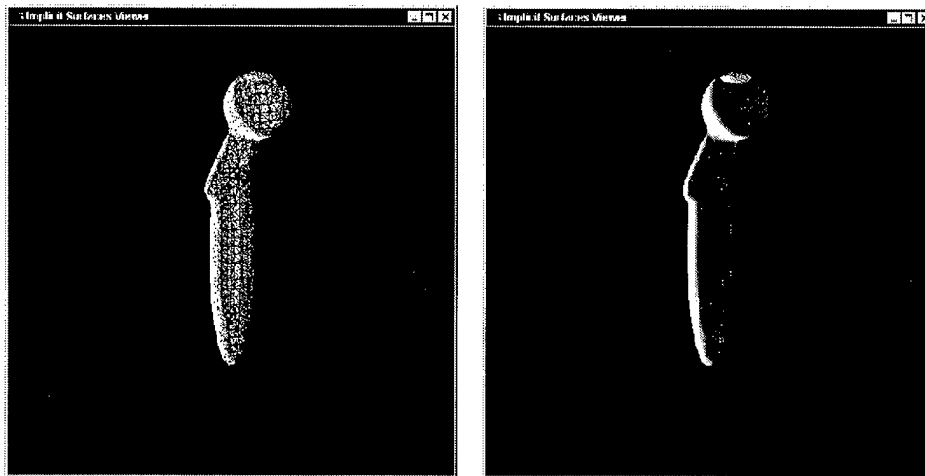


Figure 5: Implicit Model of Femur Implant

The same algebraic surface in implicit form was used for the material subspace. The gradient region in the subspace is specified as a function of radius within the range of the material subspace. Therefore, The material distribution has constant depth of a primary material shell. Localized distribution also can be achieved by modifying the blob model for the material subspace. The material gradient and the cross section along the z axis of the implant are shown in Figure 6.

4 Conclusion and Future Work

I have successfully implemented material gradient varying in three dimension in implicit algebraic surfaces. Material gradient region in the solid can be designed by generating implicit



Figure 6: Material Gradient in Femur Implant

function with the size of either equal to or smaller than the geometry. This method is very effective when the distribution is continuous and smooth. Distribution pattern can be either interpolated from discrete data sets, or sketched using Bias and Gain functions. Implicit scheme was chosen to model both geometry and material gradient. Hence, geometric and material information can be queried at any points without further interpolation.

While it is possible to model a general closed surface as a single implicit surface patches, higher-order algebraic surfaces become difficult to design because there is no readily perceived relation between polynomial coefficients and the shape of a surface. This has prompted the use of piecewise algebraic surfaces, also known as *semi-algebraic sets* or *implicit patches*. Each surface piece is low order and spans a particular cell, usually a tetrahedron, that is defined by a spatial partitioning. The formulation would become more efficient to generate complex shapes by employing implicit algebraic patches.

References

- [1] Bloomenthal, Jules, et al. (eds.), *Introduction to Implicit Surfaces*, Morgan Kaufmann Publishers, San Francisco, CA 1997.

- [2] Crawford, R. H., Computer Aspects of Solid Freeform Fabrication: Geometry, Process Control, and Design , *Proceedings of the 1993 Solid Freeform Fabrication Symposium*, Austin, TX, pp. 102-112, August 9-11, 1993.
- [3] Darrah, J. and M. Wielgus, A New CAD Model Format for SFF Machines?, *Proceedings of the 1993 Solid Freeform Fabrication Symposium*, Austin, TX, pp. 121-125, Austin, TX, 1993.
- [4] Ebert, David S., et al. (eds), *Texturing and Modeling: a Procedural Approach* , AP Professional, Chestnut Hill, MA, 1998.
- [5] Fessler, J., A. Nickel, G. Link, and F. Prinz, Functional Gradient Metallic Prototypes through Shape Deposition Manufacturing , *Proceeding of the Solid Freeform Fabrication Symposium*, The University of Texas at Austin, August, 1997.
- [6] Hirai, Toshio, and Makoto Sasaki, Vapor-Deposited Functionally Gradient Materials , *JSME International Journal*, Series I, Vol. 34, No. 2, 1991
- [7] Hoffmann, Christoph M., Implicit Curves and Surfaces in CAGD, *IEEE Computer Graphics and Applications*, January 1993.
- [8] Kumar, Vinod, D. Dutta, An Approach to Modeling Multi-Material Objects. , *Proceeding of 4th ACM Symposium on Solid Modeling*, Atlanta, GA, May 1997.
- [9] Manocha, Dinesh, Efficient Algorithms for Multi Polynomial Resultant , *The Computer Journal*, Vol.36, No. 5, 1993.
- [10] Marsan, Anne, and D Dutta, On the Application of Tensor Product Solids in Heterogeneous Solid Modeling , *Proceedings of DETC98*, 1998 ASME Design Engineering Technical Conferences, September 13-16, Atlanta, GA, 1998.
- [11] Ochiai, Yoshihiro, Generation Method of Distributed Data for FEM Analysis , *JSME International Journal*, Series A, Vol. 39, No. 1, 1996.
- [12] Perlin, Ken, Hypertexture, *Computer Graphics*, Vol 23, No. 3, July 1989.
- [13] Requicha, A. A. G. and Voelcker, H. B., Solid Modeling: a historical summary and contemporary assessment, *IEEE Computer Graphics and Applications*, Vol. 2, 2 March 1982, pp. 9 - 24.

Application of Genetic Algorithms in the Design of Multi-Material Structures Manufactured in Rapid Prototyping

Oliver König
<okoenig@ikb.mavt.ethz.ch>
Institute for Construction and Design
ETH Zurich
CH-8092 Zurich

Georges M. Fadel
<gfadel@ces.clemson.edu>
Department of Mechanical Engineering
Clemson University
Clemson, SC 29634-0921, USA

Abstract

Recent developments in the Rapid Prototyping technology establish it as a new manufacturing technique, enabling localized material addition to build a part. Thus, heterogeneous structures, consisting of more than one material can be produced. The aim of this paper is to present an optimization tool to find the best material distribution in a multi-material structure due to given objectives and constraints. The tool is based on genetic algorithms using a discrete material model and FE-analysis to evaluate the objective functions. It can optimize the distribution of different materials in 2D-structures with up to 1500 DOF's at reasonable computational costs. Its performance is shown on a bi-objective optimization of a turbine blade.

1 Introduction

In the past, the intuition and experience of engineers played the key role in designing structures. Recent years have seen the development of numerical tools, which provide conceptual designs for a given design space and specified boundary conditions. The aim of these tools is to support the intuition and the experience of an engineer. In addition, most of these tools are focused on the optimization of traditional structures consisting of one material. Examples of such software tools are the topology optimization method using homogenization introduced by Bendsøe and Kikuchi [1], and the 'Soft-Kill-Option' (SKO) method introduced by Mattheck [2].

The development of new manufacturing technologies and new materials such as Rapid Prototyping [3] or the use of composite structures expands the demands for numerical tools to design structures. These new techniques offer the possibility to manufacture anisotropic and/or multi-material structures. This makes it much more difficult to design parts just by intuition. Numerical optimization algorithms are needed to develop solutions which consider all the different aspects of such a problem. The present project starts at this point, concentrating on the design of multi-material structures manufactured in Rapid Prototyping. This leads to the main research question for this paper:

*How can one optimize the distribution of different materials
in a multi-material structure for given objectives and given constraints?*

The paper presents a methodology based on genetic algorithms to solve this type of optimization problems.

2 Genetic Algorithms

Genetic Algorithms can be described as search algorithms based on the mechanics of natural selection and natural genetics. They belong to a category of stochastic search methods,

with an additional strength that randomized search is conducted in those regions of the design space which offer the most significant potential for gain. The primary monograph on the topic is Holland's "Adaption in Natural and Artificial Systems" (referenced in [4]). The terminology of genetic search and its principal components are discussed in the book from Goldberg [4] and in a paper by Hajela [5].

GA's are not severely limited by discontinuous design spaces like techniques derived from mathematical programming principles. On the other side there is usually a stiff computational requirement associated with the use of this method. Therefore genetic algorithms represent a good solution approach for design problems where standard mathematical programming techniques are inefficient. The main advantages of GA's can be formulated as follows:

- GA's work on function evaluations, not on function derivatives.
- GA's proceed from several points in the design space, this makes it more likely to find global optima.
- GA's work on a coding of the design variables. This allows them to work in design spaces consisting of a mix of continuous, discrete, and integer variables.

2.1 GA's in Automated Design Optimization

Much work has been performed and published as shown below:

The first group of projects discusses general aspects of using genetic search for structural and topology optimization. Chapman and Jakiela [6] apply genetic algorithms to problems of structural topology design. Nair and Keane [7] investigate the combination of approximation concepts with genetic algorithm based structural optimization procedures. A flywheel optimization with a genetic algorithm is presented by the GARAGe [8] group at Michigan State University.

Other projects are more concerned in the application of genetic search on practical problems. For example there are papers investigating multidisciplinary rotor blade design [9], the design of a satellite boom [10] or the optimization of truss structures [11].

Finally, several publications examine the optimization of composite structures with genetic algorithms [12],[13],[14].

All these works establish the use of genetic search in automated design optimization.

2.2 Concept and Additional Functions of GA's

The concept is briefly discussed in this paragraph, a detailed description can be found in the book from Goldberg [4].

After the coding of the design variables an initial population is generated randomly. Then the iteration process starts. The fitness values for each individual in a population are evaluated. The first GA operator which is then applied to the population is reproduction. Individuals are selected for the next generation according to their fitness. The crossover operator mates and crosses the individuals in this newly generated pool of individuals. Mutation as the last operator is the occasional random alteration of the value of a string position. This concludes one iteration of a GA, and a new generation results.

In the following some additional GA features which are used in the project are briefly introduced:

- **Elitist Strategy.** This strategy ensures, that the best individuals stay in the population.
- **Overlapping Populations.** The pool of individuals before reproduction consists of a GA with overlapping populations in the previous population and a specific amount of new individuals. The worst individuals of the entire pool are removed in order to return the population to its

original size. Since only part of the population is generated, this strategy saves computation time.

- **Scaling the Objective Function.** In order to control the sensitivity of the GA, the objective values are linearly scaled. The aim of a scaling function is to avoid premature convergence in the GA.

2.3 Parameters in Genetic Search

The initiation of genetic search requires specification of some key parameters:

- **Population Size: popsize.** The number of strings processed in each generation must be kept small to minimize the overall computation effort. A population size between 25 and 125 represents a good choice for structural optimization problems [5].
- **Number of Generations: n_{gen} .** Usually a value in the hundreds is needed to make sure that the solution has time to converge.
- **Crossover Probability: p_{cross} .** Values ranging from 0.6 to 0.8 have been used in numerical experiments with very satisfactory results.
- **Mutation Probability: p_{mut} .** Probability values between 0.005 and 0.05 produce in general good results.
- **Overlapping Gap: p_{repl} .** The overlap parameter specifies how many new individuals are created for each generation. A typical value is $p_{repl}=0.5$, meaning that 50 % of the population has to be evaluated new for each generation.

3 Modeling of Materials and Structures

3.1 Discretization of the Design Domain

Any kind of chromosome used as a representation of the design variables in GA's is discrete. Therefore a finite design domain must be selected and discretized into elements.

For a topology optimization the design domain represents the maximal volume in which the structure is to be constructed. For a multi-material optimization, one can either fix the topology and only optimize the material distribution, or both, the topology and material distribution can be unknown.

The representation of the design space in a mathematical way is the space $T = R^3$ [15]. A typical object in the design space is called a class A, while members of this class are noted as r-sets, for example an element of the discretized structure.

3.2 Modeling of Multi-Material Structures

Currently, most solid modeling techniques are capable of capturing only the geometric and topological information of an object. In this project, a modeling method for general heterogeneous objects proposed by Kumar and Dutta [15] is used:

Modeling of Heterogeneous Objects Consisting of a Finite Number of Distinct Materials (HD) [16]. In the previous paragraph, the design space $T = R^3$ was defined in which the geometry of an object can be represented. In order to model multi-material objects, this space is expanded to include a material dimension M. The material dimension is represented with a set of integers I. The product space $T = R^3 \times I$ forms then the new modeling space including both, geometrical topology and material distribution. A new class $A_m = A \times K$ is defined where $K \subset I$ is a finite set of integers. A typical member of this class is then defined as an r_m -set. It is

composed of an r -set describing the geometry and an integer $k \in K$ defining the material. Each r_m -set, typically an element in this project, is homogeneously filled with one material.

The design variables for the optimization are now defined with the type of material for each element in the discretized design space. The approach provides thus a discrete and finite set of design variables.

3.3 Mapping the Design Variables to GA Chromosomes

The design variables for a GA must be coded, a mapping from the design domain to chromosomes must be defined. Using the HD approach above, the coding results in a binary or integer string which defines the type of material for every element in the design domain. A binary string can be used if there are only two materials to distribute, while an integer string is able to handle a whole set of materials.

Figure 1 shows the mapping for a cantilever structure with three materials mapped into a two dimensional integer string. To consider topology optimization as well as optimal material distribution, the material 1 is defined as void. To prevent numerical singularities, the material void is implemented with very small property values.

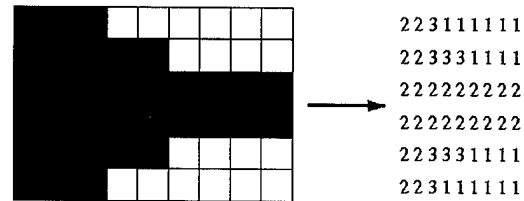


Figure 1: Mapping to GA Chromosome

4 Optimization Procedure

The genetic algorithm library GALib in C++ by Matthew Wall (MIT) provides all the needed functionality and is used in this project.

A GA needs a function which determine the fitness of each individual in a population. For a multi-material optimization this function includes an analysis of the discretized structure. For a typical GA evaluation, the fitness has to be computed for thousands of individuals. Therefore it is imperative that the analysis method has to be fast. This can only be reached if the method for the fitness evaluation has a close interface to the GA.

A first approach to evaluate the fitness of the individuals is to use **Numerical Approximation Concepts**. Keane [7] used this concept to optimize a 10 bar truss structure. It is based on the exact analysis for a limited number of individuals, the fitness for the rest of the population is evaluated using an approximation model. Although this approach can save a lot of computation time, one would have to verify the accuracy of the results carefully, because only a small part of the individuals are evaluated exactly. This method was not pursued any further in this project.

A **Finite Element Analysis** for each individual in the genetic algorithm represents another approach to evaluate the fitness values required by the genetic search. This method is favored for this project, because it provides in general a good accuracy for the solution and adaptations of the method can be found for analyses in a lot of different fields. The computational cost for analyzing each individual in the GA is the main concern. Therefore a big effort was put in minimizing the computational time needed for one single analysis. In order to keep the optimization tool as compact as possible, a FE-code in C++ was developed. With this approach, the optimization procedure can be packed in one single C++ program, the time consuming processes such as storing temporary data on the hard drive are eliminated.

The FE-code was developed to provide analyses for the applications in section 5. Therefore FE-codes for heat conduction and thermal stress analyses had to be implemented. The concepts of the FE-codes can be found in [17],[18],[19], and are not discussed here. The detailed procedure is shown in the flow chart in Figure 2.

The computational performance of this approach was tested for a simple topology optimization of a Cantilever. It represents a small application with 352 DOF's, where not much computation time should be needed to solve it. In a typical optimization for this problem the fitness function has to be evaluated approximately 3000 times. The evaluation on a computational server with 2 CPU's (200 MHz) and 1 GB RAM needs approximately 75s. This is promising for bigger applications.

In an earlier approach Ansys was used for the FE part. But the time consuming processes of storing interface files on the hard disk makes the GA evaluation for the same application about 300 times slower.

The optimization procedure using the FE-Code in C++ is therefore used for all applications.

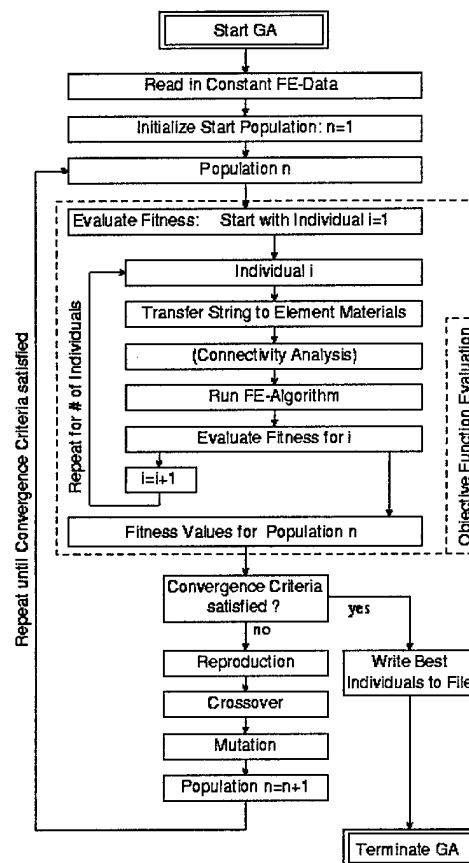


Figure 2: Procedure Using FE-Code in C++

5 Multi-Material Optimization of a Turbine Blade

The application in this section shows the performance of the developed optimization method. The distribution of two materials in a turbine blade shall be optimized.

5.1 Problem Definition

The design domain considered is a 2D cross section of a turbine blade. It is a non-cooled blade and has therefore no internal holes in the structure. This cross section is discretized into 951 linear triangle elements.

Materials. A turbine blade is subject to pressure gradients over the boundary, which introduce high mechanical stresses in the structure. Furthermore, certain regions of the blade in a gas turbine are heated to very high temperatures. This results in the wish to use one material, such as Titanium, to deal with the mechanical stresses in the structure, and a heat withstanding material such as a Ceramic to place at high temperature locations. Therefore, in this example, the materials Titanium Alloy and Silicon Nitride are used.

Boundary Conditions. The temperatures applied on the boundary are based on experimental data described in [20]. Figure 3 shows the resulting temperature distribution for a titanium blade. The purpose of this application is to show the optimization algorithm. Therefore the complex boundary conditions on a real turbine blade were simplified:

- Prescribed temperatures on the boundary replace convection and radiation effects.
- The blade is not cooled, there are no internal holes in the structure.
- Pressure distributions on the boundary are not applied.

5.2 Single Objective Optimization

The objective is to find the optimal material distribution due to given maximal service temperatures for the materials. This is an unconstrained optimization problem. The fitness function for the genetic algorithm is formulated as a maximization problem:

$$\text{Maximize} \quad \text{score} = \frac{\text{score}_{\text{norm}}}{\sum_{i=1}^{Nele} (T_i - T_{\text{service}(\text{mat})})^2}$$

The service temperature $T_{\text{service}(\text{mat})}$ does not represent a physical property of the material, it is fictive. Since the conductivities for the two materials are different, the temperature distribution in the blade changes for every new chromosome. A heat conduction analysis has to be performed for each individual in the GA. The design variables are represented by the material of each element, they are mapped in a binary string for the GA.

The GA is evaluated for 2000 generations with a population size of 100. This corresponds to 100'000 heat conduction analyses. A typical evaluation takes about 70min. Figure 4 shows the fitness scores for this evaluation, the best individual found is shown in Figure 5.

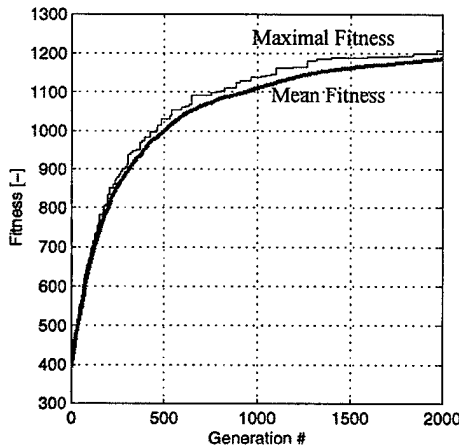


Figure 4: Fitness Scores

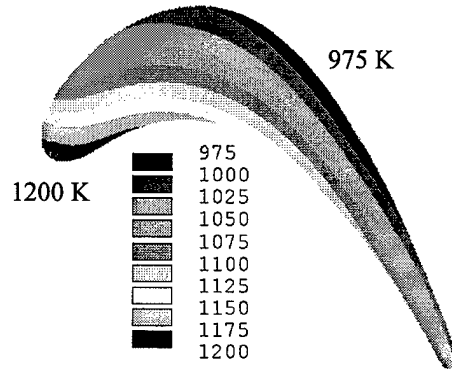


Figure 3: Temperatures in a Ti Blade [K]

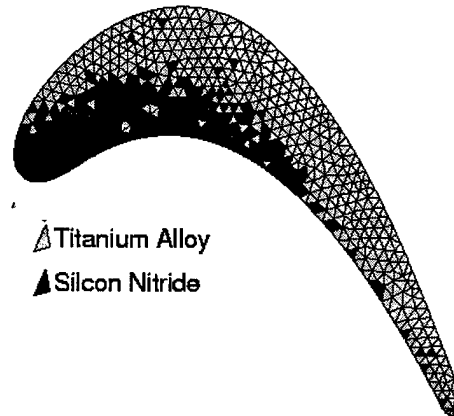


Figure 5: Resulting Material Distribution

5.3 Bi-Objective Optimization

In the solution above, high thermal stresses occur because of the different thermal expansion coefficients of Titanium and Silicon Nitride. Therefore a bi-objective optimization is carried out which combines the temperature objective with a thermal stress objective.

The fitness function is defined as a combination of the two objectives using the weighting method [21]:

$$\text{Maximize} \quad \text{fitness} = (w_{\text{temp}} \cdot \text{score}_{\text{temp}} + w_{\text{stress}} \cdot \text{score}_{\text{stress}})^{-1}$$

Where w_{temp} and w_{stress} represent the weighting factors. The objective functions are defined as:

$$\text{score}_{\text{temp}} = \frac{\sum_{i=1}^{Nele} (T_i - T_{\text{service}(\text{mat})})^2}{\text{norm}_{\text{temp}}}$$

$$\text{score}_{\text{stress}} = \frac{\sum_{i=1}^{Nele} \sigma_{eq}}{\text{norm}_{\text{stress}}}$$

The temperature objective is defined similarly to section 5.2, it controls the material distribution according to temperature distribution. The thermal stress objective aims at reducing the thermal stresses in the blade, it is the sum of an equivalent stress σ_{eq} of all elements. To evaluate the fitness of a single individual, a thermal conduction and a thermal stress analysis have to be performed.

In a bi-objective optimization, many optimal solutions can be found. Therefore a Pareto-set [21] of solutions is created in a first stage. The Pareto points result from a systematic variation of the weight factors between 0 and 1. Figure 6 shows the resulting Pareto points for such a variation. Each of this points represents the best population found by the GA in 1500 generations with a population size of 100 and the specified weight factors. The temperature objective is plotted in the x-direction, the stress objective in the y-direction. A typical GA evaluation for this problem takes about 10h, because of the two FE-analyses (thermal conduction & thermal stress) for each fitness evaluation.

A decision making process is necessary to choose a single solution out of this set of optimal Pareto solutions[21]. Figure 7 shows one single solution where the weight factors were chosen as $w_{temp} = 0.3, w_{stress} = 0.7$. In addition the GA for this result is run over 2000 generations with a population size of 150 to get a more converged result.

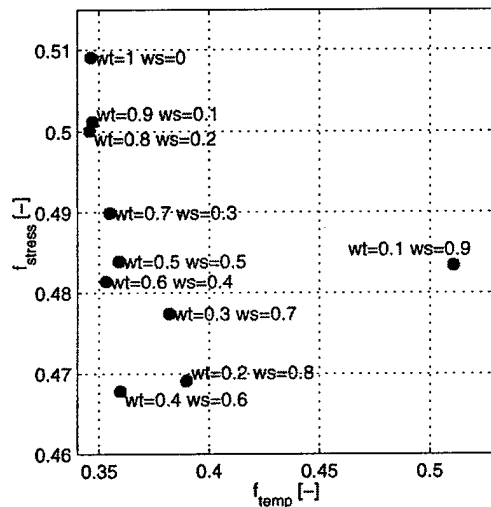


Figure 6: Pareto Points

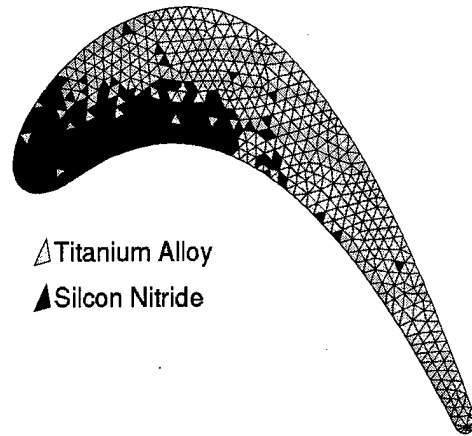


Figure 7: Best Individual for $w_{temp} = 0.3, w_{stress} = 0.3$

6 Discussion and Conclusion

For the single objective optimization in section 5.2, the optimization puts as expected Ceramic at the tip of the blade (see Figure 5), where the highest temperatures occur. The Titanium in the rest of the structure provides the needed strength. Although the GA was evaluated for 2000 generations, it's stochastic concept still influences the result. Several elements have obviously the wrong material (assigned by mutation). Because of the high temperatures and the different thermal expansion coefficients, it is imperative to include thermal stresses in the optimization.

An approach to include thermal stresses is shown in the bi-objective optimization in section 5.3. Figure 6 shows that the weight variation does not result in a convex pareto curve. This indicates that probably the GA evaluations did not fully converge to the optima.

Figure 7 with the best individual for a specific weight combination shows that the Ceramic is smaller. But it is still not clear how the interface between the two materials should be best configured. It was hoped to see a fuzzier mechanical interface between the two materials, but the problem conditions and the way the objectives were formulated prevented this from happening.

An optimization tool for 2D-multi-material structures was developed. It optimizes the distribution of materials in a structure due to given objectives and constraints using genetic algorithms. It can be said, that the developed optimization tool is able to handle structures with as many as 1000 to 1500 DOF's in a reasonable computation time (a few hours). The turbine blade application showed, how essential a fast objective function evaluation for GA's is, a run time of 10h for the bi-objective optimization shows the limits of the tool. Since the solution space for the GA grows exponentially with the number of elements, the number of generations needed to achieve a converged solution increases as well in an exponential way. This project has shown some of the potentials of GA's in structural optimization, as their flexibility, their robustness and ability to find global optima. But it has also demonstrated some of their shortcomings of high computational needs and bad convergence performance towards the end of an optimization. To overcome these shortcomings, future work could be concentrated on introducing parallel genetic algorithms, using gradient based optimizers after the GAs pointed towards possible solutions (memetic algorithms) or using a continuous material model.

References

- [1] Bendsøe, Martin Phillip, *Optimization of Structural Topology, Shape, and Material*, Springer-Verlag Berlin, Heidelberg, New York, 1995
- [2] König, O., *Application and Analysis of a Topology Optimization Method Including the Development of a Bicycle Crank*, Semester Work at the ETH Zurich, in German, 1997
- [3] Beaman, J.; Barlow, J. et al, *Solid Freeform Fabrication, a New Direction in Manufacturing*, Kluwer Academic Publishers, 101 Philip Drive, Assini Park, Norwell, Massachusetts 02061, 1997
- [4] Goldberg, David E., *Genetic Algorithms in Search, Optimization and Machine Learning*, Addison-Wesley Publishing Company, Inc., 1989
- [5] Hajela, Prabhat, *Stochastic Search in Structural Optimization: Genetic Algorithms and Simulated Annealing*, Structural Optimization: Status and Promise, Vol. 150, pp. 611-637, Progress in Astronautics and Aeronautics, 1992
- [6] Chapman, C.D.; Saitou, K.; Jakiela, M.J., *Genetic Algorithms as an Approach to Configuration and Topology Design*, Journal of Mechanical Design, Vol.116, No.4, pp. 1005-1012, 1994
- [7] Nair, P.B; Keane, A.J., *Combining Approximation Concepts with Genetic Algorithm-Based Structural Optimization Procedures*, Department of Mechanical Engineering, University of Southampton, Highfield, Southampton, SO17 1BJ, U.K., andy.keane@soton.ac.uk
- [8] Punch, William F.; Gelfand, Boris; Mathews, Owen; Goodman, Erik D., *An Injection Island GA for Flywheel Design Optimization*, Genetic Algorithm Research and Application Group (GARAGe), Michigan State University, East Lansing MI 48824 USA, goodman@egr.msu.edu
- [9] Hajela, Prabhat; Lee, Jongsoo, *Parallel Genetic Algorithm Implementation in Multidisciplinary Rotor Blade Design*, Journal of Aircraft, Vol.33, No.5, pp. 962-969, 1996

- [10] Keane, A.J.; Brown, S.M., *The Design of a Satellite Boom with Enhanced Vibration Performance Using Genetic Algorithm Techniques*, Department of Mechanical Engineering, University of Southampton, Highfield, Southampton, SO17 1BJ, U.K., andy.keane@soton.ac.uk
- [11] Hajela, Prabhat; Lee, E., *Genetic Algorithms in Truss Topological Optimization*, International Journal of Solids and Structures, Vol.32, No.22 pp. 3341-3357, 1995
- [12] Punch, William F.; Averill, Ronald C.; Goodman, Erik D.; Lin, Shyh-Chang; Ding, Ying, *Design Using Genetic Algorithms -- Some Results for Laminated Composite Structures*, Intelligent Systems Laboratory, A714 Wells Hall, Computer Science Department, Michigan State University, punch@cps.msu.edu, 1995
- [13] Punch, William F.; Averill, Ronald C.; Goodman, Erik D.; Eby, David J., *Parallel Genetic Algorithms in the Optimization of Composite Structures*, Genetic Algorithm Research and Application Group (GARAGe), Michigan State University, East Lansing MI 48824 USA, goodman@egr.msu.edu
- [14] Punch, William F.; Malott, B.; Averill, Ronald C.; Goodman, Erik D.; Ding, Y., *Use of Genetic Algorithms for Optimal Design of Laminated Composite Sandwich Panels with Bending-Twisting Coupling*, Genetic Algorithm Research and Application Group (GARAGe), Michigan State University, East Lansing MI 48824 USA, goodman@egr.msu.edu
- [15] Kumar, Vinod; Dutta, Dabasish, *Solid Model Creation of Materially Graded Objects*, Solid Freeform Fabrication Proceedings, 1997
- [16] Huang, Jinhua; Fadel, Georges, M., *Heterogeneous Flywheel Modeling and Optimization*, Department of Mechanical Engineering, Clemson University, Clemson, SC 29634-0921, USA, 1998
- [17] Dawe, J.D., *Matrix and Finite Element Displacement Analysis of Structures*, Oxford University Press, Walton Street, Oxford, 1984
- [18] Huebner, K.H.; Thornton, E.A.; Byrom, T.G., *The Finite Element Method for Engineers*, John Wiley & Sons, Inc., New York, 1995
- [19] Reddy, J.N., *An Introduction to the Finite Element Method*, McGraw-Hill, Inc., New York, 1993
- [20] Liebert, C.H.; Gaugler, R.E.; Gladden, H.J., *Measured and Calculated Wall Temperatures on Air-Cooled Turbine Vanes with Boundary Layer Transition*, National Aeronautics and Space Administration, Lewis Research Center Cleveland, Ohio, 1983
- [21] Yusheng Li, *Bi-Criteria Optimization Problems to Aid Decision Making Design*, PhD Thesis, Department of Mechanical Engineering, Clemson University, Clemson, SC 29634-0921, USA, 1998

AN EJECTION MECHANISM DESIGN METHOD FOR AIM TOOLS

Sundiata K. Jangha
Graduate Research Assistant

David W. Rosen
Associate Professor

The George W. Woodruff School of Mechanical Engineering
Georgia Institute of Technology
Atlanta, GA 30332-0405
404-894-9668 david.rosen@me.gatech.edu

Keywords: Injection Molding, Rapid Tooling, Ejection, Stereolithography, Decision-Based Design

ABSTRACT

One of the key advantages of AIM tooling is time savings when producing small batch production quality parts. However, designing suitable ejection mechanisms is becoming a bottleneck. There are two goals of this paper. First, a model is presented that effectively characterizes the stresses on the mold core and part during injection molding. Second, a method is described for ejection system design. Our approach consists of a combination of analytical, computational, and physical experiments. The ejection system design method will first determine the feasibility of ejection for a particular part geometry, then will determine the number, sizes, and locations of ejector pins. Each phase of the method will be formulated into a Compromise Decision Support Problem, a multi-objective optimization problem formulation. An example will be presented to provide an idea of the robustness and the limitations of the method. Preliminary results indicate that this methodology is sound for a simple geometry.

1. INTRODUCTION

Rapid Prototyping (RP) is fast becoming the preferred method for hastening the product realization timeframe. The deficiency in this field is the lack of the ability to perform functional tests on the produced parts. Hence the development of the field of Rapid Tooling (RT) which entails creating an injection molding tool capable of producing small batch parts, from an RP technology. RT combines the speed of RP technologies with the realistic test specimens from injection molding. For this work we will consider AIM tooling which uses the StereoLithography Apparatus (SLA) as the RP technology to create the molding tool. There are three phases to the injection molding process; filling, cooling, and ejection. While all three of the phases present issues not considered when using traditional tooling, the final phase, ejection, has become the bottleneck for the RT process. As such, the ejection phase will be considered in this work.

The practice of injection molding has always been based on heuristics. Hence the area needs some form of standardization to ensure good parts are produced independent of the manufacturer. The most glaring area where this is true is the ejection of the parts. The material properties of the SLA resin are much closer to the injected material than those of the steel tools. Thus, the user must be more wary of the mold tool being damaged and even failing during the ejection of the part. We believe that the system that has been created will help to address these concerns.

The first step in the system is to determine whether or not the part can be ejected successfully. This step is carried out before any tools have been created. Therefore there is immediate timesaving. The second step in the system is to determine the actual ejection layout. This layout consists of the number, diameter, and locations of the ejector pins. This information will be invaluable to the user since there is less need for the incorporation of a highly skilled manufacturer in the early testing phase of product development.

2. BACKGROUND

2.1 Ejection Literature

There has been quite a bit of research on ejection for traditional injection molds. This literature ranges from papers dealing with studies of the forces associated with part ejection [1-3], to sections from books describing the process in detail [4-7], to potential improvements to the ejection process [8]. However, until recently, very little work has been done with respect to RT molds. Clearly, the theory related to the forces associated with ejection would apply. Yet, the rules developed would not due to the material property differences between RT and steel tools. The difference in material properties is significant enough that it is necessary to redevelop ejection rules. Palmer [9], has established a foundation for these new rules. Her work entailed an investigation into the failure mechanisms for AIM tooling. During the course of this investigation she conducted extensive physical experiments the results of which were categorized into design rules. At the same time, CeDorge [10] has conducted research that investigates the thermal effects on the AIM molding process, and how that affects the life and productivity of the tool.

The work that has been done in the area of ejection in rapid tooling has mainly been in the area of evolving design rules for traditional tools into usable rules for RT. Dickens [11] has made strides towards this end by measuring the ejection force characteristics for both pin and stripper plate ejection systems. At the same time, there are other areas that must be considered.

2.2 Compromise Decision Support Problem

The compromise DSP is a general framework for solving multi-objective, non-linear, optimization problems [12]. Mathematically, the compromise DSP is a multi-objective decision model which is a hybrid formulation based on Mathematical Programming and Goal Programming [12]. The compromise DSP is used to determine the values of the design variables, which satisfy a set of constraints and bounds and achieve as closely as possible a set of conflicting goals. The structure of the cDSP is as follows:

- Given:* A feasible alternative, assumptions, parameter values and goals.
- Find:* Values of design and deviation variables.
- Satisfy:* System constraints, system goals, and bounds on variables
- Minimize:* Deviation variable that measures distance between goal targets and design point

The alternative in this case is a part configuration. The goals of this system are to minimize the stress experienced by the part during ejection, and to minimize the number of pins to be used. The goals are often weighted depending on the intent of the designer. The design variables to be

investigated will be the number of pins, the pin diameters and the location of the pins. The orientation of the part and the location of the part with respect to the mold will also be considered but they are not design variables. The constraints to be satisfied in this system are the ejection rules discussed earlier.

A solution to the compromise DSP is called a satisficing solution, because it is a feasible point that achieves the system goals to the "best" extent that is possible [13]. This notion of satisficing solutions is in philosophical harmony with the notion of developing a broad and robust set of top-level design specifications. The compromise DSP will be at the heart of the ejection system design methodology.

2.3 Ejection Force Determination

The ejection force (the force required to remove the part from the mold) is the primary consideration in the ejection process from a mechanics standpoint. The base equation for this force is as follows:

$$F_E = \mu * P * A \quad (1)$$

Where μ is the coefficient of friction, P is the contact pressure, and A is the contact area.

Glanvill [5] developed a more advanced formulation that considers an equivalent diameter:

$$F_e = \frac{\Delta \phi * E * A * \mu}{\phi \left[\frac{\phi}{2t} - \left(\frac{\phi}{4t} \nu \right) \right]} \quad (2)$$

where:

$$\Delta \phi = \alpha (T_m - T_e) \phi \quad (3)$$

$\Delta \phi$ = "restrained" thermal contraction of plastic material across the equivalent diameter (m)

ϕ = diameter of circle with a circumference equal to the length of perimeter of molding surrounding the male core (m)

E = plastic modulus at the temperature of ejection (Pa)

A = contact area (m²)

μ = coefficient of friction

α = plastic coefficient of thermal expansion (m/m/°C)

ν = Poisson's Ratio

T_m = "melt" temperature/softening point (°C)

T_e = part temperature at time of ejection (°C)

This formulation is more robust than the base equation, yet it still has limitations. The most glaring of these limitations are the lack of consideration of internal geometry and of draft. The ejection mechanism design method reported here is capable of dealing with both issues.

3. EJECTION MECHANISM FORMULATION

3.1 Approach

There are two main areas that have to be dealt with in order to reduce the amount of time required to develop an ejection system. The first area to be understood is the nature of the force

that results from ejecting the part with respect to both the mold and the part. The second area to be understood is the effect that each ejector pin has on the entire system. This will allow for the addition or removal of pins as necessary. The overall approach to designing the ejection mechanism will be based on the Compromise Decision Support Problem (cDSP). The word formulation for the cDSP is represented in Figure 1.

The design process for the ejection mechanism is depicted in Figure 2. The first step in designing the mechanism is to conduct a shrinkage analysis using an Finite Element Analysis (FEA). This analysis will dictate the amount of pressure that shrinkage due to the part's solidification will produce on the mold core. The second step is to formulate and solve the cDSP. The formulation of the cDSP requires only the addition of the part-specific information (part geometry, material properties). Once formulated the cDSP is solved using a computer algorithm. The output from this algorithm will be the number of ejector pins and their diameter. The next step will be to input the number of pins and their diameter into the algorithm that will be used to determine the potential ejector pin configurations. These configurations will then each be analyzed using an FEA. From these configurations the final layout will be selected, completing the design of the ejector mechanism.

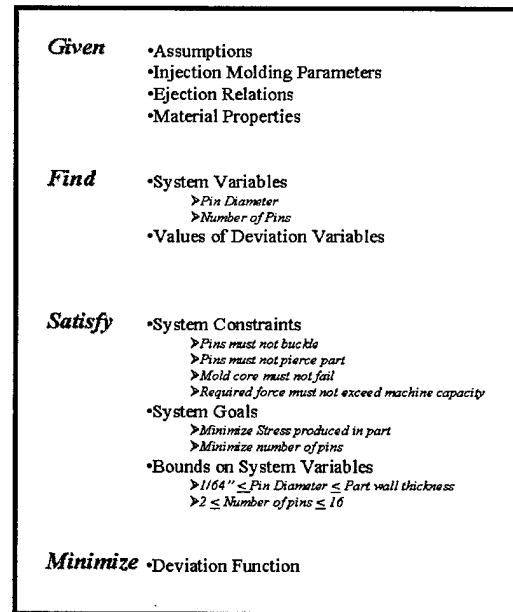


Figure 1 cDSP Word Formulation

In order to facilitate the determination of part shrinkage, a two stage FEA is performed. The first stage simulates the solidification of the part via a thermal analysis. The second stage simulates the shrinkage of the part during cooling via a structural analysis that uses the results from the thermal analysis as loading conditions. After determining the injection molding parameters, the user is required to input the parameters along with the part geometry into the Finite Element Model (FEM). With this information, the FEA is run and the result is the contact pressure between the part and mold core.

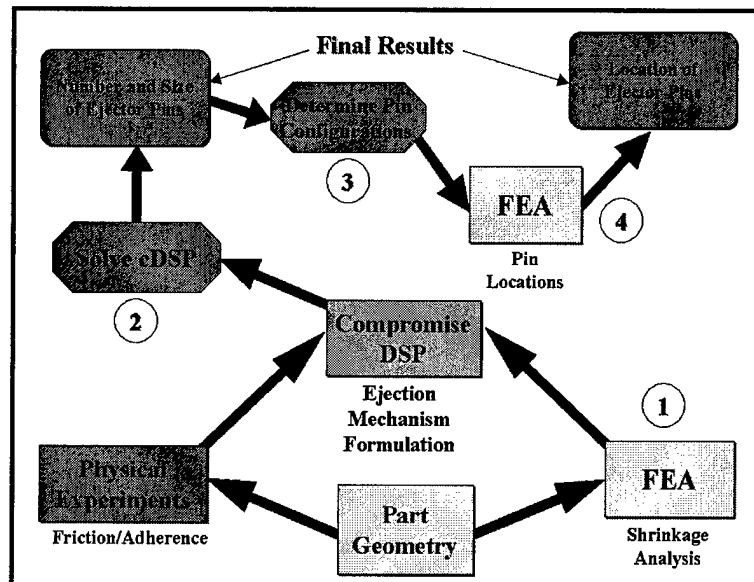


Figure 2 Process Flowchart

Once the contact pressure is known, the cDSP can be solved. The cDSP has already been formulated into a generalized form. Like the shrinkage analysis, the completion of the formulation of the cDSP requires the user to input problem specific information (part geometry, part material properties, and injection molding parameters). The formulated cDSP is solved using a computer code written in FORTRAN. The algorithm conducts an exhaustive search of the design space. In this case the deviation function is composed of deviation variables representing the number of pins and the stress produced in the part. The more pins that are used the less the amount of localized stress. At the same time, the fewer the number of ejector pins required, the less expensive the process is with respect to both time and money. Hence the combination of design variables (number of pins, Pin Diameter) that produces the minimum value for the deviation function as a whole is the desired satisficing solution. This solution is the first half of the ejector mechanism. The variable values from this solution are input into a separate algorithm to determine the other half of the ejector mechanism specifications, the pin locations.

The algorithm that has been created to determine the pin locations requires the information that is output from the solution of the cDSP. The user will have to specify certain information about the part. This includes the number of features that are to be ejected directly and the number of pins per feature. Based on the ejector pattern for the mold base, the algorithm considers a range of part orientations and the resulting pin locations. From this range the best set of pin locations is based on the desire to centrally locate the pins within the feature. Hence, for each angle, there is a part origin and a set of pin locations. The output from this algorithm will be a list of all of the different part configurations (orientations and the associated pin locations). Each one of these configurations will then be analyzed using an FEA to determine the configuration that produces the least amount of stress. This configuration will be the one selected. At this point, the specifications for the ejection mechanism are complete.

3.2 Constraints

In this work, constraints take two forms. On one hand there are boundary conditions that must be considered during the development of the ejection mechanism. On the other hand there are the design rules for injection molding and part design that must be taken into account. Both of these are depicted in the word formulation of the cDSP in Figure 1.

For the mold base used in this work, as is common with RT molds, there is an ejector plate with a set pattern of ejector holes. There is a hole at the center of the plate for the sprue. From the center of that hole, there are two sets of intervals. One set is spaced at $\frac{1}{2}$ ". The second set is offset by $\frac{1}{4}$ " and again spaced at $\frac{1}{2}$ " intervals. As such, the mechanism design system must account for the ejector plate. This compensation takes place in the computer algorithm that determines the feasible configurations.

Four design rule constraints have been derived from well-known theory. First, the ejector pins must not buckle. The equation used to enforce this constraint is Euler's column buckling formulation [14]. Second, the mold core must not fail, meaning that the tensile stress resulting from the ejection of the part can not exceed the tensile strength of the mold material. Third, the ejector pins can not pierce the part. The force acting on each pin will create a localized stress. This stress can not exceed the compressive strength of the part material. Finally, the Ejection

algorithm that will be used to solve the cDSP. The cDSP is to be solved as described in section 3.2.

Part Orientation			Pin Displacement		Pin Locations							
Angle	Origin		d1	d2	Pin 1		Pin 2		Pin 3		Pin 4	
	X	Y			X	Y	X	Y	X	Y	X	Y
-45.0000	0.25	0.75	1.011	0.7571	0.9649	0.0351	2.1996	-0.1289	2.3791	1.4493	0.7854	1.2854
0.0000	0	0	1	1	1.0000	0.0000	2.0000	1.0000	1.0000	2.0000	0.0000	1.0000
45.0000	1.5	0.5	-0.7571	1.111	0.9646	-0.0354	3.6998	2.6998	2.3789	1.3789	2.2856	1.2856

Table 1 Abbreviated Output from Pin Configurations

The formulated cDSP is solved by exhaustively searching the design space. The two system variables and the system variable bounds determine the design space as depicted in step 2 of Figure 2. The solution algorithm outputs a number of pins and the pin diameters. Since the example part has four features to be ejected and the wall thickness is 0.1 in, the results from the cDSP solution algorithm is four pins and a pin diameter of 0.093875in. (3/32"). This is to be expected due to the nature of the trade-off between number of pins and stress in the part. In order to minimize the stress produced in the part, the ejector pin diameters should be maximized to minimize the local stress. One of the geometric constraints is that the pin diameters not exceed the wall thickness of the part. The value output from the system is the largest standard pin diameter that will fit within the wall thickness. The next step is to determine the final configuration of the ejector mechanism.

The output from step 3 of the flowchart in Figure 2 is a set of feasible pin configurations. This set ranges throughout the feasible range of part angles with one feasible configuration emerging for each angle. Table 1 is an abbreviated listing of the output.

These alternative configurations are run through an FEA to determine the configuration that yields the minimum stress in the part. This is solution step 4 in Figure 2. In this example the configuration that emerged was at 45 degrees. The stress in the part produced by this configuration is illustrated in Figure 5. The maximum stress in the part is between 50 and 58 kPa. This is well under the compressive strength of the material, which is 100 MPa. At this point the ejection mechanism is complete. The final layout is configuration 3 (45-degree orientation) in Table 1. The final layout with respect to the ejector plate is depicted in Figure 6.

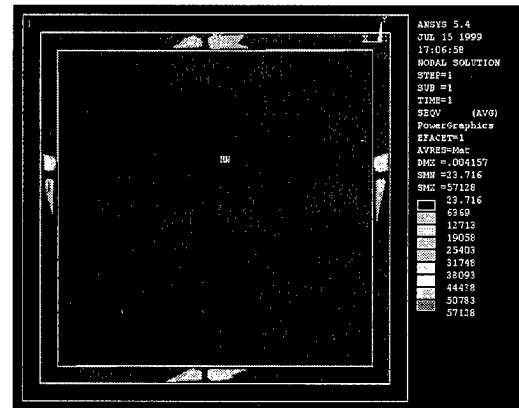


Figure 5 Resultant Stress Due to Pins Due to Ejection

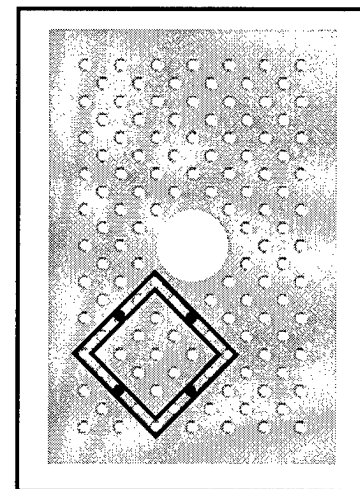


Figure 6 Ejector plate with final part configuration

5. CONCLUSIONS

An ejection mechanism design method was developed that creates a mechanism while accounting for both the part geometry and the injection molding parameters involved with the product. The goals of the design system for this mechanism are to minimize the number of pins, and the stress induced in the part due to ejection. The intent of this system is to allow the user to hasten the realization of a product by shifting the production of prototype parts that can be functionally tested to earlier in the design process. This is accomplished by the system in that it removes a bottleneck from the rapid tooling arena, and as such improves the ability of the user to achieve high quality parts relatively quickly and with a minimal amount of effort. By using the methods outlined in this paper, the ejection mechanism can be designed successfully and with little cost to the user in time. This design system will help to keep the "rapid" in rapid tooling.

While the ejection mechanism design system will significantly impact the field of rapid tooling, it is not without limitations. The reliance on the part having a fairly simple geometry is a limitation. The system is also limited in its ability to handle parts that require multiple pins per feature. Finally, as complexity is added to the requirements, (increased number of parts, number of features, etc...) the system becomes computationally expensive. Efforts are being made to further enhance the capabilities and eradicate the limitations of both the system and the underlying design methodology.

ACKNOWLEDGEMENTS

We thankfully acknowledge the support of the Rapid Prototyping and Manufacturing Institute of the Georgia Institute of Technology and its member companies, and that of the George W. Woodruff School of Mechanical Engineering.

REFERENCES

1. Malloy, R., P. Majeski. *Design of Pin ejector Systems for Injection Molds*. in *SPE Annual Technical Conference*. 1989. New York, NY: Society of Plastics Engineers.
2. Malloy, R., C. Burke. *Experimental Study of the Ejection Force Encountered During Injection Molding*. in *SPE Annual Technical Conference*. 1991. Toronto, Canada: Society of Plastics Engineers.
3. Wang, H., K. K. Kabenami, G. Salloum. *Prediction of Ejection Force and Ejection-Induced Stress in Injection Molding of Plastics*. in *Annual Technical Conference, Society of Plastics Engineers*. 1997. Toronto, Canada: Society of Plastics Engineers.
4. Bryce, D.M., *Plastic Injection Molding ...manufacturing process fundamentals*. Fundamentals of Injection Molding, ed. D. Peterson. Vol. I. 1996, Dearborn: Society of Manufacturing Engineers. 277.
5. Glanvill, A.B., *The Plastics Engineer's Handbook*. 1971, London: The Machinery Publishing Co. Ltd.
6. Rees, H., *Mold Engineering*. 1995, New York: Hanser/Gardner Publications. 608.
7. Rosato, D.V., Dominick V. Rosato, *Injection Molding Handbook*. 2nd ed. 1995, Washington D.C.: Chapman and Hall. 1118.

8. Kwak, S., Kunwoo Lee. *Optimal Layout and Sizing of Ejector Pins for Injection Mold Design*. in *American Society of Mechanical Engineers Design Automation Conference*. 1998. Atlanta, Georgia: ASME Press.
9. Palmer, A., *The Effect of Feature Geometry on the Life of Stereolithography Molds*, Masters Thesis. 1999, Georgia Institute of Technology: Atlanta, Georgia.
10. CeDorge, T., Y. Lebaut, A. Palmer, J. Colton. *Design Rules for Stereolithography Injection Molding Inserts*. in *National Stereolithography User's Group*. 1999.
11. Hopkinson, N., P. Dickens. *Research into Part Ejection in the AIM Process*. in *Solid Freeform Fabrication Symposium*. 1998. University of Texas Austin, Texas.
12. Mistree, F., W. F. Smith, B. A. Bras, *A Decision Based Approach to Concurrent Engineering*, in *Handbook of Concurrent Engineering*. 1993, Chapman and Hall: New York.
13. Simon, H.A., *The Sciences of the Artificial*. 3rd ed. 1996, Cambridge, MA: MIT Press.
14. Beer, F.P., E. Russell Johnston, Jr., *Mechanics of Materials*. Second ed. 1992, New York: McGraw-Hill Inc.

FRACTAL GROWTH MODELING OF ELECTROCHEMICAL DEPOSITION IN SOLID FREEFORM FABRICATION

Jack G. Zhou, Zongyan He and Jian Guo
Department of Mechanical Engineering and Mechanics
Drexel University, Philadelphia, PA 19104

ABSTRACT

A new rapid tooling technique ElectroChemical Liquid Deposition Based Solid Freeform Fabrication (ECLD-SFF) was introduced in this paper. In the ECLD-SFF a substrate made of or coated with conductive materials is connected to a DC power supply, and the substrate is put into a plating bath. A very thin metal pin is connected to the DC power as a positive electrode. Between the substrate and the tip of the pin there is a thin layer of metal powder. Under the effects of electric field, metal ions from electrode moving to chemical liquid will deposit onto the powder particle and growing so that the metal particles can be bound by the deposited materials to form freeform solid. By controlling the pin's movement and electrified time, a desired 3-D shape will be built through layer by layer scanning. ECLD-SFF distinguishes itself from other SFF techniques with advantages of products: high build rate, high accuracy, high density, low shrinkage and controllable microstructures. It has been found that the electrochemical deposition among metal particles during ECLD-SFF is a fractal growth process. The fractal dimension and the width of the deposited metal band are all related to electric field density, composition of electroplating liquid and processing time. Several models on the fractal growth between electrodes or metal particles were developed in order to explain these fractal growth phenomena and obtain desired process parameters and conditions for the ECLD-SFF process.

INTRODUCTION

There have been many efforts to use gas-phase laser-induced reaction to make parts. The Selective Laser Sintering system has been used to form alumina parts by oxidation of aluminum powder in air, and to form silicon nitride by laser sintering of silicon in nitrogen or ammonia (Birmingham, 1995). Other efforts are focused on converting laser-induced Chemical Vapor Deposition (CVD) from a film-forming to shape-making technique (Maxwell, 1995, Lehmann, 1994). A technique called Selective Area Laser Deposition (SALD) has been proposed by Jakubenas et al., (1997). Their proposed process, depositing material from one or more organometallic gases on a substrate selectively heated by a scanning laser beam, offers an opportunity of forming shapes under lower temperature with a wide range of materials. The primary limitation of gas-phase reaction methods is their low deposition rates. According to the listed deposition rate of organometallics, 0.1-1.0 $\mu\text{m}/\text{min}$, (Sudarshan, 1989), it may take several weeks even months to make a cubic inch solid metal part by using conventional CVD. Solids can also be free-formed by electrochemical methods. There are two SFF techniques related to electrochemical reactions: tooling with Nickel Ceramic Composite (NCC) and Expressstool (Ashley, 1998). The NCC tooling method uses plastic RP models as a master pattern, it is first coated with a conductive silver-based material, then placed in an electroforming bath of nickel sulfamate where a thin nickel layer is plated over it. The typical nickel plating thickness varies from 0.04 to 0.2 inch (Ashley, 1997). After electroforming, Chemical Bonded Ceramic (CBC) is cast to support the nickel shell. Once the CBC is cured, the ejector pins are drilled and installed. This technique is not a direct free-forming method, and the filled-in ceramic material usually has

large shrinkage that will cause shear stress on the interface and tooling distortion. In Expressstool technique, a mandrel is first made with a CNC machine, then the mandrel is put in a bath of nickel sulfamate for electroforming. The formed nickel shell with a thickness of 1 to 2 mm needs to be backed with aluminum-filled epoxy. The aluminum fraction helps heat conduction. Two main advantages of this process are the ability to produce large parts and the high accuracy of the products due to a very small shrinkage. A key disadvantage is that deep holes do not electroform well; this is also the shortcoming of conventional electroforming techniques caused by the heterogeneity of electric current density. This technique is also not a direct freeform fabrication. A new SFF technique has been developed to overcome the main limitations of other gas-phase chemical reaction or electrochemical SFF techniques. It will be introduced briefly in this paper.

On the other hand, fractal geometry (Mandelbrot, 1967, 1982) has blossomed tremendously in the past few years and has helped reconnect pure mathematics research with both the natural sciences and engineering. Within the last decade fractal geometry and its concepts have become central tools in most of the natural sciences, including physics, chemistry, biology, geology, and meteorology. The application of fractal geometry in engineering, however, is still in its infancy. Although in its infancy in engineering practice, fractal geometry has already been introduced into many disciplines of engineering research and it has great potential in developing new technologies and solving real engineering problems. The engineering field that has benefited the most from fractal research is materials science. The microstructure of such materials as metals, composites, concrete, rocks, graphite, and the majority of synthetic materials can be characterized by fractal geometry. Particle distributions and aggregations also possess fractal properties. The fractal characterization of materials has greatly helped researchers in understanding the microstructures and operative mechanisms of materials, and in implementing the manufacture of new materials. In this paper, the authors will use fractal geometry as a modeling and analysis tool to study deposits and particle growing mechanism in the electrochemical liquid deposition process for solid freeform fabrication. If the fractal growth process is realized and understood thoroughly, then it can be used to predict and control various electrochemical liquid deposition processes used in coating, plating, solid freeform fabrication, and electronic circuit and device making (Bradley et al., 1997).

A NEW SOLID FREEFORM FABRICATION TECHNIQUE

A new SFF technique, called ElectroChemical Liquid Deposition based SFF (ECLD-SFF), has been developed by the authors to overcome the main limitations of other gas-phase chemical reaction or electrochemical SFF techniques. In the ECLD-SFF (see Fig.1), the substrate is made of or coated with conductive materials (metals or graphite), and is connected to a DC power supply as a negative electrode (cathode). Then the substrate is put into a plating bath that is filled with electroplating liquid. A very thin pin that is made of deposition metal is connected to the DC power as a positive electrode (anode). Between the substrate and the tip of the pin there is a thin layer of metal powder/particles. Between cathode and anode there is an electric field named Z direction field. Two assistant electric fields are arranged perpendicular to each other to form an X-Y surface electric field. A magnetic field is applied in the Z direction of the substrate to form a tight connection of ferrite material powders. Under the effects of the electric and magnetic fields, metal ions from electrode moving to chemical liquid will deposit onto the powder particle and growing, and the metal particles will be bound by the deposited materials to

form freeform solid. By controlling the pin's movement and electrified time, a desired 3-D shape can be built through layer by layer scanning. The formed product will be further treated, such as sintering and infiltration. Fig. 2 is a conceptual diagram of the ECLD-SFF system. It consists of six sub-systems: an X-Y-Z scanning & elevating; a pin anode feeding; a metal powder feeding system; a electroplating liquid treating and recovery system; a heating system; and a central computer control unit.

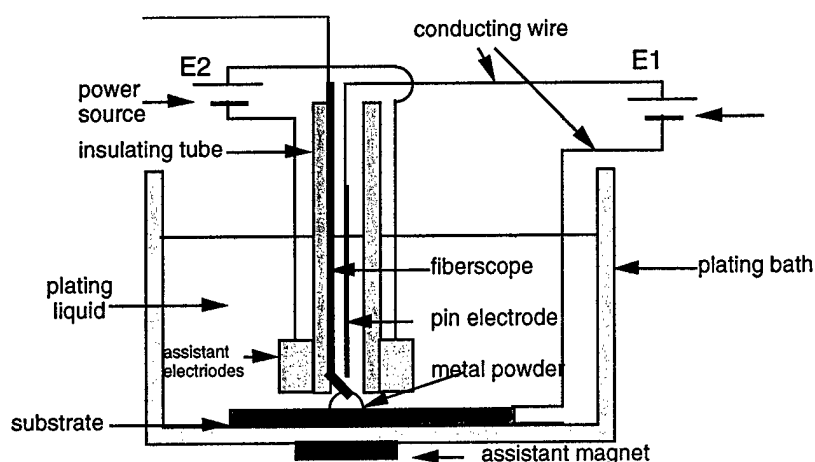


Fig. 1. A complete structure and mechanism of electrochemical liquid deposition

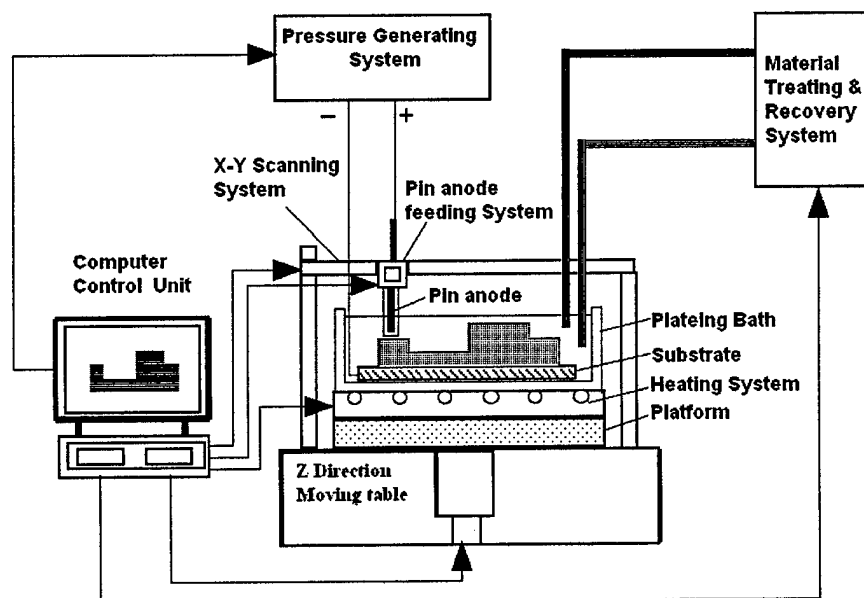


Fig. 2. The conceptual diagram of the ECLD-SFF system

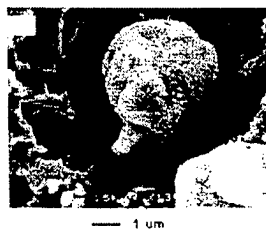
The new ECLD-SFF distinguishes itself from other SFF techniques with the following advantages: (1) High build rate. In ECLD-SFF, the deposited material serves as the binder among the particles of metal powders, and the product is formed by many layers of the powders not only the deposited materials, thus a high producing rate can be expected. Additionally, the rate can be increased greatly by changing the shape of the anode. For example, for a part with large flat surface we can choose a similar shape metal plate as an anode. (2) High accuracy. In ECLD-SFF, a specially designed insulation tube is used to constrain the electric field of the pin

anode, which will provide a concentrated electric field between the substrate and the pin so that the deposition occur only in a very small area. Since both the tube and pin wire can be made very thin, the scanning accuracy will be very high. (3) High density and low shrinkage. In ECDB-SFF, the assistant electric fields are used to increase the amount of the deposited materials among the powders, and the assistant magnetic field is used to increase the accumulation density of the ferromagnetic powders. Also, the layer thickness of the powder can affect the density. The thinner the layer of the powder, the higher the density should be. The high density will lead low shrinkage in later sintering and infiltration. (4) Controllable microstructure. In ECLD-SFF, the microstructures of the formed part can be controlled by changing the composition and the layer thickness of the powder. For example, for the working surfaces of a mold, which needs a higher hardness, we can reduce the layer thickness of the powder in order to increase the density or we can use a mixture of ceramic and metal powders.

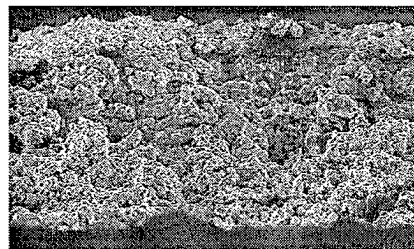
FRACTAL PHENOMENA IN ECLD-SFF

Existing researches on electrochemical deposition and our initial experiments on ECDB-SFF revealed the following interesting phenomena and also challenges. (1) Researches and experiments have shown that metal particles in a suitable electroplating medium can be connected by directed electrochemical growth (Bradley, et al., 1997, 1998). Our experiments further show that if some metal powders are laid on the cathode plate (substrate) and sunk into the liquid medium (Fig. 1), the powder particles can be bound under the action of electric fields and form a solid with a certain strength. In Fig. 3a, an SEM photo shows a ropelike deposit connecting to a particle at the initial growth stage. Our research result, in Fig. 3b, shows the formed powder layer bound by the deposits. (2) Researches and experiments have shown that the electrochemical deposition is a fractal growth process even the distance between two particles is very short, and the fractal growth always occurs in the direction of the electric field (Brady and Ball, 1984). The fractal dimensions of the growing branches and the width of the deposited metal band all decrease with the increasing electric field. Fig. 3c shows several stages of the fractal growth, from which one can see when some new fractal branches are forming, some formed fractal branches may disappear at the same time. After a longer time only a few main branches can survive. (3) Researches and experiments have shown that by using assistant electric fields in surrounding directions (Fig. 1), a web-like deposits among particles can be formed (Fig. 3d). (4) Our initial research has shown that the surface topography of the bound powder particles has fractal structures, and the fractal dimension depends mainly on the composition of the medium, the processing time and the strength of the electric and assistant magnetic fields (Fig. 3e). An assistant magnetic field can increase the particle density and affect the dimensions of the fractal surfaces. (5) Researches and experiments have shown that during the electrochemical process the voltage and current are unstable. There is a critical point of processing time for the deposition among each layer (see Fig. 4). At this critical point the constant voltage will drop sharply to a very low value. From then on the electrochemical deposition process will stop basically until new powders are added on the top surface, and then the voltage recovers to the initial value. This phenomenon can be used to detect and control the fractal growth process.

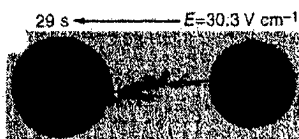
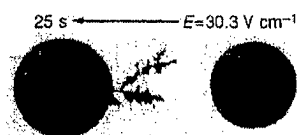
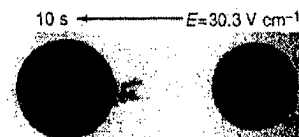
It is very obvious that the above mentioned electrochemical deposits growing process to bind metal powders under electric and magnetic fields is a complex fractal problem.



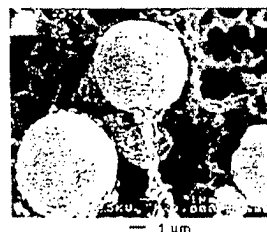
(a) A ropelike deposit on a particle at initial growing



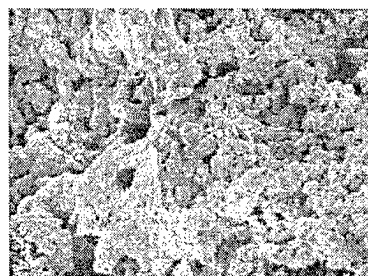
(b) The powder layer bound by deposits (1 mm thick)



(c) Three stages of fractal growth, at 10s, 25s, 29s

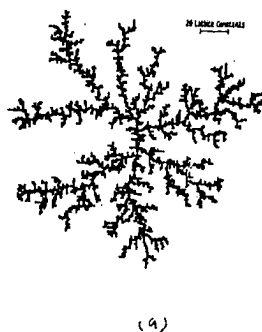
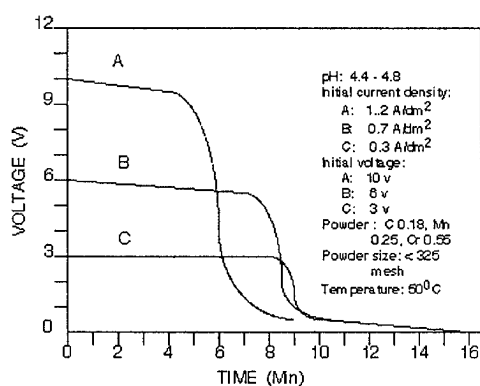


(d) Weblike deposits among particles



(e) The fractal surface topography of bound particles

Fig. 3. Five SEM photos showing fractal growth phenomena



(a)

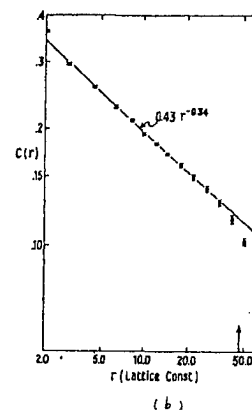


Fig. 4. Relation of the voltage and time, Fig. 5. (a) 3600 particles aggregation on a square lattice, (b) Simulation based on DLA model

FRACTAL GROWTH MODELS

The authors considered several fractal growth models to obtain information on the deposit and explain the above mentioned fractal growth phenomena. First, we consider the simplest case i.e., the fractal growth between two electrodes, then consider the model between

two powder particles in single electric field. For the growth among the powders containing a large amount of particles, we will try to use the re-normalization group method.

1. Diffusion-Limited Aggregation (DLA) Model Between Two Electrodes

The goal of this model is to find the density distribution of the deposit in a small area between the pin anode and the plate cathode. It is expected that the density distribution is related to the microstructures and accuracy of the product. The pin anode with a diameter d is above the center of a metal disc and the cathode/disc has a diameter D . We assume that d is much smaller than D , and the end of the pin is so close to the disc surface that the deposition can be assumed as a 2-D process occurring on the disc. After a metal atom in the pin anode losses its electrons and become an ion, it will move into the plating liquid. Once the ion contacts the cathode surface it will get electrons and deposit on the disc. The second, ion walks randomly until it visits a site adjacent to the first one and the walking particle becomes part of the cluster. The next particle joins the cluster at a random distant point, and so forth. With the increase of deposited atoms the average walking distance of an ion before contacting the cathode will decrease. The exposed ends of the cluster tend to grow more rapidly than other perimeter sites because these sites are "shadowed" by the deposits. The above mentioned growth process can be simulated with the Diffusion-Limited Aggregation (DLA) model. This model was first developed by Witten & Sander (1981), in which the so-called "shadow" effect is expressed as "diffusion-limited". In a 2-D DLA model a particles, i.e. ion is released from a random position on the boundary of a square lattice at regular intervals. The released particles will walk randomly in the lattice until join the aggregate. If assuming the distance γ separating two sites is much less than the size D of the aggregate, we can obtain information about the deposit-particle distribution from the following density correlation function:

$$C(\gamma) = N^{-1} \sum_{\gamma'} \rho(\gamma') \rho(\gamma' + \gamma), \quad (1)$$

where γ' denotes the distance variable, N is the total number of deposit-particles, the density $\rho(\gamma)$ is defined to be 1 for the occupied site and 0 for the others. Fig. 5a shows a 3600-particle aggregate on the lattice. Fig. 5b shows the simulation results, in which the solid line is a least-squares fit over the range $\gamma = 3$ to $\gamma = 27$. The error bars represent the spreads of values among the six samples of aggregate. The arrow marks the average radius of the gyration. The simulation shows

$$C(\gamma) = 0.43\gamma^{-0.343 \pm 0.004}. \quad (2)$$

From this we can get the following results. (1) The density distribution depends only on the distance separating two sites providing the distance is much less than the size of the aggregate. (2) The density correlation within the model aggregation falls off with distance obeying a fractal power law. (3) The maximum of density is only 0.43 (let $\gamma = 1$ in Eq. (2)). The lower density of the deposit will cause large shrinkage, distortion and low strength of product. This is why we do not use direct electrochemical deposition between two electrodes. (4) Considering that the real deposition occurs on a smaller circular area not a large square area and the ions is not released from the boundary of the deposition area, the density of the center region close to the pin anode must larger than that of others. This kind of distribution is desirous to the high accuracy of products. This 2-D model can be analogized to 3-D and was verified by experiments (Brady, 1984). However, DLA model is not so suitable to describe the fractal

growth in our ECLD-SFF study. First, according to DLA model, we can not get any formula used to calculate the growth rate. Second, our experiments showed that the fractal growth occurs between the polarized powder particles not between the electric poles. Thus the space between particles, the size and shape of the particles all affect the growth. Thirdly, according to the DLA model, the growth process can continue forever without any critical points of cease-growing like illustrated in Fig. 4. Therefore, other two models were developed.

2. Modeling on the Fractal Growth between Two Metal Particles

The main goal of this model is to obtain a formula on the growth rate of deposits between powder particles. If the boundary and initial conditions can be got, according to the formula we can calculate the growth rate, then estimate the production rate. Production rate is very important not only to ECLD-SFF but also to other rapid tooling techniques. The fractal growth between two powder particles (not atoms) is shown in Fig. 6. After an electric field is applied to a pair of particles, both of them will be polarized (Fig. 6a). Initially the particle close to the anode will liberate metal ions while the particle close to cathode will reduce solvent (Fig. 6b). The concentration of the ions near the former one is much higher than that near the latter one. The ions will move towards the latter one by diffusion, and when the ion concentration around the latter particle reaches a critical value the electrodeposition will occur and the fractal branch begin to grow to facing the other particles (Fig. 6c). It is first assumed that the single electric field between two spherical particles has a cylinder shape (Fig. 6d), the ion concentrated along the X-axial direction has a continuous distribution. If the distance between the two particles is long enough, the effect of the shape of the particle can be neglected, then the concentration distribution along the radial r-direction will be uniform. Thus we can use $U(x, t)$ denotes the concentration at point x at time t . If R denotes the radius of the particle, we have $-R < r < R$. In a very small area $\delta(x, r)$ around the center point $C(x, r)$, the ion number will be $U(x, t)\delta(x, r)$. If assuming that ions all obey Brownian motion law and are independent with each other, then it can be deduced that the ion concentration at time $t + h$ has the following normal distribution:

$$U(x', t + h) = (2\pi h)^{-1/2} \exp[-(x - x')^2/(2h)]U(x, t)dx \quad (3)$$

By differentiating x' and h , we obtain

$$\partial U / \partial t = 0.5 \nabla^2 U \quad (4)$$

where ∇^2 denotes the second order partial differentiation. The boundary conditions of this differential equation are assumed as follows: On the surface of the particle near the cathode the ion concentration is a constant during the process, i.e., $U(x = 0) = U_0$. Using F_t denotes the depositing bound at time t , on F_t all ions will lose their electric charges, so we have $U(F_t) = 0$. The growing rate of F_t in its orthogonal direction will be

$$V_n = K_n \nabla U \quad (5)$$

where ∇ denotes the first order partial differentiation and K is a coefficient of per unit time growing rate.

This model also can not describe the critical phenomenon shown in Fig. 4, because it is related to only a few particles. As we know most critical phenomena occur in the systems consisting of a large number of individual units.

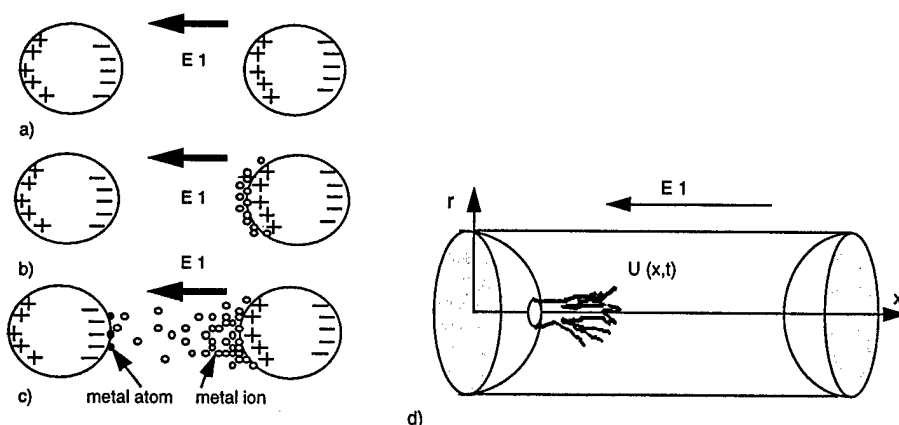


Fig. 6. Fractal growth of deposits between two particles

3. Modeling on the Fractal Growth among a Large Amount of Particles

It is impossible to treat fractal growth related to many particles by conventional analytic methods. Even if we can deduce a very complex model to describe the growth among ten particles, we are still not sure if it can be used to describe the case of more than ten particles, and whether the results can be used to explain the complex growth phenomena. So we will try to use the re-normalization group method which has been used to treat various phase transformation or critical problems (Wilson and Kogut, 1974). Considering a 2-D array which contains a large amount of particles, if four neighbor particles can be connected by deposited material just like that shown in Fig. 3, we call the unit containing four connected particles breakover cell. Under the action of the electric fields, some units in the array may become breakover cells, but others may not. With the time increasing, the number of breakover cells will be more and more. But when the number reaches a critical value the whole array will become breakover by connecting a lot of neighbor breakover cells and forming some breakover cell clusters. Once the array becomes breakover, the distribution of electric fields on the array will be changed greatly. Further depositing new material among the remained individual particles will be very difficult, so the process will stop. We think it may be the main reason why the voltage will drop down very quickly after a period in the ECLD-SFF process in Fig. 4. The goal of this model is to find the conditions that the cluster can form and the density of the breakover. If the formed clusters have the fractal structure, we also want to know their fractal dimension.

In the 2-D array model, assuming the breakover probability of a four-particle unit is p_0 , critical point probability p_c . It has been known when $0 < p_0 < p_c$, the cluster forming probability P is very small. However, when $p_c < p_0 < 1$, P will be very close to 1. Although by using Monte Carlo method one can calculate the value of p_c , when there are a lot of particles, the calculation will be very difficult and time-consuming. Here we are introducing the re-normalization group method. As shown in Fig. 7a, four adjacent particles form into an initial unit, and it has the breakover probability p_0 . Four adjacent initial units form into a first degree unit with breakover probability p_1 , and four first degree units form a second degree unit with probability p_2 , and so on. Based on the principle of re-normalization group, p_2 can be calculated from p_1 , p_3 can be calculated from p_2 , p_4 can be calculated from p_3 , and so on. Fig. 7b-7f show all probable cases of four first degree units. The probability that all four initial units are not breakover is $(1 - p_0)^4$ (Fig. 7b). The probability that only one initial unit is breakover will be $p_0(1 - p_0)^3$ (Fig. 7c). The probability that only two initial units are breakover should be $p_0^2(1 - p_0)^2$ (Fig. 7d). The

probability that only one initial unit is not breackover is $p_0^3(1-p_0)$ (Fig. 7e). The probability that all initial units are breackover is p_0^4 . Therefore, the probability that a first-degree unit is breackover will be

$$p_1 = 2 p_0^2(1 - p_0)^2 + 4 p_0^3(1 - p_0) + p_0^4 = 2 p_0^2 - p_0^4 \quad (6)$$

Then considering the second degree unit with the same method, we get $p_2 = 2 p_1^2 - p_1^4$. A general equation is

$$p_{n+1} = 2 p_n^2 - p_n^4 \quad (7)$$

Figure 8 shows the iteration relationship between p_{n+1} and p_n . This equation can be rewritten as

$$f(x) = 2x^2 - x^4 \quad (8)$$

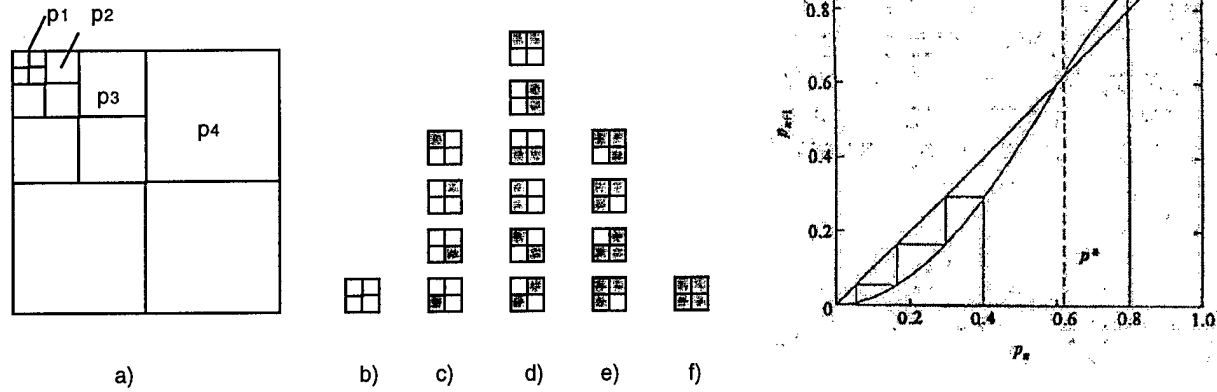


Fig. 7. The breackover probabilities of the first degree unit, Fig. 8. Iteration between p_n and p_{n+1}

Let $f(x) = x$ ($0 < x < 1$) and we get three solutions (fix points): $x_1 = 0$, $x_2 = 0.618$ and $x_3 = 1$. Their corresponding values of $df(x)/dx$ will be $\lambda_1 = 0$, $\lambda_2 = 1.582$ and $\lambda_3 = 0$. Therefore, both x_1 and x_3 are stable, but x_2 is unstable because $\lambda_2 > 1$. So the critical probability p_c will be 0.618. It is an approximate value. In order to improve the accuracy we can chose 3×3 unit instead of 2×2 unit and obtain,

$$p_{n+1} = 3 p_n^3 + 3 p_n^4 - 2 p_n^5 - 15 p_n^6 + 18 p_n^7 - 7 p_n^8 + p_n^9 \quad (9)$$

According to this equation, we calculate $p_c = 0.609$ that is closer to the value obtained from Monte Carlo method. From the obtained critical value, we can deduce the critical particle number n_c of the cluster,

$$n_c \approx n^{0.5d_f} \quad (10)$$

where n is the total number of the particles in a 2-D array, and d_f denotes the fractal dimension of the cluster. If n is big enough we can get $d_f \approx 1.896$. Then the ratio between n_c and n can be calculated. For example, when $n = 10,000$, the ratio is about 55%. It means when the depositing process stops, over a half of the metal particles can be connected. However, the real ECLD-SFF process should be considered in 3-D models. In the simplest case, the initial unit will include 2×2 particles. But there are three ideal stacking modes of the metal particles, i.e., Body

Centered Cubic(BCC), Face Centered Cubic(FCC) and Hexagonal Close-packed (HCP). For different stacking mode the critical probability will be very different. In addition, we must consider the effects of voids in real metal powders. The 3-D model of fractal growth is very challenge and promising.

CONCLUSIONS

It has been found that the electrochemical deposition among metal particles during ECLD-SFF is a fractal growth process. The fractal dimension and the width of the deposited metal band are all related to electric field density, composition of electroplating liquid and processing time. Based on the DLA model of the fractal growth between two electrodes we know that the density distribution depends only on the distance separating two sites, the density correlation within the model aggregation falls off with distance obeying a fractal power law, and the maximum of density is only 0.43. According to a 2-D re-normalization group model, the critical phenomenon on the fractal growth will occur when the whole powder layer becomes breakover. In the critical case the formed powder cluster's fractal dimension is 1.896, the ratio of the particles connected by the deposits is about 55%. Based on the fractal model we can calculate growth rate of deposits.

REFERENCES

- Ashley, S., "From CAD Art to Rapid Metal Tools," Mechanical Engineering, ASME, March 1997, pp. 1-11
- Ashley, Steven, "Rapid Prototyping Industry's Growing Pains," Mechanical Engineering, ASME, July 1998, pp. 64-68.
- Birmingham, B. R. and Marcus, H.L., In Solid Free -form Fabrication Symposium Proceedings, Beaman, H.L. et al. eds, University of Texas Press, Austin, TX, 1995, pp. 389-396
- Bradley, J. C. et al., "Creating Electrical Contacts Between Metal particles Using Directed Electrochemical Growth", Nature, Vol. 389, 1997, pp268-270
- Bradley, J. C. et al., "A Contactless Method for the Directed Formation of Submicrometer Copper Wires", J. Electrochem. Soc., Vol. 145, 1998, pp45-48
- Brady, R. M. and Ball, R. C., "Fractal Growth of Copper Electrodeposits", Nature, Vol. 309, 1984, pp225-229
- Jakubenas, K. J., Sanchez, J.M. and Marcus, H.L., Multiple Material Solid Free-Form Fabrication by Selective Area Laser Deposition, Journal of Materials and Design, 1997
- Lehmann, O. and Stuke, M., Mater. Lett., 1994, 21, 131
- Mandelbrot, B. B., "How long is the coast of Britain? Statistical self-similarity and fractal dimension", Science Vol. 156, 1967, pp636-638
- Maxwell, J., Pegna, J. and Hill, E., In Solid Free -form Fabrication Symposium Proceedings, Beaman, H.L. et al. eds, University of Texas Press, Austin, TX, 1995, pp. 143-150
- Sudarshan, T.S., Surface Modification Technologies: An Engineering's Guide, MARCEL DEKKER Inc., New York, 1989, pp135-188.
- Wilson, K. G. and Kogut, J., "The renormalization group and the expansion", Phys. Rev. C12, 1974, pp75
- Witten, T. A. Jr. and Sander L. M., "Diffusion-Limited Aggregation, a Kinetic Critical Phenomenon", Phys. Rev. Letter, Vol. 47, 1981, pp1400-1403.

Residual Stresses in Layered Manufacturing

A. Nickel, D. Barnett, G. Link, and F. Prinz

Department of Materials Science and Engineering, Stanford University

Abstract

Layered Manufacturing processes accumulate residual stresses during material build-up. These stresses may cause part warping and layer delamination. This paper presents work done on investigating residual stress accumulation and part distortion of Layered Manufactured artifacts. A simple analytical model was developed and used to determine how the number of layers and the layer thickness influences part warping. Results show that thin layers produce lower part deflection as compared with depositing fewer and thicker layers. In addition to the analytical work, a finite element model was developed and used to investigate the deposition pattern's influence on the part deflection. Finite element model and corresponding experimental analysis showed that the geometry of the deposition pattern significantly affects the resulting part distortion. This finite element model was also used to investigate an inter-layer surface defect, known as the Christmas Tree Step, that is associated with Shape Deposition Manufacturing. Results indicate that the features of this defect are influenced only by the material deposited close to the part surface and the particular material deposited. The step is not affected by the deposition pattern.

1 Introduction

Residual stresses develop in many Layered Manufacturing processes. These stresses arise from the contraction or expansion associated with the deposition of a layer, which causes distortions and possibly failure by layer delamination or cracking. Many authors have examined residual stresses in Layered Manufacturing. Jayanthi et al. [1], Ullett et al. [2], and Jacobs [3] each discuss how the scanning pattern of the laser in Stereolithography affects the resulting deflection of the part, while Karapatis et al. [4] and Dalgarno et al. [5] studied residual stresses in metal parts produced using Selective Laser Sintering. McIntosh et al. [6] examined deformation of ceramic parts produced using Fused Deposition of Ceramics. Both Maziasz et al. [7] and Griffith et al. [8] measured residual strain in H13 tool steel parts produced by Laser Engineered Net Shaping. In addition, Chin et al. [9,10] and Klingbeil et al. [11,12] examined residual stresses and deformation in microcasted metal parts produced using Shape Deposition Manufacturing (SDM). In all of these processes residual stresses accumulate and lower the quality of the manufactured parts.

This research focused on thermal stresses in laser deposited metal parts produced using SDM. SDM is a Layered Manufacturing process developed jointly at Carnegie Mellon University and Stanford University [13]. SDM's unique features include material removal after each layer is deposited and the use of a sacrificial support material to facilitate the deposition of overhanging structures. Metal parts are produced by feeding powders into a molten pool formed by a 2.4 KW Nd:YAG laser. The laser and the powder feed are then scanned over the surface of the part producing a deposited layer. After several laser passes, the desired layer thickness is achieved and the excess material is then removed with a computer controlled (CNC) milling machine. Thermal stresses in these parts were investigated using a combination of analytical modeling, finite element modeling, and experiments. Initially an analytical model was developed to predict the overall part warpage. Then both a finite element model and experiments were used to investigate how the pattern used to deposit a layer influences the substrate warpage, and to investigate the inter-layer surface defect known as the Christmas Tree Step.

2 Analytical Model

This research began by first developing an analytical model to predict substrate warpage. Both elastic and elastic-perfectly plastic models were investigated. These models are similar to the models developed by Townsend et al. [14]. In this model, the radius of curvature of the substrate, or equivalently, the substrate deflection was determined (figure 1). To solve for the deflection, the time dependent laser deposition process was approximated with two time steps. The first step includes the laser heating, and the second step includes the beam cooling after the laser energy is removed. The conditions of equilibrium, namely the summation of the forces to zero and the summation of the moments to zero were then used to determine the deflection. In the elastic-perfectly plastic model, additional continuity conditions were necessary to solve for the position of the elastic plastic boundaries.

The results of the calculation for a 6.3 mm x 25.4 mm x 152.4 mm beam substrate are shown in table 1. In addition, experiments were performed for comparison with the calculated results. The experimental values are shown in table 2. The elastic analytical

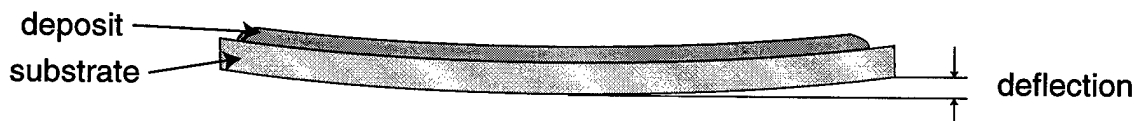


Figure 1: Deflection of a beam substrate subjected to laser deposition.

Model	Bolting Conditions	1/R	Deflection Invar 36	Deflection 1117 steel
Elastic	no constraint	$\frac{3}{4h}\alpha(T_{room} - T_{melt})(1 - (\frac{r}{h})^2)$	0.82 mm	6.21 mm
Elastic-Perfectly Plastic	no constraint	$-12\frac{\sigma_{yield}}{E}\frac{h(h-r)}{(r+h)^3}$	not valid	0.83 mm
	constrain bending	$-\frac{3}{2}\frac{\sigma_{yield}}{E}\frac{(h-r)}{h^2}$	not valid	0.50 mm
	constrain bending and axial	$-\frac{3}{4}\frac{\sigma_{yield}}{E}\frac{(h^2-r^2)}{h^3}$	not valid	0.16 mm

Table 1: Calculated deflection values for 6.3 mm x 25.4 mm x 152.4 mm (1/4 in x 1 in x 6 in) substrates where $2h$ is the thickness of the substrate, α is the expansion coefficient, T_{room} is room temperature, T_{melt} is the melting temperature, $(h - r)$ is the depth of remelting, σ_{yield} is the yield strength, and E is the elastic modulus.

model accurately predicted the deflection for Invar substrates. However, the elastic-perfectly plastic model was necessary for low carbon steel substrates due to the significant amount of plastic deformation that occurs in these substrates. As shown in table 1 the elastic-perfectly plastic equations are not valid for Invar since no plasticity occurs in the calculation for Invar substrates. The results show that for the elastic-perfectly plastic model, bolting the substrate down during deposition reduced the part deflection. Chin et. al. [9] noted a similar result for microcasted SDM metal parts. The results of this calculation also show the deflection dependence on material and process properties. In the elastic model the deflection depends on the expansion coefficient, the remelted depth, and the change in temperature that occurs during the substrate cooling. In the elastic-perfectly plastic model the deflection depends on the yield strength, the elastic modulus, and the remelted depth. Table 2 shows that the experimental deflection depends on the deposition pattern. The deflection dependence on the deposition pattern cannot be modeled analytically and is discussed using a finite element model in the next section.

Pattern	Bolting Condition	Deflection Invar 36	Deflection 1117 steel
long raster	bolted	0.79 mm	1.00 mm
short raster	bolted		0.44 mm

Table 2: Experimental deflection values for 6.3 mm x 25.4 mm x 152.4 mm (1/4 in x 1 in x 6 in) substrates

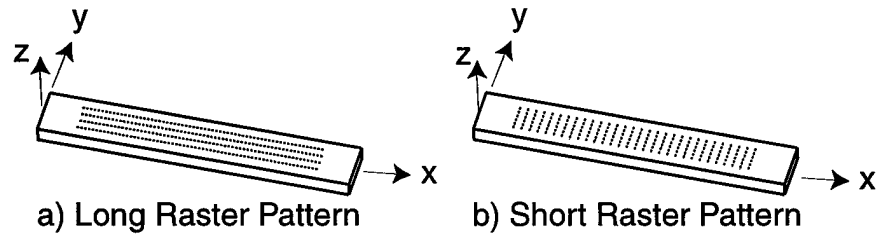


Figure 2: Long and short raster deposition patterns for a beam substrate.

This model was then used to examine how the deposit thickness and the number of layers used to produce the deposit influences the warpage of the part. The deflection of a beam substrate is plotted against the deposit thickness in figure 3. Each line in this graph represents a constant number of layers used to achieve the desired deposit thickness. The results indicate that depositing thinner layers reduces the deflection and that the majority of the deflection accumulates for deposit thicknesses up to the substrate thickness.

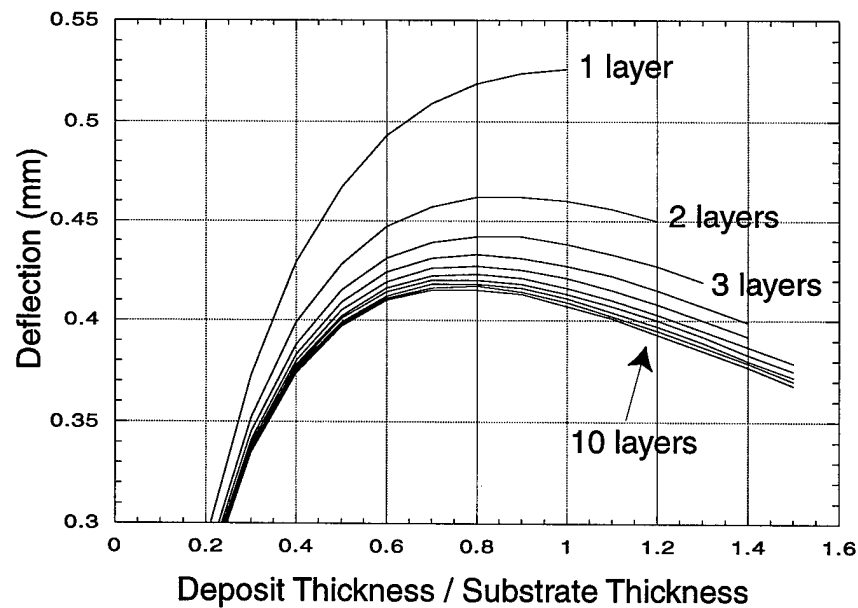


Figure 3: Deflection verses deposition thickness and the number of layers used to produce the deposition.

3 Deposition Pattern

In SDM of metal parts many deposition patterns can be used to deposit a layer. The pattern used has a significant influence on the substrate warpage. The deflection depen-

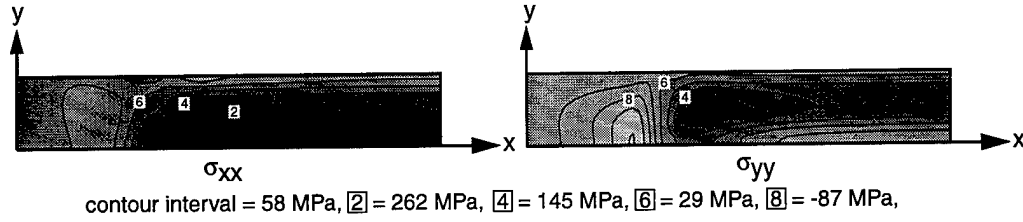


Figure 4: The finite element calculated stresses on the top surface of a beam substrate after the last line in the long raster pattern has been scanned and the substrate has cooled to room temperature.

dence on the deposition pattern was investigated using both finite element modeling and experiments.

The finite element results for a 6.3 mm x 25.4 mm x 152.4 mm beam substrate are shown in figures 4 and 5. In figure 4 the final σ_{xx} and σ_{yy} stresses on the top surface of a beam substrate is shown due to a long raster deposition pattern (figure 2). Only 1/4 of the beam is shown due to assumed symmetry planes along the x and y axis. This figure shows that the highest stresses are found along the deposition lines. Since the deposition lines are oriented in the x direction for the long raster pattern, the σ_{xx} stress is larger than the σ_{yy} stress as shown in figure 4. Similar results were reported by Andersson [15] and Jonsson et al. [16] for stresses in welded structures. In figure 5 the σ_{yy} stress is shown after the first line in the short raster pattern has cooled and after the last line in the short raster pattern has cooled. This figure shows that the highest stresses are found where the last line was deposited.

The optimal deposition patterns for both a 6.3 mm x 25.4 mm x 152.4 mm beam and a 6.3 mm x 152.4 mm x 152.4 mm plate substrates were determined from these observations. The lowest deflection for a beam substrate occurs by minimizing the σ_{xx} stress. Since the short raster pattern does not have any deposition lines oriented along the x axis, it produces

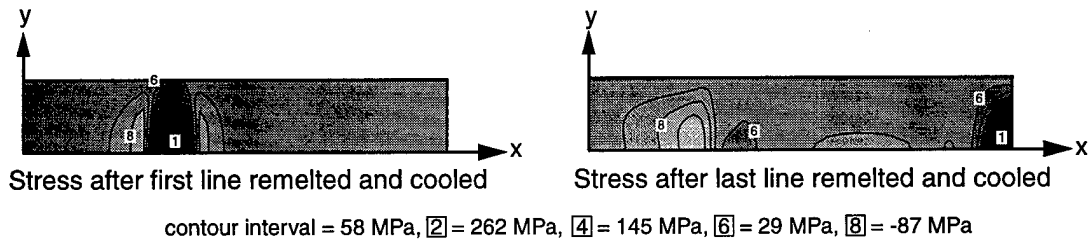


Figure 5: The finite element-calculated σ_{yy} stress at the top surface of a beam substrate after the first line and the last line in the short raster pattern has been scanned and the substrate has cooled to room temperature.

the lowest σ_{xx} stress. Therefore, this pattern results in the lowest beam deflection. The finite element calculated deflection values were 0.92 mm for the long raster pattern and 0.39 mm for the short raster pattern. These results match closely the experimental values of 1.00 mm for the long raster pattern and 0.44 mm for the short raster pattern. Using the observation that the highest stresses are found where the last line was deposited, the lowest deflection for a plate substrate occurs by minimizing the length of the last line deposited. Therefore, a spiral pattern scanned from the outside to the inside will produce low and uniform stresses for a plate substrate. The finite element-calculated value for the deflection along the centerline of the plate was 0.34 mm and the experimental value was 0.49 mm. This deflection is contrasted with a spiral pattern scanned in the opposite direction which has a calculated deflection of 0.55 mm and an experimental deflection of 0.60 mm. Klingbeil et al. [12] experimentally observed similar deflections for microcast patterns on plate substrates.

4 Christmas Tree Step

SDM suffers not only from the global distortion previously discussed, but also from a local defect known as the Christmas Tree Step. This step is found at the layer interface and results in poor surface quality and part inaccuracy. Figure 6 shows this defect on a metal part.

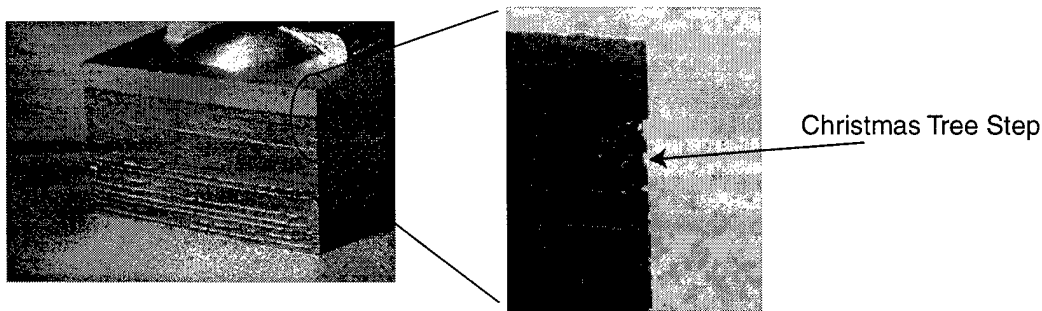


Figure 6: The Christmas Tree Step on a metal part.

An experiment was performed to investigate which processing steps influence the magnitude of the Christmas Tree Step. The experiments showed that the support material deposition and machining did not significantly distort the part edge. However, if sharp cutters and small cutting depths were not used, removal of excess support material could significantly deform the edge of the part. The experiments also show that the majority of this distortion develops during the deposition of the part material.

A finite element model and experiments were used to make three observations on the

development of the Christmas Tree Step. Firstly, it was determined that the step is an edge effect. Figure 7 shows the step size as a function of the deposition length for a 0.75 mm thick deposited layer. Both the finite element and experimental results in this figure show that the step develops due to the material deposited close to the edge of the part. Secondly, it was determined that the step size does not depend significantly on the deposition pattern. Experimentally the average step size for a 0.75 mm thick layer deposited using a long raster deposition was $46.9\text{ }\mu\text{m}$, and the step size obtained using a short raster pattern was $39.6\text{ }\mu\text{m}$. These results show that there is only a small difference in step size for the two different deposition patterns. Finally, experimentally the step size was found to depend on the particular material deposited. The step size for a 3 mm thick was $102\text{ }\mu\text{m}$, $70\text{ }\mu\text{m}$, and $33\text{ }\mu\text{m}$ for 316 stainless steel, Invar, and 410 stainless steel, respectively. It is believed that this martensitic 410 stainless steel produced the lowest step size due to the solid state phase transformations that occur upon cooling and on subsequent reheating during future depositions.

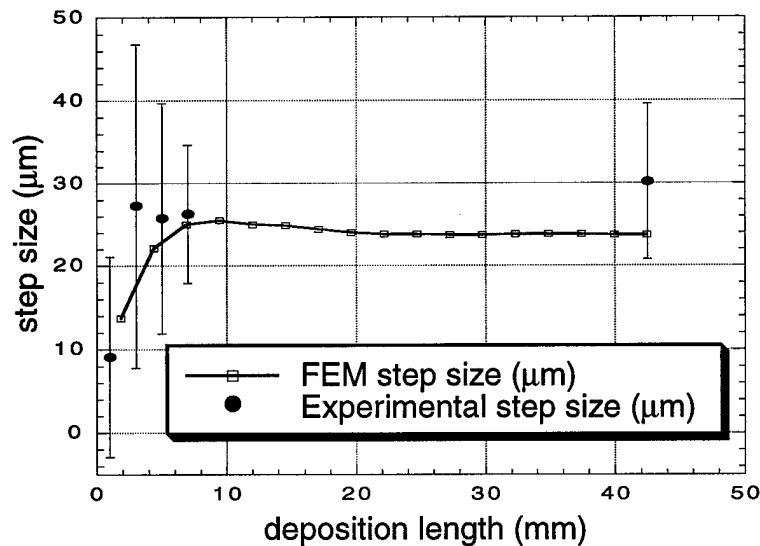


Figure 7: The Christmas Tree Step size as a function of deposition length.

5 Conclusion

This research increased the understanding of residual stress accumulation in metal parts produced using Shape Deposition Manufacturing. The combination of analytical modeling, finite element modeling and experiments was used to predict overall part deflection, to understand the influence of deposition patterns on part warpage, and to understand the

development of the Christmas Tree Step. Although these results were found while researching metal parts produced using SDM, many of the findings are applicable to parts produced using other Layered Manufacturing processes. The elastic-perfectly plastic model results are applicable to any Layered Manufacturing processes that involve some form of permanent deformation during cooling. Also, the deposition pattern findings are valid for processes that produce layers by scanning material over the part surface. In addition, the results from the Christmas Tree Step analysis give insight into the local deformation processes that occur near the part edges for many Layered Manufacturing techniques. To produce accurate Layered Manufactured parts, continuing research is necessary to understand and reduce the adverse affects of residual stress accumulation.

6 Acknowledgments

The authors gratefully acknowledge the Department of the Army for administrating contract #DAAH04-96-1-0241 for the Defense Advance Research Projects Agency and the Office of Naval Research (#N00014-96-1-0354) for their support of this research.

7 References

- [1] S. Jayanthi et al., Proc. Solid Freeform Fabrication Sym., 250-258, 1997.
- [2] J. Ullett et al., Proc. Solid Freeform Fabrication Sym., 242-249, 1994.
- [3] P. Jacobs, Rapid Prototyping and Manufacturing, 1996.
- [4] N. Karapatis et al., Proc. Solid Freeform Fabrication Sym., 79-87, 1998.
- [5] K. Dalgarno et al., Proc. Solid Freeform Fabrication Sym., 721-728, 1998.
- [6] J. McIntosh et al., Proc. of the Solid Freeform Fabrication Sym., 159-166, 1997.
- [7] P. Maziasz et al., Scripta Materialia, 39(10):1471-1476, 1998.
- [8] M. Griffith et al., Proc. Solid Freeform Fabrication Sym., 89-96, 1998.
- [9] R. Chin et al., Proc. Solid Freeform Fabrication Sym., 221-228, 1995.
- [10] R. Chin et al., Proc. Solid Freeform Fabrication Sym., 507-514, 1996.
- [11] N. Klingbeil et al., Proc. Solid Freeform Fabrication Sym., 125-132, 1997.
- [12] N. Klingbeil et al., Proc. Solid Freeform Fabrication Sym., 367-374, 1998.
- [13] R. Merz et al., Proc. Solid Freeform Fabrication Sym., 1-8, 1996.
- [14] P. Townsend et al., J. Applied Physics, 62(11):4438-4444, 1987.
- [15] B. Andersson, J. Eng. Mat. Tech., 100(4):356-362, 1978.
- [16] M. Jonsson et al., Numerical Methods in Heat Transfer, vol. 3, chap. 2, 1985.

Thermal Effects of In-Bed Rapid Prototyping Metastructures

Jeffery L. Norrell Kristin L. Wood Richard H. Crawford
Graduate Student Associate Professor Associate Professor

Mechanical Engineering Department
The University of Texas at Austin

Abstract

In an effort to produce higher quality Selective Laser Sintering (SLS) parts, a number of approaches have been taken. One such approach is the use of in-bed metastructures, such as tortillas and canisters. In past work, these metastructures have produced changes in part quality, but only qualitative analysis has been done. Using a model created during previous work, a numerical study of these in-bed metastructures is undertaken, with the goal of systematically determining the thermal effectiveness of the various structures. The thermal behavior of in-bed structures subjected to mixed mode convection and conduction is then determined. Results demonstrate that in-bed structures can be designed to *spatially* affect in-bed thermal transfer, providing SLS users the capability to remove or retain heat as a part's local geometry demands.

1 Introduction

Selective Laser Sintering (SLS), a process wherein a laser is rastered across layers of powder in the fabrication of complex 3D parts, is inherently a thermally-based process. Thermal energy in the process drives both local powder consolidation and attachment of a given layer to those layers underneath. With potential SLS part uses including geometrical design visualization, patterns for injection molding, and directly-produced parts, the overall dimensional accuracy of the SLS process is of extreme importance.

In direct conflict with this desire for accurate SLS parts are phenomena including curl, or local part warpage, and growth, or local areas of uncontrolled powder consolidation. Both factors are postulated to be due to lack of thermal control [6, 11].

Through the use of experimentation and numerical simulation [12], we have created a method satisfactory for describing a bulk powder bed's thermal behavior as a function of time and mixed mode heat transfer. But, how might this method be applied to improve SLS part quality through machine, material, or process design?

One potential process modification is the use of supplemental in-bed structures, such as tortillas, to alter a bed's behavior. The developed model [13, 14], when applied to in-bed structures, can answer a number of important questions for us. Will tortillas and other structures lead to quicker bed cooldown times, providing a quality increase through higher production rates? Will these "metadevices" hamper thermal transfer out of formed parts, delaying part extraction but potentially reducing the development of in-part stresses, resulting in higher quality parts through increased geometrical accuracy?

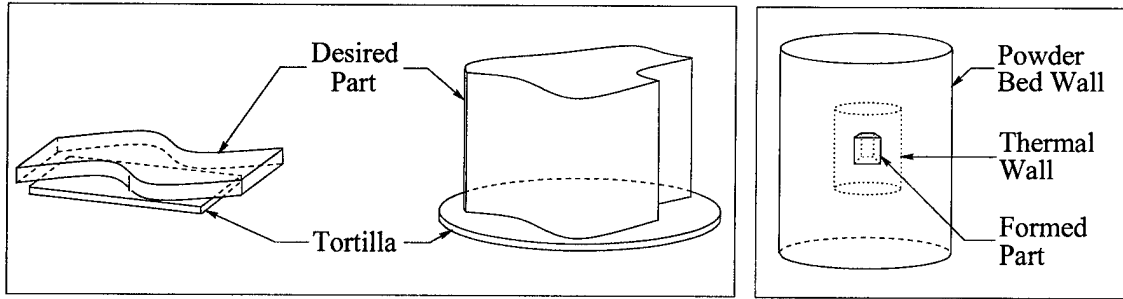
In this paper we describe tortillas and other in-bed structures, such as thermal walls. This description is followed by a discussion of parameters governing metastructure usage. An application of the developed model is next, followed by a discussion of in-bed structure parameter sensitivity with respect to affecting a powder bed's thermal state. Finally, we conclude the paper with design recommendations regarding in-bed structure usage and summarize with key points.

2 What is an In-Bed Structure?

In-bed structures are geometry produced during the SLS process, in addition to the part geometry. These structures can come in a variety of shapes and sizes. Shapes range from flat layers to structures completely enclosing a part. These various shapes can be used in different locations within a powder bed, locally modifying a bed's physical properties. Thin in-bed support bases, or "tortillas", located near the bottom of SLS parts have been qualitatively shown to reduce part curl [2]. As well, in-bed structures completely enclosing SLS-formed parts, also known as canisters or containers, have been seen to have an effect on a

bed's thermal temperature [3]. Essentially, structures such as containers and tortillas represent methods potentially capable of *spatially* modifying a part bed's mechanical and thermal properties.

Consider the sample systems shown in Figure 1(a). Created prior to fabrication of the desired part, tortillas are thin disks located below a part, typically sintered at a density below that ultimately attainable for a given powder and 20 to 40 layers thick [2]. They are also spaced 10 or 20 layers below a part, where one layer is assumed to be 125 μ m thick.



(a) Tortilla examples.

(b) Thermal wall example.

Figure 1: Examples of in-bed structures.

Extending the basic plate-like shapes shown in Figure 1(a), attempts have also been made to expand tortilla usage. Attempted expansions include different shapes and layers supplemented with anchors. As well, in contrast with full layers, simple rings of one or two scan lines below formed parts have also been considered [3].

Extensive in-bed structures are further considered with thermal walls, as shown in Figure 1(b). Essentially, the same notion of a tortilla, or base "wall", is applied along the sides and top of a formed part to supplement any structure fabricated below a part. This thermal wall, completely enclosing a formed part as it is fabricated, is postulated to affect natural convection within a powder bed, thereby limiting thermal transfer from a part and resulting in better part quality from the slower in-bed thermal transfer [3]. Though this effect has not been analytically addressed, brief experiments support this assertion [3].

A logical next step in structure extension is a combination of disks, rings, and walls. A little creativity can result in a very complex arrangement including layers comprised of single discrete scan lines, layers of double scan lines, and layers containing both disks and discrete scan lines. It is believed that this agglomeration of layers forms a barrier, or "wall", beneath an SLS-formed part [3].

A limitless variety of in-bed structures is possible when one considers tortillas or more elaborate in-bed structures. The remaining question, however, is what *exactly* do these structures do for an SLS user?

3 Motivation for the Study

The phenomenon of part curl is commonly thought to be heavily dependent upon a bed's *thermal* behavior [11]. In-bed structures, such as tortillas and thermal walls, have led to qualitative improvements in part quality through the reduction of curl [2, 3]. However, the link between part quality improvement and in-bed structure usage is, at best, only empirically understood. Improvement due to structures may be a consequence of thermal, mechanical, or thermomechanical effects. There has been little work addressing which of these physical effects may lead to an in-bed structure's contribution.

However, in-bed structure usage is not without a cost. Powder used in the fabrication of an in-bed structure is powder that cannot be utilized in the creation of an actual part. Time and energy spent creating an in-bed structure directly translates to longer, more costly fabrication procedures. Without an in-depth understanding of in-bed structure effects, balancing the cost of using tortillas with the attained benefit is difficult, if not impossible. This work provides a means with which to evaluate the attainable benefit of in-bed structure use.

The use of our developed model [14] in the consideration of a powder bed modified with in-bed structures can directly lead to a design improvement in this instance, resulting in insights to remedy the unknowns regarding tortilla usage. By examining the significance of in-bed structures through fundamental thermal science, we can directly benefit the SLS process with improved use of in-bed structures. For example, powder usage can be reduced through the use of in-bed structures which have been optimized to provide sufficient benefit while minimizing the expense reflected in used powder.

4 Construction of Thermal Simulation of In-Bed Structures

With the above background and motivation, we now turn our attention to a simulation addressing the issue of metastructure thermal effects. In the application here, let us consider the customer need of a rapid cooldown time [4, 7, 8, 15]. A quicker post-production cooldown will potentially improve the SLS process by reducing cycle times. Such a reduction positively benefits manufacturing throughput of the SLS process. In this section we describe the systems under consideration, the parameters necessary to describe those same systems, and simulation arrangements used to study the systems.

4.1 Representative Systems

We begin by describing a representative SLS system. We consider variables available to describe in-bed structure usage, the in-bed structure material properties, and the process through which in-bed structures are utilized. In this context, we examine the thermal significance of in-bed structures.

4.1.1 Geometry

Consider a cylindrical powder bed approximately 0.43 m (17") deep and 0.25 m (10") in diameter. While current SLS machines utilize rectangular powder beds with these same nominal dimensions [1], a cylindrical bed allows us to exploit symmetry and avoid concerns with corners in the simulation, as shown in Figure 2.

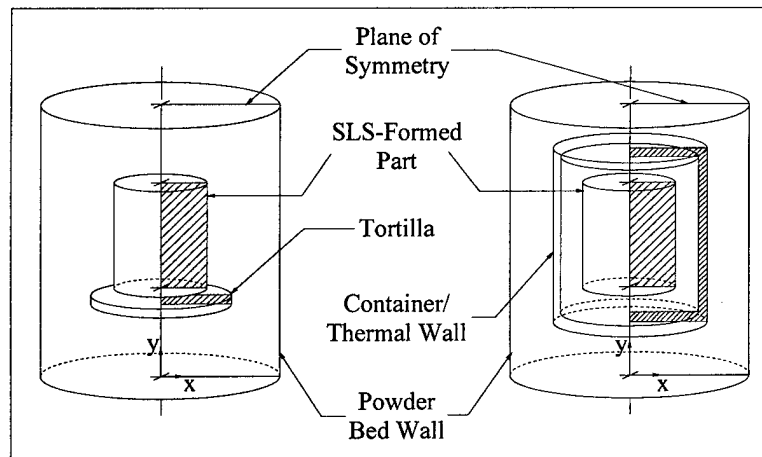


Figure 2: Representative systems, and planes of simulation.

As shown in Figure 2, the plane of symmetry which intersects each powder bed, in-bed structure, and SLS-formed part comprises our modeling domain for this study. Note that the cross-hatched regions in Figure 2 denote areas of "solid" in the symmetry plane, representing both the SLS-formed part and in-bed structure.

Unless being specifically varied, as a starting point in-bed structures are assumed to be approximately 50 layers thick, where one layer is $125\mu\text{m}$ in thickness [2]. As well, unless otherwise noted, a spacing of 20 layers is assumed above and below the SLS-formed part.

4.1.2 Material Properties

Along with the given system geometry, we need to characterize the material properties for our system. Bulk powder has a poured porosity of 0.5 [14]. For any part sintered to full density, let us assume a final porosity, ϕ , of 0.01. Assuming such a high degree of sinter ensures no fluid flow occurs through solid parts. Fluid flow through an SLS-formed part is highly dependent upon the part's geometry. The limitless geometrical variety possible in SLS machines makes this an intractable problem with respect to investigating in-bed structure thermal effects. Our assumed low porosity sufficiently scopes our problem.

Let us also initially assume that any in-bed structure, such as a tortilla or thermal wall, achieves a final porosity of 0.25. Such a porosity represents the decrease from an initial porosity of 0.5, driven by the structure being scanned with 40-50% of normal laser intensity [4, 8].

4.1.3 Extended Metastructure

One specific exception to the geometry and material properties discussed here is a more complex in-bed structure arrangement [3], akin to the thermal wall in Figure 1(b) but comprised of a multitude of rings, disk, and plates. In an effort to shed some light upon the results seen with this structure, let us also include this structure in our study.

For simulation purposes, we can calculate effective porosities and determine permeabilities for the thermal wall top, or cap, the thermal wall sides, and the extensive base. The cap is formed of several layers sintered to full density. With a resulting nominal porosity of 0.01, we assume that the cap's permeability, κ , is zero. In essence, it is assumed that no fluid flow will occur through the cap. With a bulk permeability of approximately 10^{-10}m^2 for unsintered powder [14], a permeability of zero for fully sintered powder is an acceptable assumption.

For the thermal wall sides, we have an effective porosity of 0.49. Of particular interest, however, is the permeability of the thermal wall sides. As discussed above in Section 2, the thermal wall sides are comprised of 4-ringed structures as shown in Figure 3.

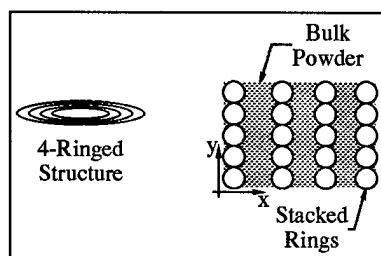


Figure 3: Detail of thermal wall construction for the extensive in-bed structure[3].

While an unintentional feature, the thermal wall morphology results in *anisotropic* permeability. With respect to the coordinate system in Figure 3, permeability in the x direction is essentially zero. In contrast, permeability in the y direction is that of the bulk material. This effect will also be addressed in our simulations.

Lastly, the thermal wall's extensive base has an effective porosity of 0.45 based upon calculating the total sintered volume and its density across all 188 layers. With effectively solid walls, top, and bottom, the base region also has a nominal permeability of zero.

4.2 Operating Parameters

With the system geometries and materials sufficiently characterized, we now turn our attention to the protocol to be simulated. Currently, entire powder beds, or "cakes", are pulled out of SLS machines after a part is formed. These blocks of powder, with the part inside, are then set aside to cool before the formed part can be safely handled. Cool down periods can range up to 24 hours for large parts, for a centerpoint temperature decrease of 393 K (120°C) to 348 K (75°C) [1], where it is deemed safe to remove the part. How will in-bed structures affect this time period?

Let us assume a starting temperature of 393 K (120°C) and a surrounding temperature of 298 K (25°C). We can now numerically examine temperature as a function of time for the case where a cake is removed from an SLS machine and set on a table to cool. Thermal transfer out of the bed is predominantly due to convective heat losses from the bed top and sides, with the table assumed to be an insulative surface. We can contrast this case with one wherein forced convection is used through a bed to enhance the net heat transfer rate.

Note that we use an average powder bed surface convection coefficient, \bar{h} , of 1 W/m²K. With an approximate coefficient of 1.4 W/m²K, based upon energy conservation for a fluid bath-based wall-heating system [12], and a value of 0.3 W/m²K based upon flat plate correlations [10], 1 W/m²K is a good approximate value for our study.

As well, the through-bed fluid velocity arises from previously-examined experimental conditions [12]. With the factorial experiment delineating, over the range tested, a maximum flow rate for improved thermal response of the bed, we opt to use the maximum tested flow rate of 70 SCFH. Note that the velocity of 0.011 m/s is equivalent to 70 SCFH of flow through the larger 0.25 m (10") diameter tube.

Along with these control parameters, we also consider those which are both easily manipulated by an SLS machine's end user *and* independent of a solid part's morphology. For example, varying the type of in-bed structure used only requires modification of appropriate .STL files. In contrast, the amount a tortilla extends beyond a SLS-formed part's edge as shown in Figure 2 is affected by overall part shape and nominal bed dimensions. This dependency makes an exhaustive consideration of the overhang's effect difficult, lending more support to our chosen control variables.

With all of these concerns in mind, we can consider a number of separate simulations to gain insight with respect to various control parameters. Simulations examined include SLS-formed parts with and without tortillas and containers. As well, these arrangements are considered for powder cakes set aside on a table to cool and for powder cakes subject to through-bed forced convection. Lastly, the potential benefit of very extensive in-bed structures [3] are also considered.

5 Simulation Results

With the system geometries and properties sufficiently described and the simulations fully constructed of 9-noded quadratic elements coupled with an implicit backward Euler solver, we can now execute our simulations and examine the results to the mixed convection, transient system. Analysis of the simulation output will offer insight into the overall influence of the various control factors mentioned above.

5.1 Effect of Tortillas and Containers, With and Without Convection

To answer the question of in-bed structure significance, let us examine temperatures along the SLS-formed solid part's centerline. By considering temperature distributions both with and without forced convection and with and without in-bed structures, significant insight can be gained into the effects of forced convection and in-bed structures.

Consider Figure 4(a) where we plot solid centerline temperatures as functions of both time and in-bed structure inclusion for systems without forced convection, analogous to an entire cake being removed from an SLS machine and set aside to cool [1]. Note that, in Figure 4(a), the x -axis' left end is the *top* of the SLS-formed solid while the right end is the *bottom*.

As shown in Figure 4(a), in-bed structure inclusion has little thermal effect on a system without forced convection. Over a 24 hour time period, there is no significant difference in predicted temperatures, regardless of tortilla or container inclusion.

Is this same trend maintained if we now include forced convection? From consideration of Figure 4(b), we can immediately see that the trend is indeed maintained. There is no significant thermal effect for in-bed structure inclusions *with the parameters considered*.

Note, however, the decided differences between Figures 4(a) and 4(b). In Figure 4(a), even after 12 hours, the center of the solid is at approximately 380 K (107°C). With a target center temperature of 348 K (75°C) for safe handling [1], the simulation predicts that the solid cannot be removed until after 24 hours, which agrees well with previously reported data [1]. With forced convection, this temperature drops to 338 K

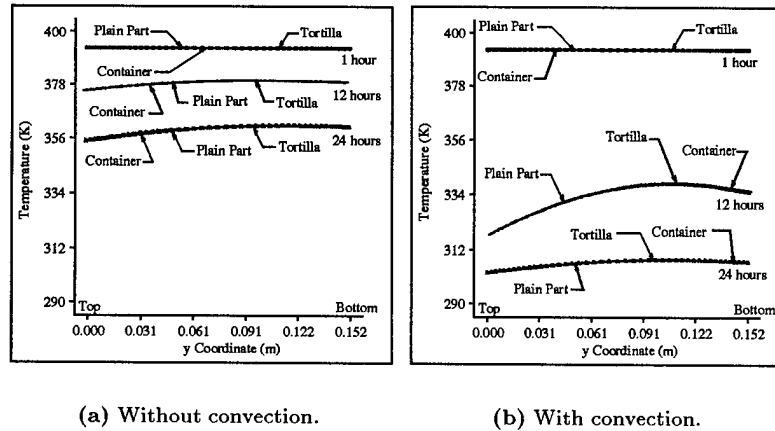


Figure 4: Comparison of temperatures along SLS-formed part centerlines with and without convection.

(65°C) at 12 hours, offering a possible remedy to the very real production limitation encountered with part cooldown times. Note that this increased cooling rate comes at the cost of an increased thermal gradient across the solid part, a factor thought to increase curl [2, 5, 11, 15].

It is worthwhile to take a moment and reiterate that the cool down time reduction results are beneficial only if we aim to satisfy the customer need of reducing cool down time as discussed in Section 4. If, instead, our desire is to maintain the thermal energy state of our part in order to delay thermal gradient-induced stresses, then the preferred solution would be to leave a cake sitting on a table to cool.

While forced convection through a cake can have significant effects, there still appears to be little in-bed structure effect at this porosity level. Does a change in metastructure porosity have any effect? Can the relatively simple change of increased sintering for in-bed structures significantly affect temperatures?

5.2 Effect of Varying In-Bed Structure Porosity

Let us begin by considering cake thermal behavior as a function of tortilla porosity in a system subjected to forced convection. From the solid centerline temperatures shown in Figure 5(a), we can see that while there is not a great difference in temperatures within the bed, there is indeed a difference near the bed bottom. The low porosity tortilla ($\phi=0.01$) system shows slightly higher temperatures at the solid's base.

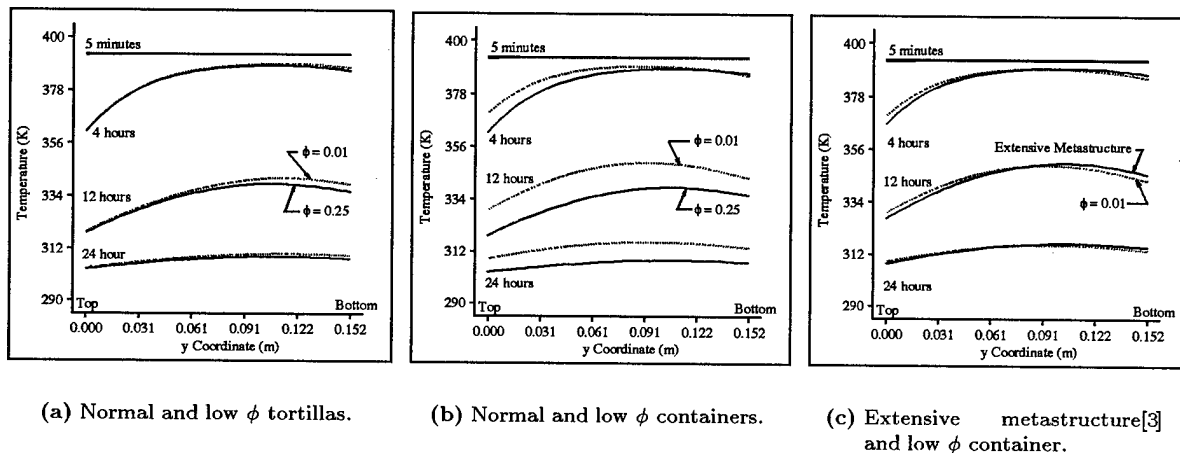


Figure 5: Solid centerline temperatures for various in-bed structure porosity configurations.

If we next consider a container with a lower porosity of 0.01, we achieve results as shown in Figure 5(b). The effect of a lower porosity is easily observed, where its use results in higher temperatures within the bed at any given time. In some instances, the temperature is almost 10 K higher within the low porosity container.

The above results are with monolithic in-bed structures, i.e., structures fabricated with uniform porosity. How will an in-bed structure with non-uniform porosity values affect the powder bed's thermal response?

Consider the aforementioned elaborate in-bed structure [3]. As discussed in Section 4.1.3, this structure has nonuniform porosity, nonuniform permeability, and nonuniform thickness. Substantial time is invested in creation of the base with its numerous layers of various construction.

Is all of this process truly required to achieve an increase in bed temperature as seen experimentally [3]? Consider Figure 5(c), which compares solid centerline temperatures at various times for a low porosity container, Section 5.2, and for the extensive metastructure, Section 4.1.3.

As shown in Figure 5(c), there is only a small difference in cake thermal behavior between the low porosity container and the extensive, varying porosity metastructure. However, the small differences that do exist offer insight into the powder bed's overall thermal sensitivity to various parameters.

For the extensive structure, the solid's centerline experiences lower temperatures at the top and higher temperatures at the bottom. Consider that the extensive structure's top is 5 times *thinner* than the low porosity container's top. As well, the metastructure's base is 4 times *thicker* than the low porosity container's base. Essentially, as an in-bed structure's thickness increases, the SLS-formed solid in that region experiences higher temperatures. Conversely, as the in-bed structure's thickness decreases, the SLS-formed part sees lower temperatures.

Lastly, it is interesting to note that, at least from a thermal standpoint, there is no significant reason to utilize the large number of layers and intricate construction as originally described [3]. A container the same thickness on all sides and of a higher density can achieve nearly the same results as a much more complicated structure, as illustrated in Figure 5(c). Given these results, what physical phenomena might lead to an explanation of this behavior?

5.3 Discussion of Effects

With the above work, we observe that container geometry makes little difference unless a lower porosity is utilized. Only at this lower porosity does in-bed structure morphology have an effect. Why does a lower porosity lead to higher in-bed temperatures for a given time?

In actuality, higher in-bed temperatures at a given time can also be viewed as lower porosity beds having a *slower response* to any thermal disturbance to which the bed is subjected. Such a point of view now leads us to consider the change in thermal diffusivity between high and low porosity regions. Given by [9],

$$\alpha = \frac{k_{eff}}{\rho_{eff} c_{p,eff}}, \quad (1)$$

thermal diffusivity, α , is a measure of how rapidly a thermal disturbance will propagate through a powder bed. Essentially, the larger α is for a system, the faster a change in temperature will propagate through that system [10].

For our system, when comparing containers at porosities of ϕ equal to 0.01 and 0.25, we have effective diffusivities of $1.25 \times 10^{-7} \text{m}^2/\text{s}$ and $1.36 \times 10^{-7} \text{m}^2/\text{s}$, respectively. The decrease in porosity seen with a fully-sintered container results in a 25% decrease in thermal diffusivity. The net result of this effect, combined with the lower permeability seen in low porosity parts, is a slower propagation of thermal disturbances to the solid within a low porosity in-bed structure-modified system.

6 Key Points

From the parameters considered in this study, including tortilla and container usage, structure porosity and geometry, and the use of forced convection, we have gained significant insight into control of SLS-formed part cooldown. With proper choice of parameters, a user can decrease cool down time or maintain a bed's thermal energy level, depending upon their desire. To decrease cool down time, forced convection through

a powder bed is mandated. Even at a relatively low flow rate of 70 SCFH, the time for an SLS-formed part to cool down to safe levels can be halved.

Conversely, a low porosity container allows a user to maintain the powder bed's temperature level over a greater length of time. With the potential of thermal gradients within a part leading to post-production curl, containers capable of slowing a part's cooling, and thereby reducing gradient levels, offer much promise.

Functioning due to a combination of lower thermal diffusivity and reduced permeability, instead of a reduction in natural convection, these in-bed containers can be of relatively simple construction. A metastructure comprised of numerous layers of rings and disks in various arrangements does not offer significantly improved control of a bed's thermal state over a simpler, low porosity container.

The important control factors, such as porosity, can also vary spatially. Not only do SLS users have the capability to control an in-bed structure's thickness and porosity, they can modify the thickness and porosity for various sections of the container. Through this approach, a user can affect cooling or thermal retention of a part on a *spatially-dependent* basis. Beds can be equipped with in-bed structures having properties that vary with location. Through such an approach, in-bed structures, near sections of an SLS part with high susceptibility to curl, can be designed with lower porosity and higher thickness. Thermal energy in these curl-sensitive regions can be drawn out more slowly than from other regions of a part.

In conclusion, in-bed structures and forced convection can both be used to significantly affect a bed's cooldown cycle and, in turn, an SLS machine's final part quality, where quality can be measured in parts per hour or final dimensional accuracy. With such process design changes, a user can effectively manipulate cooling from specific regions of SLS-formed parts.

References

- [1] S. Barnick. Manager, Technical Product Support, Personal Interview, DTM Corporation, Austin, TX, 1998.
- [2] M. Berzins, T.H.C. Childs, K.W. Dalgarno, G.R. Ryder, and G. Stein. Densification and Distortion in Selective Laser Sintering of Polycarbonate. In H.L. Marcus et al., editors, *Proceedings of the 1995 Solid Freeform Fabrication Symposium*, pages 196–203, Austin, TX, 1995. University of Texas at Austin.
- [3] K. Chen. *Intelligent Scanning in Selective Laser Sintering*. PhD thesis, University of Texas at Austin, Austin, TX, 1998.
- [4] M. Chung. Manager, Technology Development, Personal Interview, DTM Corporation, Austin, TX, 1998.
- [5] K.W. Dalgarno, T.H.C. Childs, I. Rowntree, and L. Rothwell. Finite Element Analysis of Curl Development in the Selective Laser Sintering Process. In D.L. Bourell et al., editors, *Proceedings of the 1996 Solid Freeform Fabrication Symposium*, pages 559–566, Austin, TX, 1996. University of Texas at Austin.
- [6] P. Forderhase, K. McAlea, M. Michalewicz, M. Ganninger, and K. Firestone. SLSTM Prototypes from Nylon. In H.L. Marcus et al., editors, *Proceedings of the 1994 Solid Freeform Fabrication Symposium*, pages 102–109, Austin, TX, 1994. University of Texas at Austin.
- [7] D. Gray. Staff Scientist, Personal Interview, DTM Corporation, Austin, TX, 1998.
- [8] C. Hanna. Senior Mechanical Engineer, Personal Interview, DTM Corporation, Austin, TX, 1998.
- [9] F.P. Incropera and D.P. De Witt. *Fundamentals of Heat and Mass Transfer*. John Wiley and Sons, New York, NY, 3rd edition, 1990.
- [10] A.F. Mills. *Basic Heat and Mass Transfer*. Irwin, Boston, MA, 1995.
- [11] J.C. Nelson, K. McAlea, and D. Gray. Improvements in SLS Part Accuracy. In H.L. Marcus et al., editors, *Proceedings of the 1995 Solid Freeform Fabrication Symposium*, pages 159–169, Austin, TX, 1995. University of Texas at Austin.
- [12] J. Norrell, R. Crawford, and K. Wood. Thermal Issues in the Design of an SLS Rapid Prototyping Machine. In *Proceedings of the 1997 ASME Design Engineering Technical Conferences*, Sacramento, CA, 1997. ASME.
- [13] J. Norrell, M. Kandis, and T. Bergman. The Influences of Natural Convection and Radiation Heat Transfer on Sintering of Polycarbonate Powders. In H.L. Marcus et al., editors, *Proceedings of the 1996 Solid Freeform Fabrication Symposium*, pages 619–627, Austin, TX, 1996. University of Texas at Austin.
- [14] J. Norrell, K. Wood, R. Crawford, and T. Bergman. Forced Convection in Polymeric Powders. In H.L. Marcus et al., editors, *Proceedings of the 1996 Solid Freeform Fabrication Symposium*, pages 459–470, Austin, TX, 1996. University of Texas at Austin.
- [15] Craig Wadham. Director, Systems Development, Personal Interview, DTM Corporation, Austin, TX, 1998.

OPTIMIZATION OF POWDER LAYER DENSITY IN SELECTIVE LASER SINTERING

N. P. KARAPATIS, G. EGGER, P.-E. GYGAX, R. GLARDON

Department of Mechanical Engineering, Swiss Federal Institute of Technology, Lausanne

Abstract

An important parameter for the overall quality of SLS parts is the density of powder layers before sintering. Previous studies have shown that the control of powder particle shape and size distribution can increase the density of non-packed powder beds. However, these studies concerned beds several orders of magnitude larger than the SLS layers. The purpose of this study is to determine if, and to what extent, the density of thin powder layers can be increased. Experiments show that the density of thin layers increases from 53% to 63% when adding 30% fine powder to the coarse powder, with a coarse-to-fine ratio of 1:10. Compared with the bulk experiments, this density improvement method is less efficient, because the particles do not arrange as efficiently, and the wall effects can become predominant.

1. INTRODUCTION

Metallic components made by selective laser sintering (SLS) for tooling applications generally exhibit high porosity and low surface quality that still impede a widespread application [1]. Two different SLS processes can be distinguished: the indirect and the direct sintering techniques. In the first case, the material is constituted of metallic particles (typically tool steel) coated with a specific polymer [1, 2]; the energy brought by the laser locally "remelts" the polymer, which then "glues" the metallic particles together. The polymer binder must be thermally removed. The obtained product is neither dense nor fully consolidated yet, and a third operation is necessary: the post-sintering, which, together with an infiltration with a lower melting point metal (e.g. copper), leads to the final part. Post-processing operations are required, which inevitably lead to an increased throughput time. Furthermore, due to the various thermally based operations, residual stresses and/or loss of accuracy are to be expected.

In the direct selective laser sintering route [1, 3], no post-processing is, theoretically, necessary. The material is a fully metallic powder which can contain two components: in that case, liquid phase sintering is used as the densification process. However, a single-component powder can also be selectively sintered, provided that only a fractional part of the powder is remelted under the laser. The molten phase propagates through the solid particles bed (which is in fact a thin layer), and the wetting properties of the liquid-solid couple lead to powder densification. Since the interaction times are usually very short in SLS processes compared to conventional liquid phase sintering (a few hundreds of milliseconds vs. several minutes), rearrangement is essentially the only operative densification process. After processing, the part density and surface quality are usually poor [4] and an infiltration (e.g. epoxy resin) is still required. However, the number of operations is limited and the thermal influence on the sintered components is reduced to a minimum.

In both SLS techniques, an extensive number of parameters control the quality of the sintered parts. Among them, the material properties play a major role: in particular, the characteristics of the powder bed before sintering are decisive for the quality of the finished component. More specifically, the relative density of the bed has a direct influence on the density of the sintered body. Therefore, powder materials and deposition process must be improved to insure the highest possible layer density before laser sintering.

2. THEORETICAL APPROACH

2.1. General considerations

Increasing the density of a powder requires the understanding of the mechanisms that dominate during particle motions. Such interactions have been described in detail in many other papers, such as [5]. A few simulation studies have been performed to reproduce these motions, and to identify and understand the phenomena [6, 7]. Basically, the most important factors are found among the particle shape and surface state, and the granulometry parameters of the powder.

The density of powder bulks can be increased by several methods [8]. A first approach is the optimization of the particle shape and surface state: smooth particles will move easily within the bed and will lead to a higher loose density. In addition, clean and dry surfaces prevent the formation of unwanted bonds between particles, so that particle motion is not prevented [5]. The shape of the particles will further influence the density of a powder: regular, equiaxed particles tend to arrange more efficiently (Figure 1); therefore, spherical grains are often preferred when available. Non-porous particles are evidently favored.

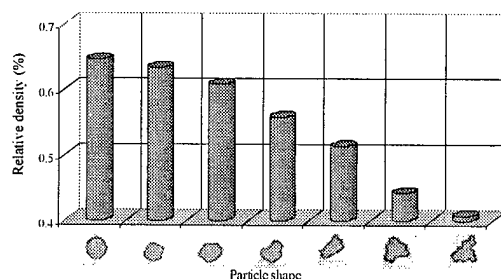


Figure 1: effect of particle shape on the achievable relative density (after R. M. German [8])

In general, the optimization approaches described above are closely related to the powder material and its production process. For instance, hard materials are generally manufactured by milling, producing angular, irregular particles, while most gas-atomized powders exhibit equiaxed, smooth spherical particles. Therefore, for a given material, there is usually little flexibility for modifying and optimizing the particle shape and quality.

The granulometry of a powder, which is not directly related to a selected material is an important parameter for density optimization. In a monomodal, monodisperse granulometry distribution, the particles will assume a stable position with the highest possible density, if sufficient energy is brought in for rearrangement. However, it is evident that an significant number of voids exist between particles: for a compact packing (fcc), the relative density is about 74%. In a monomodal but polydisperse particle size distribution, with a given peak width, some of the particles on the low diameter side of the peak can fill the holes left between the coarser particles [8]. The maximum density can be obtained when the particle size distribution follows Anderson's equation:

$$W = A \cdot D^q$$

where W is the cumulative weight fraction, D is the class diameter, A and q are empirical constants. The best results are obtained for values of q between 0.5 and 0.67, corresponding to a large fraction of fine particles ("fines") [8].

Although not fully efficient, the peak width method can increase the density of a powder, in a relatively straightforward way. A more effective means would be to determine the size or size distribution of the available voids in a starting, coarse powder and then to add suitable fine particles to fill them (multimodal granulometry). Evidently, an energy input into the system, e.g. by vibration, can further increase the final density. Further improvements can be accomplished by adding finer particles with suitable size ratios to fill in the remaining voids.

2.2. Previous studies

McGeary [9] applied the multi-modal approach to powder bulks. His experimental setup was composed of vertical transparent cylinders and vibratory equipment. The test procedure consisted in pouring a coarse powder into the tank, vibrating it until no more volume variation was noticeable; then, the first finer powder was poured, vibrated and the process was repeated for the subsequent fine fractions. The experiments were performed with various materials and powder absolute sizes, but always with particles as spherical as possible and with narrow size distributions. Blends with different size ratios and fines content were prepared and the densities were measured. Before the addition of the fine powder, McGeary observed that the coarse particles assume an arrangement close to orthorhombic.

The results showed that a size ratio about 1:7 with about 30 % of fine particles constitutes the approximate optimum achievable density increase. Higher size ratios do not present significant improvements and are usually less favored because of availability and handling problems.

The determination of the void size, and thus of the ideal coarse-to-fine ratio can be made on the basis of an orthorhombic arrangement. Two types of voids can be identified in this particular packing configuration: a triangular pore and a "square", larger passage. Since the compaction is made by allowing the fine particles to percolate through the bed of the coarse particles, the limiting

factor is the smaller diameter. The value of the small particle radius r can be determined geometrically; it is given by the relation:

$$r = \left(\frac{2}{\sqrt{3}} - 1 \right) \cdot R \cong \frac{1}{7} R$$

which is in good agreement with the experimentally determined value.

The optimum amount of fine particles X_{fines} to be added to the coarse is determined by:

$$X_{\text{fines}} = 1 - \frac{\rho_{\text{coarse}}}{\rho^*} = 1 - \frac{\rho_{\text{coarse}}}{\rho_{\text{coarse}} + (1 - \rho_{\text{coarse}}) \cdot \rho_{\text{fines}}},$$

where ρ_{coarse} is the relative density of the coarse particles and ρ_{fines} the relative density of the fine particles arrangement. Taking a relative density of about 60 % for both coarse and fine powders, the composition should be about 30 % of fine particles (with a 1:7 ratio with the coarse particles). The maximum density achievable with such a composition is $\rho^* \approx 0.84$.

The equations above can be easily extended to a larger number of size mixtures. This way, a second fine fraction with a size ratio 1:49 can be added to further improve the density. However, finer particles induce handling problems (due to aggregation). They may also be difficult to obtain. Both last equations admit implicitly that the whole space between the coarse particles can be filled with fines. However, the calculated maximum density is consistent with the data obtained by McGeary [9]. Although this study does not consider a void size distribution, it has been shown that adding 30 % of fine particles, with a size ratio of 1:7, can increase the density of a powder bulk by about 30 %.

A remarkable side conclusion of McGeary's study is that the ideal ratio and the achievable density do not depend on the particles absolute size. This is probably true only for particles larger than ca. 1 μm , i.e. such that they are not influenced by electrostatic, Van der Waals or other joining forces.

McGeary's work has been extended by B. M. Zivanovic [10] to the compaction of monodisperse, but non-spherical particles. Basically, the same results are obtained: a similar density increase can be expected, although the values of relative density are lower than those obtained with spherical particles. In this case however, the size ratio is higher than 1:7 (over 1:10), since the passages follow a size distribution. Increasing the size ratio may lead to better results due to an enhanced percolation through the coarse bed, but fine particles will fill a given volume less efficiently than a single, dense particle. Another study on particle arrangement by simulation was presented by G. T. Nolan and P. E. Kavanagh [11], considering a random arrangement of log-normal distributed particles. The influence of the peak width on the void size, number and distribution was studied: when the peak width increases, the voids size expands, their number decreases and the apparent density increases.

2.3. Application to Selective Laser Sintering

The studies presented above are valid for powder bulks, i. e. powder particles arranged in containers several orders of magnitude larger than an average particle size. In Selective Laser Sintering, the situation is drastically different. Although particles can be very spherical, their granulometry is usually not ideal (in terms of size ratios). Most importantly, the dimensional characteristics of the “container” (the powder layer) are much closer to the size of the particles: 50 μm layers can be prepared with a 30 μm mode size powder.

Therefore, “wall effects” (Figure 2) [12] will be more relevant in such layers, inducing lower densities. The wall effects can be estimated with the relation:

$$V_{\text{walls}} \approx N_s \cdot V_s \cdot S_w$$

where N_s is the number of vacant sites per unit area, V_s is the void volume per vacant site and S_w is the total wall surface area.

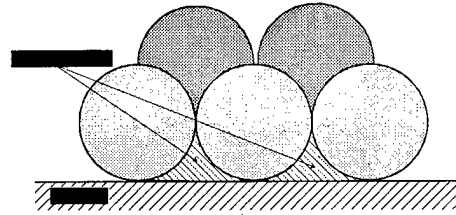


Figure 2: vacant sites created by the presence of a wall. The dotted circles represent spheres that would be present if the wall was not there. Therefore, the hatched volumes are not filled and constitute the wall voids.

Here, the wall effect is approximated by considering an orthorhombic arrangement of particles with a monodisperse radius R (bulk porosity of 40 %) deposited in a disk layer of diameter D and height h . The influence of the wall effect is:

$$\frac{V_{\text{walls}}}{V_{\text{voids}}} = \frac{\frac{1}{3}\pi^2 R \cdot D \cdot \left(\frac{D}{4} + h\right)}{0.4 \cdot \pi \frac{D^2}{4} \cdot h + \frac{1}{3}\pi^2 R \cdot D \cdot \left(\frac{D}{4} + h\right)} \approx \frac{R\left(\frac{D}{4} + h\right)}{0.4 \frac{D}{4} \cdot h + R\left(\frac{D}{4} + h\right)}$$

where V_{voids} is the total void volume in the powder layer.

In the above equation, the void volume due to the walls is the volume of the “missing” half sphere that is absent at the powder/wall interface, as shown in Figure 2. Figure 3 shows the importance of the wall effect on the powder porosity for a powder bed: with a cavity height of 100 μm , about 40 % of the porosity is due to wall voids. This value may be underestimated, since the upper surface will also be locally porous. However, it must be born in mind that subsequent layers will be sintered on a rougher surface, with a probably lesser influence of the walls.

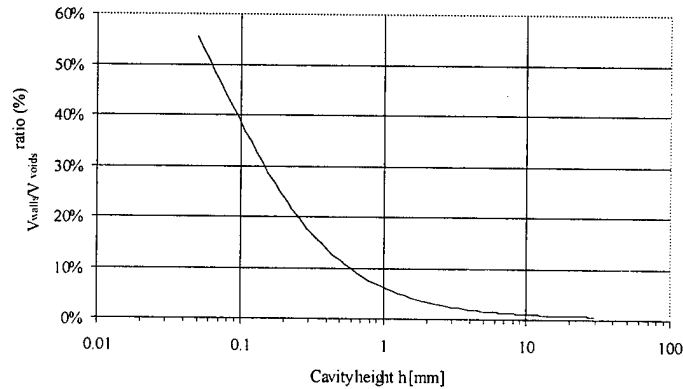


Figure 3: influence of the wall effects on the powder density (cavity/layer diameter = 60 mm; particle diameter 25 μm).

3. EXPERIMENTAL METHODS

3.1. Powders

The powders used for the experimental determination of layer density were spherical, smooth particles of nickel-base alloy (Figure 4). These materials were provided by Castolin+Eutectic SA. The powder was separated in size classes and blends with given size ratios were prepared (Table I and Table II).

Table I: available size classes.

Class	Sizes [μm]
B	150 – 200
C	100 – 150
E	50 – 75
G	25 – 40
H	< 20

Table II: composition of blends

Size ratio	Blended classes
1:2	C + E
1:5	B + G
1:10	C + H
1:18	B + H

3.2. Measurements

Conventional granulometry measurement equipment was used for the characterization of the base materials. The density of the powder layers was determined by weight measurement of a powder filled cavity (500 μm depth, 65 mm diameter). In some experiments, a deeper cavity (1500 μm) was used, because of the difficulty to deposit regular layers with the coarser powders. The container height was 5 mm and its external diameter was 80 mm. The weight of the empty container was about 57 g. The powder was deposited using a metallic ruler, taking care that as little powder as possible remained outside of the cavity.

The measurements were performed with a precision scale (± 0.02 mg). Although powder layers in SLS are usually below $100\text{ }\mu\text{m}$ ($50\text{ }\mu\text{m}$), the cavity used in this study was deeper in order to minimize measurement errors due to irregular layers.

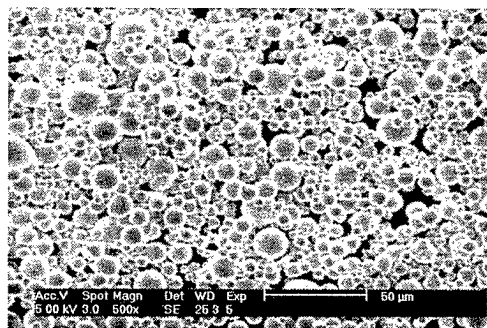


Figure 4: SEM image of the nickel model powder.

4. RESULTS AND DISCUSSION

Figure 5 presents the results obtained for different size ratios at different fines compositions. The first observation is that the 1:2 ratio, corresponding to the square void in the orthorhombic arrangement, does not bring significant improvements. Although the powders are mixed before deposition, percolation is still required and the fine particles cannot rearrange in the square voids.

The 1:5 ratio leads to a slight improvement at a rather high composition, as observed by McGeary. Due to the void size distribution (and to the locally disordered arrangement), the fine particles can still percolate through the coarse powder. With higher ratios (over 1:10), the density increase is more significant: at 30 % fines, the layer density has increased from about 55 % up to 63 %, which amounts to an over 15 % relative increase.

At higher fines content, the density decreases, probably because the passage voids are saturated and the fines tends to pull the coarse particles apart. Interestingly, the curves for bulks and for layers are quite similar, indicating that the same processes occur, although with less efficiency in the layer case. The differences observed between the pure coarse and pure fine densities are due to the different classes used, which exhibited an agglomerate structure for the finest powders.

Figure 6 compares the results of the layer density with the data obtained by McGeary for powder bulks, for the same fine content (30 %). Again, the tendency is clearly similar, but the apparent densities are more than 15 % below that of powder bulks, although the particles are also spherical (Figure 4).

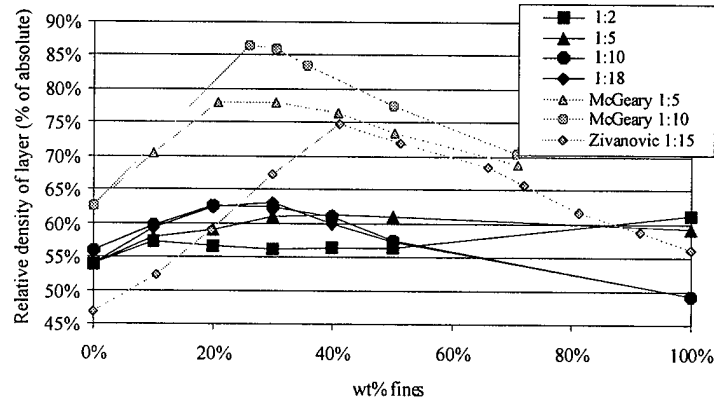


Figure 5: relative density curves for thin layer as a function of the amount of added fine fraction, for several size ratios. For comparison, data for bulks are also represented.

As expected, the value for non-spherical particles (given by Zivanovic [10]) is situated below the McGeary's curve but over that of layer density. This indicates that several effects act jointly in layer deposition. First, since the powder is not monodisperse, the voids follow a size distribution, which is a sign that probably finer particles would be required. The percolation process is also less efficient, since little energy, except gravity and friction, is provided to the powder. More importantly, the wall effects are probably very effective in this case.

Figure 3 shows that for thin layers (below 100 μm), over 40 % of the voids are generated by the wall effects. This ratio decreases rapidly when the layer height increases. The wall effects could be advantageously reduced by increasing the roughness of the walls. This way, some of the wall voids can be filled by the wall peaks. Since the layer thickness used in this study was higher than in common SLS, it can be expected that in the real case, the density and its improvement will be even lower than in Figure 6.

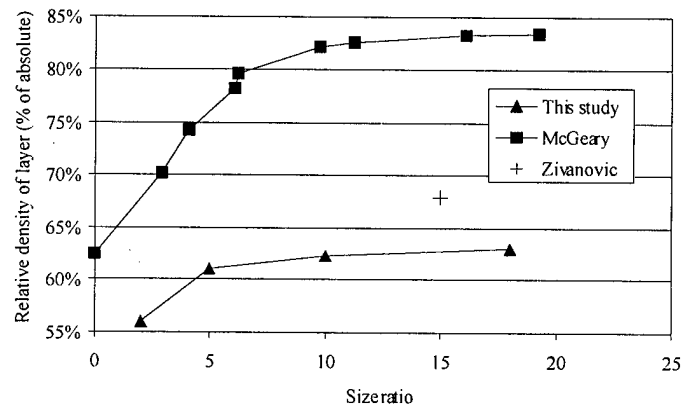


Figure 6: relative density of thin layers and bulks with 30 wt% fines as a function of size ratios.

5. CONCLUSIONS

In this paper, it has been shown that the density of powder layers can be improved by using multimodal powders. With a suitable size ratio between coarse and fine particles (over 1:10) and adequate composition (about 30 %) of fines, a density increase of about 15 % can be expected. Wall effects were approximated, showing a central influence on layer density: for layers less than 200 μm thick, the influence of the wall voids can be higher than 20 % of the total porosity in the powder. This effect may be reduced by an increased roughness of the support; the control of the roughness between layers may also be beneficial. The density values presented in this paper should be considered as an upper, achievable density, since the experiments were performed on thick layers (500 μm) compared with the thickness in the SLS process. It is to be expected that the density improvement will be less efficient in the real situation, with thinner layers.

6. REFERENCES

- 1 N.P. Karapatis ; J.-P.S. van Griethuysen ; R. Glardon, "Direct rapid tooling : a review of current research", *Rapid prototyping J.*, Vol. 4, No 2, 1997, pp.77-89
- 2 Girouard D., "Molds for Low Temperature Molding Processes using Rapid Prototyping", *Proceedings of the 4th International Conference on Rapid Prototyping*, 1993
- 3 Lohner A., "Laser sintering ushers in new route to PM parts", *MPR*, February 1997, pp. 24-30
- 4 N.P. Karapatis ; Y. Guidoux, P. E. Gygax, R. Glardon, "Thermal Behavior of Parts Made by Direct Metal Laser Sintering", 9th SFF Symposium, Austin, 1998, pp. 79-87
- 5 R. M. German, *Liquid Phase Sintering*, Plenum Press (1985)
- 6 S. Tamura et al., *J. Mat. Process. Techn.*, Vol. 42, 1994, pp. 197-207
- 7 Ferrez J.A., Müller D., Liebling Th.M., "Parallel Implementation of a Distinct Element Method for Granular Media Simulation on the Cray T3D", *EPFL Supercomputing Review* No. 8, 1996
- 8 R. M. German, *Powder Metallurgy Science*, Metal Powder Industries Federation, 1984
- 9 R.K. McGeary, *J. of The American Ceramic Society*, Vol. 44, No 10, 1961, pp.513-22
- 10 B.M. Zivanovic, *Proc. 1st Int.Conf. Compaction and Consolidation of Particulate Matter*, Brighton, 1974, pp.37-40,
- 11 G.T. Nolan, P.E. Kavanagh, *Powder Technology*, Vol. 74, 1994, pp.231-238
- 12 F. Zok, F. F. Lange, *J. Am. Ceram. Soc.*, Vol. 74, No 8, 1991, pp. 1880-1885

Atmospheric Control during Direct Selective Laser Sintering of Stainless Steel 314S powder.

C. Hauser, T.H.C. Childs, K.W. Dalgarno, R.B. Eane.
School of Mechanical Engineering,
The University of Leeds, UK.

Abstract

Stainless steel grade 314S powders have been Selective Laser Sintered (SLS) in three different argon/air (oxygen) atmospheric mixtures. The amount of oxygen present during the heating, melting and fusing of the metal powder strongly limits the range of laser powers and scanning speeds for successful processing. As oxygen levels diminish, powder oxidation reduces. This reduces absorption of laser energy as well as balling and other detrimental surface phenomena. This paper reports the conditions for creating sintered layers and observations of part quality variation within these conditions. Sintered microstructure observations are also helpful in determining thermal history changes.

Keywords

Atmosphere, Oxidation, Surface Tension, Metallography.

Introduction

The SLS processing route of heating, melting and fusing metal powders over extremely short periods of time, in a back and forth (cyclic) manner is a unique manufacturing strategy. During metal powder processing, oxygen can be present in the surrounding atmosphere, contained within the porosity of the powder bed and in the form of a passive layer of oxide on the surfaces of particles prior to sintering, the latter being common due to the large surface area associated with a powder mass. The presence of oxygen and variations in the temperature-time history during sintering can fuel surface oxide growth. This has led to a succession of reported detrimental effects during the SLS of a number of metallic powders [1,2]. However, surface oxide build up is not always a disadvantage. Other laser manufacturing routes (e.g. laser cutting) report considerable increases in the absorption of CO₂ laser radiation on oxidised metal samples where normal conditions (no oxide growth) would strongly reflect 10.6µm radiation [3]. Another concern is the liquid metal surface tension which influences the wetting angle between the solid and the liquid phases that can disrupt bonding between rastered lines and individual layers [4]. Reports indicate that certain scanning and atmospheric conditions allow surface tension phenomena to dominate causing the melt pool to solidify into a series of balls in the wake of the travelling laser beam [2,5].

This paper is for us a first step in understanding the process of metal powder melting, flow and solidification during SLS. The research as a whole is intended to clarify the affects and requirements of the SLS atmosphere. Particular attention has focused on the significance of oxygen during the formation and growth of the metal powder melt as the laser scans the powder bed surface over a range of laser powers and scanning speeds.

Material

The material under investigation was a standard grade gas atomised stainless steel powder classified as 314S HC, an austenitic steel with a high carbon content (referred to as 314S). The material composition is given in Table 1. The powder was sieved into four batches having particle size distributions of $-300+150\mu\text{m}$, $-150+75\mu\text{m}$, $-75+38\mu\text{m}$ and $-38\mu\text{m}$. Images of sectioned and polished samples of the pre-sintered powder were observed through a Scanning Electron Microscope (SEM) to help understand the re-solidification process after laser sintering. Figure 1 shows two typical SEM images of the $-150+75\mu\text{m}$ powder batch: (a) shows the general powder shape while (b) indicates a mean grain size in a particle of $\sim 5.0\mu\text{m}$.

Elements	(Fe)	(Ni)	(Cr)	(C)	(Si)
Weight %	Bal.	20.0	25.0	0.4	1.0

Table 1: Stainless steel 314S HC material composition.

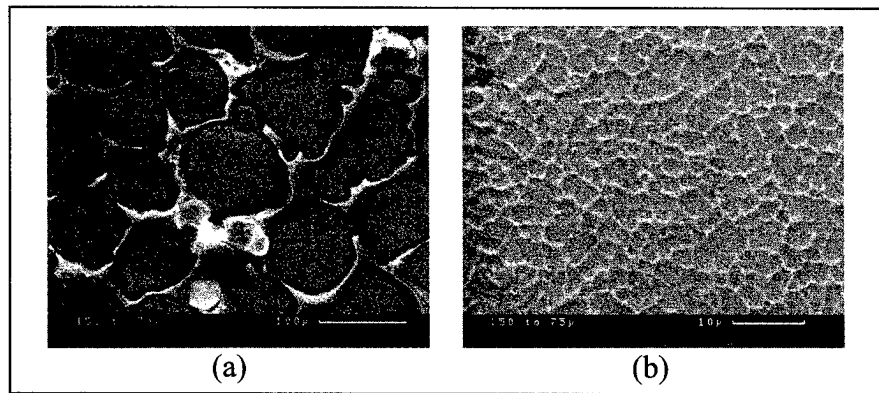


Figure 1: (a) Typical size and shape of 314S $-150 +75\mu\text{m}$ particles and (b) Grain size and shape within a single particle.

SLS Machine and Environmental Control Equipment.

The Leeds high power SLS machine includes a 250W continuous wave CO_2 laser with a spot diameter adjustable between 1.0mm and 2.0mm at the focal length. Galvanometer controlled mirrors direct the laser beam onto a 70.0mm diameter build area which is housed within a 0.03m^3 ($L=460\text{mm}$, $H=260\text{mm}$, $D=250\text{mm}$) process chamber (Figure 2a) capable of sustaining a variety of atmospheric conditions including an absolute pressure of 10mbar. Oxygen dilution within the chamber can be achieved by a combination of evacuation followed by a continuous purge of argon (bottled argon at 99.9% purity) or by targeting argon directly onto/out of the powder bed. The targeting techniques (Figure 2b) were: Method 1- by purging the build area with argon through a shroud which surrounds the powder bed; Method 2 - by percolation of argon through the powder bed. Both methods were tested.

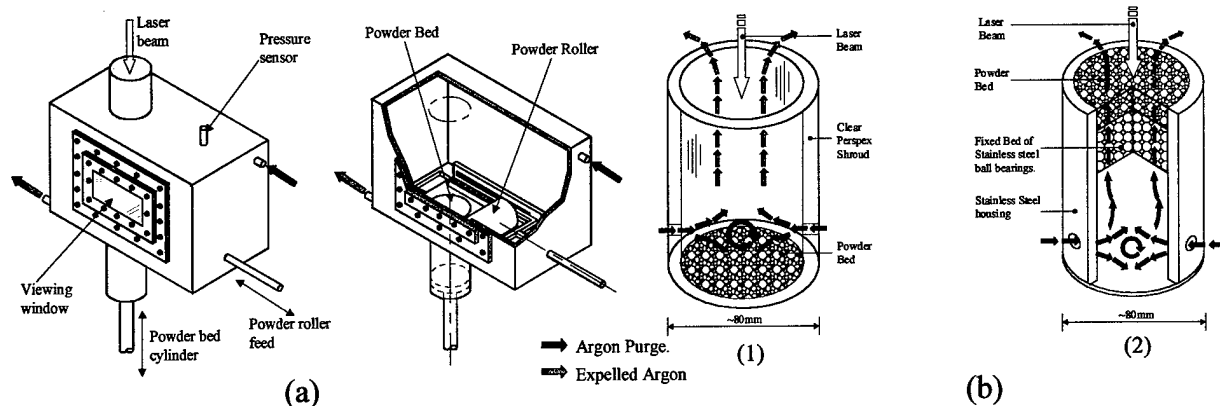


Figure 2: (a) the process chamber, (b-1) gas shrouding and (b-2) gas percolation system.

Experimental Procedure

The four batches of 314S were sintered in the conditions in Table 2. Single line scans varying in length from 15.0mm to 50.0mm were sintered in three different atmospheric gas mixtures of air, air/argon and argon while observing changes in the melt quantity and quality, oxidation and oxidation related phenomena. The results were displayed as a series of sintering charts. Single layer sintering in the same conditions as the previous experiments then followed. Observations were recorded including influences of scan spacing on the changes in oxidation behaviour, on bond quality between rastered lines, on repeatability and on thermally induced distortion. The results were superimposed onto the previous constructed charts.

The air atmosphere was achieved by exposing the powder bed to laboratory air during sintering. The air/argon atmosphere was created by both shrouding and percolating techniques in Figure 2b. A five minute pre-sinter purge of argon was applied before sintering under a continual flow of argon. The argon atmosphere (which still contained traces of oxygen) was achieved by evacuating the process chamber to a pressure of 50mbar followed by a pre-sinter purge of argon for 10 minutes. During sintering the gas inside the chamber was held at 30mbar above atmospheric pressure. The quantities of oxygen within the three atmospheres and the flow rates of the gasses were not measured. However, the three types of atmosphere were sufficiently diverse to allow judgement on the effects of oxygen depletion during SLS.

The powder was in its as received state. No powder pre-heating was carried out prior to sintering. However, only powder from containers with unbroken seals was used: prolonged atmospheric exposure caused powder agglomeration from moisture absorption in the -38 μ batch and increased the chances of further oxidation of all powders during sintering.

Exp. No.	Atmospheric Condition	Beam Diameter (mm)	Laser Power (W)	Scanning Speed (mm/s)	Scan Spacing (Fraction of beam diameter)
1	Air	1.1	0 – 185 in steps of ~10	0 – 50 in steps of ~2	0.25,0.5,0.75
2	Air/Argon	1.1	0 – 185 in steps of ~10	0 – 50 in steps of ~2	0.25,0.5,0.75
3	Argon	1.1	0 – 185 in steps of ~10	0 – 50 in steps of ~2	0.25,0.5,0.75

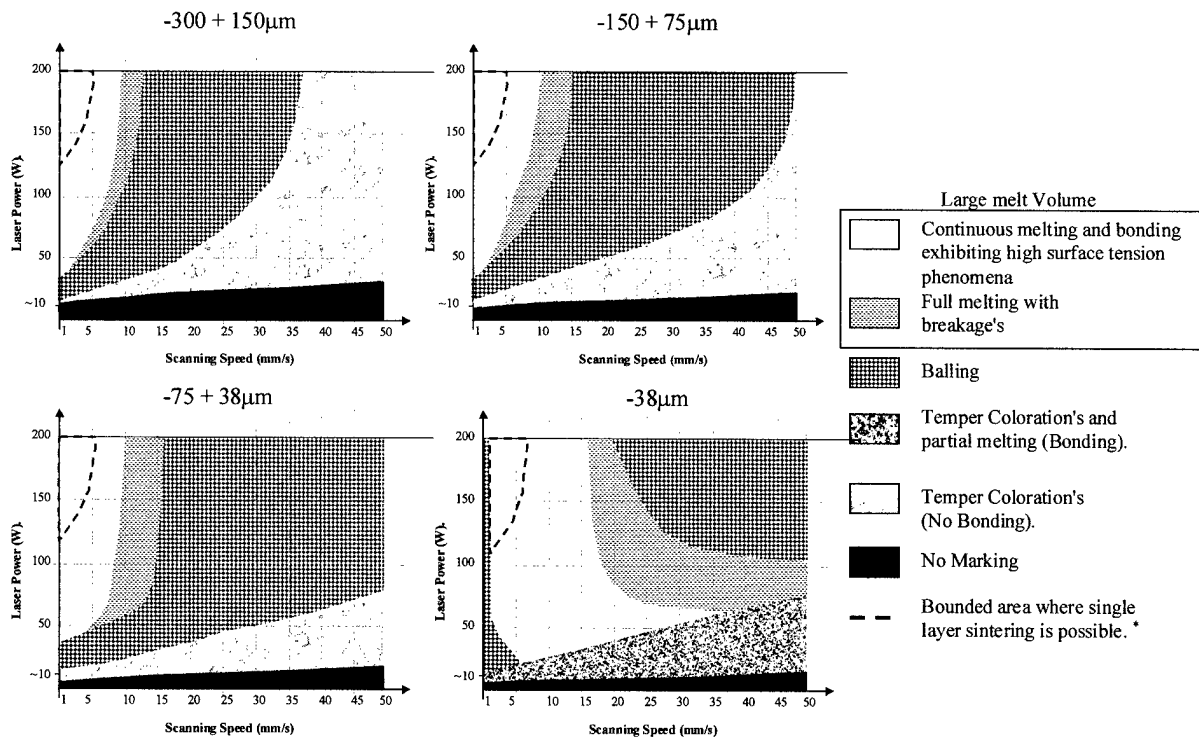
Table 2: Experimental conditions.

Sintering Maps and Observational Results

Exp. 1: Air atmosphere sintering.

Conditions for sintering single lines and single layers within an air atmosphere were found to be limited. Figure 3 maps the observed stages of oxidation behaviour, particle bonding and melt pool growth and quality during single line scanning and Figure 4 shows typical examples of single layer scanning using Figure 3 as a reference guide. During sintering temper colorations following classical oxidation theory [6] could be observed on the surfaces of individual 314S particles as the powder bed was heated by the laser beam. As the net energy density increased (power/speed), small droplets (balls) of liquid metal began to form covered by an opaque surface oxide scale and seated within a trail of oxidised powder. The phenomenon of melt pool balling and breakage was widespread during air sintering because liquid surface tension forces were allowed to dominate due to large melt volumes and the influence of the surface scale. If the scanning speed remained low ($<8.0\text{mm/s}$) and the laser power was high (dependant on speed) surface tension forces became less dominant and the melt pool began to flow more freely. This created a continuous melt pool that solidified into a tubular shape, though a single ball did exist at the start (this can be seen in Figure 4). However, such high temperature conditions dramatically increased the melt volume and a slag believed to be rich in chromium (Cr_2O_3) was observed on the surface.

Single layer scanning was carried out over the range of conditions where single line scanning was successful (white zone of Figure 3). However, it was found that single layer



* Dependant on scan spacing.

Figure 3: Sintering maps for 314S processed within an air atmosphere.

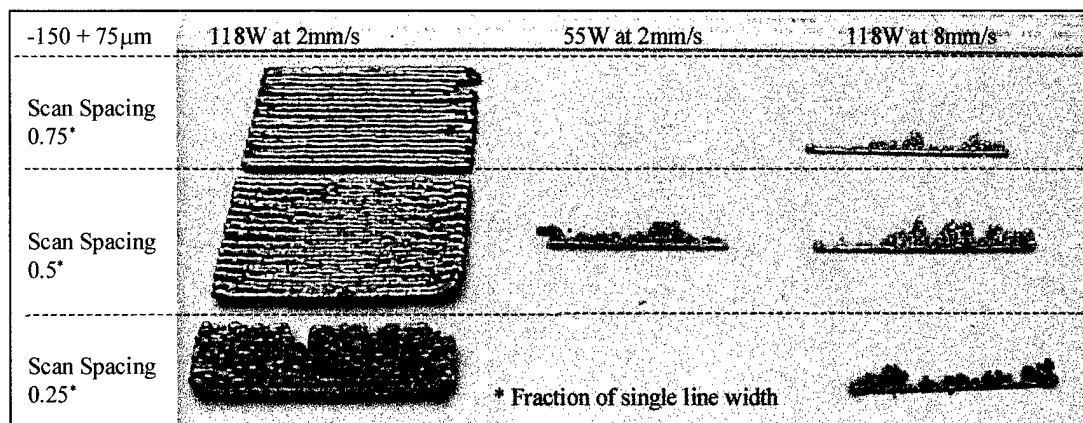


Figure 4: Examples of air atmosphere sintering.

scanning could only be achieved at very high energy densities. Lower energy densities produced a continuous First Line Scan (FLS) followed by balling of all other rastered lines (See Figure 4). Experimentation also showed that if the scan spacing was large ($>0.6 \times$ width of single line) then bonding was limited and if the scan spacing was low ($<0.4 \times$ width of single line) balling occurred.

Exp. 2: Air – Argon atmosphere sintering.

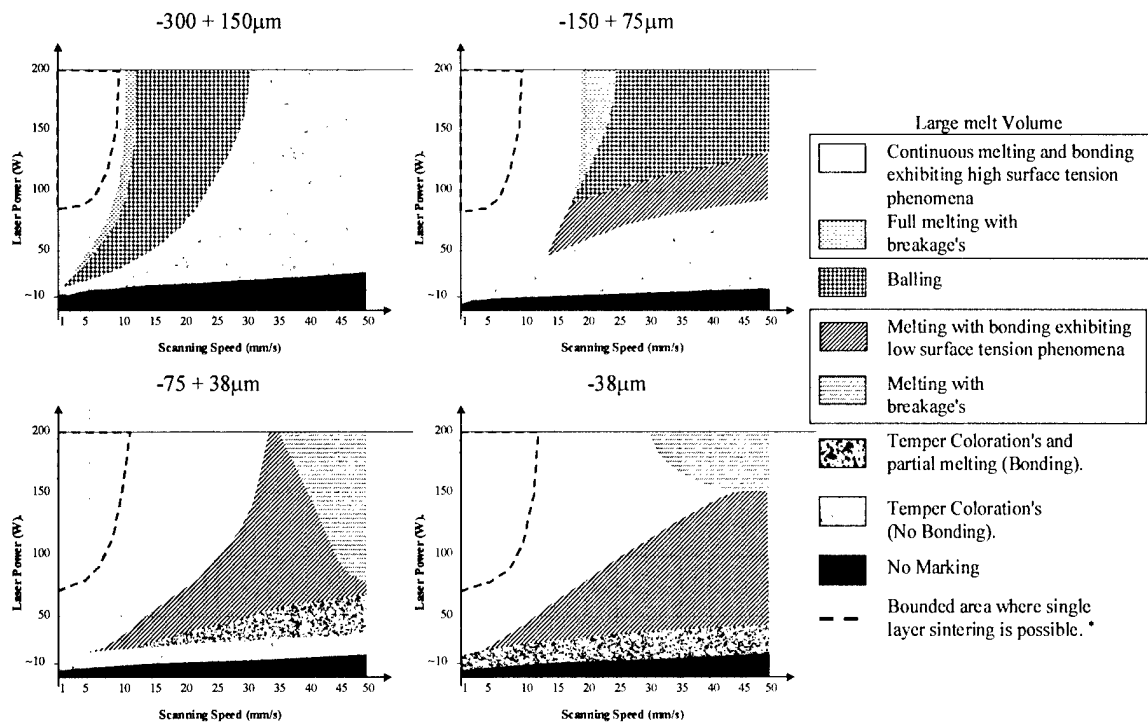
Figures 5 and 6 show the process map for single line air-argon sintering and typical examples of single layers sintered in an air-argon atmosphere respectively. A similar trend to that of air atmosphere processing is seen. However single layer scanning was more successful with improved bonding between the rastered lines over a larger range of scanning conditions, including more flexibility in the choice of scan spacing. The ball at the start of the scan length had also dramatically reduced. Warping of the single layers was also evident, showing that large bulky layers are affected by thermal distortions. All results were obtained from the gas shrouding equipment. When using the gas percolator powder was blown from the bed.

Exp. 3: Argon atmosphere sintering.

Figures 7 and 8 show examples of argon atmosphere sintering and the process map for single line sintering within an argon atmosphere respectively. Under these conditions no oxide growth occurred resulting in free flowing smaller melt volumes creating flatter (0.4mm to 1.3mm thick) and stronger bonded single layers. However, because of the lower melt volume, porosity still existed, effectively lowering the sintered density by 40 to 50%. Even extremely high energy densities (185W at 1mm/s) could not induce full melting as previously experienced in air and air – argon sintering.

Metallographic Inspection

Figure 9 shows typical results of sectioned, polished and etched single sintered lines showing how the microstructure and cross sectional shape change with changes in sintering atmosphere. Two different solidification modes were observed. Firstly, a cellular microstructure found in both air (full) and air/argon (upper half) sintering indicating resolidification from temperatures sufficient to induce full melting. Secondly, an equiaxed



* Dependant on scan spacing.

Figure 5: Sintering maps for 314S processed within an air-argon atmosphere.

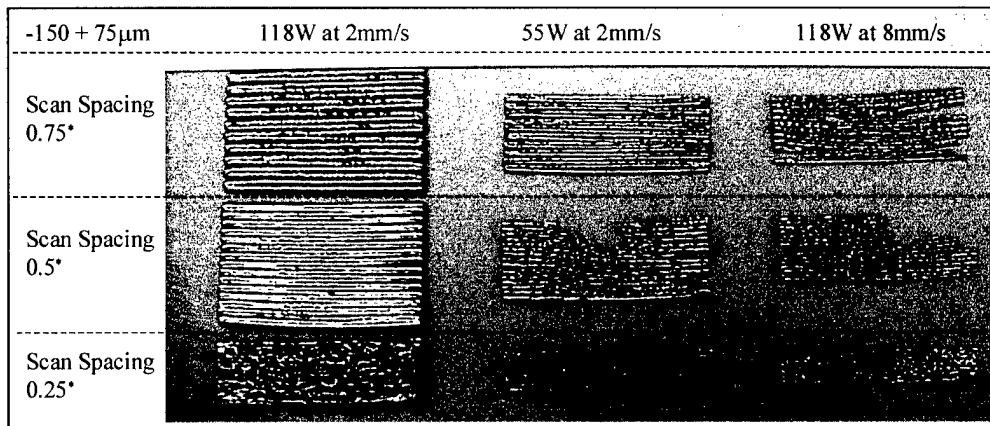


Figure 6: Examples of air-argon sintering.

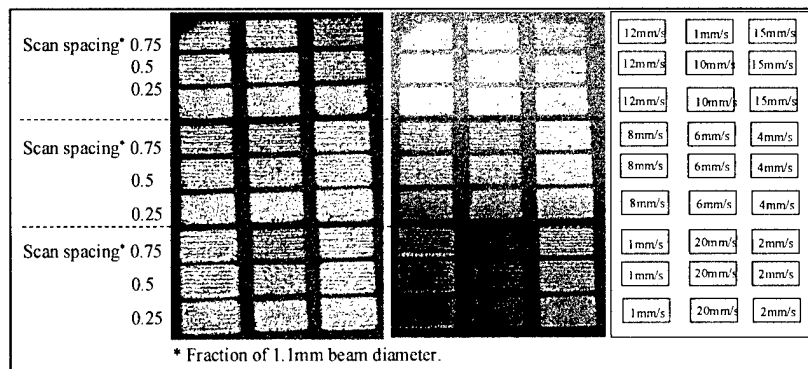


Figure 7: Examples of argon sintering.

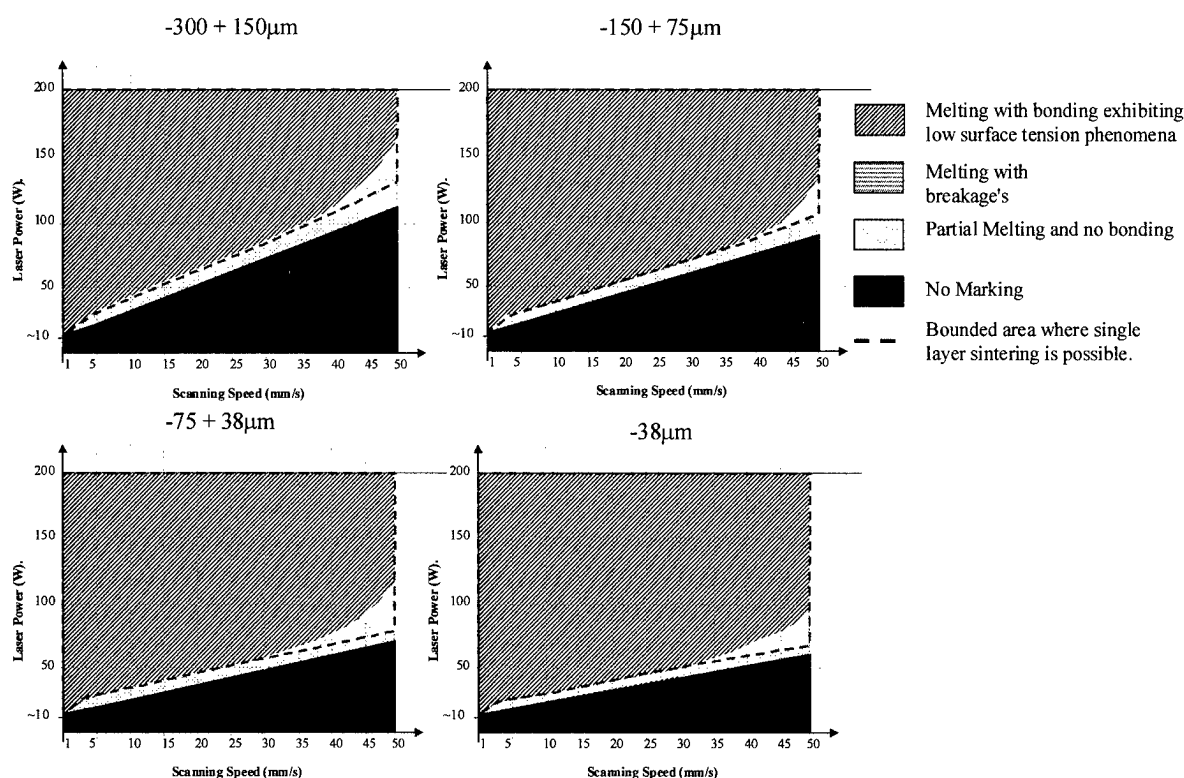


Figure 8: Sintering maps for 314S processed within an argon atmosphere.

dendritic microstructure (similar to original powder particle) found in both air/argon (lower half) and argon (full) sintering indicating re-solidification from temperatures within the solidus/liquidus or 'mushy' zone of the phase diagram where solid and liquid co-exist. The shape of the boundary is a good indication of the changing dominance of the acting surface tension force. Figure 9 also indicates the height of sintered single lines (also reflective of single layers) relative to the powder bed surface. Sinking of the sintered part was observed as the melt volume increased. This phenomenon can influence conditions during powder recoating.

Final Discussion and Conclusions

The presence of oxygen within the sintering atmosphere and powder bed allows surface oxides and slags to form as the powder is heated and melted by the scanning laser beam. Observing the growth and effects of these scales in differing atmospheric conditions has shown that elimination of all oxygen is required in order to reduce the melt volume allowing surface tension forces to become less dominant. Under these conditions liquid metal can flow and wet other solid powder particles and previously sintered areas creating strong bonds for successful single layer sintering. Average sintered densities ranged from 50 – 60 % of theoretical density. However higher densities of ~70% were attainable when using a smaller particle size(-38μm batch) and high scanning energy densities. The existence of surface oxides and slags increased the melt pool volume dramatically (5mm thick single layers were produced). Possible reasons for this include: (1) an increased coupling efficiency between the laser and the surface oxide layer, (2) the exothermic nature of some oxides and (3) the oxide acting as an insulating jacket. The large melt volumes solidified to full density at the expense of a dominant surface tension

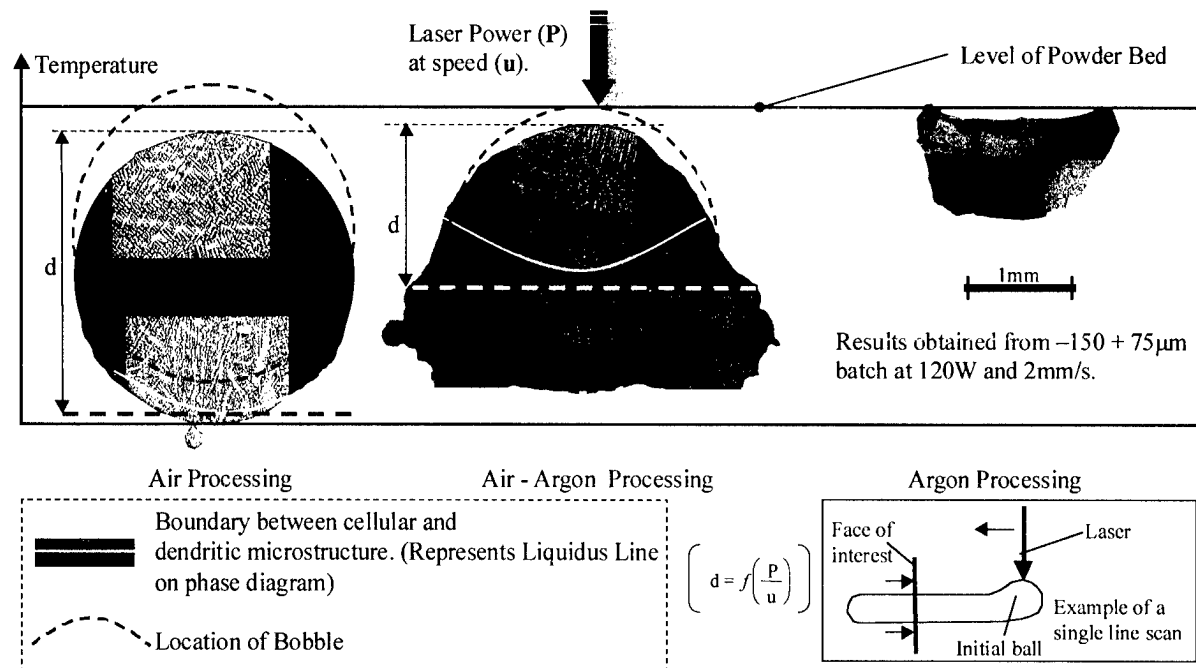


Figure 9: Changes in microstructure and shape of single sintered lines.

force which lowers wetting causing sharp reductions in the range of available scanning conditions for single layer sintering. Improved wetting and bonding was achievable in the air/argon atmosphere. However metallographic inspection has shown that bonding only occurred in areas between adjacent scans where surface tension phenomena were relaxed i.e. in regions where solid fragments and liquid co-exist.

Acknowledgements

The work reported in this paper was supported by the UK Engineering and Physical Science Research Council (EPSRC), through an IMI grant and industrial collaborators. The authors would like to thank the EPSRC and industrial partners for there support.

REFERENCES.

- [1]. U. Lakshminarayan et al, *Advances in Manufacturing Metal Objects by Selective Laser Sintering (SLSTM)*, Advances in Powder Metallurgy and Particulate Materials, Volume 4, 1996.
- [2]. W. T. Carter et al, *Direct Laser Sintering of Metals*, Solid Freeform Fabrication Symposium, The University of Texas at Austin, 1993 [pp 51 – 59].
- [3]. G. Chryssolouris, *Laser Machining: Theory and Practise*, Springer-Varlag, 1991.
- [4]. J. A. Manriquez-Fayre et al, *Selective Laser Sintering of Cu-Pb/Sn Solder Powders*, Solid Freeform Fabrication Symposium, The University of Texas at Austin, 1991.
- [5]. D.E. Bunnell et al, *Fundamentals of Liquid Phase Sintering during Selective Laser Sintering*, Solid Freeform Fabrication Symposium, The University of Texas at Austin, 1995 [pp 440 – 447].
- [6]. J. H. G. Monypenny, *Stainless Iron and Steel*, Volume 1, Third Edition, Chapman and Hall Ltd, London, 1951. [p362].

Selective Laser Sintering of Stainless Steel 314S HC processed using room temperature powder beds.

C. Hauser, T.H.C. Childs, K.W. Dalgarno.
School of Mechanical Engineering,
The University of Leeds, UK.

Abstract

Metal powder bed pre-heating is a proposed route for the homogenisation of temperature gradients that can otherwise cause individual layer warping and cracking in direct metal Selective Laser Sintering (SLS). However, the high temperatures involved complicate a relatively simple process. This paper reports on the conditions for successful small scale SLS of binderless stainless steel 314S powders within the surrounds of a room temperature powder bed. Results show that a scan length around 15.0mm and a scan spacing around 0.275mm produce sintered layers showing no signs of warping. Experimentation also indicates that single layer shape effects warping but length of layer propagation does not.

Keywords

Rapid prototyping, Selective laser sintering, Processing, Part quality.

Introduction

A three dimensional direct metal part built by SLS contains many layers. Each layer is constructed by selectively sintering a metal powder bed, locally at elevated temperatures. The heat input is supplied by a laser beam which raster scans a pre-defined area (from a CAD model), heating and consolidating thin tracks of powder as it travels. The scan spacing determines the amount of overlap between adjacent lines (See Figure 1). Values of scan spacing are often small, typically $\frac{1}{2}$, $\frac{1}{4}$ and $\frac{1}{8}$ of the beam diameter. This permits strong bonding which aids densification. After completion, the powder bed and sintered layer are lowered, allowing a fresh layer of powder to be spread into the build zone and the process repeats. Bonding must also occur between laminates as the new layer is sintered. This is achieved by appropriate selection of the layer thickness that allows heat to conduct sufficiently into the lower laminate. However, as the laser moves in a back and forth cyclic manner across the powder surface, each consolidated track can be heated several times before the laser passes. This scanning technique creates a unique temperature-time history causing thermal gradients to build up in the xy plane during single layer growth. Analogous to scan spacing, the build up of layers also allows thermal gradients to exist in the z plane. The existence of the thermal gradients permits differential shrinkage of the sintered layers during cooling, causing warping, layer cracking and inter laminae cracking [1 - 3].

There are a number of reported methods that have been investigated to prevent thermal distortions and cracking during metal sintering [4,5]. The most successful methods are: (1) powder bed pre-heating aimed at homogenising temperature distributions over entire laminates ($\sim 1000^{\circ}\text{C}$) and (2) by anchoring through sintering the first layer and any overhangs to

substrates placed within the powder bed. The substrates are usually sacrificial but could be designed as an integral part. All these techniques have proven successful though they complicate what should be a very simple process.

The research within this paper is (for us) a second step in understanding the process of metal powder solidification during SLS. This paper reports the conditions for creating single and multiple sintered layers with no powder pre-heating or conditioning and no additional support structures. Emphasis of the work is to establish a range of scanning routines that control the build up of thermal gradients during metal powder heating and cooling that will allow the creation of unwarped and uncracked layers.

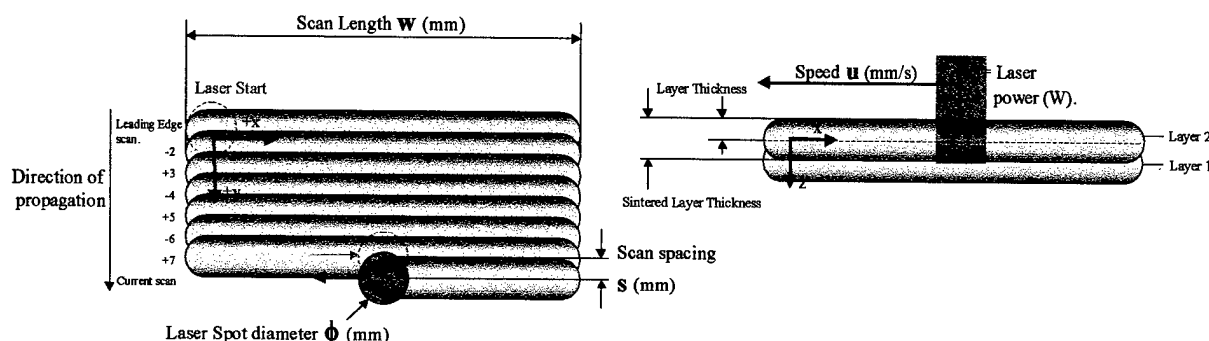


Figure 1: Clarification of scanning parameters.

Material

The material under investigation was a standard grade gas atomised stainless steel powder classified as 314S HC, an austenitic steel with a high carbon content (referred to as 314S). The material composition is given in Table 1. The powder was sieved into four batches having particle size distributions of $-300+150\mu\text{m}$, $-150+75\mu\text{m}$, $-75+38\mu\text{m}$ and $-38\mu\text{m}$. Each batch was used to examine whether thermal distortions are affected by changes in powder particle size.

Elements	(Fe)	(Ni)	(Cr)	(C)	(Si)
Weight %	Bal.	20.0	25.0	0.4	1.0

Table 1: Stainless steel 314S HC material composition.

SLS Machine and Environmental Control Equipment.

The Leeds high power SLS machine includes a 250W continuous wave CO_2 laser with a spot diameter adjustable between 1.0mm and 2.0mm at the focal length. Galvanometer controlled mirrors direct the laser beam onto a 70.0mm diameter build area which is housed within a 0.03m^3 ($L=460\text{mm}$, $H=260\text{mm}$, $D=250\text{mm}$) process chamber (Figure 2) capable of sustaining a variety of atmospheric conditions including an absolute pressure of 10mbar.

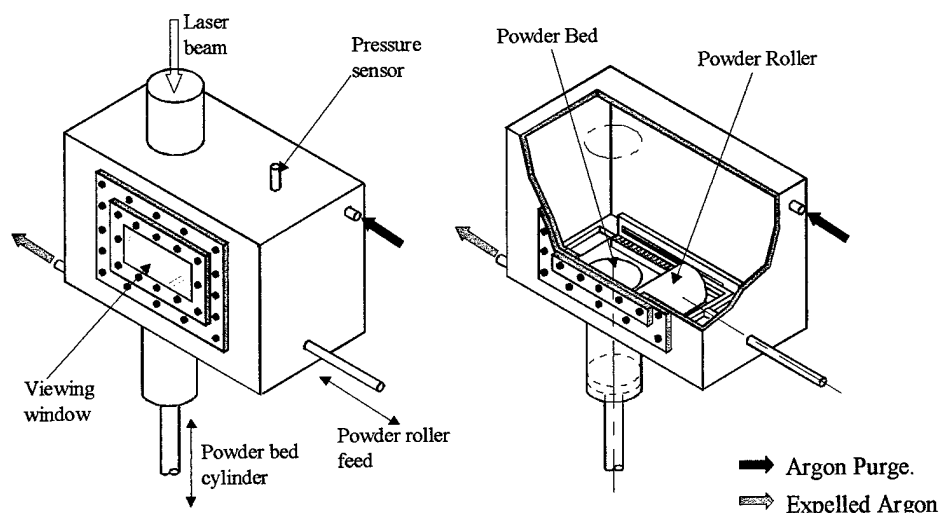


Figure 2: The process chamber.

For the work reported here, oxygen dilution within the chamber is achieved by a combination of evacuation followed by a continuous purge of argon (bottled argon at 99.9% purity). Effects of oxygen are detailed in a companion paper [6].

Experimental Procedure

The four batches of 314S were sintered in the conditions in Table 2. Single line and layer scans with scan lengths ranging from 5.0mm to 150.0mm were sintered within an argon atmosphere while observing for signs of warping and cracking. The number of scanned lines within a layer ranged from 1 to 200. Multiple layer sintering in the same conditions as the previous experiment then followed. Observations were recorded including how the layer thickness influenced warping and inter layer cracking, causing delamination.

The argon atmosphere (which still contained traces of oxygen) was achieved by evacuating the process chamber to a pressure of 50mbar followed by a pre-sinter purge of argon for 10 minutes at atmospheric pressure. During sintering the gas inside the chamber was held at 30mbar above atmospheric pressure.

Atmospheric Condition	Beam Diameter (mm)	Laser Power (W)	Scanning Speed (mm/s)	Scan Spacing (Fraction of beam diameter)
Argon	1.1	0 – 185 in steps of ~10	1 – 100 in steps of ~2	0.25, 0.5, 0.75

Table 2: Experimental conditions.

Results of single layer sintering

Single line scans varying in length from 5.0mm to 150.0mm were sintered while observing for signs of warping (See Figure 3). As has already been presented [6], single lines and layers could be obtained within an argon atmosphere above a (power/speed) energy density

range of 1.0 – 2.0 W/(mm/s). In such conditions, no warping was observed in single layer scans over powder batches of size $-75 +38\mu\text{m}$ and larger. However, some warping was observed with the $-38\mu\text{m}$ powder batch when sintering at high scanning speeds ($>40\text{mm/s}$). It was also found that higher energy densities caused the ends of sintered tracks to lift (all powder batches), a phenomenon that can be seen in figure 3. This effect is believed to be surface tension related rather than caused by temperature distortions.

During the build up of successive bonded tracks warping and stress cracking begins to occur. Two types of thermal distortion were observed: (1) in plane warping leading to arcing of the sintered tracks and (2) out of plane warping leading to dramatic elevations of the sintered layers. In plane warping takes place first and occurs within the first 2 – 10 scanned lines of a single layer though this is dependant on scan length (See Figures 4 and 5). As successive tracks cool differential shrinkage occurs causing the current hotter track to shrink and pull the cooler tracks towards it. As more tracks are produced the phenomenon escalates. The effects of the distortion causes stresses that lead to cracking. As the layer grows the resistance against in plane distortion increases and the arcing phenomenon eventually stops. However shrinkage still occurs and so stress equilibrium is achieved through out of plane warping (See Figures 4 and 5). Increases in layer length (number of lines) showed no visible changes in the magnitude of the distortion. However, the warping phenomenon was found to be periodic in nature causing a wave affect over the entire laminate as it grew (See Figure 5).

Reductions in scan length were found to dramatically reduce the amount of warping and stress cracking within a single laminate. A layer sintered with a scan length of 20.0mm showed no signs of warping but random cracking was still evident (See Figure 6). Further reductions in scan length to 15.0mm stopped both warping and cracking of sintered layers processed over powder batches of size $-75 +38\mu\text{m}$ and larger, irrespective of both energy density, scan spacing and layer length. Single layer sintering using the $-38\mu\text{m}$ powder batch was found to be limiting. Both warping and to a lesser degree cracking was observed when the scan spacing was small ($>0.3 \times$ beam diameter) and when the scanning speed was high ($>40\text{mm/s}$).

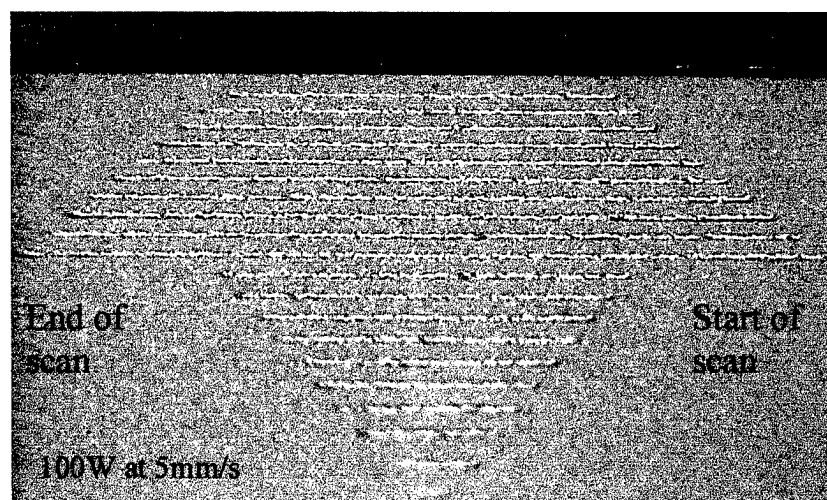


Figure 3: Single line scans.

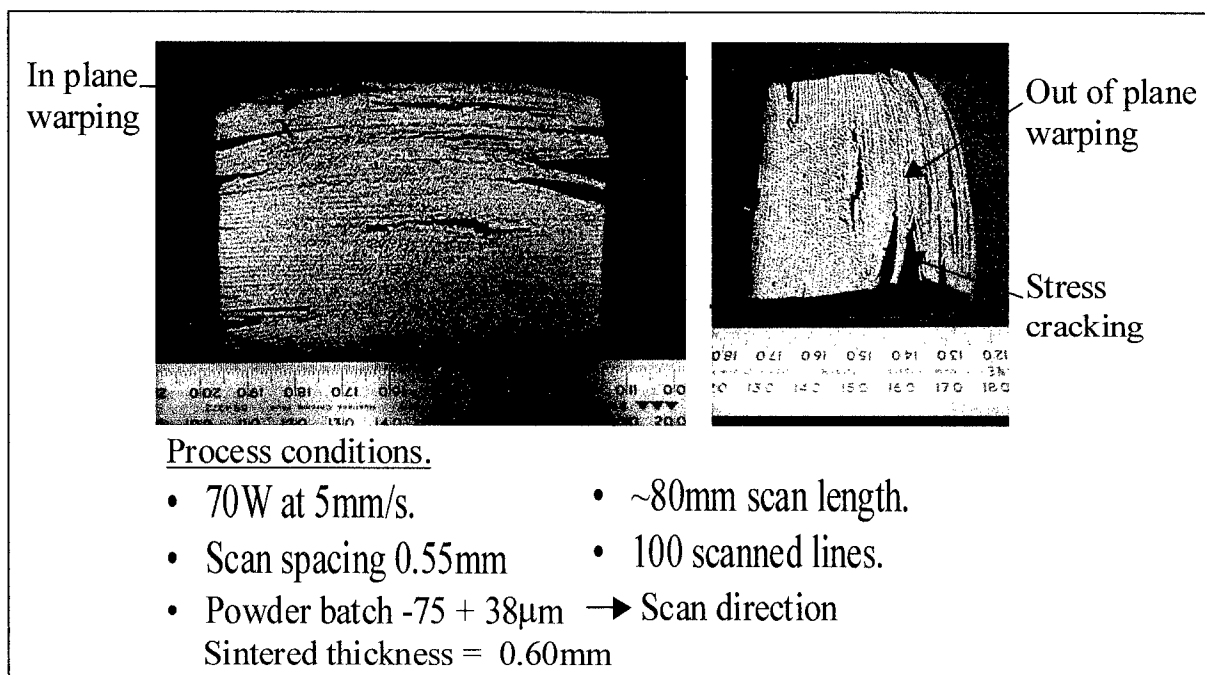


Figure 4: Single layer scan showing dramatic warping and cracking.

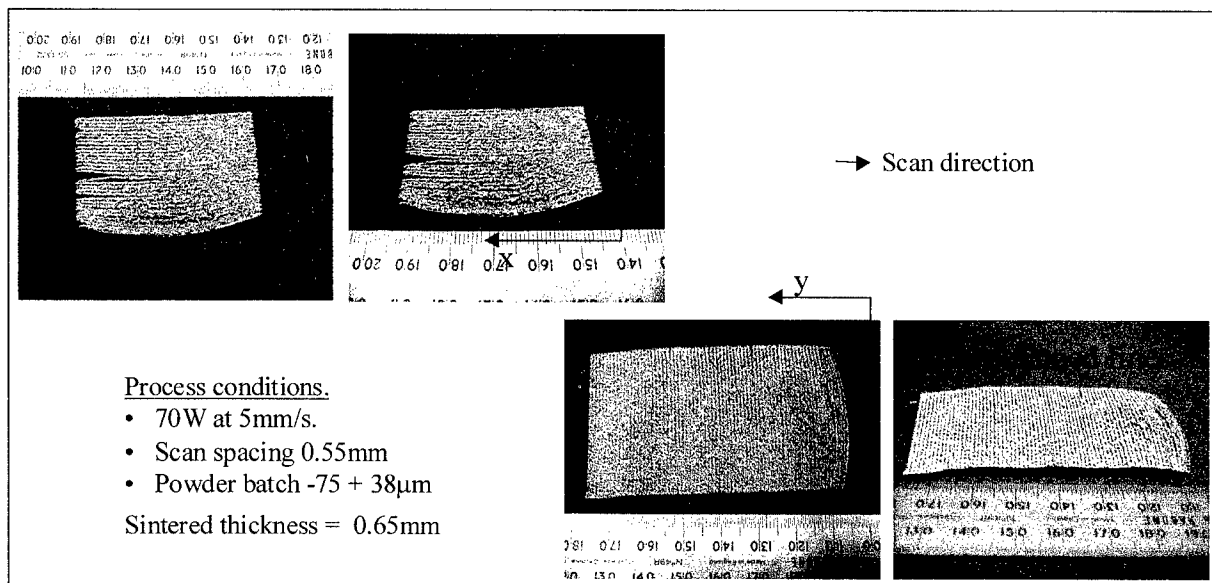


Figure 5: Single layer scan showing warping and cracking.

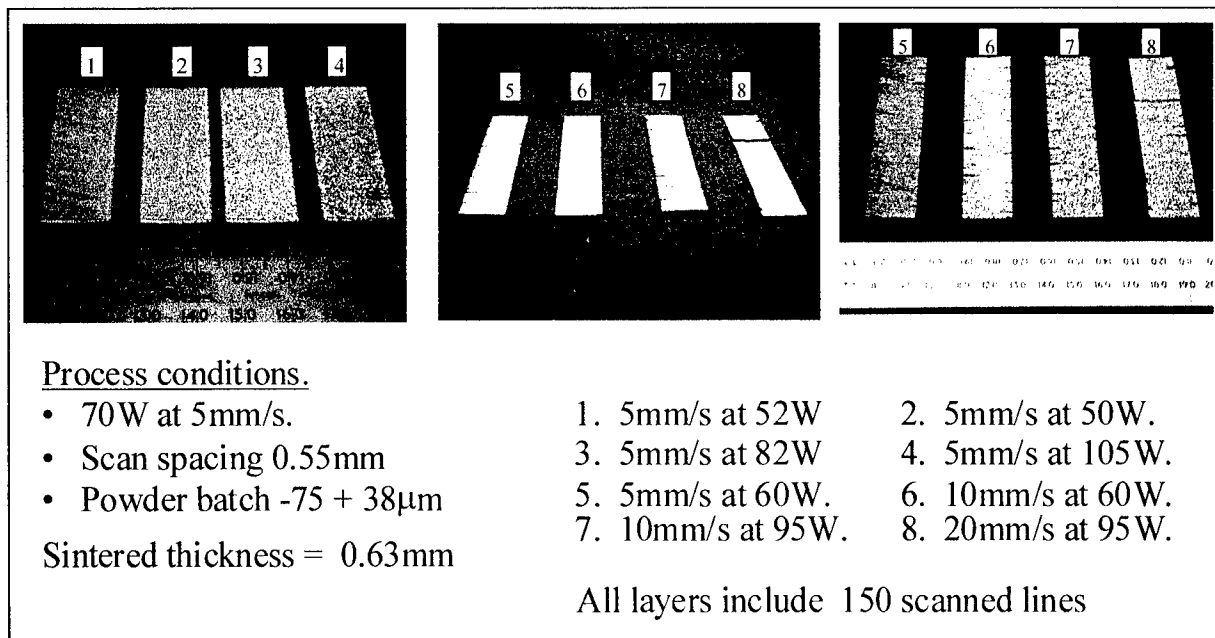


Figure 6: Short scan length single layer scanning.

Changes of single layer shape

Effects of single layer shape were studied to observe how a variable scan length changes the magnitude of warping and cracking. Of the strategies implemented, circular and triangular scanning proved the most successful. It was found that varying the scan length of each track within a single laminate stopped out of plane warping and reduced in plane arcing (See Figure 7). During scanning of circular shapes, distortions were visibly reduced when scanning from the edge to the centre but grew in stature when raster scanning from the middle of the circle back to the edge.

Results of multiple layer sintering

Multi layer sintering was carried out over the range of scanning conditions where single layer sintering was successful. However, it was found that the progressive build up of layers when the scan length was 15.0mm allowed thermal distortions to occur causing delamination. Reducing the scan length further to 12.0mm was found to be more successful. Figure 8a shows a cube with 10.0mm sides consisting of 15 layers, each layer approximately 0.7mm thick (layer overlap was 0.4mm). The sintered density of the cube was ~55%, the density of the individual layers were slightly higher at 60%. Analogous to single layer triangular scanning, a multi layer pyramid was constructed by layering a series of laminates that reduced in surface area. Figure 8b shows a 25 layer pyramid with a base area 15 x 15mm showing no signs of warping or cracking, though layer displacement (stair step effect) can be seen but is a result of roller/sintered part interaction during the recoating process.

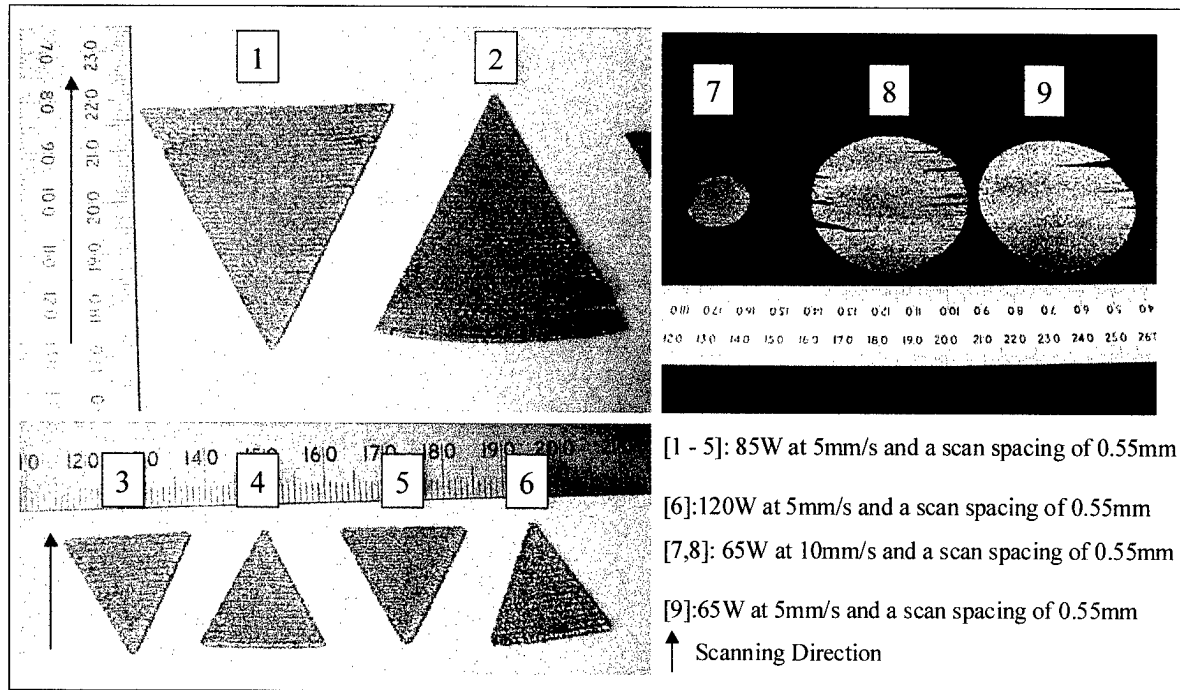


Figure 7: Effects of single layer shape on layer warping and cracking..

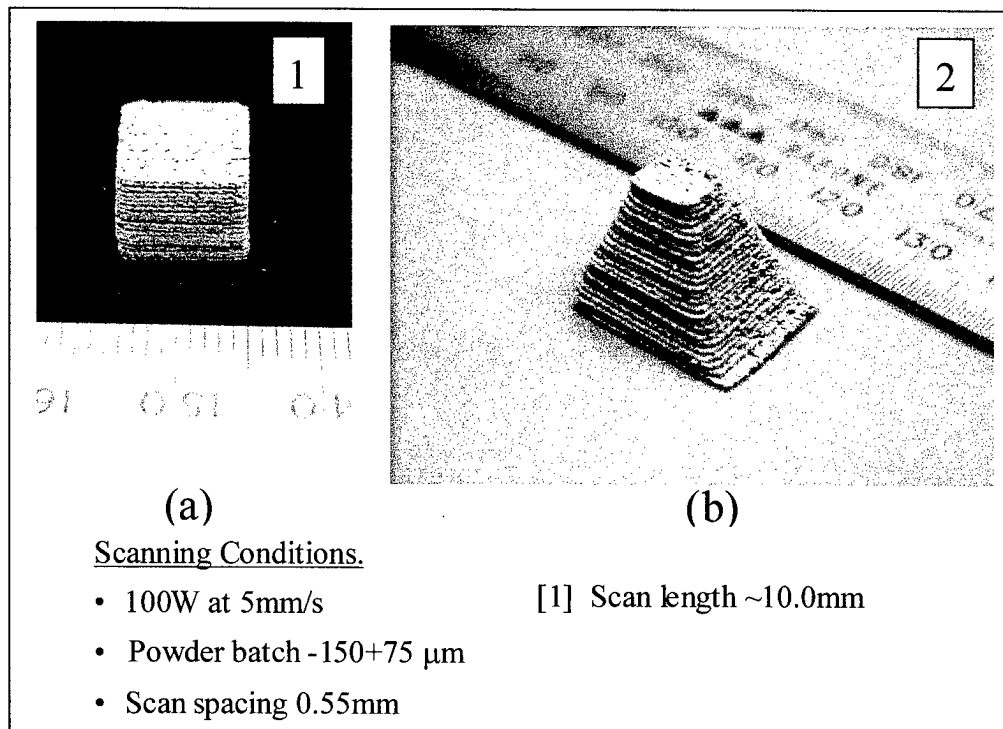


Figure 8: Examples of multiple layer sintering.

Discussion and Conclusion

Single and multiple layer SLS of a single metal alloy powder using a room temperature powder bed was found to be successful when the length of scan remained short. The thermal gradients that exist during sintering caused severe warping and stress cracking when the scan length is long. Single layers were successfully achieved with powder batches of $-75 + 38\mu\text{m}$ and larger and at energy densities greater than $\sim 1.0 \text{ W}/(\text{mm/s})$, up to the limit of the machines laser power of 250W. In these conditions, unwarped and uncracked single layers could be achieved provided the scan length was kept below 15.0mm. This was possible because the heat input into the layer is concentrated over a small area and the temperature gradients are less dominant. Low speed scanning also reduced the chances of warping and was more beneficial in attaining better sintered densities.

The range of conditions for successful multiple layer sintering were similar to conditions for single layer sintering. However higher energy densities ($>1.5 \text{ W}/(\text{mm/s})$) were needed to improve on layer bonding. Under these conditions, unwarped and uncracked multiple layers showing no signs of delamination could be achieved provided the scan length was kept below 12.0mm.

During single line scanning no build up of thermally induced distortions was observed. This evidence, although not conclusive, indicates that the temperature gradient that exists between the upper and lower surface of a single line and possibly a single laminate can be assumed to be negligible.

Acknowledgements

The work reported in this paper was supported by the UK Engineering and Physical Science Research Council (EPSRC), through an IMI grant and industrial collaborators. The authors would like to thank the EPSRC and industrial partners for their support.

REFERENCES.

- [1] J. McWilliams et al, *Design of a High Temperature Process Chamber for the Selective Laser Sintering Process*, Solid Freeform Fabrication Symposium, University of Texas at Austin, 1992, [pp 110 – 117].
- [2] C. Deckard et al, *Improved Energy Delivery for Selective Laser Sintering*, Solid Freeform Fabrication Symposium, University of Texas at Austin, 1995.
- [3] G. B. Prabhu et al, *Supersolidus Liquid Phase Selective Laser Sintering of Metals and Metal Melt Infiltration for Near Net Shape Fabrication of Components*, Solid Freeform Fabrication Symposium, University of Texas at Austin, 1993, [pp 317 – 324].
- [4] J. A. Benda, *Temperature Controlled Selective Laser Sintering*, Solid Free Form Fabrication Symposium, The University of Texas at Austin, 1994, [pp 277 – 284].
- [5] W. T. Carter et al, *Direct Laser Sintering of Metals*, Solid FreeForm Fabrication Symposium, The University of Texas at Austin, 1993, [pp 51 – 59].
- [6] C Hauser et al, *Atmospheric Control during Direct Selective Laser Sintering of Stainless Steel 314S powder*, This Conference, The University of Texas at Austin, 1999.

DIRECT LASER FABRICATION OF HIGH PERFORMANCE METAL COMPONENTS VIA SLS/HIP

Martin Wohler, Suman Das, Joseph J. Beaman, and David L. Bourell

Laboratory for Freeform Fabrication
The University of Texas at Austin
ETC 5.160 C2200
Austin, TX 78712-1063

Abstract

Recent research in the area of direct freeform fabrication of components via selective laser sintering/hot isostatic pressing (SLS/HIP) has focused on the processing of Alloy 625. Alloy 625 is a nickel-based superalloy which provides high temperature strength and corrosion resistance. Alloy 625 test specimens were successfully SLS processed with an integral gas impermeable skin or "can". These samples were subsequently HIPed to high density (>99.5%). Characterization of the test specimens indicated that microstructures similar to conventionally processed P/M materials are achieved in the HIP consolidated "core" region of the parts, while structures similar to those found in cast materials are present in the SLS processed "can" regions. Mechanical analysis of Alloy 625 SLS/HIP parts and production of complex structures will commence shortly.

Introduction

Selective laser sintering/hot isostatic pressing (SLS/HIP) is a hybrid net shape manufacturing technique under development for the production of high performance metal components¹. SLS/HIP combines the freeform shaping capability of selective laser sintering (SLS) with the full densification capability of hot isostatic pressing (HIP) to produce net shape, high value metal components with significantly reduced costs and lead times in comparison to traditional HIP processing. Components being evaluated for this process include aircraft turbine engine hardware, naval, and submarine components.

A schematic of the SLS/HIP process is shown in Figure 1. As an object is built layer by layer, the laser fuses the metal powder only at the part boundaries to form an integral, gas impermeable skin or "can" to a density exceeding 92% theoretical density. This is the fractional density at which the porosity typically changes from interconnected to closed². The powder in the interior of each layer cross-section can be left unprocessed or optionally laser sintered to an intermediate density. Thus, the component is shaped, canned, evacuated and sealed *in-situ*. The integrally canned, net shape component produced by SLS is directly post-processed by containerless HIP to full density. A final machining step may be applied if necessary.

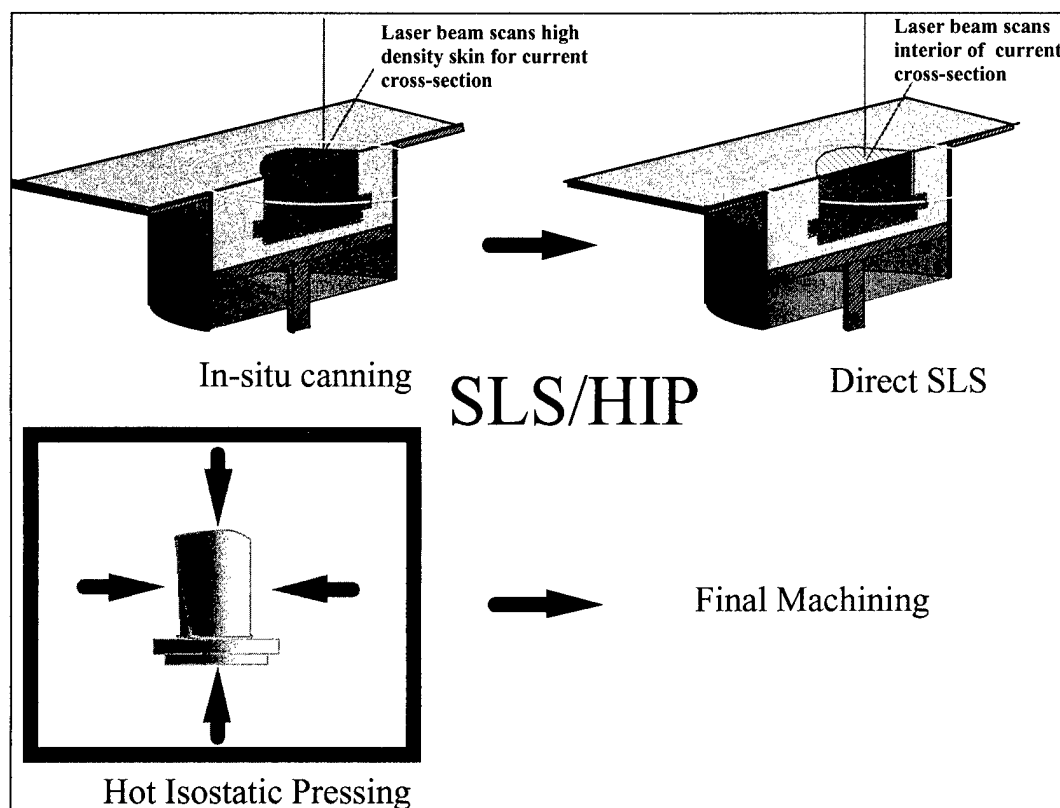


Figure 1: The SLS/HIP process.

SLS/HIP has several advantages over conventional HIP methods. Since an integral skin or “can” is formed of the same material as the component, a secondary canning step is not necessary. Adverse container-powder interactions are eliminated and post-HIP container removal is not required. Tooling and pre-processing steps associated with container fabrication and filling are also eliminated. Therefore, SLS/HIP enables production of complex shapes at reduced cost and in shorter lead-times.

As part of an ongoing research program, SLS/HIP process development is being undertaken for two materials and two demonstration components. Based on a survey¹ of several naval installations, the materials selected for technology development and demonstration are Alloy 625 and Ti-6Al-4V. Prior work on SLS/HIP development for Ti-6Al-4V has been reported elsewhere³. This paper focuses on process development for Alloy 625.

Experimental

Alloy 625 is produced by several manufacturers, under a variety of trade names. The fundamental properties and chemical composition are available in test standards such as ASTM B443, B444, and B446. The composition and metallurgy of Alloy 625 is similar to the more commonly used Alloy 718⁴. Its notable properties include high tensile and fatigue strength, as well as excellent corrosion and oxidation resistance. The corrosion resistance is largely provided by the high chromium content of the alloy, while creep strength is provided by formation of a variety of carbides and precipitates (primarily γ''). However, the precise quantity and

distribution of microconstituents can vary greatly depending on the exact composition and thermal history of the material. The supplier selected to provide a powder form of the material was Anval Inc. (301 Route 17 N., Suite 800-T, Rutherford, NJ 07070). The chemical composition and particle size distribution for the supplied powder is listed below.

Table 1. Chemical Composition

Ni	Cr	Mo	Fe	Nb	Ti	Al	Si	N	Mn	Co	C	S	P
62.2	21.3	8.22	4.00	3.36	0.27	0.21	0.16	.051	.04	.04	.028	.008	.007

Table 2. Particle Distribution (Microtrac)

Micron	44	31	22	16	11
%<	78.8	40.6	9.4	2.6	1.5

Analysis of the provided powder by SEM and optical microscopy indicates a generally spherical morphology with low internal porosity, as shown in Figure 2.

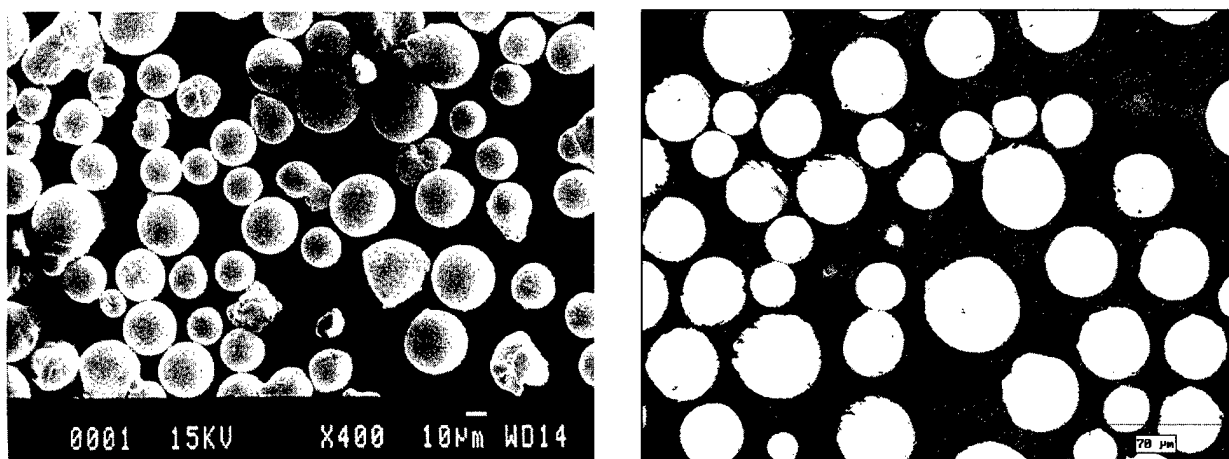


Figure 2. SEM micrograph of spherical Anval 625 powder (left). Optical Micrograph of polished powder showing low internal porosity (right).

Initial experiments with Alloy 625 were designed to demonstrate the feasibility of constructing integrally canned shapes by SLS suitable for HIP post-processing. To this end, a number of cylindrical specimens were fabricated by SLS. Processing was performed in vacuum using a 250 watt continuous wave Nd:Yag laser. Early test samples showed a high degree of porosity and cracking after processing. The presence of cracks or connected porosity cannot be tolerated in the walls of the part since a gas tight specimen is critical for successful HIPing. Further analysis of the problem indicated that contamination of the powder was a likely culprit. The problem of absorbed gases and other contaminants on powder is well known in traditional powder metallurgy⁵. The removal of contaminants can be accomplished by “degassing” the powder in vacuum. Typically, absorbed water vapor is found in the greatest quantities. The

application of heat to the powder can greatly accelerate the rate of contaminant removal. Measurement of contaminant concentration versus temperature by residual gas analysis (RGA) was performed. Scans for a typical metal powder are shown in Figure 3. A temperature increase as low as 150°C is sufficient to greatly accelerate contaminant removal. Removal of absorbed gases produced a dramatic improvement in alloy flow and densification, as shown in Figure 4.

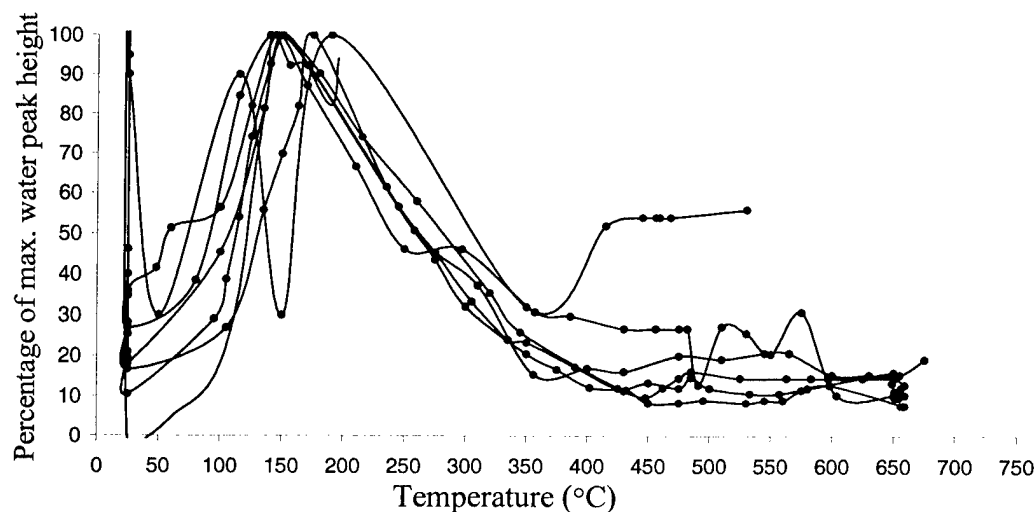


Figure 3. Residual Gas Analysis (RGA) data showing water desorption from metal powder with increasing temperature⁶.

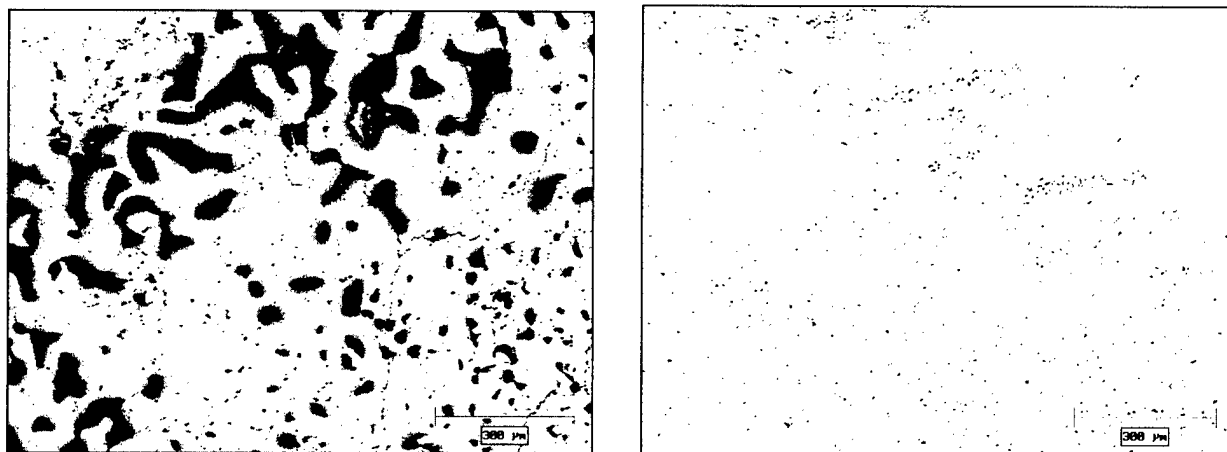


Figure 4. As-SLS processed specimens, contaminated powder (left), after 12 hour vacuum bakeout at 450°C (right).

Following optimization of the processing parameters, production of cylindrical HIP specimens commenced. A typical specimen, shown in Figure 5, has an outer diameter of 0.5 inches with a wall thickness of 0.125 inches and an unprocessed powder core. A portion of a transverse cross-section of one such cylinder is shown in the photomicrograph of Figure 6. The figure shows a section of the powder core, the right side-wall and the base of the cylinder. The

fractional density varies from 60% at the axis to more than 98.5% at the side-wall. Shown on the left in Figure 7 is a photomicrograph of the interface between the cylinder side-wall and the interior powder core while the photomicrograph on the right shows the interface between the fully dense side-wall and the porous outer layer formed by sintering due to local heat transfer.

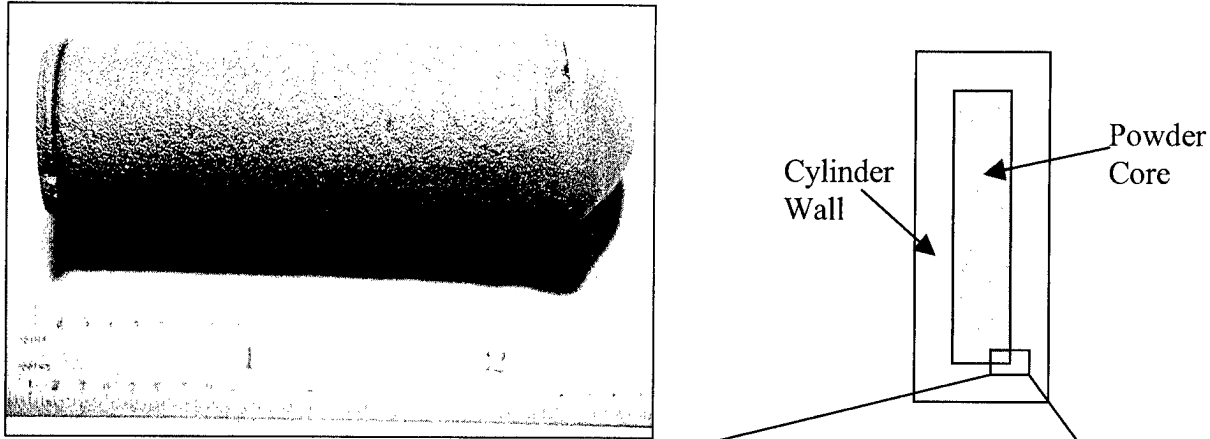


Figure 5. A typical as-SLS processed Alloy 625 cylinder.

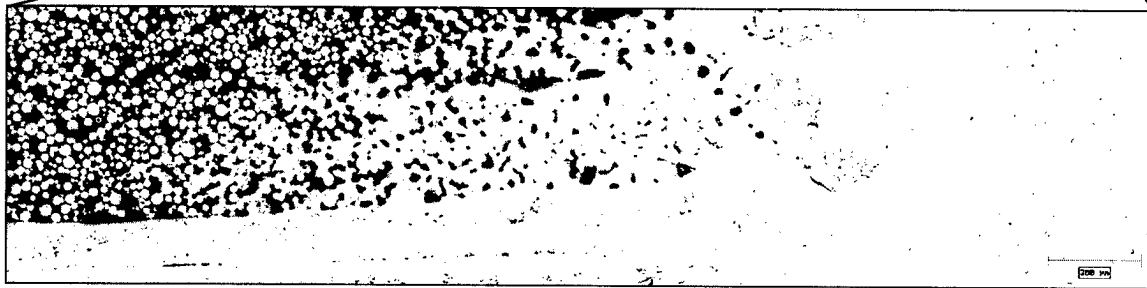


Figure 6. Transverse cross-section segment of a typical SLS processed Alloy 625 cylinder at the interface between bottom-cap, side-wall and core.

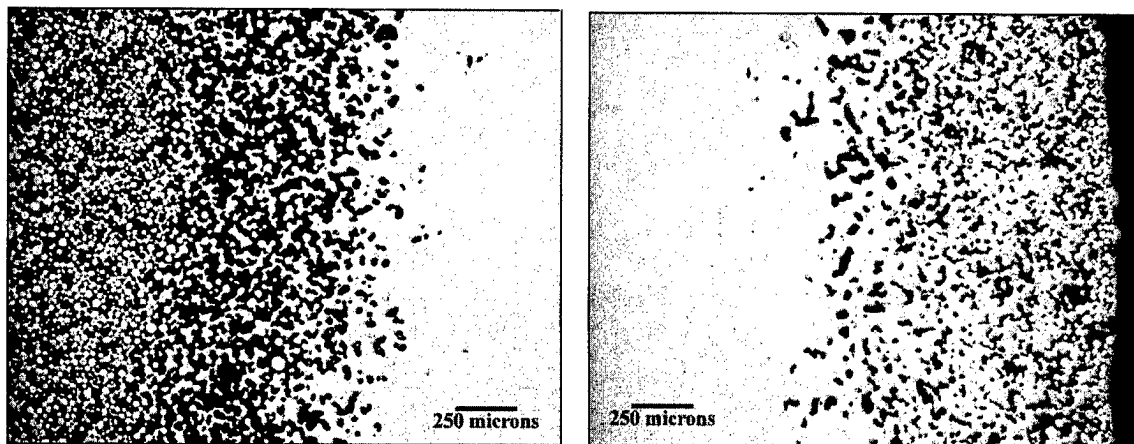


Figure 7. Interface between skin and core (left), between skin and outer layer (right).

Microstructure

Sample parts were sectioned, mounted, and polished for metallographic inspection. Grain structure was revealed by a mixed acids etchant⁷ (15 ml HCl, 5 ml acetic acid, and 5 ml HNO₃). The photomicrograph on the left in Figure 8 shows the grain structure of as-SLS processed fully dense skin in a cross-section transverse to the powder layer orientation. The image height is the equivalent of approximately 7 powder layers, each of thickness 125 μ m. The microstructure consists of elongated columnar grains oriented vertically in the build direction. The grain orientation indicates that the solidification front originates at the remelted surface of the previously solidified layer, which provides significantly better heat conduction than the loose powder surrounding the part along the sides. No distinct boundaries between individual powder layers are visible. The photomicrograph taken parallel to the powder layers exhibits the expected equiaxed grain structure, as shown on the right in Figure 8.

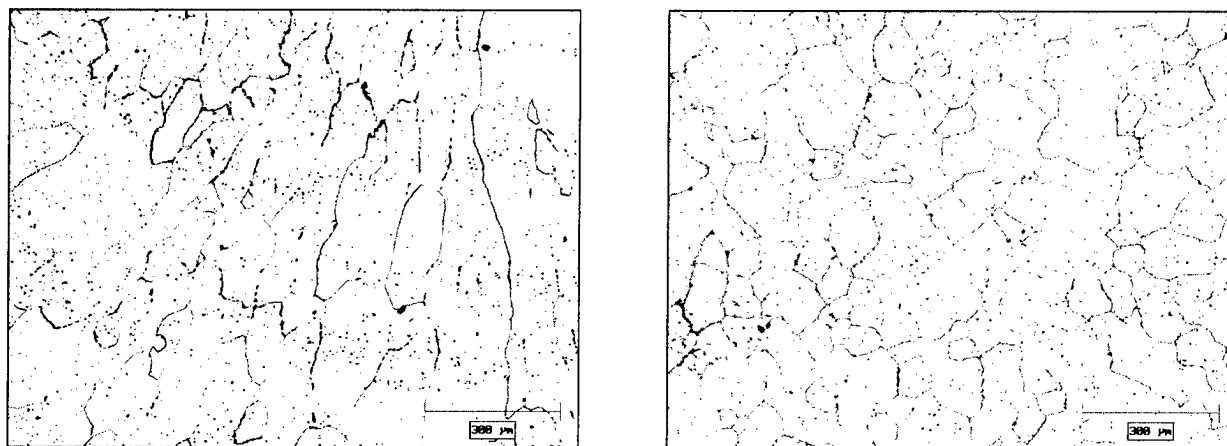


Figure 8. Etched microstructure of cylinder side-wall, transverse section (left) and longitudinal section (right).

SLS processed Alloy 625 cylinders were post-processed using the following HIP cycle: ramp from ambient temperature to 1150° C at 15° C/min, pressurize to 138 MPa (20,000psi) over 30 min, hold at 1150° C and 138 MPa for 3 hours, ramp down to ambient at 30° C/min. Figure 9 shows photomicrographs of the powder core taken prior to and after HIP. Image analysis of the unprocessed core indicates a density of 60% prior to HIP. Actual density may be slightly higher, in the range of 65%, due to errors caused by particle pullout during sectioning and polishing of the sample. Following HIP, a core density of 99.5% was achieved. Etching reveals grain boundaries formed largely along prior particle boundaries. The generally spherical geometry of the particles is preserved in the grain structure shown in Figure 9. While this is the expected microstructure for HIP processed parts, the effect of the prior particle boundaries (PPBs) on the mechanical behavior of the parts has not yet been established. The presence of contaminants or undesirable precipitates at PPBs can substantially reduce ductility and tensile strength. Because there is no additional cold working to disrupt the boundaries following HIP, the presence of a continuous impurity film can be quite detrimental. Previous researchers⁸ have identified the presence of an Al-rich oxide film as limiting mechanical and corrosion properties in improperly processed material. While great care has been taken during SLS processing to minimize the possibility of contamination, tensile test specimens will be produced in the near

future to verify the mechanical properties of the SLS/HIP processed material.

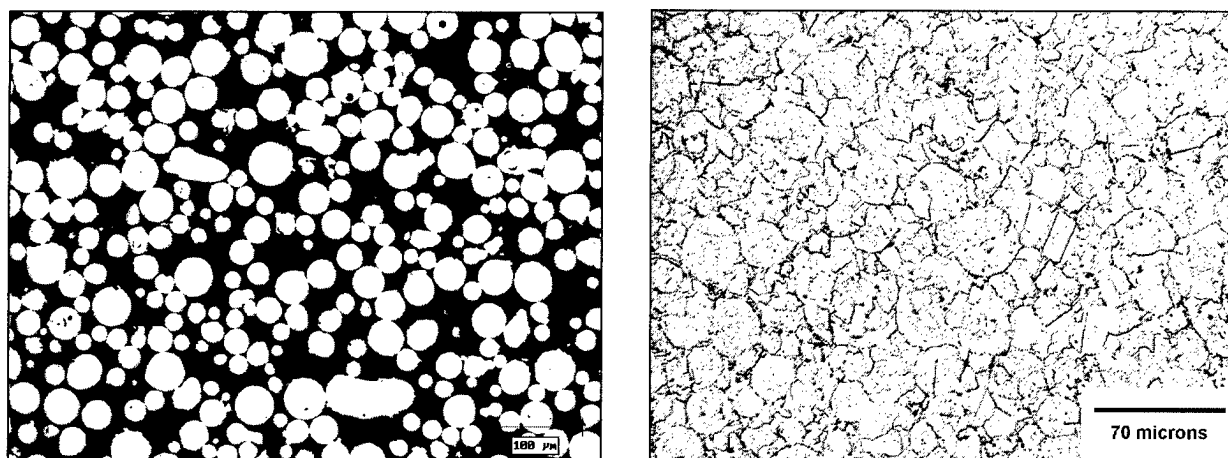


Figure 9. Unprocessed powder core, approximately 60% dense (left), etched microstructure following HIP, 99.5% dense (right).

A second type of cylinder was also processed by SLS. This cylinder, fabricated with an identical 0.5 in. diameter, was processed to near full density across the entire diameter. This type of processing is necessary to fabricate “end-caps” for an integrally canned object made by SLS suitable for HIP post-processing. Metallography revealed that the density in this type of specimen exceeded 98.5% of theoretical density. The etched microstructure, shown on the left in Figure 10 reveals equiaxed grains. This microstructure is quite comparable to that obtained in conventionally cast or annealed wrought materials⁹. The SLS processed specimen was post-processed by a HIP cycle consisting of 3 hours at 1240°C and 172 MPa (25000 psi). The microstructure in the HIP post-processed specimen (with density exceeding 99.5% of theoretical) is shown on the right in Figure 10.

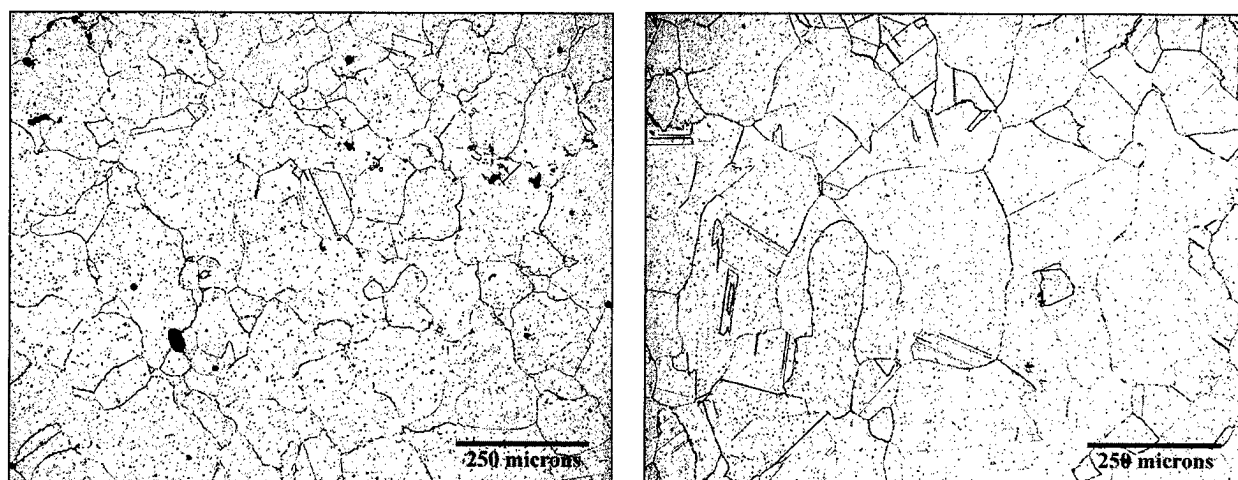


Figure 10. Etched microstructure of 98.5% dense SLS processed (left) and 99.5% dense SLS/HIP processed (right) Alloy 625.

Conclusions

Feasibility of fabricating integrally canned complex shapes by SLS for containerless HIP post-processing was demonstrated in Alloy 625. Simple cylindrical shapes were fabricated by SLS and consolidated to full density by HIP. Preliminary evaluation of microstructure reveals that material processed by the SLS/HIP technique is equivalent to conventionally processed P/M material in the part core. The small volume of material processed directly by SLS that forms the can structure is similar to conventional cast structures. Future work will focus on building a part with complex geometry as a technology demonstration for Alloy 625, further characterization of structure/property relationships as well as optimization of processing parameters for build speed, skin thickness and HIP cycle time.

Acknowledgements

The authors wish to acknowledge research funding provided by DARPA and ONR under contract N00014-95-C-0139 titled "Low Cost Metal Processing Using SLS/HIP".

References

- ¹ R. Knight et al., "Metal Processing Using Selective Laser Sintering and Hot Isostatic Pressing", *Proc. Solid Freeform Fabrication Symposium 1994*, (Austin, TX: U. of Texas, 1994).
- ² R. M. German, *Powder Metallurgy Science*, Chapter 7, pp. 257, MPIF, 1994.
- ³ S. Das et al, "Producing Metal Parts by Selective Laser Sintering/Hot Isostatic Pressing", JOM, December 1998, TMS.
- ⁴ S. Floreen et al., "The Metallurgy of Alloy 625", *Superalloys 718, 625, 706 and other Various Derivatives*, TMS 1994, pp. 13-37.
- ⁵ Cleaning of Metal Powders, *Metals Handbook 9th edition*, v7, Powder Metallurgy, American Society for Metals, 1984, pp. 171-181.
- ⁶ B. Engel, Masters Thesis "Preprocessing of Ti-6Al-4V Powder for Applications in Selective Laser Sintering / Hot Isostatic Pressing (SLS/HIP)", The University of Texas at Austin, 1998.
- ⁷ G. F. Van der Voort, J.W. Bowman and R. B. Frank, "Custom Age 625 Plus Alloy", *Superalloys 718, 625, 706 and other Various Derivatives*, TMS 1994, pp. 489-498.
- ⁸ F.J. Rizo and S. B. Justus "PM Alloy 625M – A High Strength Modification of Alloy 625", *Superalloys 718, 625, 706 and other Various Derivatives*, TMS 1994, pp. 903-911.
- ⁹ INCONEL Alloy 625, Inco Alloys International, 1985.

Si/SiC-Ceramic Prototypes via LS²I -Process (Liquid Silicon Infiltration of Laser Sintered C-SiC Parts)

Peter Stierlen*, Peter Eyerer*

* Institute of Polymer Testing and Polymer Science (IKP), University Stuttgart
with the cooperation of the DLR Stuttgart

Abstract

The liquid silicon infiltration of laser sintered C-SiC parts (LS²I) is a solid freeform fabrication technique which allows the production of complex shaped Si/SiC prototypes. A mixture of SiC powder and reactive polymer binder is used in the laser sintering process to generate a porous green part. In the postprocessing, the porous green part structure has to be infiltrated with a precursor resin, carbonised and finally infiltrated with molten silicon. The infiltrated silicon reacts with the residual carbon to build β -SiC. Results generated by the use of reduced primary particle sizes as well as alternative infiltration materials and the use of other RP-techniques for the green part fabrication will be discussed in this paper.

Introduction

Up to now, several investigations on rapid prototyping ceramics have been performed worldwide. Most investigations have focused on ceramic filled SLA-resins, binder coated ceramic powders for SLS or 3D printing processing, ceramic filled sheets for LOM and other technologies such as laser induced generating by vapour deposition /1/,/2/,/3/,/4/,/5/,/6/. The post processes debinding and sintering are necessary to obtain a high density ceramic structure. The theoretical maximum density of monomodal particles is 74 % with an increase in density during sintering to over 95 %, so, in existing processes, this leads to high shrinkage.

The presented technology relies on the debinding and sintering and is a combination of laser sintering, different infiltration and pyrolysis techniques /7/. In comparison to the other techniques, the polymeric binder is transformed to its residual carbon and must not be burnt out completely. The porous green part structure must be filled with precursors to increase the carbon yield after pyrolysis /8/,/9/. After the precursor infiltration, the binder system and the precursor are transformed in an inert pyrolysis reaction process to carbon. During pyrolysis the polymeric systems utilised result in a stable carbon binding structure penetrated by fine structured crack systems. In the final process the crack system has to be infiltrated with molten silicon. Because of the very low viscosity of the molten silicon and the capillary forces, the molten Si will fill the whole open porosity. The infiltrated silicon will finally react with the residual carbon to form β -SiC.

Si/SiC Processing with laser sintered pre-forms

Greenpart production by lasersinter process

The process technique for the green part production is similar to the well known direct croning process from EOS GmbH. The first investigations were carried out with an average SiC-powder particle size of about 70 μm and a powder density of 1.25-1.40 g/cm^3 (~39-44 % of full SiC density). Meanwhile the particle size was reduced to $d_{50}=15\mu\text{m}$ and further investigations were done with $d_{50}=1,5\mu\text{m}$ powder. The binder system, a dry powder resin, removes the need for the complex process of coating the SiC particles. Nevertheless first coating tests were carried out. A new powder resin shows a reduced melt viscosity and an improved wetting of the SiC particles. The binder content can be reduced from 18 %wt to 10-15 %wt. Therefore the shrinkage and warpage during the laser sintering of the green parts and during the pyrolysis was reduced. The complete process chain is shown in **figure 1**.

Post-infiltration with precursor

In the second step the open porosity of the laser sintered part is infiltrated with a precursor. Phenolic precursor resins must be pre-heated to get the lowest melt viscosity for the infiltration which takes place in a vacuum desiccator. Other precursor materials like PS or PAN have to be infiltrated in solution.

The following processing steps of pyrolysis and silicon infiltration are quite similar to the well known Liquid Silicon Infiltration Process (LSI) of the DLR for manufacturing fibre reinforced CMC materials /10/,/11/,/12/.

Pyrolysis of the polymeric components

The infiltrated and cured parts are now ready for the carbonisation process. During pyrolysis at a temperature of up to 900 °C under a nitrogen environment the polymer shrinks in an almost unrestricted manner in all directions. In this process the shrinkage of the polymeric components during the carbonisation is hindered by the SiC powder particles. Therefore a crack structure in the carbonised matrix is produced, which is necessary for the following silicon infiltration step. The crack system can be influenced by different parameters such as SiC particle size, particle form, binder and precursor, infiltration and carbonisation process parameters.

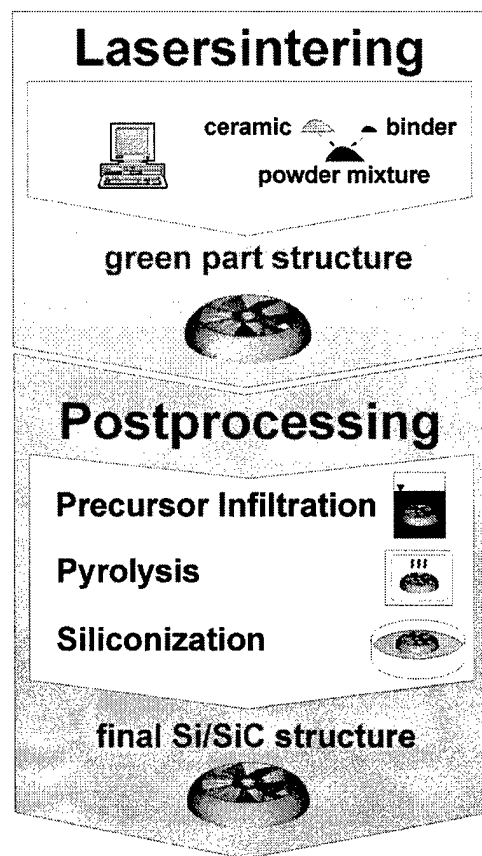


Figure 1: Process chain of the Si/SiC process

Silicon infiltration

During the last manufacturing step at temperatures up to 1600 °C, and in vacuum, the liquid silicon infiltrates the porous specimens due to the capillary forces, and reacts with the carbon of the residual matrix and forms to silicon carbide. The carbonized parts have to be placed

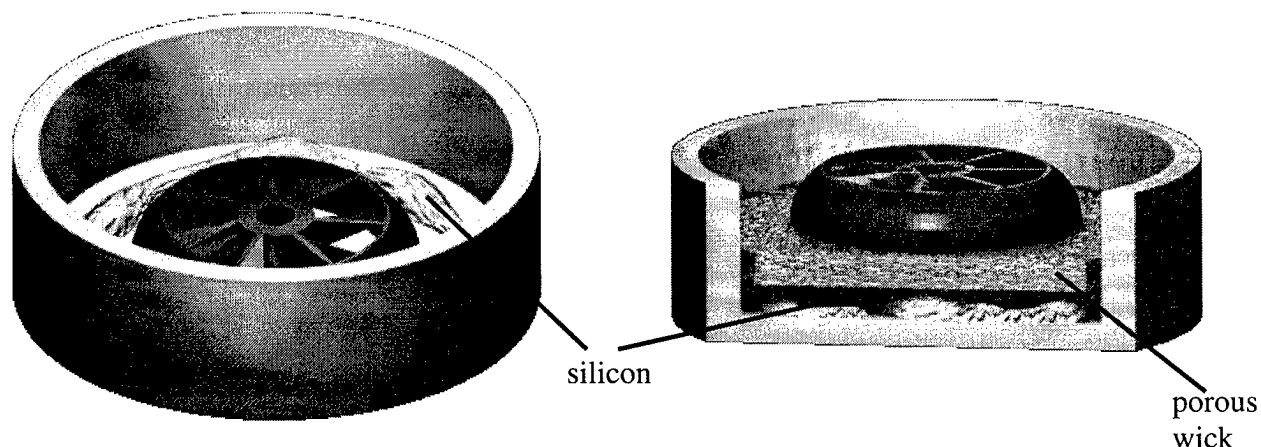


Figure 2: Left: Pyrolysed greenpart placed with silicon in bowl. Right: Pyrolysed greenpart placed on a porous wick panel

in a bowl or on a porous wick panel for a well dosed Si feeding **figure 2**. The removal of the parts after the siliconization can be simplified by placing the parts on additional weak supports. The degree of ($\text{Si} + \text{C} \rightarrow \text{SiC}$) conversion during the siliconization can be controlled by the temperature profile. Therefore it is still one of the aims to realise a stoichiometric formation of the components to get a high yield of $\beta\text{-SiC}$. The infiltration height depends on the diameter of the crack capillaries and the infiltration time. The calculated infiltration heights for the Si infiltration are shown in **figure 3** [11]. The resulting surface of the parts primarily depends on the surface of the green part. The surface quality can be improved by the use of smaller powder particles with a more uniform particle geometry. Additional finishing of the infiltrated green parts also improves the surface quality.

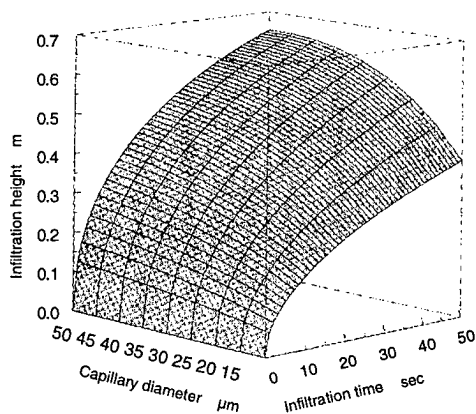


Figure 3: Calculated silicon infiltration height

Results of investigations

The aim of the first investigations was to show the feasibility of the process. Therefore a SiC-powder with a particle size of about 70 μm was chosen for easy powder recoating in the Laser Sinter machine. With the modified machine particle sizes of 10-15 μm can be used easily.

The reduction of the particle size is limited by the optical behaviour of the powder material. At the wavelength of the CO_2 -laser SiC shows a very low absorption depth of approximately 5 μm . To get a sufficient layer thickness the laser energy must be carried into the material by multi-reflection and heat transfer. The effect of multi-reflection depends on the

particle size. The smaller the particles the lower the energy transfer into the depth. Therefore the layer thickness must be reduced if smaller particle sizes should be realised. With a reduced particle size also the capillaries, necessary for the infiltration become smaller. The reduction of the particle size also reduces the maximum infiltration height **figure 3**.

Reduced particle size

The mechanical properties of ceramic parts depend on the ceramic structure and the surface quality of the parts. The strength primary depends on the fine-particle character and homogeneity of the structure. Each scratch or surface failure reduces the strength of the parts. The stairstep effects of layerwise building RP-systems are also surface failures reducing the mechanical strength. Therefore the ceramic structure and the surface quality must be improved by reduced SiC particle size and by reduced layer thickness. Additional finishing of the infiltrated green parts also improves the surface quality.

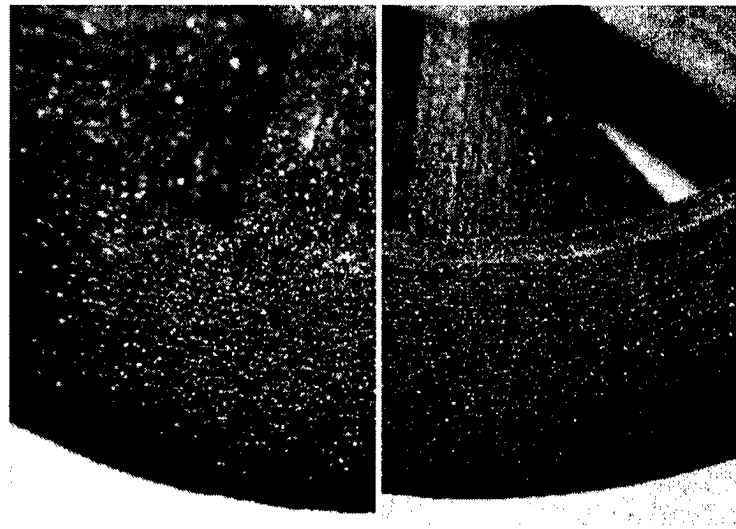


Figure 4: Left: Particle size 70 μ m, 200 μ m layers; right: particle size 15 μ m, 100 μ m layers

Figure 4 shows two samples processed with 70 μ m particle size, 200 μ m layer thickness on the left side and a sample with 15 μ m, 100 μ m layer thickness on the right side. The final structures with and without the precursor infiltration are shown in **figure 5**. The pictures show the structure for 15 μ m primary SiC particle size and for the rough 70 μ m powder.

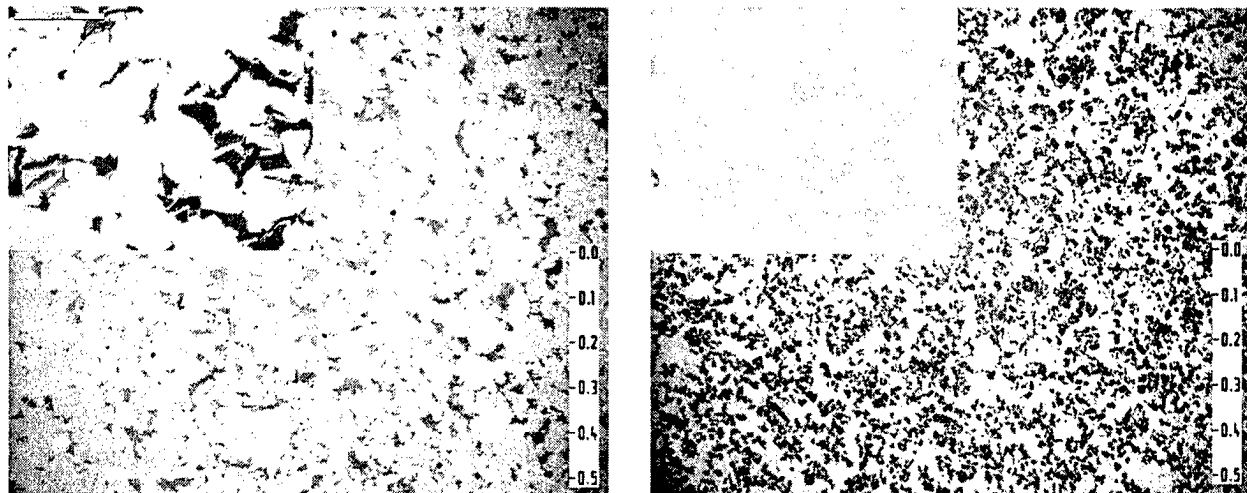


Figure 5: Left: Final Si/SiC structure with precursor infiltration. Right: Final structure without precursor infiltration. Primary particle sizes 15 μ m (70 μ m in u. l. corner)

Powder binder

The shrinkage and warpage during laser sintering of the green parts primary depends on the polymeric binder content. By the use of a new improved powder resin with a reduced melt viscosity the powder content is reduced to 10-15%wt. The warpage is eliminated almost completely. The parts can now be built without, or with very weak supports. The main problems of the new powder system are the reduced free-flowing properties. It is much more difficult to recoat in thin layers. But with a multi-recoating process the powder can be levelled very homogenously. The powder flow depends on the temperature and the humidity of the powder. Further on the lower melt viscosity reduces the resolution by the wider melting section.

Precursors

Phenolic resin was the first precursor system used in the investigations to increase the residual carbon content after the pyrolysis. Different phenol resins were tested. Phenolic resins show a good carbon yield and can be infiltrated easily into the porous green part structure

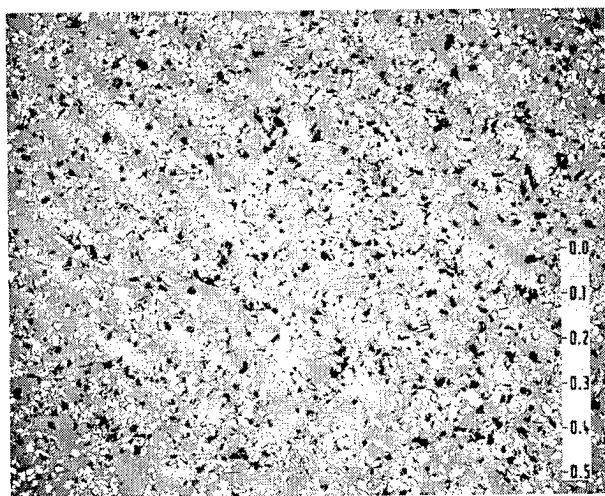


Figure 6: Green part structure infiltrated with phenolic resin

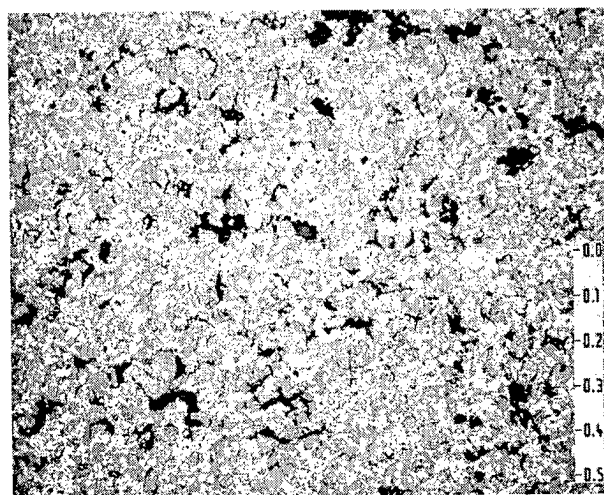


Figure 7: Final structure of a polysilazane infiltrated sample after pyrolysis

figure 6. But phenolic resins react in a polycondensation reaction by separating water. It is difficult to remove the water out of the structure without producing bubbles. Additional tests were carried out with polysilazane resin to directly form ceramic structures in the pyrolysis step. The final structure after pyrolysis and formation of the ceramic structure is shown in **figure 7**. Meanwhile other precursors like polystyrene were tested.

Test shapes and Examples

For the evaluation of the mechanical properties several test bars for bending tests were built. For the silicon infiltration via capillary action the samples have to be placed on support structures for easy removal of the buffer panel. **Figure 8** shows 7 bending test bars placed on a support panel for simplified removal of the bars after siliconization.

Also parts with overhangs undercuts and thin walls have been built successfully. With the new powder system, complex shaped green parts can be built up reliable and easily **figure 9**. All green parts were built up in the laboratory sinter station at IKP with 0.1mm slices.

The lasersinter process is quite fast with a scan speed of 900 mm/sec., 0.2 mm hatch distance and up to 0.05-0.1 mm slices. Smaller slices are also possible for the adaption of smaller particle sizes. The post-curing and the precursor infiltration is done in approximately one day and depends on the chosen precursor system and processing. The rapid pyrolysis requires two further days and the final silicon infiltration is also done in 2 days. The whole post-processing can be executed in 5 days.

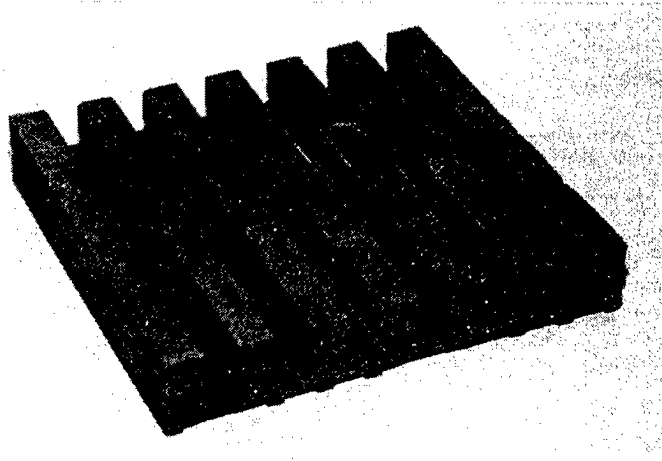


Figure 8: Test bars for bending tests with support

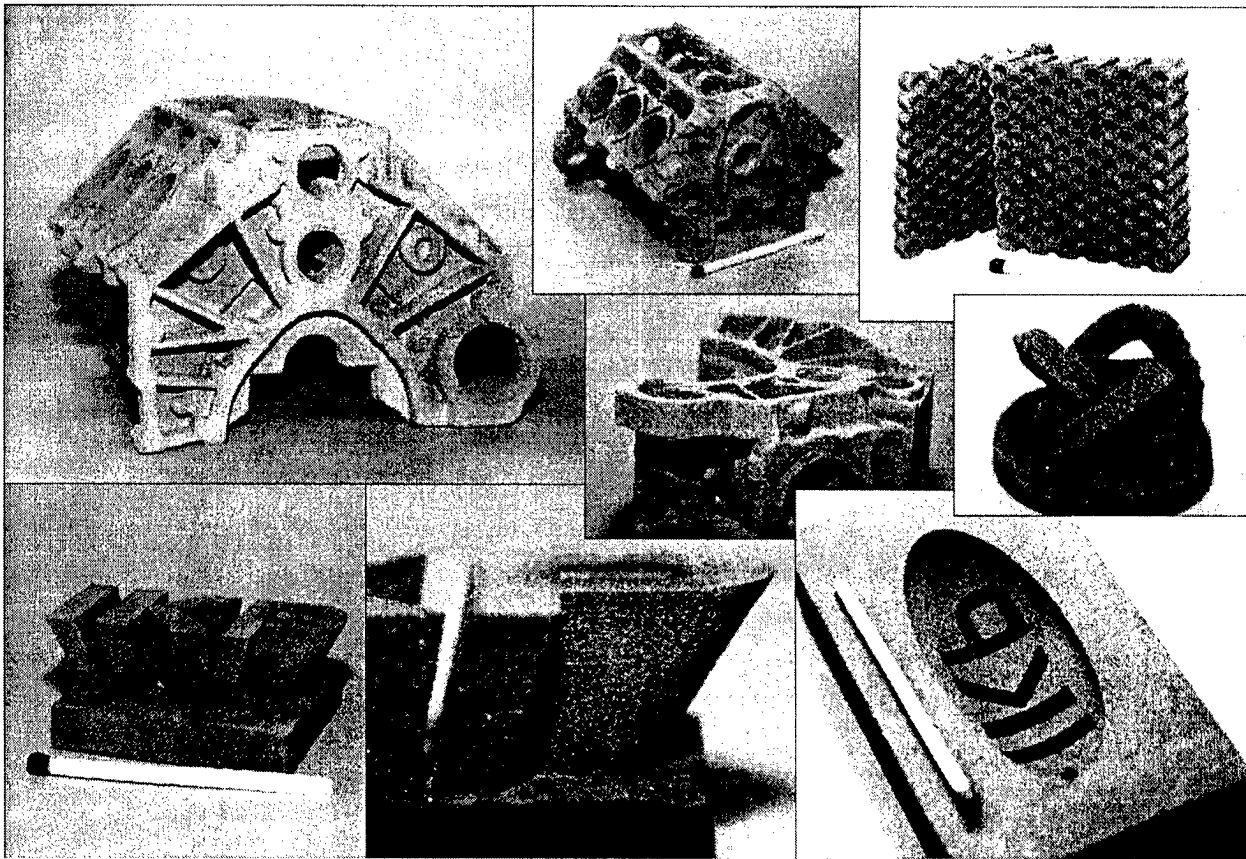


Figure 9: Complex test samples with overhangs, under cuts and inner sections like moulds and combs

Conclusion

Powders with smaller particle sizes were adapted successfully. The further reduction of the particle size is limited by the decrease of the optical absorption depth of the SiC-powder and the much more difficult layerwise recoating in the lasersinter process. Tests with agglomerated 1,5µm SiC powder showed good layerwise recoating conditions but inadequate absorption depths of the laser beam. Therefore only a small layer thickness can be realised.

The investigations must be focused on the further reduction of the particle size and higher powder packing densities. Therefore additional tests must be carried out with the laser operating at other wavelengths. First kick-off tests should be carried out with a Nd-YAG laser system also available at the IKP.

The parameters for the pyrolysis are of interest for an optimised porous crack structure. In conjunction with the parameters of the silicon infiltration, they specify the forming of the β -SiC and therefore the final structure.

Acknowledgement

Parts of the presented research were supported by the German Research Foundation (DFG/Sfb 374). The authors thank especially DLR, Stuttgart; Institut für Materialforschung (IMA), University Bayreuth; Bakelite AG, Iserlohn; ESK, Kempten; Institut für Nichtmetallische Anorganische Materialien (INAM), University of Stuttgart; Fraunhofer-Institut für Chemische Technologie (FhG/ICT), Pfinztal for the help and encouragement as well as Retallick Systems and SCAPS GmbH for the process software for our laboratory sinter machine.

Further informations:

Dipl.-Ing. Peter Stierlen
Institute for Polymer Science and Polymer Testing
University Stuttgart
phone: +49-711-641-2276
stierlen@ikp2.uni-stuttgart.de

Literature:

- /1/ Lakshminarayan, U.; et al. Selective Laser Sintering of Ceramic Materials. Proceedings of the Solid Freeform Fabrication Symposium 1990, University of Texas, Austin (TX), 1990
- /2/ Vail, N.K.; et al. Silicon Carbide Preforms for Metal Infiltration by Selective Laser Sintering of Polymer Encapsulated Powders. Proceedings of the Solid Freeform Fabrication Symposium 1993, University of Texas, Austin (TX), 1993
- /3/ Deckard, L.; Claar, T.D. Fabrication of Ceramic and Metal Matrix Composites from Selective Laser Sintered Ceramic Preforms. Proceedings of the Solid Freeform Fabrication Symposium 1993, University of Texas, Austin (TX), 1993

- /4/ Birmingham, B.R.; Marcus, H.L. Solid Freeform Fabrication of Silicon Carbide Shapes by Selective Laser Reaction Sintering (SLRS). Proceedings of the Solid Freeform Fabrication Symposium 1993, University of Texas, Austin (TX), 1993
- /5/ Birmingham, B.R.; et al. Silicon Carbide Shapes by Selected Area Laser Deposition Vapor Infiltration. Proceedings of the Solid Freeform Fabrication Symposium 1994, University of Texas, Austin (TX), 1994
- /6/ Jakubenas, H.; Marcus, H.L. Selective Laser Pyrolysis for Solid Free-Form Fabrication of Silicon Carbide. Proceedings of the Solid Freeform Fabrication Symposium 1994, University of Texas, Austin (TX), 1994
- /7/ Stierlen, P.; Schanz, P.; Eyerer, P. Si/SiC-Ceramic, low process shrinkage-high temperature material for the Laser Sinter process. In: Proceedings, Solid Freeform Fabrication Symposium SFF98, 1998
- /8/ Löschau, W. Selektives Lasersintern von Strukturkeramik. Jahresbericht FhG-IWS. Fraunhofer-Institut für Werkstoff und Strahltechnik (FhG-IWS), Dresden, 1997
- /9/ Löschau, W.; Lenk, R.; et al. Prototyping of complex shaped parts and tools of Si/SiC-ceramics by selective laser sintering. Proceedings of the 9th CIMTEC, Florence, Italy, June 14-19, 1998 (to be published)
- /10/ Schanz, P.; Krenkel, W. Description of the Mechanical and Thermal Behaviour of Liquid Siliconized C/C. Proceedings of the 6th ECCM, Bordeaux, France, Sept. 20-24, 1993
- /11/ Gern, F. Interaction between Capillary Flow and Macroscopic Silicon Concentration in Liquid Siliconized Carbon/Carbon. Proceedings of 2th HT-CMC, Santa Barbara, California, Aug. 21-24, 1995
- /12/ Fabig, J.; Krenkel, W. Principles and New Aspects in LSI-Processing. Proceedings of the 9th CIMTEC, Florence, Italy, June 14-19, 1998 (to be published)

Selective Laser Sintering of Zirconia with Micro-Scale Features

Nicole Harlan, Seok-Min Park, David L. Bourell, and Joseph J. Beaman

Laboratory for Freeform Fabrication
The University of Texas at Austin

Abstract

Recent work in Selective Laser Sintering of ceramics at the University of Texas at Austin demonstrates the capability to produce zirconia parts with fine features. Zirconia powder was pre-processed into spherical particles, laser sintered with a sacrificial polymer binder, infiltrated and post-sintered to higher density. Optical micrographs show that hole sizes of 180 μm are possible in fully ceramic components.

1 Introduction

Selective laser sintering (SLS) was limited initially to low temperature material. Recent work utilizing metals, ceramics and cermets has created new applications for SLS produced components [1, 2]. Studies show that blends of stabilized and unstabilized zirconia powder are resistant to thermal cycling through the monoclinic to tetragonal transformation temperature and exhibit a lower thermal expansion than fully stabilized zirconia [3, 4]. An investigation of indirect ceramic SLS processing has shown the potential to produce micro-scale features in "partially stabilized" zirconia. In addition to micro-scale features and high operating temperature, part impermeability was identified as a desirable feature of the ceramic components. Porosity and liquid surface tension are factors in the part impermeability, as given by the Washburn equation,

$$P = 2\gamma\cos\theta/d \quad (1)$$

where γ is the surface tension of the liquid, θ is the contact angle between the liquid and the solid, d is the pore diameter and P is the pressure head [5]. A liquid will infiltrate to a capillary restriction equal to d for a given pressure, based on the wetting characteristics of the liquid. As the pore size decreases, more pressure is needed to permeate the part.

A series of experiments have been done to characterize the SLS produced zirconia parts and quantify the minimum hole size that may be produced using an SLS Model 125 Workstation. A micro-feature part was built to demonstrate the potential of this processing technique.

2 Experimental Procedure

Granulated yttria-stabilized zirconia powder (Tosoh TZ-8Y) was de-bound and sintered at 1250°C for 2 hours. The pre-sintered powder was mixed with a copolymer and roll-milled for 24 hours. The zirconia-copolymer mixture was SLS processed using an SLS Model 125 Workstation with a CO₂ laser energy density between 10 and 13 J/cm^2 , calculated from the

Andrew number formula [6]. The laser spot size was approximately half of a millimeter. SLS green shapes were infiltrated with a colloidal solution of amorphous zirconia (Nyacol Zr100/20). Wetting of the green shapes was improved by adding a surfactant to the colloid. After several infiltration cycles, the green shapes were pyrolyzed to burn off the copolymer binder, crystallize the infiltrated zirconia and densify the parts. The heating schedule consisted of a slow ramp to 500°C, a faster ramp to 1500°C and a 10 hour soak. Infiltration and firing cycles were repeated until adequate strength was achieved.

A thin plate (0.015 inches thick) containing a series of small holes was built to determine the minimum hole size that could be produced using the processing method described above. Hole sizes were measured in the green state and after firing using an optical microscope. A micro-scale nozzle was built with holes of similar size. Green and post-fire dimensions were measured to quantify the amount of shrinkage that occurred during post-processing. Density was measured using the Archimedes method with ethanol. Bend coupons were produced and broken per ASTM C1161-94 to measure flexural strength. After each firing step, roughness was measured using a Surfanalyzer 5000. Pore size was measured via mercury porosimetry using a Micromeritics AutoPore 3000.

3 Result and Discussion

The spherical shape of the granulated zirconia powder was maintained during the de-binding and sintering step. The spherical particle shape improves powder bed packing, thereby increasing the initial density of the SLS part. The pre-sintering step prevents the particles from dissolving in the colloidal zirconia solution during infiltration and eliminates a small amount of shrinkage during post-processing. The average particle size of the pre-sintered powder was 50 μm , determined from SEM micrographs. The smallest hole size that was produced in the thin plate was 180 μm . The size of the holes did not change significantly during firing. An optical micrograph of one of the larger holes is shown in Figure 1. Spherical zirconia particles are surrounded by a crystallized matrix of infiltrated zirconia.

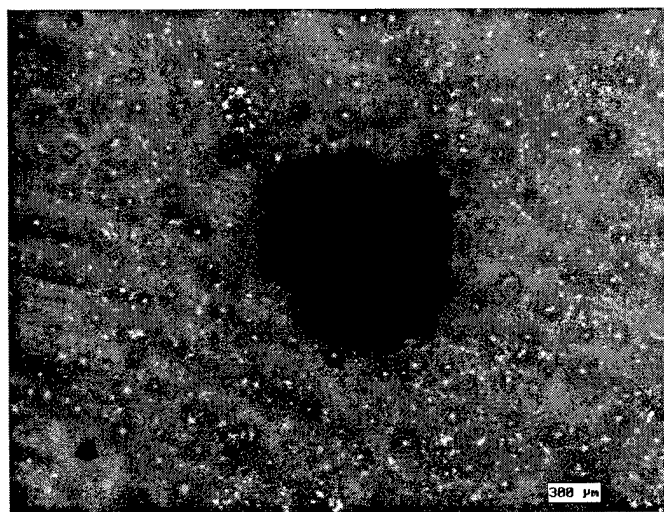


Figure 1: Hole in thin zirconia plate, post fire.

It is encouraging that such small holes can be created from a powder with an average particle size of $50\text{ }\mu\text{m}$ and using a laser spot size not much finer than $500\text{ }\mu\text{m}$. A photo of the micro-scale nozzle is shown in Figure 2. The holes are close to the same size as that shown in Figure 1. The length of the nozzle is less than $3/4$ of an inch.

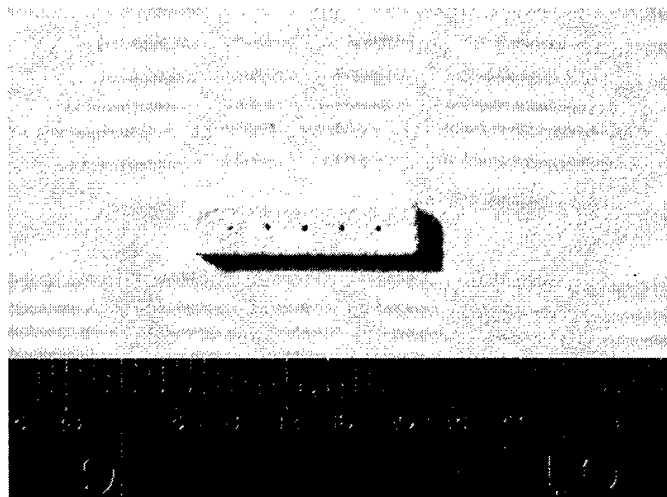


Figure 2: Zirconia Test Coupon with Features

Shrinkage measurements in the x, y and z directions are shown in Figure 3. The extent of shrinkage is not significantly different for samples fired once than for samples fired three times. Hence, the majority of the shrinkage occurred during the first firing cycle. This can be attributed to the rearrangement of the zirconia particles that occurs during initial stage sintering after copolymer burn-out. An average of 13% shrinkage occurred in each direction. No cracking was observed in the fired samples.

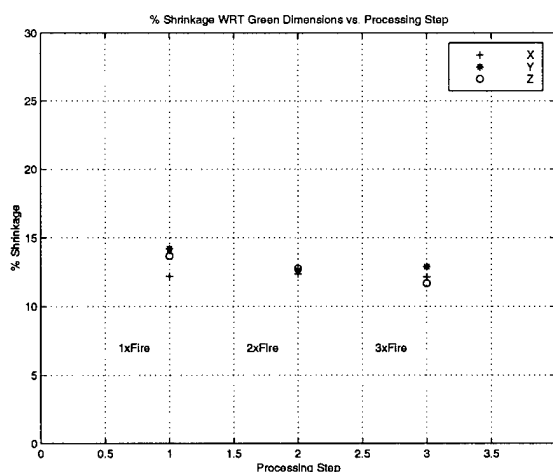


Figure 3: Shrinkage during Post Processing

The density of the SLS parts increased with colloidal zirconia weight gain. The plot in

Figure 4 shows the density of the zirconia parts versus the weight gain of infiltrated zirconia (with respect to the initial Tosoh zirconia weight). A theoretical density of 5.9 g/cm^3 was assumed. Flexural strength also increased with weight gain, as was expected. A plot of the four-point bend strength of green and ceramic specimens is shown in Figure reffig:plot3.

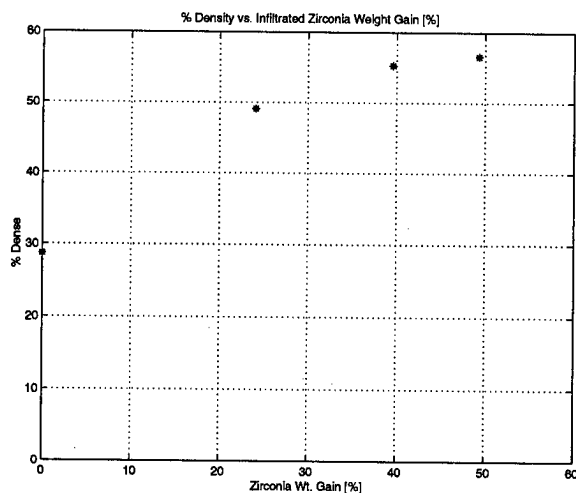


Figure 4: Density vs. Zirconia Weight Gain

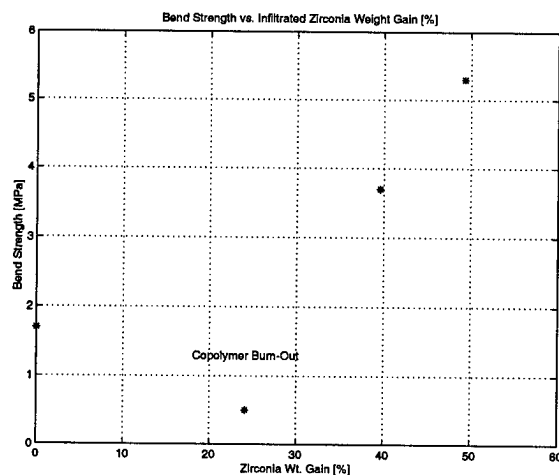


Figure 5: Bend Strength vs. Zirconia Weight Gain

Multiple colloidal infiltration steps smoothed the surface of the SLS part. The roughest surface of an SLS green part is on its side, where the stair-stepping effect is prominent. The average roughness, R_a , of the side of a zirconia SLS green part was $14 \mu\text{m}$. After multiple infiltrations, the average roughness decreased to $9 \mu\text{m}$ on all surfaces.

Mercury porosimetry was used to measure the median pore size based on volume. Figure 7 shows the decrease in size of the largest pores with colloidal zirconia weight gain.

Final pore size was less than $5 \mu\text{m}$, corresponding to an infiltrant weight gain of 50%. The pore size can be used to calculate the impermeability of the part to a specific liquid. If we

assume that a pressurized fluid has similar surface energy and wetting characteristics to those of mercury, then a pressure of 50 psia would be necessary to permeate this part through its largest pores according to the Washburn model and experimental porosimetry data.

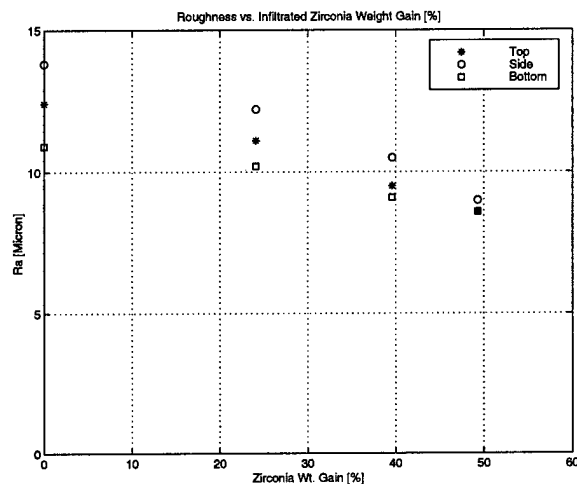


Figure 6: Roughness vs. Zirconia Weight Gain

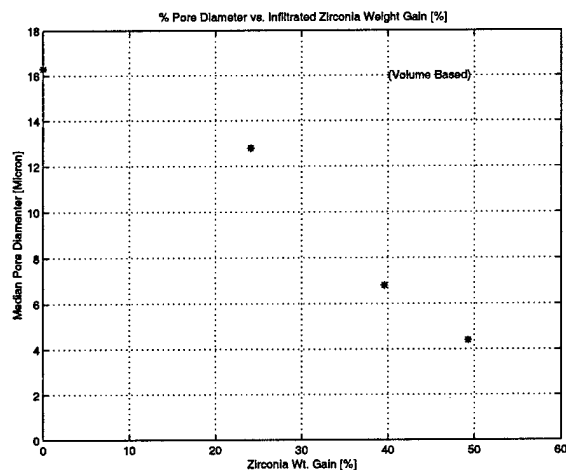


Figure 7: Pore Size vs. Zirconia Weight Gain

4 Conclusion

The work done shows that indirect processing of micro-scale zirconia ceramics via selective laser sintering is feasible. A minimum hole size of $180\text{ }\mu\text{m}$ was produced. With repeated infiltration, an average roughness of $9\text{ }\mu\text{m}$ was achieved on all surfaces, and the median pore size was reduced to less than $5\text{ }\mu\text{m}$. The small pore size supports pressures up to 50 psia before mercury permeates the part. No cracking was observed in pieces that went through multiple

firing cycles. To produce components with finer features, future experiments could incorporate a smaller laser spot size and a reduced particle size.

References

- [1] S. Das, et al., *Direct SLS Processing for Production of Cermet Composite Turbine Sealing Components*, Materials and Manufacturing Processes, Vol. 13, No. 2, pp. 241-261, (1998).
- [2] J.W. Barlow and N.K. Vail, *Method of Producing High-Temperature Parts by Way of Low-Temperature Sintering*, U.S. Patent 5,284,695, (1994).
- [3] E.D. Calvert, *An Investment Mold for Titanium Casting*, U.S. Bureau of Mines Report of Investigations, n. 8541, (1981) p.20.
- [4] N. Harlan, D. L. Bourell, J.J. Beaman, *Titanium Casting Molds via Selective Laser Sintering*, Solid Freeform Fabrication Proceedings, (UT Austin), Aug. 1998.
- [5] G. de With, *Process Control in the Manufacture of Ceramics*, Materials Science and Technology - A Comprehensive Treatment, Vol. 17A, p. 45, (1996).
- [6] N.K. Vail, *Preparation and Characterization of Microencapsulated Finely Divided Ceramic Materials for SLS*, Ph.D. Dissertation, The University of Texas at Austin, 1994.

Measurement of the Sintering Dynamics of polymeric powders at Near SLS Conditions

J. Steinberger, K. Manetsberger, J. Shen, J. Müllers

DaimlerChrysler Research Center
Ulm, Germany

Abstract

The sintering dynamics of materials used in the Selective Laser Sintering process impact greatly the thermal conditions of the powder bed. An experimental setup was developed to obtain sintering rate information at conditions very near to those of the SLS process. The system consists of a powder sample heated by a CO₂ laser while maintained at constant thermal boundary conditions. The powder height is measured by means of an optical sensor, which avoids stress on the powder and allows fast data acquisition. This paper discusses experiments conducted with this apparatus and further compares the obtained results with theoretical models and the previous work of others.

Introduction:

Selective laser sintering (SLS) can be separated into three physical processes /NEL93/, /NÖK96/:

- Propagation of electromagnetic waves such as the laser and the heat radiation,
- Heat transfer in the powder bed, and
- Powder sintering due to thermal absorption of the laser power.

Sintering dynamics affect both the propagation of the laser radiation and thermal heat diffusion due to corresponding changes in powder bed porosity /Sch88/, /THI83/, /NEL93/. Since an understanding of sintering is important to modeling the SLS-process, a fair amount of theoretical and experimental work has been reported on this subject.

Sun /SUN91/ modeled sintering with an extension of the Frenkel model /FRE49/ by introducing an empirical sintering factor ξ , which described the probability of forming a neck between two adjacent particles. Weissman and Hsu /WEI91/ simulated the SLS process using Scherer's model for densification. Neither of these models were verified by experimental results. Nelson presented a simple phenomenological model dependent only upon rheological parameters of the material /NEL93/. He described densification according to the first order decay mechanism (Eq. (1)).

$$\frac{d\Psi}{dt} = -k \cdot (\Psi - \Psi_{\infty}) \quad (1)$$

where ψ is the solid fraction at time t , ψ_{∞} is the solid fraction at $t = \infty$ and k is the sintering rate constant [1/s]. The sintering rate was described by an Arrhenius function:

$$k = A \cdot e^{-\frac{E_a}{R \cdot T}} \quad (2)$$

where A is the sintering coefficient [1/s], E_a is the activation energy [J/mol] and R is the gas constant [J/(molK)].

Sintering rate kinetics determined from isothermal, unidirectional powder densification studies as carried out by oven experiments were used to simulate SLS processing. While Nelson's empirical model showed reasonable agreement with his experimental results, the model fails to capture the true dynamics of the SLS process. Especially since, the empirical sintering rate of Eq. (1) was determined from data obtained at time scales several orders of magnitude larger than the time scales of the SLS process. Furthermore, the sintering rate was calculated by a change in powder sample height at constant temperature as determined by the aid of an applied stress. Lastly, the empirical sintering rate can not be inferred from physical material properties.

In this paper, a more suitable physical model is presented to describe the sintering dynamics of the SLS process. The model is then compared to an experiment, designed to be as close to the SLS process as possible.

Sintering Theory

German /GER96/ describes the viscous flow as the driving force for the sintering of polymers. Frenkel /FRE 45/ as corrected by Eshelby /ESH49/ first modeled sintering using viscous flow. Rosenzweig /ROS82/ verified the Frenkel model by studying the sintering of two PMMA spheres. Brink further demonstrated the Frenkel model to adequately describe the sintering of semicrystalline polymeric powders /BRI95/.

However, the Frenkel model is valid only for the initial sintering stage, since a change of the particle radius due to the sintering process is not considered. Pokluda modified the Frenkel model by considering the change in particle radius using the following equation /POK97/:

$$a(t) = a_0 \cdot \left(\frac{4}{(1 + \cos(\theta(t)))^2 \cdot (2 - \cos(\theta(t)))} \right)^{\frac{1}{3}} \quad (3)$$

where $a(t)$ is the particle radius at time t and a_0 is the initial particle radius. The sintering angle θ is defined as

$$\frac{d\theta(t)}{dt} = \frac{\sigma}{\eta \cdot a_0} \cdot \frac{2^{\frac{5}{3}} \cdot \cos(\theta) \cdot \sin(\theta) \cdot (2 - \cos(\theta))^{\frac{1}{3}}}{(1 - \cos(\theta)) \cdot (1 + \cos(\theta))^{\frac{1}{3}}} \quad (4)$$

$$\sin(\theta) = \frac{x}{a}$$

where σ is the surface tension, η is the viscosity and x is the radius of the sintering neck.

The Pokluda model describes the sintering of a two body system as the changing ratio of the sintering neck x to the particle radius a . This quantity must be used to describe densification or the change in solid fraction, ψ , in the SLS process. *Figure [1]* shows a characteristic volume element of the powder used to determine the solid fraction as a function of the sintering neck. It consists of a cylindrical unit cell containing two half-particles surrounded by an airjacket. This airjacket is used to explain the difference between the calculated solid fraction of the cell ψ_{unit} and the experimentally measured solid fraction. The solid fraction of the unit cell can be calculated as:

$$\Psi_{unitcell} = \frac{V_{neck} + V_{residual_sphere}}{V_{cylinder}} \quad (5)$$

$$\Psi_{unitcell} = x^2 + \frac{2}{3} \cdot (1 - x^2)^{\frac{3}{2}}$$

The volume of the airjacket is such that $\Psi_{theoretical}$ and $\Psi_{experimental}$ are equal for $t = 0$.

$$\Psi(t=0)_{theoretical} = \Psi(t=0)_{control_volume} = \frac{V_{solid}}{V_{control_volume}} = \frac{V_{solid}}{V_{unit_cell} + V(t=0)_{airjacket}} \quad (6)$$

If the control volume is scaled to 1, the volume of the airjacket at $t = 0$ is given by

$$V(t=0)_{airjacket} = 1 - \frac{\Psi_{experimentally}}{\Psi(t=0)_{unit_cell}} \quad (7)$$

As the neck grows, the volume of the airjacket must decrease. By assumig the decline of the airjacket being proportional to the growth of the solid fraction in the unit cell, the volume of the airjacketed at time t is given by

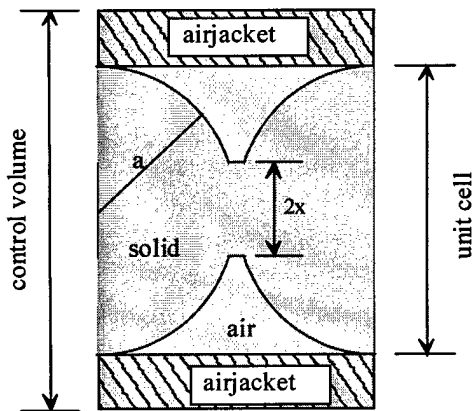
$$V_{airjacket} = \left(1 - \frac{\Psi_{experimentally}}{\Psi(t=0)_{unitcell}}\right) \cdot \frac{1 - \Psi_{unitcell}}{1 - \Psi(t=0)_{unitcell}} \quad (8)$$

Therefore, the solid fraction of the control volume becomes

$$\Psi = \Psi_{unitcell} \cdot (1 - V_{airjacket})$$

$$\Psi = \left(x^2 + \frac{2}{3} \cdot (1 - x^2)^{\frac{3}{2}}\right) \cdot \left(\left(\frac{\Psi_{experimentally}}{\frac{2}{3}}\right) \cdot \frac{1 - x^2 - \frac{2}{3} \cdot (1 - x^2)^{\frac{3}{2}}}{1 - \frac{2}{3}}\right) \quad (9)$$

Eq. (9) is material independent, so it can be compared with experimental data for any material. *Figure [2]* shows the comparison to experimental data for glass /GER96/.



Figure[1]: Characteristical volume element

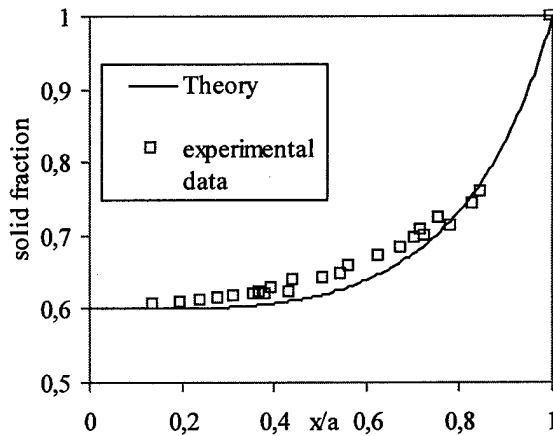


Figure [2]: Comparison of Eq. (9) and experimental data for glass

Experimental analysis of the sintering dynamics

Experimental setup: Figure [3] shows the experimental apparatus used to measure powder sintering dynamics. Powder is placed on a heating stage and preheated to the desired temperature. The powder is then exposed to CO₂ laser radiation (Synrad-laser, 10W). An optical sensor (Jurca Optoelektronik) is used to follow the change in sample height. The sensor uses the spherical aberration of a lens and therefore volume effects can be neglected. It has a focal spot of 10 μm , an accuracy of 0.1 μm , and a sampling rate of up to 1000 Hz. The working distance is 5 mm thus the laser beam had to be focused by an optical system on the powder bed under an angle δ of 13.5°.

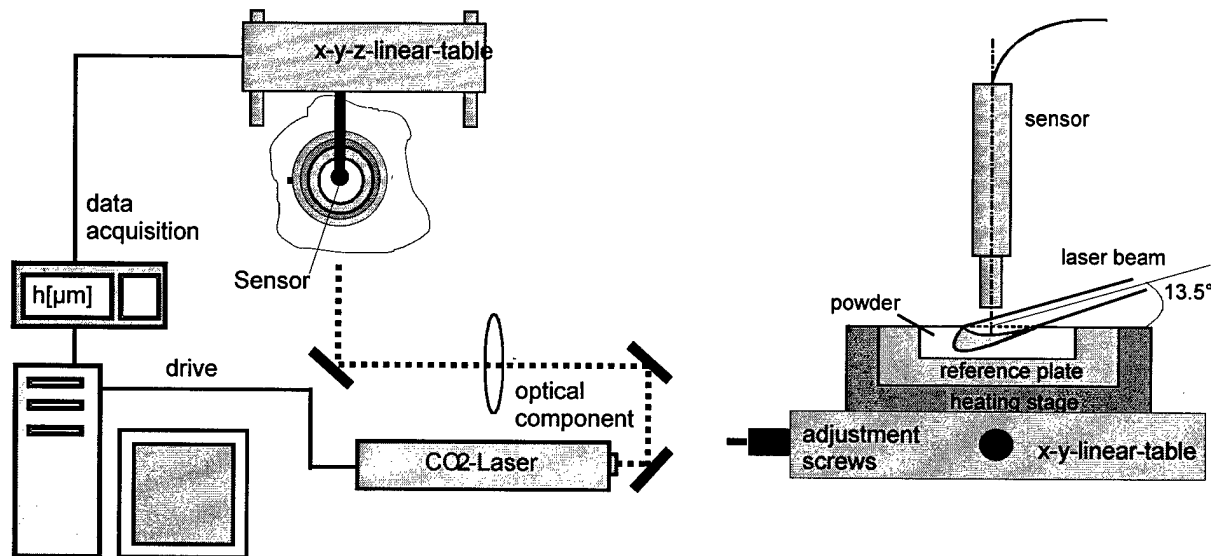


Figure [3]: experimental setup

Experimental procedure: The applied laser energy density during the experiment corresponded to values used in the SLS-process. It was changed by varying both the laserpower and the exposure time. The spot size was enlarged to 4.25 mm to minimize border effects. Thus, homogeneous conditions within the measuring spot can be assumed. To compare experimental data with theoretical predictions, the temperature in the laser spot was also measured. Variations in the applied energy density due to the 13.5° working angle were corrected by an appropriate coordinate transformation.

Since the working angle was limited to 30°, small lateral movements of the measured powder sample could lead to a loss of the sensor signal. Therefore, a series of measurements for PMMA as well as for PA were averaged for each condition. Curves represented in this paper are the result of at least seven independent measurements for each condition.

Experimental results (PMMA): Figure [4] shows the change in powder height, dh , for different laser energies for a characterized PMMA. The PMMA powder particles have a spherical shape and an average radius of 16.5 μm . The laser energy was applied to the powder bed 5 s after the measurement was started. Immediately the powder began to expand.

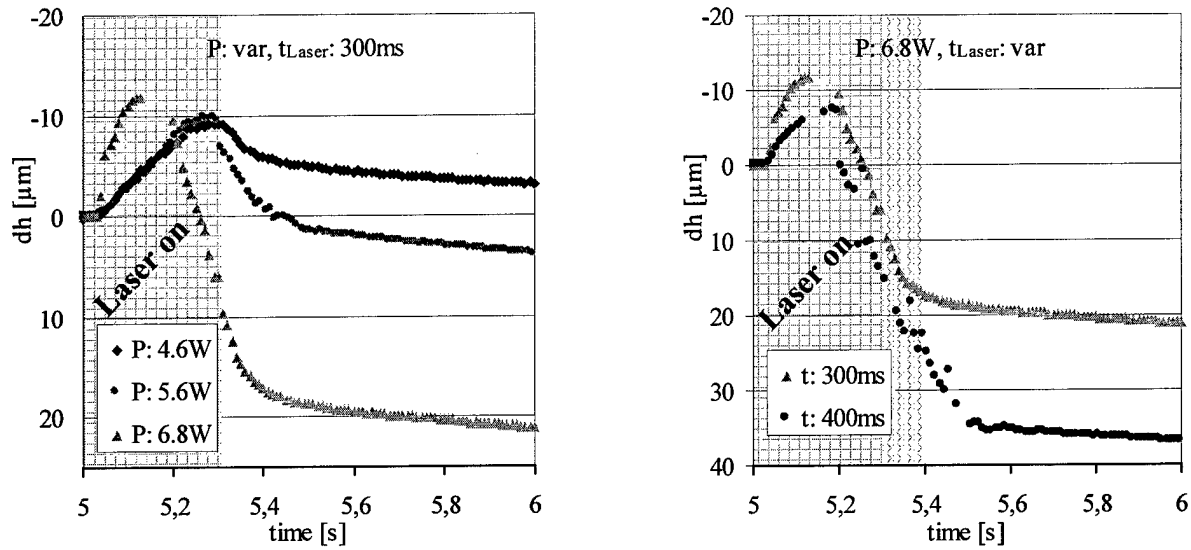


Figure [4]: change of heigth of a sintered PMMA-powder

Nelson also observed a similar expansion in his experiments and reasoned it was due to a change of particle geometry from ellipsoidal to spherical. In the present work, however, PMMA is spherical. *Figure [5]* compares the thermal expansion, dl , of PMMA powder to solid PMMA. In order to compare the expansion curves of the powder and the solid, the rate of thermal expansion is estimated by:

$$\Delta l = \alpha \cdot \Delta T \cdot D_p = \alpha \cdot \frac{P \cdot \Delta t \cdot r \cdot \cos(90 - \delta)}{\frac{\pi}{2} \cdot a_0 \cdot b_0 \cdot D_p \cdot \varphi \cdot \Psi_{\text{exp}} \cdot c_p} \cdot D_p \quad (10)$$

$$\left(\frac{\Delta l}{\Delta t} \right)_{\text{solid}} = \frac{P_{\text{solid}}}{P_{\text{powder}}} \cdot \Psi_{\text{exp}} \cdot \left(\frac{\Delta l}{\Delta t} \right)_{\text{powder}}$$

$$\left(\frac{\Delta l}{\Delta t} \right)_{\text{solid}} = 1.93 \cdot \left(\frac{\Delta l}{\Delta t} \right)_{\text{powder}} \quad \text{for } P_{\text{solid}} = 6,8\text{W and } P_{\text{powder}} = 1,9\text{W}$$

where D_p is the penetration depth of the laser beam, r is the absorbed fraction of the laser beam, a_0 and b_0 are the semiaxis of the elliptical laser beam, φ is the density of the solid material and c_p is the specific thermal capacity.

Comparing Eq. 10 to the experimental data in *Figure [5]* for $\Delta t = 150\text{ms}$, the effective thermal expansion of the powder is about 2,5 times higher than the theoretical thermal expansion. We think, this due to a possible expansion of the gas.

As the laser power is increased with constant exposure time, the sintering rate is enhanced. Moreover the onset of sintering t_{start} is decreased to shorter times. The activation energy, E_a , necessary to start the sintering process is achieved more rapidly using the higher laser power. Changing the applied energy by varying the exposure time with constant laser does not change either the sintering rate or the starting point of the sintering process. However, *Figure [6]* shows that the absolute change in height, dH , the change of height for $t = \infty$, and therefore the absolute change in solid fraction does change.

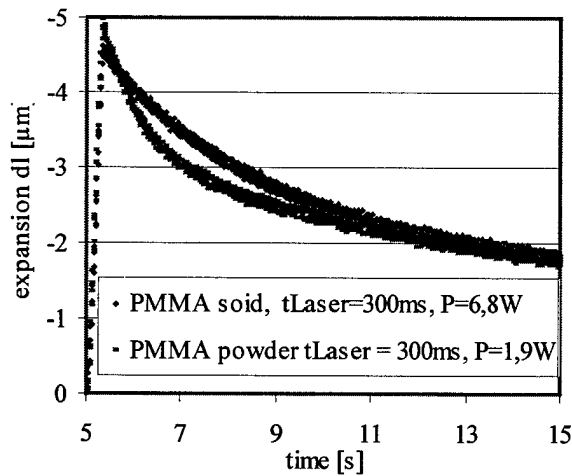


Figure [5]: Comparison of the expansion curves of solid and powder (PMMA)

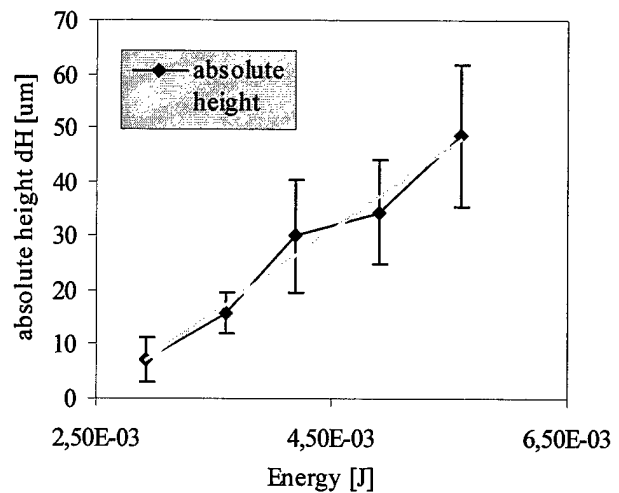


Figure [6]: Absolute change in height dH

Depending on the laser power, the sintering starts after 200ms. For the heat conduction and the propagation of electromagnetic waves, however, only the densification due to the sintering is relevant. Therefore, the thermal expansion was measured and then subtracted from the measured values as shown in Figure [4]. The result is shown in Figure [7].

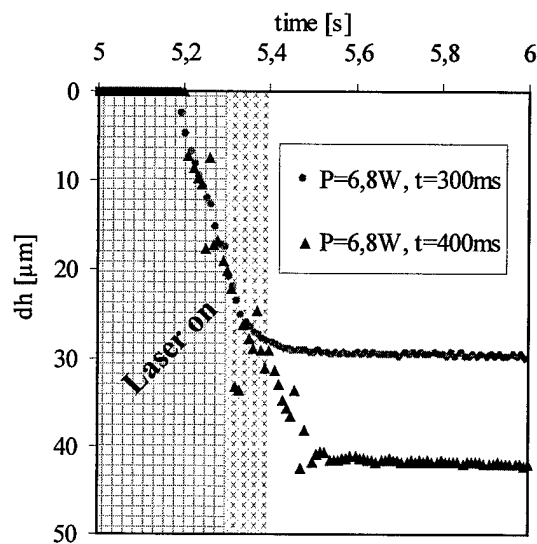
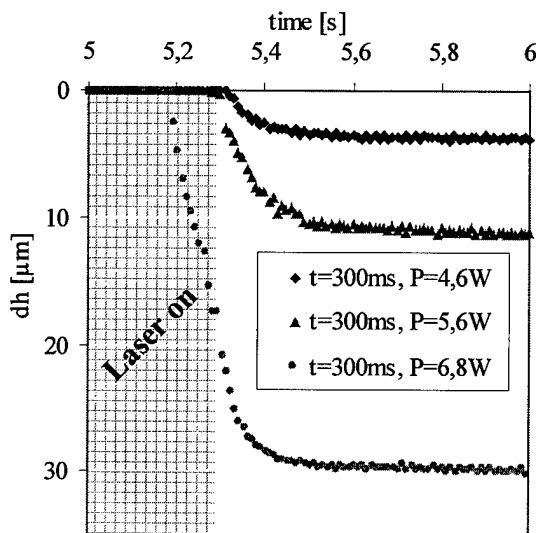


Figure [7]: Scaled sinter dynamics (PMMA)

Evaluation of the sintering theory

To compare theoretical and experimental results, the temperature at the laser spot was measured during the sintering process. The results are shown in Figure [8]. Since a temperature gradient exists in the heated spot, it follows that only an average change of solid fraction can be measured. To judge one model properly, the experiment needs to be simulated by taking the temperature distribution into account. This is our research of immediate interest. For a rough estimation, however, the solid fraction at $t = \infty$ in the experiments is compared to the solid fraction at $t = \infty$ for parts, build at the same energy densities as in the “real” SLS.

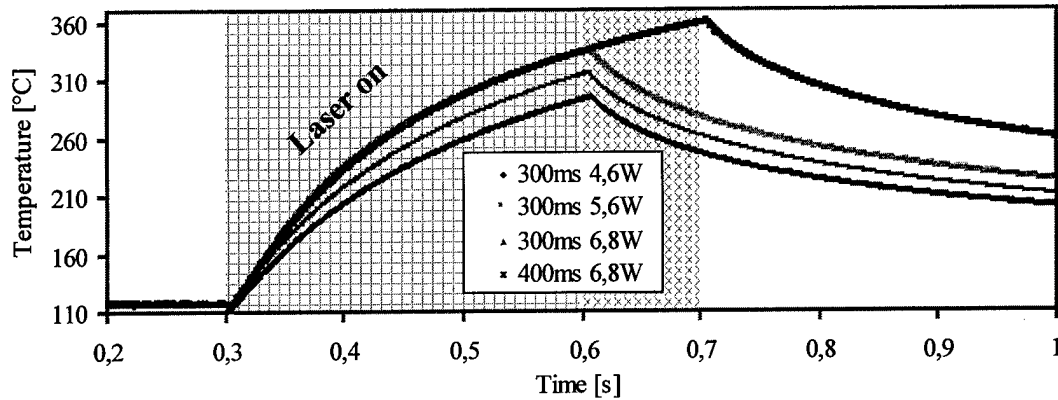
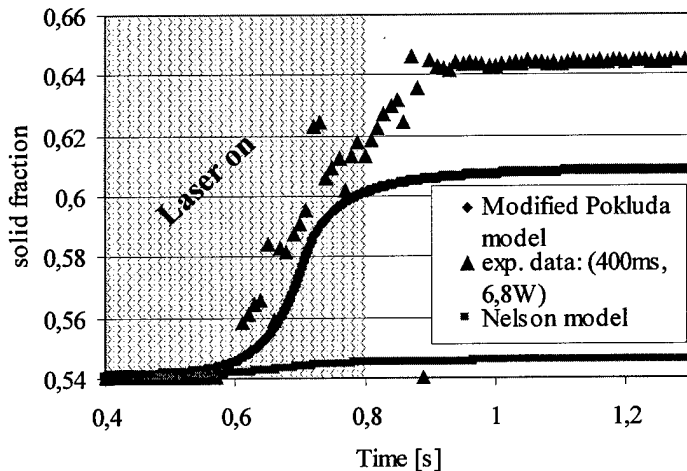


Figure [8]: Temperature in the laserspot (PMMA)

Data for Nelson's empirical model were obtained for the PMMA material used in this study to provide a comparison between the two models. The sintering rate was determined to be:

$$k = 4.15 \cdot 10^5 \cdot e^{-\frac{79.451 \cdot 10^3}{R} \cdot \frac{1}{T}} \cdot \frac{1}{s}$$

Discussion: Figure [9] shows model results compared to a set of experimental data (400ms, 6.8W). The necessary physical properties were either determined experimentally or taken out from the literature. Clearly, Nelson's model does not adequately describe the sintering dynamics. The modified Pokluda model, describes sintering dynamics better, but kinetics are still too slow, especially since temperature gradients in the powder are not taken into account.



Parameters:

$$\eta = 1.95 \cdot 10^{-8} \cdot e^{\frac{1.241 \cdot 10^5}{8.3123 T}} [Pa \cdot s]$$

$$a_0 = 15 \mu m$$

$$\sigma = 25 \cdot 10^{-3} \frac{N}{m} (/ROS81/)$$

$$\Psi_{exp} = \Psi_0 = 0.54$$

$$\Psi_{\infty} = 1$$

$$P_{Laser} = 6.8W$$

$$t_{Laser} = 400ms$$

Figure [9]: Comparing the modified Pokluda model and the Nelson model to experimental data

Sintering dynamics of Nylon:

The melting dynamics of PA-12 for the experimental conditions (300ms, 3.3W) are of the same time scale as for the sintering dynamics of PMMA (Figure [10]). The absolute change of the solid fraction, however, is higher, since PA-12 is a semi-crystalline material.

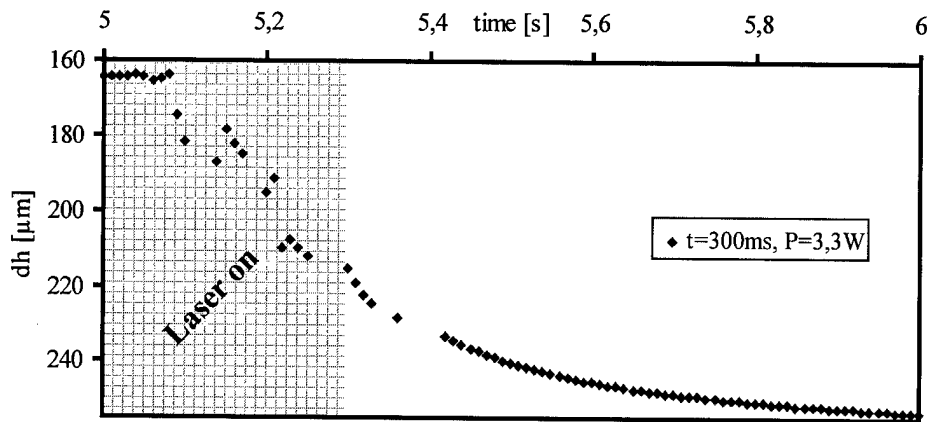


Figure [10]: sintering dynamics of PA-12

Conclusions

Unlike to other experiments, the sintering dynamics were measured at near SLS conditions. This was achieved using instantaneous heating with a laser and by data acquisition with a fast optical sensor. The results show that the modified Pokluda models describes the dynamics of the SLS process better than the Nelson model. It appears, that this modell could be improved and adapted to the SLS process. One possible improvement could be the consideration of viscoelastic effects /BEL98/, /MAZ94/. However further information can only be obtained by simulating the experiment.

Acknowledgement

The authors kindly thank Dr. Neal K. Vail for his input on this work

References

C. T. Bellehummeur /BEL98/: <i>The role of viscoelasticity in polymer sintering</i> Rheol Acta 37: 270 – 278 (1998)	S. Nöken /NÖK97/: <i>Technologie des Selektiven Lasersinterns von Thermoplasten</i> , Diss Shaker Verlag, Band 8, 1997
A. E. Brink /BRI94/: <i>Sintering high performance semicrystalline polymeric powders</i> Polymer Eng. And Science, Dec. 95, Vol. 35, No. 24	O. Pokluda /POK97/: <i>Modification of Frenkel's model for sintering</i> AIChE Journal, Dec97, Vol. 43, No. 12
J. D. Eshelby /ESH49/: <i>Seminar on the kinetics of sintering</i> Metals transaction 185 (1949), S 806 - 807	N. Rosenzweig /ROS81/: <i>Sintering Rheology of Amorphous Polymers</i> Polymer Eng. And Science, Dec. 81, Vol. 21, No. 17
J. Frenkel /FRE45/ <i>Viscous flow of crystalline bodies under the action of surface tension</i> Journal of Physics, 1945, Vol LX, No. 5	E. U. Schlünder /SCH88/: <i>Wärmeübertragung in Festbetten, Schüttgütern und Wirbelschichten</i> Georg Thieme Verlag Stuttgart, 1988
R. M. German /GER96/: <i>Sintering theory and practice</i> John Wiley & Sons, Inc. New York 1996	M. Sun /SUN91/: <i>A Model for Partial Viscous Sintering</i> Solid Freeform Fabrication Symposium 1991
S. Mazur /MAZ94/: <i>Viscoelastic effects in the coalescence of polymer particles</i> Progress in organic coatings 24 (1994) 225 - 236	C. L. Tien /TIE87/: <i>Thermal Radiation in Particulate Media with Dependent and Independent Scattering</i> Annual Review of Numerical Fluid Mechanics and Heat Transfer, 1, pp. 1-32, 1987
J. C. Nelson /NEL93/: <i>Selective Laser Sintering: A Definiton of the Process and Empirical Sintering Model</i> ; PhD, Dissertation , 1993; Univ. of Texas	E. M. Weissman /WEI91/: <i>A Finite Element Model of Multi-Layered Laser Sintering Parts</i> Solid Freeform Fabrication Symposium 1991

Cryogenic Mechanical Alloying of Poly (ether ether ketone) – Polycarbonate Composite Powders for Selective Laser Sintering

J. Schultz, R. Kander, C. Suchicital
Department of Materials Science and Engineering
Virginia Tech
Blacksburg, VA

Abstract

Mechanical alloying is a solid state processing technique traditionally used in the metallurgical industry to extend solubility limits in alloy systems. Mechanical alloying can also be used to blend polymer systems at ambient or cryogenic temperatures. In this work, cryogenic mechanical alloying was employed to create composite powders of Poly (ether ether ketone) (PEEK) – Polycarbonate (PC) for use in selective laser sintering applications. The microstructural development of the PEEK-PC system that occurs during laser sintering and the effects of this microstructure on mechanical properties of the laser sintered parts was investigated.

Key Words: Selective Laser Sintering (SLS), Mechanical Alloying, Poly (ether ether ketone) (PEEK), Polycarbonate (PC)

Introduction

Mechanical alloying (MA) was first developed at The International Nickel Company, Inc. as a means of producing oxide dispersion strengthened nickel-based superalloys. This process is now a widely used fabrication method in the metals industry. Mechanical alloying is employed to enhance microstructural control and extend solubility limits in metal alloys^[1]; however, since the late 1980s efforts have been made to apply this technology to the processing of polymer composites and blends. Research in mechanical processing of polymers has shown improved ultimate tensile strengths of mechanically processed polymers^[2] and the ability to blend immiscible polymers with no significant degradation^[3].

The device used for mechanical alloying in this study is the vibratory mill, which provides the highest energy collisions of any milling device available. Figure 4 shows a schematic representation of the motion of a vibratory mill; the arrows indicate the axis of motion of the milling vile (B). Motion of the milling vile results in collisions between the milling media (A).

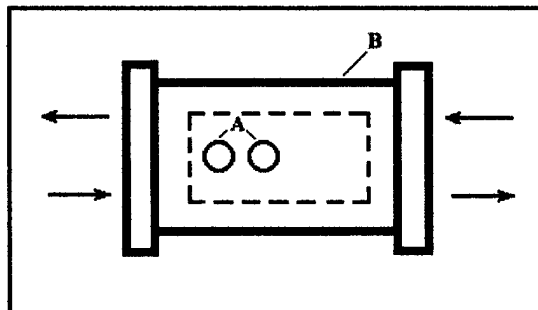


Figure 4: Schematic representation of a vibratory mill.^[1]

Typically, at least two balls (milling media) are used in this type of mill. Due to a decrease in the kinetic energy of the collisions with increasing number of collisions, there is a limit to the benefit of adding more balls. The vibratory mill can also be outfitted to operate at cryogenic temperatures, often required to mill polymers whose melting and glass transition temperature are near or below room temperature. Cryogenic mechanical alloying (CMA) also results in faster particle size reduction because of the increased brittleness of the polymer at low temperatures. Mixing of the polymers is done when powder particles are trapped between the balls during rapid high-energy collisions with each other and the container walls. The powders are repeatedly fractured and “welded” together by the collisions, which results in the mixing of the powders and refining of the particle microstructure^[4]. Figure 5 shows a schematic representation of the welding and fracture of particles. The particles in the *A* region are being welded together into a lamellar two-phase structure. The particles in region *B* are being fractured, thus reducing the particle size.

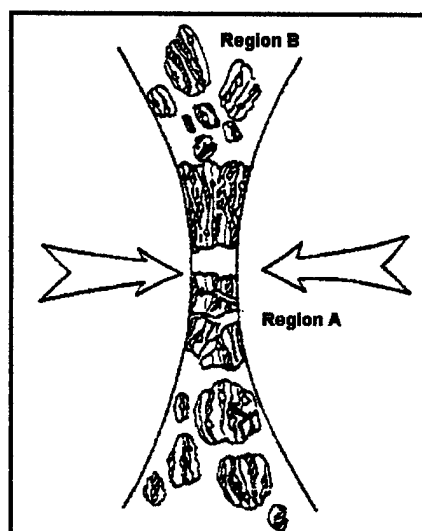


Figure 5: Schematic Representation of high-energy collision.^[1]

As the milling time increases, the number of fractures and welds per particle is increased. This results in increased refinement of the particle morphology. Figure 6 shows the progression of particle morphology refinement with increased milling time.

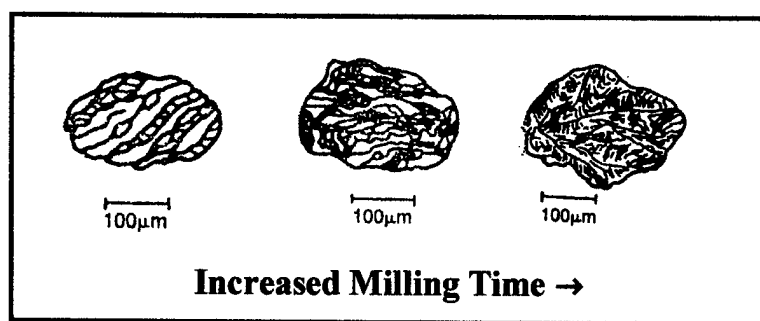


Figure 6: Particle Morphology Refinement.^[5]

The characteristic plate-like shape of mechanically alloyed polymers is also illustrated in Figure 6. The individual plates are made up of multiple lamellar structures of varying orientation. The

number of different lamellar orientations in a particle increases with time, but the spacing of the lamella decreases with time^[4], as shown in Figure 6.

The objective of the work presented here was to demonstrate the feasibility of using cryogenic mechanical alloying to produce micro-composite powders for use in selective laser sintering. The goal of using cryogenic mechanical alloying to produce powders for SLS application is to improve the mechanical properties of parts made by SLS. Therefore, parts produced by SLS could be used as fully functional parts. The material system chosen to be cryogenically mechanically alloyed is a polymer-polymer composite of polycarbonate and poly(ether ether ketone).

Experimental Equipment

Two pieces of equipment have been designed as a part of this research, a cryogenic vibratory ball mill and a laboratory scale selective laser sintering unit. The following two sections describe the operation of these two devices.

The Cryogenic Vibratory Ball Mill

Mechanical alloying of the composite blend for selective laser sintering was accomplished using a cryogenic vibratory ball mill (shown in Figure 7) designed to make polymeric composite powders. Figure 8 shows a schematic representation of the operation of the cryogenic vibratory ball mill.

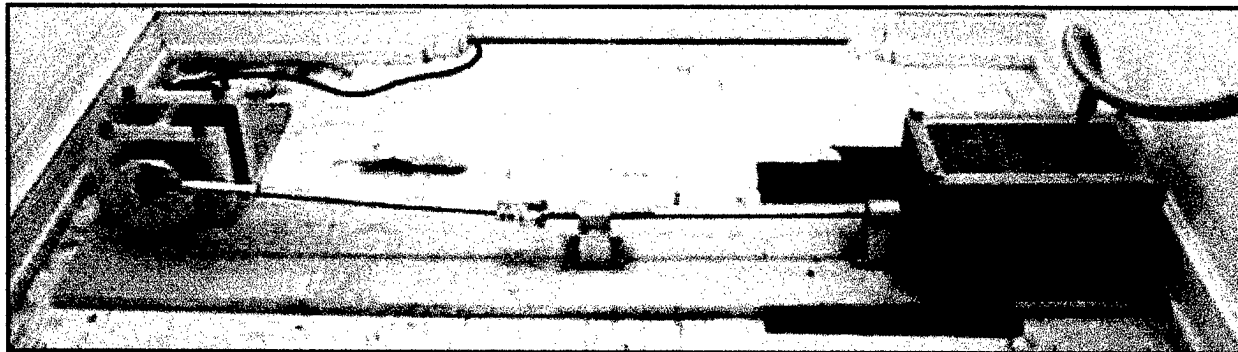


Figure 7: Cryogenic vibratory ball mill.

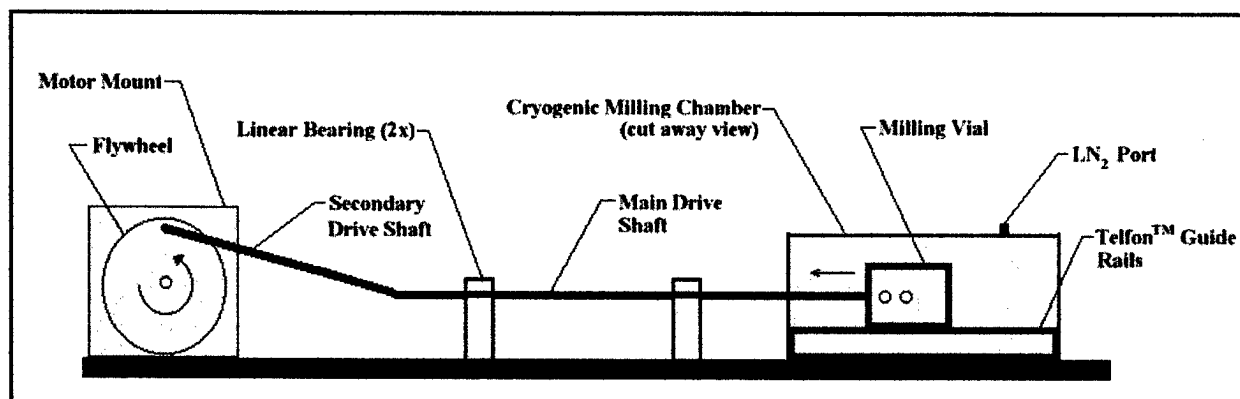


Figure 8: Schematic of the operation of the cryogenic vibratory ball mill.

A one half horsepower motor drives the cryogenic vibratory ball mill. The rotational motion of the motor is converted into linear motion by a flywheel and a wishbone linkage that connects the primary and secondary drive shafts. The milling vial, which rides on three Teflon™ guide rails, is connected to the opposite end of the main drive shaft. As the motor rotates, the milling vial and its contents (powdered material and the mixing media) are oscillated at approximately 10 Hz through a 4.2 inch linear range of motion. During operation, the bottom inch of the cryogenic milling chamber is filled with liquid nitrogen which is continuously fed through the port in the acrylic lid. The steady-state temperature in the cryogenic mill approaches that of liquid nitrogen, -196°C. Exact measurement of the temperature inside the milling vial is not possible because of the vigorous motion imparted to it. Stainless steel was chosen as the material for the milling vial and balls because its fracture toughness at cryogenic temperatures is such that the impacting surfaces do not erode and contaminate the samples. Each run of the cryogenic vibratory ball mill produces approximately 40mL of mechanically alloyed powder.

2.2 Laboratory Scale Selective Laser Sintering Unit

The selective laser sintering unit, shown in Figure 9 is a laboratory scale machine which can be used to test the applicability of a material to SLS processing using only small amounts of the material. Design and development of the lab-scale SLS unit was necessitated by the fact that only 40 ml of composite powder are produced for every run of the cryogenic vibratory ball mill. In the lab-scale SLS unit's present configuration, part geometries are limited to plaques and other flat test specimens.

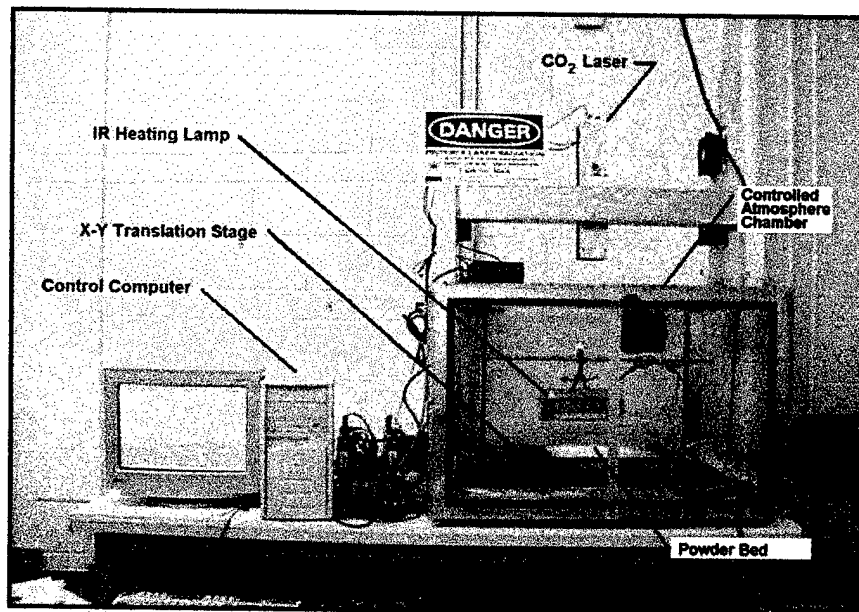


Figure 9: Laboratory scale selective laser sintering unit.

The laser, mounted vertically, in the SLS unit is a CO₂ laser with a nominal power of 10W. The translation of the system, mounted in the bottom of the enclosure, has a travel of 152mm x 152mm. The powder bed was made by smoothing the powder between two gage blocks with a doctor blade. Additional layers were added by placing shim stock on the gage blocks and smoothing the new layer of powder with the doctor blade. DTM Polycarbonate was laser sintered in the lab-scale unit to provide a benchmark for the capabilities of the unit and guide the design improvements. The benchmark tests were done on ASTM D 638 Type M-II^[6] tensile

specimens. Five tensile specimens, each consisting of five 0.25mm thick layers, were laser sintered at the following conditions: 2.6 W laser power, 66 mm/s scan speed, 0.2 mm scan spacing, 115°C bed temperature (obtained using an IR lamp), 3mm spot size. The average ultimate tensile strength (UTS), strain to failure, and elastic modulus of the specimens were 3.0 ± 0.6 MPa, 5.8 ± 0.5 % and 71.8 ± 16.8 MPa. DTM reports a UTS of 23 MPa^[7], a strain to failure of 5%^[7], and an elastic modulus of 1220 MPa^[7] for samples produced in a Sinterstation® under standard operating conditions. The porosity of each of the tensile specimens was also determined using ASTM C 373-88^[8] and the average porosity was calculated to 59 ± 2.1 %. The high porosity and low UTS relative to DTM's published value result from the fact that the lab-scale SLS unit is still in the developmental stages.

Procedure

PEEK-PC sample production

Composite powders of 50vol% Victrex™ PEEK and 50vol% DTM Polycarbonate were made using the cryogenic vibratory ball mill. The samples were milled for one hour and the charge ratio (mass of powder/ mass of milling media) used was 0.45. Each one-hour run produced 25.6 grams of the PEEK-PC composite powder. After milling, the PEEK-PC composite powder was laser sintered into ASTM D 638 Type M-II^[6] tensile specimens. Each specimen was 4 layers thick and was produced using the following conditions: 6 W laser power, 66 mm/s scan speed, 0.2 mm scan spacing, 125°C bed temperature, 3mm spot size, 0.25mm layer thickness.

Mechanical testing

Five PEEK-PC laser sintered tensile specimens, made using the aforementioned conditions, were tested at 0.2 mm/s using a Texture Technologies Texture Analyzer load frame. Stress-strain curves as well as the UTS, elastic modulus, and strain to failure were recorded for each specimen. The average and standard deviation of the UTS, strain to failure and elastic modulus for the five specimens was calculated.

Porosity testing

After mechanical testing, a 25x10 mm strip was cut from each of the tensile specimens and porosity testing was performed using the Archimedes method, based on ASTM C378-88^[8] with ethanol as the submersion liquid. The porosity of each specimen (the percentage of sample volume occupied by pores), was calculated along with the average and standard deviation for the five samples.

Scanning electron microscopy

Scanning electron micrographs of the as received DTM Polycarbonate, cryogenically mechanically alloyed PEEK-PC composite powder, and laser sintered PEEK-PC (same sintering conditions as above), were taken using an International Scientific Instruments SX-40 with an accelerating voltage of 20kV.

Results and Discussion

Figure 10 shows a PEEK-PC tensile specimen laser sintered with the lab-scale SLS unit. No gross distortion or geometric inaccuracies are visible from the photo. The tensile specimen does, however, exhibit a large number of relatively large pores throughout the surface of the specimen.

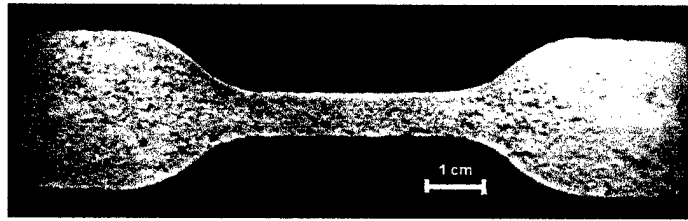


Figure 10: PEEK-PC tensile specimen made with the lab-scale SLS unit.

Mechanical testing

Figure 11 shows the stress strain curves for the PEEK-PC tensile specimens that were laser sintered using the lab scale SLS unit. The average elastic modulus, UTS and strain to failure were calculated to be 103.2 ± 12.1 MPa, 2.8 ± 0.4 MPa and $2.7 \pm 0.3\%$. The authors believe that these low UTS and strain to failure values are a result of the large porosity observed in the laser sintered tensile specimens that results from the difficulty in achieving a smooth uniformly dense powder bed with the PEEK-PC powders. The elastic modulus of the PEEK-PC laser sintered using the lab-scale SLS is 43% higher than the elastic modulus of the DTM PC laser sintered using the lab-scale SLS unit.

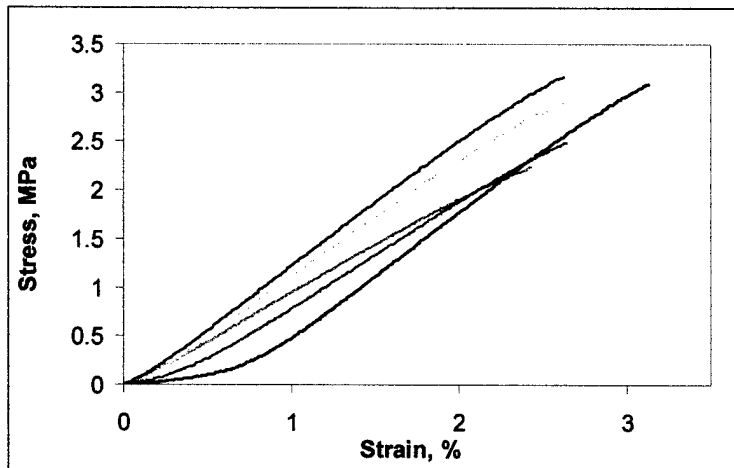


Figure 11: Stress-strain curves for laser sintered PEEK-PC tensile specimens.

Porosity testing

The porosity of the PEEK-PC samples was quantified through porosity testing and was determined to be $54.9 \pm 2.3\%$. The high degree of porosity is attributed to the aforementioned difficulties in achieving a uniform dense packing of the powder bed. The porous surface of a laser sintered PEEK-PC sample is shown in Figure 12.

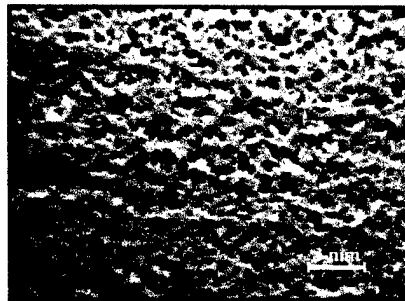


Figure 12: Laser sintered PEEK-PC surface.

Scanning electron microscopy

Figures 13 and 14 are scanning electron micrographs of the as-received DTM Polycarbonate and the PEEK-PC composite powders that resulted from 1 hour of cryogenic mechanical alloying.

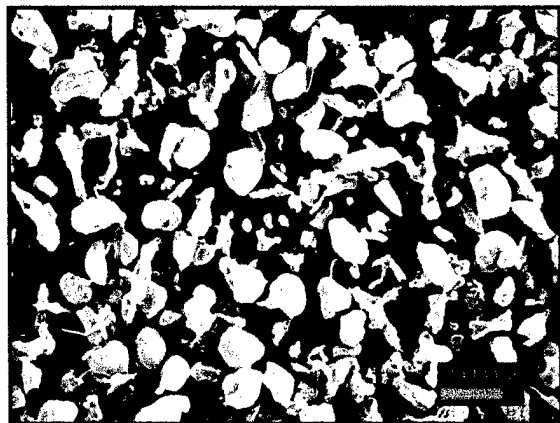


Figure 13: SEM micrograph of DTM Polycarbonate powder.

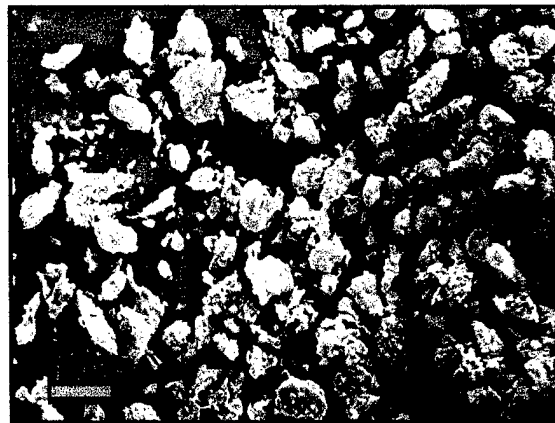


Figure 14: SEM micrograph PEEK-PC composite powder.

No drastic size differences are observed between the PC and PEEK-PC particles but the latter particles appear to be much rougher and more plate-like. The authors attribute the difficulty in obtaining a smooth powder bed to the surface roughness and plate-like shape of the powder particles since the rough plate-like particles do not roll over one another as well as particles with smooth surfaces.

Figure 15 shows a scanning electron micrograph of a cross sectioned surface of a PEEK-PC laser sintered sample. Unsintered particles are visible between the dense sintered layers shown in Figure 15. The presence of these unsintered particles suggests the laser sintering parameters employed in producing this sample were inadequate in sintering through the interlayer. Insufficient interlayer sintering could result from using a scan speed that is too high, laser power that is too low, layer thickness that is too large, or a combination of these.



Figure 15: SEM micrograph of PEEK-PC laser sintered sample.

Conclusion

The low UTS and strain to failure values measured and high porosity of the PEEK-PC samples laser sintered with the lab-scale SLS unit were attributed to difficulty in achieving a smooth, uniformly dense powder bed and inadequate laser sintering parameters which resulted in large porosity and insufficient interlayer sintering. The problem obtaining a smooth uniformly dense powder bed were attributed to the surface roughness of the PEEK-PC powder particles. It was determined from the SEM micrograph of the laser sintered PEEK-PC cross-section that the laser sintering parameters used to produce the current samples results in insufficient interlayer sintering.

Future Work

Continued development of the lab-scale SLS unit will improve the quality the samples; areas of concentration include reduction of beam spot size and improved powder delivery. These improvements are expected to result in improved mechanical properties of laser sintered samples. Investigation into methods of smoothing the rough surfaces of the PEEK-PC will also be undertaken. Investigation into the formation of other SLS material systems formed by cryogenic mechanical alloying will be ongoing.

Acknowledgements

The authors would like to thank DTM Corporation for supplying the DTM Polycarbonate. The authors would also like to thank Dr. Alex Aning for his continued support and input into our mechanical alloying research. Additional thanks goes to Julie Martin for performing the microscopy.

References

- [1] D. R. Maurice & T. H. Courtney, *Metall. Trans.*, 21, 289, 1990.
- [2] J. Pan, W. J. D. Shaw. "Effects of Processing Parameters on Material Properties of Mechanically Processed Polyamide." *Journal of Applied Polymer Science*, Vol. 56, John Wiley & Sons, 1995.
- [3] T. Ishida. Mechanical Alloying of Polytetrafluorethylene with Polyethylene." *Journal of Materials Science Letters*, 13, 1994.
- [4] Farrell, M. P., R. G. Kander, and A. O. Aning, "Polymer Blends Formed by Solid State Mechanical Alloying", *Journal of Materials Synthesis and. Processing*, 4, pp 151-161, 1996.
- [5] R. Sundaresan and F. H. Froes, *J. Metals*, 39, 22, 1987.
- [6] ASTM Standard D638M-93, "Standard Test Method for Tensile Properties of Plastics (Metric)".
- [7] <http://www.dtm-corp.com/Technology/Materials/polycarb.htm>
- [8] ASTM Standard C373-88, "Standard Test Method for Water Absorption, Bulk Density, Apparent Porosity, and Apparent Specific Gravity of Fired Whiteware Products".

Processing, Characterization and Modeling of Non-Random Porous Ceramic Structures

Ashwin Hattiangadi and Amit Bandyopadhyay

School of Mechanical and Materials Engineering,
Washington State University,
Pullman, WA 99164

Abstract

Processing of non-random porous ceramic structures via fused deposition process is discussed. These structures are characterized experimentally and statistically based on their compressive strength. Finite element modeling is used to understand the effect of stress concentration leading to the strength degradation of these brittle elastic solids.

Introduction

Porous ceramic materials are of significant technological interest due to their applications in molten metal filters, light weight core for sandwich panels, radiant burners, catalyst supports, sensors and bone grafts [1-2]. The porosity may be needed in the structures to reduce the weight of the structure at the non-critical areas, to increase the activity of the ceramics by increasing surface area or to separate the wanted from the unwanted materials during filtering. But in all the cases, a better control of the pore geometry and improvements of the mechanical properties of the porous structures are important to improve the reliability of the structures.

Various processing techniques have been utilized to fabricate porous ceramic materials. Replamineform process was utilized to fabricate porous bioceramic implants to duplicate the macroporous microstructures of corals that have interconnected pores [3]. Porous alumina ceramics have been fabricated using pore former or foaming agent that evolves gases during sintering at elevated temperatures [4]. Porous Hydroxyapatite (HAp) ceramic blocks were also fabricated using HAp slurry mixed with foaming agent followed by sintering at elevated temperature [5]. Shrout et al. and Rittenmyer et al. [6-7] reported fabrication of 3-3 piezocomposites using a mixture of volatilizable plastic spheres and PZT powder, in a process known as BURPS (BURned-out Plastic Spheres). Unfortunately, all of these processes form structures with randomly arranged pores with a wide variety of sizes and have limited flexibility to control pore volumes and porosity distribution in the final structure. In this paper, we discuss about porous ceramics with non-random pore volumes, shapes and sizes, which have been processed using solid freeform fabrication (SFF) methods. SFF offers tremendous flexibility in varying the porosity parameters which controls the strength of these ceramic structures as well.

Theoretical and experimental characterization of porous materials is not new and several theories have already been postulated to characterize the mechanical strength of polycrystalline porous ceramics. These theories to characterize the mechanical strength can be classified into three broad categories: (1) reduction in cross-section area approach, (2) stress concentration approach and (3) effective flaw size approach. Most of these studies in predicting the porosity-strength relationship have been limited to the fitting capability of the equations towards the available experimental data and no attempt has been made to quantitatively access the effects of porosity parameters on the strength degradation of the porous ceramic structures.

The effects of porosity parameters such as size, shape, and pore interaction on the strength degradation of porous ceramics under uniaxial compression loading are presented. Finite element method (FEM) is used to study the effects based on stress concentration. Statistical analysis of the experimental results shows the main factors and the interaction among them that affect compressive strength.

Processing

Solid freeform fabrication (SFF) is an approach to directly build three-dimensional components layer-by-layer from a computer data description or a CAD file of a component. SFF techniques can be used in two ways to fabricate functional metal/ceramic prototypes: (a) direct and (b) indirect. In the direct route, green metal/ceramic components are directly fabricated using SFF. Recently, researchers modified the Fused Deposition process [8] to manufacture direct ceramic parts via a process known as FDC (Fused Deposition of Ceramics) [9, 10]. In the indirect route, the negative or the mold of the desired structure is fabricated via SFF. The positive is then cast using metal/ceramic powder based slurry via a lost mold technique. Recently, using the indirect processing route, 3D honeycomb porous ceramic preforms have been fabricated [11]. Commercially available Fused Deposition Modeling (model FDM 1650, Stratasys Inc., MN) process was used for making the molds. The indirect processing route is schematically shown in Fig. 1 and the schematics of the wax mold is shown in Fig. 2a and b.

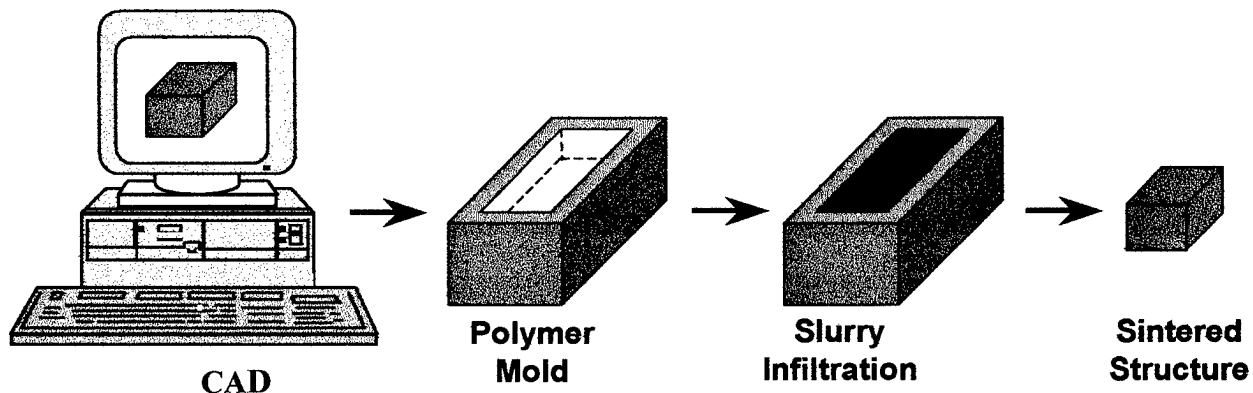


Fig.1: Schematic of the indirect processing of ceramic structures via rapid prototyping processes.

Thermoplastic polymeric molds were built using FDM 1650 machine. The raster gap (X and Y gap), road width (length a) and slice thickness (Z gap) were varied with respect to each other, to obtain desired pore size, pore shape and volume fraction porosity.

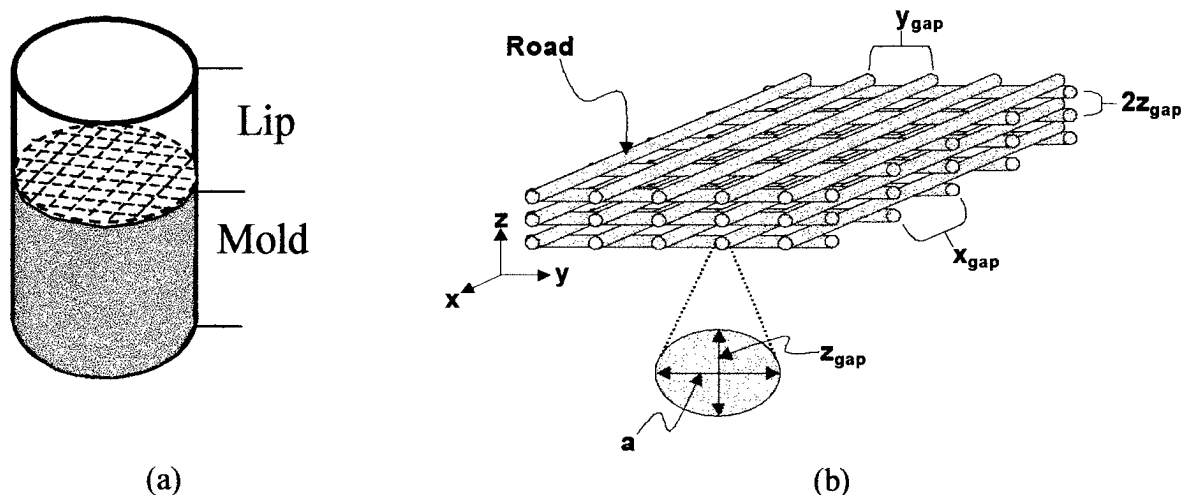


Fig.2: (a) Schematic of polymeric mold design using FDM. (b) Schematic of internal wax pattern in the mold via FDM.

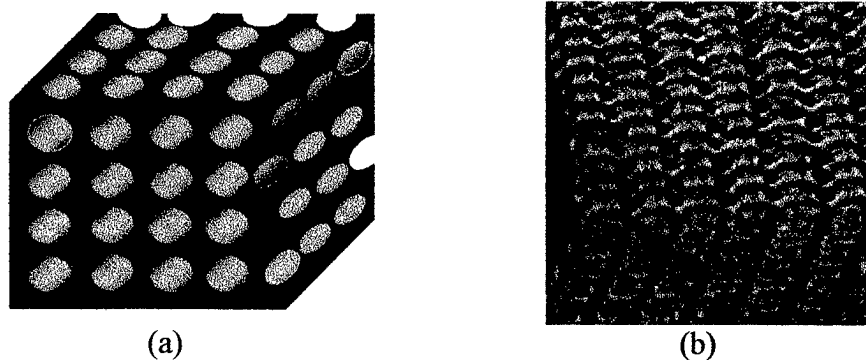


Fig.3: Microstructures of 3D honeycomb porous ceramic structures. (a) Schematic; (b) Side view of a structure with uniform porosity

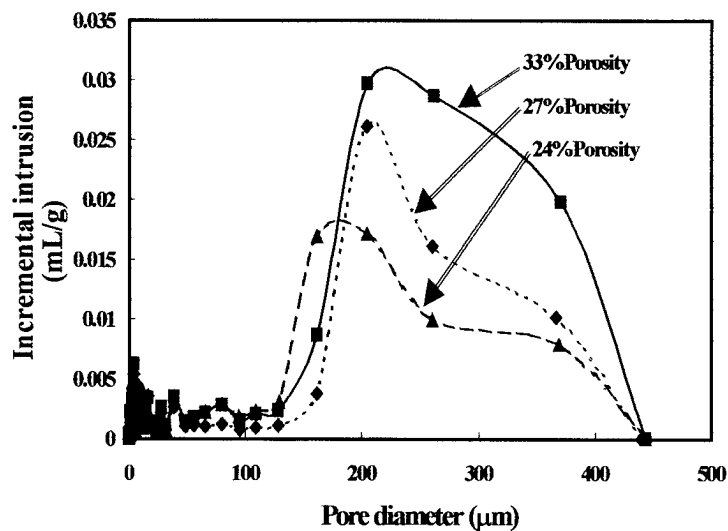


Fig.4(a): Hg-porosimetry plots show the porosity distribution in 3D honeycomb porous mullite ceramics

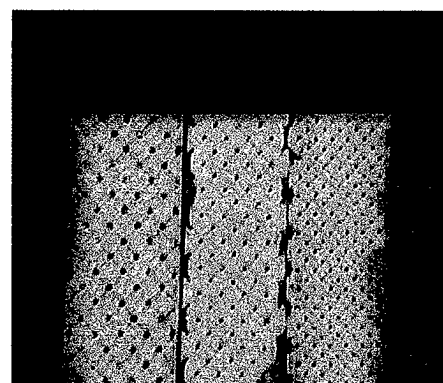


Fig. 4(b): 3D honeycomb porous ceramic structures with different volume fractions of porosity.

Fig. 3a shows the schematic of the porous structures and **Fig. 3b** is photomicrograph of the side view of porous 3D honeycomb ceramic preforms. In both the cases, it can be observed that pores are uniformly distributed and interconnected in all three directions. **Fig. 4a** shows the mercury porosimeter (model Autopore III, Micromeritics, GA) plot of incremental intrusion of mercury in the porous structures. It can be seen from this plot that the maximum volume of the mercury, that intrudes the porous ceramic, occupies the macropores in the vicinity of 150 to 300 μm , which was actually the designed pore sizes for these structures. **Fig. 4b** shows the porous ceramic structures where the pore sizes and their distribution are varied.

Experimental Testing:

Experimental result for strength degradation of mullite ceramics subjected to compressive loads is discussed in this section. Some of the trends were observed that follow the exponential equation proposed first by Ryshekewitch [12]. The equation was expressed as

$$\sigma = \sigma_0 (\exp.)^{-bP}$$

where, σ , is the stress of the porous structure in compression.

σ_0 , is the stress of non-porous structure.

b , empirical constant. Ryshekewitch (1953) determined the value of “ b ” from the slope of the curve as 6 to 9, for different loading conditions.

and P , is the volume fraction porosity for zirconia and alumina.

Cylindrical samples of 1-inch length and 0.6-inch diameter were fabricated having a non-random porous structure with predetermined pore size and pore volume. Uniaxial compressive tests were done on a servo-hydraulic load frame (MTS 4 post (44KN)) under displacement control at a stroke rate of 1.27 mm/min

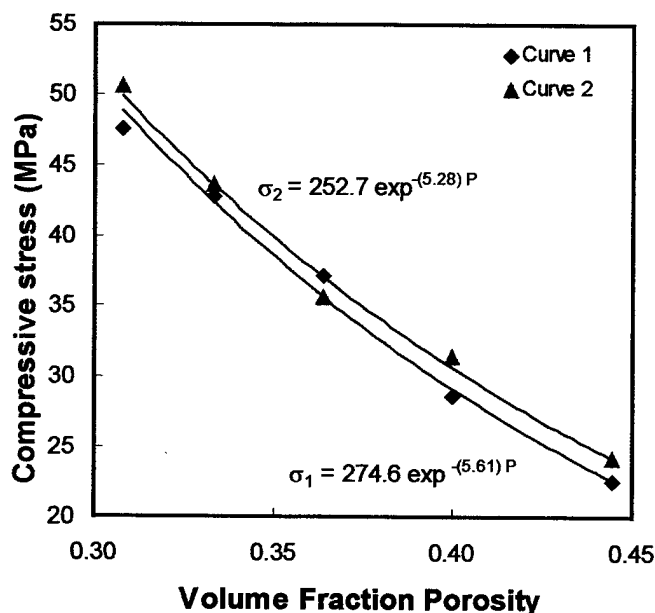


Fig. 5: Variation of Raster Gap

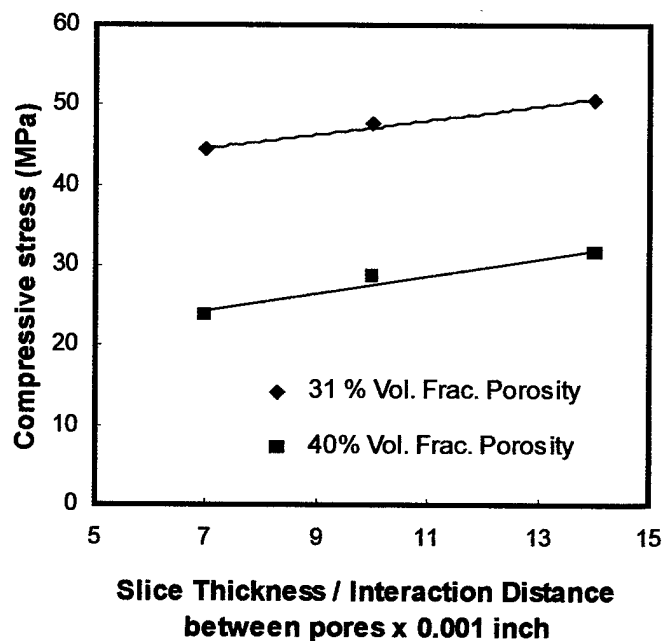


Fig. 6: Variation of Slice Thickness

By varying the raster gap (X and Y-gap in **Fig. 2b**) between the filaments in the wax mold, the interaction between pores in the horizontal plane of the ceramic structure was varied. This variation for different volume fraction porosities shows a failure trend in **Fig. 5** for which the exponential equation is a good fit. The Curve 1 and 2 in **Fig. 5** show the failure trend for two different pore heights which is achieved by varying the slice thickness (Z- gap in **Fig. 2b**). The strength is slightly lesser when a smaller slice thickness is used, shown as curve 1 compared to curve 2, where a higher values of slice thickness was used. The σ_0 based on the above Ryshekewitch equation for curve 1 and 2 are 274.6 MPa and 252.7 MPa, respectively. The variation of the slice thickness or pore shape in the vertical direction is shown in detail in **Fig. 6** for 31% and 40% volume fraction porosities.

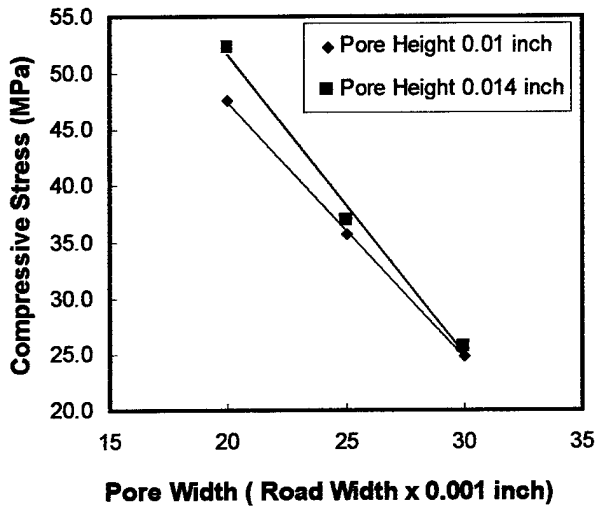


Fig. 7 : Variation of Road Width

It can be observed from **Fig. 6** that as the vertical interaction between the pores increase the strength decreases. It also suggests that as the pore shape becomes more elliptical in the vertical direction, the compressive strength decreases.

By varying the road width (length a in **Fig. 2b**) in the wax mold, the pore shape can also be changed along the horizontal direction as shown in **Fig. 7** for two slice thickness of .01 and .014 inch. The strength of the ceramic decreases as the pore width increases. In other words as the shape of the pore becomes more elliptical the strength decreases.

Statistical analysis

Analysis of Variance for the Compressive Strength Data					
Source of variation (A :- Sum of Squares of the Compressive data (Sq. MPa)	B :- Degrees of Freedom	C :- Mean Square = A / B	F-Value = C / Error	P-Value
Road Width (RW)	894.26	1	894.26	27.585	Very Low
Raster Gap (RG)	370.52	1	370.52	11.429	Very Low
Road Width-Slice Th. (RW-ST)	30.60	1	30.60	0.944	High
Slice Thickness (ST)	16.17	1	16.17	0.499	High
Raster Gap - Slice Th. (RG -ST)	6.51	1	6.51	0.201	High
RG-RW-ST	0.26	1	0.26	0.008	Very high
Raster Gap - Road Width (RG-RW)	0.03	1	0.03	0.001	Very High
Sum of Squares (Error)	259.4	8	32.4		
Sum of Squares (Total)	1577.7	15			
Std. Error Regression Coeff.	1.16				
Standard Error Limits on the Effect Estimates	(plus / minus) 4.65				

Table 1: Two level-three factorial experimental analysis of variance

A two-level three factorial design of experiment was carried out on the basis of analysis of variance (ANOVA). The **Table 1** shows statistical analysis for the three main factors, raster gap(RG), road width (RW) and slice thickness(ST). The road width (RW) and raster gap (RG) are the most important controlling parameters of the strength of porous structures. Their F-values are very high indicating that these factors have most significant effect. The probability that these factors will not control the strength (P-value) is also very low.

Finite Element Modeling

Finite element modeling (FEM) of porous ceramics for increasing porosity and varying pore shapes was studied with respect to their effects on strength degradation of the structures under compressive loading. The FEM was carried out on ANSYS (ver.5.4). Representative cross-sectional schematics of typical porous ceramic structures with uniform pore shapes and sizes are shown in two dimensions in **Fig. 8a**.

Boundary conditions, plane stress method and material properties: In **Fig. 8a**, the nodes along the bottom edge are fixed in the Y-direction but are allowed to move in the X-direction. A node at one of the bottom corners is fixed in the X-direction to prevent rigid body motion. A load is applied to the mesh in the Y-direction " σ_y " such that it is compressive in nature. In controlled porosity ceramic structures, where long cylindrical pores in the third dimension are oriented parallel to the stress direction, there should not be any stress concentration effect, which has been observed by Boccaccini et al.[13] Hence, in this study, plane stress method is used where the stresses in the Z-direction are set to zero. The Young's modulus and Poisson's ratio are selected arbitrarily as 137.8 GPa (2×10^7 psi) and 0.1, respectively. The porous structure is represented by **Fig. 8a and b** in two-dimensions and the porosity is evaluated as area fraction.

Results and discussion of the FEM: All the finite element analysis (FEA) results are shown as a variation of stress concentration factors (SCF) with respect to different porosity parameters. SCF is calculated as σ_θ / σ along the perimeter of the pore, where the angle θ defines the location, σ is the applied stress and σ_θ is the stress at that specific location. The angle θ is zero for all the cases at the perimeter which intersects the y-axis ($\theta = 0$) and increases along the clockwise direction as shown in **Fig. 8a**.

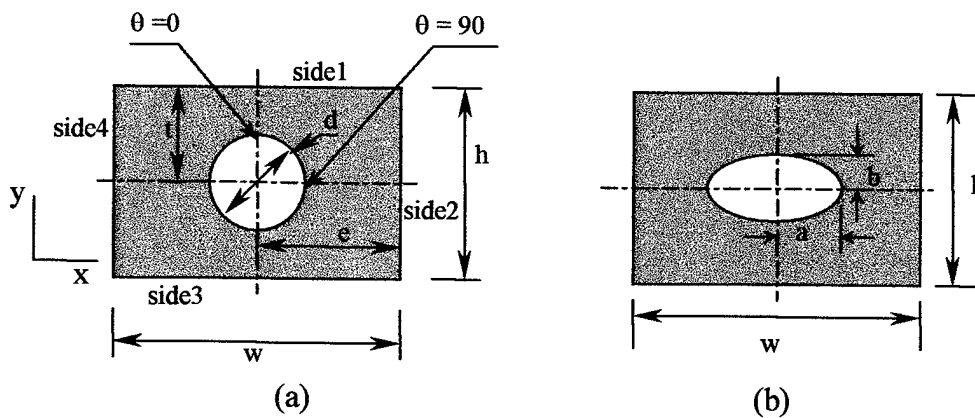


Fig. 8: (a) Finite plate with one pore (b) Plate with elliptical pore.

Effect of increasing porosity: The variation of tensile and compressive component of the SCF with volume fraction porosity is shown in Fig. 9a. This is a very ideal case and it may be difficult to manufacture porous structures with perfectly circular pores. The exponential increase of the tensile component does indicate that the strength is affected by the increasing porosity.

The experimental plot of Fig. 5 obtained by varying the raster gap shows similar effect as the increase in porosity modeled using finite elements. In the experimental study we observed an exponential decrease in strength as the volume fraction porosity or the raster gap increased. In the FEM study, we observe an exponential increase in SCF as the volume fraction porosity increases.

Effect of pore shapes: The above structure was considered for circular/spherical pores. But in reality, all pores are seldom spherical. Fig. 8c shows a schematic diagram where the pore has an elliptical shape. The ellipticity of pores will vary as the ratio of the major and the minor axis (a and b respectively) changes. Fig. 9b shows the effect of pore shapes on SCF. With the increase in ellipticity of the pores, more severe stress concentration effects are observed. The cross sectional solid area decreases in one direction compared to the other and it has been shown that minimum solid area is one of the critical parameters that predicts the strength of the porous structures [14].

The effect of change in pore shape through this FEM study matches well with the experimental results shown by Figs. 6 and 7. Varying the slice thickness and road width has experimentally shown that by decreasing the pore ellipticity controlled porous structures with higher compressive strengths can be designed and this may be caused due to a decrease in stress concentration effects.

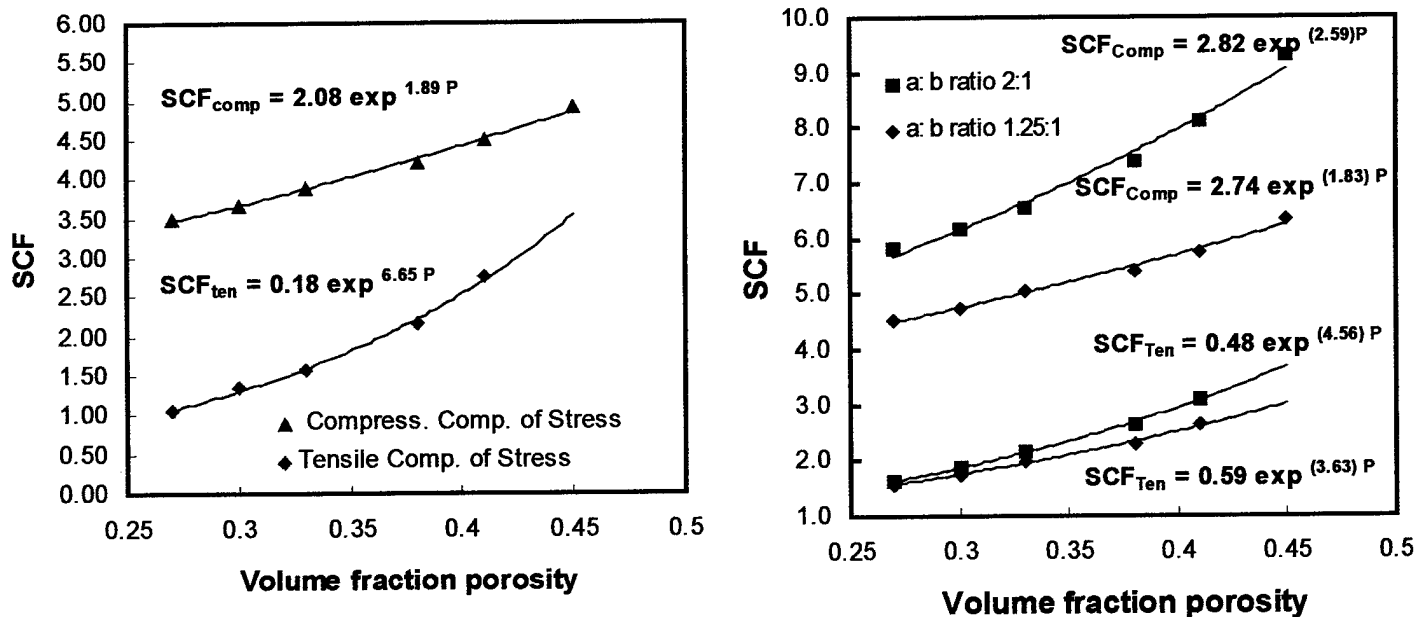


Fig. 9: (a) Effect of increasing porosity on the SCF for constant number of pores. (b) Variation of SCF with increasing porosity for constant pore shapes

Conclusions

Non-random porous ceramic structure can be processed indirectly from SFF process. Experimental results and statistical analysis show that the main parameters that affect the compressive strength of non-random porous ceramics are pore shape and distance between the pores in the horizontal plane. Since SFF process can control these parameters by changing the raster gap and road width, stronger porous structures can be produced via design optimization. Stress concentration effects by finite element modeling show similar behaviour as the failure strength trends obtained experimentally.

Acknowledgments

The authors would like to acknowledge the financial support from the Office of Naval Research under grant number N-00014-98-1-0550. The authors would also like to acknowledge the experimental help of Raj Atisivan, Susmita Bose and Sudarshan Rangaraj.

References

1. D. Hardy and D. J. Green, *J. Eur. Ceram. Soc.*, **15** (1995) 769.
2. R. M. de Souza, H. N. Yoshimura, C. Xavier and H. Goldenstein, *Key Engineering Materials* Vols. **127-131** (1997) 439.
3. E. W. White, J. N. Webber, D. M. Roy, E. L. Owen, R. T. Chiroff and R. A. White, *J. Biomed. Mater. Res. Symp.*, **6**, (1975) 23-7.
4. S. F. Hulbert, S. J. Morrison and J. J. Klawitter, *J. Biomed. Mater. Res. Symp.*, **6**, (1975) 347-74.
5. C. P. A. T. Klein, and P. Patka, *Handbook of Bioactive Ceramics II: Calcium Phosphate and Hydroxylapatite Ceramics*, edited by T. Yamamura, L. L. Hench and J. Wilson, CRC Press, Boca Raton, FL, (1990) 53-60.
6. T. Shrout, T., W. A. Schulze, and J. V. Biggers, *Mat. Res. Bull.* **14**, (1979) 1553-1559.
7. K. Rittenmyer, T. R. Shrout, W. A. Schulze, and R. E. Newnham, *Ferroelectrics* **41**, (1982) 189-195.
8. ---, "Rapid Prototyping Using FDM: A Fast, Precise, Safe Technology"; in *Solid Freeform Fabrication Symposium Proceedings*, Edited by H. L. Marcus, J. J. Beamen, J. W. Barlow, D. L. Bourell, and R. H. Crawford. University of Texas at Austin, (1992) pp. 301-308.
9. A. Bandyopadhyay, R. K. Panda, V. F. Janas, M. K. Agarwala, S. C. Danforth and A. Safari, "Processing of Piezoelectric Ceramics by Fused Deposition Technique," *J. Am. Ceram. Soc.*, **80** 1366--72 (1997).
10. M. K. Agarwala, A. Bandyopadhyay, R. van Weeren, P. Whalen, Ahmad Safari and Stephen C. Danforth, "Fused Deposition of Ceramics: Rapid Fabrication of Structural Ceramic Components," *Ceram. Bull.*, **11** 60--65 (1996).
11. S. Bose, S. Suguira and A. Bandyopadhyay, "Processing of Controlled Porosity Ceramic Structures via Fused Deposition," *Scripta Materialia*, Accepted for Publication.
12. R. Ryshkewitch, "Compression Strength of Porous Sintered Alumina and Zirconia," *J. Am. Ceram. Soc.*, **36** [2] 65--68 (1953).
13. A. R. Boccaccini, G. Ondracek and E. Mombello, "Determination of Stress Concentration Factors in Porous Materials," *J. Mater. Sci. Letters*, **14** 534--536 (1995).
14. R.W. Rice, "Comparison of Physical Property-Porosity Behavior with Minimum Solid Area Models," *J. Mater. Sci.*, **31** 1509--1528 (1996).

Extrusion Freeform Fabrication of Functional Ceramic Prototypes

R. Vaidyanathan, J. L. Lombardi, J. Walish.
Advanced Ceramics Research, Inc., Tucson, AZ 85706

S. Kasichainula, P. Calvert. University of Arizona
Arizona material Laboratories, Tucson AZ, 85712

K. Cooper. NASA Marshall Space Flight Center, Huntsville, AL 35812

Extrusion Freeforming (EFF) and Fused Deposition Modeling (FDM) processes are established freeforming techniques capable of fabricating complex shaped ceramic prototypes by the sequential deposition and solidification of green ceramic feedstock, layer by layer until the final part results. The freeforming of ceramic parts was accomplished using a commercially available Stratasys 3D Modeler retrofitted with a high-pressure extrusion head designed by Advanced Ceramics Research, Inc. (ACR). The manufactured objects had good dimensional tolerances, as well as real engineering compositions and microstructures. Ceramic feedstock based on two different silicon nitride powders were developed and successfully used to make prototype parts. Mechanical properties and microstructural characterization of prototype parts were performed.

I. Introduction

Extrusion Freeform Fabrication (EFF) is an SFF technique based on the Stratasys FDMTM approach^a for the fabrication of functional ceramic prototypes [1]. More details are given in reference 2. While possessing the benefits of Fused Deposition of Ceramics (FDCTM) [1995 Volume from reference 1] and FDMTM, EFF has the added advantages that it can handle higher viscosity feed stock materials and higher extrusion temperatures compared to FDCTM and FDMTM. Similar to other SFF techniques, EFF also allows the sequential deposition of multiple layers to form a complex ceramic shape. This has been achieved by retrofitting a high-pressure extruder head to a Stratasys FDMTM modeler (figures 1 and 2). The CAD file is processed by the QuicksliceTM software and used to control the EFF high-pressure extrusion head [1]. However, the operation parameters that are automatically set by Quickslice, are optimized for polymer filament type of feedstock. These parameters are not necessarily the optimum parameters for the SFF of ceramic parts. To further control process parameters for SFF of ceramic parts, SML PostTM, a Visual Basic based post-processing software was developed to modify selected process parameters. SML PostTM could modify the start-delay, preflow, start-flow, start-distance, main-flow, shutoff-distance, roll-back, speed, and acceleration that were originally set by QuicksliceTM. Presently, the road-width, slice-thickness, and fill-patterns are still set by Quickslice. However, SML PostTM could modify these parameters also, if needed.

The quality of the EFF green ceramic feedstock has a strong influence upon the robustness of the process and its ability to reproducibly fabricate high strength, dimensionally accurate ceramic components. A high degree of homogeneity is desirable in order to minimize density gradients between the binder and ceramic powders. If density gradients are present in the feedstock, it could lead to non-uniform firing shrinkage and formation of defects within the

^a Stratasys Inc., Eden Prairie, MN

freeformed ceramic bodies³. The feedstock should also possess a reproducible rheology so that it can be accurately freeformed into the desired green ceramic component. Further requirements for the rheology of EFF feedstock are a low melt viscosity (extrudable at low pressures) as well as the ability to undergo rapid solidification upon deposition (enabling more rapid part build rates). The binder should be easily removable from the freeformed green bodies under controlled conditions and leave minimal pyrolysis residue. Finally, the resulting bodies should be readily sinterable into dense ceramic components.



Figure 1. Stratatsys FDMTM retrofitted
With a high pressure head

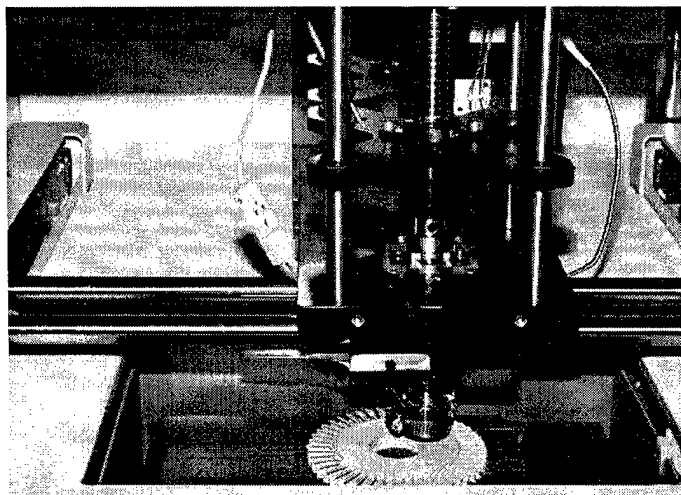


Figure 2. Close up view of the high pressure
head creating a ceramic prototype

In contrast to EFF, additional requirements must be met for the filament feedstock used in FDC processing. In particular, FDC compatible filaments should also possess sufficient strength and flexibility such that they can be continuously extruded through a conventional Stratatsys Modeler without fracturing. Significant FDC filament breakage could lead to dimensional inaccuracies and flaws within the FDC parts. Consequently, the utilization of filament feedstock possessing reproducible mechanical properties is an important issue in successful FDC part fabrication. Therefore, for successful FDC, the filament feedstock needs to meet two separate and sometimes divergent sets of property requirements. This is extremely difficult to achieve for non-ideal systems such as ceramic-loaded binder systems. The EFF process avoids this problem by the use of a ceramic feed-rod as the feedstock. This provides the EFF process certain advantages over the current FDC process.

II. Experimental Procedure

The entire EFF process involves at least five distinct processing stages that result in a structural ceramic part. In addition to the EFF process itself, there are two pre-EFF and two post EFF processing stages.⁴ The first of these stages is the formulation of a binder system which contains plasticizers, surfactants, and dispersants as well as other additives. More details of the present binder system and the rheology of the ceramic-loaded binder system has been discussed in reference 2. After a formulation is decided on, feedrods 0.625"x6" length are made by mixing the binder system with the ceramic powder and sintering aids and then pressing this batch of material into feedrods. The next step is to fabricate a part using the EFF process and burn out the

binder. The subsequent sintering stage densifies the part. Other steps could be added if necessary, such as post-finishing, depending on the quality desired.

A. Ceramic/Binder Feedstock Development

The ceramic feedstock for EFF needs many of the qualities commonly desired in raw materials for ceramic injection molding.⁵ Consequently, EFF feedstocks were developed with binder formulations similar to those employed by conventional ceramic forming processes. These formulations consisted of ≈ 55 vol% of silicon nitride powder dispersed in an organic binder. The binder is a mixture of polymer, wax, and plasticizer and serves as a vehicle for the freeformed Si_3N_4 ceramic powder. The wax is an important component in the binder since it lowers the melt viscosity of the binder polymer at elevated temperatures (ca. $> 100^\circ\text{C}$) while simultaneously enabling the green body to rapidly solidify and maintaining its dimensional accuracy after freeforming. A liquid plasticizer is believed to be an important binder constituent since it also lowers the binder melt viscosity. Its higher volatility compared to the wax and polymer enables a progressive and more controllable removal of binder components prior to sintering the freeformed ceramic bodies.⁶ The suitability of this binder composition in EFF feedstocks was demonstrated after successfully extrusion freeforming and subsequent pressureless sintering $>97\%$ dense, crack free silicon nitride parts using this type of formulation. Figure 3 depicts both green and pressureless sintered silicon nitride prototypes that were fabricated using EFF techniques.

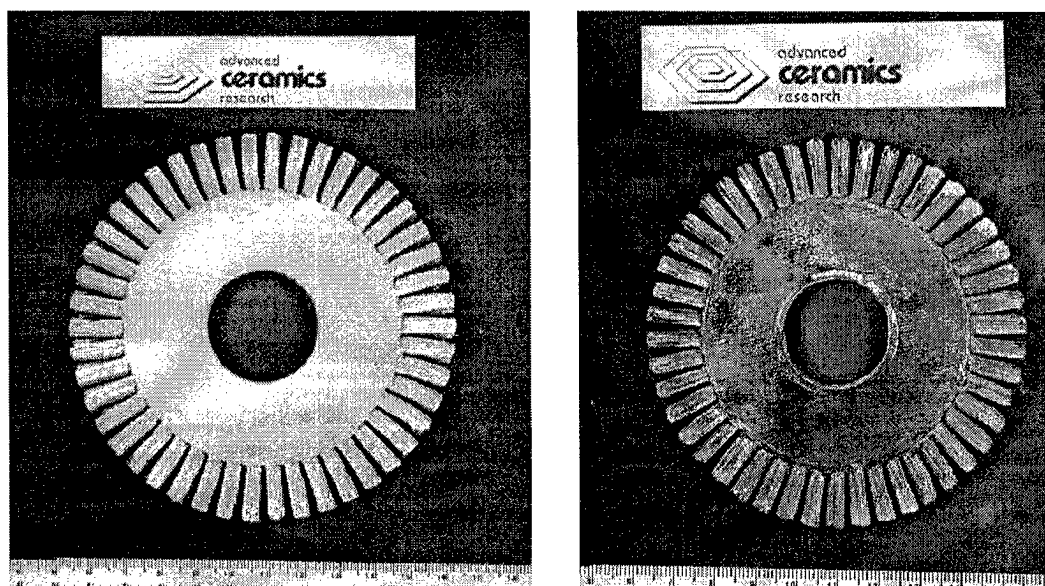


Figure 3. Photograph of green and sintered silicon nitride bladed disk fabricated using EFF techniques.

Green ceramic feedstock having a composition similar to the values in Table I was compounded using an Armoloy Prep Mixer^a. All raw materials present in the green ceramic feedstock were obtained from commercial sources. The silicon nitride powder was a pressureless

^a C. W. Brabender, Hackensack, NJ

sinterable composition containing yttrium and aluminum oxide sintering aids in a 9:3 weight ratio. The saturated elastomer in the binder was an amorphous, noncrystallizable copolymer. Gel permeation chromatography of the paraffin wax binder component reported an average molecular weight of 3779 g/mole and a polydispersity index of 2.5. The fatty acid plasticizer was a liquid under ambient conditions.

Component	Concentration (Volume %)
Silicon Nitride	≈ 55
Saturated Elastomer	≈ 25
Fatty Acid Ester Plasticizer	≈ 10
Paraffin Wax	≈ 5
Acryloid Additive	≈ 5

Table I: A typical green ceramic feedstock composition.

For rheology characterization, a plunger type Instron rheometer (Model 3211)^c was utilized for capillary rheometry at temperatures between 120 and 150°C.

B. Feedrod Processing and the EFF Process

After shear mixing, the green ceramic material was extruded into feedrods measuring 15.9 mm (5/8") in diameter by 152.4 mm (6") in length. These feedrods were then fed into the barrel of the extrusion head and extruded to produce different 3-D shapes with the EFF process. The EFF process itself was optimized by using a Design of Experiment (DOE) procedure⁷. The software-controlled parameters were optimized so that a uniform rate of material deposition was obtained. Figure 4a and 4b show simple parts that were fabricated without optimization of the EFF parameters, while figure 4c shows a simple part that was made after determination of the optimized parameters. The optimization of EFF parameters also improved the on the prototypes. Figure 5 and 6 are prototype parts made with different starting silicon nitride powder, such as Kyocera SN282 and Starck M-11. At present, Alliedsignal AS800 silicon nitride parts are also being made. These results show that the EFF process is capable of handling a variety of starting ceramic powders.

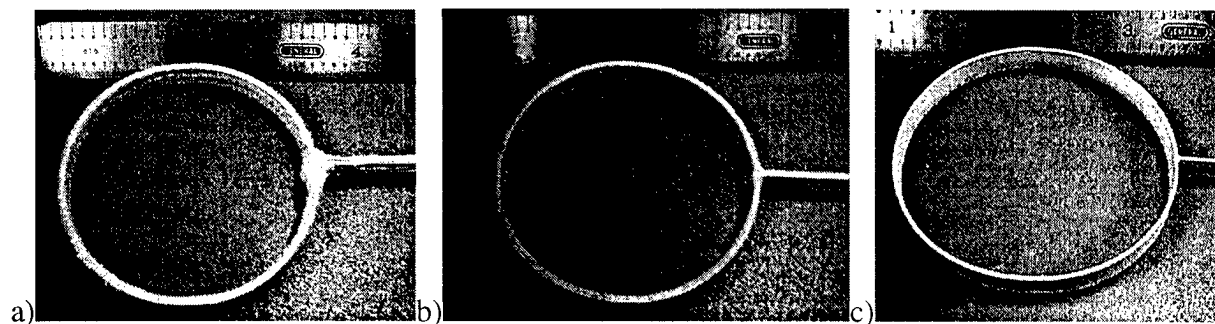


Figure 4: Cylinders a and b were fabricated prior to optimization. Cylinder c was constructed with the optimized parameters.

^b Instron, Canton, MA

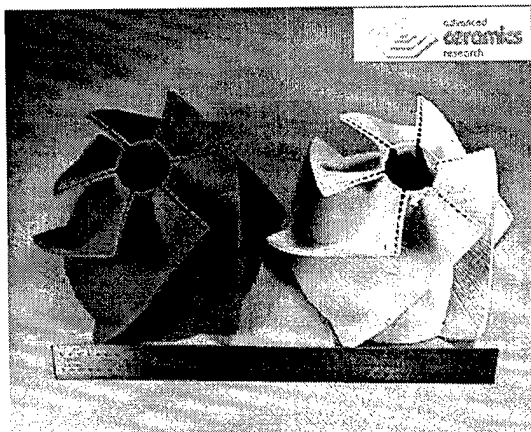


Figure 5: Impellers made with Kyocera (left) H.C. Starck (right) silicon nitride powders.

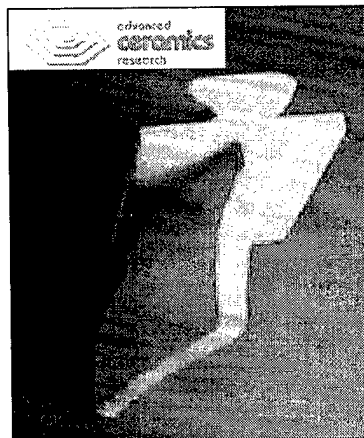


Figure 6: A turbine blade made with the Starck M-11 powder.

C. Binder Burnout and Sintering

Once the green prototype has been fabricated using EFF, the organic binder must be removed. The optimum situation is one in which all of the binder has been removed, yet there are no defects created by the removal of the binder system. Thermogravimetric Analysis (TGA) was used to study the compositional loss and degradation of a binder relative to temperature. After TGA is performed, a binder burnout cycle is then devised. Binder burnout cycles are currently being studied so that prototypes with thick cross-sections can be successfully burned out and sintered without fear of producing defects. The current binder burnout and sintering processes can produce parts with greater than 97% theoretical density.

III. Results and Discussion

A. Ceramic/Binder Feedstock Development and EFF optimization

Formulation modifications were performed in order to obtain lower viscosity and a less shear-rate dependent Si_3N_4 formulation compared to the standard binder formulation. Capillary rheology of EFF feedstock with an acryloid addition for improving the dispersion of the Si_3N_4 powders in the binder system was performed. A comparison of the shear rate-viscosity behavior on standard binder formulations with and without the acryloid addition is shown in Figure 7. The capillary rheology data shows little difference in viscosity at all shear rates. However, at the shear rate ranges operative in the EFF process, there was no difference in the viscosity between the EEA binder formulations with and without the acryloid additions. However, the significant finding here was that the extrusion forces during EFF were an order of magnitude lower for the modified formulation compared to the standard formulation. For example, the extrusion pressures for the modified formulation were of the order of 150-200 pounds, while the extrusion pressures with the standard formulation were of the order of 1500 pounds. High extrusion pressures beyond the capacity of the load cell tend to create a situation where the extrusion stops shortly and starts again, creating missed layers and defects in the part. The modified formulations resulted in improved average strength and eliminated missed layers in the part.

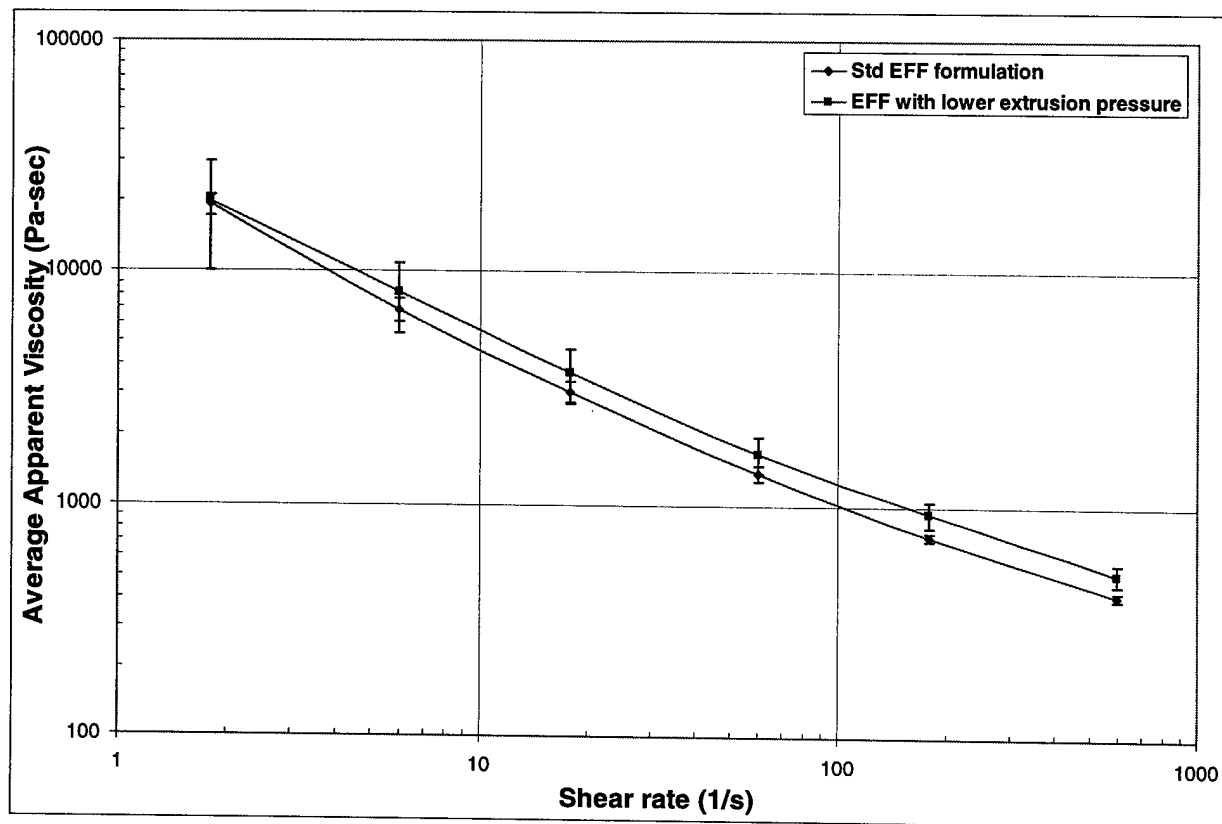


Figure 7. Comparison of shear rate-viscosity behavior of EEA binder formulations with 55 vol% Si_3N_4 with and without an acryloid addition, at 150°C .

The above result suggests that rheology measurements by themselves are not sufficient to evaluate the effectiveness of a binder formulation for EFF. The high-pressure extruder head is capable of overcoming the rheology limitations of the EFF formulations and therefore, other simple indicators of extrudability need to be developed for the EFF process. This could include extrusion force, mechanical properties of flexural bars, as well as SEM analysis of fracture surfaces. Room temperature four-point bend tests were performed on flexural bars prepared from EFF formulations with the acryloid addition. An average strength of 641 ± 107 MPa was obtained, compared to an average strength of 525 ± 110 MPa for flexural bars from the standard formulation. Figure 8 shows the fracture surface of a test bar. The fracture surface did not show any delaminations or missed layers during the freeforming process. Figure 9 shows a higher magnification image of the fracture surface from figure 8.

Room temperature flexural tests were performed on bars produced with the optimized parameters. These results are shown in table II. The strength of these bars were comparable with that of previously made bars (polished – 613 ± 12 , unpolished – 594 ± 80). These results suggest that optimization of the EFF parameters provided a good surface finish to the samples.

B. Binder Burnout and Sintering

Binder burnout and sintering currently produce parts that are greater than 97% dense with x-y shrinkages of $18 \pm 3\%$ and z shrinkage of $20 \pm 5\%$. These numbers are similar to numbers obtained from other ceramic freeforming processes⁸.

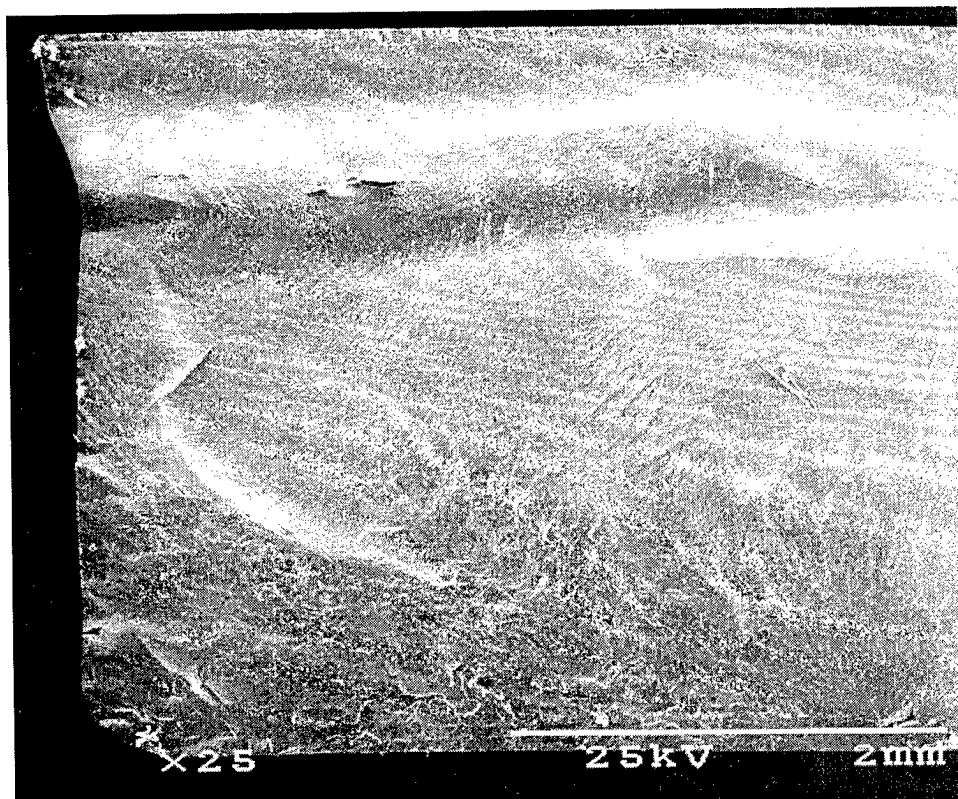


Figure 8. Low magnification image of the fracture surface of freeformed flexural test bars.

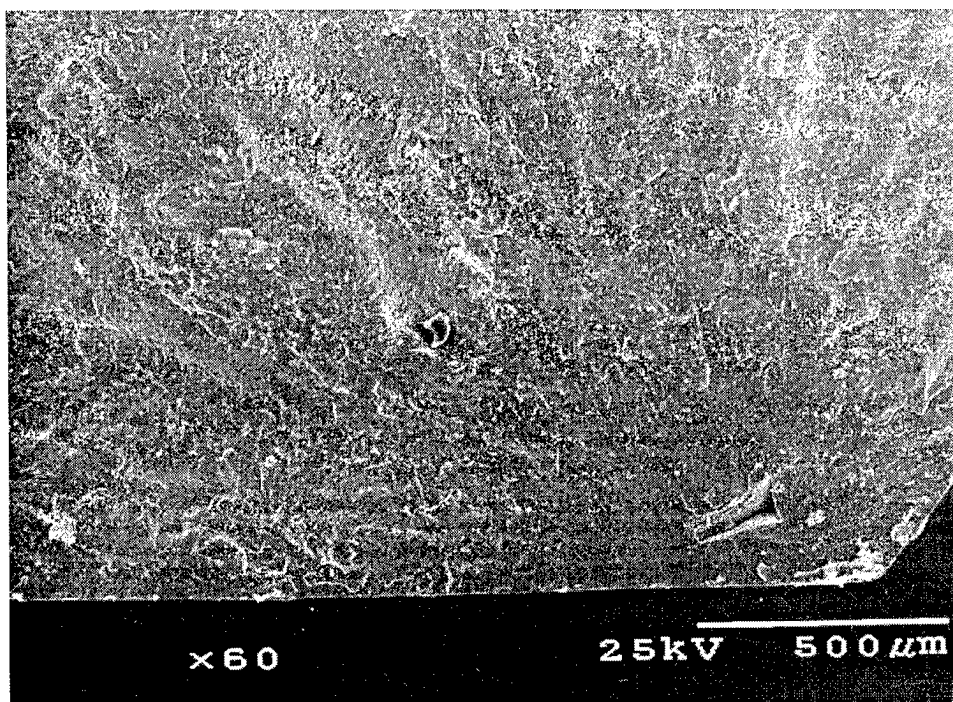


Figure 9. Higher magnification of fracture initiation point from figure 8.

IV. Conclusions

Through the improvement of feedstock and process parameters, the EFF process has

demonstrated the capability to fabricate complicated ceramic prototypes using a commercially available Stratasys 3D modeler. Prototypes with excellent surface finish and few defects can be made. Binder burnout schedules are currently being modified to assure that parts with thick cross-sections can be burned out without warping or defects.

Table II. Flexural strength data for EFF test bars as a function of raster-build direction

Raster-build direction	Surface condition	Flexural strength (MPa)
0°	Unpolished	594 ± 80
0°	Polished	613 ± 12
0°/90° alternating	Unpolished	227 ± 39
0°/90° alternating	Polished	312 ± 71

Acknowledgments

This work has been performed under NASA STTR program contract number NAS8-98025.

REFERENCES

1. Proceedings of the Solid Freeform Fabrication Symposium, Vol. 1990-1998, Edited by H.L. Marcus, et al., the University of Texas at Austin, Austin, TX.
2. R. Vaidyanathan, J. L. Lombardi, B. Tennison, S. Kasichainula and P. Calvert, "Rheological properties of ceramic formulations for Extrusion Freeform Fabrication," presented at the 23rd Annual Cocoa Beach Ceramic Society meeting on Ceramics and Composites, Cocoa Beach, FL, Jan. 1999 (in press).
3. R.M German and A. Bose: *Injection Molding of Metals and Ceramics*, Metal Powder Industries Federation, Princeton, New Jersey, pp. 23, (1997).
4. J. L. Lombardi, R. A. Hoffman, J. A. Waters, D. Popovich, C. Sovignier, and S. Boggavarapu, "Issues associated with EFF and FDM ceramic filled feedstock formulation," *Proceedings of the Eighth Solid Freeform Fabrication Symposium*, Vol. 1997, Edited by D. L. Bourell, J. J. Beaman, J. W. Barlow, H. L. Marcus and R. H. Crawford, The University of Texas Press, Austin, TX., pp. 457-464, (1997).
5. M.J. Edirisinghe and J.R.G. Evans: *Materials and Design*, vol. 8, pp. 284-8, (1987).
6. M.J. Edirisinghe and J.R.G. Evans: *Journal of Materials Science*, vol. 22, pp. 269-277, (1987).
7. J. Walish, et al., "Application of Design of Experiments to Extrusion Freeform Fabrication (EFF) of Functional Ceramic Prototypes," *Proceedings of the Eighth Solid Freeform Fabrication Symposium*, Vol. 1999, Edited by D. L. Bourell, J. J. Beaman, J. W. Barlow, H. L. Marcus and R. H. Crawford, The University of Texas Press, Austin, TX.
8. M.K Agarwala, R. van Weeren, R. Vaidyanathan, A. Bandyopadhyay, G. Carrasquillo, V. Jamalabad, N. Langrana, A. Safari, S.H. Garofalini, S.C. Danforth, J. Burlew, R. Donaldson, P. Whalen, and C. Ballard, "Fused Deposition of Ceramics," *Proceedings of the Sixth Solid Freeform Fabrication Symposium*, Vol. 1995, Edited by D. L. Bourell, J. J. Beaman, J. W. Barlow, H. L. Marcus and R. H. Crawford, The University of Texas Press, Austin, TX., pp. 1-8, (1995).

Maximizing the Strength of Fused-Deposition ABS Plastic Parts

J. F. Rodríguez, J. P. Thomas, and J. E. Renaud
University of Notre Dame
Department of Aerospace and Mechanical Engineering
Notre Dame, IN 46556-5637
USA

ABSTRACT

Fused-Deposition (FD) creates parts using robotic extrusion of a semi-liquid polymer fiber, which molecularly bonds with neighboring fibers via thermal-diffusion bonding. The strength of the part depends on the bulk polymer strength, the mesostructure (fiber layout, void geometry, extent of fiber bonding), and the fiber-to-fiber bond strength. The influence of these factors on the mechanical strength of FD-ABS plastic parts is reported along with the FD process variable settings for maximum strength. Substantial increases in transverse strength are achieved at the optimal settings and additional increases can be achieved by post-fabrication annealing.

Keywords: Stratasys, fused-deposition, ABS plastic, functional parts, strength, mesostructure, polymer diffusion.

INTRODUCTION

Fused-Deposition (FD) Modeling is a Solid Freeform Fabrication (SFF) process that creates a physical representation of a CAD model via computer-controlled robotic extrusion of a small polymeric fiber in an additive material deposition process. The fibers are extruded in a semi-liquid state and bond with the neighboring fibers via thermal-diffusion welding. FD materials take the form of laminate composites with vertically stacked layers consisting of contiguous material "roads" or "fibers" with voids. The ability of FD create geometrically complex parts with specific mesostructural characteristics endow it with unique potential for the manufacture of functional parts with tailored mechanical performance. However, better understanding of the influence of the mesostructure and FD process variables on the mechanical behavior is needed to fully capitalize on this potential.

There have been several efforts to characterize and improve the mechanical behavior of FD materials. Fodran and coworkers [1998] studied the effect of impregnating the FD material with adhesive bonding agents after manufacturing to improve stiffness and strength. Kulkarni, et al. [1997] compared experimentally measured in-plane tensile moduli for symmetric FD composites built with various deposition strategies with predictions made using laminate composite theory. Gray et al. [1998] investigated the use of fiber reinforced polypropylene for making much stronger and stiffer FD parts. Bertoldi et al. [1998] characterized the elastic moduli for FD-ABS materials with a "pseudo-isotropic" stacking sequence.

This paper summarizes the results of various studies conducted at Notre Dame on the influence of mesostructure and FD processing parameters on the strength of unidirectional FD-ABS (acrylonitrile-butadiene-styrene) plastic materials. Our studies show that the strength and stiffness of FD parts is controlled by the bulk ABS material properties, void geometry, extent of bonding between contiguous fibers, and the strength of the fiber-to-fiber bonds. Decreasing the FD gap setting from 0.0 to $-25.4\ \mu\text{m}$ reduces the void size and increases the contact between contiguous fibers resulting in a significant increase in transverse strength. Increasing the FD envelope temperature and post-build annealing increases the strength of the bonds between the fibers, which also produces an increase in the transverse strength.

We start with a description of the experiments used to characterize the mesostructure, fiber-to-fiber bond strength, and material strengths as a function of the various FD processing parameters. The experimental results are presented and discussed, and the paper ends with conclusions and recommendations for future work.

METHOD

The Stratasys FDM1600 Modeler with the P400 ABS plastic was used to make the test specimens. The P400 ABS is supplied in monofilament form (1.778 mm diameter) and is kept in the shipping container or the FDM1600 material feed chamber with desiccant to minimize the absorption of humidity.

The FDM1600 has hardware and software based parameters that can influence the material strength. The fiber-to-fiber gap, g , (0 to $-50.4\mu\text{m}$) has a large influence on the extent of bonding between fibers within a given layer and on the resulting material density. The fiber cross-section geometry is controlled by the normalized flow rate, ϕ , (16-30 \equiv nominal fiber width in mils), the layer height (0.254 mm), the nozzle diameter (0.308 mm), and the nozzle speed during extrusion (12.7 mm/sec). The fiber layout can be controlled within each layer (unidirectional, contour) and between each layer (translation: aligned or skewed; and rotation). The extrusion ($\sim 285^\circ\text{C}$ max) and envelope temperatures (70°C max) influence the viscous flow and solidification characteristics and the thermal-diffusion bonding process between fibers. Parameter settings that minimize the void and defect densities and maximize the extent of fiber-to-fiber bonding produce FD materials with the maximum elastic strength and stiffness.

Only unidirectional FD materials with aligned (vertically aligned stacking; Figures 1,2) or skewed (alternating layers with horizontal skewing one-half the fiber width) mesostructures are considered in this paper. The void areal density and the extent of circumferential fiber-to-fiber bonding have been characterized as a function of fiber-to-fiber gap, flow rate (fiber width), and the extrusion and envelope temperatures. Void density on the i^{th} material plane is defined as:

$$\rho_i = \frac{\text{Void Area}}{\text{Cross Section Area}} \quad (1)$$

The extent of circumferential fiber-to-fiber bonding is quantified using the fiber interface bond length density:

$$\text{B.L. Density} = \frac{\sum \text{Fiber Bond Lengths}}{\text{Total Circumference Length}} \quad (2)$$

Mesostructure characterization was performed using cross-section micrographs (Rodriguez et al., 1997, 1999b). Void densities in the plane normal to the fiber extrusion direction were determined using a point counting method. Bond length densities were determined by subdividing fiber circumferences into arcs and summing the respective contributions. The reported densities are averages based on ten or more measurements.

The fiber-to-fiber bond strength was characterized in terms of interface fracture toughness (Rodriguez et al., 1999a). Tests were performed to assess the influence of the extrusion and envelope temperatures, loading rate, and post-build annealing treatments on the bond strength. The test specimens are sheet-like, one fiber thick, and have an edge crack at the interface between fibers (Figure 3).

The stress-strain behavior of bulk ABS monofilament and FD-ABS under longitudinal, transverse, and off-axis loading was determined under strain control. The test specimens (Figure 4) are in a tabbed-coupon configuration with dimensions conforming to ASTM Standard D3039.

RESULTS

The fiber gap and flow rate had a large influence on mesostructure while extrusion and envelope temperatures had very little influence. The lowest void densities (6.8%A, 4.5%S) and largest bond densities (73%A, 69%S) are achieved at the following settings: $g = -25.4\mu\text{m}$, $\phi = 20$, $T_L = 270^\circ\text{C}$ and $T_E = 70^\circ\text{C}$, henceforth denoted as "optimal." Photographs of an aligned mesostructure at gap settings of 0.0 and $-25.4\mu\text{m}$ are shown in Figures 1 and 2. For skewed mesostructures with positive gap, the maximum void density achieved was 16% at $g = 152\mu\text{m}$ with a corresponding bond-length density of 39%. The fiber cross-sections were asymmetrical, and the voids were either triangular or diamond shaped depending on the gap setting and the magnitude of the extrusion-envelope temperature difference, $T_L - T_E$.

Fiber bond strengths (i.e., fracture toughness, K_c) for the envelope temperatures $T_E = 50$, 60, and 70°C are plotted in Figure 5 as a function of extrusion temperature ($T_L = 255$, 270, and 285°C). K_c increases with T_L and T_E , but the increase levels out with T_L at the machine default setting of 270°C . The increase in K_c with T_E is similar for all T_L values amounting to $0.014\text{MPa}\sqrt{\text{m}}/^\circ\text{C}$. The effect of displacement rate (0.013 to 0.85mm/sec) on K_c is relatively small, only $-0.08\text{MPa}\sqrt{\text{m}}$ per decade increase in the rate. The effect of annealing treatment (1 min to 8 hr at 118, 125, or 134°C) is shown in Figure 6. K_c increases linearly with respect to $t^{1/4}$ for a given anneal temperature. The bond strength before annealing ($1.88\text{MPa}\sqrt{\text{m}}$) corresponds to the value for specimens built with the optimal settings. It reaches a maximum of $2.48\text{MPa}\sqrt{\text{m}}$ at the so-called recovery time, t_∞ . The observed power-law form is consistent with molecular diffusion theories for strength development at A/A polymer interfaces (Rodriguez et al., 1999a).

The fracture morphology in the small region of stable crack growth that occurs prior to reaching the critical fracture load is most relevant to the mechanistic understanding of strength at the fiber interface. SEM fractographs of this region for specimens built with the optimal settings, with and without annealing (64 minutes at 134°C), are shown in Figures 7 and 8. The annealed specimen (Figure 8) shows less fibrillation (i.e., tear ridges due to crazing and molecular pullout at the interfaces between the butadiene particles and acrylonitrile-styrene matrix) and more chain scission than the unannealed specimen (Figure 7), due to increased molecular interpenetration that occurs with annealing. Defects (e.g., voids and microcracks) at the interface between the bonded fibers (Figure 9) also influence the interface bond strength.

The stress-strain responses for bulk ABS and FD-ABS specimens loaded in the longitudinal and transverse directions are shown in Figure 10. Strength values for these and other mesostructures are listed in Table 1. Stresses in the FD specimens are calculated using apparent cross-section areas that do not account for the void area. The bulk and longitudinal FD stress-strain responses are qualitatively similar, but the FD-ABS strength (i.e., the maximum stress attained) is lower than the bulk ABS strength by 6.8MPa (22%). The transverse FD stress-strain behavior is more "brittle" in nature with much lower strength and strain-to-failure values. The change in behavior is indicative of the change in failure mode from ductile fracture of the extruded FD fibers, for longitudinal loading, to brittle fracture along the fiber interfaces for transverse loading.

Figure 11 shows the strength values plotted as a function of angle, from longitudinal at $\theta = 0^\circ$ to transverse, at $\theta = 90^\circ$. The quadratic strength theory of Azzi and Tsai (1965) for

laminate composites is used to characterize the strength, S_θ , as a function of θ :

$$\frac{1}{S_\theta} = \frac{\cos^4 \theta}{S_0^2} + \left(\frac{1}{S_s^2} - \frac{1}{S_0^2} \right) \cos^2 \theta \sin^2 \theta + \frac{\sin^4 \theta}{S_{90}^2} \quad (3)$$

The coefficient, S_s , is quantified using the tensile strength at 10° (Rodriguez, 1999).

Table 1: Bulk ABS and FD-ABS Strength and (Modulus) Values

Mesostructure	Longitudinal (MPa)	Transverse (MPa)
Bulk ABS	31.2 (2230)	n/a
Aligned, $g = 0.0\mu m$	21.5	<5
Aligned, $g = -25.4\mu m$	24.4 (1972)	13.4 (1762)
Aligned, $g = -25.4\mu m$, Annealed	22.9	18.5
Skewed, $g = -25.4\mu m$	21.6 (1986)	13.4 (1701)
Skewed, $g = 76.2\mu m$	17.9 (1807)	13.4 (1400)

Figure 12 shows the effect of strain rate on the stress-strain response. A rather drastic reduction in toughness (area under the stress-strain curve) occurs at the lowest strain rate; this strain rate effect is not observed with the bulk ABS specimens. The size of the overshoot at the maximum stress also decreases with strain rate and commences at a smaller level of strain.

DISCUSSION

The strength of the FD-ABS material is lower than the bulk ABS strength for all loading orientations. The presence of voids in the FD-ABS material decreases the amount of load carrying material. The voids cannot be eliminated because the viscosity of the ABS cannot be lowered enough by high temperature to fill the voids without inducing excessive thermal damage. In transverse loading, the sharp corners at the junction of neighboring fibers and the weaker fiber-to-fiber interface material due to incomplete "mixing" of the polymer molecules promotes craze nucleation and propagation further reducing the strength.

Rule-of-mixture relations can be used with good accuracy to predict the effective tensile modulus and strength of unidirectional composite materials. In the present case, the rule of mixtures estimates for longitudinal FD-ABS modulus and strength are off by -5.4% and -19% respectively. One reason for the underestimation of these values is a suspected difference in the modulus and strength of bulk ABS versus extruded FD-ABS fibers due to increased molecular alignment in the bulk ABS. Molecular alignment can be discerned using thermal shrinkage experiments (Fritch, 1980). The larger the shrinkage experienced by a specimen, the larger is the degree of molecular alignment in the shrinkage direction. Strength and elastic modulus increase with increasing alignment. If our suspicions are correct, the bulk ABS should show more shrinkage along the extrusion axis than the FD-ABS fibers.

Shrinkage experiments were conducted at Notre Dame on bulk ABS monofilament and extruded FD-ABS fibers. Four specimens of each, equal in length (102 mm), were held in an oven at $110^\circ C$ ($T_g = 94^\circ C$) for 6 hrs. After cooling, the % shrinkage in length, $(L/L_0 - 1) \times 100$, was measured. The monofilament shrank an average of 20% while the FD fiber shrank only 0.4% indicating a much larger degree of molecular orientation in the bulk ABS. These results are consistent with the underestimates produced by the rule-of-mixtures predictions.

Polymer chain diffusion theory (i.e., reptation theory) can be used to develop additional understanding of the influence of the processing temperatures on the fiber-to-fiber bond strengths. Wool and coworkers [1986,1989] have used reptation theory to develop various models for the strength of isothermally bonded symmetric A/A polymer interfaces. An expression for interface toughness, K_c , can be derived from this work assuming the bond strength is proportional to the monomer interpenetration depth across the interface:

$$\frac{K_c(t, T, M, p)}{K_\infty} = \frac{K_0(T)}{K_\infty} + \int \frac{d}{d\tau} \left[\left(\frac{\tau}{t_\infty(T, M, p)} \right)^{1/4} \right] d\tau \quad (4)$$

This integral is evaluated over the time t at which the interface temperature, T , is above the glass transition temperature, T_g . M is the molecular weight of the polymer; p is the pressure normal to the interface, $K_0(T)$ is the interface toughness due to surface wetting; and K_∞ is the maximum attainable toughness (i.e., K_c for the virgin material). The time to reach K_∞ is known as the recovery time, $t_\infty(T, M, p)$, and is defined by:

$$t_\infty = C(M, p) \exp\left(\frac{Q_d}{RT}\right) \quad (5)$$

where C is the pre-exponential frequency factor; Q_d is the activation energy; and R is the universal gas constant ($8.314 \text{ J/mol} \cdot \text{K}$).

Based on Eqs. (4) and (5), one expects higher processing temperatures to produce diffusion-related increases in K_c due to the increase in time that the interface temperature is above T_g and the decrease in the recovery time at higher temperatures. Figure 5 shows this is true for increasing T_E and for increasing T_L between 255 and 270°C . The increase in K_c with annealing time/temperature and K_c 's conformance to the $t^{1/4}$ relationship (Figure 6) further support the applicability of Eqs. (4) and (5) to FD thermal-diffusion bonding process.

A transient heat transfer analysis of the FD thermal bonding process was conducted using the finite element method (Rodriguez et al., 1999a). The predicted interface temperatures, $T(t)$, were combined with C and Q_d estimates from Figure 6 to calculate the effect of different T_L and T_E combinations on the diffusion related contribution to bond strength (i.e., Eq. (4)). The diffusion contribution to K_c was consistently overpredicted, particularly as $T_L \rightarrow 285^\circ\text{C}$. Two reasons for the overprediction are suspected. First, the activation energy calculated from Figure 6 (i.e., 390 kJ/mol) is strictly valid only at the lower temperatures used in the annealing treatment. At the higher extrusion temperatures, Q_d is expected to decrease, which will (significantly) lower the integral contribution in Eq. (4) due to the exponential nature of t_∞ . The second factor is related to the degradation of ABS by molecular chain breaking, oxidation, and butadiene particle coalescence at the high temperatures used during FD extrusion (Casale et al., 1975; Kelleher, 1966). This temperature related degradation is being confirmed via comparison of the molecular weights and microstructures (i.e., the butadiene particle size distribution) of the bulk ABS with extruded FD-ABS. Introduction of inert gas atmosphere in the FD build envelope is also being considered as a means of preventing polymer oxidation damage.

Annealing produced a 38% increase in transverse strength and a 6.7% decrease in longitudinal strength consistent with increased molecular interpenetration at the interface and decreased polymer chain alignment via thermal randomization. Unfortunately, the annealing also leads to part distortion, which limits its usefulness as a strengthening method. Efforts are underway to devise an annealing schedule that minimizes distortion effects.

CONCLUSIONS

The results illustrate the two links between the mechanical behavior of FD-ABS materials and the FD process variables; namely, mesostructure and fiber-to-fiber bond strength. The strongest and stiffest unidirectional FD-ABS parts are obtained at the "optimal" parameter settings: $g = -25.4\mu\text{m}$, $\phi = 20$, $T_L = 270^\circ\text{C}$, and $T_E = 70^\circ\text{C}$. Advances in FD technology that will lead to improved mechanical performance of FD-ABS parts include: higher envelope temperatures (available on the newer Stratasys FDM models); ABS blends with a larger range of molecular chain lengths to increase the bond strength; and second-phase additions to the ABS (e.g., free and grafted nanotubes) to increase the FD-ABS fiber strength and the fiber-to-fiber interface strength.

REFERENCES

- Azzi, V. D., and Tsai, S. W., 1965, *Experimental Mechanics*, Vol. 5, pp. 283-288.
- Bertoldi, M., Yardimci, M. A., Pistor, C. M., Gucer, S. I., and Sala, G., 1998, *SFF Symposium Proc.*, Austin, TX, pp. 549-556.
- Brown, N., 1986, "Yield Behavior of Polymers", *Failure of Plastics*, Oxford, NY, pp. 98-118.
- Casale, A., Salvatore, O., and Pizzigono, G., 1975, *Polymer Engr. Sci.*, Vol. 15, pp. 286-293.
- Fodran E., Koch M., and Menon, U., 1996, *SFF Symposium Proc.*, Austin, TX, pp. 419-442.
- Fritch, L. W., 1980, PACTEC V Conference of the Society of Plastic Engineers, Los Angeles, CA, Vol. 1, Feb. 1980, pp. 184-216.
- Gray, R. W., Baird, D. G., and Bøhn, D. G., 1998, *Rapid Prototyping Journal*, Vol. 4, pp. 14-25.
- Kelleher, P. G., 1966, *J. Applied Polymer Science*, Vol. 10, pp. 843-857.
- Kulkarni, P., and Dutta, D., 1997, Paper #DAC3987, *Proc. ASME Design Engr. Conf.*, ASME, Sacramento, CA.
- Rodríguez, J. F., 1999, "Modeling the Mechanical Behavior of Fused Deposition Acrylonitrile-Butadiene-Styrene Polymer Components", Doctoral Dissertation, University of Notre Dame, Aerospace & Mechanical Engineering Department, Notre Dame, IN.
- Rodríguez, J. F., Thomas, J. P., and Renaud, J. E., 1999a, "Tailoring the Mechanical Properties of Fused-Deposition Manufactured Components", *Proc. Rapid Prototyping and Manufacturing Conf.*, SME, Dearborn, MI, pp.
- Rodríguez, J. F., Thomas, J. P., and Renaud, J. E., 1999b, "Characterization of the Mesostructure of Fused Deposition ABS Plastic Materials", *Rapid Prototyping Journal*, in review.
- Rodríguez, J. F., Thomas, J. P., and Renaud, J. E., 1997, *CAE and Intelligent Processing of Polymeric Materials*, MD-Vol. 79, ASME, NY, pp. 299-308.
- Wool, R. P., and O'Connor, K. M., 1981, *Journal of Applied Physics*, Vol. 52, pp. 5953-5963.
- Wool, R. P., Yuan, B.-L., and McGarel, O. J., 1989, *Polymer Engineering and Science*, Vol. 29, pp. 1340-1367.

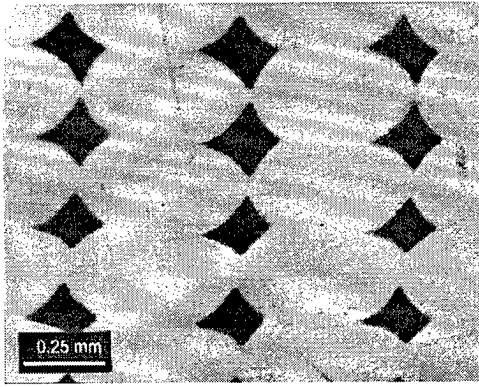


Figure 1: Mesostructure for the FD machine “default” settings: $g = 0.0\mu\text{m}$, $\phi = 20$, $T_L = 270^\circ\text{C}$, and $T_E = 70^\circ\text{C}$.

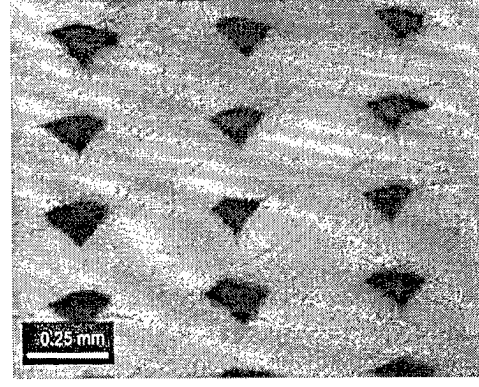


Figure 2: Mesostructure for the “optimal” FD machine settings: $g = -25.4\mu\text{m}$, $\phi = 20$, $T_L = 270^\circ\text{C}$, and $T_E = 70^\circ\text{C}$.

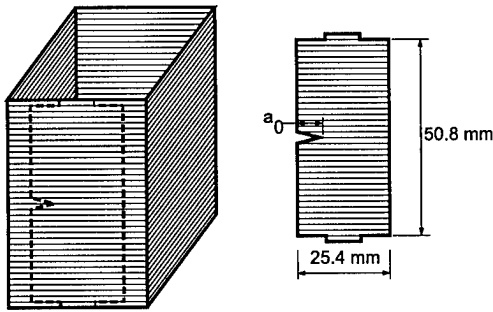


Figure 3: Fiber bond strength test specimen.

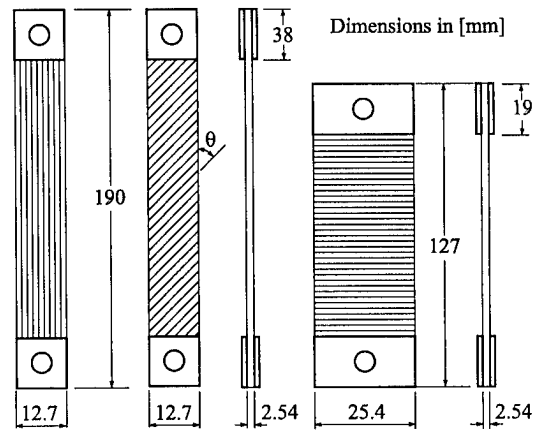


Figure 4: Tensile specimen geometries for longitudinal, off-axis, and transverse loading.

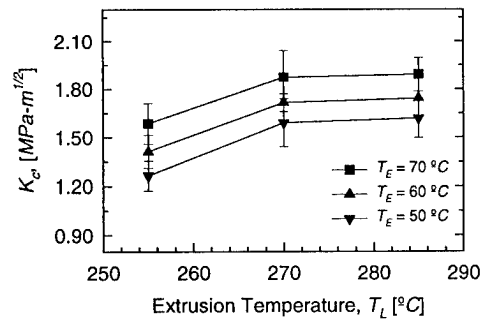


Figure 5: Fiber bond strength versus extrusion temperature for various envelope temperatures.

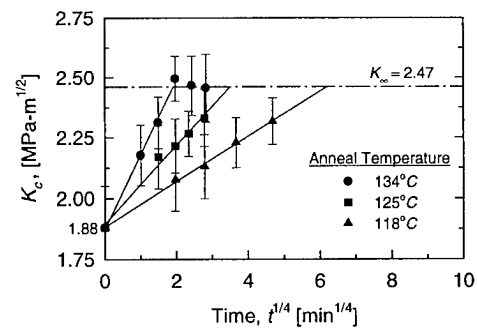


Figure 6: Fiber bond strength versus annealing time showing agreement with Equation (4).

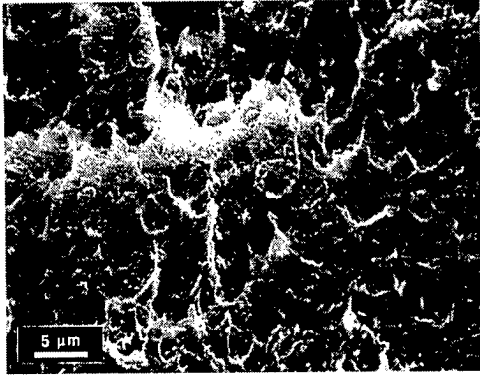


Figure 7: The fracture morphology in the stable crack growth region for a specimen built at the “optimal” machine settings, no annealing.

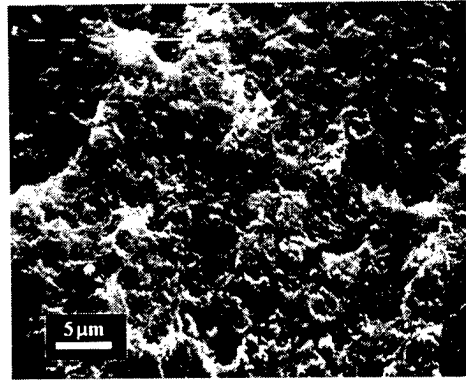


Figure 8: The fracture morphology in the stable crack growth region for a specimen built at the “optimal” machine settings and annealed at 134°C for 64 minutes.

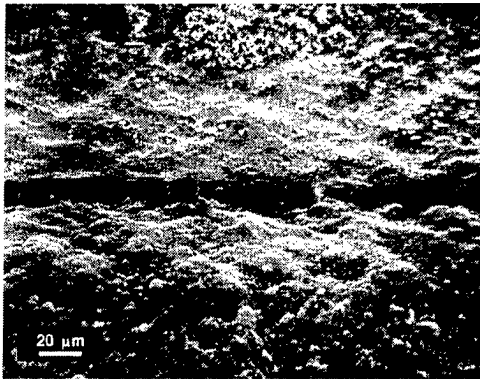


Figure 9: Interface zone between fibers showing typical void and microcrack defects.

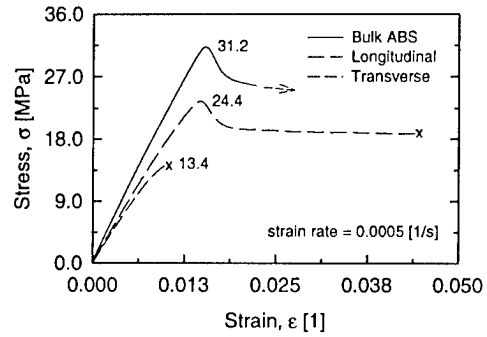


Figure 10: Stress-strain behaviors for the bulk ABS and FD-ABS built at the “optimal” FD machine settings.

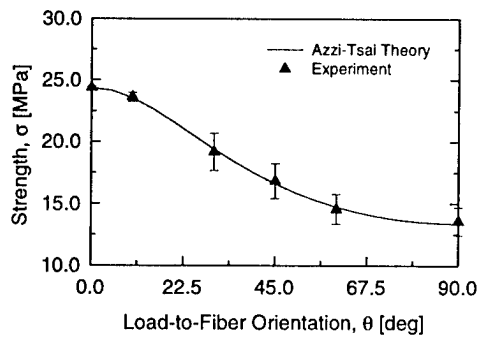


Figure 11: Experimental and predicted tensile strengths versus load-to-fiber orientation.

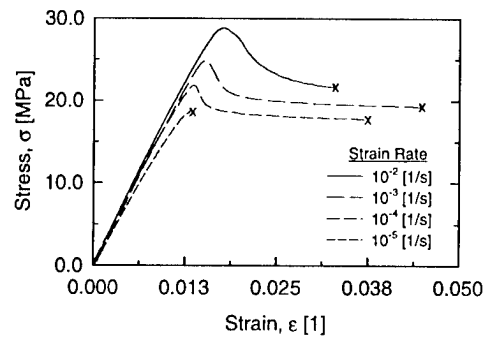


Figure 12: Influence of strain rate on the stress-strain behavior for longitudinal loading.

Thermo-mechanical Analysis of Parts Fabricated via Fused Deposition Modeling (FDM)

Manish Bharvirkar, Phong Nguyen, Christoph Pistor (Ph.D.)
University of Utah

Abstract:

The quality of Fused Deposition Modeling parts that are built using the standard parallel road approach depends significantly on the orientation of the slices. In this study the expansion coefficient, tensile strength and elastic modulus of FDM parts made from ABS were determined experimentally. The parts were built using the standard toolpath (parallel roads) with a uni-directional stacking sequence. The results were used to determine the thermo-mechanical properties for an individual slice. Classical lamination theory was applied to predict properties and stiffness matrix of parts with arbitrarily oriented stacking sequences. The results of these predictions are compared with experimental results for a quasi-isotropic stacking sequence.

Introduction:

Part Quality of FDM parts mainly relates to part strength, surface quality and dimensional accuracy. FDM parts are produced by extruding material and depositing it in layers. This result in poorer mechanical properties within a layer due to the formation of interbead interfaces and voids coupled with the inherent isotropic nature of extruded roads. Therefore, it is important to select a good orientation to achieve better strength. This paper shows how orientation, that is, the orientation of the part and orientation of roads within individual slices influences part strength. It will be also shown how various orientations affect the coefficient of thermal expansion of the part.

Thermal Expansion Experiment:

In order to identify the thermal expansion coefficients of parts built with the Fused Deposition process, three mutually orthogonal oriented specimens (see Figure 1) were made for two different stacking sequences. The xy-plane is the build plane of the machine. The stacking sequence of the roads was chosen to represent a uni-directional and a quasi-isotropic laminate [0 90 45 -45]. This resulted in a total of 20 layers for the specimen built in the xy plane and a total of 197 layers for the specimen built in the yz- and xz-plane.

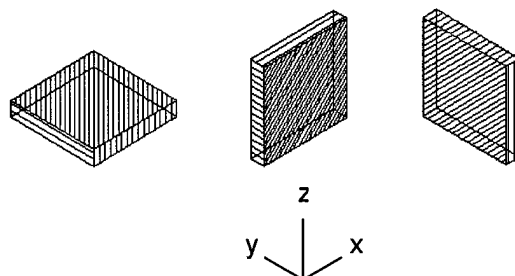


Figure 1: Sample Orientation for Thermal Expansion Measurements

These ABS parts were built using default parameters in QuickSlice 5.0. For the parts built in xy-plane, the top surface was chosen for strain-gage installation whereas no such preference was given for the remaining samples. The surfaces of the specimens were sanded to obtain a good bonding with strain gages. Standard 120 Ω strain-gages with a gage factor of 2 and M2000 Bond were used. Strain-gage installation was performed according to the gage manufacturer's specification [4].

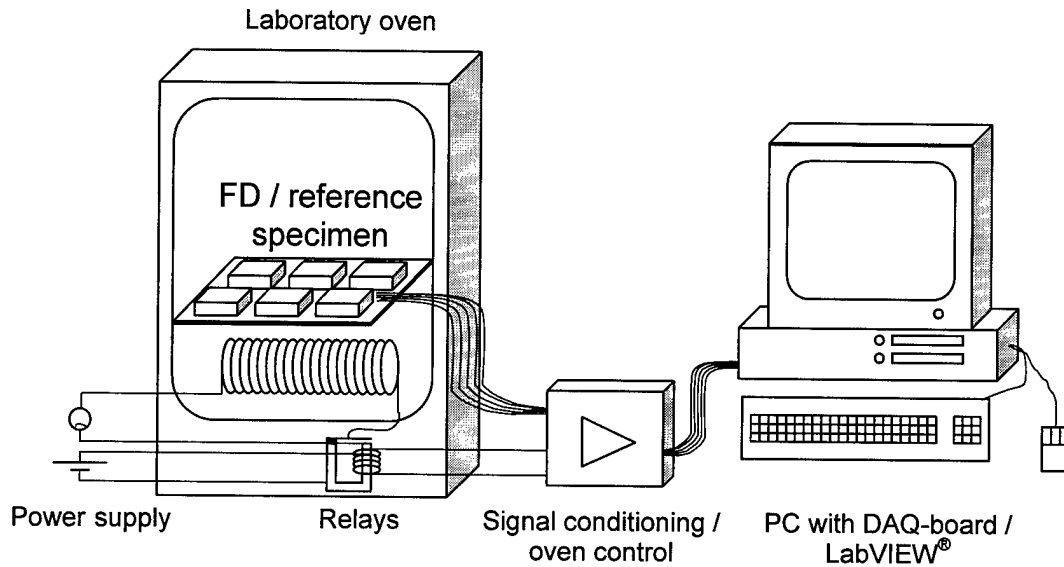


Figure 2: Experimental set-up for thermal expansion measurements

See Figure 2 for experimental set-up. It consists of a laboratory oven that is controllable with a transistor / relays arrangement connected to a digital output of the data acquisition (DAQ) board. Specific software modules for calibration were implemented in LabVIEW® and allow the temperature for the expansion measurements to follow a preset heating and cooling rate. Three Fused Deposition (FD) specimen and three glass reference specimens were placed simultaneously inside the oven with strain gages and thermocouples attached. Three half-bridge circuits (Figure 3) one for each pair of FD and glass reference specimen, were included in the signal conditioning box. The three bridge signals are then amplified using three precision signal integrated circuit amplifiers AD624 (Analog Devices, [2]). The K-type thermocouples are amplified using AD594 (Analog Devices, [1]) amplifiers that include thermocouple signal calibration and cold junction compensation.

The architecture of the half-bridge circuit, the experimental procedure, and the determination of the thermal strain are described in (Measurement Group, [4]). The circuit diagram for strain measurement is as shown in Figure 3. To account for the expansion of the gage and the adhesive, a second gage is used which is bonded to a reference material. The reference material was chosen to be Borosilicate Glass with a known expansion coefficient of 32.5×10^{-7} [m/m-K].

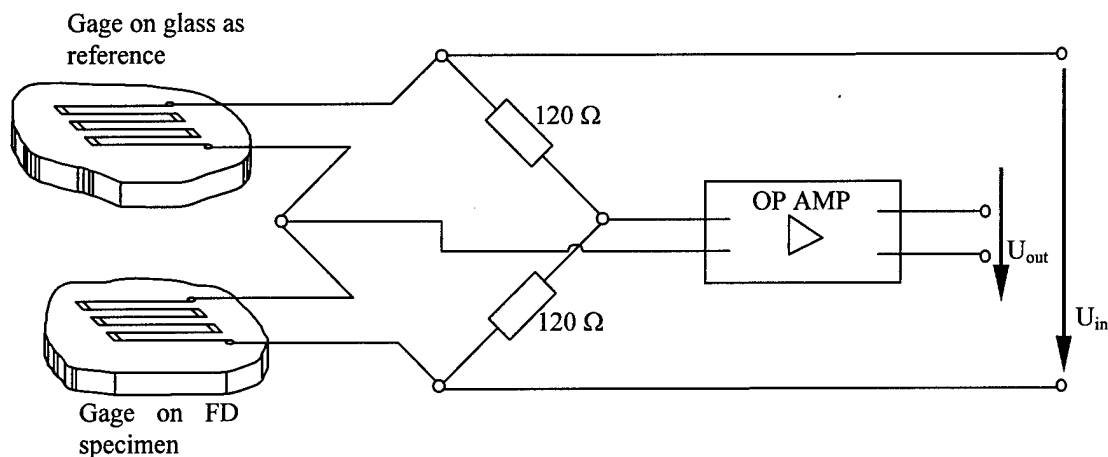


Figure 3: Half bridge circuit for strain measurements

In each experiment the specimens were placed inside the laboratory oven on a glass plate, to reduce friction during expansion. The LabVIEW[®] program controls the heating rate so that the temperature is increased linearly upto 100 °C and then decreased back to room temperature. The strains and temperatures of all FD specimens were recorded at a rate of one sample per minute. Figures 4 shows typical plots as obtained from the experiment .

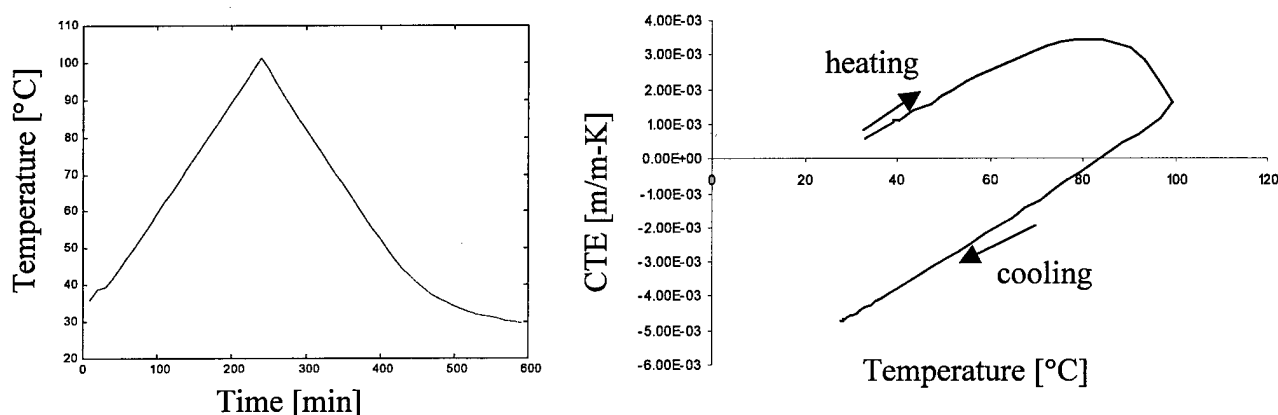


Figure 4: Temperature History (left) and Coefficient of thermal expansion (right) during Thermal Expansion Measurement

Tensile tests of uni-directional specimens:

Tensile tests were carried out on 7 specimens (designed according to ASTM D 5937-96 standard) to calculate the effective moduli of uni-directional (corresponding to continuous fiber-reinforced laminae) bars. Young's modulus was obtained from the stress-strain diagram for bars labeled 1,2 and 3 as follows:

$$E_x = \frac{\Delta\sigma_x}{\Delta\epsilon_x}$$

The longitudinal and the transverse strain are recorded using strain-gages and a data acquisition system. The Poisson ratio was obtained from data acquired by the DAQ board and is given as:

$$\nu_{xy} = - \frac{\epsilon_y}{\epsilon_x}$$

Shear Modulus was obtained from the test of bars labeled 4,5 and 6, as follows:

$$G_{ab} = \frac{E_x}{2(1+\nu_{xy})}$$

where x and y are the direction of load application and the transverse direction respectively. Also, a and b correspond to 1 and 2 for the specimen in the xy plane, 2 and 3 for the specimen in the xz plane, for and 3 and 1 for the one in yz plane.

Similar to linear and elastic composites, it is assumed that reciprocity relation holds for FDM parts. As a result the compliance matrix, and therefore the stiffness matrix, is symmetric. The complete stiffness matrix is given as follows:

$$[S] = \begin{bmatrix} \frac{(1-\nu_{23}\nu_{32})E_1}{1-\nu} & \frac{(\nu_{21}+\nu_{31}\nu_{23})E_1}{1-\nu} & \frac{(\nu_{31}+\nu_{21}\nu_{32})E_1}{1-\nu} & 0 & 0 & 0 \\ & \frac{(1-\nu_{13}\nu_{31})E_2}{1-\nu} & \frac{(\nu_{32}+\nu_{12}\nu_{31})E_2}{1-\nu} & 0 & 0 & 0 \\ & & \frac{(1-\nu_{12}\nu_{21})E_3}{1-\nu} & 0 & 0 & 0 \\ & \text{sym.} & & G_{23} & 0 & 0 \\ & & & & G_{13} & 0 \\ & & & & & G_{12} \end{bmatrix}$$

where $\nu = \nu_{12}\nu_{21} + \nu_{23}\nu_{32} + \nu_{31}\nu_{13} + 2\nu_{21}\nu_{32}\nu_{13}$

The experimental testing has been conducted on an INSTRON (series IX) machine with machine parameters as follows:

Sample rate (pts/sec) : 20.00

Crosshead Speed (mm/min): 0.300

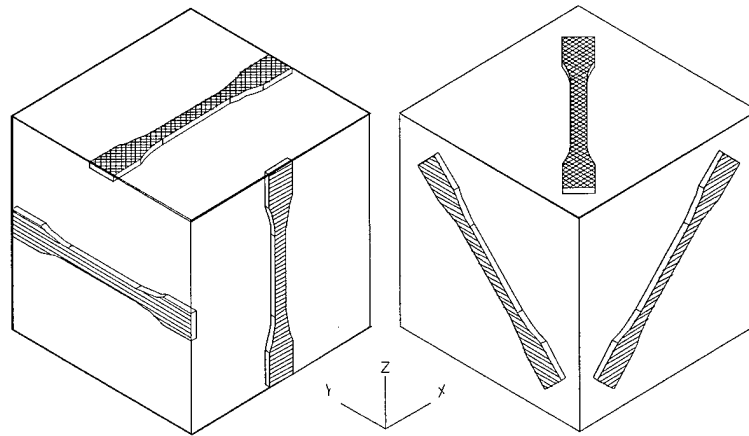


Figure 5: Tensile test specimen's orientation.

Figure 5 above shows orientation of tensile bars. The properties of these parts were found to be dependent mostly on the bar's orientation as compared to bar's individual layer lay-up and is evident from Table 1.

Bar No.	Build Plane	Orientation	Uni-directional Specimens [0°]		Quasi-Isotropic Specimens [0/90/45/-45]	
			Avg. tensile strength, MPa*	Avg. elastic modulus, MPa*	Avg. tensile strength, MPa**	Avg. elastic modulus, MPa**
1	xy	x	***	***	11.7	1072.90
2	yz	y	6.554	371.40	15.987	1652.523
3	xz	z	6.459	352.57	7.608	1391.448
4	xy	x+45	1.945	189.57	10.808	970.944
5	yz	y+45	5.605	295.1	13.465	1519.115
6	xz	z+45	6.231	300.83	14.702	1527.60

Table 1: Tensile tests results, Quasi-isotropic results from [3]

(*) Tests were performed at 0.3 mm/s crosshead speed

(**) Tests were performed at 5 mm/s crosshead speed

(***) Bar no. 1 was very weak and broke while loading it in the machine

As seen from Table 1, for the bars 2 and 3, average properties are high for yz-build plane both for uni-directional and quasi-isotropic specimens. This shows that parts with relatively shorter traverse length (corresponding to fiber length) have higher value for elastic modulus and tensile strength. This maybe because with longer traverse length, the likelihood of failure-inducing surface cracks increases. It must be noted here that loads applied were transverse to the roads for the two bars. A bar built in xz plane and oriented and tested along x-axis showed better tensile strength than bar 3. For the bars oriented at 45° to the axis, average elastic modulus is high for xz-build plane both for uni-directional and quasi-isotropic specimens. This shows that build direction strongly affects the part's strength irrespective of the stacking sequence. But the quasi bars are stronger than uni-directional bars as the total volume of voids in a particular

direction decreases because of the cross ply arrangement. The significant difference in values can be attributed to high difference in tensile testing speed of both the sets of bars.

Results:

Results of thermal expansion experiments are presented in table 2 and table 3.

	α_{xy} [m/m-K]	α_{yz} [m/m-K]	α_{xz} [m/m-K]
Experiment 1 : heating	7.636E-05	7.561E-05	7.021E-05
cooling	8.939E-05	9.726E-05	9.621E-05
Experiment 2 : heating	9.181E-05	9.246E-05	8.871E-05
cooling	9.732E-05	9.795E-05	9.687E-05
Experiment 3 : heating	9.326E-05	9.440E-05	9.233E-05
cooling	9.693E-05	9.720E-05	9.648E-05

Table 2: Expansion coefficients for Quasi-Isotropic plates

	α_{xy} [m/m-K]	α_{yz} [m/m-K]	α_{xz} [m/m-K]
Experiment 1 : heating	5.872E-05	3.570E-05	6.984E-05
cooling	7.843E-05	5.249E-05	8.335E-05
Experiment 2 : heating	7.368E-05	5.181E-05	7.698E-05
cooling	7.836E-05	5.289E-05	8.326E-05
Experiment 3 : heating	7.873E-05	5.529E-05	8.260E-05
cooling	7.864E-05	5.251E-05	8.368E-05

Table 3: Expansion coefficients for Uni-directional plates

It can be observed that the values of the Coefficient of Thermal Expansion (CTE) for the cooling portion of the experiments are higher than the heating values for both plates. CTE values for quasi plates are almost similar in all the three directions showing uniform expansion. CTE values for quasi plates are higher than those for uni directional plates, showing that there is more interfacial contact because of the cross-ply arrangement. The general trend shows that for uni-directional bars, yz orientation has lowest and xz orientation has highest CTE values. This is assumed to be related to the larger interface between rods normal to the build plane as compared to a smaller interfacial contact area in the build plane.

Experimental verification of laminate theory for FDM bars was done by comparing measured deformations with those predicted from the laminate theory. Alternatively, the compliances can be compared, an approach used in [7]. The measured normal strains on the upper surface ($z = -t/2$) are related to midplane strains and curvatures by

$$\begin{aligned}\epsilon_x(u) &= \epsilon_x(0) - (t/2)\kappa_x \\ \epsilon_y(u) &= \epsilon_y(0) - (t/2)\kappa_y\end{aligned}$$

For a uniaxial loading test of such a strain-gaged specimen, compliances can be determined as follows

$$A'_{11} = \frac{\epsilon_x(0)}{N_x} \quad A'_{12} = \frac{\epsilon_y(0)}{N_x} \quad \text{and so on.}$$

Results were as follows,

$A'_{11} = 4.6469\text{E-}01$ 1/MPa-m as predicted by laminate theory, while
 $A'_{11} = 4.4880\text{E-}01$ 1/MPa-m as measured by strain gage and equal to $\epsilon_x(0)/N_x$.

Using E_{11} , E_{22} , E_{33} , ν_{12} , ν_{13} , ν_{23} , G_{12} , G_{23} , G_{13} as determined experimentally for Uni-directional bar, stiffness matrix was calculated using laminate theory with two ply sequences, viz. $[0]_{20}$ and $[0/90/45/-45]_{20}$.

For $[0]_{20}$ laminate, stiffness matrix was found to be,

$$[S] = \begin{bmatrix} 0.4024 & 0.22694 & 0.22696 & 0.0000 & 0.0000 & 0.0000 \\ 0.22694 & 0.63790 & 0.39376 & 0.0000 & 0.0000 & 0.0000 \\ 0.22696 & 0.39376 & 0.60557 & 0.0000 & 0.0000 & 0.0000 \\ 0.0000 & 0.0000 & 0.0000 & 0.1189 & 0.0000 & 0.0000 \\ 0.0000 & 0.0000 & 0.0000 & 0.0000 & 0.2190 & 0.0000 \\ 0.0000 & 0.0000 & 0.0000 & 0.0000 & 0.0000 & 0.0799 \end{bmatrix} \text{ GPa}$$

For $[0/90/45/-45]_{20}$ laminate, stiffness matrix was found to be,

$$[S] = \begin{bmatrix} 0.4809 & 0.26615 & 0.31036 & 0.0000 & 0.0000 & 0.0000 \\ 0.26615 & 0.48053 & 0.31000 & 0.0000 & 0.0000 & 0.0000 \\ 0.31036 & 0.3100 & 0.60534 & 0.0000 & 0.0000 & 0.0000 \\ 0.0000 & 0.0000 & 0.0000 & 0.1518 & 0.0000 & 0.0000 \\ 0.0000 & 0.0000 & 0.0000 & 0.0000 & 0.1518 & 0.0000 \\ 0.0000 & 0.0000 & 0.0000 & 0.0000 & 0.0000 & 0.1070 \end{bmatrix} \text{ GPa}$$

As E_{11} value of the uni-directional bar was less than E_{22} value, we see that S_{11} term for quasi plate is higher than S_{11} term of 0° plate. It can be also seen from the fact that S_{22} term is higher than S_{11} term of 0° plate.

As compared to the stiffness matrix determined by laminate theory for quasi-isotropic lay-up (using the properties from the tensile test of uni-directional bars), the actual stiffness matrix of quasi laminate (using the properties from the tensile tests of quasi bars) was found to be (as given in [3]),

$$[S] = \begin{bmatrix} 1.8530 & 1.4348 & 1.1810 & 0.0000 & 0.0000 & 0.0000 \\ 1.4348 & 3.0843 & 1.6444 & 0.0000 & 0.0000 & 0.0000 \\ 1.1810 & 1.6444 & 2.4141 & 0.0000 & 0.0000 & 0.0000 \\ 0.0000 & 0.0000 & 0.0000 & 0.5540 & 0.0000 & 0.0000 \\ 0.0000 & 0.0000 & 0.0000 & 0.0000 & 0.5405 & 0.0000 \\ 0.0000 & 0.0000 & 0.0000 & 0.0000 & 0.0000 & 0.3696 \end{bmatrix} \text{ GPa}$$

It can be seen that although there is significant difference in values, both matrices show almost similar behavior among their 44, 55 and 66 terms. G_{12} value for quasi bar is higher than that of the uni-directional bar showing that roads with $\pm 45^\circ$ orientation will be most effective in carrying shear loads.

The difference in values can be accounted to the low modulus values of uni-directional bars. Two reasons can be given for the high difference in stiffness values of the two sets of bars: first, strain gages were used with a different data acquisition method and second, the tensile tests were carried out at a lower testing speed than those for quasi isotropic bars.

Conclusion:

It is obvious that better mechanical properties could be achieved from any FDM part by selecting a particular build orientation depending on the direction of load application in service and part geometry. The results of the experimental work conducted will provide a useful guideline to the user before building a FDM part.

The current low strength values of the parts can be improved by developing better toolpaths. This along with previous work done on surface finish (which is shown to depend on layer thickness and also orientation) will provide a useful tool in building an overall very good quality FDM part.

References:

- [1]. Analog Devices, "AD594/AD595 Monolithic Thermocouple Amplifiers with Cold Junction Compensation", Technical Note, 1997.
- [2]. Analog Devices, "AD624, Precision Instrumentation Amplifier", Technical Note, 1996.
- [3]. M. Bertoldi, M. A. Yardimci, C. Pistor, S. I. Güçeri, "Mechanical Characterization of Parts Processed via Fused Deposition", Proceedings of the 1998 Solid Freeform Fabrication Symposium, Austin, TX, 1998.
- [4]. Measurements Group, "Measurement of Thermal Expansion Coefficient", Measurements Group Tech Note TN-513-1, 1994.
- [5]. TA Instruments, "Modulated DSC® (MDSC®): How Does It Work?" <http://www.tainst.com/media/mdsc.pdf>, 1999.
- [6]. Yardimci, M.A., "Process Analysis and Planning for Fused Deposition", Ph.D. Thesis, Department of Mechanical Engineering, University of Illinois at Chicago, 1999.
- [7]. Tsai, S.W., "Structural Behavior of Composite Materials", NASA CR-71 1964.

Mechanical and Rheological Properties of Feedstock Material for Fused Deposition of Ceramics and Metals (FDC and FDMet) and their Relationship to Process Performance

N. Venkataraman, S. Rangarajan, M.J. Matthewson, A. Safari and S.C. Danforth, Rutgers University.

A. Yardimci*, S.I. Guceri, University of Illinois at Chicago.

* Advanced Engineering Design Center, Baxter International, Round lake, Illinois, USA

Abstract

Fused deposition of ceramics (FDC) is a solid freeform fabrication technique based on extrusion of a highly loaded thermoplastic binder system. The present FDC process uses filament feedstock of $1.780 \text{ mm} \pm 0.025 \text{ mm}$ diameter. The filament acts as both the piston driving the extrusion process as well as the molten feedstock being deposited. The filaments need to be able to provide and sustain the pressure needed to drive the extrusion process. Failure to do this results in failure via "buckling". The filament compressive modulus determines the ability of the filament to provide and sustain the required pressure to drive the extrusion. The viscosity of the feedstock material, nozzle geometry and volumetric flow rates employed determine the pressure needed to drive the extrusion process. In this work the extrusion pressure for a particular material termed PZT ECG9 (52.6 Vol.% PZT powder in ECG9 binder) was measured experimentally as a function of volumetric flow rate and nozzle geometry. The compressive modulus of the material was determined using a miniature materials tester (Rheometrics, Inc., Piscataway, NJ). A process map has been developed. The map is based on the quantity $\Delta P/E$, and predicts the performance of the material in a FDC process as a function of nozzle geometry and volumetric flow rate. In general, it is observed that when $\Delta P/E$ exceeds a critical value, called $\Delta P_{cr}/E$, there is an increased tendency for the filament to buckle. A preliminary fluid flow model for extrusion of PZT ECG9 through a FDC nozzle has also been developed using PolyflowTM software. The model predicts the observed trend in pressure drop with flow rate and nozzle geometry with reasonable accuracy.

Introduction

Fused deposition of ceramics and metals (FDC and FDMet) is a solid freeform fabrication process based on extrusion of highly loaded thermoplastic binder system. The present fused deposition technique uses filament feedstock of $1.78 \text{ mm} \pm 0.025 \text{ mm}$ diameter. A schematic of the fused deposition process is shown in Figure 1. The filament acts as both the piston driving the extrusion process, as well as the molten material being deposited through a nozzle of a particular orifice diameter onto a Z stage platform in the X-Y plane (Figure 1).

The extrusion of a highly particle loaded molten thermoplastic binder system through a nozzle of a given geometry requires the application of a certain amount of pressure. The actual value of the extrusion pressure required depends on: the viscosity of the material, the nozzle geometry, and the volumetric flow rate of the extrusion process. The viscosity of the material will depend on the binder chemistry, solids loading, state of agglomeration, shear rate and temperature.

In the case of the fused deposition process, the extrusion pressure is applied by the filament feedstock. If the required extrusion pressure exceeds a certain critical value, then

buckling of the filament ensues (shown schematically in Figure 1). The critical stress value is given according to Euler's criterion as [1, 2]:

$$\sigma_{cr} = \frac{\pi^2 E}{4(L/R)^2} \quad (1)$$

where: σ_{cr} is the critical buckling stress, E is the compressive elastic modulus of the filament,

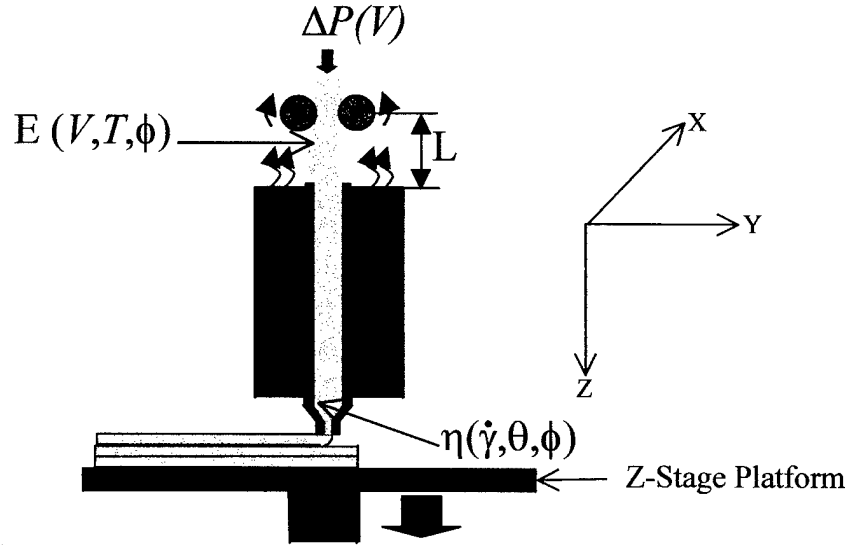


Figure 1: Schematic of the FDC liquefier showing the important process and material parameters involved in buckling (V : volumetric feed rate, T , θ : temperature, ϕ : solids loading, $\dot{\gamma}$: shear rate, η : viscosity of feedstock, E : compressive stiffness of filament)

L/R is the aspect ratio of the filament above the liquefier as shown in Figure 1. If ΔP (Figure 1) is the required extrusion pressure for a given nozzle geometry, volumetric flow rate, solids loading and temperature, then the condition for buckling can be represented as [3-4]:

$$1.1\Delta P \geq \sigma_{cr} \quad (2)$$

The correction factor 1.1 in equation 2 is due to difference in the cross section area between the filament and the liquefier barrel (the barrel diameter is larger than the filament diameter). One sees from Equation 2 that the minimum extrusion pressure needed for buckling of filaments is $\sigma_{cr}/1.1$. For sake of clarity we call this minimum extrusion pressure needed for buckling as ΔP_{cr} to differentiate from ΔP which represents any other value of extrusion pressure. One also sees from Equation 2 that $1.1 \Delta P_{cr} = \sigma_{cr}$, and therefore, applying this condition to equation 1 we find that the quantity $\Delta P_{cr}/E$ is dependent only on the ratio of the length of the filament above the liquefier to the filament radius. This is, therefore, a value characteristic of the particular fused deposition machine design. The quantity $\Delta P/E$ depends on the material used, the temperature of

operation, the nozzle geometry and the volumetric flow rate of deposition process. From equation 2 one sees that buckling occurs if $1.1 \Delta P > \sigma_{cr}$, i.e. if $\Delta P/E > \Delta P_{cr}/E$.

Experimental Procedure

The material used in this study is termed PZT ECG9. It consists of lead zirconate titanate powder (PZT Powder) dispersed in a thermoplastic binder termed ECG9. The details of the binder composition and development have been presented elsewhere [5]. The ceramic powder was obtained from TRS, Inc., State College, PA. The median particle size of the PZT powder was $1.2 \mu\text{m}$. The specific surface area of the powder, as determined by single point BET method, was $1.1 \text{ m}^2/\text{g}$. The density, as determined using helium pycnometry, was 7.83 g/cm^3 .

The powder was first coated with the dispersant by mixing PZT with a 3 wt% solution of

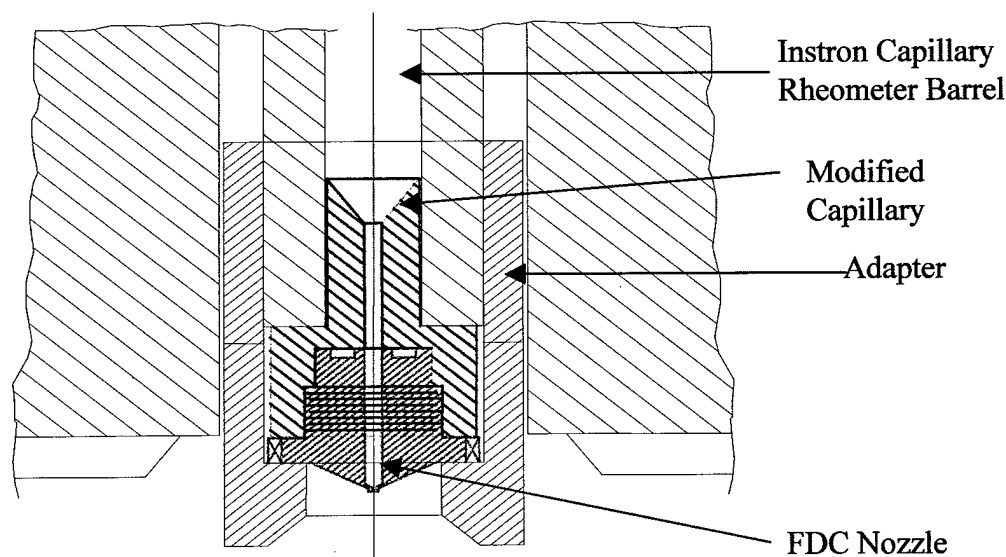


Figure 2: Schematic of modification to capillary rheometer for measurement of pressure drop across FDC nozzles.

stearic acid in toluene in a NalgeneTM bottle for four hours in a ball mill [6]. ZrO_2 media (3/8 inch, cylindrical) was used to avoid contamination of the PZT powder. The slurry obtained at the end of the mixing step was then vacuum filtered to obtain a powder cake which was then dried for 12 hours. The correct proportions of coated powder and binder were compounded at 140°C in a torque rheometer (Haake) to obtain a 52.6 vol.% ceramic-polymer mix. The compounded mix was cooled and then granulated. The granules were stored in a dessicator (25% RH) prior to extrusion. The granules were then fed via a hopper into a single screw extruder (Haake). The pressure and temperature in three zones of the screw extruder were monitored and controlled. A 120 mesh screen and breaker plate arrangement was used to remove agglomerates and also to obtain homogeneous mixing during screw extrusion. A 1.78mm extrusion diameter nozzle was used. The extruded filaments were picked up by a conveyor belt whose speed was matched to the extrusion speed to control the diameter of the filament to $1.780 \pm 0.025 \text{ mm}$. The filaments were then spooled and stored in a controlled humidity until further use.

The compressive mechanical properties of the filaments of PZT ECG9 were determined using a miniature materials tester (Rheometrics, Inc., Piscataway, NJ). The details of the mechanical testing and modulus determination procedure are described elsewhere [7].

The pressure associated with the extrusion of PZT ECG9 through a FD nozzle was measured using a modified Instron capillary rheometer. The details of the measurement technique are described elsewhere [8]. The modification consisted of an adapter custom fabricated to hold a FDC nozzle. The adapter was fabricated in such a manner as to be able to fit into the Instron capillary rheometer barrel. A schematic of the modified adapter is shown in Figure 2. The barrel was heated along with the nozzle to 140°C (the FDC temperature for PZT ECG9) following which the barrel was filled with PZT ECG9. A precision-machined piston attached to the load cell was lowered from the top end of the barrel. The barrel was then moved at a controlled displacement rate onto the piston following which the material was extruded through the FDC nozzle attached at the bottom. The load corresponding to a particular velocity and nozzle geometry was recorded. The corresponding extrusion pressure was calculated from the recorded load as a function of the volumetric flow rate and nozzle geometry. In this study the volumetric flow rates were chosen to coincide with the typical flow rates associated with the FDC process. The pressure was measured as a function of the nozzle diameter and the aspect ratio of the nozzle. The Instron capillary rheometer was also used to determine the true rheological behavior of PZT ECG9. A simple finite element model using Polyflow™ was also developed to study the physics of flow of PZT ECG9 through FDC nozzle.

Results and Discussion

The compressive modulus of PZT ECG9 as a function of displacement rate at room temperature (25°C) is presented in Table I.

Table I: Compressive Modulus of PZT ECG9 (25°C, 50% RH) as a Function of Displacement Rate

Modulus (MPa)	Displacement Rate (mm/min)
58 ± 8	0.1
80 ± 11	1
101 ± 23	10
134 ± 17	20

The data indicate a statistically significant increase in compressive modulus with displacement rate. The details of the compressive mechanical behavior of PZT ECG9 as a function of temperature and storage time have been described elsewhere [7]. As mentioned before, for a fixed geometry, the filament critical buckling stress is directly proportional to the compressive elastic modulus. In this work, the compressive modulus corresponding to the lowest displacement rate (0.1 mm/min) was chosen as a conservative estimate. The true rheological (true wall shear stress vs. true wall shear rate) behavior of PZT ECG9 as determined by the

capillary instron rheometer is shown in Figure 3. The Herschel-Buckley type equation was determined to be the best fit. The constitutive equation for a Herschel-Buckley fluid is[9,10]:

$$\tau = \tau_y + K\dot{\gamma}^n \quad (3)$$

The best fit parameters for PZT ECG9 which were used in subsequent finite element modeling are given in Table II.

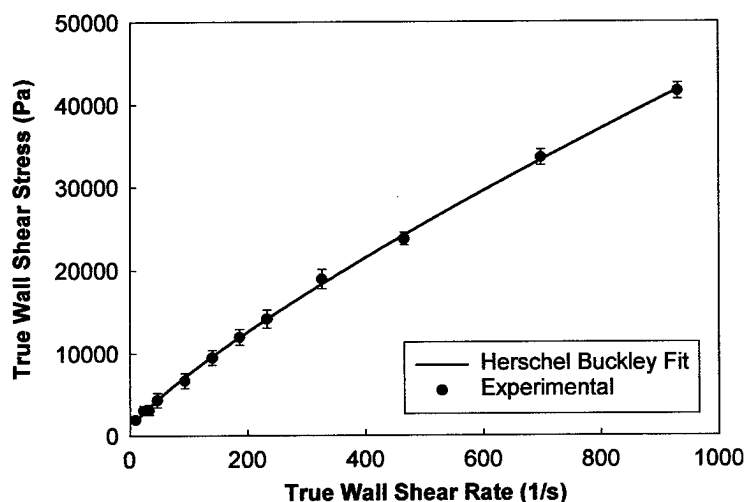


Figure 3: The true rheological behavior of PZT ECG9 at 140°C as measured using a capillary rheometer.

A schematic of the domain used in finite element model is shown in Figure 4. The domain represents the modified capillary Instron rheometer used for measurement of extrusion pressure of PZT ECG9 through the FDC nozzle. A commercial computational fluid dynamic software (Polyflow™) was used for solving the model under the following boundary conditions: isothermal, axisymmetric, no slip at walls and a fully developed flow at the inlet. The predicted pressure drop values for PZT ECG9, as calculated using Polyflow™, are shown in Figure 5

Table II: Best Fit Parameters to Herschel-Buckley Equation for PZT ECG9 at 140°C

Parameter	Value
τ_y	716 ± 290 Pa
K	165 ± 21 Pa.s ⁿ
n	0.8 ± 0.02

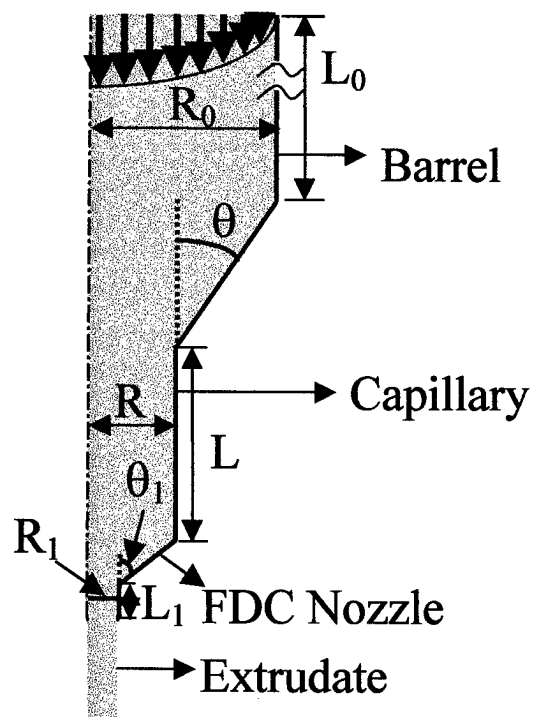


Figure 4: Schematic of domain used in finite element modeling. The values of the various parameters are: L_0 : 50 mm, R_0 : 4.7625 mm, L : 35.2 mm, R : 0.965 mm, θ : 33.5 °, R_1 : 0.127 mm, L_1/R_1 : 2, 4, 10, θ_1 : 59°.

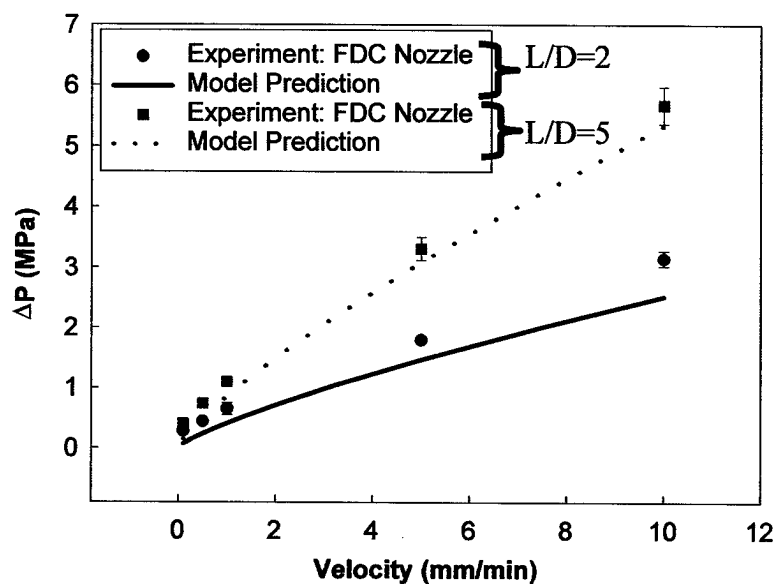


Figure 5: Experimental (symbols) and predicted (lines) pressure drop values as a function of average velocity at the inlet for flow of 52.5 Vol.% PZT in ECG9 binder in the modified capillary rheometer.

along with the experimentally determined values. One can see from Figure 5 that the finite element model accurately predicts the trend in the experimentally determined ΔP values. The model tends to underestimate the magnitude of the pressure drop values (by $\sim 30\%$). The lack of exact agreement between the experimental value and predicted value could be because the model does not accommodate for non-idealities such as end effects, non-isothermal effects and viscoelasticity of the material. The nozzle used in the measurement of the pressure drop values is not heated and therefore, the experimental pressure values are expected to be higher than the model predictions. The model also predicts that greater than 90% of the pressure drop occurs at the nozzle, and less than 10% in the barrel and modified capillary, implying that the major contribution to the measured pressure drop is from the FDC nozzle. The pressure drop for PZT ECG9 as a function of nozzle diameter and aspect ratio were measured for various volumetric flow rates. The quantity $\Delta P/E$ was calculated for the various nozzle diameters and aspect ratios as a function of volumetric flow rates. The measured pressure drop values and compressive modulus (at room temperature corresponding to 0.1 mm/min displacement rate) were used to

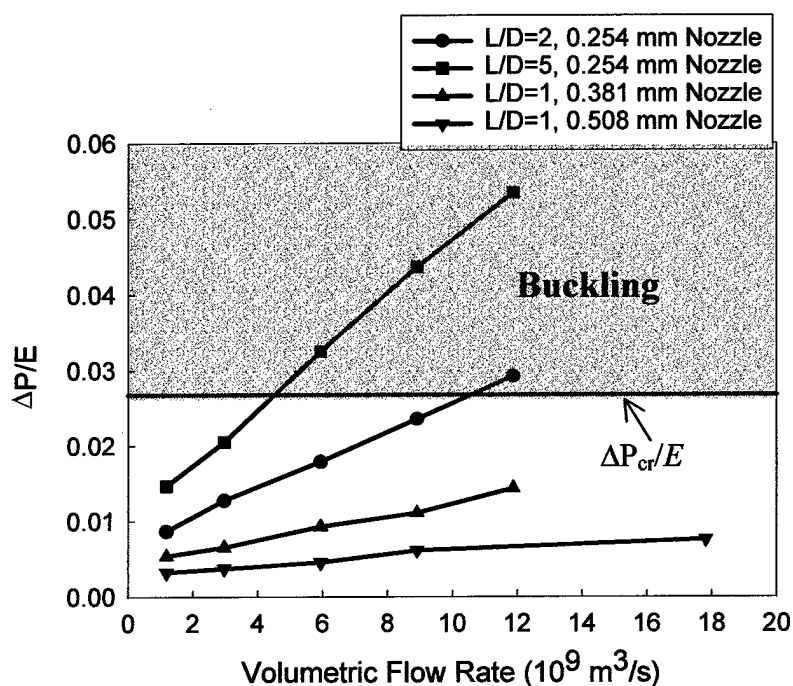


Figure 6: Process map for PZT ECG9 showing the variation of the dimensionless quantity $\Delta P/E$ (measured at 140°C) with FDC nozzle diameter, aspect ratio and volumetric flow rate.

develop a process map. A plot of $\Delta P/E$ as a function of volumetric flow rates (the process map) is shown in Figure 6. A line corresponding to $\Delta P_{cr}/E$ is also plotted on the process map. According to the theory, if $\Delta P/E$ exceeds $\Delta P_{cr}/E$ buckling should occur in the FDC process. This condition is shown in the process map as the shaded region above the $\Delta P_{cr}/E$ line. The process map predicts that with increasing volumetric flow rates, the tendency to buckle in FDC increases, as has been confirmed via independent tests. A series of independent testing have also established that PZT ECG9 does not buckle even at very high volumetric flow rates in FDC for

the 0.508 mm diameter nozzle. This is confirmed by the fact that the line corresponding to the 0.508 mm diameter nozzle for PZT ECG9 lies below the critical limit, for even up to very high flow rates. The PZT ECG9 used with a 0.254 mm diameter nozzle in FDC was found to buckle at lower volumetric flow rates than the 0.508 mm diameter nozzle. This is qualitatively confirmed by the observation that in Figure 6 the line corresponding to the 0.254 mm diameter nozzle crosses the critical line at a lower volumetric flow rate. The volumetric flow rate at which PZT ECG9 buckled with a 0.254 mm diameter nozzle is $2-3 \times 10^{-9} \text{ m}^3/\text{s}$, which is about $1/5^{\text{th}}$ the predicted value.

In the actual process, there is a temperature gradient in the filament above the liquefier. This will result in an elastic modulus gradient in the filament above the liquefier. There is also a rate dependence of the elastic modulus. The theory used in the development of the current process map does not include these effects and also it does not include possible effects of agglomeration on the elastic modulus or pressure drop. Therefore the process map in its current state gives only a good qualitative indication of the effects of nozzle geometry and volumetric flow rate on the performance of PZT ECG9 in the FDC process.

Summary and Conclusions

In this work the pressure needed for extrusion through a FDC nozzle for a particular material termed PZT ECG9 was measured experimentally as a function of volumetric flow rate and nozzle geometry. The pressure drop was found to increase with nozzle aspect ratio and volumetric flow rates, as expected. The pressure drop also increases with a decrease in nozzle diameter. The compressive modulus of the PZT ECG9 filament material was determined using a miniature materials tester (Rheometrics, Inc., Piscataway, NJ). A process map has been developed. The process map is based on the quantity $\Delta P/E$ (extrusion pressure/compressive modulus) that predicts the performance of the material in the FDC process as a function of nozzle geometry and volumetric flow rate. In general, it is observed that when $\Delta P/E$ exceeds a critical value, $\Delta P_{cr}/E$ there is an increased tendency to buckle. The predictions of the process map have been confirmed qualitatively via independent tests. It should be noted that $\Delta P_{cr}/E$ depends only on the ratio of the filament length above the liquefier to the radius of the filament. A preliminary fluid flow model for extrusion of PZT ECG9 through FDC nozzle has also been developed using PolyflowTM software. The model predicts the observed trend in pressure drop with flow rate and nozzle geometry with reasonable accuracy. The model also predicts that greater than 90% of pressure drop occurs in the FDC nozzle implying that a change in nozzle geometry will affect the pressure drop and therefore the tendency to buckle in a significant manner.

Acknowledgements

This work was sponsored by the Office of Naval Research under ONR MURI contract number N00014-96-1-1175. The authors also acknowledge the significant assistance provided by Thomas McNulty, Farhad Mohammadi, Eric Passman, Rhea Jaico, Brian Harper, Gouhua Wu and Ewan Bossett in this work. The miniature materials tester was obtained with financial support of Allied Signal under DARPA/ONR contract # N00014-94-C-0115.

References

1. F.P. Beer, and E.R. Johnston, "Mechanics of Materials", 2nd ed., McGraw-Hill Co., London, (1992).
2. S.P. Timoshenko and J.M. Gere, "Theory of Elastic Stability", Second Edition, McGraw-Hill Book Company, London, (1961).
3. "Feedstock Material Property-Process Relationships in Fused Deposition of Ceramics (FDC)", N. Venkataraman, S. Rangarajan, M.J. Matthewson, B. Harper, A. Safari, S.C. Danforth, G.Wu, N. Langrana, Submitted to Journal of Rapid Prototyping, July, 1999.
4. "Powder Processing, Rheology and Mechanical Properties of Feedstock for Fused Deposition of Silicon Nitride Ceramics", S. Rangarajan, G. Qi, N. Venkataraman, A. Safari, S.C. Danforth, Submitted to Journal of American Ceramic Society, February, 1999.
5. T. McNulty, F. Mohammadi, A. Bandyopadhyay, D.J. Shanefield, S.C. Danforth, and A. Safari, "Development of a Binder Formulation for Fused Deposition of Ceramics", Rapid Prototyping Journal, Vol. 4 No. 4, (1998), pp. 144-150.
6. T. McNulty, D.J. Shanefield, S.C. Danforth and A. Safari, "Dispersion of Lead Zirconate Titanate for Fused Deposition of Ceramics", Journal of the American Ceramic Society, Accepted for Publication, (1999).
7. N. Venkataraman, T. McNulty, S. Rangarajan, M. Vidaic, M.J. Matthewson, N. Langrana, A. Safari and S.C. Danforth, "Mechanical Properties Of Feedstock Material For Fused Deposition Of Ceramics", Proceedings of SFF Symposium, MRS Meeting, Vol. 542, (1999), pp. 111-117.
8. P. Holmstrom, "FDC Nozzle and Extrusion", M.S. Thesis, Rutgers University, November (1998).
9. J.R. van Vazer, "Viscosity and Flow Measurement; A Laboratory Handbook of Rheology", Interscience Publishers, New York, (1963).
10. H.A. Barnes, J.F. Hutton, and K. Walters, "An Introduction to Rheology", Elsevier, Amsterdam, Netherlands, (1996).

Novel Ceramics and Metal-Ceramic Composites via Fused Deposition Process

Amit Bandyopadhyay, Raj Atisivan and Susmita Bose
School of Mechanical and Materials Engineering
Washington State University
Pullman, WA 99164-2920

Abstract

Indirect fused deposition process is utilized to fabricate controlled porosity ceramic structures using alumina, mullite, zirconia, LSCF-perovskite, tricalcium phosphate and hydroxyapatite, where pore size, pore shape and pore connectivity are varied from one end to the other end of the parts. Some of these porous ceramics are then infiltrated with metals via pressureless reactive metal infiltration to form novel metal-ceramic composites. This paper will describe processing, structures of various porous and metal-infiltrated composites and their physical and mechanical properties.

Introduction

Ceramic materials possess high strength, high corrosion and oxidation resistance, excellent high temperature properties, but are brittle. The lack of toughness in ceramic materials due to their strong ionic and/or covalent bonding limits their use in numerous structural applications. Development of ceramic based composites work was started to overcome this inherent problem by incorporating ductile phases or using unidirectional ceramic fibers or ceramic cloth into another ceramics. As various novel composite materials with higher toughness were developed, several processing techniques were also invented to fabricate these materials.

In this work, novel 3D honeycomb porous ceramic structures were fabricated using indirect fused deposition (FD) process. For the past three decades, various processing techniques have been utilized to fabricate porous ceramic materials [1-4]. Unfortunately, all of these processes form structures with randomly arranged pores having a wide variety of sizes and with limited flexibility to control pore volumes and porosity distribution in the final structure. Using indirect FD, controlled porosity structures were fabricated where pore size, pore volume and porosity distributions were precisely controlled [5-6]. Different materials were used to process these structures for various applications. Porous alumina and mullite ceramics were fabricated to form interpenetrating phase metal-ceramic composites. Porous hydroxyapatite (HAp), tricalcium phosphate (TCP) and alumina structures were fabricated for bone graft application. Porous LSCF ceramics were fabricated for catalytic membrane applications and porous PZT structures for transducer and actuators. All of these structures were fabricated with uniform or functionally gradient porosity where the volume fraction porosity varies from one end of the structures to the other end. **Figure 1a, b and c** show some of the porous structures having uniform and gradient porosity.

Pressureless reactive and non-reactive metal infiltration processes were used to infiltrate the porous alumina and mullite ceramic preforms to fabricate metal-ceramic composites with a

controlled shape as well as microstructure. Reactive synthesis of composites offers the advantages of net-shape structure processing with the control of the final microstructure. Several researchers have proposed the use of molten aluminum and either silica glass or aluminosilicate ceramics to obtain alumina/metal composites by reactive penetration [7-9]. Reactions between liquid metal and ceramic oxides may be of the type $4M + 3SiO_2 = 2M_2O_3 + 3Si$, where M is a trivalent metal and the thermodynamic criterion being that at the processing conditions, the Gibbs free energy of the reaction is negative [10]. For both dense and porous ceramic substrates, reactive infiltration to take place it is necessary to reach a critical temperature. Once the infiltration starts, it is faster with higher porosity and smaller particle size. This paper describes processing and mechanical characterization of alumina-aluminum and mullite-aluminum composites.

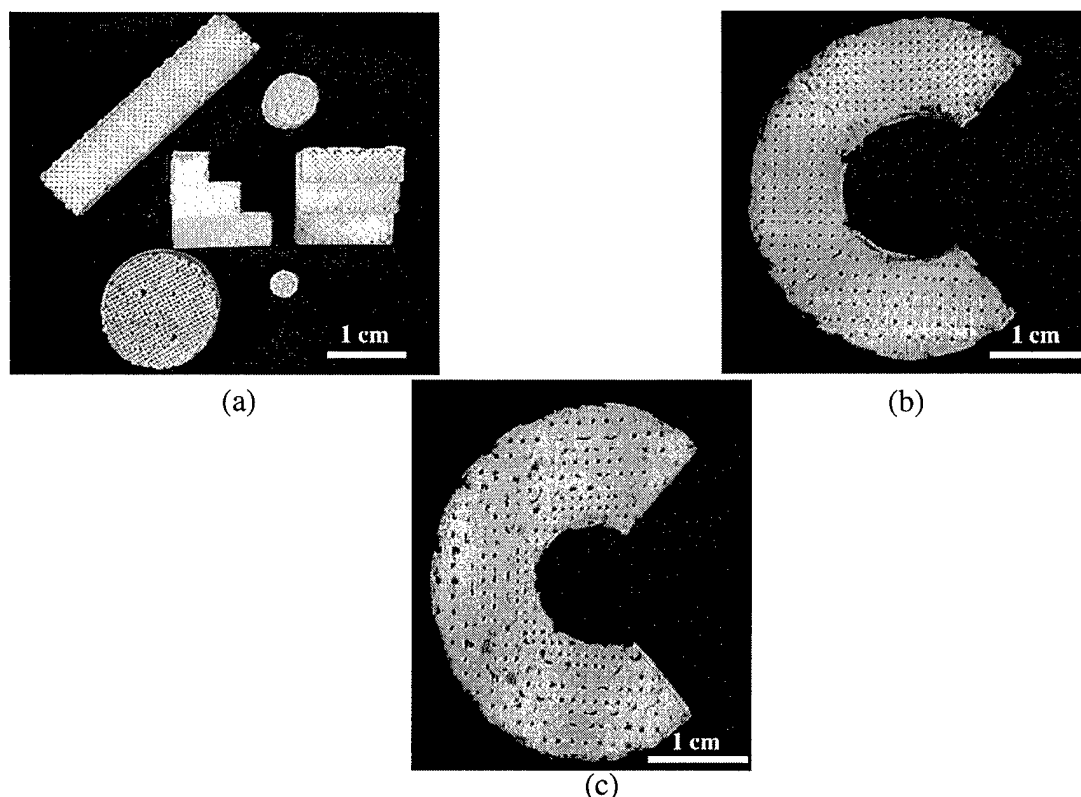
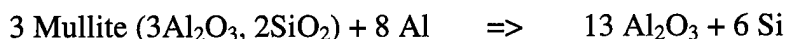


Figure 1: Porous 3D honeycomb structures processed via indirect FD process. (a) Structures having various shapes with uniform porosity; (b) structure with a gradient porosity microstructure from one end to the other and (c) structure with a gradient porosity microstructure from center to the outside of the C-ring (porosity gradient in radial direction).

Processing

Indirect FD process was used to fabricate porous ceramic structures. In this process, FDM 1650 was used to make polymeric molds having the negative of the desired structure and then was infiltrated with water based ceramic slurry. Infiltrated structures were dried for three to four days and then subjected to a binder removal and sintering cycle using a high temperature muffle furnace in furnace air environment. Structures with various pore size, pore volumes and porosity gradients were fabricated using this process.

Alumina and mullite porous ceramic preforms were then infiltrated with Al metal. In case of reactive metal infiltration, the process has two steps: infiltration and reaction. The infiltration and reaction steps can be independent of each other or can take place simultaneously. For the case of mullite-Al composites, it is expected that mullite will react with Al and form an alumina-aluminum composite via a displacement reaction given by:



Aluminum metal was infiltrated into porous preforms at 850°C temperature or higher. Porous ceramic preforms were dipped into the crucible of molten Al alloy at 750°C and furnace temperature was raised to a temperature at 850°C or higher. At that temperature, low viscosity molten Al metal filled the porous ceramic network and formed 3-3 mullite-Al composite, where both mullite and Al were connected to themselves in all three directions. Once the metal infiltration was over, the assembly was cooled to 700°C and the composite was taken out of the crucible. As the composite was taken out of the molten Al alloy, the shape of the porous ceramic became the shape of the composite. As the shape of the porous ceramic preform can be controlled by RP, this process has the flexibility to fabricate near-net-shape part with controlled microstructures.

For mullite-Al composites, it was found the complete infiltration can be achieved by going up to 850°C, but there was no reaction between mullite and Al. **Figure 2a** shows the x-ray diffraction patterns for mullite ceramic preform and composites infiltrated at 900, 950 and 1000°C. It can be observed that there was no reaction between mullite and Al, and the structure forms a mullite-Al composite. **Figure 2b** shows similar x-ray diffraction patterns for composites processed at 1050, 1100 and 1150°C and compared with mullite ceramic preform. It can be observed that the reaction between Al and mullite starts around 1050°C and completes by 1150°C and it forms α -alumina-Al metal-ceramic composite.

counts/s

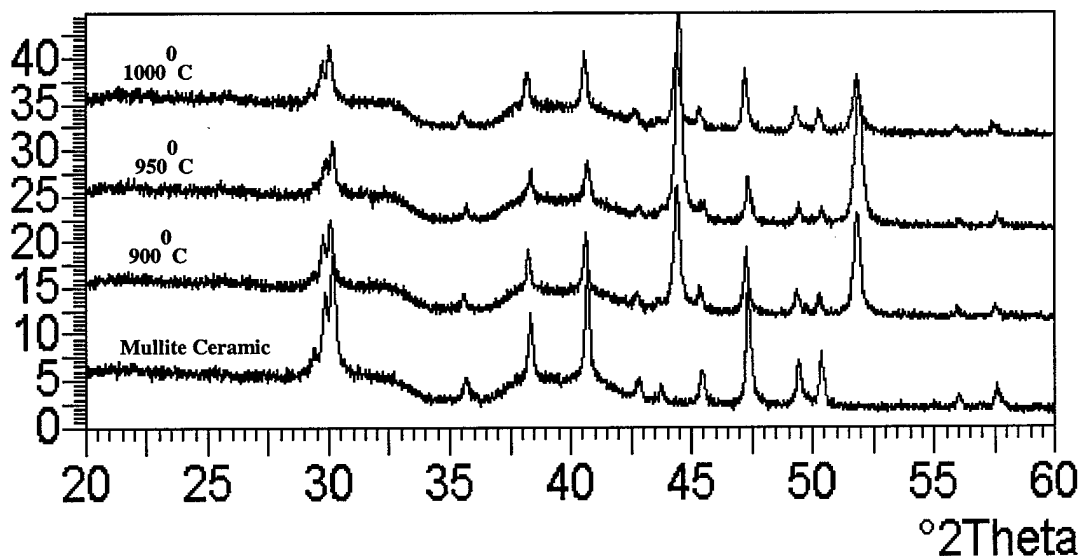


Figure 2a: X-ray diffraction patterns for porous mullite ceramic and Al infiltrated composites. Al metal was infiltrated at 900, 950 and 1000°C for one hour to form the composite.

In the case of pressureless non-reactive metal infiltration process, there is no reaction step, but only the infiltration of molten metal is involved. Low temperature Al metal infiltration of mullite ceramic preforms can serve as an example of non-reactive metal infiltration process. In this work, porous alumina ceramic preforms were infiltrated with molten Al and Cu metals to form Al-alumina and Cu-alumina composites. This process involves only infiltration of molten metal, but no reaction between Al and Cu with alumina. **Figure 3a and b** show the porous alumina preforms and a Cu infiltrated microstructure.

counts/s

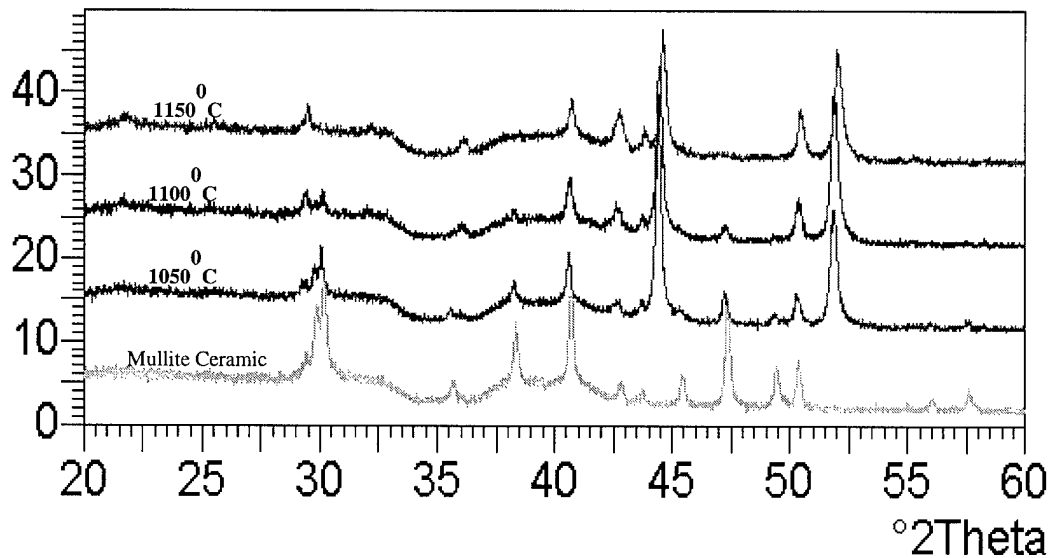
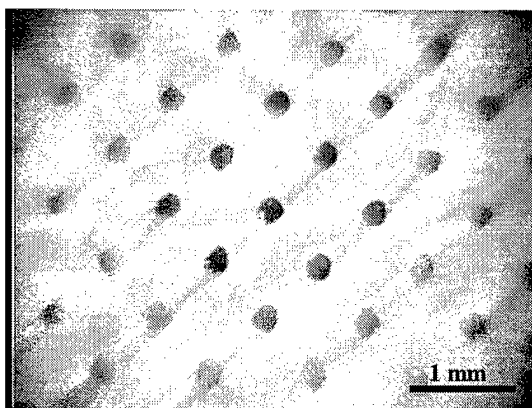
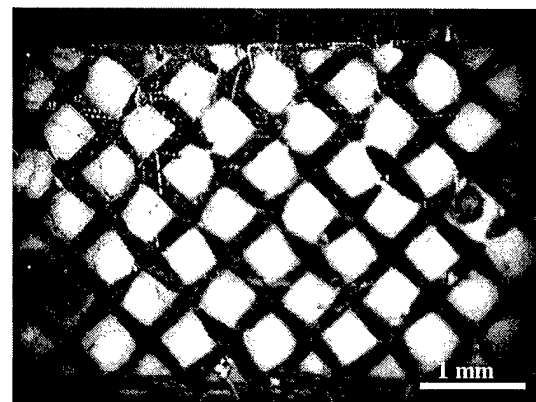


Figure 2b: X-ray diffraction patterns for porous mullite ceramic and Al infiltrated composites. Al metal was infiltrated at 1050, 1100 and 1150°C for one hour to form the composite.



(a)



(b)

Figure 3: (a) Top view of porous alumina ceramic preform and (b) top view of the Cu infiltrated alumina ceramic composites.

Results and Discussion

Composites via non-reactive infiltration process: Al-alumina and Cu-alumina composites that were processed via non-reactive metal infiltration process were all cracked during polishing or cutting operation. The cracking were observed in ceramics as can be seen in Figure 4. The coefficient of thermal expansion (CTE) mismatch between metal and ceramic were high and resulted high tensile residual stress in ceramic during cooling from the processing temperature. The inherent high residual stress caused cracking in alumina ceramic during any further operation with these composites.

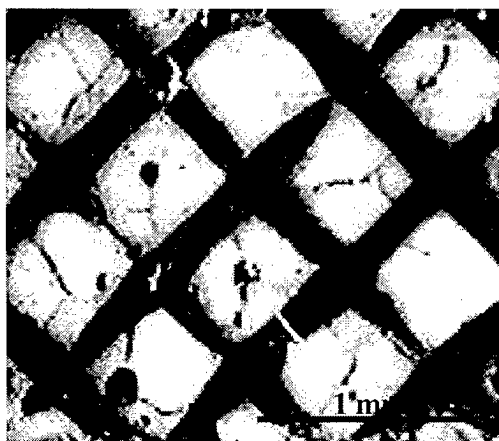
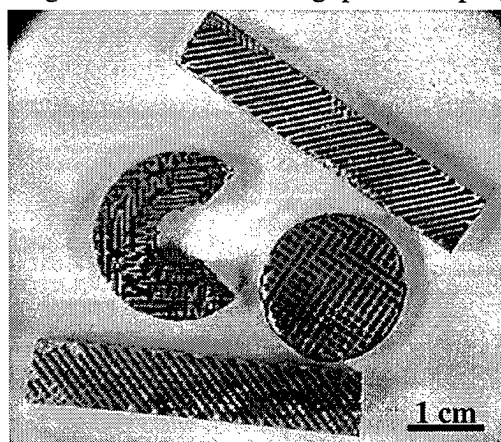
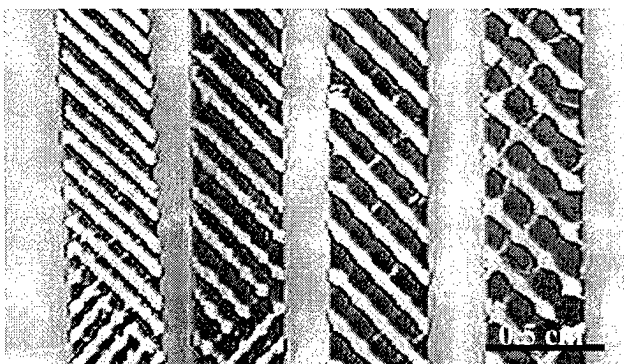


Figure 4: Alumina-Cu metal-ceramic composites showed extensive cracking during post processing in ceramics due to high residual stress.

Composites via reactive infiltration process: Mullite-Al composites were processed via reactive metal infiltration process. Porous ceramic preforms of mullite having different volume fractions of porosity were infiltrated with Al metals to form composites with different amounts of metal in it. Figure 5a shows various shapes of composites processed with mullite ceramic preforms and Figure 5b shows increasing volume fraction metals in these composites by reducing the metal-to-metal gap but keeping the width of the metal constant.



(a)



(b)

Figure 5: (a) Various mullite-Al composites processed via Al metal infiltration of porous mullite ceramic preforms. (b) Mullite-Al composites having different amount of metals.

Optical microstructures of the infiltrated composites show complete metal infiltration of the ceramic preforms. Figure 6 shows an optical micrograph of the infiltrated mullite-Al composite. Higher magnification microstructures revealed that even the micropores due to incomplete sintering was also filled with Al metal during infiltration. Microhardness measurements on the polished surfaces of the composites were made using a Vicker's indenter as a function of processing temperature. Hardness of the metal remain same for all the cases, while for ceramics, it increased from 1200 VHN to 1550 VHN due to phase transformation of mullite to α -alumina. These composite samples did not show any cracking and could be machined with regular machine tools.

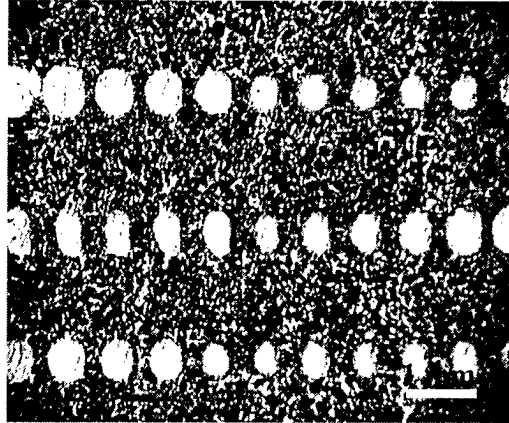


Figure 6: Low magnification optical micrograph shows the complete infiltration of pores in mullite ceramic preform by Al metal (bright areas are Al metal).

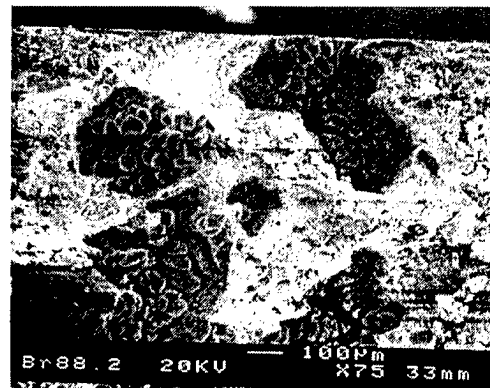
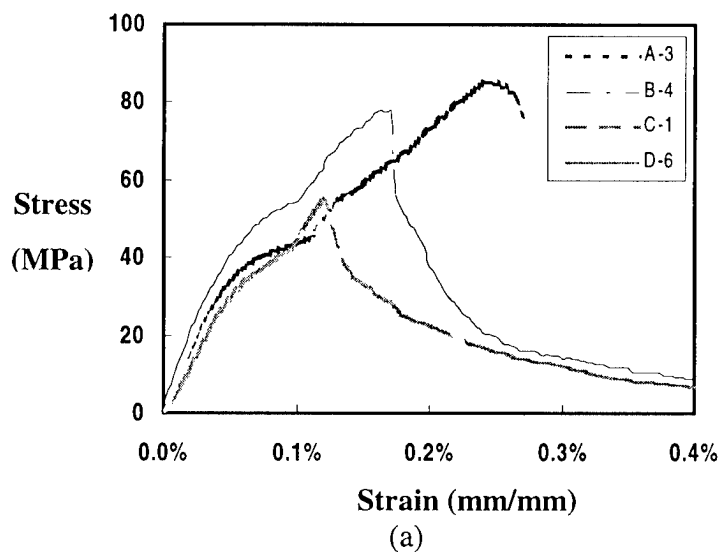


Figure 7: (a) Stress-strain curves for mullite-Al metal ceramic composites with different volume fractions of metals. (b) Low magnification fracture surface showing different types of failure for metals and ceramics.

Volume %	43%	33%	27%	24%
Strength	Metal	Metal	Metal	Metal
MOR (MPa)	87	78	50	52
Bending Modulus (GPa)	63	67	71	75

Table I: Mechanical properties of mullite-Al composites.

Four point bend flexural tests were conducted with four different types of mullite-Al composites having metal contents varied from 24% to 43% using an Instron load frame. Tests were conducted under stroke control using a 0.1mm/minute stroke rate. Flexural strengths and bending modulus are shown in Table I. It can be seen that as the metal content decreased, the bending modulus and strength increased. Increasing bending modulus can be explained due to increase in ceramic content in the composite. Figure 7a shows stress-strain curves for these composites where A means 43% metal sample and D means 24% metal. All four curves show two stages of failures and initial failure of the samples took place at ~0.1% strain. Reported bending modulus numbers were the initial modulus values. After the initial failure, there was change in modulus in the composites. Composites with higher metal contents sustained a higher load to final failure than composites with lower metal contents. The data suggests that higher metal content composites are more damage tolerant. Figure 7b shows a low magnification fracture surface of a 43% metal content sample. It can be seen that the ceramics and metal surfaces show two different types fracture surfaces. While ceramics showed a typical flat brittle failure feature with micropores, metal surfaces show ductile dimples. There was no metal pullout in all the fracture surfaces suggesting that the bonding between metals and ceramics were strong. Other samples showed a similar failure behavior.

Conclusions

Novel 3D honeycomb porous ceramic structures were fabricated using indirect FD process with various materials for applications in structural, bio-medical and piezoelectric areas. Among them, alumina and mullite ceramic preforms were used to form metal-ceramic composites having controlled macro and microstructures. Reactive and non-reactive metal infiltration processes were used to infiltrate molten Al and Cu metals to form the composites. Though composites formed via non-reactive infiltration with alumina ceramic preforms showed extensive cracking due to CTE mismatch, but composites formed with mullite ceramics did not show similar trends. Composites formed with mullite ceramic preforms showed that metal infiltration can be performed as low as 850°C, but reaction between mullite and Al starts around 1050°C and forms an α -alumina-Al composite. Four point bend flexural strengths of mullite-Al composites as a function of volume fraction metal present showed that bending modulus increases as metal content decreases and flexural strength increases as metal content increases. Fracture surfaces of the composite reveal two completely different types of fracture behavior.

Ceramic surface showed brittle flat fracture surface while the metal surface showed ductile dimples. The process allows for processing of composites with tailored microstructure along with physical and mechanical properties.

Acknowledgments

The authors would like to acknowledge the financial support from the Office of Naval Research under grant number N-00014-98-1-0550. The authors would also like to acknowledge the experimental help of Ashwin Hattiangadi, Gabe Khun, Lance Curtis and Raji Soundararajan.

References

1. E. W. White, J. N. Webber, D. M. Roy, E. L. Owen, R. T. Chiroff and R. A. White, *J. Biomed. Mater. Res. Symp.*, **6**, (1975) 23-7.
2. S.F. Hulbert, S.J. Morrison and J. J. Klawitter, *J. Biomed. Mater. Res. Symp.*, **6**, (1975) 347-74.
3. C. P. A. T. Klein, and P. Patka, *Handbook of Bioactive Ceramics II: Calcium Phosphate and Hydroxylapatite Ceramics*, edited by T. Yamamura, L. L. Hench and J. Wilson, CRC Press, Boca Raton, FL, (1990) 53-60.
4. T. Shrout, T., W. A. Schulze, and J. V. Biggers, *Mat. Res. Bull.* **14**, (1979) 1553-1559.
5. S. Bose, S. Suguira and A. Bandyopadhyay, "Processing of Controlled Porosity Ceramic Structures via Fused Deposition," *Scripta Materialia*, Accepted for Publication, June 1999.
6. A. Hattiangadi and A. Bandyopadhyay, "Processing, Characterization and Modeling of Non-Random Porous Ceramic Structures"; in *Solid Freeform Fabrication Symposium Proceedings*, Edited by H. L. Marcus, J. J. Beamen, J. W. Barlow, D. L. Bourell, and R. H. Crawford. University of Texas at Austin, (1999).
7. R. E. Loehman, K. Ewsuk and A. P. Tomsia, "Synthesis of Al_2O_3 -Al Composites by Reactive Metal Penetration," *Journal of the American Ceramic Society*, **79** [1] 27-32 (1996).
8. M. C. Breslin, J. Ringnalda, L. Xu, M. Fuller, J. Seeger, G. S. Daehn and H. L. Fraser, "Processing, Microstructure and Properties of Co-continuous Alumina/Aluminum Composites," *Material Science and Engineering*, **A195**, 113-19 (1995).
9. S. Matsuo and T. Inabe, "Fabrication of Al- Al_2O_3 Composites by Substitutional Reaction in Fused Aluminum," *Tokyo Ceramics*, 222-23 (1991).
10. M. Hanabe and P. B. Aswath, "Synthesis of In-Situ Reinforce Al Composites from Al-Si-Mg-O Precursors," *Acta Materialia*, 1-9 (1997).

PROCESS VARIABLE EFFECTS ON LASER DEPOSITED Ti-6Al-4V

C. A. Brice*, K. I. Schwendner*, D. W. Mahaffey*, E. H. Moore†, and H. L. Fraser*

*Department of Materials Science and Engineering, The Ohio State University, Columbus, OH 43210

†AFRL/MLLM Wright-Patterson Air Force Base, OH 45433

Abstract

An initial study of the processing parameters affecting deposition quality of Ti-6Al-4V was conducted using the LENS™ direct laser deposition system. The significant number of process variables presents a problem in determining relative effects. A few of the easily identifiable variables were isolated and the deposits were characterized qualitatively by comparison of layer adhesion, porosity, and dimensional accuracy. These characteristics were compared for each deposit while processing variables such as laser power, travel speed, and hatch spacing were varied. The results led to the development of a set of optimum processing conditions that produce a quality deposit.

Introduction

Direct laser manufacturing technology has developed rapidly in the recent past [1-4]. Though it has been shown to be a potentially useful manufacturing technique, there are aspects of the process that remain to be fully understood. Various systems exist with different heat sources, fixturing, and materials delivery. Although the setup of each system is unique, there exist certain process variables that are common to all. These process variables need to be interrelated to determine the optimum conditions needed to achieve a successful deposit. By studying these process interactions, a "recipe" can eventually be determined that will yield a fully dense, near-net shape part in the shortest time possible, thus making laser direct fabrication feasible in large scale manufacturing. The purpose of the present study is to develop a basic understanding of how these process parameters interrelate and also will lay the groundwork for future, more comprehensive studies.

Experimental Procedure

The experiment was planned so that appropriate data could be analyzed by statistical methods. This was done using MINITAB statistical analysis software. The following six process variables, or factors, were chosen for this analysis: travel speed, laser power, stand-off distance, hatch width, layer thickness and powder flowrate. These factors and their ranges were selected based on previous experience and process knowledge. For each factor two levels, high and low, were selected, a common strategy in a screening analysis. The optimum performance is assumed to be within these levels. The factors and their different levels are shown in Table 1.

The method of design chosen for the experiment was a 2^k factorial design, where k is the number of factors. With six factors the experiment has $2^6 = 64$ combinations (runs) to obtain a full factorial

Variables	Low	Zero	High
Laser Power (W)	300	350	400
Travel Speed (in/min)	10	15	20
Powder Flowrate (g/min)	1.30	1.95	2.60
Hatch Spacing (in)	0.010	0.015	0.020
Layer Thickness (in)	0.010	0.015	0.020
Stand-off Distance (in)	6.000	5.980	5.960

Table 1: Process variables and experimental low, zero, and high values.

design with full resolution. Performing 16 runs, 2^{6-2} factorial offers a $\frac{1}{4}$ factorial design with a resolution IV, which is sufficient for a screening design of experiments [5]. Two replicates were taken, which is important for significance testing and to obtain an error, for a total of 32 experiments. Three center points, median values between high and low, were included bringing the total number of runs to 35. These center points give additional information about the array of factors spanned. Since the sequence of experiments was randomized, every experiment was re-setup and rerun, involving complete rebuilding of the experimental trial from ground up. After designing the experiment as described above, the program created a randomized data matrix. This matrix outlines the level (high or low) for all six factors of each run. The order of the runs was randomized to account for the unknown influence between factors.

The 35 samples were deposited on four separate 0.040" thick pieces of Ti-6Al-4V sheet. Consecutive samples were placed on different substrates to minimize heat buildup. There was, however, considerable warping of the substrates due to unavoidable thermal stresses. The heat source was a 750 watt Nd:YAG laser delivered via fixed optics. Calibration of the laser power was done by pulsing the laser for a set time and reading the absorbed power on a calorimeter. 300 watts is approximately the minimum heat input needed to yield a fully remelted deposit, thus it was chosen as the lower limit and 400 watts was chosen as the high limit. The stand-off distance was determined based on the six inch focal length of the lens. Previous work had shown that working slightly overfocused produced desirable results. Thus, the low value was made to be 0.040" overfocus and the high value at sharp focus. The geometry of the deposits was 1 cm by 1 cm square by 10 layers high. Each layer alternated travel direction by 90°.

Figure 1 shows the buildup geometry of the deposits. The hatch width was calculated based on a hatch overlap of about 60%. Thus, with an approximate laser spot size of 0.050", the optimum spacing is 0.015" between each pass. This was assigned the zero value and high and low values were assigned at ± 0.005 ". Layer height values were determined by the maximum

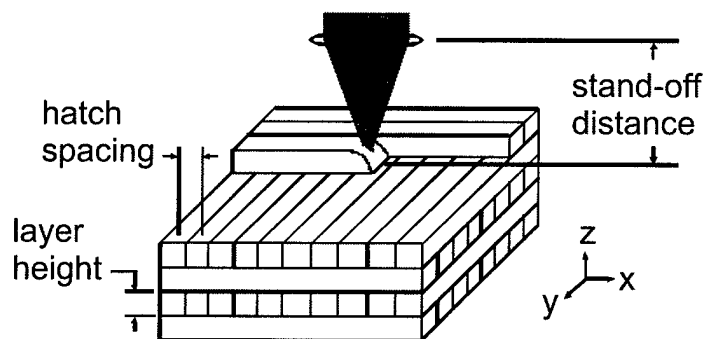


Figure 1: Schematic of test sample showing geometrically dependent process variables.

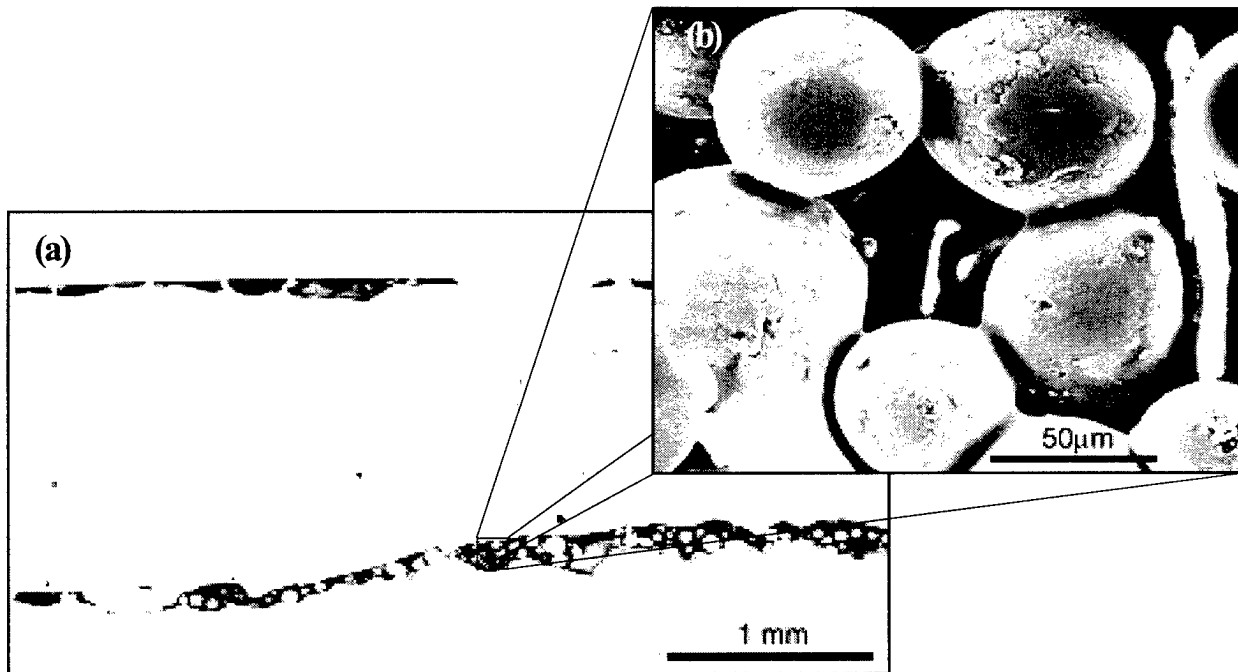


Figure 2: (a) Scanning electron micrographs of a sample showing large amounts of porosity between layers, (b) close-up of porous area showing unmelted powder.

height that could be built up by a single laser pass. Based on this, the upper limit was set at 0.020" and the lower bound was set at half this value, 0.010". Powder mass flowrate values were assigned arbitrarily since no prior calibration had been done. To calibrate the flowrate, the powder delivery motor speed was adjusted and powder was collected from the nozzles for a given time. The powder was then weighed and an approximate flowrate was assigned to each value on the motor speed dial. Travel speed values were assigned based on previous work showing that 20 inches per minute was the maximum speed that produced an acceptable deposit.

Two response variables were selected for this screening analysis; the final build height and the density. Since the expected build height varied from sample to sample (10 layers at 0.010", 0.015" or

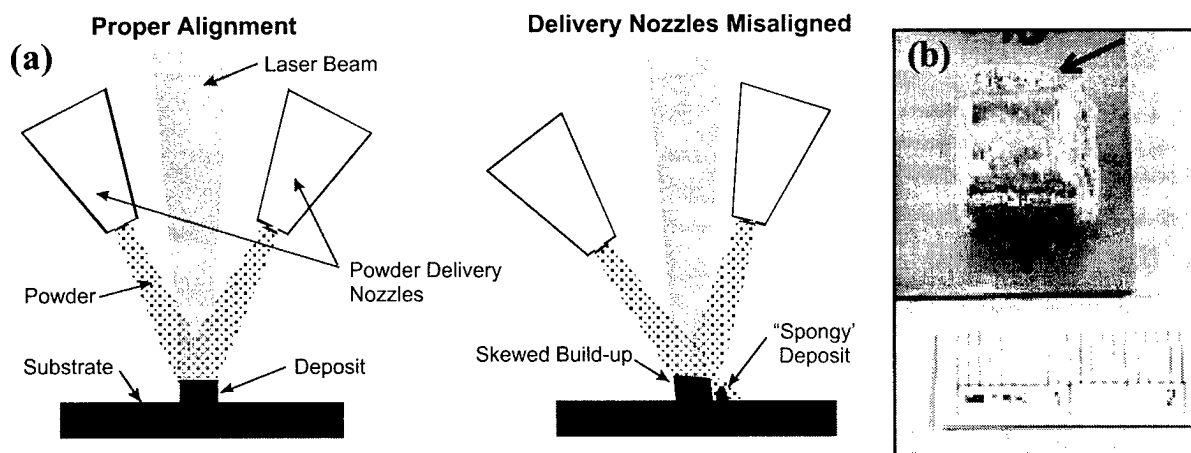


Figure 3: (a) Schematic showing how nozzle mis-alignment can affect the quality of the deposit (b) Photo of a sample showing "spongy" deposit on side of cube.

0.020" per layer) the measured response was assigned a percentage of the expected value. A transverse section was taken through each deposit and the buildup height was measured in the center of the section using calipers. Half of each sample was then mounted and examined for porosity using both optical metallography and scanning electron microscopy (utilizing a FEI/Philips XL-30 FEG). The porosity measurements were taken from top to bottom in the middle of the cross-section. This was done to reduce error since the porosity was highly localized at the layer interfaces instead of evenly distributed. This method is valid only as a comparison for samples within this study. Figure 2 depicts the localized porosity at the layer interfaces. Moreover, the close-up shows unmelted powder in the macro pores.

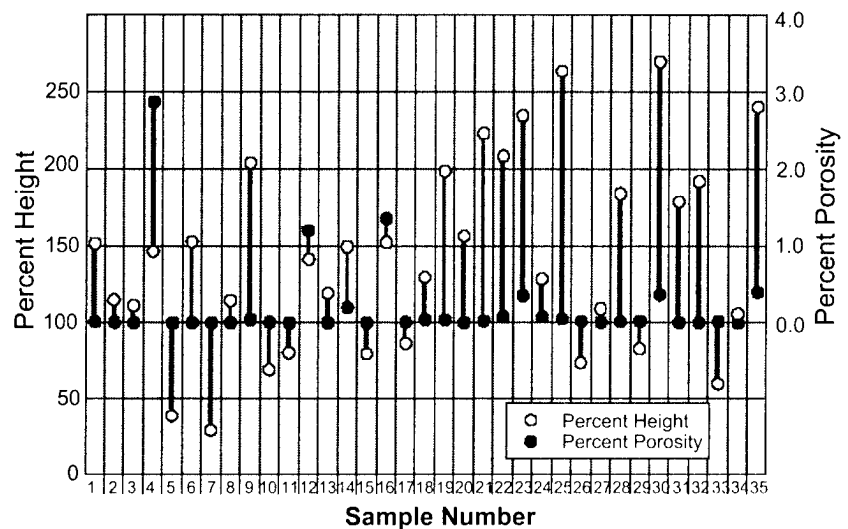


Figure 4: Graph showing the build height and density results for each sample.

Results and Discussion

Visual inspection of the finished samples showed varied results. Some deposits showed good dimensional accuracy while others were quite misshaped. Some of the thicker deposits showed an unusual spongy deposit on two sides of the cube. After breakdown and inspection of the machine, it was apparent that the four powder delivery nozzles were not aligned properly. Figure 3 shows an exaggerated schematic of the delivery head and how the spongy deposit is formed and the resultant buildup is not uniform. Some powder from the left nozzle flows through the laser focus but does not end up in the weld pool but slightly

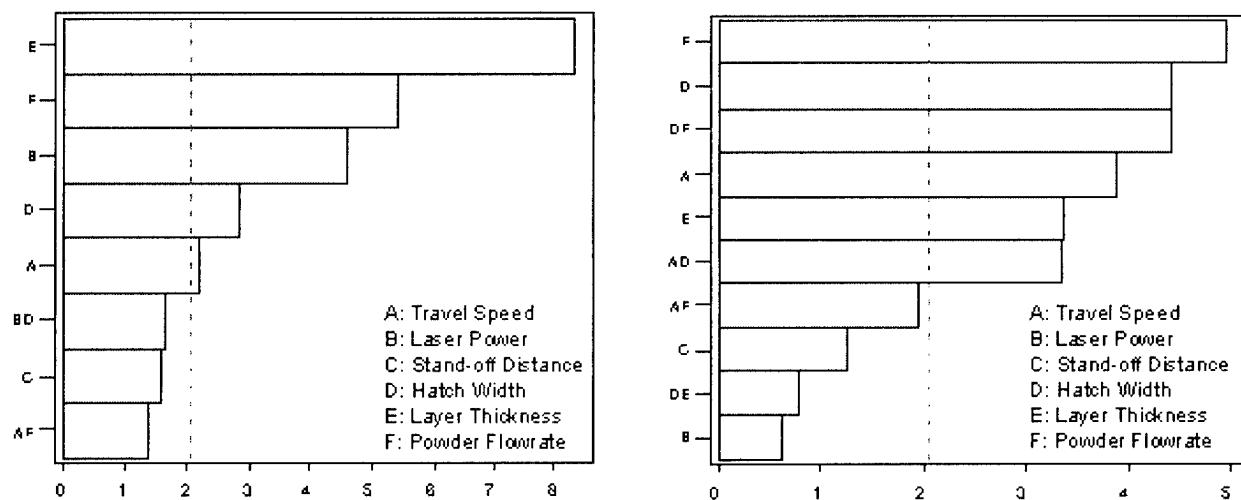


Figure 5: Pareto charts showing significance of variables. Chart on left shows response to layer height and the chart on the right shows the response of porosity.

Coefficient	Height	Porosity
Travel Speed	-10.91	-0.2086
Laser Power	22.68	-0.0295
Stand-off Distance	7.72	insignificant
Hatch Width	-14.06	-0.2381
Layer Thickness	-41.32	0.1815
Powder Flowrate	27.03	0.2651
Constant	142.62	0.2547

Table 2: Coefficients of the linear-fit model for each response.

to the side of it. This results in an overshoot of molten powder and a distorted buildup.

Subsequently, the samples were examined using microscopy and the raw data from the response variables is shown graphically in Fig. 4. From this chart, it can be seen that very few of the samples obtained both dimensional accuracy and low porosity. Finally the responses were statistically analyzed using MINITAB®. Plots of main effects versus responses were obtained. From this analysis, a model was created and the results are depicted in the Pareto charts shown in Fig. 5. The Pareto chart ranks the factors according to their importance for achieving the desired response for the process. The dashed line serves as a standardized threshold. Only factors extending to the right of that line are of statistical significance. Thus, with respect to sample height, the two most important variables are layer thickness and powder flowrate. For porosity, the two most important variables are powder flowrate and hatch width *plus* their interaction. There were no 3-factor or higher interactions of statistical significance. Some 2-factor interactions were not significant and were thus taken out of the model. The equations representing the linear model for the two responses are shown in the Table 2. These coefficients represent an equation of the form:

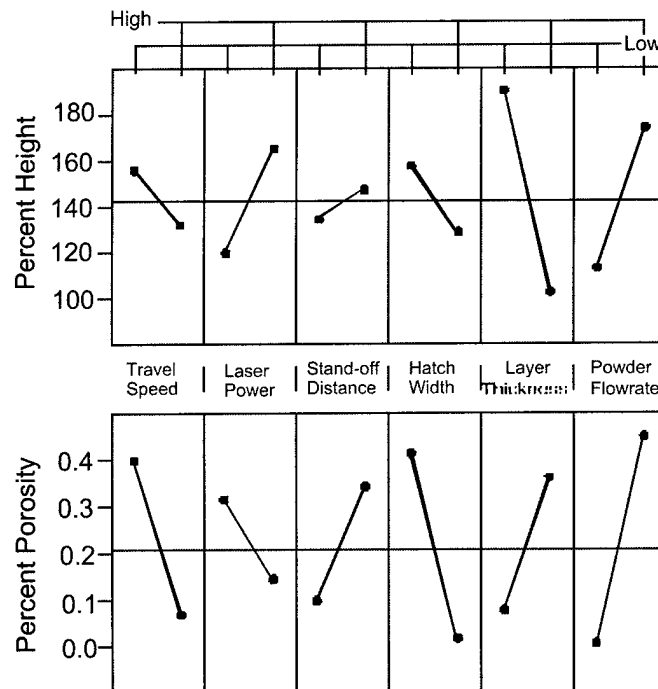


Figure 6: Graphs showing the main effects of the process variables on the given response. For these graphs, the slope determines the level of significance.

$$\text{Percent Height} = -10.91 \cdot \text{Travel Speed} + 22.68 \cdot \text{Laser Power} + 7.72 \cdot \text{Stand-off Distance} - 14.06 \cdot \text{Hatch Width} - 41.32 \cdot \text{Layer Thickness} + 27.03 \cdot \text{Powder Flowrate} + 142.62$$

The results from the model equations and the Pareto charts are different for the two responses. Eighty percent of the significant contributions in the model for height come from single factors, only 2% come from 2-factor interactions. Whereas in the model for porosity only 44% of the contribution come from single factors, but 36% from 2-factor interactions. Therefore 2-factor interactions are negligible in the first case, whereas in the latter they are of importance. Powder flow, layer thickness, hatch width and travel speed are among the most influential factors in both models. Focus does not seem to be of importance in either case, as was assumed after performing the experiment. This factor can be excluded in future analysis.

Figure 6 shows the main effects of the process parameters for both measured responses. The slope of each line is directly proportional to the importance of each variable; i.e. the steeper the slope, the more importance the variable has on the given response. Negative slopes have negative effects and positive slopes have positive effects. A comparison between the graphs of the main effects shows that travel speed and hatch width have negative effects; meaning running these parameters at a high level would produce a desirable response. Powder flow has a positive effect in both cases. To obtain a good response powder flow has to be at a low level. This can also be implied from the raw data by noting that 26 of 35 samples (74%) have higher than expected final heights. This indicates that lower powder flowrates should be examined. The effect of the laser power as well as thickness is opposite for the different cases. Comparing the responses of similar runs for the two replicates shows that the reproducibility of the experiments is not very good. The experimental error is 9% for the height and 13% for the porosity data.

Conclusions

Six process variables were chosen and their influence on the deposited samples was analyzed by means of a screening factorial design of experiments. From these experiments, it was concluded that stand-off distance could be ignored as a process variable. Also, the powder flowrate is crucial in obtaining an acceptable deposit. Unfortunately, this is the one variable that currently cannot be monitored during the process. Calibration of the flowrate must be done prior to deposition and the assumption is made that it remains constant. This issue must be addressed before further studies are conducted. Future tests must include more replicates to help reduce the error and increase the reproducibility.

References

1. D. M. Keicher, D. W. Miller, *Metal Powder Report*, 1998, Vol. 53, 12, pp. 26-28.
2. D. M. Keicher, J. E. Smugeresky, *Metal Powder Report*, 1998, Vol. 53, 1, pp. 38.
3. D. M. Keicher, J. A. Romero, C. L. Atwood, J. E. Smugeresky, M. L. Griffith, F. P. Jeanette, L. D. Harwell, D. L. Green, *Proc. of Rapid Prototyping and Manufacturing*, 1996.
4. F. G. Arcella, E. J. Whitney, D. Krantz, *ICALEO* 1995.
5. D. C. Montgomery, *Design and Analysis of Experiments*, Third Edition, John Wiley & Sons, 1991.

Microstructure and Property Optimization of LENS Deposited H13 Tool Steel

J. Brooks[†], C. Robino[‡], T. Headley[‡], S. Goods[†], M. Griffith[‡]

Sandia National Laboratories
[†]Livermore, CA and [‡]Albuquerque, NM

Introduction

Direct laser metal deposition is a means of near net shape processing that offers a number of advantages including rapid prototyping and small lot production. With the LENS (Laser Engineered Net Shape) process [Ref 1], parts are fabricated by creating a laser melted pool into which particles are injected. Fabrication proceeds by moving the work piece, thereby building the structure line by line and layer by layer. In this manner a wide variety of geometries and structures can be fabricated. During fabrication, a complex thermal history is experienced in different regions of the build. These thermal histories include remelting and numerous lower temperature thermal cycles. Furthermore, the use of a finely focused laser to form the rapidly traversing pool can result in relatively high solidification velocities and cooling rates.

Previous work has developed LENS as an advanced manufacturing tool rather than exploiting its potentially unique attributes: real time control of microstructure, tailored material properties at different part locations, the production of graded structures, etc. Very often, however, material properties are not significantly different than those of wrought materials.

The goal of this program is to exploit the unusual thermal environment experienced during fabrication, and the ability to design and vary alloy composition. In this paper we describe this approach using H13 tool steel in which only the thermal fields are varied through changing process parameters to achieve desired properties.

Approach Our desire in this program is to demonstrate the ability to "process for properties" which is necessary to fully utilize the unique attributes of this process. The approach requires at least four basic steps: (1) Select or design an alloy system with the metallurgical characteristics capable of producing the required engineering properties. (2) Develop and experimentally validate process models that can be used to describe the thermal history for different processing parameters in any region, or at least critical regions of the build. (3) Develop a material model which describes the relevant microstructural changes and properties during processing. (4) Combine the process and microstructural models to predict and tailor build properties.

In this paper we have used H-13 tool steel to demonstrate this approach. This is a commercially available secondary hardening alloy that is of significant industrial importance and which exhibits a martensitic structure tempered with the formation of alloy carbides. The alloy composition is shown in Table 1.

Table 1.
Composition of H13 (wt%)

C	Mn	Si	Cr	Mo	V	P	S	Fe
0.38	0.35	1.0	5.52	1.61	0.87	.009	0.18	Bal.

Process Thermal Model Microstructural interpretations and predictions require precise knowledge of the thermal history. In this study single line widths were used to fabricate thin wall square shells 6.35 cm on a side. Single line wall builds 5.1 cm long were also fabricated. A

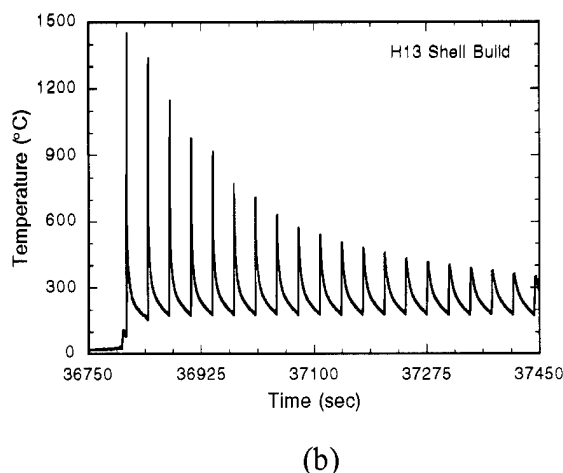
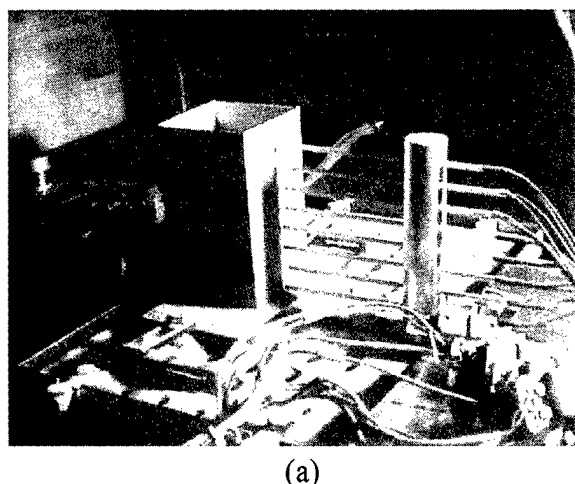


Figure 1 (a) Experimental setup for thermocouple measurements of single line width shell builds. (b) Results from one of the thermocouples shown in (a).

range of travel speeds of 5.9, 7.7, 9.3 mm/s using continuous YAG laser powers of 200, 250 and 300 watts produced individual layer thicknesses of ~ 0.25 mm with widths of ~ 0.4 mm. Temperature measurements were made using the experimental setup shown in Figure 1(a). Thermocouples 0.13 mm in diameter were inserted into parts during the build, and data was collected at 100 Hz.

Results from one of the thermocouples are shown in Figure 1(b). The first thermal cycle depicts the cooling from the molten pool. The subsequent thermal cycles, occurring every 33 seconds as the next layer is deposited, correspond to the thermal exposure of the underlying passes. Results are shown for 20 cycles, or build passes, where it can be seen that peak temperatures decrease in each succeeding pass. In the first pass the maximum cooling rate is $\sim 5 \times 10^3$ °C/sec. With these shell builds little heat is built-up with the interpass temperature remaining at ~ 150 °C. Thermal predictions have been made using simple Rosenthal analytical solutions [Ref 2] as well as with FEM using element birthing techniques. However, as has been demonstrated for weld process models [Refs 3,4], experimental data such as that shown in Figure 1(b) is critical for model validation. In this study the experimental data, rather than a thermal model, was used for microstructural predictions. However, we must point out that for true "processing for properties" a validated thermal model is required.

Microstructure The build microstructure can be related to the H13 phase diagram in Figure 2, although it must be noted that non-equilibrium conditions exist given the rapid heating and cooling rates. The microstructure shown was taken from the upper portion of a build, and for discussion has been separated into three different regions. Also shown is the height of the individual build passes. Region I is composed of as-solidified H13 (last pass) and supercritically reheated material. It can be seen that the last pass totally remelted the previous pass. Thermal cycles corresponding to these regions are also shown in the figure. Some segregation of alloying elements occurs as a result of partitioning during solidification, and little homogenization occurs due to the slow diffusion rates in austenite [Ref 5]. The exception is carbon for which the diffusivity is much more rapid and a uniform distribution is expected [Ref 5]. Microprobe measured segregation ratios (interdendritic boundaries)/(dendrite cores) were: Cr = 1.3, Mo = 1.2, and V = 1.5. The supercritical region extends from the liquidus temperature to the ferrite + carbide two-phase region, which on the equilibrium diagram is ~ 925 °C. The light etching material of the supercritical region is untempered martensite in which no carbides were detected using transmission electron microscopy (TEM).

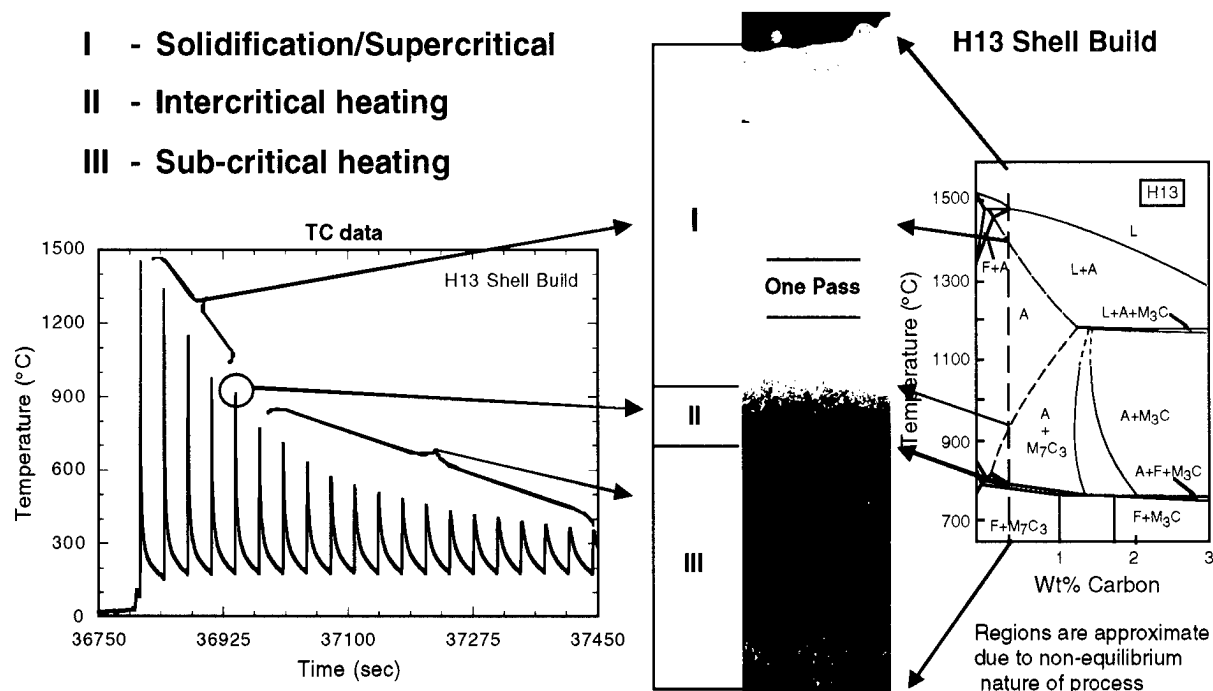


Figure 2 Correlation between measured thermal cycles, microstructure and the phase diagram used to describe H13 with 0.04 wt% C. Three thermal regions are used to describe the behavior. The pass height for these conditions is ≈ 0.25 mm.

Region II corresponds to material cycled into the intercritical two-phase and narrow three-phase regions shown on the diagram. This material had been previously cycled into the supercritical region, and corresponds to the first dark etching region noted in Figure 2. It is interesting that the height of this region is close to that of a single pass height, and based on the phase diagram, would have contained a thermal gradient of $\sim 150^\circ/0.25$ mm ($\sim 600^\circ\text{C}/\text{mm}$). For the thermal cycles shown, only the peak temperature of the fifth thermal cycle lies within this region.

Region III contains the material that in addition to having experienced thermal cycles in the upper two regions, also experienced subcritical thermal cycles. The final microstructure consists of tempered martensite with a bimodal distribution of fine V (A areas) and larger Cr (B areas) containing carbides as shown in Figure 3.

H13 Aging Model A description of the overaging process in the H13 requires a numerical model that can be applied to the rapid thermal cycles associated with the LENS process. In this section a simple kinetic parameter is defined which relates hardness to thermal history. The model is based on classical coarsening models, and the additivity rule is used to apply the model to LENS thermal cycles. In the model development, a kinetic parameter that is simply related to hardness is defined first.

It is assumed that hardness is proportional to shear strength, and that the analysis for the strengthening effect of incoherent precipitates [Ref 7] applies,

$$H \propto \tau = \frac{\alpha \mu b}{\lambda} \quad [1]$$

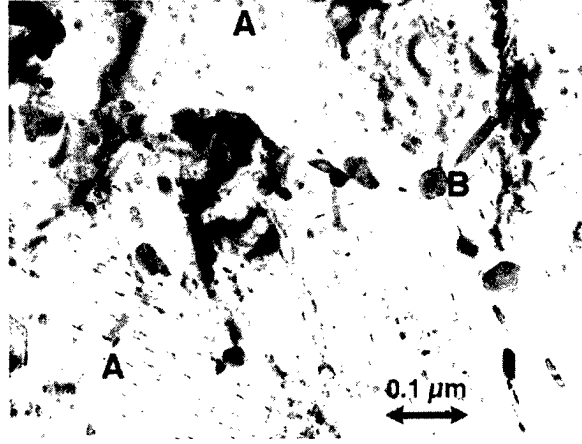


Figure 3 TEM image of H13 LENS deposit showing bimodal distribution of carbides. A and B denote typical regions of V and Cr rich carbides, respectively.

where H is the hardness, τ is the shear strength, α is a geometric factor, μ is the shear modulus, b is the burgers vector, and λ is the interparticle spacing. For overaging, the volume fraction of precipitates is assumed constant so that $\lambda \propto r$, where r is the radius of precipitates (assumed to be spherical). Thus, in the overaging regime, the following microstructural relationship is obtained:

$$H \propto \frac{1}{r}. \quad [2]$$

During aging, the precipitates are assumed to follow classical coarsening kinetics [Ref 7] (*i.e.* Lifshitz and V. V. Slyov [Ref 8], and Wagner [Ref 9], or LSW kinetics), so that

$$\bar{r}_t^3 = \bar{r}_0^3 + Kt, \quad [3]$$

where \bar{r}_0 is the mean initial particle radius and \bar{r}_t is the particle radius at time t . The coefficient K in Equation 3 is generally given by an equation of the form

$$K = \frac{8}{9} \frac{D\sigma V_m C_\alpha(\infty)}{RT} f(\phi), \quad [4]$$

where D is the diffusivity, σ is the interfacial energy, V_m is the molar volume of precipitate, $C_\alpha(\infty)$ is the solubility of the solute, R is the ideal gas constant, T is the temperature, and $f(\phi)$ is a function which depends on the particular coarsening theory ($f(\phi) = 1$ for the LSW theory). If it is assumed that all factors other than diffusivity are independent of temperature, and that the temperature dependence of D can be represented by $D = D_0 \exp(-Q/RT)$, then Equation 4 can be written as

$$K = K_1 \frac{\exp\left(\frac{-Q}{RT}\right)}{T}, \quad [5]$$

where K_1 is a constant. Combination of Equations 3 and 5 yields an expression for the coarsening rate as a function of time and temperature:

$$\bar{r}_t^3 = \bar{r}_0^3 + K_1 \frac{\exp\left(\frac{-Q}{RT}\right)}{T} t. \quad [6]$$

Substitution of Equation 6 into Equation 2 (with $\bar{r}_1 = r$) and rearranging leads to the result

$$H \propto K_2, \quad [7]$$

where K_2 has the form

$$K_2 = \left(\bar{r}_0^3 + \frac{K_1 \exp\left(\frac{-Q}{RT}\right)}{T} \right)^{-1/3} \quad [8]$$

Thus, a plot of H versus K_2 should be linear. The most direct means to apply this methodology is to search for values of \bar{r}_0 , K_1 , and Q that maximize the linearity of the plot. This can easily be accomplished in a spreadsheet application. Alternatively, if values for any of the parameters are known, such as an initial size or the activation energy for the diffusion of the rate limiting precipitating species, these can be used to reduce the number of fit parameters.

Isothermal aging experiments were conducted on single-line LENS deposits to determine the model fit parameters. The hardness for different times and temperatures are shown in Figure 4(a). The results from the procedure described above to fit this data (Equations 7 and 8) are shown in Figure 4(b). The optimized fit parameters for this data set are $\bar{r}_0 = 3.99 \times 10^{-7}$, $K_1 = 0.04048$, and $Q/R = 38143$, and the hardness for any isothermal heat treatment can be represented by a line of the form

$$\text{KHN} = 285.31 + 1.495 \times 10^{-4} (K_2) \quad r^2 = 0.9957. \quad [9]$$

These parameters linearize the data over a wide range of aging conditions, including those conditions near peak hardening and overaged. The apparent activation energy for the softening, 75,790 cal/mole, is higher than might be expected for coarsening of alloy carbides in H13. For example, the activation energy for the diffusion of Mo in ferrite is given [Ref 10] as 57,700-60,000 cal/mole (the diffusion of Cr would be expected to have a similar activation energy). However, given the assumptions inherent in the model, such as spherical precipitates, etc., this discrepancy is not thought to be a major drawback with respect to the application of the model.

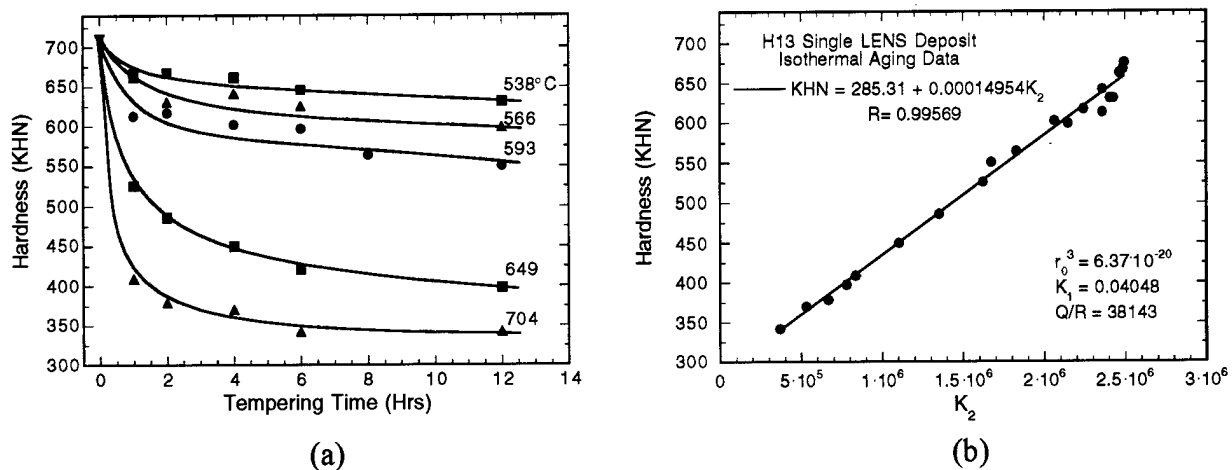


Figure 4 (a) Isothermal aging data for single line LENS deposits. (b) Correlation of data using Equations 7 and 8.

Application to LENS Thermal Cycles Application of the overaging model to LENS deposits requires a means to estimate the cumulative effect of the thermal cycle on the kinetics. A common approach for estimating this effect is the additivity principle [Ref 11, 12]. To apply the additivity principle, a thermal cycle is modeled as a series of small isothermal steps. At each step, the time elapsed is a fraction of the time required, at that temperature, to achieve a given amount of transformation or hardness. When these fractions sum to unity, the given hardness has been achieved. Formally, this can be written as

$$\int_0^t \frac{dt}{t_a(T)} = 1, \quad [10]$$

where t is the time and $t_a(T)$ is the time to reach the given hardness isothermally. For discrete time steps, Equation 10 can be written in the summation form, or

$$\sum_0^t \frac{\Delta t}{t_a(T)} = 1. \quad [11]$$

From Equation 9, $H = H_0 + mK_2$, where H_0 and m are the intercept and slope of the fit to the isothermal aging data, respectively, it is apparent that

$$H = H_0 + m \left(\bar{r}_0^3 + \frac{K_1 t \exp\left(\frac{-Q}{RT}\right)}{T} \right)^{-1/3} \quad [12]$$

or, upon rearranging,

$$t = t_a(T) = \frac{T \left[\left(\frac{m}{H - H_0} \right)^3 - \bar{r}_0^3 \right]}{K_1 \exp\left(\frac{-Q}{RT}\right)}. \quad [13]$$

For an isothermal hold, Equation 13 represents the time required to reach a given hardness, H , at a given temperature, T . Using a series of small isothermal steps to represent a thermal cycle, the summation of Equation 11 can be solved by using a goal seeking routine to find the hardness that satisfies the summation for that thermal cycle. Alternatively, the summation can be solved sequentially by calculating the softening during a given time step, adjusting the temperature to the temperature associated with the next time step and adjusting the start time to that which it would have been had the temperature always been at the new temperature, and iterating this procedure over the entire thermal cycle.

Model Predictions vs. Experiment Microhardness tests conducted on wall builds showed that the hardness of the supercritical region was the same for all processing parameters, that of untempered martensite. The hardness dropped rapidly in the region of the first intercritical pass and then decreased little after subsequent build passes. It was also found that the highest hardness build corresponded to the lowest heat input deposit (200 watts and 9.3 mm/s) and the softest deposit corresponded to the highest heat input deposit (300 watts, 5.9 mm/s). This behavior is shown in Figure 5(a), where the hardness is plotted as a function of distance from the last pass for these two process conditions. The hardness changes are consistent with the model predictions shown in Figure 5(a). As a result of the rapid softening kinetics and its exponential

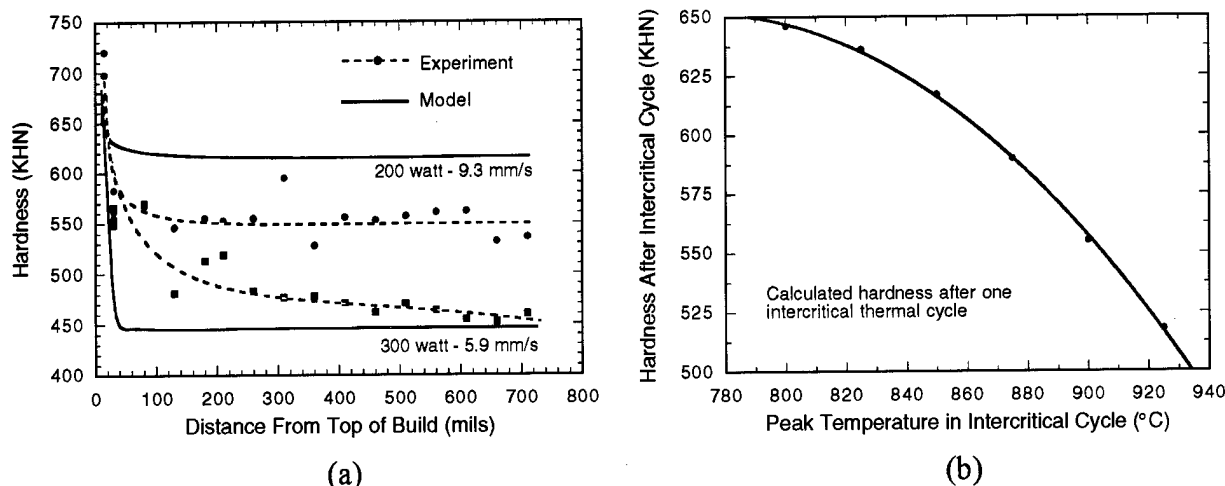


Figure 5 (a) Comparison of measured and predicted hardness distributions in LENS H13 wall build. (b) Plot of calculated hardness as a function of peak temperature within the intercritical temperature range.

temperature dependence, the calculated hardness is primarily controlled by the peak temperature of the thermal cycle within the intercritical temperature region. The measured peak temperature of the high heat input build was higher than that of the lower heat input build which accounts for the predicted hardness differences for the two sets of parameters. Subsequent tempering passes are of similar duration as the first tempering pass, but at progressively lower temperature resulting in little additional tempering.

The model predictions in Figure 5(b) show that hardness strongly depends on the peak temperature of the single thermal cycle within the intercritical region. For a region that experiences a peak temperature of 800°C, the hardness drops from ~710 KHN (that of untempered martensite) to ~645 KHN. For a peak temperature of 925°C, the hardness drops to ~515 KHN. The tempering response, or predicted hardness is, however, much more complex. It must be remembered that a thermal gradient is associated with the peak temperature of each tempering pass. All the temperatures within the intercritical and upper subcritical regions will correspond to the peak temperatures at some specific point, or line along the build. Furthermore, the height of the passes are on the order of the intercritical zone of the first tempering pass. Thus one would expect that a hardness gradient should exist over individual passes. Also, there could be regions further down the build that would be harder than regions closer to the top. This was actually observed, and accounts for some of the scatter in the data shown in Figure 5(a) and the banded etching behavior of the microstructure, Figure 2. To average some of the localized variation, Each hardness value plotted in Figure 5(a) is actually the average of three measurements made along a line at the same distance from the top of the build.

The temperature cycles used in the calculations were those experimentally measured with thermocouples. Although these thermocouples are small (0.13 mm diameter), they are still one half the height of the individual build passes. As shown in the microstructure of Figure 2, in the intercritical region the thermocouples lie within a temperature gradient of ~600°C/mm and therefore provide some average temperature within the temperature gradient. Nevertheless, the peak temperatures measured with the thermocouples resulted in the correct trend of calculated hardness for the builds, Figure 5(a). This is likely a result of the thermal gradient being flatter in the high power low speed build than in the low power high speed build, rather than the thermal couple placement. In general it was found that the hardness correlates better with travel speed than with laser power [Ref 13]. Thus, it can be seen that the details of the hardness and

tempering kinetics are highly dependent upon the height of the individual build passes as well as the thermal gradient in the intercritical region of the first tempering pass. Furthermore, accurate predictions of hardness require precise knowledge of the local thermal history.

Summary and Conclusions

The potential to use LENS to process for properties was demonstrated using H13 tool steel. The development and integration of both process and material models is necessary for precise property control. A simple kinetic model was developed that related thermal history to hardness for H13 and was combined with LENS thermal data to estimate build hardness. A good correlation was obtained between the nature of the predicted and measured hardness of single line thickness wall builds, although the features of intercritical heating require further investigation to achieve a more representative description. It was shown that the steep thermal gradients and rapid softening kinetics in H13 require very precise knowledge of the thermal history to accurately predict properties. With the rapid carbide coarsening kinetics of H13, almost all of the softening occurred during the first thermal cycle within the tempering regime.

Acknowledgements

The support of Mike Oliver in LENS processing and the metallurgical support of Annette Newman, both of Sandia Laboratories are greatly appreciated. This work was funded by the United States Department of Energy under Contract # DE-AC04-94AL85000.

References

1. M. L. Griffith, D. M. Keicher, C. L. Atwood, J. A. Romero, J. E. Smugeresky, L. D. Harwell, and D. L. Greene, *Proceedings of the Solid Freeform Fabrication Symposium*, Austin TX, , (1996), pp. 125-131.
2. D. Rosenthal, *Trans ASME*, Nov (1946), pp. 849-866.
3. J. Dike, C. Cadden, R. Corderman, C. Schultz and M. McAninch, *Trends in Welding Research, Proc. 4th International Conference*, Eds. Smart, Johnson and David, ASM, (1996), pp. 57-65.
4. J. J. Dike, J. A. Brooks, J. S. Krafcik, *Trends in Welding Research, Proc. 4th International Conference*, Eds. Smart, Johnson and David, ASM, (1996), pp.159-164.
5. J. A. Brooks, M. I. Baskes, and F. A. Greulich, *Metall. Trans. A*, 22A, (1991), pp. 915-925.
6. J. N. Dupont, C. V. Robino, and A. R. Marder, *Acta Materialia*, Vol. 46, (1998), pp. 4781-4790.
7. R. E. Smallman, *Modern Physical Metallurgy, - Fourth Edition*, Butterworths, London, (1985), pp. 394-407.
8. I. M. Lifshitz and V. V. Slyozov, *J. Phys. Chem. Solids*, Vol. 19, (1961), pp. 35-50.
9. C. Wagner, *Z. Elektrochem.*, Vol. 65, (1961), pp. 581-591.
10. E. A. Brandes, *Smithells Metals Reference Book Sixth Edition*, Butterworths, London, (1983), p. 13-64.
11. E. Scheil, *Archiv. fur Eisenhüttenwesen*, Vol. 12, (1935), pp. 565-567.
12. J. W. Christian, *The Theory of Phase Transformations in Metals and Alloys Part I*, Pergamon Press, New York, (1981), pp. 542-548.
13. M. Griffith, E. Schlinger, L. Harwell, M. Oliver, M. Baldwin, M. Ensiz, J. Brooks, C. Robino, J. Smugeresky, W. Hofmeister, M. Wert, and D. Nelson, *Materials and Design*, Vol. 20, Elsevier Science Ltd, (1999), pp. 107-213.

Process Maps for Laser Deposition of Thin-Walled Structures

Aditad Vasinonta and Jack Beuth
Department of Mechanical Engineering
Carnegie Mellon University
Pittsburgh, PA

Michelle Griffith
Sandia National Laboratories
Albuquerque, NM

Abstract

In solid freeform fabrication (SFF) processes involving thermal deposition, thermal control of the process is critical for obtaining consistent deposition conditions and in limiting residual stress-induced warping of parts. In this research, nondimensionalized plots (termed process maps) are developed from numerical models of laser-based material deposition of thin-walled structures that map out the effects of changes in laser power, deposition speed and part preheating on process parameters. The principal application of this work is to the Laser Engineered Net Shaping (LENS) process under development at Sandia Laboratories; however, the approach taken is applicable to any solid freeform fabrication process involving a moving heat source. Similarly, although thin-walled structures are treated in the current work, the same approach could be applied to other commonly fabricated geometries. A process map for predicting and controlling melt pool size is presented and numerically determined results are compared against experimentally measured melt pool lengths for stainless steel deposition in the LENS process.

Nomenclature

T	= temperature	T_m	= melting temperature
T_{base}	= baseplate and wall preheat temperature	ρ	= density
k	= thermal conductivity	c	= specific heat
t	= wall thickness	h	= wall height
L	= wall length	l	= melt pool length
Q	= laser power	V	= travel speed of laser
α	= fraction of laser power absorbed by the wall		

Introduction

Residual stress-induced warping is a concern in nearly all solid freeform fabrication (SFF) processes. This includes processes based on successive curing of polymers as well as those based on successive thermal deposition of polymers or metals. In using SFF processes for rapid prototyping, some tolerance loss due to warping is generally acceptable; however, many targeted applications for using SFF processes as rapid manufacturing techniques (to create functional parts) have strict dimensional limits. For instance, injection molds typically consist of two or more parts that must fit precisely together. Residual stress-induced warping is also becoming a greater concern as SFF processes are used to build larger and larger parts, where larger part dimensions naturally lead to larger dimensional losses.

A critical issue in developing SFF processes as rapid manufacturing techniques is the alteration of the processes to control residual stresses while maintaining optimal deposition conditions. Because SFF processes are complicated, even an intuitive trial-and-error approach is unlikely to yield success in the near term. In this research, nondimensionalized plots (termed

process maps) are developed from numerical models of laser-based material deposition of thin-walled structures for this purpose. They map out the effects of changes in laser power, deposition speed and part preheating on process parameters. This paper specifically addresses control of melt pool size, which is critical for maintaining optimal deposition conditions.

The principal application of this work is to the Laser Engineered Net Shaping (LENS) process under development at Sandia National Laboratories [1]. In the LENS process, parts are constructed by focusing a high-power laser beam onto a metal substrate, where streams of metallic powder are simultaneously injected. The laser locally melts the powder to form a molten pool on the top surface of the growing part. By moving the laser beam, parts are built up, line by line and layer by layer. Work is underway at Sandia Labs to not only optimize process parameters manually, but to use real-time thermal images of melt pool size as a feedback mechanism controlling the process [2]. Process maps presented in this paper have been developed to aid in both manual and automated process control efforts. Although this research is directed toward the LENS process, the approach taken is applicable to any solid freeform fabrication process involving a moving heat source. Similarly, although thin-walled stainless steel structures are treated in the current work, the same approach could be applied to other commonly fabricated geometries and materials.

In the next section, the geometry analyzed is presented, along with details of the finite element model and boundary conditions used. A description of the analytical solution used to choose a nondimensionalization scheme for the results is also given. In the succeeding section, numerical results are presented in the form of a process map under the assumption of temperature-independent material properties. This version of the results is important to consider because within the assumption of temperature-independent properties it is applicable to any SFF process involving a moving heat source and for deposition of any single material. Temperature-dependent simulation results are then presented as applicable specifically to the deposition of stainless steel in the LENS process. Rules are given for how these results can be applied to the prediction and control of melt pool size, and results are also compared directly with measured melt pool lengths from the LENS process. Finally, process control-related insights apparent from the results are discussed.

Geometry Considered, Numerical Model and Analytical Solution

In the current study, the thin-walled structure shown in Fig. 1 is considered. Thin-walled geometries of this type are commonly fabricated using the LENS and other SFF processes. Also, numerical simulations of a wall of large height, h , with temperature-independent properties can be verified against an existing analytical solution in the literature.

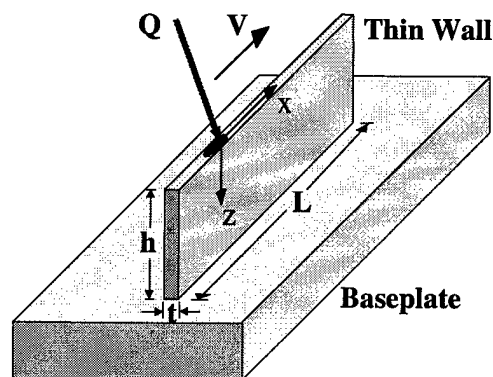


Figure 1. Thin-Walled Geometry Considered in This Study

The thin wall is assumed to be fabricated by depositing material along a single row; thus, the thickness of the wall is comparable to the molten melt pool size. The distance traveled by the laser and the length of the wall in the x direction are assumed large enough that steady-state conditions exist independent of the existence of the vertical free surfaces. It is assumed that the wall is built upon a large metallic substrate, which acts as a thermal heat sink and mechanically constrains the wall from deformation during the manufacturing process. Results presented herein demonstrate how melt pool length (extent in the x -direction) can be controlled as a function of wall height, h , absorbed laser power, αQ , laser velocity in the x direction, V , and uniform preheating of the wall and baseplate to a temperature $T = T_{base}$. Because results are presented as a function of absorbed laser power, it is presumed that the quantity α is well-defined.

The numerical models used in this study do not include effects of convective heat transfer from the wall free surfaces to the surrounding air and do not model convective flows in the melt pool itself. Work by Dobranich and Dykhuizen [3] suggests strongly that the role of these effects in determining melt pool size is not significant. The models of this study also model the laser as a point source of heat, neglecting the distribution of laser power over the melt pool region. Assuming a point source of power is reasonable given the goal of this study, which is to capture changes in melt pool size and other parameters as a function of changes in the process variables outlined above. Accuracy in the absolute predictions is of secondary importance. It is shown later in this paper, however, that model predictions still compare reasonably well with experimentally determined melt pool sizes.

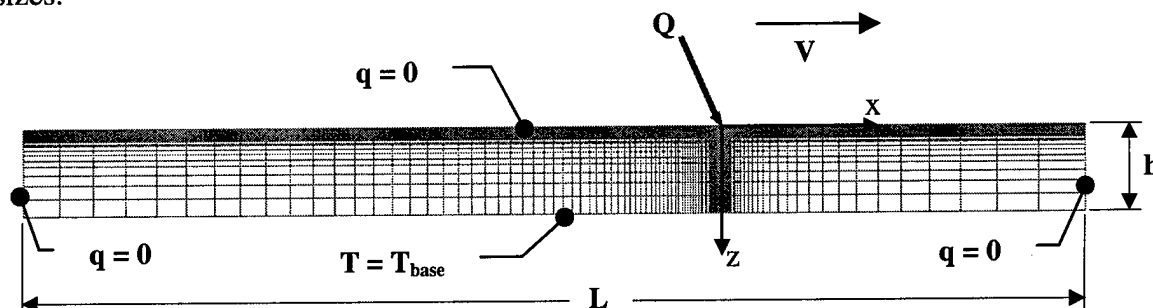


Figure 2. 2-D Thermal Model and Boundary Conditions

The mesh and boundary conditions used for a typical 2-D thermal model of this study are shown in Fig. 2. Four-noded bilinear thermal elements are used as part of the ABAQUS finite element software package. The laser beam focused on the top surface of substrate is simulated by a point source of power subsequently applied at model nodes at a rate simulating the laser velocity. Because of high temperature gradients in the region near heat source, the grid is biased toward the region that will surround the heat source at the time when results are to be extracted from the model. In addition to comparisons with an analytical solution valid for a large substrate, the convergence of this mesh was checked against a model with roughly half the resolution in the x and z directions with no noticeable change in the results.

As illustrated in Fig. 2, an insulated boundary condition is imposed on the top and both vertical sides of the substrate. The temperature along the substrate bottom is specified as fixed at a value equal to the temperature of the base plate. Sensitivity studies have shown that thermal results near the heat source are not significantly affected by boundary conditions along the substrate vertical and top surface being specified as either insulation or convective. Most of the heat transferred from the laser is conducted out through the bottom of the substrate. By using a 2-D model, it is also assumed that there is no heat loss through the front and back surfaces of the wall.

Thermal properties of AISI 304 stainless steel (SS304), which is used in the LENS and other SFF metal deposition processes, are used as inputs for the temperature-dependent simulations. Thermal properties were taken from [3] and are also comparable to those used by Klingbeil, et al. [4] in thermomechanical modeling of the Shape Deposition Manufacturing process. The properties used in the model that are set to depend on temperature are density, specific heat and thermal conductivity. The latent heat of the liquid-solid phase transition is also included in the model.

A 2-D conductive heat transfer solution for a point heat source moving across a semi-infinite thin substrate (Fig. 3) was first developed by Rosenthal [5]. The solution can be expressed in terms of modified Bessel function of second kind, zero order (K_0). An insightful study of application of this 2-D solution to the LENS process is given in [6] and [7].

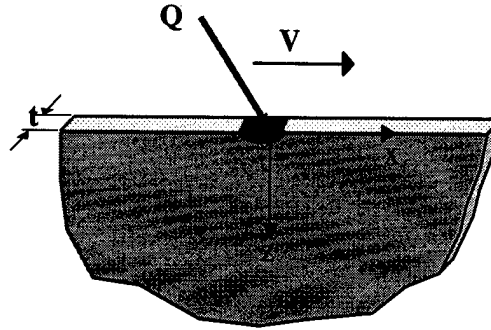


Figure 3. Geometry for the Analytical Model of Rosenthal [6]

The Rosenthal 2-D solution can be defined in terms of nondimensionalized variables as follows:

$$\bar{T} = e^{-\bar{X}_0} K_0(\sqrt{\bar{X}_0^2 + \bar{Z}_0^2}), \quad (1)$$

where

$$\bar{T} = \frac{T - T_{base}}{\alpha Q / \pi k t} \quad \bar{X}_0 = \frac{x}{2k / \rho c V} \quad \text{and} \quad \bar{Z}_0 = \frac{z}{2k / \rho c V} \quad (2)$$

and where the origin of the coordinate axes is located at the (moving) point source location.

By using the above equations, the melt pool length on the top surface can be calculated if the (temperature-independent) material properties and process parameters, namely absorbed laser power, αQ , laser velocity, V , and base temperature, T_{base} , are known. As previously mentioned, the Rosenthal solution is for a 2-D semi-infinite substrate. The simulations of this study are designed to capture behavior for thin-walled structures having a finite height. To study the relation between the melt pool size and the height of the wall, two dimensionless length variables, the normalized melt pool length (\bar{l}) and normalized height of substrate (\bar{h}) are introduced as suggested by the Rosenthal solution:

$$\bar{l} = \frac{l}{2k / \rho c V} \quad \text{and} \quad \bar{h} = \frac{h}{2k / \rho c V}. \quad (3)$$

Similarly, a dimensionless melting temperature is introduced,

$$\bar{T}_m = \frac{T_m - T_{base}}{\alpha Q / \pi k t}, \quad (4)$$

so that results for normalized melt pool length, \bar{l} , are presented as a function of normalized wall height, \bar{h} , and normalized melting temperature, \bar{T}_m .

Results Assuming Temperature-Independent Properties

Assuming temperature-independent thermal properties, a process map for a thin-walled structure with a concentrated laser heat source moving across it can be developed directly, using the normalization scheme outlined in the previous section. The resulting process map is shown in Fig. 4, which consists of a surface plotted on 3 coordinate axes. This map was developed from several numerical simulations performed with differing wall heights in order to get the dependence of \bar{l} on \bar{h} . The dependence of \bar{l} on \bar{T}_m was then determined from the same simulations by assuming different values of T_m .

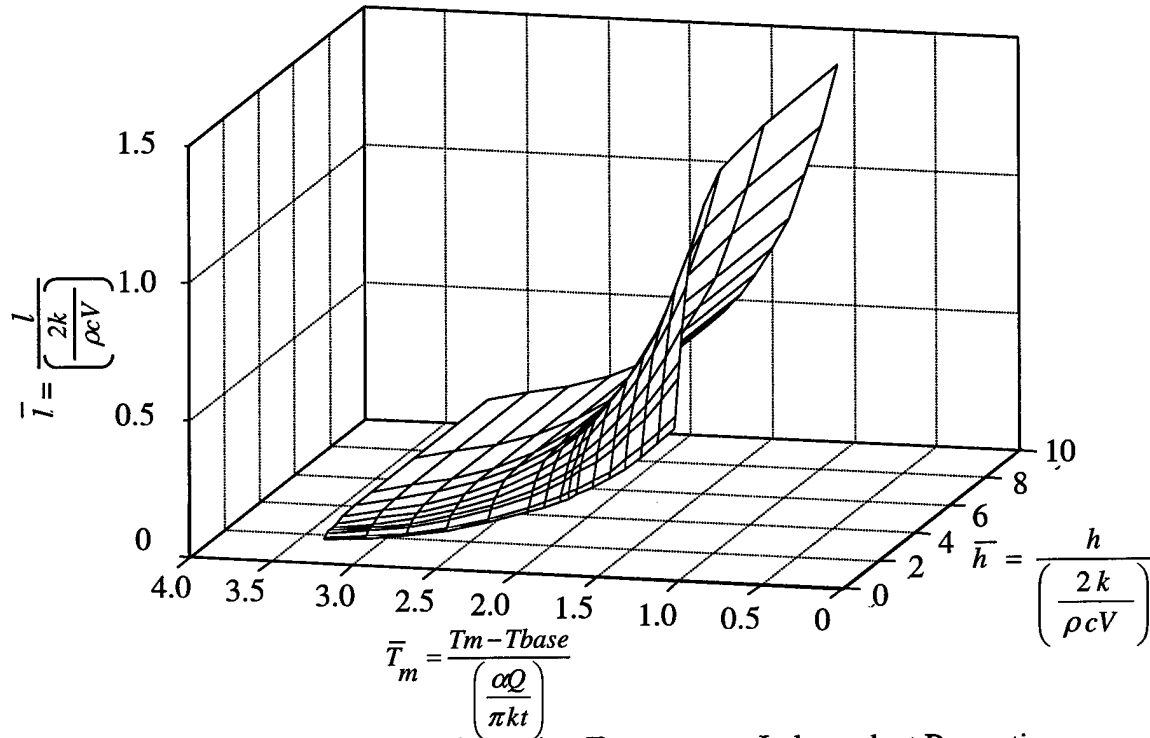


Figure 4. Process Map Assuming Temperature-Independent Properties

It can be seen from the plot that at each fixed \bar{h} , \bar{l} increases with increasing T_{base} or Q (either of which decreases \bar{T}_m). Moreover, a change in T_{base} can be compensated for by a change in Q , to retain a desired melt pool length. When the wall is relatively tall, \bar{h} has no significant effect on \bar{l} , because the wall is tall enough that the effect of the fixed temperature at the base is not felt at the melt pool. In contrast, \bar{h} has a considerable effect on melt pool length when the wall is relatively short, with \bar{l} dropping rapidly as \bar{h} is reduced. It is recognized that the fixed temperature condition assumed for the 2-D model used herein will lose its validity for very small values of wall height. Thus the process map dependence on \bar{h} is meant to only predict initial changes in melt pool size that can occur as wall height is reduced toward zero, or to predict the critical value of \bar{h} when changes in melt pool size due to changes in wall height become significant. Melt pool size can also be increased through a decrease in laser velocity, V . This is most easily seen for large values of \bar{h} (so that its dependence on V does not change \bar{l}). Through the normalization scheme used, the actual melt pool length, l , is given by:

$$l = \frac{2k\bar{l}}{\rho c V} \quad (5)$$

Thus, for a fixed value of \bar{l} as determined from the process map, l , is increased by a decrease in V .

It is important to emphasize that within the limitations of the assumption of temperature-independent properties, the process map shown in Fig. 4 is very general. It is applicable to any SFF process involving thermal deposition and for deposition of any single material and, as such, can be a useful intuitive guide to the control of SFF processes. However, for some material systems, if accurate predictions of the relationship between process variables and melt pool size are required, an accounting of the temperature dependence of thermal properties is needed.

Results for the LENS Process Using Temperature-Dependent Properties

In this section, results from modeling the LENS process for deposition of SS304 are presented, where temperature dependence of thermal properties is included in the modeling. The normalization scheme outlined in the previous section is still used, so that results are presented as a process map in terms of suitably normalized variables \bar{T}_m , \bar{l} and \bar{h} . Because properties are temperature dependent, however, the map includes "error bars" that reflect the range in results seen when process variables are varied over the range of specific interest in the LENS process. That range consists of values of αQ from 43.2 to 165 W, V from 5.93 to 9.31 mm/sec and T_{base} from 30° C to 400° C.

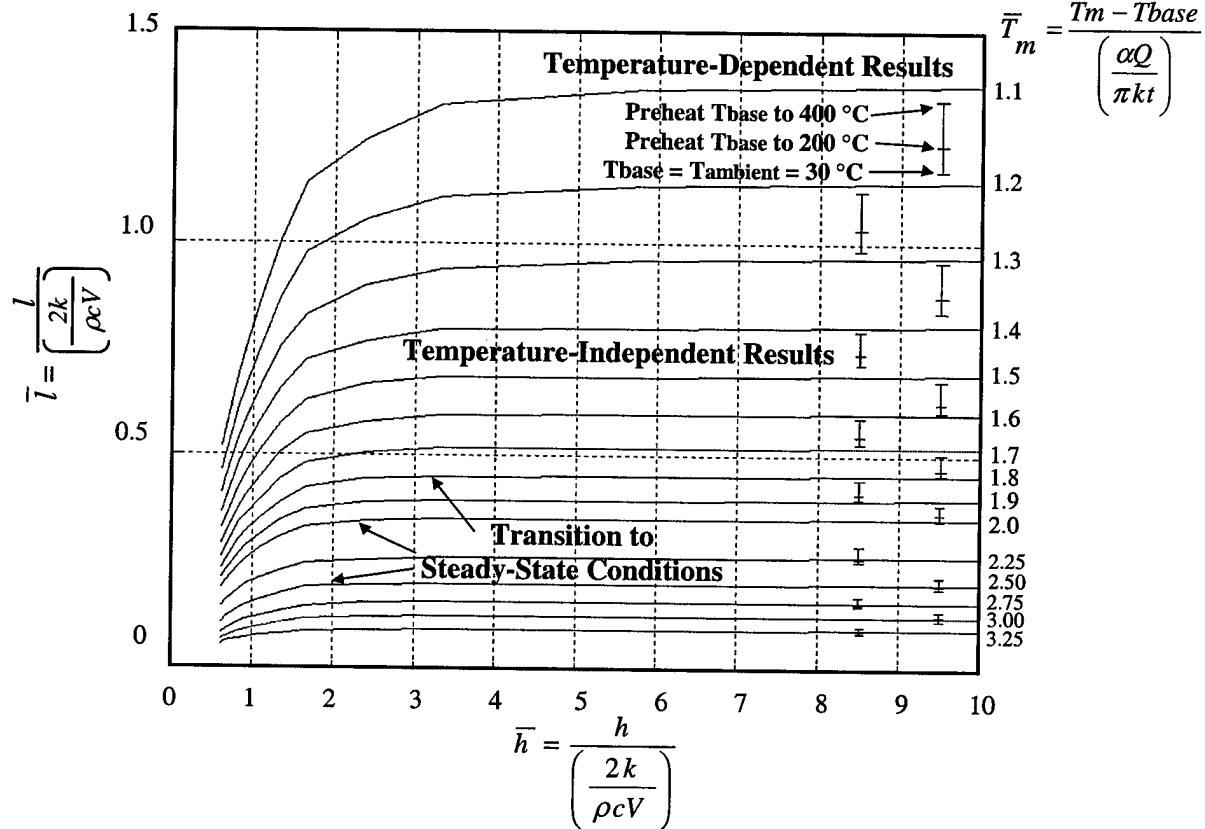


Figure 5. Temperature-Dependent Results of \bar{l} vs. \bar{h} for Various Values of \bar{T}_m for SS304

Figure 5 gives a 2-D projection of the resulting map onto \bar{l} vs. \bar{h} axes for various values of \bar{T}_m . Lines in the plot are from temperature-independent simulations and the error bars in the region of large \bar{h} values reflect results from temperature-dependent simulations. As indicated by the plot, the full range of results due to the temperature dependence of properties is less than 16% of the nominal value of \bar{l} . In order to obtain this level of agreement within the normalization scheme,

two rules were followed. First, all properties were normalized by the properties of SS304 at 1050K. This caused normalized temperature-dependent results as a function of laser power and velocity to nearly match normalized results from temperature-independent simulations for values of \bar{T}_m from 1.60 to 3.25. Second, when including a preheat in the simulations, some accounting of the temperature dependence of material properties is required. As seen in the material properties in [3], the biggest percentage change in material properties with temperature is in thermal conductivity and the change is essentially linear in temperature. Thus when normalizing results in the presence of preheating, the conductivity is varied linearly with preheat temperature (in °C) by the relationship

$$k = 25.1 + 0.013(T_{\text{base}} - 30) \quad \text{W/(m K)}. \quad (6)$$

This linear change in conductivity with temperature has been chosen to best fit the results within the preheat range of 30° C to 400° C and is less per degree C than that of the k vs. T properties from [3]. In summary, the agreement seen in Figure 5 between temperature-independent and temperature-dependent results is accomplished by normalization by what could be considered an "effective" set of properties at 1050 K and a rudimentary accounting of temperature dependence of conductivity for cases including preheating.

A final issue that must be resolved in using the results of Fig. 5 is how to account for wall thickness. Wall thickness will also change with changes in process parameters and it has to be input into the 2-D model. Analysis of experimental results from Hofmeister and Wert [8] suggests strongly that wall thickness scales with melt pool length. Thus, in using the process map given in Fig. 5, the authors assume that wall thickness scales with melt pool size and that this scaling is unaffected by velocity (within the relatively narrow velocity range of 5.93 to 9.31 mm/sec). Because thickness is in the denominator of the dimensionless variable \bar{T}_m , accounting for thickness changes requires an iterative scheme, where the wall thickness, t , is changed until the ratio of t/l reaches its original value.

In summary, the process map of Fig. 5 can be used effectively for SS 304 deposition within the range of process parameters of interest in the LENS process by applying the following four rules:

1. Properties at 1050 K are used in the normalization;
2. For cases involving a change in preheat, a linear change in thermal conductivity with a preheat temperature is assumed, as given in eq. (6);
3. Wall thickness is assumed to scale with melt pool length; and
4. It is assumed that the melt pool length/wall thickness scaling is unaffected by velocity.

Figure 6 provides a comparison of measured melt pool lengths as a function of laser power and velocity to predictions provided by the process map of Fig. 5 using the rules outlined above. The only inputs used to generate the predictions from the process map were a single experimentally measured wall thickness for ambient conditions of $V = 7.62$ mm/sec and $\alpha Q = 100$ W and an assumed value of $\alpha = 0.35$ (as suggested by Dobranich and Dykhuizen [3]). Measurements were made using real-time thermal imaging methods described briefly in [2]. The experimental results presented are for a single set of observations [8] and do not reflect the variability seen in measured results at nominally identical conditions, which can easily be on the order of $\pm 5\%$.

As seen in Fig. 6, for identical values of laser power and velocity, measured melt pool lengths are larger than predicted values. This is consistent with the model assumptions of a point source of heat and no convective flows in the melt pool, both of which tend to decrease melt pool length predictions. Clearly, however, the trends of melt pool length from both measurements and predictions are consistent for all three velocities.

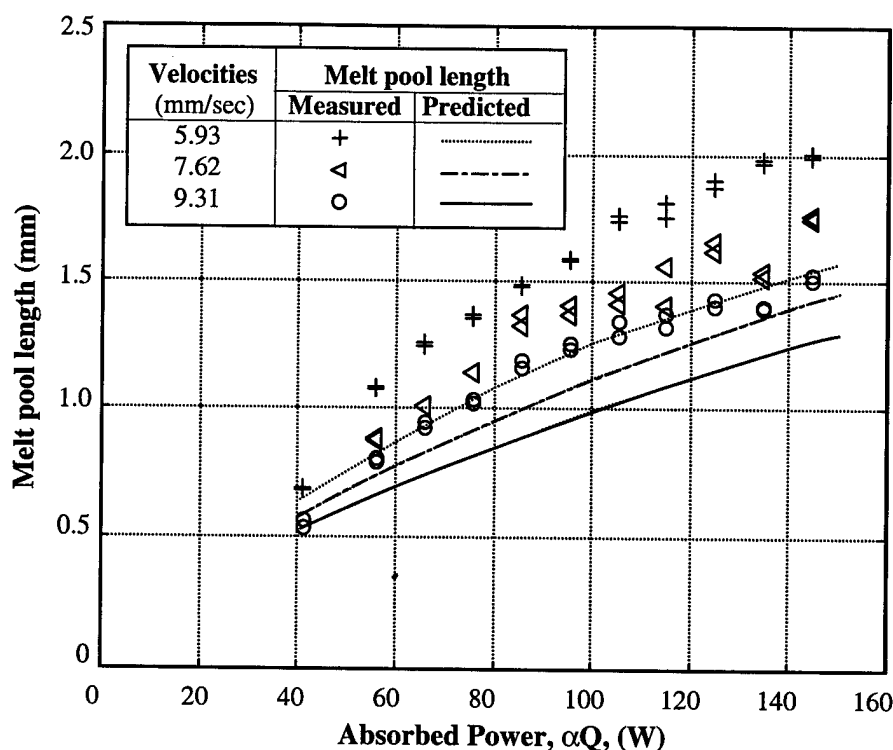


Figure 6. Predicted and Measured Melt Pool Lengths as a Function of Laser Power and Velocity

Summary and Implications of the Results

In this study, process maps have been developed for predicting or controlling melt pool size in the building of thin-walled structures by SFF processes. While the temperature-dependent results presented in this study are specifically applied to deposition of SS304 via the LENS process, temperature-independent results are applicable to any SFF process that involves a moving heat source. Furthermore, the approach taken here can be applied to other processes, materials and commonly encountered geometries. Analogous efforts are underway for developing process maps to control residual stress magnitudes primarily by part preheating. Such process maps could then be used with the process maps for melt pool length presented here to control residual stress magnitudes, while still maintaining an optimal melt pool length.

Although they are not presented in detail herein, calculations performed with the process maps described in this study have several major implications relevant to the LENS process and other similar SFF processes. First, results suggest that uniform preheating will not increase melt pool lengths significantly, and any increase in melt pool size can easily be eliminated by a small decrease in laser power or increase in laser velocity. Additionally, since uniform preheating will have an impact on residual stress magnitudes and warping, there is a clear possibility of using part preheating to reduce residual stresses with small changes in existing process parameters used to recover an optimal melt pool length. Second, a considerable change in melt pool length is predicted to occur for very short walls. It does not appear that this change can be compensated for by a base plate preheat alone. To obtain an optimal melt pool length for short walls, a change in laser power or laser velocity is needed.

Acknowledgements

This research has been supported by the National Science Foundation under grant DMI-9700320 and by Sandia National Laboratories under grant BE-0792. The authors would like to thank William Hofmeister and Melissa Wert of Vanderbilt University for providing data from their thermal imaging experiments that has proven to be vital for this research.

References

1. Griffith, M.L., Keicher, D.M., Atwood, C.L., Romero, J.A., Smugeresky, J.E., Harwell, L.D. and Greene, D.L., "Freeform Fabrication of Metallic Components Using Laser Engineered Net Shaping (LENS)," *Solid Freeform Fabrication Proceedings*, D.L. Bourell, J.J. Beaman, H.L. Marcus, R.H. Crawford and J.W. Barlow, eds., The University of Texas at Austin, August 1996, pp. 125-132.
2. Griffith, M.L., Schlienger, M.E., Harwell, L.D., Oliver, M.S., Baldwin, M.D., Ensiz, M.T., Smugeresky, J.E., Essien, M., Brooks, J., Robino, C.V., Hofmeister, W.H., Wert, M.J. and Nelson, D.V., "Understanding Thermal Behavior in the LENS Process," *Journal of Materials Design*, Vol. 20, No. 2/3, 1999, pp. 107-114.
3. Dobranich, D. and Dykhuizen, R.C., "Scoping Thermal Calculation of the LENS Process," Sandia National Laboratories Internal Report, 1998.
4. Klingbeil, N.W., Beuth, J.L., Chin, R.K. and Amon, C.H., "Measurement and Modeling of Residual Stress-Induced Warping in Direct Metal Deposition Processes," *Solid Freeform Fabrication Proceedings*, H.L. Marcus, J.J. Beaman, D.L. Bourell, J.W. Barlow, and R.H. Crawford, eds., The University of Texas at Austin, August 1998, pp. 367-374.
5. Rosenthal, D., "The Theory of Moving Sources of Heat and Its Application to Metal Treatments," *Transactions of ASME*, Vol. 68, 1946, pp. 849-866.
6. Dykhuizen, R.C. and Dobranich, D., "Cooling Rates in the LENS Process," Sandia National Laboratories Internal Report, 1998.
7. Dykhuizen, R.C. and Dobranich, D., "Analytical Thermal Models for the LENS Process," Sandia National Laboratories Internal Report, 1998.
8. Hofmeister, W.M. and Wert, M.J., personal communication.

Coated Feedstock for Fabrication of Ceramic Parts by CAM-LEM

Zhien Liu, N. Suppakarn, and James D. Cawley
Department of Materials Science and Engineering
Case Western Reserve University
10900 Euclid Avenue
Cleveland Ohio 44106-7204

Abstract

In laminated object manufacturing of ceramic components, lamination is one of the most important materials issues. Good lamination ensures monolithic component after firing. Otherwise, lamination defects that inevitably will occur in the parts will affect the properties of ceramic components. Adhesive (both liquid and non-liquid) lamination processes were developed for the cut-then-stack (CAM-LEM) procedure. The non-liquid adhesive lamination is discussed in detail.

Introduction

CAM-LEM (Computer-Aided Manufacturing of Laminated Engineering Materials) is one solid freeform fabrication technique, based on cut-then-stack procedure, which uses ceramic green tape as feedstock. One of the advantages of CAM-LEM is that ceramic parts with complex internal and external shapes can be readily produced. To achieve this requires that zero, or very small, strain is induced during stacking and lamination. One satisfactory method, called adhesive lamination, has been developed for CAM-LEM and reported elsewhere[1]. Generally, a mixture of a solvent, nonsolvent and diluent are used as adhesive. A variety of ceramic green tapes have been developed and tested [2-5], such as debased alumina, pure alumina, silicon nitride, PZT (lead-zirconate titanate) and ZTA (zirconia toughened alumina) tapes. By adjusting the details of the adhesive formulation and lamination process, 100% lamination efficiency and very low lamination strain (0-0.2%) were obtained for all systems. Recently, a non-liquid adhesive was also developed for CAM-LEM [6].

Materials and experimental

Three kinds of ceramic green tapes were used in this work: a commercial (Coors') alumina tape, in-house alumina tape and in-house silicon nitride tape. Properties of these feedstocks are shown in table 1. All these tapes are tape-casted using plasticized PVB (polyvinyl butyral) as binder. A typical liquid adhesive for these tapes is 40% ethanol, 40% PPG, and 20wt% toluene solution, although details vary with each system. To produce solid coatings of a thermally activated adhesive, a water-based suspension of ethylene/acrylic acid with 25% solids, is used. The average molecular weight and softening point of polymer are 8000 Amu and 42°C, respectively. The coating thickness can be controlled in the range of 4 to 30 μm , by doctor blading.

Properties of ceramic green tapes

	Coors' alumina tape*	In-house alumina tape+	In-house silicon nitride tape#
Powder size (μm)	3-4	~ 0.5	~ 0.5
Thickness (μm)	600	300	300
Density (g/cm^3)	2.32	2.51	1.97
Packing factor (v%)	56	56	51
Binder (v%)	21	30	30
Porosity (v%)	23	14	19

* 94% alumina, 6 wt% glass

+ A-16SG (Alcoa)

GS-44 (AllidSignal)

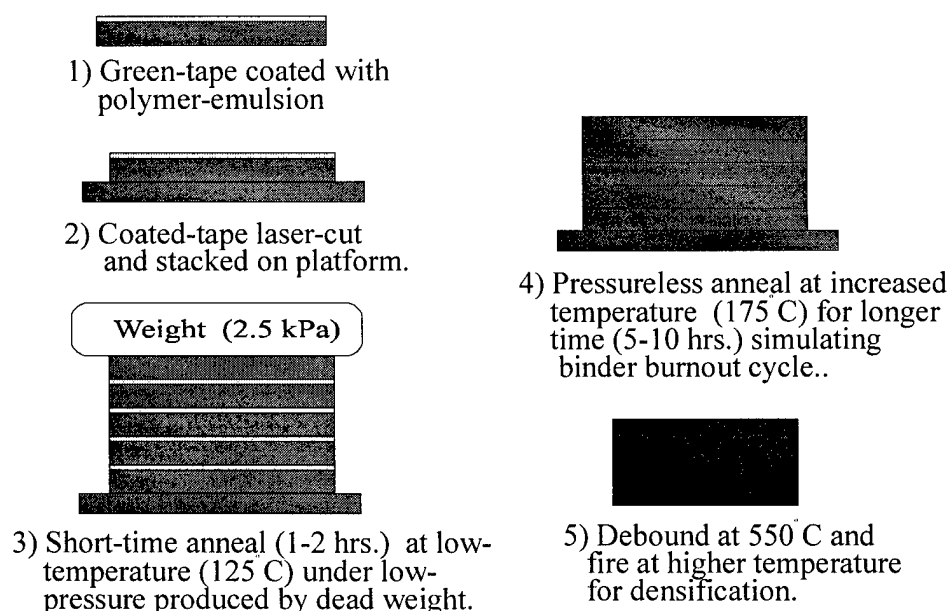


Fig.1 Schematic of lamination of ceramic green tape using water-based emulsion of tough co-polymer that becomes soluble in PVB at 100°C

A dead load lamination procedure was used to study the lamination efficiency for non-liquid adhesive (coated tape), as shown in Fig.1. After laser-cutting and stacking, the laminates were put into an oven at a low temperature ($\sim 125^\circ\text{C}$) under very low pressure ($\sim 2.5\text{ kPa}$). Under these conditions, the solid polymer film softens, becomes tacky and bonds all layers together. Subsequently, the laminates were heated without any pressure to a higher temperature (175°C) that is still below the binder decomposition onset and held for longer time (5-10 hrs). The viscosity of polymer film decreases, and it diffuses into green tape at this point. Therefore, the interface between green tapes disappears. After firing, monolithic ceramic parts are obtained. In the CAM-LEM machine, the coated film was heated to $\sim 150^\circ\text{C}$ in a few seconds to melt the polymer film using radiant

heat, then next layer was stacked and rolled to apply pressure. All the steps are robotically. The following pressureless annealing, debinding and firing are the same as shown in Fig.1.

Mass transportation during adhesive lamination

In prior work, a liquid-adhesive joining process was described that has proven very successful in terms of laminating a wide variety of ceramic green tapes. A variety of adhesive formulations have been developed for different feedstock. Solvents can be highly effective at assisting the lamination of ceramic green tape, but highly volatile solvent mixtures are difficult to control. For liquid adhesive lamination, the mass transportation during lamination is shown in Fig.2.

In the experiments, it is found that the PPG component in liquid adhesive is very important for good lamination. Therefore, the interaction of PPG with ceramic green tape was studied [7]. Fig. 3 shows the DMA (dynamic mechanical analysis) test results of PPG-coated Coors' alumina green tape. For as-received tape, there are two peaks, corresponding two organic phases. The peak at 32°C corresponds to the T_g temperature of binder and the peak at -71°C corresponds to the T_g temperature of the plasticizer. After heating a coated green tape to 80°C for a prolonged time, the binder's T_g shifted to lower temperature and the peak becomes broader. This result indicated that the diluent, PPG, diffused into binder.

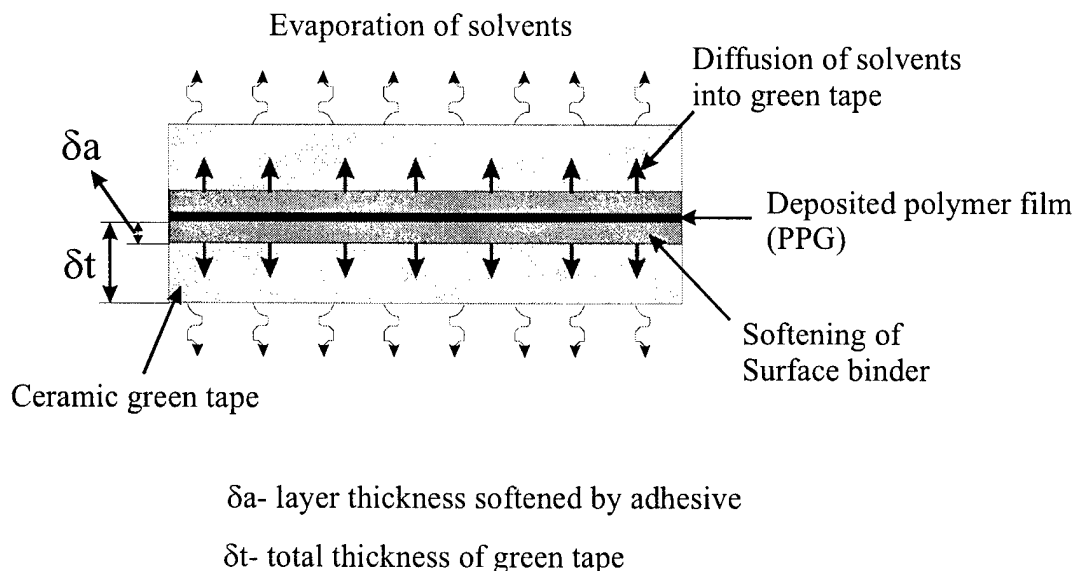


Fig.2 Mass transportation during liquid-adhesive lamination

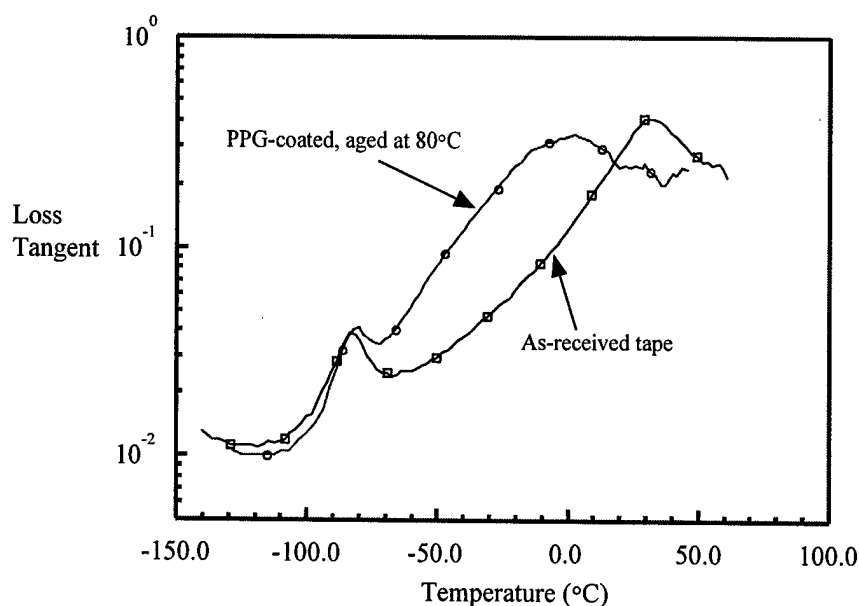


Fig.3 Dynamic mechanical behavior of Coors' alumina tape

Coated feedstock from commercial ceramic green tape

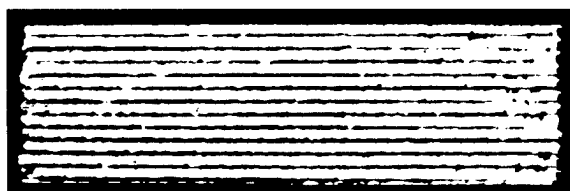
The ability of the PPG to migrate suggested that a polymer film with a low melting (or softening) point may be used as adhesive for ceramic green tape lamination at elevated

Table 2 Lamination of polymer-coated Coors; alumina tape

	1	2	3	4	5
Layers	12	12	12	12	15
Thickness	7.15	7.19	7.19	7.18	8.97
Weight	10.83	10.89	10.94	10.94	13.63
Lamination					
Temperature (°C)	80	100	125	150	175
Time (hr)	2	2	2	2	2
Pressure (kPa)	2.4	2.4	2.4	2.4	2.4
Strain (%)	-0.2	0.70	1.36	1.78	2.17
Weight loss (%)	0.08	0.11	0.13	0.17	0.59
Anneal at 175°C for 10hrs					
Strain (%)	-0.70	2.09	2.19	2.40	2.26
Weight loss (%)	3.89	3.76	3.76	3.70	3.58
Debind and Bisque Fire at 800°C					
Strain(%)	-0.98	2.26	2.29	2.44	2.28
Weight loss (%)	9.72	9.72	9.66	9.69	9.72
Lamination Result	delam	good	good	good	good
(Fired at 1560°C, 0.5hr)					

temperature. This was the underlying idea for the development at the solid system. The polymer coating on ceramic green tape was made by using a Doctor blade, as would be done in tape casting. Coated feedstocks were laminated using the procedure shown in Fig.1. Preliminary results have already presented [5]. The detailed results are shown in Table 2. Most laminates are 12 layers. Different lamination temperatures, from 80°C to 175°C, were tested while keeping lamination time and pressure constant. It can be seen that, with increasing lamination temperature, lamination strain increased due to the lowering of viscosity of the polymer film and diffusion into the green tape. After pressureless annealing at 175°C, the strain of all of specimens except for that laminated at 80°C increased to 2.1 to 2.4%, which corresponds to the original polymer film thickness. At this time, it is evident that the polymer coating is diffused into green tape, because the strain after bisque firing at 800°C did not change much. According to the laminate thickness and strain, the polymer coating thickness can be calculated in the range of 14 to 16 μm . It can also be seen that the lamination weight loss is very small if lamination temperature is lower than 175°C. The total weight loss after pressureless annealing is 3.6 to 3.9%. At that time, most plasticizer in the binder, which has much lower molecular weight (300-600) than binder and coating polymer, was evaporated. The total organic component (binder and plasticizer) in ceramic green tape is 8.5wt%. The specimen laminated at 80°C has negative strain due to the buckling delamination. Therefore, lamination temperature should be 100°C or higher. However, the green tape will too soft if temperature is too high.

Fig.4 shows a laminate of coated Coors' alumina tape. The cross-section of fired specimen subjected to a dye-penetrant indicates 100% lamination efficiency. No delamination was observed. Three layer atomizer components also were fabricated using coated Coors' alumina tape, shown in Fig.5. Fugitive tape, made from graphite and corn starch, was used in hollow area to ensure uniform pressure distribution during dead load lamination.



(a) Edge of as-laminated specimen at 125°C for 2 hrs



(b) Cross-section of fired alumina with penetrated ink (anneal at 175°C for 10 hrs, debound at 550°C, and fired at 1560°C for 30 min)

Fig.4 13-layer laminate of coated Coors' alumina (one inch square in green state)

Coated feedstocks of fine ceramic green tapes

Coated feedstock were also prepared from in-house alumina and silicon nitride ceramic green tapes. The two kinds of feedstock were laminated using polymer films of 18 and 28 μm , respectively, at 125°C and then pressureless annealed at 175°C for 15 hrs.

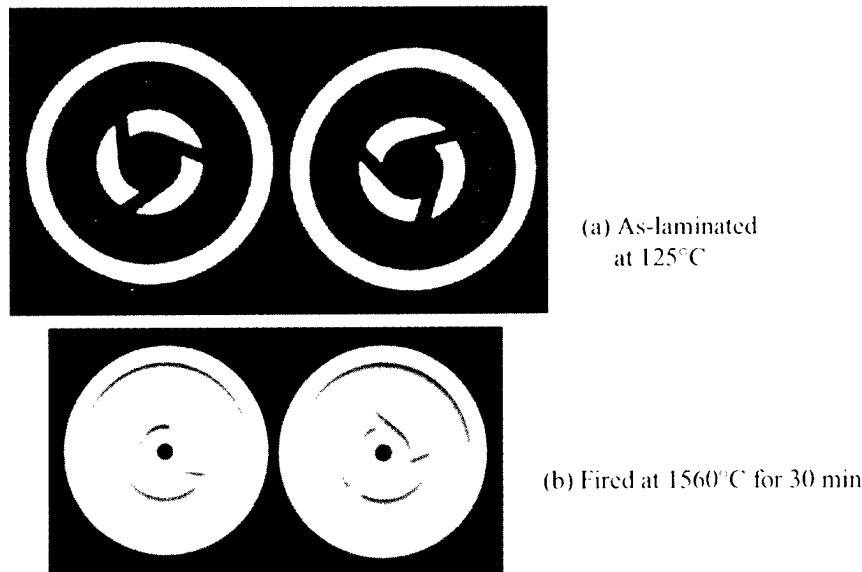


Fig.5 3-layer atomizer made from coated Coors' alumina tape

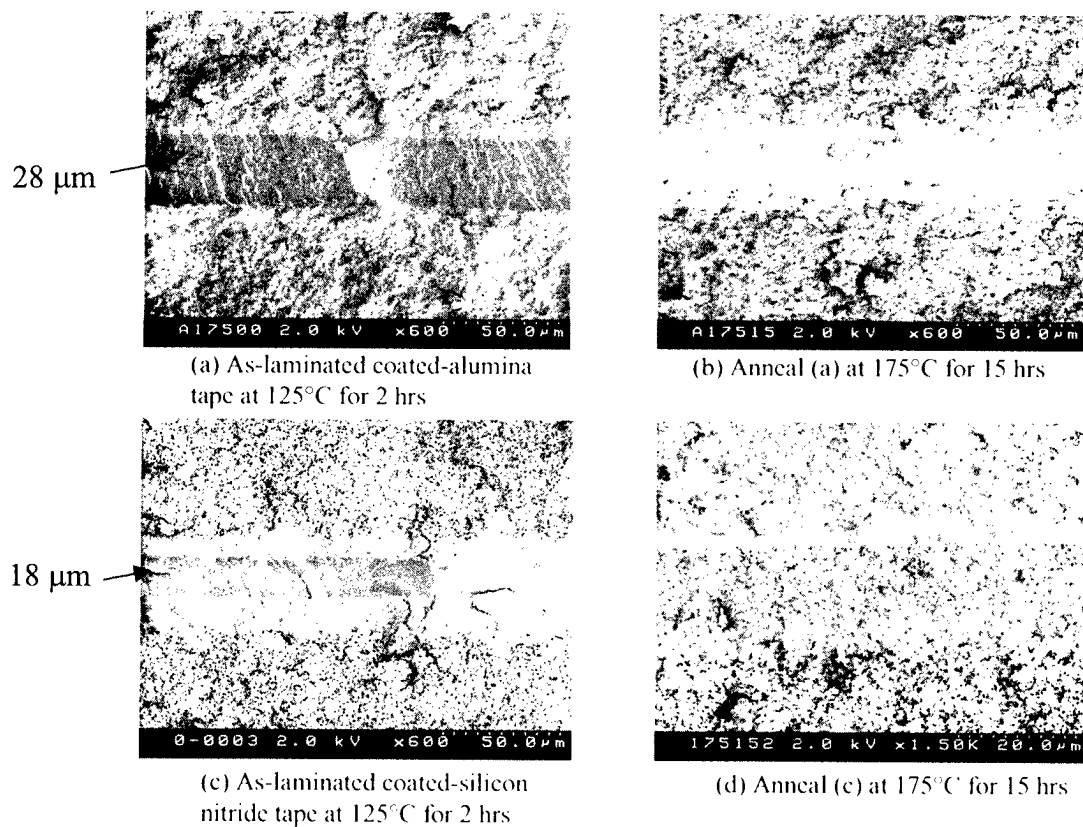


Fig.6 Cross-section of laminates of coated fine ceramic green tapes

The cross-section of laminates are shown in Fig.6. It can be seen that, unlike Coors' alumina tape, a thin polymer film (3-4 μm) still exists between green tape after 15 hrs annealing at 175°C. The reason is that the polymer coating is too thick. With the diffusion of polymer coating into green tape, the pores at near surface of green tape become saturated and a dense layer was formed at near surface, which is apparent as discoloration. Therefore, continued diffusion of the polymer coating into the green tape will meet high resistance and the diffusion rate will be very slow. It may take longer time (20 or 30 hrs) for polymer coating to diffuse into green tape completely, which is necessary to avoid delamination during firing.

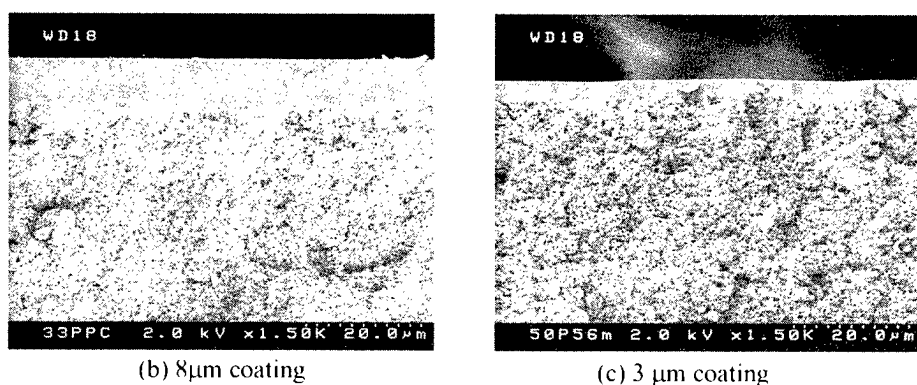


Fig.7 Thinner polymer coating on in-house alumina tape

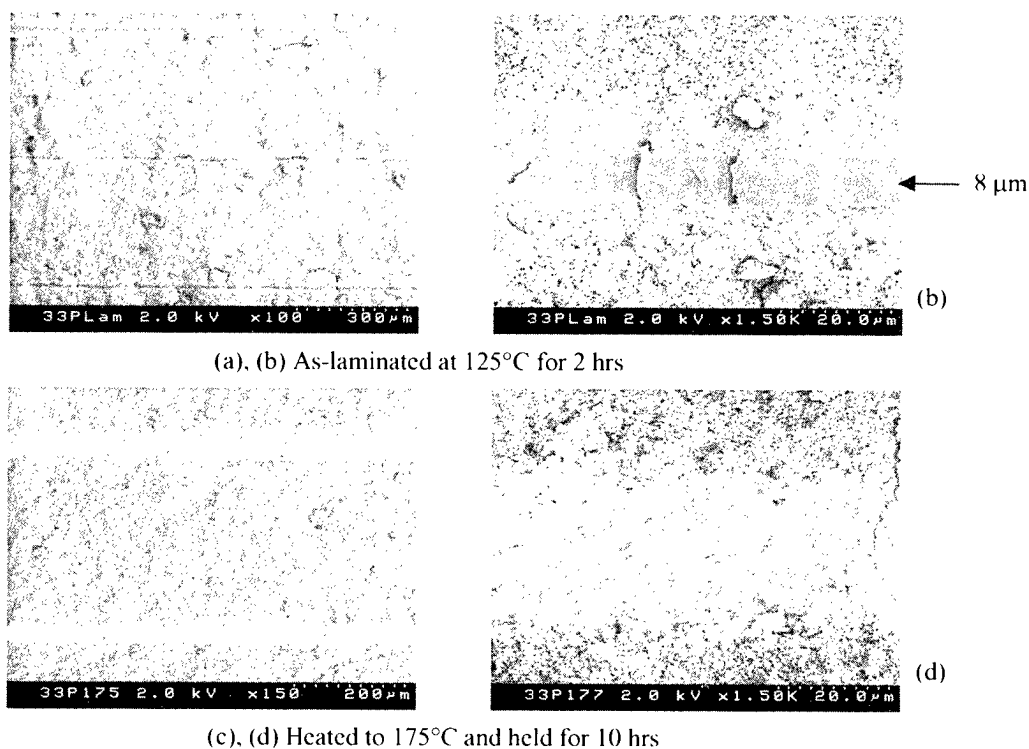


Fig.8 10-layer laminate of coated half-micron alumina tape

Therefore, thinner polymer coatings were prepared by diluting solid concentration in polymer emulsion. Coating thickness can be controlled in the range of 3 to 8 μm , as shown in Fig.7. Coated half-micron alumina tape was laminated at 125°C and then pressurelessly annealed at 175°C. SEM images of cross-section of the laminates are shown in Fig.8. It can be seen that, after annealing at 175°C, polymer coating diffused into green tape completely, and the interface between layers disappeared. Alumina atomizers were also fabricated by CAM-LEM machine. All the lamination steps were then finished robotically. Good lamination was obtained.

Conclusions

- (1) Liquid-adhesive lamination is a mature technology and has been successfully used to produce advanced ceramic parts.
- (2) Non-liquid adhesives have been developed and demonstrated. Though solid and nonsticky at room temperature, at low temperatures, it softens and bonds layers together. As temperature is increased, the adhesive becomes fluid and is dissolved in the binder.
- (3) Fine particle size green-tape require very controlled thin coating.

References

1. P. Wei, J.D. Cawley, and A.H. Heuer, CAM-LEM Processing of Ceramic Components – Lamination Technology, Proc. 6th Eur. Conf. Rapid Prototyping Manuf., edited by P.M. Dickens, Uni. of Nottingham, 1997, 95.
2. J.D. Cawley and Zhien Liu, Applying Tape Casting to Layered Manufacturing Processes, Ceramic Industry, 128[3]42(1998).
3. Zhien Liu, P.Wei, A.H. Heuer; and J.D. Cawley, Metal and Ceramic Components Made via CAM-LEM Technology, Proc. Solid Freeform Fab. Symp., University of Texas at Austin, 1996, pp. 377.
4. Zhien Liu; T-C Ko; J. Best; J.D. Cawley, and A.H. Heuer, CAM-LEM Processing: Materials Flexibility, Proc. Solid Freeform Fab. Symp., University of Texas at Austin, 1997, pp. 379.
5. J.D. Cawley; Zhien Liu; J. Mou, and A.H. Heuer, Materials Issues in Laminated Object Manufacturing of Powder-Based Systems, Proc. Solid Freeform Fab. Symp., University of Texas at Austin, 1998, pp. 503.
6. J.D. Cawley, B.D. Kernan, and W.H. Glime, US Patent Pending.
7. N.Suppakara, PhD Dissertation, Case Western Reserve University, 1999.

Acknowledgements: Brian B. Mathewson at CAM-LEM, Inc. conducted the lamination trials with the CAM-LEM machine and produced the test lot at atomizer. Funding for yhis work was provided through a NASA/CWRU Cooperative Agreement on Ceramic Processing (NCC3-404).

Direct Fabrication of Polymer Composite Structures with Curved LOM

Donald Klosterman, Richard Chartoff, Mukesh Agarwala
Ira Fiscus, John Murphy, Sean Cullen, Mark Yeazell

Rapid Prototype Development Laboratory
University of Dayton
300 College Park
Dayton, OH 45469-0131

ABSTRACT

This report describes the application of Curved LOM to the direct fabrication of polymer matrix composites (PMCs). The overall methodology of directly fabricating PMC parts involved the use of the Curved LOM machine to lay-up and shape "green" composite laminates from prepreg feedstocks, followed by vacuum bag / oven cure and consolidation. The conventional Curved LOM laminator was replaced with a vacuum thermoforming apparatus to better accommodate the bonding of commercially available prepregs. The study also demonstrated that it is possible to interface a general composite design software package with the Curved LOM machine via the curved slice file (.CSF) format. Taken together, these two improvements allow for improved flexibility in manufacturing PMC components, from both a material handling and a design point-of-view. A simple C-shaped panel was fabricated and tested to demonstrate the overall feasibility of the process for PMCs. A glass fiber / epoxy prepreg obtained from a commercial supplier was used as a model material system. It was found that the cumulative accuracy of the overall process was good, and the mechanical properties of the laminates were acceptable for non-structural applications for which the material is normally used.

INTRODUCTION

The Curved-Layer Laminated Object Manufacturing process (Curved LOM) was developed for direct, automated fabrication of curved layer structures made from high temperature materials such as ceramic matrix composites (CMCs) or monolithic ceramics. Full description of the process can be found in previous publications [1, 2, 3]. Described in this report is the application of Curved LOM to the direct fabrication of polymer matrix composites (PMCs). The availability of a direct method for rapidly and inexpensively producing PMC prototype components would be of great benefit to the composites design and manufacturing community. Currently, the effort and cost involved in the design and fabrication of PMC prototype components can be great. The design community needs a rapid, low-cost prototype manufacturing capability that can fabricate prototype parts of comparable quality to those produced via traditional techniques. In fact, aerospace designers have been recently turning to rapid prototyping technologies for potential new solutions [4]. Using LOM for the lay-up of PMC prototype laminates will allow for the simultaneous evaluation of new materials and design concepts, enabling rapid design and fabrication of competing prototypes.

The purpose of this report is to describe recent improvements made to the hardware and software capabilities of the Curved LOM apparatus (see [3] for a previous status report). These updates were made to allow for improved flexibility in manufacturing PMC components, from both a material handling and a design point-of-view. A simple C-shaped fiber glass / epoxy panel was fabricated to demonstrate the overall feasibility of the process for PMCs. Using this demonstration component and other fabricated flat panels, the dimensional accuracy of the overall process was determined, and the quality of the panels was assessed through measurements of the fiber volume fraction and interlaminar shear strength.

HARDWARE IMPROVEMENTS

Improvements were made to the Curved LOM apparatus to better accommodate commonly available PMC materials. Preimpregnated fiber preforms, or "prepregs", are widely used by manufacturers of composite products. Prepregs are flat sheets containing fibers (usually continuous unidirectional or woven fabrics) and a polymer resin. It is common industrial practice to build parts by cutting the prepregs to shape and laying them up manually. Layers are compacted manually using a roller and/or vacuum diaphragm in order to dispel air from in between layers. This compaction capability was not available on the initial version of the Curved LOM machine [3]. Thus, a vacuum thermoforming apparatus was developed in order to improve on total pressure available and pressure uniformity.

The new laminator design is illustrated in Figure 1. A flexible, resistively heated pad is sandwiched between two silicone rubber diaphragms. The composite diaphragm is stretched over and secured to the open side of a 13 inch x 13 inch x 3 inch aluminum box. This mechanism is shuttled directly over the LOM-paper mandrel, which is supported by a vacuum plate. A prepreg is placed over the mandrel, and the build platform is elevated until it seals with the laminator. A vacuum is drawn through a perimeter channel that has been bored in the vacuum plate. A porous "breather ply" (not shown), such as a woven fiberglass layer, can be placed over the lay-up to ensure even vacuum distribution over the entire part area. With a breather ply in place, the vacuum pressures at the top center and far edge of the part were measured to be 11.8 psi and 12.0 psi, respectively. It is possible to provide additional pressure via compressed gas using the vent tube. Currently, the maximum size part that can be made is 8 inch x 8 inch x 3 inch. Given the envelope of the LOM machine housing, it is possible to scale-up to 30 inch x 20 inch x 5 inch parts.

SOFTWARE IMPROVEMENTS

The interaction of software programs necessary for Curved LOM is illustrated in Figure 2 (see [1] for an expanded description). The algorithms are incorporated in two separate packages. First, LOMSlice 2.0 is used to slice an .STL file into a series of curved layers. The information of each layer, namely the X Y Z coordinates of the layer cross section, is stored in a separate .CSF (Curved Slice File) file. Thus, each part is represented by a series of .CSF files, equal to the total number of layers required to build the part. Next, the .CSF files are exported to 3D LOMSlice which drives the Curved LOM machine via an eight-axis motion control card.

This scheme is problematic for building PMC parts, based on the inherent shortcomings of the .STL file format. Because the .STL format is a surface representation, it cannot contain layer-by-layer information such as ply architecture (i.e. fiber direction) needed to fully describe a composite structure. Furthermore, engineers who design composite structures are typically not familiar with the .STL format. On the other hand, the .CSF format is of the appropriate geometrical format, although it is also relatively unknown to composite designers. One purpose of this study was to demonstrate the potential use of .CSF files as a "neutral exchange" format, providing the link between the Curved LOM machine and software/file formats typically used by composite designers.

The design of composite structures is normally accomplished with suites of software packages that have been developed to accommodate all aspects of composite design, such as ply shape definition, prepreg orientation and stacking sequence, and structural analysis and optimization [e.g. 5]. Through simulation, designers determine the best ply architecture (i.e., shape, sequence, and orientation of prepreg layers) for a given part subjected to the expected loading conditions. Some software packages [6] have the additional capability of providing a direct link from 3D CAD geometry to automated equipment, such as prepreg cutters and laser projection systems used on the manufacturing floor.

Based on this existing capability for direct machine control, it is not difficult to envision the possibility of controlling the Curved LOM machine by these packages. The motions of the various Curved LOM hardware elements are controlled by an off-the-shelf machine control board (Galil DMC-1000). However, instead of having commercial design software packages interface directly with this DMC card, it may be easier to output .CSF files. Illustrated in Figure 3 is an example of a software package that accomplishes this task. This package, referred to as Curved Composite Panel Designer (CCPD), creates the ply information for simple "C" shell composite panels. The user inputs the desired width, height, length, shell thickness, layer thickness, and layer-by-layer ply orientation of a simple "C" panel containing parabolic surfaces. The program outputs a series of .CSF files, each containing the XYZ coordinates and ply orientation of a single layer. The program is also capable of creating a simple "tool outline" file, which greatly simplifies the accurate placement and registration of the LOM-paper mandrel in the Curved LOM machine. In a similar manner, it is thought that commercially available software design packages could be readily augmented with a "Curved LOM" output module or "translator" to perform the same function, as illustrated in Figure 2. Since such software programs are CAD-based, it would also be possible to output the necessary .STL files for creating the curved mandrels, which can then be built with flat LOM or other SFF techniques. Overall, the benefit of such an effort would be to drastically improve the availability of rapid prototyping methods such as LOM to the composite design community.

PMC PROTOTYPE FABRICATION

The methodology for direct fabrication PMC components with Curved LOM is illustrated in Figure 4. Prepregs are used as feedstocks due to their wide commercial availability and ease of processing. The LOM machine is used as a means of automated lay-up and cutting, ideally eliminating touch labor and improving accuracy and consistency. Throughout the process, some heat can be used to assist lamination if necessary. However, it is desirable to keep the prepregs and the part in a state of minimal cure. It is advantageous to perform most of the cure and consolidation in one step *after* the part is completely layed-up. This approach will ensure that layer compaction, resin flow (which assists compaction), and the majority of the resin polymerization will occur simultaneously *and* uniformly throughout the part, as a result of the steady pressure and temperature conditions. This consolidation cycle can be performed using a variety of techniques, such as an autoclave cure or matched die press molding, but vacuum bag / oven cure was chosen to remain consistent with the idea of low cost processing.

A simple "C" shell panel was fabricated for the purpose of demonstrating the overall Curved LOM fabrication of a PMC, including the new hardware and software capabilities. A glass fiber / epoxy prepreg, obtained from a commercial supplier [7], was used as a model PMC material system. The prepreg was comprised of a woven E-glass fiber mat (plain weave, style 7628) impregnated with a B-staged (partially cured), catalyzed Novolac epoxy resin system. The resin content and thickness of the prepreg were 35 wt% and 0.0085 inches, respectively. The prepreg was slightly tacky to the touch at room temperature, and thus it was supplied with a removable backing ply (thin plastic sheet, like cellophane).

First, a LOM-paper mandrel was created to support the "C" shell. An .STL file for the LOM-paper mandrel was created using the .STL file of a "C" shell part and LOMSlice 2.0 software, as illustrated in Figure 2. The mandrel was built on a LOM 1015 machine using Helisys LPH008 paper. Next, the dimensions of the "C" shell, the average cured thickness of the prepreg (0.007 inches), and the lay-up sequence (16 ply, quasi-isotropic), were input to CCPD software program. The resulting sixteen .CSF files were loaded into 3D LOMSlice. The LOM-paper mandrel was placed on the Curved LOM build platform. The prepregs were layed-up on the mandrel by hand (the automatic sheet feeder was disassembled due to redesign and implementation of the new laminator). A mylar film and woven glass

fiber mat (Crowfoot weave, Style 120) were placed over each layer to serve as release and breather plies, respectively. Each layer was laminated for 30 seconds at room temperature. After lamination, the mylar and breather plies were removed prior to laser cutting. All sixteen plies were processed without problem.

The finished green part with attached LOM-paper mandrel were removed in one piece from the Curved LOM machine, placed on an aluminum sheet, vacuum bagged [8], and placed in a temperature-controlled oven. The cure cycle was 25 to 150°C in one hour, three-hour hold at 150°C, and free cool to 25°C. The vacuum pressure was maintained at >14 psi for the duration. The resulting part and a similarly fabricated body armor panel are shown in Figure 5. During the cure cycle the LOM paper mandrel shrunk by 11% in the z direction, and zero in the width and length. The "C" shell experienced spring-back (which is normally encountered in curved PMC panels), and thus, its dimensional change was much less than the mandrel. In fact, the cured "C" shell fit almost perfectly on a freshly-built mandrel, as illustrated in Figure 5.

DIMENSIONAL ACCURACY AND MECHANICAL PROPERTIES

The cumulative dimensional accuracy of the process is summarized in Table 1. No attempt was made to incorporate shrinkage compensation factors into the original dimensions. All measured final dimensions except height were within 1% of the design specification. Two possible sources of error for the height dimension are: LOM process-related error (likely due to platform motion and level control) and cure shrinkage in the direction of curvature. Due to the reinforcing fibers, it is unlikely that the second consideration is significant. Thus, additional study of the platform motion and control is needed. On the other hand, the laser gantry X Y motions seem to be highly accurate, as manifested by the small deviations in the length and width dimensions.

Table 1: Cumulative dimensional accuracy of glass fiber / epoxy "C" shell part made with Curved LOM / vacuum bag oven cure process.

Dimension	Target / Design Specification	Measured on Final Cured Part	Deviation
Length (inch)	5.00	4.98 ± 0.01	-0.4%
Width (inch)	4.818	4.775 ± .0003	-0.9%
Height (inch)	0.956	0.88 ± 0.01	-7.9%
Part Thickness (inch)	0.112	0.113 ± 0.003	+1.0%

Edge burning can clearly be seen on the PMC parts, due to charring from the cutting action of the CO₂ laser. Figure 6 shows a close-up of a laser cut line on the glass fiber / epoxy prepreg. The total laser kerf, including char zone, is about 0.5 mm. Previous studies have shown that this degradation can be minimized or eliminated only by using other types of lasers capable of photoablation [9]. The effect of the charred edges on the mechanical properties of the resulting panels is unknown.

In general, the fiber volume fraction in composite panels serves as a primary point of comparison. Based on the cured thickness, number of plies, prepreg fiber areal weight, and fiber theoretical density, the fiber volume fraction was calculated to be 44%. Given the method of consolidation, i.e. vacuum bag / oven cure, this result was promising. Furthermore, this number was moderately repeatable (41-45 volume%) for several flat and curved panels made from the same prepreg in a variety of sizes (2.5"x4" to 6"x6", 5 to 18 layers thick). In high performance aerospace applications, composites with fiber volume fraction of 60-70% are required. However, this usually necessitates the use of expensive autoclaves for consolidation and cure. Thus, the LOM / vacuum bag processing route seems to be a feasible method for quick, low-cost manufacture of reasonable quality PMC parts. If higher fiber volume fraction is desired, the uncured LOM laminates could be consolidated in an autoclave.

The interlaminar shear strength test [10] is widely used as a screening tool for PMCs. Flat panels of two different thicknesses were fabricated on the Curved LOM machine using the glass fiber / epoxy prepreg, followed by the vacuum bag / oven cure cycle as described above. Test coupons were cut from the cured panels using a diamond cutter. The test results are given in Table 2. It is often difficult to size the specimens such that a delamination/shear failure is observed in the test. In the present case, two different sized specimens failed in the proper mode, with almost identical match in the calculated interlaminar shear strength. Another specimen failed at a higher strength, but the observed failure mode was not shear. Thus, it would be prudent to report a value of approximately 3600 psi as the measured shear strength.

Table 2: shear strength results¹ for flat panel, glass fiber / epoxy composites fabricated with Curved LOM and vacuum bag / oven cure cycle.

Sample Set # (nominal width x thickness)	Bend Configuration	# layers in sample	Failure Mode	Short Beam Shear Strength (psi)	σ (4 samples each)
#1 (0.25"x0.07")	3 point (0.5" span)	10	Delamination	3637	328
#2 (0.375"x0.125")	3 point (1.0" span)	18	Delamination	3565	191
#3 (0.375"x0.125")	4 point (1.0" span)	18	Compression from pins	5838	732

¹ Span:depth ratio in all cases was ~ 8:1. Test conditions were 0.05 inches/minute crosshead speed, 0.25 inch diameter loading pins, and room temperature.

No manufacturer data was available on the shear strength properties of this prepreg. In general the highest performance composites, fabricated from structural resins and consolidated with autoclaves, have shear strength values as high as 12,000-18,000 psi. Possible reasons for the shear strength of the current material being lower than this are the following: the resin is inherently not suited for structural applications; vacuum bag consolidation does not lead to the highest possible fiber volume fraction; and the span:depth ratio (8:1) was larger than normally used in the short beam shear test (5:1), which will reduce the apparent shear strength. However, the normal use of the current material is in abrasion resistant, electrical applications, such as bearing insulation. It is thought that the shear strength is adequate for such applications.

RELATED RESEARCH

Significant related research has recently been completed that provides science-based tools to quantify the ability to laminate PMC preregs on the Curved LOM machine, predict layer compaction, and predict the extent of cure during LOM processing. These results are the subject of future publications [11, 12, 13]. This new approach will eliminate trial-and-error methods of determining the suitability of new materials in the Curved LOM process, as well as guide the user in determining machine operating conditions.

CONCLUSIONS

Hardware and software for the Curved LOM Process was upgraded to improve the ability for direct fabrication of polymer composite prototypes. A simple "C" shell was fabricated from a commercially available prepreg to demonstrate the new capabilities. The Curved LOM process was used to fabricate the "green" (uncured) part, and a vacuum bag / oven cure cycle was used to provide final consolidation and cure. The accuracy of the overall process was found to be good, as most dimensions

were within 1% of the design specification without incorporating shrinkage compensation factors. The interlaminar shear properties of the cured laminates was judged as acceptable for the normal applications of the material.

ACKNOWLEDGMENTS

The authors wish to thank Dr. William Coblenz (DARPA) and Dr. Steven Fishman (ONR) who have supported the development of Curved LOM over the past several years. Application of Curved LOM to polymer matrix composites was supported by a Research Challenge Grant from the Ohio Board of Regents. The authors would like to thank Mr. Jerry Fleeson of Lectromat, Inc. for donating the polymer prepreg used throughout the study. The authors would also like to acknowledge Mr. Don Byrge for mechanical testing advice and Mr. Gary Andrews for specimen preparation.

REFERENCES

1. Klosterman, D., R. Chartoff, N. Osborne, G. Graves, A. Lightman, G. Han, A. Bezzeredi, S. Rodrigues, "Development of a Curved Layer LOM Process for Monolithic Ceramics and Ceramic Matrix Composites," *Rapid Prototyping Journal*, Vol. 5, Issue 2, 1999.
2. Klosterman, D., R. Chartoff, N. Osborne, G. Graves, A. Lightman, G. Han, A. Bezzeredi, S. Rodrigues, "Development of a Curved Layer Process for Fiber-Reinforced Composite Materials," *Eighth European Conference on Rapid Prototyping and Manufacturing*, Nottingham, UK, July, 1999.
3. Klosterman, D., R. Chartoff, N. Osborne, G. Graves, A. Lightman, G. Han, A. Bezzeredi, S. Rodrigues, "Curved Layer LOM of Ceramics and Composites," *Solid Freeform Fabrication Symposium Proceedings*, University of Texas at Austin, Austin, TX, August, 1998, pp. 671-680.
4. Hayse, S. R., "RTM Aerospace Components Developed Using Rapid Prototype Tooling," *43rd International SAMPE Symposium Proceedings*, Anaheim, CA, May 31-June 4, 1998, pp. 1715-1723.
5. *CompositePro*, Peak Composite Innovations, 11372 W. Parkhill Dr., Littleton Colorado, 80127 USA.
6. *FiberSimTM*, Composite Design Technologies, Inc., 235 Wyman St., Suite 110, Waltham, MA 02451-1219 USA.
7. Product 95-147, Lectromat, Inc., P.O. Box 608, Mars, PA, 16046, USA.
8. According to *Standard Guide for Preparation of Flat Composite Panels with Processing Guidelines for Specimen Preparation*, ASTM Standard D5687 / D5687M-95.
9. Lightman, A., G. Han, "Laser Cutting of Ceramic Composite Layers," *Solid Freeform Fabrication Symposium Proceedings*, University of Texas at Austin, Austin, TX, August, 1996, pp. 291-298.
10. *Standard Test Method for Apparent Interlaminar Shear Strength of Parallel Fiber Composites by Short-Beam Method*, ASTM Standard D2344 - 84.
11. Popp, A., D. Klosterman, R. Chartoff, "Development of Science-Based Tools for Material and Process Considerations in Curved LOM, Part I: Application and Use of a Tack Test," *Rapid Prototyping Journal*, manuscript in development.
12. Bryant, E., D. Klosterman, L. Flach, R. Chartoff, "Development of Science-Based Tools for Material and Process Considerations in Curved LOM, Part II: Development and Verification of a Thermal / Cure Model" *Rapid Prototyping Journal*, manuscript in development.
13. Bryant, E., *Development and Verification of a Thermal and Kinetic Model for Curved-Layer Laminated Object Manufacturing of Polymer Matrix Composites*, M.S. Thesis, Chemical Engineering, University of Dayton, December, 1999.

ILLUSTRATIONS

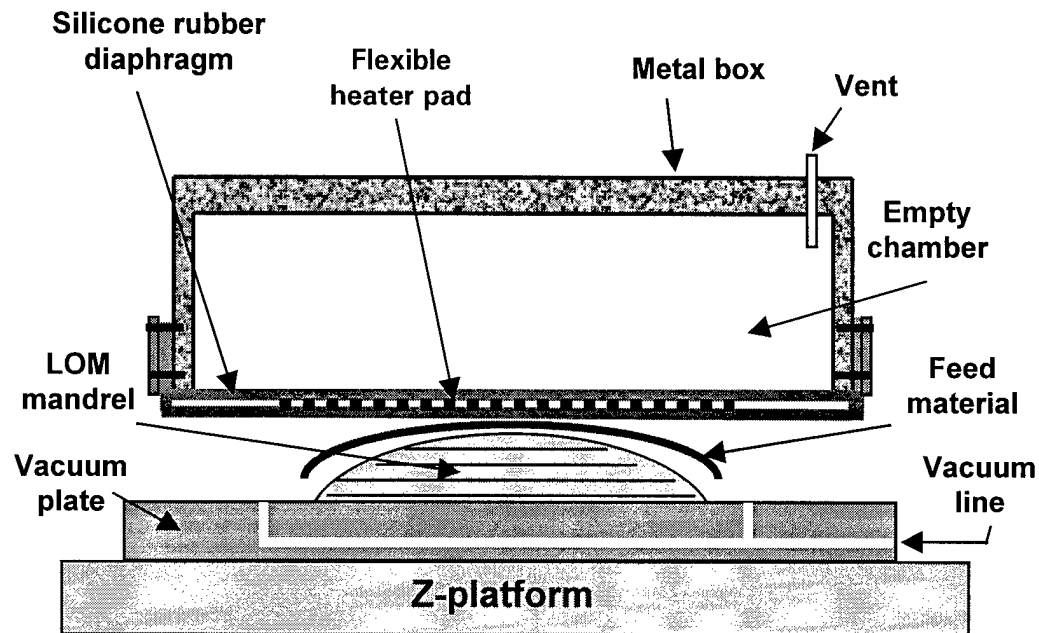


Figure 1: cross sectional schematic of Curved LOM laminator and platform.

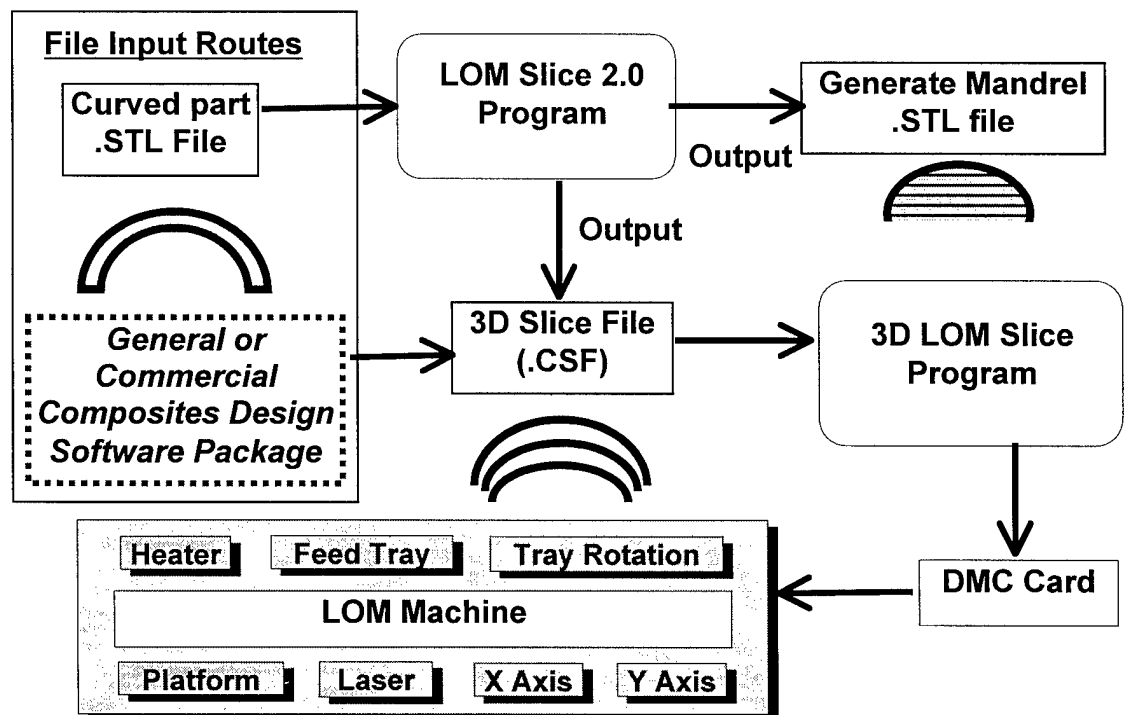


Figure 2: Interaction of software packages and file formats required for Curved LOM. The use of CSF files allows for direct use of general/commercial composite design software packages, by-passing the STL file.

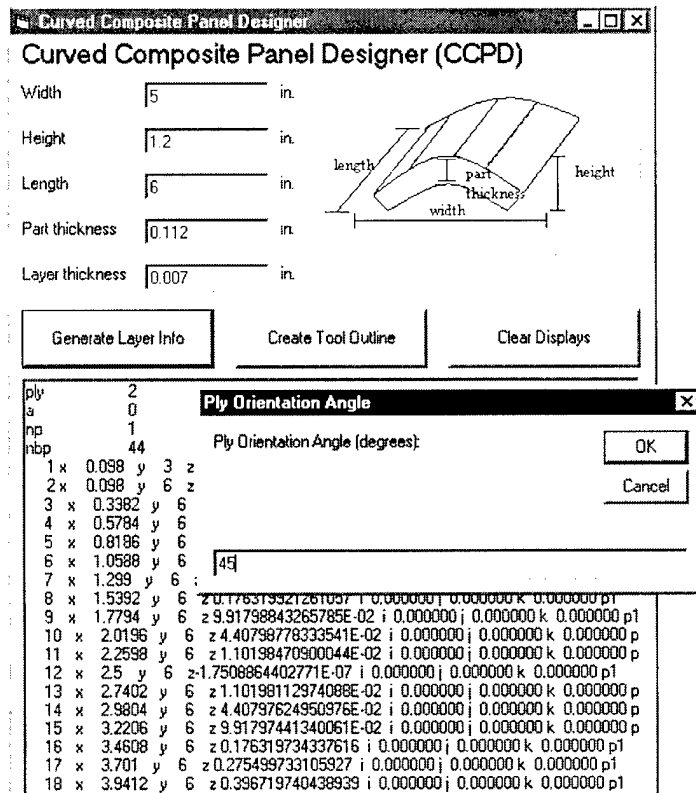


Figure 3: example of general composite design package, Curved Composite Panel Designer (CCPD), in which composite ply information is output as XYZ coordinates.

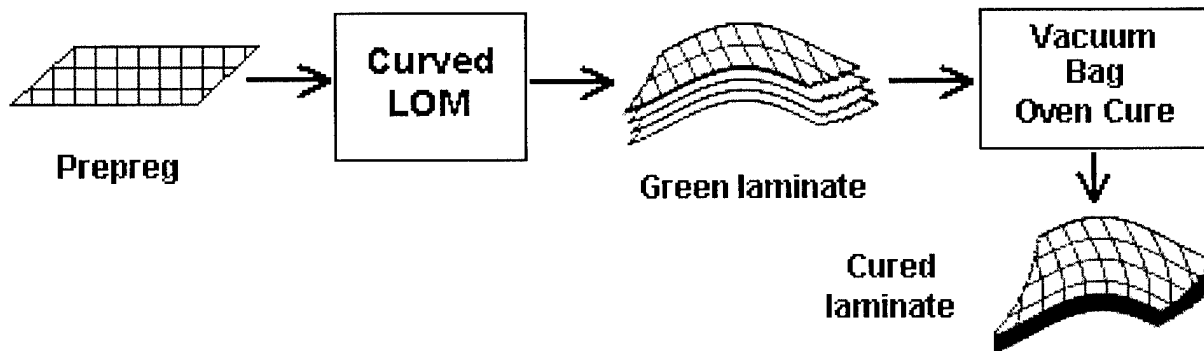


Figure 4: Curved LOM processing methodology for polymer composites, involving use of Curved LOM to form “green” (uncured) panels which are subsequently cured in a low-cost vacuum bag / oven cure cycle.

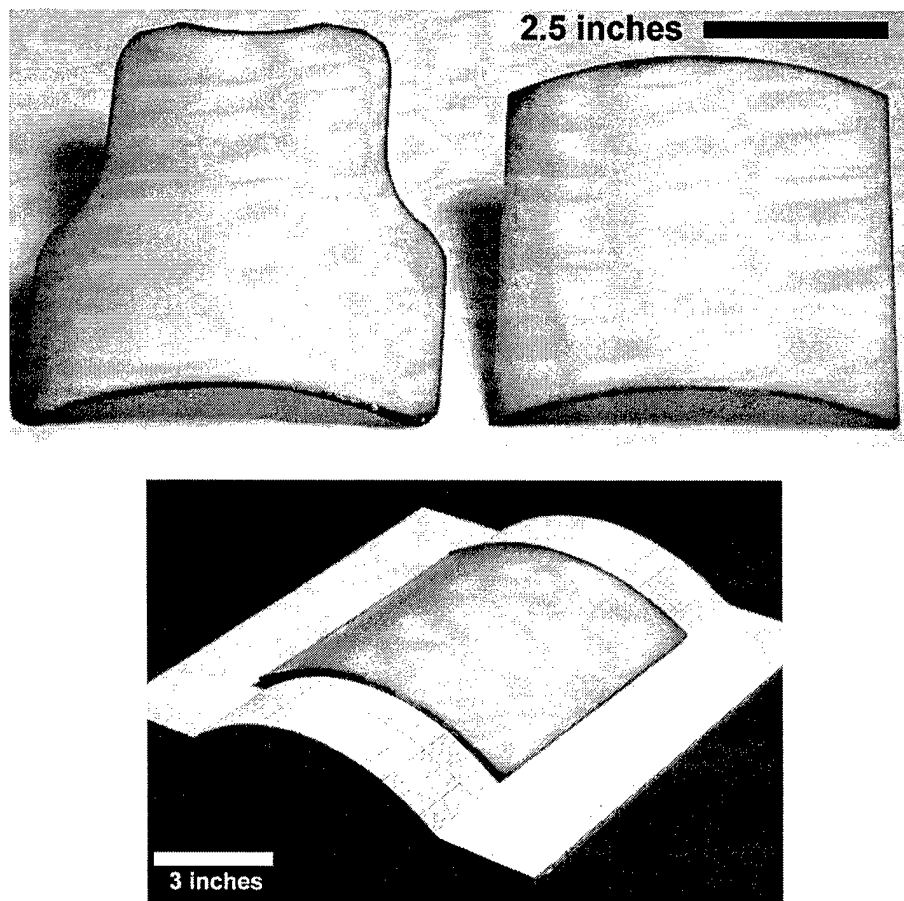


Figure 5: (above) cured, glass fiber/epoxy composite parts made with Curved LOM, and (below) cured, curved layer part resting on fresh LOM-paper mandrel.

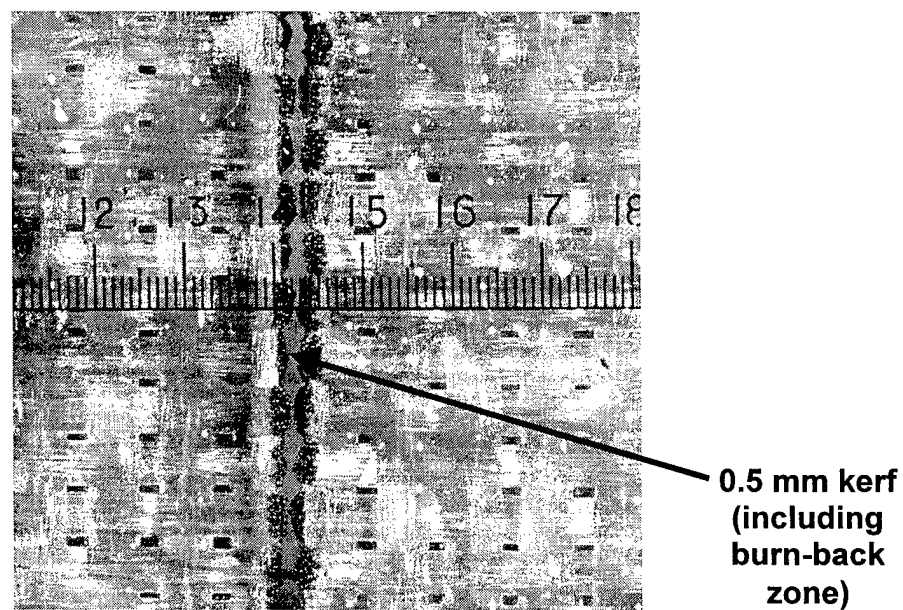


Figure 6: photomicrograph of glass fiber / epoxy prepreg cut with CO₂ laser on Curved LOM machine.

Low Shrinkage Metal Skeletons by Three Dimensional Printing

Emanuel Sachs¹, Samuel Allen², Costas Hadjiloucas¹, Jeannie Yoo³, Michael Cima²

¹Department of Mechanical Engineering, Massachusetts Institute of Technology, Cambridge, MA 02139

²Department of Materials Science and Engineering, Massachusetts Institute of Technology, Cambridge, MA 02139

³Imation Enterprises Corporation, 1 Imation Place, Oakdale, MN 55128-3414

Abstract

Three Dimensional Printing (3DP) is used to create metal parts by spreading a metal powder and printing a binder to define the geometry. In the currently used process a polymeric binder is used to define a green component. The polymer is burned out and the component lightly sintered to produce a skeleton. This sintering operation is causing $1.5 \pm 0.2\%$ shrinkage. The 3DP process can compensate for a given amount of predicted shrinkage by beginning with a larger part. However, the $\pm 0.2\%$ uncertainty in the value of shrinkage translates directly to the loss of dimensional control of the parts. Therefore, there is a need to improve the dimensional control of metal parts produced by 3D Printing.

The current work investigates the possibility of decreasing the average shrinkage by eliminating the sintering step. The concept under investigation is an alternative method of forming the skeleton where the metal needed to create the necks between powder particles is provided through the binder - a salt solution. The metal is obtained from the salt by means of a heat treatment in a reducing atmosphere. It was found that strong metallic bonding can be obtained by melting the metal or the alloy derived from the salt solutions resulting, essentially, in brazing of the powder particles. Injection molding tools were fabricated by printing a copper nitrate solution into a dry mixture of $66\mu\text{m}$ molybdenum and $1\mu\text{m}$ silver powder. The metal skeletons were infiltrated with epoxies. The shrinkage caused by the brazing step on the $66\mu\text{m}$ Mo powder is approximately 0.15% which compares favorably with the 1.5% shrinkage obtained by the standard sinter-based method. It was hypothesized that the shrinkage of this new binding method is due to the capillary forces induced by the molten metal necks. The traction force due to molten metal necks was modeled analytically and the compressibility of the powder was measured. The shrinkage determined by the equilibrium of these two effects match observed shrinkages well. The model suggests certain approaches to the further reduction of shrinkage, including attaining a higher packing fraction of the powder-bed.

1 Introduction

1.1 Background

Three Dimensional Printing (3DP) is a process for the rapid fabrication of three dimensional parts directly from computer models [1-3]. A solid object is created by printing a sequence of two-dimensional layers. The creation of each layer involves the spreading of a thin layer of powdered material followed by the selective joining of powder in the layer by printing binder material. The powder bed is lowered at the completion of each layer by lowering the bottom of

the rectangular cylinder which contains the powder bed allowing for the next layer of powder to be spread. Unbound powder temporarily supports unconnected portions of the component, allowing overhangs, undercuts and internal volumes to be created. The unbound powder is removed upon process completion, leaving the finished part (green part).

An important application of the 3DP is in the direct printing of injection molding tools. This application has two focus areas : i) the rapid fabrication (within a day or two) of tooling for a few hundred prototype parts and ii) the fabrication of production tooling which has unique capabilities such as cooling lines which are conformal to the molding cavity [4]. Direct printing of tooling involves the following steps:

- 1) Geometry Definition: A polymeric binder is printed into stainless or tool steel powder to create the green part within the powder bed. The loose powder is removed, thereby revealing the green part.
- 2) Formation of Skeleton: The green part is placed in a ceramic powder (alumina and zirconia powders are usually used) in order to support the green part during sintering. The polymeric binder is burned out in a furnace (at 500 °C) and the part is lightly sintered (at 1200 °C). The ceramic powder does not sinter at this temperature and it can be removed after the heat treatment. At the end of this step the parts are strongly bonded due to the formation of necks between powder particles during sintering.
- 3) Infiltration: The part is infiltrated with a copper alloy in a second furnace operation, typically performed at 1200 °C. At the end of this step the part is fully dense.
- 4) Finishing: The tooling is finished to achieve desired surface finish and dimension as required.

1.2 Motivation

Tools made by the process described above have been successfully finished and used to injection mold parts in large quantity. A primary issue with this process is that the dimensional control is approximately $\pm 0.2\%$ of the part dimension. The growth of the necks during the sintering step causes a shrinkage of the part which, in general, is not uniform and has a certain amount of error associated with it. As currently practiced, the magnitude of the shrinkage is 1.5% and the uncertainty is 0.2%. The 3DP process can compensate for a given amount of predicted shrinkage by beginning with a larger green part. However, the uncertainty in the value of shrinkage, translates directly to the loss of dimensional control of the parts. Therefore, there is a need to improve the dimensional control of metal parts produced by 3D Printing.

1.3 Approach to Eliminate Sintering

The current work investigates the possibility of decreasing the average shrinkage by eliminating the sintering step. The concept under investigation is an alternative method of forming the skeleton where the metal needed to create the necks between powder particles is

provided by adding it through the binder rather than relying on mass transport from the powder particles during the sintering operation.

Figure 1 illustrates one method that can be used to add metal through the printed binder: a salt solution is printed into the powder bed and then the entire (printed and un-printed) powder bed is fired at an appropriate temperature, resulting in the reduction of the salt to metal. After an appropriate heat treatment, the metal of the salt binds the printed powder.

The advantages of adding the metal by printing it in the binder include:

- 1) The elimination of the sintering step will most likely result in an average shrinkage significantly lower than the 1.5% of the current process. In addition, it is expected that the uncertainty (error) in shrinkage would be reduced commensurately.
- 2) The approach eliminates the need to burn out a polymer binder, a substantial convenience. Furthermore, some materials (i.e. titanium) are extremely sensitive to trace carbon left from the binder burn out.
- 3) The approach enables the firing of the printed parts in their original powder. Such a process eliminates the necessity to remove the green parts from their original powder bed and repack them in a ceramic powder. This is advantageous because the green parts are fragile and because the operation of packing the green parts in a ceramic powder-bed is difficult to do with reproducible results.

The following section discusses the formation of metallic skeletons bonded with necks derived from salt solutions and their application to the rapid fabrication of short run tooling. The shrinkage associated with the salt binding method and the experimental technique to measure it, is discussed in section 3. Section 4 presents a model for the shrinkage and provides direction for future work based on this model.

2 Metal Necks By Salt Reduction

2.1 Silver Carbonate on Mo Powder – Electrochemical Displacement Reaction

Silver carbonate (Ag_2CO_3) can be dissolved in an ammoniated solution of water. Droplets of a 0.3 molar solution of silver carbonate were placed onto 66 μm Mo powder. The solvent consists of 87 v.o % H_2O and 13 v.o % ammonium hydroxide (ACS, 29.6% NH_3).

Upon contact with the Mo powder, silver is deposited on the powder by means of an electrochemical displacement reaction (Mo transfers electrons to the metallic ions of the salt converting them to metal (silver)). Figure 2 shows a Scanning Electron Microscopy (SEM) picture of the powder after printing; silver appears to coat the powder surface uniformly. At this stage, the printed part has no strength; the silver is porous and does not adhere to the powder.

To obtain strong bonding, the printed part was fired at 1000 °C for one hour under forming gas (silver melts at 960.8 °C). Figure 3 shows an SEM picture of the powder after firing. Silver no longer covers the entire powder surface; it is randomly concentrated at various locations on the powder. Some of these locations are at the contact points of two adjacent powder particles and hold them together. The volume of the silver is calculated from the molarity of the solution and the volume fraction of the powder (about 60%) to be approximately 0.41% of the volume of the Mo powder. In this calculation it is assumed that the silver carbonate solution fills entirely the voids of the powder-bed. Silver carbonate, although less aggressive than silver nitrate, also causes irritation and silver staining of human skin and thus, continuous jet printing of silver carbonate is practical only as a research vehicle at this time.

2.2 Copper Nitrate on Mo Powder – Thermal Reduction

Noting that silver salts, in general, tend to cause skin irritation, attention was turned to copper salts. Copper nitrate solution was found not to cause skin burns or machine corrosion. The danger of inhalation posed by aerosol formation was mitigated by enclosing the 3D Printing machine and exhausting air from the enclosure through a ventilation system.

Droplets of a 0.43 molar water solution of copper nitrate ($\text{Cu}(\text{NO}_3)_2 \cdot 2\frac{1}{2}\text{H}_2\text{O}$) were placed onto 66µm Mo powder and the powder was fired under forming gas for one hour at 1100 °C. The salt melts at about 114 °C and it reduces to the solid copper oxide (CuO). In the presence of hydrogen, CuO reduces to copper at about 240 °C. At 1083 °C the copper melts and binds the Mo powder. Assuming that the volume fraction of the powder is 60% and that the copper nitrate solution fully saturates the voids of the powder-bed, the volume of the copper is approximated as 0.20% of the volume of the Mo powder. Figure 4 shows an SEM picture of the resulting Cu necks that bind the 66µm Mo powder. The copper shows a clear tendency to concentrate in the “neck region” forming a well-defined neck. This tendency can be attributed to capillary forces which drive the salt to the necks while it dries and while it is melted.

However, parts made by the 3DP process with Mo powder can not be fired at a temperature high enough to melt copper due to the onset of sintering of the Mo powder. Firing the parts at a temperature close to the melting temperature of copper causes extensive sintering of the copper which holds the powder particles together. Although the strength of such a bonding was expected to be less than the one where the copper had melted it was not known if it was sufficient to result in parts with good handleable strength. This question was answered by firing printed parts at 1000 °C (Figure 5). These parts were intended for use as short run injection molding tools. The handling strength of the part was not satisfactory. A similar part, fired at 1030 °C, was equally weak (in this case removing the loose powder was problematic since the firing temperature was above the powder's T_g). Therefore, heat treating the copper necks below the melting point of copper is not an option if parts with good handleable strength are to be produced.

The heat treatments described in the previous paragraph were done under a hydrogen atmosphere. Earlier attempts to fire the 2 in. x 3 in. x 7/8 in. part in a tube furnace under a forming gas atmosphere led to an incomplete reduction of the copper oxide. In particular, after

the forming gas heat treatment, the bottom-center portion of the part was black (the color of copper oxide). This incomplete reduction may be due to a slow diffusion rate of the hydrogen (of the forming gas) through the skeleton and/or due to a slow reduction rate.

2.3 Copper Nitrate and Silver Nitrate on Mo Powder – Forming an Alloy

To obtain necks that can be melted at temperatures less than the powder's T_s , printing a mixture of salt solutions from which a low melting temperature alloy can be derived, was considered. The following experiment demonstrates that strong bonding can be obtained by melting Ag-Cu alloy necks derived from a mixture of silver and copper nitrate salts.

The mixture used was a 2.21 molar AgNO_3 / 1.46 molar $\text{Cu}(\text{NO}_3)_2 \cdot 2\frac{1}{2}\text{H}_2\text{O}$ water solution (the solution was made by adding water to a mixture of 7.5g of AgNO_3 and 6.8g of $\text{Cu}(\text{NO}_3)_2 \cdot 2\frac{1}{2}\text{H}_2\text{O}$ to make a 20 ml solution). The copper to silver mass ratio in this solution is 0.39 which corresponds to the eutectic composition of the Ag-Cu system which has a melting temperature of 780 °C. Droplets of the solution were placed onto 31 μm Mo powder and the powder was fired at 850 °C for one hour in a forming gas atmosphere. During this heat treatment the copper and silver salts reduced to their metals, which form an alloy. The Ag-Cu alloy melts and forms necks that bind the Mo powder. Figure 6 shows an SEM picture of the resulting Ag-Cu neck. Assuming that the volume fraction of the powder is 60% and that the salts solution fully saturates the voids of the powder-bed, the volume of the Ag-Cu alloy is calculated as 2.2% of the volume of the Mo powder.

This solution reduces the firing temperature to the point where the T_s requirement is satisfied even for the 31 μm Mo powder. However, as noted previously, silver nitrate is extremely corrosive and hence, this material system is presented in this work as a point of reference for understanding and modeling shrinkage.

3 Shrinkage Measurements

Shrinkage usually occurs during drying of the binding solution and during firing. The former will be referred to as wet-dry shrinkage and the latter as dry-fired shrinkage. The shrinkage is measured by the following experimental technique.

3.1 Experimental Technique

A rectangular alumina tray is filled with powder and is struck 4-5 times in an attempt to obtain a packing density of the powder similar to that of the powder-bed in the printing machine (the piston that spreads the powder in the printing machine vibrates, while spreading, resulting in an increased packing density of the powder). Silicon carbide fibers (Textron Inc. of Lowell, MA) are then placed in the powder as shown in Figure 7. The fibers are approximately 5 mm long and

are placed approximately 25 mm apart; about 1 mm of the fibers extend above the powder. Using a pipette, the region between each pair of fibers is saturated with the binding solution [6].

The tray is then placed on a micrometer-driven x-y positioning stage with a resolution of $1\mu\text{m}$, which is under an optical microscope. By moving the x-y stage and focusing on the fibers, the two perpendicular components (Δx and Δy) of the distance between the two fibers are measured and they are used to calculate the fiber-to-fiber distance. The diameter of the SiC fibers is $140\mu\text{m}$ and there is an inner carbon core of diameter $33\mu\text{m}$ within the fiber which is distinctly visible. The crosshairs of the optical microscope can be positioned at the center of this circle with repeatability of $5\mu\text{m}$ or less.

With the optical microscope and micrometer stage, each Δx and Δy measurement is reproducible to within $5\mu\text{m}$. In the worst case, this results in an error of approximately $10\mu\text{m}$ in the fiber-to-fiber distance; therefore it results in an error of $\pm 20\mu\text{m}$ in a shrinkage measurement (which consists of two distance measurements). For a 25 mm sample, this is an error of about $\pm 0.1\%$. As discussed below, the measurements were seen to be more reproducible than this rough estimation would indicate.

3.2 Results

Table 1a lists various shrinkage measurements. Data is presented for two powder materials, Mo and, for reference, alumina, a ceramic powder. In all cases, the powders are spherical and made by plasma melting. The alumina powder was chosen as a reference because it is available in spherical form in the proper size range, and because it is inert to water, a property that may not be shared by metals. Two sizes of Mo powder are used, a $66\mu\text{m}$ average and a smaller powder, which ranges in size from 25-38 μm (denoted as 31 μm Mo powder). Shrinkage measurements were made with water alone, copper nitrate salt solution, silver carbonate salt solution, and copper-silver nitrate salt solution. Firing temperatures were chosen appropriate to the size of the Mo powder and the metal of the salt solution. As a result, not all combinations were tested. For example, only the copper silver salt solutions were tested for the smaller Mo powder because the lower sintering temperature of the small powder prevents its use with copper or silver alone. The multiple values for every powder-binder combination correspond to measurements from different samples. Table 1b lists the average and the sample standard deviation of the measurements shown in Table 1a.

As may be seen from these Tables, the results for the $66\mu\text{m}$ powder support the hypothesis that adding metal by printing through the binder can lead to low shrinkage systems in 3D Printing. In particular, the wet-to-dry shrinkage for $66\mu\text{m}$ Mo powder averages 0.03% over the two salts tested and this result may represent primarily measurement noise. Further, the dry-to-fired shrinkage averages 0.15% over the three salts tested. This result compares favorably with the 1.5% shrinkage typical in the standard process.

Nonetheless, the shrinkage for $66\mu\text{m}$ Mo powder is clearly non-zero. Further, it is noted that the smaller Mo powder exhibits significantly higher shrinkages, both in the wet-to-dry

shrinkage and in the dry-to-fired shrinkage. With the goal of understanding this shrinkage behavior and, hopefully, of controlling it and further reducing its magnitude, a modeling effort was undertaken.

4 Modeling Of Shrinkage Caused By Liquid Necks

4.1 Mechanism Causing Shrinkage

Liquid necks impose attractive forces on neighboring powder particles and attempt to pull them closer together. On the other hand, the powder particles are not entirely free to move because they are mechanically constrained by their adjacent neighbors (Figure 8). Relative movement of the powder particles (and consequently shrinkage) occurs only when the attractive forces overcome the inter-particle friction of the powder. Therefore, shrinkage can be viewed as an equilibrium among the attractive forces between powder particles due to the liquid necks and the stiffness of the powder bed.

The shrinkage mechanism was investigated by independently studying the compressibility properties of the powder and the attractive forces induced by the liquid necks. This approach is analogous with the one used by Charnnarong [7] to study the shrinkage mechanism of alumina powder printed with colloidal silica. In that case, the attractive force was caused by the gelling and consolidation of the colloidal silica during drying and sintering.

In the following section, the attractive force, F , induced by the liquid necks is quantified. In section 4.3 we calculate an equivalent external isostatic pressure, P_{eq} , which when applied to a collection of spherical particles results in inter-particle forces approximately equal to F . In section 4.4 we measure the compressibility of loose powder under external isostatic pressure. In section 4.5 the compressibility measurements are combined with the calculations of P_{eq} to predict the shrinkage that should be expected due to the presence of liquid necks.

4.2 Attractive Forces Between Spherical Powder Particles Induced by Liquids in the Necks

Figure 9, shows two spherical particles of radius R , held together by a liquid neck. The inter-particle force, F , due to capillary action of the liquid neck has two contributions, one due to the pressure difference caused by surface curvature and one due to the surface tension itself. As will be shown, the inter-particle force is relatively insensitive to the amount of liquid present, especially for small amounts of liquid. If the amount is increased from zero, the force due to the pressure difference starts out as attractive and decreases as more liquid is added, eventually becoming repulsive. At the same time, as liquid is increased from zero, the force due to surface tension starts out at zero and progressively increases, always being attractive between particles. Thus, as liquid is added to the necks, the two forces tend to compensate for one another, resulting in a force that is relatively constant with the amount of liquid.

Heady and Cahn [8] solved numerically the problem of capillary forces imposed on spherical particles by liquid necks, (they also solved the equivalent problem for the case of jagged particles

[9]). They used numerical means to solve for the shape of the liquid surface. Their results, are summarized in Figure 10. The attractive force is plotted as a function of the volume of the liquid neck, V , for different contact angles. The force, and the volume are non-dimensionalized by $R\sigma$ and R^3 respectively. F^* decreases monotonically with V^* from its maximum value at infinitesimal liquid volumes. F^* also decreases with increasing contact angle. For the case of $\theta = 0$, and small liquid volumes, the case of interest here, the attractive force can be approximated as:

$$F = 2 \pi \sigma R. \quad (4.1)$$

4.3 Calculation of Equivalent Pressure

An estimate needs to be found of the equivalent external pressure, P_{eq} , that when applied isostatically to a balloon filled with spherical particles of radius, R , will result in an inter-particle force, F . Such an estimate can be obtained by making a simplified assumption on the way spheres arrange themselves when they are poured into a balloon. For the purposes of this calculation, it is important that the assumed arrangement will correspond to a coordination number (the number of other particles in contact with a given particle) and a packing fraction close to that obtained when uniform size spheres are poured into a balloon. It was found [10] that lead shot with a particle size of 3.78 mm poured into a glass beaker have a packing fraction equal to 55.3% and a coordination number equal to 6.92. A simple-cubic arrangement has a packing fraction of 52% and coordination number of six. It is therefore expected to give a reasonable estimate of P_{eq} . By dividing the sum of the forces acting on a side (the (100) crystallographic plane) of the cubic cell (F) by the area of the side of the cube ($4R^2$), P_{eq} is calculated as:

$$P_{eq} = F/(4R^2) \quad (4.2)$$

The same value is obtained by summing the forces acting on the diagonal plane of the cubic cell (the (110) crystallographic plane) and dividing by the corresponding area.

Therefore, by substituting equation (4.1) into equation (4.2) we find,

$$P_{eq} = \pi \sigma / (2R) \quad (4.3)$$

Table 2 shows the values of P_{eq} for different powders and liquid necks as calculated from equation (4.7). The following values for surface tension were used: $\sigma_{water} = 0.073$ N/m, $\sigma_{Ag} = 0.893$ N/m, $\sigma_{Cu} = 1.301$ N/m, and $\sigma_{Ag-Cu [71.9:28.1]} = 1.008$ N/m. The surface tension of the Ag-Cu alloy can be calculated [12] from the values of the surface tension of the silver and the copper by means of an additive rule (mass fraction of Ag $\times \sigma_{Ag}$ + mass fraction of Cu $\times \sigma_{Cu}$).

4.4 Compressibility of Loose Powder

4.4.1 Response of Loose Powder to an External Isostatic Pressure

There are two mechanisms involved in the isostatic deformation of loose powder; (i) rearrangement-restacking of the particles, and ii) elastic-plastic deformation. Particle rearrangement and restacking takes place at low pressure as particles slide relative to one another and reorder into a tighter formation [7]. The elastic-plastic deformation mechanism is not relevant to this study because it occurs at pressures above those listed in Table 2. The rearrangement and restacking response of loose powder to an external pressure is expected to depend on the powder's shape, size, size distribution, surface characteristics and initial packing fraction. The complexity of the problem makes it intractable to any analytical investigation and points to an experimental study.

4.4.2 Experimental Set-Up

The compressibility of loose powder is measured by placing the powder in a balloon, applying an external isostatic pressure to it and measuring its change of volume. Figure 11 shows a sketch of the experimental set-up. The external isostatic pressure is created by generating a vacuum inside the balloon. A tube is attached to a balloon. The tube has a filter at its end, which prevents the passage of water and powder but allows the passage of air. The balloon is submerged in water; the volume change of the balloon is determined by recording the surface level of the water.

The linear shrinkage, S_L , is calculated from the measured volumetric shrinkage, $S_V = \Delta V_p / V_o$, according to the relationship:

$$S_L = 1 - (1 - S_V)^{1/3}.$$

The maximum pressure (1 atm.) that can be obtained with this experimental set-up is sufficient for the needs of this study (see Table 2).

4.4.3 Measurements

Figure 12, shows the percentage linear shrinkage of 31 μm and 66 μm Mo powders as a function of pressure for different initial packing fractions. The finer powder is more compressible than the larger one. It can be seen that the compressibility of the powder depends strongly on the initial packing fraction. Powder which starts with a higher initial packing density is stiffer. A higher initial packing fraction indicates a more stable particle arrangement and consequently higher resistance to rearrangement. The initial packing fraction of the 31 μm Mo powder tends to be less than that of the 66 μm powder. This behavior can be attributed to the larger surface area of the smaller powder which results in higher inter-particle adhesion and friction and consequently to higher resistance to tighter packing.

The initial packing fractions obtained with this experimental set-up are close to that obtained by pouring the powder in a graduated cylinder and striking the cylinder a few times. For instance, 66 μm Mo powder was poured into a graduate cylinder and its packing fraction was measured as 57.1%. After the cylinder was manually struck 4-5 times, its packing fraction was measured as 60.2% (the powder was then tapped causing an increase in its packing fraction to 63%). Therefore, it is expected that the packing fractions involved in the compressibility measurements are comparable to those involved in the shrinkage measurements of section 3 (the powder was struck before taking the shrinkage measurements).

4.5 Combination

The compressibility measurements, combined with the analysis of section 5.2 and 5.3 can be used to predict the shrinkage caused by liquid necks. Figure 13 shows the compressibility measurements of the 66 μm Mo powder for three different initial packing fractions.

Four vertical lines are drawn to identify the P_{eq} that correspond to water (1.7 KPa), silver (21.2 KPa), silver/copper eutectic alloy (24.0 KPa) and copper (30.9 KPa) necks; these values are taken from Table 2. The intersections of these lines with those of the compressibility measurements can be used to predict the shrinkage caused by the related liquid necks. The $P_{\text{eq}} = 1.7$ KPa line predicts that the shrinkage caused by water necks, will be less than 0.05% for all three initial packing fractions. For comparison, the wet-dry shrinkage measurements of the water-printed 66 μm Mo powder (taken from Table 1a) are superimposed on the figure as the marks on this vertical line. The $P_{\text{eq}} = 30.9$ KPa line predicts that the shrinkage caused by liquid copper necks will range from 0.12% to 0.17% depending on the initial packing fraction. The marks on this line represent the dry-fired (1100 $^{\circ}\text{C}$) shrinkage of the copper nitrate printed 66 μm Mo powder and they illustrate the proximity between predicted and measured shrinkage. The same consistency is found for the cases of silver and silver/copper necks.

Figure 14 shows the compressibility measurements of the 31 μm powder. The two vertical lines identify the P_{eq} that correspond to water (3.7 KPa) and silver/copper (51.1 KPa) necks. The marks on these lines, which identify the measured shrinkage (see Table 1a) caused by water and silver/copper nitrates, are close to the predicted values of shrinkage.

A note should be made on the effect of the liquid salts on shrinkage. Although the surface tension of the melted salts under consideration are not known, they are expected to be close to that of water [12]. Therefore they are expected to cause shrinkage similar to that of water during drying. This expectation was verified by measuring the dry-fired (300 $^{\circ}\text{C}$) shrinkage of the copper nitrate printed 66 μm Mo powder and the dry-fired (490 $^{\circ}\text{C}$) shrinkage of the copper/silver nitrate printed 31 μm Mo powder (Table 1a). These heat treatments were carried out at temperatures higher than the melting point of the salts.

The larger shrinkage of the 31 μm Mo powder, compared to that of 66 μm Mo powder, caused by water and silver/copper necks, can be explained by the fact that the former powder is

more compressible than the latter (Figure 12) in combination with the fact that the P_{eq} is inversely proportional to the size of the powder. Finally, it should be noted that the wet-dry water shrinkage of the 31 μ m Mo powder is larger than that of the 30 μ m alumina powder (see Table 1); this deviation can be explained by a possible reaction between the water and the Mo powder.

5 Conclusion

Salt solutions can be used by 3D Printing to produce metal skeletons. With the appropriate heat treatment, the metal of the salt can form metallic necks that bind the powder particles; melting the metal (or alloy) of the salts is critical to obtain strong skeletons. The average shrinkage caused by silver, copper and silver-copper necks on the 66 μ m Mo powder is ~0.15% and the shrinkage caused by the silver-copper necks on the 31 μ m Mo powder is 0.35%. These shrinkages compare favorably with the 1.5% shrinkage obtained by the standard sinter-based method. To fully evaluate the potentials of these systems in improving the dimensional control of the printed parts, the uncertainty associated with these shrinkages should be determined.

Issues concerning operator safety and damage to the machine, restrict the type of salt solutions that may be used in a given type of ink-jet printhead. Improved automation of the printing machine combined with the use of corrosion resistant materials are expected to mitigate the effect this restriction. However, even the highly corrosive silver salts can be used in Three Dimensional Printing when dispensed by a drop-on-demand printhead, where the volume of material dispensed is small and easily controlled. Despite its health hazards, the copper nitrate solution may be practically applied to 3DP with minor modifications on the printing machine. This solution was printed into a Mo/Ag powder bed and injection molding tools were fabricated which suggest that this material system can potentially be used to fabricate parts with good surface finish and good handle-able strength.

It was hypothesized that the capillary forces induced by the liquid necks was causing a shrinkage of the metal skeleton. By studying independently the compressibility of the powder and the capillary forces, sufficient support for this hypothesis was found. The compressibility of the powder was determined by applying an external isostatic pressure on a balloon filled with loose powder and measuring its change of volume. The force between spherical powder particles induced by liquid necks was determined analytically assuming a circular profile for the liquid meniscus.

This study also explains the difference in the shrinkage between the 31 μ m and 66 μ m Mo powder. The compressibility measurements indicate that the shrinkage caused by liquid necks can be drastically reduced by increasing the packing fraction of the spread powder.

References

- [1] Sachs, E. Haggerty, J., Williams, P., and Cima, M., *U.S. Patent*, 5204055, 1993.

- [2] Sachs, E, Cima, M., Williams, P., Brancazio, D., and Cornie, J., "Three Dimensional Printing: Rapid Tooling and Prototypes Directly From a CAD Model", Journal of Engineering for Industry, Vol 114, No. 4, November 1992, p. 481-488.
- [3] Sachs, E., Cima, M., Bredt, J., Curodeau, A. "CAD-Casting: The Direct Fabrication of Ceramic Shells and Cores by Three Dimensional Printing", Manufacturing Review, Vol 5, No 2, June 1992, p. 118-126.
- [4] Sachs, E., et al. "Injection Molding Tooling by Three Dimensional Printing.", Rapid Prototyping and Manufacturing '96, Dearborn MI, Rapid Prototyping Association of SME, 1996.
- [5] Sachs, E., Hadjiloucas, C., Allen, S., Yoo, H., "Metal and Ceramic Containing Parts Produced From Powder Using Binders Derived From Salt," Patent Pending.
- [6] Yoo, H., "Reactive Binders for Metal Parts Produced by Three Dimensional Printing," M.S. Thesis, Massachusetts Institute of Technology, Cambridge, 1997.
- [7] Charnnarong, J., "The Drying Shrinkage in Three Dimensional Printing and its Dependence on the Properties of the Powder and the Binder," Ph.D. Thesis, Massachusetts Institute of Technology, Cambridge 1996.
- [8] Heady, R. B., Cahn, J. W., "Analysis of the Capillary Forces in Liquid-Phase Sintering of Spherical Particles," Journal of the American Ceramic Society, vol. 1, January 1970 [7], p. 185-189.
- [9] Cahn, J. W., Heady, R. B., "Analysis of the Capillary Forces in Liquid-Phase Sintering of Jagged Particles," Journal of the American Ceramic Society, vol. 53, January 1970 [7], p. 406-409.
- [10] ASM Handbook, Vol. 7. Powder Metallurgy, p. 296.
- [11] R. K. McGeary "Mechanical Packing of Spherical Particles," Journal of the American Ceramic Society, vol. 44, 1961, p.513.
- [12] "Surface Chemistry" Bikerman, Second Edition.

Tables and Figures

	Water	$\text{Cu}(\text{NO}_3)_2$	Ag_2CO_3	Cu/Ag Nitrates
31 μm Mo				
wet-dry:	0.08; 0.08; 0.11			0.04; 0.08; 0.05
dry-490 °C				0.03; 0.05
dry-850 °C				0.36; 0.35; 0.35
66 μm Mo				
wet-dry:	0.01; 0.02; 0.02	0.01; 0.04; 0.02; 0.05	0.00; 0.06; 0.02	
dry-300 °C		0.02; 0.01; 0.03		
dry-1000 °C			0.13; 0.15; 0.11	0.12; 0.17; 0.14
dry-1100 °C		0.17; 0.17; 0.18		
30 μm Alumina				
wet-dry:	0.02; 0.02; 0.03			

Table 1a Percentage Linear Shrinkage: Wet-dry is the shrinkage due to drying and dry-fired is the shrinkage due to firing. The multiple values for each powder-binder combination correspond to different measurements

	Water	$\text{Cu}(\text{NO}_3)_2$	Ag_2CO_3	Cu/Ag Nitrates
31 μm Mo				
wet-dry:	0.09 ± 0.02			0.06 ± 0.02
dry-490 °C				0.04 ± 0.01
dry-850 °C				0.35 ± 0.01
66 μm Mo				
wet-dry:	0.02 ± 0.01	0.03 ± 0.02	0.03 ± 0.03	
dry-300 °C		0.02 ± 0.01		
dry-1000 °C			0.13 ± 0.02	0.14 ± 0.03
dry-1100 °C		0.17 ± 0.01		
30 μm Alumina				
wet-dry:	0.02 ± 0.01			

Table 1b The results of Table 1a are presented here as: average \pm sample standard deviation

	Equivalent Pressure [KPa]			
	Water	Ag	Cu	Ag/Cu
31 μm Mo	3.7			51.1
66 μm Mo	1.7	21.2	30.9	24.0
30 μm Alumina	3.8			

Table 2 Equivalent Pressure

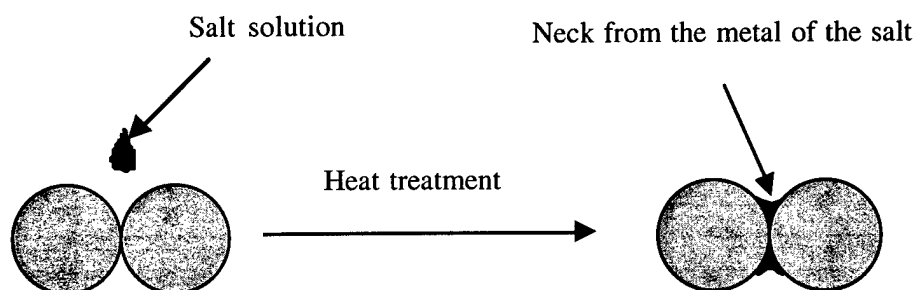


Figure 1 Principle of the Salt Binding Method

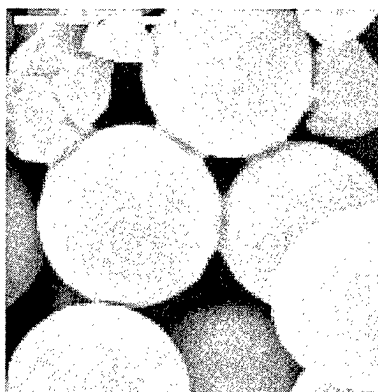


Figure 2 Mo Powder Printed with Silver Carbonate

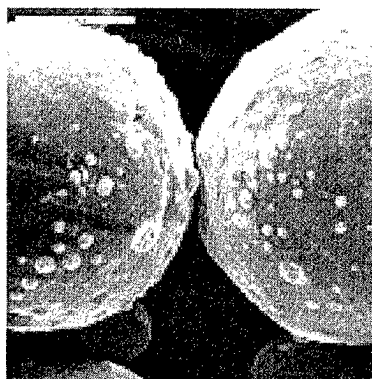


Figure 3 Mo Powder Printed with Silver Carbonate and Fired at 1000°C



Figure 4 66 µm Mo Powder Printed with Copper Nitrate and Fired at 1100 °C

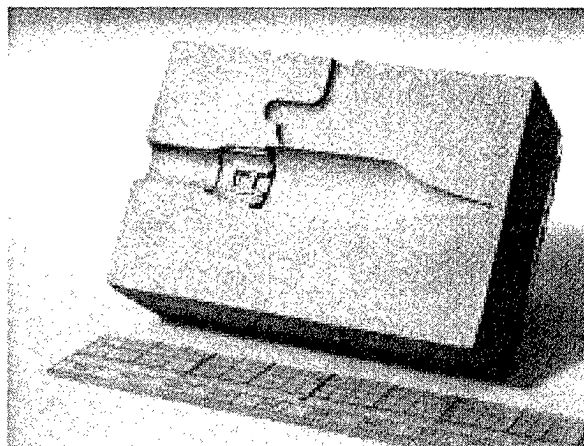


Figure 5 Mo-Cu Injection Molding Tool

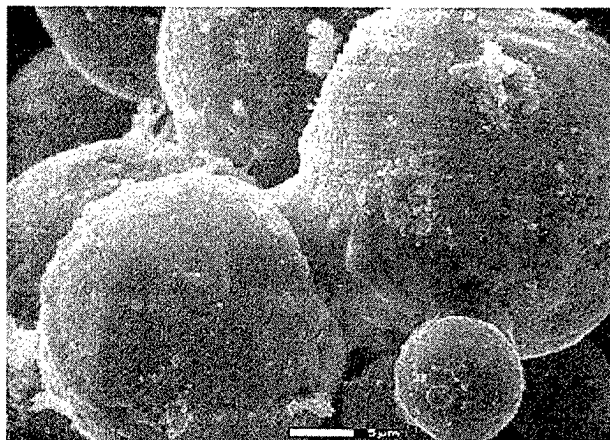


Figure 6 31µm Mo Powder Printed with Silver Nitrate and Copper Nitrate and Fired at 850°C

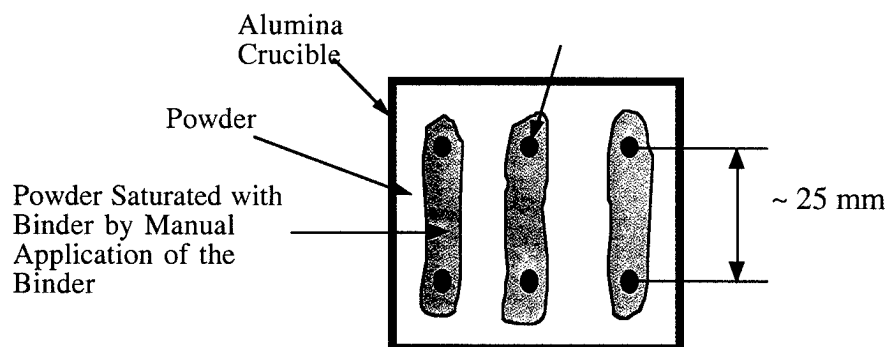


Figure 7 Shrinkage Test Set-Up

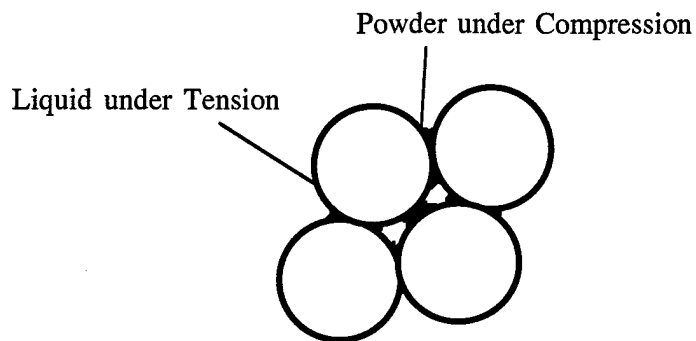


Figure 8 Liquid Necks Attempt to Pull Neighboring Particles Closer Together; Contiguous Particles Resist this Motion.

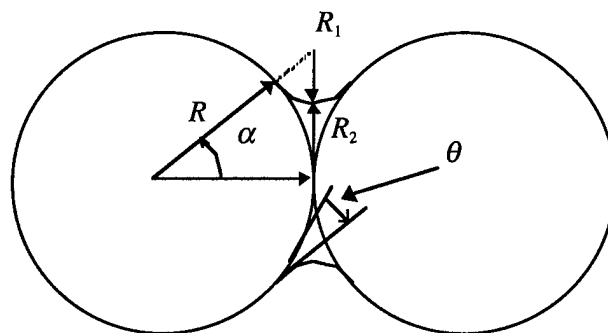


Figure 9 Liquid Neck between Spherical Particles

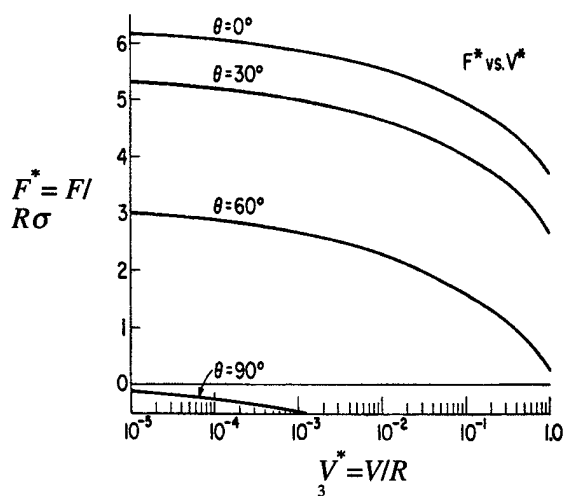


Figure 10 Interparticle Force as a Function of the Volume of the Liquid Neck; Taken from Heady and Cahn Study [8]

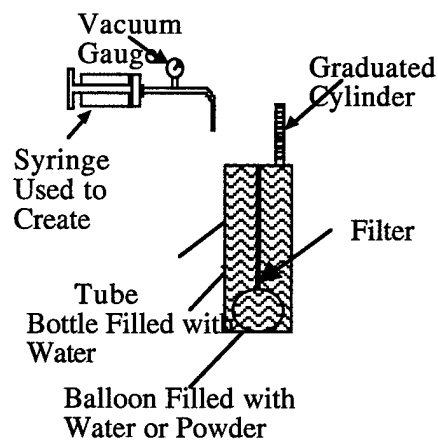


Figure 11 Experimental Set-up Used to Measure the Compressibility of Loose Powder

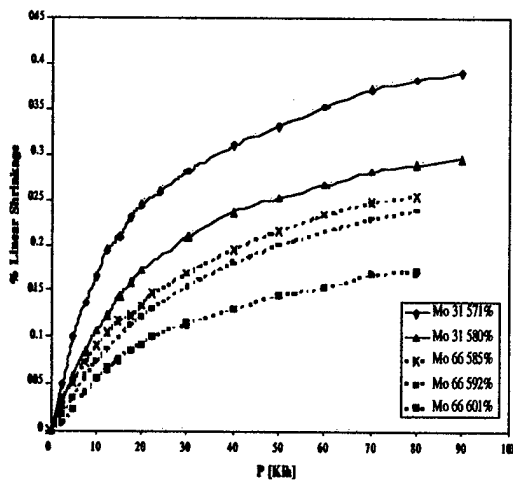


Figure 12 Compressibility Measurements of the 31 μ m and 66 μ m Mo Powder

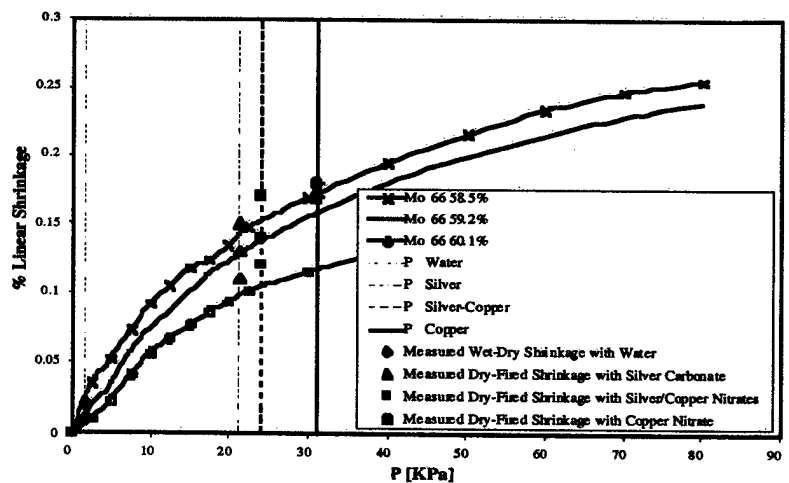


Figure 13 Predicted and Measured Shrinkage of the 66 μ m Mo Powder

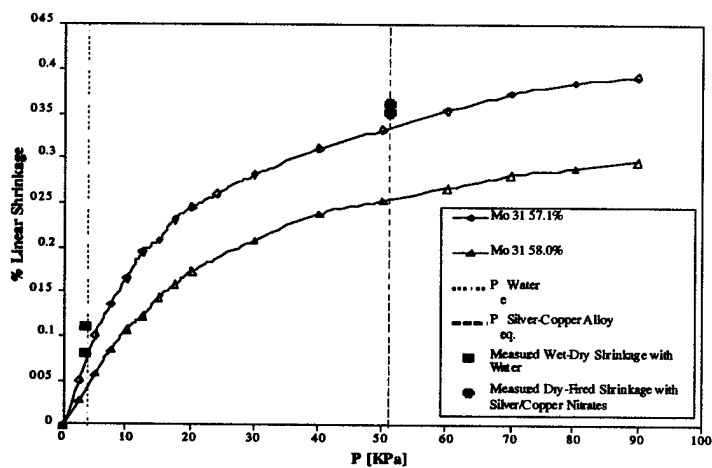


Figure 14 Predicted and Measured Shrinkage of the 31 μ m Mo Powder

Fabrication of High Quality Ceramic Parts Using Mold SDM

S. Kang¹, A. G. Cooper¹, J. Stampfl¹, F. Prinz¹, J. Lombardi², L. Weiss³, J. Sherbeck⁴

1. Stanford University, Stanford CA,
2. Advanced Ceramics Research, Tucson AZ,
3. Carnegie Mellon University, Pittsburgh PA,
4. M-DOT Inc., Phoenix AZ

Abstract

Mold Shape Deposition Manufacturing (Mold SDM) is being developed in order to fabricate complex structural ceramic parts such as components for miniature turbine engines. For this application, the ceramic parts must not only be strong, but they also must have high dimensional accuracy and superior surface quality. This paper presents current progress with process development and characterizes fabricated silicon nitride (Si_3N_4) parts including their surface quality, part density, isotropic shrinkage and build rate. The microstructure of the sintered parts has been characterized. Mechanical testing gave flexural strength values ranging from 400 to 800 MPa. The isotropic linear shrinkage of $18 \pm 0.5\%$ and best RMS surface roughness of $0.45 \mu\text{m}$ was observed. A number of process improvements that lead to better quality parts will also be described.

Introduction

Micro-turbine engines (Figure 1) are attractive because their power density is expected to increase with decreasing size. Power density is proportional to the 'thrust to weight' ratio, a key performance parameter of any thrust producing engine. However, as engine size decreases efficiency may decrease as well. This is caused by additional friction losses stemming from an enlarged surface to volume ratio at smaller scales. To retain engine efficiency at acceptable levels operational temperatures can be elevated. However, the latter is limited by the high temperature properties of engine materials such as nickel based alloys. To further increase engine efficiency ceramic materials have been considered.

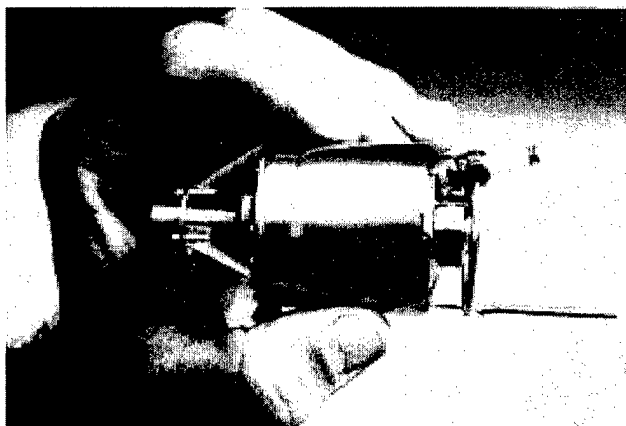


Figure 1. M-DOT micro-turbine engine

From the range of available engineering ceramic materials silicon nitride (Si_3N_4) is an excellent candidate for the small turbine engine application because of the lower density in comparison to super alloys and superior high temperature properties such as high strength, good

creep, and chemical resistance. Low CTE and moderate thermal conductivity of Si_3N_4 deliver acceptable thermal shock resistance and enable maintaining adequate temperature gradients for steady state engine operation.

Requirements

Ceramic engine components must have high dimensional accuracy and exhibit high strength at elevated temperatures. The overall part strength is a function of not only inherent material properties, but also of surface finish. Today's Solid Freeform Fabrication (SFF) methods can produce ceramic parts with complex shapes, but limited surface quality. In particular, SFF processes generate 'stair-steps' on inclined surfaces. Stair-steps reduce the benefits of ceramic materials in two ways. First, they make the inclined surfaces rough. Surface discontinuities give rise to stress concentrations and hence may reduce overall part strength. Second, traditional SFF processes are accompanied by a loss of dimensional accuracy. Inclined surfaces formed with stair-steps represent only an approximation of desired geometry, within a certain deviation h (Figure 2). Some stair-steps can be removed by post processing of the ceramic parts such as machining of green or sintered parts. However, this may not always be feasible due to limited tool accessibility and challenges associated with accurately fixturing and indexing complex part shapes.

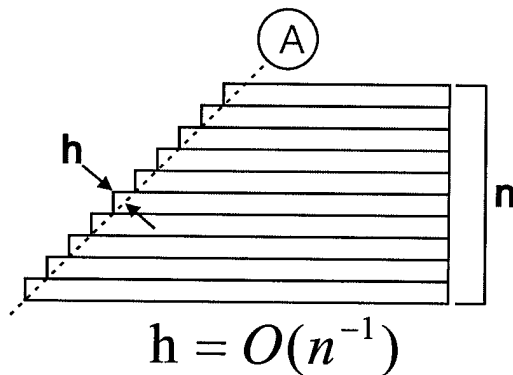


Figure 2. Inclined surface formed with layers of constant thickness converges to surface A with the rate of n^1 (n : number of layers)

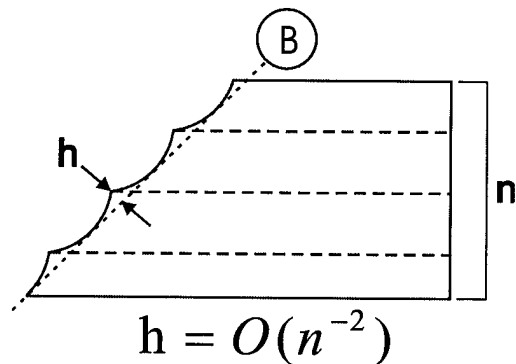


Figure 3. Inclined surface shaped with ball endmill converges to surface B with the rate of n^2 (n : number of machining path)

An inclined surface shaped by conventional CNC machining using a ball endmill (Figure 3) has advantages in strength and dimensional accuracy over the one formed by layers of constant thickness (Figure 2). In Figure 2 and 3, h is the deviation from the designated surface, which can be considered as measure for surface roughness and dimensional accuracy. Assuming surfaces A and B have the same h (i.e., have similar surface roughness), surface A is formed with sharp concave corners that induce high stress concentrations, while surface B is formed with smoother surfaces that exhibit lower stress concentrations. Surface B is less susceptible to failure at a given stress level and can preserve the inherent strength of the ceramics material. Also, the convergence rate of h to the designated surface is faster for surface B (n^2) than for surface A (n^1). Therefore, CNC machining can improve dimensional accuracy more efficiently than layered manufacturing.

While traditional ceramics fabrication processes, such as machining of green ceramic blanks, can produce parts with good surface quality, they have limitations in achievable shape

complexity. Mold SDM is an additive-subtractive process that combines the advantages of layered manufacturing and CNC milling process in order to produce parts of high shape complexity with high surface quality. This paper presents current efforts made in Mold SDM to build quality ceramic parts.

Mold SDM Process

Shape Deposition Manufacturing (SDM) is a layered manufacturing process involving an iterative combination of material addition and material removal. Parts are built up within a sacrificial support material that encases each layer to provide a platform for deposition of the next layer and to support overhanging part geometry features. Unlike most other SFF techniques which decompose models into thin 2-1/2 dimensional layers, SDM retains a three dimensional representation of the parts so that parts are built without stair-steps [1, 2].

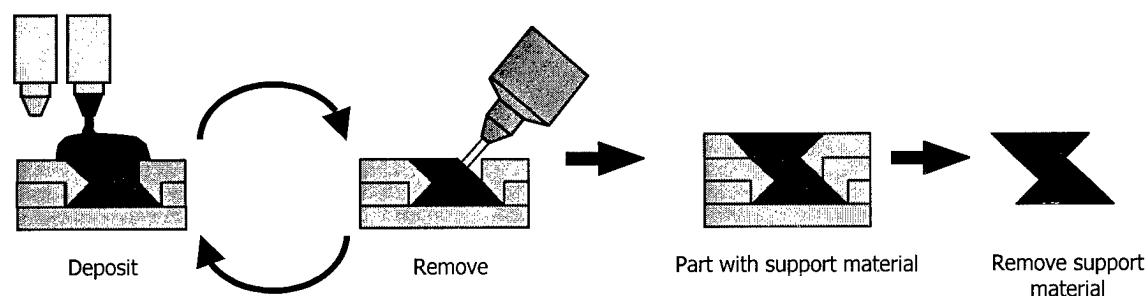


Figure 4. Schematic of SDM process

Mold SDM, illustrated in Figure 5, is a technique in which an intermediate, fugitive mold is fabricated using SDM. The mold is fabricated using SDM with a sacrificial support material occupying the mold cavity. Once the mold is complete, the support material is removed, exposing the mold cavity into which the final part material is cast. The final part material can be any compatible castable material. Green ceramic parts are formed by gelcasting ceramic slurry into the mold and subsequently curing of the slurry. Then, the mold is removed by melting and the remaining green ceramic material is sintered to produce the final ceramic part.

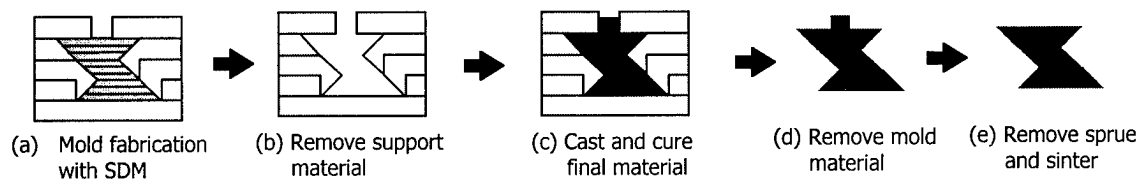


Figure 5. Schematic of Mold SDM process

While this process adds an additional step in the production of green ceramic parts, it does have significant advantages. First, since the mold itself is built using the SDM technique, high geometric complexity can be achieved. Also, the mold design is significantly simplified because the mold is sacrificed, which means no parting surfaces are necessary. Second, the molding approach produces monolithically cast parts, so there will be no layer boundaries or interlayer voids. Third, every surface of the mold is formed by direct machining or by replication of

machined surface. In this way, the merits of machined surfaces are transferred to the final ceramic parts. This enables Mold SDM to efficiently achieve dimensional accuracy [3].

Current Process Issues

While Mold SDM has a number of benefits for the fabrication of parts for small turbine engines, there are several issues regarding surface quality and part build rate. The choice of the support material is critical for addressing these issues. One support material for Mold SDM is a commercially available, ultraviolet-photopolymerizable, water-soluble soldermask. It is cast as a liquid, then transformed into a machinable solid by curing it with UV light. The water-solubility of cured soldermask provides a convenient way to remove the support material from the mold to expose the cavity for casting the final material.

Soldermask, however, has undesirable properties that lead to lower building rates and that degrade the surface quality of the final parts. The cured soldermask tends to be brittle and prone to cracking, which severely limits the speeds at which it can be machined. This material also has a maximum cure depth of only around 1 mm, so multiple steps of deposition and curing are required for building thick part layers as depicted in Figure 5 (a). Also, the soldermask does not cure evenly. In many cases, there is a thin poorly cured region at the boundaries between layers of soldermask. During the wax deposition step, the incompletely cured regions can deform which results in surface ripples (see Figure 6).

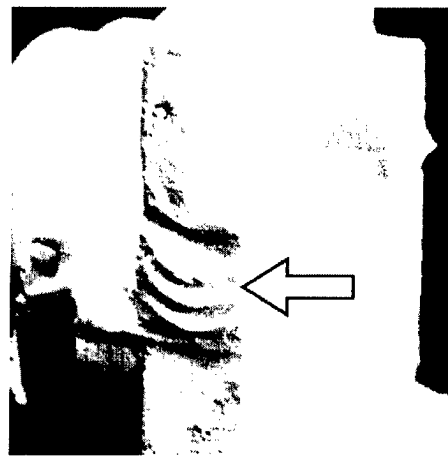


Figure 6. An example of surface ripples.

Water-soluble wax has been investigated as an alternative support material. However, unlike soldermask, a thick layer of water-soluble wax can be deposited by a single casting. Since a thick layer is built-up in one step, the chance of surface ripple is eliminated. Also, the water-soluble wax has better machinability than soldermask. Therefore higher machining feed rates can be used with the water-soluble wax and the build rate can be significantly increased.

The selection of the melting point of the water-soluble wax is critical. If the melting points of the water-soluble wax and the mold wax are very different, then features created in the lower melting point material will be damaged during casting of the higher melting point material. Features in the higher melting point material will not be damaged much, if at all, during casting of the lower melting point material. To minimize the risk of feature damage the best compromise is to use materials with similar melting points. With the materials used to fabricate parts, it was found that casting at 10°C above the melting point produced negligible remelting and feature damage. However, because of the low casting temperatures, the cast material tends to solidify very rapidly when it contacts the surface and does not always have sufficient time in the liquid state to fully and accurately replicate the surface details. Mild preheating of the surfaces prior to casting overcomes this effect. Excessive preheating can cause feature damage either during preheating by melting or during casting if the material has softened too much.

Part Characterization

The slurry used to cast the parts shown in this paper is a proprietary formulation developed by Advanced Ceramics Research (Tucson, AZ) based on Si_3N_4 powders from UBE or Starck. Alumina and yttria serve as sintering aids. The solid loading of the slurry is 50-53%. Before casting the slurry into the wax mold, an initiator is added which helps polymerizing the monomers dissolved in the slurry. The slurry gels in 1 to 2 hours at elevated temperatures.

After melting off the wax mold, the green part is dried and debinded. Depending on the maximum section thickness in the part this process takes 2 - 4 days. Debinding is done at temperatures between 200°C and 600°C in air. In a first stage the binder begins to decompose and in a second stage the remaining carbon residue is burnt out by the oxygen in the debinding atmosphere. Sintering has been done at temperatures between 1650°C and 1800°C.

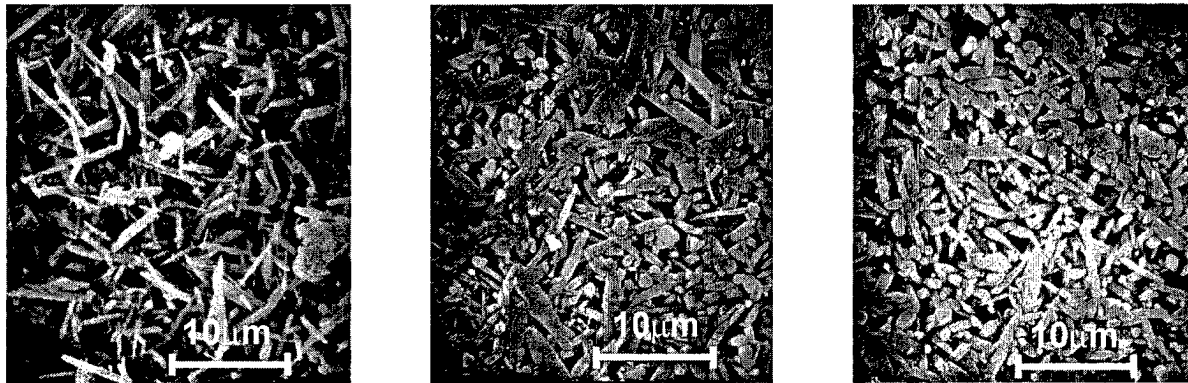


Figure 7. Microstructure of silicon nitride. From left, UBE powder sintered at 1700°C, at 1750°C and Starck powder sintered at 1750°C.

The microstructure of three samples sintered between 1700°C and 1750°C are shown in Figure 7. All samples were etched in molten NaOH at 400°C between 30 seconds and 2 minutes. The microstructure shows the typical needle-shape of the $\beta\text{-Si}_3\text{N}_4$ grains which toughen the material. The density of the samples sintered at 1750°C was 97% of full density.

Two types of samples were tested for their mechanical properties: polished bars gelcast with the Starck powder and unpolished bars made with the UBE powder. An average strength (4-point bending) of 414 MPa with standard deviation of 70 MPa was measured for the as cast bars. The corresponding value for the polished samples was 650 MPa with standard deviation of 200 MPa. The Weibull modulus for the as cast bars was $n = 9.6$. The maximum strength values were 600 MPa for the as cast beams and 800 MPa for the polished samples.

Table 1. Shrinkage of sintered silicon nitride parts. The small differences implies isotropy of sintered parts

Parts	X-Y plane	Along height	Difference
Center seal	17.7%	18.0%	0.3%
1 st inlet nozzle	17.6%	17.7%	0.1%
2 nd inlet nozzle	18.2%	17.7%	0.5%

The sintering shrinkage of Mold SDM parts are summarized in Table 1. The results show that the linear shrinkage is about $18 \pm 0.5\%$. The difference between the shrinkage in X-Y plane and Z direction (along the height) is less than 0.5%, which indicates the isotropic nature of sintering shrinkage and density of the final parts.

The surface roughness of the faces of center seal components, which are turbine components described in the next section, were measured using a profilometer over distances of approximately 6 mm. The bottom surfaces, where the geometry was replicated from a machined surface, had root mean square (RMS) roughness of $0.5 - 0.7 \mu\text{m}$. The upper surfaces, where the casting features were cut off by manual machining of the green part, had RMS roughness of $1.3 - 1.8 \mu\text{m}$. These values compare favorably with values of $4 \mu\text{m}$ reported for ceramic parts produced by stereolithography [4].

One of the advantages of using gelcasting for the fabrication of ceramic parts is the small feature size that can be achieved with this technique. As an example the green part of a small turbine is shown in Figure 8. The mold for this turbine has been manufactured with micromachining techniques [5]. The blade thickness is about $100 \mu\text{m}$. The mold has been replicated very well, and even the gray-shades originating from the triangulation of the blade curvature can be seen.

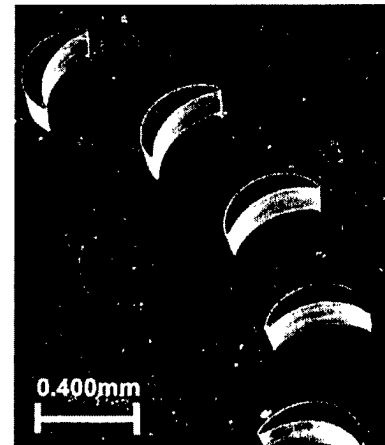


Figure 8: Gelcasting can replicate feature sizes of $100 \mu\text{m}$ and less as can be seen in this Si_3N_4 green part of a small turbine.

Example Silicon Nitride Parts

Center Seal

Figure 9 shows a pair of center seals for a miniature turbine engine design. Each piece is a semi-circular shape that has a tongue on one end and slot on the other end such that two of them can fit together to form a complete center seal. The seal prevents gas leakage between the hot turbine side of the engine and the cold compressor side. They also work as thermal barrier between the two sections. It's 26 mm in diameter and 1.8 mm in thickness. The slot and tongue are about 0.5 mm thick. They fit together with $40 \mu\text{m}$ clearance. The RMS roughness of bottom surfaces is $0.5 \mu\text{m}$. It took 6 hours to build the mold and 4 hours to dissolve out the water-soluble wax support material.

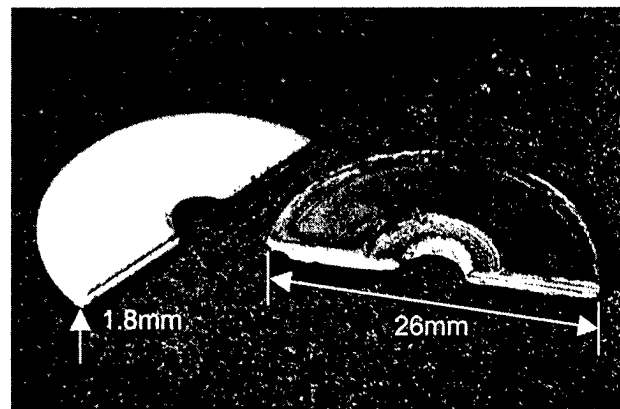


Figure 9. A pair of center seals will form a complete center seal. Left one shows bottom, right one shows top surface. The bottom surface gives $0.5 \mu\text{m}$ RMS roughness.

Inlet Nozzle

The turbine inlet nozzles shown in Figure 10 and 11 are two design versions for a non-rotating part that directs the hot gasses from the combustion chamber into the turbine. The first design, in Figure 10, has sharp corner features, while every edge of the second design, in Figure 11, is round with a radius of about 0.3 mm. The parts are about 35 mm in diameter. The height is around 9 mm for the 1st version and 16 mm for the 2nd version. It experiences the highest static temperatures in the engine. Estimates indicate that a ceramic inlet nozzle could increase engine performance by 7%, in terms of thrust/weight ratio, compared with a metal nozzle. The first design of the inlet nozzle was tested on a jet engine test rig and survived under the flow of 1250°C, high pressure gas expected in the turbine engine application. This shows the capability of mold SDM to build functional ceramic parts.

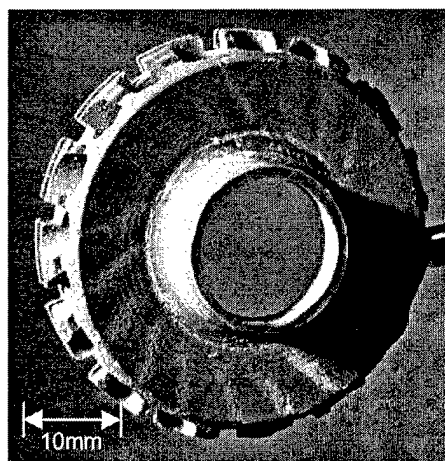


Figure 10: Top view of 1st version inlet nozzle. It was tested and survived under flow of 1250°C gas.

Conclusion

Mold SDM is a suitable process for building small ceramic engine parts. Mold SDM combines the accuracy of CNC machining with the shape complexity which is frequently associated with pure additive SFF processing techniques. Wax molds were used to fabricate green silicon nitride parts with high geometric complexity. The sintered components showed β - Si_3N_4 grain structure which is characteristic of high performance Si_3N_4 materials. The maximum flexural strength ranges between 600 MPa for unpolished samples and 800 MPa for polished samples. The isotropic linear shrinkage is $18 \pm 0.5\%$ and the best achievable RMS surface roughness was determined to be better than $0.5 \mu\text{m}$.

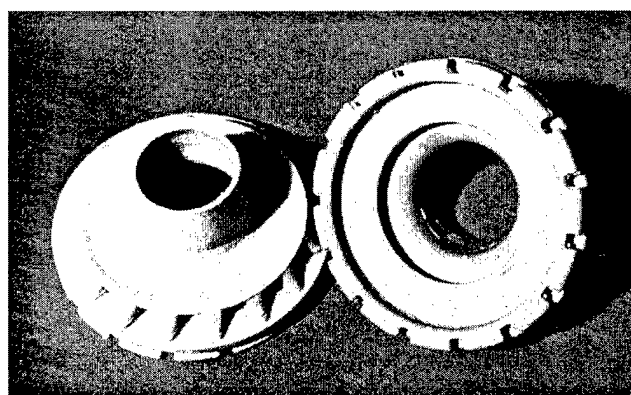


Figure 11: 2nd version inlet nozzles. The surface roughness is $0.45 \mu\text{m}$ (RMS) for bottom and $1.75 \mu\text{m}$ (RMS) for top surface.

Acknowledgements

This work has been supported by Defense Advanced Research Projects Agency and Office of Naval Research under contract N00014-98-1-0734 titled "Solid Freeform Fabrication of Ceramic Components for Microturbine Engines"

The authors would like to acknowledge Larry Schultz and Gennady Neplotnik at Carnegie Mellon University for their effort in part building and process development. The authors also thanks to Mike Stargie and Eric Lundahl at Stanford Linear Accelerator Center for their help for surface roughness measurement of ceramic parts.

References

- [1] R. Merz, F. B. Prinz, K. Ramaswami, M. Terk, and L. E. Weiss, "Shape Deposition Manufacturing", Proceedings of the 1994 Solid Freeform Fabrication Symposium, The University of Texas at Austin, August 1994, pp. 1-8
- [2] F. Prinz and L. Weiss, "Method for Fabrication of Three-Dimensional Articles", U. S. Pat. No. 5,301,415, April 12, 1994
- [3] A. G. Cooper, S. Kang, J. W. Kietzman, F. B. Prinz, J. L. Lombardi and L. Weiss, "Automated Fabrication of Complex Molded Parts Using Mold SDM", Proceedings of the 1998 Solid Freeform Fabrication Symposium, The University of Texas at Austin, August 1998, pp. 721-728
- [4] G. A. Brady and J. W. Halloran, "Solid Freeform Fabrication of Ceramics via Stereolithography", Naval Research Reviews, Office of Naval Research, Vol. L, 3, 1998, 39-43.
- [5] Y. Cheng, J. Stampfl, R. Leitzgeb, F.B. Prinz, "Additive/Subtractive Material Processing for Mesoscopic Parts", Proceedings of the 1999 Solid Freeform Fabrication Symposium, The University of Texas at Austin, August 1999

Net-Form Manufacturing of Aluminum Components: the Dependence of Processing Parameters on Component Quality

By Melissa Orme[†], Qingbin Liu[†], Robert Smith[†], Charles Huang[†], and John Fischer[‡]

[†]Department of Mechanical and Aerospace Engineering
University of California, Irvine 92607-3975

[‡]Boeing Commercial Airplane Group, P.O. Box 3707, MC 5L-14
Seattle, WA 98124-2207

ABSTRACT

High precision droplet-based net-form manufacturing of structural components is gaining considerable academic and industrial interest due to the promise of improved component quality resulting from rapid solidification processing and the economic benefits associated with fabricating a structural component in one integrated operation. In this work circular cylinders that are 35 mm in diameter and up to 11 cm in height are fabricated in their net-form by depositing molten 2024 aluminum alloy droplets onto a flat-plate substrate and building the cylinder layer by layer in the direction of its long axis. Droplets are generated from capillary stream break-up from 150-micron diameter orifices at rates typically on the order of 18,000 droplets/second depending on stream conditions. The mechanical and microstructural characteristics of the net-formed components are studied and their dependence on the processing parameters such as droplet temperature, substrate temperature and mass flow rate delivered to the substrate is ascertained.

Introduction

A droplet-based net-form manufacturing technique is under development at UCI which is termed Precision Droplet-Based Net-Form Manufacturing (PDM). The crux of the technique lies in the ability to generate highly uniform streams of molten metal droplets such as aluminum or aluminum alloys. Though virtually any metal that can be melted and contained in a crucible is suitable for use with PDM, the results presented in this paper focus on droplet deposition with molten aluminum alloy (2024) droplet streams that are generated from capillary stream break-up in an inert environment (Argon or Nitrogen). Other results that concentrate on fabrication of pure aluminum components with PDM are presented elsewhere.¹ In the final realization of the PDM process, the droplets will be electrostatically charged and deflected onto the substrate where they "splat," which entails simultaneous spreading and solidification. The charging and deflection of droplets bears many similarities to the technology of ink-jet printing,^{2, 3} except that in the current application of PDM, the droplet charges are significantly higher in order to print large lateral areas. We have found that large electrostatic charges on closely spaced droplets can result in mutual inter-droplet interactions,⁴ which are not evident in the ink-jet printing technology. Successive droplet deliveries build a component layer by layer.

Figure 1 illustrates the generation of molten metal droplet streams from capillary stream break-up. The orifice diameter is 150 microns, which, for the conditions employed in this work, results in 284 μm diameter droplets. The droplet stream speed, V , was varied over the range of 10 m/s to 13 m/s, and the droplet production frequency, f , was varied according to the relation

$f = (k_o^* V) / (2\pi r_o)$, where k_o^* is the nondimensional wavenumber equal to the ratio of the stream circumference to the wavelength, λ , of the applied disturbance. It is well known in the field of droplet formation from capillary stream break-up that the fastest growing disturbance on an inviscid capillary stream occurs when k_o^*

is equal to 0.697.^{5,6,7} Most molten metals can be approximated as inviscid. It has also been shown in previous work, that droplet generation at the k_o^* of the fastest growing disturbance results in the most uniform droplet stream.⁸ Using the above relation for f insures equally spaced droplets at a variety of droplet speeds with droplet production frequencies in the range of 15,000 Hz to 19,000 Hz for the droplet speeds employed in this work.

PDM bears similarities with other emerging technologies of net-form manufacturing such as Shape Deposition Manufacturing, SDM,^{9,10,11,12} and 3-D printing.¹³ In SDM, a feedstock wire located directly over the substrate is melted using a plasma-welding torch. A discrete droplet of typical dimension 1-10 mm (depending on plasma conditions) falls off the wire and onto the substrate and builds the material component by droplet deposition at a rate on the order of 100 Hz, i.e., over two orders of magnitude slower than with the PDM technology. The advantage of SDM is that refractory metals can be melted with the plasma-welding torch.

In 3-D Printing, a green part is created by printing a stream of binder droplets onto a metal powder bed according to CAD information. However in that process, several post-treatment steps are necessary to insure a mechanically sound component.

As an intermediate step in the development of the PDM process, we have chosen to fabricate circular cylinders by depositing molten aluminum 2024 alloy droplets onto a flat plate substrate whose motion is in a circular path as shown in Figure 2. Hence, we have eliminated charging and deflection in this phase in order to systematically develop the PDM process. Cylinders are built on a flat plate substrate (instead of on a circular cylinder substrate) as a demonstration of the relative arbitrariness of the shapes that can be net-formed and to investigate issues associated with fabrication of structures with large dimensions in the direction normal to the substrate.

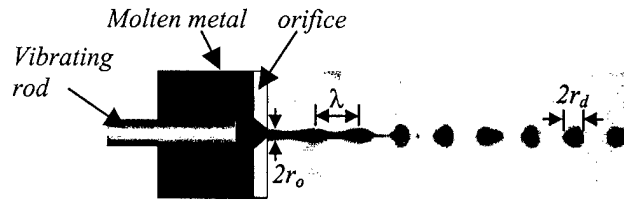


Figure 1: Photograph and sketch depicting molten droplet formation from capillary stream break-up.

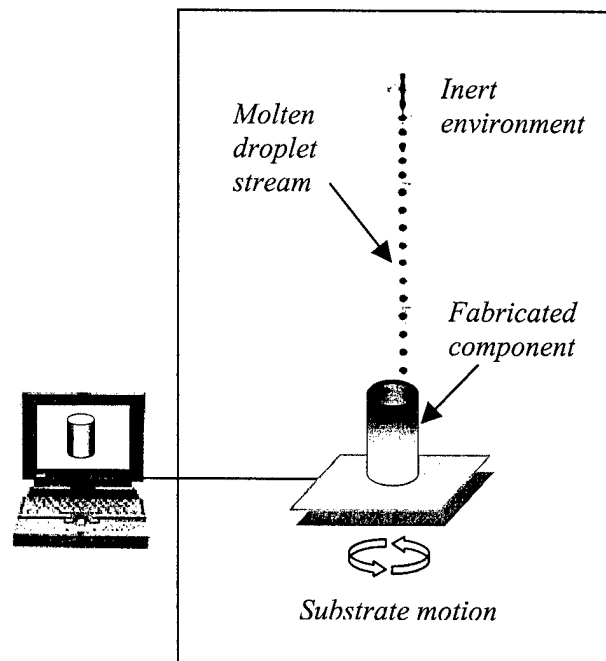


Figure 2: Conceptual schematic of cylinder fabrication on a flat-plate substrate with controlled droplet deposition.

Experimental Considerations

As depicted in Fig. 2, the droplets are injected into an inert environment where they splat on the substrate, thereby building the net-formed component. This is necessary since the presence of oxygen in the background environment will have a deleterious effect on: 1) the basic mechanism of droplet formation from capillary streams, 2) the droplet stream stability during flight to the substrate, and 3) the quality of the fabricated component. Furthermore, the presence of aluminum oxides in the melt will also degrade the droplet stream stability, if not completely plug the orifice, since the density of the oxides are on a par with that of the aluminum alloy melt. Hence, care has been taken to filter the oxides from the melt before the jetting stage and to remove the trace oxygen elements from the background environment. The purity of the bottled gas (nitrogen or argon) is specified at 99.998%, and the oxygen level of gas in the environmental chamber is monitored to insure that the O_2 level does not exceed 25 PPM. A background pressure of 14.7 psi is used in this work. More details on the apparatus are found in Reference 1.

The material used in this study was commercially available 2024 aluminum alloy. Its chemical composition was analyzed before and after filtration and jetting and was found in both cases to be consistent with industrial 2024 alloy specifications.

Experimental Results

Uniform molten 2024 aluminum alloy droplet streams have been generated in an inert environment where they travel 50.0cm before they impinge onto the substrate. The long travel distance is not a requirement for the PDM process, but is rather imposed upon this work by means of the available apparatus. The long travel distance has not been found to degrade the stream stability (which is a significant finding in its own right), however it plays a significant role in droplet cooling during flight and droplet speed reduction due to aerodynamic drag. The latter two factors can be accounted for in model predictions.¹⁴

A photograph of a typical fabricated cylinder is shown in Figure 3. Two sections have been removed (at 180° separations) from the base for microstructural analysis. It is acknowledged that the component shown is preliminary, inasmuch as it does not possess the geometric smoothness required for industrial applications, yet it is included in this paper as documentation of the current state of the PDM development. Ongoing work includes the development of a numerical model for the determination of processing parameters (substrate temperature, droplet temperature, environmental temperature, and mass delivery rate to the substrate) that yield components of high geometric, mechanical, and microstructural fidelity.¹⁴ Nevertheless, it is found that microstructural and mechanical analysis of components such as that shown in Figure 3 play a useful role in the development of the PDM process. Cylinders have been fabricated at heights up to 11 cm from the substrate.

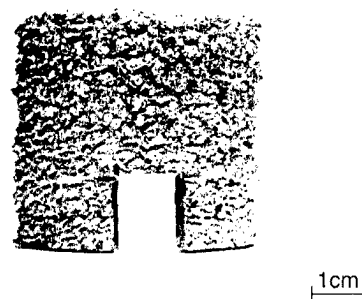


Figure 3: Photograph of droplet deposited aluminum alloy cylinder. Two samples have been removed from the cylinder base at 180° separations for analysis.

This paper reports on the microstructural results, hardness and density of six such cylinders that were fabricated over a wide range of processing parameters that are included below in Table 1. In the table, T_0 is the initial capillary stream temperature, T_s is the substrate

temperature and m/l is the mass delivered per unit length to the substrate, which is directly related to the droplet speed and substrate speed. We chose not to characterize the results in terms of the mass flow rate, \dot{m} , since it contains no information regarding the amount of material overlap on the substrate (a function of substrate speed), which is of critical importance for the geometric and mechanical quality of the component. The cylinders were sectioned as indicated in Figure 3, and the sections were polished and subsequently photographed with an optical microscope. The samples were etched with a modified version of Keller's Reagent, which consists of 31% H_2O , 31% HCl , 31% HNO_3 and 7% HF .

Microstructural Results

Figure 4 illustrates the microstructure of the cylindrical component shown in Figure 3. This sample has been labeled "#1" and its processing parameters are found in Table 1. It can be seen that the microstructure, which was photographed at a section 5.0 mm from the substrate surface, is on the order of 50 μm .

Figure 5 is a photomicrograph of sample #2a taken 35 mm from the substrate surface. The average grain size is also on the order of 50 μm , however, large voids can be seen in the lower center of the photograph.

Figure 6 shows the microstructure of sample #2b that was taken from the same cylinder as that of #2a, however at a distance of 6.0 mm from the substrate as opposed to 35.0 mm. Additionally, the droplet impact speed was 10 m/s in sample #2a, which was changed from 11 m/s in sample #2b. Hence, m/l was higher in sample #2b, thereby transferring more heat from the molten droplet stream to the cylinder. Therefore, there exist two reasons for greater exposure to heat in sample #2b

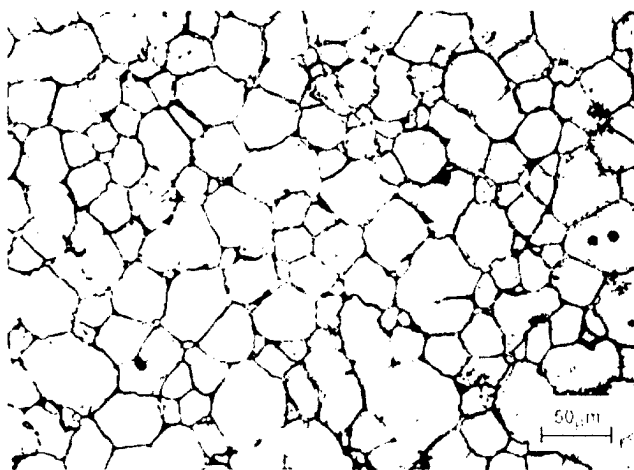


Figure 4: Microstructure of cylinder #1.

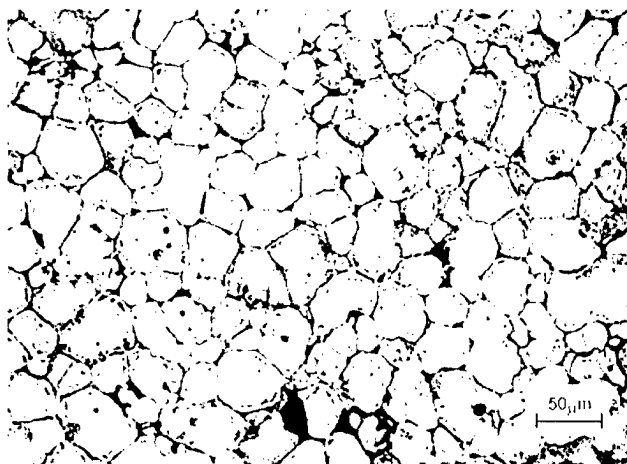


Figure 5: Microstructure of cylinder #2a.

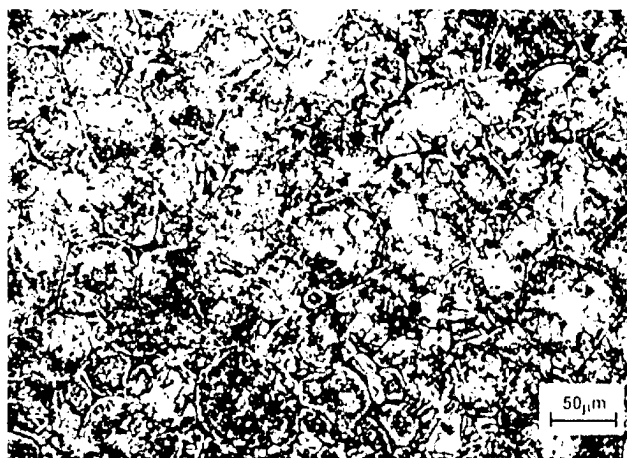


Figure 6: Microstructure of sample #2b

than in sample #2a: 1) increased heat transfer due to higher values of m/l , and 2) closer proximity to the heated substrate. This is one explanation for the coarser precipitates in the microstructure of Figure 6.

The microstructure shown in Figure 7 was taken from sample #3, at a distance of 10.0 cm from the substrate. Again, the grains are typically on the order of 50 μm . This result is significant, since it is clear that components can be fabricated at relatively great distances from the substrate surface with little change in microstructure or hardness.

Figure 8 is a photograph of the microstructure of sample #4. It is apparent that this sample possesses the largest grains of all of the specimens studied. The reason for the larger grain structure is due to the fact that the combination of the droplet temperature and the substrate temperature is higher than in any other case studied, thereby increasing the splat solidification time, which is well known to cause larger grain sizes.

The microstructure shown in Figure 9 is from a cylinder that was fabricated with an extremely high m/l compared to the other cylinders in this study (see Table 1 for sample #5) and a moderate substrate temperature. The microstructure shown occurred at a vertical distance of 20.0mm from the substrate surface. Clearly observable in the figure are dark precipitation zones, which are a result of the elevated temperature in the deposited material due to the high mass flow rate to the substrate.

Figure 10 is a photomicrograph of cylinder #6. The microstructure is distinguished by fine grains that are 10 μm or less. The large black areas on the upper part of the photograph are not voids but rather are the irregular outer boundary of

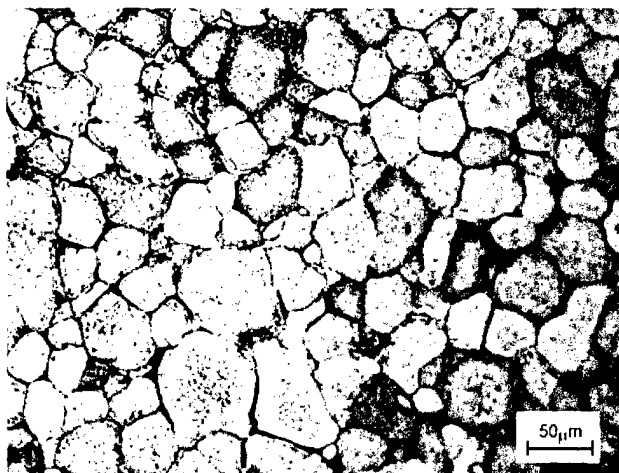


Figure 7: Microstructure of sample #3

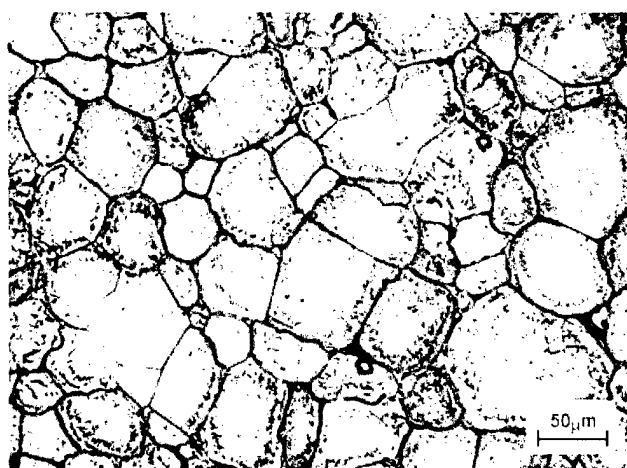


Figure 8: Microstructure of sample #4

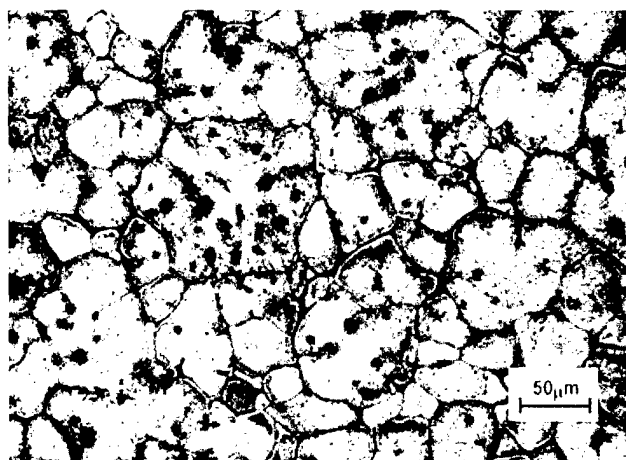


Figure 9: Microstructure of sample #5

the specimen. Unlike the other samples presented in this work, the microstructure of this sample reveals the outline of an isolated droplet that has fused relatively intact, preserving its identity. The existence of relatively refined grain structures and pristine droplet boundaries would intuitively lead to the correct judgement that the droplet and substrate temperatures were lower than in previous cases presented here. The processing parameters listed in Table 1, albeit accurate, provide misleading information for this sample, since this particular experimental realization was anomalous in the sense that the droplet stream was characterized by an angular “jitter” that greatly enhanced the convective cooling of the droplets during flight (and severely degraded the cylinder geometry). Since the droplets were no longer traveling in tandem, the aerodynamic and thermal protection of the neighboring droplet wake was eliminated, thereby causing greater droplet cooling. Hence, the droplets were much cooler than their highly stable counterparts. While the fabricated component is not useful in a practical sense, this experimental result has indicated that fine microstructures can be achieved without any loss of density as will be discussed below.

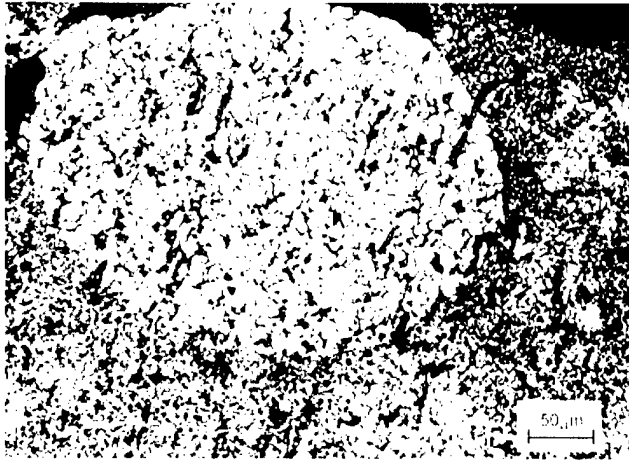


Figure 10: Microstructure of sample #6

	1	2a	2b	3	4	5	6
Microstructures shown in Figure number	4	5	6	7	8	9	10
T_o (°C)	787	830	830	732	845	810	778
T_s (°C)	176	149	149	315	454	260	460
m/l (kg/m)	1.02	1.04	1.19	1.65	0.82	8.53	1.10
Rockwell “B” Hardness	57	49	26	51	54	57	44
BNH* Hardness (conversion)	101	93	77	95	98	101	89
Specific gravity (g/cc)	2.62	2.66	2.66	2.57	2.63	2.71	2.70

Table 1: Processing parameters associated with the microstructures shown in Figures 4-10.

Hardness

Micro-hardness tests were conducted on each of the above samples directly after fabrication (with no post-working) at OCM Test Laboratory in Anaheim California. The results are included in Table 1 in the row entitled Rockwell “B” Hardness. The Rockwell “B” values were then converted to BNH values (500 kg load and a 10 mm diameter ball) in order to compare to the unworked 2024 reference stock which has a Rockwell “B” Hardness value of less than zero, and a BNH value of 47. Each hardness entry included in the table is the average of five readings taken over a vertical distance of 1.0 cm in the sample. The test procedure is identified as ASTM-E-384.

The samples with the greatest hardness are those that are characterized by the larger grain sizes. This finding is counter-intuitive since fine grain sizes are generally known to result in enhanced mechanical properties. However, in samples 1, 4, and 5 (which possess the highest values of hardness), the heat flux received by the cylinder during deposition (either through the delivery of large values of mass per unit length of cylinder or through high droplet temperatures) was sufficiently high to insure that the droplet material spread prior to solidification so that no pores could be embedded within the component. Hence, higher melt temperatures result in larger grain sizes, but also act to reduce porosity, thereby increasing the hardness of the component. The value of hardness for sample 2b is significantly lower than that of any of the other samples and it is concluded to be a result of the coarse precipitates which are observable in the micrographs and thought to be due to elevated heating during processing

Specific gravity

The specific gravity was also measured by OCM Test Laboratories for each of the above specimens, and found to vary from 2.57 to 2.71 g/cc, where the raw stock value of 2.70 g/cc is used as a reference. Hence cylinders have been fabricated that are fully dense and devoid of measurable porosity at best and others have been fabricated with a porosity of 4.8 % at worst. A measured specific gravity greater than the reference value is believed to be due to experimental uncertainties. With the exception of the anomalous sample #6, and sample 2b with coarse precipitates, the fully dense and nearly fully dense parts are those which have the highest measured hardness. Hence, the conclusion that porosity is the cause of lower hardness is corroborated in part by these measurements. Sample #6 is peculiar inasmuch as the sample is fully dense, yet the hardness is relatively low. However, it is stressed that this sample was anomalous since the droplet stream was not stable in an angular sense, and the resulting fabricated cylinder was grossly irregular. Additionally, specimen 2b is only 1.5% less dense than our reference value, yet the hardness is significantly lower than the other samples in this work. Hence, the generation of *widespread coarse precipitates* appears to be the influencing factor for the generation of softer components and porosity is of secondary importance. Alternatively, the generation of *somewhat finer precipitates*, such as those in specimen #5 acts to harden the component.

Summary

Several important findings have been reported in this paper which chronicles the development of the PDM process and are summarized here. The five most important findings are that: 1) molten aluminum alloy 2024 droplet streams can be generated from capillary stream break-up and travel a distance of 50.0 cm in an inert environment without observable degradation in stream uniformity (it is believed that this is the first time such a result has been reported); 2) it has been found that structures as high as 11.0 cm can be formed (11.0 cm is the greatest height that our current apparatus will permit) with little measurable changes in component characteristics; 3) BNH of as-deposited material is roughly twice that of (annealed) raw stock; 4) 2024 droplets can be generated and deposited without deviation from specified alloy composition limits and 5) fully dense components can be fabricated.

The processing parameters that govern the mechanical and microstructural integrity of the net-formed component are coupled with each other. It has been found that the most important factor is the heat flux received by the cylinder during droplet deposition. The heat flux can be affected by varying the mass delivered per unit length, the droplet temperature or the substrate

temperature. Extreme heating of the cylinder through any of the mechanisms discussed above results in coarsely precipitated microstructure, which can reduce the hardness of the component. Additionally, extreme heat fluxes also thickened cylinder walls due to slow solidification times. It is also important, however, that the droplets not be too cool prior to impingement, else the droplet boundaries will remain intact thereby reducing the structural integrity of the component. Hence, there is a trade-off between high heat fluxes to reduce porosity and increase hardness, and low heat fluxes for higher control over component geometry and finer microstructures.

Acknowledgements

The authors wish to acknowledge the generous grants from the Boeing Commercial Airplane Group (grant number BCA-23483), Lawrence Livermore National Laboratories (grant number B345710), and the National Science Foundation (grant number DMI-9622400).

References

- ¹ Orme M., and Smith, R. "Enhanced Aluminum Properties with Precise Droplet Deposition" *ASME Journal of Manufacturing Science and Engineering*, under review, 1999
- ² Sweet R. G. "High-Frequency Oscillography with Electrostatically Deflected Ink Jets," *Stanford Electronics Laboratories Technical Report No. 1722-1*, Stanford University, CA, 1964
- ³ Sweet R. G. "High Frequency Recording with Electrostatically Deflected Ink Jets", *Rev. Sci. Instrum.* 36, 2, 131, 1965
- ⁴ Orme M., Liu Q., and Huang, C., "Mutual Electrostatic Interactions between Closely Spaced Charged Solder Droplets, *Submitted* 1999
- ⁵ Rayleigh, Lord, [1879] On the instability of jets. *Proc. London Math. Soc.* 10, 4-13
- ⁶ Bidone, G. Experiences sur la forme et sur la direction des veines et des courants d'eau lances par diverses ouvertures. *Imp. Royale*, Turin, 1829
- ⁷ Savart, F. "Memoire sur la constitution des veines lequides lancees par des orifices circulaires en mince paroi" *Annales de Chimie et de Physique* 53, 1833
- ⁸ Orme M, "On the Genesis of Droplet Stream Microspeed Dispersions," *Physics of Fluids*, 3, (12) 1991
- ⁹ Prinz, F.B., Weiss, L.E., Amon, C.H. and Beuth, J.L., 1995, "Processing, Thermal and Mechanical Issues in Shape Deposition Manufacturing" *Solid Freeform Fabrication Symposium*, Austin, Texas, 118-129
- ¹⁰ Amon, C.H., Schmaltz, K.S., Merz, R., Prinz, F.B., 1996 "Numerical and Experimental Investigation of Interface Bonding Via Substrate Remelting of an Impinging Molten Metal Droplet" *ASME J. of Heat Transfer*, 118, 164-172
- ¹¹ Amon, C.H., Beuth, J.L., Merz, R., Prinz, F.B., and Weiss. L.E., 1998, "Shape Deposition Manufacturing with Microcasting: Processing, Thermal and Mechanical Issues, *ASME J. Manufacturing Science and Engineering*, Vol. 120, pp 656-667
- ¹² Chin, R.K., Beuth, J.L., and Amon, C.H., 1996 "Thermomechanical Modeling of Molten Metal Droplet Solidification Applied to Layered Manufacturing," *Mechanics of Materials*, Vol. 24, pp 257-271
- ¹³ Sachs E., Cima M., Williams P., Brancazio D., Cornie J., 1992, *J. of Eng. For Ind.*, 114, 4, 481-488
- ¹⁴ Shapiro, A. and Orme, Melissa, 1999, "Numerical Modeling for Droplet-Based Net-Form Manufacturing", a collaborative effort between Lawrence Livermore National Laboratory and UCI.

Design for Controlled Thermal Expansion Using Anisotropy in Parts Made from Liquid Crystal Stereolithography Resins

Richard P. Chartoff, Jill S. Ullett¹, and John W. Schultz¹

The University of Dayton
Rapid Prototype Development Laboratory and
Center for Basic and Applied Polymer Research
Dayton, Ohio 45469-0130 USA

¹ Current address: Georgia Tech Research Institute, Atlanta, Georgia

Abstract

In previous publications we showed that liquid crystal stereolithography resins can be cured in a magnetic field to yield polymers with anisotropic mechanical and physical properties. A modified stereolithography (SL) process developed as a part of this research provides the flexibility to change alignment directions from one layer to the next. This is akin to altering the fiber direction in continuous fiber reinforced composites. In traditional continuous-fiber composites, parts are often constructed of plies containing unidirectional fibers. When the fiber alignment varies from layer to layer throughout the structure, lamination theory developed for composite mechanics can be used effectively to model the characteristic mechanical and physical properties. Of particular interest is that by using such a model, layered polymeric parts with very low thermal expansion coefficients in the x-y plane can be designed. In this paper we demonstrate that composite lamination theory provides a basis for estimating the thermal expansion properties of liquid crystal polymer SL parts with aligned layers.

Introduction

In order to expand the usefulness of stereolithography, it is of interest to develop new resins that have functional mechanical properties at high temperatures. Current SL resins have softening temperatures under 100°C. As a result, they have limited value as high temperature structural materials. By increasing their high temperature mechanical stiffness and strength, SL resins will find new and expanded applications in areas such as direct injection molding, wind tunnel testing, and under-the-hood automotive applications.

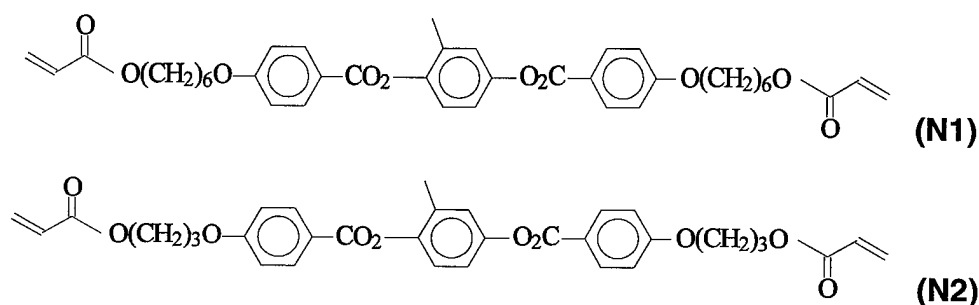
Photo-curable liquid crystal (LC) diacrylate monomers represent a new class of stereolithography resins. These LC materials contain stiff, rod-like molecules, which produce high glass transition (T_g) temperatures. The exact T_g developed depends on the monomer chemical structure and processing conditions. It has been demonstrated that T_g values in excess of 250°C can be achieved [1].

Because the rod-like molecules exhibit liquid crystalline phase behavior, they can be aligned by an external force. When cured in the aligned state, the aligned structure is "locked in" resulting in polymers with anisotropic physical and mechanical properties. By varying the alignment of the layers, properties such as the thermal expansion coefficient can be optimized. In this paper we demonstrate that composite lamination theory effectively provides a basis for estimating the thermal expansion properties of liquid crystal polymer SL parts with aligned layers. Of particular interest is that using

such a model, layered polymeric parts with very low thermal expansion coefficients in the x-y plane can be designed. This is demonstrated by measurements of the thermal expansion behavior for multilayer SL parts fabricated using the prescribed layer alignment sequences.

Experimental

Materials: Two liquid crystal monomers having the structures shown below were studied. The monomers differ only in the length of the alkane spacer groups. Monomer N1 has a spacer length of six $-\text{CH}_2-$ groups while monomer N2 has a spacer length of three. Both monomers exhibit liquid crystal phases over a broad temperature range above room temperature. Considerable information has been published on them previously [1-7]. The photo-initiator used was Irgacure 369 (Ciba-Geigy), referred to here as PI-A. The photo-initiator was solvent blended with the monomers and the solvent was removed prior to processing.



Thermal expansion measurements: The thermal expansion properties of thin films were first evaluated to study the effects of processing parameters on the linear coefficient of thermal expansion values and to establish benchmark values for comparison with thick, multilayer parts made via stereolithography. The thin film specimens were made under carefully controlled conditions by a non-SL method. A description of the method and some results of the thin film CTE measurements were presented in an earlier publication [5]. In this paper we focus on the thermal expansion properties of multilayer SL parts. A TA Instruments model 2940 Thermal Mechanical Analyzer (TMA) was used to measure CTE values. A tensile TMA probe was used for x-y plane CTE measurements; a flat tip probe was used for z dimension (thickness) measurements [8]. Samples were heated at 5°C per minute to just above their glass transition temperatures (to erase thermal history and residual stresses), cooled at $5^\circ\text{C}/\text{minute}$ to below room temperature and then heated a second time at $5^\circ\text{C}/\text{minute}$ to 120°C or above. All data shown are from the second heat. Due to imposed page constraints, in this paper data are presented only for polymer N1. These data fully illustrate the issues involved. Representative data for polymer N2 will be considered further in the SFF Conference presentation.

Specimen Fabrication: A modified table-top stereolithography apparatus (TTSLA) equipped with a rotating magnetic field was developed as a part of this project [9, 10]. This provides the flexibility to change alignment directions of the LC monomer from one layer to the next. This is akin to altering the fiber direction in a continuous fiber reinforced composite. Multi-layer specimens were made with the TTSLA using an

Argon ion laser tuned to 364 nm. Both the N1 and N2 resins containing 0.5 % Irgacure 369 photo-initiator (Ciba-Giegy) were used for fabricating specimens. The N1 resin temperature was maintained at 85 °C during part building. The N2 resin temperature was set at 100 °C. These temperatures are within the nematic phase temperature range for both resins.

The poles of the magnet used for alignment were adjusted so that the magnetic field was either parallel or perpendicular to the principal build direction. All parts were made using an alternating draw style with a center-to-center spacing of 6 mils (0.152 mm). The layer thickness used was either 10 mils (0.254 mm) or 8 mils (0.203) depending on the part. All parts made for the thermal expansion studies were rectangular in shape with the short side measuring about 10 mm and the long side measuring about 25 mm.

When the magnetic field was aligned parallel to the long direction of the part the orientation was labeled 0 degrees. When the magnetic field was aligned perpendicular to the long direction of the part, the orientation was labeled 90 degrees. The types of multilayer parts made for this study include those with 0 degree, 0/90 symmetric, and 0/0/90 symmetric layer sequences ranging from 12 to 16 layers. The symmetric nomenclature in composite mechanics means that the ply orientation lay-up is symmetric about the mid-plane of the part.

After each part was built, it was removed from the elevator platform and support structures attached to the part were removed before post-cure. The parts were post-cured at an ambient temperature of 150 °C using a broad-band Mercury vapor lamp. They were post-cured bottom-side up for two hours; and then top-side up for two hours.

Results and Discussion

We first consider how the thermal expansion properties of multilayer parts fabricated via stereolithography compared with those of thin films that were made under more ideal conditions. Figure 1 shows the thermal expansion of a 16 layer uni-directional N1 part compared with the thermal expansion of an N1 film. Table 1 lists CTE values above and below the T_g for these specimens. The transverse, or 90 degree, data matched well with no significant differences noted for the 90 degree film and multilayer part. There were greater differences between the 0 degree film and part. The slight differences observed, however, may be due to procedural errors either in aligning the magnet poles before scanning the film or part, or in mounting the sample for thermal expansion measurement.

Table 1 Thermal Expansion Coefficient Values for N1 Films and Multilayer Parts

N1 Specimen	α , from 25 to 40 °C	α , from 85 to 100°C
Film, 0 degree	-17.6 ppm/°C	-139 ppm/°C
Part, 0 degree	7.9 ppm/°C	-102 ppm/°C
Film, 90 degree	179 ppm/°C	315 ppm/°C
Part, 90 degree	180 ppm/°C	328 ppm/°C

Another possibility is that the differences in the slopes of the expansion curves indicate that the molecular alignment in the multi-layer part is not as good as in the thin film. There are certain possible sources for disorder that may result from the laser scanning process. These are:

- Convective flow within the resin at the interface surrounding a new polymer strand-- [11]. Such gradients in temperature and density result from the released heat of reaction. Both the scan speed (energy density) and scan pattern will affect thermal gradients and convective flow [11]. Such process parameter variations can influence the properties of the photocured material. As evidence of this, Schultz [13] found that laser draw speed influenced both the degree of anisotropy and the mechanical properties of aligned N2 parts.
- Since the degree of order in the LC state decreases with increasing temperature [7], thermal gradients inherently cause a certain amount of disorder within the monomer phase independent of local convection.

The N1 data in Figure 1 indicate that multilayer parts made with a significant degree of alignment result in anisotropic thermal expansion properties. A similar anisotropy in thermal expansion properties is characteristically found in continuous fiber-reinforced composite plies. In-plane thermal expansion is minimized in composite laminates by arranging the plies at different angles. The same technique was evaluated with aligned layers of the N1 resin. A 13 layer part was made having layers with alignment alternating between 0 degrees (angle between magnetic field and long side of part) and 90 degrees.

For this 13 layer part the thermal expansion in the longitudinal direction was then measured and compared with the thermal expansion of the uni-directionally aligned 16 layer part as shown in Figure 2. As expected, the thermal expansion of the 0/90 part falls somewhere in between the expansion curves for the 0 degree and the 90 degree part. It will be shown below that composite mechanics can be used to predict the thermal expansion properties of multi-angle aligned parts.

Based on the 0/90 symmetric part design, the thermal expansion of the part should be the same measured in the 0 degree direction (length) as it is measured in the 90 degree (width) direction. The thermal expansion properties in the 0 degree, 90 degree, and thickness direction were analyzed and are shown in Figure 3. The curves for the two in-plane directions are nearly the same showing good dimensional stability over the temperature range evaluated. The out-of-plane (part thickness) direction, however, exhibits a large positive thermal expansion coefficient of about 184 ppm/°C below the glass transition temperature.

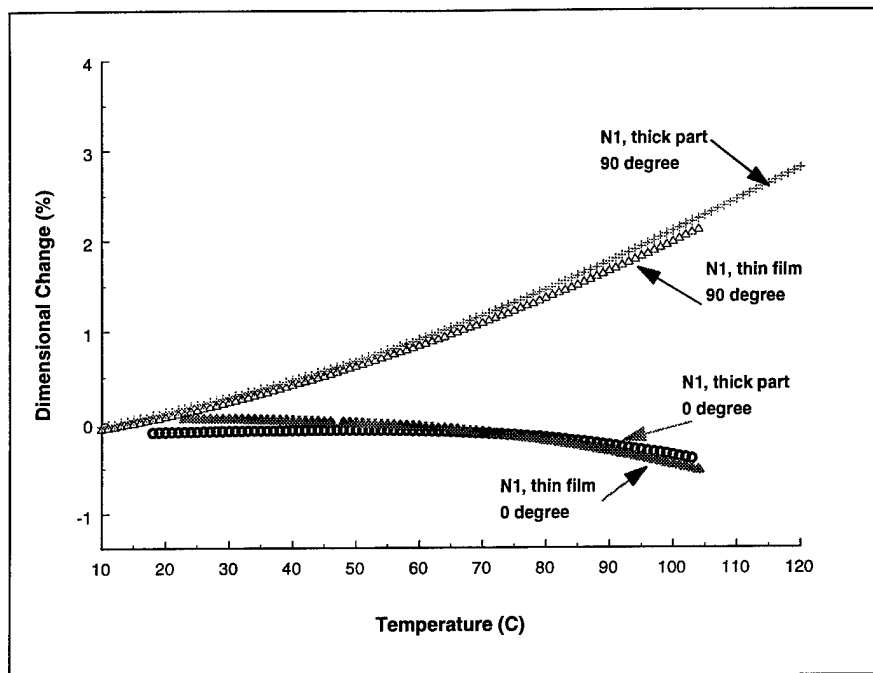


Figure 1. Comparison of linear thermal expansion data for N1 thin film and multilayer part specimens.

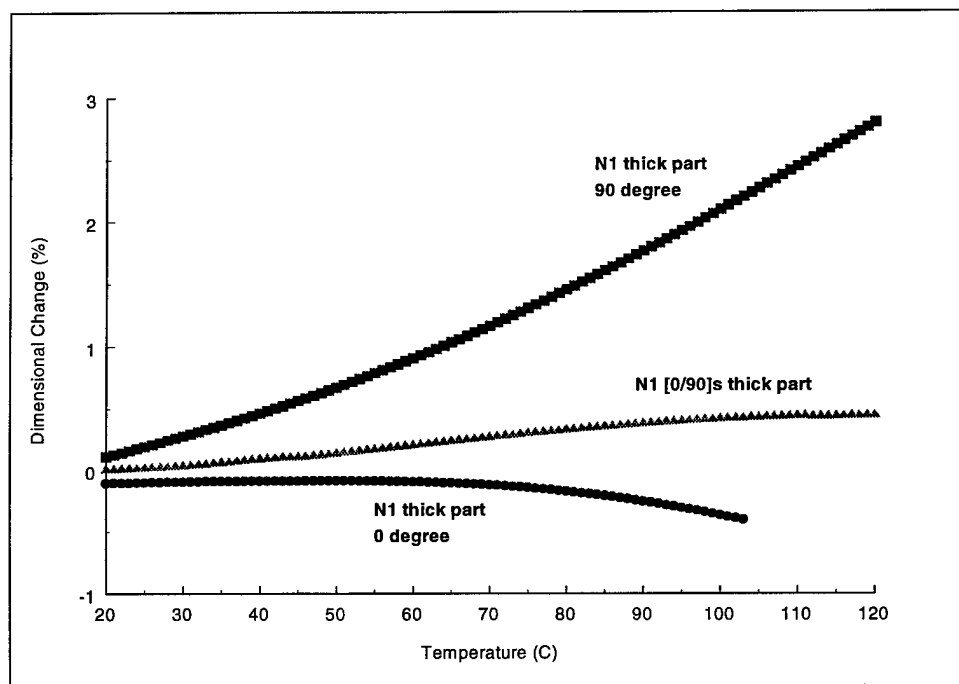


Figure 2. Comparison of N1 thermal expansion data for a 0/90 symmetric part with data for a uni-directionally aligned part.

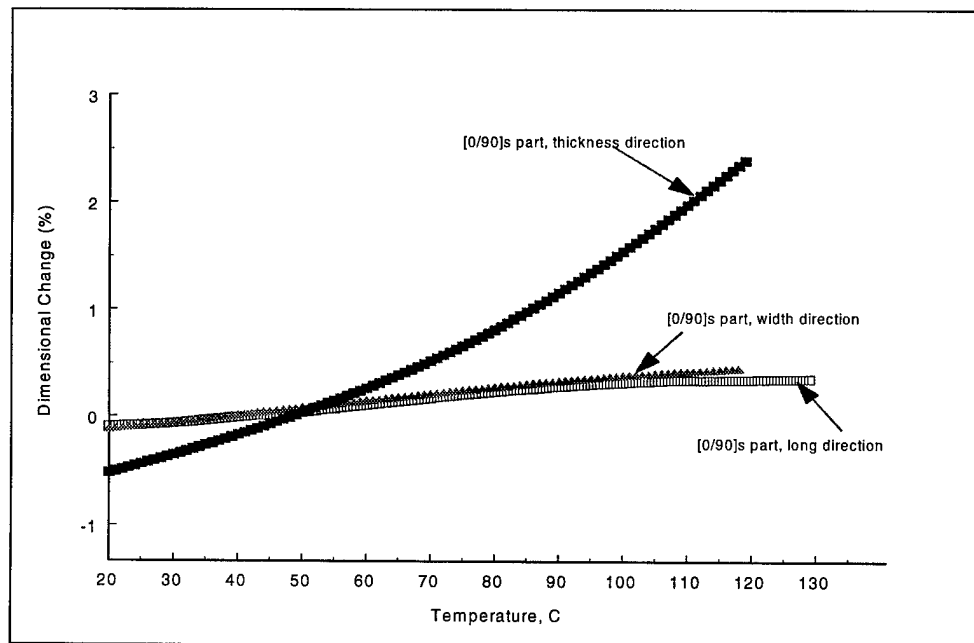


Figure 3. Comparison of N1 linear thermal expansion as a function of part orientation for [0/90]s part.

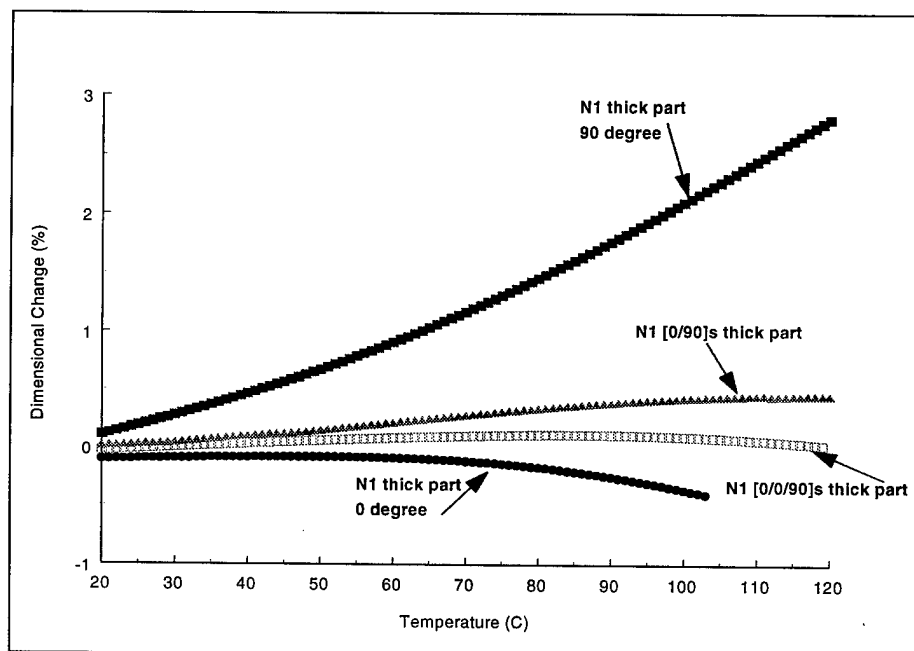


Figure 4. Comparison of the thermal expansion properties of N1 thick parts.

A second multi-angle part, containing a total of 12 layers, was made using a 0/0/90 symmetric layer sequence. The thermal expansion of the part was evaluated in the long direction and the results are shown in Figure 4. The 0/0/90 symmetric part analyzed in the long, or 0 degree, direction has a CTE of 31 ppm/°C below the glass transition temperature and a CTE of -35 ppm/°C above it. Depending on the sequence of alignment angles relative to the part axis system, one may achieve any desired in plane thermal expansion coefficients intermediate between the 0 degree and 90 degree values. Composite mechanics provides a way to predict laminate or part properties as a function of layer properties and stacking sequence.

Composite Mechanics Analysis

In an aligned liquid crystal thermoset, the physical and mechanical properties are anisotropic, with anisotropy similar to that in fiber/polymer lamina. For example, in the direction of orientation the modulus is greater than in the transverse direction and the linear CTE is lower. As a result, it is postulated that composite lamination theory can be used to predict the properties of layered, aligned liquid crystal parts. The thermal expansion of the layered structures fabricated in this study were analyzed by composite lamination theory for symmetric laminate plates where the ply alignment may vary throughout the structure. The analytical treatment of this problem is described in detail by Halpin [12].

A computer spreadsheet analysis program developed by Tsai [14] was used to perform the composite mechanics calculations. The spreadsheet program was developed to do integrated micro-macromechanical analysis and is called Mic-Mac (as discussed in Section 27 of [14]). The user enters a series of material parameters, as well as the laminate ply lay-up sequence and any applied stresses or strains (in our case these are zero). There are also additional parameters that can be entered for hygrothermal expansion and strength degradation. In this study moisture absorption was not considered.

The analysis was performed for the N1 resin. Two operating temperatures were considered: 25 °C and 100 °C. The input single ply (thin film) coefficient of thermal expansion (α) data, the predicted values as a function of part stacking sequence, and the measured values are given in Tables 2 and 3. As shown in Table 2, the composite mechanics approach predicts the in-plane thermal expansion coefficient to be 38.7 ppm/°C in both the x and y directions for the [0/90] symmetric part at 25 °C. The measured α 's were somewhat higher and not equivalent in the x and y directions. At 100 °C the predicted values for α_x and α_y were 34 ppm/°C, while the measured values were 21.3 and 44.6 respectively.

The [0/0/90]s part was only analyzed in the length, or x, direction. At 25 °C the mechanics approach predicts the in-plane thermal expansion in the x direction to be 17 ppm/°C while the measured value was 30.7 ppm/°C. At 100°C there was closer agreement with the predicted value at -30 ppm/°C and the measured value at -23.3 ppm/°C.

Starting with the CTE data for unidirectional parts, the composite mechanics approach provided a reasonable estimate of the thermal expansion coefficients of multi-angle symmetric layered parts at different temperatures. It is thought that closer agreement would be achieved between the model and experiment if the magnet in the TTSLA apparatus were on a precision controlled turntable. This would permit the alignment angle to be more precisely controlled. The effect of process variables such as layer thickness, scan speed, and resin temperature on the degree of alignment achieved was not considered in detail. In order to achieve more exact results these also would need to be considered. It is important to note as well that molecular alignment of the polymers cured in a magnetic field is not perfect as reflected in the order parameter data of Schultz [7, 13]. The theory assumes perfect fiber orientation.

Table 2. Comparison of Measured and Predicted Thermal Expansion Coefficients at 25°C for Multi-Angle Symmetric Parts Made from Polymer N1

Part	One Ply α_x, α_y (ppm/°C)	Predicted part α_x, α_y (ppm/°C)	Measured part α_x, α_y (ppm/°C)
16 layer, 0°	-----	-----	7.9, 180
[0/90]s part	7.9, 180	38.7, 38.7	47.5, 62
[0/0/90]s part	7.9, 180	17.0, 63.0	30.7, (α_y not measured)

Table 3. Comparison of Measured and Predicted Thermal Expansion Coefficients at 100°C for Multi-Angle Symmetric Parts Made from Polymer N1

Part	One Ply α_x, α_y (ppm/°C)	Predicted part α_x, α_y (ppm/°C)	Measured part α_x, α_y (ppm/°C)
16 layer, 0°	-----	-----	-117, 342
[0/90]s part	-117, 342	34.0, 34.0	21.3, 44.6
[0/0/90]s part	-117, 342	-30, 107.0	-23.3, (α_y not measured)

Conclusions

A modified stereolithography (SL) process was developed which uses a magnetic field to align liquid crystal monomers in each layer of a multilayer SL part. This is akin to altering the fiber direction in continuous fiber reinforced composites. Using this process, multilayer SL parts with various layer alignment patterns were fabricated. Multilayer parts were made that contained 13 to 16 layers having unidirectional, 0/90 symmetric, and 0/0/90 symmetric layer sequences. Their thermal expansion behavior in the x-y plane and the z plane were characterized using thermomechanical analysis (TMA).

Analysis of the 0/0/90 symmetric construction in the long, or 0 degree, direction demonstrated a particularly low x-y CTE of 31 ppm/°C below the glass transition

temperature and a CTE of $-35 \text{ ppm}/^{\circ}\text{C}$ above it. From the results obtained it was noted that, depending on the sequence of alignment angles relative to the part axis system, it is possible to achieve any desired in plane CTE values intermediate between the 0 degree and 90 degree values for unidirectional parts.

When the fiber alignment varies from layer to layer throughout the structure, lamination theory developed for composite mechanics can be used effectively to model the characteristic mechanical and physical properties. Reasonable agreement between the model predictions and experimental CTE values was obtained. Thus it was shown that by using such a model the CTE values of layered polymeric parts may be estimated. By following this procedure multilayer parts can be designed that have very low thermal expansion coefficients in the x-y plane.

References

1. Schultz, J.W., Bhatt, J., Chartoff, R.P., Pogue, R.T., and Ullett, J.S., (1999), *J. Polym. Sci.:Part B, Polym. Phys.*, **37**, 1183-1190.
2. Broer, D. J., Boven, J. et al., (1989), *Makromol. Chem.*, **190**, 2255-2268.
3. Broer, D. J., Hikmet, R. A. M., Challa, G., (1989), *Makromol. Chem.*, **190**, 3201- 3215.
4. Broer, D. J., Mol, G. N., and Challa, G., (1991), *Makromol. Chem.*, **192**, 59-74.
5. Ullett, J.S., Schultz, J. W., Benson-Tolle, T., and Chartoff, R.P., (1998), *Proc. of the Solid Freeform Fabrication Symposium*, University of Texas, Austin, TX, 519-528
6. Schultz, J.W., Chartoff, R.P., and Ullett, J.S.(1998, *J. Polym. Sci.:Part B, Polym. Phys*, **36**, 1081-1089
7. Schultz, J.W., Chartoff, R.P. (1998), *Polymer*, **39** (2), 319-325.
8. Gallagher, P.K., (1997) in "Thermal Characterization of Polymeric Materials", 2nd ed., E. Turi, ed., Academic Press, New York, Ch1-pp 121-148.
9. Pellechia, M. and Lightman, A., (1994) Proceedings of The Fifth Int. Conf. on Rapid Prototyping, Dayton, OH, June 12 - 15, pp 99-108,.
10. Ullett, J.S., Schultz, J.W, and Chartoff, R.P., (1999), accepted for publication in Rapid Prototyping J.; Chartoff, RP, Ullett, J.S., Schultz, J.W. (1997), Proceedings of the 7th International Conference on Rapid Prototyping, SanFrancisco, CA, University of Dayton, pp 203-212.
11. Xu, Y., Imamura, M., and Nakagawa, T., (1997), *Proceedings of the 1997 Solid Freeform Fabrication Symposium*, Austin, TX, April 11 - 13, 177-184.
12. Halpin, J. C., (1984) *Primer on Composite Materials Analysis*, Technomic Publishing Company, Lancaster, PA.
13. Schultz, J. W., (1997) "Processing, Network Formation, and Mechanical Behavior of Liquid Crystal Photopolymers for Structural Applications," Ph.D. Dissertation, The University of Dayton.
14. Tsai, S. W., (1988) *Composites Design 4th Edition*, Ed., S. W. Tsai, Think Composites, Dayton, OH.

Comparison of the Curing Process of Epoxy and Acrylate Resins for Stereolithography by Means of Experimental Investigations and FEM-Simulation

J. Eschl, T. Blumenstock, P. Eyerer

Institute for Polymer Testing and Polymer Science

IKP - University of Stuttgart

Böblinger Straße 78 E

D - 70199 Stuttgart

<http://www.ikp.uni-stuttgart.de>

Abstract

An improved method of investigating the mechanical properties of stereolithography resins during the curing process is described. With this method a typical acrylate material and a common epoxy resin are compared. An example of a finite element analysis shows the suitability of a material model (Burger) to simulate the mechanical stress due to polymerisation stress.

1 Introduction:

There have been many investigations into the curing process of stereolithography resins to determine the reaction rate or shrinkage. Both are crucial for the building process, especially the delay, building time or the accuracy. Previously shrinkage has been regarded as the direct and only reason for warpage. FEM simulation of the curing process, mainly the mechanics, is an attempt to enhance the accuracy of parts built with acrylic resins which showed reasonable curl. The IKP developed a testing method for stereolithography resins to determine the linear shrinkage, the resulting mechanical stress (which cause warpage) as well as the progression of the mechanical properties from the liquid resin till the green part. This data can then be used for FEM simulation.

2 Measuring method

With the measuring device shown in figure 1 the most important influences of the building process on part accuracy can be determined directly in the stereolithography system. A Stereos Desktop system manufactured by EOS GmbH was used. This system is quite similar to others

using a HeCd- Laser. The measuring equipment device has been constructed and optimized for several time intervals especially for these investigations.

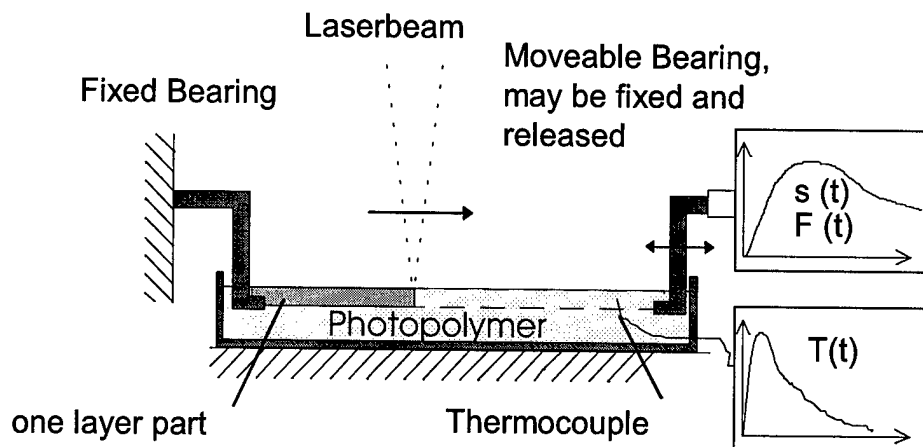


Figure 1: Measuring apparatus

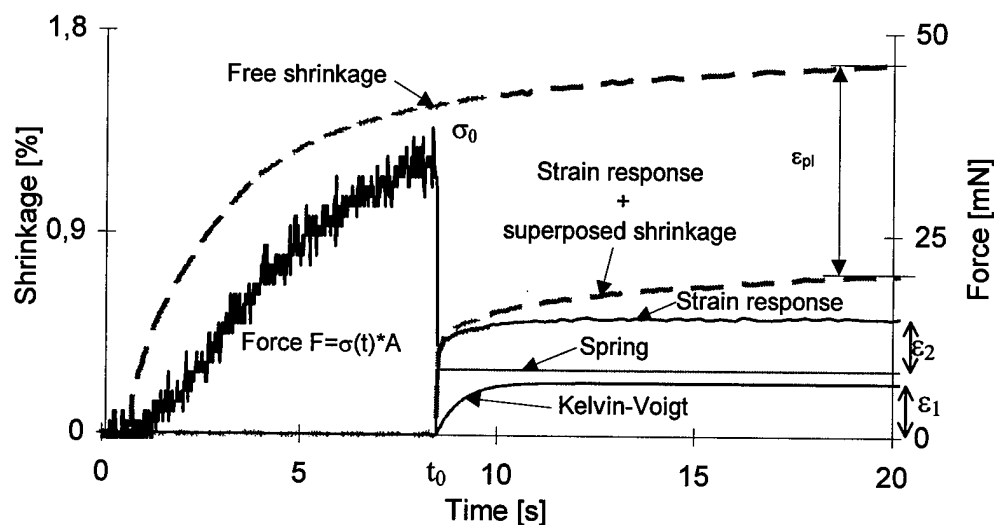


Figure 2: Measuring curves of shrinkage- and force. The response at the end of force measuring leads to the material parameters.

The geometry of the test parts were determined by the structure elements of the stereolithography process. These are single lines but also the hatching of plates (single layers) with a typical length of 10 mm. They are scanned so that they stick immediately with both ends to the measuring device, thus clamping is not necessary. The experiments may be performed in a variety of modes. In one case only one end of the specimen is fixed and the movement due to the shrinkage of the other end is measured. This is called the free shrinkage. With a stepping drive it is also possible to control the length of the part. When it is kept constantly, as it is the case when curing a layer on top of a part, the necessary force is measured. This measurement is called force test or hindered shrinkage. From the force and the cross section of the part the stress can be calculated as one reason for curl. As a combination of both tests one can start with measuring the force and

release the bearing at a certain time (Figure 2). This experiment then leads to the mechanical material properties.

3 Determination of the mechanical material behavior –curing dependent creep law

The standard tests to determine the mechanical material properties are the tensile test, dynamic mechanical analysis or creep and relaxation tests. Tensile tests can be done but the Young's modulus does not describe the material completely. With stereolithography resins where the material properties vary from liquid to brittle depending on their respective times for the curing state, these tests are problematic. For example the creep test: Shortly after the irradiation very small forces will cause high strain. However after a few seconds with the progression of the reaction, the material becomes harder and the applied force leads to only small strains which are not measurable.

To avoid these problems the following method is used:

Firstly the free shrinkage is measured. This is required as it is superimposed to all measurements and has to be eliminated afterwards. Then the length of the specimen is kept constant. The polymerization shrinkage now induces strain and according to the strength of the material stress which also is measured. At a specific starting time t_0 one bearing will be released. The force drops to zero and the part becomes shorter. The elimination of the superposed shrinkage gives the strain response. This experiment is similar to a "reverse relaxation" test. The strain response can be divided into the elastic strain ε_1 and the time dependent retardation part ε_2 . The elastic strain ε_1 leads to the young's modulus E_1 . The course of ε_2 can be described with one, or if necessary, several Kelvin-Voigt models (E_2, η_2).

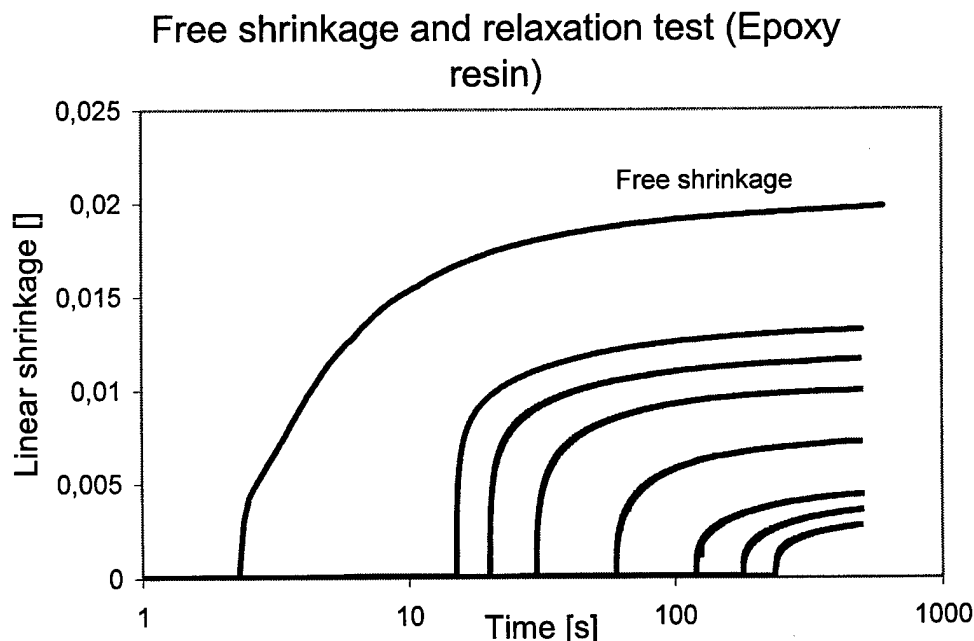


Figure 3: Measurements of free shrinkage and relaxation tests

This experiment can be repeated for several starting times t_i (Figure 3). The later the part is released, the lower are the strain responses due to plastic deformation ε_{pl} . This behavior is modeled (Figure 4) with one more damping element η_{pl} . It is stepwise determined (Boltzmann Superposition) through Equation 1.

Equation 1:

$$\varepsilon_{pl}(t) = \int_0^t \frac{\sigma(\tau)}{\eta_{pl}(\tau)} d\tau$$

The complete model together with typical courses of the parameters is shown in Figure 4. Other tests showed that for the obtained strains (smaller than 5 %) linear visco-elastic material laws may be used.

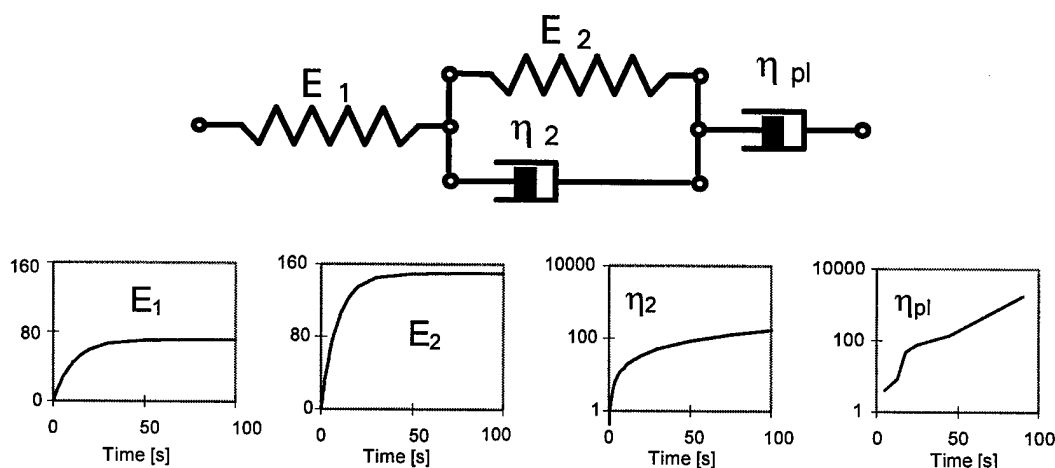


Figure 4: Burger model with its time dependent parameters (acrylate material)

4 Comparison of acrylate and epoxy resins

There already have been many comparisons of both material classes. The most important difference is that the degree of polymerization of the acrylates which can only be influenced by the duration of exposure of UV light. This is due to initiation by radicals and the inhibition by oxygen. The oxygen in the material and from the environment stops the reaction quickly. Thermal curing has only little effect. Only by increasing the number of exposures and the total amount of used UV energy, the degree of polymerization can be raised /1/. Contrary the epoxies, which are initiated by cations, once exposed with enough UV- light to start the reaction properly, cure by themselves with time. This is also called dark reaction. Heating accelerates the reaction /2/.

The investigated materials are Silacure 1485 from Siemens /3/, one of the latest acrylate materials developed which shows good accuracy. And on the other hand the well known Somos 6110 from DSM (former DuPont) which is a hybrid resin of mainly epoxy and acrylate. Both are cured with the HeCd- laser. The comparison was made on parts (length 10 mm, width 3 mm) with the same

cure depth c_d of 0,4 mm. This is a typically used when building parts with a layer thickness of 0,2 mm and is most suited for the measurements. With less cure depth the stress is too small to be measured properly. The parts were scanned with a laser power of 18 mW on the vat, a hatching distance of 0,05 mm at a temperature of 27 °C. For the acrylate material an exposure of 100 mJ/cm² was used, for the epoxy 144 mJ/cm².

Figure 5 and Figure 6 show the course of the four parameters that can be calculated from the relaxation tests using the Burger model. As explained below, for the epoxy resin a material model with 7 parameters should be applied, but comparing only four parameters is far more practical. Again the much slower reaction of the epoxy can be seen. However, the increase of strength of the acrylate material stops at about 60 seconds, whereas the properties of the epoxy resin seem to increase still after 240 seconds. Further experiments have to be done to investigate the final values. Of course in simple tensile test (also done in this apparatus) it was observed, that the young's modulus rises for more than two hours [1/].

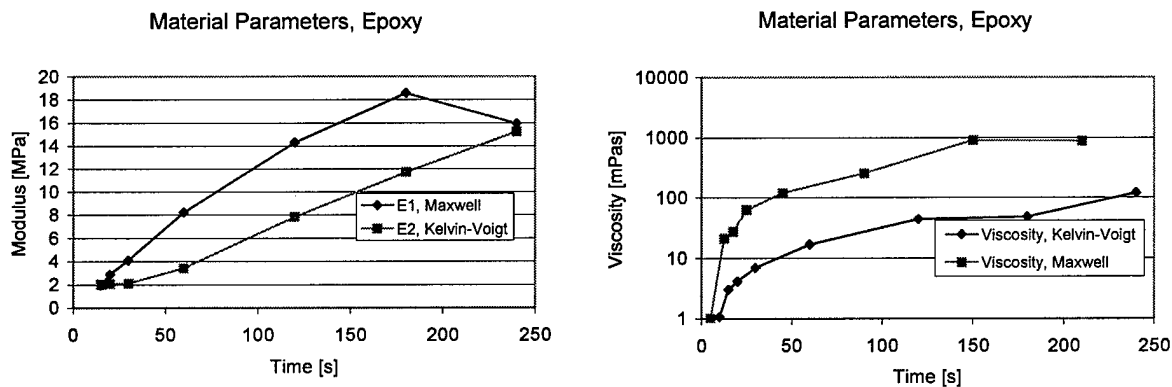


Figure 5: Material Parameters of Epoxy resin (4 Parameter Approximation)

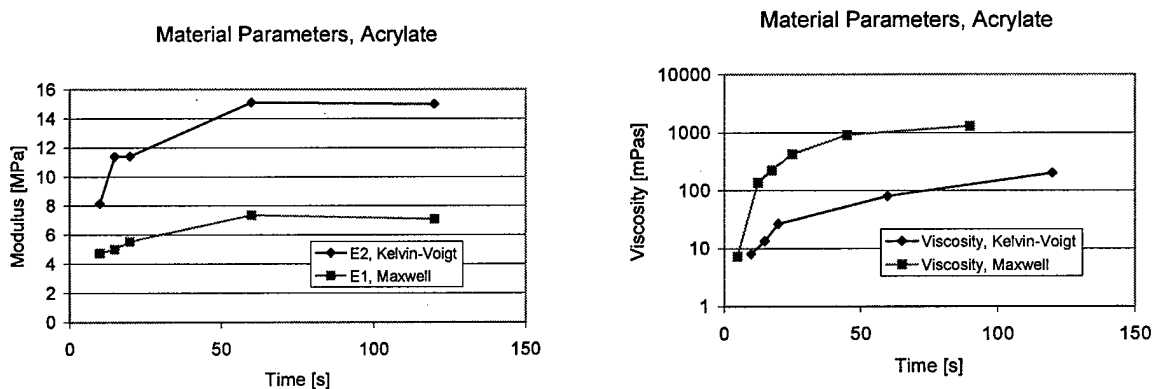


Figure 6: Material Parameters of Acrylate resin (4 Parameter Approximation)

It has to be considered that the epoxy material has, in contrast to the acrylate, reasonable reaction energy (exothermy). So that the part becomes warm during the first seconds. Accordingly the increase of strength partly is caused by the temperature change while cooling. This effect lasts for about 50 seconds [4/]. It has to be considered that the overall Modulus E is calculated with Equation 2. So the total modulus is always smaller than the single ones. For the acrylate as example E_1 ,

keeps below 8 MPa, E reaches a value of about 5 MPa, whereas the Modulus of the epoxy resin at the end of the measurement is about 8 MPa .

Equation 2:

$$E = \frac{1}{\frac{1}{E_1} + \frac{1}{E_2}}$$

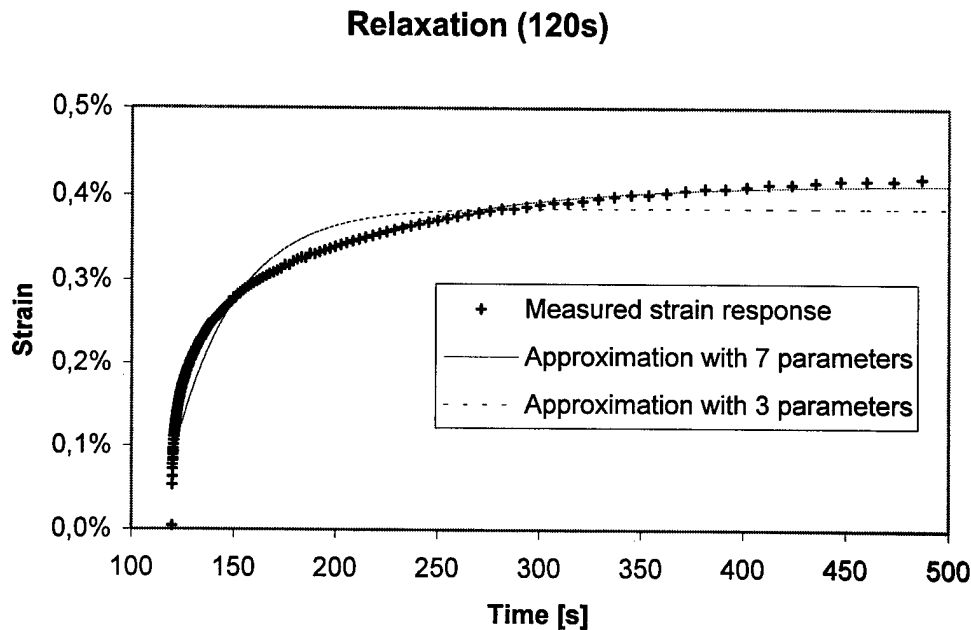


Figure 7: Fittings of the measured strain response (starting time 120s) with two material models (3 and 7 parameters)

The determination of the material parameters showed an other difference between the acrylates and the epoxies: The strain responses of the acrylates can be approximated very well using a three parameter model (E_1 , E_2 , η_2), to have a good approximation for the epoxy material a material model with seven parameteres (E_1 , E_2 , η_2 , E_3 , η_3 , E_4 , η_4) has to be used. This can be explained by the compound of the material of epoxy and acrylate material, but also by swelling effects. The part is cured within the vat, so substances of the liquid resin tend to diffuse into the network, this may be faster when the network is under stress. Either this material is involved in the reaction and causes additional shrinkage, or when the stress is released, the network tries to tighten, but this is retarded by the diffused material.

5 Simulation

To validate the material model the tests were simulated by the finite element method. Thus it is also possible to investigate the curing process not only of the whole layer but also of parts of the layer or the distribution of stress within the layer. Further observations on the influence of the

uncured material, like the material flow of the liquid due to the volume shrinkage of the curing material, may be made (Figure 8).

The material law and the time dependent shrinkage of each element were implemented in the commercial FE solver MARC through the subroutine HYPELA. In the simulation the part is built as in the stereolithography process by single scan tracks. Based on the position of the laser the program calculates which elements begin to cure for each time step.

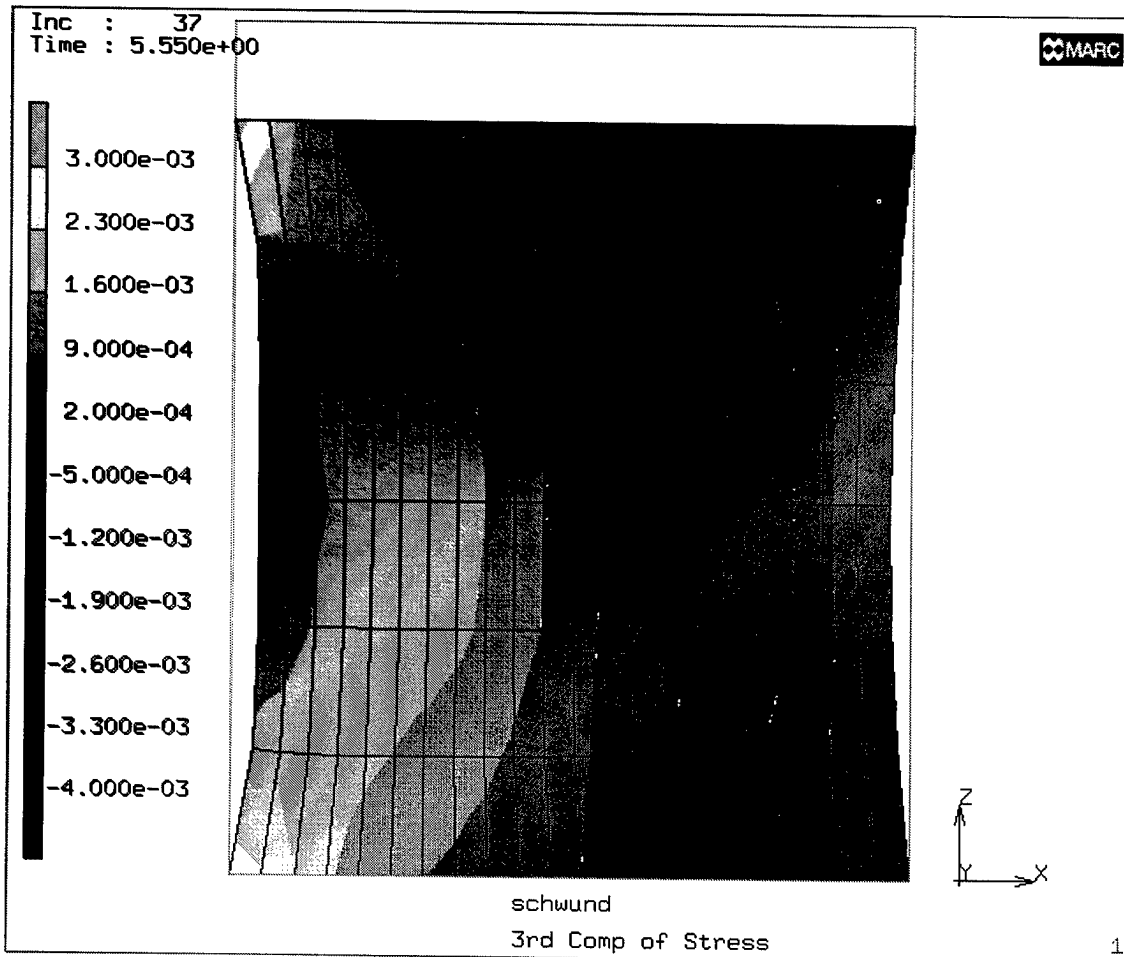


Figure 8: Simulation of free shrinkage (deformations scaled by 10, viewed from the top), colors show stress in length.

The comparison of measurements and simulations of several relaxation tests (different times, but same process parameters) shows good conformity (Figure 9). Of course, since in the simulation the Burger model with only 4 parameters was used, there is a deviation between simulation and experiments, this can be reduced when using a material model with more than 4 parameters (see above).

This model can be the basis to simulate the stress and distortion of complete parts. With the dramatic increase of computing power during the last few years, for small parts, this may already be achieved with work stations as they are used for CAD.

Comparison of Measurements and Simulation

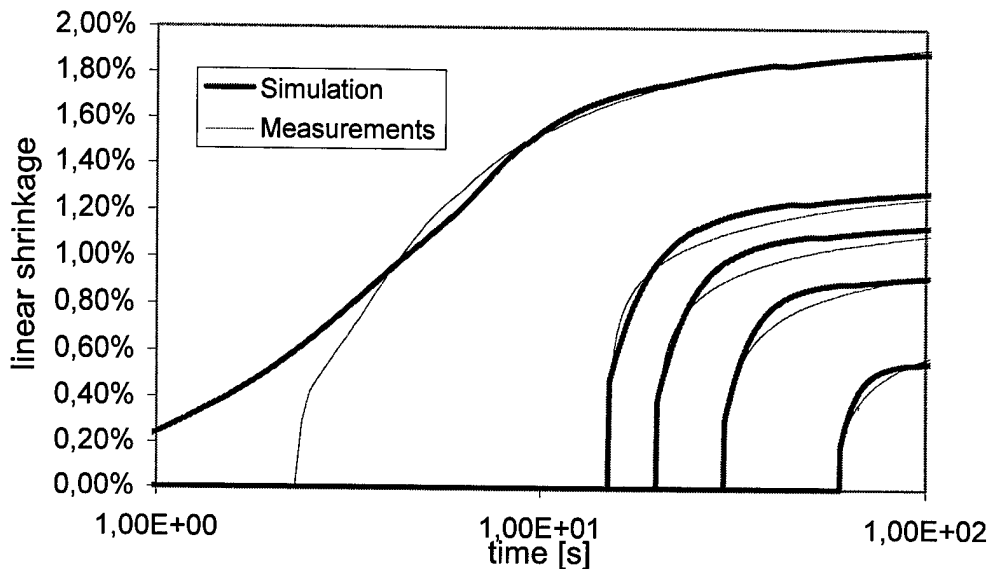


Figure 9: Comparison of simulation and experiments (Epoxy)

6 Conclusions

The differences between epoxy and acrylate resins become quite clear when investigating the material properties during the curing process. The epoxy resin show the same linear shrinkage, but because the cure slower, the stress due to the shrinkage is smaller. Together with the higher final stiffness this explains the better accuracy of parts.

References

- /1/ Dusel K.-H.; Eschl J.; Wiedemann B.: Improvement of Part Accuracy - Investigation into the Basics of Photopolymerisation; In: 5th European Conference on RPM, University of Nottingham, 4th-6th of June, 1996.
- /2/ Colton Jonathan, Bryan Blair: Experimental study of post build cure of stereolithography polymers for injection molds. Rapid Prototyping Journal, Volume 5, Number 2, 1999, MCB University Press, Great Britain. 1999.
- /3/ Schön Lothar, Bayer Heiner, Fischer Walter, Muhrer Volker, Approaches to improve photopolymers for stereolithography. 6 th European Conference on RPM, University of Nottingham, 1st – 3rd of July, 1997.
- /4/ Xu Yi, Imamura Masato, Nakagawa Takeo, Heat Generation of Photopolymer by UV-Laser Exposure, Proceedings of the 7th International Conference on Rapid Prototyping, March 31-April 3, 1997, University of Dayton

RAPID PATTERN BASED POWDER SINTERING WITH ROOM TEMPERATURE POLYMER INFILTRATION

Zongyan He, Yong S. Kim, Monnappa Kokkengada and Jack G. Zhou
Department of Mechanical Engineering and Mechanics
Drexel University, Philadelphia, PA 19104

ABSTRACT

In this paper a new rapid tooling technique, named Rapid Pattern Based Powder Sintering (RPBPS), is introduced. Due to limitations of common infiltration methods used in rapid tooling such as high temperature caused cracks, distortion, shrinkage and poor surface quality, a low temperature polymer infiltration method is proposed. Based on the curing principles of polymer materials, several kinds of infiltration materials were selected, and their main mechanical and thermal properties and chemical resistances were discussed. With various infiltration methods and materials, a series of testing samples were made, and their microstructures and thermal resistances were observed and tested. In order to calculate the needed amount of the polymer materials and their infiltration height in the sintered molds or parts, an infiltration model was also proposed and compared with experiments.

INTRODUCTION

Rapid prototyping/tooling and manufacturing have experienced tremendous growing and drawn great attention in national and international manufacturing industry (Jocobs, 1996). Although rapid prototyping has brought in a new revolution in manufacturing processes of materials by using additive and layer by layer material processing technique, its crown has gradually shifted to rapid tooling/manufacturing, i.e. not only prototype but also functional products. The development list of Rapid Tooling (RT) technology based on rapid prototyping and manufacturing has been growing during recent years (Vanputte, 1994). Over ten RT methods have been proposed, and examples are 3D Systems's Keltool, DTM's RapidSteel, CEMCOM's NCC Tooling, Dynamic Tooling's PolySteel, ExpressTool's Electroforming, and Extrudehone's PROMETAL (Ashley, 1998). Rapid Pattern Based Powder Sintering (RPBPS) technique (Zhou and He, 1998, 1999) developed by the authors is a new rapid tooling technique. This technique is suitable for a variety of materials and any complex geometry, and also has the advantages of rapid process and low cost. Like many other RT techniques, such as Keltool, RapidSteel and NCC Tooling, RPBPS technique involves two main processing steps: sintering and infiltration. After a green mold or part, having desired cavity/geometry, is made through laser scanning (such as in RapidSteel) or casting the mixture of metal powder and polymer binder (such as in Keltool, NCC Tooling and RPBPS), it will be sintered in protective atmosphere. During this process the binder material will vaporize and/or carbonize and then escape from the green products, and the remains, i.e. the metal particles will be sintered to form a solid body. To increase the strength and hardness, the sintered mold/part will be infiltrated with some alloys, such as brass and bronze. In general, the infiltration alloy should have a lower melting temperature than that of the powder material, so that the melted alloy can soak into the sintered product and fill into all porous. During the infiltration process the product will have a linear shrinkage of 2%-5%. The shrinkage depends mainly on two factors. First is the temperature for melting the infiltration alloy. For brass, zinc amount is over 30% by weight and

copper around 70%. For bronze, the tin amount is over 35% by weight and copper around 65%. Their melting temperature are both over 1830 F. The second factor is the time for maintaining the high temperature which depends on the size and geometry of the product to be infiltrated. In general, the time will be controlled as short as possible. Based on our experiments when infiltrating a sintered one-inch-cube part of low carbon steel powder with brass, the furnace should maintain a temperature of 1830 F for at least 25 minutes. Under these conditions the linear shrinkage of the infiltrated product will reach 2.5%-3%. Another problem in the infiltration process is the distortion of the product caused by the non-uniform temperature distribution in the furnace and the complex geometry of the product. In some special cases the product may crack on the positions with sharp angle change or discontinuous change of wall thickness. The research presented in this paper is an effort toward a new infiltration method. Based on RPBPS technique some special polymer materials to infiltrate the sintered mold/part in room temperature have been used. First, a brief introduction on RPBPS technique and main processing steps is given. According to the desired characteristics the infiltration materials are chosen, and their properties are listed and compared. Then some details on the infiltration process are discussed. Furthermore, the microstructures and thermal properties of the infiltrated samples is illustrated and tested. Finally, a model on the infiltration process was deduced and compared with experiments.

TECHNICAL PROCESSES

Rapid Pattern Based Powder Sintering (RPBPS) technique is to seek out more efficient way to make rapid tooling and manufacturing. This new technique includes the following main steps (see Figure 1). First, a master pattern made of polymer material is fabricated by using a rapid prototyping machine based on a 3-D solid model designed in a CAD system. Then the pattern is positioned on a substrate in a metal box or frame, and then a mixture of metal or ceramic powder and binder is cast around the pattern under certain pressure. After removing the pattern and separating the substrate, a green compact having desired cavity/geometry can be obtained. Then the green compact will be sintered and infiltrated in a protective gas, such as nitrogen or hydrogen, to finally form a tool, mold or part. The reason that the RPBPS is better than other rapid tooling methods can be concluded as that it overcomes the defects of other RT methods and adopts the merit from various tooling techniques. RPBPS technique is suitable for a variety of materials and any complex geometry, and also has the advantages of rapid process and low cost. In order to save time and energy and reduce the shrinkage, the sintering and infiltration processes can be carried out in one step (see Zhou and He, 1998). Figure 2 shows a typical program on the sintering/infiltration process, in which the powder material is carbon steel, the infiltration alloy is brass, and the protective gas is nitrogen. There are still some problems when using this program. One is the reaction between the escaping carbon smoke and the infiltration alloy. Based on our experiments, from about 600–650 F the binder material will carbonize to form a large amount of carbon smoke. a temperature-keeping stage (see Figure 2) for the escape of smoke from the furnace is designed. However, some carbon particles will still remain on the surface of infiltration alloy, with the increase of temperature the alloy will react with carbon to form carbide.

On the other hand, for improving the temperature distribution to reduce the distortion of the green compact we can use ceramic powder, such as alumina, to fill all concave angles, hollows or holes of the compact to reduce uneven temperature distribution. But the powder may

hinder the carbon smoke's escape so that some carbon particles will remain in the compact. The remainder will cause two problems: the metal particles can not be sintered well and the melted alloy can not soak into the compact well due to the poor wettability of the metal particles. Using some special polymer materials to infiltrate the sintered compact in room temperature have been developed. We hope by using this technique not only the products will have very small shrinkage and distortion, but also the time and energy can be saved. We also hope the infiltrated parts have better mechanical and thermal properties to be applied in practical production.

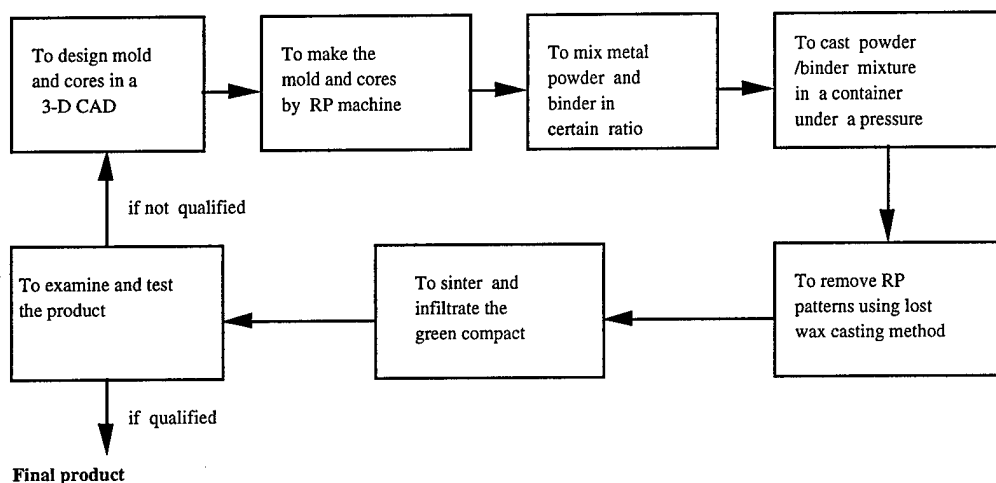


Figure 1. The main steps of RPBPS process

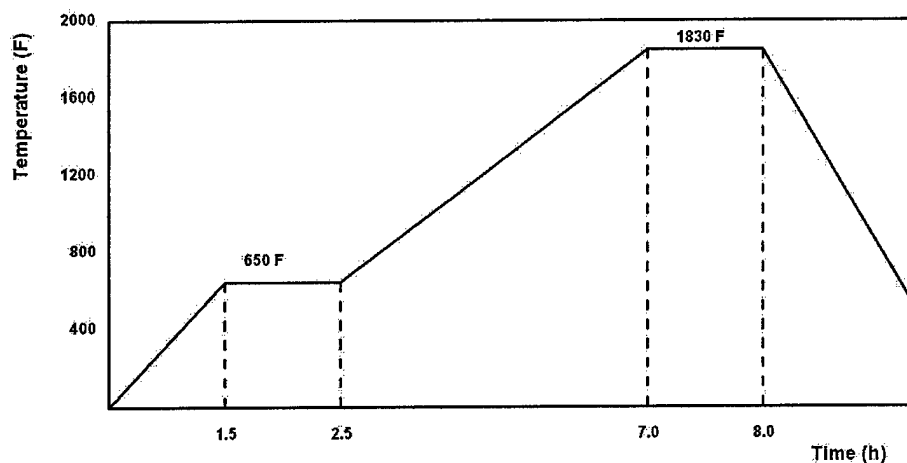


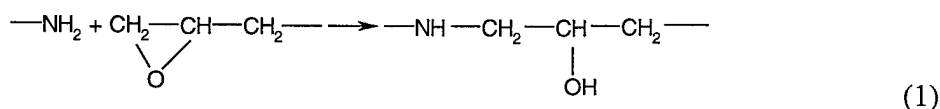
Figure 2. The program of sintering/infiltration process

SELECTION OF INFILTRATION MATERIALS

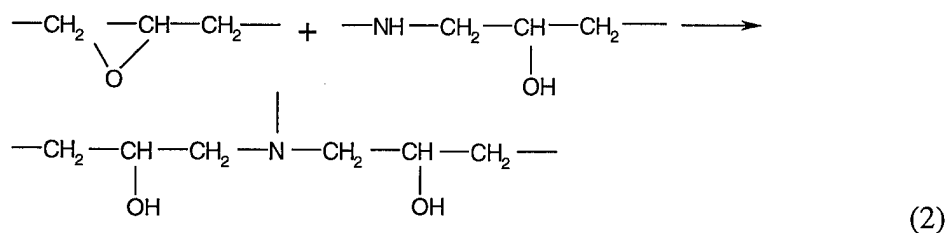
It is expected that a suitable infiltration material should have the following characteristics. (1) It should have a liquid state in room temperature, but in certain conditions it can transform into solid. (2) The transformation from liquid to solid should be irreversible, and the volume change caused by the transformation should be as small as possible. (3) In liquid state the material should have a lower viscosity and higher wettability to the metal powder in order to soak into the sintered compact easily and quickly. (4) When solidified the material

should have a certain strength, hardness and chemical resistance. (5) For making mold or tool the solid material should bear a higher temperature and a hot-cold temperature cycle for a longer time, and it has a higher thermal conductivity.

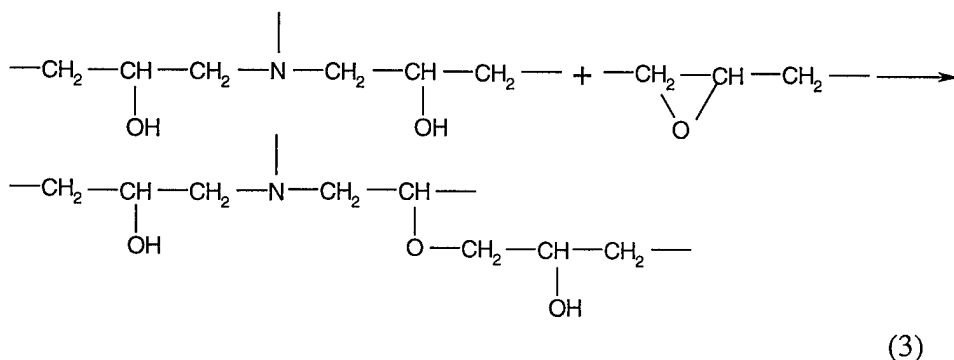
Metallic materials have high strength, hardness, heat-resistance and thermal conductivity, but they can not satisfy the above condition (1). It is also difficult for ceramic or inorganic materials to meet the above conditions (1) to (3). Most organic materials have lower strength and hardness. Especially they can not withstand higher temperature. However some polymer materials can meet above mentioned five requirements. Because of the advantages of its very applicable structure, behavior, and fundamental properties, polymers are used in many manufacture areas (Flory, 1953, Gedde, 1996). Our focus is on special resins and their thermal properties. For example, before cured an epoxy resin may have a lower viscosity like a liquid, but after cured it may have a higher strength and rigidity like a solid. A resin's cure can be carried through cross-linking of linear molecules. The degree of cross-linking depends mainly on the hardener and/or surrounding temperature. If using polyamine or other kinds of amine as hardener, the cross-linking process can be described as follows. First a cyclic chain in epoxy resin radical will be opened:



Then another cyclic chain can be opened under the action of the resultant of the first step reaction.



The next etherification reaction is



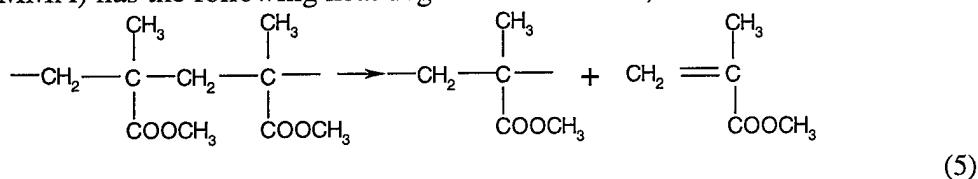
The produced hydroxyl can continuously react with epoxy resin radical to form net structure. Some resins can be cured through heating not using any hardener, and the curing temperature is only little higher than room temperature. In general the cure of resin is an irreversible process, and its volume change during the process is very small (for most epoxy resins it is less than 0.15%). So the second condition can be satisfied. Because some resins or their solutions have very low viscosity, and most metal materials can be wetted by them. So the third condition is also not a problem. But the strength and hardness of most resins are not so high. Especially,

their heat deformation resistance and heat stabilization are all much lower than that of metallic materials. The last two conditions limit our choice space greatly.

For polymer materials, a high heat deformation resistance means the high glass transition temperature T_g . The glass transition is analogous to a melt. As the temperature is raised, crystalline solid like metal or polyethylene melt and become liquids. Amorphous solids like glass and resin pass through a temperature range where the molecules rapidly gain in mobility. This molecular mobility results in flow or creep, and in rapid dimensional change. We are able to use several methods to increase T_g : (1) To change the structures of main chain of the existing polymer binders. If the main chain is composed with saturated single bond, such as $-C-C-$, $-O-C-$ or $-Si-O-$, its T_g will be very low; (2) To increase the polarity of lateral group. Due to stronger forces between bonds, the polymers with strong polar lateral group will have a higher T_g ; (3) To increase the molecular weight M . In general, T_g will increase with the increase of M . There is a relationship between them,

$$T_g = T_g(\infty) - K / Mn \quad (4)$$

where $T_g(\infty)$ denotes the glass transition temperature when molecular weight is infinite, K is a constant and Mn denotes the number mean molecular weight. (From this equation one can see when Mn is big enough the effect of increasing T_g will decrease greatly.) (4) To use cross linking method. Cross-linking among molecules can hinder the movement of molecular chain segments, thus T_g will be raised; (5) To use copolymerization method. In fact, if the monomers have similar properties, the T_g of the copolymer has a linear relationship with the weight ratios of monomers. The heat stabilization means the thermal decomposition resistance. In general, degradation and cross-linking of polymers can occur simultaneously under high temperature. The two reactions are both related to the break of chemical bonds. The heat degradation has two modes: depolymerization and random break of bonds. For example, polymethyl methacrylate (PMMA) has the following heat degradation reaction,



Degradation will result in tacky and soft of polymers. We can use several methods to increase the heat stabilization of the existing polymer binder. (1) To increase the strength of bond in the molecular chains and avoid weak bonds, such as $(C-Cl)$, $(C-S)$ and $(O-O)$. (2) To add in aryl heterocycle structure and decrease $(-CH_2-)$ structure in main chain. (3) To add in some heat stabilization agents, such as stearates. The above analyses provide us a choice direction among hundreds of resins.

PROPERTIES OF SELECTED INFILTRATION MATERIALS

We have found several kinds of resins as the candidates. (1) Phenolic resin. Phenolic resin is classified as a condensation reaction polymer. In this type of reaction, the polymer grows by combining two large molecules and releasing a third small molecule, usually water. A wide range of characteristics can be designed into a phenolic resin. Reactivity, moisture content, molecular weight, pH value, monomer level, viscosity, flow and lubricity all may determine the suitability of the resin for our needs. A key property of phenolic resin is the ability to withstand higher temperature. Unlike most polymers, the T_g of phenolic resin can be further elevated to

levels in excess of 260°C by a correct design. Considering that an injection mold needs to bear only 100°C-150°C for the manufacture of common plastic parts (for ABS parts, the mold needs to withstand 215°C), we select phenolic resin for the infiltration of injection molds. The solution can penetrate and soak very easily into the sintered compacts no matter what kind of powder materials. Its curing temperature is around 150°C, the shrinkage during the cure process depends on the density of the solution. The lower the viscosity, the lower the density, but the larger the shrinkage will be. Main specifications of Plenco 06582 are in Table 1.

Table 1 Typical Properties of Infiltration Materials

Resin	AboCast50-3	AboCast50-6	AboCast50-24	Plenco 06582
Hardener	Cure50-17	Cure50-17	Cure50-17	
Ratio (resin/hardener) by wt.	100/26	100/28	100/115	100/0
BI. Viscosity (cps/°C)	110/70	70/70	80/25	50/25(50%alcohol)
Specific Gravity (H ₂ O=1)	1.87	1.75	1.89	1.59
Flexural Strength (Mpa)	94.9	107.3	90.5	93.8
Flexural Modulus (Mpa)	3,900	3,520	3,450	7,952
Tensile Strength (Mpa)	67.1	70.3	57.8	59.0
Tensile Modulus (Mpa)	3,750	2,170	4,250	8,982.0
Compressive Strength (Mpa)	118.1	124.0	110.6	115.0
Tensile Elongation (%)	4.4	3.0	4.7	0.7
Hardness, Rockwell	106(M scale)	109(M scale)	104(M scale)	42(E scale)
Mold Shrinkage (m/m)	0.001	0.0012	0.002	0.0023
Water Absorption (%)				0.17
Deflection Temperature (°C)	160	157	170	221
Heat Resistance (°C)	230	257	298	238
Thermal Expansion (°C)				5.3E-5
Thermal Conduction(W/m°C)				0.44
Thermal Degradation (wt. loss) After 100 hrs, 160°C	0.55%	0.44%	0.65%	
Chemical Resistance (wt. loss) Aft 120days, 30% Sulfuric Acid	2.60%	1.96%	1.96%	
Chemical Resistance (wt. loss) After 120 days, 50% Sodium Hydroxide	0.05%	-0.12%		
Chemical Resistance (wt. loss) After 120 days, JP 4 Fuel	0.27%	0.11%		
Cure temp.& time (°C/hour)	80/1.5	80/2.5	25/14	80/(12-20)

(2) Epoxy resin. The principle of the cure of epoxy resin has been shown in Equations (1)-(3). Most epoxy resins have higher viscosity and lower heat-resistance. But some modified epoxy resins can be as ideal candidates. For example, the viscosity of Resin AboCast 50-3 (see Table 1) is 110 cps (at 70°C), it is just like that of light motor oil. The viscosity of Resin AboCast 50-16 is even less than 110 cps. However, as above mentioned in phenolic resin, the resin with lower viscosity must have a lower strength and heat-resistance and a larger shrinkage. We should compare all properties of various resins to make the decision, see Table 1.

METHODS OF INFILTRATION PROCESS

Before infiltration, the green compact will be sintered. For steel powders the sintering temperature and keeping time are controlled not over 1400 F (760°C) and 30 minutes. In this case the linear shrinkage of the sintered compact can be controlled less than 1%. After sintered the surface of the compact needs to clean carefully to remove oxidized layers, then the compact will be put into the prepared infiltration material. Figure 3 shows three methods for infiltrating a sintered mold. If the infiltration material has a higher viscosity and the viscosity increases continuously even in room temperature, the process may be carried so slowly that the sintered

mold can not be infiltrated completely. In other word, before the center parts of the mold are infiltrated the materials close to the surface have been cured to form a solid "outside shell". Thereby, when using some epoxy resins, such as AboCast 50-3 or AboCast 50-6, we must consider the thickness of the mold and the surrounding temperature. If the thickness is bigger and the temperature is higher we will use the Method (a) shown in Figure 3. In this method the inside surface of the mold (called working surface) is kept to not contact with the resin, which will soak into the mold from its bottom and outside wall. The whole container is kept in a refrigerator with a lower temperature for a longer time until the top surface of the mold is infiltrated. Because the above two kinds of epoxy resins have dark colors, the color of the infiltrated surface is different from that not treated, from which we can guess if the process has been finished. Then the infiltrated mold will be heated for further cure of the resin.

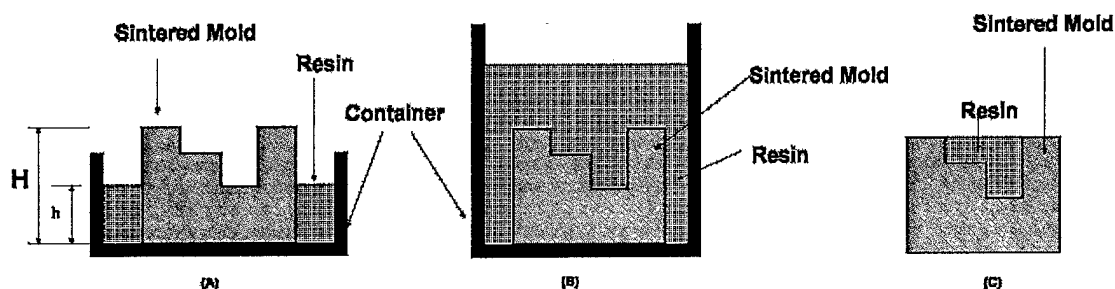


Figure 3 Three methods for infiltrating a sintered mold

If the infiltration material has a lower viscosity and it increases very slowly during the process, then we can choose Method (b). In this method the whole mold sinks into the resin for a period of time, then it is taken form the container to remove remain resins. Then the mold will be heated for the cure of the infiltration material. For those molds with a smaller thickness we can use Method (c). In this method the resin is directly poured into the concave part of the mold, more resin will be added until whole mold is infiltrated, then the mold will be heated. No matter what methods we use, we must guarantee all porous to be filled and the mold has a clear working surface. For this object we should know the accurate amount of the needed resin and the mechanism of the infiltration process.

MODELING OF INFILTRATION PROCESS

When a sintered mold or part sinks into a resin that has a lower viscosity and higher wettability to the sintered material, the resin can enter the inside of the mold automatically. This is caused by the capillarity. The capillarity effect depends on several factors: the surface tension of resin, the size of the capillary tube and the contact angle between resin and tube wall that represents the wettability of the resin. In a straight circular tube a pressure difference caused by the capillarity effect will be (Sears et al, 1984),

$$\Delta p_s = 2\sigma \cos\theta / r \quad (6)$$

here σ denotes the coefficient of surface tension, θ is the contacting angle and r is the radius of the tube. The height difference that the liquid can rise in the tube from its top surface due to the capillarity will be

$$H - h = \Delta p_s / d \quad (7)$$

here H is the height of the tube, h is the height of the liquid top surface and d is the density of the liquid. We can not directly use the above formulas to calculate the infiltration height of a sintered mold as shown in Figure 3(a), because gaps and holes contained in the sintered mold are not straight circular tubes. If we want to simplify them into straight circular tubes, we must first know their equivalent radius r' , i.e. the radius of a circular cross section that has the same area as that of the gap/hole. In fact, r' is related to the size of the powder particle and the gap ratio of the sintered mold. As shown in Figure 4, we assume that the microstructures of sintered mold can be simplified as many cylinders that are bonded together after sintered. From the cross section view there are several simplified arrangement modes (see Figure 4). Every mode has the corresponding gap ratio λ . For Mode (a), we have $\lambda_a = [S_{abc} - 3(\pi R^2)/6]/S_{abc} \approx 0.092$, in which S_{abc} denotes the area of triangle abc and R denotes the radius of a particle. For Mode (b), we have $\lambda_b = [S_{abcd} - 4(\pi R^2/4)]/S_{abcd} \approx 0.215$, in which S_{abcd} denotes the area of square $abcd$. For Mode (c), we have $\lambda_c = [S_{abcdef} - 6(\pi R^2/3)]/S_{abcdef} \approx 0.395$, in which S_{abcdef} denotes the area of hexagon $abcdef$. Based on our experiments the gap ratio of sintered molds or parts is about 0.20-0.42, so Mode (b) and (c) are more reasonable than Mode (a). Considering that the gap ratio depends mainly on the binder ratio in the green compact and the casting pressure, when the binder ratio is smaller and the casting pressure is bigger we select Mode (b), or select Mode (c).

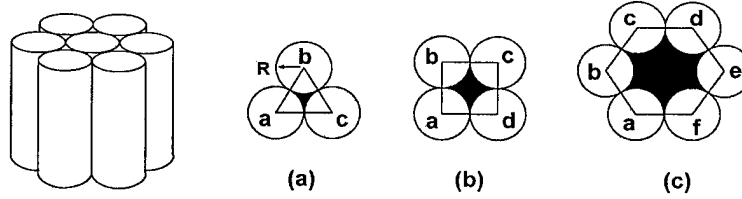


Figure 4. The simplified microstructure of sintered particles and three arrange modes

Now we calculate the equivalent radius r' . In the Mode (b), the area of the black part will be $S_b = (2R)^2 - 4(\pi R^2/4) = \pi r'^2$, from which we have

$$r' = \sqrt{4/\pi - 1}R \quad (8)$$

Considering that $\lambda_b = S_b/(2R)^2$, we have

$$r' = \sqrt{4\lambda_b/\pi}R \quad (9)$$

In the Mode (c), the area of the black part will be $S_c = 6\sqrt{3}R^2 - 2\pi R^2 = \pi r'^2$, which will be

$$r' = \sqrt{6\sqrt{3}/\pi - 2}R \quad (10)$$

Considering $\lambda_c = S_c/(6\sqrt{3}R^2)$, we have

$$r' = \sqrt{6\sqrt{3}\lambda_c/\pi}R \quad (11)$$

Let r in Eq. (6) be replaced by r' in Eq. (9) and (11) and considering Eq. (7), we can deduce two relationship formulas

$$H - h = \sqrt{\pi} \sigma \cos \theta / (dR\sqrt{\lambda}) \approx 1.77 \sigma \cos \theta / (dR\sqrt{\lambda}) \quad (12)$$

$$\text{and} \quad H - h = 2\sqrt{\pi} \sigma \cos \theta / (\sqrt{6\sqrt{3}} dR\sqrt{\lambda}) \approx 1.10 \sigma \cos \theta / (dR\sqrt{\lambda}) \quad (13)$$

As above mentioned, only when the ratio of binder is very small (less than 1% by wt.) we can use Eq. (12), in general case we use Eq. (13) to estimate the infiltration height (see Figure 3). For example, if the infiltration material is water, then $\sigma = 7.3 \times 10^{-2} \text{ N/m}$, $\theta = 0^\circ$ (complete wettability), $d = 1 \text{ g/cm}^3$, $R = 50 \times 10^{-6} \text{ m}$, $\lambda = 0.3$. According Eq.(13), the height that water can rise automatically in the sintered sample is about 0.286m. But if using brass alloy (zinc 35% by wt) as infiltration material, we have $\sigma = 0.12 \text{ N/m}$, $\theta = 0^\circ$ (complete wettability), $d = 6.4 \text{ g/cm}^3$, $R = 50 \times 10^{-6} \text{ m}$, $\lambda = 0.3$. Then the infiltration height is about 0.075m, so if the thickness of the sintered sample is over 8cm the top surface may not be infiltrated by the melted alloy. If using epoxy resin AboCast 50-24 for infiltration, we have $\sigma = 4.0 \times 10^{-2} \text{ N/m}$, $\theta = 30^\circ$ (good wettability), $d = 1.89 \text{ g/cm}^3$, $R = 50 \times 10^{-6} \text{ m}$, $\lambda = 0.3$. Then the infiltration height is 0.074m, so if the thickness of the sample is not over 7cm we will use the method (a) shown in Figure 3. But for a mold with a much bigger thickness we may consider other methods or using different infiltration materials. The above calculation results are in better accord with experiments.

CONCLUSIONS

RPBPS is a rapid tooling technique and is suitable for a variety of materials and any complex geometry, and also has the advantages of rapid process and low cost. Some epoxy and phenolic resins with lower viscosity and higher thermal resistance can be used in the RPBPS technique as infiltration materials. Based on the simulation, the parts infiltrated with phenolic resins have enough thermal resistances so that we can use them in injection machining process. According to the deduced infiltration model, we can estimate the needed amount of the resin and their infiltration height in the sintered molds or parts.

REFERENCES

- Ashley, Steven, "Rapid Prototyping Industry's Growing Pains," *Mechanical Engineering*, ASME, July 1998, pp. 64-68.
- Jacobs, P.F. (1996), *Stereolithography and other RP&M Technologies, from Rapid Prototyping to Rapid Tooling*, SME Press, New York.
- Vanputte, D.A. (1994), "Rapid Tooling is a Key Factor in Future Achieving Rapid Product Development", *Proceeding of 27th ISATA Conference*, Aachen, Germany, Paper No. 94RA024.
- Gedde, U.W. (1996), *Polymer Physics*, Chapman & Hall, London, pp.13-15 & 217-237.
- Flory, P.J. (1953), *Principles of Polymer Chemistry*, Cornell University Press, Chap.10.
- Sears, F.W., Zemansky, M.W. and Young, H.D. (1984), *University Physics*, sixth edition, Addison-wesley Publishing Company, Massachusetts, reprinted in Feb., 1984, pp253-255
- Zhou, J., and Z. He, "A New Rapid Tooling Technique and Its Special Binder Study," *Journal of Rapid Prototyping*, Vol. 5, No. 2, 1999.
- Zhou, J., and Z. He, "Rapid Pattern Based Powder Sintering Technique and Related Shrinkage Control," *Journal of Materials and Design*, Vol. 19, pp. 241-248, 1998.

Structural Analysis of Silicon Carbide Deposited by Gas-Phase Selective Area Laser Deposition (SALD)

by S. Harrison and H.L. Marcus

Institute of Materials Science
97 North Eagleville Road
Storrs, CT 06269-3136

(860) 486-4623
Fax: (860) 486-4745

Abstract: Silicon carbide deposited by the gas-phase Selective Area Laser Deposition (SALD) process underwent extensive structural analysis in this investigation. The silicon carbide material was locally formed from a gas precursor mixture of tetramethylsilane and hydrogen, at a deposition temperature of approximately 1100°C and maintained by a closed-loop laser control system. Ground powder samples of the SALD silicon carbide material were examined by Magic Angle Spinning-Nuclear Magnetic Resonance, X-ray Diffraction and Transmission Electron Microscopy. The results from these analytical tools show a significant level of twinning in the SALD SiC material which explains the significant differences between the NMR and X-ray spectra.

Introduction: Gas-phase Selective Area Laser Deposition (SALD) is a laser-driven chemical vapor deposition (CVD) process that locally forms the desired solid material in the laser beam heated zone. A schematic of the process is found in figure 1. Silicon carbide has been repeatedly deposited from a gas mixture of tetramethylsilane (TMS, $\text{Si}(\text{CH}_3)_4$) and hydrogen in several SALD-based techniques, such as SALDVI and SALD Joining¹⁻⁴. The SALD SiC material, as well as other, similar CVD SiC deposits, was previously revealed to be the beta, face-centered cubic crystalline polytype through x-ray diffraction analysis (XRD)⁵⁻⁷. Magic Angle Spinning Nuclear Magnetic Resonance (MAS-NMR) was performed on SiC SALD samples as a secondary identification tool but the resulting spectra showed significant deviation from the expected beta silicon carbide pattern. Further investigation using fine structure XRD pattern modeling and transmission electron microscopy (TEM) dark field imaging and selective area electron diffraction methods were undertaken to reconcile the initial XRD findings and the MAS-NMR results. The explanation focuses on the nano- and sub-nanometer structure in the SALD SiC material, specifically the formation of twins.

Experimental: The SALD silicon carbide material was fabricated using a continuous wave Neodymium:YAG laser ($\lambda = 1.064$ microns) directed into a stainless steel vacuum chamber. The gas precursor environment was a 1:2 ratio of TMS to hydrogen and the deposition temperature was approximately 1100°C, as maintained by the closed-loop temperature control program. After the silicon carbide deposited onto a silicon carbide substrate, the SALD material was broken off and ground to a powder with a mortar and pestle. This powder then underwent the various investigative procedures.

The magic-angle spinning method is the necessary technique for NMR analysis of inorganic solids. Until the early 1970's, NMR spectra of inorganics suffered from broad peak

structure and high background noise due to orientation effects and nuclear interactions⁸. This was addressed by spinning the sample at an angle of 54.7° to the applied magnetic field. The magic angle orientation mitigated these secondary interactions and the resulting NMR spectra have sharper peaks and lower background noise. The SALD silicon carbide powder samples were packed into a zirconia pencil rotor and spun at the magic angle at a 5 kHz spinning rate in a Chemagnetics CMX300 NMR spectrometer. The spectrometer utilized a commercial double-bearing 7.5 millimeter MAS probe with the following acquisition parameters: 90° pulse width for ²⁹Si, 40 kHz spectral width and Fourier transformation with 40 Hz line broadening. The chemical shifts presented in the spectrum are relative to the silicon environment in liquid TMS using an external sample of solid tetrakis-trimethylsilyl-silane (TTMS) as the secondary reference.

The x-ray diffraction experimental patterns were acquired with a Bruker 5005 x-ray diffractometer using a copper source. The x-ray diffraction pattern modeling originated from a computer simulation program that was devised to replicate x-ray diffraction patterns of dominantly beta silicon carbide. Based on considerations of the amount, type and manner of production of stacking faults in the material morphology, the diffraction simulation produces patterns by selecting the type and frequency of stacking errors in the beta polytype sequence, ABCABC^{9,10}. This simulation generates 1000 silicon-carbon layers to form a supercell, with the layers labeled A, B or C depending on the atom position determined for the specific layer. The type of layer created depends on three user-controlled variables that set the probability of forming a stacking fault in a regular cubic lattice, the likelihood of whether the initiated fault continues and the distribution of faults in a certain region. After 15 supercells are formed, the model calculates structure factors and d-spacings in the 15000 layer structure for (hkl) planes in the 2θ range of interest. Diffraction intensities are evaluated on per volume basis, making the calculations independent of the supercell size. In the SALD SiC investigation, the 30° to 45° 2θ region was modeled to examine the background intensity surrounding the (111), 35.6° peak, the intensity of the (200), 41.6° peak and possible shifts in the peak positions.

TEM dark field imaging and selective area electron diffraction were performed on a Phillips EM420 unit with an accelerating voltage of 100 kilovolts.

Results: The typical SALD silicon carbide x-ray pattern is found in figure 2, with three dominant peaks at approximately 35.6°, 60° and 72°. The NMR spectra of SALD SiC (A), a 50/50 weight % alpha/beta SiC powder physical mixture(B), a 100% beta SiC powder standard (C) and a 100% alpha SiC powder standard (D) are shown for comparison in figure 3. The x-ray diffraction modeling results appear in figure 4. The black line pattern is from an experimental SALD SiC sample, while the gray line pattern represents the attempt of the computer model to match the experimental result. The accompanying stacking fault data that the model produced in replicating the experimental pattern is found in table 1. TEM bright field and electron diffraction images are presented in figures 5 and 6 respectively. The zone axis of the diffraction pattern from the FCC silicon carbide is [110].

Discussion: As mentioned previously, the SALD SiC XRD pattern indicates the 3C, beta polytype crystal structure, although the 4th main peak at 41.6° is not significant. The NMR patterns, which are discussed more fully in another publication¹¹, show significant variation of the SALD SiC from the one dominant peak pattern of the beta powder standard NMR spectra. Although the SALD pattern appears to be a mixture of the alpha and beta standards, the

characteristic shape could not be reproduced by physically mixing the 2 polytypes in various ratios, including the 50:50 weight % combination in figure 3D. Because the NMR probes the local chemical environment at the Angstrom level, the SALD results point to a change in the atomic structure and order from the pure beta stacking sequence. The XRD modeling data support this hypothesis. The fine detail of the SALD XRD pattern shows a broad hump before the 35.6° peak and a very broad, low intensity peak at 41.6°. The model output pattern shows excellent correlation to the experimental pattern and the raw data indicates a significant presence of 1, 2 and 3 layer stacking faults, over 75% of the faults generated. The stacking sequences for these faults, i.e. AA'AA'AA' for 1 layer, ABA'B'AB for 2 layer and ABCB'A'C' for 3 layer, correspond to hexagonal alpha polytype regions of 2H, 4H and 6H respectively. These faults are twin structures, with a 180° rotation of orientation across the twin plane. Further modeling efforts showed that as the quantity of faults was reduced, the intensity and sharpness of the 41.6° peak increased.

The physical evidence of twins was provided by the TEM analysis. Twins are indicated in TEM bright and dark field images by alternating contrast bands in the twinned regions. This contrast alternation arises from the 180° phase orientation rotation of adjacent regions. Similarly, the electron diffraction patterns show diffraction spot reflections across the twin plane. These reflections are the result of two diffraction patterns superimposed onto one image again due to the orientation rotation caused by the twin. Multiple spots occur at expected diffraction positions except along the twin plane, which produces only one spot per position because the plane acts as the mirror plane. Streaking of the diffraction spots also points to the presence of twins. The TEM images in figures 5 and 6 show these anticipated features. The twin plane from the diffraction pattern in figure 6 is a (111) type as is typical in FCC materials. The twin bands in figure 5 range from .5 nanometer to several nanometers across. This is consistent with the belief that stacking disruptions led to the unique NMR results for the SALD SiC material. These twin features were widespread throughout the TEM SALD silicon carbide samples.

Conclusions: SALD silicon carbide is a bulk face-centered cubic crystalline material that shows a significant level of twinning in the stacking structure. These twin features are in effect alpha polytype, hexagonal domains on the Angstrom/nanometer scale. The presence of the alpha regions in the bulk material is the source of the unique NMR spectra and x-ray diffraction fine structure for the SALD silicon carbide material.

Acknowledgments: The authors would like to acknowledge Dr. Vijay Pujar and Dr. Sean Xie for their aid and effort during this project, as well as the partial funding support of the Office of Naval Research, grant # N00014-95-1-0978.

Figures and Tables

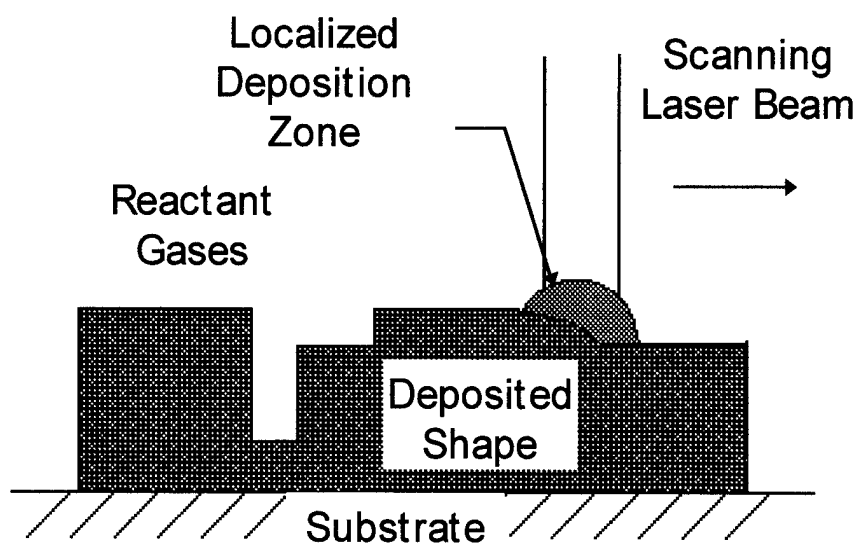


Figure 1: Schematic of Selective Area Laser Deposition (SALD) Process

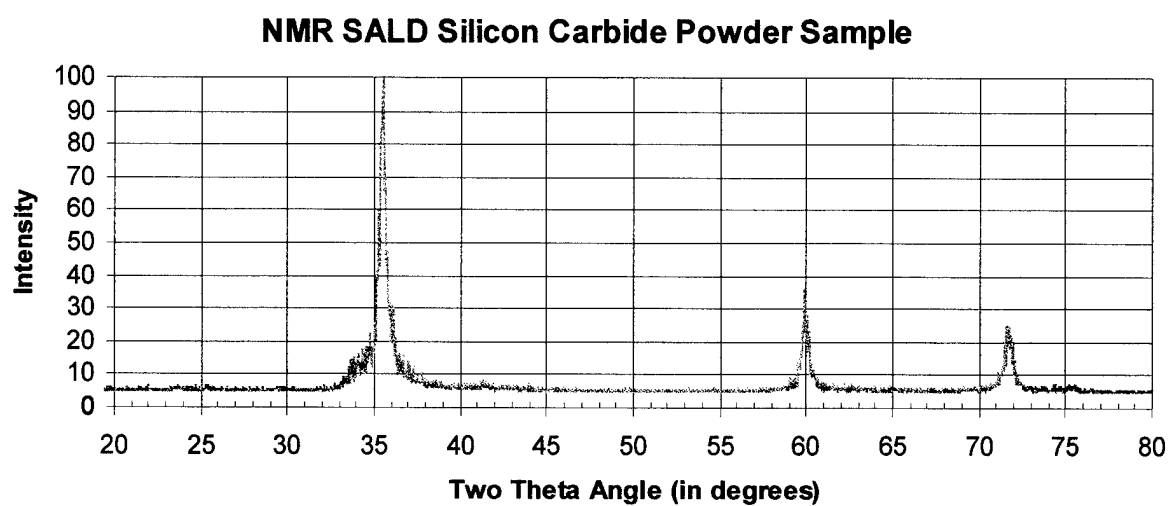


Figure 2: Powder X-ray Diffraction Pattern for Typical SALD Silicon Carbide Sample

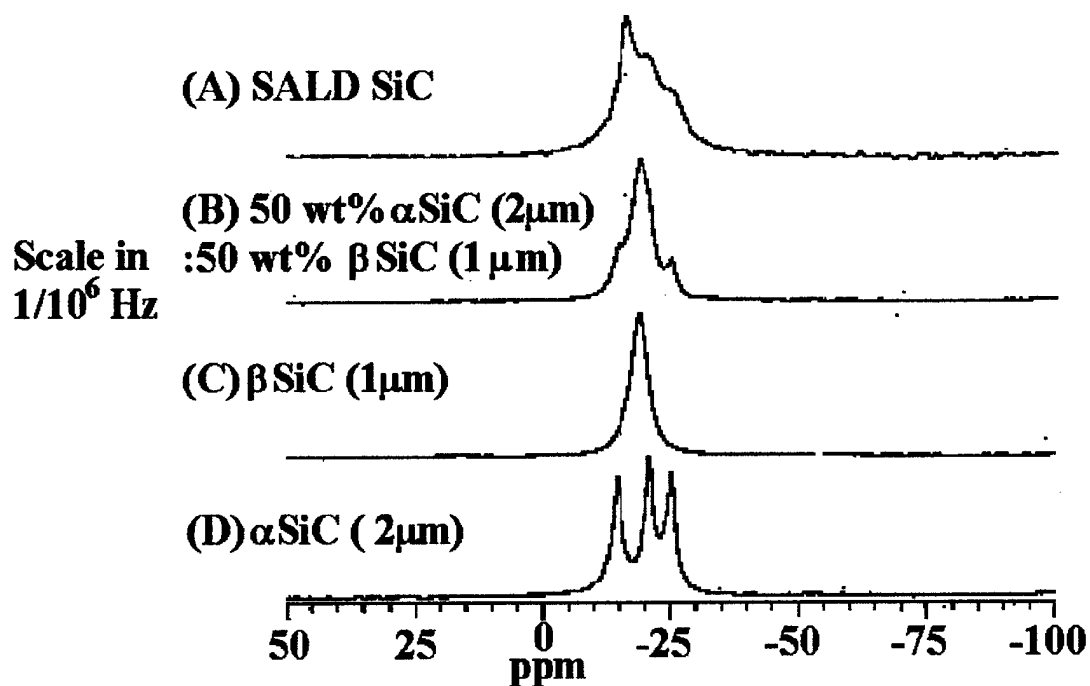


Figure 3: Magic-Angle-Spinning Nuclear Magnetic Resonance Spectra for SALD Silicon Carbide (A), 50/50 Weight % Alpha/Beta SiC Powder Mixture (B), 100% Beta Silicon Carbide Powder Standard (C) and 100% Alpha Silicon Carbide Powder Standard (D)

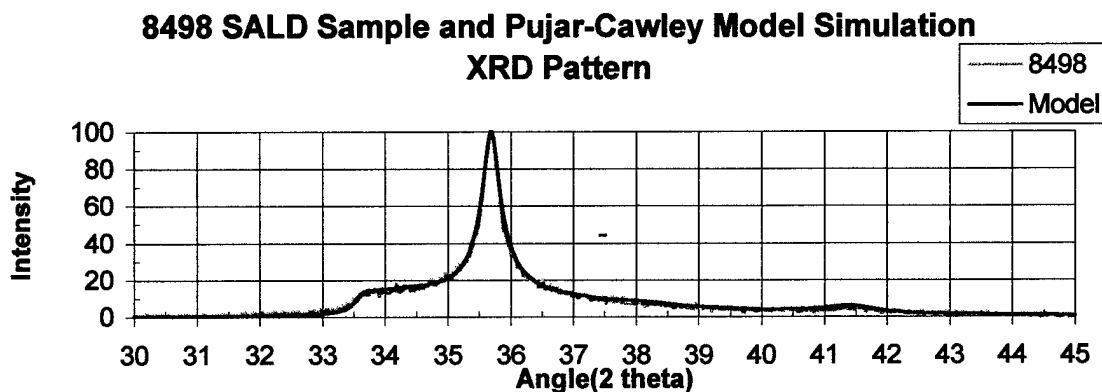


Figure 4: XRD Computer Model Simulation of Experimental SALD Silicon Carbide Pattern

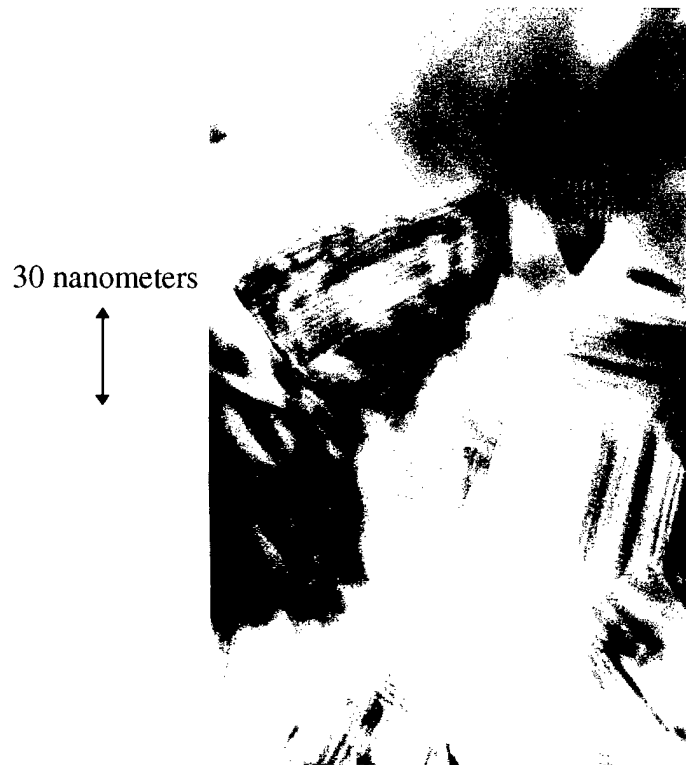


Figure 5: Bright Field TEM Image of Twin Bands in SALD Silicon Carbide

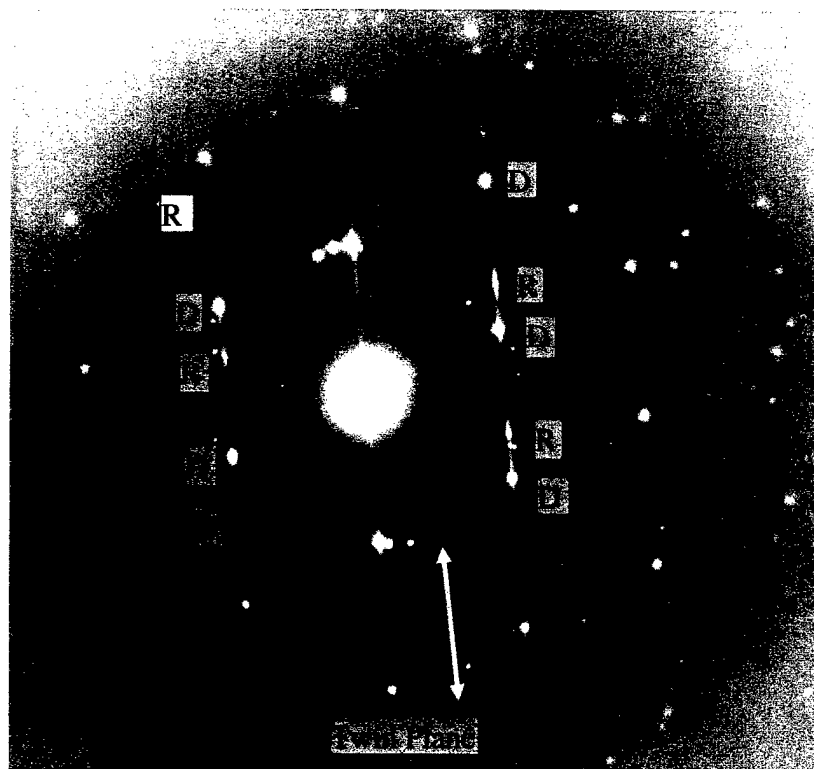


Figure 6: Electron Diffraction Pattern for SALD Silicon Carbide, Camera Length = 684 cm, [110] Zone Axis
(D = Diffraction spot, R = Reflected spot)

Fault Width	Frequency	Normalized Frequency
1	1160	0.2548
2	1121	0.2463
3	1133	0.2489
4	485	0.1065
5	233	0.0512
6	119	0.0261
7	63	0.0138
8	22	0.0048
9	20	0.0044
10	23	0.0051
11	26	0.0057
12	19	0.0042
13	14	0.0031
14	10	0.0022
15	6	0.0013

Table 1: Raw Fault Data from XRD Simulation Model Shown in Figure 4 (Note: 4552 Total Number of Faults)

Footnotes

1. Laser-Based Solid Freeform Fabrication Techniques for the Direct Production of Ceramic and Metal/Ceramic Shapes by B.R. Birmingham, PhD Dissertation, University of Texas at Austin, May, 1995, pg. 18
2. Joining Ceramics by Selective Beam Deposition by J.V. Tompkins, University of Texas at Austin, PhD Dissertation Thesis, May, 1998, 129 pages
3. "Preparation and Properties of In-Situ Devices Using the SALD and SALDVI Techniques" by J.E. Crocker, L. Sun, L.L. Shaw and H.L. Marcus, *Proceedings of the 1998 Solid Freeform Fabrication Symposium*, pp. 543-548, Austin, TX, August, 1998
4. "Gas-Phase Selective Area Laser Deposition (SALD) Joining of SiC" by S. Harrison and H.L. Marcus, *Materials and Design*, June, 1999, Vol. 20 #2/3, pp. 147-152
5. "Influence of Temperature and Tetramethylsilane Partial Pressure on the Beta-SiC Deposition by Cold Wall Chemical Vapor Deposition" by R. Rodriguez-Clemente, A. Figueras, S. Garelik, B. Armas and C. Combescure, *Journal of Crystal Growth*, Vol. 125, 1992, pp. 533-542
6. "Codeposition of Free Silicon During CVD of Silicon Carbide" by J. Yeheskel and M.S. Dariel, *Journal of the American Ceramic Society*, Vol. 78, January, 1995, pp. 229-232
7. "Growth Characteristics of CVD Beta-Silicon Carbide" by D. Cheng, W.J. Shyy and D.H. Kuo, *Journal of the Electrochemical Society*, Vol. 134, December, 1987, pp. 3145-3149

8. "The Narrowing of NMR Spectra of Solids by High-speed Specimen Rotation and the Resolution of Chemical Shift and Spin Multiplet Structures for Solids" by E.R. Andrew, *Progress in Nuclear Magnetic Resonance Spectroscopy*, vol. 8, #1, 1971, pp. 1-39.
9. V.V. Pujar and J.D. Cawley, "Effect of Stacking Faults on the X-ray Diffraction Profiles of β -SiC Powders", *Journal of the American Ceramic Society*, vol. 78 number 3, 1995, pp. 774-782
10. V.V. Pujar and J.D. Cawley, "Computer Simulations of Diffraction Effects due to Stacking Faults in β -SiC: I, Simulation Results", *Journal of the American Ceramic Society*, vol. 80 number 7, 1997, pp. 1653-1662
11. "²⁹Silicon Solid-State MAS NMR Investigation of Selective Area Laser Deposition(SALD) Silicon Carbide Material" by S. Harrison, X.-Q. Xie, K.J. Jakubenas, H.L. Marcus, accepted to be published in the *Journal of the American Ceramic Society*

Effect of Hydrogen on Silicon Carbide Deposition from Tetramethylsilane – Raman Scattering Studies

Lianchao Sun, James E. Crocker, Leon L. Shaw and Harris L. Marcus
Institute of Materials Science
University of Connecticut, Storrs, CT 06268-3136

1. Introduction

Silicon carbide has long been recognized as an ideal material for applications where superior attributes such as stiffness and hardness, strength at elevated temperatures, high thermal conductivity, low coefficient of thermal expansion and resistance to corrosion, oxidation, wear and abrasion are of primary value. Silicon carbide or its composites for structural applications are usually fabricated using hot pressing (HP), sintering, reaction sintering, pressureless sintering, or hot isostatic pressing (HIPing). All these belong to powder metallurgy approach. To reduce processing temperature and/or processing time, the second phase is almost widely strategically used in above techniques. In other words, the "impurity" materials, at least two phases, act to compromise the true performance of the silicon carbide. For example, some reaction bonded SiC contains as much as 40% second phase. This, of course, is not a case in the electronic applications of SiC where high purity SiC is required. It is also obvious that using powder metallurgy is difficult to produce SiC parts with a complex shape because of its high hardness and low toughness.

Selective area laser deposition (SALD) is a unique technique for fabricating complex ceramic shapes, tailoring functionally graded structures and embedding in-situ sensors into ceramic parts. In general, high deposition rate is desired. For the case of fabricating in-situ sensors, the chemical composition must also be controlled. Proper shapes and deposition rate using tetramethylsilane (TMS) precursor to deposit SiC has been demonstrated in previous studies ¹⁻³. However, carbon contamination has been found to be a potential obstacle for the further application of this precursor in sensor-related fabrication. It has been suggested using the thermodynamic calculation that hydrogen has significant effect on the composition of SiC deposits ⁴. In this study, therefore, the effect of hydrogen on the SALD SiC will be experimentally evaluated.

2. Experimental procedures

The SALD system used for this study has been described elsewhere in detail⁵. To avoid the carbon tail phenomenon⁶, a stationary beam was used to grow the SiC dots. TMS precursor was chosen for deposition of SiC. Its pressure varied from 2 torr to 75 torr. Hydrogen pressure varied from 0 to 500 torr. The target temperature varied from 800 to 1200°C.

In this study, Renishaw Raman Imaging Microscope system (2000) was used to characterize the SALD SiC products. This system is a compact laser Raman microprobe/microscope that can collect both Raman spectra and global images. An argon ion laser (514.5nm) provides the light for illuminating the sample and exciting Raman scattering. The sample was measured in the as-deposited state and at a near backscattering geometry. The wave number range was set to 100 - 2000 cm^{-1} , within which all the first-order Raman scattering

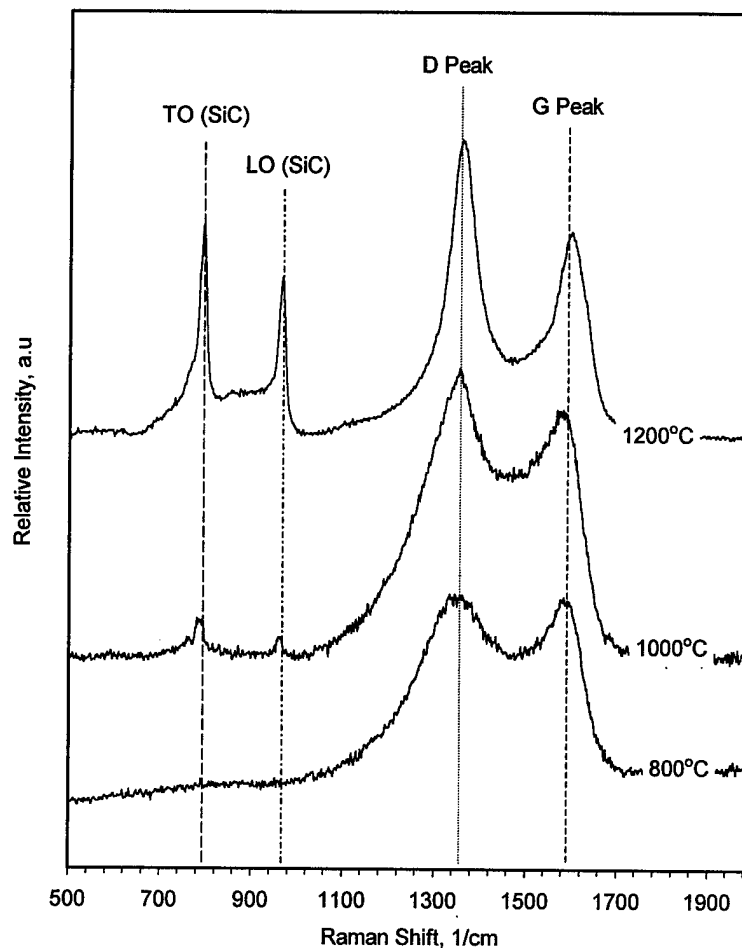
can be recorded for SiC and graphite. For 3C-SiC, there are a longitudinal optical (LO) mode and a doubly degenerate transverse optical (TO) mode in optical branches. The Raman shift corresponding to LO active mode appears at 972 cm^{-1} while that of TO mode appears at 796 cm^{-1} in spectra.⁷

3 Results

3.1 Temperature Effect

The typical Raman spectra from SiC deposited at different target temperatures using 20 torr TMS were shown in Figure 1. There are four Raman peaks. Two peaks labeled as G and D are ascribed to graphite and the other two peaks labeled as LO and TO are contributed by SiC. Presence of the graphite peaks clearly indicates the existence of excess carbon in the deposited SiC samples. It is also found that graphite peaks appear in other samples when only TMS precursor is used.

Figure 1. Effects of target temperatures (800, 900 and 1200°C) on the Raman spectra of SiC deposits (preparation conditions: 20 torr TMS, stationary beam, 100 seconds of growth time; measured at the spot center)



3.2 Raman Mapping

It is important to know the structure information from point to point for a laser deposited materials because the structure and/or composition at any specific location could be related to the local growth temperature. At the spot center, the temperature is highest due to the non-linear Gaussian distribution. Thus, it is supposed that microstructure distribution along the radial position of a spot has a similar result to the target temperature effect. This study was performed using a 20 torr TMS at different target temperatures. Because there is no attempt to perform quantitative analysis, only spectra plots are given here for qualitative purpose. Figure 2 to Figure 4 give the information of radial Raman measurements corresponding to 800, 1000 and 1200°C target temperature, respectively.

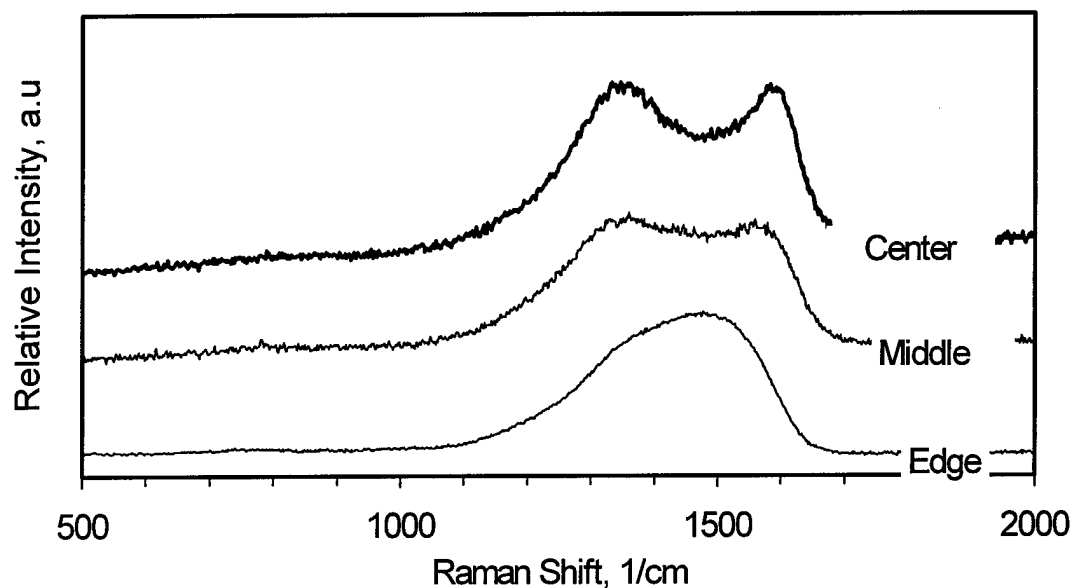


Figure 2. Raman mapping on the sample deposited at a target temperature of 800°C using 20 torr TMS.

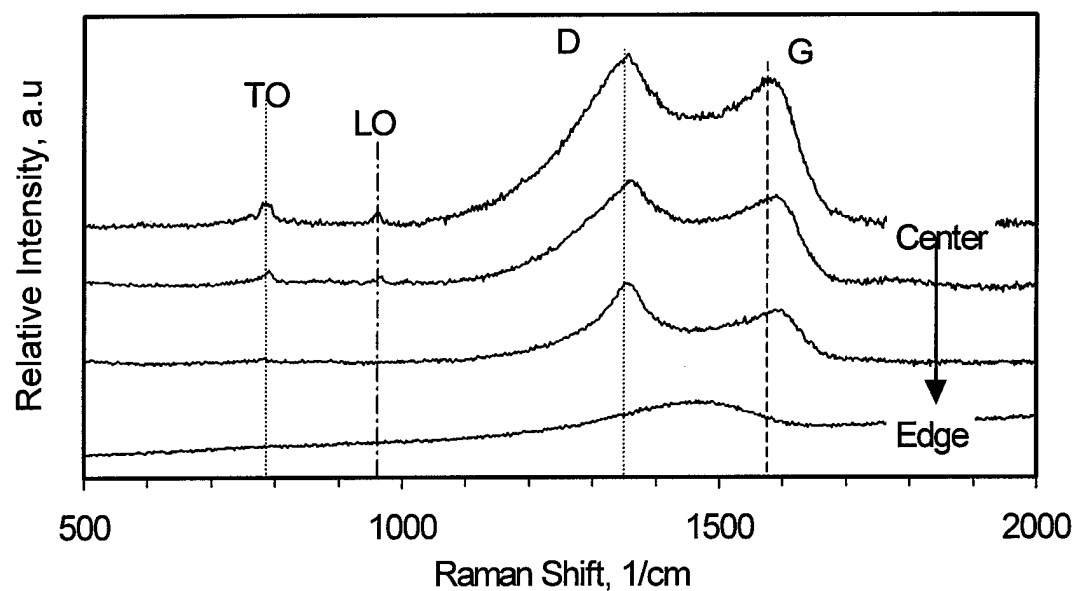


Figure 3. Raman mapping on the sample deposited at a target temperature of 1000°C using 20 torr TMS.

Based on the Raman mapping results from Figure 2-4, it can be concluded that carbon always codeposits with SiC over a wide temperature range (from spot center to its edge) when only pure TMS is used. The crystallinity of deposits increases with the local temperature as

reflected in the increasing peak sharpness seen in Figure 2-4. The co-deposited carbon within SiC has very small crystallite size.

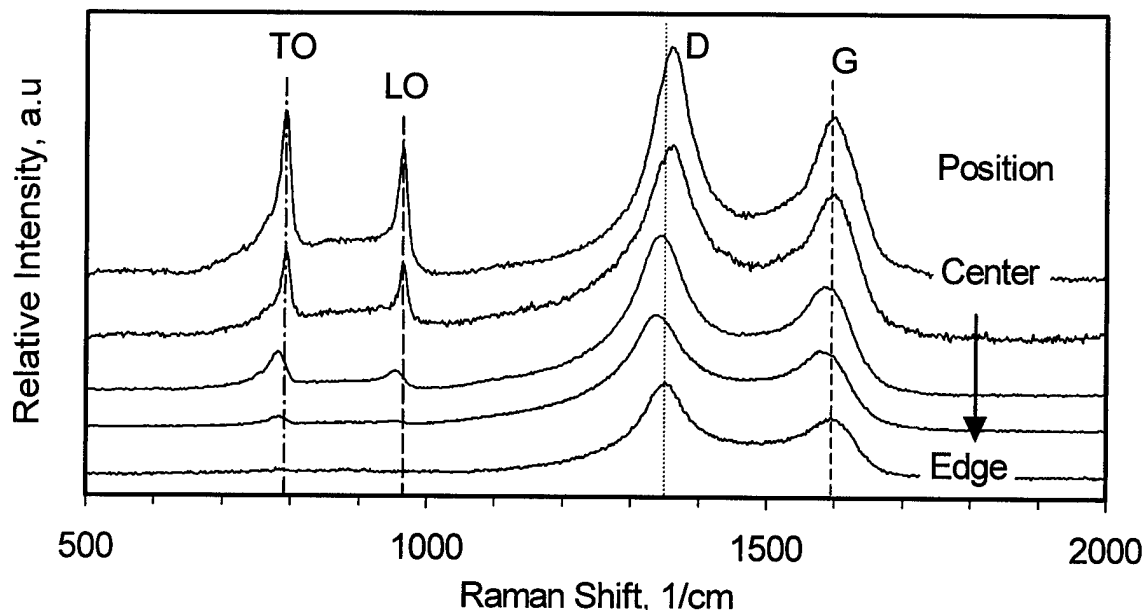


Figure 4. Raman mapping on the sample deposited at a target temperature of 1200°C using 20 torr TMS.

3.3 Hydrogen Effect

Raman mapping on a sample prepared using 2 torr TMS and 500 torr H₂ at a target temperature of 1200°C is shown in Figure 5. It can be seen that graphite still exists at the spot center under current experimental conditions. In the middle region of the spot, however, crystalline SiC was identified without the graphite contamination. At the outer region of the deposited spot, pure SiC exists in amorphous state. In Figure 5b, a small peak around 1500cm⁻¹ was observed and denoted as DO shift. The same peak has been observed from the commercial SiC samples. Some investigators have also reported this peak and ascribed to disordered SiC^{7,8}. Since this peak is located between G and D peak, it is not visible when there exists a certain amount of carbon in the SiC sample.

This result clearly indicates that it is possible to achieve pure SiC deposition as long as the target temperature can be controlled below a certain level. Additional experimental studies on the systems containing 20 torr TMS and up to 500 torr H₂ indicate that small amount of carbon still coexists with SiC and thus it is believed that in addition to temperature there is an upper limit for TMS pressure to achieve pure SiC deposition.

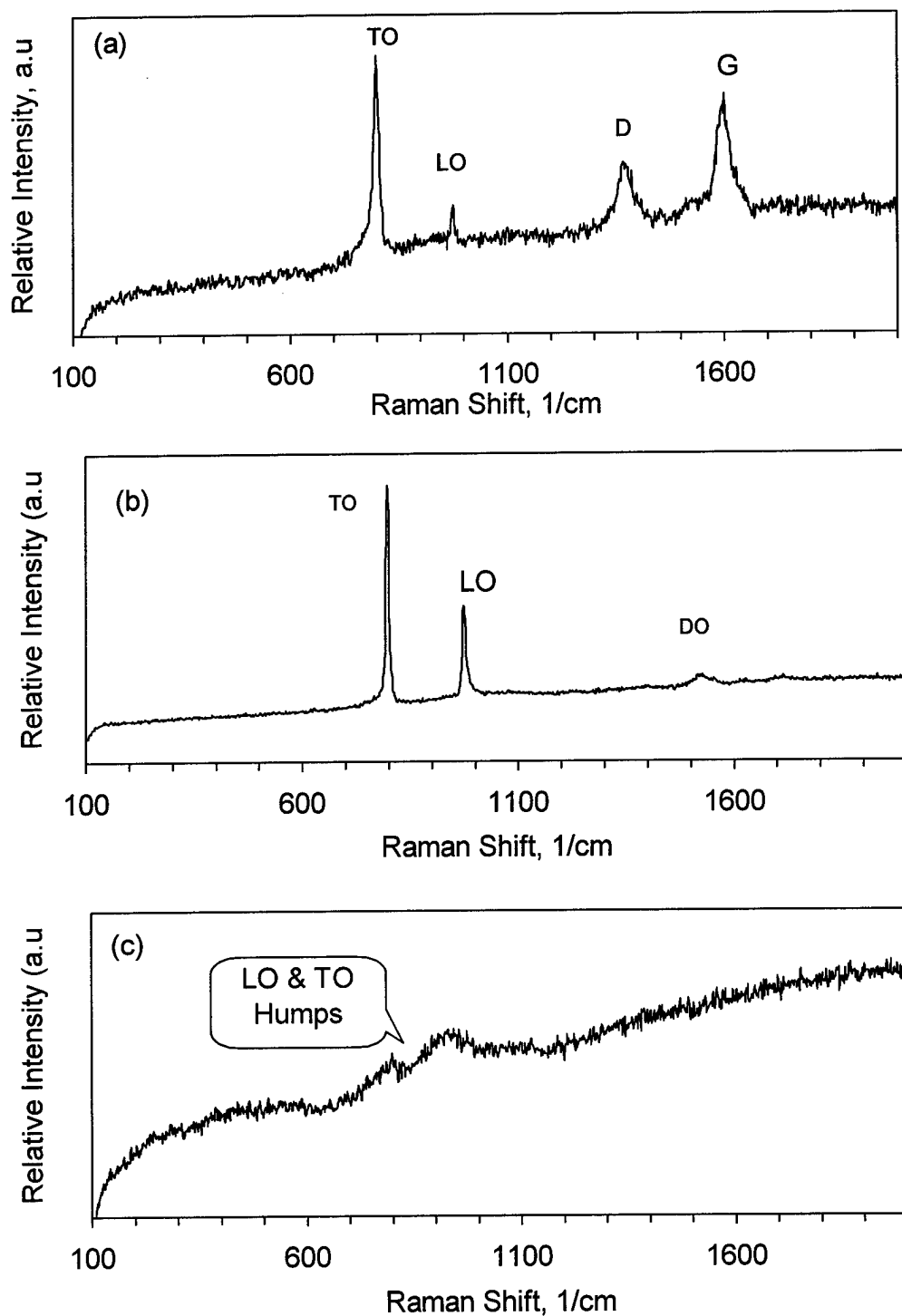


Figure 5. Raman spectra from the sample deposited using 2 torr TMS and 500 torr hydrogen at 1200°C. They were collected from (a) spot center, (b) middle (between center and edge of the spot), and (c) edge.

4. Discussions

No carbon co-deposition has been reported by many researchers^{9,10}. For example, using the same precursor TMS and a ratio of about 6 P_{H_2}/P_{TMS} between 1100°C - 1500°C, Figueras et al claimed that no excess C was detected. Although it is possible that no carbon co-deposition takes place due to the use of high partial pressure of hydrogen, it can not be completely eliminated at high temperatures. It is expected that graphite should be co-deposited based on thermodynamic modeling and present experimental results under the same experimental conditions as those used by the above researchers. The conclusion made by these researchers was based on the X-ray diffraction. It is well known that carbon has a very low mass absorption coefficient at a wavelength of 1.5 Å. It is also believed that the very small crystallite size (nano-size) itself makes diffraction very weak or not sensitive. For example, the previous study by the authors showed that carbon is not detectable in the as deposited samples. However, it could be revealed after heat treatment⁵.

Within the visible light range, the situation would be totally different. The absorption coefficients of carbon and β -SiC crystals have been experimentally determined¹¹. The relevant data are given in Table 1. It can be seen that carbon has a much higher absorption coefficient than SiC. The penetration depth is thus much smaller than that of SiC. The small penetration depth, only 50 nm for carbon, indicates that relatively strong Raman scattering intensity can be obtained for even a very small amount of carbon coexisted with SiC. For example, if there exists a 50 nm thick carbon tail on the surface, SiC signal may not be detectable.

Table 1. Absorption data for C, Si and SiC at 514.4nm

$\lambda=514.5$ nm	C	Si	SiC
Absorption coefficient (α), um^{-1}	20	1.47	25×10^{-4}
Extinction coefficient (κ)	0.82	0.06	1.024×10^{-4}
Depth of the exciting radiation (δ), μm	0.05	0.68	400

Thus, the Raman scattering technique is an effective tool for detecting excess carbon. By using this technique, it has been clearly confirmed that hydrogen could significantly reduce the amount of carbon co-deposited with SiC or even completely eliminate carbon co-deposition. It is believed that the observed phenomena such as decrease in growth rate and increase in electrical resistivity after adding hydrogen are related to the hydrogen's role in reducing the carbon amount⁶.

The hydrogen's role observed in this study could be discussed based on the thermodynamic calculations. Using the CET89 code (calculation method has been described elsewhere⁴), effect of hydrogen on the decomposition of TMS precursor has been calculated and it is found that hydrogen's role lies in its inhibition to the hydrocarbon's further decomposition. A 3D solid phase diagram from thermodynamic calculation showing the stable zone of pure SiC is given in Figure 6

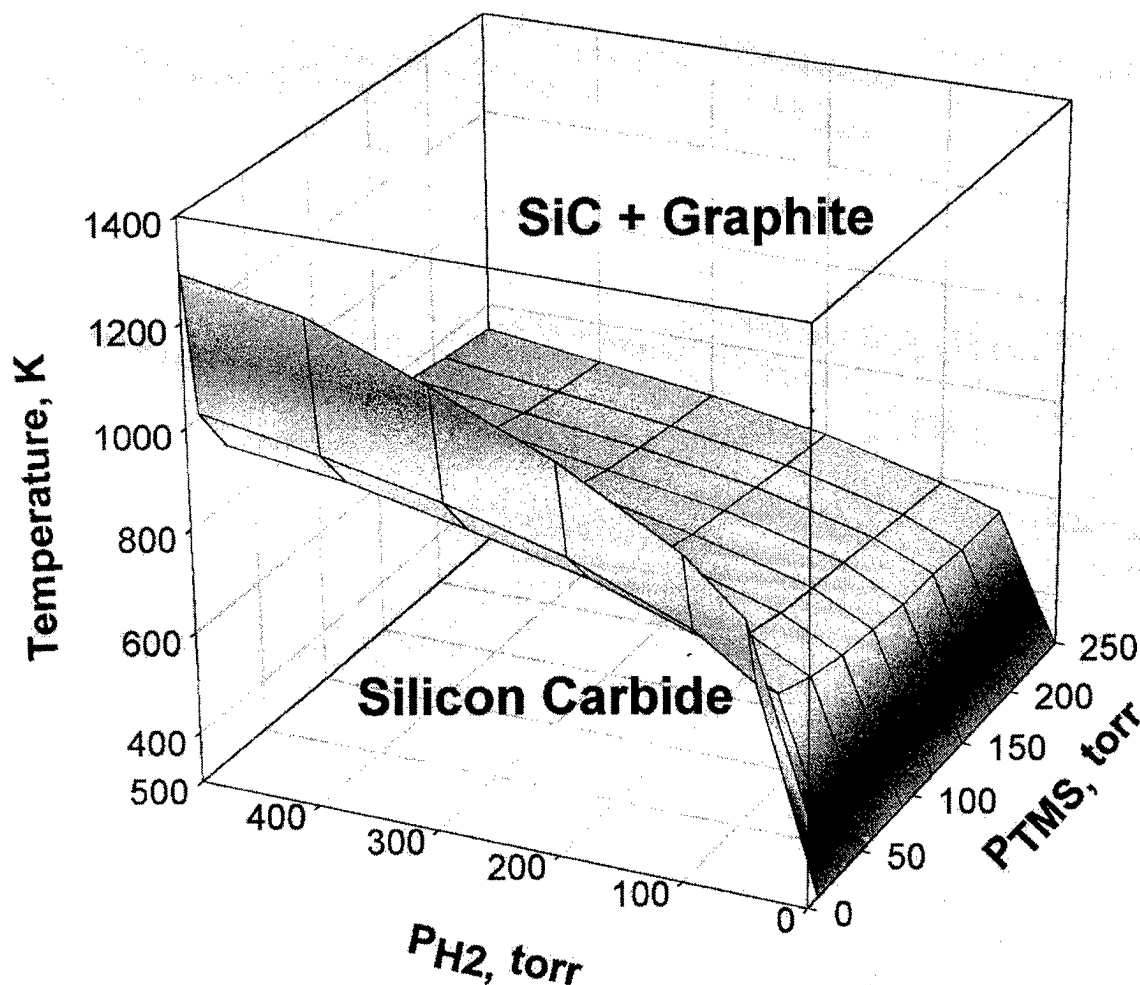


Figure 6. 3D diagram – effect of hydrogen on TMS decomposition

From Figure 6, it can be seen that pure SiC can only be deposited through adding hydrogen. The phenomenon that carbon still codeposits at the spot center even with the addition of 500 torr H_2 to 2 torr TMS can be explained as follows. It has been calculated that the temperature rise at the beam center is higher than the target temperature¹². For example, at a target temperature of 1200°C, the estimated center temperature at the beam center is about 1800°C. Examining Figure 6, the co-deposition will take place because the local temperature at the beam center has exceeded the threshold temperature for carbon codeposition. At the middle position of the spot, the temperature there may have dropped to the pure SiC deposition region, but the temperature is still fairly high and therefore the pure crystalline SiC can be obtained. At the outer region of the spot, temperature is low, and therefore deposited SiC has very short-range order or is amorphous due to low diffusivity or mobility of species.

5. Summary and Conclusions

Selective area laser deposition of silicon carbide from the tetramethylsilane precursor has been studied using the Raman scattering technique. It is found that carbon always codeposits with SiC when pure TMS gas is used. Hydrogen significantly reduces the amount of excess carbon under low TMS pressures. Pure SiC without carbon contamination can be achieved at low temperatures and low TMS pressures with addition of hydrogen. Raman mapping of the deposited SiC revealed that the composition of the deposit varies with the local deposition temperature. The finding is consistent with the thermodynamic prediction and confirms that temperature is one of the most important factors in depositing pure SiC using TMS precursor. Thermodynamic analysis also indicates that reduction or elimination of carbon codeposition through addition of hydrogen is due to the inhibition of H₂ to the hydrocarbon decomposition.

Acknowledgment:

The authors acknowledge the support of ONR Grant N00014-95-1-0978 in funding this research. We also appreciate the helpful discussions with Dr. John E. Morral, Mr. Gary Lavigne, Dr. Shay Harrison, Mr. Erik Geiss and Ms. Helene Ansquer.

Reference:

- ¹ J. V. Tompkins, B. R. Birmingham, and H. L. Marcus, *Advances in Selective Area Laser Deposition of Silicon Carbide* (The University of Texas at Austin, 1994).
- ² J. E. Crocker, S. Harrison, L. Sun, L. L. Shaw, and H. L. Marcus, *JOM* **50**, 21-23 (1998).
- ³ K. J. Jakubenas, J. M. Sanchez, and H. L. Marcus, *Materials & Design* **19**, 11-18 (1998).
- ⁴ L. Sun, K. J. Jakubenas, J. E. Crocker, S. Harrison, L. L. Shaw, and H. L. Marcus, *Materials and Manufacturing Processes* **13**, 859-882 (1998).
- ⁵ L. Sun, K. J. Jakubenas, J. E. Crocker, S. Harrison, L. L. Shaw, and H. L. Marcus, *Materials and Manufacturing Processes* **13**, 883-907 (1998).
- ⁶ L. Sun, Ph.D. Thesis, The University of Connecticut, 1999.
- ⁷ A. Perez-Rodriguez, C. Serre, L. Calvo-Barrio, A. Romano-Rodriguez, J. R. Morante, Y. Pacaud, R. Koegler, and W. Skorupa, *Proceedings of SPIE - The International Society for Optical Engineering* **2648**, 481-494 (1995).
- ⁸ H. Hobert, H. Dunken, R. Menzel, T. Bachmann, and W. Wesch, *Journal of Non-Crystalline Solids* **220**, 187-194 (1997).
- ⁹ A. Figueras, S. Garelik, R. Rodriguez-Clemente, B. Armas, C. Combescure, and C. Dupuy, *Journal of Crystal Growth* **110**, 528-542 (1991).
- ¹⁰ T. Noda, H. Suzuki, H. Araki, F. Abe, and M. Okada, *Journal of Materials Science*, **28** 2763-2768 (1993).
- ¹¹ Z. C. Feng, I. Ferguson, R. A. Stall, K. Li, Y. Shi, H. Singh, K. Tone, J. H. Zhao, A. T. S. Wee, K. L. Tan, F. Adar, and B. Lenain, *Materials Science Forum* **264-268**, 693-696 (1998).
- ¹² L. Sun, J. E. Crocker, L. L. Shaw, and H. L. Marcus, *Materials Research Society Symposium Proceedings*, **542**, p. 37-42. (1999)

Conceptual Design of a Smart Portable SFF System

Zbigniew M. Bzymek*), Chandrasekhar Roychoudhuri**), Leon L. Shaw**) and Wojciech Marks***)

*) Department of Mechanical Engineering, University of Connecticut, Storrs CT

**) Photonics Research Center, University of Connecticut, Storrs CT

***) Department of Metallurgy and Materials Engineering, University of Connecticut, Storrs CT

*****) Institute of Fundamental Technical Problems of the Polish Academy of Science, Warsaw, Poland

Abstract

This paper describes the conceptual design of a portable Solid Freeform Fabrication (SFF) system. The work is based on previous concepts of modeling systems [Manzur et. al., 1997], [Bzymek et al., 1996], [Lotko et. al., 1998] and research in which a desk-top SFF system was developed [Manzur et. al., 1997], [Bzymek, Manzur et al., 1998], [Bzymek, Theis et al., 1998]. Such a system allowed the rendering of parts of 80% to 90% density. The optimized laser path programming [Bzymek, Shaw & Marks, 1998] and diode laser development [Chen & Roychoudhuri, 1994] added new features to that concept. The newly designed system will be compact and light. It will be equipped with a new powerful diode laser based on the newest technology, and will use new achievements in programming concepts, and a new portable high performance computer. An intelligent CAD program, as well as slicing and laser path control software, will be incorporated in the system. The parts to be rendered will have size and loading limitations. Due to the method of rendering, the points of load applications are limited to certain areas and in certain directions. In conclusion, one can state that the newly designed system will be intelligent in use, light in weight, easily assembled and disassembled, and will be able to produce parts of a limited size, presumably up to 3x5x2 inches, with loads supported in certain directions, areas, and points of the part.

Introduction

During the last three years a desk-top SFF system was developed at the University of Connecticut [Manzur et. al., 1997]. The hardware part of the system was composed of a laser diode, powder delivery mechanism, oxidation prevention device, laser scan control, data acquisition and transmission, and control subsystem. The slicing software and laser path control were developed at the Computer - Aided Design & Computer - Aided Modeling (CAD&CAM) and Expert Systems Laboratory for Thermo-Printing [Bzymek, Benson et al., 1996] and for low cost Computer- Aided Modeling [Lotko et. al, 1998], and adapted to the SFF system. The part model was designed using the CAD (Computer -Aided Design) system to generate data supplied to a STL (STereo Lithography) file. The STL file was transformed into slices that were used to render the parts after calculating an optimum laser path. The software was implemented on an IBM PC. In preliminary tests, a significant number of different parts were sintered achieving approximately 80% and, in some cases, 90%, (when using 45 μm powder) of their theoretical density [Manzur et. al., 1997]. The parts rendered in later stages were sintered using Fe and Bronze-Fe and Bronze-Ni premixed powders of 100 to 150 μm size. Two series of four and six sample plates 250 x 175 x 1 mm and 250 x 175 x 2 mm were fabricated [Bzymek, Theis et al., 1998]. The system was effective. The plates demonstrated considerable strength and precision, with very little warping along with good surface properties [Bzymek, Theis et al., 1998], [Bzymek, Manzur et al., 1998]. However the system was heavy, large, and bulky mainly due to the weight of the diode laser and PC computer. Research developments in three areas: laser diode, parts design and CAD software, and miniaturization of computer hardware gave us the opportunity to build a smaller, lighter and

smarter portable SFF system. The conceptual design of the new Smart Portable Slid Freeform Fabrication (SP SFF) system discussed in this paper is based on experiments with desk - top system [Bzymek, Manzur et al., 1998].

Smart Rendering SFF Parts

Optimized design for maximum strength of the force-carrying members and minimum deformation due to the fabrication. Smart rendering of the part is based on creating a non-uniform structure for the part, i.e. composed density. It is assumed that the part will be loaded in known way, that the loads will not be moving, and that the loads are applied in a known direction. In such cases the interior of the part will be composed of strong rod like members (vertical, horizontal or inclined) that will carry the load and pass it to the points of support. Those members will lie in planes parallel to the larger dimensions of the rendered part. Thus, the part is rendered as a composite structure composed of strong members of high density with weaker areas surrounding them. The weaker surrounding areas will also provide a media for speeding heat dissipation. The thermo-elasticity theory is used to calculate the laser passes which will build such a composite structure. In the dynamic problem of thermoelasticity [Nowacki W., 1986], the heat conduction equation is completed by the equation of motion in displacements in the form of

$$\sigma_{ji,j} + X_i = \rho u_i^{**} \quad (1)$$

where: $\sigma_{ji,j}$ expresses a set of partial differential equations, u_i^{**} - second derivative of displacement with respect to time, X_i are the mass forces and ρ represents a set of constants. The rod system should be located in an optimum way, such that the load-carrying strength is maximized and the thermal stresses are minimized. Based on these assumptions, the following object function expressing thermal stresses (deformations) due to the temperature changes was assumed:

$$F(\phi, k, \omega, v, \delta, p, T) \quad (2)$$

where: $\phi(x, y, t)$ is laser pattern function, k - thermal conductivity of the rendered layer, ω - laser power, v - scanning speed, δ - scan spacing, p - gas pressure, $T(t)$ - temperature as function of time.

In this study, which can be applied to any method of SFF [Bzymek, Show, Marks, 1998], it is assumed that rendered elements optimized for the maximum ultimate strength under the given static load possess the following attributes:

- deformation of every layer due to fabrication should be as small as possible,
- the sintered part should have mechanical properties close to the isotropic material,
- the time necessary to render every layer should be as long as possible.

There are two kinds of deformations mentioned in this proposal: one occurring during rendering due to thermal conditions, and a second, occurring when the part is in use and subject to loads. To satisfy these requirements, the following criteria for the four -criterion (A, B, C, and D) optimization are assumed:

A -the ultimate strength σ_u for tension or compression

$$F_A = \sigma_u = F_C^{\max} \quad (3)$$

B -the vertical deformations of any layer of the material and deformations resulting from fabrication of that layer should be minimal

$$F_B = \int_S w^2 = F_A^{\min} \quad (4)$$

where w is the vertical deformation and S the area of the rendered plate.

C -the difference of the constants μ (or E - Young Modulus) in the two orthogonal directions should be minimal:

$$F_C = |\mu_x - \mu_y| = F_C^{\min} \quad (5)$$

D - minimum time needed to render the layer i of the part:

$$F_D = \frac{S_i}{\delta \tilde{v}} = F_D^{\min} \quad (6)$$

where:

S_i - the area of the layer i ,

\tilde{v} - the average velocity of the laser,

δ - the width of the material strip rendered with single pass of laser.

The decision variables are: $\varphi(x,y,t)$, ω , v , T , k , δ and p . Note that the decision variables are functions or parameters of the material used to render the element and characteristics of the laser. Further, the decision variables have to comply with the following constraints:

$$\delta \int_s \varphi(x,y,t) dS = S \quad (7)$$

$$\underline{\omega} \leq \omega \leq \overline{\omega} \quad (8)$$

$$v \leq \overline{v} \quad (9)$$

$$\tilde{v} = \frac{v_1 L_1 + v_2 L_2}{L_1 + L_2} \quad (10)$$

where:

L_1 - the length of the longer laser path,

L_2 - the length of the shorter laser path,

$\underline{\omega}$ and $\overline{\omega}$ - the maximum and minimum laser powers,

\overline{v} - the maximum laser scanning speed,

v_1 and v_2 - the laser scanning speed along L_1 and L_2 , respectively.

The solution to the problem formulated above is a multicriteria optimization task [Marks W., 1997] and the multicriteria solution method proposed by Hwang [Hwang C.L. 1979] is used. It can be solved using dimensionless object functions, Φ_i , such that :

$$\Phi_i = \frac{F_i}{F_i^-} \quad (11)$$

where: $i = A, B, C, D$ and $\Phi_i \leq 1$ and F_i^- is the maximum value of the function F_i which belongs to the set of compromises. The introduction of the dimensionless object function facilitates the identification of the preferred solution.

The preferred solution can be found using one of the two approaches as described by Bzymek, Shaw and Marks [Bzymek et al., 1998].

Taking partial derivatives of the function (11) with respect to different arguments, one can find the optimal mechanical properties and optimum deformation conditions, with respect to the fabrication conditions, (i.e. laser pattern, gas temperature, laser impulse due to the rendering of the slices) the

preferred point for the different function F values can be established.

Once we know the properties of the optimum slice, the three dimensional (stereometric) part is designed by rendering the slices in an optimum way so as to minimize the thermal stresses and maximize the material properties. We are then ready to perform the design and fabrication of parts in three dimensions. To perform the design, the part's STL or VRML files will be generated and sliced to enable rendering.

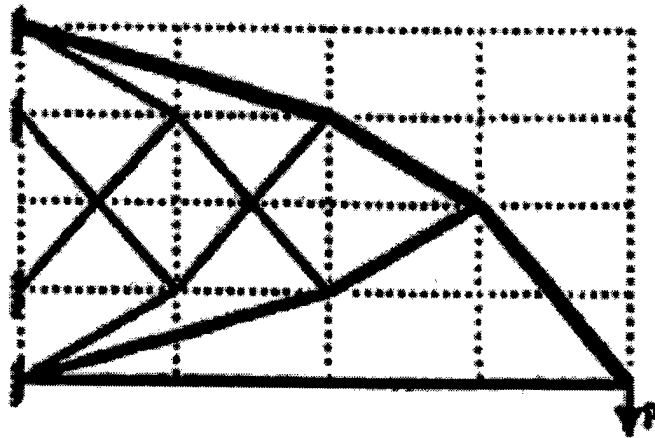


Figure 1.: Example of the straight laser path under concentrated load

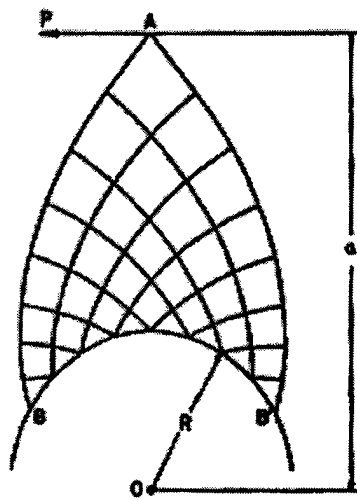


Figure 2: Example of the elliptical laser path under concentrated load

The Computer-Aided Design Laboratory has experience in slicing both types of files. The examples of path planning [Kolchowski, 1998] are shown on Figures 1 and 2. The CAD system to serve the PS SFF fabrication system will be supported by a portable PC.

There are actually two optimization problems that concern design of a part. One problem exists on the fabrication layer level. The solution to this problem should give us information about how to set production parameters in order to obtain the best mechanical properties, the maximum strength, or the minimum deformation.

The second optimization problem should define the laser pattern used to obtain the lowest thermal stresses. Solving this problem will give us information about which laser pattern obtains the minimum thermal stress and deformation under a given load.

The CAD system, which is used to design the part and to determine the parameters of

fabrication, will be chosen. An advisory module in which design rules will be incorporated will be added to it. At the end of the fabrication process, the quality of parts will be determined by laboratory tests.

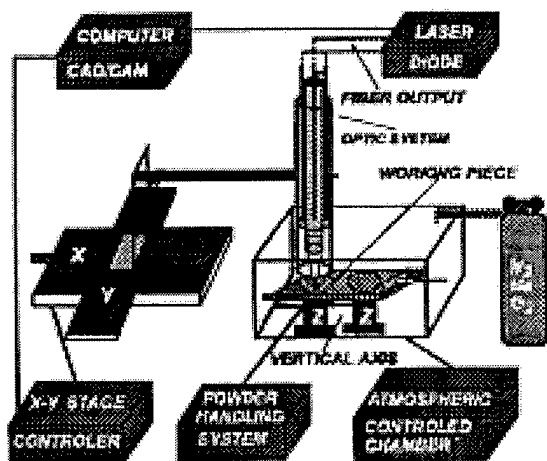


Figure 3: Schematics of the SFF portable system.

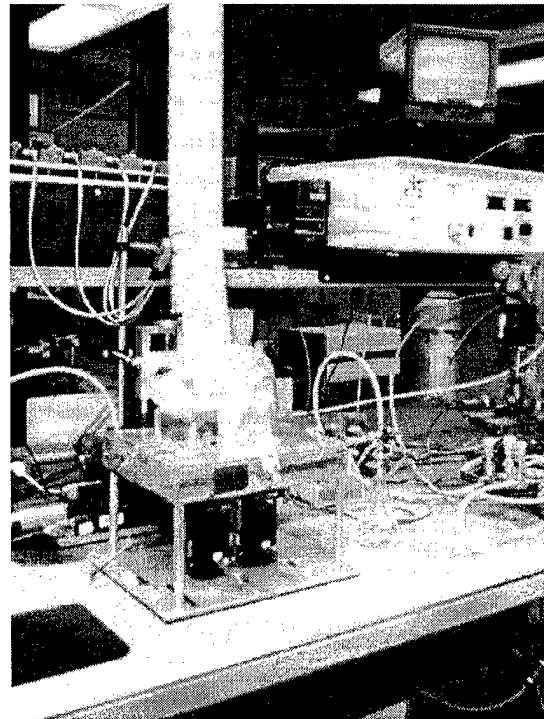


Figure 4: A photograph of the previously developed desktop SFF system.

The object function (11) will serve two purposes: first, for the optimization of mechanical properties (maximum strength or minimum deflection) of the part, and subsequently for optimization of laser scanning patterns. In both optimizations, the general criterion is the minimum deformation and maximum strength of the part under a given load. The criteria object function utilized depends on many fabrication variables including the optimization for optimum stiffness (minimum deformation), which can be performed analogously to the outlined optimization for maximum strength.

The results of optimization can be presented in an analytic way as a function or functions of the aforementioned variables or as an algorithm that will generate results on the computer. It may also be generated as a n-dimensional matrix in one of the known forms [Bzymek, Show, Marks, 1998].

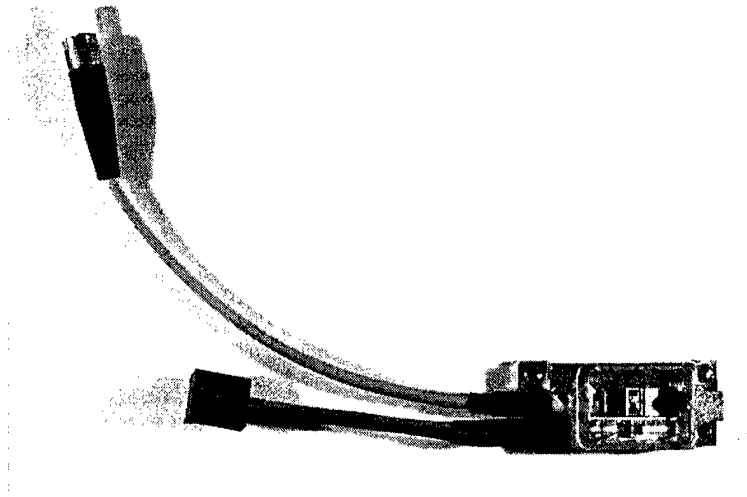


Figure 5: A general view of 1 Watt diode (1X)

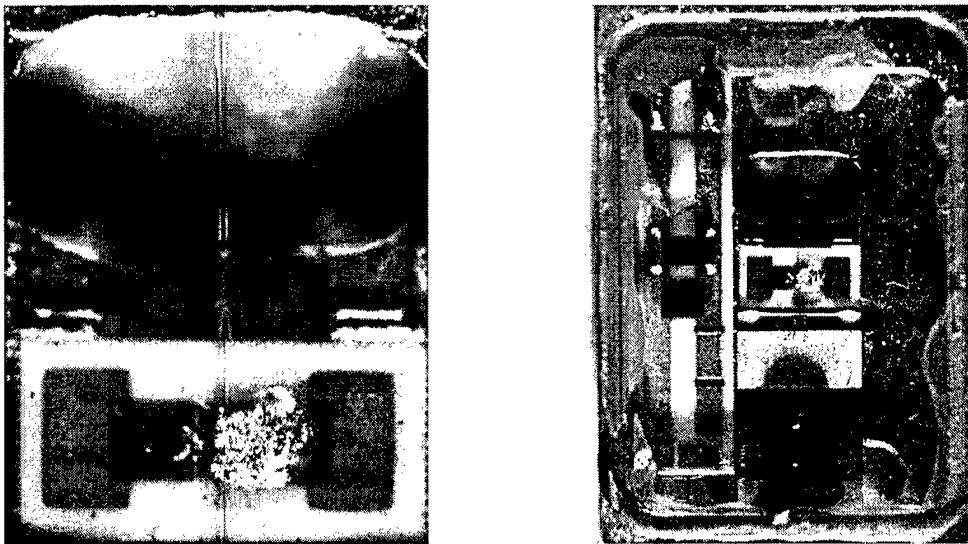


Figure 6: Close views of 1 Watt diode (4X) and (8X)

Hardware

The SP SFF system was designed using experience gained in building the desk top system (Figures 3 and 4). Generally, it is composed of the same subsystems. It is suitable for micro-structure optimization under given loads (with fabrication constraints), calculation of laser path coordinates, slicing the model, and rendering of the part. The two major hardware components that differ from the desktop system are the diode laser and the computer.

Laser Diode.

One of the main components of the portable SFF system is a diode laser composed of a series of diodes. Laser diode fiber couples the 1 Watt system. The diode is 0.4 mm in thickness, less than 1mm^2 in cross-section, and with a wavelength of 810 to 850 nm (Figures 5 ,6 and 7). They can be pre-packaged in a cluster of 20 stripes [Chen W. et al., 1994]. The effectiveness coefficient , less than 1.0, is a function of the number of diodes in a cluster and has to be

considered in calculations of the laser pulse power. Bigger clusters are possible, however they require additional heat dissipation solutions. The design proposes three to eight 20 diode clusters which will give yield a power of 40 to 80 Watt; sufficient laser power for most SP SFF system applications.

Computer System

Out of many portable systems, the TOSHIBA 2590CDT portable system (TOSHIBA Portables, 1999) is proposed as the computer for the portable SFF system. It is equipped with the Mobil Intel Celeron 400MHz processor, an integrated coprocessor, 32 (KB) internal cache, 128KB on-die Level 2 cache, PCI Bus V 2.1, with 64 MB to 192 MB RAM and 6.4 GB disk. The 3.5 inch disk and CD-ROM are built in. The operating system is Windows 98 with AT&T WorldNet service. With these specifications, the TOSHIBA is able to run the Smart Portable SFF system software. This is only an example solution. The development of portable computers is so rapid that within the next few years, Celeron and Pentium III processors will be probably supplanted by Merced (about 1000MHz). Russian and Polish newspapers [Pilawski K., 1999] are already reporting about even newer new chip, Elbrus-2000, that will be twice as fast as Merced, half the size, and with a lower energy consumption. The present weight of the TOSHIBA 2590CDT (6.7 lbs) will also probably dwindle since the weight of portable computers is dropping and will drop further.

Concluding Remarks

The presented conceptual design of a Smart Portable Solid Freeform Fabrication system is feasible and real. The intensive research that preceded this design has resulted in software and hardware solutions that can be readily implemented. However, the final test of the design is a prototype which has not yet been built. All of the qualities cannot be stated with certainty until the actual system is built and tested. The design of the SP SFF system is based on previous modeling systems and research in which a desktop SFF system was developed. The system allowed rendering of parts of 80% to 90% of theoretical density and of considerable strength. The optimized laser path programming added new features to that concept. The newly designed portable system will be composed of new hardware and software and will be compact and light. It will be equipped with a new powerful diode laser based on the newest diode laser technology, and will use new achievements in programming concepts and hardware architecture. The CAD, slicing, and laser path control will be incorporated into the system. The parts to be rendered will have size and loading limitations. Due to the method of rendering, the points and planes of load applications will be limited to certain areas, directions and planes.

The described design represents a system which is light and practical. It still has some limitations to be eliminated in future research, especially in regard to three dimensional volume rendering and space location of the members under different loads without limitations on the direction of plane or orientation.

Acknowledgment

The work was initiated by the Photonics Center, CAD&CAM and ES laboratory and the Institute of Material Science (IMS). The authors would like to thank colleagues from those institutions for their help and support. The SP SFF system design is based on a desktop solution developed previously. Dr. Tariq Manzur made key contributions to the desktop SFF system development. The authors would like to acknowledge the help of the Institute of Material Science, Photonics Center, the Institute of Fundamental Research of the Polish Academy of Science, the Mechanical Engineering Department and the Research Foundation of the University of Connecticut, as well as Professors Harris Marcus, Jan Holnicki, and Stefan Owczarek, for their help and support. The authors would also like to thank the members of the IMS SFF Seminar for their valuable comments on the SP SFF system design.

References:

Bzymek Z.M., Benson S., Garrett R.E. and Ramakrishnan B.T., "Thermo-Printing and Laser Sintering Slicing Simulation for Rapid Prototyping of Engine Parts", 29th ISATA International Symposium on Automotive Technology and Automation, June 6-9, 1996, Florence, Italy; *29th ISATA Conference Proceedings: Simulation, Diagnosis and Virtual Reality Applications in the Automotive Industry*, 1996, pp. 291-298.

Bzymek Z. M., Tariq Manzur, Chandrasekhar Roychoudhuri and Scott Theis, 1998, "Design Aspects of Desk-Top Selected Laser Sintering of Stereometric Shapes", SMART - 98 Advanced Research Workshop Proceedings, pp. 16 - 22, June 16 - June 19, 1998, Pultusk, Poland;

Bzymek Z. M., Scott Theis, Tariq Manzur and Chandra Roychaudhuri, 1998, "Stereometric Design for Desk - Top SFF Fabrication", The Ninth Annual SFF Symposium, The Univ. of Texas at Austin, Aug. 10 - 12, 1998.

Bzymek, Z. M., Shaw L. D., Marks, W. : A Theoretical Model for SALD Parameters, Solid Freeform Symposium 1998, *Proceedings - August 10-12, 1998*, Edited by: David L. Bourell, Joseph J. Beaman, Richard H. Crawford, Harris L. Marcus and Joel W. Barlow, The University of Texas at Austin, pp. 399 - 406.

Chen W., Roychaudhuri C. S. , Banas C.M. : "Design Approaches for Laser-Diode Material-Processing System Using Fibers and Micro - Optics", *Optical Engineering*, November 1994, Vol. 33, Number 11, pp. 3662 - 406.

Pilawski K., Grease from Nucleids, (in Polish), NIE , No.28 (459), July 15,1999.

Hwan C.L. and Masus A.S.M., "Multiple objective decision making - methods and applications - a state-of-the-art survey", *Lecture Notes in Economics and Mathematical Systems*, Springer-Verlag, Berlin, 1979.

Kolchowski, P. : " Analysis and possibilities of optimization of truss structures by virtual distortion", (in Polish), IPPT Works, No. 1/1998.

Lotko John III, Z. M. Bzymek, S, Billatos: Design of a Low Cost Computer - Aided Modeling System, 1998 International Mechanical Engineering Congress & Exposition, November 1998;

Manzur Tariq , Chandrasekhar Roychoudhuri and Puneid Dua, Fahmida Hossain, Harris Marcus, 1997, "Net shape Functional Parts Using Diode Laser", *Proceedings of the The Eight Annual SFF Symposium*, The University of Texas at Austin, Aug. 11 - 13, 1997.

Marks W., 1997, "Multicriteria Optimization of Shape of Energy-Saving Buildings", *Building and Engineering*, Elsevier Science Ltd., Printed in Great Britain, Vol. 32, No. 4, p. 331 - 339.

Nowacki W., Thermoelasticity, 1986, PWN Warszawa, Pergam Press, Oxford, New York, Toronto, Sidney, Paris, Frankfurt.

"Processing and Characterization of SALDVI Ceramic Structures"

James E. Crocker, Lianchao Sun, Helene Ansquer, Leon L. Shaw, and Harris L. Marcus
Institute of Materials Science
University of Connecticut

Abstract

Selective Area Laser Deposition Vapor Infiltration (SALDVI) ceramic structures and composites are fabricated by the localized chemical vapor infiltration of powder layers. A matrix of vapor deposited ceramic material is selectively deposited from gas precursors into a bed of ceramic powder particles using laser heating. An important aspect of the SALDVI process for building 3-D structures is the depth of penetration of the infiltration zone into the powder layer. The infiltration behavior of vapor deposited silicon carbide from tetramethylsilane gas was investigated for a range of ceramic powders with different optical, thermal, and physical properties using image analysis. The porosity distribution in the silicon carbide matrix SALDVI structure was found to vary with particle size and particle material. These results will be used to guide experiments on the effect of layer thickness on the microstructure of multiple layer SALDVI composites.

Introduction

Selective Area Laser Deposition Vapor Infiltration (SALDVI) is a developing Solid Freeform Fabrication technique for fabricating, using a layer-by-layer approach, ceramic and composite structures and multiple material shapes containing embedded devices¹⁻⁴. By the process of chemical vapor deposition (CVD), a matrix of solid material is deposited from a gas precursor into a layer of ceramic powder by a chemical reaction. Laser beam heating of the powder bed localizes the CVD reaction and enables the formation of shapes via laser beam scanning. By choosing different gas precursors and starting powders, a variety of SALDVI structures with tailored compositions and properties can be produced. Figure 1 shows an example of a 15 layer SALDVI shape made from 20 μm diameter SiC starting powder and tetramethylsilane gas, and the laser scan pattern used to build the part.

SALDVI is a complex process involving the laser heating and localized chemical vapor infiltration of layers of powder. Chemical vapor infiltration of bulk preforms has been experimentally⁵⁻⁶ and theoretically⁷⁻⁹ studied in many forms. The infiltration kinetics are difficult to predict and understand theoretically, and depend on the temperature distribution in the preform and on the transport rate of reactants into and products out of the preform. Both of these quantities change continually as the workpiece evolves during infiltration. SALDVI adds the complication of laser heating, where the particle size, particle material, matrix material, gas precursor pressure, laser wavelength, and instantaneous density all contribute to the temperature distribution¹⁰. The depth of penetration for a given set of SALDVI processing conditions is important in determining the thickness of layers and the mechanism by which adjacent layers bond. In this work the effect of particle size on the laser-induced chemical vapor infiltration of silicon carbide into loose silicon carbide or alumina powder layers is experimentally studied.

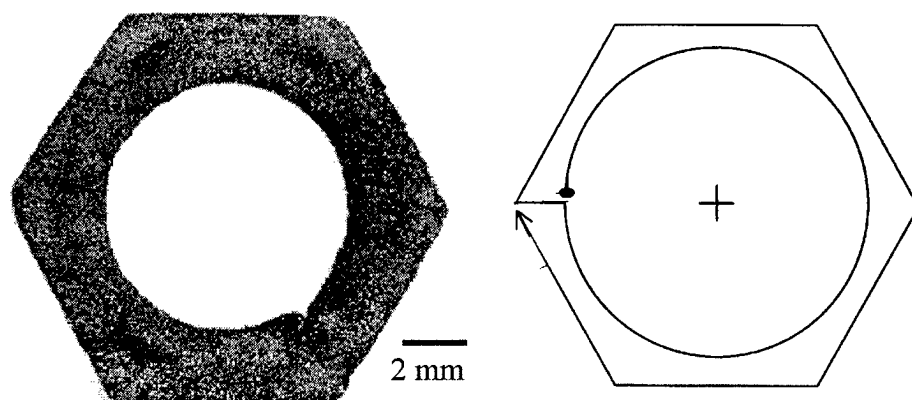


Figure 1. SALDVI SiC 15 layer shape and build pattern.

Experimental

Three sizes of silicon carbide powder and two sizes of alumina powder were used as starting powders for SALDVI in this study. Each powder was characterized by average size, packing fraction, and transmissivity at the CO₂ laser wavelength (10.64 μm). Average size was determined by optical microscopy. Packing fraction was calculated by measuring the mass of each powder as poured into a cavity of a known volume. Transmissivity is defined as the fraction of incident laser power passing through a layer of powder of a given thickness. Layers of powder ranging in thickness from 25 to 250 μm were spread on a transparent window. A 10 watt, 3.5 mm diameter CO₂ laser beam was directed at each layer, and the amount of power transmitted through the layer was detected by a laser power meter.

The SALDVI workstation consists of a 50 Watt CO₂ laser, a vacuum chamber, a powder delivery system, an xy table with scanning mirrors, and an optical pyrometer, all controlled and automated by a computer. SALDVI experiments are performed in closed loop temperature control mode, where the surface temperature of the laser heated workpiece measured by the pyrometer is used as feedback to adjust the laser power to maintain a constant temperature referred to as the target temperature parameter. SALDVI samples were fabricated for each of the five starting powders using tetramethylsilane, Si(CH₃)₄, as the gas precursor for the vapor-deposited SiC matrix. The following processing conditions for each starting powder were fixed: 1 mm beam spot size, 10 Torr Si(CH₃)₄ gas precursor pressure, and 950 C target temperature parameter. Samples 10 mm in length were fabricated by scanning the laser beam in a single line over a semi-infinite powder bed. The laser beam scan speed was varied from 25 to 800 seconds dwell time to study the time evolution of the infiltration. The samples were mounted in epoxy, cross-sectioned at the mid-length, and polished for microscopic evaluation of the infiltrated regions. Image analysis was used to characterize the infiltration behavior for each experimental condition. Area fractions of the powder, vapor deposited matrix, and porous phases were obtained for different regions on the cross-section in 110 μm by 110 μm frames. By taking a series of frames starting from the free powder surface, the extent of infiltration was mapped as a function of depth into the layer. These measurements were obtained at four different locations along the length of each sample and the average value is reported here.

Results and Discussion

The powder size and packing fraction results are listed in Table 1. The 7 μm SiC powder forms a less dense powder bed than the two larger SiC powders because of its poor flowability and tendency to agglomerate. The other four powders range in packing fractions from 0.38 to 0.46. The poor flow properties of the 7 μm SiC powder made it difficult to spread thin layers for the transmissivity measurement. The transmissivity results are plotted in Figure 2 for the other four powders as a function of powder layer thickness for the CO_2 laser wavelength. The measurements show that nearly all of the incident beam is absorbed by the two SiC powders for layers thicker than 100 μm . Only when the powder layer thickness approaches the powder size, essentially a monolayer of powder, does transmission of the beam begin to occur. The Al_2O_3 powder showed better transmissivity than the SiC powder, and the larger powder sizes transmit more power than the smaller powders for both materials.

Table 1. Starting powder characteristics:

<u>Particle Size</u>	<u>Packing Fraction</u>
7 μm SiC	0.30
20 μm SiC	0.44
80 μm SiC	0.42
20 μm Al_2O_3	0.38
100 μm Al_2O_3	0.46

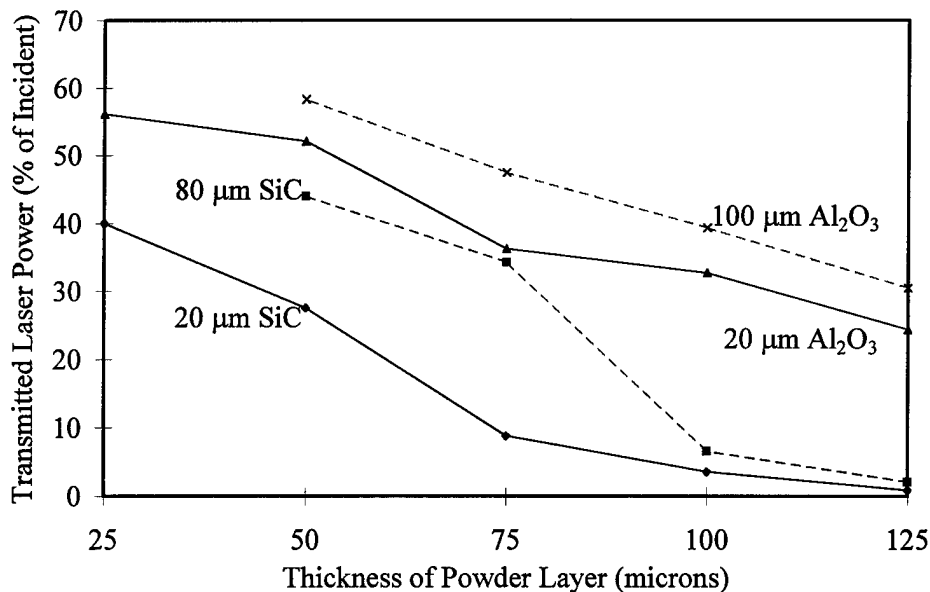


Figure 2. Transmissivity of CO_2 laser beam vs. powder layer thickness for four SALDVI starting powders.

The cross-sections of SALDVI samples made from the five different starting powders are compared in Figure 3 for a laser beam dwell time of 800 seconds. The cross-sections reveal the presence of three phases in the SALDVI sample: the starting powder particles, the vapor deposited matrix, and uninfiltrated regions or porosity. The distribution of vapor deposited matrix material in the infiltration zone is expected to be a function of two factors: the temperature distribution in the workpiece, and the flux of gas by diffusion into and out of the pore structure. The SiC and Al_2O_3 starting powders should provide different temperature distributions in the workpiece, while the different powder sizes will yield different scales of pore structure and thus different rates of gas transport. Infiltration occurs most readily at the free surface of the powder and decreases with distance into the powder bed and from the centerline of the scanning laser path. Penetration of the vapor deposited phase appears deepest for the $7\text{ }\mu\text{m}$ SiC powder. The shape of the cross-sections reflects the Gaussian distribution of the power in the laser beam.

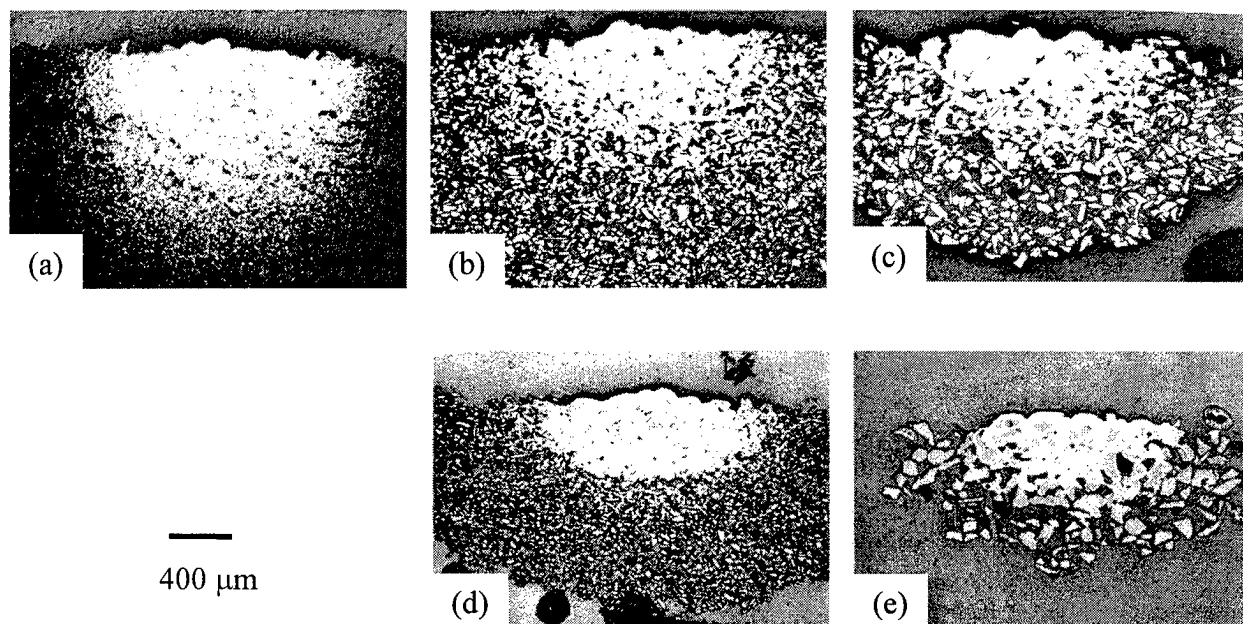


Figure 3. Cross-sections of single line SALDVI samples with starting powders of (a) $7\text{ }\mu\text{m}$ SiC, (b) $20\text{ }\mu\text{m}$ SiC, (c) $80\text{ }\mu\text{m}$ SiC, (d) $20\text{ }\mu\text{m}$ Al_2O_3 , and (e) $100\text{ }\mu\text{m}$ Al_2O_3 .

Image analysis was used to quantify the distribution of the porosity in each cross-section. Area fractions of the porous phase were measured as a function of depth from the free surface of the powder layer in $110\text{ by }110\text{ }\mu\text{m}$ frames. Figure 4 shows an example of three such frames used for image analysis for a SALDVI sample made using the $20\text{ }\mu\text{m}$ Al_2O_3 starting powder. The white regions are the vapor deposited matrix, the gray regions are the starting powder particles, and the black regions are porosity. Figure 5 shows the porous phase area fractions as a function of depth into the sample for samples fabricated from $7\text{ }\mu\text{m}$ SiC powder at four laser dwell times. As the laser heating time increases from 100 to 400 seconds, the infiltrated region extends deeper into the sample. Also, the amount of porosity at a particular location in the sample decreases with increasing heating time. When the dwell time increases to 800 seconds, the infiltrated region continues to extend deeper into the sample. However, the porosity within

the first 250 μm of the surface stays the same, likely due to the presence of trapped porosity. That is, when the infiltration has progressed sufficiently that the pores are no longer interconnected, they become isolated from the bulk gas and vapor deposition within the pore stops. Nevertheless, the areal density in the sample within 250 μm of the surface exceeds 90 % for a powder with an initial packing fraction of 30 %.



Figure 4. Image analysis frames for 20 μm Al_2O_3 starting powder at three locations from the free surface of the powder: (a) 0-100 μm , (b) 300-400 μm , and (c) 500-600 μm .

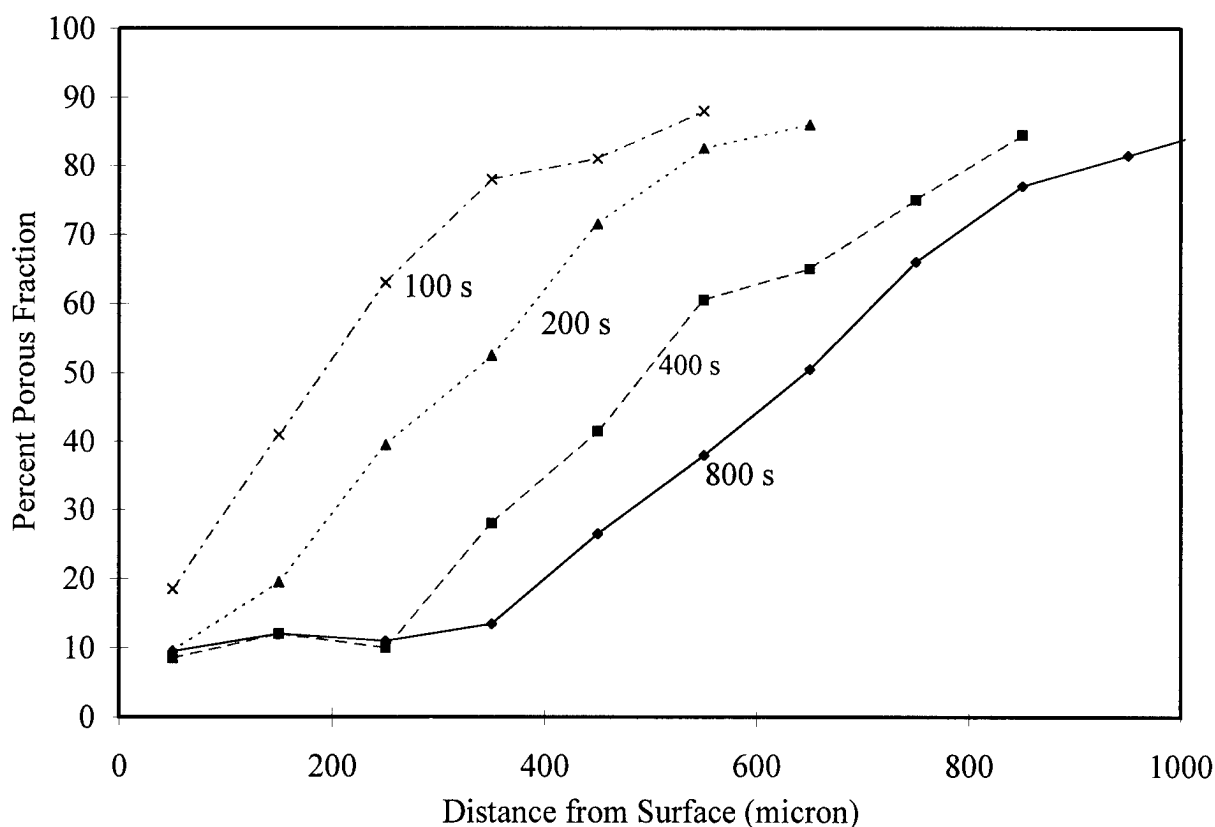


Figure 5. Area fraction porosity vs. distance from free surface of 7 μm SiC starting powder for four laser dwell times.

The porosity distributions in SALDVI samples of the three SiC starting powders and the 20 μm Al_2O_3 starting powder are compared in Figure 6 for a laser dwell time of 800 seconds. Near the surface, the 20 μm SiC and 20 μm Al_2O_3 starting powder samples show a slightly higher final density than the 7 μm SiC powder. The final density is the least for the 80 μm SiC powder, due to the presence of large pores between the larger particles in the sample. Comparing the porosity distributions of the SiC samples with the 20 μm Al_2O_3 sample, the SiC samples show a more diffuse density gradient while the Al_2O_3 sample shows a sharper gradient between the infiltrated and uninfiltrated regions. This difference could be explained by considering the difference in thermal conductivity of the two materials. The thermal conductivity of the SiC powder bed is greater than that of the Al_2O_3 powder bed, so the temperature distribution would be expected to extend deeper into the SiC powder. Remember that the surface temperature parameter is the same regardless of the starting powder since the incident laser power is varied to yield the same surface temperature parameter as measured by the pyrometer. Also, the result that the Al_2O_3 powder transmits the CO_2 wavelength better than the SiC powder does not greatly affect the depth of the infiltration zone. Toward the later stages of infiltration, the vapor deposited SiC matrix accounts for about 50 volume % of the workpiece and certainly affects its optical behavior since SiC is a strong absorber at the wavelength used in this study. A $1/e$ extinction length of 9 μm was reported for hot-pressed 6H SiC at a wavelength of 10.6 μm ¹¹. Therefore, it appears that heat transfer in the SALDVI workpiece using a CO_2 laser and SiC matrix is by laser heating near the surface and by thermal conduction elsewhere.

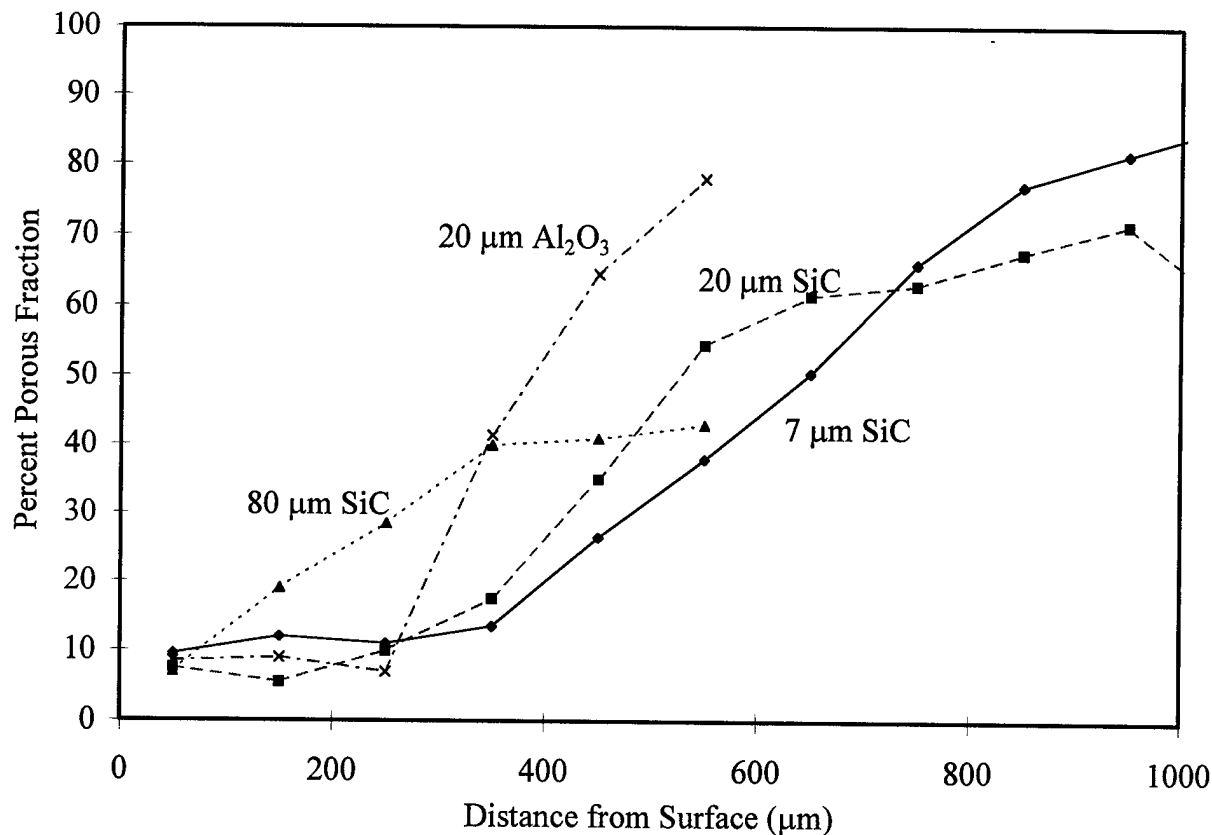


Figure 6. Area fraction porosity vs. distance from free surface for four starting powders at 800 second dwell time.

Summary

Image analysis was used to quantify the distribution of the various phases in SALDVI samples fabricated from tetramethylsilane gas and several starting powders. Area fractions of the porous phase varied with the powder size and powder material. Solid area fractions of 95 % were measured for samples containing 20 μm particles. Samples with particles over 80 μm contained large pores and lower solid fractions. The thermal conductivity of the starting powders influenced the density gradients. Samples containing starting powders of higher thermal conductivity have a more diffuse infiltration zone than those of the lower thermal conductivity. The transmissivity of the starting powders does not affect the size of the infiltration zone when the vapor deposited matrix material strongly absorbs the incident wavelength.

Acknowledgements

The authors gratefully acknowledge the support of the Office of Naval Research (grant #N00014-95-1-0978).

References

1. B.R. Birmingham and H.L. Marcus, "Silicon Carbide Shapes by Selective Area Laser Deposition Vapor Infiltration," Proceedings of the Solid Freeform Fabrication Symposium, The University of Texas at Austin, 1994, pp. 348-355.
2. L. Sun, K.J. Jakubenas, J.E. Crocker, S. Harrison, L. Shaw, and H.L. Marcus, "In-Situ Thermocouples in Macro-Components Fabricated Using SALD and SALDVI Techniques: III. Fabrication and Properties of the SiC/C Thermocouple Device," *Materials and Manufacturing Processes*, **13**, 883-907, 1998.
3. J.E. Crocker, S. Harrison, L. Sun, L.L. Shaw, and H.L. Marcus, "Using SALDVI and SALD with Multi-Material Structures," *JOM*, **50**, 21-23, December 1998.
4. J.E. Crocker, L. Sun, L.L. Shaw, and H.L. Marcus, "Preparation and Properties of In-Situ Devices Using the SALD and SALDVI Techniques," Proceedings of the Solid Freeform Fabrication Symposium, The University of Texas at Austin, 1998, pp. 543-547.
5. D.P. Stinton, T.M. Besmann, and R.A. Lowden, Advanced Ceramics by Chemical Vapor Deposition Techniques, *Ceramic Bulletin*, Vol. 67, No. 2, 1988, pp. 350-355.
6. K. Sygiyama and K. Yoshida, Pressure Pulsed Chemical Vapour Infiltration of SiC to Two-Dimensional-Tyranno/SiC-C Preforms, *J. Mat. Sci.*, Vol. 30, No. 20, 15 Oct 1995, pp. 5125-5129.
7. Sotirchos and Ofori, "Multidimensional Transport Effects on Forced-Flow CVI," *Ind. Eng. Chem. Res.*, 1997.
8. H-C Chang, T.F. Morse, and B.W. Sheldon, "Minimizing Infiltration Times During Isothermal CVI with MTS," *J. Am. Ceram. Soc.*, **80**, 1805-1811, 1997.
9. S.M. Gupte and J.A. Tsamopoulos, "An Effective Medium Approach for Modeling CVI of Porous Ceramic Materials," *J. Electrochem. Soc.*, vol. 137, no. 5, 1626-1638, 1990.
10. D. Bauerle, *Chemical Processing with Lasers*, (Springer-Verlag Berlin Heidelberg, 1986), pp. 41-48.
11. F. Shaapur and S. Allen, "Infrared Optical Absorptivity and Reflectivity of Hot-pressed SiC," *Applied Optics*, 26:2, January 1987.

Fabrication of Inorganic Material Models with Local Chemical Reaction Heat by Laser Scanning

Takayuki KAMITANI, Osamu YAMADA*, and Yoji MARUTANI

Department of Information Systems Engineering, Faculty of Engineering,
Osaka Sangyo University, 3-1-1 Nakagaito, Daito, Osaka, 574-8530 Japan

*College of General Education, Osaka Sangyo University,
3-1-1 Nakagaito, Daito, Osaka, 574-8530 Japan

ABSTRACT

In this paper, we propose a new method of fabricating 3-D models of the inorganic materials having high melting points such as ceramics and intermetallic compounds by laser scanning. To save the laser energy, we adopted the combustion synthesis which is the exothermic reaction between the raw materials. By adding chemical reaction heat to laser heat, the particles of the products of the reaction were bonded together by relatively low laser energy. The combinations of the raw materials and the laser scanning conditions for solidifying the products of the reaction and laminating the solidified layers were investigated experimentally. By mixing the powdered binder with the reactive raw materials, the simple layered models were fabricated. Since burning in the furnace is unnecessary in the proposed method, it is possible to fabricate the models in a short time.

1. INTRODUCTION

Metal and ceramics are widely used in the mechanical parts required the strength and the heat resistance. Ceramics are also used as the casting molds. Metal models are generally fabricated by cutting, milling, electrical discharge machining (EDM), casting, etc. Ceramics models are mostly fabricated by pouring the ceramics slurry into the molds and sintering at high temperature.

In recent years, selective laser sintering (SLS)[1], three dimensional printing (3DP)[2], fused deposition modeling (FDM)[3], and laminated object manufacturing (LOM)[4] have been developed as the methods of fabricating 3-D models of the ceramics and the metal directly from CAD data like the stereolithography.

In any of these methods, since the powders or the sheets of the materials are connected

temporarily by the binder, sintering at high temperature near the melting points above 1000°C is required to connect the materials together firmly. Therefore, the fabrication takes for a long time and a high degree of skill about burning process is required.

There is the method of fabricating the models directly by heating and fusing the metal powder sprayed on the laser beam spot. However, laser power of more than 500W is necessary even in the case of Co alloy having the melting point of 1200°C[5]. It is difficult to apply this method to the ceramics models which has to be sintered by keeping the materials at high temperature for a long time.

In this paper, we propose a new method of fabricating the 3-D models of high-temperature structural materials by using combustion synthesis[6] induced by laser heating. In this method, the synthesis of the compounds and the fabrication of the 3-D models progress simultaneously. By adding the chemical reaction heat to laser heat, the fabrication of the 3-D models of the heat-resistant inorganic materials such as the ceramics and the intermetallic compounds can be realized with low laser energy. Since the proposed method dispenses with sintering in the furnace, the knowledge and the skill about the process are unnecessary and the models can be fabricated in a short time. The principle of this method and the experiments are described in the following chapters.

2. COMBUSTION SYNTHESIS

Generally, combustion means the chain-reacting chemical reaction between an element and oxygen with the generation of heat and luminescence. In the case of using the element near the oxygen in the periodic table instead of the oxygen, similar reaction often occurs. The former which is the oxidation reaction and the latter are known as oxidative combustion and nonoxidative combustion, respectively.

The method of producing the compounds as the condensate by these combustion reaction is called combustion synthesis[6]. The Combustion synthesis is a highly efficient method of obtaining the compounds, because it advances to spontaneously after the ignition and the compounds are synthesized in a few seconds. In the oxidative combustion, ceramics such as Al_2O_3 is obtained. The nonoxidative combustion by using N, C, B, and Si produce the nonoxide ceramics which are nitride, carbide, boride, and silicide, respectively. In the case where Al is used, the intermetallic compound termed aluminide is produced. In this study, we adopted the reaction heat of the combustion synthesis to solidify the materials having high melting points with low laser energy.

3. EXPERIMENT OF SOLIDIFICATION AND LAMINATION OF POWDERED MATERIALS

3.1 Tested materials

Cermet of Cu and Al_2O_3 , intermetallic compound TiAl, and ceramics MoSi_2 were used as the structural materials of the models. TiAl and MoSi_2 are known as the promising high-temperature structural materials. Tested materials and their chemical reaction formulas are shown in Table1. Particle sizes of the raw materials were CuO: $1\text{--}2\mu\text{m}$, Cu: $15\mu\text{m}$, Al: $27.6\mu\text{m}$, Ti: $45\mu\text{m}$, TiAl: $40\mu\text{m}$, Mo: $1.5\mu\text{m}$, and Si: $2\text{--}3\mu\text{m}$.

Table1 Combinations of the tested materials and their chemical reaction formulas.

No.	Raw materials (molar ratio)	Chemical reaction formula	Calorific power	Products	Melting point of the products
①	CuO: 10%, Cu: 84%, Al: 6%	$0.3\text{CuO} + 2.7\text{Cu} + 0.2\text{Al} = 3.0\text{Cu} + 0.1\text{Al}_2\text{O}_3$	38.8kJ/mol	Cu Al_2O_3	Cu: 1084°C Al_2O_3 : 2054°C
②	Ti: 33%, Al: 33%, TiAl: 34%	$0.5\text{Ti} + 0.5\text{Al} + 0.5\text{TiAl} = \text{TiAl}$	37.7kJ/mol	TiAl	TiAl: 1460°C
③	Ti: 43%, Al: 43%, TiAl: 14%	$0.75\text{Ti} + 0.75\text{Al} + 0.25\text{TiAl} = \text{TiAl}$	56.5kJ/mol	TiAl	TiAl: 1460°C
④	Ti: 50%, Al: 50%	$\text{Ti} + \text{Al} = \text{TiAl}$	75.3kJ/mol	TiAl	TiAl: 1460°C
⑤	Mo: 33%, Si: 67%	$\text{Mo} + 2\text{Si} = \text{MoSi}_2$	118.4kJ/mol	MoSi_2	MoSi_2 : 2027°C

In the combustion synthesis, the product which is inert substance is sometimes added to the raw materials for the purpose of controlling the calorific power[6]. The inert materials in Table1 are Cu of ①, and TiAl of ② and ③.

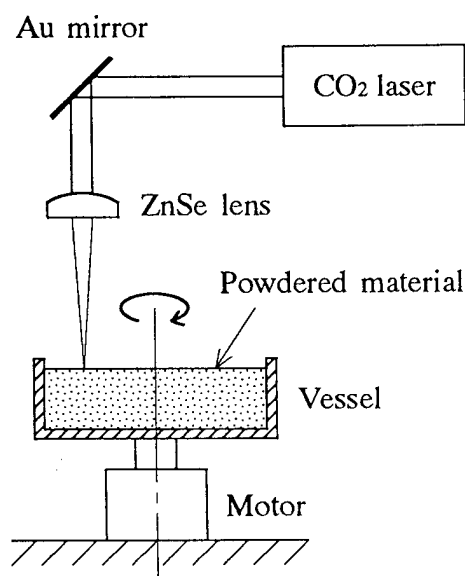


Fig.1 Experimental system.

3.2 Experimental apparatus

Fig.1 shows the experimental apparatus. Output beam of CO₂ laser (SYNRAD Co.: Model 48-1-28, wave length: 10.6 μ m, TEM00 mode) is focused on the raw materials by ZnSe lens (lens aperture: 30mm, focal length: 50mm) and then scans the surface of the raw materials. To simplify the scan, the vessel is rotated by a motor. Spot size of the laser is 117 μ m at the calculated value.

The selective laser sintering which solidifies the spread powdered materials selectively by laser heating is used as the method of forming the solidified layers. By repeating the spread of the powders and the beam scan alternately, a 3-D model is fabricated. In this method, it is necessary that the material only in the scanned area solidifies stably and the layers are connected firmly.

3.3 Experiment of solidification and lamination with only reactive materials

Firstly, several materials were investigated whether or not the combustion reaction was limited in the scanned area. The raw material was spread with the thickness of 3 mm and scanned from the above by the laser. Fig.2 shows the state of the material during laser scanning. The material in the irradiated area incandesced and sparked, and turned black after the irradiation.

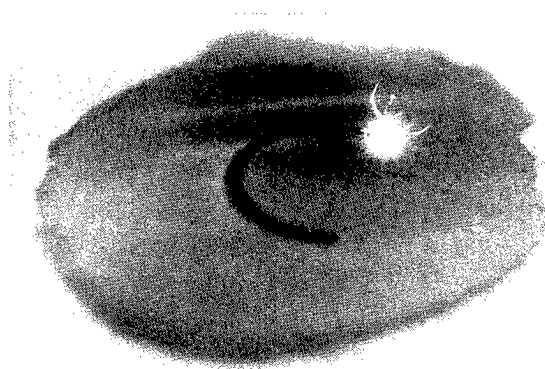


Fig.2 Material during laser scanning.
(material ③, laser power: 4W, scanning speed: 1.65mm/sec)

Fig.3 shows the experimental results. Reactions are classified into the next 3 states by the scanning condition of the laser and the constitution of the raw material.

- (1) The material only in the scanned area were solidified.
- (2) The whole material were burned out by the chain reaction.
- (3) The powders in the irradiated area were scattered by the excess laser power.

Increment of the supplied energy [W/mm/sec] makes the reaction move from (1) to (3). Material ④Ti+Al is easy to burn out by the chain reaction. Solidified object made from material ② and ③ that the product TiAl was mixed previously is significantly brittle. Accordingly, ① Cu+Al+CuO and ⑤Mo+Si are in prospect as the raw materials.

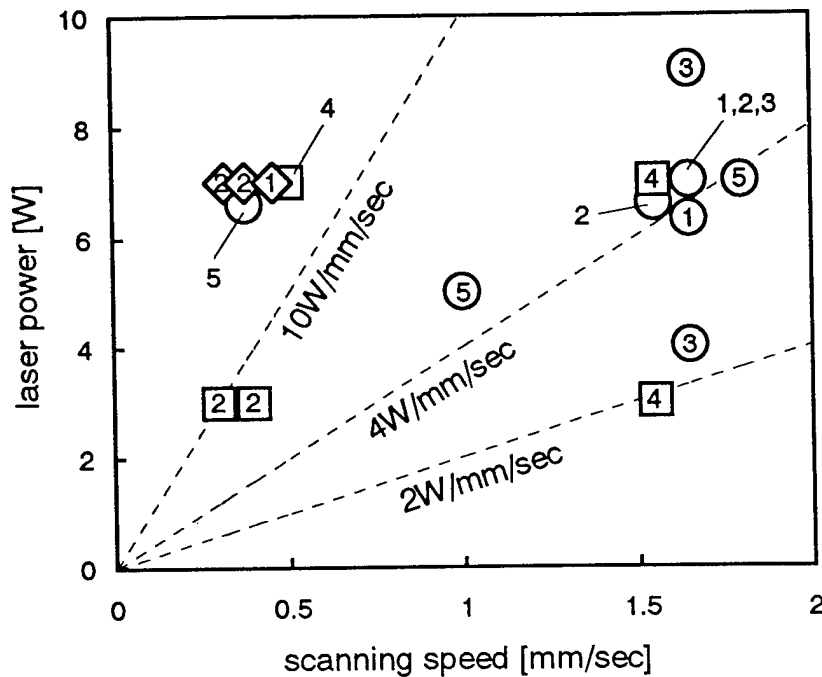


Fig.3 Relationship between the scanning condition and the stability of the solidification.

(The numbers in the symbols show the material numbers.

○: The material only in the scanned area were solidified.

□: The whole material were burned out.

◇: The powders in the irradiated area were scattered.)

To know the effect of the reaction heat, the same solidification experiment as the above was done by using Fe powder (particle size: $50\mu\text{m}$, melting point: 1535°C). In the case of the reactive materials, the materials could be solidified with the laser power of a few W. On the other hand, to solidify the Fe powders with the scanning speed of 1mm/sec , not less than 10W was required. Thus the combustion reaction plays a part which reduces the external energy required for the solidification.

Next, lamination experiment was done by using material ① and ⑤. Since the solidified depth was not less than 0.3mm in the above solidification experiment, the experimental condition was set as the following:

laser power: 7W
scanning speed: 1.65mm/sec
layer thickness: 0.2mm

However, in this condition, the layers did not connect each other and unified object could not be fabricated. On the other hand, when the supplied energy [W/mm/sec] was increased, burning out by the chain reaction was occurred.

3.4 Experiment of solidification and lamination by addition of binder

We attempted to add an inorganic inert binder to the raw reactive materials and connect the reactive material particles with the combustion synthesis and the help of the binder. In this case, it is thought that the binder materials restrain the calorific power same as the inert materials and reduce the reactivity of the total system. For this reason, we considered that the reactivity of the raw materials themselves have to be high in the case of using the binder. ④Ti+Al was selected as the reactive raw materials and the glass powder (particle size: $100\mu\text{m}$, softening point: 550°C) which was easy to obtain was used as the binder. The mixed material was spread with the thickness of 3 mm as paragraph 3.3. In the case that the material ④ : glass powder weight ratio was 1:1, even if the laser power was 3W and the scanning speed was 1.55mm/sec, the materials burned out by the chain reaction. To reduce the reactivity further, the ratio was changed to be 1:2. In this ratio, the solidification reaction stabilized, but the solidified object was porous and fragile. To strengthen the solidified object, the ratio was chosen to be 1:3. As a result, the solidified object became dense and rigid. The materials could be solidified with the laser power of not less than 2W.

On the other hand, in the case of only the glass powder, not less than 3W was needed for the solidification. Thus, it is clear that the reaction heat assists the melting of the binder.

Next, to confirm the connectivity between the layers, lamination experiment was done by using the above mixed material of 1:3 weight ratio. Experimental condition is maintained as the following based on the above solidification data.

laser power: 3W
scanning speed: 0.5mm/sec
layer thickness: 0.2mm
the number of layers: 15 layers

Fig.4 shows an example of the layered model. In this example, the center of the circular

solidified objects are shifted from the fifth layer. Contact area between the fourth layer and the fifth is significantly narrow, but the connectivity between the layers is firm enough.

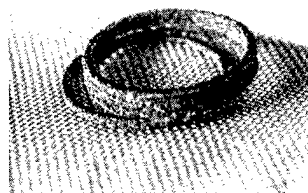


Fig.4 An example of the layered model.

4. CONCLUSIONS

We have proposed the new method for fabricating 3-D models of the inorganic materials with low laser energy by using the exothermic reaction and have done some fundamental experiments. Since the combinations of the tested materials were significantly reactive, the top of the solidified layers could not be heated to the melting point by the laser to avoid burning out by the chain reaction. Thus, it is not easy to connect the layers only the reactive materials.

We are planning to try to melt the top of the solidified layers through the use of the raw materials having a slightly lower reactivity than the tested materials. In the case, the required laser energy becomes larger than that of this time, but it is expected that the laminated models can be fabricated without the binder.

REFERENCES

- [1] I. Lee, A. Manthiram, and H. L. Marcus: "Selective Laser Sintering of Alumina-Zinc Borosilicate Glass Composites using Monoclinic HBO_2 as a Binder", *Solid Freeform Fabrication Proceedings, Austin, 1995*, pp.46-54 (The University of Texas at Austin, 1995).
- [2] S. Michaels, E. M. Sachs, and M. J. Cima: "Metal Parts Generation by Three Dimensional Printing", *Proceedings of the 4th International Conference on Rapid Prototyping, Dayton, 1993*, pp.25-31 (The University of Dayton, 1993).
- [3] T. F. McNulty, F. Mohammadi, A. Bandyopadhyay, D. J. Shanefield, S. C. Danforth, and A. Safari: "Development of a Binder Formulation for Fused Deposition of Ceramics", *Rapid Prototyping Journal*, Vol.4, No.4, pp.144-150 (1998).

- [4] B. B. Mathewson, W. S. Newman, A. H. Heuer, and J. D. Cawley: "Automated Fabrication of Ceramic Components from Tape-Cast Ceramic", *Solid Freeform Fabrication Proceedings, Austin, 1995*, pp.253-260 (The University of Texas at Austin, 1995).
- [5] W. Konig, T. Celiker, and H. J. Herfurth: "Approaches to Prototyping of Metallic Parts", *Proceedings of the 2nd European Conference on Rapid Prototyping and Manufacturing, Nottingham, 1993*, pp.303-316 (The University of Nottingham, 1993).
- [6] O. Yamada: "Basic Research and Applications of Combustion Synthesis Process", *Journal of Science and Industry*, Vol.65, No.10, pp.460-466 (in Japanese) (1991).

ELECTRICALLY STIMULATED BILAYER HYDROGELS AS MUSCLES

Paul Calvert and Zengshe Liu,

Department of Materials Science and Engineering, University of Arizona, Tucson, AZ 85721.

ABSTRACT

Muscle-like actuators have been made from bilayers of crosslinked polyacrylamide and polyacrylic acid hydrogels sandwiched between electrodes. The polyacrylic acid responds to applied positive polarity field by contracting and expelling water which is taken up by the polyacrylamide layer. Previous studies have shown that the effective swelling modulus of polyacrylamide is much lower than polyacrylic acid. Hence the polyacrylamide acts as a sponge. As the polyacrylic acid layer contracts in the x,y and z directions the polyacrylamide is also pulled in on x and y, so that the whole stack becomes narrower and expands along the z-axis. Reversing the field reverses this effect with a time constant of about 1 minute for 1 mm thick layers with a thickness change of about 10%. Linear changes up to 50% have been obtained.

Other gel actuators either transfer water across a sheet and so bend, or contract by expelling water. This new system shows a linear contraction and expansion without a volume change and so can be run (sealed) in a dry environment.

INTRODUCTION

There is an obvious need in robotics for synthetic actuators with properties close to those of biological muscle. These requirements could include contractions of about 50% in a time of about 1 second, a maximum stress above 200 kPa and a power density of 50 W/kg. In the absence of other convenient energy sources, the synthetic muscle should be powered electrically.

Only polymer gels seem capable of producing sufficiently large strains. There have been demonstration systems which promise to meet most of the requirements listed above, but only when powered chemically, by added solvent or a pH change^{1,2}. Outfitting a robot with a metabolic system and blood supply to provide the necessary reagents would be a major inconvenience.

There have been many studies of the electrical response of polymer gels. The archetypal system is a cross-linked hydrogel of polyacrylic acid. When a strip of gel is placed in water between two electrodes, it bends. The bending direction is dependent on the details of the experiment, whether the electrodes are touching the gel surface³ and the relationship between the gel composition and the surrounding fluid. This complexity reflects the fact that the electrical field provides an asymmetric stimulus and any differential response between the two surfaces will lead to bending.

The primary response of these gels is ionization at high pH. In the acid form, at a pH below 4, the gel is slightly swollen but it swells strongly in base, at a pH above 7. However, a number of secondary effects also lead to volume changes and will cause the gel to bend in an electrical field under the right circumstances.

We have been exploring the use of multilayer gels to produce better actuators. The aim was to produce an electrically-driven actuator that provides a linear contraction or expansion, rather than bending. It should also be able to run dry, in the sense of being sealed in a cell not much larger than the swollen gel, rather than requiring a water bath. It should also be possible to group many thin layers of gels and actuators to make a larger "muscle". Bending actuators do not lend themselves to being stacked in order to get larger forces. The underlying philosophy for our work is that the asymmetry of the field can be balanced by an asymmetry in the gel structure in order to provide a symmetric response. This response should be a shape change, rather than a volume change.

GEL FORMATION

Gel stacks were made by extrusion freeform fabrication. Acrylic monomer, water and catalyst is extruded from a syringe through a fine (0.2-1 mm diameter) nozzle which writes on a heated substrate. The composition of the gel can be changed by swapping syringes or by using a Y-junction between two syringe feeds. To prevent the monomer solution from flowing off the substrate before curing, 8 wt% of fumed silica is added to the solution, to give it a toothpaste-like rheology. The solution cures to cross-linked gel by thermally activated free radical polymerization within a few minutes of being deposited on the plate. Typically 6-layer stacks were formed into bars 5 cm x 0.5 cm (wide) x 0.4 cm (thick), before swelling.

A typical stack would have a polyacrylic acid face with 1-5 (x) layers and a polyacrylamide face of (6-x) layers with a combination of dense and open-mesh layers (written as a series of spaced lines). When used, wire electrodes were usually placed between layers 1&2 and 5&6.

The system used on this work was solutions of acrylamide or acrylic acid at 2-4g/10ml of water. The cross-linking agent was methylenebisacrylamide at levels from 0.2g to 0.5 g. for the acrylamide, the initiator was potassium persulfate, 0.0025g and the accelerator was tetramethylethylenediamine (TEMED) 0.036g. For the acrylic acid, the catalyst system was a potassium persulfate (0.0114g)-potassium metabisulfite (0.0094g) redox couple. Fumed silica (2.1 g) was added and the pH adjusted to 3.8-4.0.

BENDING OF MULTILAYER GEL STACKS IN BASE

Initially this study sought to demonstrate very strong bending responses in six layer gel stacks with from one to five layers of polyacrylic acid gel and the remainder polyacrylamide⁴. It seemed reasonable that the acid gel would swell strongly in base, while the acrylamide would not. As a result the bars should bend with the polyacrylamide surface concave.

The results for the weight change of such bars on immersion in base are shown in figure 1. In fact relatively little bending was observed. In addition, the weight change of a bar with two polyacrylic acid layers and four polyacrylamide layers was quite comparable to that for six layers of polyacrylic acid.

The absence of bending implies that the polyacrylamide gel is relatively soft and does not constrain the polyacrylic acid layers. Similarly, little bending would be expected on heating a strip of metal with attached rubber layers. Since our experiment is being carried out in water, the polyacrylamide is soft to deformation in water with a volume change. It is not unexpectedly soft when tested in air⁴. It would also be expected that the polyacrylamide section of the bar would be extended in the length and width directions but would contract along the thickness direction. In fact the weight change shows that the polyacrylamide layer is increasing in volume and so must have a small or negative Poisson's ratio. Such effects have been described for immersed gels^{5,6}.

These observations suggested to us that the polyacrylamide layers can act as a bellows and increase or decrease in volume under the force applied by the polyacrylic acid gel. Thus it should be possible to form an electrically driven stack where contraction of a polyacrylic acid layer would drive water into an attached polyacrylamide layer, which would contract in the length and width directions but would expand in the thickness direction to accommodate the increased volume of water. A sketch of this is shown in figure 2.

ELECTRICALLY-DRIVEN CONTRACTION OF GEL STACKS

Initially, we built stacks of six gel layers : three of polyacrylic acid gel followed by three of polyacrylamide gel with palladium wire electrodes between layers 1&2 and 5&6. The shrinkage of these gels was studied in response to applied field.

The response of the system was made complicated by the strong dependence on the state of the gels. First the stack was swollen in dilute base to allow the acid gel to ionize fully and to swell the acrylamide gel to equilibrium. It was then washed in deionized water. The stack was then treated briefly for 5 minutes with dilute acid (0.25M HCl) to bring the acid gel close the point at which a large volume change occurs in response to a small change in the degree of ionization. From this state, a potential of 6 Volts, with the acrylic acid side positive, was applied for 12 minutes and the stack contracted by about 50% along the x and y axes. The contraction of the resulting gel is shown in figure 3. During this process, some water exuded from the system with a weight loss of 20-30%. Thus the area of the sample changed by a factor of four, the weight decreased by about 30% and the thickness must increase. The current flowing during this process was about 8 mA/cm². This system was not wholly satisfactory as there was tendency of the gel to burn around the wire electrodes and for the electrodes to pull out with these large shape changes.

An alternative system was developed with carbon foil electrodes placed above and below a gel stack. The system was taken through the cycle of swelling in base and then deswelling in acid, as before. The shape change on applying a potential was then followed by recording the deflection of a laser reflected off the surface of the stack. The results of this are shown in figure 4. It can be seen that the thickness changes by about 10% in 1 minute and the change at 3V is roughly twice that at 1.5V. We were concerned that this height change might be due to bending, rather than a thickness change. No difference was seen between height changes at the edge and center, so this is believed to be a simple thickness change, occurring as the acid gel contracts along the x-y directions and displaces water into the acrylamide gel, which expands along the z-

direction. A sample was subjected to a series of 10 cycles, with current on for 1 minute, off for 1 minute, reversed for one minute then off for 1 minute, as shown in figure 5. These preliminary results show that the 10% thickness change is quite reversible.

DISCUSSION

A swollen, ionized gel is not a simple material. As made it will normally not be in swelling equilibrium with the liquid it contains. If it is allowed to equilibrate, the degree of swelling, per gram of dry gel, will depend on the crosslink density and on the pH and ionic strength of the medium. We believe that the responses of our gels can be interpreted in these terms plus the effect of applied field in lowering the pH next to the positive electrode and raising the pH next to the negative electrode. The response of a gel to applied field is strongest in the range of pH4-pH5 where the degree of swelling changes fastest with pH. This is not where the degree of ionization changes fastest with pH.

By coupling a soft neutral gel to an ionizable gel, get can obtain a linear contraction, and no volume change, with applied potential. A synthetic muscle that would change thickness, like an electrically-driven jack, seems quite feasible with this system. For a faster response, many thin layers are needed, with interleaved electrodes. The gels probably also need to be reinforced with flexible fibers to provide mechanical strength without compromising the shrinkage.

ACKNOWLEDGMENTS

We would like to thank the Army Research Office for support of this work.

REFERENCES

1. S. Umemoto, N. Okui and T. Sakai. in *Polymer Gels* (eds. DeRossi, D., K.Kajiware, Osada, Y. & Yamauchi, A.) pp. 257-270 (Plenum, NY, 1991).
2. M. Suzuki. in *Polymer Gels* (eds. deRossi, D.) pp.221-236 (Plenum, New York, 1991).
3. M. Doi, M. Matsumoto and Y. Hirose, *Macromolecules* **25**, 5504-5511, 1992.
4. P. Calvert and Z. Liu, "Freeform Fabrication of Hydrogels", *Acta Materialia* **46**, 2565-2571, 1998.
5. T. Takigawa, Y. Morino, K. Urayama and T. Masuda, "Osmotic Poisson's ratio and equilibrium stress of Poly(acrylamide) gels", *Polymer Journal*. **28**, 1012-1013, 1996.
6. C. Li, Z. Hu and Y. Li, "Poisson's ratio in polymer gels near the phase-transition point", *Phys. Rev. E* **48**, pp. 603-606, 1993.

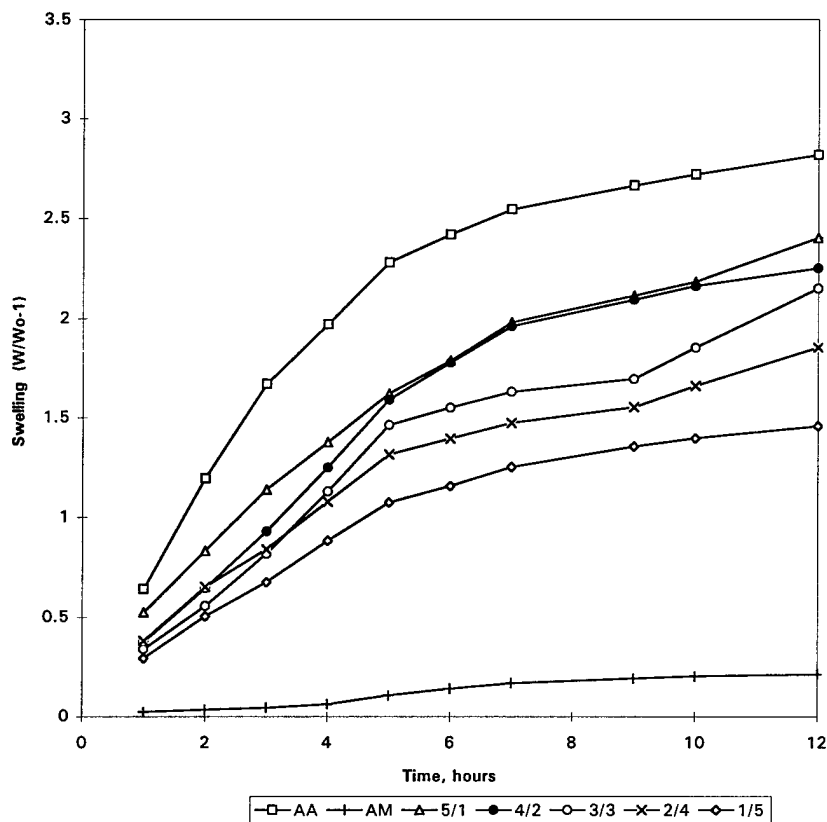


Figure 1) Swelling of multilayer stacks of acrylamide and acrylic acid gels. 0.03M monomers, 4%(vs. monomer) crosslinking. (AA: 6 layers, Acrylic acid; AM: 6 layers Acrylamide; 5/1: 5 layers AA and 1 layer AM)

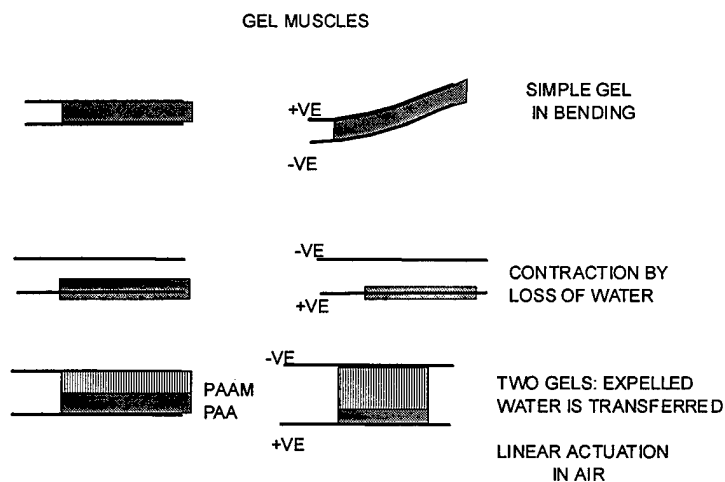


Figure 2: Sketch of response of one- and two-layer gels to an applied field. Left, no field, right, field applied.

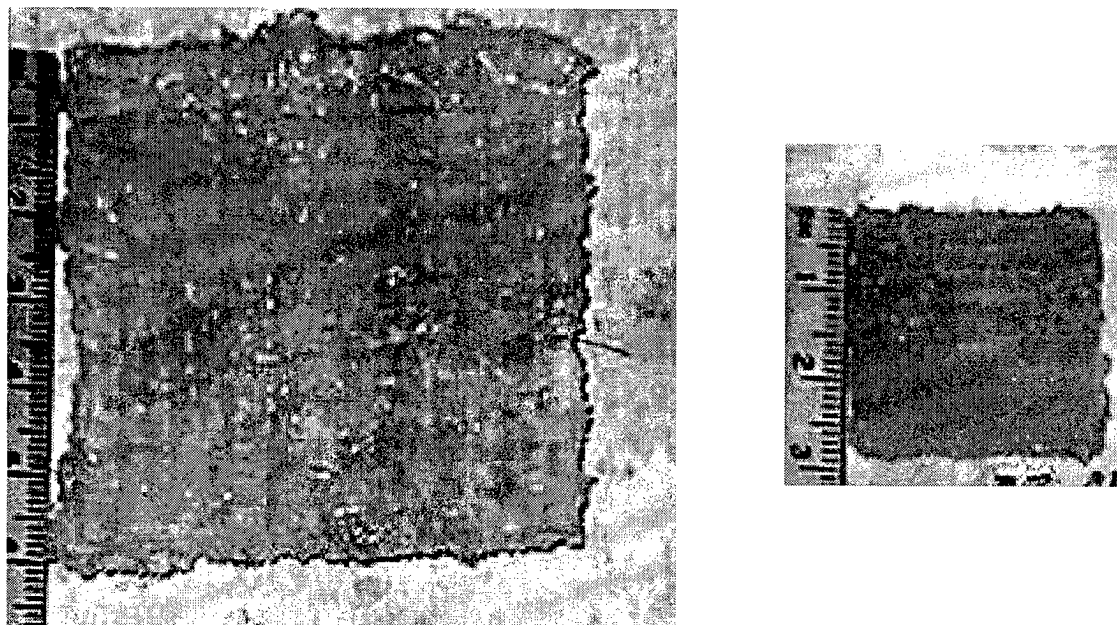


Figure 3: Gel sheet before (left) and after (right) applied potential of 6V for 12 minutes

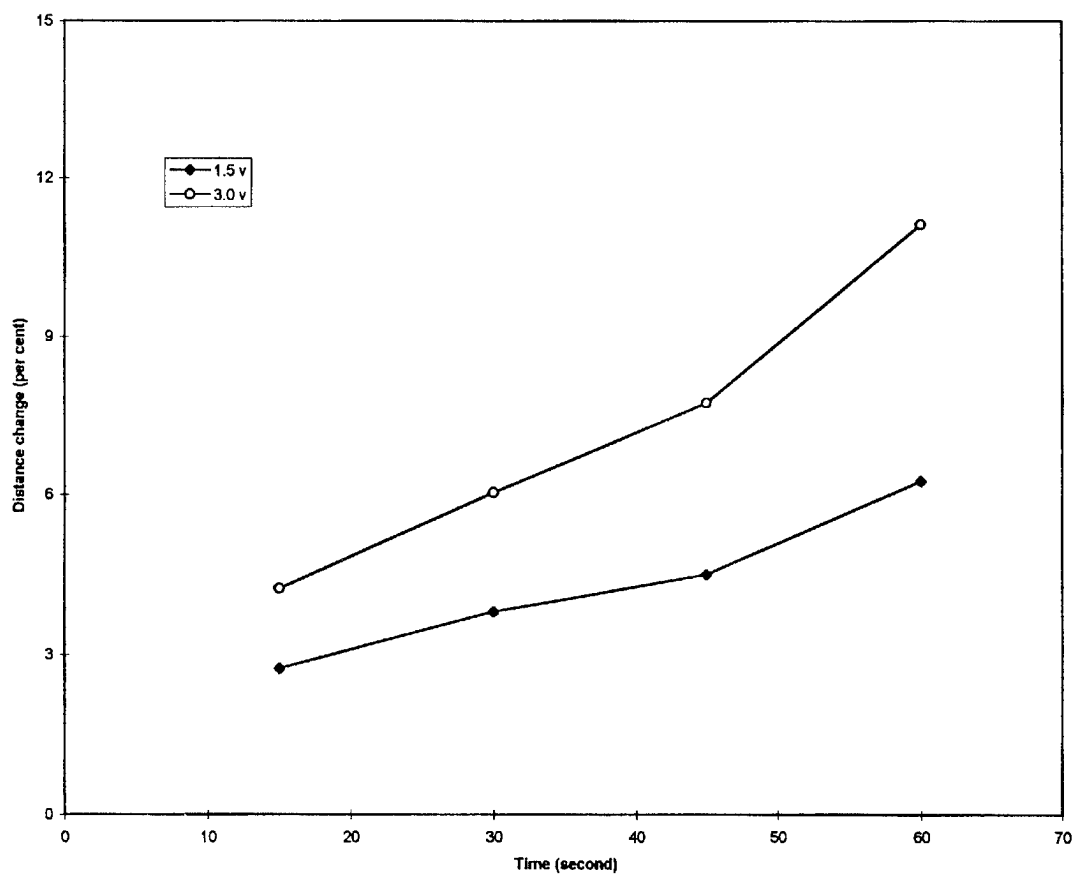


Figure 4: % thickness change in a gel stack between graphite foil electrodes.

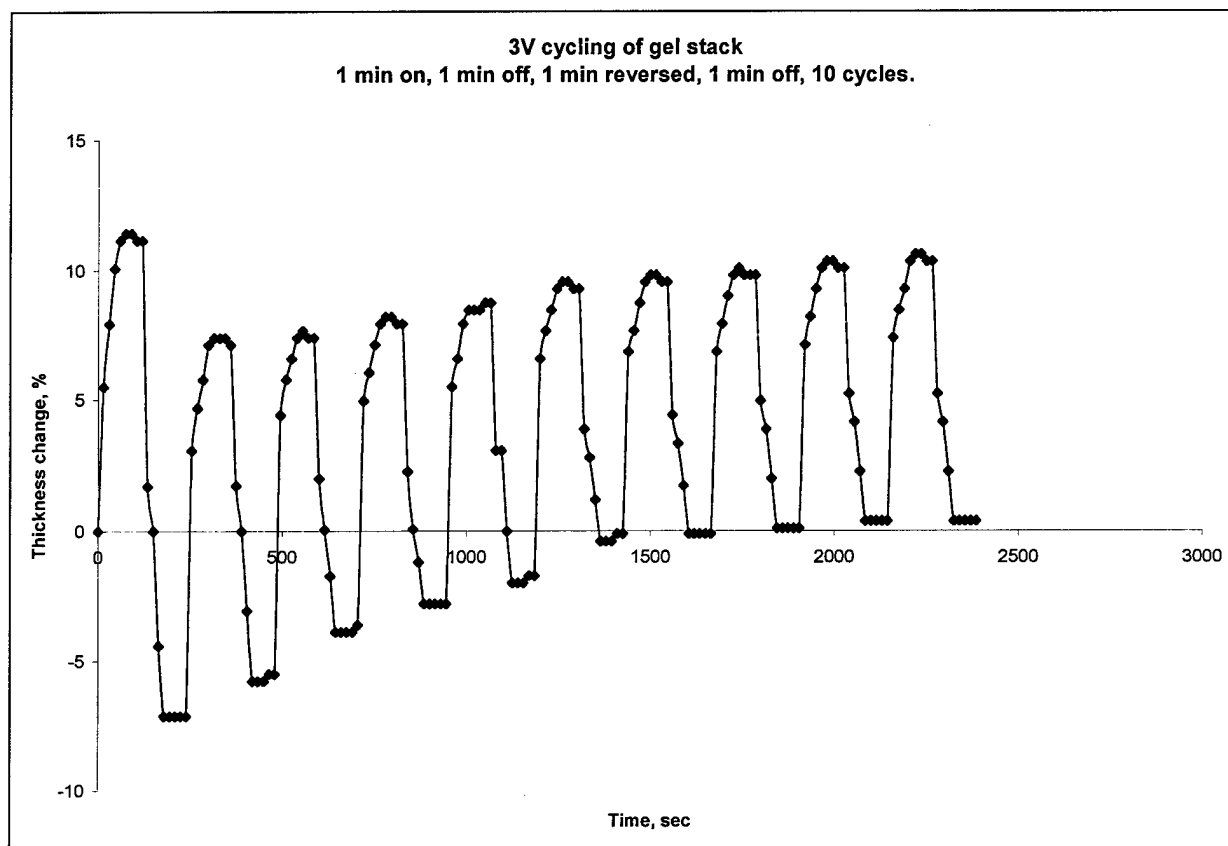


Figure 5: Cycling of a gel stack from +3V to 0V to -3V to 0V.

Intelligent Toolpath for Extrusion-based LM Process

Dan Qiu¹, Noshir A. Langrana¹, Stephen C. Danforth²,
Ahmad Safari², Mohsen Jafari³.

¹Mechanical & Aerospace Engineering, ²Ceramic & Materials Engineering, ³Industrial Engineering, Rutgers - The State University of New Jersey, Piscataway, NJ, 08854-8058

1. Abstract

At Rutgers University, in an ONR funded MURI program, we've built the hardware and developed the corresponding advanced computer software for multi-material layered manufacturing. Based on our ongoing research, we determined that the build characteristic is heavily dependent on the material being used. This has direct implications on toolpath creation. Therefore, it is important to develop the hardware/software that will accommodate this requirement. In recent past, we have developed CAD models and their .stl files using commercially available software such as I-DEAS and ProE. Using this information, the slice file is generated in QuickSilce. To fabricate high quality part's, to have better control on the toolpath in relation to the materials, and to make the development generic yet compatible with our hardware, we are developing an in house intelligent toolpath generation system. This new development includes the issues such as multiple fill-toolpaths for the same material, deposited road characteristics, the interface mismatch between adjacent materials and the intelligent toolpath features needed for machine control. After the component toolpath file generated by the in house toolpath software, our multi-material build file algorithm, systematically, layer by layer, integrates all component toolpaths into one multi-material toolpath. The existing virtual graphical simulation as well as well selected part fabrication experiments are being used to validate the current development. The development is kept modular and it is developed with the intention to be used for the majority of Layered Manufacturing systems.

2. Background

LM refers to the process of fabricating three-dimensional objects from CAD-generated solid models layer by layer [1]. Since the first commercial inception of Stereolithography technology in 1988, LM technologies have been developed rapidly. There are many success stories giving specific comparative examples of time and cost savings relative to the more traditional ways of completing the same steps in the product development and commercialization cycle [2]. A representative list [3] [4] includes: 3D System's Stereolithography Apparatus (SLA) series, Stratasys's Fused Deposition Modeling Process (FDM), DTM's Selective Laser Sintering (SLS), Helisys's Laminated Object Manufacturing (LOM), Sanders, and 3D Printing. Each technology has various materials options before starting the manufacturing process; Yet typically, they can only handle one component material during one building process.

Multi-material LM technologies are needed. For example, there is already a need for multi-color parts for surgical applications. There are two kinds of multi-material solids, those where material distribution is changing gradually from one material to another, and

those made of a collection of discrete materials. Multi-material solids are also called heterogeneous solids [5]. Multi-material LM refers to a process of fabricating a part consisting of more than one component material from CAD models layer by layer. The multi-material LM system under development at Rutgers University is designed to fabricate parts consisting of a collection of discrete materials with boundary interfaces. This multi-material LM system should be able of generating CAD models, slicing files, toolpath files and fabrication of multi-material parts in one manufacturing process. The development of our multi-material LM system is still at the research stage. At university of Texas at Austin, Multi-material Selective Laser Sintering (M^2SLS) is under development. This process could allow fabrication of functionally gradient materials (FGMs) in which blended material interfaces exist [6]. A new development of M^2SLS for an application in complex sand casting core arrays is discretely laying down two different materials and removing one after sintering. This will allow more complex geometries and drastically decrease the production times of sand cores [7]. At Sandia National Laboratories, Robocasting technology is a direct fabrication technique that relies on automated extrusion of highly concentrated ceramic slurries, which is able to fabricate either single material or multi-material parts [8].

3. Objective

Currently, at Rutgers University, under an Office of Navy Research (ONR) funded MURI program [9], An Intelligent Layered Manufacturing System (Fig 1) for fabrication of multiphase electromechanical parts has been developed. This program requires design and construction of an intelligent multi-material LM system, processing science for multi-material LM, CAD based design and manufacture of multi-phase electromechanical components. The intelligent multi-material LM system should include a high quality multi-material layered manufacturing machine (hardware) and a CAD based intelligent multi-material LM software system. In the recent past, the MURI hardware as well as corresponding software has been developed and several multi-material parts have been successfully fabricated.

Multi-material CAD System

MURI Machine

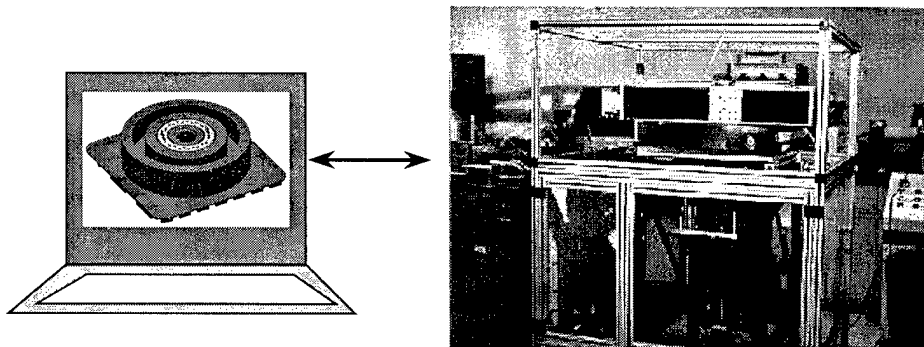


Figure 1: An intelligent Layered Manufacturing System

The multi-material CAD system in the intelligent Layered Manufacturing System will generate toolpath data file ready for the MURI machine and virtually fabricate

defect free multi-material parts. In the present program, quality of a part is considered to be very important. To have full control over the building toolpath, which has important influence on the part's quality, an in house intelligent toolpath generation software is needed. This paper discusses the implementation of the intelligent multi-material toolpath generation algorithm and its results. The objective of this study is to develop a virtually void free toolpath file for the multi-material LM process. The toolpath file generated here will be input to the simulation software developed last year [10] to visualize the virtual LM process. If the virtual part has voids and defects, the toolpath parameters will be adjusted and the toolpath will be regenerated until the virtual part is defect free.

4. Method

Multi-material CAD

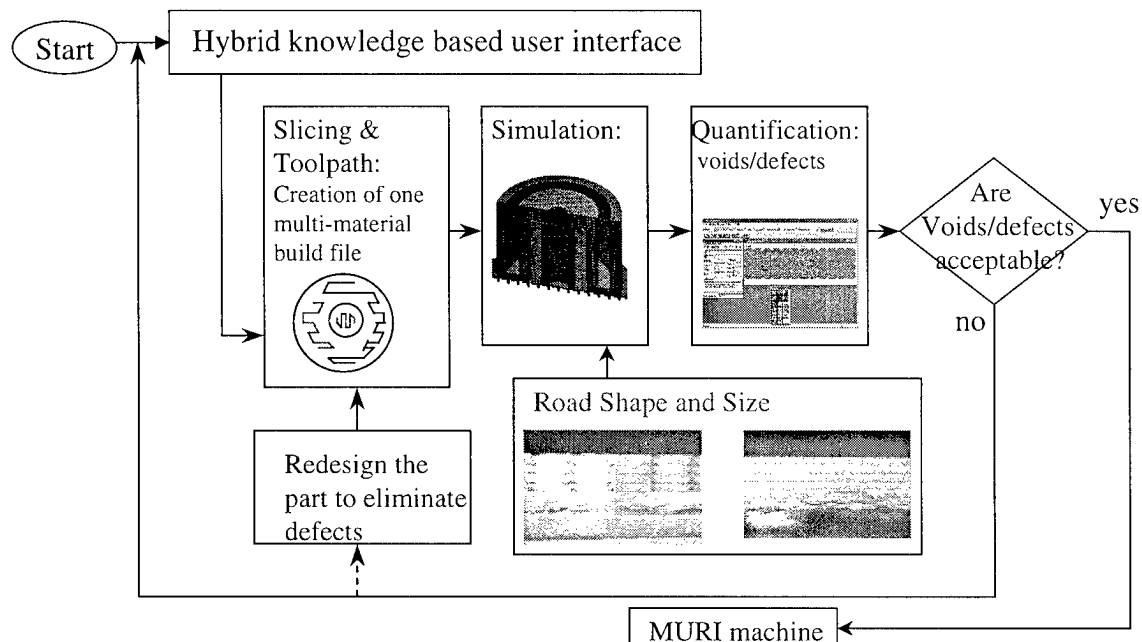


Figure 2: Multi-Material CAD System

The Multi-material CAD system (Fig 2) includes multi-material build file generation, virtual simulation and quantification of the defects in virtual part. The virtual simulation [10] uses the in-house multi-material build file as the input data and virtually fabricates the multi-material part. Surface and internal defects can be quantified from the images captured from the outside view or sectional view of the simulation. If the part quality is not acceptable, modifying the toolpath parameters to regenerate the build file or redesigning of the part is needed. The iteration runs until the virtual part quality is acceptable. Finally the multi-material build file is ready for the hardware – MURI machine.

To create the multi-material build file, we use IDEAS, ProE, or Auto CAD to generate a n-material solid model and orient the part for the “best” build direction. For the n-material solid model, n .stl files and n-slice files (.slc file currently) are generated while maintaining their geometric relationships [11]. The open issues related to the fabrication

are the offset between the material boundaries and the order of the solid models. Once the slice files are loaded, the toolpath parameters are defined for each material and for all intersecting boundaries, the in-house toolpath software can generate n-build files for n-slice files. The in-house integration software integrates the n-build files with their locations into one multi-material build file.

Toolpath generation software

The toolpath generation software developed here is designed to create a single-material build file for the MURI machine, which has toolpath information mainly. Taking a slice file as the input data, the program extracts one slice from the file at a time. Boundary path and raster path for the slice are generated and written into the output file. The program continues to extract the next available slice and generate paths until all the slices in the file are finished (Fig 3).

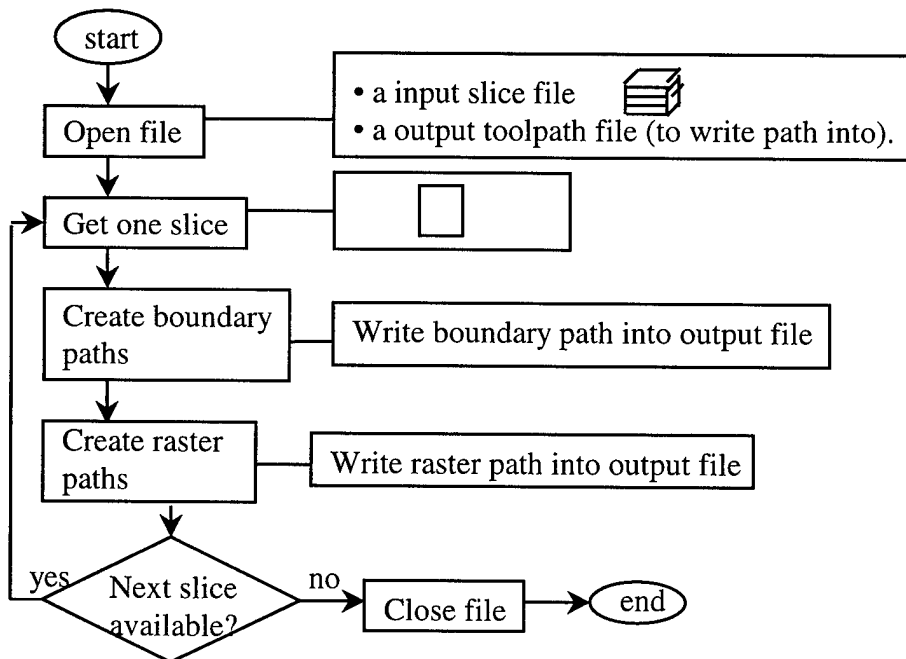


Figure 3: Toolpath generation process

The main data structures in this program are a file manager structure, a surface structure, a boundary structure and a quantized point structure. The file manager structure contains all the toolpath parameters and the method, which extract a slice from the input file. A surface structure contains boundaries on this slice, quantized points structure, and methods which rotate and reduce boundaries, write boundary paths, quantize boundaries into points and write vector paths respectively. A boundary structure contains boundary points, methods that rotate boundary points and calculates the reduced boundary point locations respectively. The quantized point structure contains all the quantized points and the information related to the point, which help to form the raster paths.

5. Results

First version

The first version of the toolpath generation software was able to successfully handle simple convex shapes such as a triangle and a square. To test the software, two representative complex-shaped surfaces are generated. One is a hollowed circular surface; the other one is a concave polygon. For these two shapes, the first version of the software gave the following results (Fig 4): 9 zigzag paths, 3 straight-line paths are generated for the hollowed surface; 6 zigzag paths and one erroneous jump were generated for the concave polygon. The number of paths on each surface is high, which will make the depositing nozzle jump many times and will likely result in poor surface quality.

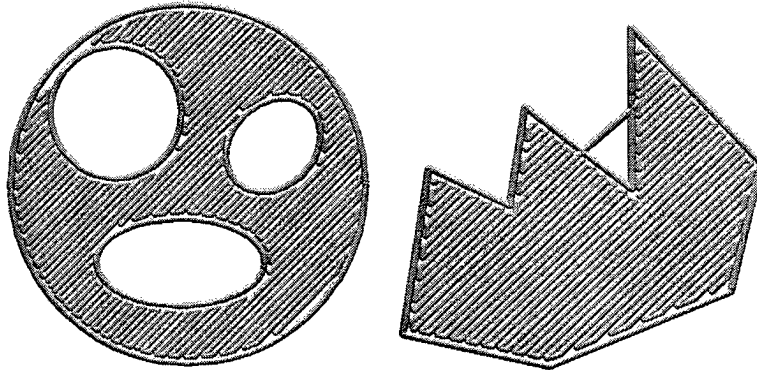


Figure 4: Simulated toolpath generated by 1st version of the software

Second version

We learned from version 1 that the location and occurrence of any discontinuities in the different toolpaths. Additional logic was added to create version 2. This improved the toolpath. The result is as follows (Fig 5): 5 zigzag paths generated for the hollowed surface; And 3 zigzag paths and no erroneous jump for the concave polygon. The toolpath generated in version 2 is comparable to the results generated for a commercial software result like QuickSlice.

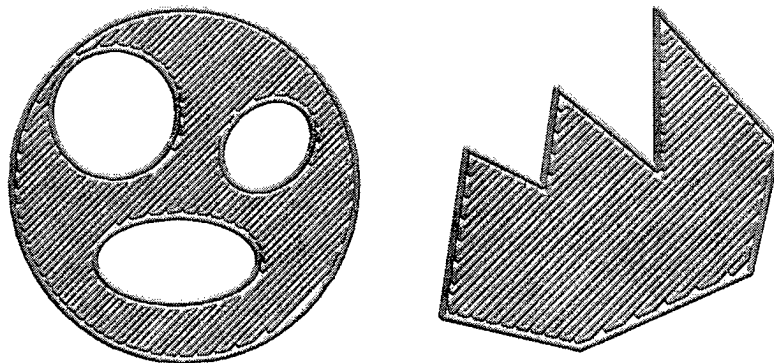


Figure 5: Simulated toolpath generated by 2nd version of the software

Third version

To improve the toolpath further, the third version of the software was developed.

The third version has two intelligent features: a “least number of paths” and the “closest next starting point identification” algorithms. From this version of the software, 4 zigzag paths were generated for the hollowed surface and 3 zigzag paths for the concave polygon. The start and end for each path are marked in Figure 6. Except for the starting point of the first path, each start point of the current path is the closest one to the end point of last path.

There are many voids at the road turns and road ends in the results of version 2. To make the part full dense, two toolpath parameters are altered: roadwidth and offset. As can be seen from the simulation image (Fig 6), the surfaces are much denser, fewer voids exist on both surfaces. Most existing voids are located at the road ends and sub-perimeters. New intelligent toolpath features need to be developed deal with these kinds of voids.

To test if the software can handle different road raster angles, the -45° raster angle toolpath was also generated. For the hollowed surface, the same number of zigzag toolpaths was generated. For the concave polygon, one zigzag toolpath was generated (Fig 6).

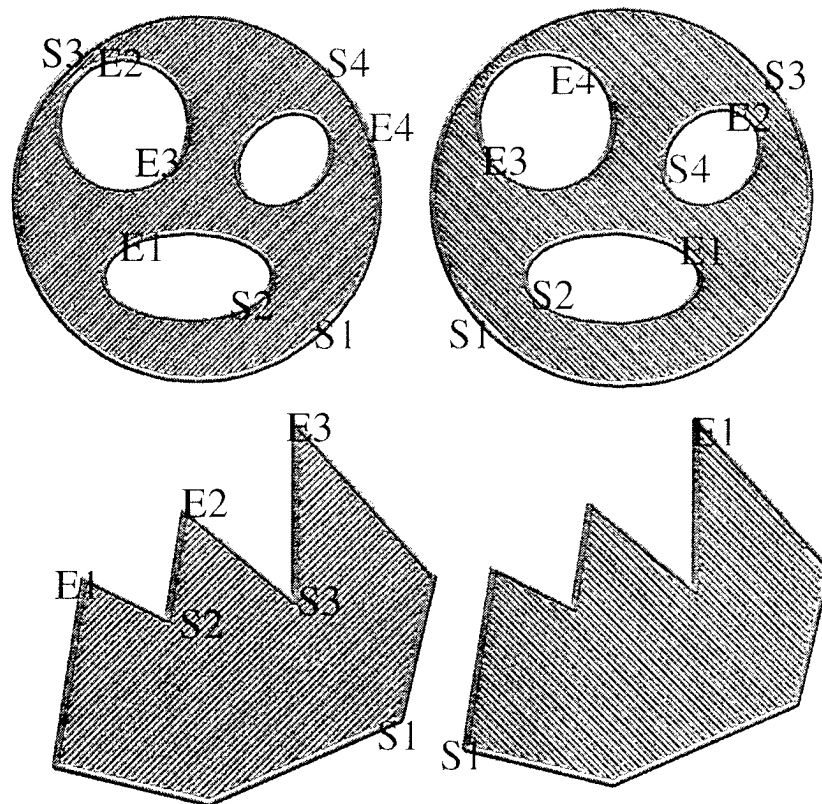


Figure 6: Simulated toolpaths of $\pm 45^\circ$ raster angles generated by 3rd version

A two material part

A two-material square-in-square part (Fig 7) was designed to investigate material boundary mismatch problems. The toolpath for this two-material part was generated by the in house toolpath generation software version 3. This part was simulated. The two materials touch at the inner square boundary. For the first set of toolpath parameters, there

are voids at this boundary (Fig 8). After changing the material offset and sub-perimeter offset, the voids were eliminated (Fig 9).

Specifications:

Nozzle: 15 mil
Roadwidth: 20 mil
Layer Thickness: 10 mil
Number of layers: 20
Red material: Wax
(0.5"X0.5")
Green material: PZT
(1"x1")
Blue material: support
(Can be any material)

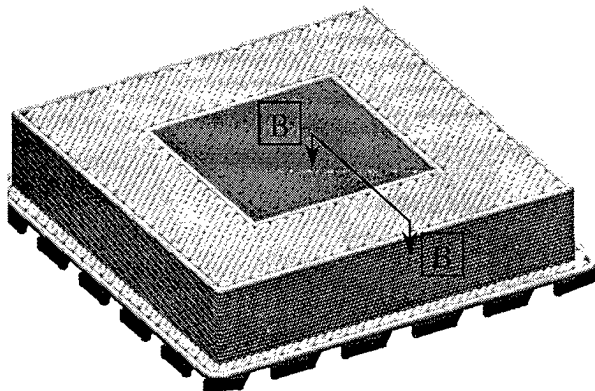


Figure 7: A two-material square-in-square part

Sub-perimeter offset for wax (red material): -2 mil
Offset between two materials: 0 mil

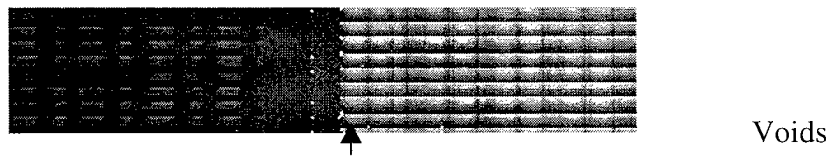


Figure 8: B-B cross section view of Figure 7 (the 1st set of parameters)

Sub-perimeter offset for wax (red material): -4 mil
Offset between two materials: -3 mil



Figure 9: B-B cross section view of Figure 7 (the 2nd set of parameters)

A two-material telescope part

To demonstrate the capability of the in house toolpath generation software, a more complicated two material telescope actuator part was designed. Toolpaths for both materials and the support layers were created and merged into one multi-material build file. The telescope part was visualized (Fig 10). This part has 59 layers high. The multi-material build file can also be created by manually editing the commercially available single material build files. But this takes approximately 2 hours for this part. Using our in house software, this multi-material build file was generated in seconds.

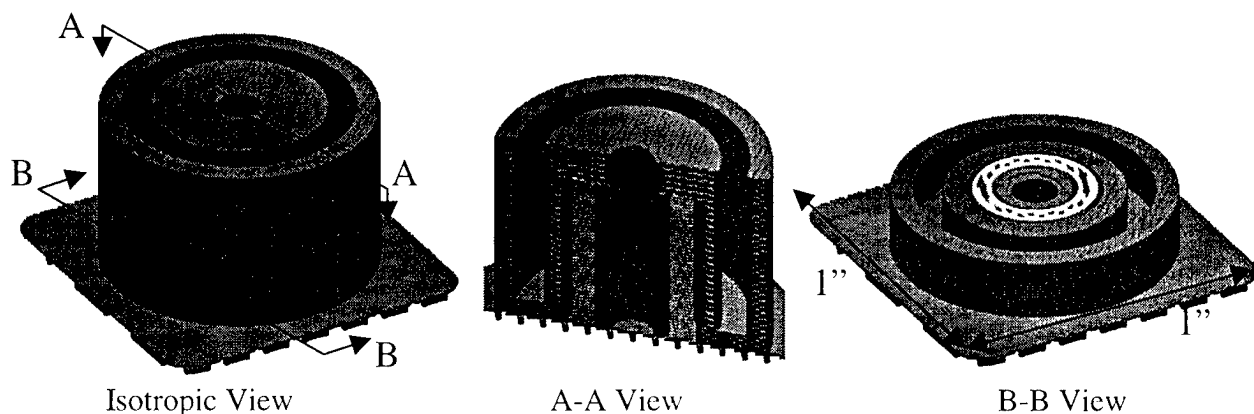


Figure 10 A telescope part

8. Conclusion

A multi-material toolpath generation system (Version 3) with new intelligent features has been developed. A variety of parts with complex boundary shapes and multi-material parts with interconnectivity have been visualized and quantified. The multi-material CAD system provides tools to investigate the multi-material toolpath parameters, alter the toolpaths to create defect free green parts. This software is flexible and general purpose and should be applicable to a number of SFF methods.

9. Acknowledgments

The research reported here has been performed towards the partial fulfillment of the requirements for a Ph.D. thesis of the first author.

The authors would like to thank the Office of Naval Research (ONR) Drs. R. Wachters, G. Spanos and K. Cooper for the financial support under #N00014-96-1-1175 Multidisciplinary Research Program of the Univ. Research Initiative (MURI).

10. References

1. M. Agarwala, A. Bandyopadhyay, R. van Weeren, V. Jamalabad, P. Whalen, N. A. Langrana, A. Safari, S. C. Danforth, "Fused Deposition of Ceramics", J. Rapid Prototyping, Vol. 2, 4, pp. 681-684-19, 1996.
2. P. F. Jacobs, "Stereolithography and other RP&M Technologies", Society of Manufacturing Engineers, pp.21-23, 1996.

3. R. F. Aubin, "A World Wide Assessment of Rapid Prototyping Technologies", January 1994.
4. C. C. Kai and L. K. Fai, "Rapid Prototyping: Principles and Applications in Manufacturing", John Wiley & Sons Inc, Singapore, 1997.
5. S. M. Morvan, G. M. Fadel, "Heterogeneous Solids Possible Representation Schemes", Proceedings of the Solid Freeform Fabrication Symposium, The University of Texas at Austin, TX, August 1999.
6. L. Jepson, "Multi-material Selective Laser Sintering (M²SLS): Hardware Development and Experimental Analysis", Proceedings of the Solid Freeform Fabrication Symposium, The University of Texas at Austin, TX, August 1999.
7. B. Jackson, "Discrete Multi-material Selective Laser Sintering (M²SLS): Development for an Application in Complex Sand Casting Core Arrays", Proceedings of the Solid Freeform Fabrication Symposium, The University of Texas at Austin, TX, August 1999.
8. J. Cesarano III, H. B. Denham, B. H. King, "Overview of Robocasting Technology: Current Capabilities and Future Directions", Proceedings of the Solid Freeform Fabrication Symposium, The University of Texas at Austin, TX, August 1999.
9. Office of Naval Research (ONR), # N00014-96-1-1175 Multidisciplinary Research Program of the Univ. Research Initiative (MURI): An Intelligent CAD Based System
10. D. Qiu, "Multi-material Layered Manufacturing Virtual Simulation", Graduate School - New Brunswick, Rutgers, The State University of New Jersey, May 1999.
11. D. Qiu, N. Langrana, S. Danforth, M. Jafari, A. Safari, "Virtual Simulation for Multi-material LM Process", Proceedings of the Solid Freeform Fabrication Symposium, pp. 681—688, August 1998.

Key words:

Layered Manufacturing, Multi-material, Toolpath Generation

SOLID FREEFORM FABRICATION USING THE WIREFEED PROCESS

M. L. Griffith, M. T. Ensz, D. L. Greene, D. E. Reckaway, J. A. Romero,
T. B. Crenshaw, L. D. Harwell, T. E. Buchheit, and V. Tikare

Sandia National Laboratories
Albuquerque, NM 87185

Abstract

Direct metal deposition technologies produce complex, near net shape components from CAD solid models. Most of these techniques fabricate a component by melting powder in a laser weld pool, rastering this weld bead to form a layer, and additively constructing subsequent layers. This talk will describe a new direct metal deposition process, known as WireFeed, whereby a small diameter wire is used instead of powder as the feed material to fabricate components. Currently, parts are being fabricated from stainless steel. Microscopy studies show the WireFeed parts to be fully dense with fine microstructural features. Initial mechanical tests show stainless steel parts to have good strength values with retained ductility.

Introduction

Laser processing has the potential for revolutionizing the rapid prototyping field to impact rapid manufacturing of metallic components. Various groups are coupling high power lasers with metal powders to fabricate metallic components, layer additively (1-4). Typically, a laser beam is focused onto a substrate to create a molten pool into which powder particles are injected to build up each layer. The substrate is moved beneath the laser beam to deposit a thin cross section of the desired geometry. Subsequent layers are additively fabricated, thereby building a three dimensional (3-D) component.

While metallic powders work well for the described direct metal deposition technologies, they do have drawbacks. A key aspect is material or powder utilization. Typical systems require a high velocity spray of powder to insure consistent material build up; however, only a small amount of the powder is actually retained in the molten pool, approximately 20%. In the WireFeed process, powder is replaced with wire feedstock to fabricate components. With wire feedstock, 100% utilization is achieved during fabrication, since all wire injected into the molten pool is used to fabricate the part. Therefore no recycling system is required and faster build times can be accommodated. Furthermore, even flow of the powder material is crucial to the success of fabrication in laser/powder technologies, where control can be difficult to maintain. It is relatively simple to maintain constant wire feed rates. Another consideration is availability of material; many materials are readily available in wire form. Direct metal deposition with powder feedstock requires a good powder source, where size distribution and composition must

be carefully controlled. This paper will describe the WireFeed process, the resultant material properties for as-processed 308L and 304L stainless steel, and modeling results of the microstructural evolution.

WireFeed Process

Figure 1 shows a schematic of the initial prototype WireFeed system. The system consists of a CW 600W Nd:YAG laser, a 4-axis computer controlled positioning system, and a wire feed unit (5). The positioning system and wire feed unit are mounted inside a box with localized gas purge capability. During fabrication, the workpiece and surrounding area are purged with argon to minimize oxidation of the workpiece. The laser beam is brought into the box through a window mounted on the top of the box and directed to the deposition region using a six inch focal length lens. The wire feed unit is designed to inject the wire into the molten pool from one side, and the lens and wire feed unit move as an integral subsystem.

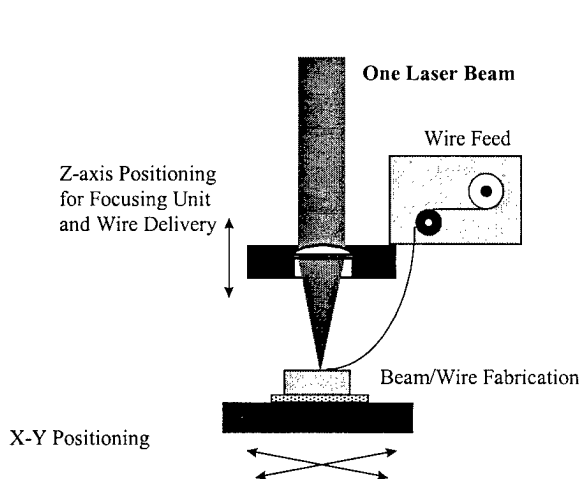


Figure 1: Schematic of the prototype WireFeed system showing laser perpendicular to substrate and wire feed from side.

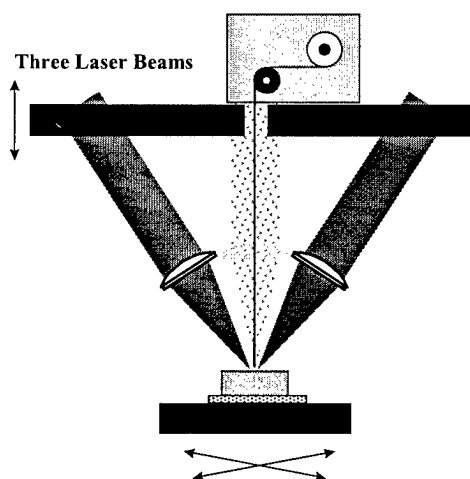


Figure 2: Schematic of improved system with three laser beams at 120° placement surrounding wire.

Geometries are written into a series of tool path patterns to build each layer. This file is combined with other commands to drive the laser, the positioning stages, and the wire feed unit to produce the desired component one layer at a time, starting from the bottom of the part. A solid substrate is used as a base for building the WireFeed object. The laser beam is focused onto the substrate to create a weld pool in which fine wire is injected, typically 250 micron diameter. The substrate is moved beneath the laser beam to deposit a thin cross section, thereby creating the desired geometry for each layer. After deposition of each layer, the wire feed mechanism and focusing assembly are incremented in the positive Z-direction, building a three dimensional component layer additively.

Shape Fabrication

Initially, test matrices were developed and implemented to identify the key factors controlling the WireFeed process. The key processing variables include: laser power, wire feed rate, wire feed direction and angle, and traverse velocity. From previous work with LENS (6), laser power, wire feed rate, and traverse velocity are the key factors to control deposition in direct metal fabrication. Along with those tests, extra experimental studies were required to understand the relationship between the wire and the weld pool for the system shown in Figure 1. This study included varying the wire feed direction, wire feed height (w.r.t. the substrate), and insertion angle. Diagnostic tools, such as high magnification video camera techniques, were used to monitor and understand the wire/molten pool interaction.

From these studies, it was determined that the wire must intersect the molten pool in such a manner to maintain stability along the solidification front. If the wire is inserted too high (w.r.t. the substrate or previous layer), it does not remain connected with the pool; if the wire is inserted too low, the wire either stubs on the substrate/layer or is pushed around by the force of the weld pool. After choosing the intersection point, the insertion angle and direction must be determined. An insertion angle of 45 degrees maintains the best stability, and uniform deposition is only maintained with wire insertion perpendicular to the deposition direction. The consistency of build is not maintained if the wire is inserted either from the trailing or leading edge of the weld pool, because the molten pool has difficulty forming and maintaining the bead as the source material or energy moves away.

Since the process was highly dependent on the position of the wire in relation to the deposition direction, a new system was configured to remove this geometric processing constraint. As shown in Figure 2, the wire is fed down the center and the laser beam is split into three beams (by use of fiber optics) to surround the wire. The laser heads are stationed 120 degrees apart from each other. Now, the wire always enters the pool at the 'hot spot' and there are no constraints on direction of travel. This new design was imperative for complex part fabrication.

From the process variable experiments, the laser wire deposition parameters were optimized to demonstrate feasibility of part fabrication. Test matrices were added to understand how layer thickness and hatch (fill) spacing affected part fabrication. Process studies to control the wire feed during layer increments for simple block shapes were a major activity. After a layer is fabricated in a serpentine draw pattern, the laser shutter closes, and the focusing and wire feed subsystems must increment in the positive Z direction to fabricate the next layer. Before the Z increment, the wire must reliably detach from the part. This knowledge is required for complex part fabrication with increasing area complexity.

Various shapes with increasing complexity are shown in Figure 3. We have fabricated four types of geometries: 1) uni-directional fabrication using a rotary stage to build hollow cylinders (Figure 3a), 2) bi-directional patterns to fabricate walls, and 3) with an understanding of wire detachment, hatch spacing and layer thickness, it was possible to fabricate dense, rectangular shapes from 308L stainless steel (Figure 3b). Finally, we have initiated complex part

fabrication with the challenge of building two cubes, where each layer is deposited side by side (Figure 3c). This was only possible with the new WireFeed system design shown in Figure 2. All shapes possess 100% utilization of the wire, where the material inserted into the molten pool is directly used to produce a part. WireFeed parts are quickly fabricated, between 0.5 to 1 hour per cubic inch.

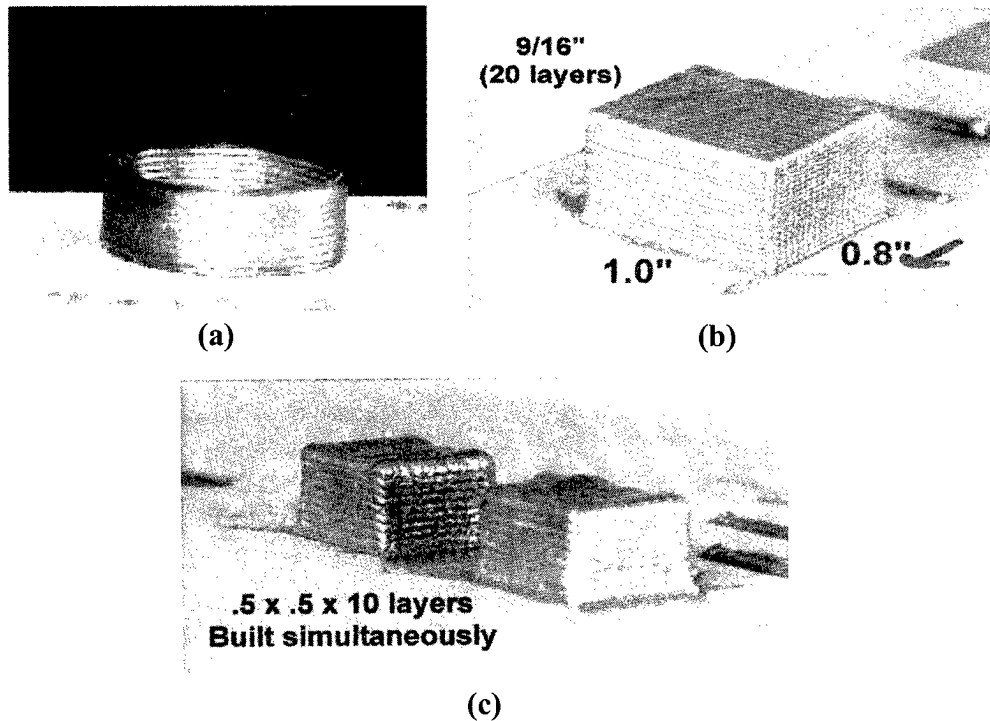


Figure 3: (a) cross-sectional micrograph of uni-directional fabrication, (b) block fabrication with wire detachment between layers, and (c) complex part fabrication with start and stop capability in each layer.

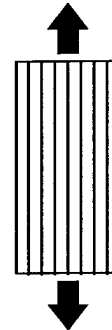
Materials Characterization

Mechanical Behavior

Coupons were machined from the as-processed 308L stainless steel for room temperature tensile testing, where the pull direction is parallel to the build plane in the WireFeed system (longitudinal). All samples had densities greater than 98%. The results for WireFeed-processed material is compared to typical annealed material in Table I. With grain size refinement, the WireFeed material possesses strengths greater than annealed, where the yield strength is 58 ksi as compared to 35 ksi for the annealed material. However, the ductility remains consistent with elongation values of 65-75%, which are slightly higher than the annealed values (55-65%). High strengths and hardness with retained ductility is a good combination for WireFeed-processed material.

Table I. Room temperature mechanical properties for as-processed 308L stainless steel compared to typical annealed material.

Property	WireFeed	Annealed material
Hardness	87 HRB	80 HRB
Microstructure feature size	4 Micron	40 Micron
Tensile strength (Yield)	58.2 ksi	35 ksi
Tensile strength (Ultimate)	94.2 ksi	85 ksi
Ductility (Elongation)	64.9%	55%
Ductility (Reduction in area)	74.6%	65%



The effect of deposition style was studied for 304L stainless steel material. Two types of patterns were fabricated: 1) longitudinal and 2) cross hatch where every other layer is deposited 90 degrees to the previous layer. The results are shown in Table II. Both deposition patterns show similar strength properties, with yield values much greater in comparison to annealed material. However, there is a trade-off with a decrease in ductility, especially for the cross hatch pattern style. Any flaws in adhesion between layers would be more evident in the cross hatch deposition material because the weak layers are perpendicular to the tensile pull direction. Overall, the material properties for these stainless steel alloys show benefit in strength values compared to traditional annealed material and in some cases the ductility is maintained.

Table II. The effect of deposition pattern on room temperature mechanical properties for as-processed 304L stainless steel.

Property	Longitudinal Pattern	Cross Hatch Pattern	Annealed 304L
Tensile strength (Yield)	75.9 ksi	76.1 ksi	42.8
Tensile strength (Ultimate)	104.2 ksi	102.0 ksi	95.9
Ductility (Elongation)	48.3%	34.6%	56.0
Ductility (Reduction in area)	40.0%	32.8%	---

Microstructures

Metallographic analysis reveals dense, fine grain microstructures for 308L stainless steel produced by the WireFeed process as shown in Figure 4. Figure 4(a) is a cross-sectional view of a line drawn by the WireFeed process. Typical microstructural features are on the order of 4 microns, due to the high solidification rate in the WireFeed process. Figure 4(b) is a top view showing one full line and two partial lines (interfaces between lines marked at A). The fine microstructural features show directional solidification behavior resulting in textured features.

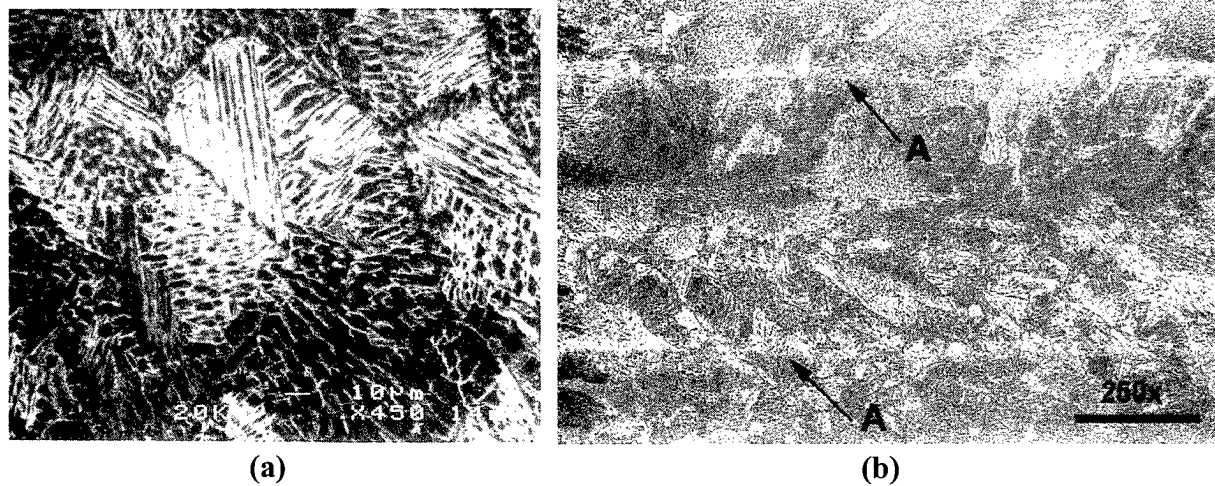


Figure 4: Typical microstructures for 308L stainless steel, where (a) is a view inside a fabrication line (450x) and (b) is a view of three lines fabricated in a layer.

Simulation of Coarsening in WireFeed Microstructures

Components manufactured by the WireFeed process have unique microstructures. The prediction and control of these microstructures is important to tailoring the components to their respective application. We have extended the previously developed 2-D simulation (7) of coarsening during WireFeed to 3-D. A kinetic, Monte Carlo model was used to simulate coarsening in the presence of a non-linear, dynamic temperature profile. This model utilizes a cubic lattice populated by a canonical ensemble of domains. The equation of state is the sum of bond energies between unlike neighboring domains and simulates grain growth in response to capillary forces of the grain boundaries. The simulation was adapted to 3-D by extending the neighbor interaction energies from X- and Y-directions to X-, Y- and Z-directions. The mobility of the grain boundaries scales with temperature in the simulations. The temperature profile used in the simulations is the Rosenthal solution to a moving point source of heat given by:

$$T_m - T = \left(\frac{\alpha Q}{2\pi k r_p} \right) \exp \left(\frac{-C}{2k} (x_p + r_p) \right)$$

where T_m = melting temperature, T is temperature at r_p , the distance from the center of the laser spot and x_p , the distance from the laser spot along the direction of travel and are:

$$r_p = \sqrt{(x_p - vt)^2 + y^2 + z^2} \quad \text{and} \quad x_p = x - vt$$

and x is the laser travel direction, z is depth, vt is the current laser position along the x -direction, α is the heat transfer efficiency, Q is heat input, k is conductivity and C is heat capacity. The temperature profile at the surface is shown in Figure 5.

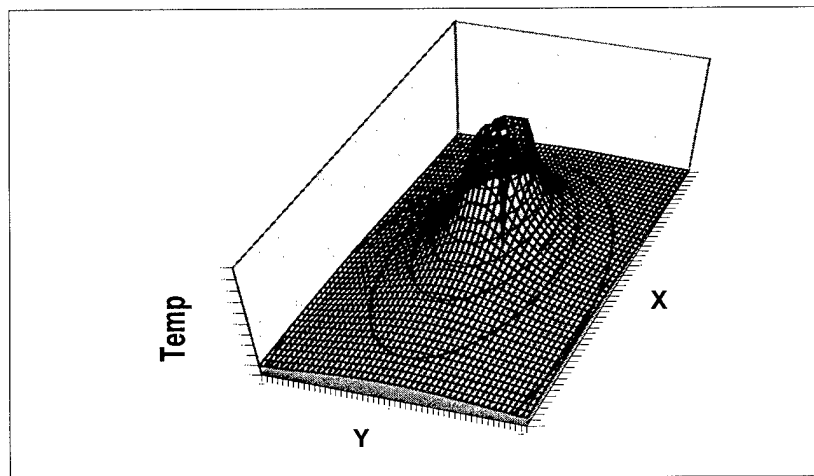


Figure 5. Rosenthal temperature profile at the surface, with heat source moving along the X-direction.

The results of the 3-D simulations are shown in Figures 6a and 6b, with simulated microstructures of grains after a laser has passed across at velocity $v = .01$ and $v = .02$ sites/MCS, respectively. The laser travel direction is from right to left, and features of the same shades are grains. The microstructures show that the grains grew faster in the center region, which is the hottest area and much slower at the outside cooler region as was expected since grain boundaries have higher mobility at higher temperatures. The elongation of the grains was dependent on the velocity of the laser. At slower laser velocity, grains are highly elongated as the grain boundary mobility is able to keep pace with the laser. At high laser velocity, the grains were smaller and less elongated because the laser velocity was faster than the grain boundary mobility. Furthermore, the direction of grain elongation was perpendicular to the Rosenthal isotherm as seen in Figure 6b. The microstructures in Figure 6b are similar to those of actual WireFeed microstructures as seen in Figure 4b.

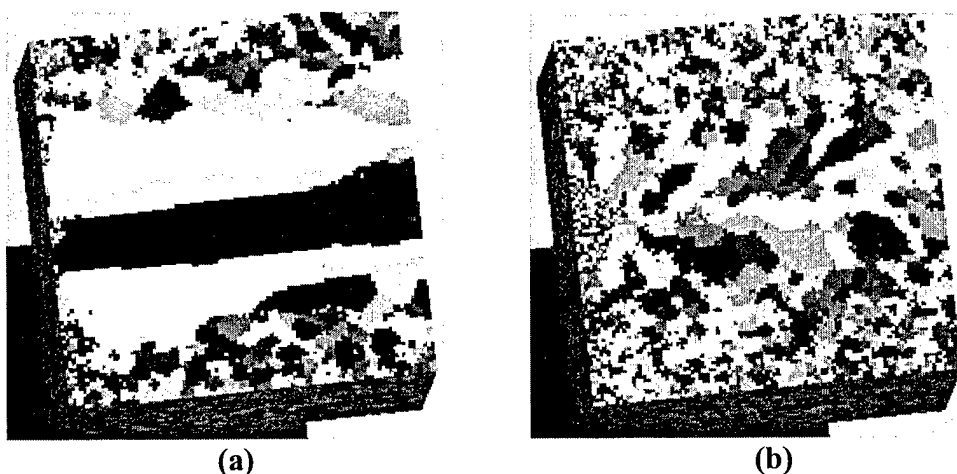


Figure 6: Simulated microstructures of grains at two laser velocities: (a) 0.01 sites/MCS and (b) 0.02 sites/MCS (where MCS = Monte Carlo Step). Laser travel direction is from right to left.

Conclusions

With the WireFeed process, high fabrication rates (one hour per cubic inch) can be achieved with 100% utilization of feed material. As-processed stainless steel parts have strengths greater than traditional annealed material, but with retained ductility if there are no flaws (porosity) during fabrication. Preliminary modeling of the WireFeed process shows the correlation between the laser beam profile and raster speed with the resulting microstructure. The WireFeed system is simple in design, requiring only a localized gas purge to removed unwanted oxidation during fabrication. This allows for easy part removal and change of wire material. Future work will develop complex geometry fabrication, where the theoretical model will be able to predict the resulting microstructure for a given material and process conditions.

References

1. M. L. Griffith et al., "Free Form Fabrication of Metallic Components using Laser Engineered Net Shaping (LENS)", Solid Freeform Fabrication Symposium Proceedings, August 12-14, 1996, Austin, TX, p.125.
2. J. R. Fessler et al., "Laser Deposition of Metals for Shape Deposition Manufacturing", Solid Freeform Fabrication Symposium Proceedings, August 12-14, 1996, Austin, TX, p. 117.
3. F. Klocke, H. Wirtz, and W. Meiners, "Direct Manufacturing of Metal Prototypes and Prototype Tools", Solid Freeform Fabrication Symposium Proceedings, August 12-14, 1996, Austin, TX, p.141.
4. J. Mazumder et al., "The Direct Metal Deposition of H13 Tool Steel for 3-D Components", Journal of Materials, Vol 49, Number 5 (1997), p. 55.
5. E. Brandon, F. Hooper, and M. Reichenbach, "Precision Wire Feeder for Small Diameter Wire" (U. S. Patent #5137223, August 11, 1992).
6. D. M Keicher et al. , "Towards a Reliable Laser Powder Deposition System through Process Characterization", Proceedings of SAMPE '95, Albuquerque, NM, October 12-14, 1995, p. 1029.
7. V. Tikare et al., "Simulation of Coarsening during Laser Engineered Net Shaping", Solid Freeform Fabrication Symposium Proceedings, August 11-13, 1997, Austin, TX, p.699.

A SFF Approach Utilizing Condensed Gas Precursors and Pulsed Laser Deposition

Erik Geiss, and Harris L. Marcus
Institute of Material Science
University of Connecticut
Storrs, CT

Abstract

Two techniques were studied in an effort to direct write diamond-like carbon (DLC) films. The first process employed a pulsed YAG laser to decompose a frozen precursor and deposit thin films directly on SiC and 304 stainless steel. After the initial film is deposited, additional layers may be subsequently condensed and deposited onto the substrate. A second approach is considered, whereby, the pulsed YAG is used to ablate the frozen precursor target and deposit a film on a nearby SiO₂ substrate that was locally heated by a CO₂ laser in an effort to augment the surface reaction rates.

Introduction

Diamond-like carbon (DLC) films synthesized by the decomposition of hydrocarbons by an energy source (electrical, thermal, or electromagnetic) have generated a lot of interest due to their wear resistance, hardness and chemical inertness. The diamond-like character of the film is controlled by the proportion of the sp₃ bonds relative to the sp₂ bonds. The Gibbs free energy difference between these two forms of carbon bonding is very small, on the order of 0.5 Kca/g-atom, so under most deposition conditions there is probability that some carbon atoms will bond in the sp₂ configuration and some in the sp₃ configuration. The role of atomic hydrogen can be critical in maximizing the sp₃/sp₂ ratio. Atomic hydrogen is considered to play an important role in diamond nucleation and growth through differential etching of sp₂ and sp₃ bond stabilization. [1] Although there has been a great deal of progress in the technological aspects of diamond CVD, the underlying gas/diamond interface chemistry is still not completely understood. The focus of this paper is to explore two methods of depositing DLC via variations of Selective Area Laser Deposition (SALD), which is a Solid Free Form Fabrication (SFF) technique.

SALD is a deposition process that uses localized chemical vapor deposition to deposit solid materials from precursor gases to create shapes in an additive manner. [2] The chemistry of the deposited material can be controlled through various process parameters like temperature, laser wavelength, and precursor pressure and composition. [3] The first approach used in this study involves condensing and solidifying the gaseous precursor onto the substrate and decomposing the precursor and directly depositing on the substrate. The solidification of the precursor allows for a high concentration of the precursor molecule in the SALD process zone, which can lead to increased deposition rates, and creates a highly uniform initial film. Acetylene is the precursor used for carbon deposition, owing to its relatively low melting and sublimation points (MP 191k SubT 193K) and the relatively weak C-H bond [0.36 eV]. [4] After the initial deposition, additional layers of the precursor may be subsequently condensed and decomposed. This technique is obviously suited for pulsed lasers, which don't require pyrolytic decomposition of the precursor and hence is ideal for low temperature processing. This methodology also allows for depositing on substrates that do not absorb the laser's

wavelength, however the problem of ablation of the substrates does arise. The second technique, pulsed laser deposition (PLD), relies on an increased laser energy density to ablate the condensed target precursor and essentially sputter the energetic dissociated precursor onto a locally heated substrate. PLD is widely used to produce DLC films by sputtering graphite. [5,6,7] The substrate is locally heated to augment the surface reaction rates and provide a method of controlling the deposition area. [8] Both 1064 and 266 nm wavelengths were used to sputter the acetylene, as it has been suggested that photon energy plays a role in the diamond-like properties of the film. [6,9]

Experiment

Film depositions were conducted in a stainless steel vacuum chamber evacuated by a rotary vane pump to a base pressure of 100 mTorr. Acetylene gas was then introduced into the reaction chamber, where it was condensed and solidified on a liquid nitrogen chilled substrate. A pulsed YAG laser ($\lambda=1064$ nm, 5-7ns pulse width) was operated at 10 Hz at approximately 45 degrees to normal at an energy density of 15 to 20 J/cm². This laser was equipped with several harmonic generators capable of producing wavelengths at 266, 355, and 532 nm at decreased energy densities. For PLD, a secondary 25 W CO₂ laser was directed through a ZnSe window to heat a SiO₂ substrate to 300 C as measured by an infrared pyrometer. To increase the ratio of sp₃ sites in the deposited material H₂ gas was added into the system and thermally cracked by a heated Tungsten filament to produce atomic hydrogen. The Raman measurements were collected by micro-Raman device utilizing a $\lambda=514$ nm green laser as an excitation source.

Results and Discussion

Several films were deposited under various conditions of substrate type, partial hydrogen pressure, laser wavelength, and laser energy density. The deposited films were characterized by Raman spectroscopy and determined to be either microcrystalline graphite or DLC depending upon the deposition conditions and technique. The films that could be deposited by PLD were observed to be very smooth except for an area of irregular crystal growth. Both the regular film surface and the larger crystallites displayed Raman spectra generally attributed to DLC. The direct deposition technique, by comparison, created depositions whose film density was highly irregular, due to ablation, and whose Raman spectra could be generally characterized as microcrystalline graphite.

Raman spectra is ideally suited for examining DLC deposits, as both crystalline diamond and to a greater extent graphitic carbon are strong Raman scatters. Raman spectra of amorphous carbon films are generally composed of 2 peaks: the G line centered at 1550 cm⁻¹; and the D line which is centered around 1350 cm⁻¹. The D peak becomes active in the presence of small graphite crystallites. Normally a sharp peak at 1332cm⁻¹ is to be expected for diamond, but the sensitivity of the Raman line is approximately 50 times lower than graphite. The G peak is due to C=C stretching vibrations of graphite. The positions, widths and relative intensities of these G and D peaks have been found to vary systematically with film properties. [10, 11] It was observed by Tamer *et al* [11 that an increase in G line width corresponds with increased density and hardness. The ratio of the intensities of the D to G peaks is also used as an indicator of the nature of the films, as a high I_D/I_G ratio indicates very small graphite crystals which may be indicative of DLC films. [10] DLC Raman spectra generally consists of a broadband from 1540 to 1600 overlapped by a component lying between the two graphite bands. [10, 12]

The direct deposition method utilized 304 stainless steel, SiC and amorphous SiO₂ as substrates. The majority of deposits on stainless steel displayed Raman spectra with relatively narrow G and D lines of roughly the same intensities as seen in fig 1. In particular, for steel lower energy densities (15 J/cm²) were conducive to greater film densities as ablation of films was often a problem. A combination of the 1st, 2nd and 4th harmonics of the YAG did yield a DLC Raman spectra for distinct parts of the deposit as shown in figure 2. Figure 3 depicts the silicon carbide substrate which was coated with a thin deposit of polycrystalline graphite. We have been unable to deposit on the SiO₂, which is transparent to the YAG wavelength, thus far. It was noted that a very low concentration of hydrogen, less than 10 torr, often leads to a slight decrease in the intensity of the D peak, but for higher hydrogen partial pressures no noticeable difference was detected.

The PLD technique was able to consistently deposit DLC on a quartz substrate. Raman characterization yielded a distinct DLC spectra as shown in figure 4. The ability to direct write with PLD by attempting to control the process zone via localized heating of the quartz, however, is admittedly more technically difficult than the direct deposit method. The partial pressure of hydrogen was varied but it was determined that any benefit a higher density of atomic hydrogen might produce was negated by the decrease in the mean free path of the sputtered hydrocarbons. Various combinations of wavelengths were also explored, but only the primary beam had a sufficient energy density to ablate the target.

Conclusion

While much still remains to be optimized in the process both methods have been shown to be able to deposit DLC. Future work will focus on attempting to create rudimentary DLC structures and more extensive characterization of the films.

Acknowledgements

The authors gratefully acknowledge the generous support of the Office of Naval Research (grant #N00014-95-1-0978)

References

1. J. Angus, C. Hayman, Science 241, 913 (1988)
2. G.S. Zong, R. Carnes, H.G. Wheat, H.L. Marcus, SFF Symposium, 83 (1990)
3. J.E. Crocker, K.J. Jakubenas, S. Harrison, L. Shaw, H.L. Marcus, SFF Symposium, 489 (1997)
4. D. Haninollahzadeh, J. Murray, M. Grodzichi, J. Seminario, P. Politzer, Inter. J. Quant. Chem 42, 276 (1992)
5. A.P. Malshe, S.M. Kanethar, S.B. Ogale, S.T. Kshirgagar, J. Appl. Phys 68, 5648 (1990)
6. P.T. Murray, D.T. Peeler, J. Elec. Mater. 23, 855 (1994)
7. M.C. Polo, J. Cifre, G. Sanchez, R. Aguiar, M. Varela, J. Esteve, Appl Phys Lett. 67, 485 (1995)
8. H. Chen, N. Maffei, R.H. Prince, J. Appl. Phys. 76, 8113 (1994)
9. F. Xiong, Y.Y. Wang, V. Leppert, R.P. Chang, J. Mater. Res 8, 2265 (1993)
10. D.S. Knight, W.B. White, J. Mater. Res 4, 385 (1989)
11. M.A. Tamer, W.C. Vassell, J. Appl. Phys. 76, 3823 (1994)
12. M. Yoshikawa, G. Katagiri, H. Ishida, A. Ishitani, T. Akamatsu, J. Appl. Phys 64, 6464 (1988)

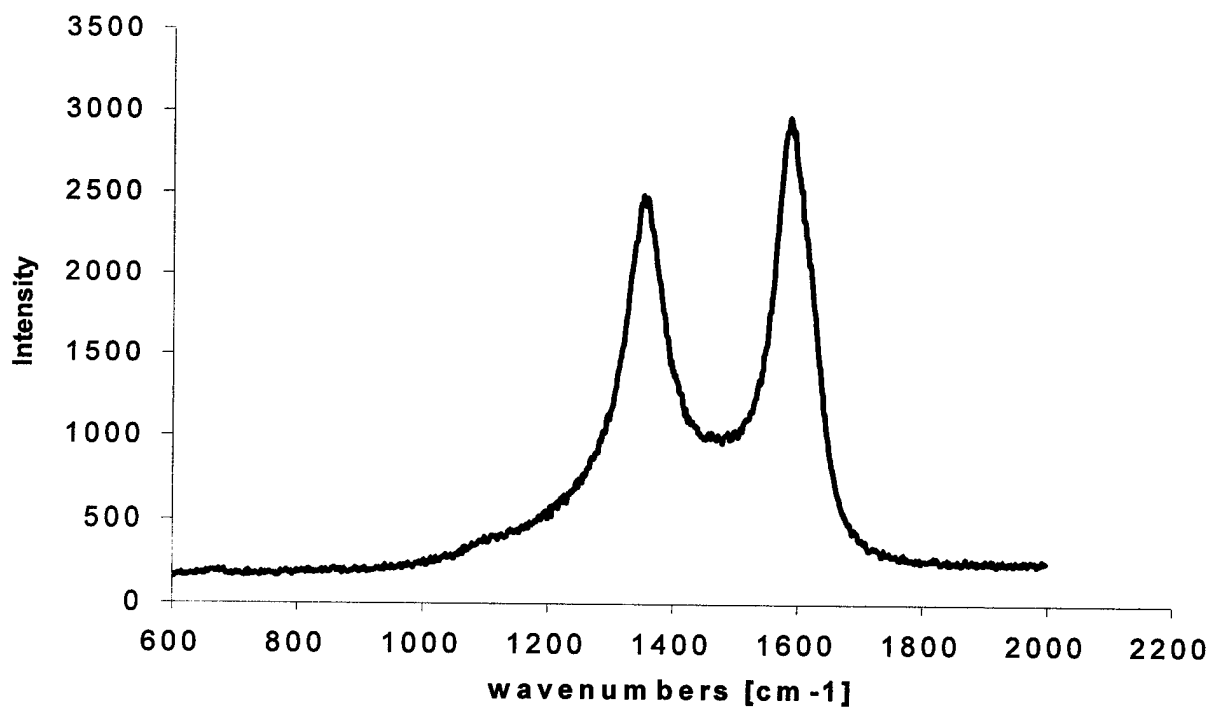


FIG 1 Raman spectra of microcrystalline graphite on 304 stainless steel by direct deposition

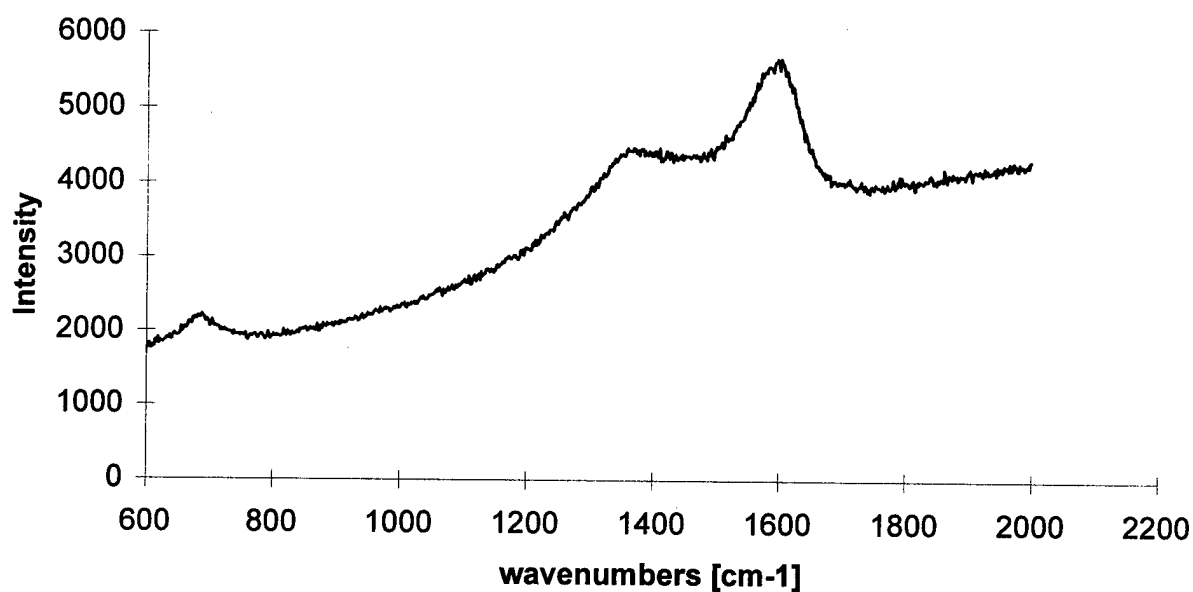


FIG 2 Raman spectra of DLC on 304 stainless steel by direct deposition

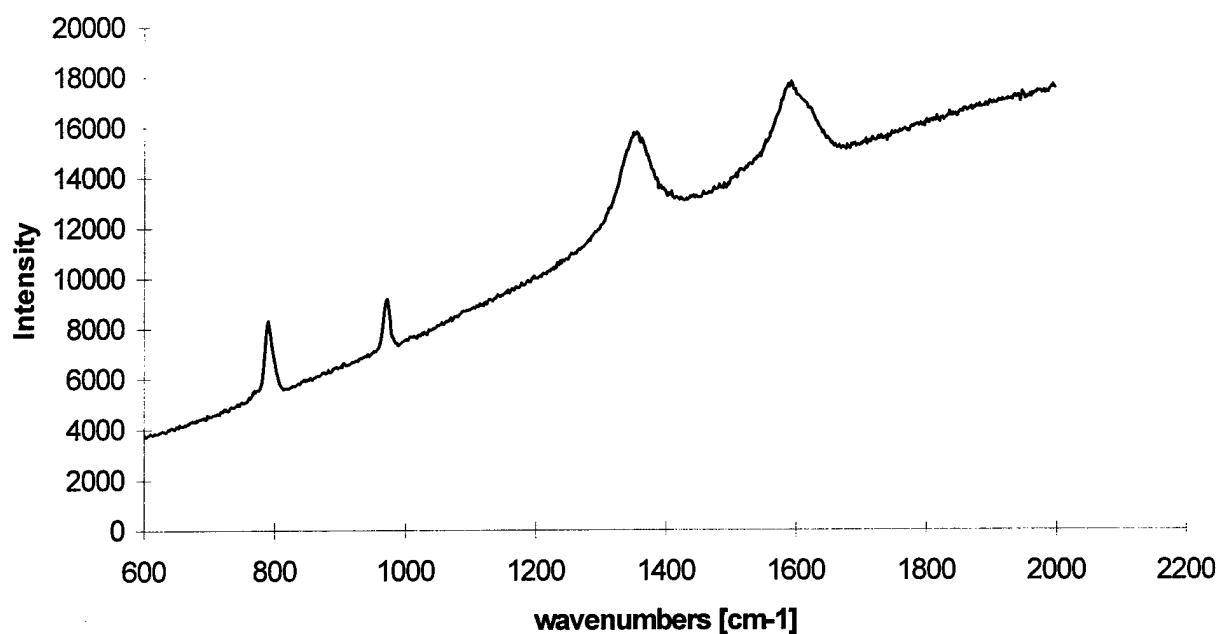


FIG 3 Raman spectra of microcrystalline graphite on SiC by direct deposition

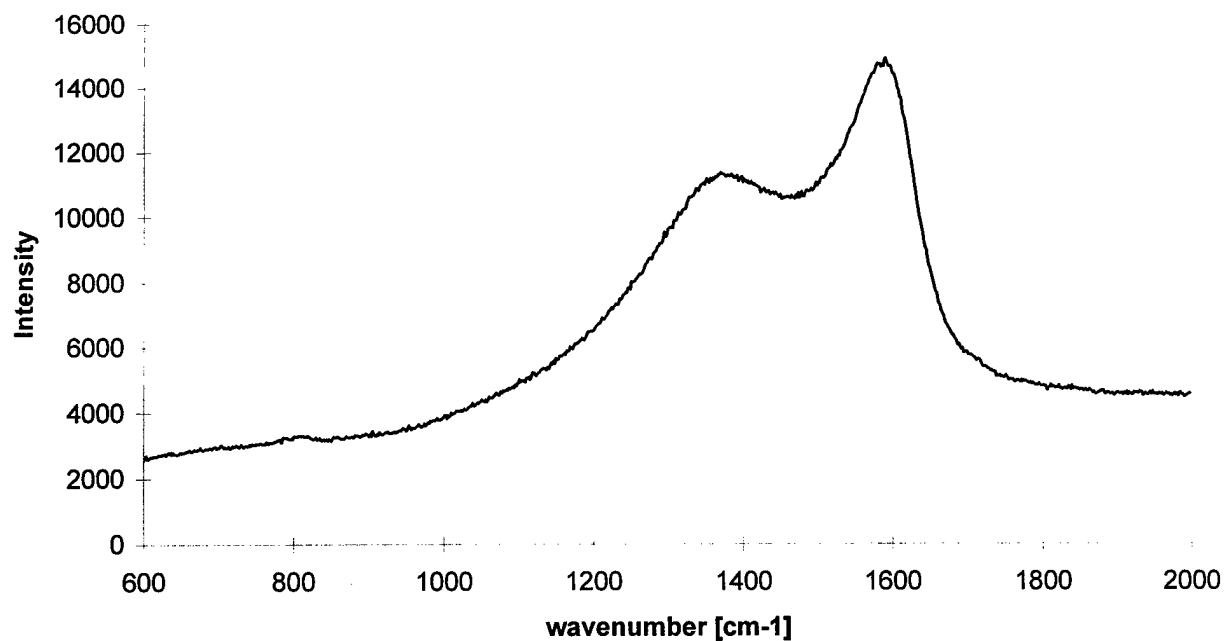


FIG 4 Raman spectra of DLC on SiO₂ by PLD technique

The Laser Microchemical Lathe: Rapid Freeform Part Fabrication from the Vapor Phase

K. Williams, N. Jaikumar, G. Saiprasanna, M. Hegler, J. Maxwell*

Institute for Micromanufacturing, Louisiana Tech Univ., 911 Hergot Ave., Ruston, LA, USA

This paper reports the development of a two-beam Laser Microchemical Lathe (LML) used for prototyping freeform axi-symmetric parts from the vapor phase. In the LML, one beam is focused along the rotational axis of the lathe, while another is scanned at right angles to the first. The first beam is used for alignment and to deposit a fiber-like mandrel from a vapor-phase precursor. The second beam is then applied to add or remove material on this rotating mandrel, either through high pressure laser chemical vapor deposition (LCVD) or laser chemical vapor etching (LCVE). Material is added when an appropriate precursor is present, or removed when a reducing atmosphere such as chlorine, iodine, or hydrogen is employed. In LCVE mode, the second beam may be scanned in profile along the length of a rotating part—thereby profiling the part by laser etching. The ability to correct for errors in the deposition process through such laser profiling allows accurate prototyping of milli-scale axi-symmetric parts, such as lead screws, cams, and sharp needles. Very rapid deposition and etching rates were achieved; at ethylene pressures above 10 atmospheres, diamond-like carbon was grown at linear rates exceeding 120,000 microns per second (12 cm/s). This record-setting growth rate allows the computer-controlled prototyping of carbon-fiber reinforced structures with volumes surpassing 1 cubic centimeter in only 10-20 minutes.

Keywords: High Pressure Laser Chemical Vapor Deposition, Carbon, Alkenes, Direct-writing, Freeform Growth.

I. Introduction

Previous efforts in vapor-phase solid freeform fabrication have concentrated on the growth of transition and refractory metals,¹ implementation of emissions and temperature feedback control methods,^{2,3} exploring self-limiting effects,⁴ and prototyping functional devices such as springs, microsolenoids, and waveguides.^{5,6} The rapid growth of fibers at axial rates approaching 1 mm/s has also been demonstrated at elevated pressures.⁷

While it has been shown that three-dimensional laser chemical vapor deposition (LCVD) may be employed to grow simple freeform parts, the process is inherently unstable when operating in the kinetically-limited regime; this is especially apparent during repetitive laser scanning, where irregularities in one layer are amplified in the next, resulting in very irregular deposits.⁸ It is for this reason that the emissions and temperature feedback control methods mentioned above are being investigated, as well as the use of elevated pressures which facilitate mass-transport limited growth.

An alternate feedback approach also holds promise, where imperfections in the laser deposited surface are corrected through laser ablation or three-dimensional laser chemical vapor etching (3D-LCVE). In this case, a reducing atmosphere is employed, rather than a CVD precursor, and the by-products are volatile. Rapid chlorine etching of silicon and other materials via 3D-LCVE has been demonstrated by various investigators.⁹ Note that it is possible to switch between 3D-LCVD and 3D-LCVE on-the-fly by merely changing chamber gases; this allows material to be added to (or deleted from) any portion of an object, either to correct for machining errors produced during laser deposition or to generate three-dimensional shapes

* Corresponding Author: maxwell@coes.latech.edu

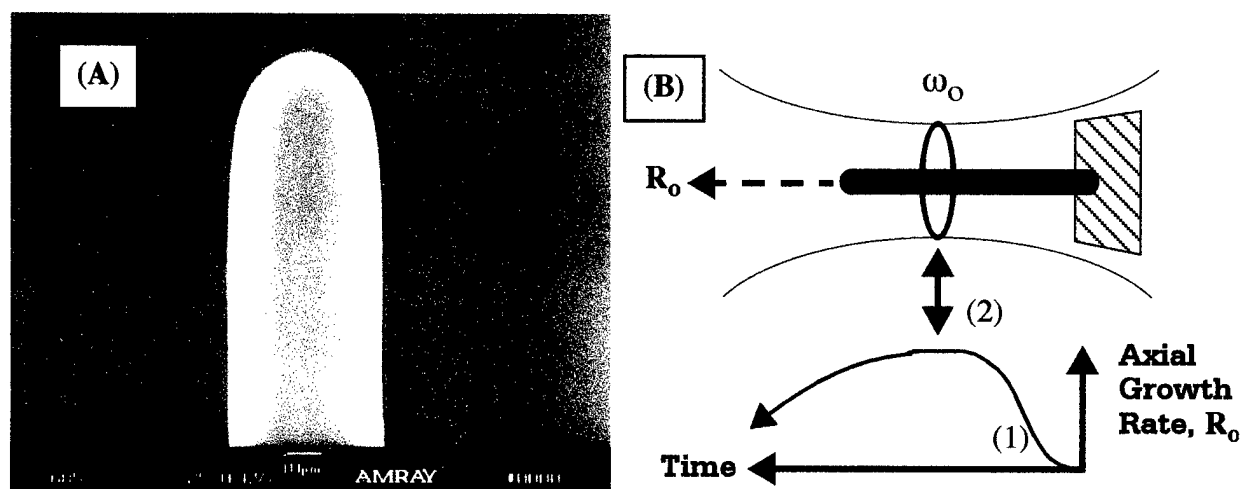


Fig. 1: (A) Carbon Fiber, (B) Rod Growth Rate Measurements

which cannot be fabricated by usual means. The emissions and temperature feedback techniques currently under development will also be essential for this task, allowing precise volumes of material to be deposited or removed in a selected area. The combined 3D-LCVD/E processes may also be used to build up or etch the surfaces of existing objects, creating periodic or arbitrary perturbations over surfaces in a controlled manner.

The objective of this paper is two-fold: first to demonstrate the potential of high pressure, convectively-enhanced, laser chemical vapor deposition (HPCE-LCVD) for high-speed prototyping through fiber growth in excess of 1 mm/s; and second, to implement a new laser prototyping tool, termed the Laser Microchemical Lathe (LML), which may be harnessed to accurately machine small axi-symmetric parts with the combined 3D-LCVD/E processes. To this end, growth rate data for carbon fibers grown from the alkenes, including ethylene, butene, pentene, hexene, and heptene will be presented, as well as preliminary results in part fabrication with the LML.

II. Experimental Method

A) Fiber Growth

For the carbon growth experiments, several hundred fibers were grown from the alkenes. To accurately measure the steady-state axial fiber growth rate, the prime focus of the laser beam was fixed 250-300 microns in front of the substrate, as shown in Fig. 1B. In this way, it was possible to eliminate focal offset errors which may occur during laser tracking, and ensure that the fibers had passed out of the transient growth regime (1), where conduction to the substrate influences the growth rate. A minimum of 12 axial rate measurements were then performed along the length of each rod, to decouple the effects of varying beam waist on the axial rate. The maximum measured rate corresponded to the position of the optimal focus—point (2) in Fig. 1B. A full description of rod growth throughout the transient, steady-state, and tail regimes has been previously provided.¹⁰

For the fiber growth experiments, a small chamber was employed with double windows at each port. The space between each window-assembly was heated continuously with a flow of hot air to eliminate precursor condensation on the inside window. The entire chamber and gas delivery system were also heated to a temperature greater than that of the precursor source cyl-

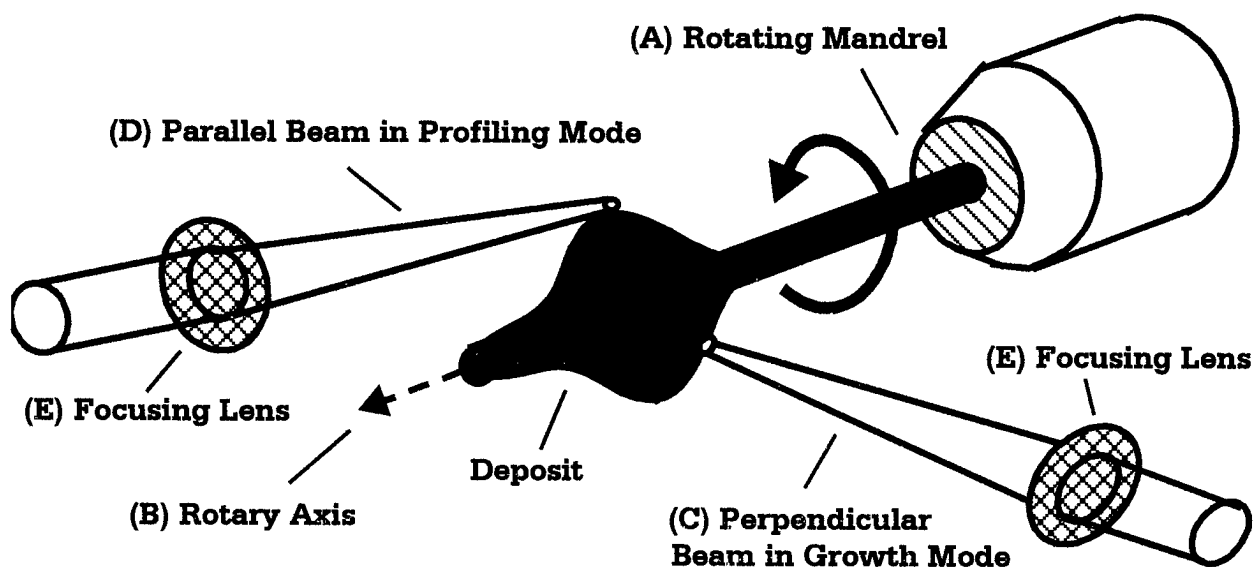


Fig. 2: Principle of the Laser Microchemical Lathe

inder. Two gas regulators were attached at the inlet and outlet of the chamber, so that a high pressure flow of gas could be maintained through the chamber, while the chamber pressure remained constant. At the inlet, this precursor gas stream was directed toward the substrate through a 2 mm ID nozzle, allowing forced convection over the reaction zone. This nozzle could be oriented in a variety of configurations (parallel, perpendicular, or behind the substrate). In this case, a 40 W Nd:YAG laser beam was focused to a 20-25 μm spot using a laser best-form lens. Tungsten light bulb filaments 40 μm in diameter were used as substrates.

B) The LML: Principle and Design

To implement the Laser Microchemical Lathe (LML), an initial fiber (the substrate) was grown on a rotating mandrel—as shown in Fig. 2 (A), so that the substrate was auto-aligned to the rotary axis (B). Two beams were then focused at right angles onto this substrate, one perpendicular to the rotary axis (C), and the other parallel to the axis (D). Depending on the ambient gas present, either beam could be used for 3D-LCVD or 3D-LCVE. In the first case, the beam was focused normal to the deposit surface as in (C)—so that material could be added to the cross section of the part. In the latter case (LCVE), the beam was passed at grazing incidence to the deposit surface, removing excess material which protruded beyond the desired contour—as in Fig. 2 (D). Either beam could be used for profiling or deposition, and the beams could be focused to a common point, or used independently as desired.

A schematic of the entire LML system is shown in Fig. 3. As before, a small chamber with heated windows (a) was employed with a heated gas delivery system and a nozzle (b) directed at the substrate. In this case, however, a mandrel (such as that in Fig. 2) was supported by two precision bearings inside the chamber and driven by a rotary feedthrough (c) with stepper-motor actuation. The parallel and perpendicular beams were delivered to the LML through fiber optics (d), plate beamsplitters (e), and objective lenses (f). In both cases, the beamsplitters and lenses rode on 6-axis piezoelectric stages (g), so that each beam could be independently aligned to the deposit. The piezoelectric stages and rotary axis stepper motor were positioned with a high-speed data acquisition system and motion controller. The beamsplitters were designed to reflect the beam efficiently at 1064 nm, while passing higher wavelengths

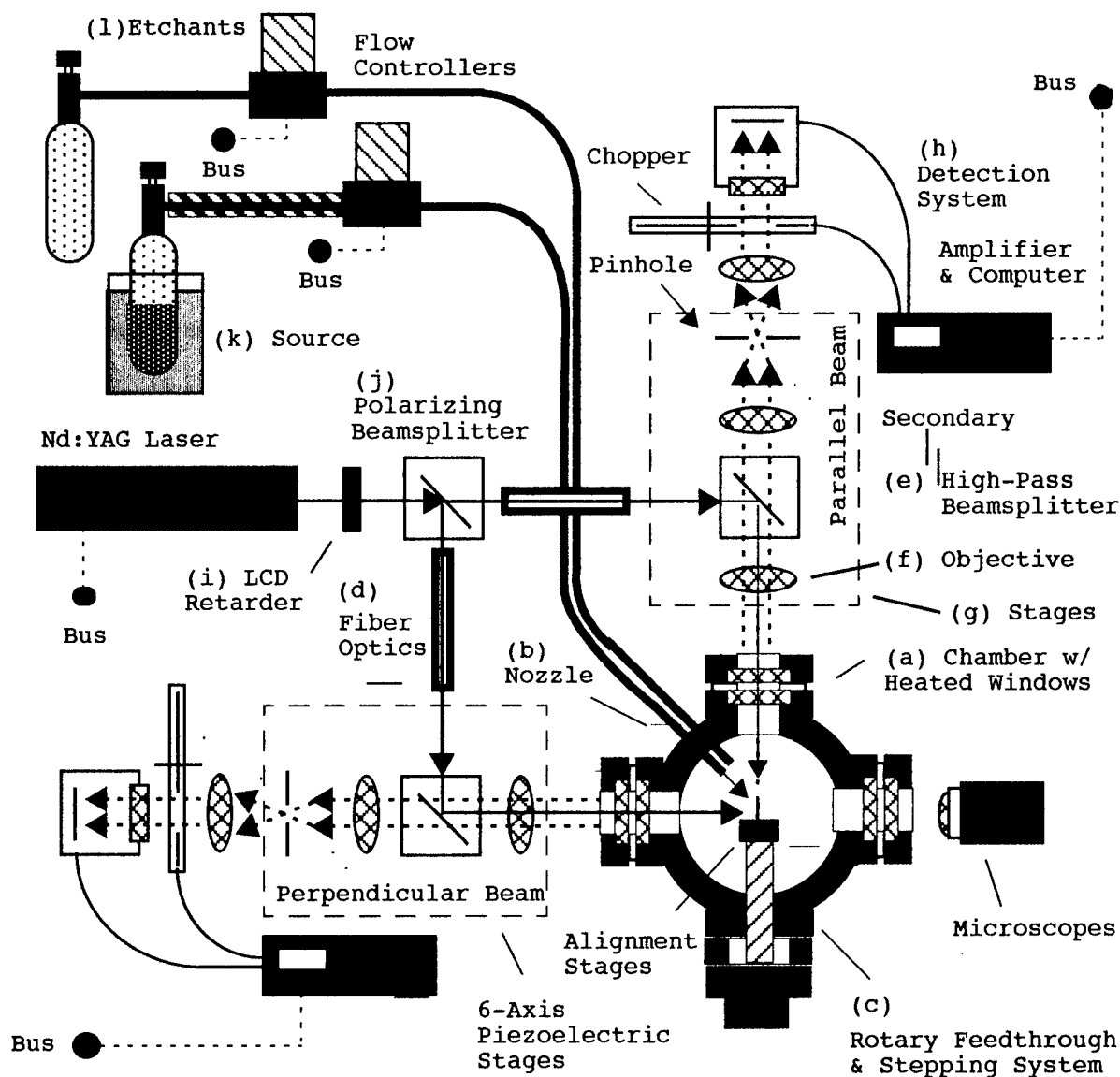


Fig. 3: Experimental Apparatus (Overview)

from 1300 to 1600 nm. In this way, the reaction could be monitored from behind the beam-splitter, with the detection system (h), which has been previously described for temperature and emissions feedback control.¹¹ Finally, to allow for both deposition and profiling, the gas delivery system allowed the introduction of both precursors (k) and etchants (l) into the chamber through the nozzle (b).

For deposition, the Nd:YAG laser was operated in cw mode, while for profiling the laser was Q-switched, with peak powers of up to 60kW. At low powers, the beam was modulated with a liquid crystal retarder (i) through a polarizing beamsplitter (j), with peak-to-peak power swings in under 20 ms. All laser powers reported herein were corrected for optical losses, and represent the actual beam power present at the deposit.

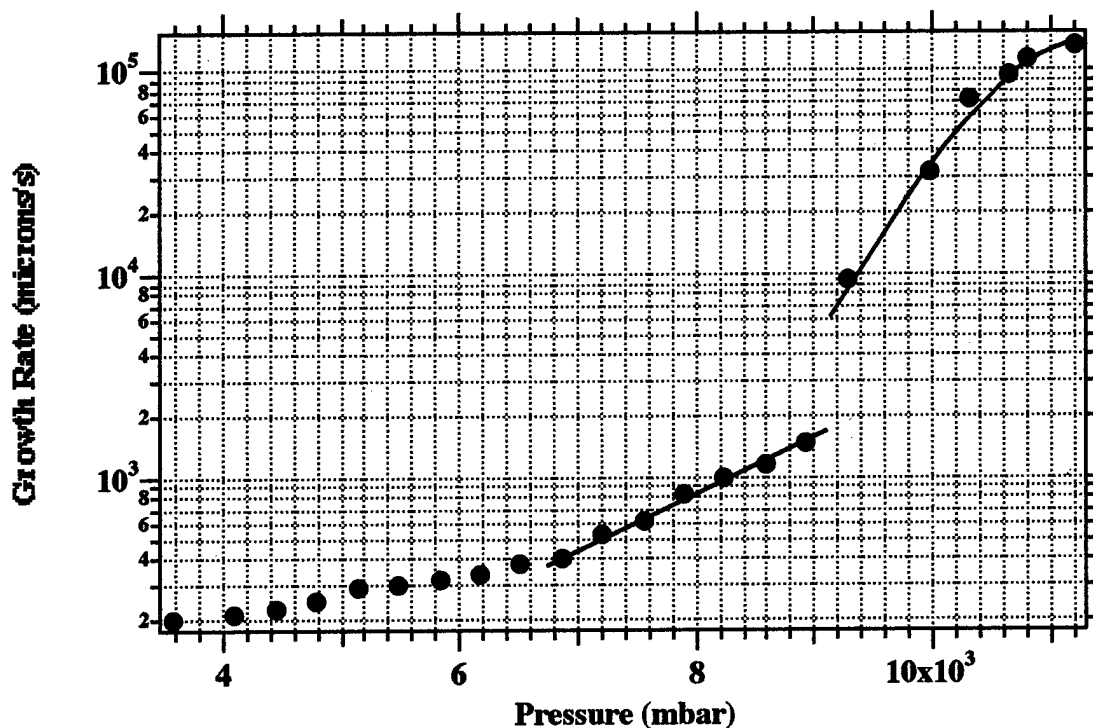


Fig. 4: Fiber Axial Growth Rate vs. Ethylene Pressure at Constant Laser Power (950 mW)

III. Results

A) Carbon Growth Experiments from the Alkenes

While carbon rods have been grown previously from acetylene,¹² methane,¹³ and ethylene,¹⁴ there appears to be no previous data of vapor-phase fiber growth from heavier molecular weight hydrocarbons. For this paper, the ethylene series, including ethylene, butene, pentene, hexene, and heptene was investigated at elevated vapor pressures.

As a baseline for comparison, several hundred fibers were grown from pure ethylene. The axial growth rate of the carbon fibers is shown in Fig. 4 for ethylene pressures from 4–11 bar. In this case, the laser power was held constant at 0.95 W. The most striking feature of this graph is the sudden discontinuity and rapid rise in growth rates above pressures of 9.3 bar; on a linear plot, it appears that the growth rate is directly proportional to the pressure in this regime, with no apparent sign of saturating. At 11 bar, the carbon fibers grew at an impressive 120,000 $\mu\text{m/s}$ (12 cm/s), a record setting growth rate for LCVD. The data points at the highest pressures were repeated several times to confirm these axial rates. One 120 μm diameter fiber grew at over 130,000 $\mu\text{m/s}$, corresponding to a volumetric deposition rate of 1.5 mm^3/s . At this speed, a 1 cm^3 object could be prototyped in 11 minutes—sufficient for large scale rapid prototyping.

Another notable feature of Fig. 4 is the change in growth rate at 6.5 bar. At lower pressures, the growth rate rises linearly from 4 bar to approximately 6.5 bar, then begins an exponential rise which continues until 9.3 bar. As the reaction rate was transport limited at these pressures,

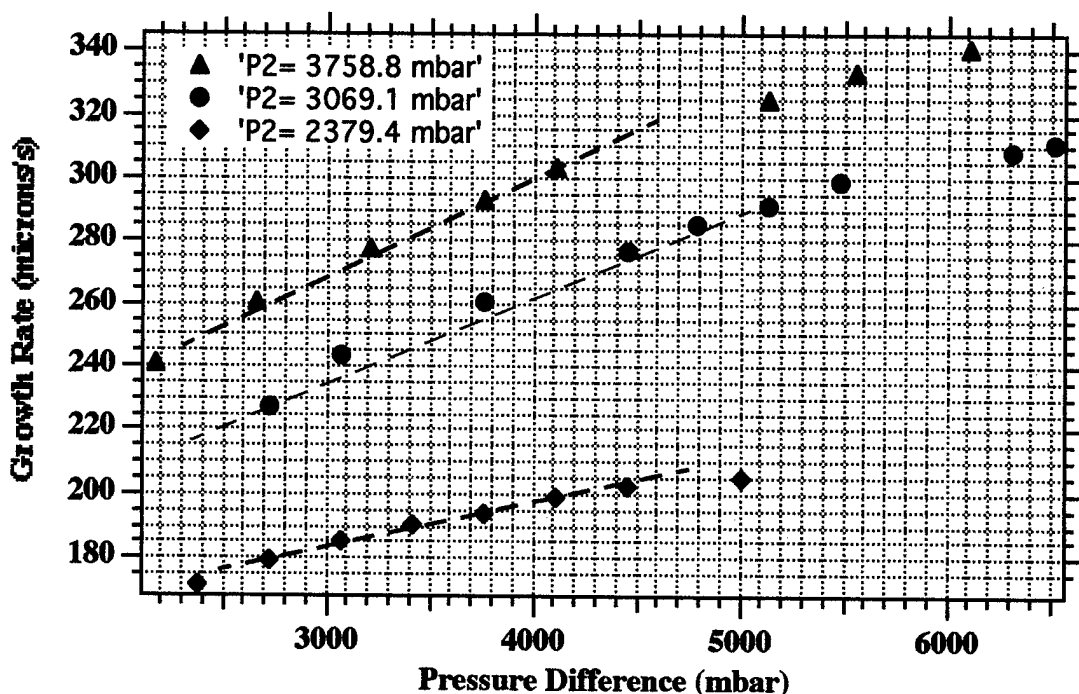


Fig. 5: Axial Growth Rate vs. Mass Flow Rate: Ethylene

it appears that increasing pressure allowed greater transport through enhanced convection and supersaturation of the reaction zone with ethylene molecules.

At 9.3 bar, a corresponding change in rod morphology was also observed; fully-dense diamond-like carbon grew below 9.3 bar, while porous carbon fibers were obtained at higher pressures. However, the porous fibers were still cohesive and highly flexible. The diamond-like carbon fibers exhibited the same highly elastic properties described previously;⁵ they were fully-dense over a wide range of laser powers—allowing the fiber diameter to be tailored to particular applications without a significant change in material properties. At laser powers above approximately 2.5-3.0 W (depending on the pressure) graphite fibers formed which were comparatively brittle. In Fig. 7A, a fiber is shown which passed through the optimal focus as a graphitic deposit, then as the incident laser power density dropped, smooth diamond-like deposits were obtained. At powers above 3.0 W homogeneous nucleation of carbon particles in the gas phase also occurred around the growth zone; these particles could be used to track the fluid flow around the fiber. Very rapid convection was observed, in excess of meter/second velocities near the laser heated zone. At the highest powers, carbon particles accumulated at the upper window of the chamber, directly above the carbon fibers—marking the rapid upward convection of the precursor fluid.

Forced convection experiments were also performed, using the two-regulator system described above. To obtain a variety of mass flow rates, the inlet regulator pressure was varied while maintaining a constant chamber pressure with the outlet regulator. In this case, a 50-200% increase in axial growth rate was observed over static data. The nozzle was directed normal to the fiber axis, and horizontally, i.e. perpendicular to the axis of natural convection. This can be seen in Fig. 5, where the ethylene flow rate is represented by the difference in chamber and inlet-regulator pressures—for three different base pressures. As the pressure difference (flow rate) rose, so did the axial rate—with a slope of approximately 20-30 $\mu\text{m/s}\cdot\text{bar}$. The fibers grew visibly faster as they passed through the forced nozzle flow; while no axial direc-

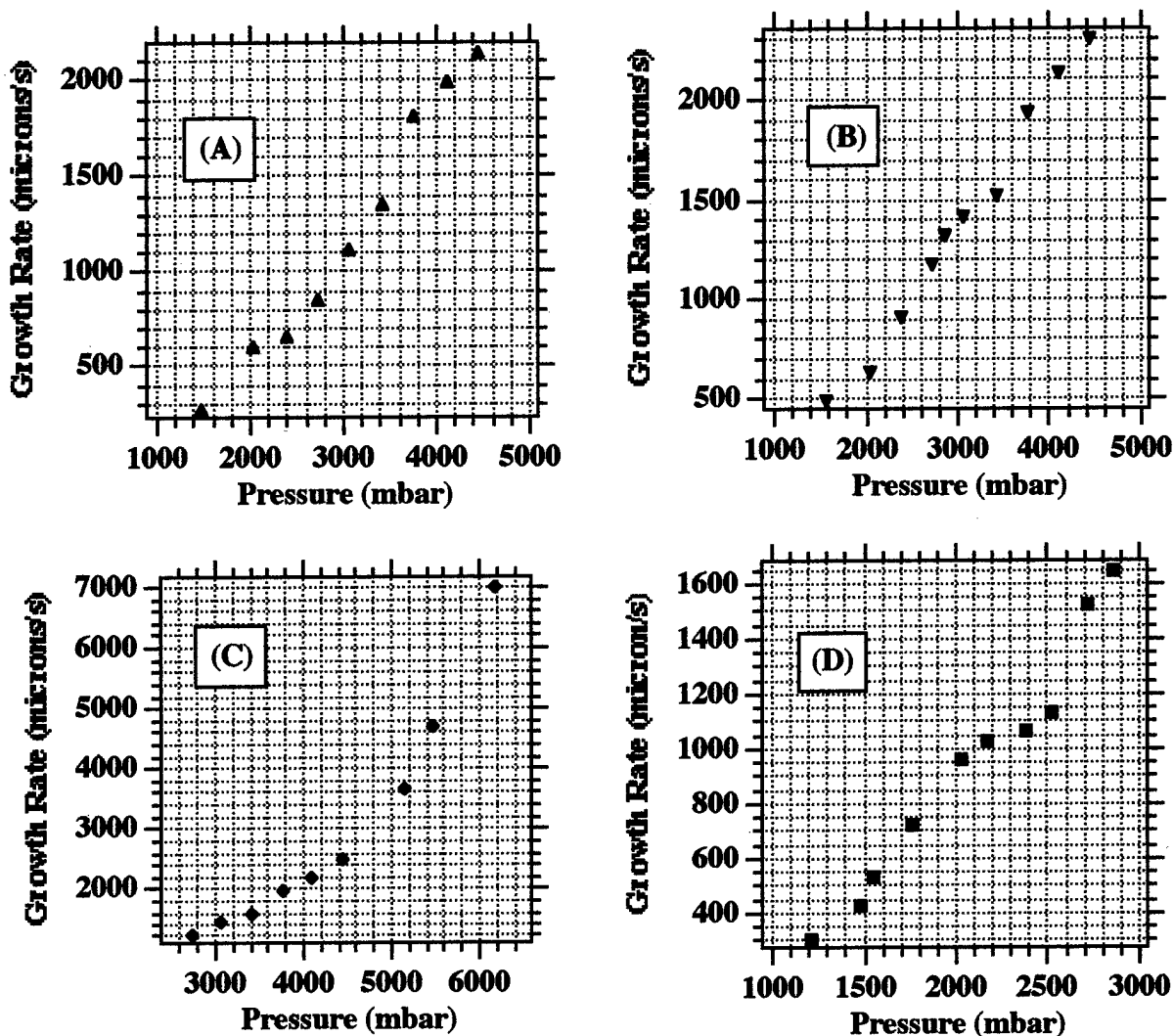


Fig. 6: Growth Rates vs. Pressure:
(A) Butene, (B) Pentene, (C) Hexene, (D) Heptene

tionality has as yet been observed, the fibers were slightly out-of-round due to the cross-flow. Note that the nozzle diameter of 2 mm was large compared to the growth zone on the fiber. An important feature to note in Fig. 5 is that the rate enhancement tends to saturate at the highest flow velocities; this is tentatively explained by forced cooling of the rods—as the same laser power was used throughout the experiment. It remains to be seen whether it is possible to compensate for the forced cooling with an increase in the incident laser power. However, the potential for more rapid growth through forced convection is apparent.

To investigate the potential of the longer chain hydrocarbons, fibers were also grown from 1-butene (C_4H_8), 1-pentene (C_5H_{10}), 1-hexene (C_6H_{12}), and 1-heptene (C_7H_{14}), respectively. As these precursors are all liquids at room temperature, the heated chamber and gas delivery system were employed. In Fig. 6, the axial growth rate for each these precursors is displayed; while the pressure was varied, a constant laser power of 950 mW was maintained throughout the growth experiments. The slowest axial rates among these precursors were obtained with butene in Fig. 6A. However, a comparison of Fig. 4 (ethylene) and Fig. 6A (butene), reveals

that for equivalent vapor pressures and laser powers, butene provides the greater deposition rate, by nearly an order of magnitude!

A further comparison of Fig. 6B, Fig. 6C, and Fig. 6D shows that for equivalent pressures, the growth rate rises with increasing molecular weight of the precursor, with heptene yielding the highest deposition rates. While not surprising, this result confirms that longer-chain hydrocarbons are desirable for the maximum possible growth rates, despite lower diffusion constants due to increased molecular weight. While each of the alkenes were studied at pressures of up to 3 bar, hexene (C) was investigated at pressures of up to 6.15 bar, yielding smooth fibers at axial rates of 7 mm/s! At an equivalent pressure, ethylene produced fibers at only 320 $\mu\text{m/s}$. Finally, the morphologies of the fibers grown from the longer-chain alkenes were similar to those obtained with ethylene. At laser powers below 2-3 W, diamond-like fibers resulted, while excessive powers yielded graphitic rods.

B) The Laser Microchemical Lathe

The LML was also implemented, as seen in Fig. 7A, using ethylene as a precursor. As expected, the diameter of the carbon mandrel fiber could be broadened through laser deposition, such as in Fig. 2 (C)—and etched as in Fig. 2 (D). Preliminary runs with the system yielded several sample parts, including rings, helices, pinafore spirals, and spur-gear-like parts. In the latter case, the teeth of the gear were laser-ablated to obtain uniform tooth heights, and then filleted between the teeth by laser deposition (see Fig. 7C). Future work will concentrate on implementing feedback control schemes to obtain consistently smooth deposits during repetitive scanning operations, as well as the growth of more complex and useful axi-symmetric parts.

IV. Acknowledgments

The authors would like to thanks the National Science Foundation and the Louisiana Board of Regents Research Competitiveness Program for their generous support for this work. We would also like to thank Robert Giasolli and Philip Coane for their contributions in facilities installations and chemical handling and disposal.

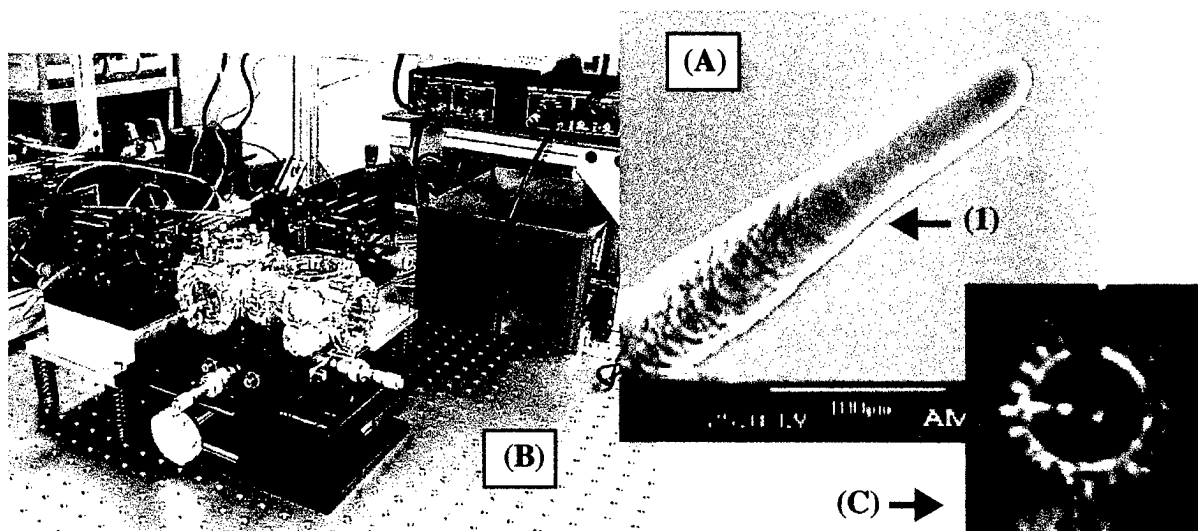


Fig. 7: (A) Transition Between Graphitic and Diamond-like carbon, (B) CarbonThe Laser Microchemical Lathe, (C) Gear-like Deposit (video)

V. Bibliography

1. Maxwell, J., Pegna, J., DeAngelis, D., Messia, D., "Three-dimensional Laser Chemical Vapor Deposition of Nickel-Iron Alloys," Material Research Society Symposium Proceedings, v. 397 (B3.30): Advanced Laser Processing, MRS Fall 1995 Meeting, Boston, MA (Nov. 27--Dec.1, 1995).
2. Maxwell, J., Pegna, J., DeAngelis, D., "Feedback Control and Reaction Kinetics of Three-dimensional Laser Chemical Vapor Deposition" Applied Physics A, Vol. 67, (1998), pp. 323-329.
3. Thissell, W., Marcus, H. L., "New Developments in Processing and Control of Selected Area Laser Deposition of Carbon," Proc. Solid Freeform Fabrication Symposium, Austin, Texas, (Aug. 1994), pp. 311-320.
4. Maxwell, J., Krishnan, K., "High-Pressure, Convectively-Enhanced, Laser Chemical Vapor Deposition of Titanium," Proc. Solid Freeform Fabrication Symposium, Austin, Texas, (Aug. 1997).
5. Maxwell, J., Larsson, K., Boman, M., "Rapid Prototyping of Functional Three-Dimensional Microsolenoids and Electromagnets by High-Pressure Laser Chemical Vapor Deposition" Proc. Solid Freeform Fabrication Symposium, Austin, Texas, (Aug. 1998).
6. Wanke, M. C., Lehmann, O., Stuke, M., "Laser Rapid Prototyping of Photonic Band Gap Microstructures," Science, Vol. 275, No. 5304, (Feb. 28 1997), p. 1284.
7. Wallenberger, F. T., Nordine, P. C. "Amorphous Silicon Nitride Fibers Grown from the Vapor Phase," J. Mater. Res., Vol. 9, No. 3, (Mar. 1994), pp. 527-530.
8. Pegna, J., Messia, D., Maxwell, J., DeAngelis, D., "Real-time Control and Modelling for the Laser Chemical Vapor Deposition of Walled-Structures," Material Research Society Symposium: Rapid Prototyping, MRS Spring 1997 Meeting, San Francisco, CA (Apr. 1997).
9. Bloomstein, T. M., Ehrlich, D. J., "Stereo Laser Micromachining of Silicon," Applied Physics Letters, Vol. 61, No. 6, (10 Aug. 1992), pp. 708-710.
10. Maxwell, J., Ph.D. Thesis, Rensselaer Polytechnic Institute, Ch. 5 and 6.
11. Maxwell, J., Williams, K., Larsson, K., Boman, M., "Freeform Fabrication of Functional Microsolenoids, Electromagnets and Helical Springs Using High-Pressure Laser Chemical Vapor Deposition," IEEE Micro Electro Mechanical Systems (MEMS) Conference, Orlando, FL, Jan. 1999.
12. Zong, G., Tompkins, J., Thissell, W., Sajot, E., Marcus, H., "Processing Problems Associated with Gas Phase Solid Freeform Fabrication Using Pyrolytic Selective Area Laser Deposition," Proc. Solid Freeform Fabrication Symposium, (1991), pp. 271-278.
13. Wallenberger, F. T., Nordine, P., "Strong, Pure, and Uniform Carbon Fibers Obtained Directly from the Vapor Phase," Science, Vol. 260, (1993), pp. 66-68.
14. Maxwell, J., Pegna, J., "Laser-induced Pyrolysis of Tapered Microstructures," Proc. Solid Freeform Fabrication Symposium, Austin, Texas, (Aug. 1995).

COOLING CONFIGURATIONS FOR RAPID TOOLING

"A Comparison Study"

Vito Gervasi, Christopher J. Urban, Steven E. Gerritsma

Rapid Prototyping Center
Milwaukee School of Engineering

Abstract

With advances in solid freeform fabrication and rapid tooling methods, true conformal cooling is becoming more feasible each year. As conformal cooling becomes more commonplace, methods for comparing cooling configurations are increasingly necessary. Milwaukee School of Engineering has developed a "simulated core-cavity" which was used to compare various cooling methods. The simulated core-cavity combines many features one might find in typical molds. In addition to developing a simulated core cavity, we have also developed a test fixture for collecting heat-removal-rate information. Heat removal rate information was gathered from difficult to cool locations on each simulated core-cavity. Several cooling configurations were tested, including conformal cooling and traditional cooling. Conclusions and recommendations for the use of conformal cooling with various tooling materials will be presented.

Introduction

"Conformal cooling" is used here to describe a system of cooling channels and openings – inline with or equidistant from – the surface of an object to be cooled. The cooling channels direct a fluid in a controlled manner, receiving heat from the surface which is then carried away from the system. Conformal cooling has several objectives aimed at improving the effectiveness of heat transfer from the object surface, through a material, and to the cooling fluid. One objective of conformal cooling is to bring the cooling channels as close as possible to the heated surface while maintaining structural integrity and tolerances. Another objective is to maximize the channel surface area through which heat may be transferred. A third objective is to induce turbulence for enhanced convection cooling, within the cooling channel. In many applications conformal cooling must remove heat in a uniform controlled manner; therefore controlling channel size and placement become critical objectives. In other applications, such as cooling objects with low thermal conductivity, the objective becomes the removal of as much heat as quickly as possible.

For many years the primary obstacle for the integration of conformal cooling into structures has been synthesis techniques. With traditional manufacturing, material is typically removed from a large billet, making it difficult and expensive to add internal features such as cooling channels. One approach is to machine multiple pieces which are assembled into a conformally cooled object. Near-net castings with expendable cores molded-in-place to form conformal cooling is another approach used by industry, with limited success, limited by channel size and length. A new approach, overcoming limitations of traditional manufacturing, is Solid Freeform Fabrication (SFF).

Unlike traditional material removal fabrication techniques, such as CNC machining, SFF is an additive process, starting with a void, and adding material one layer at a time to create a 3D object. CAD data is used to define the surface and interior of the solid 3D object, making complex part geometries as well as complex internal structures possible and commonplace. No expensive patterns, molds, or parting-lines are required when using SFF directly, making it a widely accepted, accelerated prototyping process.

The ability to create detailed complex conformal cooling systems with SFF is advancing each year. Powder based SFF approaches such as Selective Laser Sintering (SLSTM, Rapid Steel 2.0 MetalTM)¹ or 3D printingTM (Pro-metalTM)² are capable of producing complex channels. The current limitation of these powder-based processes is the difficulty of removing powder from channels in a green body state without damaging the object. To minimize this difficulty, channels are made with wider diameters and shorter lengths, significantly reducing the effectiveness of the cooling system in some applications. With improvements in green strength, cooling channels will undoubtedly become longer and more complex. Another technique is to directly or indirectly create an expendable ceramic core, which is molded into a near-net-shape casting and later removed. SFF processes continue to advance, making very complex objects with intricate conformal cooling systems. With the known benefits of conformal cooling^{3,4} for heat removal and the continual evolution of SFF technologies, a study was conducted to compare the effectiveness of several cooling systems.

Background

The Rapid Prototyping Center at the Milwaukee School of Engineering has been developing a new composite based epoxy matrix rapid tooling methodology for several years. With epoxy being a poor thermal conductor, improved heat removal was important. Current techniques for producing conformal cooling within cast RT tooling such as formed copper tubing or gun-drilled holes, seemed inferior to the potential of fine, contoured cooling channels.

The conformal cooling technique developed uses an expendable core, molded in place within the tooling material. Many geometries are possible including serpentine, zig-zag, straight-line, TetraLattice⁵ and others. The expendable cores are first generated using CAD and later produced using SFF. The SFF can be used directly to form the channels or indirectly as an expendable-core mold. In the final stage, the expendable core is placed accurately within the mold face and cast in place. After the tool is cured, the expendable core material is removed, forming the conformal cooling channels.

Although this paper focuses on cooling systems comparisons, the thrust of this investigation was to develop a method for producing conformal cooling within RT. The goal for the conformal cooling configuration design was to bring the tightly spaced channels as close to the surface as possible, while maintaining structural integrity needed for injection molding.

Objectives

The first objective was to compare several standard RT cooling systems against a conformal cooling system. The second objective was to compare these systems under similar conditions using a standard pump and standard plumbing to gain a better understanding of the benefits of

conformal cooling. The final objective was to form the conformal cooling channels as close to the surface as possible while still maintaining adequate wall thickness for injection molding pressures.

Methodology

To compare four cooling configurations an experimental tool called a "Simulated Core-Cavity" was developed and analyzed in a test apparatus. The following pages will describe the simulated core cavity, the four cooling configurations, as well as the test apparatus.

Simulated Core Cavity

The simulated core-cavity was designed to mimic characteristics of both the core and cavity halves of a typical injection mold. A shape was sought, which had irregular curves, sharp and rounded edges, as well as primitive recessed and protruding features. After considering a number of possible geometries the simulated core-cavity shown in figure 1 resulted. This design uses a 3D face scan with complex, difficult to machine, features. One half of the face is protruding from the theoretical parting line, and the other half is recessed into the simulated core-cavity. There are also two cylindrical shapes, with draft, one protruding and one recessed. The simulated core-cavity has indentations for snap-fitting into the test apparatus.

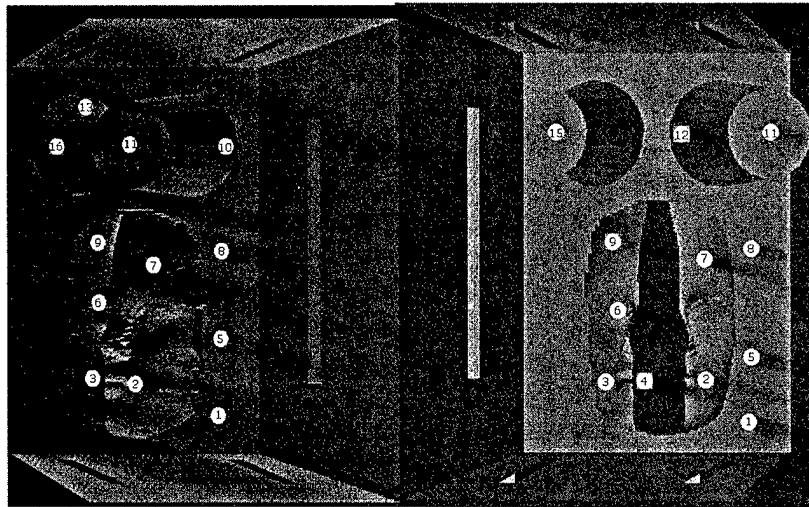


**Figure 1. Simulated Core-Cavity with Data
16 Collection Points Displayed**

To create the simulated core-cavities a silicone mold was used. Silicone walls were approximately 2 inches thick and reinforced with 1/4 inch aluminum rods *-to reduce mold deflection*. Simulated core-cavities were cast using standard aluminum filled epoxy. Cooling systems were cast-in-place or machined after casting *-depending on cooling type*. All simulated core-cavities were cast and post cured following a standard schedule and temperatures. Brass tubes were added to union with coolant pumping systems. Brass tubes were coated with silicone to minimize heat transfer to surroundings.

Cooling Configurations (figure 2)

No-Cooling

One option in RT is to not use any coolant channels, relying upon air cooling. This option is represented in the first simulated core-cavity which used no coolant channels.

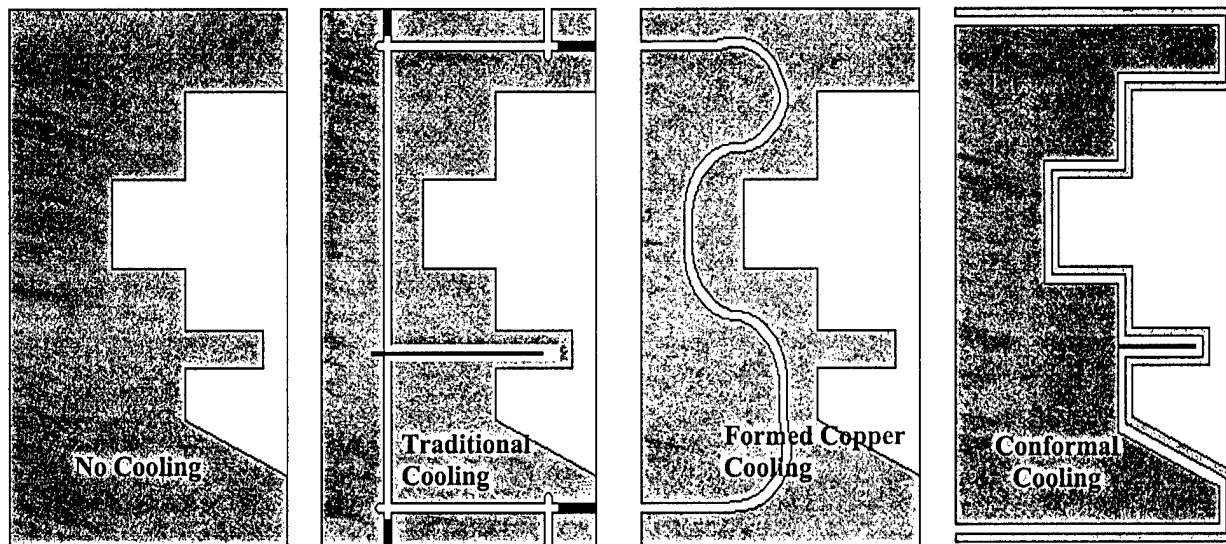


Figure 2. Cooling Configurations

Traditional Cooling

In some RT processes, such as DTM's RapidSteel2^{TM,1} or 3D System's KelTool^{TM,6}, it is desirable to add a coolant channel network after the mold is created. For this traditionally-cooled simulated core-cavity, a network of interconnected drilled holes was capped off to direct coolant throughout the object. In addition to drilled channels, a baffle was used on one tall narrow feature.

Formed Copper Cooling

Many RT processes, such as AIM or composite tooling, use formed copper tubing to improve heat removal rates. Two cast-in-place methods can be employed for this type of cooling. The first method is a plumbed coolant system with elbows and tees soldered together, forming a near conformal cooling system. The second method (used for this study) uses formed copper tubing, bent to contour within the cooled surface. In both cases the copper is molded-in-place. To achieve maximum coverage on this simulated core cavity two formed copper tubes were used.

Zig-Zag Conformal Cooling

Conformal cooling is the ideal coolant system for injection molding applications. As fine channels get closer to the cooled surface the ability to cool small, detailed features becomes more feasible. A simulated core-cavity with eleven 2.5 mm diameter channels, conforming to the surface in a zig-zag pattern was formed (figure 3). The channels were spaced 5 mm between centers at the minimum and 2.5 mm

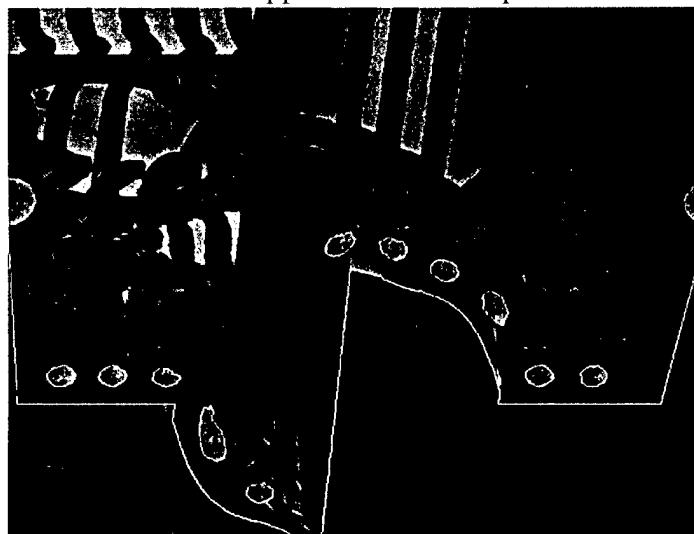


Figure 3. Zig-Zag Conformal Cooling Channels

from the surface throughout. Channel spacing increased as surfaces became more vertical as a result of CAD modeling methodology.

Test Apparatus

A method was developed to test and record the heat removal rate at multiple points on the simulated core-cavity surface. To measure the heat removal rate at the same location on all simulated core-cavities an apparatus was created, with 16 test cells located at specific surface positions.

Figure 4 illustrates the basic design of the 16 test cells. The liquid volume of the cell, labeled pseudo-part, represents a plastic part. To measure heat transfer from the cell liquid to the simulated core-cavity coolant, a thermocouple and data acquisition system were used. Figure 5 illustrates the entire test apparatus.

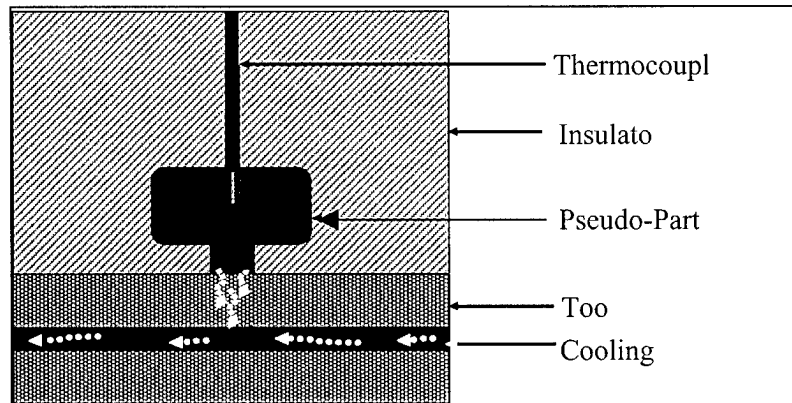


Figure 4. Test Cell Design

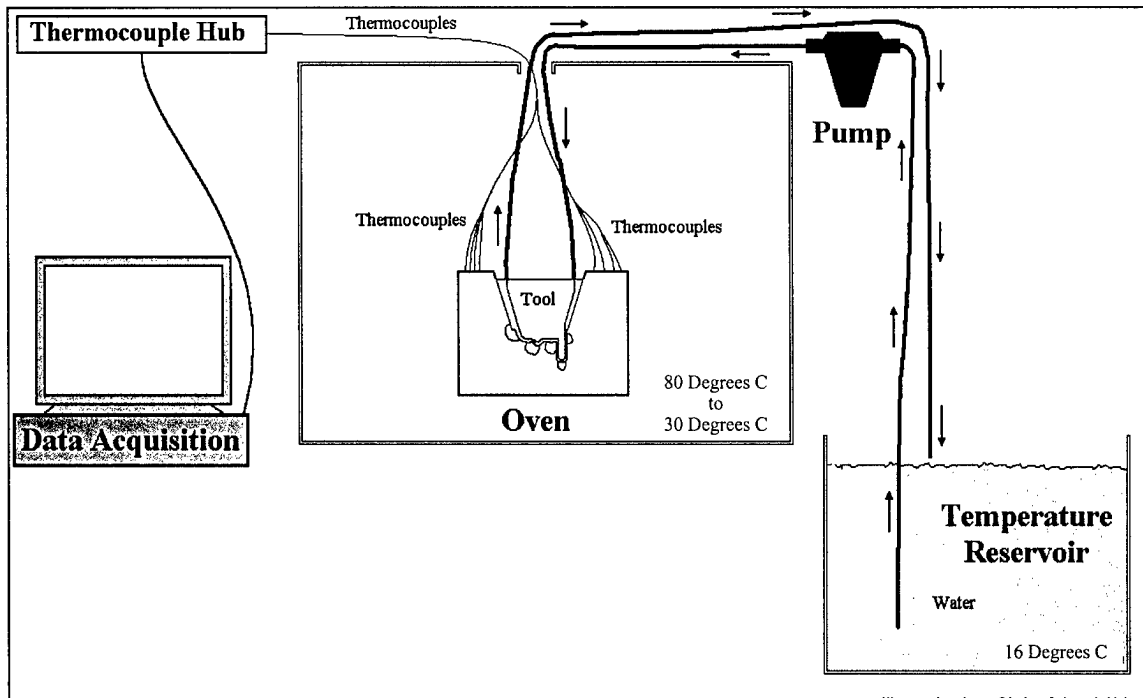


Figure 5. Complete Test Apparatus

To run the test, the simulated core-cavity was placed in the test apparatus and the test cells were filled with glycerol under vacuum. The coolant pump was connected to the simulated core-cavity, and the thermal couples were placed. The test cells and simulated core-cavity were heated to 80° C in a convection oven. To initiate the test the oven temperature setting was

reduced to 30° C, the coolant pump was activated, and data collection began. When the temperature of all test cells fell below 45° C the test was stopped and data was analyzed.

Results/Discussion

All four simulated core-cavities were tested under similar conditions to determine the rate of heat removal for each system. The results were verified by testing the zig-zag conformal cooling system and the traditional cooling system a second time. The resulting data points were analyzed and used to generate three charts illustrated and discussed in the following pages.

Figure 6 illustrates an overall cooling configuration comparison. Performance of all four simulated core cavities is shown. Each line shown is an average of all 16 data points for each configuration. The slope of the curves for each configuration represents the rate of heat removal. The line for "no cooling channels" has a gradual slope with a relatively slow rate of heat removal. The traditional and copper tubing performed similarly to each other and significantly better than a lack of cooling channels. The conformal cooling has a steep curve, cooling the cells noticeably faster than traditional and copper tubing.

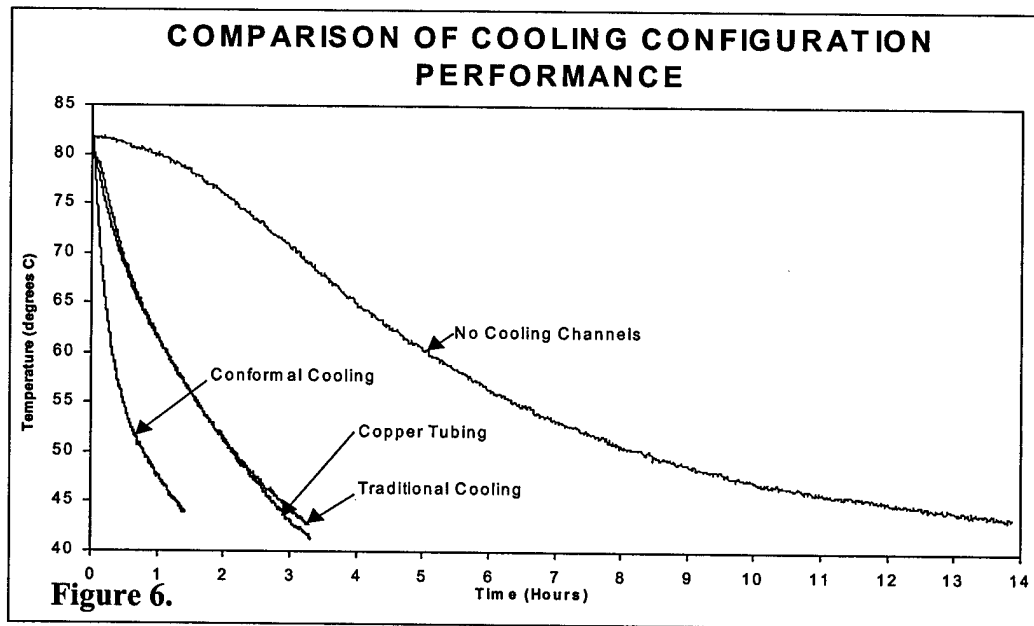
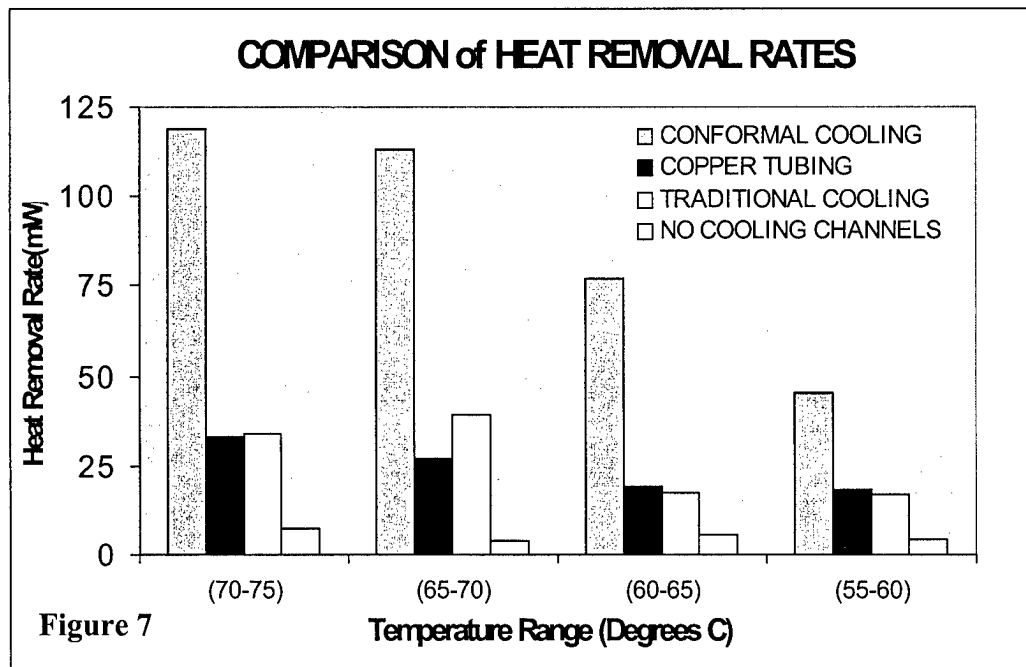
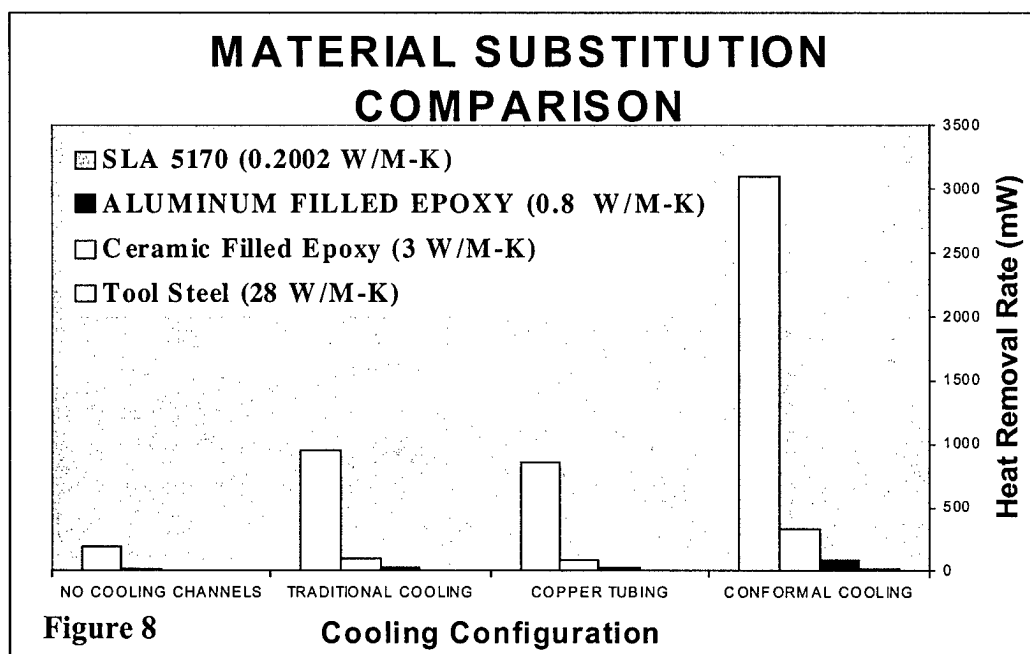


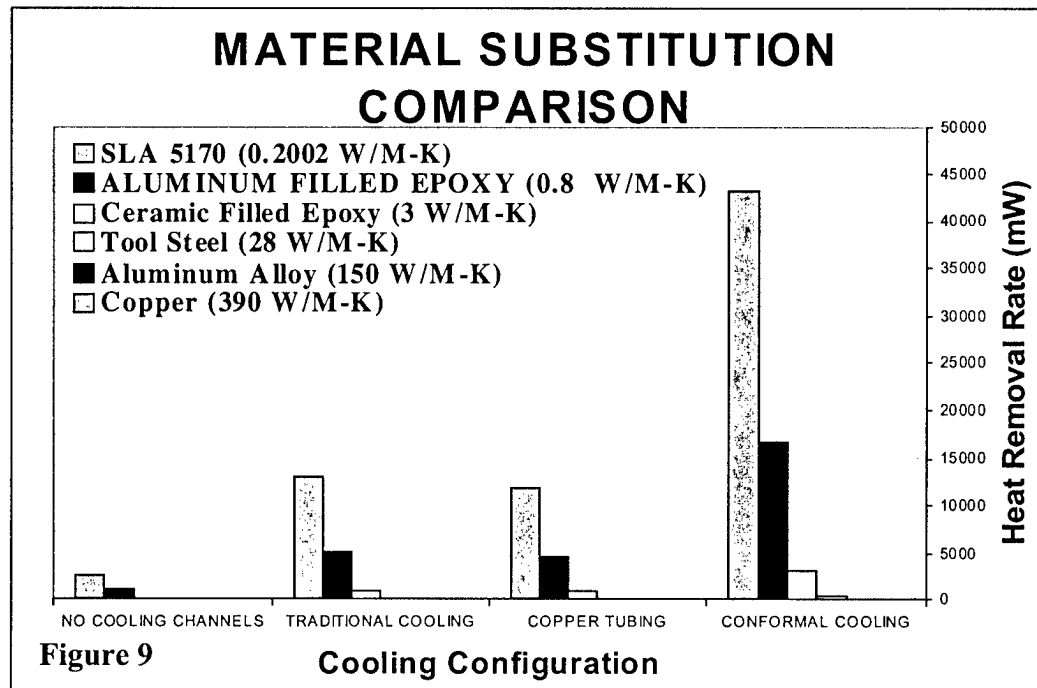
Figure 7 illustrates the heat removal rates of each cooling configuration over a temperature range. No cooling has a relatively low heat removal rate. The traditional cooling has a comparable heat removal rate to that of the copper tubing: both rates are about three times that of no cooling. Conformal cooling has a heat removal rate about three times higher than the copper and traditional cooling. Therefore, conformal cooling also has a heat removal rate 9 times higher than no cooling.



As SFF expands material capabilities it becomes of interest to predict how these materials may perform in conformally cooled injection molding applications. This portion of the paper will attempt to give some material performance insight into, not only current SFF materials, but also SFF materials of the future. The material used for this study was aluminum filled epoxy with a thermal conductivity of $0.8 \text{ W/(M}\cdot\text{K)}$. The heat removal rates of figure 7 were averaged to obtain one heat removal rate for each cooling system. These average heat removal rates for the aluminum filled epoxy were used to theoretically estimate the heat removal rate of other materials. To do this, thermal conductivity (K) for Stereolithography epoxy, ceramic filled epoxy, tool steel, aluminum, and copper were substituted in place of the thermal conductivity of aluminum filled epoxy. As shown in figure 8, stereolithography materials are considerably more



challenging to transfer heat through. Ceramic filled epoxy⁷ is a significant improvement over aluminum filled epoxy while tool steel is even a greater improvement over the ceramic filled epoxy. Figure 9 illustrates the addition of aluminum and copper to figure 8, again a significant improvement over tool steel.



Conclusions

Any cooling is useful for standard tooling and rapid tooling. If channels of any form are created within a mold, heat removal rates can improve as much as three times with formed copper or traditional cooling and nine times with conformal cooling.

Conformal cooling is a significant improvement over traditional cooling and formed copper cooling and may increase mold life by reducing thermal shock after plastic injection.

Conformal cooling has significant potential for reducing cycle times by improving heat removal from injection molded parts.

To cool detailed features of parts cooling channels should be located as closely to the cooled surface as possible while still maintaining structural integrity.

Mold materials with higher thermal conductivity will improve heat removal rates significantly over epoxy based materials.

Acknowledgments

We gratefully acknowledge the support of the National Science Foundation (EEC-99619715, Undergraduate Research in Solid Freeform Materials and Technology).

Thank you to the Rapid Prototyping Consortium and the Rapid Prototyping Center staff at Milwaukee School of Engineering for their contribution to this applied research project.

Thanks also to Rich Phillips of the Mechanical Engineering Department at Milwaukee School of Engineering for facilitating this project.

References

1. <http://www.dtm-corp.com/Technology/Materials/rapidstl.htm>
2. <http://www.prometal-rt.com/>
3. Sachs, Emanuel, Samuel Allen, Honglin Guo, James Banos, Michael Cima, James Serdy, and David Brancazio, "Progress on Tooling by 3D Printing; Conformal Cooling, Dimensional Control, Surface Finish, and Hardness," 1997 SFF Symposium Proceedings pp 115-123
4. Bartkus, Eric K., Chuck Ondrejka, "Rapid Product Development and Tooling at Amway Corporation," 1999 Rapid Prototyping and Manufacturing Conference Proceedings, pp 205-216
5. Gervasi, V., L. Milkowski, J. Canino, R. Zick, "MSOE TetraLattice, Applications and Simplified CAD Representation," SFF Symposium Proceedings, August 1999
6. http://www.3dsystems.com/index_nav.asp?nav=products&content=products/index.asp
7. Adtech EC-430, ceramic filled epoxy tooling system, product bulletin
8. Rao, Suanth, "How to make Injection Molds," Hanser Publishing, Munchen, Germany

A Vacuum Furnace Process for DTM's RapidSteel 2.0 Material

Klas Boivie, Torsten Kjellberg
Woxéncentrum, KTH, The Royal Institute of Technology
Sweden

Abstract

The work described in this paper investigates the possibility to use a vacuum furnace in DTM's RapidTool LR process. This alternative process route is brought about to allow the usage of a more common type of furnace than the one recommended by DTM.

Based on the specified, well established H_2/N_2 furnace processing, a similar procedure, adapted to conventional cold wall vacuum furnaces has been developed and tested. The testing is described in detail, and the results so far are promising enough to justify the practical usage of this process, and more of in-depth analysis of all the various aspects of the procedure.

Introduction

The field of Rapid Prototyping (RP), or Solid Free Form Fabrication (SFF), has gone through quite a rapid development on its own during the last decade. From crude concept models made of brittle polymer material to more and more production like objects from a variety of materials including ceramics and metals. A major challenge has been to extend the application of RP-technology into the field of RT, -Rapid Tooling, thus a wide array of RT processes has been developed, all with their own limits and benefits. Among the most widely used of those is the Rapid Tool LR process from DTM Corp. Austin, TX.

The Rapid Tool LR process is an indirect SLS based process, where a powder material, RapidSteel 2.0, is processed in the Sinterstation system, followed by two subsequent furnace cycles. During the SLS stage a scanning laser melts the polymeric binder in each powder layer, thus gluing the metal powder together forming a fragile, but solid mass called the "green" part. The green part is placed in a crucible and sintered, at 1120°C in a 30/70 H_2/N_2 furnace atmosphere, forming a rigid but porous object called the "brown" part. A second furnace cycle at 1050°C in the same atmosphere infiltrates the part with bronze giving a final, ideally, fully dense part.

The specified furnace atmosphere with 30% H_2 requires a specialized furnace that in many cases has little other use. Vacuum furnaces, on the other hand, are often used in various heat treatments and brazing operations, and could in many cases, be available to use as an alternative. This paper describes the adaptation of the Rapid Tool LR process for processing in vacuum furnaces.

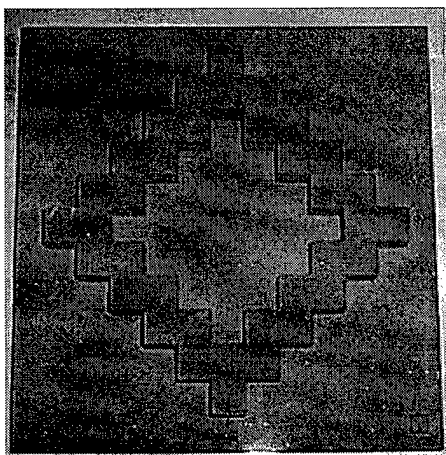


Fig. 1.
Standard sample part used to determine the scaling factors for the whole RapidTool LR process, from SLS processing to completed infiltration. The same geometry was used during the evolution of the vacuum furnace process. This picture shows the infiltrated sample 3.

Our Approach

Vacuum furnaces are used in conventional powder metallurgy to "maintain a clean reproducible, and controlled non reactive atmosphere" [4], especially for "corrosion resistant materials (stainless steels), vacuum is the most reliable atmosphere"[4]. The RapidSteel 2.0 powder metal is stainless steel, and our hypothesis was that it would process well in a vacuum furnace.

Most sintering practices in the powder metallurgy industry are set by trial and error techniques, but since there is a designated process at hand in this case, it is reasonable that a similar process could be deducted from the effect given by the H_2/N_2 atmosphere during the process and comparing that to the likely effect of vacuum.

Atmosphere: According to [1], the "hydrogen reduces any oxides in the surface of the iron powder and aids in infiltrating the bronze into the part". The nitrogen is simply inert, (and to a small extent dissolves into the metal, thus adding a hardening effect). Apart from chemical activity, the atmosphere gas is also an important medium for heat distribution by means of convection. That is obviously not the case with vacuum, and this difference should be accounted for in the settlement of times for the different process steps.

Temperatures: DTM has settled suitable temperatures for sintering (1120°C) and infiltration (1050°C). Ramp rates are mainly set by the equipment's (crucible and alumina plate) sensitivity to thermal shock, and a maximum ramp is given to 180°C/h . These values are determined by material properties and there are no reasons to make any changes at this stage.

Chemical activity: In DTM's standard furnace atmosphere, hydrogen reduces metal oxides,—and the better reduction, the better sintering and infiltration. A similar effect can be obtained in a vacuum furnace too; by lowering the partial pressure of oxygen in the equilibrium: $\text{MeO} \leftrightarrow \text{Me} + \text{O}$.

Thus, the higher vacuum, the better reduction, and the better sintering and infiltration. But high vacuum at high temperatures would not only evaporate the binder, but also risks to evaporate some alloying elements in the metal powder. In relation to that, it can be justified to assume that the organic binder would evaporate at a far lower temperature and pressure than the alloy components. In the H_2/N_2 atmosphere, burnout temperatures are between 450-650°C. Therefore, for the most likely success; -find the highest vacuum that, with reasonable security, does not evaporate the alloying elements.

The activity of any chemical reaction that takes place in the crucible is dependent of temperature and chemical composition. Since the proportions of the alloying elements are given within rather wide ranges, all calculations will be coarse and all resulting values must include large safety margins. The alloying component with the highest gas pressure at process temperatures gives the lowest possible gas pressure in the vacuum furnace, i.e. the highest vacuum acceptable.

Calculation

The Rapidsteel 2.0 powder is an iron based steel powder. According to [2] the alloying elements are ;

Chromium: 12 - 30%

Molybdenum: 0 - 7%

Nickel:..... 0 - 35%

Manganese:... 1 - 4%

Given that

p: gas pressure; atm

ΔH_m : enthalpy for the phase transformation (s) \rightarrow (g); cal

T: temperature; K

R: constant = 1.987 cal deg⁻¹mol⁻¹

$$d \ln p / dT = \Delta H_m / (RT^2) \Rightarrow d \ln P = \Delta H_m / R \cdot dT \cdot T^{-2} \Rightarrow \int d \ln p = \Delta H_m / R \cdot \int T^{-2} dT \Rightarrow$$

$\ln p_1 - \ln p_2 = -\Delta H_m / R \cdot (T_1 - T_2)$, where index (1) is referring to the triple point equilibrium, and index (2) is referring to the process conditions.

For an ideal gas solution, partial pressure of a component = $p_2 \cdot (\text{fraction of element}) = p_p$.

For Cr, in the sintering stage, (fractions according to worst case scenario):

$$p_1 = 1 \text{ atm} \Rightarrow \ln p_1 = 0$$

$$\Delta H_m = 81.7 \text{ kcal/mol}$$

$$T_1 = 2893 \text{ K}$$

$$T_2 = 1393 \text{ K}$$

$$-\ln p_2 = -81.7 \cdot 10^3 / 1.987 \cdot (2893^{-1} - 1393^{-1}) = -15.3 \Rightarrow p_2 = 2.26 \cdot 10^{-7} \text{ atm}$$

$$\text{fraction of Cr; } X_{\text{Cr}} = 0.32 ; \Rightarrow p_{\text{p,Cr}} = 2.26 \cdot 10^{-7} \cdot 0.32 = 7.8 \cdot 10^{-8} \text{ atm}$$

In a similar manner (fractions picked according to worst case scenario):

$$p_{\text{p,Mn}} = 3.98 \cdot 10^{-4} \cdot 0.019 = 7.57 \cdot 10^{-6} \text{ atm}$$

$$p_{\text{p,Mo}} = 1.37 \cdot 10^{-16} \cdot 0.0234 = 3.2 \cdot 10^{-16} \text{ atm}$$

$$p_{\text{p,Ni}} = 1.8 \cdot 10^{-8} \cdot 0.1632 = 2.89 \cdot 10^{-9} \text{ atm}$$

With a calculated partial gas pressure of $7.57 \cdot 10^{-6}$ atm, manganese is the critical component..

A reasonable safety margin gives \Rightarrow set point value $49.3 \cdot 10^{-6}$ atm, or in a common scale among vacuum furnaces; $50 \cdot 10^{-3}$ mbar.

Experimental

The experimental furnace cycles were run in a conventional cold wall vacuum furnace at Järfälla Hårdverkstad AB, Järfälla, Sweden. Green bodies were manufactured following recommendations according to DTM's "Guide to Materials: The Rapid Tool LR Process Using RapidSteel 2.0"[1] and "RapidSteel 2.0 Mold Inserts for Plastic Injection Molding"[3]. Crucible setup was likewise according to recommendations from the same sources, but with one small exception: for increased safety during transportation, the fine grain alumina powder (240 grit) was used for both the infiltration and sintering cycles.

Sample 1. Sintering: The standard setup, ramp rate (180°C/h) and sintering temperature (1120°C) according to [1] was used. Since no other mechanism of heat transfer than radiation is active in vacuum, the dwell time at sintering temperature was prolonged from 3 hrs [1] to 3.5 hrs. For practical reason was the furnace allowed to cool down in its own pace from 500°C . Furnace temperature and pressure was monitored during the whole cycle.

The sintering result was quite satisfactory regarding strength, shape accuracy and sharpness of edges. However due to the fact that the equipment (crucible, bricks etc.) had not previously been subjected to a vacuum furnace cycle, some unaccounted gas was released during the furnace cycle, and it was not possible to draw any conclusions from the furnace atmosphere pressure.

Sample 1. Infiltration: The standard setup for solid bar bronze was used. The temperature (1050°C) and ramp rate (180°C/h) was set according to [1]. For reasons mentioned earlier the dwell time at 1050°C was prolonged from 2 hrs [1] to 2.5 hrs.

The infiltration could be termed "half successful", meaning that only half the bronze was infiltrated. Two infiltration plates had at some time lost contact with the sample and no infiltration was possible from those plates.

Sample1. Conclusion: The sintering cycle seemed good enough, so no further modifications were necessary at this stage. Instead securing the contact between the sample and the plates was the primary aim for the next sample.

Sample 2. Sintering: The setup, ramp rate, sintering temperature and dwell time was identical to sample1. To secure the best possible contact between infiltration plates and sample, they were sintered in direct contact with each other. Identical, still quite satisfactory results as for the previous sample1. The plates had bonded to the sample thus forming one large object with the plates stuck like wings to the sides.

Sample 2. Infiltration: Standard setup, and the same procedure as previous sample. All infiltrant bars were infiltrated, but still the result could only be termed a partial success. Each bar left a "foam" of nickel rich residue on the plates.

The sample was measured and scaling factors were calculated in the standard data sheet provided with the RapidSteel powder from DTM. See table1.

Sample 2. Conclusion: Connection between plates and sample secured infiltration, however since the brown specimen could not be weighed separately infiltration success could not be calculated. Still the nickel rich foam suggests that a modification of the infiltration procedure would be necessary to achieve a completely successful infiltration. It is also possible that the prolonged sintering time in combination with the extremely low gas pressure in the furnace has allowed the sample to sinter, and shrink a little bit more than expected.

Sample 3. Sintering: The sintering of sample 3 followed the same standard set up as previous samples and the result is also as good as previous samples. From the Time/Temperature/Vacuum-diagram (Fig.2) we find that the Time/Temperature relationship follows the expected program with almost perfect precision. The vacuum likewise behaves as might be expected: after it had reached the set point, it stayed fairly constant with a sharp dip during the binder's evaporation (burnout).

Sintering Sample 3.

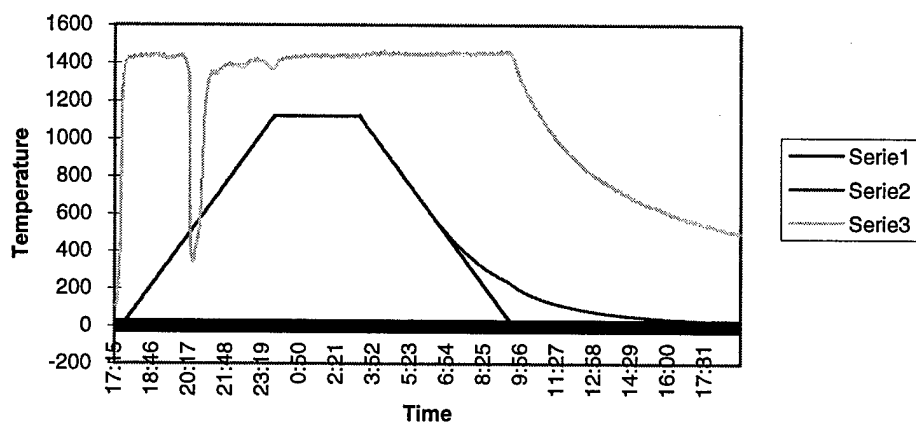


Fig.2.

Sintering of sample3. Temperatures in Celsius, "serie1" gives the temperature set point, "serie2" gives the actual temperature and although no scale values are given in the figure "serie3" indicates the vacuum. Notice the dip in the vacuum between 443°C and 586°C. Apparently, that is the interval where the binder evaporates under these circumstances. The fact that there no other dip is indicated verifies that no alloying elements are being evaporated.

Sample 3. Infiltration: To avoid the same problems as were experienced with the previous samples, some modifications of the procedure was necessary. The joints between the infiltration plates and the sample were powdered with some loose powder. If any vibration would separate the plates from the sample, the void would still be filled with RapidSteel powder thus ensuring free flow of the infiltrant. Since this powder was not weighed together with the plates and sample when the mass of infiltrant was calculated, and in order to assure that there would be enough bronze, 50g extra bronze was added to the calculated amount. To ensure that the nickel rich phases would melt and infiltrate with the rest of the infiltrant, a recommendation from [3] was followed and the temperature was ramped up at a rate of 120°C/h. The furnace was kept at infiltration temperature (1050°C) for 3hrs and lowered, as the previous samples, at a rate of 180°C/h.

This time infiltration was quite satisfactory apart from the fact that the color of the sample was not completely even, and that there still was small amounts of infiltrant remaining on the plates. Still, according to the calculation of the infiltration in [1] and [3], the amount of bronze infiltrated should equal 85% of the mass of the brown part. Since the mass of this brown part was 1360g, $\Rightarrow 1360 \cdot 85\% = 1156\text{g}$, and, $1360 + 1156 = 2516\text{g}$. Hence 2516g is the theoretical mass of the full density object. The actual mass of the infiltrated sample 3 is 2513g, that gives an infiltration success of 99.8%, which we consider satisfactory.

Similar to the previous sample, the offset and scaling factors were calculated. See table 1.

The Time/Temperature/Vacuum-diagram (Fig 3,) shows a stable behavior, where the temperature follows time according to program, and vacuum keeps around the set point.

Infiltration Sample 3

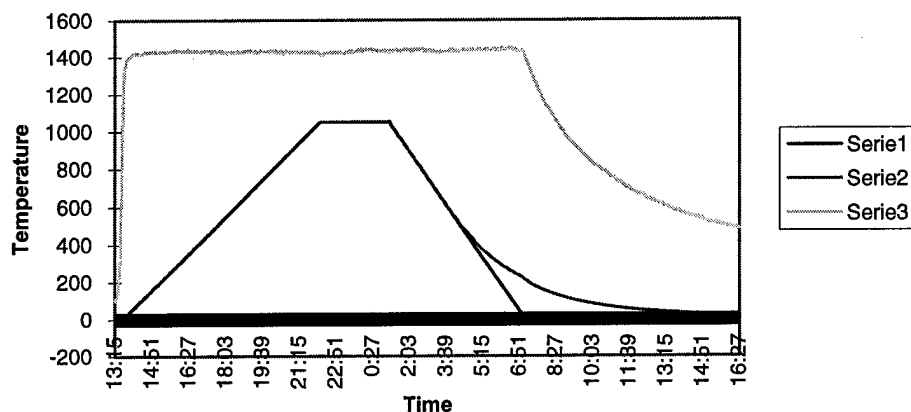


Fig.3. Infiltration of sample 3. Temperatures in Celsius, "serie1" gives the temperature set point, "serie2" gives the actual temperature and "serie3" gives the vacuum all identical to Fig.2. The decreased ramp rate has given a longer warm up time. The vacuum stays at the set point during the whole cycle, which verifies that there is no evaporation of any alloying components (or anything else).

Sample 3. Conclusion: The process used for sample 3 gives satisfactory results for DTM's RapidSteel 2.0 material and could be useful to manufacture functional molds.

Table 1.

	X offset	X Scale	Y offset	Y scale
Sample2	0.0070	1.019	0.0086	1.0133
Sample3	0.0041	1.0173	0.0070	1.0130
H2/N2*	0.1825	1.0072	0.1603	1.0001

**) Scaling and offset values for the conventional H₂/N₂ furnaces have been supplied by courtesy from DTM GmbH, Germany. All individual machines have different scale and offset values, especially between Sinterstation 2000 and 2500(+) there are big differences. In addition to that, comes the difference between individual furnaces. In this case however, all objects, Swedish and German, have been SLS processed on Sinterstation 2000s, and even with the individual differences accounted for, there still remains a significant difference in scaling factors. This must be referred to the difference in furnace processing. Apparently the shrinkage is larger with the used vacuum procedure. Among other things this means that the value of infiltration success in reality is higher than the calculated value of 99.8%.*

Conclusion and Further Study

This investigation has showed that it is possible to process DTM's RapidSteel 2.0 material to satisfactory objects in a vacuum furnace process. Little experience of this process has been accumulated so far, and more work is required to fine tune every aspect of a large number of variables. For example: it is likely that the prolonged dwell time at sintering temperature introduced in the sintering cycle for sample 1, in combination with low the gas pressure in the pores, (vacuum) could have led to higher shrinkage, higher sintering density and more closed pores which could not be infiltrated, which in turn led to the unevenness in color and the comparably large scaling factors in the infiltrated sample 3.

This effect could possible be turned into something very positive. By making use of the enhanced sintering of liquid phase sintering it could be possible to sinter full density objects in a single furnace cycle. During sintering the "liquid phase provides a high diffusivity pathway for atomic motion, and a strong capillary force that induces particle compression at point contacts" [4]. This phenomena continues until the connections between the pores are closed and the remaining pores are filled with furnace atmosphere, which is exerting a gas pressure and thus locking further pore closure. Since vacuum furnace atmosphere means virtually no atmosphere, nothing would fill the pores and nothing could lock the pore closure, thus it would be possible to reach full density.

Acknowledgments

We would like to thank Mr. Berndt Holmer, Mr. Gunnar Palm, and Ms Lena Thorsson, all from IVF, Stockholm, for their interest and good advice during the research and the work with this paper.

References

1. DTM Corporation "Guide to Materials: The Rapid Tool LR Process Using RapidSteel 2.0", (Draft), The Sinterstation Systems, DCN: 8001-10011, May 1998.
2. DTM Corporation "Material Safety Data Sheet: RapidSteel 2.0", DCN: 8001-20002, May 1998.
3. Nelson C, "RapidSteel 2.0 Mold Inserts for Plastic Injection Molding", DTM Corporation 1998.
4. German R.M. " Powder Metallurgy Science" Chapter 7, MPIF 1994.
5. ASM, Metals Handbook, Ninth Edition, vol. 7. "Powder Metallurgy", ASM International, 1987, pg. 345-346, 368-374.

MSOE TetraLattice™

"Applications and Simplified CAD Representation"

Vito R. Gervasi, Lisa M. Milkowski,
James V. Canino, & Rebecca J. Zick

Rapid Prototyping Center
Milwaukee School of Engineering

Abstract

Applications for the MSOE TetraLattice™ used for SFF structures are growing. The simplicity of the tetragonal lattice morphology makes this structure useful for composite and metal castings, gradient morphologies, conformal cooling & heating systems, transfer and filtering systems, rapid build style, and stress-reducing build style. As more applications emerge, the need for a simplified 3D CAD representation, with easily adjustable void-solid ratios, has become increasingly important. The volume was determined as a function of node spacing and node size in a simplified, minimal surface representation. Reducing the points required to define the lattice surface is key in reducing processing time and improving synthesis quality. The simplified CAD representation and mathematical model, used to determine percent volume, will be presented followed by TetraLattice applications.

Introduction

Unlike traditional material removal fabrication techniques, such as CNC machining, Solid Freeform Fabrication (SFF) is an additive process, starting with a void, and adding material one layer at a time to create a 3D object. CAD data is used to define the surface and interior of the solid 3D object making complex part geometries, as well as complex internal structures, possible and commonplace. No expensive patterns, molds, or parting-lines are required when SFF is used directly, making it a widely accepted, accelerated prototyping tool.

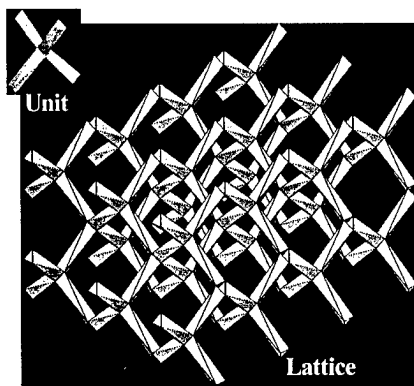


Figure 1. TetraLattice structure with repeating unit shown

With the additive nature of SFF it is possible to create structures never thought possible, such as complex, three dimensional lattice structures. TetraLattice, the topic of this paper, (TL, figure 1) is one of these structures made possible by SFF. TL is modeled after the molecular bond geometry found in diamond -*tetrahedron*- offering a simple repeating lattice unit, that lends itself to SFF. Arrays of TL units form complex structures as well as complex channels within objects, resulting in many useful characteristics. Based on this TL geometry -interconnected in all directions- several applications have emerged and more will likely follow. Initially, TL was used for metal and composite castings. Now, TL applications in the areas of gradient materials, conformal heating and cooling, transfer systems, and stress reduction are being discovered.

As new applications emerged, the CAD design of the early TL was limiting, for some uses, due to the large file size and square geometry. To reduce file sizes as well as improve the TL design, a completely new CAD representation was developed. The new CAD representation is a solid with a minimal number of triangles defining its surface. The volume ratio of TL solid to void space was determined using a tetrahedron breakdown, making this new representation better suited for gradient materials. The volume ratio is determined as a function of several variables related to node spacing and node size.

This paper will discuss three main topics, starting with a detailed description of the new, simplified TL CAD representation. Next, the volume ratio of TL versus Negative TL is represented mathematically and verified. Finally, six TL applications, some benefiting from the simplified CAD representation and volume model, will be discussed.

Simplified TL CAD Representation

Various methods can be employed to define a lattice structure for SFF. Masks could be used, changing masks for each layer until the lattice repeats. Another method would be to form a computer generated hatch within the parameter of the desired part. The hatch would change depending on the current layer. Yet another method is to form a solid three-dimensional model of the desired lattice structure which is boolean intersected with the desired CAD part resulting in lattice structure of the desired form. This portion of the paper will briefly describe several solid CAD representations and a new, simplistic CAD representation.

TL is based on the repeating crystallographic structure of diamond. The repeating or base unit of TL is made up of four “legs”, which are joined end to end at specific angles to form an intersection, or “node”. Therefore, the shape of the end face of the four legs will dictate the geometry of the intersection. The geometry of the leg also impacts computer file size, as different geometries require different number of facets to create a surface file (.stl format). The TL base unit could be defined utilizing at least four geometric structures: square, hexagonal, rectangular, or triangular as shown in Figure 2.

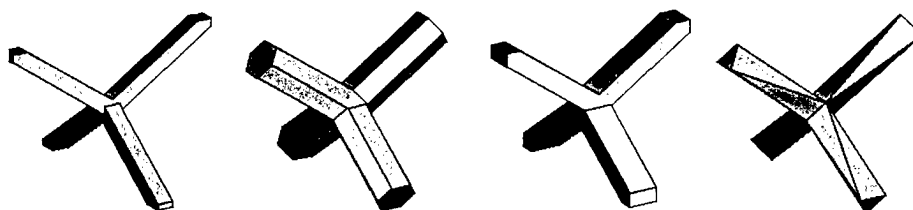


Figure 2. Four possible TetraLattice base unit geometries: square, hexagonal, rectangular, and triangular, respectively

Figure 3 shows the comparison of the number of facets required to define a base unit depending on the base unit geometry. It is shown that using triangular legs to construct the base unit will yield the smallest file sizes. The triangular geometry, shown in figure 2 uses four triangular legs, joining to form a regular tetrahedron node. Legs are twisted 60° to allow fields of units to join with minimal faceting. It should be noted that for certain applications a base unit created using a different geometry may be desired, however this paper will focus on the triangular format.

TL Volume Calculation Methodology

In many of the applications described later, it is beneficial to control the volume ratio of the TL volume to its void space volume. This section will focus on mathematically representing the volume of TL and TL void space. Two variables can be used to describe the volumes, the side lengths of a tetrahedron node, S , and the length of a leg, L . A base unit, created using triangles, is shown in Figure 4.

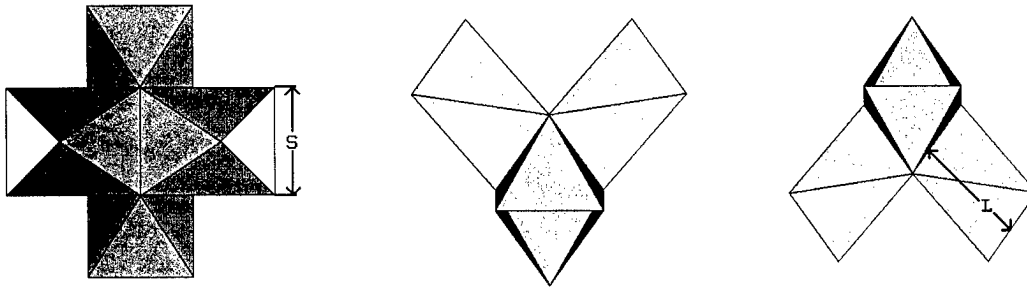
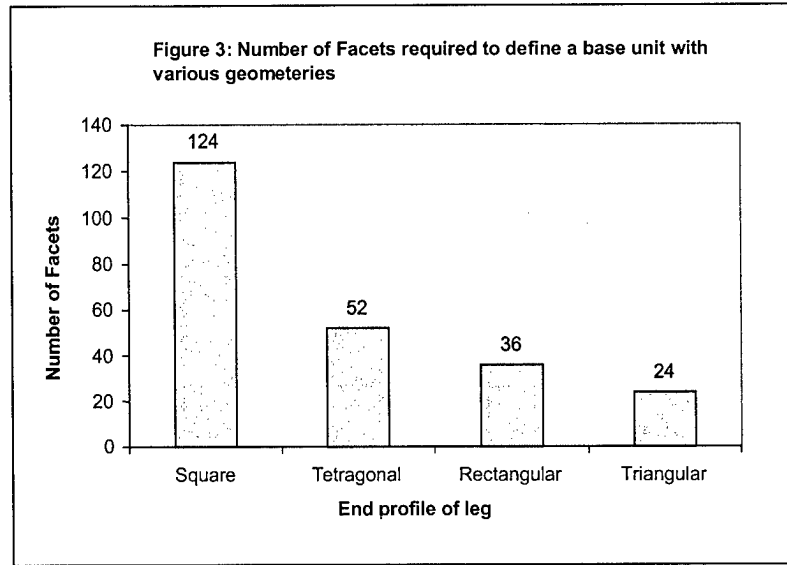


Figure 4: Top, right side, and front of a TetraLattice base or repeating unit. The side length, S , is shown on the top view and the leg length, L , is shown on the right side view.

TL Volume calculation

As stated before, the ends of the four legs join to form a regular tetrahedron node of side length S . The volumes of a regular tetrahedron and the four legs are required to find the volume of a base unit.

The regular tetrahedron belongs to all four legs; hence, one quarter of the tetrahedron volume can be assigned to each of the legs. The same argument can be applied to the other end of each leg. Therefore, $\frac{1}{2}$ of an intersection is assigned to each leg, and two intersections are assigned to a base unit.

The volume of a regular tetrahedron is

$$V_{tetrahedron} = \frac{S^3 \sqrt{2}}{12} \quad (1)$$

where S is the side length of the tetrahedron.

The height of the leg, L , is measured perpendicularly between the equilateral end triangles, as seen in Figures 5a and 5b. The leg is a triangular shaped column that twists from one end to the other. While the center points of the end triangles align, the ends are rotated 60° about the center of the leg, as can be seen in the end view in Figure 5c.

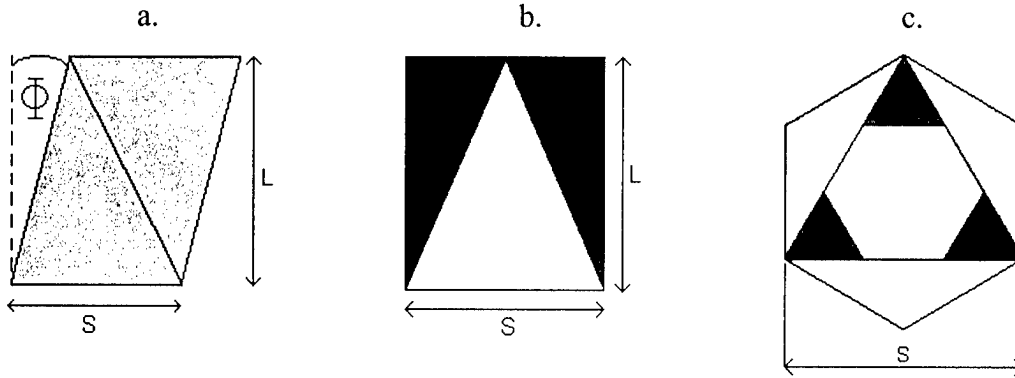


Figure 5: Illustrated is a triangular leg of TetraLattice. Variables, S and L , are used to describe its volume. a. Side view of leg. b. Front view of leg. c. End view of leg.

To find the volume of the TL leg, it was assumed that the leg was a hexagonal tube from which six triangular pyramids have been removed. The volumes of the hexagonal tube and the pyramids were found to be

$$V_{\text{hexagon}} = \frac{3S^2L}{2\sqrt{3}} \quad (2)$$

$$\text{and } V_{\text{pyramid}} = \frac{S^2L}{12\sqrt{3}} \quad (3)$$

The leg volume is $V_{\text{hexagon}} - 6(V_{\text{pyramid}})$ which reduces to

$$V_{\text{leg}} = \frac{S^2L}{\sqrt{3}} \quad (4)$$

As explained earlier the TL base unit volume is

$$V_{\text{TetraLattice_Unit}} = 2(V_{\text{tetrahedron}}) + 4(V_{\text{leg}}) \quad (5)$$

$$V_{\text{TetraLattice_Unit}} = \frac{S^3\sqrt{2}}{6} + \frac{4S^2L}{\sqrt{3}} \quad (6)$$

TL Negative Volume

TL occupies a certain percentage of an object's volume. In order to predict the percent volume a TL field will occupy, the space surrounding each base unit or the void space was mathematically characterized. This will be referred to as Negative TL. The geometry of a negative unit was found by enclosing a space with four base units. The geometry was checked by enclosing one base unit with four negative units. This assured that the spatial relationship between TL and Negative TL is one to one and that the geometry of the volume is correct.

The orientation of the TL legs (the 60° twist) causes the angle between side faces to change as the dimensions of S and L change. If the angle between faces of a tetrahedron is measured

from the center point then the angle (α) is a constant of 109.47° . If the legs were not twisted, measuring between the adjacent faces of each leg would also result in this angle. However, as the faces of the tetrahedron are extruded and rotated to form the legs, the angle measured between the side faces changes. The angle Φ (Figure 6) will reflect dimensional changes in both S and L. This relationship is shown in the following equation.

$$\Phi = \tan^{-1}\left(\frac{S}{2L\sqrt{3}}\right) \quad (7)$$

To find Θ , the angle between two adjacent faces, 2Φ is subtracted from α since both of the legs will be causing the reduction in α . This is shown in Figure 6.

$$\Theta = \alpha - 2\Phi = 109.47^\circ - 2 \tan^{-1}\left(\frac{S}{2L\sqrt{3}}\right) \quad (8)$$

Several dimensions of the TL base unit are necessary to calculate dimensions of the negative unit. These dimensions are shown in Figure 5 and the relationships to S and L are found by the Pythagorean theorem.

For simplicity, these new variables will be used in subsequent equations.

$$F = \sqrt{L^2 + \frac{S^2}{12}} \quad (9)$$

$$E = \sqrt{L^2 + \frac{S^2}{3}} \quad (10)$$

Several dimensions must also be obtained from the Negative TL unit. These are shown in Figure 8.

$$T = 2F \sin\left(\frac{\Theta}{2}\right) \quad (11)$$

$$B = \sqrt{F^2 - \frac{T^2}{4}} \quad (12)$$

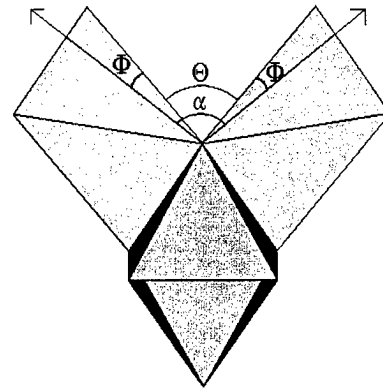


Figure 6: Illustration of TetraLattice base unit showing the relationship between various

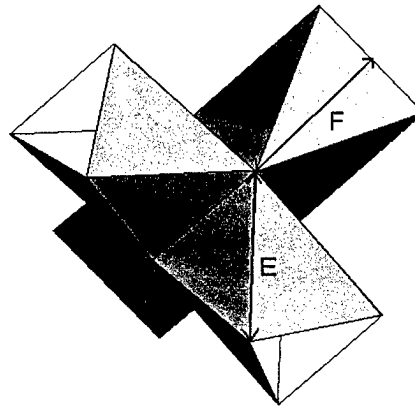


Figure 7: Triangular TetraLattice base unit with E and F shown.

The negative TL unit also has tetrahedrons as the nodes with “legs” connecting them. The legs have a different geometry than that of TL. The side length of the tetrahedron is T, so substituting into Equation (1) we find the volume of the node tetrahedron. Note that, there are two tetrahedron and 4 legs that make up each unit of negative TL.

T can be substituted for S in Equation (4) but the height of the leg is still needed. This height, H, can be calculated as the height of a tetrahedron composed of three isosceles triangles

for the sides, with symmetrical sides E and base side, T. Therefore the base is an equilateral triangle of side length T. The height can be found using the Pythagorean Theorem. To do this, the center to corner distance of the equilateral triangle measured along the angular bisector (R) is needed. This is simply,

$$R = \frac{T}{\sqrt{3}} \quad (13)$$

Therefore,

$$H = \sqrt{E^2 - R^2} \quad (14)$$

The negative TL leg volume differs from the TL leg volume by the formation of an additional wedge on each side face of the leg. The volume of the wedge is the volume of a pyramid, which reduces to

$$V_{Wedge} = \frac{BTS}{12} \quad (15)$$

Substituting into Equation (6) with H for L and T for S, and adding the wedge volume to each face, the leg volume reduces to

$$V_{Neg_Leg} = \frac{T^2 H}{\sqrt{3}} + \frac{BTS}{2} \quad (16)$$

Finally, the volume of the Negative TL unit is two tetrahedron and 4 legs resulting in the following equation.

$$V_{Negative_TetraLattice} = \frac{T^3 \sqrt{2}}{6} + \frac{4T^2 H}{\sqrt{3}} + 2BTS \quad (17)$$

Final Volume Calculation

Since the summation of TL volume with negative TL volume results in the total volume occupied by both, the following equation can be written:

$$V_{Total} = V_{TetraLattice_Unit} + V_{Negative_TetraLattice} \quad (18)$$

TL Volume Verification

The volume equations for both TL and Inverse TL were validated using a MATLAB program. The program allows the user to input the percent volume of TL desired, as well as the node to node distance (This distance is measured from the centers of the intersection node tetrahedra). Using an iterative solution method, the program determines the dimensions of S and L that are necessary to construct a TL field with the desired volume percentage. These dimensions were used to create a base unit. The base unit was multiplied and arranged to create a field. Several object geometries with known volumes were created. Using Magics RP software, these objects were intersected with the TL field. After the boolean intersection, the

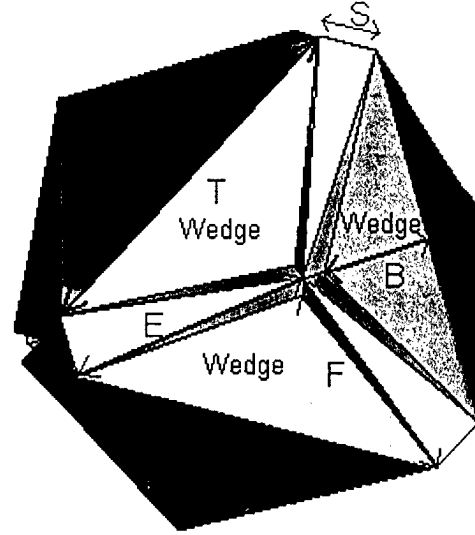


Figure 8: Illustration of negative or void TetraLattice

remaining part was a TL field having the shape of the object. The volume of this TL object was estimated in software and divided by the volume of the original part. The division resulted in a percent volume of TL for this test. This calculated percent volume was compared to the percent volume input into the MATLAB program.

This test procedure was performed using several object geometries. Five volume percentages were also tested. Results shown in table 1 indicate that the percent difference between the input amount of TL and the actual measured amount varied between 0.0% and 2.1% (Table 1). This was dependent on the orientation of the TL in the object and on the iterative method used. The MATLAB program was written for calculation speed, rather than the highest accuracy. This could be changed depending on the need for accuracy in the application.

Volume Percent desired	Volume Percent achieved	Percent difference
10.00	10.20	2.00
20.00	20.41	2.10
40.00	40.00	0.00
60.00	60.15	0.25
80.00	80.09	0.11

Table 1: Data for Varification of TL equations

TL Applications

Net-shape composite and metal castings were the original applications of TL. Since then, many additional applications have emerged, such as: gradient morphologies, conformal cooling & heating systems, micro lattices, transfer and filtering systems, fast build style, and stress reducing build style. Benefits of TL vary depending on the application. Some applications require a fine, minimal lattice volume with open communication throughout the lattice void space. Others require a TL void where the TL is completely interconnected and allows fluid flow in a controlled yet continuous manner. Although the new simplified TL CAD representation benefits most TL applications the goal of this portion of the paper is to describe where this lattice morphology—*defined using any of the representations*—is useful to the SFF community.

Net-shape Composites and Castings

As mentioned previously, net-shape composite and metal castings were early applications of TL.^{1,2} The three-dimensional TL structure is generated inside a hollow shell (the desired pattern geometry) typically using the stereolithographic process. TL legs are thin, providing internal structure for the SLA skin, while adding minimal overall material to the low-density pattern.

Patterns with this unique internal structure currently have two particular applications including rapid composite prototyping and investment casting. Rapid composite prototyping is a process wherein the TL void space is filled with reinforced plastic to form a composite with enhanced mechanical properties. When TL is used for composite casting, TL patterns have three unique characteristics: (1) ease of uncured photopolymer drainage (2) ease of filling with viscous reinforcement plastics, and (3) near-isotropic physical properties after filling.

TL-filled investment casting patterns offer foundries three beneficial characteristics: (1) quick, complete drainage of photopolymer (2) reduced danger of refractory shell cracking and

(3) minimal ash content after burn-out. SLA TL patterns are especially useful when large, thin walls are required. Wall thicknesses of less than 0.040 inches will drain sufficiently for investment casting.

Gradient Materials

Functionally gradient materials³ (FGMs) have enormous potential in the industrial world today. The ability to fuse two entirely different materials together to form one hybrid material results in the possibility of forming a vast range of new engineering materials. With this technology, engineers can tailor properties within a mechanical component to handle a full spectrum of application requirements, without changing design geometry. FGM's transform from one material (part A) to another (part B), unlike traditionally bonded materials having a distinctive –typically planar– seam.

Gradient TetraLattice^{4,5} (GTL) is a three-dimensional FGM morphology, transforming from one material to another, in a controlled manner (this morphology can be likened to M.C. Escher artwork in three dimensions). To create Gradient TL, spacing between standard TL units can remain constant while the branch thickness is increased in a controlled manner, as shown in Figure 9.

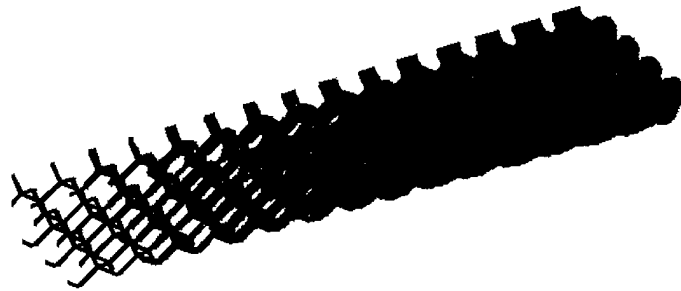


Figure 9: Gradient TetraLattice morphology

This controlled increase in branch thickness results in a proportional change in volume percentage of material combinations. In theory, this volume percentage will transform from 100 percent of material A to 100 % of material B, at any rate, in any direction. With Gradient TL, the transformation is three-dimensional and mechanically inter-linked. GTL becomes two TL with varying branch thickness. Part A is the negative of part B. Another benefit of GTL is the ability to transition from one material to another through a series of layers. Figure 10 illustrates the first Gradient TL sample.

Conformal Cooling & Heating

With the layerwise build mode of SFF arises the opportunity to produce cooling and heating systems conformal to complex contoured surfaces, where heat exchange is critical. Applications such as injection molding, where a large percentage of cycle time is spent cooling, benefit significantly from conformal cooling channels.^{6,7}

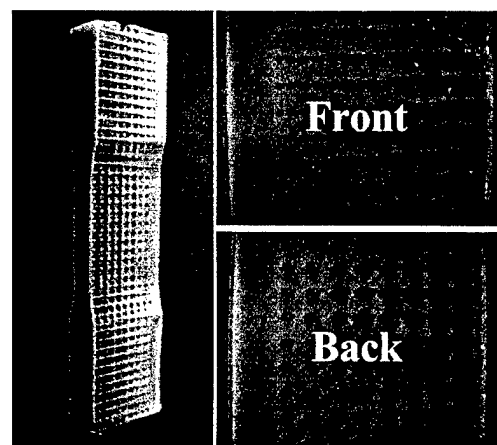


Figure 10: Photopolymer-glass reinforced epoxy gradient TL

TL can be used for conformal cooling and heating as illustrated in figure 11. In this case a TL void is formed to create the conformal fluid channels. Interconnections between TL nodes make this morphology useful when deep cavities or tall irregular features are present. Leg angles induce beneficial turbulent flow resulting in improved convective heat transfer within the fluid. To ensure even flow over a complex surface or variable heat removal at various locations node size or depth of the TL field can be tuned. Normally the stair-stepping effect of SFF is undesired; here it is beneficial for conformal cooling and may be increased to induce further turbulent flow.

Transfer and Filtering Systems

TL can be useful for transfer applications where entities (heat, electrons, ions, molecules, other) need to be moved efficiently from one object to another in a controlled manner. The basic concept here is to intermesh two TLs to form two distinctly separate objects separated by a thin wall. The two objects could be liquid, solid, or gas and the thin wall could be a solid, liquid, gas or vacuum. The simplest approach to describe TL of this form would be the heat exchanger as illustrated in Figure 12. In the case of a heat exchanger two intermeshing TL voids are separated by a thermally conductive wall. The wall transfers heat from one TL void fluid to the other. The TL flow path is non-linear and can be optimized to induce turbulent flow.

Another application, where the wall separating the two TL channels is a liquid and the TL channels become a solid, would be for a battery cell. One TL solid becomes the anode, the other the cathode and the liquid wall would be an electrolyte.

Listed below are other possible applications of TL based transfer or filtering systems:

- Hemodialysis (A semipermeable membrane separates the two hollow TL regions. In one TC chamber flows the patient's blood, while the other chamber contains a dialysate consisting of water and solutes.)
- Anatomical Micro-circulation modeling (A porous frame work separates the two hollow TL regions.

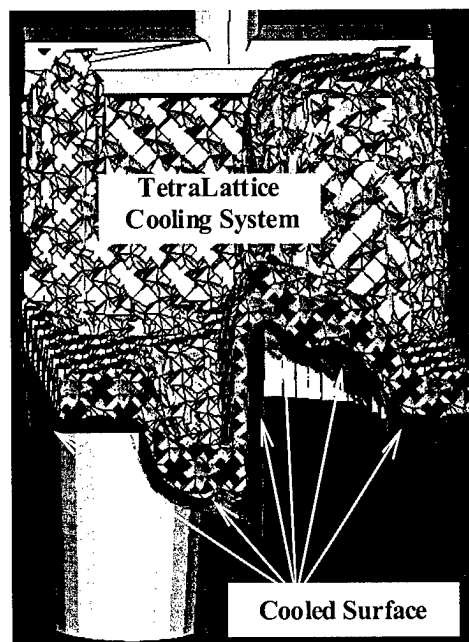


Figure 11: Illustration of Conformal TetraLattice Cooling

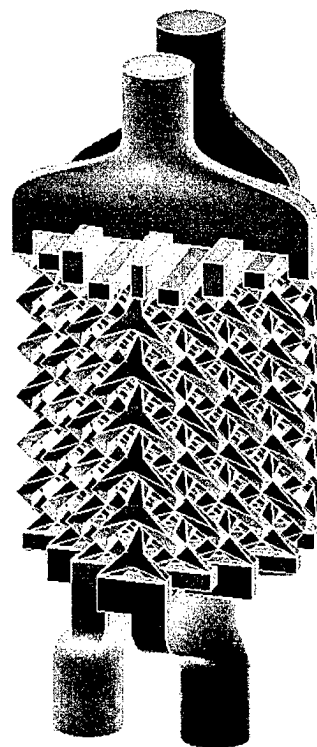


Figure 12: Possible orientation of a liquid to liquid heat exchanger using TetraLattice. The two shaded regions represent the fluid within the heat exchanger (illustration by Adrian Sikorski).

One TL chamber represents the arterial system in anatomical tissue and the other TL chamber represents the venous system. The separation region or porous region represents the organ bank or tissue specific cells.)

- Filters/separation devices (A porous wall separates the two hollow TLs)

Stress Reduction

In SFF processes where layer-to-layer stresses are locked into objects, resulting in warpage or deflection, TL may be beneficial. This type of warpage is typically due to shrinkage induced stress. When building a solid part, a new layer is added on top of a solid layer and the new layer has a tendency to shrink during solidification and cooling while the previous layer is stable. The result is a planar stress, locked into the new layer. If more layers are added the stress becomes so great that without sufficient support the part will curl or warp. One approach to reduce this stress is to build the part using an array of columns that are independent of one another. The shrinkage is held locally, in the column cross-section, and the stress lines, formed across a large cross-sectional area, are discontinuous. The main problem with building a part consisting of columns is the discontinuity in the X and Y directions (Z being the build direction.) If one TL or two intermeshed TLs are used to fill the desired volume of the object the result will be, in effect, intertwined columns. The cross-section of one layer will be significantly discontinuous. Thereby, breaking the lines of planar stress, but still keeping the part as one entity enclosed by an outer skin.

Build Time Reduction

Quite often rapid prototyping requires a part that will not be used for functional testing nor secondary operations. In many cases the part will be used only as a visual model. In this case a TL internal structure can be used to shorten build time. Stereolithography parts produced with "thick skins" (0.045 inch) often take less than half the time to build as an identical solid model⁸. The option to solidify the part, for improved functionality, via the rapid composite process remains, resulting in a much more efficient and effective usage of RP equipment.

As SFF continues to advance with larger and smaller size capabilities, expanded material capabilities, and multiple material capabilities the aforementioned applications will advance and new applications will likely emerge. SFF enables more than unique objects to be produced —*SFF enables unique objects with complex, functional internal features to be produced*— quite often with negligible added cost.

Conclusions

A new TL CAD representation was developed for faster computing and reduced human intervention. The new representation reduced file sizes and computer processing time significantly when compared to previous CAD representations. A mathematical model of the volume for the new TL CAD was determined. The ability to easily specify volume ratios in gradient TL applications is important and was accomplished and verified. Applications of TL are expanding into unforeseen areas beyond original applications of composite and metal

castings to gradient morphologies, conformal cooling & heating systems, transfer and filtering systems, fast build style, and stress reducing build.

Acknowledgments

We gratefully acknowledge the support of the National Science Foundation (REU program – “Undergraduate research in solid freeform materials and technology - #EEC-9619715)

The authors would like to thank Sheku Kamara, Matt Panhans, Robert Crockett, Christopher Kreuser, Doug Cook, Vadim Pikhovich, Darius Daruwala, Jesse Upp, Steven Shaffer, John McCray, and Adrian Sikorski of the Milwaukee School of Engineering for efforts in technical assistance and application development.

Special thanks to the Rapid Prototyping Consortium members for their involvement in this and other applied research.

References

1. Gervasi, Vito R., Dr. Daniel Brandt, Steven D. Shaffer, King Lim, "TetraCast SLA Build Style," International Conference on RP, 1997, pp 309-317
2. Gervasi, V. "Net Shape Composites using Stereolithography TetraCAst Build Style", Solid Freeform Fabrication Symposium Conference Proceedings, August 1997, Austin, Texas.
3. Holt, J. Birch, Mitsue Koizuma, Toshio Hirai, Zuhair A. Munir, A. "Functionally Gradient Materials", American Ceramics Society, 1993, chaps 1 and 2.
4. Gervasi, V., R.S. Crockett, "Composites with Gradient Properties From Solid Freeform Fabrication", Solid Freeform Fabrication Symposium Conference Proceedings, August 1998, Austin, Texas
5. Crockett, R.S., V.R. Gervasi, "Gradient and Discrete Region Composites Produced by Solid Freeform Fabrication Techniques", Materials Research Conference Proceedings, November 1998
6. Sachs, Emanuel, Samuel Allen, Honglin Guo, James Banos, Michael Cima, James Serdy, and David Brancazio, "Progress on Tooling by 3D Printing; Conformal Cooling, Dimensional Control, Surface Finish, and Hardness," 1997 SFF Symposium Proceedings pp 115-123
7. Gervasi, V., Christopher J. Urban, Steven E. Gerritsma, "Cooling Configurations For Rapid Tooling -a Comparison Study," SFF Symposium Proceedings, August 1999
8. Kamara, Sheku, Interview on TetraLattice Performance, May 1999

Refrigerative Stereolithography for Support-Free and Accurate Fabrication

Akiya KAMIMURA, Tamotsu MURAKAMI and Naomasa NAKAJIMA

Department of Engineering Synthesis
Graduate School of Engineering
The University of Tokyo
Hongo 7-3-1, Bunkyo-ku, Tokyo 113-8656, Japan

ABSTRACT

A "refrigerative stereolithography" process is presented in this paper. In this process, a photopolymer resin for one building layer is supplied in a liquid state and cooled to become gel state before photopolymerization by laser. After repeating this process for all layers, a fabricated object is obtained by heating, melting and removing the non-photopolymerized resin from around the object. Since the object is fabricated in gel state resin, support structures are unnecessary and distortion by photopolymerization is reduced. A method of restraining surplus growth, which is caused by the overcuring of the bottom surface of solidified parts, is also proposed. The effectiveness of the method is confirmed by fabrication experiments using a prototype machine.

INTRODUCTION

In conventional stereolithography, support shapes are necessary for accurate fabrication. The design of the support shapes is currently performed automatically by software; however, users must remove them manually after fabrication and this takes much time and effort. Furthermore, it is difficult to fabricate complicated objects that include jointed structures or any other assembled structures, because support shapes, in these cases, are difficult to remove. Support shapes are one of the factors preventing the fabrication of objects with a high degree of freedom. Also, in stereolithography, since a solidified layer must be connected in principle to the previous layer, excessive exposure is needed to solidify the resin layer beyond one layer thickness [1]. Therefore, surplus growth caused by overcuring occurs at the bottom surface of the solidified layers and leads to a dimensional error in the height direction [2]. The objective of this paper is to propose a new stereolithography method referred to as "refrigerative stereolithography" to overcome the problems described above, and to describe the effectiveness and possibility of the method on the basis of fabrication experiments using a prototype machine.

REFRIGERATIVE STEREOLITHOGRAPHY

The refrigerative stereolithography fabrication process is shown in Figure 1. In this process, photopolymer resin is supplied in a liquid state on a platform for one layer thickness and flattened at first (Figure 1(a)), then rapidly cooled to turn to a solid state (Figure 1(b)). The resin surface is selectively exposed using a laser beam to solidify the photopolymer resin (Figure 1(c)), and then the platform is lowered by one layer thickness (Figure 1(d)). After repeating these processes for all layers, a solid block which contains the target object inside is removed from the platform, and by heating, melting and removing the non-photopolymerized resin remaining around the object (Figure 1(e)), the desired product is obtained (Figure 1(f)). During steps (a) through (d) in Figure 1, as the solidified parts cured using a laser beam are completely supported

by non-photopolymerized resin, there is no need for supports for these parts. The main advantages of refrigerative stereolithography are as follows.

1. There is no need for support structures during the part building process.
2. The fabrication of the objects with a high degree of freedom such as jointed structures is available.
3. An accurate resin surface is possible because there is no surface tension when the resin is used in the liquid state.
4. Additional mechanical treatments on the resin surface are possible since the resin surface is in a frozen solid state [3].

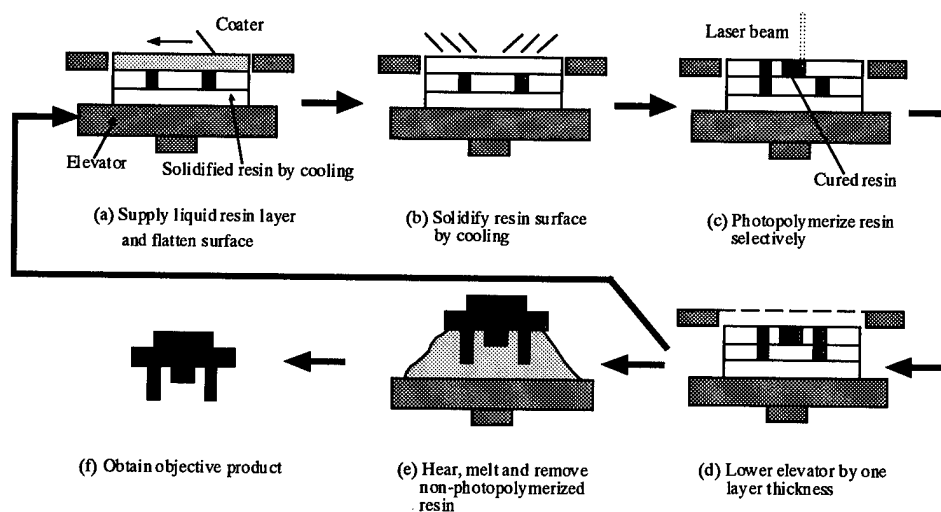


Figure 1: Process of refrigerative stereolithography

RESIN FOR REFRIGERATIVE STEREOLITHOGRAPHY

The photopolymer resin used in the refrigerative stereolithography process is required to be in a liquid state with a low viscosity while it is supplied at a temperature above but as close as possible to room temperature. In addition, it is required to be in a solid state for supporting the cured parts at room temperature. Therefore, we selected a new type of resin that exists in a gel state at room temperature but turns to a sol state at about 80°C. This photopolymer resin, ST1214-LW25, is composed of two ingredients, commercial urethane-acrylate photopolymer resin and sol-gel changeable resin. The resin changes phases, from gel to sol or from sol to gel, very sharply in a narrow temperature range. The gel strength at room temperature is very important for preventing the deformation of cured resin layers. The resin ST1214-LW25 has the gel strength of 600kPa; this is sufficient for restraining the deformation of the solidified parts as supports.

In the refrigerative stereolithography fabrication process, the heated sol-state resin is supplied onto the surface of the cooled gel state resin. Therefore, if the gel-state resin surface in the previous layer is melted by the heat from the heated sol-state resin, cured parts may move while recoating or deform due to the heat. To confirm how the temperature of the resin surface

changes during recoating, we carried out some experiments. In these experiments, as shown in Figure 2, two small thermocouples were placed on the resin surface in the building area separated by 2cm, and the temperatures at the position of these thermocouples were measured. The resin was manually supplied by a metal blade which was heated to 110°C, and the resin surface was cooled to room temperature by a fan. Table 1 lists the experimental conditions. The results are illustrated in Figure 3. From the results, it is clear that the temperatures of the two points on the resin surface drop slightly after the resin is supplied, and that about 20 seconds is needed for the supplied resin to cool down to room temperature. The highest temperature of the thermocouple (a) is about 60°C, which is below the phase change temperature of the resin ST1214-LW25. Therefore, during the process of resin supply there is no possibility of cured part movement or deformation.

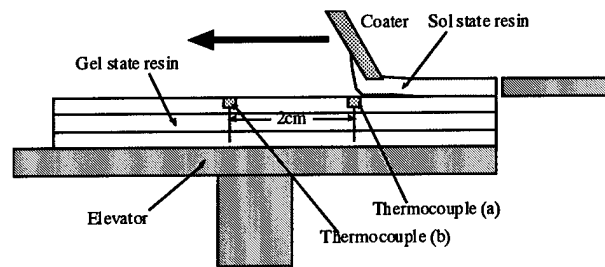


Figure 2: Schematic of experiment for measurement of resin surface temperature while recoating

Table 1: Conditions of experiments for measurement of resin surface temperature

	Data
Recoating speed [cm/sec]	8
Layer thickness [μ m]	100
Blade temperature [°C]	110
Resin temperature [°C]	100
Circumstance temperature [°C]	27

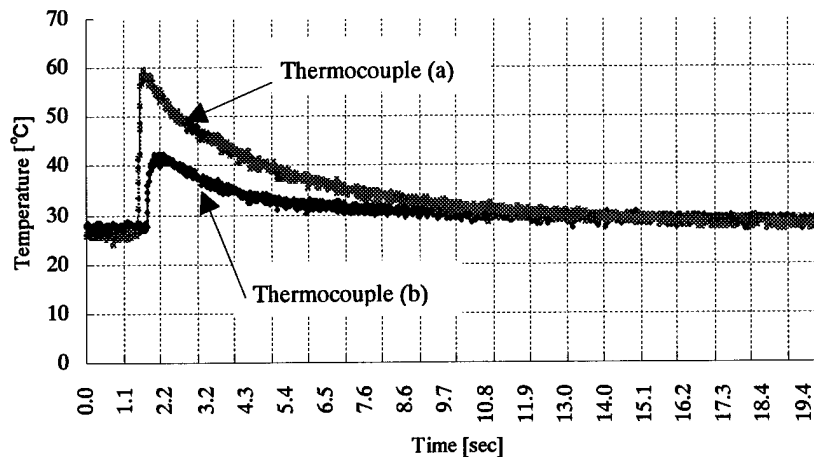
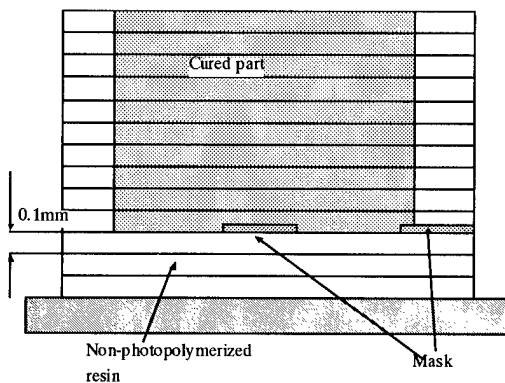


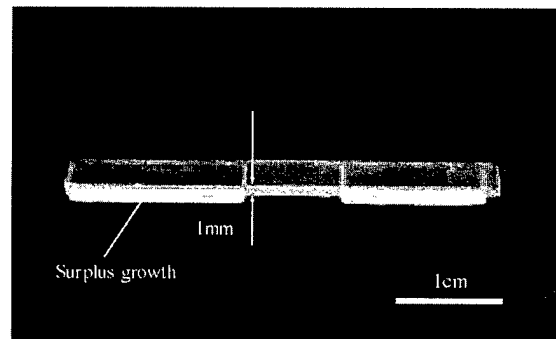
Figure 3: Temperature vs time during recoating process

NEW METHOD FOR RESTRAINING SURPLUS GROWTH

In the stereolithography fabrication process, since a solidified layer must be bonded to the previous layer, excessive laser exposure is needed to solidify the resin beyond one layer thickness. Therefore, surplus growth caused by the overcuring occurs at the bottom surface of the solidified layers and leads to a dimensional error in the height direction. Refrigerative stereolithography makes it possible to fabricate the assemblies in a single process, therefore accurate clearance between each individual component becomes important. To build clearances accurately, we propose a new method of drawing masking layers on the resin surface which intercept surplus laser light. Experiments were carried out to verify the effectiveness of this method. In these experiments, as shown in Figure 4(a), the masking layers were drawn manually with a white pen for masking directly on the resin surface only once at the bottom layer of the desired product. The resin for one layer of thickness of $100\mu\text{m}$ is supplied and then cured by the laser beam. After repeating this process ten times, the fabricated part shown in Figure 4(b) was obtained. Figure 4(b) shows that there is no surplus growth at the masked regions and the thickness there is just 1mm as measured by a micrometer. Also, the bottom surface at the masked regions is flatter than those of objects produced using conventional stereolithography.



(a) Schematic of masking experiment



(b) Fabricated object

Figure 4: Experiment for surplus growth

PROTOTYPE MACHINE FOR REFRIGERATIVE STEREOLITHOGRAPHY

A prototype machine based on refrigerative stereolithography and the new masking method was designed and produced. In designing the prototype machine, the following elements were examined.

Laser and scanning mechanism

In the prototype machine, a 40mW He-Cd laser(325nm) is used. The laser beam derived from the laser source is reflected by four sets of optical mirrors and then focused on the resin surface by an optical convexo-plane lens which is placed on a carrier equipped with the XY-plotter. The XY-plotter mechanism works to scan the laser beam across the resin surface. The resolutions in the X and Y axes of the XY-plotter are $10\mu\text{m}$ and $25\mu\text{m}$ respectively and the

iteration accuracy of the two axes is approximately $\pm 100\mu\text{m}$. The power of the laser beam focused on the resin surface is controlled by an AOM (audio optical modulation) device, while in conventional machines it is used to shut off the laser beam.

Resin supply unit

The ST1214-LW25 photopolymer resin currently used in our system is stored in a heated resin tank and led to the resin supply unit through a heated pipe. The amount of resin being supplied at any one time is controlled by an electric valve which is attached to the resin supply unit. Since the resin tank is located at a position higher than the resin supply unit, no special pump is required. The resin supply is performed by a coater which is connected to the XY-plotter carrier by a magnet only when the resin is supplied, and detached after the recoating process. Figure 5 schematically shows the process of resin supply. All of the components used for the resin supply are heated to 100°C and maintained at that temperature.

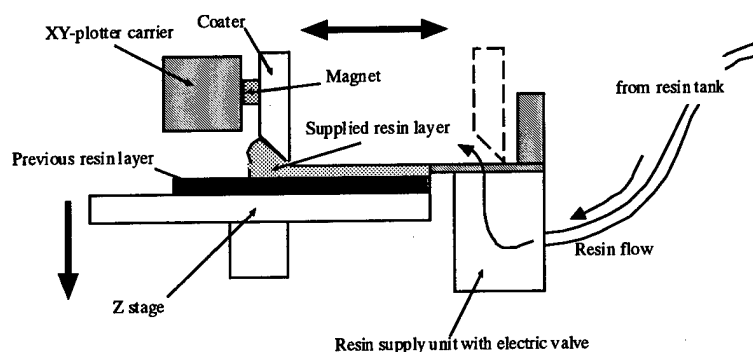


Figure 5: Schematic of resin supply process

MECHANISM FOR DRAWING MASK

The masks for intercepting the surplus light from upper layers are drawn by an inkjet head, which is located below the XY-plotter carrier and moves with it. The inkjet head has a nozzle $40\mu\text{m}$ in diameter. Ink dots are discharged from the nozzle by the vibration of a metal plate connected to a piezo actuator. The diameter of the ink dot when it drops onto the resin surface is approximately $200\mu\text{m}$. Therefore, it is currently impossible to mask areas that are smaller than the ink dot, such as a line of width of $150\mu\text{m}$.

SLICE DATA OF PROTOTYPE MACHINE

Slice data of a 3-D object is obtained by the following processes. At first, a solid model of the object is designed in a 3-D CAD system and converted into a STL file. Next, the STL file is loaded into a developed slice software by which the STL file is "sliced" into a series of slice datum for the prototype machine. The slice data is a bitmap format file for each one of the layers, compressed by a run length method. It also consists of information such as the object sizes, the resolution of one dot which is equivalent to the minimum building unit size, and the masking

data.

POSTPROCESSING OF FABRICATED OBJECT

After the fabrication, the obtained solid blocks are immersed in toluene solvent in an ultrasonic cleaner to rinse and remove the non-photopolymerized portions. After that, the object is post-cured using a UV lamp and the desired product is obtained.

Figure 6 is a configuration of the experimental prototype machine. The specifications of the prototype machine are listed in Table 2.

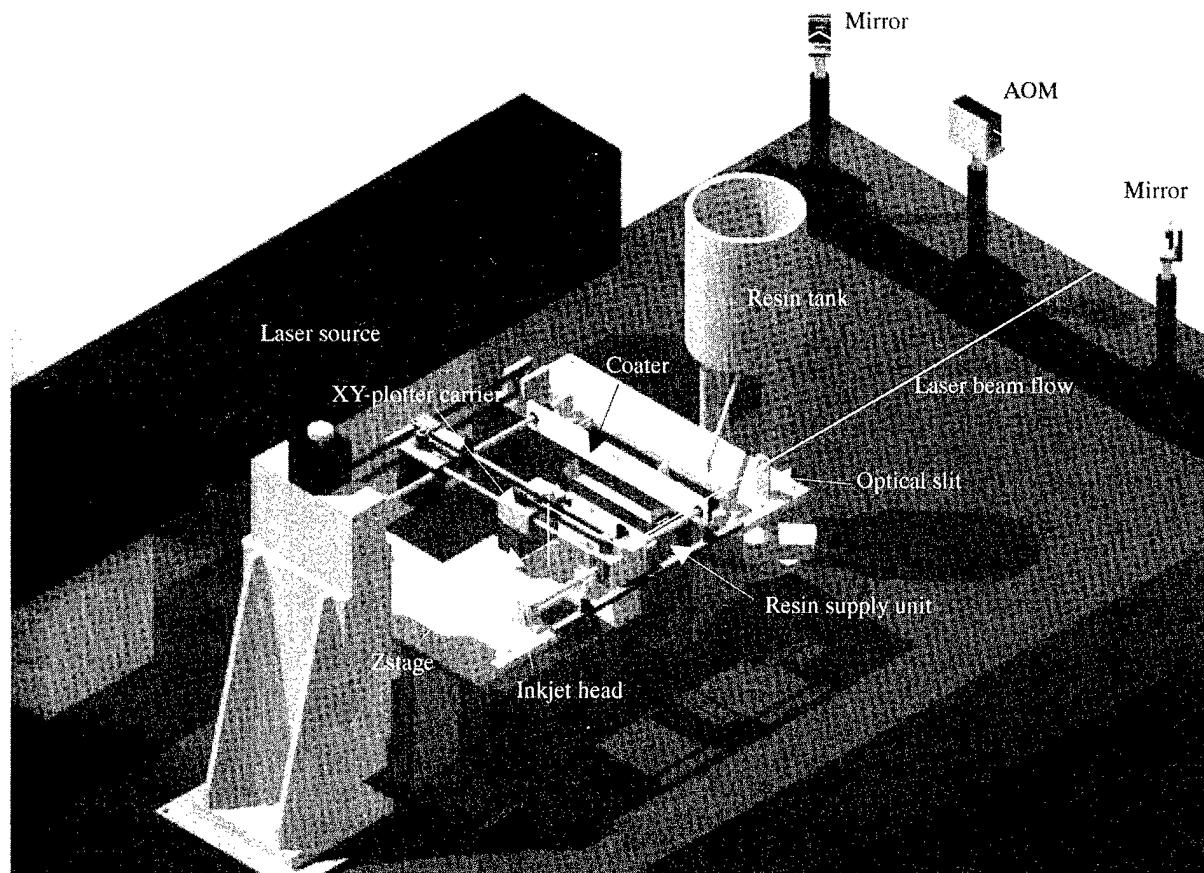


Figure 6: Configuration of designed and produced prototype machine

FABRICATION EXPERIMENT

To confirm the effectiveness of the prototype machine based on refrigerative stereolithography and the masking method, we carried out fabrication experiments. The main objective of these experiments was to attempt to fabricate assemblies which contain small, accurate clearances between individual components. Figure 7 shows a designed sample model which contains two individual components, and the clearances between them are 100 μ m in the height direction. The plate located in the middle of the object can rotate around the shaft. The

clearance between the shaft and the plate is 200 μ m. The parameters for the fabrication experiment are listed in Table 3.

RESULTS AND DISCUSSION

Photographs of the object fabricated in the experiment above are shown in Figure 8. From these photos, it is verified that the clearances between the two components in the height direction were accurately fabricated and the plate in the middle could be turned smoothly around the shaft. The clearances between the top of the plate and the casing part, and between the bottom of the plate and the casing part are 105 μ m, and 106 μ m, respectively. The fabricated object is colored which is due to residual inks from the masking layers. Since commercial pigment colored ink is currently used, there are some problems with the reflection and penetration of light, and also the objects lose their transparency. Each mask is drawn three times at the same place on the resin surface, so as to block the penetration of light. However, this causes another problem in that it increases the mask thickness. To avoid this problem, we plan to use particulate oxidized titanium as the ink, which has excellent transparency and blocking capability of UV light.

Table 2: Specifications of produced prototype machine

Laser	He-Cd, 40mW, 325nm
Laser beam power control	AOM
XY scanning of laser beam	XY-plotter Resolution X 10 μ m, Y 25 μ m Iteration accuracy \pm 100 μ m Maximum scanning speed 50cm/sec
Z feed of elevator	Z stage with stepping motor Resolution 1 μ m Iteration accuracy \pm 10 μ m
Maximum work size (X,Y,Z)	120, 120, 100 mm
Photopolymer resin	ST1214-LW25
Inkjet head	One nozzle, 40 μ m diameter

Table 3: Parameters for fabrication experiment

Photopolymer resin	ST1214-LW25
Resin supply temperature	100 °C
Layer thickness	100 μ m
Laser power	3 mW
Scanning speed	30 mm/sec
Scanning interval	0.1 mm
Object size	9 \times 28 \times 5.2 mm

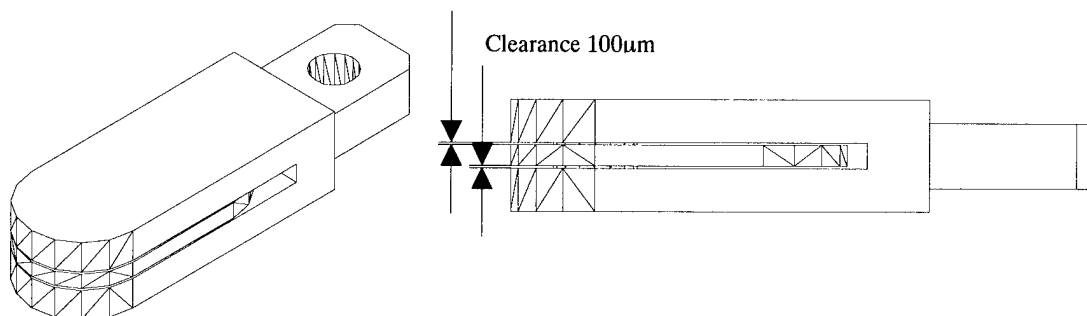


Figure 7: Designed 3D-CAD model

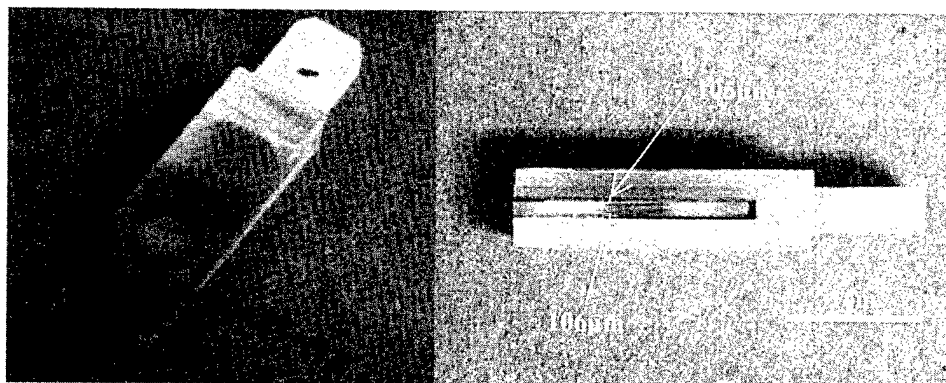


Figure 8: Fabricated object

CONCLUSIONS

1. Refrigerative stereolithography and a new method for masking the light from upper layers to restrain surplus growth and improve resolution in the height direction were proposed.
2. A prototype machine using the above methods was produced.
3. The effectiveness of the refrigerative stereolithography and the new masking method were confirmed by fabrication experiments.

REFERENCES

- [1] P. F. Jacobs, "Rapid Prototyping & Manufacturing Fundamentals of Stereolithography," Society of Manufacturing Engineers, (1992).
- [2] T. Watanabe, A. Matsumura, and T. Ukachi, "Study on Spectral Sensitivity of Resins for Stereolithography," Proc. of RadTech Asia'95, Guilin, Nov. 20-24, (1995), pp.301-306.
- [3] A. Kamimura, T. Murakami and N. Nakajima, "Research on Refrigerative Stereolithography," " Proc. of RadTech Asia'97, RadTech Japan, Yokohama, Nov. 4-7, (1997), pp.614-617

AN EXPERIMENTAL AND ANALYTICAL STUDY OF ICE PART FABRICATION WITH RAPID FREEZE PROTOTYPING

Wei Zhang, Ming C. Leu, Guanghua Sui, Zhiming Ji

Department of Mechanical Engineering

New Jersey Institute of Technology, Newark, NJ 07102

E-mail: zhangwei@oak.njit.edu

ABSTRACT

Rapid Freeze Prototyping (RFP) is a new solid freeform fabrication process that builds an ice part by rapidly freezing water layer by layer. In this paper, we will present our recent progress in the development of this novel process. An experimental system has been built for conducting the research. It consists of an XY-table and Z-stroke driven by micro-stepping motors and a water dispensing and deposition subsystem which incorporates a solenoid valve and a syringe pump placed inside a freezer. Simple heat transfer analysis is made to help select proper values of process parameters and predict part building failures. Example ice parts have been successfully built with this process. Key factors of this freeform fabrication process are identified.

KEYWORDS

Solid Freeform Fabrication, Layered Manufacturing, Rapid Freeze Prototyping, Ice Patterns

1. INTRODUCTION

The solid freeform fabrication processes which deposit material directly to build parts through thermal extrusion or drop-on-demand ejection play an important role today in the SFF research field and equipment market. These processes include Fused Deposition modeling (FDM), Shape Deposition Manufacturing (SDM), Multi-Jet Modeling (MJM), etc. Material diversity, relative cleanness, and cheap material and equipment cost are strengths that contribute to their success. For example, the building process usually only involves material melting /solidifying and thermal extrusion without substantial chemical reaction and laser processing. This means more applicable building materials and lower cost. Accordingly, these processes can more easily be used for developing desktop rapid prototyping systems. However, most of these processes also have drawbacks and could further benefit from improvements such as surface smoothness and build accuracy, reduction of building time and thermal stress for large solid parts, and adaptability of process parameters to part building quality. Due to various technical limitations of material flow control such as surface tension, nozzle dragging effect, start-stop response delay, etc., part building accuracy and surface smoothness of some of these processes cannot compete with laser based processes. On the other hand, the part building quality is sensitive to the change of process parameters because these processes are heat based and are sensitive to the amount of heat and the condition of heat consumption. Any change in process parameters, such as layer thickness and depositing speed, affect not only the total heat which needs to be consumed but also the condition of heat consumption [1-4].

The concept of Rapid Freeze Prototyping (RFP) process was recently developed by us to address the above issues. It is a novel SFF process that makes a part by selectively depositing and freezing the material (water or brine) layer by layer. Figure 1 [4] illustrates the process of Rapid Freeze Prototyping. In this process, the building environment is kept at a temperature

below water's freezing point (-20°C in our experimental system). Water is extruded or ejected from the nozzle and deposited onto the previously solidified ice surface. The newly deposited water is cooled by the low temperature environment through convection and by the ice surface of the previous layer through conduction. As a result, the deposited material freezes rapidly and binds to the previous layer, forming a new layer of the part. The part is built with water (pure or with some agent) and the support, where necessary, is built with either brine or water of a different color. The nozzles and feeding pipes are kept at certain temperatures to pre-cool water close to its freezing point but remaining in the liquid state so that the material can flow freely. During the deposition process, the ratio of material flow rate in continuous method or liquid droplet frequency in drop-on-demand method versus the nozzle moving speed is set according to predetermined layer thickness and line width.

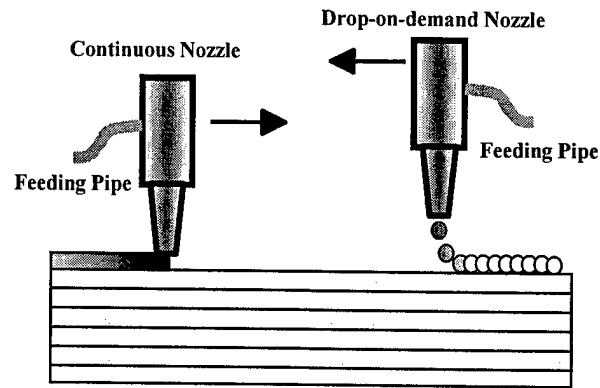


Figure 1. Principles of Rapid Freeze Prototyping

The advantages of this novel process, including cleanness, lower cost, potential better surface finish and building accuracy, and ease of stress compensation and potentially faster building speed, were discussed in [3-4]. The potential applications of this process include part design visualization and rapid tooling such as RTV silicone molding, investment casting and sand casting [3-5]. For example, in a patented investment casting process, called Freeze Cast Process (FCP), ice patterns are used to make metal parts instead of traditional wax patterns. This process was developed to obviate problems and technical difficulties of traditional investment casting method such as wax pattern expanding, ceramic shell cracking, highly skilled operation requirement, etc.[6-7]. However, one major concern in this process is ice pattern making. Traditional methods to make ice patterns is injecting water in a mould and making it frozen. Some main issues in this method include water expansion compensation during freezing, air bubble removal, ice pattern de-molding, and part complexity limitations. With RFP it is possible to make accurate ice patterns directly from CAD models in a very short time, without the cost of mold making and without the above issues. This is especially valuable in case that a small amount of complex ice patterns and metal parts is needed with an extreme time concern.

The paper presents our recent progress in the development of RFP. It is organized as follows. Section 2 introduces the experimental setup for conducting the RFP part building experiment. Section 3 presents the method and result of the heat transfer analysis for the RFP part building process. Section 4 demonstrates some results of three-dimensional ice part building. Section 5 concludes this paper.

2. EXPERIMENTAL SETUP

An experimental setup was developed to conduct the study of this process, as shown in Figure 2. The software of this system accepts an .STL file from Pro/Engineer or other CAD packages and slice the CAD file into a .CLI file which represents the contour information of each sliced layer. This software further generates NC codes according to the contour information of the sliced layer and the specific process parameters of RFP such as building speed and material ejection rate. Then the NC code is sent to a motion control card to control the building of ice

parts. The hardware of this experimental system consists of three major parts: XY table and Z elevator, a material extrusion subsystem, and electronic control devices. The three-axis moving mechanism is driven by three stepping motors. The XY table is placed in a freezer at a low temperature of -20°C . The heat generated by stepping motors, however, increases the temperature of the table to about 0°C which may vary $\pm 2^{\circ}\text{C}$ depending on the working status of the motors. A metal plate is mounted on the XY table as the building substrate. This plate is isolated from the table so that its temperature is kept at a constant temperature of -20°C . The nozzle is mounted on the Z elevator and can move only in Z direction. However, the movement of the building substrate relative to the nozzle makes it possible to deposit material in the XY plane. After one layer is finished, the nozzle is elevated upwards a height of one layer thickness, waiting for the XY table to move and depositing material to build the next layer.

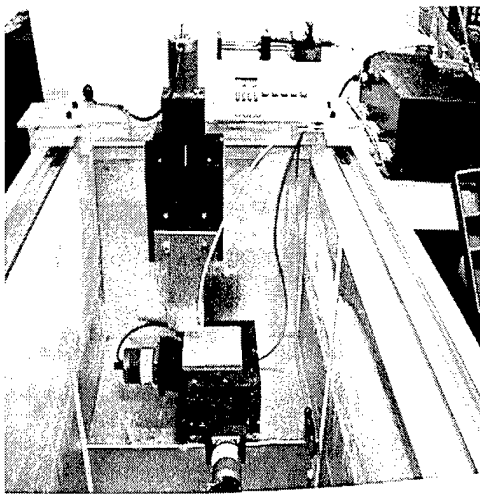


Figure 2. Rapid Freeze Prototyping Experimental Setup

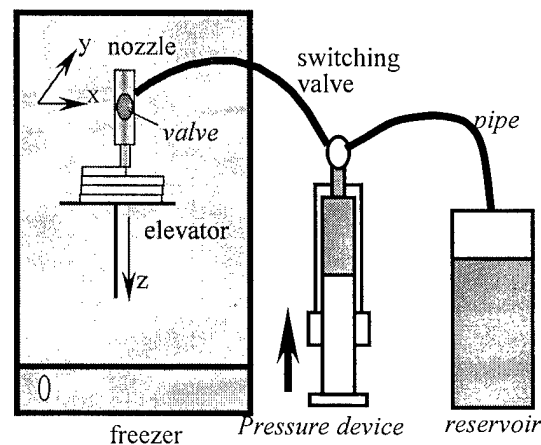


Figure 3. Material Extruding Subsystem

The material extrusion subsystem consists of a constant pressure device, a material reservoir, a feeding pipe with temperature control capability, and a miniature solenoid valve based nozzle, as shown in Figure 3. The pressure device provides a constant preset pressure according to the extrusion rate requirement. The feeding pipe is controlled at a proper temperature range, allowing the water in it to be pre-cooled but still in liquid state. The miniature solenoid valve controls material flow on and off in continuous method, and generates water droplets in drop-on-demand method. In the latter case, the response time of the valve determines the minimum achievable droplet size and the material flow resistance determines the minimum pressure required to generate droplets, both of which are vital to the success of making ice parts with drop-on-demand method.

The electronic control device (Figure 4) of this system is used to control the three stepping motors of the XYZ moving axes and to control the material flow rate, which is proportional to the resultant linear moving speed of the XY table. Motors are driven to move with a linear resolution of up to $0.25\mu\text{m}$. The motion control card (AT 6400, provided by Compumotor company) can output a pulsed signal with a pulse width of $0.3\mu\text{s}$ to the fourth axis at a frequency proportional to the resultant moving speed of XY table. The speed proportion factor is treated as a process parameter before NC code generation and is configured by software. The output signal is sent to a circuit which widens the pulse to 0.2ms , making it compatible with the response of the valve. In this circuit, the frequency of the signal determines the droplet frequency and the pulse width determines the droplet size. Since the pulse width is constant, the pulse

frequency (i.e. number of droplets per second) is proportional to the material flow rate. Accordingly, the material flow rate is proportional to the resultant moving speed of the XY table. The proportion factor can be changed by either varying the speed proportion factor or by adjusting the pulse width.

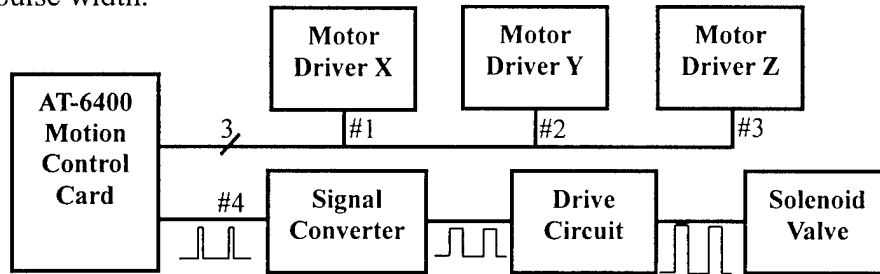


Figure 4. Schematics of the electronic control device

3. ANALYTICAL STUDY OF ICE LAYER BUILDING

Before starting to build ice parts, analysis with the ANSYS software package is conducted to help understand the water freezing process when depositing a new layer of water on a previously built ice layer. The analytical result will be used to guide the process parameter settings, such as layer thickness, drawing speed, and waiting time between two successive layer. In this study, only the heat conduction in Z direction (or between layers) and convection with the environment is considered while the heat transfer in the direction of nozzle movement and that between neighboring lines are neglected. This simplification is reasonable because the nozzle drawing (resulting from XY table movement) speed is much faster than heat transfer rate in the nozzle movement direction. On the other hand, we concern contour building more than interior filling. For contour building, there is no neighboring lines perpendicular to the drawing direction. The built contour is exposed entirely to the environment and consumes heat mostly through conduction between layers in Z direction and through convection to the air. This is a two-dimensional, non-linear transient heat transfer problem and can be analyzed by ANSYS [8]. The simplified calculation model is shown in Figure 5. The height of the model, H , is proportional to the number of layers built. It is varied from 0.5 mm to 20 mm while the newly deposited layer thickness δ is kept at 0.1 mm to see the influence of height on new layer freezing time. In another analysis, the height is kept at 5 mm constant while the newly deposited layer thickness is varied from 0.05 mm to 0.20 mm to see the influence of layer thickness on new layer freezing time. In both cases, according to the condition of the experimental system, we assume that the previously built layers has an initial temperature of -20°C , the newly deposited layer of water has an initial temperature of 10°C , and the building metal substrate and the environment have a constant temperature of -20°C . The time T required for the newly deposited water to freeze completely is investigated with this assumption.

The above initial condition can be expressed by

$$\begin{aligned} T &= 10^{\circ}\text{C} && \text{for } H \leq y \leq y_0 \\ T &= -20^{\circ}\text{C} && \text{for } 0 \leq y < H \end{aligned}$$

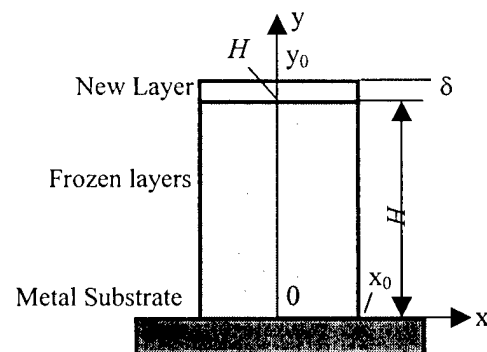


Figure 5. Heat transfer calculation model for Rapid Freeze Prototyping process

The boundary condition can be expressed by

$$T = -20^{\circ}\text{C} \quad (\text{including the substrate and air environment})$$

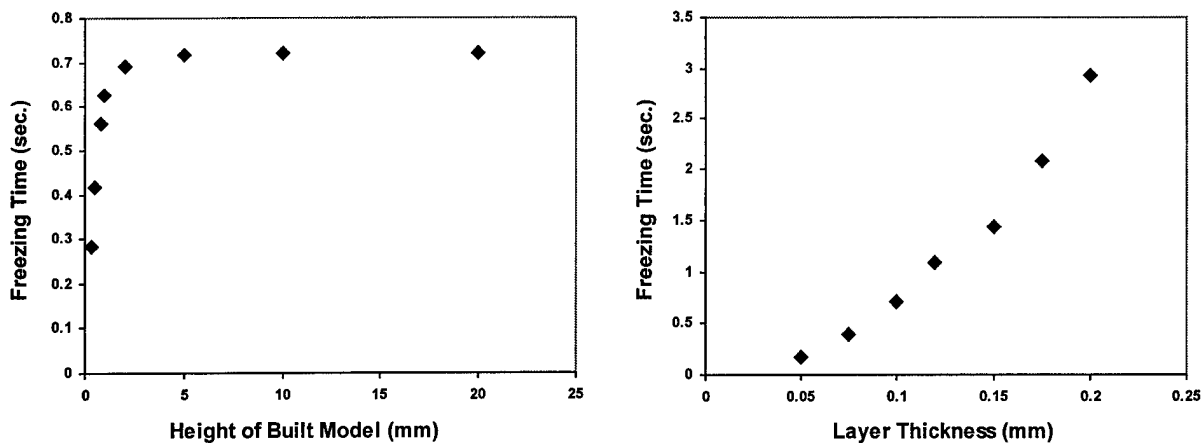


Figure 6. Influence of built model height and newly deposited layer thickness on freezing time

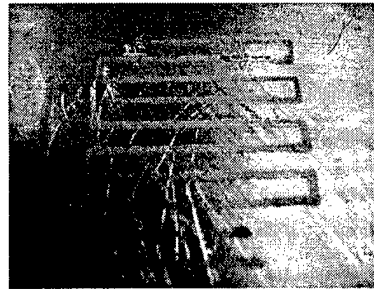
Figure 6 shows the result. From this figure, we observe that:

- 1) As height H becomes larger, a longer time T is needed to freeze the newly deposited layer. However, when H is over 2 mm, this influence becomes negligible. This means that the additional material in Z direction over 2 mm does not significantly decrease the cooling speed.
- 2) As layer thickness δ becomes larger, a longer time T is needed for the water to freeze. So reducing building layer thickness can effectively shorten the freezing time, which means better freezing process control and thus better building resolution.

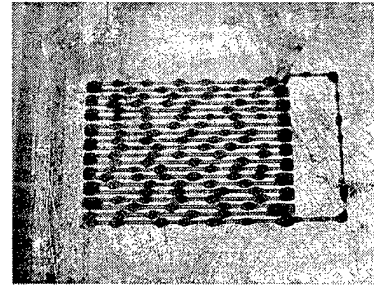
4. ICE PART BUILDING EXPERIMENTS

In the experiments described below, only drop-on-demand method is given because it can provide better control on material flow with our current experimental system. Continuous extrusion method will be investigated after an upgrade of the experimental system to include a valve on-off control device and a new nozzle design. Ice part building experiments were conducted in the following steps:

- 1) **Building ice lines.** This step is to provide optimal building parameter values such as building substrate temperature, drawing speed (i.e. XY table movement speed), layer thickness, droplet frequency and size. From the experiments, we can see the influence of these parameters on ice line building quality. We have observed that insufficient substrate temperature can cause uneven line width as shown in Figure 7. Proper ratio of droplet frequency versus drawing speed have been obtained from these experiments. Another goal of ice line building experiments is to help find out the relationship between the drawing speed and the material deposition delay error. There exists a time delay between on-off of the control signal and open-close of the valve. There exists another time delay between open-close of the valve and start-stop deposition of the materials because there is a distance between the nozzle and the building surface. The two delays will result in material deposition errors in the drawing direction. Figure 8 shows an experiment that is done to measure the deposition error and to help optimize the most suitable drawing speed and valve distance.



(a) Fine ice lines



(b) Poor ice lines

Figure 7. Ice lines built

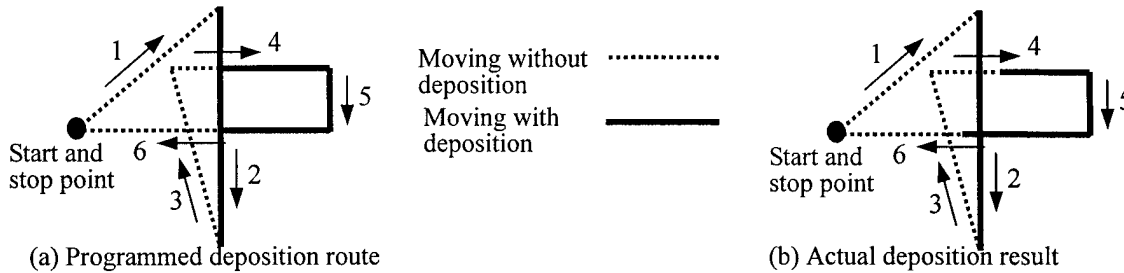
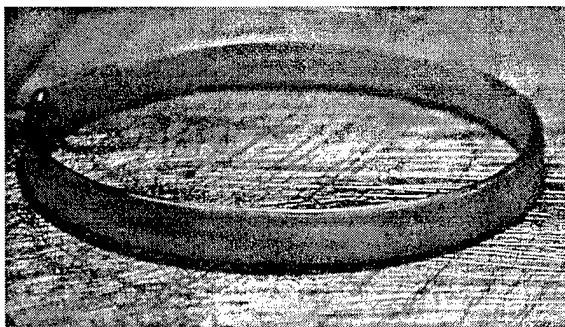
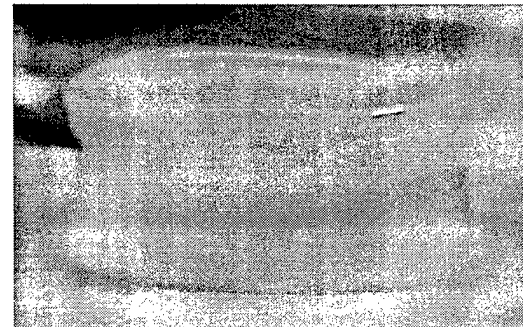


Figure 8. Drawing route to measure valve start-stop errors

2) **Building ice rings.** The purpose of this experiment is to find out a suitable waiting time between two layers for successive part building, in addition to the practical knowledge obtained from ice line building. From the heat transfer analysis above, it is found that the complete freezing time for a new layer is around 0.7 second when the model height is over 2 mm. However, for successive part building, in order to prevent heat accumulation with layer building, the previous built layer should have been cooled down to almost the environment temperature before starting to build the next layer. The analysis shows that the time to cool down the previous layer could be tens of seconds depending on many heat consumption factors. A group of experiments with different waiting time is taken to figure out the suitable waiting time value. Samples with insufficient waiting time show unevenness of ring height and wall thickness. On the other hand, samples with sufficient waiting time have an even ring height and wall thickness, and fine surface smoothness, as shown in Figure 9.



(a) Fine ice ring



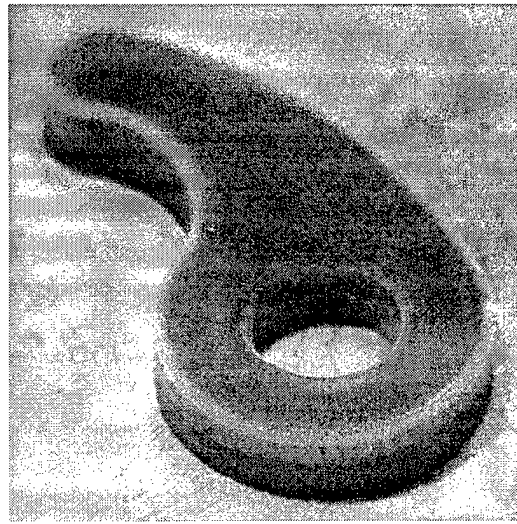
(b) Ice ring with uneven height and wall thickness

Figure 9. The effect of waiting time on ice ring building

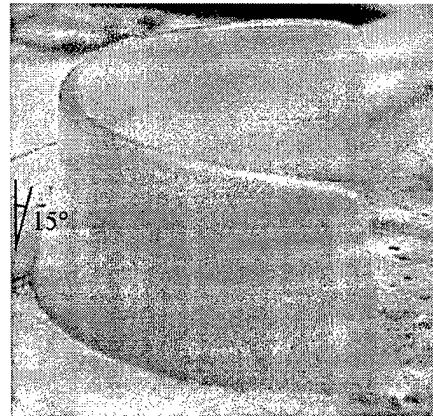
Table I. Three-dimensional ice part parameters

Layer Thickness	Drawing Speed	Extrusion Pressure	Ejecting Frequency	Pulse Width	Environment Temperature	Nozzle Temperature
0.12 mm	40 mm/sec.	$1.5 \times 10^5 \text{ N/m}^2$	400 Hz	0.2 msec.	-20°C	10°C

3) Building three-dimensional ice parts. Table 1 lists the optimal parameter values that were obtained from the above experiments and were used for three-dimensional ice part building. Figure 10 shows an ice link-rod and two ice conoids. The conoids are built to see the maximum angle that can be achieved without support. In our experiments, a conoid of 35° angle was successfully made, as shown in Figure 10. The surface smoothness for both the conoids and the link-rod is very good as compared to parts made by other deposition based SFF processes without machining.



(a) Ice link-rod



(b) Ice conoids of two different angles

Figure 10. Built three-dimensional ice parts

From the above experiments, we have observed that allowing enough cooling time before building the next layer and having high heat transfer rate are extremely important for the successful building of ice lines, rings, and three-dimensional parts. Insufficient cooling rate or cooling time can cause part building failure. This is because if the newly deposited water is kept in liquid state for some time, the surface tension will cause the water unevenly distributed, forming some water sweats on the building surface as shown in Figure 7(b). This surface tension effect can be restrained if the cooling rate is fast enough.

6. CONCLUSION

An experimental system has been developed to conduct the study of rapid freeze prototyping. The experiments conducted on this system have demonstrated the feasibility of making three dimensional ice parts by depositing and rapidly freezing water. The heat transfer analysis helps understand the freezing process and provides useful information to the selection of building parameters. Cooling rate, which depends on the environment temperature and cooling time between two successive layers, is a parameter critical to the success of part building.

Future work will focus on improving building resolution and part accuracy, and on process parameter optimization. Software will be developed to make complex three-dimensional ice parts with supports. Applications of ice parts will be another important issue in this research.

ACKNOWLEDGEMENT

The authors gratefully acknowledge the support of the Multi-lifecycle Engineering Research Center at New Jersey Institute of Technology. Dr. Ming C. Leu was on leave at the National Science Foundation as the Program Director for Manufacturing Machines & Equipment when the work described in the paper was done.

REFERENCES

- 1) Leu, M. C. and Zhang, W., "Research and Development in Rapid Prototyping and Tooling in the United States," *Proceedings of the International Conference on Rapid Prototyping and Manufacturing*, Tsinghua University, Beijing, China, July 21-23, 1998.
- 2) McIntosh, J. J., Danforth, S. C., and Jamalabad, V. R., "Shrinkage and Deformation in Components Manufactured by Fused Deposition of Ceramics" *Proceedings of the 8th Annual Solid Freeform Fabrication Symposium*, University of Texas at Austin, Austin, TX, August 1998.
- 3) Zhang, W., Leu, M. C., Ji, Z., and Yan, Y., "Rapid Freezing Prototyping with Water," *Proceedings of the 9th Annual Solid Freeform Fabrication Symposium*, University of Texas at Austin, Austin, TX, August 1998.
- 4) Zhang, W., Leu, M. C., Ji, Z., and Yan, Y., "Rapid Freezing Prototyping with Water," *Materials and Design*, Vol. 20, pp. 139-145, June, 1999.
- 5) Skeehan, M., "Artificial Ice Shapes for FAA Certification of the C130J Aircraft," *Proceedings of the 1998 North American Stereolithography Users Group Conference*, San Antonio, TX, March 1-5 1998.
- 6) Yodice, A., "Freeze Process Cuts Casting Costs," *Advanced Materials & Processes*, Vol. 155, No. 4, pp.35-37, 1999.
- 7) Yodice, A., *Investment Casting Process*, US Patent 5,072,770, issued in 1991.
- 8) Carslaw, H. S. and Jaeger, J. C., *Conduction of Heat in Solids*, Oxford University Press Inc., New York, pp. 466-479, 1997.

Direct Thick Layer Rapid Prototyping From Medical Images

Peter B. Chamberlain and Charles L. Thomas
University of Utah

Abstract

This paper discusses a technique for building medical prototypes directly from medical image data using ruled thick layers directly from medical image data. Medical image slices are currently much thicker than the layers used by most RP machines, but a direct slice to layer correspondence can be established with the use of thick layers. The proposed algorithm uses three image planes to interpolate a ruled edge cutter path using an adapted form of the marching squares algorithm. The algorithm has no problems with bifurcations or multiple loop contours and can create cutter paths from any high contrast image volume.

Introduction

Medical prototyping is an emerging and increasingly important form of rapid prototyping. Medical prototypes are created from scanned volume data such as CT and MRI scans. Prototypes are used for surgical planning, practicing surgical steps, diagnosis, and direct creation of implants. Wilford Hall Medical Center at Lackland Air Force Base has been using medical rapid prototyping for surgical planning and has used the technique with more than 70 different patients including a conjoined twin separation (US Air Force Press Release, 1997, 1998). A company called Anatomics in Australia provides medical rapid prototyping services. Customers send a CT or MRI file and Anatomics will return models of the desired tissues made with the SLA or FDM rapid prototyping processes. The company website gives more information, including case studies (<http://www.qmi.asn.au/anatomics>). In the future, direct prototyping of implants using implantable biocompatible materials will make medical prototyping more attractive. Researchers are currently developing bioceramics that are compatible with tradition SLS, FDM, and 3D Printing RP Systems (Bose, 1998, Steidle, 1998, Vail, 1998).

Medical prototyping is a three step process (see Figure 1). First, a medical image is made. Second, the image volume is processed to extract geometric surface information describing the tissue to be built. Third, the geometric surface data is used to construct a physical prototype using a rapid prototyping machine or NC machine. Most of the research related to medical rapid prototyping is in the areas of medical imaging scanners, image segmentation, and rapid prototyping materials development. Image segmentation is the focus

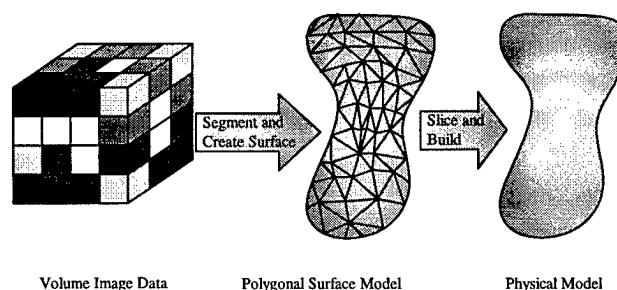


Figure 1
Generalized Medical Prototyping Process

of this paper.

All algorithms for medical image segmentation are based on the same principles and can be classified into two groups, contour segmentation or surface segmentation. In contour segmentation, each slice of the medical image is processed separately to produce a two-dimensional contour with one or more loops. The contour slices are then laced together to create a three dimensional surface. In surface segmentation, the entire volume is processed simultaneously to generate the three-dimensional surface directly. Both techniques are based on pixel or voxel intensity thresholding.

All segmentation algorithms are based intensity interpolation of a unit cell. In two dimensions the unit cell is the unit square, and in three dimensions the unit cell is the unit cube (Schroeder, 1997). The unit square is defined by the centers of four adjacent pixels in an image plane. The set of all unit squares for a plane forms a grid passing through the center of each pixel (see Figure 2 A). The unit cube is defined similarly with eight adjacent voxels from two image planes. Figure 2 B shows how to interpolate to find a line segment representing a given intensity value as it passes through the unit cell. The plus sign represents a pixel with an intensity higher than the desired value and the minus signs represent a pixels with an intensity with lower than the desired value. A simple linear interpolation of the intensities and coordinates of the points defining unit square produces the desired intensity line segment. Schroeder discusses all of the special cases for the unit cell and the unit square with a description of the marching squares and marching cubes algorithms.

Current segmentation techniques focus on obtaining a good surface representation of the tissue to be prototyped. That surface is then converted to an STL which can then be used to build a physical model by re-slicing it and running it through a rapid prototyping machine. The STL surface model must be generated from the medical image volume because the slice thickness of a rapid prototyping machine, ~0.1 mm, is much less than the slice thickness of medical image data, ~0.5 to 5 mm. The STL file is also the standard input to most RP machines, they will not accept medical image data. The creation of the STL surface also allows for surface smoothing to make the model

look better, but the process can be slow and does not improve accuracy (Manichovich, 1994).

Ruled thick layer rapid prototyping techniques allow layer thicknesses ranging from 0.5 mm to several inches (Chamberlain, 1997). Thick layers could speed the prototyping process by eliminating the creation of a surface data set because

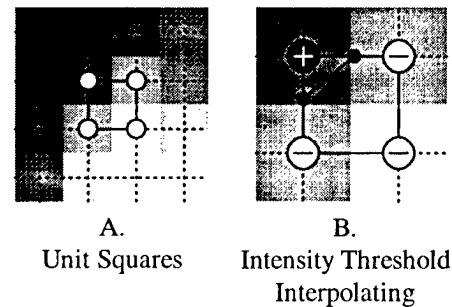


Figure 2
Unit Square Definition and Intensity
Threshold Interpolation

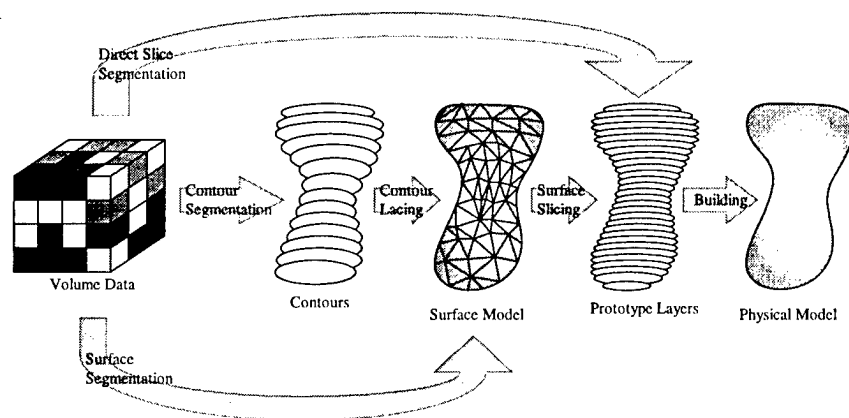


Figure 3
Ruled thick layer prototyping allows direct prototyping without the creation of an intermediate surface

layers with the same thickness as the image slices can be used. That means that it is possible to directly process the medical image data to create the layers for the RP machine (see Figure 3). The latest version of the thick layer ruled edge machine at the University of Utah is called ShapeMaker 2000. It is a four-axis waterjet cutter capable of building prototypes of 20 or more feet in size. It uses a semi-manual process that requires manual stacking and manual STL file splitting to remain within the machine's 3 ft x 5 ft cutting envelope. The waterjet cutter operates at pressures up to 40,000 psi and can cut low density foams several inches thick or plastic sheet about 1 to 2 mm thick.

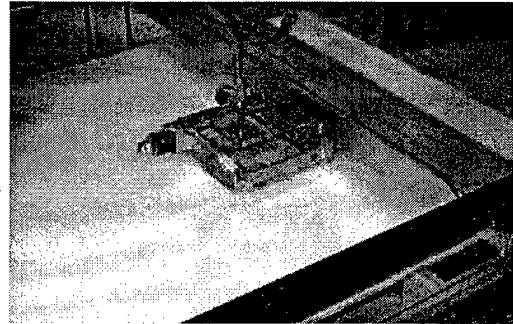


Figure 4
Photograph of ShapeMaker 2000 cutting head

Direct Slicing Algorithm

In order to create a direct slicing algorithm, one must first determine the image slice to prototype layer correspondence. One option would be to define layers with vertical edges based on the contours from a single image slice. This option has the disadvantage of thick stepped layers. A second option would be to use two adjacent image slice contours to create a general ruled edge. With this option it is difficult to connect rapidly changing contours or contours without the same number of loops. A third option would be to use three adjacent image slices to define a general ruled edge (see Figure 5). The prototype layer would be centered on the middle image slice, which would control the geometric topology of the layer (number of loops and general shape of contour). The top and bottom image slices would be used to define the cutter angle of the layer. This option has the disadvantage of being a tangent cut algorithm, meaning the layers form a model with jagged edges (Hope, 1997). This third layer definition provides the most robust algorithm because it does not break down with complex geometry, yet still provides a ruled edge result.

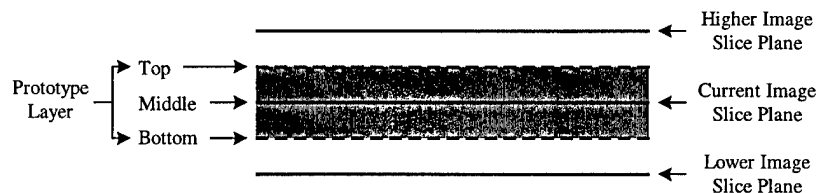


Figure 5
Prototype layer definition using three image slice planes

Implementation of the three plane layer definition required the creation of a new segmentation algorithm

which will be referred to as the three plane marching squares algorithm. It is a modification of the basic marching squares algorithm as presented by Schroeder. The marching squares algorithm is a two loop search and sort algorithm. In the first loop, each unit cell in the image is intensity interpolated to determine if a contour segment crosses through it. If a segment does cross through it, that segment is added to an unordered segment list. In the second loop, the segments in the list are sorted to create the loops of the intensity contour. The three plane algorithm works with a similar search and sort method.

The searching step of the three plane marching squares algorithm is more complex than the searching step of marching squares algorithm. Figure 6 is a schematic of the steps involved

in the algorithm. The first noticeable difference is that the unit cell is defined by twelve voxels, three from each image plane, instead of four pixels. The first step of the algorithm (Fig. 6A) is identical to the marching squares algorithm. The four voxels on the mid-plane are used to define a unit square which returns a mid-plane contour segment. Each mid-layer segment endpoint then becomes the pivot point for a cutting angle at each end of the contour segment. The cutting angle at each end of the segment is determined independently in a multiple step process. Figure 6B is a schematic of the process for one end of the mid-plane contour. Two unit squares, one above and one below the mid-plane, are formed using the top, middle, and bottom image planes. A line is intensity interpolated in the top and bottom square independently, shown as the thick dotted lines terminated with small squares in Figure 6B. The average slope of the two interpolated lines is used to create a cutter angle line centered on the mid-plane contour and extending halfway to the top and bottom planes. The process is repeated for the other end of the intersection to produce a segment of the ruled edge cutter path, as shown in Figure 6C.

After the three plane marching squares algorithm is executed, the result is an unordered

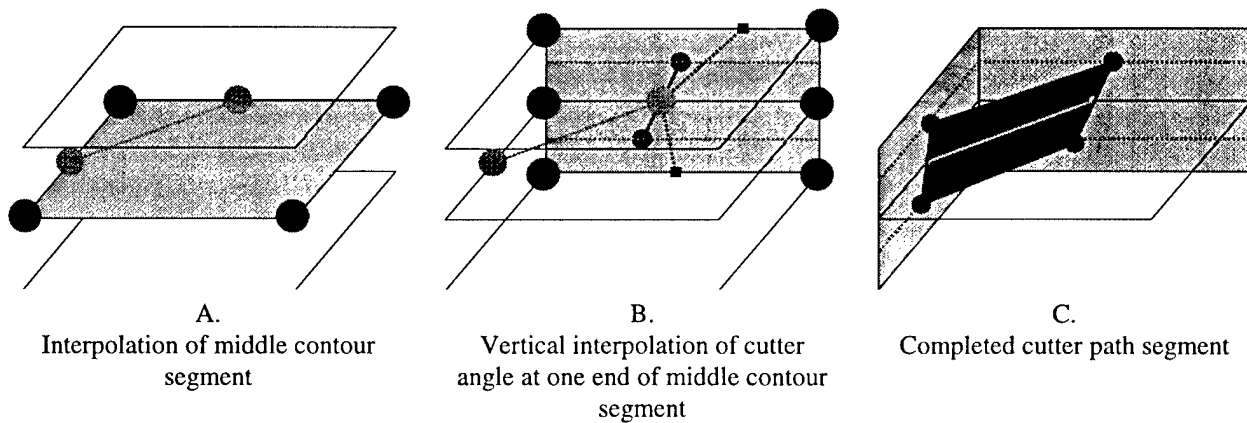


Figure 6

Three plane square for the three plane marching squares algorithm

list of cutter path segments which are sorted using the mid-plane contour segments to produce the loops of the cutter path contours. The top and bottom contours, calculated from the cutter path angles, are added to the contour list along with the mid-plane contour. Several fixes are required to produce proper cutter paths that can be used by ShapeMaker 2000. First, angle limits are applied to bring the top and bottom contours closer together so that the angle of the cutting head is never more than the current 55 degree limit of the wajerjet(see Figure 7). Next, the cutter path must be examined for cutter path crossovers, which result in unnecessary motions that slow the cutting process and reduce the layer surface quality. Crossed cutter lines are fixed by swapping cutter lines, as shown in Figure 8. Cutter lines are always swapped on the side with the shortest cutter path segment. Cutter line crossovers are detected and fixed in a two dimension projection. Note that a cutter line represents a three dimensional line in space that the wajerjet will pass through as

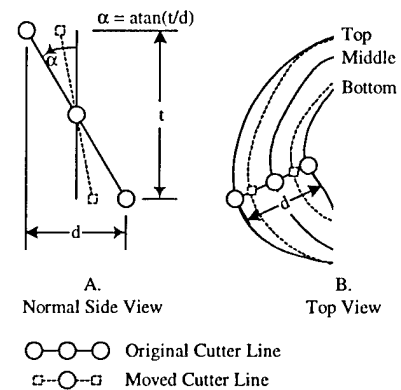


Figure 7
Setting cutter angle limits

it moves along the cutter path.

Three further modifications were added because of the small size of the bones to be prototyped. First, each layer was surrounded by a registration box which was cut into the material surrounding the layer. During stacking, the registration boxes can be aligned corner to corner to provide registration for gluing the layers together with high accuracy. Second, the waterjet tends to blow small pieces off from the cutting table after they have been cut. All of the smallest pieces of any layer were cut first, generally it does not matter if they blow off from the table because they are usually internal cavities that will be thrown out later. If the larger cuts that surrounded the internal cavity cuts blew off the table it would mean that the internal cavities would not be cut. Third, because ShapeMaker 2000's cutting table is several feet across, it was possible to cut a hundred or more layers one sheet of material by writing all of the layers into a single cutter file with an offset for each layer.

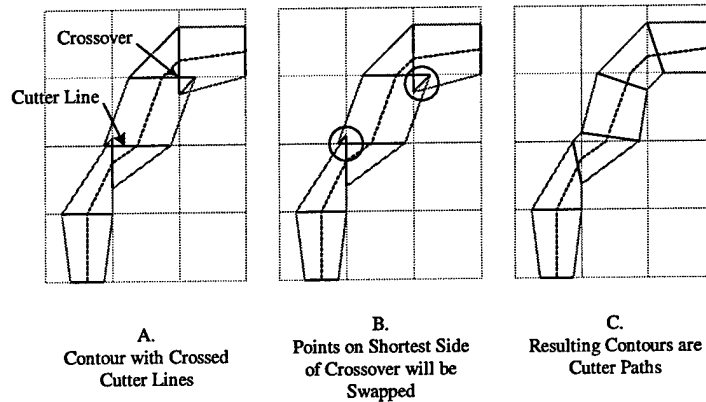


Figure 8
Swapping cutter line crossovers

Results

The software was tested with data sets obtained from the website of the Laboratory of Human Anatomy and Embryology, University of Brussels (ULB), Belgium. Two windowed high contrast data sets were used, a C1 vertebrae from the top of a human neck and a human humerus shaft. The C1 vertebrae data set is 24 MB in size. The voxels are stored in a 16 bit format with 512x512x47 voxels, 0.5x0.5x0.5 mm in size. The humerus data set is 200 MB in size. The voxels are stored in a 16 bit format with 512x512x298 voxels, 0.5x0.5x1.0 mm in size. Figure 9 shows a rendering of part of the processed C1 dataset displayed as a series of stacked layers with a 47.5 degree angle limit. A physical model of the part was built at 2.54 times actual size because at the proper scale the layers were too small to glue manually. The total build time for the C1 model was 16 hours, about 4 hours of cutting and 12 hours of manual stacking. The physical model was built from Sintra sheet, a high density PVC foam, and assembled with clear PVC adhesive. Figure 10 shows a scanned image of the built humerus shaft. This was also built using Sintra sheet and purple PVC adhesive primer was used to accentuate the layers. The total build time for the humerus model with 8 hours, about 1.5 hours of cutting and 6.5 hours of manual stacking.

Conclusions

The three plane marching squares algorithm is robust and easy to use. This was proven by the C1 vertebrae data set which had anywhere from one to 30 loops on a layer and multiple bifurcations on most layers. It would be difficult to extract a surface from the dataset and it would be even more difficult to construct a set of ruled edge cutter paths from the resulting STL

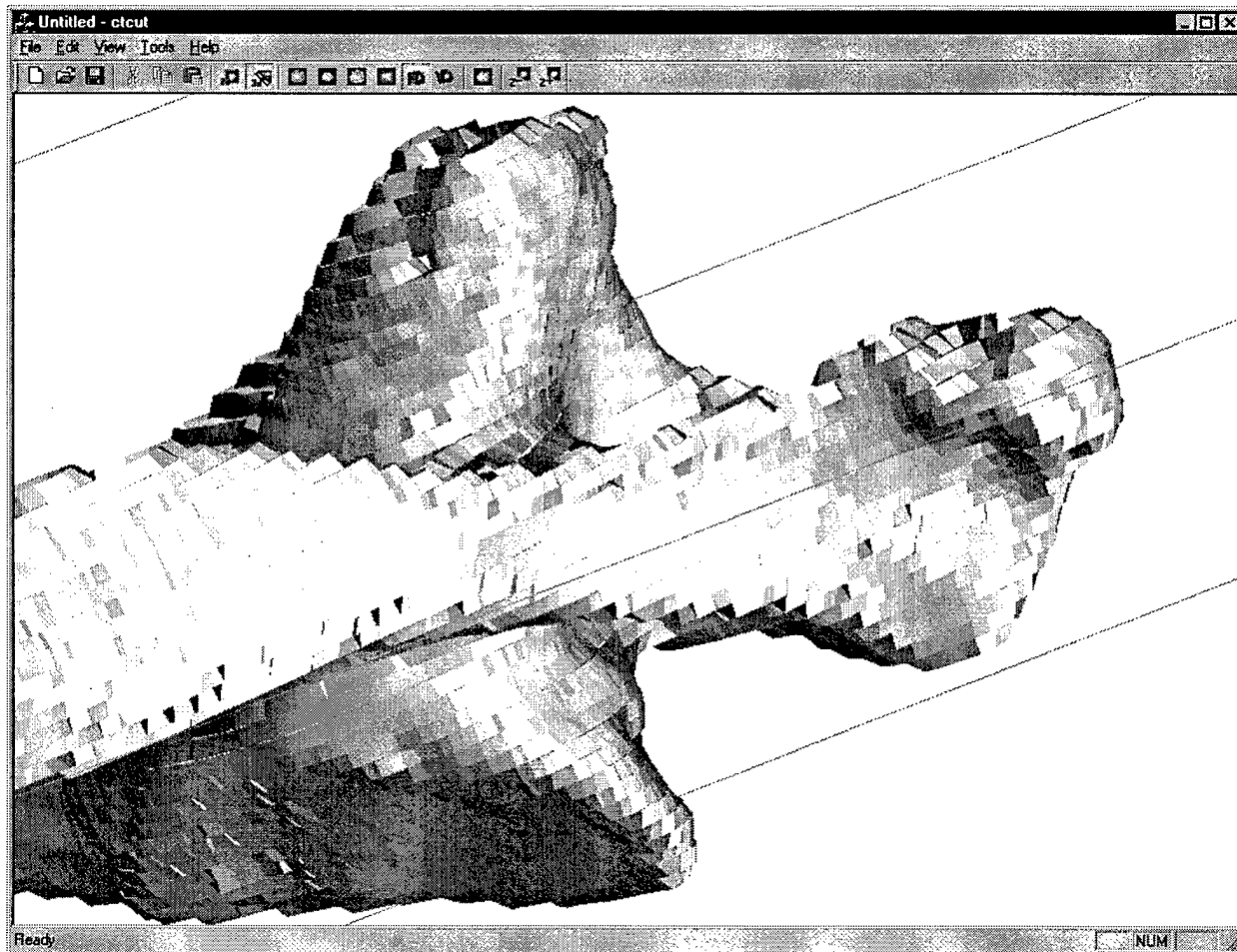


Figure 9

Screen capture of human C1 vertebrae rendered in OpenGL as stacked ruled edge layers with an angle limit of 47.5 degrees

file. The humerus prototype showed particularly good results. The near vertical edges cut and stacked accurately, giving a model with great surface quality. This shows the potential of a ruled edge RP machine to improve surface quality when it is working within its angle limits.

The current research implementation of ShapeMaker 2000 is not suitable for building models of human bones or organs because the machine is designed for objects an order of magnitude larger. A smaller version of ShapeMaker with automatic stacking might make this particular prototyping process practical.

References

- Bose, Susmita, Avila, Marisol., and Bandyopadhyay, Amit. "Processing of bioceramic implants via fused deposition process". *Solid Freeform Fabrication Symposium Proceedings*. 1998. pp. 629-36.
- Chamberlain, Peter, Van Roosendaal, Mark, Thomas, Charles. "Variable thickness ruled edge slice generation and three-dimensional graphical error visualization." *Solid Freeform Fabrication Symposium Proceedings*. 1998. pp. 311-8.
- Hope, R.L, Roth, R.N., and Jacobs, P.A. Rapid prototyping with sloping surfaces. *Rapid Prototyping Journal*. Vol. 3 No. 1. 1997. pp. 12-19.
- "Cutting edge technology improves lives, saves money." United States Air Force Press Release. January 27, 1998.
- "Twins celebrate successful surgery." United States Air Force Press Release. March 15, 1997.
- Mankovich, Nicholas, et. al. "Surgical planning using three-dimensional imaging and computer modeling." *The Otolaryngologic Clinics of North America: Craniofacial Skeletal Augmentation and Replacement*. 1994, 27(5). pp. 875-89.
- Schroeder, Will, Martin, Ken, and Lorensen, Bill. *The Visualization Toolkit*. 2 ed. 1997.
- Steidle, Cheri, et. al. "Automated fabrication of nonresorbable bone implants using laminated object manufacturing (LOM)." *Solid Freeform Fabrication Symposium Proceedings*. 1998. pp. 637-38.
- Vail, N. K., et. al. "Materials for Biomedical Applications." *Solid Freeform Fabrication Symposium Proceedings*. 1998. pp. 621-628.

Anatomics web site: <http://www.qmi.asn.au/anatomics>

The image datasets used in this experiment were from the Laboratory of Human Anatomy and Embryology, University of Brussels (ULB), Belgium

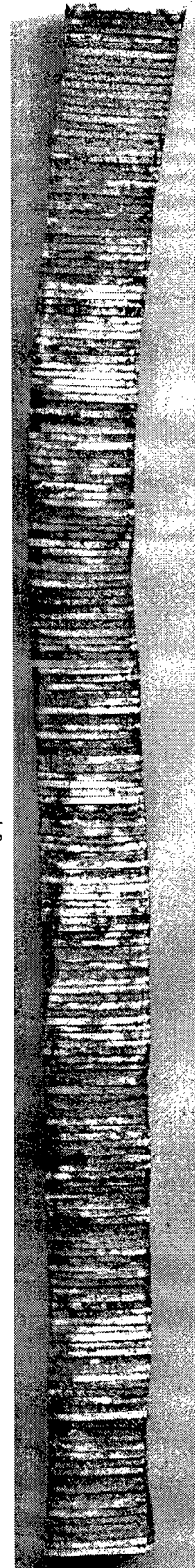


Figure 10
Human humerus

Rapid Prototyping by Injection Molding

Shaun D Compton, Charles L. Thomas, Vipul Lotke
University of Utah

Abstract

Thick layered rapid manufacturing, using injection molding techniques, integrates the concept of layered manufacturing into the molding process. This process takes an STL file of a part and decomposes it into layers that can be milled on a 3-axis machine. New STL files are then created of each layer, where upon these layers are used to create mold cavities. Machining code is then written for each mold, and the mold is cut using the 3-axis mill. The layers of the part are then molded and combined to form the whole part. In this way, complex parts can be molded without concern for injection molding flaws in the part or complicated mold design. This technique allows the production of thousands of complex parts directly from a CAD file in a few days.

Introduction

The goal of Rapid Prototyping by Injection Molding (RPIM) is to produce a medium to large quantity of prototypes/parts directly from a CAD file in a short time. In addition, the process should be relatively unskilled and automatic. The techniques used in RPIM, layered manufacturing, NC machining, and injection molding, are common techniques that have been around for a number of years. Each of them have their advantages and disadvantages, and this process is intended to combine the advantages from these techniques while minimizing the disadvantages.

Layered Manufacturing

Most rapid prototyping systems currently available employ an additive process for the prototype construction (Thomas, 1995). This means that the part in question is decomposed into layers, and each individual layer is constructed and "stacked" upon the previous layer, hence, an additive process. This process is also known as layered manufacturing or solid freeform fabrication (Deckard, 1987). The advantage of creating parts in layers and then stacking them is that the complexity of the manufacturing process is greatly reduced. One only needs to know the contour of any specific layer to create that layer. As a result, this process can produce almost any geometry.

One disadvantage of a process such as this is that it is not as accurate as one might wish. An example of the tolerances available with this type of process would be from 8 to 12 thousandths of an inch for a Stratasys® FDM1650 fused deposition modeling machine (Stratasys®, 1996). The available surface finish for this process is also relatively poor. This process is also quite fast at producing an individual part, but very slow in terms of mass production.

Numerical Controlled Machining

One might also consider another type of rapid prototyping to be a subtractive method such as NC machining. In NC machining, the part is simply "cut" out of an existing block of material; unwanted material is removed from the block to reveal the part. This process is extremely accurate in its tolerances and provides an excellent surface finish. For example, the repeatable tolerance on a Bridgeport® Discovery Torq-Cut 22 Vertical CNC machine is ± 0.00015 inches (Bridgeport®, 1995).

The disadvantages to this technique are that it requires a skilled operator to run the machine, with extensive planning and design in the manufacturing process, and it also requires a wide range of tooling to produce a wide range of parts. Another disadvantage, perhaps the biggest, is that some geometries are very difficult to produce or even impossible. For example, a cavity in the middle of the part would be impossible since there is no way to get to it to remove the material.

Injection Molding

The next technique used in this process is injection molding. Injection molding is a process through which a mold is created, where upon the mold is injected with a heated polymer to produce the part. This technique is a very fast and efficient means for producing many, identical parts.

A disadvantage to this process is that the mold design can be very complicated and expensive. Injection molding also limits the geometry that can be manufactured. For example, thick walled parts are difficult or impossible to mold.

RPIM Concept

Previous researchers have developed prototyping techniques based on the decomposition of complex 3D parts into thick layers. L.E. Weiss and F. B. Prinz developed an automated manufacturing process known as Shape Deposition Manufacturing, or SDM (Weiss, 1998). SDM combines the concepts of molten metal droplet deposition and CNC machining to produce 3D, complex-shaped, multi-material structures. F. Zafar Shaikh and coworkers developed a manual process known as Precision Stratiform® Machining, which decomposes a complex, 3D part into layers that can be machined with an NC machine (Shaikh, 1997). The Stratiform® process then combines the machined layers using a vacuum furnace brazing process that creates leak free, brazed joints between the connecting layers. Cheol H. Lee developed a method known as Ruled Thick Layered Rapid Prototyping, which incorporates ruled edges on the layer decomposition to build large, 3D, complex geometries (Chamberlain, 1998).

RPIM begins with an automated adaptation of the Stratiform® process, except that it machines molds of the thick layers. The end product of RPIM is a collection of thick injection molded slices instead of a unitary part as with SDM. The concept of RPIM takes the techniques

of layered manufacturing, NC machining, and injection molding and combines these three processes into a single new process. The following steps outline the operation of RPIM:

- Decomposition of a general 3D CAD object into 3 axis machinable layers
- Generation of 2 part mold surfaces from layers
- Generation of interlocking features to lock adjoining layers
- Generation of tool paths to machine mold cavities
- Machining of the cavities into standard mold inserts
- Molding of the layers
- Assembly of molded layers

Decomposition of general 3D CAD object into 3 axis machinable layers

The first thing that must be accomplished is to decompose the part into layers that are machinable by a 3-axis NC machine. In order to accomplish this, the part must be split at intersections where, in the splitting plane, downward facing surfaces meet upward facing surfaces. In this way all layer surfaces will be seen either from a top view or from a bottom view, allowing the surfaces to be machined with a 3-axis NC machine. This will also allow for a two-part mold.

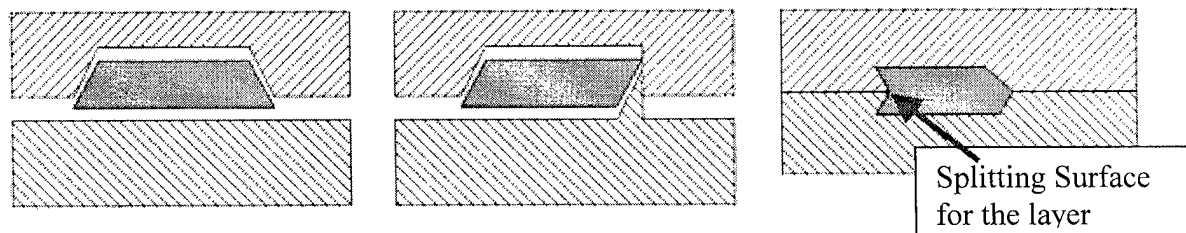


Figure 1
Parting Surface Between Layers

Another consideration to take into account when decomposing each layer is to be aware that a single layer thickness must not exceed approximately 0.125 inches. This is the approximate maximum thickness at which any part should be molded to do shrinkage/sinking. Sinking occurs when the part is removed from the mold and begins to cool. If the part is too thick, the internal stresses created by the cooling process will pull the outer walls inward creating a "sink" in the part (Dym, 1987).

Figure 2 shows an example of a die that is very difficult to injection mold. This die has concave surfaces on all six sides with further concave

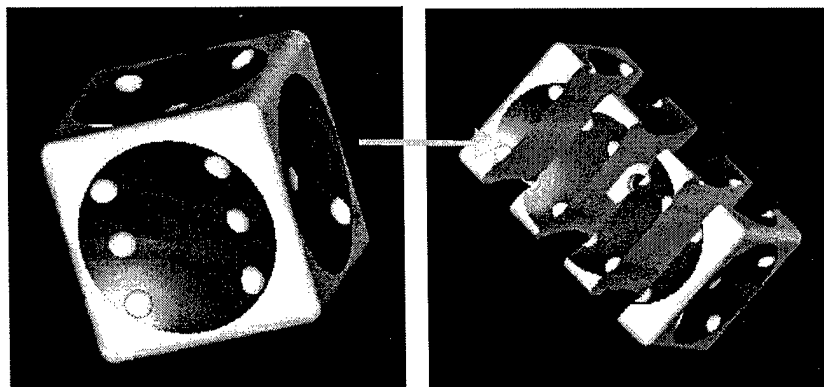


Figure 2
Example of Thick Part Decomposition

indentations to represent the number markings on each side. This die also contains a cavity within the core. All of these factors make this die difficult, or even impossible to injection mold. It is therefore split into layers along horizontal planes where downward facing surfaces meet upward facing surfaces. This occurs in the middle of each concave indentation.

Generation of 2 part mold surface from layers

The next phase of the process is to place the layers within a mold, creating a two-half mold to inject the layers. During this phase of the process, consideration must be given for injection molding constraints. A standard mold insert will be used for the injection process, limiting the number of layers that will fit into any one mold. Allowances must also be made to fit runners within the mold, which are channels for the heated polymer to reach the part layers. Ejector pin placement is also a factor when placing the layers in the mold. The layers must be ejected from the mold with the ejector pins. This reduces the possibility of the part sticking in the mold cavity. A final consideration is for vertical edges in the mold. If the layers have vertical surfaces in the mold relative to the mold face, draft angles will have to be implemented on those surfaces to facilitate the ejection of the part layer. Figure 3 show the example of the die layers within the standard mold inserts.

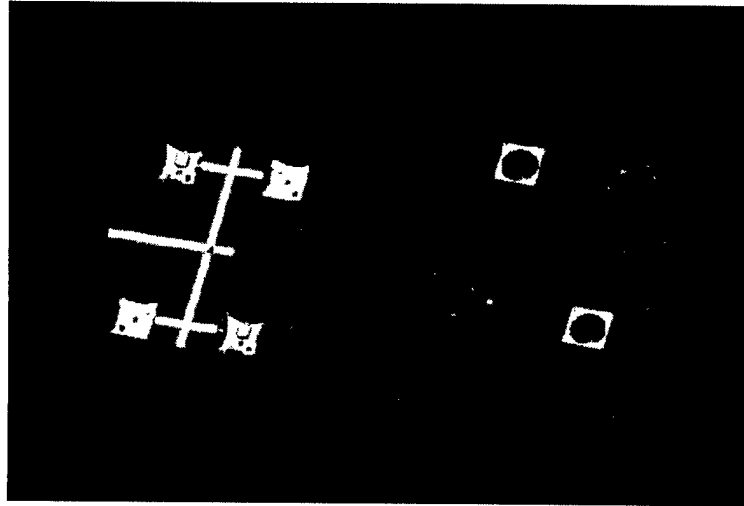


Figure 3
Mold Halves for Die Example

Generation of Interlocking Features to Lock Adjoining Layers

Interlocking features are necessary to reference one layer with another. This can be accomplished in several different ways. One way is to create a small hemisphere that protrudes from the surface of one layer, and then to create a matching cavity of the hemisphere on the adjoining layer. When the layers are brought together, the hemisphere from the first layer will go into the cavity on the second layer referencing the two layers together. Figure 4 shows how this may be accomplished.

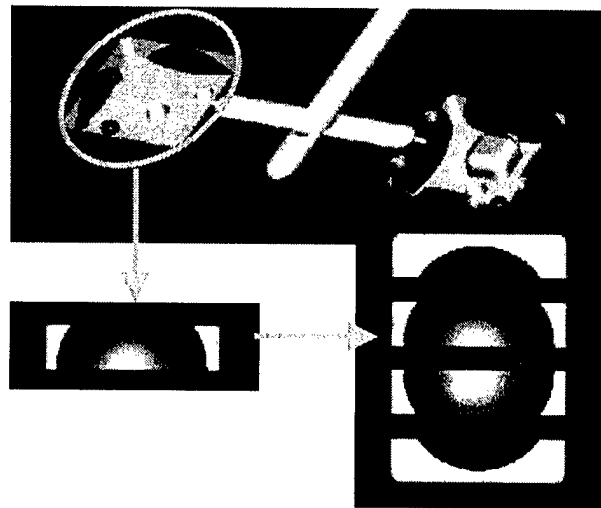


Figure 4
Example of Interlocking Features to
Position Adjoining Layers

Another possibility would be to use the ejector pins to create the locking features. This could be accomplished by making the ejector pins a little too long for one layer, thereby creating a cavity on that layer; and making the ejector pins a little too short on the adjoining layer, creating a small protrusion. However, in order for the layers to be positioned correctly with respect to each other, the pins would have to be positioned in such a manner as to be at the same place on each adjoining surface. Figure 5 shows the interlocking features created by the ejector pins on another example part.

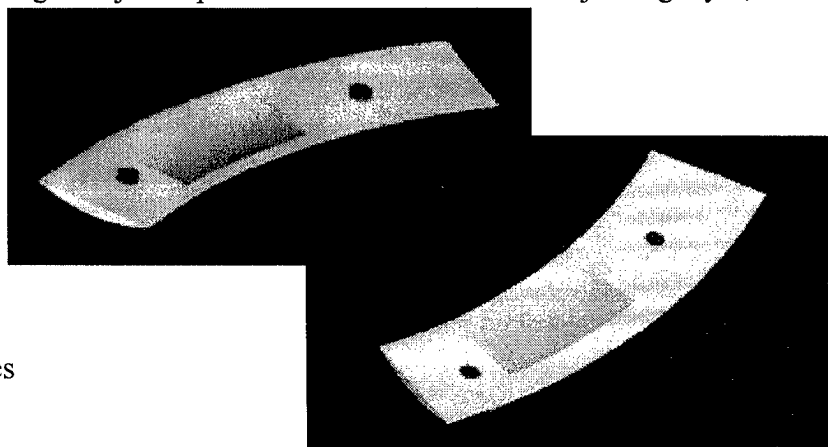


Figure 5

Interlocking Features Created Using the Ejector Pins

Generation of Tool Paths to Machine Mold Cavities

After the layers are inlaid into the mold halves and the interlocking features have been created, tool paths are then generated. Tool paths are the code that tells a certain CNC machine how to move the cutting tools to create the part that has been designed. Different codes exist for different machines. Therefore, the determination of what code is to be implemented will depend on the machine that will be used for the cutting process. The tool paths, in this case, will tell the NC machine to cut the cavities for the each part layer that has been created.

Machining of the cavities into standard mold inserts

The machining of the cavities will be done on a 3-axis mill. This means that the cutting tool of the mill will only be able to move in three planes of motion: left-right, forward-backward, and up-down. Each layer of the part has been generated so that their cavities will be machinable with this type of NC machine, reducing the complexity of the machining process. Figure 6 shows a simulation of a die cavity being machined. As can be seen in the figure, the cutting tool can reach each point on the surface of the cavity by moving in the three planes of motion.

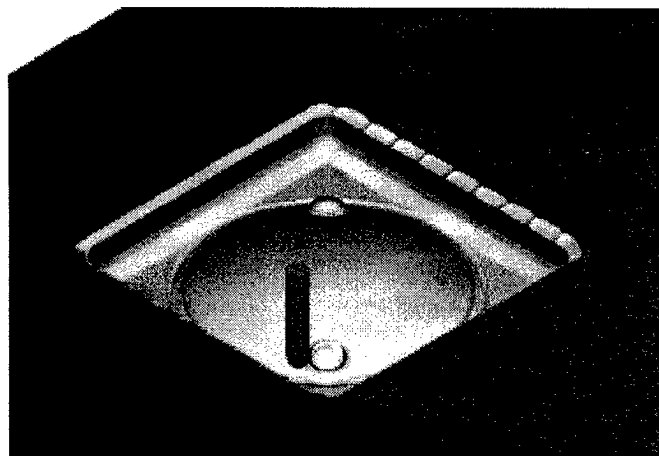


Figure 6

Simulation of NC Machining of Mold Cavities

Molding and Stacking the layers

The next phase in the process is to mold the individual layers on a standard injection molding machine. Once each layer has been molded, it can then be stacked and bonded together with the other layers to form the entire part. The interlocking features will align each layer to the adjoining layer, referencing the entire part together.

Conclusion

Rapid Prototyping by Injection Molding uses the best features of layered manufacturing, NC machining, and injection molding to produce a medium to large quantity of prototypes/parts. With layered manufacturing, one can produce almost any geometry imaginable, including overhanging dimensions and cavities. This process also significantly reduces the complexity of the entire part by decomposing it into several layers, each of which are simple to construct. NC machining, which is very accurate in its dimensioning and surface finish, is used in the mold construction; and since the design of the mold has been simplified by the decomposition process, an expert machinist will not have to be employed to operate the NC machine. Injection molding is the final technique used which is the perfect process for producing a large quantity of the same part. Therefore, Rapid Prototyping by Injection Molding is the perfect process for creating a medium to large quantity of prototypes/parts.

Future Work

Future work for this process will be its automation. At present, software is being constructed that will take an STL file of a part, and automatically decompose it into the necessary layers for the process. It will then generate new STL files for each individual layer. Additional software will be created to take these new layer files and inlay them into a mold with the necessary locking features, ejector pin locations, and runners for the mold halves. It will then take these mold halves and generate the tool paths for the NC machine. Additional work can be done to index the layers, once molded, to stack them automatically.

References

- Bridgeport®, *Installation & Maintenance Manual*, Discovery Torq-Cut 22 with Bridgeport DX-32 Control, Bed-Type Vertical Machining Center with Power Drawbar and Automatic Toolchanger, Bridgeport Machines, Inc., 1995.
- Chamberlain, Peter, Van Roosendaal, Mark, Thomas, Charles, "Variable Thickness ruled edge slice generation and three-dimensional graphical error visualization," *Solid Freeform Fabrication Symposium Proceedings*, 1998.
- Deckard, C. R., Beaman, J. J., "Solid Freeform Fabrication and Selective Powder Sintering," *15th North American Manufacturing Research Conference Proceedings*, Volume 2, SME, May 1987.

Dym, Joseph B., *Injection Molds and Molding*, A Practical Manual, Second Edition, Van Nostrand Reinhold Company Inc., New York, New York, 1987.

Shaikh, F. Zafar, et. al., " Precision Stratiform[®] Machining - 100 Day engine project", *Prototyping International*, 1997.

Thomas, C. L., *An Introduction to Rapid Prototyping*, Schroff Development Corp., Mission, Kansas, 1995

Weiss, L. E., Prinz, F. B. and coworkers, *Journal of Manufacturing Science and Engineering*, Transactions of the ASME v 120 n 3, ASME Fairfield, New Jersey, August, 1998.

Rapid Tooling of Ceramic Parts and Molds using High-Pressure Slip Casting of Si_3N_4

Rolf Pfeifer*, Liwu Wang**, Peter Eyerer*

* Institute of Polymer Testing and Polymer Science, IKP - University of Stuttgart

** Max-Planck-Institut für Metallforschung and INAM - University of Stuttgart

ABSTRACT

A novel rapid tooling technology for the fabrication of ceramic parts has been developed. A concentrated Si_3N_4 slurry is cast in a porous mold. Therefore, a high pressure slip casting device has been constructed which enables the use of relatively fragile polystyrene molds. Polystyrene molds have been produced using rapid prototyping techniques e.g. selective laser sintering. The required porosity is adjustable by variation of the process parameters. Mechanical and chemical methods to demold the ceramic green parts are demonstrated. The technology enables the fabrication of crackless Si_3N_4 parts, particularly molds with high and homogenous density and illustrates the possibility to transfer the results to other ceramics.

1 INTRODUCTION

The processing challenge in the forming of advanced ceramic parts is to achieve a defect-free microstructure in the final body. Forming a ceramic powder into an engineering part can be performed with a variety of methods, such as powder compaction, injection molding, extrusion, slip casting, pressure casting and more. In general the choice between these methods often depends on several important factors, such as product volume, size tolerance, cost, short cycle time to mention a few. Due to the high hardness of ceramic materials, it is almost always cost prohibitive to form a component by removing material from a solid ceramic block or shape.

In the last few years rapid prototyping technologies have been developed to a very high level and allow the direct production of components with complex shapes directly from CAD data. One drawback of most of these processes is the fact that only plastic and metal parts can be accomplished by these technologies /1/. To generate ceramic parts for industrial applications, especially for producing ceramic parts with complex geometries, there are still less possibilities.

Consolidating powders into uniform, near-net-shape powder compacts is an essential element of ceramic processing. Today there exist two major forming techniques for large-scale fabrication of ceramic components with complex shapes: injection molding and slip casting. In injection molding relatively large amounts of polymers are added, which have to be removed before sintering. In the slip casting process there is a liquid which has to be removed from the cast component. Pressure casting or pressure filtration in which a porous mold or a filter was used has been developed to accelerate the drying stage and to get more dense particle packing and hence a more favorable microstructure /2/.

The paper illustrates a rapid tooling technology and apparatus for the rapid production of Si_3N_4 -parts and -molds using high-pressure slip casting in polystyrene molds. Procedures to

obtain porous polystyrene molds applying selective laser sintering (SLS) and sintering in silicone molds are shown. In addition, demolding strategies were investigated to separate green part and polystyrene mold.

2 PRESSURE SLIP CASTING

Unlike slip casting, pressure casting derives its main driving force from an external pressure applied to the ceramic slurry which results in an increased rate of cake formation /8/. The kinetics of pressure casting obeys Darcy's differential equation /3/ for fluid flow through porous media, which, when integrated with appropriate boundary conditions, shows that the thickness of the consolidated layer L , formed when either pressure P , or time t , is kept constant, is parabolically related to the variation in the other of these experimental variables by the equation

$$L^2 = 2K\phi Pt/\eta(\phi_c - \phi)$$

where η is the viscosity of the slurry and ϕ and ϕ_c are the volume fractions of particles within the slurry and cake. The permeability K is inversely related to the resistance to fluid flow through the consolidated layer. This equation assumes unidirectional filtration, negligible mold resistance, constant rheological properties of the slurry, absence of particle setting, and constant permeability, i.e. the body is incompressible.

In practice, cakes are more or less compressible, depending on pressure level, interaction forces between particles and particle size distribution /4//5/. The rate of cake growth is therefore expected to follow a parabolic behavior /4/. That is, the cake should grow as a function of $(\text{time})^{1/2}$. This means that the cake builds up very quickly at the beginning of the casting, then slowly. When the thickness of the cake reaches some value, the rate of consolidation is about zero, because the thick cake will resist any further filtration. This is illustrated by the study of Schwelm /6/.

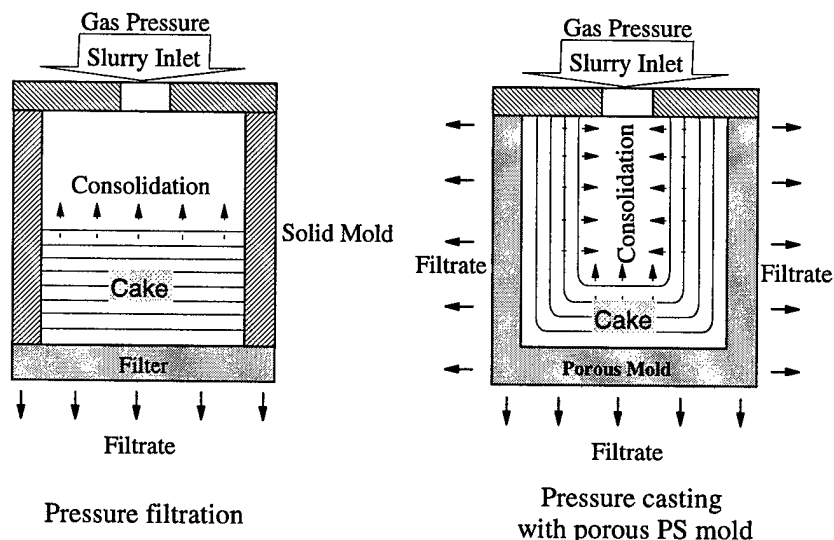


Figure 1: Schematic description of consolidation progress during pressure slip casting

Figure 1 is a schematic description of consolidation progress during casting. The progress of the consolidated fronts are indicated. According to the theory of consolidation, the cake builds up layer by layer until filtration ceases. By usual pressure filtration using a solid mold and plate filter, it is difficult to produce thick components, because at some thickness the consolidation rate

is very slow. Besides this, there also exists a detectable gradient of green density in the direction of consolidation by unidirectional casting /6/. These density differences will cause anisotropic shrinkage during sintering.

These problems could be resolved by pressure casting with a porous PS mold. Unlike usual pressure filtration, the consolidation by pressure casting with PS molds occurs not only in a direction opposite to that of the pressure, but also circumferentially, because the filtrate can go out around the mold, as indicated in right figure of figure 1. It should be noted that the consolidation rate in this way will increase with the additional surface area of the mold and therefore the possibility to cast a thick component will then be increased. Moreover with this new processing the density gradient will also be limited.

2.1 POWDER AND SLURRY PREPARATION

A submicron α -phase Si_3N_4 powder (M11, H.C. Starck, Germany) with a BET specific area of $11.5 \text{ m}^2/\text{g}$ and a mean particle size (d_{50}) of $0.74 \mu\text{m}$, containing 5mass% of Y_2O_3 (AKP247, H.C. Starck, Germany) and 3mass% Al_2O_3 (AKP53, Sumitomo, Japan) as sintering additive, was mainly used for the slurry preparation. The particle size distribution of the powders was measured by He-Ne-Laser-Granulometer HR 850 (Cilas, France).

The slurries containing a 0.31 solid volume fraction of ceramic powder was homogenized by ball milling (a planetary ball mill, Si_3N_4 balls) for one hour in a Teflon container. The aqueous Si_3N_4 -slurry was prepared by addition of 2-amino-2-methyl-propanol ($\text{C}_4\text{H}_{11}\text{NO}$, Fluka Chemie AG) as dispersant. For some slurries PVA was added as a binder and PEG as a plasticizer. After milling dissolved gas in the slurry was removed in a closed vessel under vacuum to prevent the formation of bubbles in the green body. The slurries were characterized by viscosity. The rheological measurements were performed with a rotational viscometer (SR500, Rheometric Scientific, USA) at a constant temperature of 25°C .

3 RAPID TOOLING PROCESS

Figure 2 schematically shows the developed pressure slip casting device designed to cast high concentrated ceramic slurries in porous polystyrene molds. The device consists of two major parts, a store tank and a pressure device. The porous polystyrene mold is glued on a silicone grease coated aluminium plate. The plate is used as a substratum to remove the mold after casting without damaging the inner ceramic cake. Silicone grease is necessary to allow a stress free shrinkage of the drying ceramic on its substratum. The pressure slip casting device has to be turned to fill the pressure device container with fine sand. The whole device is put on a vibraxer to compress the sand, simultaneously the clamped support has to be installed and screwed in. After fixing the clamped support the device is turned and an amount of slurry (according to the volume of the mold) poured into the store tank. The store tank is air tight and a pressure pipeline is installed. The pressure, regulated by a ER2000 pressure device from Dräger-Tescom, can be applied and the cake formation occurs. Pressurized N_2 gas was used to apply the pressure.

As the cake fills the whole mold pressure casting is finished, the pressure is reduced to atmospheric level and the device can be opened. Subsequently the pressure device has to be dismantled and the now solvent tintured sand is poured out. To separate the mold from the pressure device the plate with the filled mold is pushed to the side. Experiments showed, that to ensure a crackfree shear the cake from the pressure device, the sprue gate of the substrate plate has to be edged. The porous polystyrene mold is glued on a silicone grease coated aluminium plate. The plate is used as a substratum to remove the mold after casting without damaging the

inner ceramic cake. Silicone grease is necessary to admit a stress free shrinkage of the drying ceramic on its substratum.

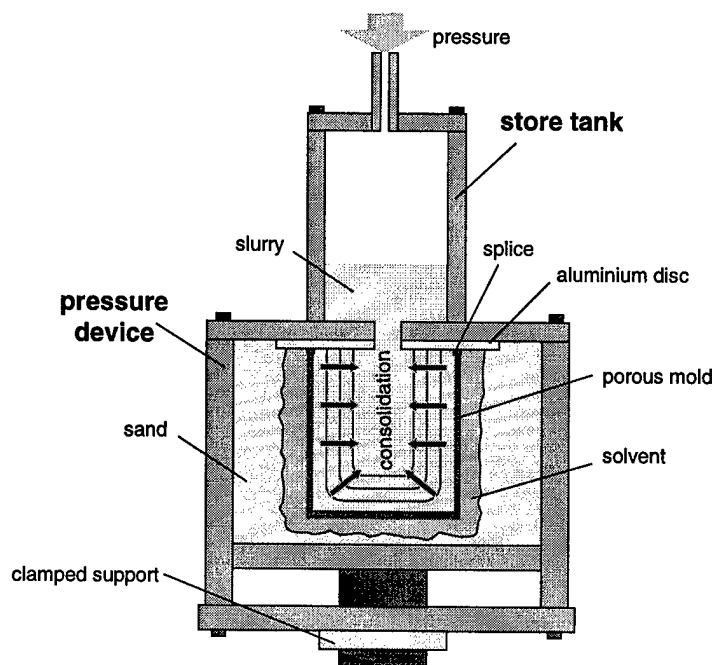


Figure 2: Pressure slip casting device

As the ceramic cakes still contain a high percentage of solvent (in this case we used water as a solvent) the cake has to be dried to get a green body. As during the drying, the ceramic shrinks, it is essential to demold the ceramic cake before drying, otherwise cracks are inevitable. As a matter of principle there exist two demolding methods: mechanical and chemical demolding. A thermal demolding is not applicable because by firing the polystyrene mold the outer regions of the cake are dried too fast and the moisture gradient in the cake causes innumerable cracks on the surface. The other demolding techniques are explained in section 4.3.

4 POROUS MOLDS

Polystyrene powder (from EOS), specially developed for the laser sintering process with an average particle size of 100 μm was used to generate the molds.

4.1 SELECTIVE LASER SINTERING

The laser sintering equipment was an EOSINT 350P having a cw CO_2 laser of 42W. In the experiments the beam power was kept at the maximum value to get a high process speed. Usually laser sintered prototypes should be as dense as possible. In contrast to that a porous polystyrene mold with an amount of pores was desired in this work. Therefore the building parameters have to be optimized to get porous molds with proper porosity and sufficient strength. At a constant hatch distance of 0,2 mm the beam energy density was adjusted by varying the beam scanning velocity from 1000 to 2500 mm/s. The layer thickness was 0,2 mm for all experiments. As support structures influence the homogenous density of the polystyrene molds the building process had to be realized without the commonly used support grid. Hence the first layer was sintered directly on the working platform by treble exposure at maximum power and a scanning velocity of 800 mm/s.

Considering the mechanical strength, samples built at 2500 mm/s cannot be used for pressure casting. Samples scanned at 2000 mm/s provide sufficient strength and proper porosity. For this reason they were chosen as mold material for further experiments. The open pores of these PS samples were measured by means of mercury porosimetry. It reveals an open porosity of about 11% with an average pore diameter of 27 μm . About 2/3 of pores are closed.

The beginning of cake formation is usually different from the rest of the process and depends on interactions between the particles of the slurry and the porous mold. The first consolidation behavior is very important and strongly affected by the characteristics of the ceramic powder and the slurry. Lyckfeldt /3/ summarized the factors which were found to have the main influence on the consolidation behavior of ceramic slurry. As the mean pore size of the sintered PS-molds is 20-50 times larger than the ceramic particle size used, a great amount of slurry gets infiltrated in the mold. To prevent this effect the mold had to be coated with gypsum. Therefore gypsum powder has been dissolved in isopropanol and painted on the molds by means of a paint-brush. The liquid gypsum infiltrates and occludes the pores establishing a porosity in the pores comparable with a gypsum mold. Experiments showed that the gypsum coating prevents the PS-mold from slurry infiltration and consequently accelerates the cake formation.

4.2 SINTERING IN SILICON MOLDS

In order to gain time and accuracy, another sintering procedure (see fig.3) has been applied. Starting from a stereolithography or other RP-model a silicone mold is cast.

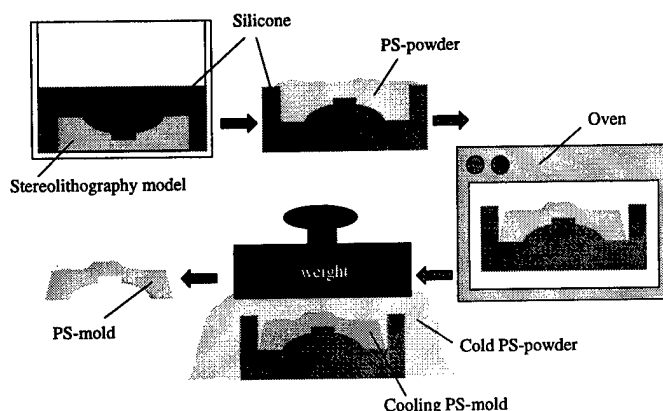


Figure 3: Sintering process in silicone molds

The silicone mold is filled with PS-powder, covered, and given in an oven which is gently heated up. The slow increase of temperature guarantees an equable heating of silicone mold and powder. After reaching the sintering temperature range (about 125°C) of the PS-powder the temperature is held until a sufficient firm sintering is reached. As silicone is a bad heat conductor the sintering time is widely dependent of the thickness and the silicone used.

After sintering the mold is taken out of the oven, covered with cold PS-powder and a weight placed on top. During the cooling the weighted powder prevents the shrinking mold from curling and guarantees an exact molding of the silicone model. The advantages of that sintering concept are obvious: no staircase effect, better surface quality and the opportunity to produce as many molds as required.

4.3 DEMOLDING TECHNIQUES

As mentioned before there exist two demolding principles: mechanical and chemical demolding.

4.3.1 MECHANICAL DEMOLDING

The first green bodies were demolded mechanically by carefully paring the sintered layers with a scalpel. With this the major problem are the sintering parameters. A hard sintered mold with high strength is difficult to demold because the layers hold together too much, whereas a soft sintered mold is easy to peel but contains defects which can precipitate an intrusion of slurry into the mold or at worst a fracture of the mold. Furthermore, experiment showed that this demolding strategy is unapplicable on complex geometries.

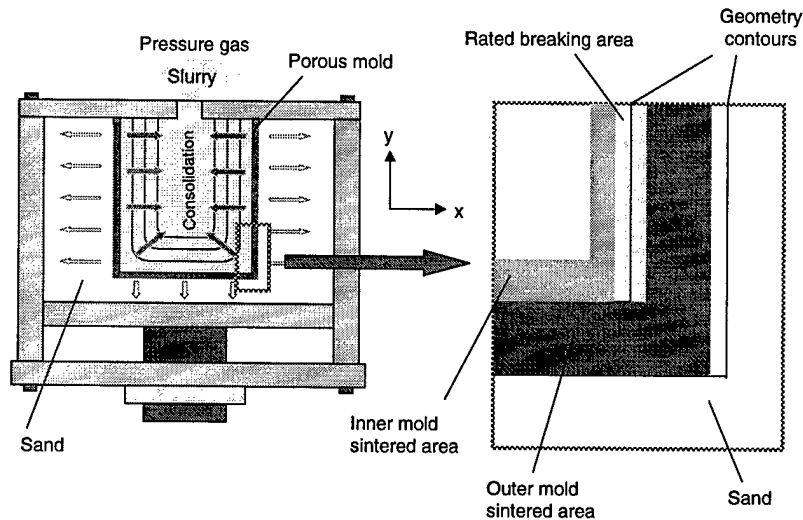


Figure 4: Double mold production with rated breaking area

On this account an improved sintering concept for mechanical demolding was developed (figure 4). The produced part consists of a thin inner and a stabilizing outer mold separated by an unsintered region in the layer (x-direction) direction. In the building direction (y-direction) there is no unsintered area applied because on one hand, only an unsintered region of layer thickness is possible which causes problems in the sintering process, on the other hand the layers can easily be separated by paring with a scalpel. As the geometries of inner and outer mold have to be constructed at a tangent to each other, the rated breaking point between them is reached by implementing a bigger hatch compensation (0,6 - 0,8 mm) for the laser scanning parameters than usual. After the slurry is cast in the mold, the outer mold is removed with a scalpel and then the inner mold with a thickness about 1,5 mm can be peeled from the ceramic cake.

4.3.2 CHEMICAL DEMOLDING

As experiments showed that mechanical demolding is complicated and labour-intensive, dissolvers were tried to dissolve the polystyrene molds. After casting the mold was placed in a dissolver filled, closed exicator with a magnetic mixer. After some hours the polystyrene mold is dissolved and the ceramic green body lies demolded in the bath. The gypsum coating still adheres to the cake and as the gypsum binds to water, it mainly prevents toluene from penetration in the slurry. The part is taken out of the toluene bath and immersed in clean PS-free toluene. After that the wet green body is taken out and cautiously dried. Before sintering, remnants of gypsum and PS have to be remotely rubbed off with a stiff paint-brush.

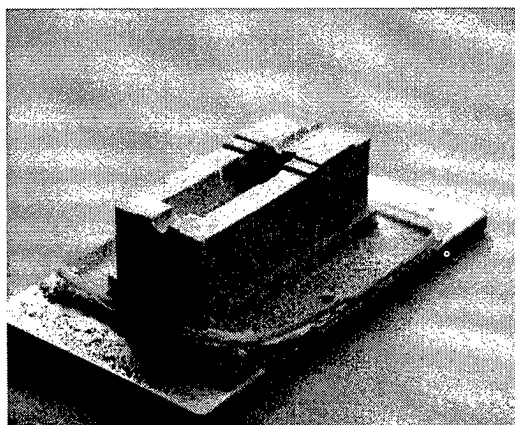


Figure 5: Green body after demolding with Toluene

5 RESULTS

Specimens fabricated with this new processing achieved a high sintered density of $> 97\%$ of the theoretical value, as shown in Tab.1. All the samples were cast using the slurries with a solid volume fraction of 0.31. The value for the sample PSC (pressure slip casting) is a mean value of many samples.

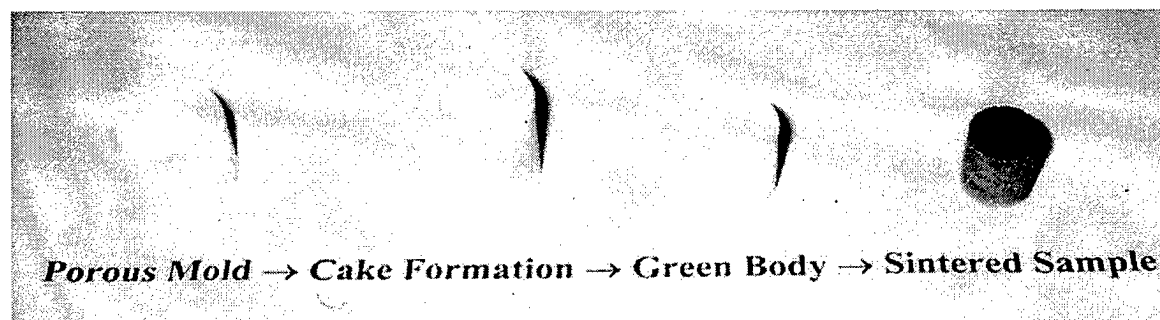


Figure 6: Steps of the process

There is a correlation between the green density and the final sintered density. It should be noted that the green density appeared to be the most important parameter for the final product and it depends strongly on the properties of the slurry in this process. The remaining porosity within the samples is, in general, very small, and well dispersed throughout the matrix.

Sample	Green density (% of theor.)	Sintered density (% of theor.)	Linear shrinkage (%)	Note
PSC	57.2	97.6	radial $\Delta\Phi$: 18.5 Δh : 18.5	pressure slip casting with homogeneous slurry
CIP	56.0	96.0	radial $\Delta\Phi$: 18.4 Δh : 18.4	cold isostatic pressing (600MPa)

Tab.1: Green and sintered densities and the shrinkage of Si_3N_4 samples

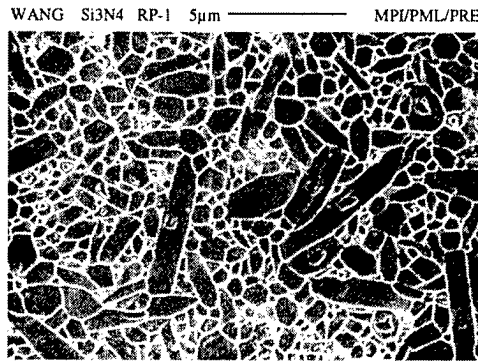


Figure 7: SEM micrograph of a polished specimen (plasma etched) showing the grain structure of sintered Si_3N_4

In order to investigate the sinterability, a sample prepared by cold isostatic pressing with the same composition was also sintered at the same sintering conditions. The Si_3N_4 parts produced by this new technology has the highest relative density (Tab.1). The $\beta\text{-Si}_3\text{N}_4$ phase with homogeneous microstructure is very well developed (as shown in Fig. 7). The glass phase is also uniform. From Tab.1 we know that the linear shrinkage after sintering both in radial and high directions of the simple cylinder specimen is nearly the same. No inhomogeneous shrinkage could be detected. This means that the green density before sintering is very uniform, just like the specimen produced by cold isostatic pressing.

6 ACKNOWLEDGMENT

This work is supported by the state of Baden-Wuerttemberg under contract 07-105-406 in cooperation with Bertrand Fahrzeugtechnik GmbH, Cardenas GbR, Oxidkeramik J. Cardenas GmbH and VEPA GmbH.

References

- /1/ P M Dickens, Rapid prototyping of Metal Parts and Tools, Competitive Advantages by Near-Net-Shape Manufacturing, edited by H.-D. Kunze, 311-317, 1997
- /2/ T. Betz, W. Rieß, J. Lehmann & G. Ziegler, Wichtige Parameter beim Schlickerdruckguß von Al_2O_3 (Teil 1), Cfi/Ber. DKG 74 (1997) No.2 101-105
- /3/ O. Lyckfeldt, E. Liden, M. Persson, R. Carlsson & P. Apell, Progress in the Fabrication of Si_3N_4 Turbine Rotors by Pressure Slip Casting, J. Europ. Ceram. Soc., 14 (1994) 383-395
- /4/ F.M. Tiller & C.D. Tsai, Theory of Filtration of Ceramics: I. Slip Casting, J. Am. Ceram. Soc., 69 (1986) 882
- /5/ J.H.D. Hampton, S.B. Savage & R.A.L. Drew, Experimental Analysis of fine-Particle Migration during Ceramic Filtration Processes, J. Am. Ceram. Soc., 75 [10] 2726-32 (1992)
- /6/ F.F. Lange & K.T. Miller, Pressure Filtration: Consolidation Kinetics and Mechanics, Am. Ceram. Soc. Bull. 66 [10] 1498-1504 (1987)
- /7/ M. Schwelm, Untersuchungen zur Dispergierbarkeit und zum Druckschlickerguß von Si_3N_4 mit $\text{Y}_2\text{O}_3\text{-Al}_2\text{O}_3$ Sinteradditiven, Dissertation, 1992
- /8/ E.G. Blanchard, Pressure casting improves productivity, J. Am. Ceram. Bull., 67 (1988) 1680

Rapid Tooling of Al_2O_3 Parts using Temperature Induced Forming

Rolf Pfeifer*, Liwu Wang**, Peter Eyerer*

* Institute of Polymer Testing and Polymer Science, IKP - University of Stuttgart

** Max-Planck-Institut für Metallforschung and INAM - University of Stuttgart

ABSTRACT

A novel near-net shape process for the rapid production of complex-shaped ceramic prototypes has been developed. By using a newly developed in situ temperature induced forming (TIF) technology, concentrated ceramic slurries are vacuum cast into a mold, which has been produced in a rapid tooling process. The tooling process enables the production of complex-shaped molds which allow powerless demolding. The TIF technology enables the change of particle potential in the slurry from a repulsive into a weakly attractive particle network during consolidation. In combination of TIF- and rapid tooling technology a green body with a high and homogeneous density without any cracks can be realized.

1 INTRODUCTION

The processing challenge in the forming of advanced ceramic parts is to achieve a defect-free microstructure in the final body. Forming a ceramic powder into an engineering part can be performed with a variety of methods, such as powder compaction, injection molding, extrusion, slip casting, pressure casting and more. In general the choice among these methods often depends on several important factors, such as product volume, size tolerance, cost, short cycle time and more. Due to the high hardness of ceramic materials, it is almost always cost prohibitive to form a component by removing material from a solid ceramic block or shape. Therefore, near-net-shape forming is regarded as the most efficient, economical and reliable pathway for practical applications /1/.

Temperature induced forming (TIF) /2/ is a novel forming method for ceramics via a colloidal processing route. Consolidation of a highly filled ceramic slurry is induced simply by an increase in temperature. No dispersing media needs to be removed and so a nonporous mold can be used. TIF produces not only near-net-shape parts, but also complex shapes limited only by the mold design.

Consequently, a novel rapid tooling process for the production of complex-shaped ceramic prototypes has been developed by combining temperature induced forming with a rapid tooling technology allowing an almost powerfree demoulding. This novel process allows the production of advanced ceramics with a high surface finish, near-net shape and reliability in their mechanical properties.

2 TEMPERATURE INDUCED FORMING (TIF)

Figure 1 presents a flowchart for the TIF process. Al_2O_3 powder (AKP 53, Sumitomo, Japan) with mean particle size of $0.24 \mu\text{m}$ was used for the experiments. Aqueous Al_2O_3 slurry at a solid volume fraction of 0.55 with tri-ammonium citrate (TAC) (Fluka, Germany) as dispersant was homogenized by ball milling (a planetary ball mill, ZrO_2 balls) for two hours in a Teflon container. As reported by Luther /3/, the isoelectric point of Al_2O_3 shifts from about pH 9 to pH 3 when a large amount of tribasic ammonium citrate is added. The pH value of the Al_2O_3 slurry is stable at about pH 10 due to the dissociation of TAC. Therefore, TAC is a very good dispersant

for Al_2O_3 with which a highly concentrated slurry with low viscosity can be realized. Poly(acrylic acid) (PAA) from Polyscience, Inc. was added to a dispersed Al_2O_3 slurry and further ball milled at lower speed. After milling, the dissolved gas in the slurry was removed in a vacuum chamber at about 20 mbar.

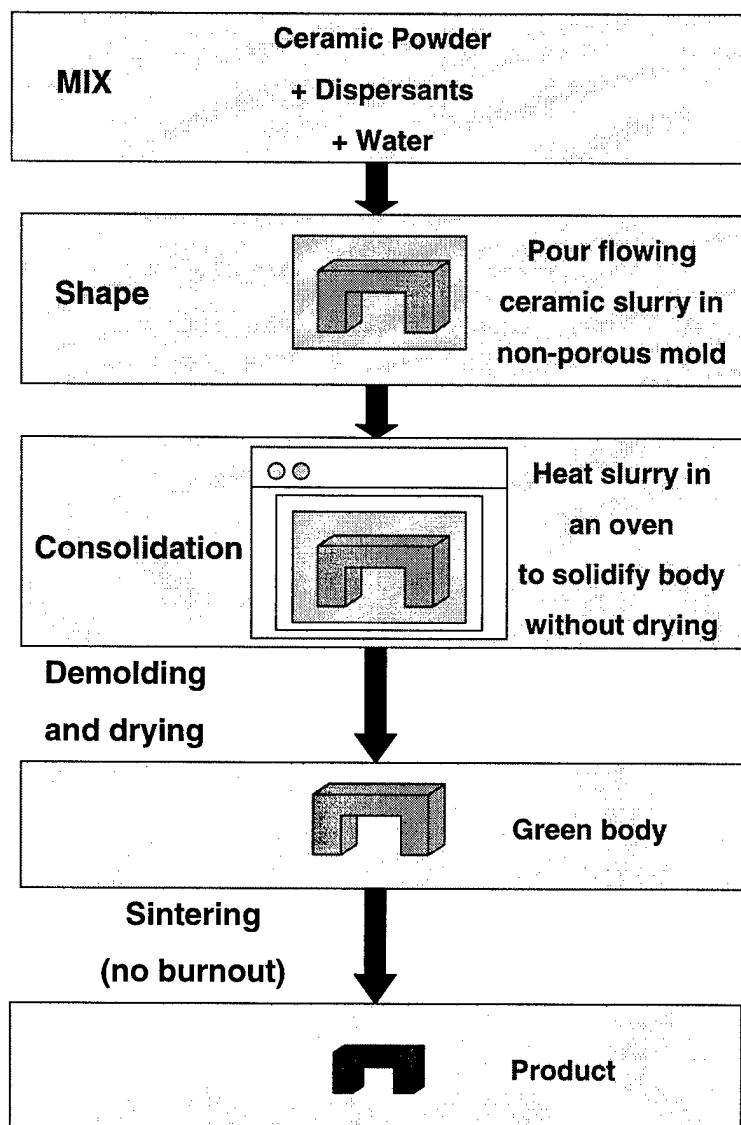


Figure 1: TIF process

This highly concentrated Al_2O_3 slurry is then poured into a non-porous mold. After casting, the slurry together with the mold is sealed and warmed up in a furnace. The temperature treatment at about 60°C yields coagulated slurry in the mold. An elastic wet green body can be achieved without drying. After demolding, drying and sintering, a near-net shape ceramic prototype with a high degree of surface finish and reliable mechanical properties is achieved.

Recent studies indicated that the consolidation of Al_2O_3 slurry results from bridging flocculation of the polyacrylic acid caused by a competitive adsorption of the dispersants that is enhanced with increasing temperature. The rheological properties are a key to monitor this

gelation behavior. Figure 2 shows the relationship between the viscosity of Al_2O_3 slurry and temperature. Aqueous Al_2O_3 slurry at a solid volume fraction of 0.34 was used for the rheology measurement. The pH value of the slurry was adjusted to pH 9.12 with KOH. The measurement was performed with a rotational viscometer (SR500, Rheometric Scientific, USA) at a shear rate of 20 s^{-1} as the temperature was increased from 25°C to 60°C . Vegetable oil was placed on top of the slurry to prevent evaporation of water. By increasing the temperature, the viscosity of the slurry increases rapidly because of bridging flocculation. The significant gelation occurs at temperatures between 30°C and 40°C . The plateau region in the viscosity curve is due to the break down of the gelled network by rotation during measurement.

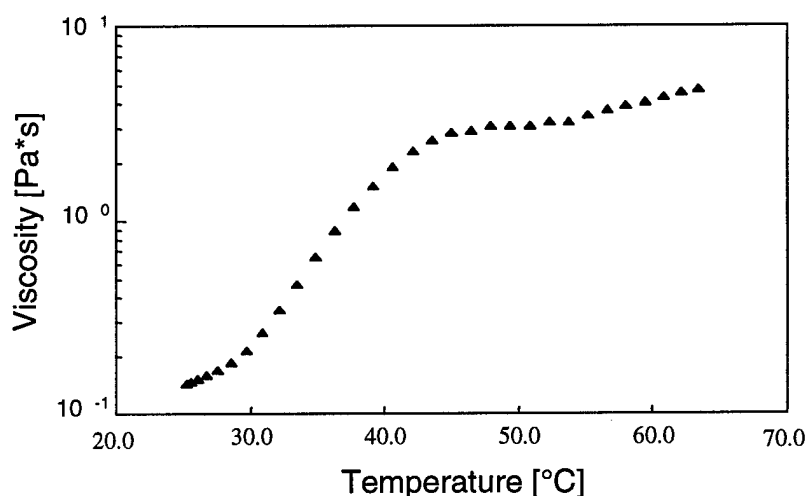


Figure 2: Gelation of TIF-slurry by temperature

Thus, green parts are easily produced by heating alumina slurry at high solid loading in such a way that evaporation is minimized. Once the system is cooled and has sufficient green strength, the body can be removed from the mold and then dried.

The consolidation of the slurry occurs in the mold without any external stress and the shaped parts are dried after demolding. Therefore, a green body with high and homogeneous density (about 65 %) as well as fine surface structure without cracks can be realized.

3 RAPID TOOLING PROCESSES

During the consolidation of the slurry the particle potential changes from a repulsive into a weakly attractive particle network. This weak attraction results in a green body strength comparable with gelatin. To demold simple geometries silicone molds can be used, but in order to obtain complex-shaped green bodies containing undercuts and thin structures an almost powerless demolding process is required. Figure 3 and 4 show the applied rapid tooling processes.

Figure 3 illustrates a process specially for producing small complex-shaped parts. At the beginning of the process a model of an acid-soluble wax has to be manufactured. Applicable techniques are milling or casting in silicone or solid molds. Depending on the melting temperature of the waxes used, the wax model is dipped or immersed in an insoluble wax. Short time dipping or additional cooling of the acid-soluble wax could prevent a blending of the applied waxes. Subsequently the coated acid-soluble wax is immersed and dissolved in an acid-solution.

The TIF-slurry is casted in the hollow wax body generated. The sealed mold is placed in an vegetable oil bath and heated-up to about 60°C to effectuate the coagulation of the TIF-slurry in the mold. As wax is a very bad heat conductor the heating time is relatively long. After the coagulation of the whole slurry the temperature of the oil bath is raised over the melting range of the encasing wax. The wax gets partially dissolved in the oil, the rest is sinks to the bottom of the bin. The oil prevents the ceramic body from air contact and drying at high temperature. The demolded green body remains in the oil until room temperature is reached. Afterwards the part is taken out of the oil and dried under controlled environmental conditions. This way the rapid tooling procedure ensures a powerless demolding and a controlled drying, the requirement to obtain complex shaped, crack free green bodies. If the self weight and the geometry of the ceramic part is under certain limits, the process allows production of green parts without a plane bottom.

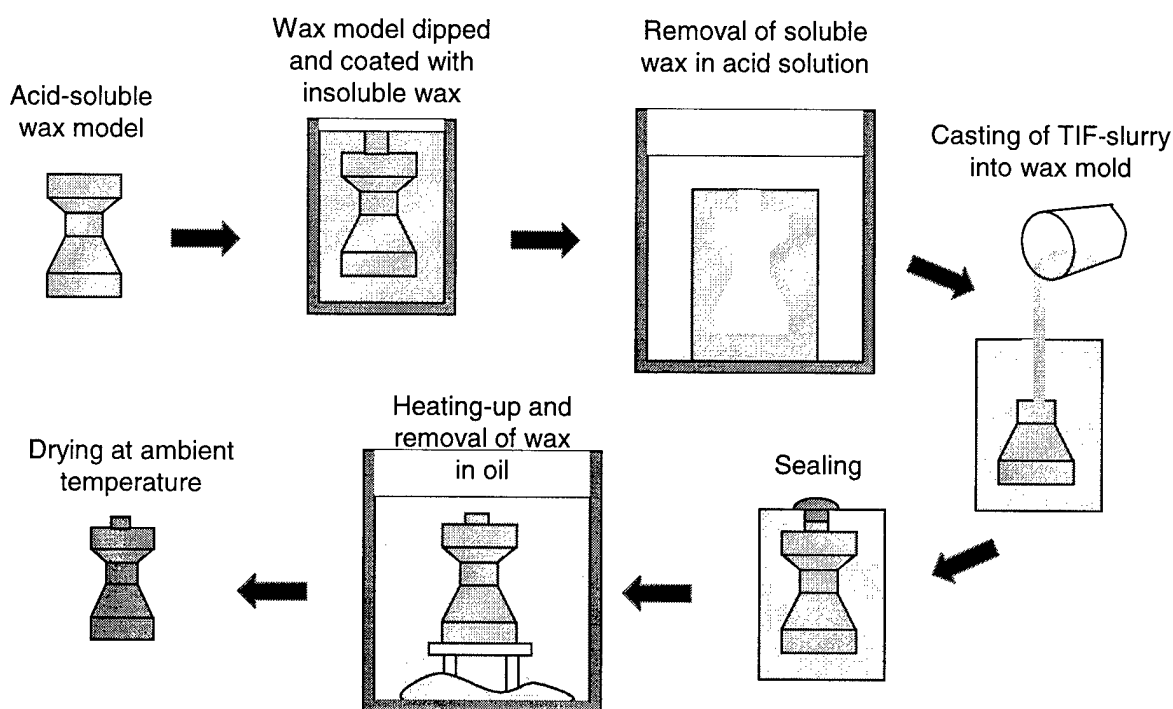


Figure 3: Rapid tooling process using acid-soluble wax

Figure 4 shows a simplified rapid tooling process. The process enables the production of TIF-parts of restricted geometry.

In a first step a silicone part with a plane bottom had to be produced and immersed in a wax. The silicone part is placed on a small substructure that enables the wax to flow around the silicone body. This procedure ensures that the wax is shrinking from all directions on the silicone body and no undesirable warp of the cooling wax occurs. The top side of the solidified wax is milled even and the silicone part is pulled out. TIF-slurry is cast in the wax mold until a meniscus, caused by the surface tension of the slurry, is reached at the top of the mold. A silicone grease coated disk is pushed over the top of the mold sliding away excessive slurry. This procedure ensures that the slurry is airless and covered. Afterwards the mold is turned upside-

down in the oil bath. The remaining process is as described above. The process enables the rapid production of more voluminous green bodies.

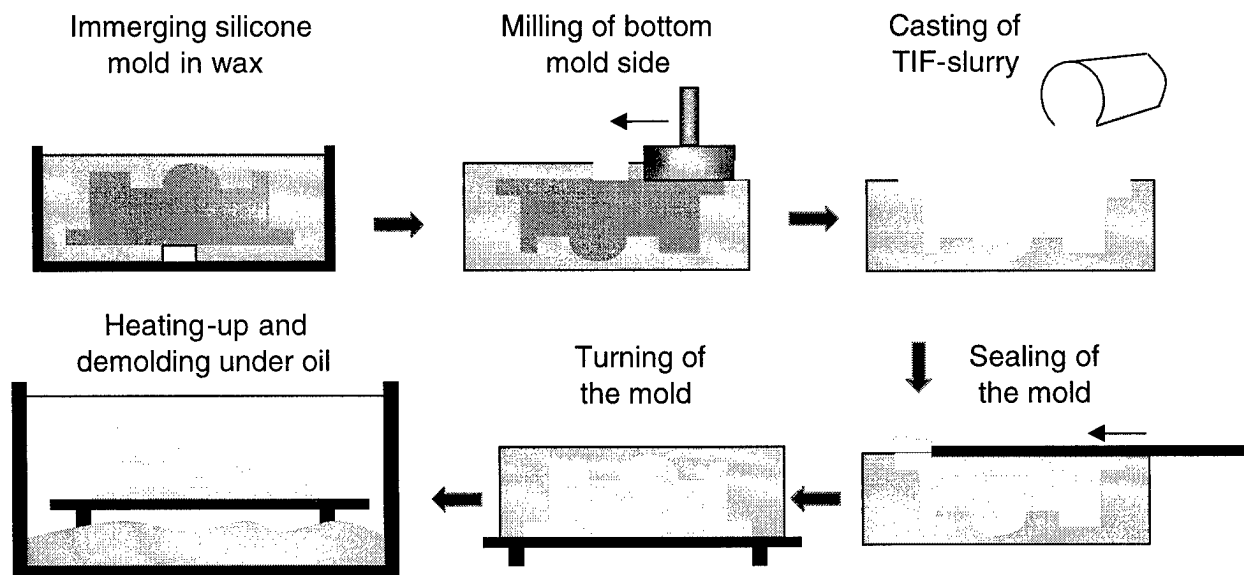


Figure 4: Rapid tooling process using silicone models

4 Results

One example of a stereolithography model and sintered Al_2O_3 is shown in figure 5. Figure 6 shows a complex shaped ceramic tool after removal from the oil bath with wax rests on the surface.

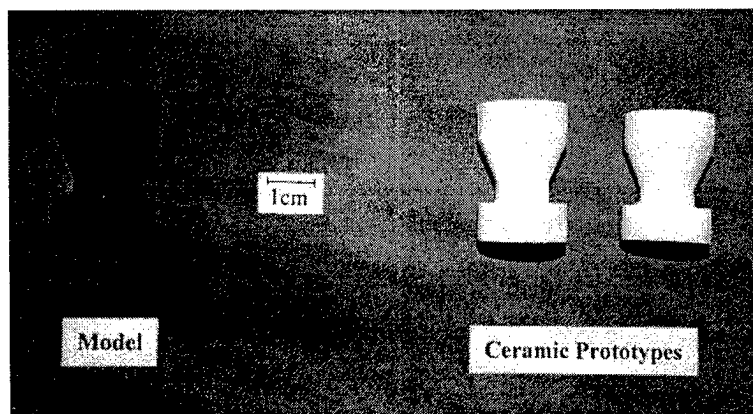


Figure 5: One example of a stereolithography model and the sintered Al_2O_3 parts

The microstructure of the sintered parts is very homogeneous with a mean grain size of about $1\text{ }\mu\text{m}$ (Figure 7). Sintering was performed at 1400°C for two hours in air. Highly densified microstructures are found with only a very small amount of pores in the grains and some

abnormal grain growth because of the absence of sintering aids. Therefore, we conclude that this process can achieve homogeneous microstructures.

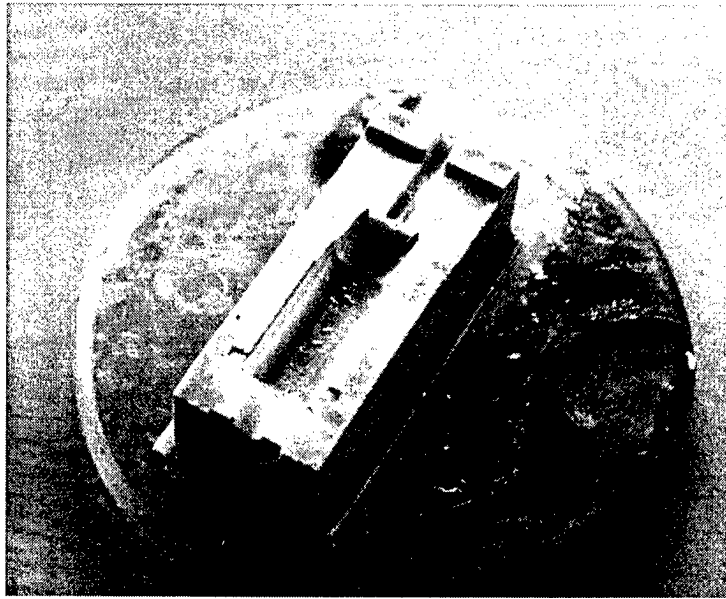


Figure 6: TIF-Ceramic after removing of the oil bath

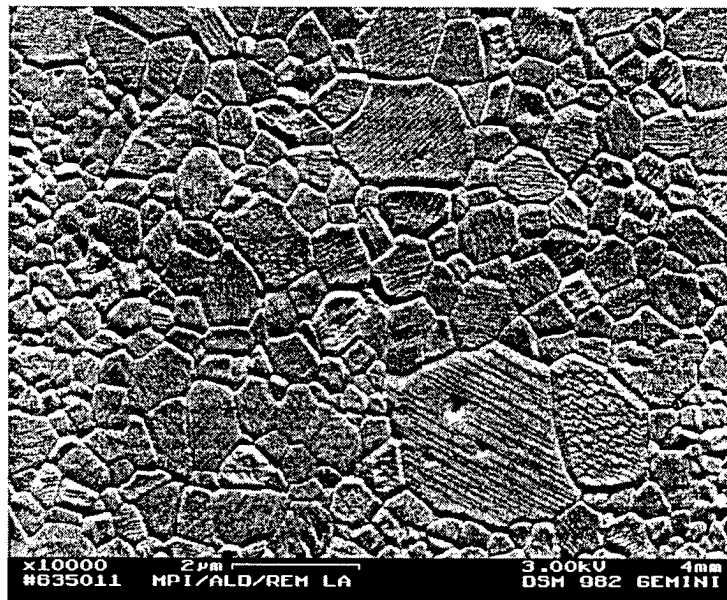


Figure 7: Sintered Al_2O_3 made by the TIF process showing fully dense microstructure with grain size between 0.5 and 2 μm .

The advantage is obvious if the mechanical properties of sintered Al_2O_3 are considered for the TIF process in comparison to conventional cold isostatic pressing (CIP) at 200 MPa. The bending strength at room temperature (RT) was tested on a 20/40 mm four-point fixture with bend specimens of 3 x 4 x 45 mm³ followed by cutting and polishing from sintered Al_2O_3 bars at 1400°C for 2 hours in air without sintering aids. The bending strength for the TIF processed

Al₂O₃ bars (5 specimens) was 455 ± 30 MPa, whereas for CIP processed Al₂O₃ bars only 269 ± 28 MPa were achieved. The significant increase in the bending strength can be attributed to a very high degree of deagglomeration and good dispersion of the originally strong agglomerated sub-micron Al₂O₃ powders. It also indicates homogeneous consolidation as well as stress-free drying by TIF. Further improvements of the mechanical properties by optimizing the TIF processing with filtration to remove heterogeneities and introducing sintering aids, such as MgO are under investigation.

5 CONCLUSIONS

In this work a novel process for the fabrication of advanced ceramic prototypes has been developed by combining rapid tooling technology and temperature induced forming to produce reliable and complex-shaped ceramic prototypes quickly. Complex-shaped molds with high surface quality can be produced. Highly concentrated Al₂O₃ slurry is consolidated in non-porous molds simply by mildly increasing the temperature. Therefore, fine and dense green parts without any cracks can be realized. Apart from the near-net shape, the process also has significance for production of advanced ceramics with reliable mechanical properties. Higher bending strength at RT is achieved for the TIF process in comparison to conventionally processed (CIP) powder.

This novel near-net shape technique offers the opportunity to significantly shorten the time to market for the production of new ceramic parts. TIF enables the forming of advanced ceramic prototypes and the process also seems suitable for small series production. This new forming method has many advantages, such as rapidly produced complex-shaped ceramic parts, a more homogeneous density distribution of the green body and consequently more reliable mechanical properties than conventional pressing techniques offer.

6 ACKNOWLEDGMENT

This work is supported by the state of Baden-Wuerttemberg under contract 07-105-406 in cooperation with Bertrandt Fahrzeugtechnik GmbH, Cardenas GbR, Oxidkeramik J. Cardenas GmbH and VEPA GmbH.

REFERENCES

- /1/ M.N. Rahaman, „Plastic Forming Methods”; pp. 309-15 in *Ceramic Processing and Sintering*, Marcel Dekker, Inc., New York, 1995
- /2/ W. Sigmund, J. Yanez and F. Aldinger, „Forming Method for Ceramics and Metals in Aqueous System by Temperature,” European Patent Application, PCT/EP98/03555, 1998
- /3/ E. P. Luther, J.A. Yanez, G.V. Franks, F. F. Lange and D. S. Person, „Effect of Ammonium Citrate on the Rheology and Particle Packing of Alumina Slurries, *Journal of the American Ceramic Society*, **78** [6] 1495-500 (1995)

FAST INK-JET BASED PROCESS

I. Ederer*, H. Seitz*, A. Welisch**

*FGB, TU Munich, Germany

**FORWISS Passau, Germany

ABSTRACT

With a new ink-jet based SFF processes, the building rate can be improved dramatically compared to single laser based processes. One reason for that is the multi-jet-technology well known in ink-jet-printing. Process velocity can be additionally increased by dividing material application and geometry information transfer. Theoretically, the cross section of an object can be described only by its outline. This paper describes a new ink-jet based process reducing printing times by using a combination of creating thin shells and a rapid application of building material.

INTRODUCTION

Three Dimensional Printing technique becomes more and more important: because it is accurate, cost effective and can be fast. At the moment we can find three different ink-jet based processes at the market.

- MIT's powder-based "Three Dimensional Printing" with different applications
- Multi-Jet-Modeling by 3D Systems
- Model-Maker by Sanders

The common problems of all these processes are:

- the jetted material must have special properties (low viscosity, enough surface tension)
- typically the droplet volume amounts about 113 fl. This means for 1 liter dosed material about 8840 billion droplets are needed!
- the support structure should be easily removable

For each problem we find different solutions used by these processes. Sanders and 3D Systems use wax in a melted state as dosing material, MIT uses liquid binder. Due to that, stiffness and rigidity of the models are limited. Likewise the volume problematic is solved differently. As the name expresses, the MJM uses numerous parallel addressable nozzles to increase speed. A 3DP model consists out of powder material at the main part, thus a comparable small part of binder has to be jetted.

The idea behind the development is to achieve a fast process with good model properties by combining the positive characteristics of the described processes.

3D PRINTING METHOD

To set up this new process, two steps are necessary: the amount of the jetted material must be reduced to a minimum, and the dosed material mustn't be a part of the desired object.

This will be achieved by segregation of the process in information transfer and material deposition. The minimum information to create the cross section of an object is the boundary line. This outline will be printed by means of a droplet generator. Thus a thin shell of the model will be formed. For example, the shell material could be a release wax with a high melting point. In the next step the layer is filled with building material by a rapid application. This material could be also wax with a lower melting point or a fast curing resin etc.

Figure 1 shows the new printing method for making a three-dimensional body:

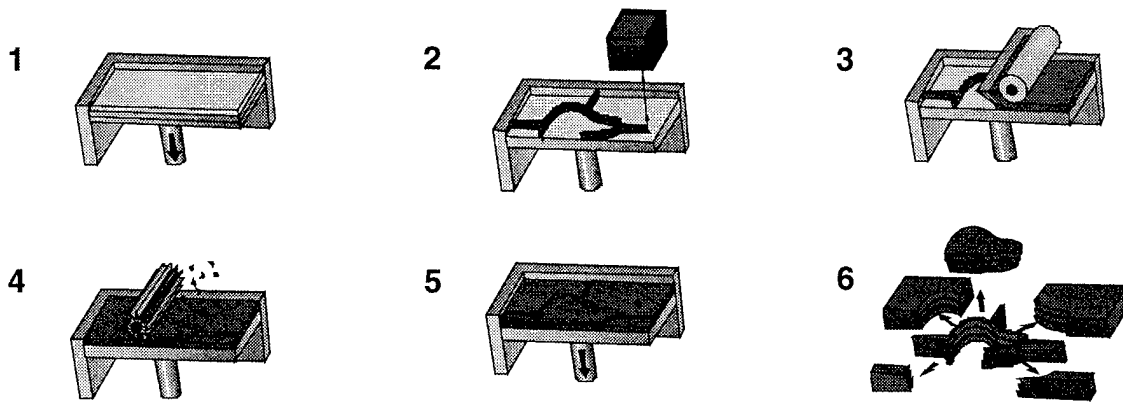


Figure 1: 3D Printing Process

The repeated steps are:

- 1) Lowering the platform according to the layer thickness.
- 2) Applying a release wax in its liquid state onto selected areas of a building platform by a multi-jet printhead, using a pattern according to the cross-section of a thin-walled shell around the three-dimensional body, and a grid pattern (not shown in Figure 1) across the remaining area of the building platform.
- 3) After finishing of the pattern of the current layer, the areas enclosed by the release wax are filled with the building wax.
- 4) Smoothing and planing of the layer in order to expose the upper surface of the release wax.
- 5) Ready for the next layer. Repetition of the steps 1) to 4) with patterns according to the current cross-section of the three-dimensional body, thereby making the body itself.
- 6) Removing the structures not belonging to the body by dissolving the release wax.

FEATURES

The advantages of the described process in comparison with the state of the art consists of the combination of a selective material deposition, mostly in lines and a non selective, rapid application of building material for filling up the layer. Due to the application of the release agent in small regions during the first step the whole process will be accelerated significantly.

Moreover, the differentiation between building and support material can be neglected because both structures will be formed by the same material during the rapid application of the building material. The differentiation is made due to the location of the material, either it is located inside the region enclosed by the border corresponding to the section plane of the object and therefore building material, or outside the border and therefore support material. The applied release agent is the preposition for this decision.

The building of a cavity is possible by filling the release wax layerwise in regions which belong to the cavity volume. By solving the release wax after the process, extracting the object and emptying the cavity through a provided hole the designated object will be demoulded.

Due to the use of a ink-jet like drop-on-demand dosing device for the application of the release agent, cost-effective and accurate systems can be designed which will reduce the overall system price.

Additionally the choice of building materials is much wider than with the processes described above, because material properties like viscosity and surface tension in the liquid state are affecting the application much less. Due to that, objects with much better properties like rigidity, stiffness, hardness and surface quality can be made.

Because of the wide choice of materials, it is possible to find material combinations which will produce less emissions during the building process and which are not affective to skin. Due to that, the most important requirement for an office compatible device is fulfilled.

After the process the complete building volume is taken from the device as a solid cube. Therefore no special handling devices are necessary. There are no loose particles or unhardened resin which can pollute the environment or affect the user.

With a suitable composition of a release wax the removal of the non-object-parts can be done without any tools. Solving of the release agent is possible by a solvent, preferably water or by means of heat.

Due to the complete hardening of the wax there is no hazardous waste.

Any object geometry can be produced in short time and without use of other means, provided that object defining three-dimensional computer data exist, for example CAD-data. Other data sources can be used as well, for example output of three-dimensional scanners.

DROP-ON-DEMAND DOSING DEVICE

A printhead has been developed to apply the release wax in its melted state onto selected areas. The dosing device (see Figure 2) is a multi-jet drop-on-demand printhead that can be heated up to 130 °C. Due to the rheologic characteristics of the release wax a piezoelectric multilayer bending

actuator is used. Existing acoustically systems can't generate the necessary impulse and bubble jet systems have negative effect on release wax because of the heat transfer into the release wax.

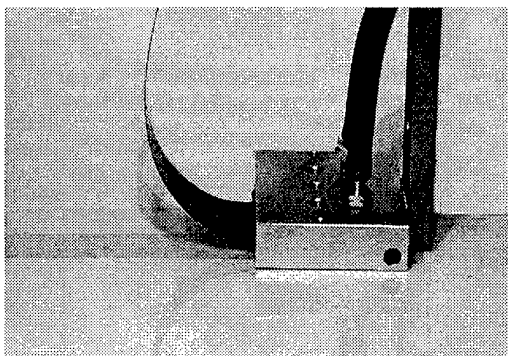


Figure 2: Piezo Printhead

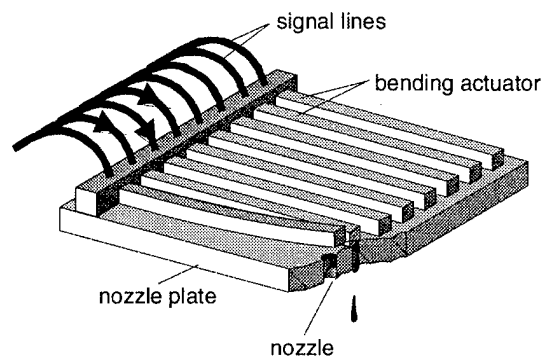


Figure 3: Nozzle plate with actuators

The nozzle plate (see Figure 3) indicates a row of very small, precise nozzles. An actuator is assigned to every nozzle. This assembly is covered by the chassis which has the function of a fluid chamber to provide the actuators with fluid. Each of the actuators can be run independently from the remaining actuators. The bending actuators are fixed at one end. The nozzles are placed below the free ends of the actuators.

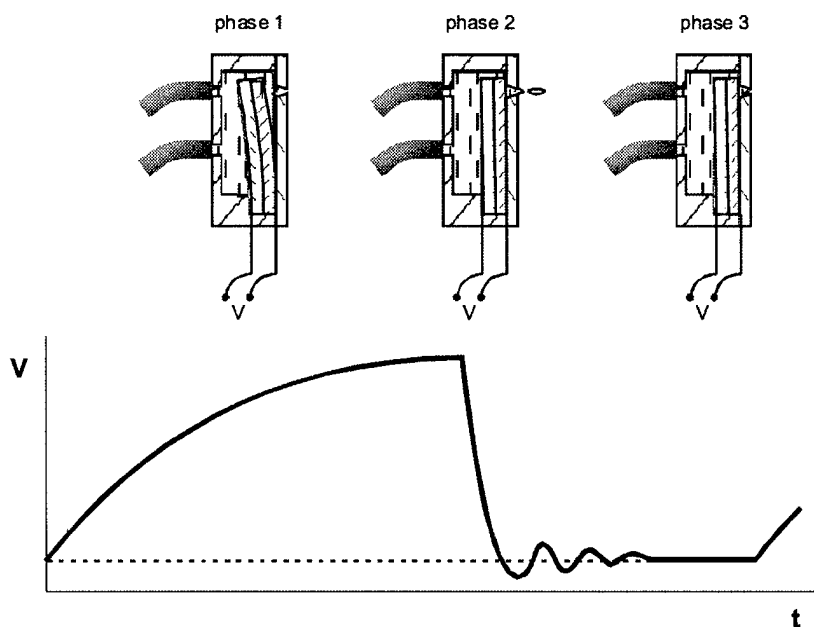


Figure 4: Functionality of the Piezo Printhead

The piezoactuator is a bending actuator. The functionality of the printhead is shown in Figure 4. After applying a voltage the bending actuator deviates at its free end away from the nozzle plate,

so the fluid can flow in the gap between the bending actuator and the nozzle plate. After discharging, the bending actuator relaxes suddenly towards the nozzle plate and forces the liquid through the nozzle. The resulting droplet is moving perpendicularly away from the nozzle plate. Piezo bending actuators combine a high deflection with a high velocity of the actuator. Thus a high fluid-mechanical impulse is transferred to the fluid. Due to that it is possible to dose a wide range of release waxes.

Figure 5 shows the features of a single printhead:

number of nozzles	32	
viscosity	0,7 - 20	mPa s
temperature range	20 – 130 (68 – 266)	°C (°F)
nozzle pitch	50	dpi
continuous frequency	5	kHz
nozzle diameter	50	µm
supply voltage	35 - 55	V

Figure 5: Features of the printhead

SOFTWARE

For the shell production a special layer-based algorithm is needed. The following lines show a method to calculate the dividing shell given the outline of the objects as CLI-data.

From slice-data to the object-shell

If the workspace is assumed as a room with voxels representing the drops of the release material, the cross sections of the dividing shell would be monochrome bitmaps. The presented algorithm operates directly on these bitmaps being printed by the wax-jet later on.

Let w be the necessary width of the dividing shell in the xy-plane. Then the easiest way to produce the shell is to draw a w pixels thick line (i.e. with a standard Bresenham-algorithm) around the border of the object-area. This line is called an offset-line.

However, some circumstances require that we consider the sections lying above and below the layer currently processed. In order to describe these facts we need some definitions:

- L_z is the layer currently processed.
- $r \in \mathbb{N}$ recoating interval (recoating takes place every r layers).
- $s \in \mathbb{N}$ is the thickness of a layer.
- $inner(z)$ the union of all regions covered by the part within layer L_z .
- $outer(z)$ is the complement of $inner(z)$.

The requirements for considering layers in the neighborhood are

- a) We only want to recoat the layers $L_{i \cdot r}$ with $i \in \square$. Therefore we have to take into account the layers L_{z+1} up to $L_{n(r)}$ in order to support overhangs directed to the outside, where $n(r) = \min\{x \geq z \mid x = i \cdot r, i \in \square\}$.
- b) The boarding of the current layer requires to look at the layers $\{L_{z-s}, \dots, L_{z-1}\} \cup \{L_{z+1}, \dots, L_{z+s}\}$.
- c) All regions covered by the part must not contain release material, so if $inner(z) \cap outer(z+1) \neq \emptyset$ (the part tapers) \Rightarrow we have to recoat after layer L_z .

Additional application of release material to facilitate a thermic separation

To uncover the prototype after the building process, we need extra dividing walls. For example we could cut the workspace into cubes with our dividing material. The cubes could have different sizes - outside the prototype big cubes would shorten the building time, in hollow spaces the cubes have to be small enough in order to get them out through the holes of the object.

The Algorithm

The above considerations lead to the following algorithm for the shell around a prototype using it's CLI-Data:

$$\begin{aligned}
 shell(z) = & (outer(z) \cap (cubeshell(z) \cup offsetshell(z))) \cup \\
 & (outer(z) \cap (inner(z-s) \cup offsetshell(z-s))) \cup \\
 & \dots \cup \\
 & (outer(z) \cap (inner(z-1) \cup offsetshell(z-1))) \cup \\
 & (outer(z) \cap (inner(z+1) \cup offsetshell(z+1))) \cup \\
 & \dots \cup \\
 & (outer(z) \cap (inner(max(n(r), z+s)) \cup offsetshell(max(n(r), z+s)))) \\
 = & outer(z) \cap [\quad inner(z-s) \cup \dots \cup inner(max(n(r), z+s)) \cup \\
 & \quad offsetshell(z-s) \cup \dots \cup offsetshell(max(n(r), z+s)) \cup \\
 & \quad cubeshell(z)]
 \end{aligned}$$

Figure 6 illustrates the formula above for $r = 3$ and $s = 2$. It is a vertical section through a part showing the points of dividing material.

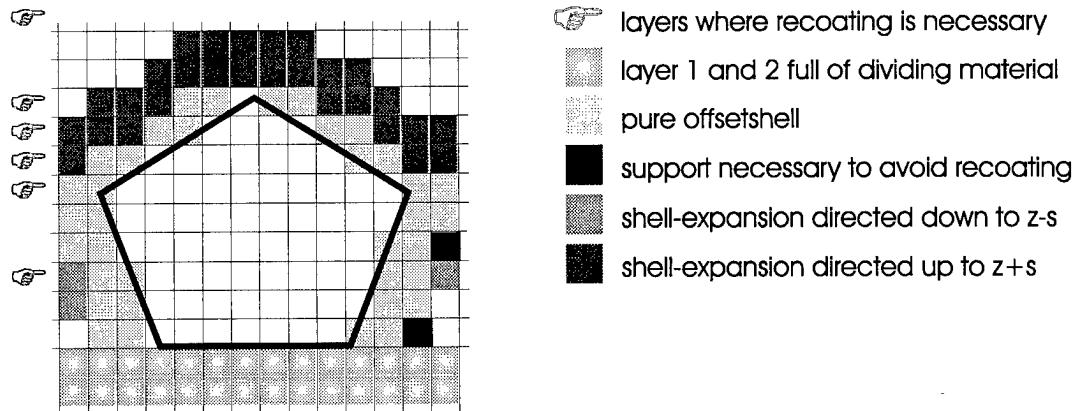


Figure 6: Vertical section through a part

In the illustration you can see that in some cases the shell is 3 pixels high. To avoid this, we change our formula to:

$$\begin{aligned} shell(z) = & outer(z) \cap [inner(z-s) \cup \dots \cup inner(max(n(r), z+s)) \cup \\ & offsetshell(z-s+1) \cup \dots \cup offsetshell(max(n(r), z+s-1)) \cup \\ & cubeshell(z)] \end{aligned}$$

Then we consider that the layer L_{z-1} is already top-covered partly by the offsetshell of layer L_z and layer L_{z+1} is already bottom-covered in an analogous way.

The union- and intersection-operators can be implemented by *or*- and *and*-operations on the bitmap. Better performance can be reached by intersecting the CLI-polygons directly without drawing them into a bitmap. However this requires more complicated algorithms to calculate the offset-polygons and their intersections or unions.

STATE OF THE DEVELOPMENT

Presently, we have already demonstrated the functionality of the basic processes such as printing of the release wax and applying thin layers of building wax.

A prototype of the pinhead has already been realised. A first printing sample of the release wax is shown in Figure 7. This sample has a size of about 0.6 x 1.65. The printed areas have not been filled in order to see the details of the structure.

Some waxes have been tested in regard to find a building wax with the desired properties. Now a suitable combination of release and building wax is disposable and some application tests can be executed.

Furthermore a software with GUI has been programmed.

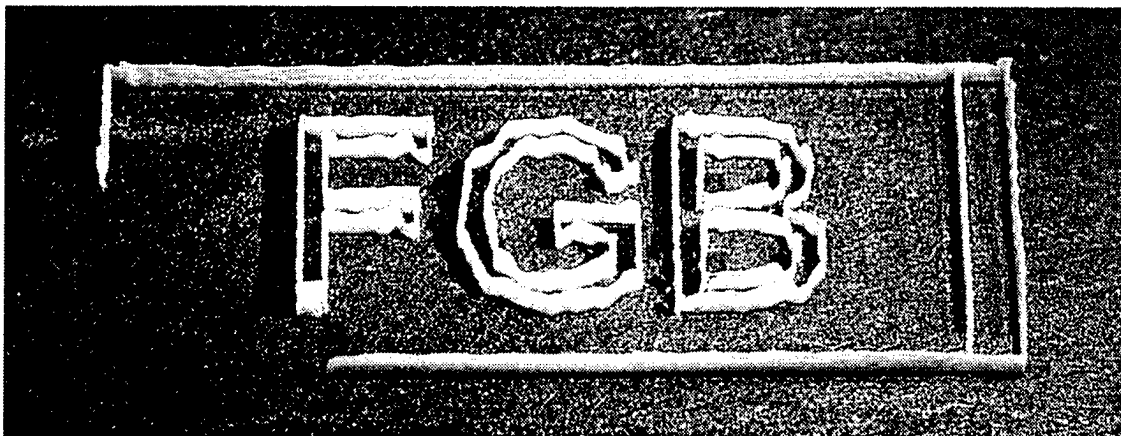


Figure 7: Printed release wax structure

CONCLUSION

A fast 3DP process has been developed. In this process, only the thin shell of the model has to be printed by a multi-jet printhead. The building material is applied by a rapid process. The next steps are the realization of a prototype of the 3D printer and the optimization of process parameters. Future enhancements to these systems will lead to improvements of the rapid prototyping system in accuracy, surface finish and in application development.

REFERENCES

1. Ederer I. "A 3D Print Process For Inexpensive Plastic Parts", Solid Freeform Fabrication Symposium, Austin, Texas, 1995
2. Cima, M. J., Yoo, J., Khanuja, S., Rynerson, M., Nammour, D., Giritlioglu, B., Grau, J., Sachs, E. M., "Structural Ceramic Components by 3D Printing", Solid Freeform Fabrication Symposium, Austin, Texas, 1995
3. Ederer I. "Mit Inkjet-Technologie schnell und preiswert zum Bauteil", EuroMold '98, Frankfurt a. M. 1998
4. Kretschmer, J., Ederer, I., Tille, C., "A Dop-on-Demand Inkjet Printhead for Wide Range of Applications", IS&T's 15th International Conference on Digital Printing Technologies, Toronto 1998

Extrusion and Deposition of Semi-Solid Metals

Steffi Finke^a, William Wei^b, Frits Feenstra^a

^aTNO Institute of Industrial Technology, Rapid Prototyping R&D, Delft, The Netherlands

^bUniversity of Twente/W.E.I. Consulting, Enschede, The Netherlands

Abstract

Interest in Rapid Prototyping (RP) with fully dense metals is increasing and with it the development of rapid prototyping techniques. A feasibility study for using semi-solid metals as construction materials for rapid prototyping is currently being carried out by TNO and the University of Twente. Semi-solid low melting point alloys are being investigated. Work is being conducted in a number of areas including rheological properties, layerwise deposition and interlayer bonding. An experimental apparatus has been built and tested for the extrusion of these materials. Preliminary results indicate that these materials can be successfully extruded, and the interlayer bonding between layers is satisfactory for the generation of three dimensional objects.

1. Introduction

Rapid Prototyping is becoming an increasingly important part of product development. The rapid production of prototypes enables the manufacturer to adapt his/her design and development process faster to constantly changing requirements.

The Netherlands Organization of Applied Scientific Research (TNO), Institute of Industrial Technology has had considerable success in the development and application of RP techniques, such as Fused Deposition Modeling (FDM), Layered Object Manufacturing (LOM, KIRA) and Multiphase Jet Modeling (MJM) in a wide variety of industries. The FDM technique involves the generation of a near net-shape physical model by extrusion and layered deposition of material based on 3D-CAD files. The systems currently available allow the production of prototypes from thermoplastic materials. However, there is an increasing interest in RP with metals. The use of an FDM-based technique with metals will provide industry with far broader capabilities for product development and a cost effective manner for producing small series of metal products.

The extrusion and deposition of metals, as separate tasks are established production processes. However, for a layered manufacturing technique (LMT) process such as FDM, extrusion and deposition have to be combined in such a manner that the final product fulfils all requirements regarding accuracy and strength. That involves processing the metals in the semi-solid state. In order to control such processes, knowledge about the flow and solidification behavior of semi-solid metals (SSM) is therefore necessary. In particular the design of the equipment for SSM processing requires quantitative data about flow properties, viscosity and solidification behavior. Research is thus being carried out in the fields of semi-solid slurry production, slurry morphology, viscosity, mechanical and metallurgical properties of semi-solids and characteristics of the final products [1].

TNO and the University of Twente have started a co-operative research program to investigate the feasibility of an FDM-based process for the production of 3D metallic objects. Experimental work has begun with low melting point alloys in order to make use of existing testing equipment with minor modifications. Initial work is being conducted to investigate the solidification process of these materials and their flow behavior in the semi-solid state. The preliminary results of this work are presented in this communication.

2. Experimental

Material

For an extrusion process it is fundamental that the material shows a suitable flow behavior. This can be achieved and controlled adequately if the material is being brought into a semi-solid condition. Metals with a wide temperature range where liquid and solid phase coexist are thus required. Properties such as low shrinkage on solidification and no formation of undesired second phase particles have to be considered. The alloys must also have good bonding qualities upon deposition. The alloys shown in Table 1 were found to be suitable with respect to these aspects. These are listed with their respective liquidus and solidus temperatures.

Table 1-Composition and characteristic temperatures of the low melting point alloys

Composition [wt%]	T _{liquidus} [°C]	T _{solidus} [°C]
70%Sn-30%Bi	185	133
35%Sn-35%Pb-30%Bi	140	96
17%Sn-51.5%Pb-31.5%Bi	158	96
60%Pb-40%Sn	235	183

The solidification behavior of these materials was investigated by determining their microstructure after quenching from either the liquid, or the semi-solid state at various cooling rates. The actual goal is to determine the cooling rates during processing based on microstructure since temperature measurement is virtually impossible.

Rheological Data

The flow behavior of the semi-solid materials was investigated by extrusion using a plate/plate rheometer (Fig. 1a) and a capillary viscometer (Fig. 1b). For the latter the material was extruded using several defined ram velocities (see Table 2) and the pressure drop over the capillary was measured. The apparent shear rate can be calculated from the pressure drop as [2]

$$\dot{\gamma}_a = \frac{4Q}{\pi R^3} \quad (1)$$

where Q is the flow rate in the cylindrical part of the capillary and R is the radius. Using the apparent shear rate, the shear rate on the cylinder wall can be calculated according to the Rabinowitsch correction,

$$\dot{\gamma}_w = \dot{\gamma}_a * \left(\frac{3}{4} + \frac{1}{4} \frac{\partial(\ln Q)}{\partial(\ln \tau_w)} \right) \quad (2).$$

In eqn. 2, τ_w is the shear stress at the cylinder wall and is calculated as

$$\tau_w = \frac{\Delta p}{2 \frac{L}{R}} \quad (3)$$

where Δp is the pressure drop and L is the length of the capillary.
The viscosity can then be calculated as

$$\eta_w = \frac{\tau_w}{\dot{\gamma}_w} \quad (4).$$

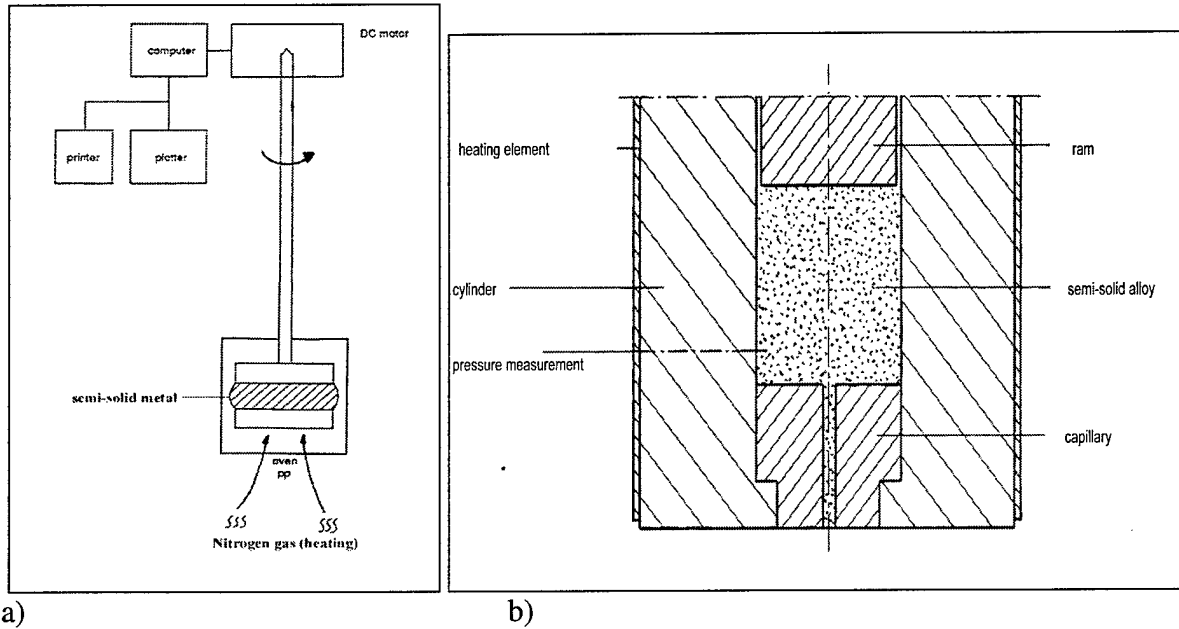


Figure 1: a) Plate/plate rheometer for the determination of the viscosity as a function of the shear rate and b) Capillary viscometer used for viscosity measurements by extrusion

Table 2- Flow rates for given dimensions and six different ram velocities

Ram velocity [cm/s]	Q [mm ³ /s]
0.0051	41.2
0.0103	82.5
0.0257	206
0.0515	412
0.103	825
0.257	2056

Initial extrusion trials have been conducted using an extrusion apparatus built similar to the viscometer described above (see Fig 2). There are however, three main differences, the materials, the pressure supply and the nozzle size. The material is supplied in wire form and is transported with a set of 4 friction wheels. The pressure can be varied through the velocity of the friction wheels. In order to create layers of material, the material was extruded through the extrusion head onto a base-plate which could be moved in the x and y directions. Z-axis movement was carried out manually and further layers could thus be deposited.

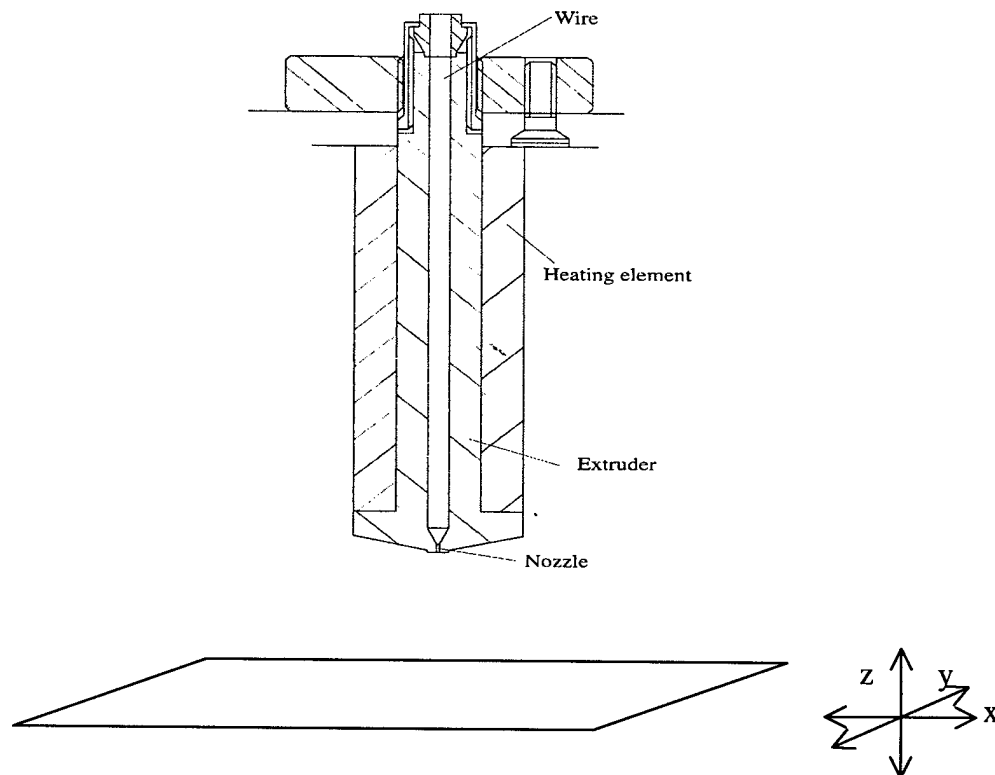


Figure 2: Extrusion head

3. Results and Discussion

Fig. 3 shows the results of the viscosity measurements using the plate/plate rheometer. The flow curves show a shear thinning behavior which is typical for pseudoplastic materials (Fig. 4). These figures show that the viscosity strongly depends on the shear rate (pseudoplasticity). The shear rate and the time of shearing (thixotropy) are in turn dependent on structural aspects, such as fraction of solid or shape and distribution of particles.

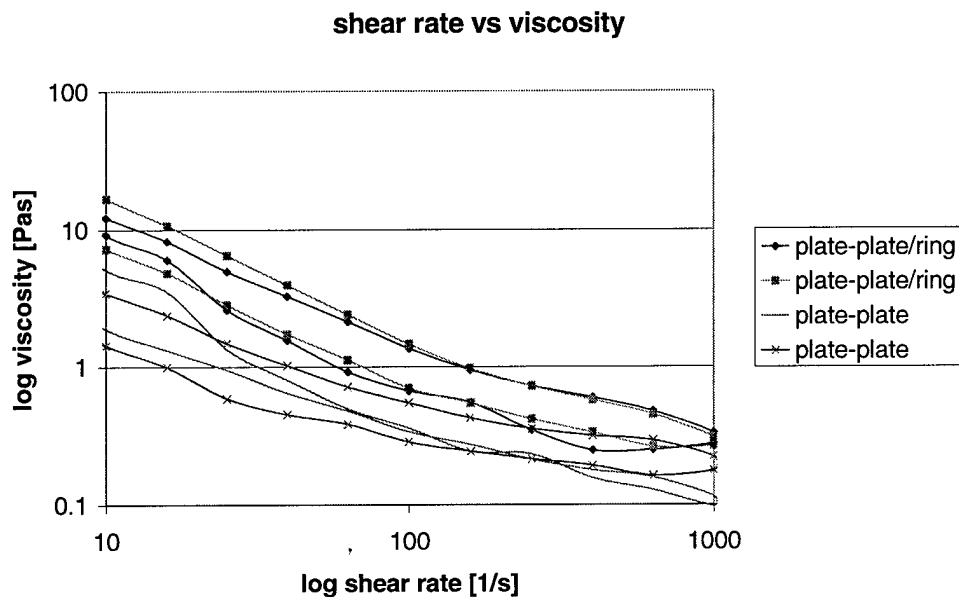


Figure 3: Shear rate vs viscosity measured values

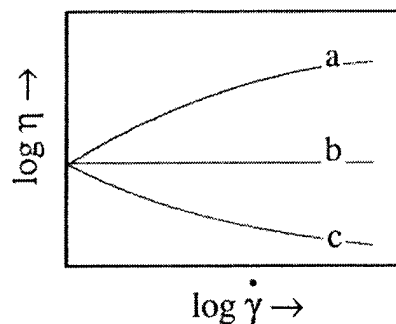


Figure 4: Principal flow curves with a) shear thickening, b) Newtonian and c) shear thinning behavior [3]

The flow curves in Figure 3 and 4 reveal information about the materials reaction to shear forces. Obtaining rheological data on semi-solid systems still remains a problem when it comes to high solid fraction subject to higher shear rates. The torques required are usually too high for conventional viscometers [4]. Extrusion methods in particular have been tried to overcome this problem [5,6]. Fig. 5 shows a typical p-t curve obtained from the extrusion experiments, using the capillary viscometer. After an initial pressure increase the extrusion process starts and the pressure value decreases to a certain level and remains stable. The viscosity at the point where the extrusion starts was determined indirectly using eqns. 1-4 as 884.3 Pa-s.

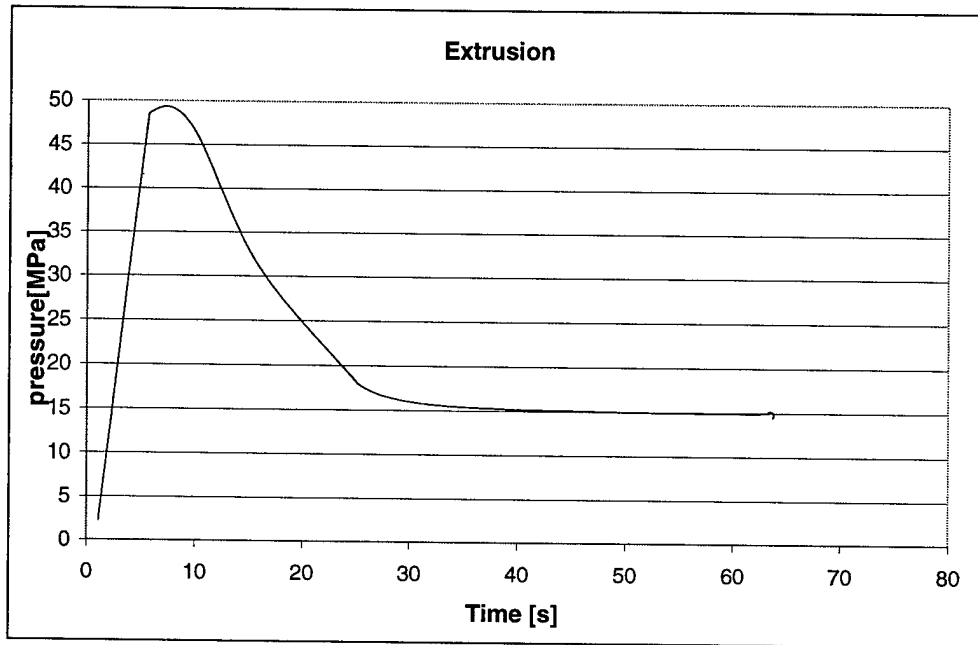


Figure 5: Pressure-time curve obtained from extrusion tests

Several layers of material have been deposited onto a target using the extrusion device based on these first rheological results. Despite limitations in the experimental setup, it has been possible to deposit not only single layers of metal, but multi-layers as well. The material deposited has been examined using optical and electron microscopy. Fig. 6 shows the areas from which the samples have been prepared and Fig. 7 the microstructure of a) extruded material and b) an interlayer area. Microstructures of all extruded specimens appeared globular, which is typical for semi-solid metal, having been subjected to shear forces. Quenching tests showed that this microstructure can be related to a cooling rate of approx. 6°C/s . Clear bonding between the two layers can be observed. The bonding could be further improved if a protective atmosphere and elevated chamber temperatures are introduced in the process.

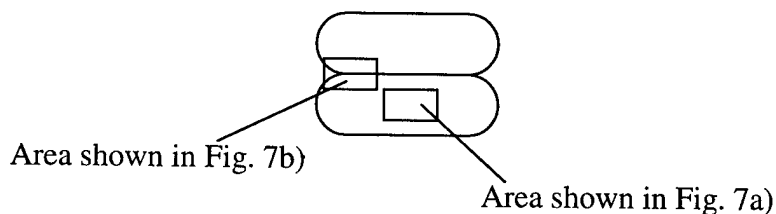


Figure 6: Cross section of two layers indicating areas from which the micrographs shown in Fig. 7 were taken.

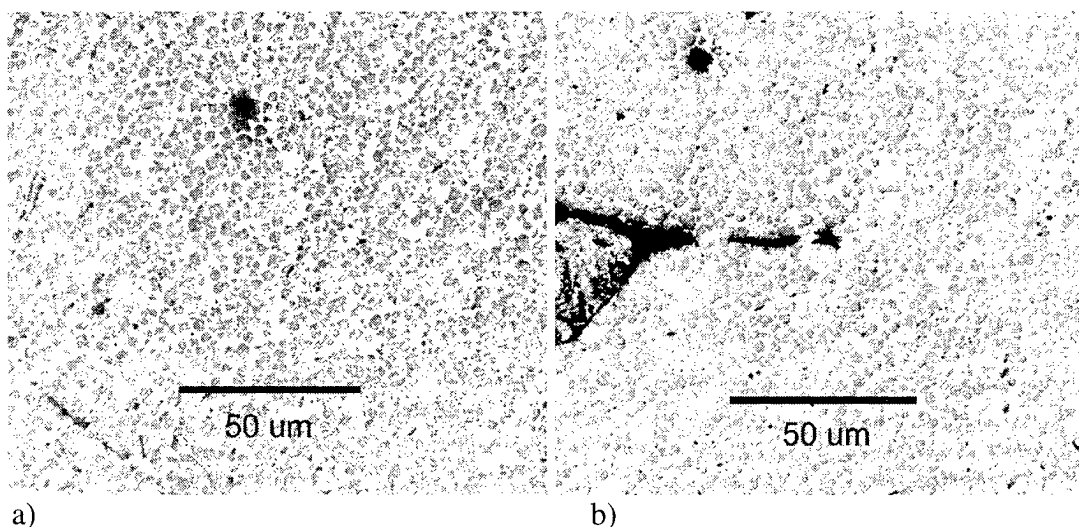


Figure 7: Micrograph showing a) the microstructure of extruded material and b) an interlayer region

The work conducted thus far has shown that the extrusion and deposition of metallic materials is feasible for the creation of physical 3D objects. Further work will concentrate on the deposition process. The x-y-z-movement will be fully automated so that controlled deposition is possible. The relationship between the extrusion velocity and x-y movement are critical to the process and require optimization. This also applies to the start-stop control of the materials flow. Rheological models will be employed in order to optimize the nozzle design and thus improve the extrusion process.

The mechanical properties of the extruded material will be tested. Preliminary tests showed that under certain circumstances the bismuth containing alloys became brittle. SEM analysis of these materials revealed that a bismuth-rich phase in the form of coarse particles formed at grain boundaries and caused embrittlement. This problem could be solved through a variation of process parameters or materials composition.

4. Conclusions

A program is being conducted to show the feasibility of Rapid Prototyping with metals using an FDM-based technique. Initial work with Sn-based low melting point alloys has shown that layer deposition of these materials is possible by extrusion in the semi-solid state. Further studies on the relationship between microstructural and rheological properties of these metals are being conducted in order to optimize the equipment and process.

5. References

- [1] Kiuchi, M.: Proceedings of the Third International Conference on Processing of Semi-Solid Alloys and Composites, Tokyo, (1994)

- [2] Brüggeman, H.M.; Feenstra, F.K.; Kunen, J.M.G.; den Otter, J.L.; Simons, H.J.: Reometrie van Kunststofsmelten, Course material, TNO Industrie, Delft (1992)
- [3] Quaak, C.J. Rheology of Partially Solidified Aluminium Alloys and Composites, Ph.D. Thesis, University of Delft, (1996)
- [4] Kirkwood, D.H.: European trends in Semi-Solid Processing, Proceedings of the Third International Conference on Processing of Semi-Solid Alloys and Composites, Tokyo, (1994)
- [5] Wan, G.; Witulski, T.; Hirt, G.: Proceedings of International Conference of Aluminium Alloys, Ravenna, (1993)
- [6] Loue, W.R.; Suery, M.; Querbès, J.L.: Proc. 2nd. Int. Conf. on SSM Processing, MIT, Cambridge, (1992), pp266

Electrophotographic powder deposition for freeform fabrication

Ashok V. Kumar and Hongxin Zhang

Department of Mechanical Engineering
University of Florida, Gainesville, FL 32611-6300

Abstract

Research at the University of Florida on electrophotographic freeform fabrication is presented. In this fabrication technique, powder is picked up and deposited using a charged photoconducting surface and deposited layer by layer on a build platform. The process enables precise deposition of powder in the desired shape on each layer. A test-bed was designed and constructed to study this approach to solid freeform fabrication. Methods for charging and depositing powders on a platform using a photoconducting drum were studied. Preliminary results obtained using this test-bed are presented.

1. Introduction

Solid Freeform Fabrication (SFF) is a new class of manufacturing technologies that is characterized by a layer-by-layer build-up of parts (Ashley, 1991, Kochan, 1993). Due to the layer-by-layer building approach, it is possible to create significantly more complex parts in one fabrication step than was previously possible. In addition, due to the relatively simple process planning required, the potential has been demonstrated to automatically fabricate a part under computer control given a solid model of the part.

Over the last decade many different technologies for Solid Freeform Fabrication have evolved. Broadly, the SFF techniques available currently can be classified as stereolithography, solid fusion and solidification, laminated object manufacturing, and powder based techniques (Kochan 1993). The earliest solid freeform fabrication technology was based on stereolithography (Kodama, 1981). Stereolithography builds parts by solidifying a liquid photopolymer using a laser beam. Parts are constructed layer by layer by hardening the photopolymer using a laser beam that is projected in the shape of the cross-section of the part. Examples of solid fusion and solidification technique are Fused Deposition Modeling (FDM) and Shape Deposition Manufacturing (SDM). FDM involves depositing ABS plastic, wax, etc by extruding the material through a nozzle in a fused state (Crump, 1992). Shape Deposition Manufacturing (SDM) integrates material deposition and material removal (Amon et al 1998). Layers of part material are deposited by microcasting and machined to net-shape before additional material and further layers are deposited. Laminated object Manufacturing (LOM) builds parts by gluing foils or sheets of material on top of the one another (Feygin et al 1991). A laser beam is used to cut the sheet into the desired shape of the cross-section.

The two main powder-based techniques that have been commercialized are Selective Laser Sintering and 3D printing. For powder based methods no support structures are

typically required to create complex shapes. Powder is selectively consolidated into a part and the remaining powder can be easily removed. In the SLS process (Bourell, 1992) a thin layer of powder is deposited in a workspace container and the powder is then fused together using a laser beam that traces the shape of the desired cross-section. The process is repeated by depositing layers of powder thus building the part layer by layer. In the 3D printing process (Sachs et al 1992), a binder material selectively binds powder deposited in layers. Ink-jet printing technology is used to print the binder in the shape of the cross-section of the part on each layer of powder.

Freeform Powder Molding (FPM) process is a two-powder method, that uses a "tool" powder of a different material than the part to be manufactured. The two powders are deposited layer-by-layer. Although, no specific method for powder deposition has been developed a method of depositing powders through nozzles has been proposed. Rock and Gilman (1995), have presented application of this process for tool manufacture using metal powders.

A powder based freeform fabrication technology is described here that builds parts by depositing powders layer-by-layer. Powder is deposited using electrophotographic powder deposition method described in section 2. Section 3 describes the compaction or sintering process required for consolidating the part. Implementation of the test-bed and conclusion are presented in sections 4 and 5 respectively.

2. Electrophotographic powder deposition technique

A solid freeform fabrication method is described where powder is deposited layer-by-layer using electrophotography. The powder particles are picked up and deposited by electrostatic force by a charged surface. This process is currently patent pending. Powder

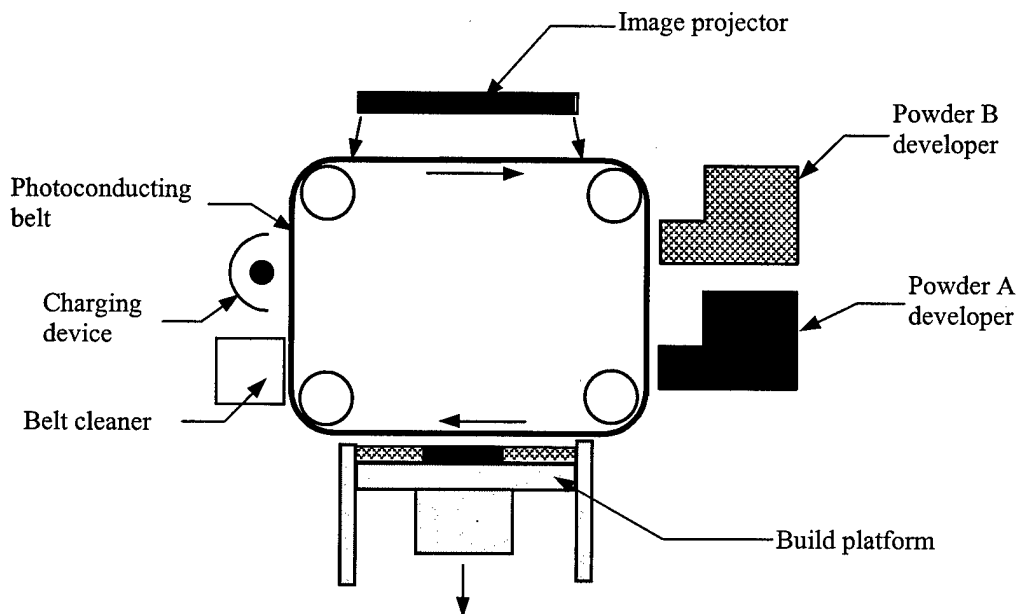


Figure 1. Powder deposition system

can be picked up using a photoconducting belt or a drum. A configuration based on photoconducting belt is illustrated in Figure 1. The belt has a coating of photoreceptive material on one side. This material is non-conducting in the dark but becomes conducting when light falls on the surface. The belt is cleaned and charged by the belt cleaner and charging device respectively. The image projector then discharges the belt selectively by projecting light on the belt so that only an area in the desired shape remains charged. Light can discharge the photoconductor because it becomes conductive in the region where the light falls and charge flows to the ground in such regions. Later, when the belt comes in contact with the image developer, powder particles jump on to the region of the belt that is still charged. The developer not only acts as powder container but it also charges and transports the powder to the photoconductor. The figure shows two developers so that the system could deposit more than one powder. The powder picked up by the belt is deposited on to the build platform, which is charged in the opposite polarity to attract the powder particles. This process is repeated to deposit powder layer by layer. Very fine powder can be used in this process so that each layer can be as little as 5-10 microns thick. The sub-systems and the process involved are described in more detail below.

2.1 Corona charging

Photoconducting material (also called the photoreceptor) can be charged using a corona-charging device. The device is schematically shown in Figure 2. High voltage is applied between the corona wire and the shield. Due to this high voltage, the air near the wire is ionized. The ions having the same polarity as the wire are repelled from the wire towards the photoconducting surface.

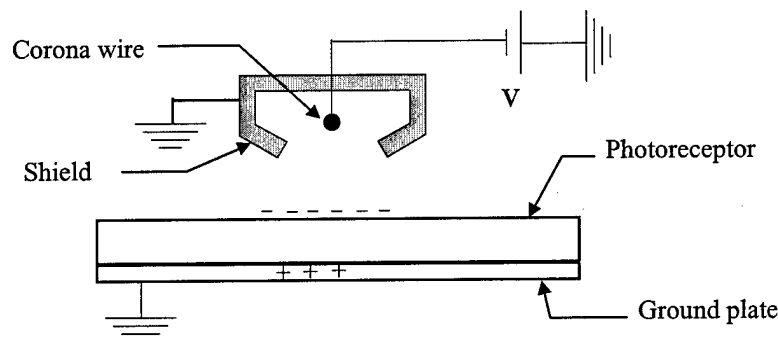


Figure 2. Charging the photoconductor

2.2 Image projection

Photoconducting surfaces are widely used in many image-processing applications such as photocopiers. In most small copiers, photoconducting drums are used that have a layer of photoreceptor deposited on the surface of the drum. Some of the larger and high-speed photocopiers use photoconducting belts. Many photoreceptors have now been developed. The earliest material used in photocopiers was amorphous selenium. More recently, many organic photoreceptors (Schien, 1988) have been developed. The photoconductor

becomes conductive and gets discharged when light falls on it. A latent image of the desired shape can be formed on the photoconducting surface by projecting light on the region to be discharged. This was achieved using an array of laser beams that project the desired image line by line on to the photoconductor.

2.3 Image developing system

The image developing system (or image developer) must electrostatically charge the powder to be deposited and bring it to the vicinity of the latent image on the photoconducting belt. The charged particles would then adhere to the latent image due to the electric field created by the charge on the photoreceptor. This will create a real image on the belt consisting of a uniform layer of powder deposited on the charged areas of the belt.

We are currently experimenting with various types of development systems to identify the system most suitable for our application. Most photocopiers and printers use a two component developing system, where "carrier" particles are mixed with the toner particles. These carrier particles are made of a magnetic material so that they can be transported using magnetic force. The carrier particles serve two purposes. Firstly, they induce electrostatic charge on the toner particle during mixing. Secondly, toner particles, which are much smaller in size than the carrier particles, adhere to the carrier particle. Therefore, they get transported along with the carrier particles on magnetic rollers.

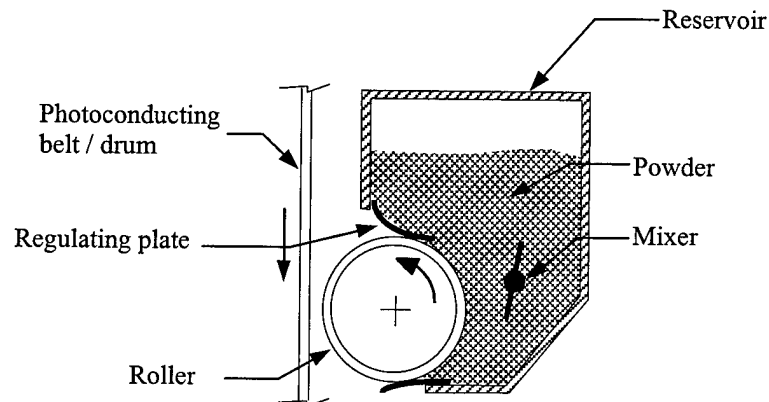


Figure 3. Image developer for depositing powder on belt

Currently, we are using a mono-component development system where the powder particles are charged using an a.c. field. The field creates a powder cloud that gets charged tribo-electrically due to the contact with a regulating plate. A schematic illustration of the developer depositing powder on the belt or drum is shown in Figure 3.

2.4 Powder deposition or transfer

The powder picked up by the belt has to be deposited on the build platform so that it is deposited over the previous layers with precise alignment. To facilitate the transfer of

powder from the belt to the platform, it is necessary to charge the platform / top layer of powder to a reverse polarity than the belt and the powder. In addition, after depositing each layer the powder has to be fused to the previous layers to build green strength by applying a compressive load / heat.

2.5 Cleaning system

After the powder has been deposited, the photoconducting belt has to be discharged and cleaned to remove any residual particles. This can be achieved by exposing the belt to a bright light to discharge it and subsequently using brushes and / or scraper blades to remove residual particles.

3. Consolidating the part

Parts can be built by depositing powder of a single material layer by layer and fusing each layer to the previous layer by application of pressure and heat via a compacting device. In this case temporary support structures have to be created to support any overhanging features. Alternatively, the powder deposition method described above can be used to deposit two powders in each layer, one powder of the material with which the part is to be made while the other powder provides support by holding the part powder in the required shape during subsequent compaction and sintering. The idea is illustrated in Figure 4. Powders of materials A and B are deposited as shown in a box-like container. Powder B acts as *support material* that surrounds powder A, the *part material*.

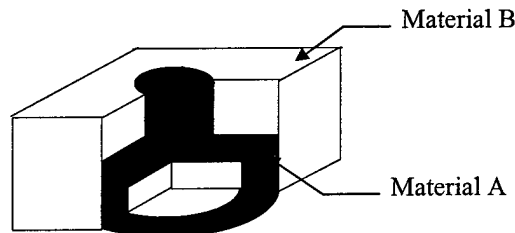


Figure 4. Powder based freeform fabrication

If material B has a relatively high melting point compared to material A, then upon compacting and sintering, powder A will fuse together and consolidate while material B will remain in powder form. The material B therefore serves as a die within which powder A is compacted and sintered. Since both powders are deposited layer by layer, the part and the “die” are being built simultaneously.

Compaction and sintering will enable the creation of fully dense parts. The powder layers will be compacted by subjecting it to uniaxial compression within a die during sintering. The support powder will transmit the pressure around the part being consolidated to apply nearly isostatic pressure on the part. If fully dense parts are not required then compaction is not necessary. Both compacting and sintering are associated with shrinkage in volume. In order to hold the part dimensions within a desired tolerance, it is essential to be able to predict the shrinkage fairly accurately.

4. Test-bed results

A test-bed was designed and constructed to test the powder deposition scheme described here. It consists of a movable build platform on which powder is deposited by a photoconductor drum. The photoconductor drum was charged using a charging roller, which is a contact charging device (Kadonaga et al, 1999). The latent image is formed on the drum using an array of laser beams. The developer used consists of a container for holding powder and a magnetic roller that transports powder. A magnetized polymer toner powder was deposited layer by layer on to the platform. To transfer the powder on to the platform or the previous layers of powder, the top layer was charged using a charging roller. After the deposition of each layer, a heat roller was used to fuse the powder to the platform or previous layers. The test-bed is not yet fully automated and requires manual set up to print each layer. However, it serves as a useful facility to test layer by layer deposition of powder.

Preliminary results indicate that the approach described here is capable of printing powder with precision consistent with electrophotography used in printing and photocopying applications. The test-bed is capable of achieving an accuracy of roughly 600 dots per inch. However, positioning subsequent layers precisely over previous layers will require robust control system which is currently being designed.

5. Conclusions

Electrophotography appears to be a promising means of depositing powder in desired shapes of freeform fabrication or rapid prototyping. The process is capable of highly accurate control over the shape of powder deposition. Further research is needed to study and model techniques for charging and transporting a variety of powders. A test-bed was constructed to enable this research.

6. Acknowledgement

Funding for this research from ONR grant N00014-98-1-0694 is gratefully acknowledged.

7. References

- [1] Ashley, S., 1991, "Rapid Prototyping Systems", Mechanical Engineering, pp. 34-43.
- [2] Kochan, D., 1993, Solid Freeform Manufacturing: Advanced Rapid Prototyping, Manufacturing research and technology, vol. 19, Elsevier.
- [3] Kodama, 1981, "Display 3 dimensional information to a physical formed model", Trans. of Electronics and Communications Society, vol. 17, no. 6, pp. 237-241.
- [4] Crump, S., 1992, "The extrusion process of Fused Deposition Modeling", in the Proceedings of the 3rd International conference on Rapid Prototyping, Dayton, OH.
- [5] Feygin, M. and Hsieh, B., 1991, "Laminated Object Manufacturing: A simpler process" in Proceedings of Solid Freeform Fabrication Symposium, Austin, Texas.

- [6] Amon, C.H., Beuth, J.L., Weiss, L.E., Merz, R. and Prinz, F.B., 1998, "Shape deposition manufacturing with microcasting: Processing, thermal and mechanical issues", *Journal of Manufacturing Science and Engineering, Transactions of the ASME* v 120 n 3 pp. 656-665.
- [7] Kadonaga, M., Katoh T., and Takahashi T., "Study of non-uniform charging by charging roller with DC voltage", 1999, *Journal of Imaging Science and Technology*, vol. 43, no. 3, pp. 274-279.
- [8] Bourell, D.L., Marcus, H.L., Barlow, J.W. and Beaman, J.J., 1992, "Selective laser sintering of metals and ceramics", *International Journal of Powder Metallurgy* (Princeton, New Jersey) v 28 n 4. pp. 369-381.
- [9] Sachs E., Cima M., Williams P., Brancazio D., and Cornie J., 1992, "Three Dimensional Printing: Rapid Tooling and Prototypes Directly from a CAD Model," *Journal of Engineering for Industry*, vol. 114, pp. 481-488.
- [10] Rock S.J. and Gilman C.R., 1995, "A New SFF Process for Functional Part Rapid Prototyping and Manufacturing: Freeform Powder Molding," in *Solid Freeform Fabrication Symposium Proceedings*, H.L. Marcus et al. (eds.), The University of Texas at Austin, (Austin, TX, USA), August 1995.
- [11] Schien L., B., "Electrophotography and Development Physics", Springer-Verlag, NY, 1988.

Direct Generation of Metal Parts and Tools by Selective Laser Powder Remelting (SLPR)

W. Meiners, C. Over, K. Wissenbach, R. Poprawe

Fraunhofer Institute for Laser Technology (ILT)

Steinbachstraße 15, 52074 Aachen, Germany

Abstract

For the direct manufacture of metallic prototypes and tools Fraunhofer ILT is developing the new rapid prototyping (RP) process Selective Laser Powder Remelting (SLPR). The objective of this development is to manufacture metallic prototypes and tool prototypes out of serial materials with a density of 100 %, thus the manufactured parts can be immediately installed without time consuming post-processing like e.g. infiltration. Therefore, basic investigations for process analysis are being carried out to attain a fundamental understanding of the process. Process parameters have been determined and process procedure strategies have been developed to manufacture parts of different materials with a density > 99 % without any binder component. The materials under investigation are stainless steel, tool steel, aluminum alloys and titanium alloys. Due to the high density the tensile strength and yield strength of the parts produced by SLPR are in the range of the specification of the bulk material.

Based on these results a prototype plant for SLPR is being designed and realized. With this machine complex functional prototypes as well as prototype mold inserts for injection molding and die casting can be manufactured out of different materials.

Introduction

A relatively large number of rapid prototyping techniques are available on the market [1]. All these techniques depend on very special materials. The functional properties of the models produced by these techniques are limited extensively by the material used and the manufacturing process. For many functional tests, especially for tests of loading ability, it is nevertheless required to have functional prototypes that have at least serial properties and are available in large numbers. This is certainly not directly possible with the current commercially available RP techniques, especially not with metals. The way to achieve metal parts relies on different time-consuming post processes, e.g. vacuum casting or waste wax casting, where the RP model serves as a master pattern.

In order to manufacture metal parts directly by a RP-technique, the powder based process

Selective Laser Sintering (SLS) has been enlarged for the processing of metal powder. Right now two strategies for the manufacture of metallic components through SLS are being followed, the so called indirect and the direct selective laser sintering. Both strategies rely on their own very special metal powder systems [2],[3]. A problem arises through the development of a special powder, which is well adapted to the SLS process, but the functional properties of the manufactured part are severely limited. The reason is, that the properties of the special sinter material differ from the later production material to a high degree. Therefore, the part must be infiltrated or sintered again to increase the density and strength [4]. To avoid this problem, the development of SLPR for metallic materials at the Fraunhofer Institute for Laser Technology is consequently focused on the demands for serial metal components. ILT is carrying out a process development with serial single component metal powder materials.

The Principle of Selective Laser Powder Remelting

The basic principal of SLPR is similar to SLS. The parts are manufactured layer by layer using a laser beam, which locally fuses a powder material. The SLPR plant is also very similar to a SLS plant. The prototype plant for SLPR, shown in Fig.1, fulfills the basic functions of a SLS- machine. It mainly consists of the SLPR chamber with lowerable work platform and powder feeding platform as well as the powder leveling system. The SLPR chamber is closed and can be floated with an inert gas like argon. A Nd:YAG laser with a maximal output power of about 110W is used in cw-operation. The beam scanning is done by a scanner unit. The software, which is used for the SLPR process, is a stereolithography software of the company Fockele & Schwarze GmbH with special modifications for the SLPR process.

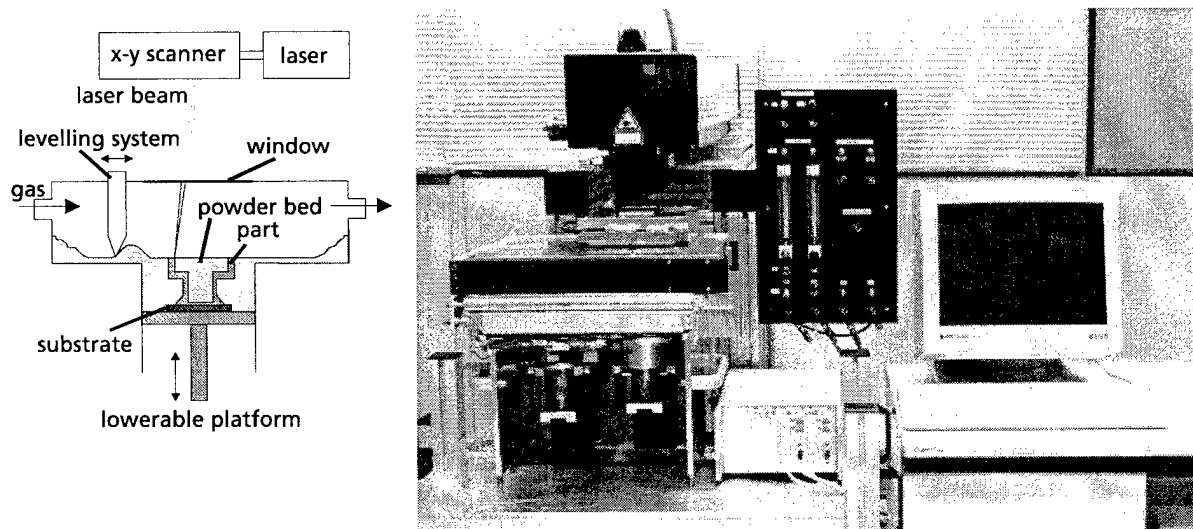


Fig. 1 Prototype plant for the SLPR process

The first main difference between SLS and SLPR is the kind of powder, which is used for the process. While the SLS process requires very special powder systems with a binder component, the SLPR technique uses common single component powder. The powder is processed without any binder material and without any kind of pre-treatment. Serial materials like stainless steel (309 L, 316 L) and tool steel (1.2343) can be processed. The only requirement is a spherical particle shape with a particle size in the range of 20 - 50 μm (Fig. 2).

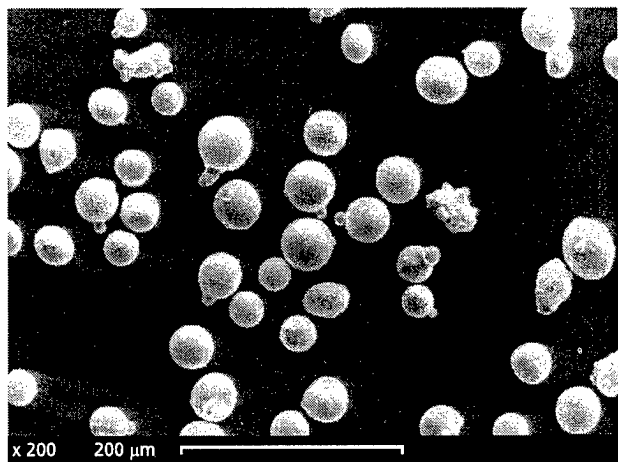


Fig. 2 Stainless steel powder for the SLPR process

In order to manufacture parts with a high density using one-component powders without any binder material, it is necessary to melt the powder particles completely. If these particles are only partially melted, the powder layer cannot sufficiently densify and the density of the part will not be significantly higher than the density of the powder layer. A problem of a complete melting of the powder particles is that the physical processes in the interaction zone of melt and laser beam lead to the formation of spherical structures of the metal melt due to its relatively high surface tension (Fig. 3 a).

Hollow areas remain and a porous structure

is formed. This leads to low strength and rough surfaces, which does not match the user requirements.

To avoid this problem fundamental investigations of the physical interrelations between the process parameters and the behavior of the metal melt were carried out [1],[5],[7],[8]. The process parameters which influence the behavior of the melt were determined. The parameters laser power, scan speed, hatch distance and layer thickness are crucial for the processing results. These parameters are dependant upon one another and therefore have to be adapted accordingly to each other. The influence of scanning strategies and protection gas flow was determined. An effective shielding of the interaction zone for atmospheric oxygen through a protection gas (such as argon) is of great importance so that the wetting properties of the melt are not reduced by formation of an oxide skin layer. In addition a special scanning strategy with a limited length of each scan vector has to be used to achieve high density of the parts. Based upon this knowledge a suitable process layout could be set up, which enables the influence and control of the melt's behavior. By the SLPR process the powder of each single track is completely melted by the laser beam and the melted material solidifies without forming spherical structures (Fig. 3, b).

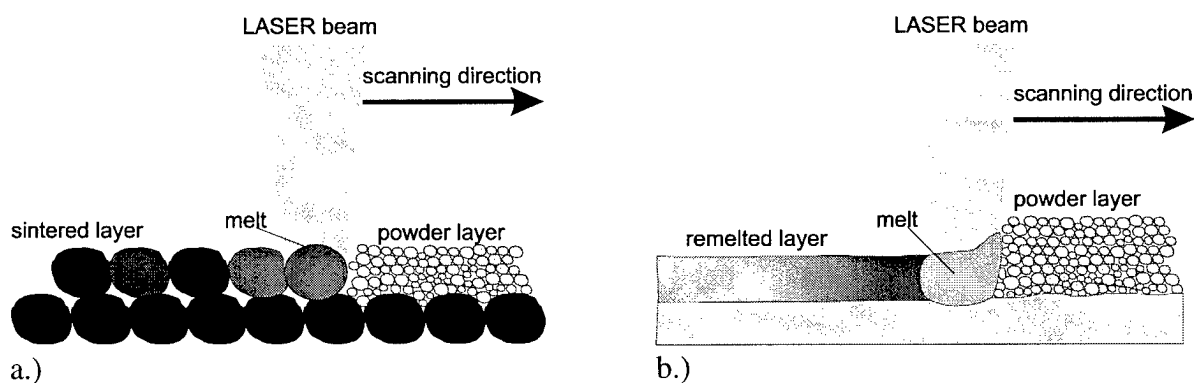


Fig. 3. Melting process of single component powder with a laser beam.

a.) porous structure by SLS

b.) dense structure by SLPR

Quality of the SLPR - parts

Considering the suitable process procedure strategies, process parameters can be determined with which parts out of different materials can be manufactured with a density up to 99% directly by the SLPR-process. Post-processes like infiltration to improve density and strength are not necessary. Fig. 4 shows cross sections of a stainless steel 316 L sample and a TiAl6V4 sample produced by SLPR. The cross sections show, that the material of every track is bonded to the next track as well as to the layer below through a melt metallurgical bond.

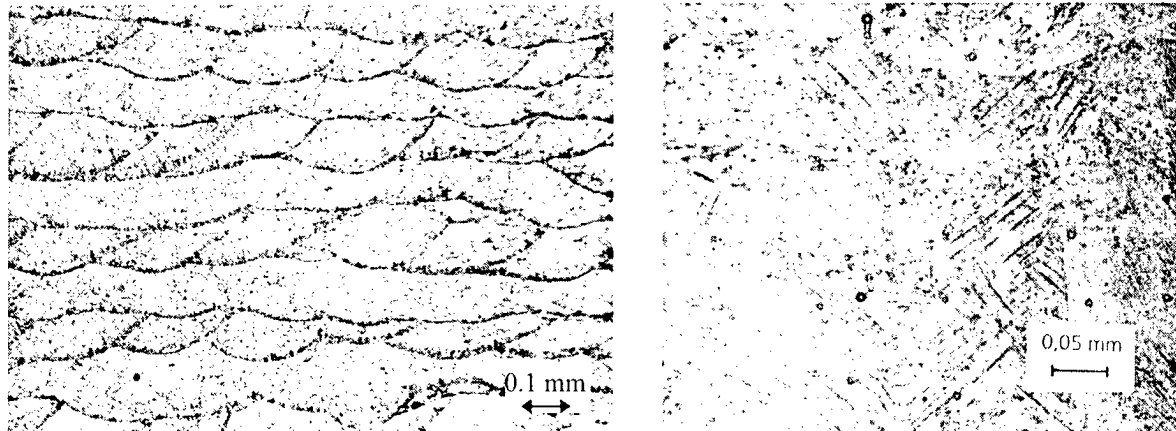


Fig. 4 Cross section of a sample manufactured out of stainless steel 316 L (left) and TiAl6V4 (right) by SLPR. The density of the samples is approx. 99 %.

The high density leads to a high strength of the parts. Tensile strength, yield strength and breaking elongation have been determined by a tensile test. Tensile test rods have been build out of stainless steel 316 L and TiAl6V4. For stainless steel test rods with an orientation of the layers perpendicular and parallel to the tension direction have been tested separately.

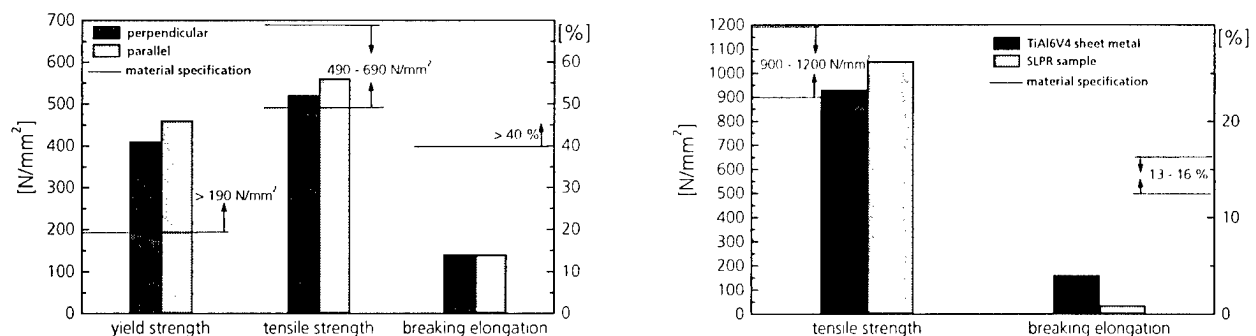


Fig. 5 Results of tensile tests of SLPR-parts out of stainless steel 316 L (left) and TiAl6V4 (right)

The tensile test results of the parts manufactured by SLPR are compared with the material specification and in case of TiAl6V4 with a sheet sample. The results are demonstrated in Fig. 5. The diagrams show that the tensile strength of the SLPR-steel parts of approx. 550 N/mm² as well as yield strength with approx. 450 N/mm² are in the range of the materials specification. There is no significant difference between the parts with perpendicular and parallel orientation of the layers to the tension direction. The tensile test for TiAl6V4 shows similar results. The tensile strength of approx. 1050 N/mm² of the SLPR test rods is in the range of the material specification. Both of the tested materials show a brittle fracture which leads to significant less breaking elongation of the SLPR parts in comparison to the material

specification. The rapid solidification of the metal melt during the SLPR process leads to a more brittle material structure in comparison to sheet metal.

In addition to density and strength the accuracy and surface quality of the parts are important properties which determine the acceptance of this technique for industrial applications.

Investigations have shown, that an accuracy of approx. 0.1 mm can be achieved by the SLPR process for parts without undercuts. The accuracy of overhangs depends on position and shape of the support structure.

The surface roughness of the parts strongly depends on the layer thickness. The Rz value of parts built with a layer thickness of 0.05 to 0.1 mm is in the range of 60 to 80 μm . Depending on different applications, a surface finish with manual techniques like grinding and polishing is necessary. With these techniques a mirror-like surface can be achieved (Fig. 6).

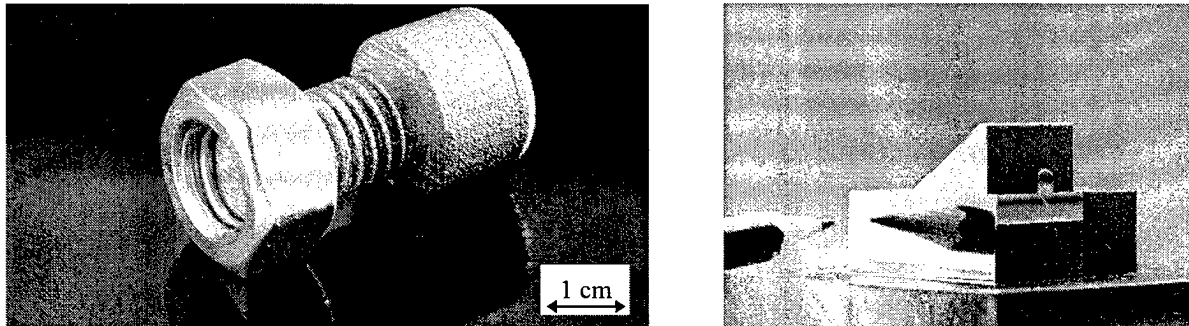


Fig. 6 Test parts for the demonstration of accuracy and surface quality of the SLPR technique. Left: Screw M12 manufactured by SLPR out of 316 L. Nut can be screwed on by hand without any reworking at the screw. Right: Mirror-like surface of an SLPR-part by manual surface finish technique.

Applications of SLPR

One of the most important application of the SLPR technique is Rapid Tooling. The complex shape of injection mold tools and die casting tools can be manufactured rapidly by SLPR. Thus, prototype plastic parts can be manufactured out of the serial material and with the serial manufacturing process, e.g. injection molding. As an example for this application Fig. 7 shows an injection mold tool which has been manufactured by SLPR out of stainless steel 316 L. The manufacturing time was approx. 4 hours for the core and approx. 7 hours for the cavity. After the manufacturing process the mold release surfaces had to be manually smoothed and core and cavity had to be fitted into a mother tool.

With this tool thermoplastic parts as well as rubber parts have been manufactured. The lifetime test of the tool is in process.

In order to manufacture prototype tools with properties as close to the serial tool as possible, investigations with the tool steel 1.2343 were carried out.



Fig. 7 Prototype tool out of 316 L, manufactured by SLPR

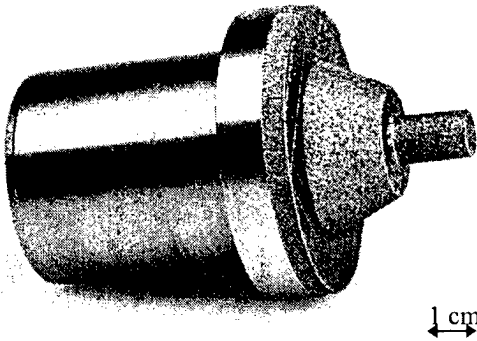


Fig. 8 Slider for a die casting tool manufactured out of 1.2343 by SLPR.

A slider for a die casting tool has been manufactured out of 1.2343 (Fig. 8). The slider was fitted into the tool, which was manufactured with conventional techniques. With this tool housings made out of AlSi12 where produced at a casting temperature of 700°C and a pressure of approx. 800 bar. A check of the slider after the production of 4800 parts showed no visible wear at the slider.

In addition to prototype tools functional prototypes are also manufacturable with the SLPR technique. Due to the high density and strength the prototypes can be used for almost all functional tests. Generally the SLPR technique allows the manufacturing of all shapes with almost no limitation in complexity. Parts with undercuts can be manufactured without a support structure if the angle between the perpendicular axis and the surface of the undercut is less than 50°. If the angle exceeds 50°, the undercuts have to be fixed by a support structure to avoid or minimize distortion during the building process. Once the part is completed, the support structure can be removed manually and distortion is avoided by the stiffness of the part itself. Fig. 9 shows examples of prototypes out of different materials. The parts have been build with a layer thickness of 0,05 mm without support structure. The building time is approx. 4 hours per part.

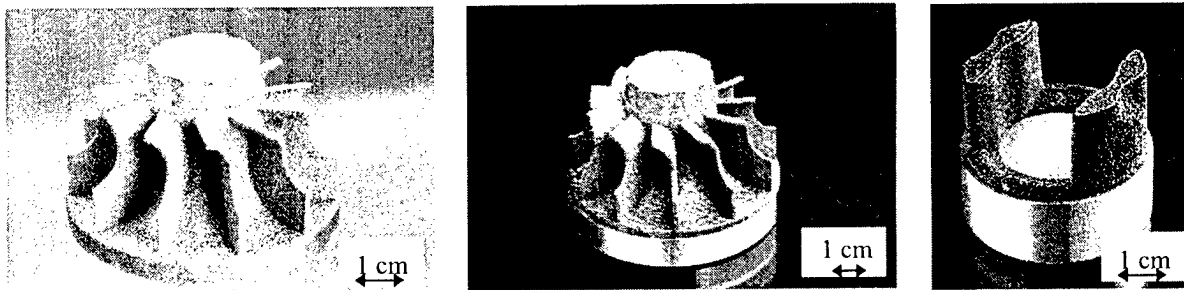


Fig. 9 Functional prototypes out of stainless steel 316 L (left), TiAl6V4 (center) and AlSi30 (right) manufactured by SLPR

In future works other components like tools and functional prototypes will be produced and will be tested in cooperation with industrial users in practice.

In the area of process development, the aims of further investigations are the improvement of surface quality and form precision of the components.

References

- [1] A. Gebhardt Rapid Prototyping: Werkzeuge für die schnelle Produktentwicklung Hanser Verlag München Wien, 1996

- [2] Hejmadi, McAlea
Selective Laser Sintering of Metal Molds: The Rapid Tool Process
Proceedings of the Solid Freeform Fabrication Symposium, Austin, Texas 1996
- [3] C. Wilkening Fast Production of Technical Prototypes Using Direct Laser Sintering
of Metals and Foundry Sand.
Proceedings of the Solid Freeform Fabrication Symposium, Austin, Texas 1996
- [4] J. Lorenzen, F. Breitingner
Rapid Tooling- Verfahren zur schnellen Herstellung von Prototypwerkzeugen
Euroforum Konferenz Rapid Prototyping in der Anwendung, Bad Homburg, Juni 1997
- [5] W. Meiners, K. Wissenbach, R. Poprawe
Mit Selektivem Laser Sintern zu metallischen Prototypen aus seriennahen Werkstoffen
Proceedings of 6th European Conference on Laser Treatment of Materials, ECLAT'96
Stuttgart 1996
- [6] E. Hoffmann
Herstellung metallischer Bauteile durch Laserstrahlgenerieren
Dissertation RWTH Aachen, Shaker Verlag, Aachen 1998
- [7] W. Meiners, A. Gasser, K. Wissenbach, R. Poprawe
Direct Selective Laser Sintering of steel powder
Proceedings of LANE '97, Meisenbach Bamberg 1997
- [8] W. Meiners
Direktes Selektives Laser Sintern einkomponentiger metallischer Werkstoffe
Dissertation RWTH Aachen, 1998

Design and Evaluation of a Novel Laser-Cutting Machine for Computer-Aided Manufacturing of Laminated Engineering Materials

Sangeun Choi¹, and Wyatt S. Newman²

Abstract

This paper presents the recent redesign of a tangent-cutting machine for CAM-LEM (Computer-Aided Manufacturing of Laminated Engineering Materials). Our former 5-axis, serial-joint, open-chain mechanism for laser cutting has been reduced to two parallel, 2-axis kinematic chains and articulated optics. The redesign results in lower inertias, higher stiffnesses, and less calibration sensitivity to homing and misalignment of axes. As a result, the system has higher acceleration capability, higher tracking bandwidth (translating into faster laser cutting) and greater precision, enabling improved build rates. The new design is presented, along with experimental evaluation of the performance improvements. Performance improvements are quantified in terms of calibration sensitivity, tracking bandwidth, and resonant frequencies.

1. Introduction

Computer-Aided Manufacturing of Laminated Engineering Materials (CAM-LEM), being pursued at Case Western Reserve University, is an approach to Solid Freeform Fabrication (SFF) that offers the potential for fast build rates and flexibility in material selection [1], [2], [3]. While a wide variety of both commercial and experimental SFF approaches exists, most are additive techniques. Notably, Stereolithography [6], Selective Laser Sintering [7], Fused Deposition Modeling [8], and 3-D Printing [9] are well-known approaches for building up 3-D solids through incremental deposition, solidification, or fusing of material for layer-by-layer growth in the vertical direction. In contrast, Laminated Object Manufacturing [10], ShapeMaker [11] and CAM-LEM use sheet-based feedstock, and objects are built up by cutting and stacking (or stacking then cutting) successive layers. This latter approach has the potential for much faster build rates, particularly for large objects, since material removal about a perimeter can be significantly faster than material deposition throughout the enclosed area.

Another distinguishing feature of CAM-LEM is exploitation of a model's surface-normal information. By forming tapered edges on each layer (i.e., tangent cutting), thicker build layers can be used without compromising surface finish (see, e.g., [4], [5], [12]). Shape Deposition Modelling [13], ShapeMaker, Stratoconception [14] and CAM-LEM are unusual among SFF methods in exploiting tangent cutting.

Our 5-axis "alpha" CAM-LEM machine design has been described in [2], [3]. This design was successful in laser cutting thick sheet materials to produce ruled-surface edges. In the current presentation, we describe redesign of the CAM-LEM system to achieve lower cost, better precision and faster cutting. We first present a review of the 5-axis "alpha" design, then compare it to our new "beta" design—a simpler, cheaper 4-axis system. We present analysis showing

¹ graduate student, Dept of Mechanical Engineering, Case Western Reserve University

² Professor, Dept of Electrical Engineering and Computer Science, Case Western Reserve University

that the precision of the 4-axis design is less sensitive to parametric uncertainties than the 5-axis design. Subsequently, we present the measured dynamic properties of both the alpha and beta machines, including consideration of mechanical resonances. It is shown that the new system is capable of higher-speed laser cutting than the former design.

2. Review of CAM-LEM 5-Axis Alpha Design

Our 5-axis system, shown in Fig 1, consists of 3 translational axes (x,y,z) and two rotational axes (roll and pitch) that position and orient a 6"x 6" cutting table beneath a stationary laser source. Sheet material is clamped to the cutting table with vacuum pressure exerted through aluminum honeycomb cells. The cutting table is mounted with an offset 77.5 mm above the intersection of the two rotary axes to maximize clearance with the laser. To achieve the required positions and orientations for cutting the desired tangents about the boundary of a part slice, motion of the x and y axes must be coordinated with the roll and pitch angles of the cutting table. Vertical (z-axis) motion is incorporated in order to keep the material at the laser focal point, at which air ejected from a nozzle helps remove debris and assist cutting. The maximum orientation angle of the cutting table surface is constrained by the clearance of the laser nozzle such that the pitch and roll axes are limited to ± 73 degrees of motion from vertical during cutting.



Fig1: The 5-axis cutting machine

Kinematics of the alpha design are shown schematically in Fig 2. This design has all five axes connected serially. While this construction has achieved the desired kinematic range of motions, it includes some undesirable dynamic and calibration problems. The relatively tall z axis must carry both the roll and pitch axes, which rotate the cutting table under the stationary laser beam. The z translation is necessary to keep the cutting point at the laser focus when the cutting table is tilted. However, the pitch and roll axes are relatively heavy, resulting in problematic z-axis vibration modes. Further, the weight of the pitch and roll axes carried by the x, y and z axes results in a gravity pre-load that increases the Coulomb friction and the inertia seen by the translational axes, resulting in reduced trajectory-tracking performance. In addition to the dynamic features, by stacking all axes serially, relatively small calibration errors (e.g., misalignment of the roll axis with respect to the x axis and non-orthogonality and non-intersection of the roll and pitch axes) are amplified in terms of laser-cutting distortions, particularly at extreme tangent angles.

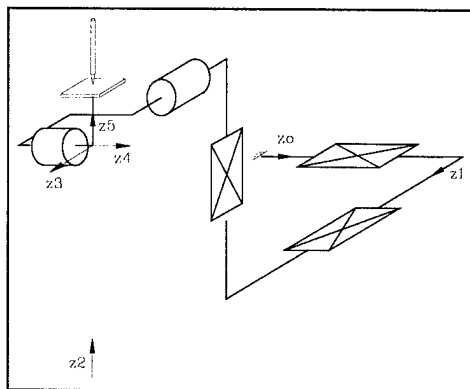


Fig 2: Five axis system architecture

3. The CAM-LEM 4-Axis Beta Design

Fig. 3 shows a schematic description of the 4-axis beta design. In this design, the four controlled axes are configured as two, 2-DOF kinematic chains with separate paths to ground. To accomplish this, an x-y cutting platform is used in combination with an articulated laser head. The laser head rotates about a fixed center of rotation—the focal point of the laser—via two orthogonal rotation axes lying in the cutting plane. With this design variation, multiple benefits accrue. First, the required number of servoed degrees of freedom is reduced from 5 to 4, reducing complexity and still achieving the required mobility. Second, the pitch and roll axes do not have to be supported by x, y and z axes, reducing the gravity force and moment loading on these axes. Third, the decoupled system has lower x-y table inertia, enabling more nimble contour following during laser cutting. Fourth, by providing parallel paths to ground for the x-y table and for the pitch-roll axes, the system can be much stiffer and have less resonance problems. Fifth, by separating the x-y vs. pitch-roll degrees of freedom, the system is easier to calibrate. Finally, since the beta design does not require tilting the cutting platform, the cutting table is easier to design and the clamping requirement on the sheet material being cut is less demanding.

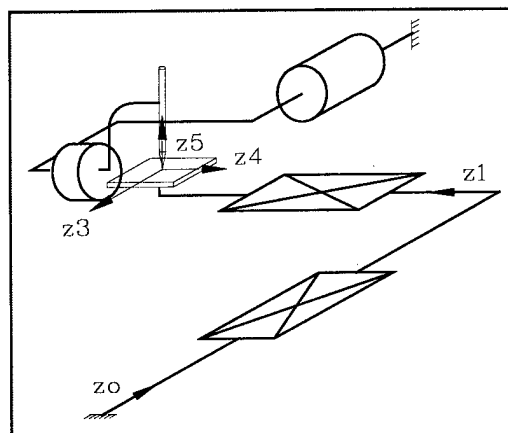


Fig 3: Four axis system architecture

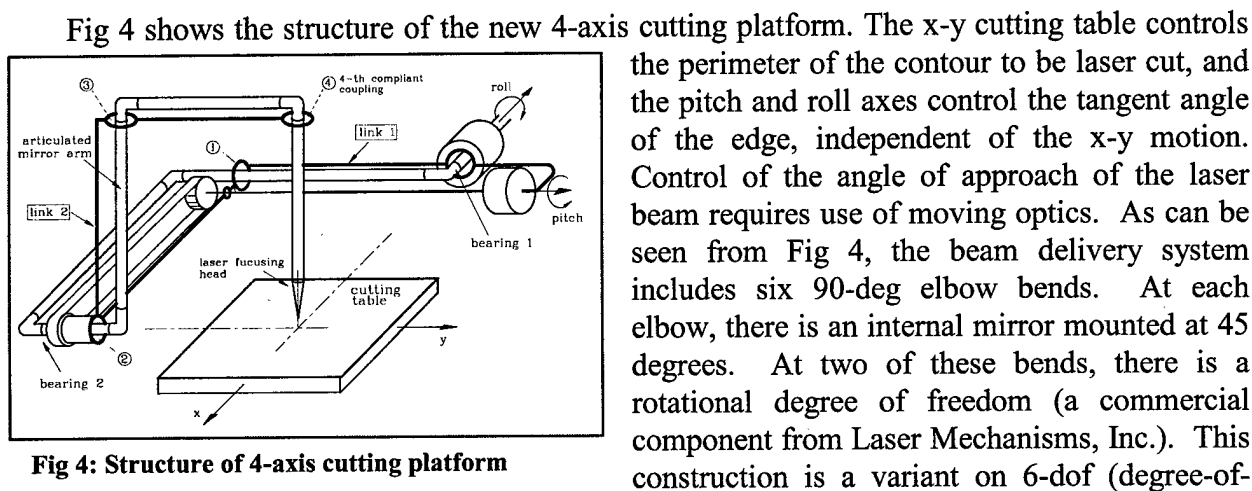


Fig 4: Structure of 4-axis cutting platform

The x-y cutting table controls the perimeter of the contour to be laser cut, and the pitch and roll axes control the tangent angle of the edge, independent of the x-y motion. Control of the angle of approach of the laser beam requires use of moving optics. As can be seen from Fig 4, the beam delivery system includes six 90-deg elbow bends. At each elbow, there is an internal mirror mounted at 45 degrees. At two of these bends, there is a rotational degree of freedom (a commercial component from Laser Mechanisms, Inc.). This construction is a variant on 6-dof (degree-of-freedom) and 7-dof passive beam delivery systems used in laser surgery. It permits maintenance of good optical alignment while providing for redirection of the laser-beam. In our laser-cutting design, we require only two degrees of freedom of the articulated optics—provided these degrees of freedom are aligned as shown in Figs 3 and 4.

The resulting beam-delivery system is capable of rotating the direction of approach of the laser beam about a fixed point in space, which is designed to coincide with the laser focal point at the surface of the x-y cutting table. Actuation of the passive laser mechanism is performed by

two rotational motors. If the axes of these motors are not precisely aligned with the axes of the beam-delivery elbow bearings, large binding moments will be exerted on the elbows, resulting in beam misalignment and possible damage to the precision bearings of the articulated optics. To accommodate inevitable small misalignments, the passive beam-delivery mechanism is driven via compliant couplings to the drive mechanism. The drive mechanism is a 2-dof serial-link, open kinematic chain (a 2-dof robot). Four compliant couplings are used, as labeled in Fig 4.

The roll axis of the drive mechanism drives a yoke, which rotates the entire beam-delivery mechanism as well as the pitch motor. The pitch motor actuates the second degree of freedom, moving only the beam-delivery components past the second articulated mirror. To reduce the inertia and gravity load seen by the roll actuator, the pitch motor is located near the roll motor, offset from the roll axis to act as a counterbalance. The pitch motor drives the second degree of freedom via a shaft extension to a pulley and toothed belt.

The fully-assembled beta machine is shown in Fig 5. The 6"x6" cutting table is cantilevered from a vertical support mounted on the x-y sled. This support structure permits the roll axis to swing the yoke below the cutting table, extending the range of accessible angles. The reachable range of roll and pitch angles is at least ± 80 deg over the full 6"x6" cutting table range of motion.

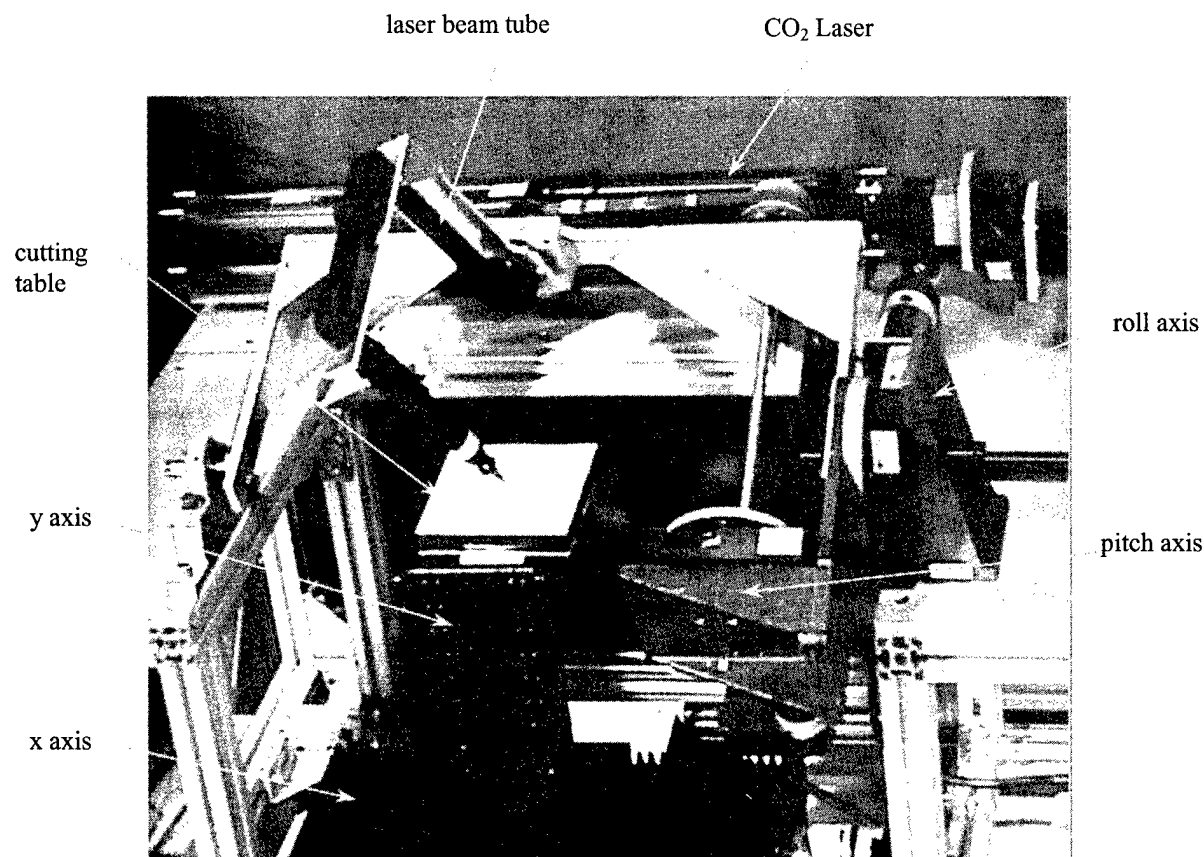


Fig 5: The new 4-axis cutting platform

4. Analysis of Alpha and Beta Machine Calibration Sensitivities

One of the advantages of the new 4-axis design is reduced sensitivity to calibration errors. To evaluate this claim, a sensitivity analysis was performed, as described by Fig 6.

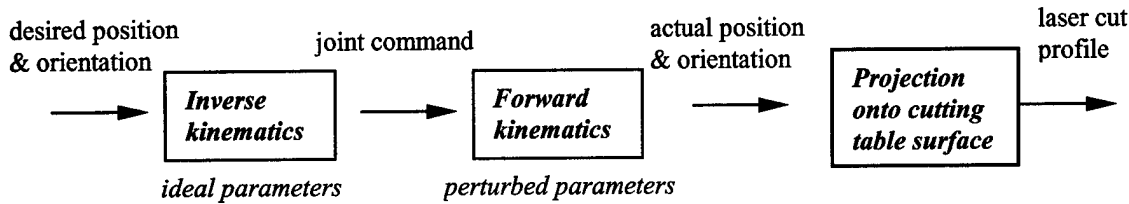


Fig 6: Scheme for the sensitivity analysis

To illustrate this analysis, we consider cutting a simple shape—a frustum of a cone with a 4 mm top (minor) diameter and a 7.73 mm bottom (major) diameter cut from a 0.5 mm thick sheet, constituting a tangent angle of 75 deg. For the beta design, the inverse kinematics corresponding to the desired cut shape prescribes sinusoidal x and y displacements, phase shifted by 90 deg, and sinusoidal roll and pitch displacements, also phase shifted by 90 deg. In the case of the alpha design, if the frustum is to be cut at the center of the cutting table, then sinusoidal x, y, roll and pitch angles are also required, while the z-axis is at a constant elevation.

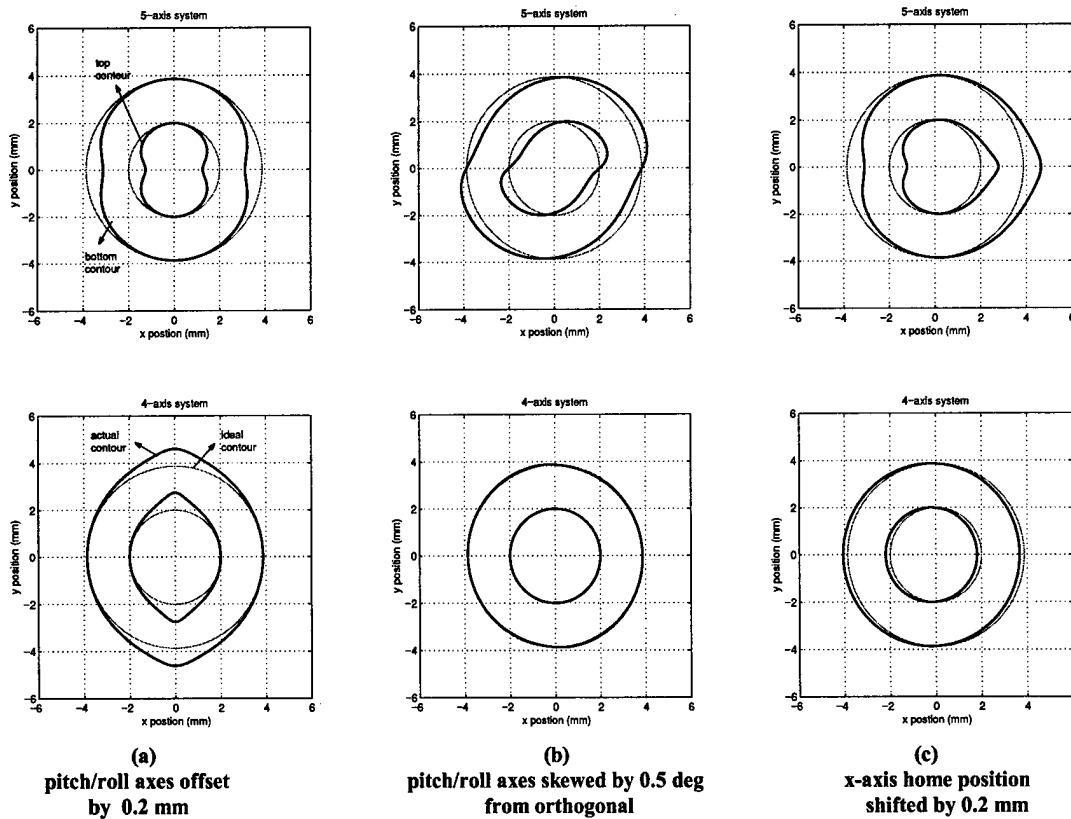


Fig 7: Contour cut shapes due to calibration errors

We illustrate three relatively strong influences on cut accuracy vs. alignment errors. The first is an offset between the (ideally intersecting) pitch and roll axes. The second is non-orthogonal pitch and roll axes, and the third is an error in the home position of the x axis. Fig 7 shows the results of the analysis per Fig 6. In Fig. 7a, the pitch and roll axes are offset by 0.2 mm. In Fig 7b, the pitch and roll axes are skewed by 0.5 deg from perpendicular. In Fig 7c, the x-axis home position is shifted by 0.2 mm.

For case 7a, an offset between the pitch and roll axes, the alpha and beta machines produce comparable magnitudes of distortion. However, for cases b and c, the alpha design shows significant distortions while the beta design is virtually immune to these types of errors. The distortion in Fig. 7b, due to non-orthogonal axes, is negligible for the beta machine. Further, for the beta design an x-home error results in a pure shift; there is no distortion of the cut shape. We thus see that the beta design has low sensitivity to kinematic imprecisions. We further see, however, that it is important to align the roll and pitch axes to be (ideally) coplanar (intersecting). In the beta machine design, this was done by assembling all parts using a precision jig designed for this purpose.

5. Analysis of Alpha and Beta Machine Dynamics

In addition to improved calibration precision, we had further proposed that the new design would be capable of faster laser cutting. To validate this proposition, we performed two sets of characterization: identification of dynamic parameters, and evaluation of influence of mechanical resonances on laser cutting. The dynamic parameters evaluated included: Coulomb friction, gravity loading, viscous friction, maximum velocity, maximum acceleration, and inertia. These terms were identified by tuning feedforward control efforts and analyzing net feedforward and feedback control terms resulting from tracking trial trajectories. Using low-speed sinusoidal trajectories, Coulomb friction and gravity terms dominated the required control efforts. Having identified the Coulomb and gravity terms, the frequency of the test sinusoidal motion was increased, introducing significant viscous friction effects in the net control effort. At still higher frequencies, inertial terms dominate. (The amplitude of the sinusoids had to be decreased at higher frequencies to avoid nonlinear distortions due to velocity saturation and force/torque saturation.) Finally, trapezoidal velocity profile trajectories were commanded for each joint, and the commanded maximum velocity and maximum acceleration were increased incrementally until saturation effects were observed.

The beta design did exhibit improved dynamic properties for the x and y axes. Coulomb and viscous friction are lower, inertias are lower, and maximum accelerations are higher. These benefits are relatively modest, however, since the lead-screw pitches constitute relatively large gear reductions, and thus the reflected inertias of the motors dominate the dynamic loads. As a result, the net improvement in acceleration of the slowest translational axis is only about 26 %. A stronger advantage of the 4-axis design is that there is no third translational axis, and thus the dynamic limitations of the z-axis do not restrict the beta design performance.

A drawback of the beta design is that orientation (pitch and roll) acceleration is slower than that of the alpha design, at 67 % of the original worst-case available angular acceleration. This

reduced response is due to the inertia of the yoke in the beta design used to drive the articulated optics. Thus, the beta design is somewhat faster in position control, but slower in orientation control. The resulting speed comparison for coordinated laser cutting depends on the shape of the part to be cut; outlines with high spatial frequencies and relatively low tangent curvatures could be cut more rapidly with the beta design, whereas part shapes with rapid tangent variations would be cut more slowly by the beta design.

A more dramatic improvement in dynamic performance is due to the stiffer structure and correspondingly higher resonant frequencies of the beta design. Notably, the serial-link structure of the alpha design resulted in a lowest translational resonant frequency of 22 Hz. With the new design, this frequency increased to 65 Hz. Within the velocity and acceleration saturation constraints, this higher resonant frequency corresponds to a higher tracking bandwidth. The higher resonance theoretically enables cutting speeds 3 times higher. However, incorporating consideration the nonlinear effects of acceleration and velocity saturation reduces the magnitude of potential cutting-speed improvement.

To illustrate the effects of mechanical resonances on laser cutting, including consideration of

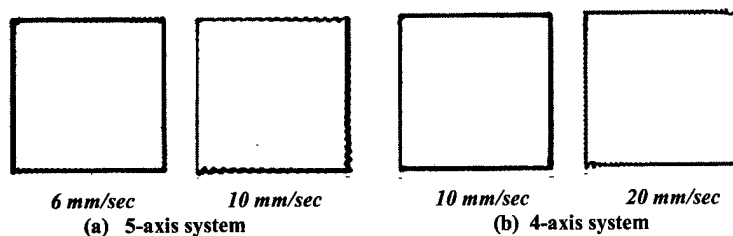


Fig 8: Square-cut (10mmx10mm) with various cutting speeds

acceleration saturation, we performed a simple test of cutting squares from poster board on both the alpha and beta machines. The results are shown in Fig.8. The trajectory specified for these test patterns was not dynamically feasible, since the cutting speed was held constant. As

a result, the corners of the desired square trajectories corresponded to infinite accelerations in the x and y directions. In attempting to follow these untrackable trajectories, the alpha and beta designs exerted maximum accelerations and induced excitations of resonances. The influence of such ringing is apparent in the spatial oscillations of the laser-cut edges.

For the alpha design, a cutting speed of 10 mm/sec resulted in significant ringing. For the beta design, comparable imperfections occurred at cutting speeds approximately twice as fast. Correspondingly, the new design should be capable of building parts 2 times faster.

6. Conclusion

Our new CAM-LEM machine design demonstrates significant performance improvements over our alpha design. By restructuring the former 5-axis, single kinematic chain into 2, 2-axis subsystems, the resulting system is faster and more precise. While the altered inertial loads did not improve system performance, the higher structural stiffness enabled faster cutting speeds. The anticipated improvement in build speed is roughly a factor of two. In addition, the new system is less complex, due to elimination of one servoed axis and decoupling of the translation and orientation axes, and less prone to disturbances during cutting, since parts on the cutting table do not need to be reoriented. Analysis predicts that the new design will be easier to calibrate, though this has not yet been experimentally verified.

In future work, the new system will be evaluated in terms of maximum practical build speeds for representative parts. Cutting precision will be experimentally quantified. In addition, the system will be integrated with automated material handling for sheet feeding and cut-part extraction and assembly.

Acknowledgments

This work was supported by the National Science Foundation under NSF grant DMI-98-00-187. This support is gratefully acknowledged.

7. References

1. Newman, W.S., Zheng, Y., and Fong, C.C., "Trajectory Generation from CAD Models for Computer-Aided Manufacturing of Laminated Engineering Materials", *Proceedings of the 26th International Symposium on Industrial Robots*, Singapore, pp. 153-158, Oct 1995.
2. Choi, S., Hebbar, R., Zheng, Y., Newman, W.S., "CAD and Control Technologies for Computer-Aided Manufacturing of Laminated Engineering Materials", *Proceedings of the Solid Freeform Fabrication Symposium*, University of Texas at Austin, Austin, Texas, pp. 643-651, Aug 1997.
3. Mathewson, B. B., Hebbar, R., Choi, S., Newman, W. S., Cawley, J. D., Heuer, A. H., "Machine Design, Control and Performance of Laminated Engineering Materials", *Proceedings of the Solid Freeform Fabrication Symposium*, University of Texas at Austin, Austin, Texas, Aug. 1998.
4. Zheng, Y., "Enabling Computational Techniques for Tangential-Building Solid Freeform Fabrication", Ph.D. Thesis, Aug 1997, Department of Electrical Engineering and Applied Physics, Case Western Reserve University.
5. Zheng, Y., and W.S. Newman, "Software Design Challenges for Computer-Aided Manufacturing of Laminated Engineering Materials", *the Sixth European Conference on Rapid Prototyping and Manufacturing*, Nottingham, UK, July 1997.
6. Paul Jacobs, "Stereolithography 1993: Epoxy Resins, Improved Accuracy and Investment Casting," *Conference Proceedings of the Fourth International Conference on Rapid Prototyping*, Dayton, OH, June 1993, pp. 249-262.
7. G. Zong, Y. Wu, N. Tran, I. Lee, D. L. Bourell, J. J. Beaman and H. L. Marcus, "Direct Selective Laser Sintering of High Temperature Metals", *Proceedings of the Solid Freeform Fabrication Symposium*, University of Texas at Austin, August, 1992, pp. 72-85.
8. Kumar, C., Jones, L., and Roscoe, L., "Support Generation for Fused Deposition Modeling", *proceedings of the Solid Freeform Fabrication Symposium*, University of Texas at Austin, Austin, Texas, pp. 229-241, Aug. 1995.
9. E. Sachs, M. J. Cima, J. Cornie, "Three Dimensional Printing: Rapid Tooling and Prototypes Directly from a CAD Model," *CIRP Annals*, 39, [1], 1990, pp. 210-214.
10. Griffin, C., Daufenbach, J., and McMillin, S., "Solid Freeform Fabrication of Functional Ceramic Components Using a Laminated Object Manufacturing Technique", *proceedings of the Solid Freeform Fabrication Symposium*, University of Texas at Austin, Austin, Texas, pp. 17-24, Aug. 1994.
11. Lee, C. H., T. M. Gaffney, and C. L. Thomas, "Soft Tooling for Low Production Manufacturing of Large Structures," in *Solid Freeform Symposium Proceedings*, University of Texas at Austin, Austin, Texas, pp. 207-214, Aug. 1996.
12. P. J. de Jager, "Development of a New Slicing Methodology to Improve Layered Manufacturing", *Delft University Press*, Netherlands, 1997.
13. Weiss, L., Prinz, F., Neplotnik, G., Padmanabhan, K., Schultz, L. And Merz, R., "Shape Deposition Manufacturing of Wearable Computers," in *Solid Freeform Symposium Proceedings*, University of Texas at Austin, Austin, Texas, pp. 31-38, Aug. 1996.
14. Philippe Bonaldi and Claude Barlier, "Examination of Various Stochastic Algorithms . Research on Placement Methods Dedicated to the Rapid Prototyping Process: Stratoconception ," *Proceedings of the 6th European Conference on Rapid Prototyping and Manufacturing* , Nottingham , UK, July 1997.

FUSED DEPOSITION MODELING IN MICROGRAVITY

Robert Crockett¹, Dan Petersen², Ken Cooper³

¹ Rapid Prototyping Center
Milwaukee School of Engineering, Milwaukee, WI 53202

² Manufacturing, Materials & Process Technology Division
NASA Johnson Space Center, Houston, TX 77058

³ Rapid Prototyping Laboratory
NASA George C. Marshall Space Flight Center, Huntsville, AL 35812

Introduction

Because of its manufacturing flexibility, Solid Freeform Fabrication will be of enormous value to human exploration of space. Storing a large number of replacement parts on long duration missions, such as a journey to Mars, is impractical, and waiting for replacement parts will not be an option. SFF has a number of potential advantages over traditional machining for use in a space-based manufacturing facility, but the reduced gravity environment imposes a unique set of design constraints on SFF systems¹. Besides materials, resolution, and throughput, additional considerations include equipment mass / complexity / power requirements, feedstock containment and handling, and the ability of a single machine to produce objects from multiple materials.

Deposition systems such as Fused Deposition Modeling and Shape Deposition Manufacturing are attractive candidates for meeting these challenges. Because they employ a very small melt volume that solidifies rapidly, these techniques are well suited to reduced gravity operations. By adding particles to the feedstock (FDC/FDMet) and obtaining the final material properties in a second sintering step, a variety of materials can be deposited from single piece of equipment. We have performed an initial evaluation of the potential for reduced gravity manufacturing using a stock Fused Deposition Modeling system (FDM 1600) as well as a fluid deposition system optimized for zero-gravity operation. These systems were flown on the NASA KC-135 Reduced Gravity Aircraft this June, in preparation for an upcoming Space Shuttle experiment.

Liquid Handling in Reduced Gravity

Deposition of sheets of liquid is an extreme challenge in reduced gravity. The surface tension of the liquid will force the deposited sheet towards a geometry with reduced surface area; depending on the liquid and the surface, this could be a spherical drop or an unstable system, which breaks into many free-floating droplets. The key is to deposit liquid not as 2-D sheets, but as a series of 1-D beads that undergo rapid solidification after placement.

The spreading of a drop or bead is driven by reductions in interfacial energies, at a rate controlled by the viscosity of the liquid. A drop of liquid on a flat, rigid substrate will

drive toward a sessile shape (spherical in 0-g), stopping at an equilibrium configuration which minimizes the Helmholtz Free Energy of the system². In the absence of gravity, this equilibrium configuration is defined by the *equilibrium contact angle*, determined from Young's Equation:

$$\gamma_{SV} - \gamma_{LV} = \gamma_{LV} \cos \theta \quad (1)$$

Where γ represents the surface tension, or specific interfacial energy between the substrate-vapor (SV), the substrate-liquid (SL), and the liquid-vapor (LV), and θ is the equilibrium contact angle that the drop makes with the substrate at the end of spreading. The driving force for spreading of a drop on a *self-similar* surface (as would occur in FDM) is a function only of the liquid's surface tension and current angle to the surface:

$$\gamma_{LV}(1 - \cos \theta) \quad (2)$$

The force of gravity is ignored in these equations, as surface tension is the overwhelming force in the spreading of small drops. The same is true for beads deposited in FDM processes. The dimensions of a deposited liquid below which gravity can be reasonably neglected is defined by the *capillary limit*³, κ :

$$\kappa^{-1} = \left(\frac{\gamma_{LV}}{\rho \bullet g} \right)^{\frac{1}{2}} \quad (3)$$

Where ρ is the density of the liquid and g is the gravitational constant. For materials associated with deposition systems, this limit ranges from about 1-5 mm. The diameter of FDM beads is below this, thus there should be little change in the shape between zero gravity and 1 g. NASA MSFC has recently performed a series of tests using a Stratasys FDM 1600 (Figure 1). Objects were built with the machine on its side (perpendicular to

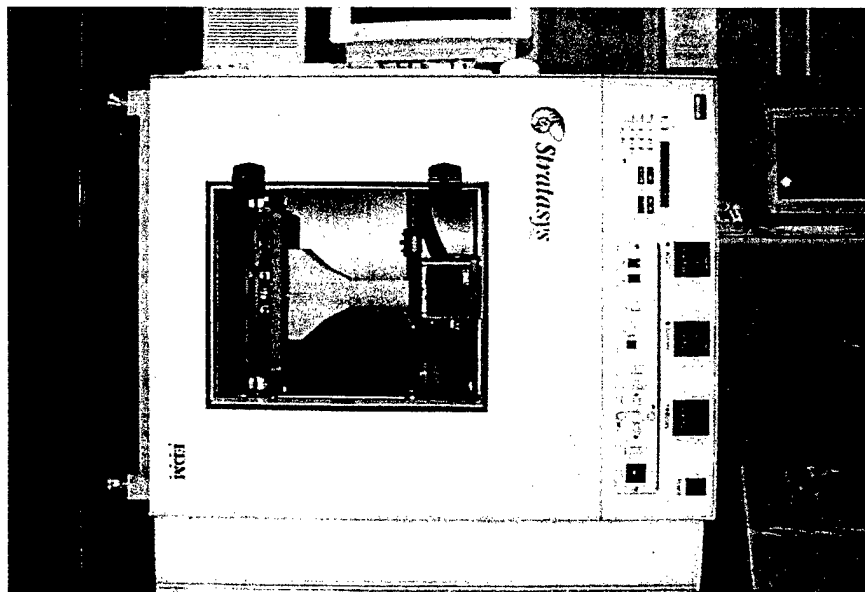


Figure 1. Stratasys 1600 ground-based test, building parts perpendicular to gravitational field.

the gravitational field) and upside down (counter to gravity). Visually, these objects were identical to parts built in the normal orientation.

The key to FDM in reduced gravity will be ensuring a continuous substrate (the previous layer). While surface tension is an effective force for spreading, it requires intimate contact with a surface. Above a certain tip height for a given bead diameter in a FDM process, the bead will tear due to unbalanced forces produced by the liquid surface tension. In 1g, this can create flaws or gaps in the final part; in reduced gravity, the consequences are potentially more severe, as droplets will likely form and bead continuity will be lost. It has been proposed by one of the authors⁴ that this is a similar geometry to the problem of an axisymmetric liquid bridge. The slenderness ratio of the tip height above the surface (l) divided by the diameter of the bead (d) must be below a height limit on the order of π to remain stable, or:

$$l < \pi d \quad (4)$$

Above this limit, high surface tension liquids are more susceptible to forming individual droplets. The force of gravity acts to stabilize the bead through minor l or d fluctuations during deposition (e.g. head speed, tip height, flow rate). It is expected that continuous contact between the deposited melt and a solid surface will be critical without this stabilizing force.

KC-135 Reduced Gravity Aircraft Experiments

A Stratasys FDM 1600 was recently flown aboard the NASA KC-135 Reduced Gravity Aircraft (Figure 2). The goal of these experiments was to obtain a set of initial qualitative observations on the feasibility of using FDM in a microgravity environment. Several ABS specimens of varying geometry were fabricated during a series of 160 parabolas, each of which provided nominally 25 s of reduced gravity. The geometry of the specimens allowed observations of inter- and intra-layer bonding, unsupported structures, and dimensional stability of specimens compared to the same designs fabricated in 1g.

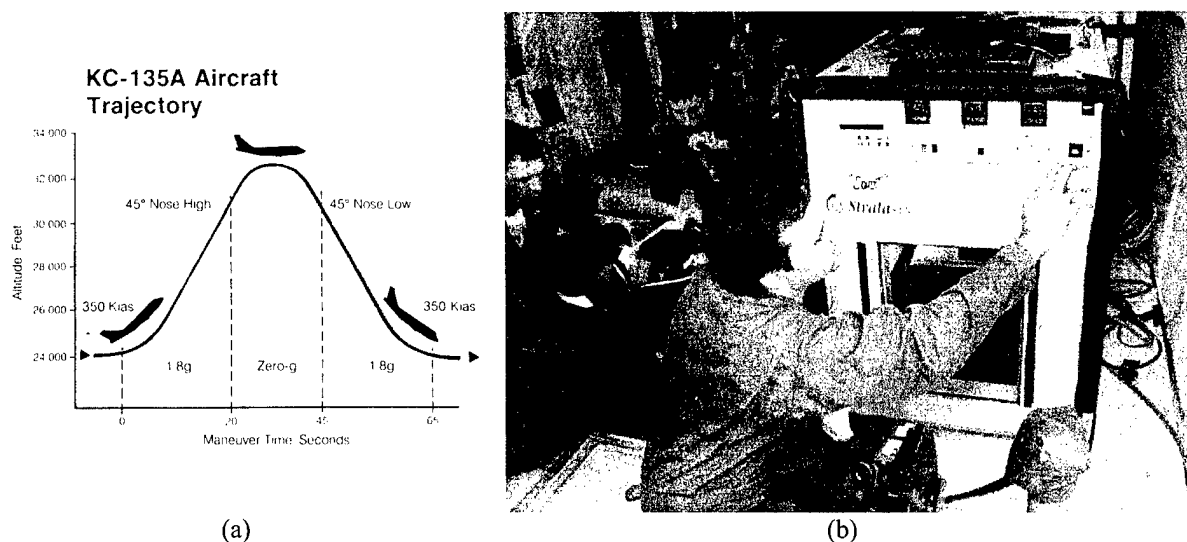


Figure 2. (a) KC-135 aircraft trajectory. (b) Stratasys 1600 during KC-135 reduced-gravity testing.

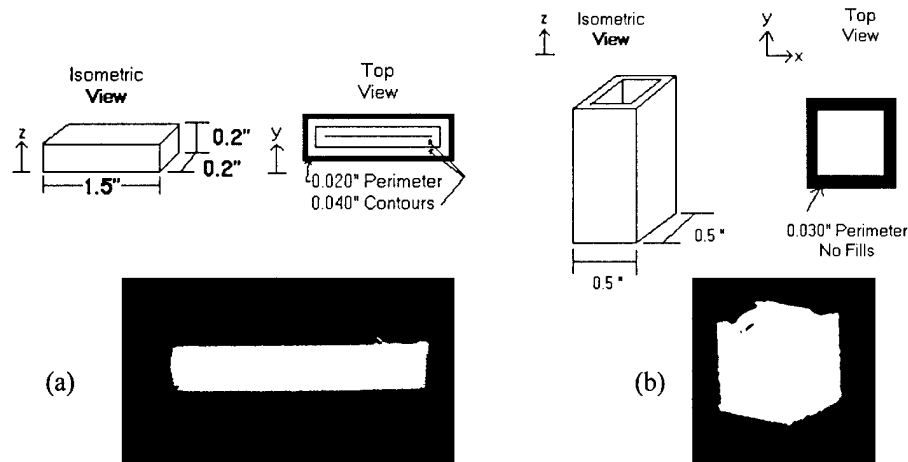


Figure 3. Continuous substrate geometries and results: (a) horizontal test bar. (b) vertical column.

Experiment Set #1: Continuous Substrate: Bars and Columns

Horizontal test bars were fabricated twice during the first flight, requiring approximately 10 parabolas each. Bars were fabricated using concentric extrusion paths, from the outside inward until a solid part was achieved. Dimensions are shown in Figure 3(a). Two vertical columns were fabricated during the remainder of the first flight sequence (Figure 3(b)). The columns consisted of a hollow box with 0.020" walls, with an operator-determined height of approximately 1".

Intra-layer bonding between concentric extrusion paths was of interest for the horizontal test bars. If the absence of a gravitational force on the extruded beads reduced the magnitude of spreading or bead contact to the surface, the beads would be narrower than designed. This could cause delamination between the perimeters and contours, resulting in a series of unconnected concentric boxes as opposed to a solid structure. Results, however, were very much the same in microgravity as in one-g. Both inter- and intra-layer bonding was good, and overall dimensions of the flight parts compared to the ground parts were: $x = \pm 0.00"$; $y = \pm 0.00"$; $z = \pm 0.00"$. It should be noted that, under normal conditions, the FDM deposition tip is designed to actually "smear" the material out to the required width (i.e. $l < d$). The absence of gravity for this type of simple geometry deposited on a continuous substrate should thus not affect the properties of the final object.

The vertical column was designed to verify the capability to build a tall, thin-walled structure in the absence of gravity. It was suggested that the thin walls would probably remain intact, however a taller structure may topple during a multi-g aircraft pullout. Although the structure remained intact during the pullout, the thin walls experienced a small amount of sag. Successive layers bonded only in areas where the previous bead didn't sag (i.e. bonding occurred only where there was a continuous substrate, generally at the corners). These failures continued to propagate throughout the remainder of the part, although it appeared that some process correction occurred during the zero-g segments of the flight.

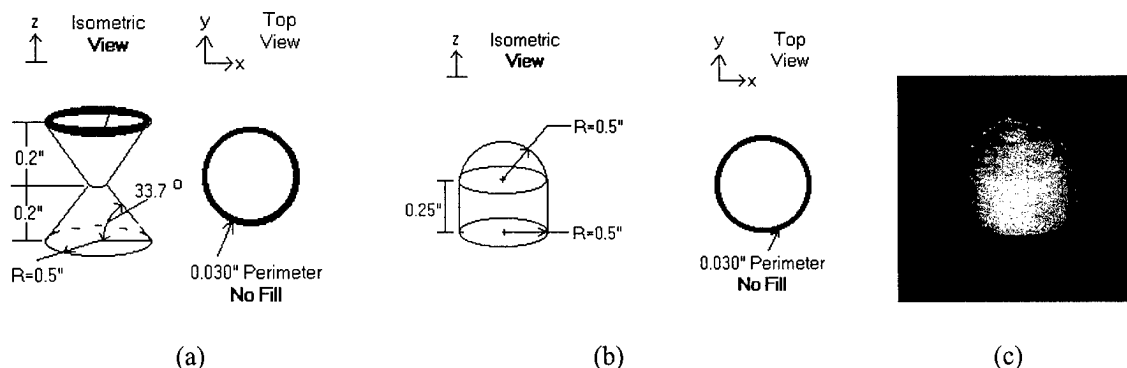


Figure 4. Moderate overhang geometries: (a) hourglass. (b) domed column. (c) results (dome).

Throughout these experiments, the FDM operated properly, holding to its designed patterns and extruding the proper volume of material. There was only one noticeable "side-step" during construction of the horizontal bar, resulting from one of the multi-g pullouts of the aircraft.

Experiment Set #2: Reduced Substrate: Hourglass and Dome

Geometries were fabricated that provided constant or increasing overhangs, reducing the substrate contact area for the successive layer. These geometries cannot be built in 1g without support structures. The hourglass design, Figure 4(a), consisted of two blunted cones with 33.7° angles to the horizontal, connected vertically at their apex. This design prescribed that each consecutive horizontal layer was only attached to the previous layer by 25% of the surface area of the bead. The dome design, Figure 4(b), consisted of a straight hollow vertical cylinder, capped by a constant radius dome. During fabrication in one-g, this part failed (delaminated and slumped) near the upper 25% of the dome with a collapse induced by gravity.

It was assumed that the steep hourglass design and upper unsupported area of the dome would have a better chance at survival in zero-g. Due to the extreme changes in cross section per layer at the tip of the dome, however, some failure was expected as a result of reduced substrate contact. It was also expected that the multi-g segments of the flight would possibly cause failure due to the weight of the overhanging structure.

As predicted, the hourglass did survive farther in reduced gravity compared to one-g tests. Also as predicted, the multi-g flight segments caused a great strain on the excessive overhangs, causing a significant "waviness" to the once-horizontal layers. In the dome geometry, the horizontal layers in the cylinder and lower dome sections bonded properly. The cylinder radius was within $\pm 0.00"$ of the one-g test. As per expectations, the hollow dome structure built higher successfully than did its one-g counterpart. These preliminary observations point to a potential reduction in support structures that will be required for fabricating components in micro-gravity, as long as a minimum contact is provided with the previous layer. The FDM system performed properly during these experiments.

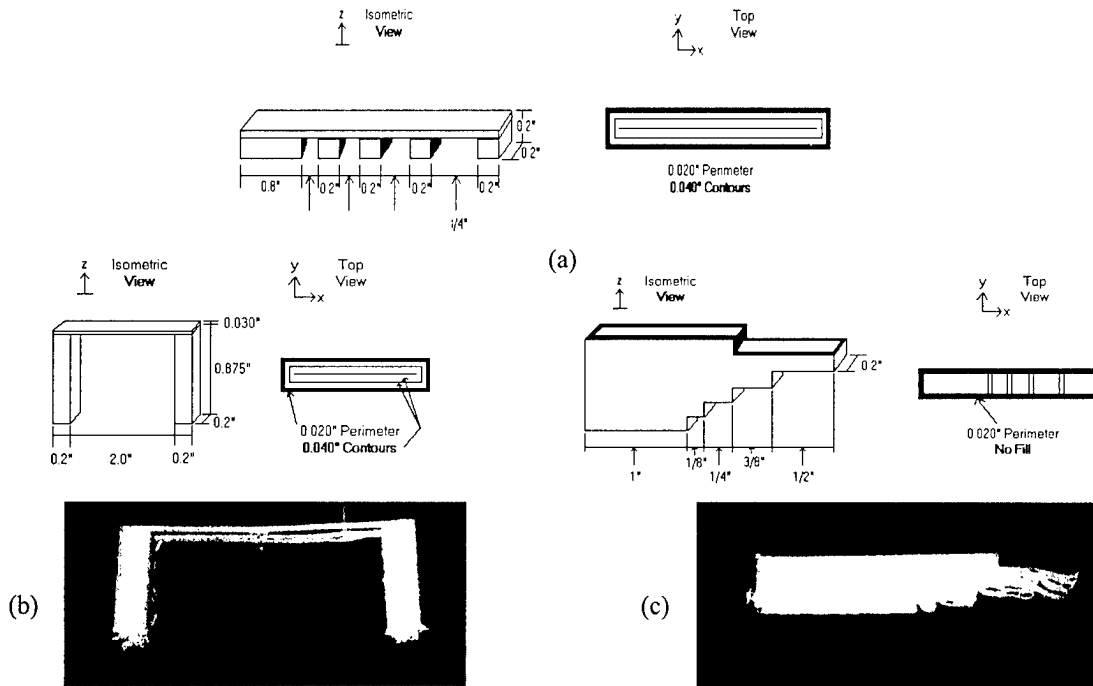


Figure 5. Bridge and cantilever geometries and results: (a) Initial bridge with increasing spans. (b) modified bridge with tall vertical columns. (c) cantilever.

Experiment Set #3: No Substrate: Bridges and Cantilevers

A bridge-and-piers structure was fabricated at the beginning of the second flight day, during the first 10 parabolas. Several pier columns were built pre-flight at consecutively increasing horizontal gap spacings. The beginning pier was elongated to allow the material to reach its full flow volume before leaving contact with the substrate. Dimensions and specifications are shown in Figure 5(a). A second design, consisting of two tall vertical columns with a long span between them, was fabricated on the final flight day (Figure 5(b)). Columns for this design were fabricated during the one-g portion of the flight, and the span was fabricated in reduced gravity.

The design in Figure 5(a) failed as expected when fabricated under one-g conditions, with the unsupported bridge sections sagging down to the bottom of their corresponding voids. The flight test was to determine whether, at moderate head speeds, the rapid solidification of the thermoplastic would provide sufficient continuity between the initial substrate and the melt to allow extended unsupported deposition. Unexpectedly, the bridges sagged during reduced-gravity deposition to contact the lowest surface (the FDM foam platform), just as occurred in one-g. It is likely that surface adhesion to the previous pier wall, in addition to frictional attraction of the foam platform, pulled the extruded beads down to this “undesired” substrate. Once in contact with the foam, it acted as the substrate for the remainder of the deposition. To avoid contacting the foam, the design in Figure 5(b) was used in successive experiments, with taller bridge piers acting to separate the span sufficiently from the base substrate. Results were positive in that the entire free span was connected by a smooth, horizontal bridge during the reduced gravity segments of the flight.

The cantilever design (Figure 5(c)) was similar to the bridge-and-pier experiment, in that free-hanging "shelves" of consecutively increasing gaps were fabricated. In this case, however, the unsupported sections of the object had no second pier on which to attach. This design required that the extruded bead make a 180-degree turn in free space in order to return to the single supporting pier.

It was believed that the surface tension of the liquid would pull the soft, solidifying portion of the bead out of position during the about-face of the tip, destroying the desired geometry. Results showed that the horizontal layers of the solid part section bonded properly, however those layers in free space did not: the unsupported segments did appear to "fall" some, as in the case of the bridge-and-pier; the turnaround and return of the tip indeed caused the free hanging material to deform slightly, although the layers achieved moderate self-correction as the build progressed. Extremely unsupported structures such as this would most likely require a small amount of support in microgravity applications, due to the shear stresses imparted by the moving extrusion tip.

These experiments demonstrated that free spans of extended length can be fabricated without supporting structures in microgravity, as long as: 1) the head speed is sufficiently slow to allow solidification and maintain continuity with a "launching" substrate or pier, and 2) there is a "landing" substrate, or secondary pier on the opposing side of the void to be spanned.

One problem experienced throughout the test session was the effects of atmospheric humidity on the ABS build material. The build material is known to be moderately sensitive to high humidity levels, which were experienced in the test geographical area and season (Houston, TX in June). This high air moisture content caused the molten material to continue oozing from the extrusion tip long after it had been shut off at the end of a build layer. This would then cause a clump of material at the beginning of the following layer, along with a following gap as the flow caught back up to the ooze void in the extrusion tip. The result was a large "fuzzy" build seam along the start points of each layer. A much dryer climate would be needed for follow-up testing conditions.

Space Shuttle "Get Away Special" Payload

A significant limitation of the above tests was the affects of the multi-g segments of the flight during aircraft pullout. This was especially limiting on parts with overhangs. Further testing is required in an extended microgravity environment. Such testing is planned for late summer of 2000, when a deposition experiment will fly as a Space Shuttle "Get Away Special" (GAS) payload. Undergraduate students at Milwaukee School of Engineering developed and constructed a mini-FDM to evaluate material flow and solidification (Figure 6(a)). The hardware was tested on the same KC-135 flight as discussed above (test apparatus is visible on the left side of Figure 2(b)).

The experimental apparatus consists of a 3-axis positioning system in cylindrical coordinates. Material is deposited on a rotating surface to provide the equivalent of ~ 25

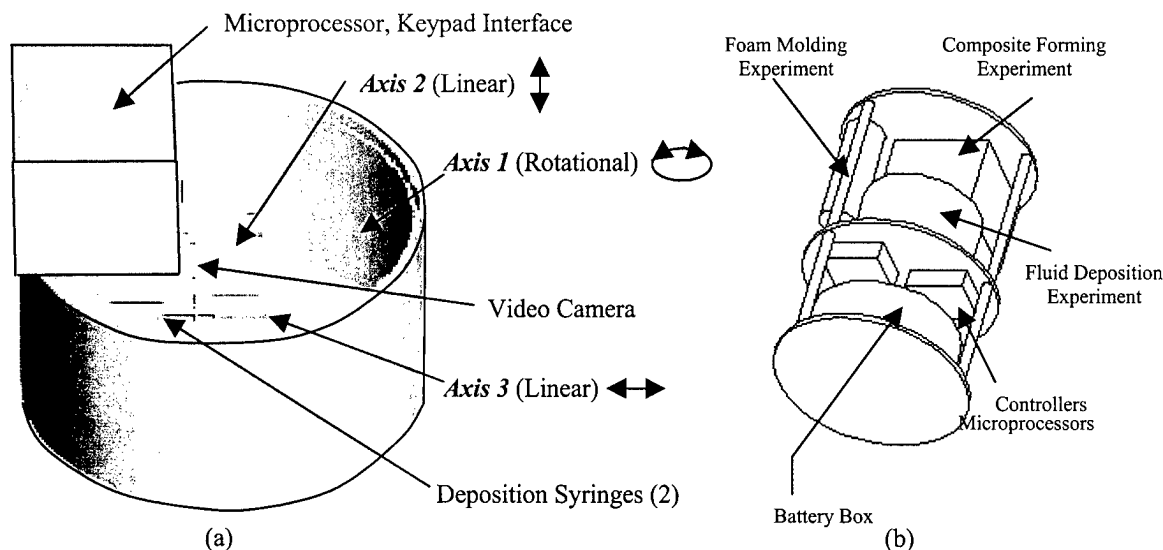


Figure 6. (a) deposition apparatus. (b) Get Away Special (GAS) experiment layout.

linear inches of deposition real estate. Cameras are mounted to the dispensing head to provide a fixed, close view of initial deposition and material flow. This system uses standard 25-gage Stratasys FDM tips and ABS plastic. Due to space limitations, however, the feedstock for the experiment is contained within a syringe (3cc), and is melted fully before extrusion. Eliminating all air from this large a melt volume is absolutely critical, and has been a design challenge. Although the positioning hardware and data collection systems performed well in the KC-135 tests, there will be some fluid delivery system modifications based on lessons learned. The modified system will ultimately be repackaged into a NASA GAS container (Figure 6(b)), which must provide all power, control, thermal management, and data collection/storage for the experiments. In addition to the FDM apparatus, a set of composite forming and foam molding experiments will take advantage of the reduced gravity environment to build complex freeform shapes without forms or mandrels.

The application of layered fabrication techniques is apparently feasible for standard and some non-standard part designs in a reduced gravity environment. Further testing and development is planned to study the interaction between a deposited melt and substrate, as well as processing limits for free spans and partial substrates.

REFERENCES

- ¹ K. Watson, D. Petersen, and R. Crockett, "Application of Solid Freeform Fabrication Technology to NASA Exploration Missions", paper presented at this conference.
- ² P. Kralchevsky, A. Dimitrov, and K. Nagayama, "Analytical Expressions for the Shape of Small Drops and Bubbles", *Journal of Colloid and Interface Science* **160** (1993) 236-242.
- ³ A. Zosel, "Studies of the Wetting Kinetics of Liquid Drops on Solid Surfaces", *Colloid Polym Sci* **271** (1993) 680-687.
- ⁴ R. Crockett and P. Calvert, "The Liquid-to-Solid Transition in Stereodeposition Techniques", in *1996 Solid Freeform Fabrication Symposium Proceedings*. Austin, TX: University of Texas at Austin (1996) 257-264.

Automated Loading and Unloading of FDM Systems

Øivind Brockmeier, Christopher Westcott, and Jan Helge Bøhn

Mechanical Engineering, Virginia Tech

Blacksburg, VA 24061-0238, U.S.A.

tel.: 540-231-3276, fax.: 540-231-9100, e-mail.: bohn@vt.edu

Rapid prototyping systems have advanced significantly with respect to material capabilities, fabrication speed, and surface quality. However, build jobs are still manually activated one at a time. The result is wasted idle time whenever an operator is not at hand to make a job change. A low-cost auxiliary system has been developed and implemented to automatically load and unload FDM 1600 (and FDM 1650 / FDM 2000) rapid prototyping systems. The modifications to the FDM 1600 system are minimal. The door to the FDM 1600 build chamber has been removed, a new build tray has been developed, and the .SML build files have been slightly modified at both ends to facilitate synchronized operation between the FDM 1600 and the automated loading and unloading systems.

1 Introduction

Layered manufacturing was commercially introduced by 3D Systems, Inc. in 1987. Since then, several more systems and advancements to existing systems have been commercialized, and research has primarily been concerned with increasing the build speed, improving part quality, and developing new fabrication materials. Hence, today the utility of layered manufacturing spans the range from rapid physical visualization to low volume manufacture. Unfortunately, layered manufacturing systems remain relative expensive compared to equivalent build-volume size computer numerical control (CNC) machining systems and most other computer peripherals. It is therefore important that layered manufacturing systems are used efficiently to justify their high capital cost.

The efficiency of layered manufacturing systems has thus far been addressed by increasing the material deposition rate and by making it easier to "print a part." Examples of advances to increase the material deposition rate include adaptive build layer thicknesses, slanted build layer contours, adaptive material area deposition, parallel material deposition, and faster motion systems. The ease of use has been facilitated by more intuitive and less complex user interfaces, and by the implementation of print queues to ease the movement of customer build files to the fabrication unit. An example of the latter includes the network print queue for a laminated object manufacturing (LOM) system (Helisys, Inc.) that was demonstrated by Bailey

in 1995 [1]. Today print queues are increasingly more common. For instance, the Genisys X (Stratasys, Inc.) [2] and the ThermoJet (3D Systems, Inc.) [3] have print queues to help users submit build jobs and administrators order these jobs for optimal utilization of their respective fabrication systems.

Being able to optimize the order of the build jobs is essential for the effective utilization of most layered manufacturing systems. Today's systems require an operator to manually change build jobs, and most systems are installed in an environment where an operator is available only during regular working hours on weekdays. Hence, to maximize system throughput over time and to maximize the number of hours over which to share fixed costs (e.g., capital depreciation and maintenance contracts), operators will attempt to schedule long build jobs over night and over weekends, and short build jobs during the time operators are available to manually change build jobs. Too often this strategy is insufficient to ensure continuous operation, and a choice must be made between letting the system stand idle for hours at a time or absorbing the additional expense of having an operator come in after hours to make a build job change.

For instance, in the course *ME 4644 Introduction to Rapid Prototyping* at Virginia Tech, 20 student teams each have an FDM 1600 (Stratasys, Inc.) reserved for 24 hours twice during the semester, with each build job taking on average about 15 hours to complete. Hence the system stands idle for about 360 of the 960 reserved hours (63% system utilization). With continuous operation, these 40 build jobs could be completed in 25 days instead of the current 8 weeks.

Burns [4] argued in 1993 the need for automating the loading and unloading of layered manufacturing system to make them true automated fabrication systems, similar to many CNC machining and EDM systems [5]. Gibson [6] discussed the use of robots for loading, unloading, and finishing operations, and is currently working to simulate robot loading and unloading of selective laser sintering (SLS) systems (DTM Corp.) [7].

This paper presents the complete implementation of a fully automated loading and unloading system for FDM 1600 rapid prototyping systems. With minimal modification it should also work with FDM 1650 and FDM 2000 rapid prototyping systems. The following sections discuss the characteristics of FDM systems and the design and implementation of this auxiliary loading and unloading system.

2 Fused Deposition Modeling

Fused deposition modeling (FDM) systems fabricate parts by extruding a thermoplastic material (typically ABS plastic) through a small die to produce a thin bead that, when routed back and forth across a horizontal plane, combines to produce a horizontal cross-sectional build layer, bonded to the build layer below (Figure 1). The instructions for this fully automated motion are contained in a text file that is uploaded from a host computer to the FDM unit. This text file is often referred to as an .SML build job file. However, currently, both before and after

this automation, an operator must perform a series of trivial, though manual, tasks for each build job:

1. Bring system up to temperature;
2. Open door;
3. Place new build tray on build table;
4. Close door;
5. Upload build job file;
6. Position relative start point;
7. Continue build job;
8. Open door;
9. Remove build tray with part; and
10. Close door.

Hence, in order to fully automate FDM rapid prototyping systems, so they can operate unassisted across multiple build jobs, analogous to how a laser printer is loaded with a ream of paper, it is necessary to automate the above loading and unloading process. The following section will describe one such solution.

3 Continuous Layered Manufacturing

A low-cost auxiliary loading and unloading system has been developed to enable continuous layered manufacturing (CLM) with FDM 1600 and similar rapid prototyping systems (e.g., FDM 1650 and FDM 2000 systems). The CLM system attaches to the front of the FDM system on a steel frame that slides beneath the FDM system (Figure 2) and requires only three minor modifications to the FDM system: First, the front door on the FDM system is removed and replaced by a slender frame holding a weather strip seal. Second, a redesigned build tray is used in place of the original build tray. The redesigned tray features several guides that enable it to reliably go into and come out of the fixture on the FDM build table (no modification is made to the FDM system). Finally, custom software is used to automatically modify the .SML build files at the time of job submission, and to coordinate the operations of the CLM and FDM systems across two independent RS232 serial lines. Hence, setting up the CLM—or resetting the FDM back to its original state—takes less than 10 minutes.

The following describes in more detail the CLM's mechanical and electrical systems and the software used to coordinate the CLM and FDM operations.

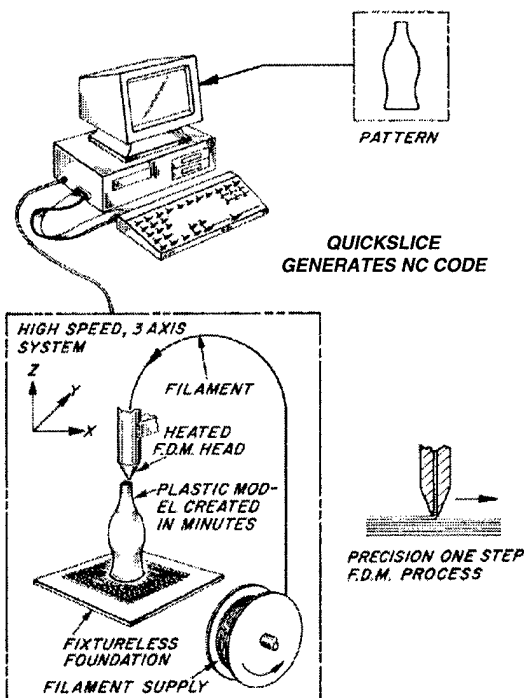


Figure 1 Fused deposition modeling (FDM).

3.1 Mechanical System

The mechanical system for the CLM consists of four parts; a roller conveyor table, a new rotating door, a loading and unloading linkage, and a new build tray that actually forms the only physical interface between the CLM and FDM systems.

The conveyor table, which consists of several driven and idle rollers in a frame, has three zones over which it can store five build trays: The first zone is where up to two unused build trays rest prior to fabrication; the second zone is where the active build tray is moved into and out of the FDM build chamber; and the third zone is where up to two build trays with parts rest after fabrication. The driven rollers are connected by o-rings to, and powered by, a driveshaft that runs perpendicular to the rollers below the conveyor table. Three spring-loaded position guides are placed in between the rollers to control the flow and positioning of the build shelves along the conveyor table.

The original door to the FDM build chamber was removed because it swings outward and would interfere with the CLM. A new door was put in its place. This door is attached to and driven by the CLM such that it rotates in its plane. Finally, a slender frame with weather stripping was attached to the FDM to provide a seal between the FDM and the new door.

The build shelves are moved between the CLM and FDM by an electromagnet attached to a Chebyshev Type One four-bar linkage [8] with a parallel wire linkage (Figure 3). This linkage combination ensures that the electromagnet travels in a straight line without rotation.

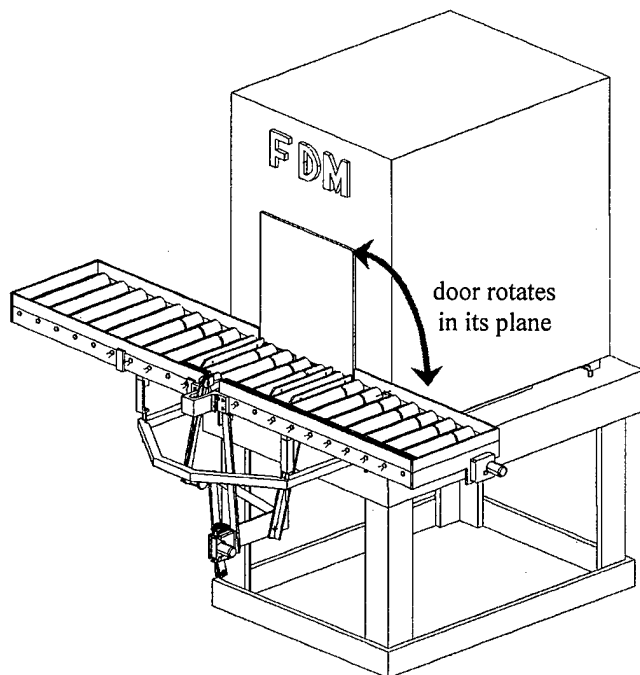


Figure 2 Continuous layered manufacturing (CLM) system positioned relative to FDM system.

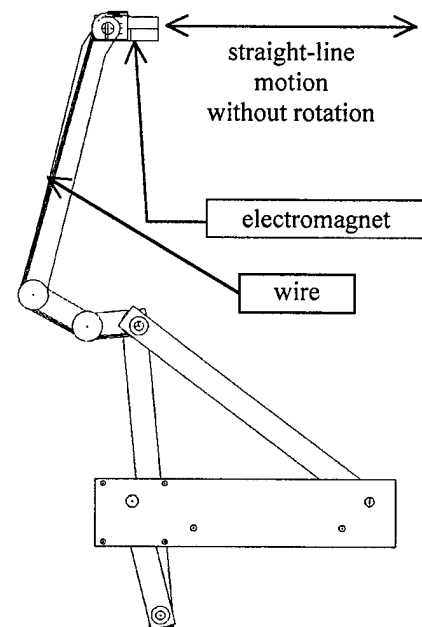


Figure 3 The Chebyshev Type One four-bar linkage with a parallel wire linkage is used to insert and remove the build shelves into and out of the FDM build chamber.

The original FDM build shelves were designed for manual operation. Two modifications were therefore made to these build shelves to enable their use with the CLM: First, the handle was replaced by an iron plate to enable the use of an electromagnet. Second, the bottom plate and the guides on the sides were elongated and heavily beveled to ensure that the tray easily guides itself into and out of position without jamming. These changes are shown in Figure 4.

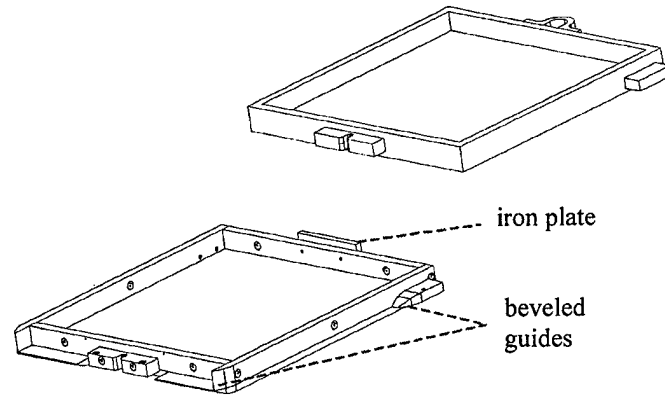


Figure 4 The new elongated build shelf (lower left) has guides to facilitate reliable loading and unloading. The original build shelf (top right) is shown for comparison.

3.2 Electrical System

Seven electrical devices actuate the CLM system: three solenoids, three DC gear motors, and an electromagnet. The three spring-loaded position guides between the rollers are actuated by separate pull-style solenoids. When a solenoid is energized, the corresponding guide retracts beneath the rollers, which allows build shelves to pass. The DC gear motors open and close the door, drive the conveyor table, and move the linkage. Lastly, the electromagnet is used to connect the build shelf to the linkage during loading and unloading.

Six infrared proximity sensors provide feedback to control the CLM system. Four of these sensors act as limit switches; two for the door, and two for the linkage. The remaining two are positioned between the rollers of the conveyor table: One sensor is placed close to the linkage to sense when the build shelf reaches the load/unload position; the other is placed at the start of the storage zone for finished parts to sense if this zone is full.

The CLM control system is located on a circuit board inside an enclosure attached below the conveyor table. A microprocessor controls the CLM electrical devices via motor drivers and relays, and receives input from the six proximity sensors, a numerical keypad, and a serial port connected to the host computer driving the FDM system. The electrical devices can therefore be activated manually via the keypad or by a program over the serial line. This includes the *load* and *unload* sequences, which, for convenience, have been programmed directly into the microprocessor memory. A brief overview of these two predefined sequences follows:

Load Sequence

1. Retract linkage (moves the linkage out of the way)
2. Retract position guides (allows the free flow of build shelves)
3. Run conveyor table until the first build shelf reaches the loading position
4. Release position guides (positions the build shelf for loading)
5. Open door

6. Turn on electromagnet (grabs onto the build shelf)
7. Extend linkage (pushes the build shelf into the FDM machine)
8. Turn off electromagnet (lets go of the build shelf)
9. Retract linkage
10. Close Door

Unload Sequence

1. Check storage sensor (make sure there is storage space available)
2. Retract position guides (allows free flow of build shelves)
3. Open door
4. Extend linkage
5. Turn on electromagnet (grabs onto the build shelf)
6. Retract linkage (removes build shelf with finished part from the FDM machine)
7. Turn off electromagnet (lets go of the build shelf)
8. Close door
9. Run conveyor table for 15 seconds (moves build shelf with finished part to the storage zone)

3.3 Software

The software for controlling and coordinating the CLM and FDM systems has been designed to take the place of the program *ssend* that is shipped with the FDM systems. It assumes that the CLM and FDM systems are connected to the same host computer via two independent RS232 serial lines operating at 9600 baud. The new program incorporates a basic print queue. For each file it attempts to "print", it verifies the file; modifies its beginning and end; and then sends it to the FDM system while coordinating with the CLM system.

Since modifications are made to the original .SML file that is fed to the FDM system, it is important that the format of the .SML file is well understood to avoid sending the FDM system instructions that might cause damage. This is achieved by verifying the version of the .SML file and by checking the file for certain constant characteristics (e.g., the standard instruction preamble sequence). Once the version and integrity of a file has been verified, the beginning and end of this file are modified to accommodate synchronous operation between the CLM and FDM systems. These modifications are made in memory (RAM) as the FDM fabrication instructions are read from the disk and resent to the serial port; they do not affect the actual file on disk itself.

The coordinated operations of the CLM and FDM systems assume that the FDM system temperatures are set appropriately for the materials to be used; that the FDM has been loaded with material; and that build trays with new foam have been loaded onto the CLM unused build tray storage zone. Once these one-time manual operations have been completed, the coordinated operations under program control are repeated for each file in the print queue as follows:

FDM system

1. Lower build table (avoid collision during Find (0,0) operation)
2. Find (0,0) in XY build plane (enable moving to safe position)
3. Move head to safe position (avoid collision during subsequent Find Z=0 operation)
4. Find Z=0 level (enable moving to CLM loading/unloading level)
5. Lower table to CLM loading/unloading level

CLM system

6. Execute the preprogrammed CLM loading sequence (see Section 3.2)

FDM system

7. Move to standard start position (left front corner with tip slightly submerged in foam)
8. Continue with actual build instructions — stop before entering final standard FDM sequence
9. Lower table to CLM loading/unloading level

CLM system

10. Execute the preprogrammed CLM unloading sequence (see Section 3.2)

4 Results

A fully operational prototype of the CLM has been built and installed with an FDM 1600 rapid prototyping system, with both systems controlled concurrently by an SGI Octane workstation running IRIX 6.5.4. The control program was written in C++ and should easily port to other systems. The estimated construction cost was less than US\$5,000.

The CLM system has the capacity to complete three build jobs before operator intervention is required. However, completed build jobs can be removed from the CLM, new ready-to-use build trays can be added to the CLM, and build jobs can be added to the print queue—all at any time. Hence, sustained continuous automated FDM fabrication is feasible.

It takes close to seven minutes to load a new build shelf. The vast majority of this time is for the build table to find the Z=0 level and then move to the CLM loading/unloading position, which is towards the bottom of the FDM build chamber. Unloading is faster and depends on the position of the build table at the end of the build; the closer it is to the CLM loading/unloading level, the faster the unloading is completed.

The FDM productivity increase with the CLM system will still vary with build times. For instance, a series of three short build jobs overnight or over the weekend will still cause significant down time. However, in most cases a series of three build jobs will continue through the night or over the weekend, which will reduce the downtime between build jobs to less than 15 minutes. Alternatively, the CLM can easily be extended in both directions to accommodate more build jobs without operator intervention.

5 Conclusion

This paper has presented a low-cost auxiliary system for automated loading and unloading of build trays for FDM 1600 systems (and, with minimal modification, FDM 1650 and FDM 2000 systems). The new system has the potential to provide continuous FDM operation with only occasional operator attendance at his or her convenience. For instance, it is expected that the 40 build jobs during a semester in the course *ME 4644 Introduction to Rapid Prototyping* at Virginia Tech will now take 25 days to complete instead of the customary 8 weeks.

Acknowledgment

FDM® is a registered trademark of Stratasys, Inc. of Minneapolis, Minnesota, U.S.A., Reg. No. 1,663,961.

References

- [1] Michael J. Bailey, "Tele-Manufacturing: Rapid Prototyping on the Internet," *IEEE Computer Graphics & Applications*, vol. 15, no. 6, November 1995, pp. 20-26.
- [2] Stratasys, Inc., Eden Prairie, Minnesota, August 1999,
URL: <http://www.stratasys.com/genisys.html>
- [3] 3D Systems, Inc., Valencia, California, August 1999,
URL: <http://www.3dsystems.com/products/solidobject/thermojet>
- [4] Marshall Burns, *Automated Fabrication: Improving Productivity in Manufacturing*, Prentice-Hall, Englewood Cliffs, New Jersey, USA, 1993, ISBN 0-13-119462-3.
- [5] Erowa AG, Reinach and Büron, Switzerland, August 1999,
URL: <http://www.erowa.com>
- [6] Ian Gibson, "A Discussion on the concept of a flexible rapid prototyping cell," *Rapid Prototyping Journal*, vol. 2, no. 2, 1996, pp. 32-38.
- [7] Matthew Lai, University of Hong Kong, personal correspondence, July 1999.
- [8] Kevin Riutort, "Applied Design and Implementation of Straight-Line Mechanisms," M.S. thesis, Mechanical Engineering, Virginia Tech, Blacksburg, Virginia, USA, July 1996.

Additive/Subtractive Material Processing for Mesoscopic Parts

Yih-Lin Cheng, Jurgen Stampfl, Rudolf Leitgeb, and Fritz B. Prinz
Stanford University, Stanford, CA

Abstract

Mesoscopic additive/subtractive material processing (Meso A/SMP) is a solid freeform fabrication technique capable of producing engineering parts in mesoscopic (100 micron to several millimeters) scales. This process integrates silicon processing, electroplating, hot pressing, casting, and traditional machining methods to provide opportunities for 3D layer fabrication and parallel production, and opportunity to build small dimension parts. The proposed approach overcomes material constraints in MEMS fabrication and current layered manufacturing processes. In this paper, various manufacturing strategies are discussed for generating engineering parts with mesoscopic dimensions. In particular, processes to build components of magnetic field based micro motors and 3D thin airfoils are described.

Introduction

Most of the current solid freeform fabrication techniques are restricted to a small range of materials. Shape Deposition Manufacturing (SDM) [1] and Mold Shape Deposition Manufacturing (Mold SDM) [2] are capable of building objects of various engineering materials, but with a lower limit part size of several millimeters. The development of Micro-Electro-Mechanical Systems (MEMS) has enabled designers to conceive applications for smaller scale parts. However, the processes involved in MEMS have material and geometric limitations.

Mesoscopic additive/subtractive material processing (Meso A/SMP) expands solid freeform fabrication into the mesoscopic scale, which is defined as 100 microns to several millimeters. Meso A/SMP integrates silicon processing, electroplating, hot pressing, casting, and traditional machining methods to provide opportunities for 3D layer fabrication and the possibility of parallel production for mesoscopic parts. It allows a wide range of engineering materials to be used in this range, so that the material constraints in MEMS fabrication and current layered manufacturing processes can be overcome.

In this paper, manufacturing strategies and fabrication techniques in Meso A/SMP are discussed. Also, its application to build components of a magnetic field based micro-motor and a small flying vehicle, "mesicopter," are illustrated.

Meso A/SMP Approach

For large-scale parts, additive/subtractive SFF techniques typically employ traditional machining methods and novel deposition methods for material addition and removal. In order to reach smaller dimensions, Very Large Scale Integration (VLSI)

techniques have been used. Meso A/SMP integrates the processes innovatively by combining processes from traditional and VLSI regimes, and can be treated as a 2-stage process— planning and fabrication. Planning involves three main issues: 1. material selection, 2. decision of shaping strategies, and 3. determination of supporting operations for shaping strategies. Integrated in this approach are considerations for CAD modeling and checking of manufacturability. Once the fabrication strategies are determined, parts will be built according to the processes selected. Processes involved in material addition are electroplating, hot pressing, gelcasting, polymer casting, and casting of powder filled polymers. Likewise, EDM, CNC machining, and plasma etching are employed in material subtraction.

Planning

In the planning stage, the part's function and material requirements are considered. Under these constraints, materials for building the parts are selected first. Once the part material is selected and its characteristics are assessed, shaping techniques are chosen. Analysis is then performed on the selected shaping strategy to determine if support operations are required and how to coordinate them accordingly. Before starting the fabrication, one should also complete manufacturability checks and any necessary post-processing of CAD modeling.

Five groups of materials are considered in the material selection phase of planning—ceramics, polymers, magnetic materials, electroplated materials, and other conductive materials. The shaping strategies for different materials are summarized in the following table.

Material	Example	Shaping Strategy
Ceramics	Silicon Nitride	Gelcasting
Polymer	Epoxy, Polyurethane	Casting
Magnetic materials	Amorphous metal, Nd-Fe-B	EDM, Casting of powder
Electroplated metals	Cu, Ni	Electroplating
Other conductive materials	Alloys	EDM

For ceramics and polymers, the shaping strategies mainly rely on gelcasting and polymer casting. The supporting operation for these two fabrication techniques is to build molds. Molds can be made of wax or silicon. The molds may be generated by CNC machining and plasma etching, respectively. Wax, compared to aluminum, is easier to machine in the mesoscopic scale, and easier to remove by melting out. Wax allows for less tool wear and less machining time when working with high spindle speeds which is required for miniature end mills. Commercial miniature end mills have a size limitation of 0.01 inch (0.254mm) in diameter. Features smaller than this will require modifying machining sequences or using silicon molds. Part of the manufacturability analysis would determine if smaller dimensions exist on the potential part and modify the fabrication strategy. Silicon molds can be obtained by stacking thin etched silicon wafers.

Hard magnetic and soft magnetic materials are hard to machine and deposit. Most micro machining techniques cannot directly shape magnetic materials, whereas most large-scale material subtraction techniques for these materials cannot be used easily for micro and mesoscopic scale. Moreover, their crystalline structure has a strong impact on their performance, and deposition techniques in micro fabrication, such as electroplating or physical vapor deposition (PVD), do not allow enough control over the resulting microstructure. Complicated heat treatment cycles are involved to develop good magnetic properties. Parts in the mesoscopic scale have high surface to volume ratios, making them difficult to be heat-treated. Therefore, shaping stock materials is a better option. Two possible shaping techniques are proposed here—EDM and casting of powder in polymer binders. The supporting operations are building electrodes for EDM and molds for casting, respectively. EDM electrodes are made either by electroplating copper or by hot pressing silver-tungsten into silicon cavities, while casting of powder in polymer binder uses silicon or wax as molds.

Materials that can be electroplated, such as copper and nickel, are widely used in micro fabrication. LIGA ("Lithographie, Galvanoformung Abformung") is a well-known process using deep X-ray lithography to create electroplating masks out of PMMA (plexiglass), and is capable of making high aspect ratio structures. However, the cost of LIGA setup is very high. In our approach, we chose plasma-etched silicon wafers as electroplating masks, which is a more economical technique. Photolithography and plasma etching are the necessary supporting operations. Stacking of wafers may be employed if the part geometry is complex and needs more than one layer to build up. Through electroplating, parts can be obtained which closely resemble parts fabricated with LIGA.

EDM technology can be applied to most conductive materials. In order to reach a satisfying surface finish, several experiments need to be conducted to find out the optimal operating conditions for the selected material. Electrodes needed for EDM can be made by the same methods as mentioned before, electroplating or hot pressing.

Once fabrication strategies and related supporting operations are decided, the examination of part features for manufacturability is important, especially in small scale. In addition, certain post-processing of CAD models is required. For example, machining code needs to be generated for CNC milling. Moreover, most of the strategies mentioned above need patterned silicon wafers for molding or pattern transfer. Therefore, it is necessary to determine how to slice the 3D CAD model and translate layer information into standard format for mask making. A software package that converts STL files to CIF format, a standard commonly used by semiconductor mask makers, was developed in the Rapid Prototyping Lab at Stanford. If the part is prismatic, the bottom surface will be exported as an STL file. If the part is non-prismatic, it has to be approximated by a stair-step profile and a patterned wafer has to be fabricated for every step. Once the slice heights are determined, the surfaces at different heights can be exported as STL files and then converted to CIF format. Since an individual part is usually much smaller than the

wafer size, several patterns can be put onto one photolithography mask, allowing parallel fabrication of parts.

Fabrication

The fabrication step implements the strategies decided in the planning stage to build the parts. Patterning silicon for molding or masking is a common supporting operation in the shaping strategies. Silicon wafers are coated with a layer of liquid photoresist and selectively exposed to UV light through photomasks. After the unexposed section of photoresist is chemically removed, the wafers are patterned by plasma etching. The resulting wafers have prismatic patterns etched into them or etched all the way through, depending on their application. Silicon molds and masks can be removed later by etching in boiling KOH solution.

Three major shaping techniques are described and discussed—casting, electroplating, and EDM.

Casting: *Molding -> Casting -> Mold Removal*

Consider building polymer thin 3D airfoils for a small flying vehicle, "the mesicopter," (Figure 1). The shaping strategy selected to build the part is casting. Molds can provide either complete geometry or only bottom geometry that will require further machining after casting. Silicon is a good mold material because it is hard, insensitive to most solvents and common acids, and has a high melting point. Several patterned wafers can be stacked to form a more complex mold. The individual wafer pieces can have different thickness, allowing variable height steps to approximate the desired geometry. Wax molds are currently used in Mold SDM [2]. For the dimension that miniature end mills can achieve, wax mold would still be a good option, since it provides the opportunity to build full 3D objects and to build functional prototypes with short lead-time.

Casting can be used for thermosetting polymers or ceramics and metals mixed with a gel. These materials can be cast into cavities and then solidified either through cooling or chemical reaction. For polymer thin airfoils, casting of thermosetting polymer, such as epoxy and polyurethane, was used. Polymers that cure at room temperature and require short curing time are preferred. For the ceramics blades, gelcasting was used. Gelcasting is a casting process in which a high ratio of ceramic or metal powders is mixed into the uncured slurry, polymers and solvent. Parts with these filled polymers would be sintered after mold removal. During the sintering process, the polymer binder burns out with little or no residue and the ceramic or metal powder particles bond together strongly. Gelcasting is well suited for ceramic or metal parts with very fine features. Figure 2 shows a thin 3D airfoil made by wax mold, epoxy casting, and CNC machining with miniature end mills. Figure 3 shows silicon nitride blades made by gelcasting into a silicon mold.

In addition to the two casting processes discussed above, casting of powder filled polymer may be used. It is similar to gelcasting but the polymer binder is used as structural material for the final part, and the part is not sintered after casting. For those magnetic materials that are hard to deposit and cannot tolerate high temperature processing, casting of powders filled with polymer is a technique that is able to process the material. Although the resulting structures are weaker magnets than the pure magnets, this method is highly parallelizable and thus much more suitable for mass production.

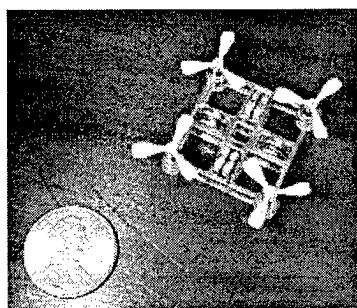


Figure 1 Prototype of 16mm x 16mm Mesicopter.

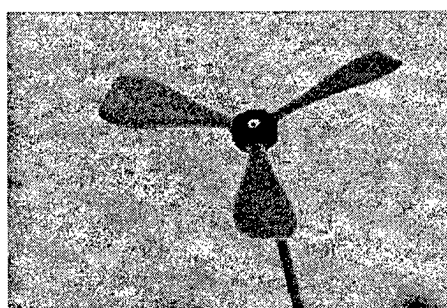


Figure 2 True 3D epoxy rotors for the mesicopter. The rotor (right) is 80 μm thin and 15 mm in diameter.

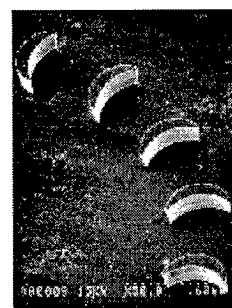


Figure 3 SEM of gelcasted Si_3N_4 blades (500 μm high and <150 μm thick).

Electroplating: Patterning silicon wafers-> masking-> electroplating-> silicon removal

Figure 4 shows a copper structure, which is used as one turn armature coil for a four-phase miniature stepper motor. Highly conductive bulk structures are required; therefore, copper is selected as the structural material and electroplating is the shaping strategy. Another example part that can be built by electroplating is a micro propeller with small uniform thickness.

Electroplating has been used for decades in metal finishing. In micro fabrication, electroplating is used to build up thicker layers than PVD can do at a faster deposition rate. In Meso A/SMP, electroplating is used to make bulk structures of pure metals, thin uniform thickness objects, and, moreover, EDM electrodes. A supporting operation for electroplating is the development of masks or molds.

Depending on the application, "non-through plating" and "through plating" are two different electroplating approaches. Non-through plating is to electroplate metal onto the silicon. Highly doped silicon with a copper seed layer on the surface is used in this process. On the other hand, through plating uses silicon as a mask, hence nonconductive silicon is preferred. In the latter case, the nonconductive silicon wafers can be further passivated by creating a silicon dioxide layer on their surface. After attaching the silicon mask to the substrate and covering the area that is not to be electroplated, the part is placed in the electroplating bath.

For copper electroplating a commercial acid copper-electroplating bath containing copper sulfate and sulfuric acid is used. For mesoscopic structures with high aspect ratio

cavities, a periodic-pulse-reverse (PPR) [4] current source is recommended. The PPR output waveform is a forward cathodic current interrupted by specific short anodic pulses to ensure dense and even electroplating through the deep cavities. The current density used is about 30 mA/cm^2 . Figure 4 and 5 show copper structures for the DC micro motor. High aspect ratio structures are achieved by this silicon-masking approach. Layers with different geometries can be electroplated one after another. Once the first layer of the cavities is filled, the second layer mask can be stacked on to the previous one by precision alignment system. Then the deposition process is repeated. Figure 6 shows the copper coils on a circular base, which was done by two layers of through plating. Objects with thin uniform thickness can be built through electroplating as well. True 3D geometry can be approximated by stacking sufficiently thin 2D layers. A copper micro-propeller approximated by two-layer silicon mold is shown in Figure 7.

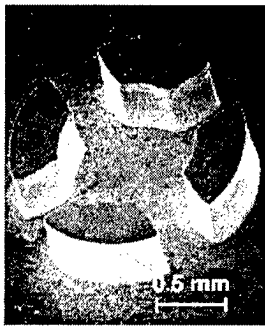


Figure 4 SEM image of electroplated Cu structure. It is $500 \mu\text{m}$ high and 1.6 mm in diameter.

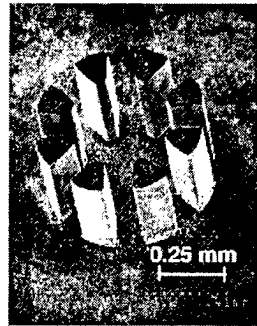


Figure 5 SEM image of electroplated Cu structure. It is $500 \mu\text{m}$ high and $800 \mu\text{m}$ in diameter.

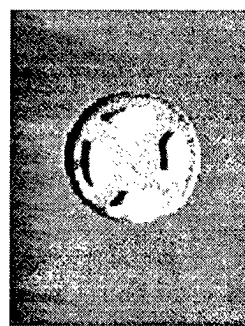


Figure 6 Electroplated Cu structure on a circular base. It is $500 \mu\text{m}$ high and 1.6 mm in diameter.

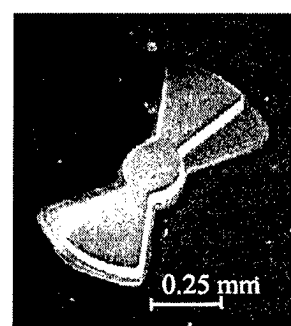


Figure 7 SEM image of electroplated Cu propeller. The structure is $200 \mu\text{m}$ high and 1 mm in diameter.

Electric-Discharge-Machining: Patterning Silicon wafers-> making electrodes-> EDM

Casting of powder filled polymers provided a way of mass producing soft and hard magnetic components. However, their magnetic properties were weak compared to pure stock materials. Most magnetic materials are electrically conductive and can therefore be shaped by EDM. Since EDM does not attempt to cut materials but, instead, removes materials with electrical discharge, it can be used to shape hard and brittle materials. EDM transfers patterns from the electrode to work piece by controlled spark erosion. Most popular materials for EDM electrodes are graphite and copper. However, graphite is mainly shaped by conventional machining techniques like milling or turning, and therefore is not a suitable electrode material for mesoscopic scale. Here we propose two ways to obtain EDM electrodes—electroplating and hot pressing of metal powder into the silicon mold. Electroplated copper electrodes can be obtained with the method described in the previous section. Figure 8 shows a copper electrode made by electroplating.

Besides copper, other high melting-point materials like graphite or tungsten are ideal for EDM electrodes. However, their processing temperatures are above the melting point of silicon that is used as molds. Therefore, the combination of tungsten with highly

thermal conductive materials, such as silver and copper, is used through hot pressing blended powders. Copper forms alloys with silicon at low temperatures and would destroy the mold during hot pressing. Silver, on the other hand, can be easily hot pressed into silicon, since its melting point is closer to the hot pressing temperature and it does not form alloys with silicon. All hot pressing experiments are done at 750°C and 30 MPa for one hour. This temperature and pressure setting was low enough to avoid plastic deformation of the silicon. The final AgW part has around 93% of the theoretical full density, and replicates the mold sufficiently well (Figure 9).

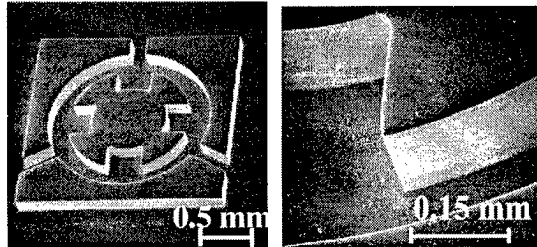


Figure 8 SEM images (full and detailed view) of electroplated Cu electrode.

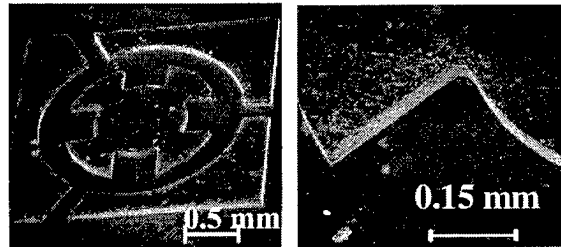


Figure 9 SEM images (full and detailed view) of hot pressed AgW electrode.

Once the EDM electrodes with fine features are fabricated, we can transfer the patterns to conductive work pieces through EDM process. The energy and shape of the individual electric discharge pulses control the resulting surface finish. The lower the energy of the pulses, the smoother the surface that can be achieved; yet this increases machining time and tool wear. From experiments, pulses with sufficiently low energy, 40 $\mu\text{J}/\text{spark}$, can produce a surface finish (2-5 μm) which is acceptable for our application. Finer surface finish can be achieved with special micro EDM machines. Figure 10 shows amorphous Fe-Co sheets shaped by EDM with electroplated and hot pressed electrodes.

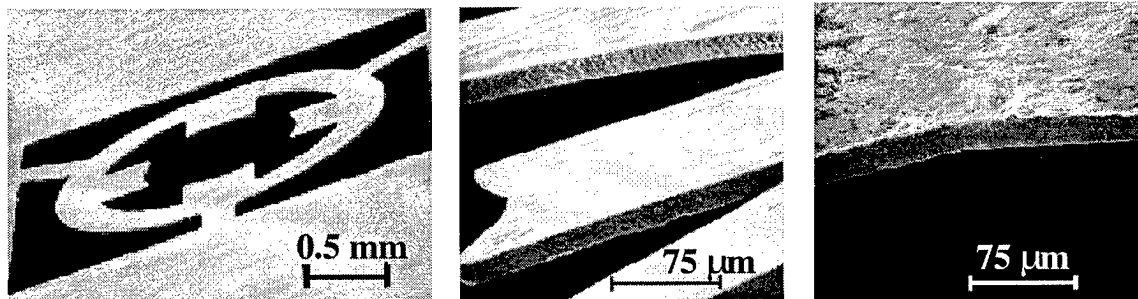


Figure 10 SEM images (full and detailed view) of amorphous metal sheet shaped by EDM with electroplated Cu electrode (left and middle) and with hot pressed AgW electrode (right).

Advantages of Meso A/SMP

1. Meso A/SMP suggests various fabrication strategies for different types of engineering materials, therefore overcomes material constraints in 3D layered fabrication and in micro fabrication.
2. Most of the process steps (silicon process, electroplating, hot pressing, and casting) are parallelizable, allowing mass production and group assembly of mesoscopic parts.

3. With the integration of VLSI techniques and conventional fabrication processes, parts can be built within 100 μm range and potentially even smaller.

Conclusion

A planning and fabrication approach for mesoscopic parts has been suggested which uses fabrication processes from VLSI and traditional machining. The planning stage includes material selection and coordinating fabrication techniques and support operations. The research presented here discusses five groups of engineering materials (ceramics, polymer, magnetic materials, electroplated metals, and other conductive materials) and their corresponding fabrication strategies. Casting, electroplating and EDM are the main shaping techniques. Meso A/SMP overcomes the material constraints in the current layered manufacturing processes and MEMS, and provides opportunities for mesoscopic 3D layer fabrication and parallel production. The ability to produce mesoscopic parts in a variety of engineering materials has now been attained.

Acknowledgements

The authors would like to acknowledge support from the National Science Foundation and National Aeronautics and Space Administration. The authors would also like to acknowledge Ali Farvid from Stanford Linear Accelerator Center for his advice and help with the electroplating process and setup.

References

- [1] R. Merz, F.B. Prinz, K. Ramaswami, M. Terk, L. Weiss, "Shape Deposition Manufacturing", Proceedings of the Solid Freeform Fabrication Symposium, University of Texas at Austin, August 8-10, 1994, pp. 1-8.
- [2] J. W. Kietzman, A. G. Cooper, L. E. Weiss, L. Schultz, J. L. Lombardi, and F. B. Prinz, "Layered Manufacturing Material Issues for SDM of Polymers and Ceramics", Proceedings of the Solid Freeform Fabrication Symposium, The University of Texas at Austin, Austin, Texas, August 1997, pp. 133-140.
- [3] G. Milad, "Periodic Pulse Reverse—The new wave in acid copper plating", Printed Circuit Fabrication, Vol. 20, No.7, July 1997, pp.36-38.

THE SAND-PAINTER: Two-dimensional powder deposition

Joseph Pegna
Stéphane Pattofatto, Raphael Bergé,
Carol Bangalan, Henry Herring,
Mathias LeSaux, Jason Engler

Department of Mechanical Engineering, Concordia University
Montréal, Québec H3G1M8, Canada
Tel: (514) 848-4193 — Fax: (514) 848-3175
email: pegnaj@alcor.concordia.ca

Abstract: *The Sand-Painter project addresses the problem of pointwise deposition of multi-material powders in layered manufacturing. This approach is key to the development of selective aggregation processes capable of producing functional prototypes with internal sub-structures not achievable by any of the extant layered manufacturing processes. The solution adopted for this project is an automated version of the ancient Native American art of sand painting. Preliminary results pertaining to powder flow and deposition characterization are presented. A proof of concept multi-material deposition process was demonstrated.*

Keywords: *Sand painting, layered manufacturing, SLS, 3D-Printing, selective aggregation, multi-material, multi-modal structures, functionally graded materials., mechatronics.*

1 PRE-HISTORY OF THE SAND-PAINTER PROJECT

The Sand-Painter Project is the extension of a long-term, low-budget undergraduate research supervised by the lead author between 1993 and 1997 [Pegna, 1995a],[Pegna, 1995b],[Pegna, 1997]. The main objective of this project was a low-cost investigation and evaluation of the avenues left unexplored in the Solid Freeform Fabrication community, especially as they pertain to the fabrication of large, multi-material, functional prototypes from bulk material.

For more details on the rationale and methodology of the preliminary research, the reader is referred to the 1995 Solid Freeform Fabrication Proceedings [Pegna, 1995a]. The main outcome of this and other [Rock and Gilman, 1995] works was a proof of concept that patterned deposition of powder layers can be used as the basis for free-form fabrication. Two other important predictions came out of [Pegna, 1995a]. First it showed that the proposed approach lends itself to the fabrication of multi-material structures by either processing multiple powders in a single layer, or by inclusion of prefabricated sub-structures. Second, the volumetric flowrates experimentally feasible were compatible with the fabrication of large functional structures, and made the technology a viable alternative for construction automation.

An incidental result came from the low-cost constraint which led to the choice of cement and sand as the building materials. The processing of each patterned layer with water vapor resulted in a concrete with unusual and anisotropic material properties [Pegna, 1997]. Though these results would need to be confirmed by repeating the experiment, they illustrate the potential of multi-powder processes in the creation of hitherto undiscovered material properties.

Regardless of researcher and project however, one main obstacle remained after 1997. Powder deposition had been primarily effected by ad-hoc combination of masks, manual hoppers, or both. A pointwise, low-volumetric flow powder deposition system was still needed to automate the proposed free-form fabrication process. This has now become the primary objective of the Sand-Painter Project.

The Sand-Painter Project is therefore geared toward the investigation of powder handling, flow, and deposition characterization. The main challenge of this project lies in the geometric characteristics and flow ranges needed for free-form fabrication, which are outside the commonly studied types of particulate flows. The benefits of this research however go well beyond the proposed free-form fabrication processes of [Pegna, 1995a], and [Rock and Gilman, 1995]. Indeed, all current powder-based free-form fabrication processes rely on a powder blanket deposition. The availability of multi-powder patterned deposition is a generic increment to existing powder-based layered manufacturing technologies.

Organization of the manuscript: The main objective of this paper is to report on the experimental design of a two-dimensional powder deposition apparatus. Whenever existing results support it, a characterization of the flow and deposition will be presented. To this end this paper is organized in four main parts. Section 2 will review the prior art in powder deposition, and in powder flow control. Section 3 introduces the vibratory L-Valve concept, which is the keystone of the proposed process. Section 4 focuses on experimental characterization of the powder flow. Section 5 presents preliminary results in characterization of the deposit geometry, as well as a proof of concept of multi-material deposition.

2 PRIOR ART

2.1 Powder Deposition.

Seldom has the expression "prior art" taken as literal a meaning as it will in this section. A review of prior powder deposition techniques to form prescribed 2-dimensional patterns turned almost exclusively to the graphic arts. Of all these the only bone fide automated technique for 2D pattern deposition is the well-known and well documented electrostatic drum used in laser printers. All other approaches to depositing patterns consisting of different powders turn out to be ancient art forms. The first and most common form is enamel work, originating it seems with the Mycenaean (Cyprus) between the 13th and 11th century BC. A similar art form consisting of depositing loose powder patterns has been practiced as part of religious rituals by Navajo Indians and Tibetan monks for at least 1000 years. Among the Navajo Indians, it is known as "Sand-Painting", while the Tibetan word for it is "Mandala". While none of the above graphic art forms would qualify as modern manufacturing technique, they are definitely part of our world heritage of manufacturing science. As such, they are worth investigating in the context of freeform fabrication and we shall now review them in details.

Electrostatic drum: The electrostatic drum used in laser printers allows for accurate (about a 1/1000th inch or 25 μ m at best) location of a small quantity of non-conductive powders (spot diameter 25-100 μ m x by up to 10 μ m high). However, given the material restrictions, low volumetric build rate, and cost, this approach to powder deposition was not pursued further.

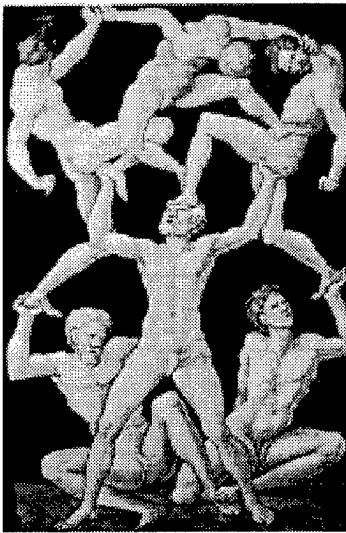


FIGURE 1. Details of "Les Acrobats," Enamel work in Grisaille from Limoges, France c. 1550 (Walters Art Gallery, Baltimore, 43.5cm x 30.5cm)

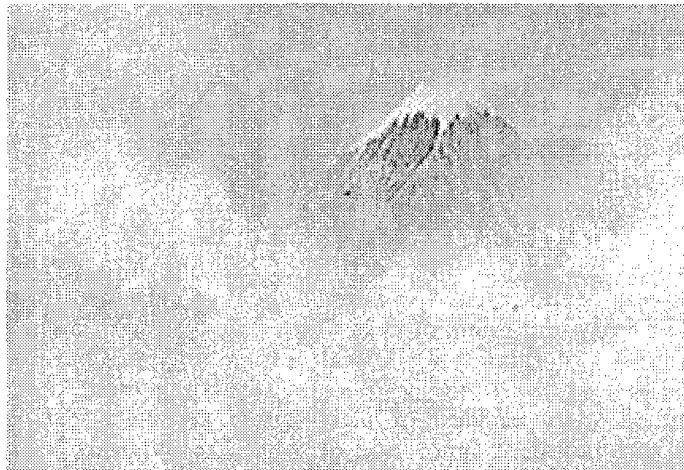


FIGURE 2. Details "Mount Fuji seen through clouds." Lineless cloisonné by Namakawa Sosuke, 1893. Tokyo National Museum (63cmx113.6cm).

Enamel work: Enamel work is a graphic art form whereby colored glass powders are deposited into patterns drawn on a metal plate. The deposit is subsequently fired to fuse the glass; thus preserving the design upon cooling and solidification. This art form appears to have been initiated by the Mycenaean between the 13th and 11th century BC, perfected by the Celts between the 3rd and 2nd century BC, and reached its pinnacle during the European Renaissance, even rivaling oil paint in details. A sample of European art is shown in Figure 1. Enamel work appears to have migrated out of Europe and into East Asia, where it also evolved into an elaborate art form illustrated by Figure 2

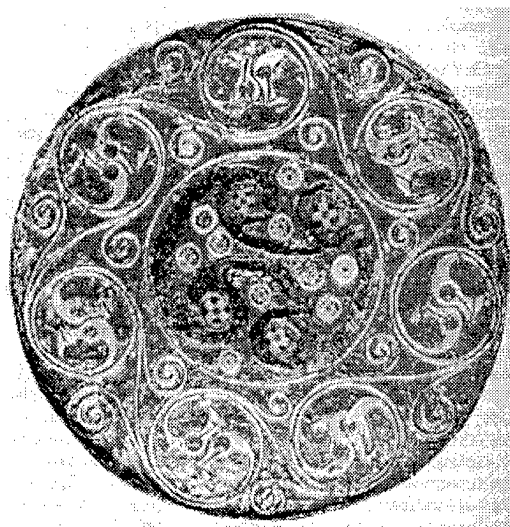


FIGURE 3. Anglo-Saxon champlevé enamel circa 650. British Museum 6cm.

For the most part, the patterning of powder deposits is done by blanket deposition over areas delimited by masks, retaining walls or groves. The "cloisonné" process uses thin metal strips that are bent to form the outline for the decorative pattern, and then attached to the base metal plate where they form miniatures cofferdam-like cells. Each cell is then filled with powders. The "champlevé" process is the opposite. Instead of walls being added, groves are gauged into the metal base, and then filled with colored glass powders. The cloisonné and champlevé processes allow multiple powders to be deposited in adjacent cells, but without mixing. Hence only discontinuous coloring is obtained as illustrated in Figure 3.

A few alternative processes allow gradation of color —i.e. of powders— and are used either alone or in addition to cloisonné or champlevé; most notably, the “*Painted Enamel*” and “*Grisaille Enamel*”. In the painted enamel process the various color enamels are applied in wet powdered state by masking or brushing without metal strip or ridges separating them. Each layer is allowed to dry before the next is applied to avoid blurring of the boundary. Grisaille enamel provides a wide range of contrast by depositing white enamel over colored enamel, which is then selectively removed or hashed before firing. In that respect, Grisaille enamel does not affect the resulting color by changing materials, but rather by varying the mixing ratio of two colors.

For the most part, powder deposition in enamel work is effected though blanket deposition into 2-D molds, be they masks, ridges or groves and do not differ fundamentally from the work intensive method used by [Pegna, 1995a].

Sand Painting: Another form of ancient graphic art offers insights into powder deposition. Although the history of sand-painting is far less well documented than that of enamel works, it appears to have developed independently in different parts of the world for a at least a thousand years. The approach taken for this alternative art form is to deposit dry powders pointwise by using hoppers, sometimes rearranging it with small brushes. Curiously similar in their techniques and religious natures, sand paintings by Navajo Native Americans of New Mexico, and Mandalas done by Tibetan monks are left as loose powders for the elements to partake. With the advent of tourism, Navajo sand-painting can now be found in a more resilient version, with glue sprayed over it to preserve the design. Figure 4 illustrates the level of detail and complexity achieved with Navajo sand-painting.

The size and complexity exhibited by Tibetan Mandalas clearly illustrates the potential of pointwise powder deposition in creating two dimensional patterns. Figure 5 shows the result of three Seraje monks work over four weeks in creating a Mandala. The automation and mechanization of this art form is in essence our project goal.

2.2 Powder transport and flow control

In pursuit of our goal of automated Sand-Painting, one of the critical issues to be addressed is that of bulk material transport to its eventual destination in the deposit. This is a new problem in the freeform fabrication arena, which has only seen blanket deposition and compaction by counter-



FIGURE 4. Sample Navajo sand painting (From the author's collection).

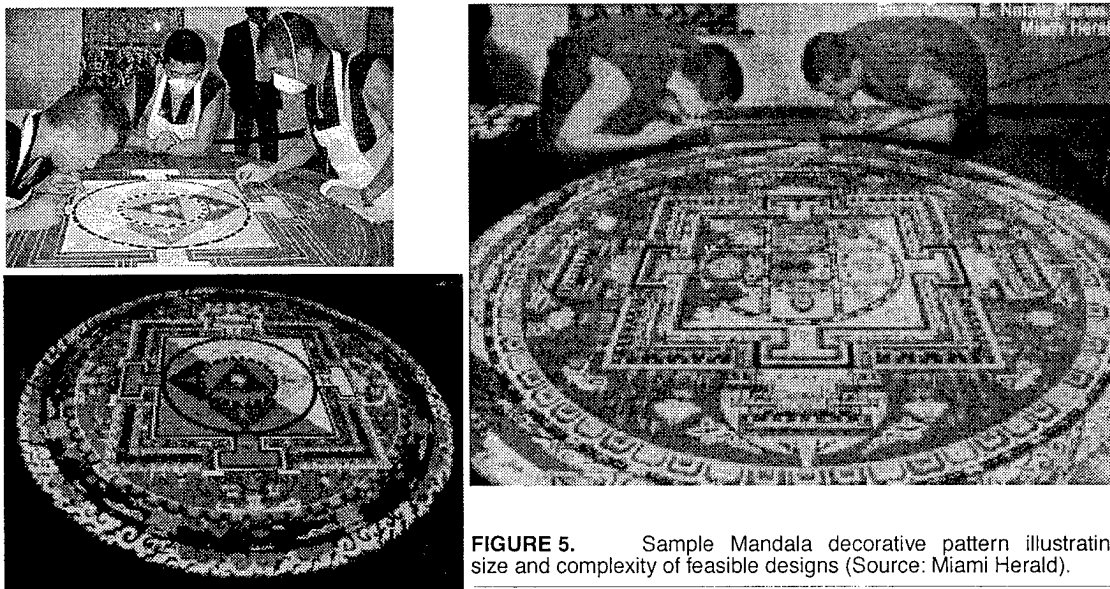


FIGURE 5. Sample Mandala decorative pattern illustrating size and complexity of feasible designs (Source: Miami Herald).

rotating roller mechanisms (see [Deckard and Beaman, 1987], or [Sachs et al., 1990] for example.) The state of the art in granular material flow can contribute to our research both from the point of view of understanding the flow mechanisms, and from the point of view of flow control, or valving. The former really belongs to a branch of mechanics which is best addressed by a specialized reference such as [Brown and Richards, 1982], [Mason and Woodcock, 1987], or [Hans, 1990]. The latter question of valving and flow control is of more immediate concern and will be addressed now.

Valving of granular material flow: The deposition mechanism sought for our free-form deposition process is well outside of the mainstream applications in bulk material transports. While the electrostatic drum provides a resolution that equals or surpass freeform fabrication processes, the build rate (about $10\mu\text{m}$ per pass) is so minute is so minute that the process may only apply to micrometric devices. Alternate flow control processes that can support on/off or flow modulation are intended for large flowrates (0.1 to 10^3 liter/s) or fluidized powder flows in which the particulates represent only a small fraction (usually $<10\%$) of the volume. A particularly interesting alternative for our purpose is the L-Valve shown in Figure 6.

A typical L-Valve consists of a downcomer section and a characteristic elbow giving the valve its name. At the junction of the down-

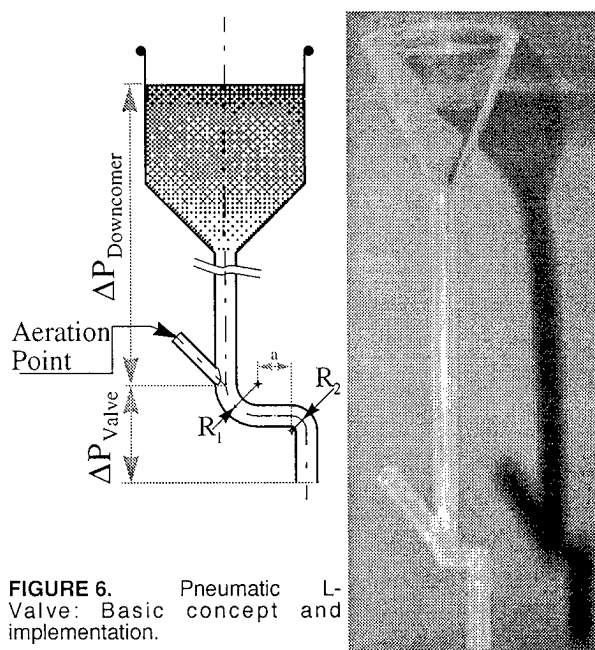


FIGURE 6. Pneumatic L-Valve: Basic concept and implementation.

corner and elbow is inserted an aeration point through which a jet of pressurized fluid can be injected. This injection fluidizes the powder bed, allowing it to flow down the L-Valve. When the fluid injection stops, the powders re-compact and the flow stops. This type of valve allows on/off as well as modulated flow control over a wide range of flowrates and materials. Yet the typical use for L-Valves involves flowrates at least one order of magnitude larger than that of concern to our design.

Experimentations were conducted with vented glass L-valves with diameters 1, 2, and 3 mm downcomers such as illustrated in Figure 6. The powders used were 33 μ m and 200 μ m spherical glass beads, uncalibrated silicon carbide, cement and sand powders. The source of pressurized air was a fish tank air pump with an adjustable restriction for pressure regulation. The results however were far from satisfactory. While on/off control was somewhat achievable. Even at pressures as low as 1cm H₂O above ambient, the fluid flow was dominant. Both flow and deposition of the powders was highly irregular and of no practical use for the range of flowrates.

The main conclusion from this section is that none of the existing powder flow control technologies could address our required volumetric flowrates and deposition requirements. Our main challenge therefore would be the invention of flow control and deposition processes that can serve our fabrication requirements.

3 VIBRATORY L-VALVE

In search of a satisfactory design to achieve powder handling and deposition within ranges needed for free form layer deposition, no solution were found in extant technologies; be it from coal, mineral, mining, food, cosmetic, or pharmaceutical industry. Yet the most ancient arts of sand painting, mandala, and enamel achieve feats of feature definition in powder deposits that rival oil paint in color definition and geometric complexity. The flowrates involved in sand-painting range from the mm³/s to tens of cm³/s. Feature definition ranges from the mm² (Figure 4) to a few m² (Figure 5.) How can such a performance be achieved with mostly rudimentary hand-tools?

Besides brushes and needles —mostly used to rearrange the deposit— the main instrument used for powder deposition is a small hand held hopper. It would seem therefore that vibratory fluidization is the most time tested technique for transport and deposition of powdered solids. This remark, and the L-Valve design naturally leads to the concept of vibratory actuated L-Valve, which is developed below.

3.1 Design

The L-Valve design was implemented in various experimental versions intended to characterize both flow and deposition. Figure 7 shows some sample glass designs. An experimental design methodology was followed in this



FIGURE 7. Sample experimental vibratory L-Valve designs.

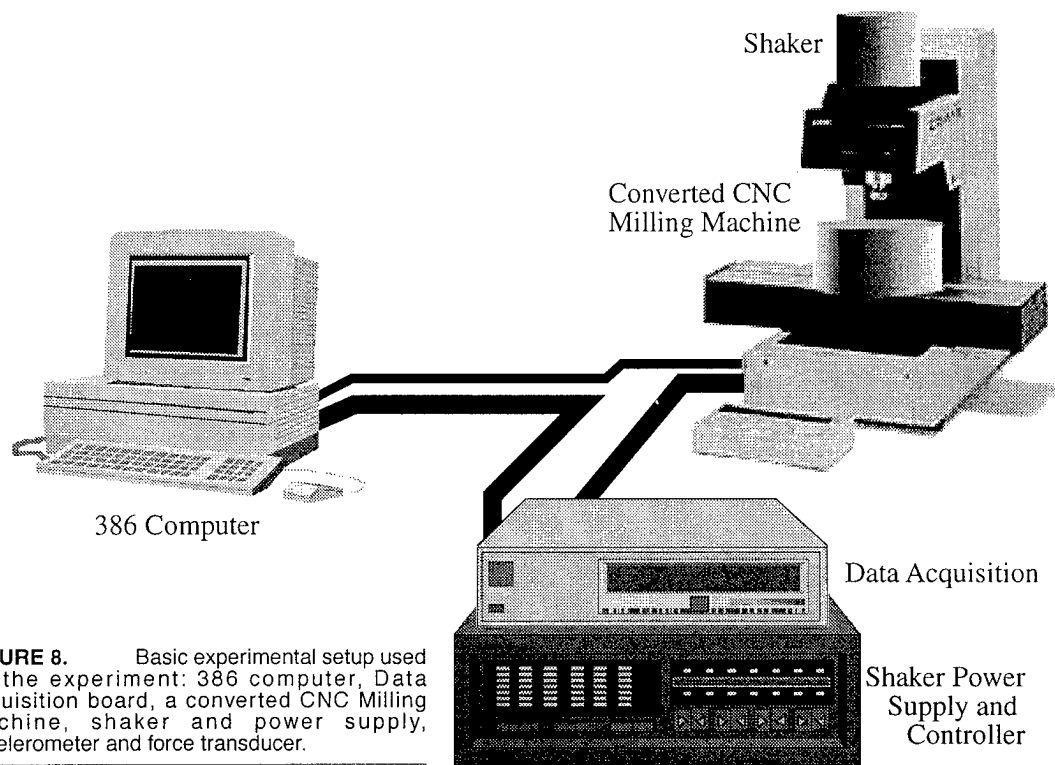


FIGURE 8. Basic experimental setup used for the experiment: 386 computer, Data acquisition board, a converted CNC Milling machine, shaker and power supply, accelerometer and force transducer.

study. Despite the use of a rational methodology, the number of data points needed is still such that we can only present preliminary results in this paper. Those results, as we shall see, are promising enough to warrant continuation of this study.

3.2 Experimental

The basic experimental set up is shown in Figure 8. The centerpiece is an old CNC CAMM3 milling machine in which the vertical spindle has been removed and replaced by a shaker. Control of the milling machine is effected by a 386 computer using G-Code. The computer also communicates with the shaker controller via an RS232 interface. In the initial implementation, real-time flow measurements were performed by means of a load cell accelerometer mounted in series with the hopper. The signal to noise ratio was such however that the only average results were of any use. A further verification of flow rate was done simply by timing the deposition of a known mass of powders. Powder flow visualization was done using a stroboscopic flash synchronized to the shaker; an example of which is shown in Figure 9.

Note that an indirect implication of this experimental setup is the possibility of using a regular CNC machine tool as the support for layered manufacturing. Indeed, the proposed approach offers the prospect of an inexpensive tool

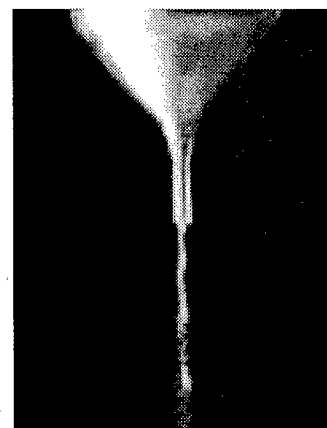


FIGURE 9. In-phase stroboscopic view of the powder flow through a straight downcomer.

kit alternative to dedicated rapid prototyping machines, assuming of course that the shop is already equipped with an available CNC vertical milling machine or lathe.

4 EXPERIMENTAL FLOW CHARACTERIZATION

When used in conjunction with powders, vibrations are mostly intended for compaction of a bed. In our instance, vibrations are called upon for fluidization. Preliminary experiments had shown that at certain combinations of powders and hopper mass, vibrations could be used as a mean of modulation or on/off control.

Table 1 below outlines the key parameters which determine the outcome of the powder flow through the downcomer, and which must be controlled.

TABLE 1. Process parameters affecting powder flow through the downcomer.			
FLOW CONTROL PROCESS PARAMETERS			
POWDERS			
Size	Geometry	Material/Density	Hygrometry
HOPPER			
Mass	Downcomer Geometry	Dimensions.	
VIBRATIONS			
Amplitude	Frequency	Waveform	

We begin by conducting a series of experiments, designed to expose the relationship between the flow rate and the process parameters. This experimentation is necessary as little data exists in the literature which can be used to formulate a complete deposition model. In future developments, a theoretical study of powder flow must be carried out to compare with our experimental results. The ultimate goal, of course, is that the analytical model be simplified and perfected through this comparison, so that, wherever possible, real-time numerical prediction of process parameters can be achieved. However, as all imaginable design cases cannot be predicted analytically, it is not realistic to obtain a complete model solely from theory. In the short term however, our goal is to obtain a set of design rules (in tabular/look-up form) to allow rapid computer control of the process. We seek to employ empirical solutions where results cannot be obtained analyti-

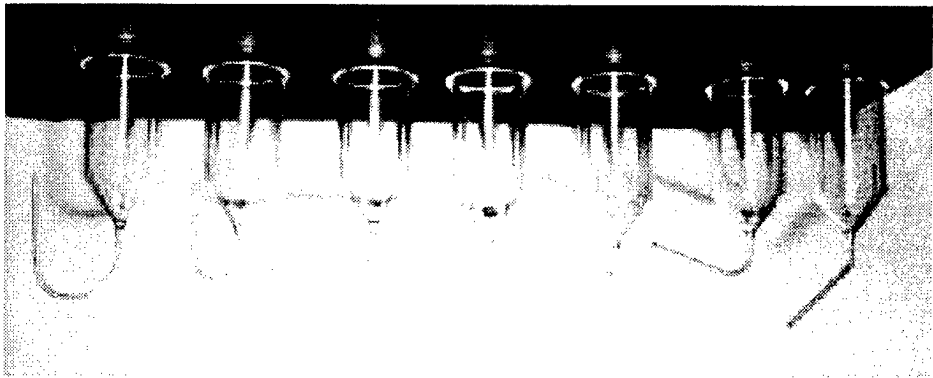


FIGURE 10. Sample hoppers developed for powder flow analysis.

cally. As dedicated sensing becomes available —e.g. real-time mass flow measurements— the model will be refined and adaptive control of the process can be investigated.

In order to perform a complete analysis of the powder flow however, a series of glass hoppers were fabricated with various 45° cone angle, various elbow radii and elbow angles, all using a $\phi 1\text{mm}$ downcomer. A few sample hoppers are shown in Figure 10. The amount of data collection required for such experiments is so large however, that only straight downcomer results are presented here.

Various types of powders were subjected to the experiment:

- $\phi 22\mu\text{m}$ and $\phi 250\mu\text{m}$ spherical glass beads.
- Uncalibrated Silicon Carbide powders.
- Uncalibrated sand.
- Uncalibrated cement powder.

For the most part free gravity flow was observed with

$\phi 22\mu\text{m}$ spherical glass bead, as should be expected from the mechanics of granular material flow [Hans, 1990]. As the particle diameter increases to about one quarter of the diameter opening, the

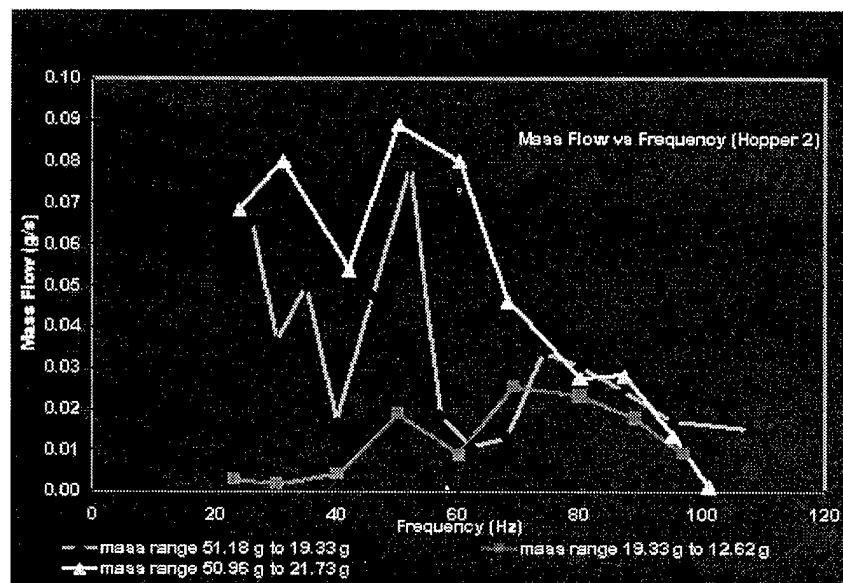


FIGURE 11. Sample mass flow rates vs. frequency plots for series of runs through variable hopper masses.

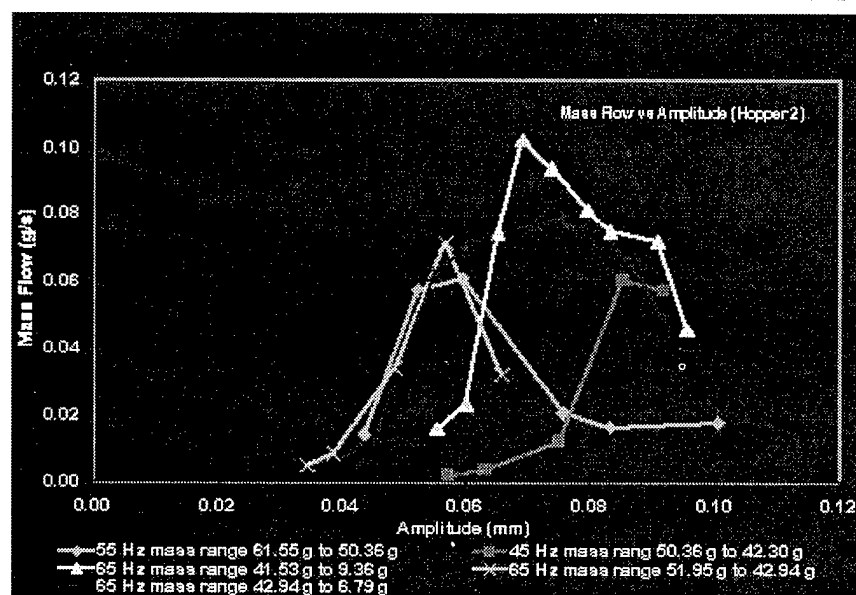


FIGURE 12. Sample mass flow rates vs. amplitude plots for series of runs through variable hopper masses.

mechanics enters a domain outside classical powder flow analysis. Yet it is in this domain that the best flow control were observed, as shown by the diagrams in figures 11-15.

Hygrometry, while not measured, was critical to the flow of cement powder. Indeed, results with cement powders were best reproduced by first baking the powders.

One of the most challenging tasks in operating the experiment described herein is the real-time mass flowrate measurement. Typical mass flows are of the order of hundreds to tenth of gram per second while typical hopper masses vary from 50 to 150 grams.

An accelerometer and force transducer mounted in series with the hopper offer only a tentative solution to this problem, as the significant fraction of the force transducer RMS signal is of the order of 10^{-7} to 10^{-6} for the typical flow-rates, masses, frequencies, and amplitude state above. Hence measurements reported in this study are only limited to average measurements confirmed by timing the flow of a known amount of powder. This renders the characterization of

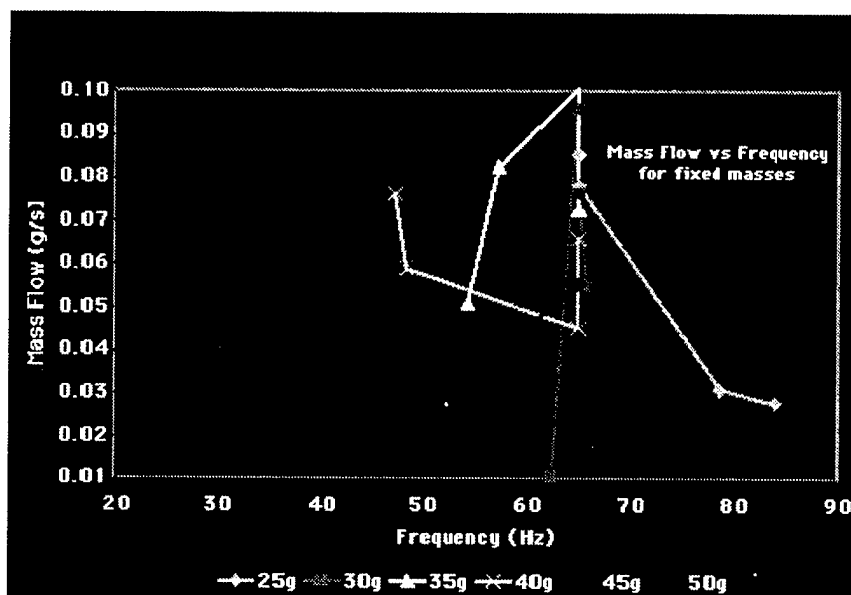


FIGURE 13. Mass flow vs. frequency characteristics interpolated for fixed hopper masses (but varying amplitudes).

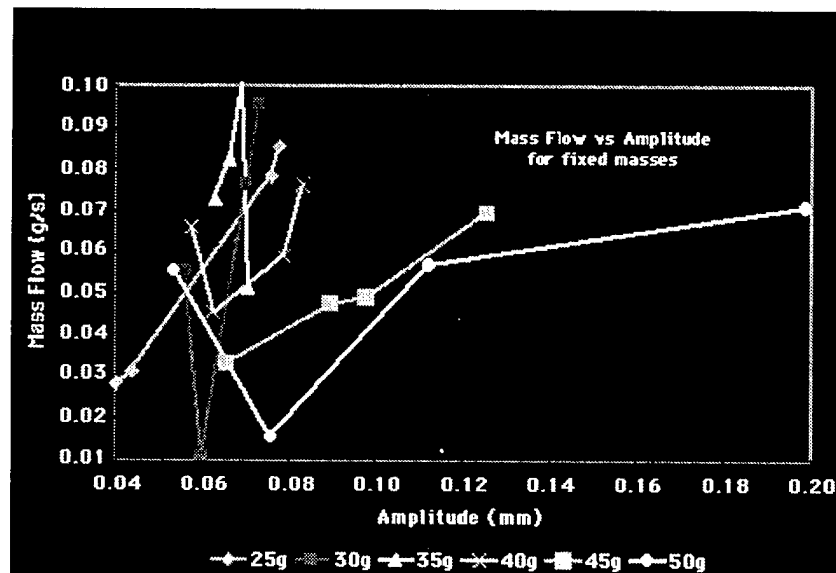


FIGURE 14. Mass flow vs. amplitude characteristics interpolated for fixed hopper masses (but varying frequency).

powder flow through the downcomer particularly difficult since we cannot isolate instances of flowrates for a set hopper mass. The measurements exposed herein can only be regarded as preliminary data, and further improvements to mass flow measurements will have to occur in order to pursue a rational experimental approach to the design.

Given the absence of a direct sampling method for flow rate measurement, exposing the relationship between powder flow and process parameters ends up being a laborious process illustrated by Figure 15. Each data point in figures 11 and 12 is obtained by timing a deposit and then weighing it. Since the flowrate is not known ahead of time and the hopper mass is varying, one can only measure flow

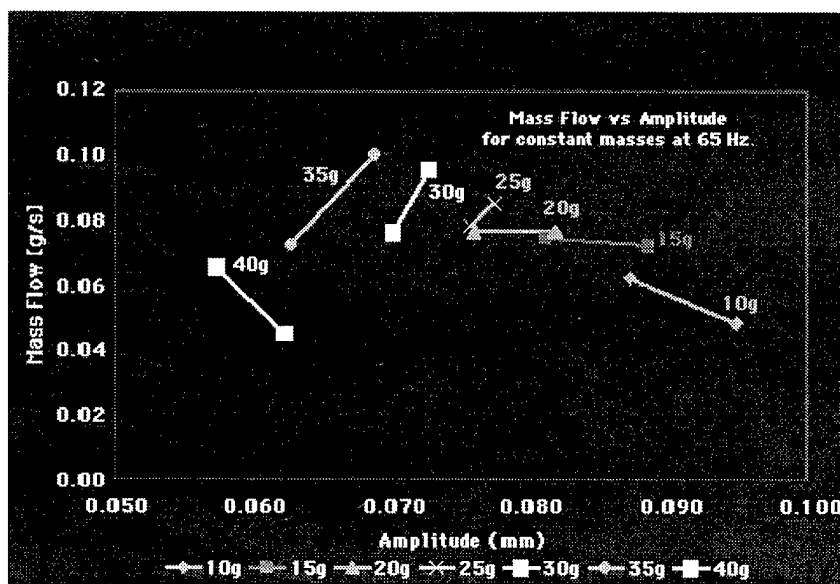


FIGURE 15. Composite of the mass flowrate vs. amplitude derived from Figures 11-14 for fixed hopper masses of 10, 15, 20, 25, 30, 35, and 40 grams, and fixed frequency of 65 Hertz.

rate at the expense of not knowing the mass precisely; an uncertainty principle of sort!

On the basis of measurements in Figures 11 and 12, one can interpolate for fixed masses and plot flow rate vs. frequency in Figure 13, in which case the amplitude cannot be constant, or flow rate versus amplitude in Figure 14, in which the frequency cannot be constant. Only by interpolation of all the above data can we derive a crude 2 point measurement each for fixed mass at a set frequency. The summarized results are shown in Figure 15, which plots flowrate vs. amplitudes for set masses of 10 to 40 grams in 5 grams increments for a fixed frequency of 65 Hertz.

As limited as they may be, the results obtained to date demonstrate that the two main goals of our flow control are achievable:

- On/off control of the flow is achievable by either starting or stopping the vibrations, or by vibrating at a frequency or amplitude regime where no flow happens.
- Flow modulation can be achieved by either frequency or amplitude modulation.

Having determined that flowrate can be controlled, a truth that Navajo Natives and Tibetan monks discovered eons ago, we can now turn our attention to the object of this study: namely the deposit itself.

5 EXPERIMENTAL DEPOSITION CHARACTERIZATION

Before one even embarks on a characterization of the deposit, one must develop an understanding of the powder's transition from the downcomer to the substrate. Such an understanding also leads to a correct identification of relevant process parameters.

Experimental powder flow visualization is notoriously difficult. Given the periodic nature of the excitation though, it was legitimate to observe the flow and flight characteristics under a stroboscope. Such observation already provides a valuable insight into the deposition process. In Figure 9 for example, one can observe the flow through a straight downcomer using a stroboscope in phase with the vibrations of the hopper. The flow can be observed primarily as a series of "powder droplets" being stretched by gravity. While the flow is observed to disperse as it falls, it remains well focused and almost as narrow as the nozzle opening within a centimeter of the orifice.

The flow from a downcomer at 45° illustrated on Figure 16 is representative of the types of hopper used by Navajo Native American and Tibetans for sand painting. This picture was taken using a stroboscope at twice the hopper frequency. It reveals that even though the flow has a horizontal velocity component, it exhibits a quasi-periodic nature. In particular the width of the flow is not uniform and reaches its minima at the nodes. Mark that the first node is indeed well focused and exhibits a diameter close to that of the orifice. This observation may help explain the level of fine details achieved by manual hopper deposition in sand-painting.



FIGURE 16. In-phase stroboscopic view of the powder flow through a downcomer at 45°.

In order to study the geometric characteristics of the deposit, various automated scanning pattern depositions were used, as illustrated in Figures 17 and 18. Such patterns—rectilinear or circular—allowed direct measurement of the deposit width.

Beside downcomer diameter, slope and height, another factor involved in the shape of the deposit is the roughness of the substrate. To simulate a substrate roughness and establish this relationship, a variety of calibrated grit sandpaper were used as deposition substrates.

It is understood at this stage that a sandpaper substrate represents a worst case condition as compared to a loose powder bed with greater energy absorption capacity. For the purpose of this paper, the results presented in Figure 19 only relate to 120 grit sandpaper.

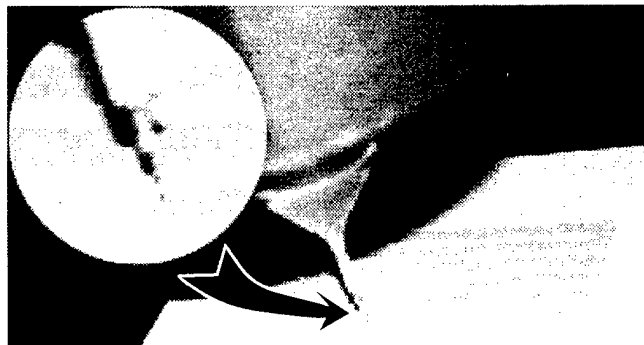


FIGURE 17. Sample scanning pattern used to measure deposit width (Type I Portland Cement on paper). The strobe flash was synchronized with the up swing of the hopper. The enlargement on the left shows a distinctive "droplet" pattern.

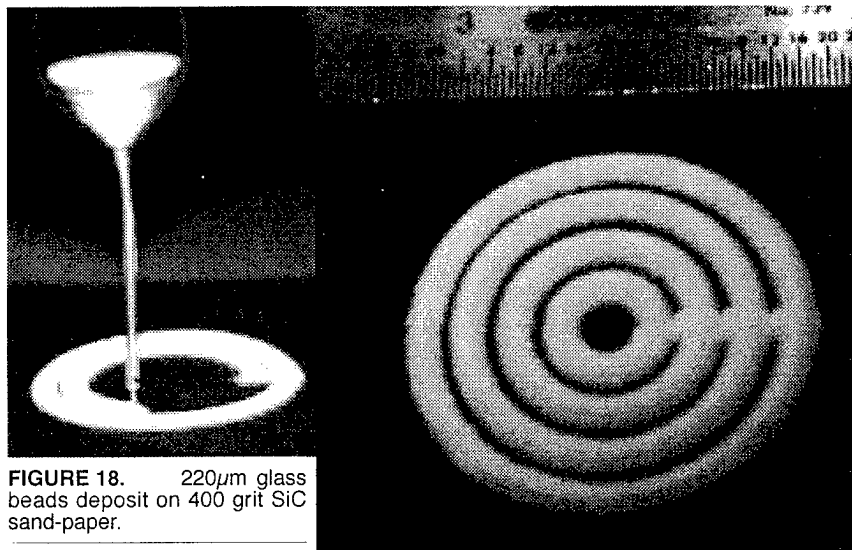


FIGURE 18. 220 μ m glass beads deposit on 400 grit SiC sand-paper.

Finally, one comes to what appears to be the most influential process parameters influencing the deposit geometry: Frequency and amplitude.

At first sight, it may appear reasonable to assume that a droplet of powder separates from the bulk during the downswing motion of the hopper, approximately syn-

chronized with the reversal of acceleration. Hence the kinetic energy of the droplet would simply be proportional to its mass, the square of the amplitude, and the square of the frequency. This view is consistent with the results shown in Figure 19, parts A, C, and D. From the bottom up in part A, and top down in part C and D, the quality of the deposit at 52Hz (respectively 30Hz and 60Hz) decreases when the amplitude of the vibrations increases. Up to the point (respectively fourth, sixth, and eighth line from the top) where the area directly under the nozzle is devoid of any powder and the deposit is scattered around the line.

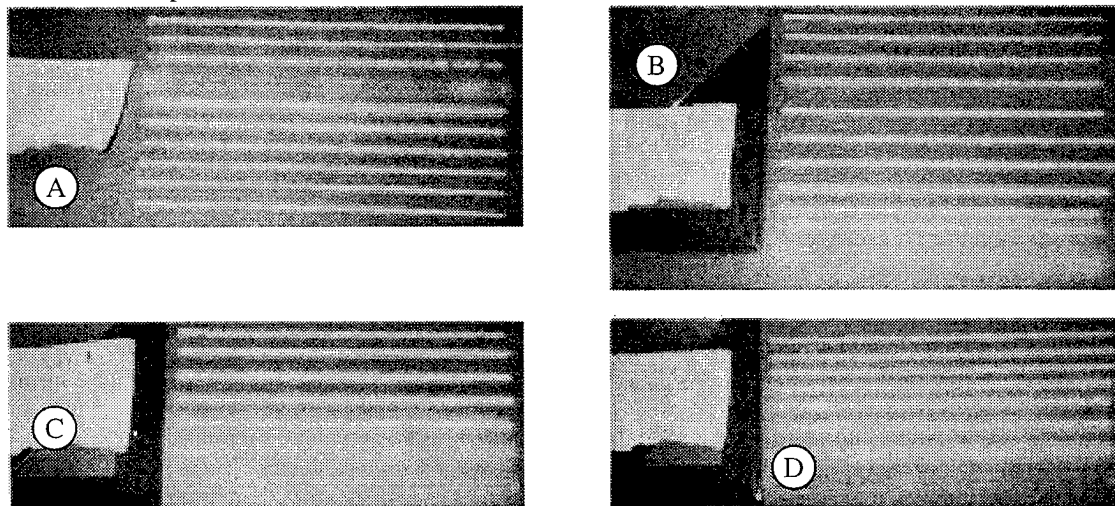


FIGURE 19. Sample deposition lines of $\phi 220\mu$ m spherical glass beads on 120 grit sandpaper. Listed below are frequency and amplitudes, from top to bottom. Average position of the nozzle opening is 2-3mm above the substrate.

- Figure **(A)**: (30Hz, 31 μ m), (41Hz, 43 μ m), (41Hz, 48 μ m), (52Hz, 42 μ m), (52Hz, 38 μ m), (52Hz, 35 μ m), (52Hz, 31 μ m), (52Hz, 29 μ m).
- Figure **(B)**: (80Hz, 18 μ m), (80Hz, 18 μ m), (80Hz, 19 μ m), (80Hz, 23 μ m), (80Hz, 4 μ m), (80Hz, 4 μ m), (80Hz, 5 μ m), (80Hz, 6 μ m), (80Hz, 5 μ m), (80Hz, 6 μ m), (80Hz, 7 μ m).
- Figure **(C)**: (30Hz, 62 μ m), (30Hz, 105 μ m), (30Hz, 71 μ m), (30Hz, 76 μ m), (30Hz, 84 μ m), (30Hz, 96 μ m), (30Hz, 107 μ m).
- Figure **(D)**: (60Hz, 27 μ m), (60Hz, 32 μ m), (60Hz, 33 μ m), (60Hz, 36 μ m), (60Hz, 38 μ m), (60Hz, 42 μ m), (60Hz, 47 μ m).

Part B of Figure 19 however, appear to contradict this simple view of the deposition mechanics. Indeed at 80Hz, the quality of the deposit deteriorates rapidly between 4 and 7 μ m amplitude, to be restored between 18 and 23 μ m. At this time, we do not have any analytic interpretation for the cause of this singular behavior.

Despite the lack of an analytical model of the deposition process, the experiments described herein did identify the process parameters influencing the deposit geometry. They are listed below in Table 2.

TABLE 2. Process parameters affecting the deposit geometry.

FLOW CONTROL PROCESS PARAMETERS			
POWDERS			
Size	Geometry	Material/Density	Hygrometry
DOWNCOMER			
Size of opening		Angle of opening	
VIBRATIONS			
Amplitude	Frequency		Waveform
SUBSTRATE			
Material	Energy Absorption		Roughness

Multiple Powder Deposition. We conclude this section with a brief note on the process of greatest interest to layered manufacturing. The pattern deposited in Figure 20 points to the feasibility of multi-material deposition. This layer was generated by the juxtaposition of type I Portland cement and $\phi 220\mu$ m spherical glass beads in a single layer.

6 CONCLUSION

Layered manufacturing processes based on selective aggregation of powders (E.g: SLS, 3D Printing) all rely on blanket deposition of the build material. This geometric constraint severely limits the prospect of expansion into multi-material and functional materials of an otherwise well developed technology.

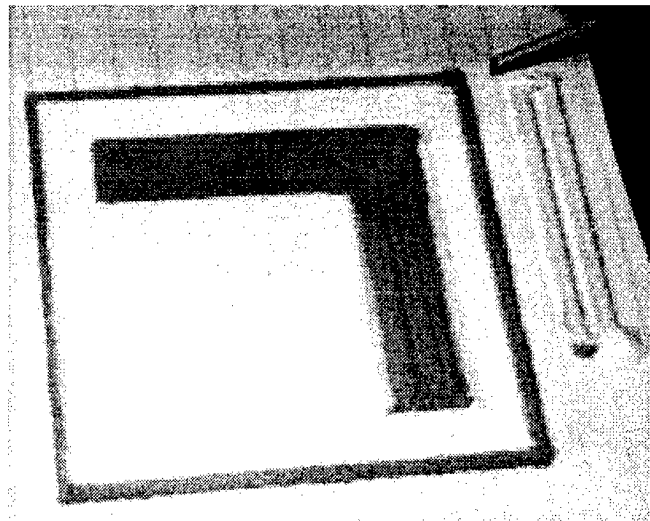


FIGURE 20. Sample two-powder deposition: Type I Portland Cement and 220 μ m spherical glass beads.

This paper introduces the Sand-Painter project. It derives from the ancestral art by the same name, which consist of decorating a flat substrate by depositing colored sand patterns. The present article focuses on reporting the results of an experimental design approach to the Sand-Painting process. Investigations reported herein focus on the experimental characterization of powder flows though the downcomer of a vibrationally actuated hopper and its corresponding deposition

characteristics. The results to date validate the Sand-Painter concept. The results to date though, are insufficient for an analytical characterization of the process. Yet, they establish a methodology and approach, which can open selective aggregation processes to the realm of multi-material structures.

7 ACKNOWLEDGMENTS

The project presented in this paper is above all an exercise in shoestring research and scavenging. It owes much to the cooperation of the Mechanical Engineering Department at Concordia University, the Concordia Center for Advanced Vehicle Engineering (CONCAVE), and above all it owes a debt of gratitude to the undergraduate students involved. The Mechanical Engineering Department provided the computer, data acquisition, and CNC. CONCAVE provided the shaker. The undergraduate research assistant acknowledged as co-authors provided their resourcefulness, energy and commitment.

Partial funding for this project was provided by the Natural Science and Engineering Research Council (NSERC) of Canada, and by the Concordia University Faculty Research and Development Program. All contributors are gratefully acknowledged.

8 REFERENCES

- [Pegna, 1995a] "Application of Cementitious Bulk Materials to Site Processed Solid Freeform Construction," Proceedings of the Solid Freeform Fabrication Symposium, Ed. by H.L Marcus, J.J. Beaman, D.L. Bourell, Joel W. Barlow, and R. H. Crawford, Austin, Tx, August 1995, pp.39-45.
- [Pegna, 1995b] "Exploratory Investigation Of Layered Fabrication Applied To Construction Automation," Proceedings of the ASME Design Technical Conferences, Design Automation Conference, Sept. 17-21, 1995, Boston, Ma., DE-Vol. 82, pp.219-226.
- [Pegna, 1997] "Exploratory Investigation of Solid Freeform Construction," *Automation in Construction*, Vol. 5, no.5, pp. 427-437 (Mar. 97)
- [Rock and Gilman, 1995] "A New SFF Process for Functional Part Rapid Prototyping and Manufacturing: Freeform Powder Molding", Proceedings of the Solid Freeform Fabrication Symposium, Ed. by H.L Marcus, J.J. Beaman, D.L. Bourell, Joel W. Barlow, and R. H. Crawford, Austin, Tx, August 1995, pp.80-87.
- [Sachs et al., 1990] Sachs, E., Cima, M., Cornie, J.; "Three Dimensional Printing: Rapid Tooling and Prototypes Directly for a CAD Model," Annals of CIRP, Vol.39, 1, pp. 201-204 (1990)
- [Deckard and Beaman, 1987] "Solid Freeform Fabrication and Selective Laser Sintering" Proceedings of the 15th NAMRC-SME, (1987)
- [Brown and Richards, 1982] Principles of Powder Mechanics, Pergamon Press, 2nd ed. (1987)
- [Mason and Woodcock, 1987] Bulk Solids Handling, Leonard Hill, N.Y., 1987
- [Hans, 1990] Particle Technology, Chapman And Hall, N.Y. 1990
- [Taguchi, 1987] System of Experimental Design I & II, UNIPUB Kraus International Publications (1987).

Accuracy Study on Laminated Object Manufacturing for the Metallic Functional Parts with Complex Surface

Yi Suping¹, Tamotsu Murakami² and Naomasa Nakajima²

1.Chongqing University, Chongqing, 400044, P. R. of China

2.The University of Tokyo, Tokyo, 113-8656, Japan

ABSTRACT

The feasibility of using the Laminated Object Manufacturing (LOM) process for rapid manufacturing of the metallic functional parts with complex surface was studied in this paper. The theoretical manufacturing error and the quantity of remaining material to be removed by finish manufacturing process caused from current LOM process were analyzed, and compared with 3-D numerical control manufacturing. A new approach for cutting metallic laminating layer was presented for reducing theoretical manufacturing error and quantity of remaining materials. Case study of cylinder surface demonstrates the effects of new LOM process that it could increase the thickness of the laminating layer from 0.05-0.1mm to 1.0mm grade. Even with such thicker metallic laminating layer, we also can get similar to or lower theoretical manufacturing error and remaining material quantity than current LOM process. It may indicate that metallic functional parts with complex surface could be rapidly manufactured with new LOM process.

INTRODUCTION

In past decade, a lot of important breakthroughs have been made in the theoretical research and its application about the rapid prototyping and manufacturing (RP/M) technology ^[1]. Although there are some reports in which the ceramic is used as the modeling materials ^[2], in the most case the modeling materials used are those such as plastics, paper or wood. During its initial development stage, RP/M technique is usually used to evaluate the correctness of the three dimensional model resulted from CAD, the materials such as plastics used as modeling materials are good enough for that purpose. With its application extending to the fields such as the check of design, the evaluation of performance, the trial fabrication or the manufacturing of the functional parts, RP/M technique must be further improved with the effort to use some other materials rather than the ones mentioned above. One of the attempts is to use metal as the modeling materials ^[3].

There are some reports using the sheet metal as modeling materials by laminated object manufacturing (LOM) for manufacturing the metallic functional parts ^[4]. After examining on the available results, we have realized that there are some problems to be solved when using the sheet metal as the modeling materials in LOM process, one of them is how to get the expected laminating accuracy. It is well known that the thinner the laminating layer is, the higher the modeling accuracy is. The thickness of laminating layer for the available LOM processes, which use paper, plastics or wood plate as modeling materials, is usually only 0.05-0.1mm. For using metal plate as modeling material, there is a research report of using sheet steel of 0.2mm thick, and the attempt would be made to use thinner sheet metal plates. But using thinner sheet metal brings about other problems, for example, the strength of steel decreases with the increase of the modeling time. In addition, the sheet steel thinner than 0.2 mm with the bond coated on its both surface is difficult to be made practically.

In this paper the accuracy study on LOM is presented. Authors have done a basic analysis on theoretical manufacturing error for LOM in reference [5]. Based on the further analysis of the

theoretical manufacturing error and the quantity of remaining material to be removed by finish process (that is said as remaining quantity) caused by LOM process and 3-D numerical control manufacturing (that is said as 3-D NC process), a new LOM process to reduce the theoretical manufacturing error and remaining quantity is proposed.

THE ANALYSIS OF THEORETICAL ERROR AND REMAINING QUANTITY

Here we use a quarter cylinder surface as the object of research. With this object, the theoretical manufacturing error and remaining quantity for both of the current LOM process and 3-D NC process are explored.

Current LOM Process

Laminating principle of the LOM method for the quarter cylinder surface is shown by fig.1, from the figure we know that there exist stair steps between each laminating layer and the modeling surface. To get the correct surface these stair steps have to be removed by the

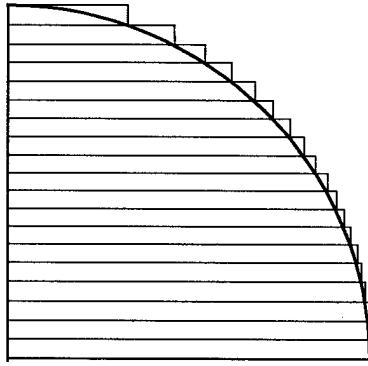


Fig.1 Laminating principle of LOM

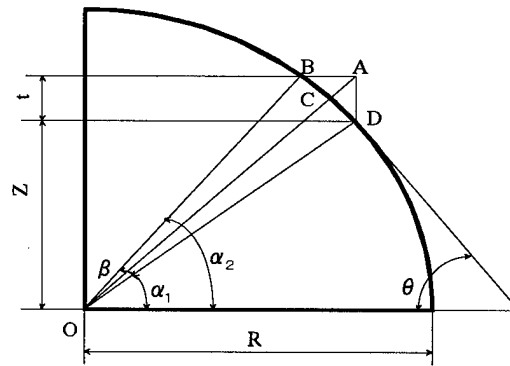


Fig.2 Theoretical error and remaining quantity of LOM

successive finish process, here the stair steps are called remaining quantity. The largest distance between each laminating layer and the modeling surface is defined as the theoretical manufacturing error of this layer. In fig.2 one laminating layer taken from the quarter cylinder surface is shown. In more detail, where the height of the layer is z , the thickness of the layer is t , the area of the curved triangle ABD is the remaining area to be removed, which is represented by S_1 . The volume formed by the area of S_1 stretching W (the width of the cylinder surface) along the axle of cylinder is the remaining quantity, which is represented by V_1 . The height AC of the curved triangle ABD along the direction of radius is the theoretical manufacturing error, which is represented by Δ_1 . Then we have the following equation:

$$\Delta_1 = \sqrt{t^2 + R^2 + 2zt} - R \quad (1)$$

$$S_1 = \frac{1}{2} [Rt(\cos \alpha_1 - \cos \alpha_2) - R^2(\beta - \sin \beta)] \quad (2)$$

$$V_1 = S_1 W \quad (3)$$

Where

$$\alpha_1 = \sin^{-1}(z/R)$$

$$\alpha_2 = \sin^{-1}[(z+t)/R]$$

$$\beta = \alpha_2 - \alpha_1$$

α_1 , α_2 , β and all the quantities of angles are measured in radian measurement.

3-D NC Process

Suppose the process of the 3-D numerical control manufacturing is the same as that of LOM, i.e. the process goes along the cylinder surface of the radius of R , the radius of ball end mill is r (as shown in fig. 3). The center of the ball end mill is O_1 on the height of z , and after one circle it changes to O_2 . The feed quantity between the two cutting along the direction z is f . From the figure we know that the area between the two cuttings and modeling surface (the area of the curved triangle ABD) is the remaining area to be removed, which is represented by S_2 . The volume formed by the area of S_2 stretching W

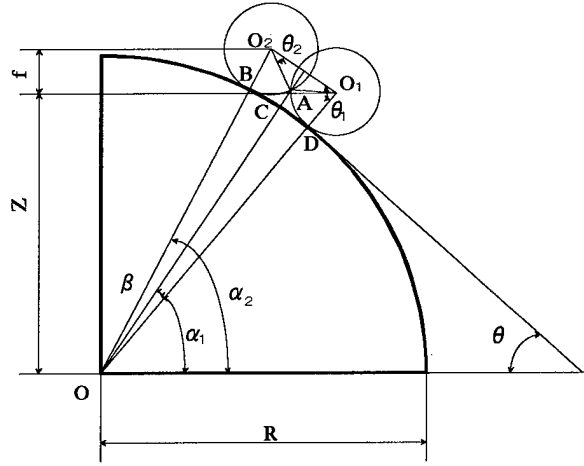


Fig.3 Theoretical error and remaining quantity of materials of 3-D NC process

along the axle of the cylinder is the quantity of remaining materials, which is represented by V_2 . The height AC of the curved triangle ABD along the direction of radius is the theoretical manufacturing error, which is represented by Δ_2 . By analysis we have the following results:

$$\Delta_2 = (R + r) \cos \beta - R - \sqrt{r^2 - [(R + r) \sin \beta]^2} \quad (4)$$

$$S_2 = (R + r)^2 \cos \beta \sin \beta - R^2 \beta - r(R + r) \sin \beta \sin \theta_2 - r^2(\theta_1 - \theta_2) \quad (5)$$

$$V_2 = S_2 W \quad (6)$$

Where

$$\alpha_1 = \sin^{-1}[z/(R + r)]$$

$$\alpha_2 = \sin^{-1}[(z + f)/(R + r)]$$

$$\beta = \frac{1}{2}(\alpha_2 - \alpha_1)$$

$$\theta_1 = \frac{\pi}{2} - \beta$$

$$\theta_2 = \cos^{-1}[(R + r) \sin \beta / r]$$

Analysis for the Theoretical Manufacturing Error and Remaining Quantity

Let $R=100\text{mm}$, $W=50\text{mm}$, $t=1\text{mm}$, $r=5\text{mm}$, and $f=1\text{mm}$, where R is the curvature's radius of the three-dimensional surface, and W is its width, t is the thickness of laminating layer, r is the radius of ball end mill, f is the feed quantity of finish milling.

By equations of (1) and (4), the theoretical manufacturing error curves of both the LOM process and 3-D NC process can be computed, which are shown by fig.4, where Δ_1 and Δ_2 are the theoretical manufacturing error curves of LOM and 3-D NC process correspondingly. With the increase of the z coordinate's value of laminating layer, the included angle of θ between the

tangent plane of the three dimensional surface and the laminating layer changes from $\pi/2$ (90°) to 0, as a result the theoretical errors of both processes increase and reach their maximums where θ approaches to 0. The maximums of the theoretical error are $\Delta_{1\max}=0.99\text{mm}$ (almost the same as the thickness of the laminating layer), and $\Delta_{2\max}=0.24\text{mm}$ ($1/4$ of the feed quantity). In addition, if we have a look at the distribution property of the error, we know that the theoretical error from current LOM process is far larger than the one from 3-D NC process.

By equation (3) and (6) the quantity of remaining material for each laminating layer or between twice cutting can be computed, the sum of the quantity of remaining materials for the all laminating layer on the quarter cylinder or among all cutting paths are $\sum V_1=2353.0\text{mm}^3$, $\sum V_2=124.8\text{mm}^3$, which are shown in fig.5. Both the remaining materials of the LOM and 3-D NC processes increase with the decrease of the included angle θ between the

tangent vector of modeling surface and the laminating layer, and reach their maximum where θ approaches to 0, i.e. the maximum values are $V_{1\max}=234.6\text{mm}^3$, $V_{2\max}=11.8\text{mm}^3$. The results show that the maximum quantity of the remaining materials of the current LOM process is 18.9 times greater, and the sum of the quantity of remaining materials is 17.9 times greater than that of the 3-D NC process.

Based on the analysis above, it is proved that although the current LOM process has high efficiency than 3-D NC process and it also simplifies the complexity of the 3-D surface to be manufactured, but it has the disadvantage of poor manufacturing accuracy, which means there is more quantity of remaining materials left, so it needs much time for further finish process. To improve the accuracy of the current LOM process, there are two choices, one is to decrease the thickness of the laminating layer, which is 0.05-0.1mm in available LOM processes, and the other is to search for more efficient LOM process. In this paper we explore some more efficient LOM process to improve the manufacturing accuracy of current LOM process.

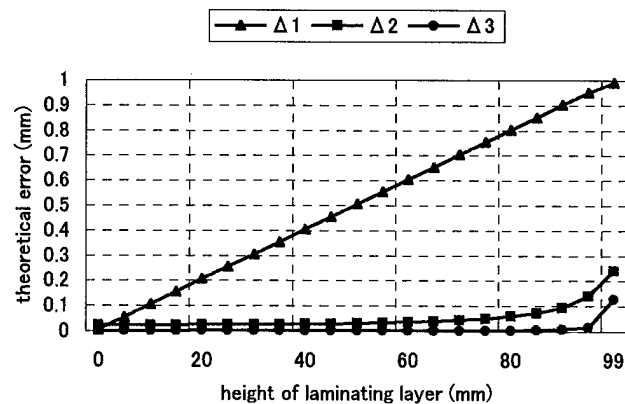


Fig.4 The theoretical manufacturing error curves

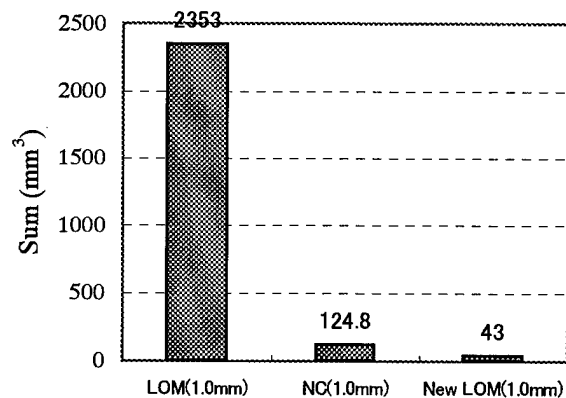


Fig.5 The sum of remaining materials quantity

NEW METHOD OF LOM PROCESS

The New Approach for Improving the Manufacturing Accuracy

From the analysis above we know that in order to reduce the theoretical error and the quantity of remaining materials, we have to reduce or eliminate the left steps between each laminating layer and modeling surface, which are the main source of the error. Let us have a look at the manufacturing process of each laminating layer. From the bottom to top along the direction of z coordinate, the laser or ball end mill cuts the perimeter of the cross sectional area of the 3-D surface in LOM at present. When θ is small, the left stair steps are large, and as a result the manufacturing error and the quantity of the remaining materials are also large. Here we suppose that in new LOM process the laminating layer is cut by laser or ball end mill along the tangent vector CD of modeling surface passing the mid point E of the laminating layer for the convex surface, or along the direction $C'B'$ of intersection points between modeling surface and up and down sides of laminating layer for concave surface, shown as fig. 6. By the figure it is obvious that the area of remaining materials of the new LOM process is much smaller than that of current LOM process (the curved triangle ABF for convex surface or $A'B'C'$ for concave surface).

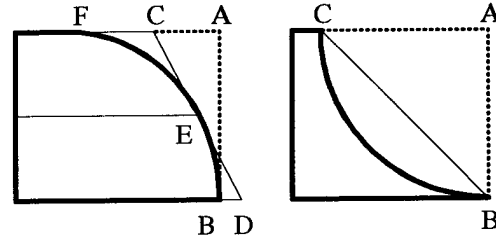


Fig. 6 The principle of new LOM process

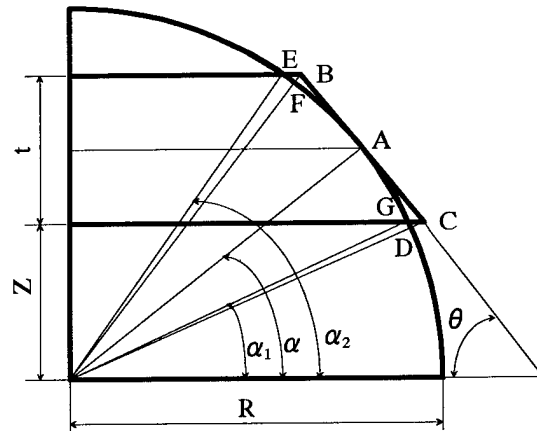


Fig. 7 Theoretical error and quantity of remaining materials of new LOM process

The Analysis for the New LOM Process

Here we use the same convex quarter cylinder surface as the example of computation, as shown in fig. 7. Where A is the intersection point between the center point plate of laminating layer and modeling surface. The points B and C are the intersection points between up and down sides of the laminating layer and the tangent line of modeling surface passing the point A . From the figure, we know that the sum of the area of curved triangle ABE and ACG is the remaining area for the new LOM process, which is represented by S_3 . The larger one of the height along the radius direction, i.e. Δ_{31} and Δ_{32} , is the theoretical error of the laminating layer, which is represented by Δ_3 . The remaining area and quantity to be removed can be computed by equation (7)-(11):

$$\Delta_{31} = \sqrt{\left(R \cos \alpha - \frac{t}{2} \tan \alpha\right)^2 + (z + t)^2} - R \quad (7)$$

$$\Delta_{32} = \sqrt{\left(R \cos \alpha + \frac{t}{2} \tan \alpha\right)^2 + z^2} - R \quad (8)$$

$$\Delta_3 = \max[\Delta_{31}, \Delta_{32}] \quad (9)$$

$$S_3 = \frac{tR}{4}(2\cos\alpha - \cos\alpha_2 - \cos\alpha_1) - \frac{R^2}{2}[\alpha_2 - \alpha_1 - \sin(\alpha_2 - \alpha) - \sin(\alpha - \alpha_1)] \quad (10)$$

$$V_3 = S_3 W \quad (11)$$

Where

$$\alpha_1 = \sin^{-1}(z/R)$$

$$\alpha_2 = \sin^{-1}[(z+t)/R]$$

$$\alpha = \sin^{-1}\left(\frac{z+t/2}{R}\right)$$

Comparison Analysis

The same as above, let $R=100\text{mm}$, $W=50\text{mm}$, $t=1\text{mm}$, the theoretical error and quantity of remaining materials are computed here.

According to equation (7)-(9), the theoretical manufacturing error is computed, and its curve is shown as Δ_3 in fig. 4, which is far lower than that of current LOM process and the 3-D NC process. Its maximum is $\Delta_{3\max}=0.125\text{mm}$, which is only 12.6% of that of current LOM process, and 52.1% of that of 3-D NC process.

The quantity of remaining materials of new LOM process can be computed by equation (11), and its maximum value is $V_{3\max}=28.7\text{mm}^3$, which is 7.1 times smaller than the same quantity of current LOM process, and 1.4 times larger than the same quantity of 3-D NC process. But the sum of the quantity of remaining materials is $\sum V_3=43.0\text{mm}^3$, shown in fig.5, which is 53.7 times smaller than the same quantity of current LOM process ($\sum V_1=2353.0\text{mm}^3$), and 1.9 times smaller than the same quantity of 3-D NC process ($\sum V_2=124.8\text{mm}^3$).

In the following we further compare the new LOM process with the available practical LOM process. The thickness of laminating layer is from 0.05 to 0.1mm in available practical LOM process and 0.2mm in reference [4], so we compute the theoretical error and the quantity of remaining materials for available practical LOM process when the thickness

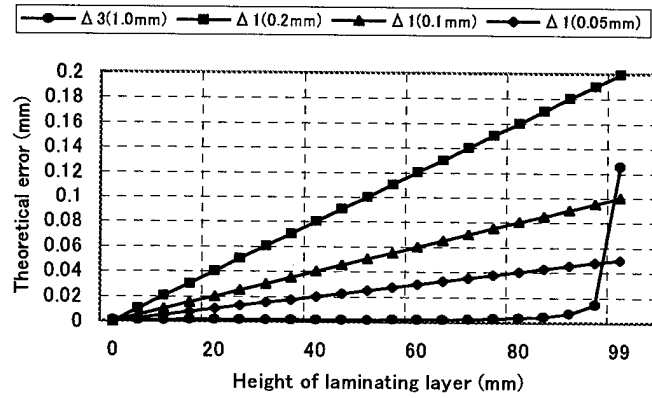


Fig.8 The comparison curve of theoretical error

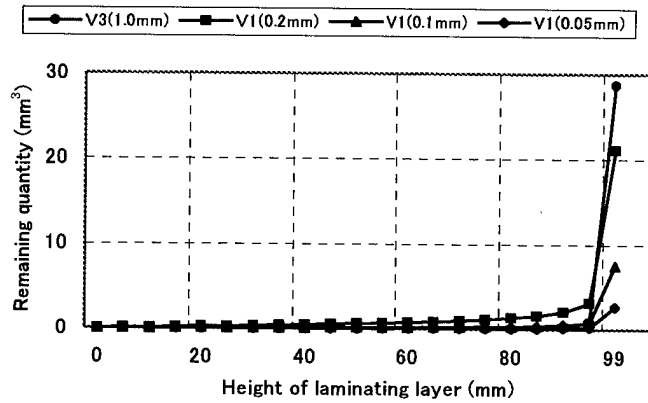


Fig. 9 The comparison of remaining material quantity

of laminating layer are $t=0.05$, 0.1 , and 0.2mm , and compare the results with those obtained by new LOM process.

In fig. 8 the theoretical errors are compared. Although when $t=0.05$ and 0.1mm , the maximum theoretical error of current LOM process are smaller than the same quantity of the new LOM process in which the thickness of laminating layer is $t=1\text{mm}$, but in overall distribution, the new LOM has the most small theoretical error.

In fig.9 the quantities of remaining materials for the single laminating layer are compared. Although the new LOM has the largest maximum remaining quantity for the single laminating layer, because it has the much larger thickness than current LOM process, but the sums of the remaining quantity for three different thickness of laminating layer in current LOM process are larger than that of the new LOM process, i.e., $\sum V_1(0.2)=3139.5\text{mm}^3$, $\sum V_1(0.1)=1570.3\text{mm}^3$, $\sum V_1(0.05)=785.3\text{mm}^3$, which are 33 times, 16.7 times and 8.5 times larger than that of the new LOM process ($\sum V_3(1.0)=95.1\text{mm}^3$) respectively, shown in fig.10.

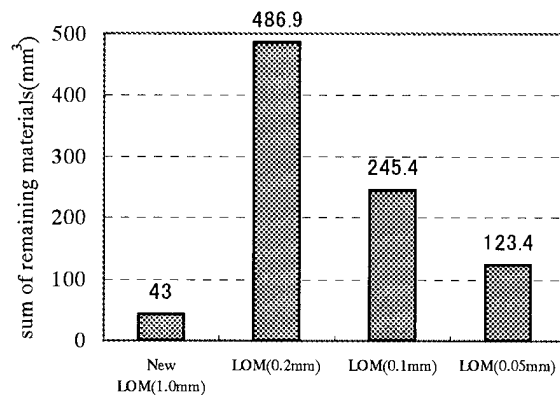


Fig.10 the comparison of remaining materials

EXAMPLE PARTS

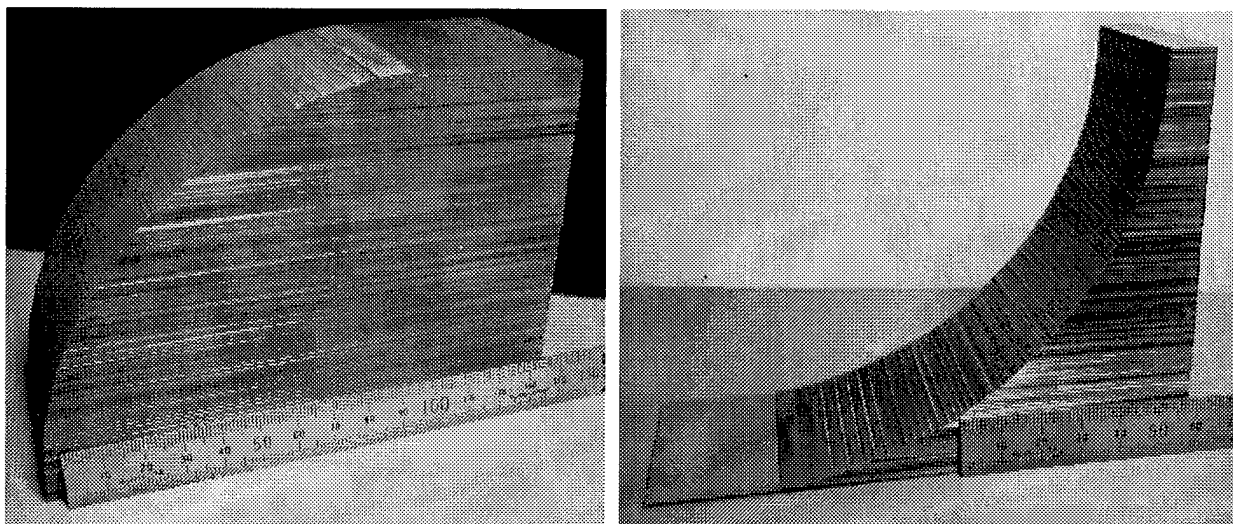


Fig.11 the photo picture of example parts

The example parts of quarter cylinder surface were made by new LOM process. In this case, sheet steel of 1.0mm thickness was used as modeling materials, the radius of cylinder surface is 100mm , and its width is 50mm , just like the analysis above. The wire electrical discharge machine was used to cut the laminating layers along the tangent vector of modeling surface. We have gotten two example parts, one was a convex cylinder surface part, and the other

was a concave cylinder part shown as fig. 10. From this photo picture we can see that stair step effect was obviously restrained and smooth modeling surface have been obtained.

CONCLUSION

Based on the analysis above, the following conclusions can be drawn:

1. In the current LOM process, the stair steps are used to make close to the modeling surface, which result in larger theoretical manufacturing error and remaining materials quantity to be removed. To get higher manufacturing accuracy and reduce the remaining materials quantity fairly thin laminating layer (about 0.05-0.1mm) must be used.
2. When sheet metal is used to manufacture the functional parts by the LOM process, available thickness of laminating layer being 0.05-0.1mm could not be used for the limitation on the modeling strength and building time of model.
3. By the new LOM process proposed in this paper, the thickness of laminating layer of the modeling materials can reach 1.0mm grade. In addition the resulting accuracy and remaining quantity are near or superior to those obtained by the current practical LOM process with the thickness of laminating layer being 0.05-0.1mm. This means the new LOM process can be treated as a rapid manufacturing method for metallic functional parts.
4. To use the new LOM process to manufacture metallic functional parts with metal sheet as modeling materials, some topics such as NC programming of four-dimension, the process of laser cutting, the bond technology for laminating layer, must be studied further.

ACKNOWLEDGMENTS

This work was supported by the National Natural Science Foundation of China (NSFC) under the grant number 59875088. It was also supported by the University of Tokyo as the first author's visiting scholar research topic.

REFERENCES

1. J. P. Kruth, M. C. Leu, T. Nakagawa, "Progress in Additive Manufacturing and Rapid Prototyping", *Annals of the CIRP*, Vol. 47/2/1998, pp.525-540
2. Donald A. Klosterman, Richard P. Chartoff, Nora R. Osborne, George A. Graves, Allan Lightman, Gyoowan Han, Akos Bezeredi, Stan Rodrigues, "Curved Layer LOM of Ceramics and Composites", *Proceedings of the 1998 Solid Freeform Fabrication Symposium*, The University of Texas at Austin, August 1998, pp. 671-680.
3. T. Nakagawa, M. Anzai, "Rapid Prototyping for Direct Manufacturing of Metallic Parts", *OPTRONICS* (in Japanese), No.4, 1996, pp. 114-118
4. T.Obikawa, M.Yoshino, T.Matsumura, H.Sasahara, J.Shinozuka, K.Furusawa, "Rapid Manufacturing System by Sheet Steel Lamination", *Proceedings of 14th International Conference on Computer Aided Production Engineering*, Tokyo, Sep. 1998, pp. 265-270
5. Zhang Genbao, Yi Shuping, "Study on Increasing the Accuracy of Laminated Object Manufacturing ", *Computer Aided Design and Manufacturing* (in Chinese), No.8, 1998, pp45-51

SPIN CASTING AS A TOOL IN RAPID PROTOTYPING

(CENTRIFUGAL RUBBER MOULD CASTING)

L J BARNARD

TECHNIKON FREE STATE, SOUTH AFRICA

Abstract

The one thing that comes to mind when parts are manufactured by means of spin casting is the dimensions of the parts, the reason being that it is very difficult to produce castings with high tolerances.

There are numerous factors in the spin casting process that influence the final product. Some of these factors are the temperature of the mould, the temperature of the material used for casting, the spin speed of the mould and the clamping pressure on the mould. The type of material used for casting will also influence the accuracy of the final product.

In our research we control these factors to see what influence a certain factor has on the process. We are working towards being able to predict what the shrinkage of a part cast will be in a certain material, to incorporate a shrinkage factor in the prototype, to ensure that the final product will be on size.

1. INTRODUCTION

It is very important to be able to reproduce parts that have been developed by Rapid Prototyping to be able to evaluate the product and to manufacture them after the development stage. Spin Casting or Centrifugal Rubber Mould Casting is the cheapest means of achieving this. There is only one problem and that is the accuracy with which this can be done. Shrinkage of the material with which you cast is the main reason for the difficulty to cast parts with a high dimensional tolerance. The other process factors can be changed to get the required results. These factors are the temperature of the casting material, the spin speed of the mould, the clamping pressure applied on the mould and the temperature of the mould when you cast. This research is aimed to be able to get the best parameters at which to cast and to get the smallest shrinkage of your part. If you can predict the shrinkage of your part at certain casting parameters you are able to alter your master so that you will get the wanted final product.

2. TYPICAL SPIN CASTING SET-UP

Figure 1 shows the typical spin casting set-up, which consist of a spin caster, an LP-gas or electric furnace, and a vulcaniser with applicable vulcanizing frames. This normally can be purchased for less than the cost of a moderately complex mould.

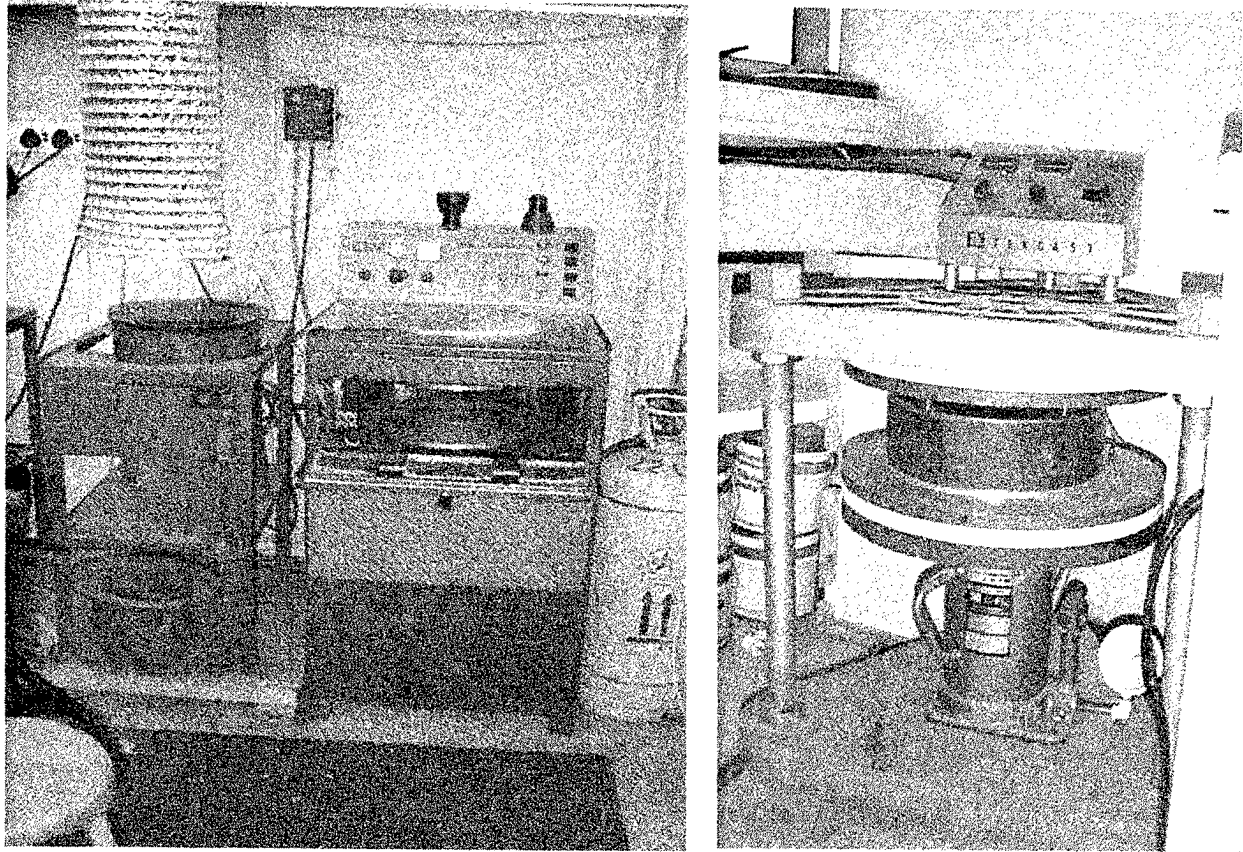


Figure 1 – A complete Spin Casting set-up.

3. PROCESS OVERVIEW

3.1 PROCESS CONTROL

The front loading system as shown in figure 1, provides three key functions for the production of functional, highly engineered or detailed parts. [1]

3.1.1. Mould stabilization without distortion:

The special mould clamping system centers and supports the mould in a horizontal plane, while a pneumatic cylinder applies an even, closely controlled clamp pressure which holds the mould halves firmly together during pouring without distorting the mould cavity by over-squeezing.

3.1.2. Mould pouring under pressure:

Rapid, speed-controlled rotation provides the adjustable centrifugal force that distributes the liquid metal or plastic throughout the mould, filling all cavities and intricate details under pressure before the material can solidify or set up.

3.1.3. Complete control of centrifugal force and pressure:

The system is fully controlled and automated to provide a complete range of spin speeds and clamp pressures. This optimizes the part's quality, tolerances, precision and detail, while improving productivity of the spin casting cycle.

3.2 SPIN CASTING PROCEDURE FOR HEAT-CURED (VULCANISED) MOULDS

3.2.1. Mould making

Parts are laid out on a disc of uncured silicone rubber. [2] Depending upon model/pattern thickness and shape, cavities may be cut or moulded by hand to accommodate the part. The uncured silicone material is soft and hand-mouldable like clay. (Figure 2) The mould parting line is formed at this stage and can be built up or lowered around any section of the model/pattern, to accommodate critical edges, surfaces, etc. Parts of any complexity can be handled.

At this time, cores and pullout sections can also be incorporated, if required. When special features like holes or bosses need to be incorporated, virgin grade Teflon inserts can be used. Through the use of a CNC lathe, an interchangeable core system has been developed, which speeds up the process for mass production, and contribute to accuracy. A special jacket-approach, as shown in figure 3, has been developed to get rid of the parting line on critical surfaces. Release agent is sprayed on the mould and "Acorn" nuts are arranged around the edge where-like pins of a die- they precisely position the mould halves to each other.

3.2.2. Vulcanization

The uncured mould is placed in a ring-shaped vulcanising frame. This frame is placed in the electrically heated vulcanising press for curing. Hydraulic force (15 MPa for WACKER™ silicones, and 14 MPa - 21 MPa for TEKSIL™ silicones) clamps the mould frame shut between the heated platens, forcing the silicone into all details of the model/patterns.

The heat cross-links the uncured silicone. The resulting mould is tough, resilient, dimensionally accurate, and heat and chemically resistant. After vulcanisation the mould is easily flexed to released the patterns (and later, parts) from the cavities. This is true even for patterns with a wide variety of undercuts.

3.2.3. Gating and venting

The gates, runner system and air vents are easily cut into the rubber with a sharp knife or scalpel. (Figure 4) If the initial spin-casting tests show a need for faster flow or more air venting, the in-gates can be cut thicker and the air vents may also be drilled into the cavity to aid in the removal of entrapped air or gases. Similar gating and venting systems is used for both metals and plastics, so both materials can be cast in the exact same mould for evaluation, if desired.

3.2.4. Spin-casting set-up

The mould is placed into the front loading unit; automatically centred and closing the door actuates a pneumatic mould clamp. Spin speed, clamping pressure and cycle time can be fully adjusted.

3.2.5. Pouring

After the spin cycle starts, the liquid metal or plastic is poured into the caster. Pressure caused by centrifugal force pushes the liquid through the mould's runner system, completely filling every section; corner, detail and surface finish in each mould cavity. (Figure 5)

3.2.6. Parts removal and mould recycling

After metals solidify and plastics set up, the parts are quickly removed from the mould.



Figure 2 - Mould lay-out and design

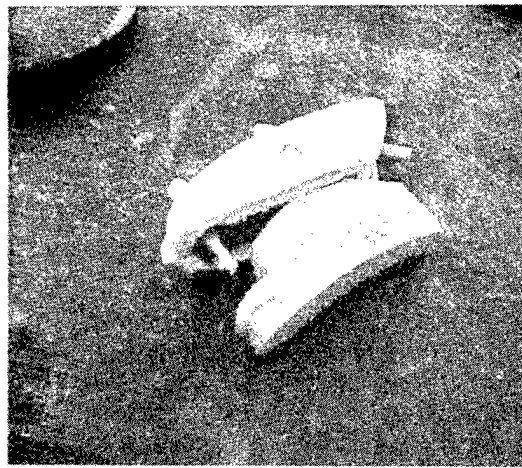


Figure 3 - Development of a "Jacket"

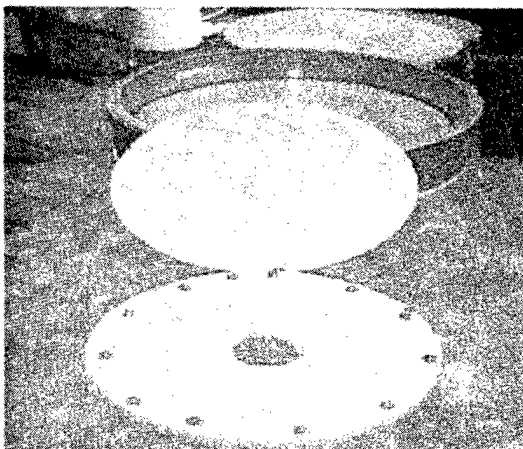


Figure 4 - Gating and Venting

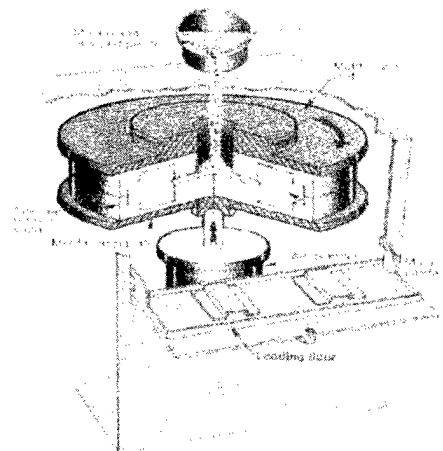


Figure 5 - Pouring by hand

4. THE WAY RESEARCH WAS DONE

To obtain the shrinkage factor of the parts numerous experiments were done to control some of the factors that influence the casting process and change one factor after a set of results were obtained. The experiments were done with the Wacker Silicones using the same vulcanizing parameters. The temperature of the melted metal was kept constant by the automatic temperature control of the Tekcast furnace. The mould temperature was checked by drilling a hole in the side of the mould and inserting a temperature probe in the hole and reading the mould temperature at the inside of the mould. The mould was only cast after it reached the required temperature.

The parts that were machined were rectangular prisms with dimensions of 40.17-mm length, 19.38-mm width and 9.79-mm thickness. These masters were machined out of mild steel to the required size. Experiments are being done on cylindrical parts to see what the effect is on round objects. The cylinder's dimensions were 40.65 mm outside diameter, 9.36 mm thickness and a hole drilled through with a diameter of 13.17 mm. It was machined from mild steel, copper and vesconite.

The mould layout was done in such a way that the ingates were the same distance from the centre so that the centrifugal force did not influence the outcome of the experiments. Ten prisms were placed at certain angles to the centerline. The first prism was placed with its longitudinal side on the centerline. The tenth prism was placed 90° with the centerline. The ingates were cut to the same size so that the melted metal would flow into the cavity at the same speed. All the experiments were done with AZM 6 Zinc and JM 90 Pewter as the casting material. The measurements were done with a digital vernier with accuracy of 10^{-2} mm.

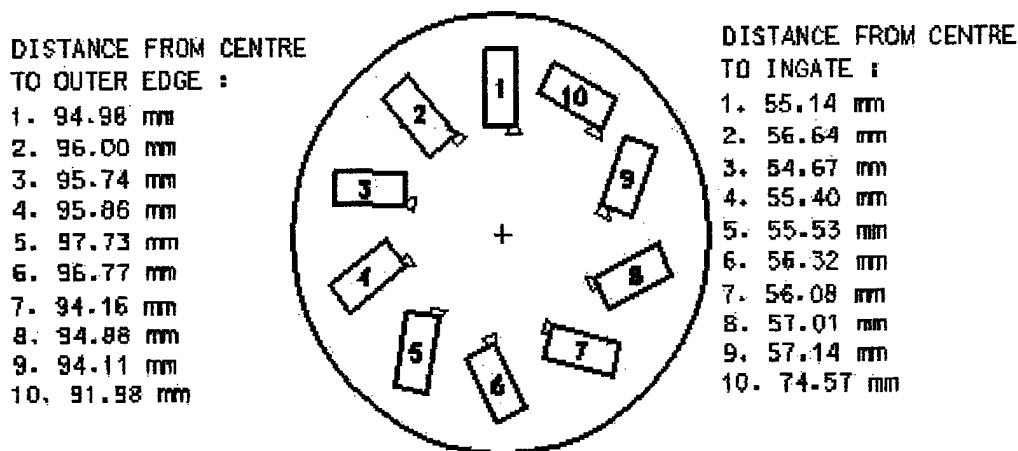


Figure 6 –Placing of masters in mould

5. RESULTS OBTAINED

5.1. Results from the rectangular prisms with AZM 6 zinc

From all the experiments done the best position of the master in the mould was position 10 which was 90^0 with the center of the mould. Looking at the different speeds at which the mould was spun the best results were obtained from 650 rpm. At this speed the percentage fill of the cavity was 98% which was also the best of all the experiments. All results shown are the percentage deviation from the original master model.

PRESSURE PSI	MATERIAL TEMP.	MOULD TEMP.	SPIN DIRECTION	MEDIANS	RESULT
20	388	50	CLOCKWISE	LENGTH	0.66
				WIDTH	-0.18
				THICKNESS	0.41
				AVERAGE MED.	0.3
				% FILL	98

Table 1: Results at 650 rpm

When the speed was kept constant at 450 rpm and the clamping pressure was changed ,it was found that the higher the pressure the bigger the thickness deviation from the original thickness. The other dimension did not change that much. But with the lower pressure, the parting line was more visible and in some cases there were signs of shifting of the two mould halves. This is unacceptable in the production of parts with high tolerances.

PRES-SURE	MAT. TEMP	MOULD TEMP	LENGTH	WIDTH	THICK.	AVE-RAGE	% FILL
20	388	35	1.72	1.08	3.32	1.85	100
25	388	35	1.83	1.06	4.81	2.56	100
30	388	35	1.62	1.24	4.29	2.38	90
35	388	35	1.68	1.34	5.42	2.81	100

Table 2: Results at 450 rpm

The change in mould temperature had the effect that with higher temperature the deviation increased.

PRES-SURE	MAT. TEMP	MOULD TEMP	LENGTH	WIDTH	THICK.	AVE-RAGE	% FILL
25	388	35	1.83	1.06	4.81	2.56	100
25	388	50	1.20	1.7	5.62	2.84	90

Table 3: Results at 450 rpm with different mould temperature

By changing the spin direction, the deviation decreased due to the fact that the speed with which the melted metal flowed into the cavity was reduced by the change in direction. This also had a negative effect because it was more difficult to fill the cavity.

5.2 Results from the rectangular prisms with JM 90 Pewter

The same results as for the zinc were obtained. The best results were at the higher speeds due to the centrifugal forces and the moment of inertia of the material. As a result of the fluidity of the pewter, the highest speed at which the experiments were done was 550 rpm. With the higher speeds, the pewter flashed through the mould split line.

PRESSURE PSI	MATERIAL TEMP.	MOULD TEMP.	SPIN DIRECTION	MEDIANS	RESULT
30	280	50	CLOCKWISE	LENGTH	0.29
				WIDTH	-0.08
				THICKNESS	2.5
				AVERAGE MED.	0.94
				% FILL	100

Table 4: Results at 550 rpm

By increasing the clamping pressure, the other dimensions stayed almost constant but the thickness deviation increased due to the fact that the cavity became smaller with the higher pressure. With the lower pressure, the parting line was unacceptable. The best results were obtained at 30 psi.

5.3 Preliminary results from the cylindrical parts

From the results obtained so far it was found that the shape of the parts became elliptical to a lesser degree. The outside diameter decreased and the inside diameter of the hole increased. More experiments should be done on the cylindrical parts to be able to make a prediction on what the shrinkage in the different axes will be.

6. CONCLUSION

With these results it is possible to predict what the dimensional deviation of a certain material will be when used in the spin casting process under certain conditions. By making use of these shrinkage factors the master can be upscaled and then from that produce the parts required. The next step in this research is to produce a master which has been scaled up with the SLA machine and then cast a few parts. This is in order to test the results and see if the predictions are correct and to see if it works in practice as indicated by the experiments.

7. References

- [1] Schaer, L.S & De Santis, E (1994) Moldmaking & Spin-casting Instruction Manual, Tekcast Industries.
- [2] de Beer, D.J. (1998) From CAD Models to Multiple Parts Using SLA and Spin Casting. Proceedings of the Time-compression Technologies Conference 1998, Nottingham, UK.

Reducing Part Deformation by Inducing Phase Transformation

Gayle Link, Tonya Huntley, Alex Nickel, Rudolf Leitgeb, Tony Nguyen, Fritz Prinz

Department of Mechanical Engineering, Stanford University, Stanford, CA 94305

Abstract

Fabrication of solid freeform fully dense metal parts involves large temperature gradients and fast cooling rates. These conditions may lead to the accumulation of residual stress or part failure by deformation. However, in tool steels, certain phase transformations can cause volumetric changes, which have the potential to reduce part deformation and stress. This research optimized process parameters for inducing controlled phase transformation in Shape Deposition Manufacturing (SDM). By manipulating SDM laser deposition process parameters, the deformation of planar beams was significantly reduced or eliminated.

1. Introduction

Influencing or altering the microstructure of a formed object to achieve certain materials properties is a common aspect of producing viable parts. Heat treatment is often used to homogenize the microstructure of newly formed sand castings or machined metal prototypes to attain uniform hardness and reduce residual stress. The surface microstructure of metal parts like gears may be deformed by peening to impose compressive stress to increase wear resistance. Die surfaces may be impregnated with alloying agents to improve die life. Laser hardening has been used on camshafts to improve wear resistance.

Layered manufacturing techniques of solid freeform fabrication have the ability to influence or control the microstructure of the prototype. Like heat treatment and casting processes, laser deposition can affect the microstructure of the part. However, unlike these bulk processes, laser deposition techniques like surface cladding can have a more localized effect (Figure 1). Yang et al. [4] showed that a CO₂ laser hardening process can produce a microstructurally altered region near a part's surface 350 μm thick.

Laser deposition produces rapid solidification or quenching because of fast heat conduction from the laser melt pool into the base metal. This solidification rate can also be influenced by changing deposition parameters such as scanning speed and laser power. When depositing carbon steels, rapid solidification can cause metastable phases to occur, primarily martensite. Martensite formation is a diffusionless process which occurs when the deposit cools from high temperatures (like the steel melting point) to below the martensitic start temperature in less than 10 sec. The arrows shown in Figure 2 illustrate the isothermal transformation of H13 and 410 stainless steel to martensite by rapidly cooling to room temperature. Cooling slower than this would not produce martensite but result in the production of ferrite and cementite.

When the laser melts the powder, the first solid metal to nucleate within the liquid is austenite. Austenite has a face center cubic structure. The rapid quenching causes the carbon in the austenite phase to transform to body center-tetragonal (BCT) martensite trapping carbon in the BCT lattice which has not had a chance to diffuse.

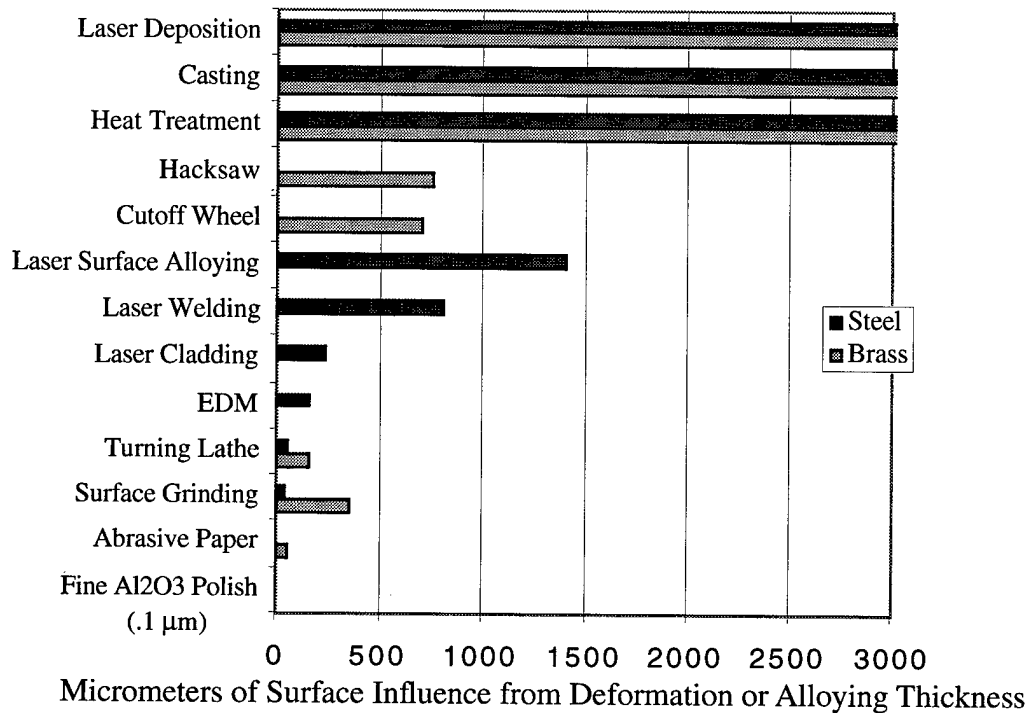


Figure 1. Aggregate Vs. Local Influence on a parts microstructure. Compiled from [1,2,4,5]

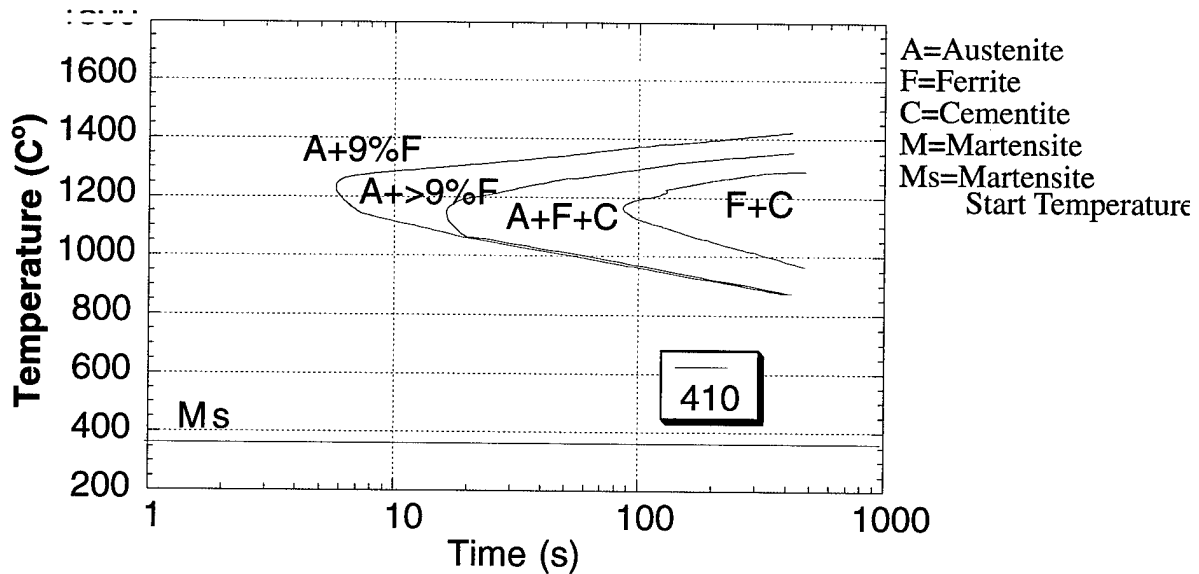


Figure 2. Isothermal Transformation Diagram of 410 steels. Compiled from [7].

This transformation results in an expansion in volume. This expansion can be as big as 4%. This is the same order of magnitude as the thermal shrinkage which arises from cooling of the metal. If martensite transformation can be induced and controlled by layered laser deposition, then the potential to balance the solidification shrinkage with phase volumetric expansion may exist.

The use of lasers to change part or surface microstructure has been extensively researched for laser cladding and surface hardening. Several researchers have shown a relationship between laser parameters and microstructural evolution for laser cladding and surfacing. Wang et al. [3] showed that metastable phases can be produced on material surfaces by laser quenching, a process in which laser melting and quenching of a material occurs by using a very short laser pulses. Yang et. al. [4] used a CO₂ laser to show that case depth or the depth of phase transformation and morphology of materials can be influenced by laser power and laser scan rate. Fouquet et. al [5] used a continuous wave CO₂ laser to transform the surface of grey cast iron from austenite to a mixture of austenite, cementite and martensite by using overlapping multiple laser scan paths. Rieker, et. al [6] uses a remelting second pass of the laser to homogenize the chemistry and microstructure of a laser hardened surface on ferritic stainless steel.

2. Experimentation

Experiments were performed to determine the influence on martensitic phase percentage on deformation. Using the SDM lasing technique [8,9], beams were laser deposited using the 400 series martensitic stainless steels. This technique uses a 2.4KW Nd:YAG continuous wave laser whose fiber optic is mounted on a robot which is used for 3D translation. Only additive processes were used to build test beams. Table 1 shows the chemical composition of the steels used. A 127 mm x 6 mm x 12.5 mm beam was deposited in 5 layers on substrates which were 152.4 mm x 6.25 mm x 25.4 mm in size. Substrates were annealed to 74 Rb (HK). Beams were built in single pass or double pass configuration. Single pass (SP) allowed for the powder material to melt and fuse upon the substrate or previously deposited layer. Double pass (DP) allowed for one laser scan to melt and fuse the powdered material while a second scan remelted and heated the newly deposited layer without the addition of any new material. The second pass occurred within seconds of the completion of the first at the same scanning speed and power. Three to five beams for each material and at each condition, single pass or double pass, were built. The deflection of the beams was measured using coordinate measurement machine in a process similar to measuring warp in silicon wafers (ASTM F657-1992). Microhardness testing was also performed on cross sections of the beams.

The cross sections were repolished and etched with solutions which leave colored films upon individual phases of the materials [10]. Phase percentages were determined by a color met-

allography analysis program called "Blue." Metallographic RGB color standards are determined for each phase of a particular material. Blue uses a polygonal RGB pixel value matching algorithm to isolate phase regions. The program matches RGB pixel values with a region in RGB color space and can automatically isolate different material phases. Blue when tested with known phase percentage color metallographs was within 3% of those values and was within 4% of X ray diffraction SDM tool steel samples [10, 11]. This produces an accuracy comparable to manual assessment using ASTM Standard E45-1997 and E1268-1994. Over 3000 metallographs were analyzed using this method. Transmission electron microscopy was also used to analyze material phases following the indexing procedure described by Williams and Carter[12]. Picral pre-etches were used with sodium metabisulfite to reveal as-quenched martensite (M_{AQ}). Hydrochloric acid plus nitric acid and sodium thiosulfite etches were used to reveal tempered martensite. Klemm's reagent was used to reveal ferrite. Table 1 is a list of the materials compositions tested.

Table 1: Test Material Composition

	C%	Mn%	Si%	Cr%	Ni%	Mo%	Nb%	Al%	P%	S%
410	.06	.17	.53	12.5	.07	0	0	0	.017	.007
420	.45	.49	.54	13.6	0	0	0	0	.017	.007
431	.18	.69	.57	15.6	1.78	0	0	0	.016	.003
SDM Tool Steel	.01	1	1.23	21.5	2.8	0	.84	0	0	0
316L	.02	1.74	.73	17.3	13.1	2.66	0	0	0	0

3. Results

Once the deposition of the beams was completed, the beams were tested for deflection and phase composition. Table 2 lists the average results for each type of material tested.

Table 2: Results of Deposition Experiments

	Laser Pass	Deflection (mm)	% As-quenched Martensite (M_{AQ})	% Tempered Martensite (M_T)	% Austenite	% Ferrite	M_{AQ}/M_T
410	1	.97	7	55	36	0	.125
420	1	1.26	19	74	3	2	.249

	Laser Pass	Deflection (mm)	% As-quenched Martensite (M _{AQ})	% Tempered Martensite (M _T)	% Austenite	% Ferrite	M _{AQ} /M _T
431	1	.432	29	62	4	0	.471
SDM -Tool	1	.89	9	68	21	0	.129
316L	1	.97	0	0	98	0	.0
410	2	1.14	4	88	6	0	.047
420	2	.33	29	58	10	0	.506
431	2	.33	32	63	5	2	.51

Selective etchants revealed martensitic and austenitic phases in all the metals with the exception of 316L which is only austenitic. Martensitic stainless steel, 420, had three phases: austenite, martensite, and ferrite (Figure 3 and Figure 4).

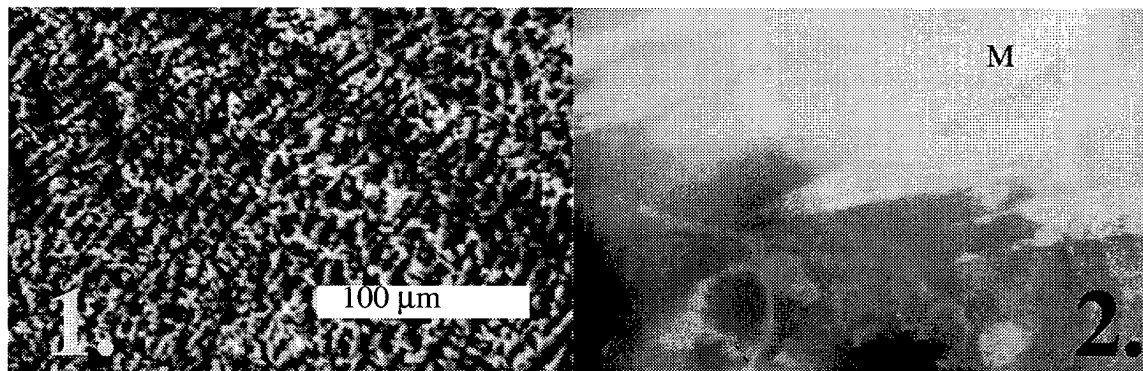


Figure 3. Pictures of 431 stainless: 1. Optical microscope with light brown reflecting tempered martensite, black - as-quenched martensite, white - retained austenite. 2. Brightfield image of TEM with white regions - martensite, black regions - austenite. @30,700 X.

Microhardness for the specimens ranged between 400-540 HK. For each of the metals, the hardness ranges were typically below the value of typical as-quenched or hardened steel ranges. The reheating affect of subsequent layer deposition or the retention of softer phases like austenite could cause this reduction in hardness. Figure 5 compares the quench/hardness ranges for the martensitic stainless steels used in the experiments.

For certain materials increasing the martensite percentage reduced deflection while it increased it in others. Figure 6 shows that by increasing the ratio of as-quenched martensite to tempered martensite, deflection is reduced.

More as-quenched martensite is found in base layers than in N+I layers (middle and top layers). This suggests that the quenching rate is much faster near the substrate than for subsequent layers. The double laser pass condition increases the quenching rate for middle sections of the beams than the single pass condition. The inset in figure 6 compares middle and bottom layers of 420 in single pass and double pass condition.

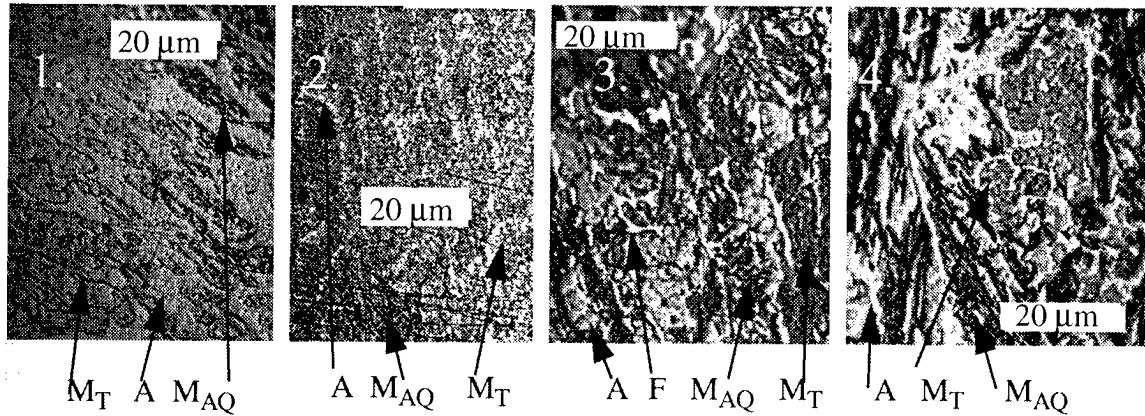


Figure 4. Optical Microscope pictures of :1. 410 - SP, 2. 410 - DP, 3. 420 - SP, 4. 420 - DP.

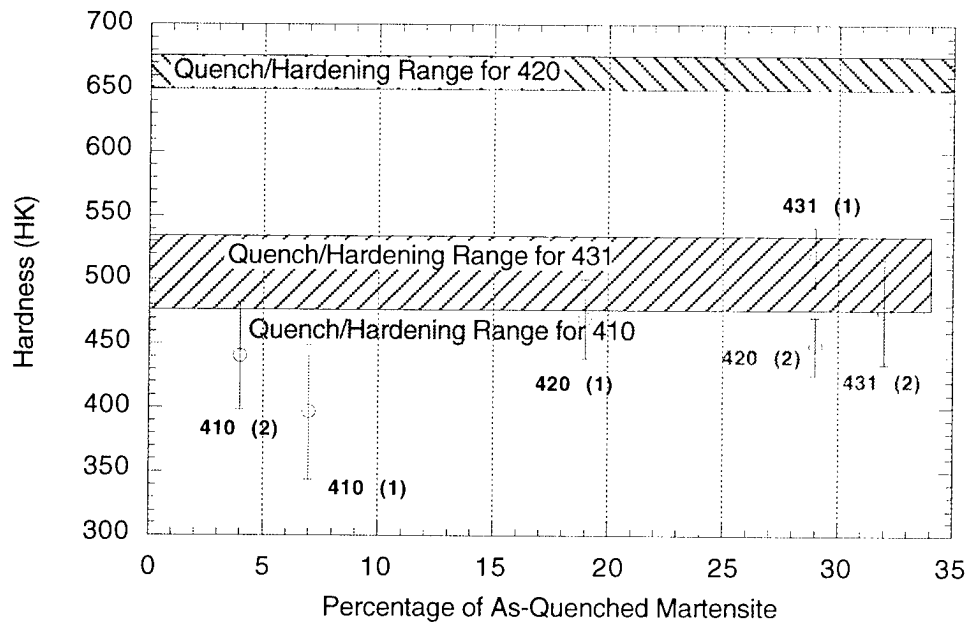


Figure 5. Comparison of the hardness values for martensitic stainless steel beams: 1 - Single Pass, 2- Double Pass. Quenching range compiled from [13].

4. Discussion

Increasing the amount of as-quenched martensite retained in the beams reduced the deflection of SDM deposited beams. As-quenched martensite allowed for maximum volumetric expansion. Tempered martensite allowed the carbon to diffuse, shrinking the lattice and reducing the

amount of volumetric expansion achieved. SDM laser manufacturing induced as-quenched martensite. However, reheating of layers during the deposition of subsequent layers tempered much of the as-quenched martensite. The addition of a second laser pass increased the quenching rate and helped maintain more as-quenched martensite for most of the metals tested. Attaining a ratio of at least .45 as-quenched to tempered martensite produced a 30-75% reduction in deformation in the SDM deposited beams.

These tests upon the SDM layered process indicate that continuous deposition of material layers influences the microstructure of N, N-1, N+1 layers. The layer that is being deposited, N, is obviously affected because of the melting and solidifying of the material. The N-1 microstructure is affected because of the reheating of the layer due to the newly deposited layer. The next layer, N+1 is affected because its grain growth direction is seeded from the prior layer N. As more layers are deposited, more heat is retained in the bulk. Grain growth in both austenitic and martensitic steels increases with each additional layer. Grain size in layer N+1 is larger than in N. However, in martensitic steels, this increased heat retention produces more tempered martensite in the bulk and upper layers than near the interface between substrate and first layer. The difference in the heat characteristics is an important element to modelling and understanding the phase development within layered metal parts.

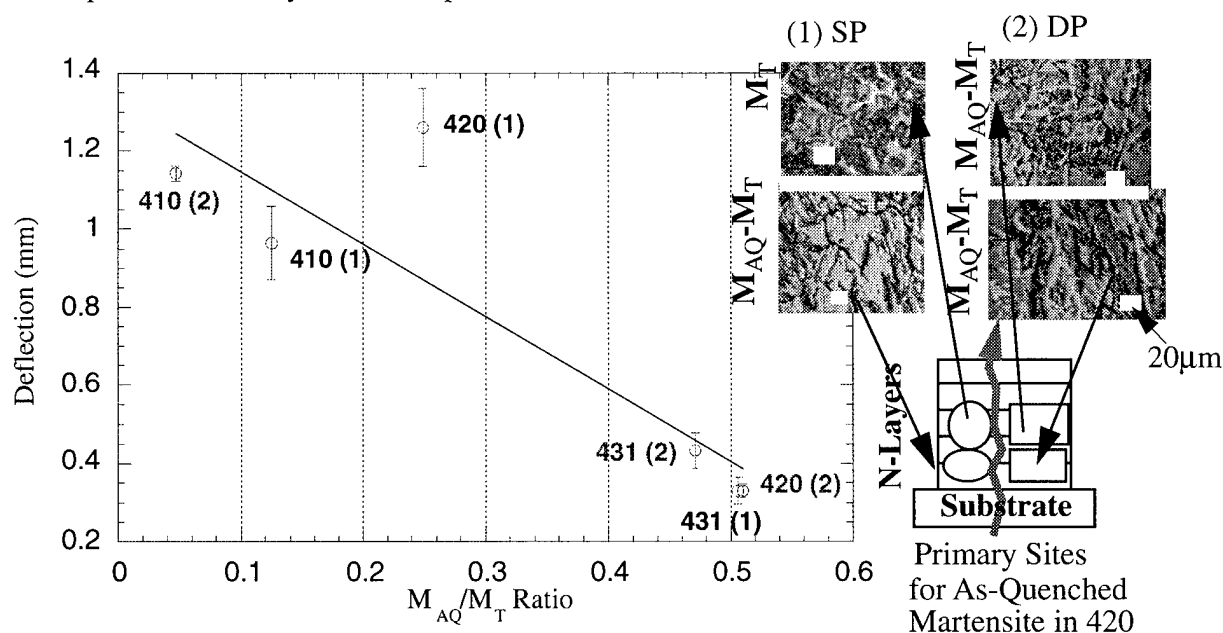


Figure 6. The effect of increasing M_{AQ}/M_T Ratio on deflection.

Multiple phases may be both detrimental and beneficial to material properties. A fully martensitic beam that is in the as-quenched phase may be too brittle to use. A beam that has ferritic phases could develop sigma ferrite which is a brittle phase often related to crack initiation points in metal. However, the retention of austenite or delta ferrite has been shown to increase

the toughness of martensitic parts [14]. Because of increased material toughness, prototype die inserts may be a promising use of this technology. Characterizing phase development in layered laser deposition will be one of the keys to reducing part deformation.

5. Conclusion

Solid Freeform Fabrication metal parts are disposed to failure from deformation caused by material responses to large temperature gradients and cooling rates. Deformation can be controlled with special fabrication strategies and heat treatment but with a trade-off of increased build time and finishing operations. However, laser layered manufacturing of carbon steels parts produces martensitic phase transformation which causes volumetric expansion, which has the potential to reduce or eliminate part deformation. Planar beams built by SDM technology significantly reduced deformation by inducing an as-quenched to tempered martensite ratio of .45 or higher.

6. References

- [1] L. Samuels, *Metallographic Polishing By Mechanical Methods*, 3rd Ed. 1982.
- [2] Fournery, "Surface Engineering of Tool and Die Steel," *ASM Specialty Handbook: Tool Materials*, (1995), pp.391-392.
- [3] W. K. Wang, C.J. Lobb, and F. Spaepen, "Formation of Metastable Nb-Si Phases by Picosecond and Nanosecond Pulsed Laser Quenching," *Materials Science and Engineering*, 98, (1988) 325-328.
- [4] L.J. Yang, S. Jana, S. C. Tam, and L. E. N. Lim, "The Effects of Process Variables on the Case Depth of Laser Transformation Hardened AISI 01 Tool Steel Specimens
- [5] F. Fouquet and E. Szmatura, "Laser Surface Melting of a Pearlitic Grey Cast Iron," *Material Science and Engineering*, 98 (1988) 305-308.
- [6] C. Rieker, D. G. Morris and M. A. Morris, "Microcrystalline surface layers created by laser alloying," *Journal of Less-Common Metals*, 145 (1988) 595-600.
- [7] Crucible Steel (1949), Rickett, Waltin, Butler (1952), Wang, Lobb, & Spaepen, (1988)
- [8] R. Merz, F.B. Prinz, K. Ramaswani, M. Terk, and L.E. Weiss, "Shape Deposition Manufacturing," *Proc. of Solid Freeform Fabrication Symposium*, The University of Texas at Austin, (1994) pp.1-8.
- [9] J. R. Fessler, Merz, A.H, Nickel and F. B. Prinz, *Proceedings of Solid Freeform Fabrication Symposium*, The University of Texas at Austin, (1996) pp.117.
- [10] E. Beraha and B. Shpigler, *Color Metallography*, (1977).
- [11] B. L. Averbach, L. S. Castleman, and M. Cohen, "Measurment of Retained Austenite in Carbon Steels," *Transactions of the ASM*, (1949) Vol. 42, pp112-120.
- [12] N. Williams and C. Carter, *Transmission Electron Microscopy - Diffraction*, Vol 2, (1996), pp.267-288.
- [13] D. Olson, T. Siewert, S. Liu and G. Edwards, "Selection of Wrought Martensitic Stainless Steels," *ASM Handbook: Welds, Brazing, and Soldering*, Vol. 6, (1993), pp.432-442.
- [14] G. R. Link, J. Fessler, A. Nickel and F. Prinz, "Rapid Tooling Die Case Inserts Using Shape Deposition Manufacturing," *Material and Manufacturing*, Vol 13, No, 2, (1998), pp. 263-274.

Acknowledgements: NSF, DARPA and the General Motors Metallurgy Lab

Controlling Heat Input, Spatter and Weld Penetration in GMA Welding for Solid Freeform Fabrication

I. Kmecko, D. Hu and R. Kovacevic
Southern Methodist University, Dallas, TX

Abstract

Two new approaches for metal transfer control during the GMA welding process, one based on a laser beam placed through the arc and the other based on real-time image processing, allow lower heat input, reducing spatter and weld penetration. The controlled welding process and CNC milling operation are combined together to form a hybrid rapid prototyping process. Test parts obtained in this procedure show better surface quality, dimensional accuracy and high density, while demonstrating new technological opportunities in rapid prototyping of real metallic parts.

Introduction

It has been recognized by several research teams [1, 2, 3] that the principles of the GMAW process could be used in the development of a cost effective method for layered deposition manufacturing or rapid prototyping (RP) of full dense metallic parts and tools. These attempts to use 3-D welding for building metal parts failed to incorporate a feedback control system between the controller and the welding system. Sensory feedback is a necessary requirement for improving the stability of the welding process [4]. Another way to stabilize the welding process is to use a milling operation to prepare the surface for a new layer. In several SFF techniques currently under development, a CNC milling operation is used to remove the metal build-ups in order to secure constant height of the generated layer [5].

The primary barrier to achieving quality welds in GMAW is the irregularity of the metal transfer process, i.e. the irregular growth and detachment of the droplets. Our interest is to develop a 3-D welding process for RP of real metallic parts using GMAW principles. 3-D welding process for RP requires low heat input and low weld penetration which is the exact opposite of the conventional welding process. Low heat input and weld penetration require low values of welding parameters such as current and wire feeding speed. On the other hand low values of the welding parameters provoke arc instability because associated short circuiting metal transfer or globular metal transfer mode can cause significant spatter [4]. This paper presents two new approaches for metal transfer control, one based on a laser beam placed through the arc and the other based on real-time image processing. Welding and milling are combined together to form a hybrid rapid prototyping process. Test parts obtained in this procedure show better surface quality and new technological opportunities in producing real metal parts.

Techniques for Low Current GMA Welding

The characteristics of the GMAW are best described in terms of the three means by which metal is transferred from the electrode to the workpiece: short circuiting,

globular and spray transfer. With low values of welding current and wire feeding speed, short circuiting or globular metal transfer will take place [6].

With short circuiting transfer, the molten weld metal necks down from the end of the electrode and touches the weld pool. During the shorting phase, the voltage drops and the amperage increases. The increased amperage produces what is called a pinching effect that causes the molten metal to detach (Figure 1a). As it separates from the electrode end, the arc reignites. If the pinch force current is too high, the weld metal will detach violently, creating spatter. The globular transfer is likely to produce the most spatter. With this transfer mode, a molten drop is formed on the end of the electrode, growing in size until it is detached by the force of gravity (Figure 1b). The droplet is usually larger than the diameter of the electrode and it separates in a nonaxial direction, which can result in metal droplets falling outside the weld pool. The droplet might even touch the weld pool before it detaches creating a mini-explosion that spews spatter.

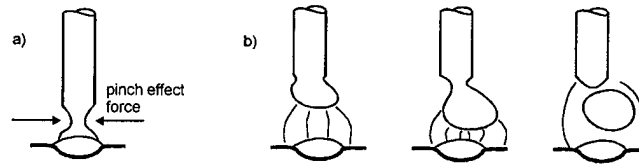


Figure 1. Short circuiting and globular metal transfer mode

Pulsed mode has been introduced to address problems with globular transfer mode. In pulsed mode, a power source provides two levels of current: one a constant, low background current which sustains the arc without providing enough energy to cause drops to form on the wire tip, and the other a superimposed pulsing current with an amplitude greater than the transition current necessary for spray transfer [6]. However, to guarantee one droplet per pulse, intensity and duration of the pulse current has to be carefully adjusted. Because of narrowness of the optimal range of welding parameters, such an open-loop selection of the pulse intensity and duration is often not robust with respect to the welding conditions. If the instant of detachment can be detected, the current may be switched to the base current to prevent multiple drops in a single pulse [7].

Active metal transfer control has been used to achieve one droplet per pulse [8]. A pulse cycle is divided into two periods: growth period and detachment period shown in Figure 2. In the growth period, a current level below the transition current is used. When the growth period ends, the current is switched to the base level and the process enters the detachment period. Sudden change in the welding current causes the droplet to oscillate vertically.

When the droplet moves down, the current is changed to the high level above the transition current for a very short time. The sudden increase of current provokes a high pinch force and together with the downward momentum it detaches the droplet. The process utilizes mechanical momentum to reduce the level of electromagnetic force required for the detachment, resulting in a reduction of the overall heat input.

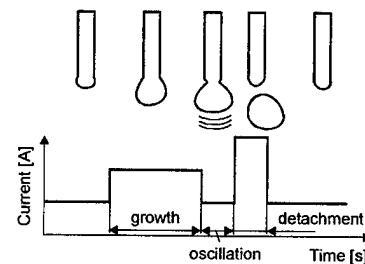


Figure 2. Droplet growth and droplet detachment pulse

Heat input is calculated as the ratio of the power (i.e., voltage x current) to the velocity of the heat source (i.e., the arc) as follows [9]:

$$H = 6 \frac{EI}{S}, \quad \left[\frac{\text{kJ}}{\text{m}} \right]$$

where E [V] is the arc voltage, I [A] current through the arc and S [cm/min] arc velocity.

In this paper we present two approaches that allow use of pulsed mode with low average current. These techniques for self-adjusting droplet transfer rate are based on:

- a) a signal provided by a laser beam placed through the arc and
- b) real-time image processing.

a) GMAW Control Based on Laser Beam Placed through the Arc

In 3-D welding, precise metal deposition is of crucial importance. One way to make metal deposition more accurate is to keep the arc length short so that a detached droplet can not be diverted out of the weld pool. The presented technique manages the arc to any desired length. An arc can be just long enough to avoid short circuiting. The control device consisting of a laser diode and photo diode positioned in such a way that the laser beam passes through the arc, as shown in Figure 3, has been used to control the welding process with wire 1.2 mm in diameter.

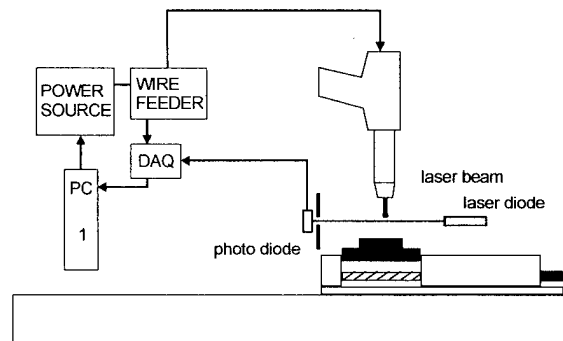


Figure 3. GMAW controlled by feedback signal from laser beam placed through the arc

While the wire tip is above the laser beam, background level current flows through the arc (Figure 4). Background current is very low and only keeps the arc on. Although wire tip melting should be avoided or at least minimized during the background current period, a droplet of molten metal slowly grows because of very low wire feed speed (~100 cm/min) and a relatively long duration (~ 65 ms, Figure 5). When the wire

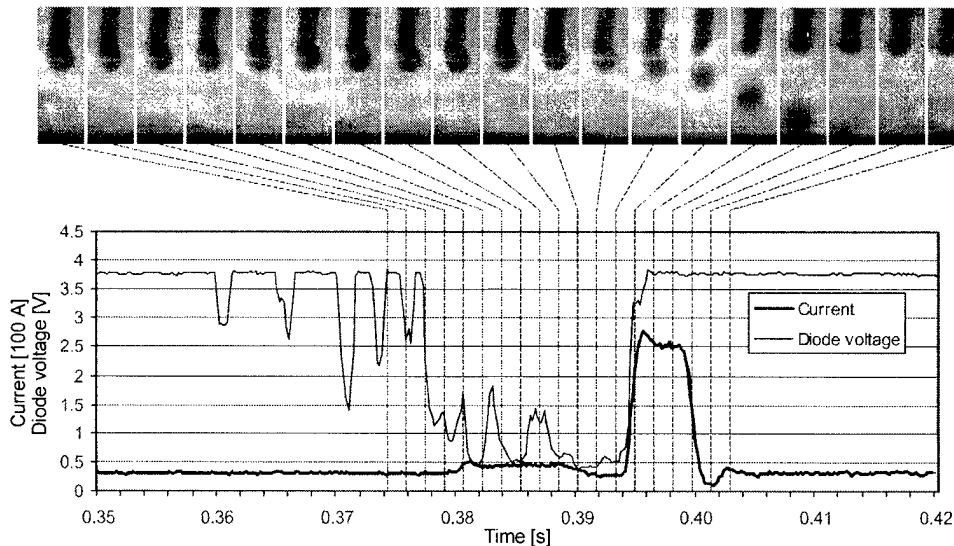


Figure 4. Feedback signal from photo diode, current through the arc and images of droplet growth and detachment

tip cuts the laser beam, diode voltage drops and a growing pulse is provoked. An increase of current by 25 % (from 40 A to 50 A, for 10 ms) means an increase of heat generation by about 50 % and is mainly intended to heat up the droplet and alleviate detachment. Current is then decreased to background level and suddenly increased to peak level introducing the detachment pulse (250 A, 5 ms). An increased electromagnetic force generates a large enough detachment force to detach the droplet from the electrode. Then the diode voltage signal is sensed and if it is still low (this is to say that droplet is still pending on the wire tip), another detachment pulse is provoked. Immediately following the detachment instant, the current is returned back to the background level. Workpiece speed was 40 cm/min, heat input 242 kJ/m.

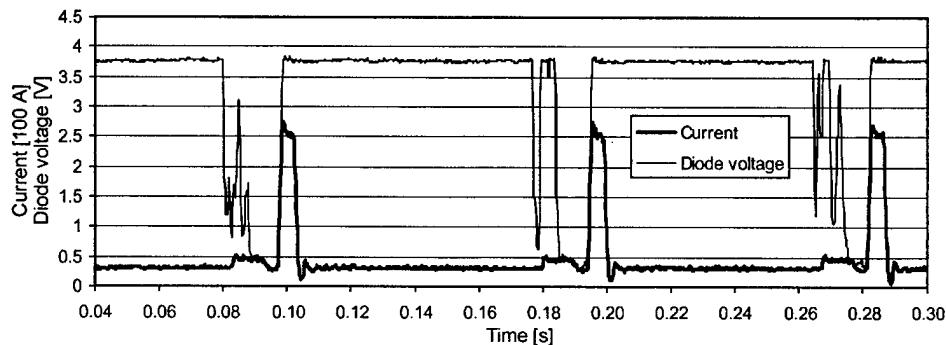


Figure 5. Feedback signal form photo diode and current through the arc

The number of pulses per second (i.e., droplet transfer rate) will be adjusted automatically based on wire feed speed. This allows the metal transfer rate to be regulated using the wire feeding speed as the lone variable ranging from 90 to 150 cm/min. It is especially useful in 3-D welding situations where for a short period of time the quantity of metal added to the weld pool has to be reduced (e.g., corner) or it is necessary to add more metal (e.g., root filling). In the hybrid welding and milling process (Figure 12), the motion control computer (PC 2) sends a signal to the welding control computer (PC 1) which metal transfer rate is appropriate, choosing from three possibilities: normal, minimal or maximal. This technique ensures constant arc length, automatically adjusts pulse rate and senses droplet detachment. Properly selected growth and detachment pulses ensure one droplet per pulse mode for a wide range of wire feed speed without changing any other welding parameter making this technique very robust and reliable.

b) GMAW Control Based on Real-Time Image Processing

A high frame rate digital camera (128x128 pixels) assisted with a He-Ne laser for back lighting, and a real-time image processing algorithm have been used to control the droplet formation during a welding operation (Figure 6). Images were captured by PCI-1424 Frame Grabber (838 images/s, PCI-bus 100 MB/s) and processed by PC based on Pentium II (350 MHz, 64 MB).

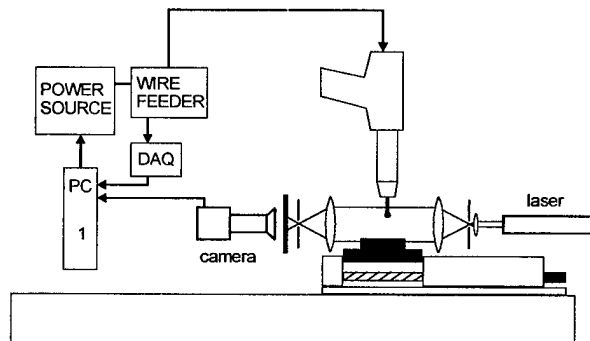


Figure 6. GMAW control based on real-time image processing

Real-time images are very valuable sources of information, and simple image processing can extract data such as arc length, droplet size and shape or droplet detachment instant. After thresholding, the binary image is processed in one of the three ways depending on the level of current flowing through the arc as it is shown in Figure 7. During the background current period the wire tip is continuously tracked by counting the number of lines that contain more than five black pixels from the top of the image to the bottom. When the wire tip is close enough to the weld pool, current is increased and growth period begins. During this period the number of black pixels in the last 20 lines used to determine wire tip position determines the droplet size. When the droplet reaches the desired size, current is decreased to the background level and then suddenly increased to initiate droplet detachment. During the detachment pulse, a simple artificial neural network (ANN) shown in Figure 8 has been employed to detect the droplet detachment instant.

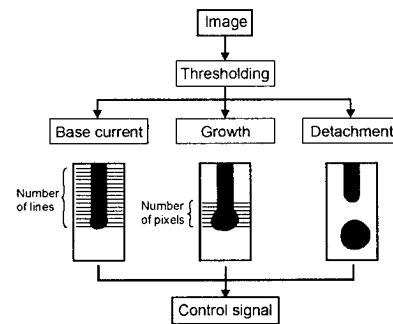


Figure 7. Schematically shown image processing sequence

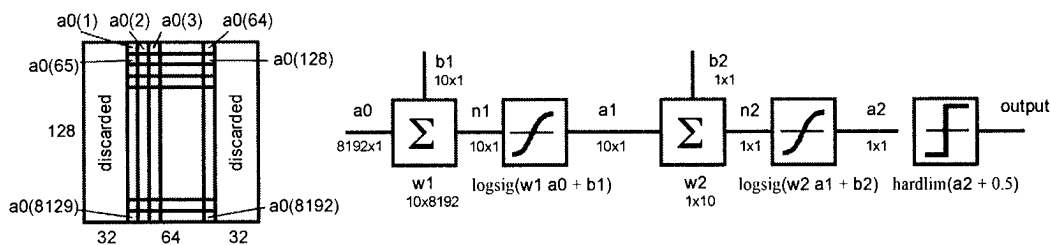


Figure 8. Artificial neural network used to detect instant of droplet detachment

ANN is a Multilayer Perceptron with one hidden layer containing 10 nodes. Input vector a_0 is a 128x64 region of interest transformed in a vector of 8192 elements (Figure 8). Transfer functions for the hidden layer and the output layer are log-sigmoid functions. At the end, a hard-limiter ensures that output will be 0 for a non-detachment situation or 1 when ANN recognizes droplet detachment. The network has been trained by alternatively presenting 25 images of a non-detachment situation and 25 images of a detachment situation. In Figure 9 real-time images presented to the network and corresponding outputs are shown.

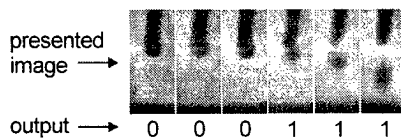


Figure 9. Images presented to the ANN and network outputs

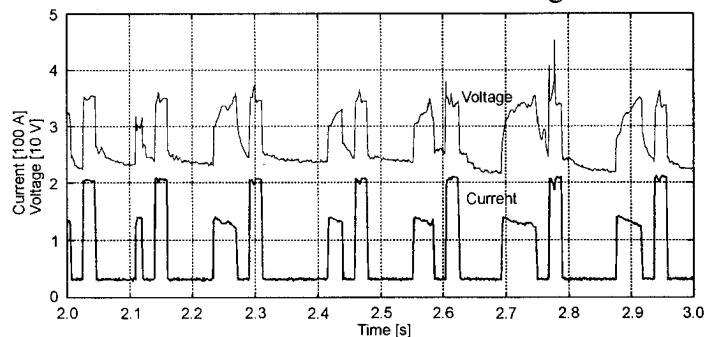


Figure 10. Current and voltage recorded during welding process

This technique ensures constant arc length, automatically adjusts pulse rate, controls droplet size and senses droplet detachment. With workpiece speed 45 cm/min heat input was 320 kJ/m. On the other hand, using an imaging system has its drawbacks. CPU speed and PCI bus capacity only allow successful control of up to 10 droplets per second. Also, the equipment is expensive and not suitable for industrial applications.

c) Short circuiting mode with thin wire (0.6 mm in diameter)

Short circuiting encompasses the lowest range of welding currents and smallest electrode diameters associated with GMAW [6]. This type of metal transfer produces a small, fast-freezing weld pool and is preferred in production of small parts and thin walls in 3-D welding. Metal is transferred from the electrode to the workpiece only during a period when the electrode is in contact with the weld pool. No metal is transferred across the arc gap, and this ensures precise metal deposition directly to the weld pool.

With wire of 0.6 mm in diameter, the welding current was 40 A, voltage 23 V, wire feed speed 290 cm/min ($0.82 \text{ cm}^3/\text{min}$), workpiece speed 36 cm/min, heat input 155 kJ/m. Shielding gas was

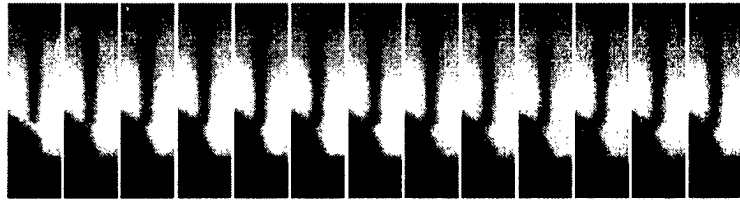


Figure 11. Short circuiting metal transfer mode

a mixture of 95 % Argon and 5 % CO_2 . Short circuiting metal transfer mode has the lowest heat input and the lowest possible metal transfer rate, but it is not the appropriate technique for welding with thicker wire (1.2 mm) because of significant spatter. The lowest values of welding parameters with 1.2 mm thick wire (globular metal transfer mode) were: average current 48 A, wire feed speed 90 cm/min ($1 \text{ cm}^3/\text{min}$), workpiece speed 36 cm/min, heat input 200 kJ/m.

Hybrid Rapid Prototyping Process Based on Welding and Milling

In spite of our success in controlling the welding process, the rapid prototyping process based on 3-D welding alone does not provide satisfactory dimensional accuracy and surface quality. Because of complete melting, the accuracy as well as the surface quality of parts are generally lower than that of machined parts. To overcome this difficulty, a combination of welding as an additive process with a subtractive technique such as milling can be an appropriate solution [3, 5]. This computer-controlled hybrid rapid prototyping system integrates the controlled GMAW process, which provides the controlled heat and mass transfer and precision depth control of bead penetration with a 2-1/2 axis CNC end and face milling operation (Figure 12).

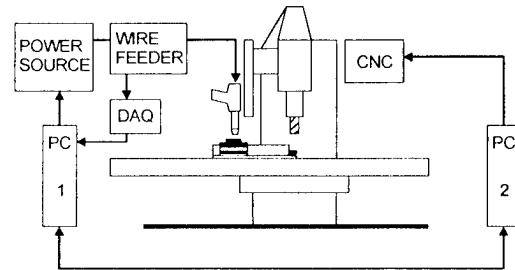


Figure 12. 2½ axis CNC hybrid rapid prototyping machine

The control system consists of two parallel microprocessors. The first processor (PC 1) controls the welding process and simultaneously acquires data from four channels. The first two channels are reserved for voltage and current measurements and the other two for acquiring signals from an infrared pyrometer and the light sensor. The second microprocessor (PC 2) controls the CNC milling machine. These two processors communicate, providing synchronization between the welding process and workpiece motion. This system offers a new way of building metallic parts in layered fashion with full density, high mechanical and metallurgical properties, high dimensional accuracy and good surface quality with complex geometrical features and sharp edges.

a) Building a wall

Building a metal wall consisting of single weld beads placed on top of each other is one of the basic procedures in 3-D welding. Poor surface quality and low dimensional accuracy are obtained by depositing metal layers without the milling operation because of small defects in the previous layer that become more and more amplified in subsequent layers. Using milling to prepare the surface for a new layer significantly improves surface roughness as shown in Table 1:

End milling can be used together with combined welding and face milling for further surface quality improvement. Additional milling operation increases time necessary to complete the layer, although the milling operation can be significantly shortened if high cutting speed machining is used due to small amounts of material that need to be removed. Also, surface quality is improved by making thinner layers. With face milling only, better surface quality was found in case when 0.5 mm thick layers were deposited comparing to the case with 1 mm thick layers.

Table 1. Surface quality in dependence of layer thickness and milling operations

Layer thickness	Face milling	End milling	Roughness
1.5	No	No	~ 1.3 mm
1.0	Yes	No	~ 0.9 mm
0.5	No	No	~ 0.6 mm
0.5	Yes	No	~ 0.3 mm
0.5	Yes	Yes	< 0.2 mm



Figure 13. Samples

b) Path planning for multiple beads layer

There is a number of commercially-available software for tool path planning for a subtractive milling operation, but we are not aware of the software that can generate the path plan suitable for an additive welding operation. Previous research [10] shows that

it is of highest importance to provide symmetric weld bead geometry and temperature conditions in order to have uniform metal flow. We tried to make multiple bead layers with various torch path plans and the best results were obtained with the path plan shown in Figure 14. A circumference bead is necessary to fill gaps created by irregular arc ignition and lower metal deposition at the end of the weld bead.

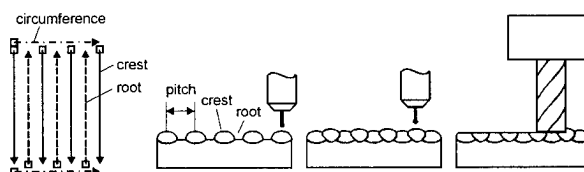


Figure 14. Correct weld trajectory

c) Making conformal channels

Making conformal channels is another basic technique in 3-D welding RP. The procedure of making conformal channels consists of the following steps: the part is built up layer by layer (every welded layer is face milled) to the point reaching the top of the channel, end milling is used to mill the conformal channel into the layered part (any shape in x-y plane), the milled channel is filled up with the support material (e.g. casting sand) covered on top with a thin sheet of metal in order to provide conditions to form an electrical arc, continue applying layers by welding and with successive face milling until part is finished, and finally, remove the support material in order to open up the channel.



Figure 15. Making channel by Hybrid RP

Conclusion

Sensory feedback is a necessary requirement to accommodate the welding process to suit 3-D rapid prototyping needs. Two new approaches for globular metal transfer control, one based on a laser beam placed through the arc and the other based on real-time image processing, allow welding with low heat input, reduced spatter and shallow weld penetration. Test parts produced on the hybrid rapid prototyping machine, consisting of controlled welding and CNC milling, showed better surface quality, dimensional accuracy and high density demonstrating new technological opportunities and manufacturing flexibility in producing real metal parts in a layered fashion.

Acknowledgment: This work is supported by the Texas Advanced Technology Program under Grant No. 003613-005-1997, National Science Foundation under Grants DMI-9700102 and DMI-9809198, Raytheon Co. in Dallas and Waco, TX and Leadwell CNC Machines Mfg. Corp., Taiwan.

References

1. P. Dickens, R. Cobb, I. Gibbson and M. Pridham, *Rapid Prototyping Using 3D Welding*, Journal of Design and Manufacturing, No. 3, 1993
2. R. Merz, F. Prinz, K. Ramaswami, M. Turk and L. Weiss, *Shape Deposition Manufacturing*, Proceedings of the Solid Freeform Fabrication Symposium, University of Texas, Austin, Texas, August 8-10, 1994
3. K. Karunakaran, P. Shanmuganathan, S. Roth-Koch and K. Koch, *Direct Rapid Prototyping of Tools*, Proc. of the SFF Symposium, University of Texas at Austin, Austin TX, August 1998, pp. 105-112
4. A. Cullison, *Get That Spatter under Control*, Welding Journal, April 1999, pp. 43-45
5. S. Yong-Ak, P. Sehyung, H. Kyunghyun, C. Doosun and J. Haeseong, *3D Welding and Milling for Direct Prototyping of Metallic Parts*, Proc. of the SFF Symposium, University of Texas at Austin, Austin TX, August 1998, pp. 495-502
6. *Gas Metal Arc Welding*, Welding Handbook, Chapter 4, AWS, 1996
7. Q. Wang and P. Li, *Arc Light Sensing of Droplet Transfer and its Analysis in Pulsed GMAW Process*, Welding Journal, November, 1997
8. R. Kovacevic and H. Beardsley, *Process Control of 3D Welding as a Droplet-Based Rapid Prototyping Technique*, Proc. of the SFF Symposium, Univ. of Texas at Austin, Austin TX, August 1998, pp. 57-64
9. R. S. Funderburk, *A Look at Heat Input*, Welding Innovation Vol. XVI, No. 1, 1999, pp. 8-11
10. J. Spencer, P. Dickens and C. Wykes, *Production of Metal Parts Featuring Heavy Sections Using 3D Welding*, Rapid Prototyping and Tooling Research, Edited by G. Bennett, Mech. Eng. Publications LTD., London, 1995, pp. 127-138.

CONTOUR CRAFTING – STATE OF DEVELOPMENT

**Behrokh Khoshnevis, Professor
Industrial & Systems Engineering
University of Southern California
Los Angeles, CA 90089-0193
Khoshnevi@usc.edu**

Contour Crafting, an additive fabrication technology that uses computer control to exploit the superior surface-forming capability of troweling to create smooth and accurate planar and free-form surfaces, is under development at the University of Southern California (USC). Using the layering approach afforded by troweling, an ancient process, a wide range of surface shapes may be created with fewer types of troweling tools than are needed for traditional plaster handwork and sculpting. Some of the important advantages of the patented Contour Crafting method compared with other rapid prototyping processes are better surface quality, higher fabrication speed, and a wider choice of materials.

Surface finish is a key issue that must be addressed in most rapid prototyping processes. The surface of the component is often rough because the component is created layer-by-layer, and in some techniques the layers are generated point-by-point. This roughness generally has a wavelength and amplitude that are proportional to the layer thickness. The approaches commonly employed to reduce the roughness include reducing the layer thickness and/or using post-fabrication grinding. Modifications to existing processes that improve the surface finish would be desirable for reducing fabrication time and cost.

A second limitation associated with most current rapid prototyping methods is the maximum size of the component that can be fabricated, which is generally not larger than a meter in any dimension. However, there is a need to fabricate large-scale components of various materials within a cost-effective time frame, particularly in the automotive and aerospace industries. With Contour Crafting components as large as real scale concept car models, can be made at relatively high speed with a variety of materials.

The key feature of Contour Crafting is the use of two trowels, which in effect act as two solid planar surfaces, to create surfaces on the object being fabricated that are exceptionally smooth and accurate. Artists and craftsmen have effectively used simple tools such as trowels, blades, sculpturing knives, and putty knives, shown in Figure 1, with one or two planar surfaces for forming materials in paste form since ancient times. Their versatility and effectiveness for fabricating complex free-form as well as

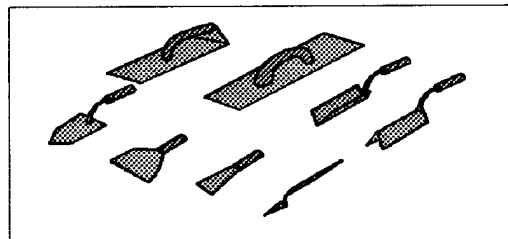


Figure 1. Traditional surface-forming tool

splanar surfaces is evidenced by ancient ceramic containers and sculptures with intricate or complex surface geometries as well as detailed plaster work that have shapes as complicated as flowers, on the walls of rooms. Surface shaping knives are used today for industrial model making (e.g., for building clay models of car bodies). However, despite the progress in process mechanization with computer numerical control and robotics, the method of using these simple but powerful tools is still manual, and their use in manufacturing is limited to model building.

In Contour Crafting, computer control is used to take advantage of the superior surface forming capability of troweling to create smooth and accurate, planar and free-form surfaces. The layering approach enables the creation of various surface shapes using fewer different troweling tools than in traditional plaster handwork and sculpting. It is a hybrid method that combines an extrusion process for forming the object surfaces and a filling process (pouring or injection) to build the object core. As shown in Figure 2, the extrusion nozzle has a top and a side trowel. As the material is extruded, the travel of the trowels creates smooth outer and top surfaces on the layer. The side trowel can be deflected to create non-orthogonal surfaces. The extrusion process builds only the outside edges (rims) of each layer of the object. After complete extrusion of each closed section of a given layer, if needed filler material can be poured (liquid monomers, for example) or injected (material in paste form, such as thermosets, ceramic or metal powders, cements,) to fill the area defined by the extruded rims.

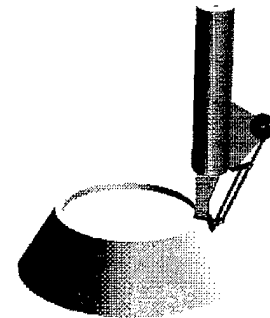


Figure 2. The extrusion assembly with top and side trowels

Some internal walls can be extruded within each layer to create square hatches or other types of hatches (see Figure 3). The hatching process may be required for large objects, since curing can start before the filler material gets a chance to spread over the entire surface of the layer. However, when hatching is used each of the small hatches is filled separately, which because of their small size allows more control over the spreading and curing of the filler material. Hatching can also accelerate the forming process because it provides for concurrent extrusion and filling (i.e., as the extrusion nozzle creates new hatches, previously made hatches can be filled). The computer positions the pouring outlet (or the injection mechanism) so that the liquid material is spread evenly within the enclosed layer. To control the amount of filler to be poured or injected, various types of sensors

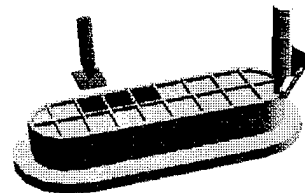
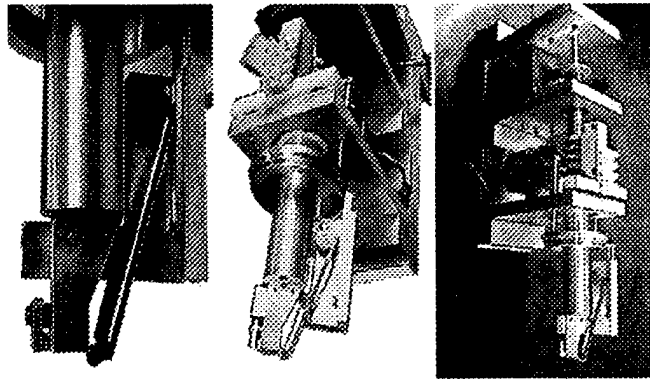


Figure 3. Internal hatches filled by pouring or injection

can be used.

One important characteristic of the special extrusion process used in this method is that the rim surface that faces the interior of the object does not require a smooth surface because it will be covered and bonded with the filler material. Therefore, despite unavoidable variations in the rate of extrusion, the outer and top sides of the extruded rim will be sharply defined and accurately controlled by the trowels, while excess material will be accommodated on the inner flank. Because of the intrinsic tolerance of this process simpler and less costly extrusion mechanisms can be used compared with those required in current fused deposition machines.

Configurations of the trowel assembly have been designed that can make top surfaces (and internal walls) and oblique surfaces with opposing slopes, that can fabricate overhangs and undercuts, as shown in Figure 4. Other designed variations can create doubly curved (e.g., spherical) surfaces.



Some advantages of Contour Crafting compared with existing rapid prototyping methods are:

Figure 4. Various views of the prototype nozzle

- ❑ Exceptionally smooth and accurate surfaces are created because of the elimination of surface discontinuities.
- ❑ Fabrication of a part is considerably faster because the layer thickness is typically much larger than layer thickness in other rapid prototyping processes.
- ❑ A wide variety of materials can be used, including thermosets, thermoplastics, metal and ceramic pastes mixed with a binder, and also materials that are not commonly used in rapid prototyping such as plaster, cement, clay, and concrete.
- ❑ Better structural properties afforded by the large size of the nozzle orifice which allows the addition of filler materials such as loose or continuous fiber.
- ❑ Prototypes and final parts much larger than 1 to 2 meters can be fabricated such as parts for airplane, automotive, marine, and building construction components (e.g., doors and windows) using large gantry-type robots for nozzle movement.
- ❑ Smooth internal surfaces of casting molds can be rapidly fabricated using the process.

Contour Crafting has certain limitations arising from the use of the side trowel. For example, very small hollow volumes, such as small holes, can't be made because they cannot accommodate the side trowel. Also it is not possible to use the side trowel to create features that are relatively thin (e.g., a vertical blade). In such cases, the extrusion deposition thickness may exceed the feature thickness. The extent of this limitation,

however, depends on the size of the side trowel, which could be 3 mm x 3 mm for fabricating small objects and 2 cm x 2 cm for large objects.

The principle feature of the Contour Crafting process is the use of a simple tool, i.e., trowel. However, despite the apparent simplicity of its principle, there are major challenges that must be overcome to successfully implement the concept. Two especially noteworthy challenges are: a) complicated shrinkage patterns due to bulk deposition of various materials, and b) complications in generation of tool (i.e., nozzle assembly) path, especially for sharp corners.

Experiments with Thermoplastics:

To date, we have constructed two Contour Crafting fabricators that can produce simple parts such as cylinders, cones, and planar surfaces using polystyrene. The extrusion system in these fabricators consists of a temperature-controlled nozzle and barrel assembly through which thermoplastic material, in the form of filament coils 3 mm in diameter, is fed via a system of gears and rollers. The first machine (Figure 5) has no environment control, while the second one (Figure 6) has a closed chamber the temperature of which can be controlled. With these machines we have built polystyrene parts that have a surface quality of 2.4 microns (96 micro inches). Note that for high quality die cast parts this figure is generally 3.1 micron (125 micro inches). The layers used to build the polystyrene parts were ranged from 1 mm to 5 mm thick. Figure 7 shows various rotational parts made by the process using polystyrene. Larger parts in this figure are 25 cm in height and each part is built in less than 20 minutes. A third machine for making more complicated shapes is under construction. The second machine was used extensively to study the impact of various process parameters such as trowel angle, extrusion rate, nozzle travel speed, layer thickness, cooling rate, etc. The informative results of these experiments are compiled in a Ph.D. dissertation [Russell, 1999].

Experiments with Ceramics:

We have applied the CC process to uncured ceramics such as plaster and clay-like materials, with

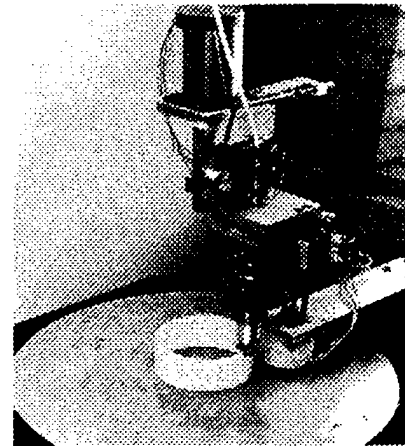


Figure 5. Machine 1 used for thermoplastics fabrication

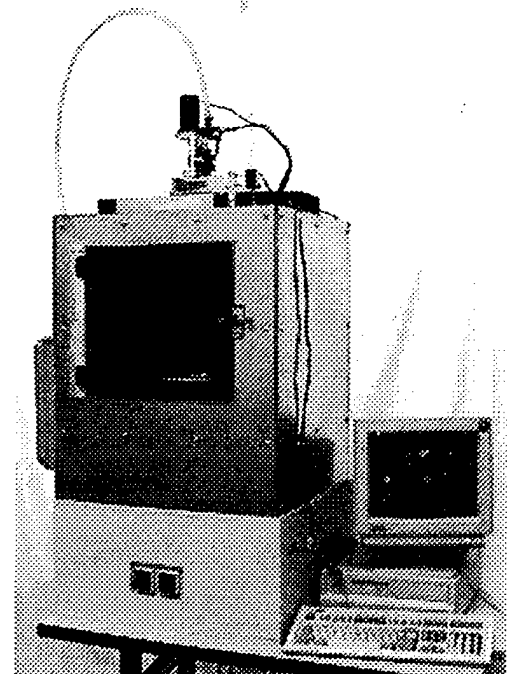


Figure 6. An environment controlled CC machine.

specific focus on achieving a high surface-finish with a minimum processing time, with the highest geometric accuracy. The machine shown in Figure 8 is customized for the CC processing of uncured ceramic materials such as spackling compound and clay models. The machine consists of a flat rotary worktable and a vertical extrusion system capable of rotary motion along its vertical axis and linear motion along three coordinate axes (i.e., a 4 axis machine).

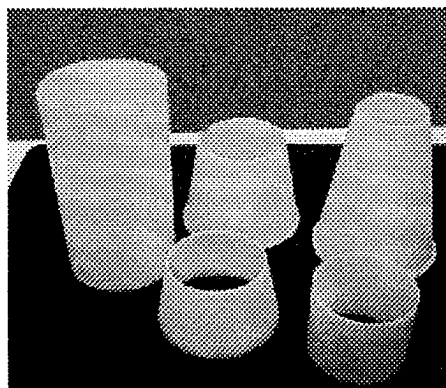


Figure 7. Some experimental rotational parts made out of polystyrene

An off the shelf spackling compound made by Custom Building Products, Inc. was used. It had the advantages of being commercially available, inexpensive, light in weight, and having quick setting time. The paste contains Acrylic Copolymer, Amorphous Silicate, 3% water per unit volume of material, and small spherical hollow glass fillers. The paste models have a complete setting time of approximately three hours after being exposed to air.

The clay used in our experiments was procured from America Ware, Inc. in Los Angeles. The clay contained: Pioneer Tak 2882, Taylor Ball clay, Barium Carbonate, Soda Ash, Sodium Silicate, and 35% water per unit mass. The clay models were produced at room temperature and then bisque-fired in a kiln at 1063°C - 1066°C for 10 hours. For glazing, a second firing at 1003°C was carried out for eight-nine hours.

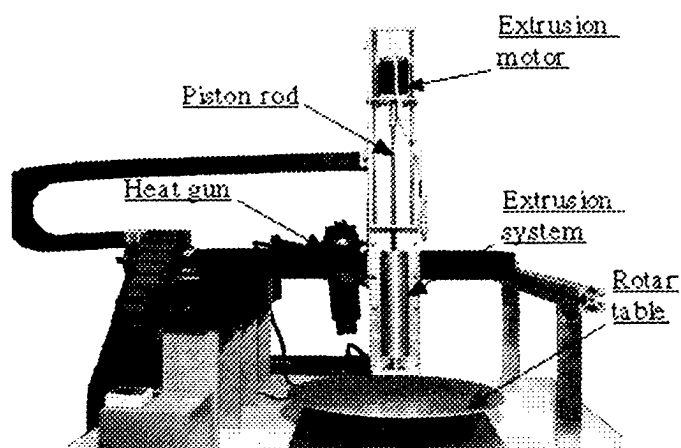


Figure 8. CC machine for ceramic part fabrication

Both the clay and paste models showed improved compressive strength qualities after compression through the extrusion system. This enabled the lower layers made of these two materials to maintain their shape and dimension even as additional deposited on them. As can be seen in Fig. 10 and 11, the layers directly below the point at which material was being deposited, compressed vertically and expanded horizontally but returned to their original form (spring-back) once the pressure was released. We believe that if the homogeneity of the material in the cylinder can be maintained, these effects would be consistent through every section of each layer, thus giving the model superior mechanical properties as compared to die casting methods of manufacturing.

Our current research efforts are focused on improving the process technology using spackling compound and clay, especially with regard to gaining physical and

experimental understanding of the influence of the various identified design parameters on the product quality. Furthermore, we are investigating the compressibility of clay, as well as the adaptability of the process mechanism to produce parts of different shapes. We are also working on a method of filling the extrusion cylinder, by which air pores contained in the raw material could be excluded simultaneously. A better surface finish and structural strength is expected to result from these endeavors.



Figure 9. Making clay parts with 3 mm layers

The pressure between the trowel and the upper layer of the model is a core factor affecting the surface quality of the CC process. Hence, we are thoroughly studying the correlation between pressure, and linear speed and extrusion rate with a finite element analysis method. We

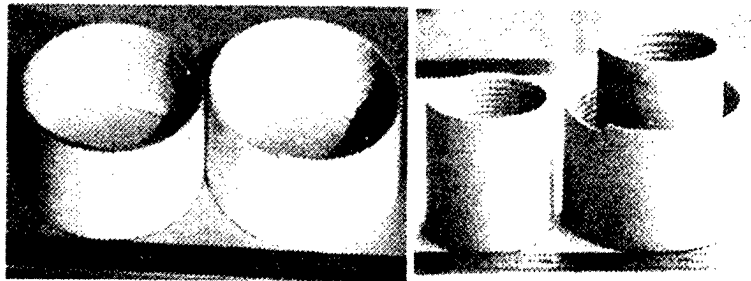


Figure 10. Parts made with spackling paste and clay

have also started creating non-rotational parts and refining our algorithms for creation of sharp corners. As the process is improved and refined, it is anticipated that composite as well as metal and ceramic parts will be fabricated. Blending the reinforcement phase with the powder particles prior to extrusion and deposition could make composite parts with particulate or short fiber reinforcements.

Software Development:

Unlike existing layering techniques, which assume uniform layer thickness and vertical sides for each layer, actual slopes of the sides of each layer must be considered in Contour Crafting. Therefore, an interface with solid modeling is required that involves approximating the surface with a series of horizontal slices that are not simply extrusions of a contour. This is because the apparatus has a trowel with variable orientation that can also be shaped for a better fit to the surface. This operation is more like 5-axis machining than the usual slicing for rapid prototyping, consequently, rather than working with an STL file, which is a polygonal approximation, Contour Crafting has to work directly from an exact solid model.

The path generated by moving the trowel to create a given surface is called trowel-path, which is different from conventional NC cutter-path. There are two major differences between the two paths: 1) cutter-path is based on cutting while trowel-path is based on press-forming, and 2) NC cutters are usually cylindrical while trowels are planar. Because of these differences, trowel-path generation should be based on new

concepts. totally new concept. Ultimately we should generate trowel-paths for 3D parts. Since parts are made layer by layer in CC, the 3D model of parts have to be sliced. Slicing is not a trivial in CC because of peaks and flat areas [Dolenc, 1994]. Again, unlike in other RP methods, slicing in CC has to incorporate an accessibility analysis, and hence it is a complicated procedure. We have approached this part of our research in two phases. First we have considered only 2.5D parts (i.e., sweeping models). Note that the profiles of several layers cut from each segment of a 2.5D model remain identical. Experiment on 2.5D will lay a foundation for dealing with other 3D cases, which we have started studying.

We classify the 2.5D model into three categories: polygon, composite curve (lines and arcs are mixed) and parametric curves such as B-Spline or NURBS. If any of these shapes is convex, then the trowel can access the entire surface and the trowel paths can be generated easily. In most cases, however, these curves are not convex. How to access the concave corner becomes an interesting challenge. We have developed a software system that deals with the above shapes. Convexity has to be determined in the beginning. For the polygon, we use the cross product of the forward and the backward vectors on each vertex to determine its convexity. Composite curves can be processed in the same way as polygons, however, they are always concave except in the tangential connection case. Determining the convexity of a parametric curve is different. In this case the whole curve is recursively sub-divided into small segments, then the cross product of consecutive normal vectors are used to determine the convexity of the curve.

After the shape is determined as concave, a special algorithm called tail-wiping is used to make the concave corner. The concept is that the trowel may go off the edge and the nozzle extrudes material outside the shape. But just before the material is solidified, the trowel's tail wipes it into the boundary of the shape. The tail-wiping can also deal with the inward arcs of the composite curve and the inward curve of the parametric curve.

Slicing a true 3D model faces different problems. First, the best direction for slicing has to be determined and the directions that results in more variations in contours must be eliminated. Second, the thickness of each slice has to be adjusted to avoid peak and flat surfaces. Finally, since the peripheral surface may not be parallel to the slicing direction, the appropriate trowel deflection angles have to be determined for each point around the slice. Our preliminary algorithm determining the deflection angle calculates the best-fit normal vector of the peripheral surface. Three normal vectors: top, bottom and middle are averaged to a mean vector. Then a delta of the surface and the best-fit surface is calculated. All features of a given part may be fabricated by CC if delta is within the tolerance of accuracy, otherwise the part may have features too small or tight for side trowel positioning.

We have developed a trowel path generator and an animation module for 2.5D designs using OLE Automation. The input of this path generator is a CAD system (IronCAD). The outputs are the G-code for CC machine and the simulation for visual verification.

The trowel paths are generated successfully from different shapes. We also have a Java version of trowel-path generator, which is more flexible than using a CAD system. We are working on an interface (using VBA) between CAD and our path generator to deal with true 3-D models. The path generator will optimize the slices, will compose 2D paths for each slice while determining trowel deflection angles, presents and animation of the toolpath, and finally generates the G-code for the CC machine.

Acknowledgement:

The research and development activities reported in this paper have been supported by two National Science Foundation grants.

References:

1. A Dolenc and I Makela, "Slicing procedures for layered manufacturing techniques" *Computer-Aided Design*, Vol. 26, No. 2, February 1994, pp 119-126
2. Debasish Dutta and Prashant Kulkarni, "Improving Surface Quality and Throughput in Layered Manufacturing by Adaptive Slicing," 7th International Rapid Prototyping Conference, San Francisco, 1997, pp 94-101.
3. Andrei S. Novac, Cheol H. Lee, Charles L. Thomas, "Automated Thchnique for Adaptive Slicing in Layered Manufacturing," 7th International Rapid Prototyping Conference, San Francisco, 1997, pp 85-93.
4. Calvert, P. "Extrusion Freedom Fabrication of Epoxy Resins," Proceedings of the 1996 NSF Design and Manufacturing Grantees Conference, Albuquerque, New Mexico, January 1996.
5. Crockett, R., O'Kely, J., Calvert, P., Fabes, B. Stuffle, K., Creegan, P, and R. Hoffman, "Predicting the Controlling Resolution and Surface Finish of Ceramic Objects Produced by Sterodeposition Processes," Proceedings of Solid Freeform Fabrication Conference, Austin, Texas, August 1995.
6. Khoshnevis, B. "Innovative rapid prototyping process makes large sized complex shapes in a variety of materials," *Material Technology*, Vol 13, No. 2, 1988, pp 53-56.
7. Khoshnevis, B. S. Bukkapatnam, H. Kwon, j. Sato "Experimental investigations into Contour Crafting for ceramic materials," Proceedings of NSF Grantees Conference, Long Beach, January 1999.
8. Russell, R. "An experimental approach to analyzing polystyrene melt flow when troweling using the Contour Crafting Process," PhD dissertation, University of Southern California, August 1999.
9. Tunaboylu, B., McKittrick, J., Nellis, W.J., and Nutt, S.R., "Dynamic Compaction of $\text{Al}_2\text{O}_3\text{-ZrO}_2$ Compositions," *J. Am. Ceram. Soc.* 77 [6] (1994) 1605-12.
10. Yeh, Z., "Trowel Path Generation for Contour Crafting," Research Progress Report, University of Southern California, June, 1999.



Large Scale Prototyping A Case Study

Alair Griffin
CEO
Javelin, Salt Lake City, UT

Dr. Charles Thomas
Professor
University of Utah

Introduction

Imagine a statue, made out of bronze, more than three times taller than the Statue of Liberty, designed to last 1000 years. That is what Javelin was asked to do when the Maitreya Project contacted them for prototyping assistance in the summer of 1998 .

The Maitreya Project, an international Buddhist organization plans to build the largest statue in the world. They plan to build a 500 foot representation of the Maitreya Buddha in Bodhgaya, India, a Buddhist holy place located in northeast India, just south of Nepal. The Maitreya statue will be significantly larger than Japan's 394 foot high Ushiku Buddha [1, 2].

A hand-sculpted original model of the statue was created by commissioned artists. In order to evaluate architectural perspective, the hand-sculpted statue was sent to Javelin's facility in Salt Lake City, Utah so that the original artwork could be captured digitally and a 5:1 scale-up produced.

Accurately and rapidly reproducing the original statue while at the same time minimizing costs pushed the current limits of Solid Freeform Fabrication (SFF) technology. While the original intent of the work conducted in Salt Lake City was to create a computerized version of the hand-sculpted statue's geometry, produce a 5:1 scaled model and verify the CAD file, the project grew to encompass much more than that.

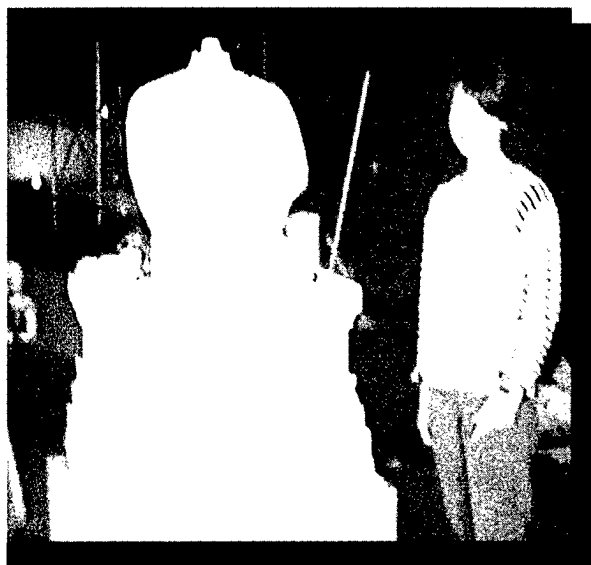
Approach

The Maitreya Buddha model, built by Javelin, made use of the several reverse engineering (RE) and SFF technologies that included:

- Computer-aided design (CAD)
- Digitizing
- Fused Deposition Modeling (FDM)
- CT scanning
- 3D Printing
- Soft Tooling
- U-of-U Shapemaker 2000™ System

It was recognized, from the start, that building a 20 foot statue entirely using one of the more common rapid prototyping systems, such as stereolithography or FDM, would be both too expensive and slow for the Maitreya Project budget and time-frame constraints. Computer Numerical Control (CNC) machining was initially considered but the approach was rejected because the costs required to produce CNC code were out-of-line for the budget. One group estimated that it would take at least a month to generate the multiple 5 axis machine code and they would not guarantee specific geometry features associated with undercuts and overhangs.

After a review of model-making options, a water-jet system under development at the University of Utah, appeared to have the best potential for building the majority of the statue's geometry. The decision was made to proceed with the 5:1 scale-up using their water-jet based rapid prototyping system. 3D Printing and FDM systems were selected as backup for features that were too small to build in foam, based on cost and strength, respectively. Because no computer model existed for the hand-crafted Maitreya Buddha, significant effort was required to create polygon and NURBS-based solid models.



Original Artwork and Denise Griffin,
Maitreya Artist



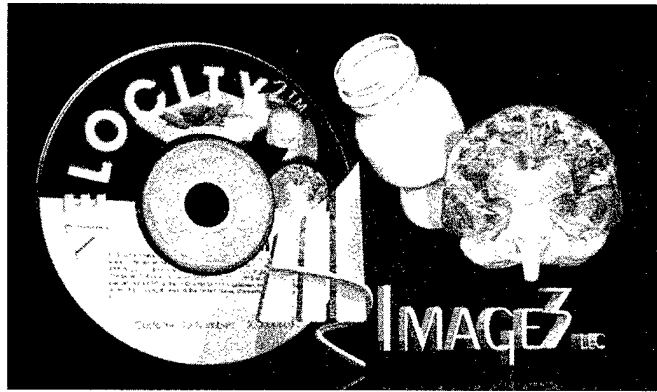
Maitreya Buddha [3]

Reverse Engineering

Reverse engineering (RE) involves taking an existing part for which there is no accurate CAD data (perhaps because the part is old or was modified after the mold was made) and essentially recreating the part. Most RE approaches involve imaging or digitizing the RE object and then cre-

TM University of Utah's Ruled Edge Layer Prototyping System

ating a computerized reconstruction that can be integrated, in 3D, into the particular design environment. The process of capturing the geometry, extracting contours and surfaces from reconstructed images, and creating a CAD-compatible representation is the most common example of reverse engineering. Related activities, such as extracting defect and dimensional data from the image and comparing the results with an already existing CAD model is commonly referred to as part characterization.



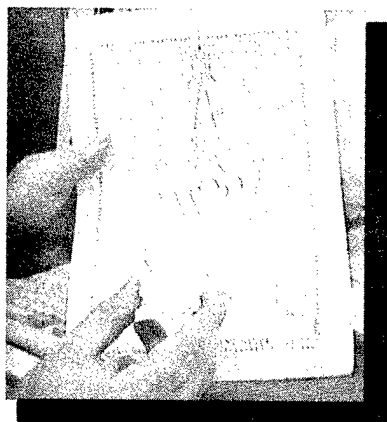
CT Scans Were Reconstructed
Using Velocity² Software [4]

The Maitreya statue sent to Javelin was a work-in-progress. This created significant RE challenges. When received at Javelin's studio, the statue's head was not attached to the body. Neither were the ears, hair curls, hair knot, stupa or the third eye. Only one foot had been sculpted, and that too, was not attached to the body. The original artwork arrived in Salt Lake City at the end of September. The goal was to finish the 5:1 foam scale-up by the end of November. Because laser scanning typically creates very large data sets, digitizing was selected to capture the majority of the geometry. Even with an approach that concentrated on file size minimization, the medium resolution polygon model contained over 800,000 polygons.

Digitizing was supplemented by CT scanning and/or CAD for geometry features that were either missing or too small for digitizing. In this case, digitizing also produced a "cleaner" model - one where imperfections pointed out by the artist could be avoided versus laser scanning that will faithfully reproduce the item - including flaws.

Some pieces of the art were not suitable for digitizing as the hand-crafted pieces were either very small, on the order of a few inches, or missing. Some pieces, such as the decorative patterns that will be found on the statue's throne, underwent CT scanning and the images were

reconstructed using Velocity² software to produce the STL file needed for SFF.



Artist's Stupa Drawing and
Small Sculpture Representation

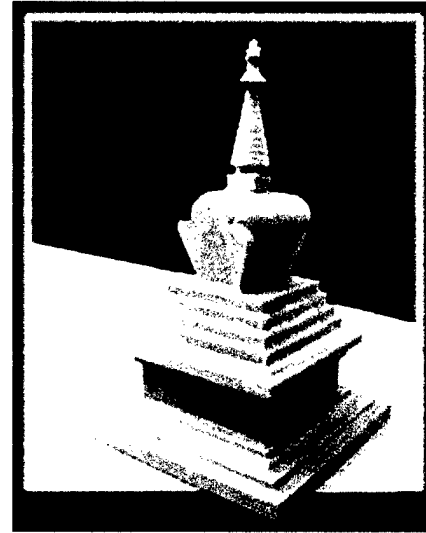
Computer Aided Design

Wherever possible, features were identified that could be modeled using high-end CAD packages such as SDRC's I-DEAS, Pro-Engineer, Maya, and Alias Wavefront. In some cases, artistic sketches were available. Other features were created from information provided by the artists. The Stupa, Hair Curls, Hair Knot, and the Third Eye of the Maitreya Statue were computer designed by engineers using advanced CAD programs.

Mirroring

The Project also wanted to mirror sections of the statue. The artists felt that features on the right side of the statue were better defined and more artistically pleasing than the left side. Wherever possible, they wanted to mirror right-side features. With digitizing it is fairly easy to define mirror regions. Items that were mirrored during digitizing include:

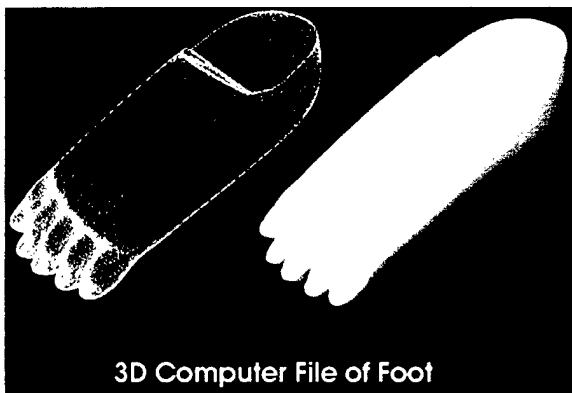
- Left side of the face was mirrored from the digitized data from the right side,
- Right half of the neck was mirrored from the digitized data from the left side,
- Left half of the torso's lap and lower legs were mirrored from the digitized data from the right side, and
- Left foot was mirrored from the right foot.



3D Printed Stupa Formed From
CAD File Modeled By Javelin
5:1 Scale

While mirroring assures that left and right halves are identical, it created unique computer file and actual statue alignment “fit” problems. Specific problem areas included:

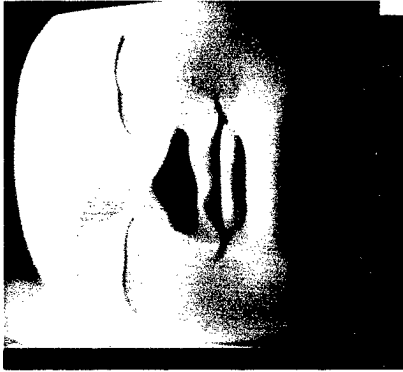
1. Making the Hair Curls fit on the curvature of the head. Imagine a bathing cap that fit snugly on a head. Then a different version of the head was created by mirroring the right side of the head. The new, mirrored head will have a slightly different size and curvature. Fitting the same bathing cap, snugly, to the new head could be difficult, if not impossible without changing the size of the bathing cap.
2. Making the “mirrored” lap torso fit identically to the upper body torso that was not mirrored.
3. Extended hand placement. The statue's extended left arm rests on top of the left knee. On the original statue, the thigh of the left knee is actually longer than the thigh of the right knee. For the computer file, the mirrored right knee was used. However, in the mirrored version the back of the hand touches in a slightly different location because of the “shorter” knee. With a 5 times scale-up, this different hand placement created visual concerns.



3D Computer File of Foot

Computer File Created From Digitized Right Foot. The Left Foot Was Created From the Mirror Image of the Right Foot.

4. The face presented the most significant “mirroring” problems. This was done to allow the artists to choose between faces. The left mirrored face was rejected outright by the artists, they absolutely did not like the left mirrored face.



Polystyrene Head
Built on the U of U system.
Right Side of the Face was Mirrored

While mirroring allows a computer file to be created that is more "exact" in its geometry features than an original piece of art, it can also result in visually different geometry. Care should be taken to understand the impact of mirroring and not assume that visual differences are due to problems in construction or computer modeling.

File Sectioning and Manipulation

The University's system employs a 4' by 5' build envelope. The 3D file had to undergo electronic sectioning to fit within the build envelope. Several CAD packages were used to achieve this. Sectioning of the computer file was further complicated by eventual statue shipping requirements. Each portion of the 20 foot statue could not exceed, including packaging materials, the maximum allowable crate size for air cargo.

Solid Freeform Fabrication

Once the STL file was approved by the artists, the University's system was used to cut over 90 % of the statue's geometry, layer-by-layer, out of 1 lb density polystyrene foam sheets. Cutting occurred over 25 days and 256 hours were logged. The statue contains over 2000 layers. Most of the layers were 1/2" thick, although quarter inch sheets were used to build the head and the hands.

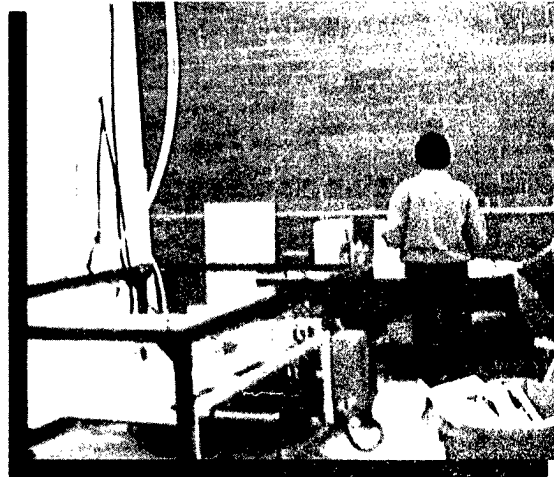
The Ruled Edge Layer Prototyping System (Shapemaker 2000™) under development at the University of Utah allows the production of prototypes directly from STL files. The Shapemaker software first slices the STL file into thick layers (1/4" to 2") where the layer edge is approximated by a sloped surface to better approximate the CAD geometry. A high pressure water jet is then used to cut these ruled edged layers from plastic foam. The dramatic advantage provided by the water jet cutter is that the cutting tool has a diameter of less than 0.01". The com-



Upper Statue Torso After Computer File Sectioning

bination of layered decomposition and a small diameter cutting tool allows the Shapemaker to produce a complex geometry quite easily.

For example, the hand shown below contains geometry that would be difficult to machine. Machining would require a skilled machinist to develop a manufacturing plan including multiple setups and probably sectioning of the hand into smaller machinable parts (in order to machine between the fingers). The Shapemaker was used to build the part in a single standard procedure. Each slice, often containing multiple pieces, was contained in a registration box that allowed the entire slice to be handled as a single piece during registration and bonding. This piece was cut, registered, and bonded in roughly 4 hours.



University's System Running in
Javelin's Studio

Some of the statue's features were too small to be built on the Shapemaker. The Third eye, Stupa, and Hair Knot were built in ABS using FDM. Also, a mirrored ABS foot was built for the original statue, as the artists never created a left foot for their original artwork. The artists covered the ABS foot with the same resin that they sculpt with and then attached the coated ABS foot to the original statue.

3D Printing was the SFF process used to create sign-off models for the artists as different sections of the large model were being produced. 3D Printing was also used as patterns for soft tooling of the Hair Curls and Ears.

Rapid Tooling

About 300 hair curls were needed for the statue's head. Hair Curl patterns were built on Javelin's 3DP machine. These patterns were used during the creation of soft tools. Polyurethane foam was shot into the tools to produce each hair curl. The statue's ears were also produced in this manner.

Measurements

Over 80 measurement points were used to document build accuracy. A Design Factor (DF) was calculated for each measurement and the difference between the actual and calculated



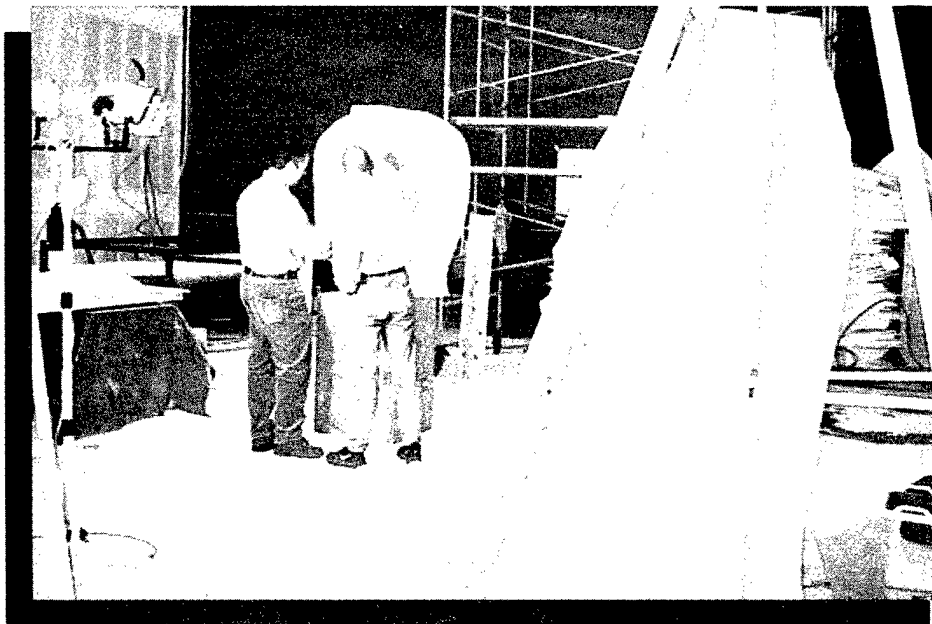
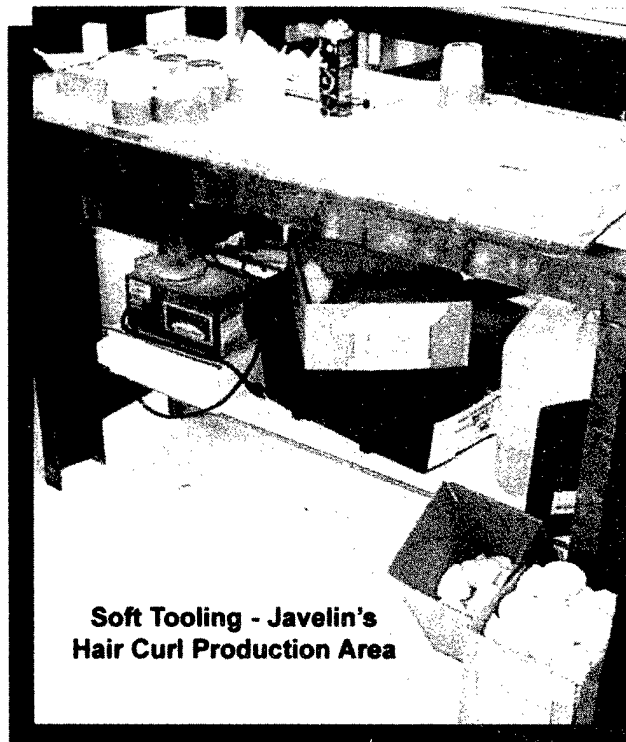
Computer Model
of the Raised
Hand (left) and
the Actual 5:1
Hand Built in
Foam (above)

5 times scale-up was determined. An overall DF of 5.05 was achieved. That Design Factor, for a scale-up of this magnitude, is very good. An overall build variance of 1.06% was obtained.

Realistically, variations should be expected from the original statue. Because the artists felt that the left side of the hand-sculpted statue was not as "finished" as the right side, portions of the statue were not digitized but were improvised by mirroring the opposite digitized sections designated by the artists.

Additionally, many portions of the hand-sculpted statue simply were not completely finished. The artists gave directions to compensate for the missing geometry and feature placement so that the CAD files could be created. As a result, some of the geometry does not exist on the hand-sculpted statue. For example, the ears were never attached to the original statue, therefore measurements cannot be taken for comparative purposes with respect to the ears.

Similarly, final placement of the Stupa, Hair Knot and Hair Curls were not completed by the artists on the original statue. These minor issues with the original statue complicated measurement comparisons.



**Peter Griffin, Maitreya Project Artist and Scott McMillin, Javelin Engineer,
Discuss Foam Head Build Progress in Javelin's Studio**

Finishing

The decision to have Javelin finish the statue rather than artists employed by the Project occurred during the actual build period. Finishing consisted of:

1. Hand sanding,
2. Coating / patching with a latex-based filler,
3. Sealing with a latex paint,
4. Polyurethane protective hard coat, and
5. Metallic gold paint.

More hand work was done on the foam model than had been anticipated due to a combination of factors. The thickness (z height) of 1 lb density foam sheets was found to vary considerably. Since the statue was built in several "blocks", problems were encountered with aligning different glued sections. Additionally, it was found that the artists had a tendency to re-work the polystyrene foam statue as if it had become the art-piece rather than a copy of the original art. This created quality control problems and greatly contributed to the amount of hand finishing required.



Hand Sculpted Statue Shown with the 5:1 Scale-up in the Background



20 Foot Statue Assembled in Javelin's Parking Lot Prior to Painting. Small, Hand-sculpted Statue is in Front of the Large Statue.

Summary

The completed statue was shipped to the Land of Medicine Buddhist Center in California where it is currently on display. A second 20 foot statue is planned for the Fall of 1999.

References

1. "Big Buddha Takes Shape in South Salt Lake" in the *Salt Lake Tribune*, 12/5/98.
2. "Rapid Prototyping Builds Karma for the Next Millennium", March, 1999, in *Rapid Prototyping Report*, Vol 9, No. 3, CAD/CAM Publishing.
3. Rendering produced by CounterPoint Studios, Salt Lake City, UT. CAD file created by Javelin, Salt Lake City, UT and Viewpoint DataLabs, Provo, UT.
4. Velocity² software is an Image3, Salt Lake City, UT product.

HARD METAL TOOLING VIA SFF OF CERAMICS AND POWDER METALLURGY

Mukesh Agarwala, Donald Klosterman, Nora Osborne, and Allan Lightman
University of Dayton Research Institute, 300 College Park, Dayton, OH 45469-0150

Robert Dzugan, EMTEC, 3171 Research Blvd., Dayton, OH 45420.

Geoff Rhodes, Crucible Materials Corp., 6003 Campbells Run Road, Pittsburgh, PA 15205

Christian Nelson, DTM Corp., 1611 Headway Circle, Bldg. #2, Austin, TX 78754

ABSTRACT

In the past five years, Solid Freeform Fabrication (SFF) Technologies have been explored for fabrication of functional ceramic components. This presentation describes the use of SFF ceramic components as pre-forms in a Powder Metallurgical process to form net shape metal tooling for manufacturing processes, such as injection molding, die casting, etc. The approach involves metal powder consolidation around a SFF ceramic pre-form. Two different SFF approaches, Laminated Object Manufacturing (LOM) and Selective Laser Sintering (SLS), were used to fabricate ceramic pre-forms. The SFF ceramic pre-forms and the consolidated metal tooling were evaluated for density, dimensional accuracy, and surface finish. Results will be presented on the consolidation of tool steel using both the SFF ceramic pre-forms.

BACKGROUND

Dies and molds constitute one of the most significant costs associated with manufacturing processes such as injection molding, die casting, etc. Currently these dies and molds are fabricated by machining wrought tool steels, such as H13. Machining is extremely costly, time consuming, and generates high amount of scrap. The machined die or mold is then subjected to appropriate heat treatment to impart the desired microstructure and properties. The heat treatment often causes dimensional instability and warpage. Machining also imposes restrictions on the tool geometry that can be fabricated. Incorporation of cooling passages, a critical feature for enhanced performance, is almost prohibited by machining. Use of conformal channels in dies and molds can increase manufacturing throughput by over 25% to as much as 70% [1,2].

Hot Isostatic Pressing (HIP) is a preferred Powder Metallurgical (P/M) process for hard to consolidate materials such as ceramics and refractory metals. A major benefit of using P/M dies and molds is the ability to produce near-net shape cavities directly by HIP; thus, minimizing input material and subsequent machining. Furthermore, HIPed dies and molds, using rapidly solidified pre-alloyed powders, have been shown to out-perform cast and wrought-machined tools [3]. However, widespread use of HIPed dies and molds has been precluded due to the difficulty and high costs in fabrication of pre-shaped HIP cans with complex geometry.

In a prior effort, Crucible Materials Corp. has demonstrated that a ceramic pre-form can be successfully used in HIPing of pre-alloyed tool steel powders to fabricate dies and molds [4]. Use of a ceramic pre-form precluded the need for pre-shaped HIP can and also allowed incorporation of conformal cooling passages in the dies and molds. Widespread use of this approach has been hampered by conventional issues associated with use and insertion of ceramics in industry, namely, high cost and long lead times for ceramic component fabrication.

Solid Freeform Fabrication (SFF) technologies have demonstrated that the long lead times and costs for ceramic prototype fabrication can be cut significantly [5]. Use of SFF technologies to fabricate ceramic components has largely been limited to demanding aerospace type applications. The use of ceramics as pre-forms in the HIP process mandates that the ceramic pre-form be low cost and easy to fabricate to keep the dies and molds affordable.

This article describes the fabrication of ceramic pre-forms using two SFF processes, Laminated Object Manufacturing (LOM) and Selective Laser Sintering (SLS), and their use in the HIP process to fabricate tool steel mold cavities, Figure 1. To keep the fabricated dies and molds cost effective, it is important to keep the time and costs low in fabricating the ceramic pre-forms. Also, to avoid carburization and/or nitridation of the tool steel during HIPing, it is preferable not to use carbide and/or nitride ceramics. Prior work has shown that fully dense or high density ceramic pre-forms are not required for successful HIPing of tool steel cavities. In fact, high density ceramic pre-forms make their removal from the HIPed steel cavity difficult. Conversely, very low density ceramic (<70%) is not suitable for successful HIPing. Therefore, it is necessary to determine the minimum density under which HIPing can be successfully performed. Furthermore, lower density ceramic pre-form fabrication will require low sintering temperature and/or time, which result in lower shrinkage during the process.

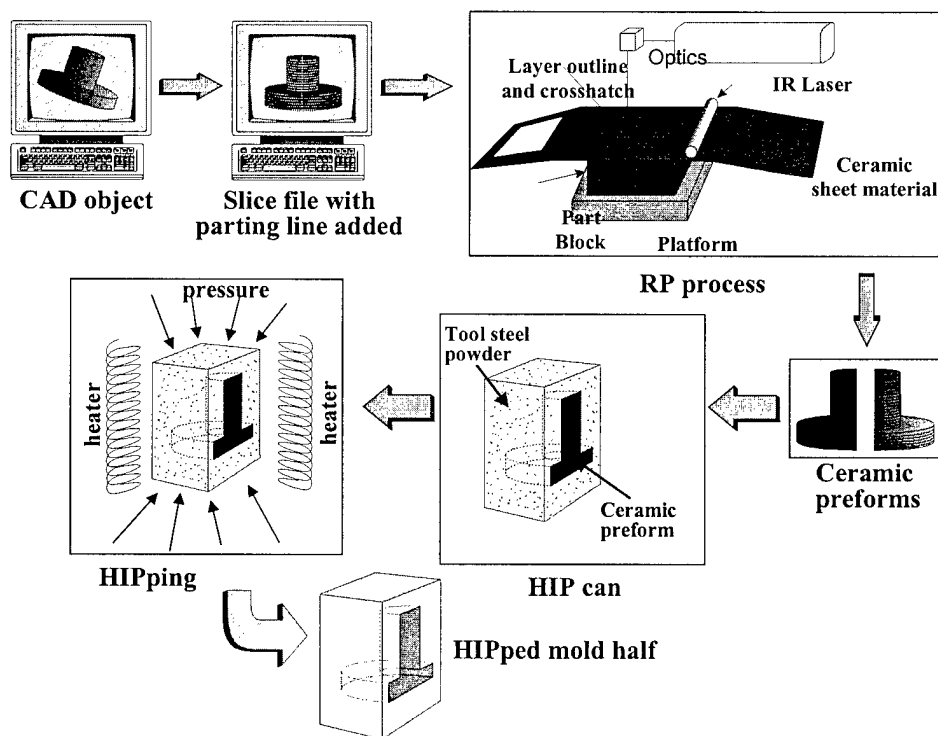


Figure 1: Schematic representation of the entire process employed in this study to fabricate mold and die cavity from SFF ceramic pre-forms.

LAMINATED OBJECT MANUFACTURING (LOM) OF CERAMICS

In the past five years, the University of Dayton and Lone Peak Engineering (LPE), Salt Lake City, Utah, have successfully developed the Laminated Object Manufacturing (LOM) process to fabricate ceramic components using green ceramic sheets as feed materials [6-8]. The LOM process results in a green ceramic part, which is then subjected to conventional thermal cycles of binder burn out and sintering/infiltration to produce a dense ceramic component.

LOM of Alumina:

LOM of alumina has been successfully developed and is commercially practiced by LPE. Continuous rolls of 12" wide and 0.010" thick green alumina tapes, from LPE, were used for this effort. The alumina tapes consist of 55 volume percent Alcoa A16 alumina powder with the balance a thermoplastic binder suitable for LOM processing. The tapes were successfully used

in the LOM process to fabricate simple green shapes and were analyzed by Scanning Electron Microscopy (SEM) for inter-layer bonding. The green alumina LOM parts were then used to develop the appropriate binder burn out cycle. The fully burned out LOM alumina parts were also analyzed by SEM. Through a series of LOM trials, binder burn out trials, and analysis, suitable LOM processing and binder burn out conditions were established for defect-free part (1" to 2" cross-section) generation.

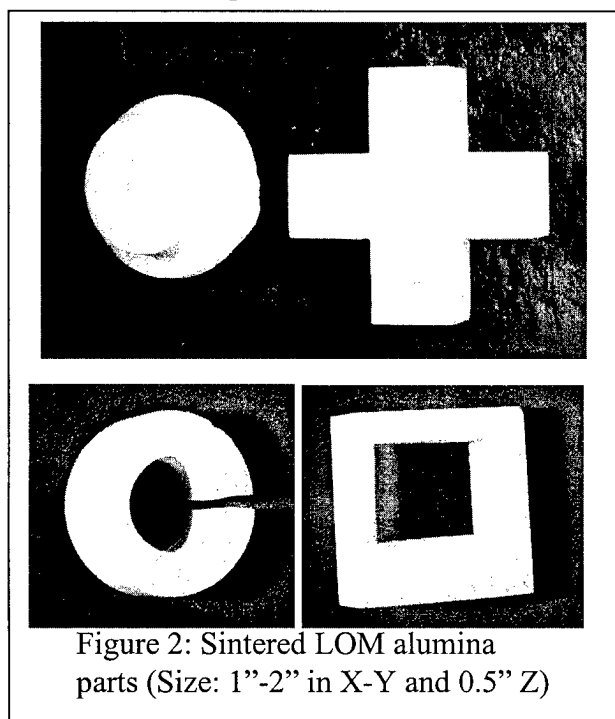


Figure 2: Sintered LOM alumina parts (Size: 1"-2" in X-Y and 0.5" Z)

To evaluate the feasibility of using LOM alumina pre-forms in HIPing, four simple LOM alumina samples (1"-2" dimension) were fabricated and subjected to binder burn out and sintering at 1650°C for 6 hours, Figure 2. The bulk density of these samples was 90%-92%. The average linear

shrinkage was: ~17% in X and Y and ~20% in Z (LOM build direction). These samples were then used in the HIPing of tool steel to form mold cavities, discussed later.

A series of sintering experiments were performed with the LOM alumina parts. Through

Table 1: LOM Alumina Sintering Data

Sintering Condition	Sintered Density (%)	% Shrinkage	
		X & Y	Z
1650 °C, 6 hours	90	15	17
1500 °C, 4 hours	77	10.8	12.7
1450 °C, 4 hours	72	8.9	10
1500 °C, 1 hour	68	7	8.5
1450 °C, 1 hour	65	5.75	7

these experiments, sintered density and shrinkage data was established as a function of sintering temperature and time, Table 1. This data will be used in fabricating LOM alumina samples with varying density for evaluation in HIPing of tool steel mold and die cavities.

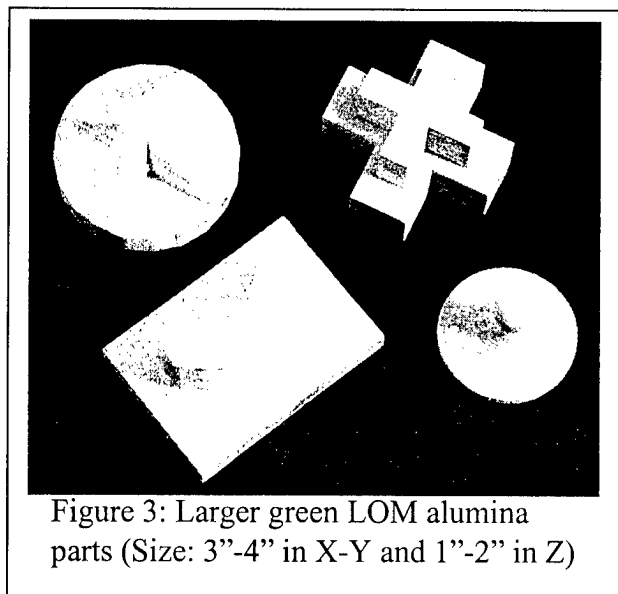


Figure 3: Larger green LOM alumina parts (Size: 3"-4" in X-Y and 1"-2" in Z)

Molds and dies used in manufacturing processes can be from a few inches to several feet in dimension. Fabrication of large ceramic pre-forms are prohibited due to the limited size of the SFF systems and due to difficulty in successfully removing binder from large ceramic pre-forms. The technology in this article is expected to be suitable to fabricate molds and dies with sizes limited to less than 8" – 10". To demonstrate the ability to fabricate larger LOM ceramic pre-forms, a series of four 3"-4" samples were fabricated using alumina, Figure 3. These samples have been successfully processed to 70% - 80% sintered densities and are currently being used in HIPing of steel cavity.

LOM of Silica:

Fused silica is low cost and is the most commonly used ceramic in industry. Therefore, it is most desirable to develop and use silica pre-forms for HIPing of tool steel molds and dies. However, LOM of fused silica has not been explored or developed. The silica powder selected for the process is a refractory grade fused silica. The average particle size of the powder is -325 mesh and its typical chemical composition is: 99.7% SiO_2 , 1150 ppm Al_2O_3 , 185 ppm Fe_2O_3 , 57 ppm CaO , 29 ppm Na_2O , and 58 ppm K_2O .

Green silica tapes for LOM were developed with a binder system used successfully in prior ceramic LOM efforts. 10" wide and 0.008" thick tapes were cast with 84 weight % silica powder and 16 weight % binder. The silica tapes have been successfully used in fabricating simple parts by the LOM process.

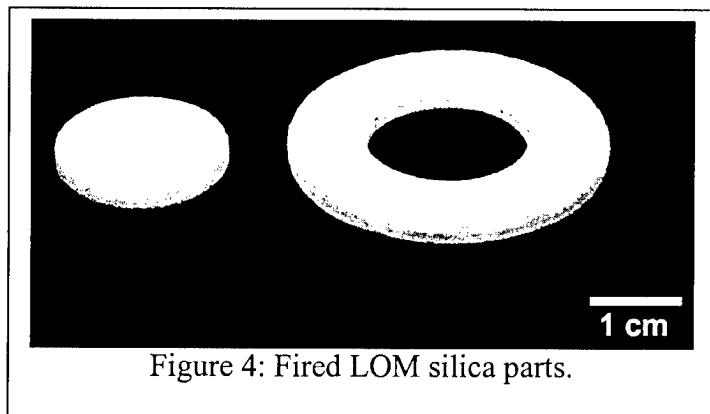


Figure 4: Fired LOM silica parts.

Simple LOM green silica parts were used to establish suitable binder burn out schedules. Following successful binder burn out, the samples were subjected to firing at temperatures of 1100°C and 1300°C for 2 to 6 hours, Figure 4. The fired part density ranged between 70% and 80% of theoretical density of fused silica (2.2 g/cc). Associated firing shrinkage was 1% - 3% in X and Y and 3%-5% in Z.

Simple LOM silica samples are currently being processed (similar to those shown in Figure 2 for alumina) for their use in HIPing of tool steel cavity.

SELECTIVE LASER SINTERING (SLS) OF CERAMICS

Selective Laser Sintering (SLS) is a SFF process, commercialized by DTM Corp., Austin, Texas. Several ceramic systems, with binder, have been explored for use in the SLS process. Due to the low packing density of the powder bed during the SLS process, the green SLS processed parts have relatively low green densities. The low green densities of the SLS processed ceramics have limited their use in many applications. However, two ceramic systems, called SandForm™ Si and Zr, have been successfully developed and commercialized by DTM for use as shell foundry cores in the casting industry. SandForm™ Si and SandForm™ Zr are polymer (thermoset resin) coated silica and zircon sand materials. Under the current practice of SLS SandForm™, the resin partially cures to hold the sand particles together during SLS processing. Following the SLS processing, the resin is fully cured in an oven at 50 to 150°C. The sand (ceramic) particles employed in the process are considerably coarse (140 mesh average particle size). Further, the green density of the parts is extremely low (<50%). These conditions are sufficient for their use as casting cores and match very closely with those used conventionally in foundries. For this study, SLS SandForm™ parts require complete removal of the resin binder followed by firing to achieve the desired density.

Based on thermal analysis of the SandForm™ powders, suitable conservative binder removal cycles were employed to completely remove binder from the SLS processed SandForm™ Si and Zr parts. Under all burn out cycles and conditions, although the binder was completely removed from the samples, due to the low green density of the parts and the coarse particle size, the parts did not retain structural integrity.

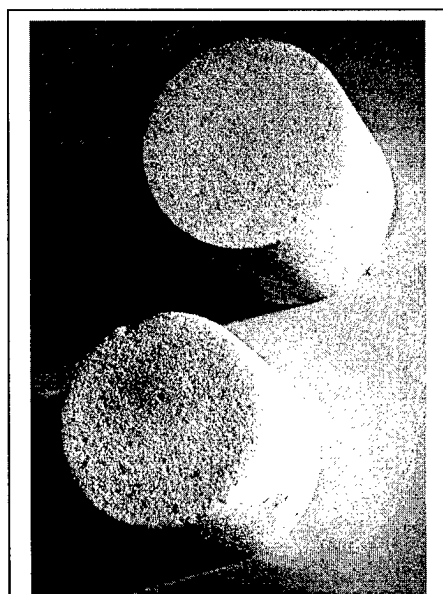


Figure 5: Pressed and fired SandForm silica parts

Improving the green density of SLS processed SandForm™ parts requires modifications to the material and/or the SLS process itself. Therefore, an alternative strategy was explored to first evaluate the suitability of the SandForm™ materials for HIPing of tool steels. This strategy involved fabricating higher green density SandForm™ parts by pressing the powders instead of subjecting them to SLS processing. If it is found that the pressed SandForm™ samples, with improved green density, are suitable for HIPing, then it will form the basis to pursue increasing the green density of SLS processed parts by tailoring the material and the SLS process.

SandForm™ silica powder was pressed in a 1" diameter die in a pneumatic press capable of heating. The pressing temperature and pressure was varied to achieve maximum green density in the pressed samples. The maximum silica green density achieved was 1.88 g/cc, which is 34% higher than the green density of SLS processed silica SandForm™ parts (1.4 g/cc). The pressed silica samples were subjected to binder burn out followed by firing under different firing temperatures and times. The fired density of the samples varied between 65% - 80% theoretical density of silica (2.2 g/cc). The pressed and fired samples, Figure 5, were then used in HIPing of tool steel.

HOT ISOSTATIC PRESSING OF TOOL STEEL WITH SFF CERAMIC PRE-FORMS

Hot Isostatic Pressing (HIP) of tool steel was performed using the LOM alumina samples, shown in Figure 2, and the pressed SandForm silica samples, shown in Figure 5. The tool steel powder used in this effort was a rapidly solidified, pre-alloyed tool steel powder called CPM Nu-Die V that is equivalent to AISI H-13. The chemical composition of the powder is 0.39C, 0.39Mn, 0.010S, 1.01Si, 5.23Cr, 0.43Mo, 0.96V and balance Fe.

The first step in HIPing is the preparation of the “can” (HIP container) containing the powder to be HIPed. In this effort, tool steel cans with 0.25” wall thickness were used. The cans had a 0.25” thick base and lid plates, with the lids drilled to accept a fill/evacuation stem. In addition, the lids were machined to have a stepped diameter fitted into the can ID to facilitate welding without contamination of the powder. After grinding the inside surfaces to a 60 grit finish, the bases and can bodies were welded together.

A 1/8” uniformly distributed layer of tool steel powder was filled in the can and then the ceramic pre-form is placed at the center of the can body. The can was then filled to within 1/8” of the top with tool steel powder. The powder in the can was not packed mechanically to prevent the ceramic pre-form from moving. The lid was then placed atop the can body and welded into place. Additional powder was added to the cans to bring the powder level about 1/2” up into the fill stems. This entire process is shown schematically in Figure 6. The stem is then topped off with some more tool steel powder. The entire assembly is then evacuated from the fill stem to -10 μ m with a -10 μ m/minute leak rate at 300°F. The stem is then sealed under vacuum. The evacuated and sealed can assembly is placed in a Hot Isostatic Press for HIP operation.

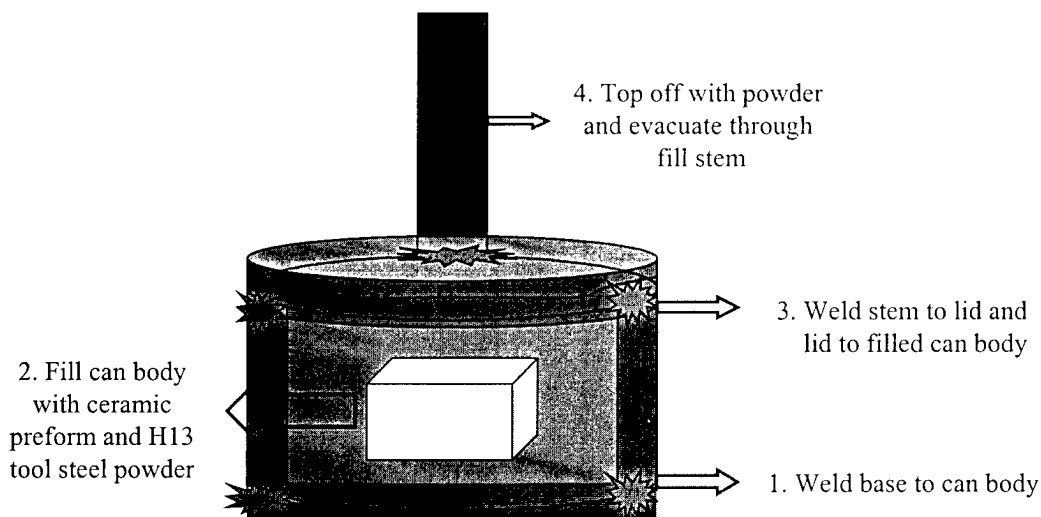


Figure 6: Schematic of the HIP “can” assembly employed in this study.

The HIP cycle used in this study was specifically developed by Crucible for HIPing of the tool steel with ceramic pre-forms [4], shown in Figure 7. In the HIP cycle, the HIP chamber is first evacuated. The temperature is then increased to 2100°F and then the pressure is increased to 1,000 psi. The temperature and pressure are kept constant for 2 hours. The low pressure heating is specifically designed for HIPing when using ceramic pre-forms, to prevent ceramic cracking due to thermal or mechanical shock. The low pressure heating and hold also allows the

tool steel to undergo preliminary densification and conform around the ceramic pre-form. The pressure is then increased to the final consolidation pressure of 15,000 psi, with the temperature held at 2100°F. The final pressure and temperature are held constant for 4 hours.

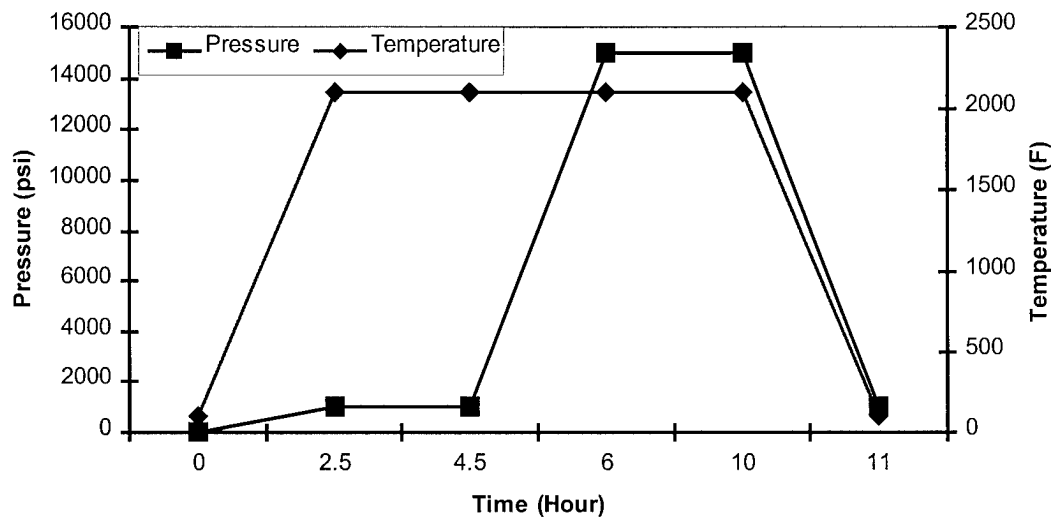


Figure 7: HIP cycle employed in this study

After HIP, the cans exhibited expected shrinkage indicative that the tool steel powder had densified during HIP. The fill stems were cut off flush with the tops of the can lids. The bottom plate in the can assembly is machined to expose the HIPed tool steel layer. The top plate is then machined parallel to the bottom. This is followed by blanchard grinding from the bottom until the ceramic pre-form surface is exposed.

Although the ceramic pre-forms did not exhibit any deformation or change in size, surface cracks were observed in the LOM alumina pre-forms. However, close examination of the HIPed tool steel powder and the alumina surface cracks indicated that there was no

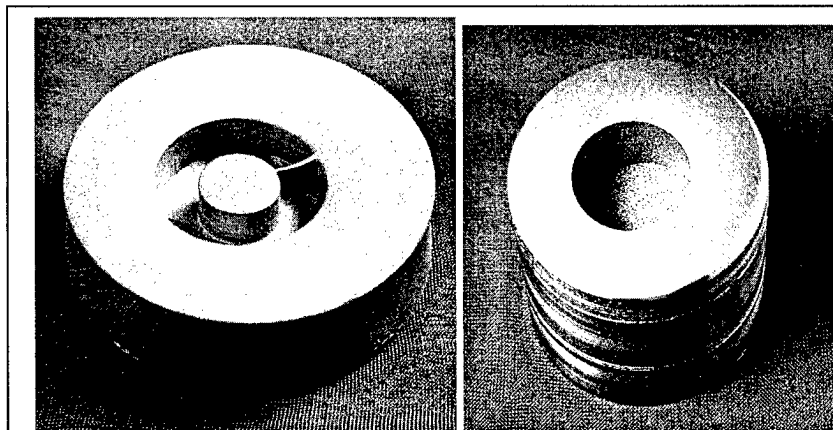


Figure 8: HIPed tool steel cavity fabricated using LOM alumina (left) and pressed SandForm silica (right)

penetration of tool steel powder into the cracks. This observation suggests that the ceramic pre-forms cracked during the HIP cool down stage, after complete consolidation of the tool steel. The cracks occurred during the cooling process due to the thermal expansion mismatch between alumina and steel. No such cracks were observed in the pressed SandForm silica samples.

Removal of the LOM alumina pre-form from the HIPed steel cavity has proven to be difficult. Due to high density of the alumina pre-forms, destructive techniques using diamond

drilling and other techniques resulted in partial removal of the pre-forms. Grit blasting resulted in complete removal of the ceramic pre-form. However, grit blasting caused some wear of the HIPed steel, Figure 8. Removal of the pressed SandForm silica pre-forms was much easier. The silica pre-forms were removed by blowing away the ceramic using pressurized air, Figure 8.

The dimensions of the tool steel cavities formed using LOM alumina as well as SandForm silica were within 1% of the dimensions of the ceramic pre-forms used in forming them. The surface finish of the cavities formed using LOM alumina reflected the layered finish present in the LOM alumina pre-forms. Similarly, the surface finish of the cavities formed using the pressed SandForm silica reflected the coarse surface finish arising due to the coarse particle size of the SandForm powder.

FURTHER EFFORT

LOM of alumina and silica and SLS of SandForm™ ceramic pre-forms are being further developed for HIPing of tool steel mold and die cavities. This effort involves:

- Optimizing the alumina and silica LOM process for larger parts (8").
- HIPing with lower density alumina and silica LOM samples.
- Efficient ceramic removal approaches, including coating of the pre-forms.
- Tailoring the SandForm™ material and the SLS process for higher green densities.
- Fabrication of demonstration injection mold inserts and their performance evaluation in the molding process.
- Incorporation of conformal cooling channels during HIPing in the mold inserts, using the SFF ceramic pre-forms.

Reference:

1. E. Sachs, "Rapid Low Cost Tooling for Injection Molding," DARPA Defense Sciences Manufacturing Programs Meeting, November 1997, Washington DC.
2. P.F. Jacobs, "New Frontiers in Mold Construction," NASA Tech Briefs, Vol. 23, No. 3, March 1999.
3. W. Stasko, et. al., "Tool and Die Material from Rapidly Solidified Powders," Rapidly Solidified Materials: Properties and Processing, Annual Meeting of ASM International, 1988.
4. V.K. Chandhok, et. al., "Process for Producing Parts with Deep Pocketed Cavities Using P/M Shape Technology," Titanium Net Shape Technologies, F.H. Froes and D. Eylon Eds., TMS-AIME, Warrendale, PA, 1980.
5. Proceedings of the Solid Freeform Fabrication Symposium, 1990-1998, The University of Texas at Austin, Austin, TX.
6. D. Klosterman, et. al., "Direct Fabrication of Ceramics, CMCs by Rapid Prototyping," Amer. Ceram. Soc. Bull., 77(10), October 1998.
7. D. Klosterman, et. al., "Automated Fabrication of Monolithic and Ceramic Matrix Composites via Laminated Object Manufacturing (LOM)," Proc. of the 8th Solid Freeform Fabrication Symposium, August 1997, The University of Texas at Austin, Austin, TX.
8. C. Griffin, J. Daufenbach, S. McMillin, "Desktop Manufacturing: LOM versus Pressing," American Ceramic Society Bulletin, 73 (8), August 1994.

Applications of FFF in The Metal Casting Industry

Rui Jiang, Wanlong Wang, James G. Conley
Department of Mechanical Engineering
Northwestern University
Evanston, IL 60208

Abstract

Fast Freeform Fabrication (FFF) is widely used in the casting industry, for tooling in sand casting, investment casting and die casting to save time and to take advantage of the variety of build materials, e.g. polymer, paper, ABS plastics, powder, wax and so on. A FFF process chosen to make patterns or cores depends on the nature of the casting processes, the availability and capability of the FFF machines among other requirements, e.g. production volume, accuracy, time, cost, and durability. This paper investigates applications of FFF in foundry processes. Issues discussed include the application of FFF models and the limitations and frontiers of those applications.

Key words: Fast Freeform Fabrication(FFF), casting, mold, master pattern.

Introduction

Fast Freeform Fabrication(FFF) refers to the physical layered production of digital design representations using a special class of machine technology. FFF systems quickly produce models and prototype parts from computer-aided design(CAD) model data, CT and MRI scan data, and data created from 3D object digitizing systems. Using an additive approach to build shapes, FFF systems join liquid, powder and sheet materials to form physical objects. Layer-by-layer, FFF machines fabricate plastic, wood, ceramic, and metal parts using thin, horizontal cross sections of the computer model^[1]. Table 1 gives a brief overview of several FFF processes.

Casting is a pervasive material forming process in which parts are produced by casting melt material into precise molds. It is estimated that more than 90% of metal parts are created by sand casting processes^[2]. Figure 1 shows a cross section view of a typical sand casting mold with terminology defining significant features^[3].

Market competition has intensified in all industries with the advent of information technology and global economy. Companies are experiencing increasing pressure to reduce product introduction lead time and cost as part of their continuous effort to gain and sustain competitive advantage. These pressures have led to far reaching new developments in the fabrication of tooling for traditional manufacturing processes such as casting. In particular, it is now possible to generate tooling directly from a CAD database by using a variety of fast freeform fabrication processes. These methods are widely referred to as *rapid tooling*(RT) processes

because the tool geometry is created in relatively short time^[4]. In this manuscript we limit our discussion to Rapid Tooling in foundry processes.

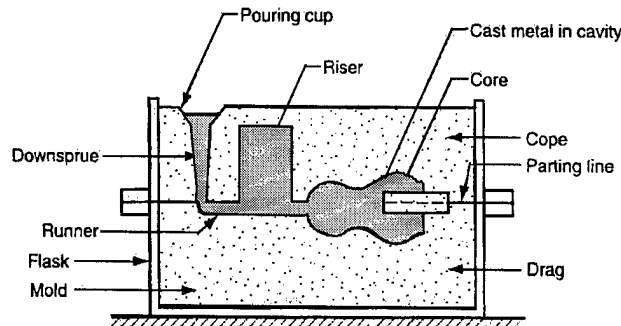


Figure 1. The cross section view of the typical sand casting mold

OEM	FFF process	Raw materials
3D Systems	SLA	Acrylate and epoxy photopolymer resin
Cubital	SGC	Acrylate and epoxy photopolymer resin
DTM	SLS	Nylon, polycarbonate, copper polyamide, resin-coated sand and polystyrene
Helisys	LOM	Paper, sheet plastic, Glass-ceramic composite, ceramic tape and metal tape
Stratasys	FDM	ABS, elastomer, investment casting wax
Soligen	DSPC	Ceramic powder, polymer binder
Z Corp.	3DP	Starch-based powder

Table 1. FFF Processes

Figure 2. is an illustration of how companies are using FFF models at present. From the chart, we can see that about 28% of FFF models are being used as patterns for prototype tooling and metal casting, as well as for tooling inserts.

Casting Methods

Casting is a manufacturing technology with a history of about 5,000 years^[5]. At present there are numerous methods of making a casting by either expendable, permanent or semi-permanent mold

techniques. In this paper, we limit our investigation to sand casting, investment casting, die casting and plaster molding. Each method has its own advantages and disadvantages.

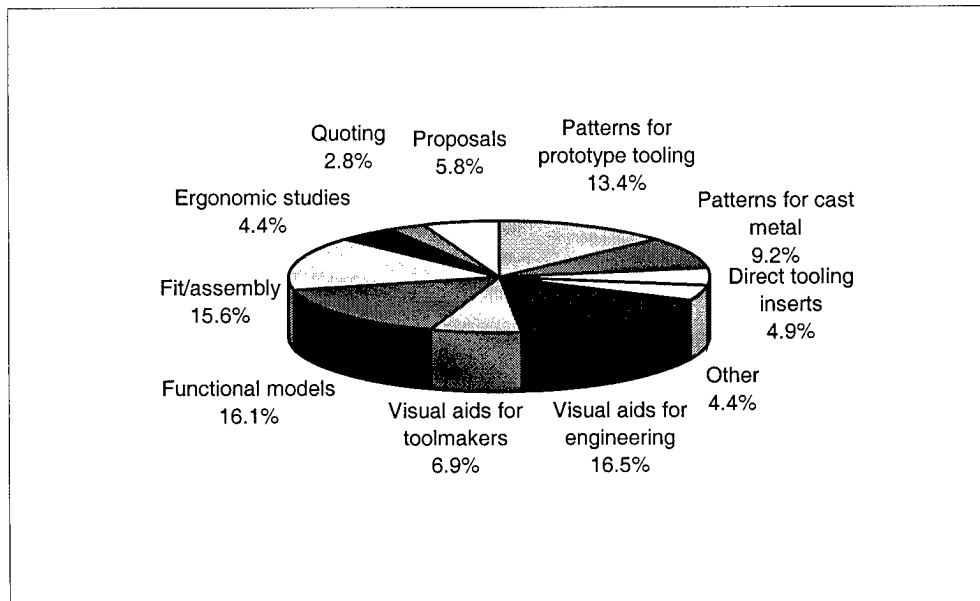


Figure 2. Applications of FFF in Industry^[6]

Sand Casting

As its name implies, this process uses sand as the material to make the mold cavity. It is an expendable mold process because the mold must be destroyed to remove the casting. Tooling for this process consists of a pattern that is rammed with sand and removed to form the casting cavity.

Advantages: Most metals can be cast by this method. Pattern costs and material costs are relatively low. The method is adaptable to large or small quantities.

Disadvantages: There are practical limits to complexity of design. Machining is often required to achieve the finished product. Dimensional accuracy can not be controlled as well as with other molding processes, though accuracy is achievable with quality pattern equipment, modern process control, and high-density molding^{[5][7]}. Thin, deep sections and very thin walls are difficult to cast.

Investment Casting

Investment casting denotes the mechanical manner of obtaining a mold rather than the material used. It is the process of completely investing a three-dimensional pattern to produce a one piece

expendable mold into which molten metal will be poured. A wax pattern elements can be created directly from either wax injection molding methods (high volume) or by RP techniques. These wax patterns are assembled on a "tree" and dipped into a ceramic slurry. The slurry wets the entire surface of the wax replicating every detail. The tree is then immersed in a fluidized bed of refractory particles to form the first layer of the ceramic shell. The mold is allowed to dry and the process repeated with coarser material until sufficient thickness has been built up to withstand the dynamics of hot metal filling and solidification. The wax is melted out of the plaster mold in an autoclave for subsequent recovery and reuse. The molds are fired prior to casting.

Advantages: Extreme accuracy and flexibility of design. Useful for casting alloys that are difficult to machine. Exceptionally fine finish. Suitable for large or small quantities.

Disadvantages: Limitation on size of casting. Material & tooling costs make it important to take full advantage of the process to eliminate as many machining operations as possible.

Die Casting

The Die casting process is widely used for producing large volumes of zinc, aluminum, and magnesium parts of intricate shape. The essential feature of die casting is the use of permanent metal dies into which the molten metal is injected under high pressure (normally 5,000 psi or more).

Advantages: Low piece cost for high volumes of castings, high degree of complexity and good surface finish. High degree of accuracy. As with other processes, inserts can be cast in if needed to enhance design capability. Suitable for relatively low melting point metal (1600 F/871 C) (lead, zinc, aluminum, magnesium, and some copper alloys) and high volume production.

Disadvantages: Limit on size of castings and on geometry with respect to parting line. Most suitable for small casting up to approximately 75 pounds. Equipment and die costs are significant. Some risk of porosity. Good design is essential.

Plaster Mold Casting

Plaster molds are made from a mixture of metal casting plaster, talc, or other refractory materials, and water. The slurry is poured or piped from the mixer into a flask containing the pattern. Which usually is made of metal. The finest engraved detail of the pattern is reproduced.

Molds are dried in a continuously circulating air oven until there is no moisture present. When the molds are poured and the castings solidify, plaster is broken away. Both rigid and flexible patterns are used. Rigid patterns are usually sealed wood, metal, plaster, or lightly lacquered plaster. Flexible patterns made of polysulfide elastomer (thiokol rubber) and urethane elastomers are used widely to make intricate molds with minimal draft.

Advantages: High degree of accuracy, excellent surface finish and dimensional tolerances and repeatability.

Disadvantage: Due to the composition of plaster, only zinc, aluminum and brass alloys can be used in the plaster-mold process.

Applications of FFF in Casting

FFF patterns or pattern elements are frequently used in the foundry industry. Due to the variety of materials used in FFF methods, the accuracy of the processes and the nature of each casting process, each FFF process has different applications in the various casting processes. Some technologies can make molds directly from FFF, such as Direct Shell Production Casting(DSPC) performed by Soligen. At least two advantages can be obtained using such methods:

- No patterns
- No draft required

Companies can also use FFF products as master patterns or use FFF products to produce master patterns or match plates. The way by which we use the FFF products depends on the material properties of the product and the volume of cast parts required. Figure 3 and Figure 4 are the diagrams of the direct approach and indirect approach for tooling production, respectively.

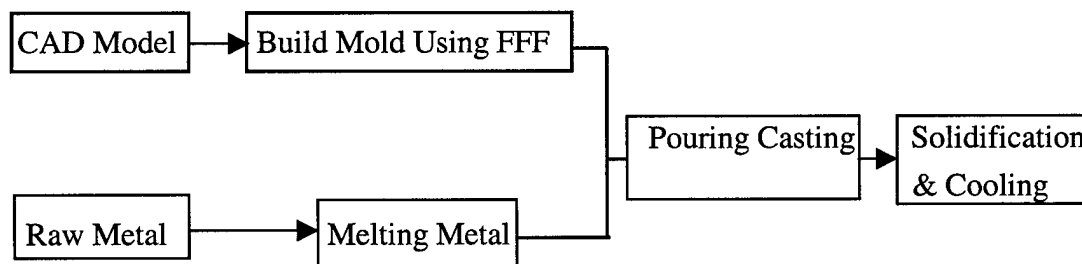


Figure 3 Direct Method of Rapid Tooling

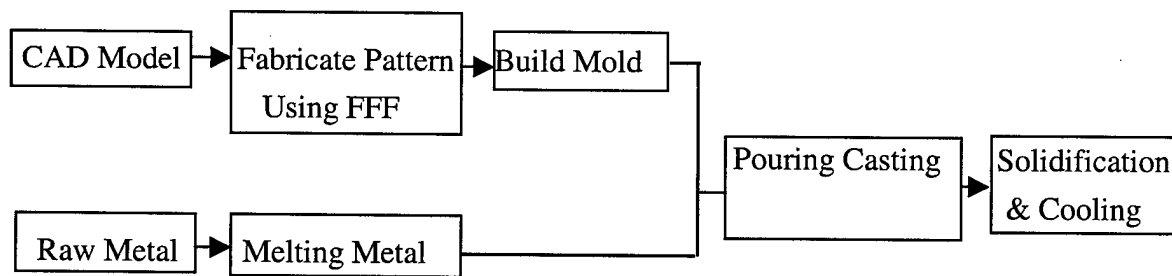


Figure 4 Indirect Method of Rapid Tooling

SLA and SGC patterns can be used in sand casting, investment casting and plaster molding. SLA Quickcast patterns are commonly used for direct investment casting. SLA patterns can also be used to produce wax patterns for investment casting by creating a silicone rubber negative mold from FFF masters and casting wax into the cavity. Companies can also use patterns made by SLA and SGC as master patterns in sand casting and plaster casting. In sand casting, if large number of castings are required, patterns are used to make a match plate type of tool. Because the plaster mold is not as abrasive as a sand mold, SLA and SGC patterns can be directly used in plaster molding even when high volume production is desired^[8].

SLS patterns can be used in sand casting, investment casting, die casting and plaster molding. In sand casting, SLS can be used in the same manner as other FFF patterns are used. Mostly, SLS patterns are used in temporary tooling to make wax patterns in investment casting. One characteristic of SLS is SLS can make the mold for sand casting directly. Parts cast using FFF sand method display mechanical and physical properties similar to the parts cast in a production sand foundry^[8]. This process allows cores to be integrated into the mold as it is built, providing a method to build parts with virtually no limitations on complexity. But due to the expense, this method has been limited to parts with complex geometry.

Although die casting and injection molding are similar processes, i.e., injecting a liquid material into a die under pressure, the die material characteristics and requirements are quite different. The molten die casting materials are less viscous than the polymer melt in injection molding and have greater tendency to flow between the contacting surfaces. The combination of flashing and high injection temperatures requires the die casting dies to be more robust^[9]. A recent study by Peter J. Hardro & Dr. Brent Stucker has demonstrated the feasibility of die casting into RapidSteel 2.0 and has indicated that composite tools made via FFF can be used for die casting.

When just a few castings are required, a LOMPaperTM patterns can be used to make direct impressions in sand. Typically, a LOM pattern can create up to 50 sand molds if geometry is not too complex. Upwards of 100 replications can be taken from such patterns, if proper care is

taken. If higher number of castings is required, LOM patterns can be used to produce master patterns or match plates. Also, LOM masters can be used as a one-to-one replacement of wax masters in investment casting. LOM masters however behave substantially different from wax. With wax, temperatures above 77 °C are sufficient to melt the master with nothing left in the shell. LOM masters on the other hand have to be flash fired at temperature higher than 574 °C. The ash left in the shell is either blown out with compressed air or flushed out with water. A LOM pattern is not the best choice for direct use in the plaster molding process because of the moisture in plaster can be absorbed by the LOM pattern.

Like other forms of fast freeform fabrication, FDM patterns can be used in sand casting, investment casting and plaster casting. Wax patterns made by FDM can be directly used in investment casting. ABS patterns are suited to sand casting and plaster casting. It is also reported that FDM ABS patterns are suitable for use in investment casting^[10]. Removing the ash requires an additional step when casting with a FDM ABS pattern.

Here, we should also mention DSPC(Direct Shell Production Casting) which produces the actual ceramic molds for metal casting. Three Dimensional Printing is used in this method^[8]. First, design a virtual pattern for net shape casting, including a gating system through which molten metal will flow. Then create a digital model of the mold and transfers the model to the 3DP system. The mold includes integral cores to produce hollow sections. The 3DP system automatically generates the mold from thin layers of ceramic powder. After lowering the previous layer, a new layer of powder is spread. Then, liquid binder is "printed" onto the powder layer to define a cross section of the mold. The process is repeated until the entire mold is printed. This is then fired, resulting in a rigid ceramic mold surrounded by unbound powder. The unbound powder is removed from the mold. The last step is to fill the mold with molten metal at our foundry. After the metal solidifies, the ceramic and gating metal are removed and the part is finished.

Conclusion

This paper has discussed the applications of several major FFF processes in the tooling of sand casting, investment casting, die casting and plaster mold casting. The FFF processes can be directly or indirectly used in casting processes. The application depends on the material used by the FFF process, the production volume and the geometric complexity of the part.

REFERENCES

- [1] Wanlong Wang, James G. Conley, Henry W. Stoll, "Rapid Tooling for Sand Casting Using Laminated Object Manufacturing Process", Accepted by *Rapid Prototyping Journal*, November 1998(in process).
- [2] Sung S. Pak, Donald A. Klosterman, David R. Tolin, "Prototype Tooling and Low Volume Manufacturing Through Laminated Object Manufacturing(LOM)", *Proceedings of The Seventh International Conference on Rapid Prototyping*, March 31 - April 3, 1997, p325-331.
- [3] Groover, M. P. (1996), *Fundamentals of Modern Manufacturing: Materials, Processes and Systems*, Chapter 12 & 13, Prentice Hall, Upper Saddle River, NJ.
- [4] Henry W. Stoll, James G. Conley, Wanlong Wang, "Tool Path Selection For Sand Casting", *AFS 103rd Casting Congress and CastExpo*, America's Center, St. Louis, MO, March 13-16, 1999
- [5] American Foundrymen's Society, Inc., *Metalcaster's Reference & Guide*, Second Edition, 1989
- [6] Terry Wohlers, "Rapid Prototyping & Tooling State of the Industry", Wohlers Associates, Inc., 1999
- [7] Fred Waters, *Fundamentals of Manufacturing for Engineers*, Bell & Bain Ltd, Glasgow, 1996
- [8] Reg Gustafson, "Rapid Prototyping: A Tool for Casting Design and Verification", *Modern Casting*, March, 1999, p44-47
- [9] Peter J. Hardro & Dr. Brent Stucker, "Die Casting Tooling from Rapid Prototyping", *Proceedings of the Rapid Prototyping and Manufacturing '99 Conference and Exposition* held at Rosemont, IL, April 20-22, 1999. P611-626
- [10] Paul Blake, Eric Fodran, "FDM of Patterns for Investment Casting", *Proceedings of Solid Freeform Fabrication Symposium*, August 11-13, 1997, P195-202

Fabrication of Metal Components using FDMet: Fused Deposition of Metals

Guohua Wu*, Noshir A. Langrana*, Sriram Rangarajan**, Ryan McCuiston**,
Rajendra Sadanji**, Stephen Danforth**, and Ahmad Safari**

* Department of Mechanical and Aerospace Engineering, Rutgers, The State University of New Jersey, 98 Brett Road, Piscataway, NJ 08854.

** Department of Ceramic and Materials Engineering, Rutgers, The State University of New Jersey, Piscataway, NJ 08854.

Abstract

The Fused Deposition of Metals (FDMet) technique has been developed to directly fabricate complex functional components. The goals of this study are to successfully fabricate reasonably long filament which could be used to successfully fabricate parts using FDMet, and to optimize the build parameters in the fused deposition technology specifically for metals. In this research, two types of stainless steel powders (spherical and irregular) were investigated. The issues related to filament fabrication and FDMet were investigated. A number of parts have been successfully fabricated (FDMet) using about a foot long filament. The parts are currently being characterized and evaluated.

Keywords: FDMet Layer Manufacturing Feedstock 17-4PH Metals

Introduction

There are many techniques available to fabricate metal components directly and indirectly. The traditional methods such as forging, drawing, welding and cutting have been used to fabricate metal parts for a long time^[1], but unfortunately these methods can only be used to fabricate simple shape components and cost is very high on low volume production.

Layered Manufacturing (LM) techniques as advanced fabrication techniques have been developed very quickly over the last 12 years due to their capability of fabricating highly complex geometric components quickly with low cost under small volume production. Currently a lot effort has been devoted to research in metal powder based fabrication: MIT has introduced metal powder into 3DP^[2], DTM has developed a new kind of Rapid Steel2.0 for SLS^[3], Laser Engineering Net Shaping(LENS) from Sandia National Laboratory^[4] and Fraunhofer Institute is working on Multiphase Jet Solidification(MJS)^[5].

Fused Deposition of Ceramics has been a research focus within Center for Ceramics Research of Rutgers University in the last five years^[6]. A lot of research work has been done on process development, material characterization, binder burn out (BBO) and sintering on silicon nitride and PZT. Now they are trying broaden their material list to graphite, alumina oxide.

As an initial effort to investigate the feasibility of fabricating metal components by RP method, RTV molding was developed by our research group at Rutgers University^[7]. The results showed that 17-4PH stainless steel is a suitable metal powder material. During the fabrication process, we found that this molding technique could not be used to fabricate very complex geometric shape. The current efforts are directed at developing a direct metal component fabrication method: Fused Deposition of Metals (FDMet). FDMet is very similar to FDC, yet since the material is different, several alterations must be made during the feedstock preparation to satisfy the requirement of the metal powder, FDMet parameters are also different from FDC and FDM of wax or ABS polymer.

Methodology

FDMet, as its name implies, is a method to fabricate metal component through deposition concept. This method combines various kinds of techniques such as advanced metal powder material, Computer Numerical Control, Rheologic characteristic and Thermal Debinding(BBO) and sintering.

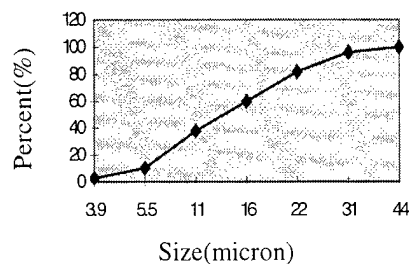
Basically this method is divided into three sections: FeedStock Preparation, FDMet (Green Fabrication), BBO and Sintering. Within the feedstock preparation process, ball milling was used to coat the metal powder with stearic acid which is dissolved in acetone before coating. Stainless steel grinding media was used this time and size is 3/8". After the coating process, the grinding media was removed by sieving and the coated powder was dried in an oven. Sieving was introduced to remove some agglomerates inside dried powder. A Haake rehometer was used to compound the coated powder with ECG2^[8] binder for 2 hours, then the compounded material was graluated process. As will be introduced later the compounded material was used to fabricate filament for FDMet. In the FDMet green fabrication process, the metal filament was used to feed into the liquifier and deposit material through a nozzle to form the part layer by layer. Since there are ECG2 binder and Stearic Acid (SA) inside the green part, Binder Burn Out (BBO) was introduced to remove the binder and SA by thermal decomposition and vaporization.

Feedstock Preparation

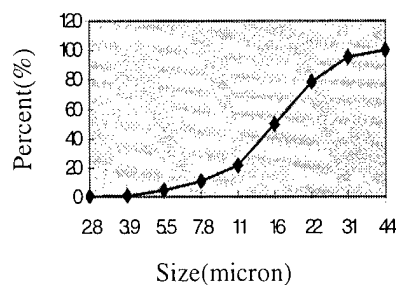
As introduced above, the feedstock preparation was used to fabricate filament needs in the following FDMet green fabrication process.

Powder characterization

Two kinds of 17-4 PH stainless steel powder were used in this process. One is a spherical powder, 22 microns, and the other is irregular powder, 10 microns. The size distribution of these two kinds of powder is shown as in Fig.1. The SEM of these two kinds of powder is shown in Fig.2.

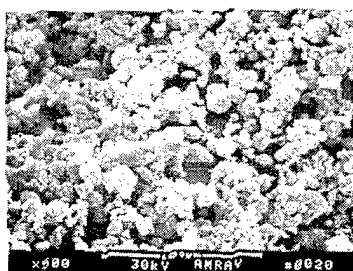


(a) Spherical powder.



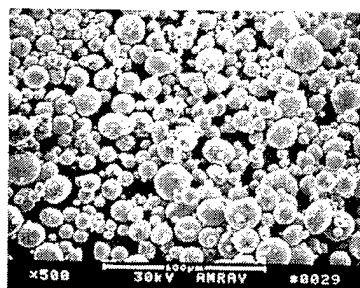
(b) Irregular powder.

Fig. 1 Size distribution of 17-4PH stainless steel powders



375×

Irregular Powder (-10 microns) as received



375×

Spherical Powder (-22 microns) as received

Fig. 2 SEM of 17-4 PH stainless steel powders

Fine powder is preferable, as we would like to use smaller possible nozzle diameters. If the powder size is too big, agglomerates will clog the nozzle, thereby ruining the fabrication process. Another requirement is the viscosity should be low enough so that the compounded material could be easily pushed out of the nozzle. Therefore spherical powder is preferred.

Compounding

Compounding is a very critical process whose aim is to provide a homogenous mixture. A HAAKE 900 rheometer was used to mix the powder and ECG2 binder. The addition schedule of the powder was 40%,30%,20%, 10%. The magnitude of the torque in the process could be used to identify the viscosity of the feedstock, the variation of the torque during the process could be used to judge the homogeneity of the feedstock. Normally the process takes two hours.

Filament Fabrication

Filament fabrication is the next very critical process in FDMet, because it provides filament which acts as the piston to push the melt material out of the nozzle to deposit to fabricate green parts.

Two types of processes are available now for filament fabrication, a screw extrusion process and a piston extrusion process. In the single screw extrusion process, the compounded feedstock was fed through the valve at one end into the tunnel continuously and the single screw was used to push the melt material out through a nozzle at the other end to become filament. A dimension control system was used to make sure the size of the filament is uniform.

In the piston extrusion process, the compounded material was fed into a barrel at a certain temperature 80°C-100°C, after holding for some time, a rod was used to push the molten material out through a nozzle at the bottom of barrel to fabricate the filament. This process could only produce short lengths of filament and speed is very low at the rate of 1 mm/min. The screw extrusion could produce long filaments (in many feet length) since the compounded material could be fed continuously, and speed is very fast: hundreds of feet/hour.

Our experience shows that the screw extrusion process could produce more flexible filament than the piston extrusion process.

FDMet

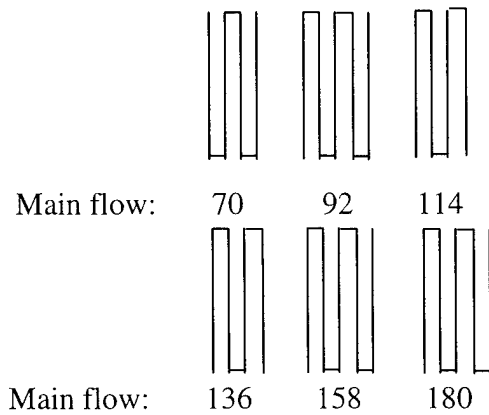
Parameters Determination

In the green fabrication process of FDMet, the stainless steel filament was used to be fed into the heated liquifier and pushed through a nozzle to deposit onto a platform layer by layer to form a part.

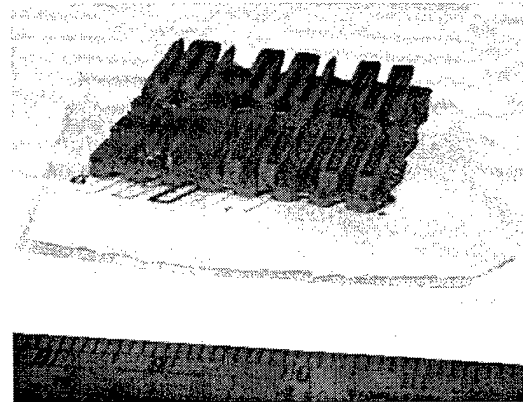
The CAD model and .STL file were created by IDEAS-5 software. The QuickSlice 2.0 software was used to slice the model and create the tool path needed in the actual fabrication process. Since stainless steel is a new kind of material used in FD technique, basic parameters such as main flow, preflow, start distance, start delay, shutoff distance, speed, acceleration and roll back had to be determined. Based on our experience with processes, we determined that the main road width is related to main flow, the start road width is related to start delay and preflow, the ending road width is related to the shut off distance and roll back. Several experiments were performed to generate workable tool path parameters for stainless steel filament.

A CAD design was created to quantify the proper main flow for a certain road width as showed in Fig. 3. This design has six sections. In each section, only main flow parameter was different. Since the range was not known, the initial experiment had a

larger range between upper & lower bounds. Based on an inspection, we can judge the material flow condition for all sections. In some sections, material flow is not enough. In some others, there is too much flow. In the next iterations, the range between upper & lower bound were reduced, and finally the lower bound (76) and upper bound of the main flow (180) were selected.

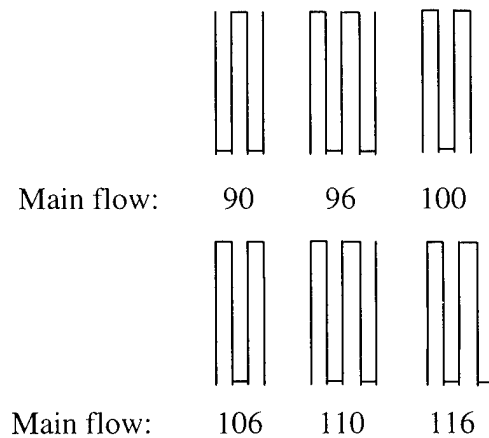


(a) CAD Design

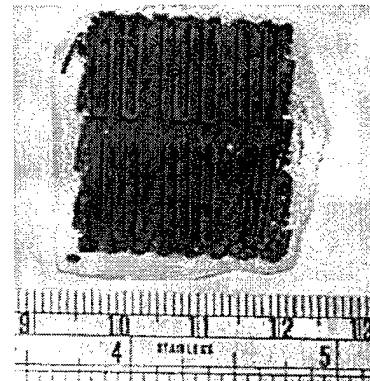


(b) Fabricated Part

Fig. 3 CAD design and real part for main flow range determination



(a) CAD Design



(b) Fabricated Part

Fig.4 Relationship between main flow and road width

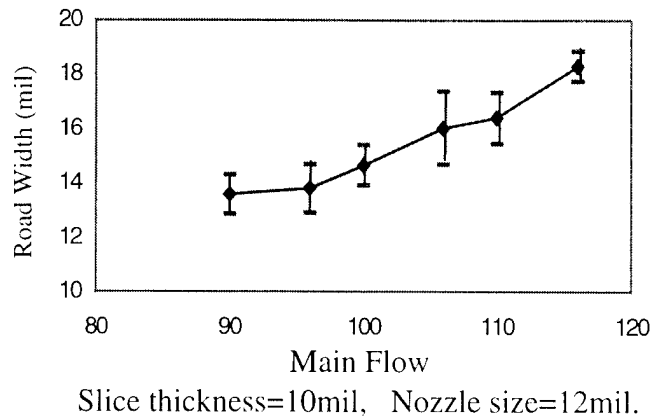


Fig.5 Relation of acceptable main flow and road width

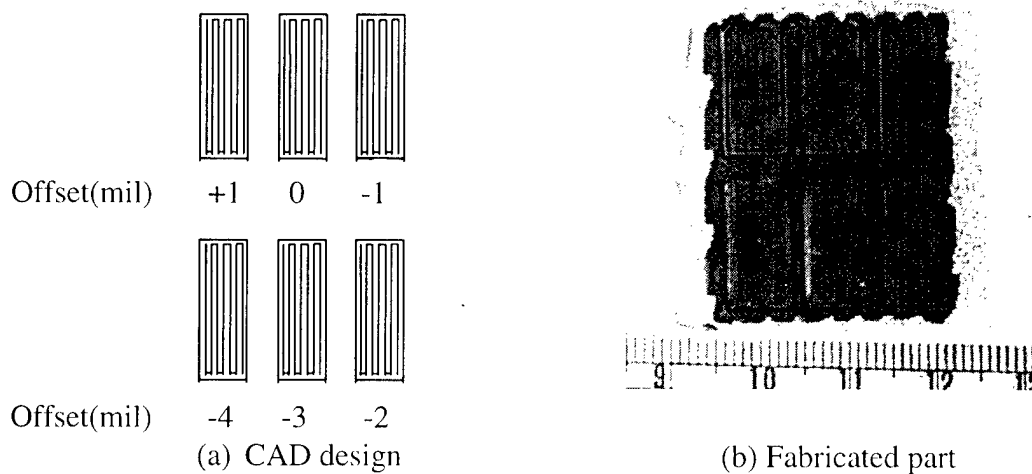


Fig. 6 CAD design and part for proper offset of a road width

Once the main flow range was determined, the specific relationship between the road width and main flow was determined, a similar CAD design as in Fig. 4 was created in which the main flow was confined between 90 and 116. Then three parts were created according to the design and the road width in each section was measured by video microscopy^[9]. The results of the acceptable main flow are shown in Fig 5.

Since raster/raster offset is very important for making fully dense FDMet green parts, a CAD design was created to identify the acceptable offset for a certain road width. As shown in Fig.6, this design has six sections, each has only different parameter, the offset changes from +1 to -4 mil. As we can see from the images of the fabricated part, Fig. 7, the acceptable offset for road width 17 mil is -2 mil.

Green fabrication

Several green parts including a lug fit fastner and wrench part have been made through FDMet process. A fabricated wrench part from FDMet is shown in Fig. 7. Dimensions of the part were measured and compared with RTV mold wrench shown in Fig. 8. The results (average of three measurements) shown in Table I indicate that FDMet has better accuracy compared to RTV mold.

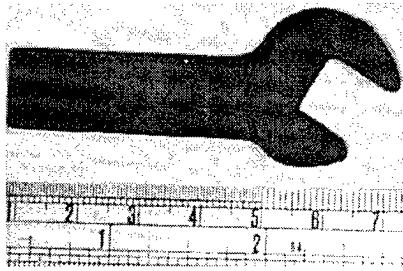


Fig. 7 FDMet wrench part

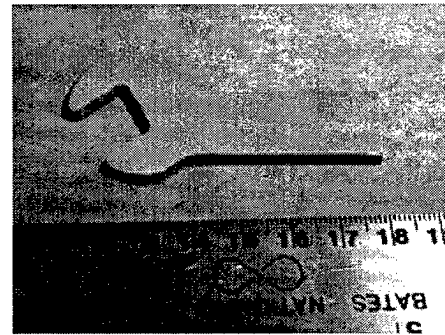


Fig. 8 RTV mold wrench part

Table I Dimensions of wrench parts

	CAD	RTV Molding	FDMet
Length (in.)	2.544	2.599	2.542
Height (in.)	0.195	0.217	0.210
Width (in.)	0.984	0.990	0.980

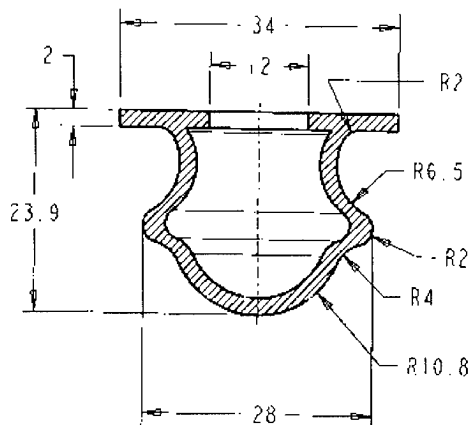


Fig. 9 Lug fit fastner CAD design

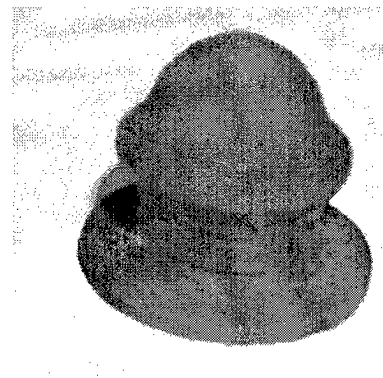


Fig. 10 FDMet lug fit fastner

Table II Dimensions of lug fit parts

	CAD	RTV Molding	FDMet
Inner Diameter (in.)	0.466	0.471	0.461
Middle Outside Diameter (in.)	1.053	1.059	1.050
Bottom Outside Diameter (in.)	1.353	1.368	1.336
Height (in.)	0.935	0.974	0.966

Fig. 9 shows the CAD design for the lug fit part and the fabricated lug fit part from FDMet is shown in Fig. 10. Since the internal structure is very complex and could not be fabricated by RTV molding (or by any other molding methods), the RTV mold lug fit was fabricated with simplified internal structure and the internal hole was a cylindrical shape [6] instead as shown in Fig. 9. The dimensions of the two parts were measured and compared with RTV mold lug fit, the results are shown in Table II.

Conclusion

A novel metal component fabrication method (FDMet) has been developed. Feed stock preparation for FDMet was established and characterized. Green fabrication of several complex geometrical components has been demonstrated and the results show that FDMet has better accuracy compared to RTV mold.

Acknowledgement

This research reported here has been performed towards the partial fulfillment of the requirements for PHD thesis of the first author. The authors would like to thank the New Jersey Commission of Science and Technology for the financial support under Grant #97-2890-14 through the NJIT Multi-Lifecycle Engineering Research Center Program. Also the authors would like to thank Drs. Reggie J. Caudill and Sanchoy Das, NJIT for their cooperation. The authors wish to thank B. Harper, N. Venkataraman, M. Muller and John Petrowski (MAE staff) for their help in the experimental work.

Reference

- [1] J.R.Davis, Davis & Associate, Handbook of Stainless Steel, ASM, 1998.
- [2] E. Sachs, S. Allen, M. Cima, X. Xu, J. Banos, J.Serdy, D. Brancazio, H. Guo, "Fabricating Metal Tooling and Metal Parts by 3D Printing.", Naval Research Reviews, Office of Naval Research, Three/1998, Vol. L pp9-18.
- [3] Suman Das, Martin Wohler, Joseph J. Beanman, and David L. Bourell, "Producing Metal Parts with Selective Laser Sintering/Hot Isostatic Pressing", Journal of Materials, 50(12)(1998), pp17-20.
- [4] Griffith, M.L., Keicher, D.M., Atwood, J.T. Romero, J.E., Smugersky, J.E., Harwell, L.D., Greene, D.L., "Free Form Fabrication of Metallic Components using Laser Engineering Net Shaping(LENS), Proceedings of the Solid Freeform Fabrication Symposium, Aug. 1996, Austin, TX, 125-32.
- [5] D. Kupp, H. Eifert, M. Greul and M. Kunstner "Rapid Prototyping of Functional Metal and Ceramic Components by the Multisphase Jet Solidification(MJS) Process", Proceedings of the Solid Freeform Fabrication Symposium, 1997, pp.203.
- [6] Danforth, S, Safari, A, Jafari, M, and Langrana, NA, "Solid Freeform Fabrication (SFF) of Functional Advanced Ceramic Components", Journal of Naval Research, an invited review article, Vol. L, pp. 27-39, THREE/1998.
- [7] G. Wu, N. Langrana, S. Rangarajan, R. Sadangi, A. Safari, S. C. Danforth, "Feasibility of Fabricating Metal Parts from 17-4PH Stainless Steel Powder", Proceedings of the Solid Freeform Fabrication Symposium, 1998, pp.479-486.
- [8] T.F.McNulty, I. Cornejo, F. Mohammadi, S. C. Danforth, A. Safari, "Development of a Binder Formulation for Fused Deposition of Ceramics", Proceedings of the Solid Freeform Fabrication Symposium, 1998, pp.613-620.
- [9] Evan Bossett, Lorna Rivera, Dan Qiu, Ryan McCuiston, Noshir Langrana, Sriram Rangarajan, Natesan Venkataraman, Stephen Danforth, Ahmad Safari, "Real Time Video Microscopy for the Fused Deposition Method", Proceedings of the Solid Freeform Fabrication Symposium, 1998, pp.113-120.

ASSESSMENT OF ENVIRONMENTAL PERFORMANCE OF RAPID PROTOTYPING AND RAPID TOOLING PROCESSES

Yanchun Luo, Ming C. Leu¹, Zhiming Ji

Department of Mechanical Engineering
New Jersey Institute of Technology
Newark, New Jersey 07102

Tel: (973)596-5668, Fax: (973)596-5601, E-mail: yxl6622@oak.njit.edu

Abstract: A method for assessing the environmental performance of solid freeform fabrication (SFF) based rapid prototyping and rapid tooling processes is presented in this paper. In this method of assessment, each process is divided into a number of life stages. The environmental effect of each process stage is analyzed and evaluated based on an environmental index utilizing the Eco-indicators that were compiled by PreConsultants of the Netherlands. The effects of various life stages are then combined to obtain the environmental performance of a process. In the assessment of SFF processes, we consider the material use in the fabrication of a part, energy consumption, process wastes, and disposal of a part after its normal life. An example is given to illustrate this assessment method applied to the stereolithography (SLA) process and two SLA based rapid tooling processes.

Keywords: Solid Freeform Fabrication, Rapid Prototyping, Rapid Tooling, Environmental Performance, Lifecycle Analysis.

1 INTRODUCTION

Industrial ecology involves both manufacturing processes and products. The interaction of process design with environmental concerns is somewhat different from that of product design. The industry-environment interaction is thus influenced by two rather separate groups of designers. On the side of product design, much of research effort has been taken to develop the concepts, methodologies and implementation of product lifecycle, end of lifecycle factors, and even multi-lifecycle issues [1-3]. However, processes are more universal than products, and a successful process design often has great importance to an entire industry. More recently, focused studies on process-level environmental performance have been developed, particularly for conventional machining processes [5-7].

Solid Freeform Fabrication (SFF), or often referred to as Rapid Prototyping (RP), produces the physical model of a CAD design using an additive process that builds the physical part layer by layer. This new manufacturing technology has been experiencing tremendous development and growth since its introduction a little over one decade ago. By the end of 1998, more than 3,000 commercial units of SFF machines were sold and installed worldwide [9]. As a prototyping and visualization tool, SFF enables the manufacturer to reduce the overall cost and time to market in the introduction of a new product. Furthermore, in the application of Rapid Tooling (RT), SFF

¹ Dr. Ming C. Leu is currently on leave as the Program Director for Manufacturing Machines & Equipment, National Science Foundation, Arlington, Virginia.

technique allows direct or indirect manufacture of production tools, which has created a competitive edge [12]. SFF has been widely adopted in aerospace and automotive industries, and is quickly spreading to other industries that manufacture medical devices, electronics products, etc.

In view of the fast growth and wide adoption of various SFF processes, it is important to study the lifecycle performance of SFF processes, including consumption of natural resources and energy, and impact on human health and the environment, together with other process attributes such as cost, accuracy, productivity, and functionality, so that the SFF technology can become more sustainable. SFF processes have some good environmental characteristics. The waste streams are less in SFF processes than in conventional manufacturing processes such as machining. Worn tools and scraps seldom occur in SFF processes and equipment. Cutting fluids, which are the major source of hazard in machining [5-7], are not used in SFF processes. Comparing with conventional manufacturing processes, SFF processes have distinguishing features in process mechanisms, materials, energy use, etc. It is essential to look into these processes, investigating how the process variables influence the environmental consequences, and apply a systematic method to assess the process environmental performance so that these processes can be optimized with consideration of their environmental properties.

In [14], we reported some preliminary results of our research towards a systematic approach that we developed for SFF processes based on lifecycle concept. A lifecycle process model was proposed, in which a process' entire lifecycle is considered and it is divided into several life stages. Environmental impact is evaluated for each life stage and then combined to obtain the overall environmental performance for a process. This method has been used to assess Stereolithography (SL), Selective Laser Sintering (SLS), and Fused Deposition Modeling (FDM) processes. Besides the environmental performance, process cost, process quality, and other factors can be incorporated to develop a multi-objective decision making method. The approach was introduced in [15].

In this paper, we extend the previous method to assess SFF based rapid tooling processes. As for the SFF processes, the method holistically incorporates the entire process lifecycle, including material extraction, pattern fabrication, shape replication, post processing, and material disposal. The environmental performance is evaluated, based on Lifecycle Assessment (LCA) principle [1-3] and with an environmental impact index called the Eco-indicator [8]. Details of this method and an example illustrating its use will be given.

2 LIFECYCLE ENVIRONMENTAL PERFORMANCE OF RAPID PROTOTYPING AND RAPID TOOLING PROCESSES

LCA has been found useful for examining the design of products and processes to reduce the impact upon human health and the environment and to achieve sustainable industrial development. From the lifecycle point of view, a part produced with a SFF process generally goes through the following stages: (a) inputting the building material into the system, (b) building the part layer by layer, (c) shape replication and sintering or burning (for tooling processes) and (d) post-processing. When the user finishes using the part fabricated by SFF, the part goes to the disposal stage: to be landfilled, incinerated, or recycled. While the material, part usage and part disposal are not exactly part of a process, their inclusion provides a holistic view of the environmental performance of an SFF process. Thus, factors taken into account in process

environmental performance should include the material extraction stage, energy consumption and process wastes in the fabrication and replication stages, and the disposal stage. In terms of these environmental factors, we first provide a general comparison between conventional machining process and several SFF processes, as given in Table 1.

Table 1. Comparison of Machining with SFF Processes

	<i>Materials</i>	<i>Material Utilization</i>	<i>Energy Source</i>	<i>Process Residues</i>	<i>Disposal</i>
<i>Machining</i>	<i>metals, alloys, ceramics, etc.</i>	<i>material-removal process. Material Utilization Rate (MUR) is 60% - 90%</i>	<i>electromotor power (mechanical energy)</i>	<i>material chips, tool scraps & chips, cutting fluids, fluid vapor</i>	<i>landfill, recycling</i>
<i>SLA</i>	<i>liquid photo-polymers etc.</i>	<i>material-additive process. MUR almost 100%</i>	<i>UV laser (chemical energy)</i>	<i>material chips, removed support structures</i>	<i>incineration, landfill</i>
<i>SLS</i>	<i>powder of nylon, plastics, metals, ceramics, etc.</i>	<i>material-additive process. MUR about 100%</i>	<i>high power laser (thermal energy)</i>	<i>material chips</i>	<i>incineration, landfill, recycling</i>
<i>FDM</i>	<i>nylon, ABS, wax, ceramics, etc.</i>	<i>material-additive process. MUR almost 100%</i>	<i>heat (thermal energy)</i>	<i>material chips, removed support structures</i>	<i>incineration, landfill, recycling</i>

To evaluate the environmental performance, we propose a process model based on lifecycle concept. The steps of an SFF process can be viewed as the process lifecycle stages, and thus the environmental impact factors in all process stages can be included in this model. The model is then extended for assessment of SFF based Rapid Tooling (RT) processes.

The environmental performance process model is shown in Figure 1. Figure 2 is an extension of this model for RT processes. In the process model, the overall environmental performance value is the sum of the environmental performance values of the various life stages, each of which has one or more corresponding environmental impacts. The environmental performance of a process is evaluated by defining the lifecycle stages of the process, identifying the individual environmental impact factors, obtaining the environmental impact values, and summing these values.

Figure 1 shows that the lifecycle of a process can be divided into n stages. For SFF process, there are generally four lifecycle stages: 1) material preparation, 2) part build, 3) part use, and 4) part disposal. Environmental impacts that occur in each lifecycle stage are identified as follows. In the material preparation stage, the environmental impact is material extraction & production. During the part building stage, the main environmental impact is energy consumption. Process residues, such as cutting fluids, which exist and have severe environmental consequences in the part cutting stage of machining process, are rare in most of SFF processes, and can be ignored in evaluation. Material toxicity may cause negative impact to human health in the part use stage. Finally in the disposal stage, the part can be landfilled, incinerated or recycled. Different disposal methods have different environmental impacts.

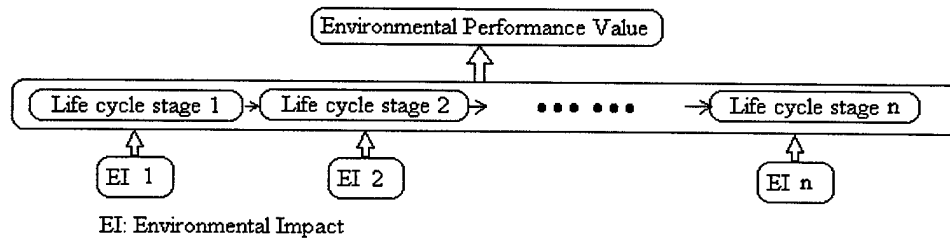


Figure 1. Lifecycle environmental performance model

The model presented above is the basic process model for SFF processes. It can be extended to SFF based RT processes. Here we consider indirect RT processes, in these processes, a few additional steps are needed to duplicate the shape of the pattern made by SFF, and then sintering or burning the duplicate part is needed to get the tool. These steps are needed for the mold creation, and they can be seen in, for example, 3D Keltool and the rapid tooling process that integrates SFF with electroforming. The extended process model for indirect RT processes is shown in Figure 2. The environmental impacts corresponding to every lifecycle stage need to be identified. In the figure 2, EI1 is for material extraction & production. EI2 is for energy consumption. EI3 includes material consumption, energy consumption and process residue. And EI4 results from the tool disposal stage where the tool can be landfilled, incinerated or recycled.

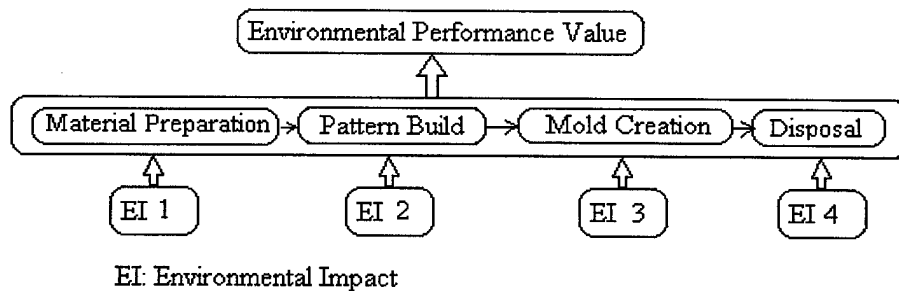


Figure 2. Lifecycle environmental performance model of indirect RT process

The environmental performance value obtained should provide an unambiguous measure for the combined environmental impact of material, process, energy, etc. This kind of data quantifies the impact of the process to the environment. It should be noted that there is no database of this kind available today. For performing the quantitative assessment, we use the Eco-indicator index [8] that was made available by PréConsultants of the Netherlands. The provided database contains 100 indicators for commonly used materials and processes. The higher the indicator, the greater the negative environmental impact.

To summarize, our process model deals with the process complexity by dividing a process into several life stages. The environmental impact index provides a quantitative measure of environmental impact for each stage of the process. The implementation of this evaluation method can be carried out as follows. First, every process stage and the elements of its associated environmental impact factors are identified. Then, the value of eco-indicator is obtained for each environmental impact factor. Finally, the environmental index values for all process stages are summed up to generate the total environmental performance value.

3 EXAMPLE: ASSESSMENT OF SLA PROCESS AND SLA BASED RAPID TOOLING PROCESS

This example considers the StereoLithography (SLA) process and two rapid tooling processes that utilize SLA to build patterns: 3D System's Keltool process [14] and an SFF based electroforming process [13]. SLA is one of the most widely used SFF processes today. It is a fabrication process that builds a part by controlling a laser beam to selectively cure liquid photopolymer layer by layer. 3DKeltool and electroforming tooling processes are two rapid tooling processes that utilize SLA to quickly create highly detailed and accurate patterns.

For the SLA process, the process parameters that influence the environmental performance are identified as follows:

M: Material used (cm^3)

V: Scanning speed (mm/sec)

W: Line width (mm)

T: Layer thickness (mm)

P: Power rate of the equipment (kW)

k: Process time delay between layers (coefficient = 0.6~0.9)

The scanning speed can be estimated using the following equation [4]:

$$V = \sqrt{\frac{2}{\pi}} \left[\frac{P_L}{W_0 E_c} \right] \exp \left[-\frac{T}{D} \right] \quad (1)$$

in which P_L is the laser power, W_0 is the half line width, E_c is the critical laser exposure, and D is a material constant of the polymer.

The Process Productivity (PP) and the Energy Consumption Rate (ECR) for each unit volume of material processed can be calculated as follows:

$$\text{PP} (\text{cm}^3/\text{h}) = V \times W \times T \times k \times 3600 / 10^3 \quad (2)$$

and

$$\text{ECR} (\text{kWh}/\text{cm}^3) = P / \text{PP} \quad (3)$$

The environmental performance of SLA process is evaluated according to the assessment method introduced in section 2.

3.1 Assessment of SLA Process

The building material in the SLA process is photopolymetric resin. The process is evaluated with three models of the equipment, SLA-250, SLA-3500, and SLA-5000. The manufacturer's recommended process parameter values are used in the assessment. First we need to obtain the environmental impact due to energy consumption in the process. Here we use equation (1) to calculate the process scanning speed V , then use equation (2) and (3) to estimate the process energy consumption rate (ECR). Finally we obtain the environmental impact of energy consumption. Table 2 shows the result representing the environmental impact of the energy used to process one cm^3 of epoxy resin. Because SLA-5000 has the highest laser power, resulting in the highest scanning speed, and the least ECR. While for SLA-3500 and SLA-250, the former one has higher scanning speed but also higher power rate of equipment than the later one. The result gives that the SLA-250 has less ECR than SLA-3500.

Table 3 shows the environmental indicators of the environmental impact occurring in each lifecycle stage of the process, and the environmental performance value representing the total environmental impact. As we discussed in section 2, the environmental impacts in various

lifecycle stage are identified and the corresponding index values are obtained from the Eco-indicator database, and converted to the values representing effect of one cm^3 of specific material. Since there are usually two alternatives of disposal, two values are given for the disposal stage. The value before “/” is for disposal using landfill and the one after “/” is for disposal using incineration.

Table 2. Environmental Impact Due to Energy Use of SLA Process

	SLA-250	SLA-3500	SLA-5000
<i>V</i> (mm/sec)	340	1000	2000
<i>W</i> (mm)	0.25	0.25	0.25
<i>T</i> (mm)	0.15	0.1	0.1
<i>k</i>	0.7	0.7	0.7
<i>P</i> (kW)	1.2	3	3
<i>PP</i> (cm^3/h)	32.13	63.00	126.00
<i>ECR</i> (kWh/cm^3)	0.037	0.048	0.024
Eco-indicator ($/\text{kWh}$) [8]	0.57	0.57	0.57
Environmental Impact	0.021	0.027	0.014

$$\text{Environmental Impact} = \text{ECR} \times \text{Eco-indicator}$$

Table 3. Environmental Impact of SLA Process

Process	Project		
SLA	Environmental effect for 1 cm^3 material processed		
Equipment	Environmental impact index		
SLA-250, SLA-3500, SLA-5000	Eco-indicator		
	SLA-250	SLA-3500	SLA-5000
Material preparation			
SLA 5170 Epoxy resin	0.012	0.012	0.012
Part build			
Energy use	0.021	0.027	0.014
Disposal			
Landfill/Incineration	4.03e-5/0.0021	4.03e-5/0.0021	4.03e-5/0.0021
Total Impact	0.033/0.036	0.039/0.042	0.026/0.029

3.2 Assessment of Two Rapid Tooling Processes

3D KelTool and the SFF based electroforming process are two indirect rapid tooling processes. Indirect tooling requires a master pattern built by SFF process. At least one intermediate step is needed. The intermediate steps may include shape replication and sintering or burning in the manufacture of the production tool.

3D Keltool process [14] can be used to rapidly create injection molds or die casting inserts. It begins with an SLA master pattern. The pattern is used to produce an RTV silicone rubber mold. Once the RTV mold is produced, it is then filled with a mix of tooling steel powder, tungsten carbide powder and epoxy binder. After this material has cured in the mold, this “green part” is sintered in a hydrogen-reduction furnace and the binder material is burning off. The final step is to infiltrate the sintered part with copper.

The SFF based electroforming process [13] can be used to produce EDM electrodes, molds and dies. First, an SLA pattern is fabricated. Then the pattern is metalized and electroformed in nickel or copper solution. When the desired thickness of metal shell is reached, the SLA pattern

is removed by burning out. Finally, the metal shell is backed with other materials to form the production tool.

Figure 3 illustrates the concepts of these two indirect tooling processes. When a cylindrical metal mold cavity is required to be manufactured, both 3D Keltool and SFF & Electroforming processes have this function, although they differ from each other in type and amount of materials use and specific intermediate steps. If we are going to look into the environmental performance, the model introduced in section 2 can be used to assess them from the lifecycle viewpoint.

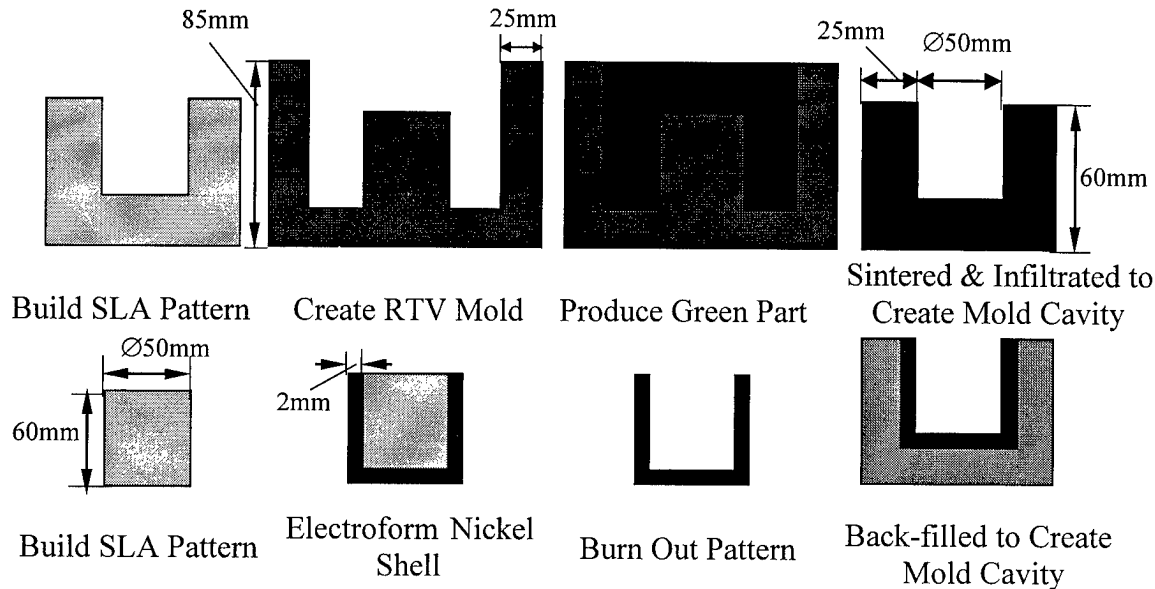


Figure 3. Indirect Tooling Process

Unlike the assessment of SFF process in which only unit volume of material is considered, In evaluating indirect RT processes, the volume of final tool should be accounted in order to estimate the amount of intermediate material consumed. In the following assessment, the cylindrical mold cavity in figure 3 is used as an example with dimensions of diameter 50mm and height 60mm.

In the pattern building stage, we can use the assessment result for the SLA process and assume the two RT processes both use SLA 250 to fabricate the master pattern. The environmental impact for unit volume (cm^3) SLA material consumed is 0.034. Since 3D Keltool uses the negative pattern and SFF & Electroforming uses positive pattern, different volume of materials used yield different impact values for this stage. Here we assume the dimensions of the mold is 100mm diameter and 90mm height. The material volumes of 3D Keltool process used to build the pattern is 589.4cm^3 and that of SFF & Electroforming process used is 117.2cm^3 .

In the mold creation stage, material consumption, process residues and energy consumption during sintering or burning step should all be considered. In this stage, 3D Keltool typically consumes silicone and mixed steel powder, The environmental indices for unit volume (cm^3) of silicone and mixed steel are 0.036 and 0.156 respectively. And the volumes of RTV mold and the final mold also need too be calculated. Therefore the material consumption impact in this stage

can then be estimated. Similarly, SFF & Electroforming process usually use nickel to electroplate certain thickness of metal shell, and then back filled with aluminum. For unit volume (cm^3) of nickel and aluminum, the environmental indices are 0.534 and 0.049 respectively. The nickel shell thickness is typically 2mm. So the volume of nickel and aluminum used can be calculated. And hence we can get the material consumption impact in this stage for SFF & Electroforming process. The results can be seen in the table 4. Sintering and burning in 3D Keltool and the electroforming tooling process require to consume energy. The energy consumption is estimated as production of furnace power rate and sintering or burning time. The electroforming tooling process needs more energy than 3D Keltool in this stage because burning off the SLA pattern consumes more energy.

In the disposal stage, The 3D Keltool process produces wastes such as SLA material and silicone. Electroforming tooling process only has residue of SLA material. If the process residue are all disposed to landfill, the environmental impact can be assessed by considering the impact indices and the volume disposed. The results are shown in table 4. In addition, we expect the disposed tools can be recycled by material recovering. The mixed metal of the tool made by 3D Keltool is less preferable than laminated nickel and aluminum used in the electroforming tooling process. The impact indices for recycling unit volume (cm^3) of mixed steel, nickel, and aluminum are -0.023, -0.311, and -0.035 respectively.

Table 4 shows the assessment results for the above two indirect RT processes.

Table 4. Environmental Performance of RT Process

Process 3D KelTool SFF based Electroforming Tooling	Project Environmental effect for RT processes	
Base SFF process SLA	Environmental impact index Eco-indicator	
	3D KelTool	SFF & Electroforming
Pattern build		
Material use	7.07 (SLA material)	1.41 (SLA material)
Energy use	12.38 (energy used in pattern building)	2.46 (energy used in pattern building)
Mold creation		
Material use	80.97 (silicon and mixed steel powder)	40.61 (nickel and aluminum)
Energy use	0.25 (energy used by furnace)	0.57 (energy used by furnace)
Disposal		
Process residues landfill	0.088 (SLA material and silicon)	0.033 (SLA material)
Material recovery	-13.56 (mixed steel)	-26.67 (nickel and aluminum)
Total impact	87.76	18.52

From the above assessment, we can see that the environmental performance of a rapid tooling process depends on several factors. First, the selection of the base SFF process is an important factor. It is desirable to select an SFF process that has good environmental performance. Secondly, the tooling materials, and process residues can further impact on the environmental performance due to the use of natural resources and possible generation of process residues. Finally, the method of disposal or recovery of tool material will also influence the total environmental performance of a process.

4 CONCLUSION

A lifecycle based process model for analyzing environmental performance of SFF processes and SFF based rapid tooling processes is extended for analyzing SFF based RT processes. The process environmental performance assessment model considers material, energy, and disposal scenarios. The material use, process parameters (e.g. scanning speed) and power use can affect the environmental consequence of a process when material resource, energy, human health and environmental damage are taken into account. The presented method is applied to the SLA process and two SLA based rapid tooling processes. The method can be used to compare different RP and RT processes in terms of their environmental friendliness.

5 REFERENCE

1. Kolluru, R., *Environmental Strategies Handbook*, McGraw-Hill, Inc. 1994.
2. Alting, L., and Jorgensen, J., "The lifecycle Concept as a Basis for Sustainable Industrial Production," *CIRP Annals*, Vol. 42/1/1993, pp. 163-167.
3. Zust, R., "Approach to the Identification and Quantification of Environmental Effects During Product Life," *CIRP Annals*, Vol. 41/1/1992, pp. 473-477.
4. Chen, C., and Sullivan, P., "Predicting Total Build-time and the Resultant Cure Depth of the 3D Stereolithography Process," *Rapid Prototyping Journal*, Vol.2, No.4, 1996, pp. 27-40.
5. Sheng, P., Bennet, D., and Thurwachter, S., "Environmental-Based System Planning for Machining," *CIRP Annals*, Vol. 47/1/1998, pp. 409-414.
6. Sheng, P., and Srinivasan, M., "A Hierarchical Part Planning Strategy for Environmentally Conscious Machining," *CIRP Annals*, Vol. 45/1/1996, pp. 455-460.
7. Howes, T. D., Tonshoff, H. K., and Heuer, W., "Environmental Aspects of Grinding Fluids," *CIRP Annals*, Vol. 40/2/1991, pp. 621-631.
8. PRé Consultants, *The Eco-indicator 95*, <http://www.pre.nl>, Netherlands, 1996.
9. Leu, M. C., and Zhang, W., "Research and Development in Rapid Prototyping And Tooling in the United States," *Proceeding of ICRPM'98*, Beijing, China, 1998, pp. 707-718.
10. Aubin, R. F., "A World Wide Assessment of Rapid Prototyping Technologies.," *Proceeding of Solid Freeform Fabrication*, Austin, Texas, 1994, pp. 118-145.
11. Karapatis, N. P., Griethuysen, J., and Glardon, R., "Direct Rapid Tooling: A Review of Current Research," *Rapid Prototyping Journal*, Vol. 4, Num. 2, 1998, pp. 77-89.
12. Yang, B., and Leu, M. C., "Integration of Rapid Prototyping and Electroforming for Tooling Application," *CIRP Annals*, Vol. 48/1/1999.
13. Raetz, T., "3D Keltool", *Proceedings of the North American Stereolithography Users Group Conference*, San Antonio, Texas, 1998.
14. Luo, Y., Ji, Z., Leu, M. C., and Caudill, R., "Environmental Performance Analysis of Solid Freeform Fabrication Processes," *Proceedings of the 1999 International Symposium on Electronics & the Environment*, Danvers, MA, 1999, pp1-6.
15. Luo, Y., Leu, M. C., Ji, Z., and Caudill, R., "Lifecycle Assessment of Solid Freeform Fabrication Processes," *Proceedings of 6th International Seminar on Life Cycle Engineering*, Kingston, Canada, 1999, pp350-360.

3D Welding and Milling - A Direct Approach for Fabrication of Injection Molds -

Yong-Ak Song*, Sehyung Park*, Haeseong Jee**, Doosun Choi***, Bosung Shin***,

** Korea Institute of Science and Technology KIST, CAD/CAM Research Center*

*** Hong-Ik University, Mechanical Engineering Dept.*

**** Korea Institute of Machinery and Metals KIMM*

Abstract:

Solid Freeform Fabrication (SFF) gives designers a new freedom to build parts which have been not able to be manufactured by conventional techniques. However, the surface finish and the accuracy of SFF parts are still lower compared to that of conventionally machined parts. To overcome this problem, a process combination of additive and subtractive techniques is being developed. This hybrid approach called "3D Welding and Milling" makes use of welding as additive and conventional milling as subtractive technique, thereby exploiting the advantages of the both processes. In this paper, it is shown whether this process combination can be applied for the fabrication of injection molds.

1. Introduction

With an increasing demand for metallic prototypes and tools, several direct SFF techniques have been developed. The common feature of these approaches consists in direct melting of metals which are normally supplied either in form of powder or wire. Due to the complete melting, however, the accuracy as well as the surface quality are generally lower than that of machined parts.

To overcome this process inherent problem, a combination of additive and subtractive technique offers as a possible solution. This kind of process combination has been already implemented in SDM (Shape Deposition Manufacturing) of Stanford University [1,2] and CMB (Controlled Material Buildup) developed by IPT Aachen [3]. In these processes, each layer is deposited as a near-net shape using thermal deposition including spraying, welding or laser cladding. The layer is then shaped with CNC milling to net shape before proceeding with the next layer.

The combination of welding as additive and milling as subtractive operation offers distinctive advantages over conventional machining. First, in case of parts with a large amount of volume to remove, the fabrication of near net-shape with the additive method and the

consecutive surface finishing can be a competitive approach. In addition, if the material is difficult to machine, the additive fabrication of a near net-shape with welding and subsequent surface finishing with milling can be an alternative method. Second, features either impossible or difficult to be produced by conventional milling can be easily manufactured by this process combination. Such features include arbitrary internal channels such as conformal cooling channel. Third, the process combination enables the fabrication of parts with different materials.

Although the process combination demonstrates a great potential so far, process inherent problems such as warpage due to thermal stress [4] put a severe obstacle to its wide application. Therefore, a continuous process development regarding effective thermal management and increased speed are necessary. In this paper, it is investigated how far this process combination of welding and milling can be used as direct approach for the fabrication of mold inserts.

2. Process Principle and Equipment

The principle of 3D Welding and Milling is shown in **Fig. 1**. First, arc welding is used to build a layer by depositing single beads side by side. After the deposition, the top surface of the layer is machined to obtain a smooth surface for the further deposition with an exact thickness in z direction. The side faces of the layer, however, remain unmachined. The successive operation of deposition and face milling repeats until the part is completed. As a result of this procedure, a near net-shaped metal part is built. To remove remaining stair steps on the surface and to increase the accuracy, a surface finishing by milling is applied in the final stage. All the necessary steps take place with only one set-up in the machine, therefore errors caused by set-up changes are avoided.

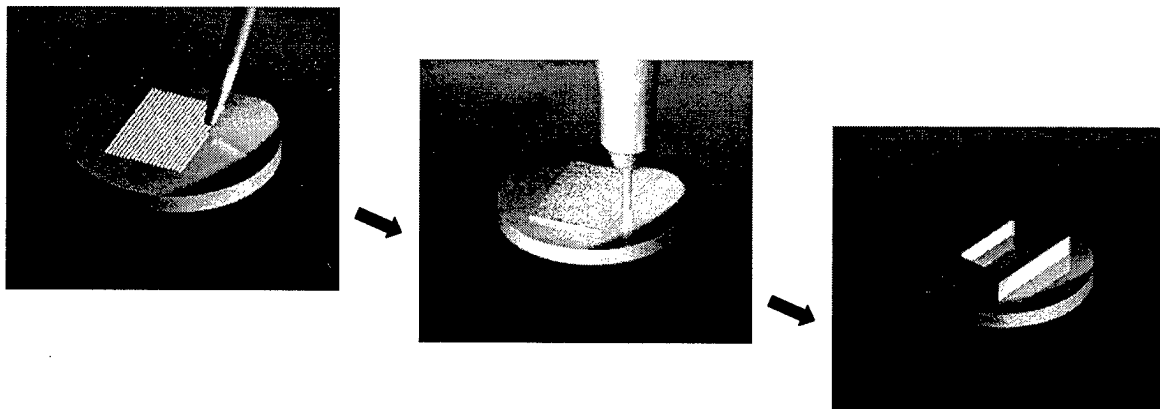


Fig. 1: Process principle of 3D Welding and Milling

In contrast to SDM, there is no support structure used in the 3D Welding and Milling process. Due to this process characteristic, the process is currently only able to produce metallic parts with 2 1/2 features such as injection molds.

The 3D Welding and Milling facility consists of a conventional 3-axis vertical milling machine and an arc welding equipment. To use different materials, the machine can be equipped with two arc welding guns. As wire material, mild steel or stainless steel is used. The substrate plate is mounted on the linear x-y table of the machine. This kind of configuration has an distinct advantage over other additive processes in that only a simple retrofitting of an existing 3-axis machine is required to realize the process instead of acquiring a special equipment.

3. Mechanical Strength and Microstructure of Welded Structure

In order to find out the mechanical value of multiple-welded structures, three tensile specimens according to the specification of ASTM were made and tested, **Fig. 2**. The values measured parallel to the building direction are 60 kgf/mm², whereas the used mild steel material has a tensile strength of 55 kgf/mm². This result shows that the strength of the multiple-welded structure is comparable to conventional mild steel, therefore an application in injection molding seems to be possible regarding the mechanical strength.

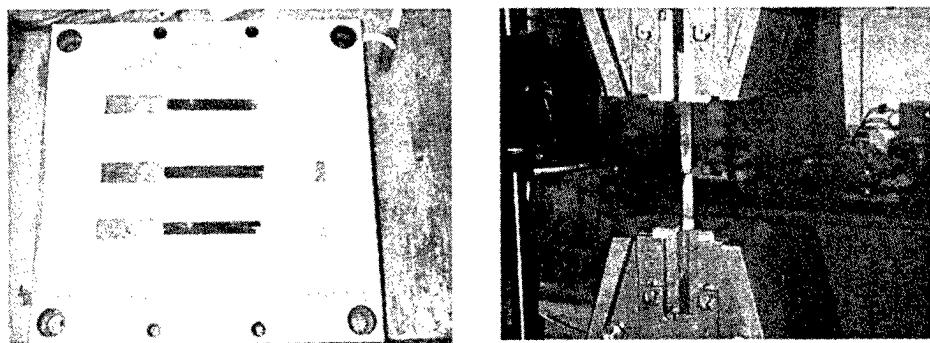


Fig. 2: Tension test specimens fabricated by 3D Welding and Milling

The analysis of microstructure shows a nearly full dense structure, as shown in **Fig. 3**. Only a few number of process inherent pores are recognizable in the microstructure. Most of the pores which are normally detected in the overlapping areas between the beads are removed during the face milling operation, therefore the number of pores is kept relatively small in the microstructure. The investigation also shows a change of the microstructure along the height of the part. This result is due to the changing heat condition during the deposition. Adjacent to the substrate plate, the microstructure is coarse because of the rapid heat dissipation into the cold substrate plate when the first beads are deposited on the substrate plate. With the increasing height, however, the cooling rate is reduced due to the decreased heat dissipating area which corresponds to the cross section area of the part and moreover, the accumulated heat from the previously deposited layers. Therefore, the grains take a globular structure.

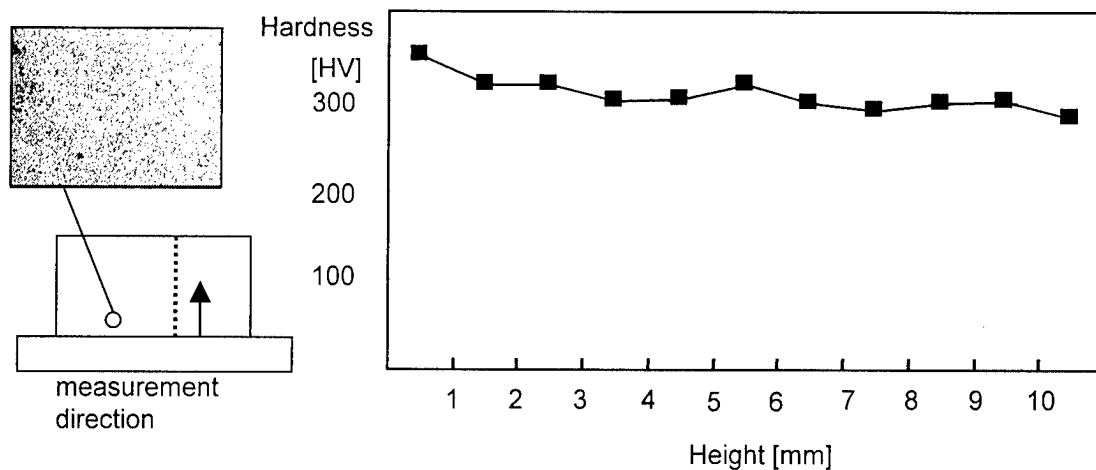


Fig. 3: Microstructure and hardness in the test specimen

The measurement of hardness proves the different microstructures along the height of the tensile specimen. As shown in Fig. 3, the hardness is decreasing from near the substrate plate to the top of the specimen. Starting from a hardness value of 331.8 HV at the bottom where mostly coarse grains are located, the hardness decreases to 280.5 HV at the top of the specimen. To avoid such a difference in microstructure, a preheating of the substrate plate can be used.

4. Experimental Results of Fabricating Injection Molds

To see whether this process combination is applicable for the fabrication of mold inserts, different sets of cavity and core inserts are selected as test parts and fabricated by the 3D Welding and Milling process. In Fig. 4, the fabricated parts of the core and the cavity inserts for cellular phone cover are shown with its CAD model. In Fig. 5, the lamp cover as test part and its injection molds are also shown.

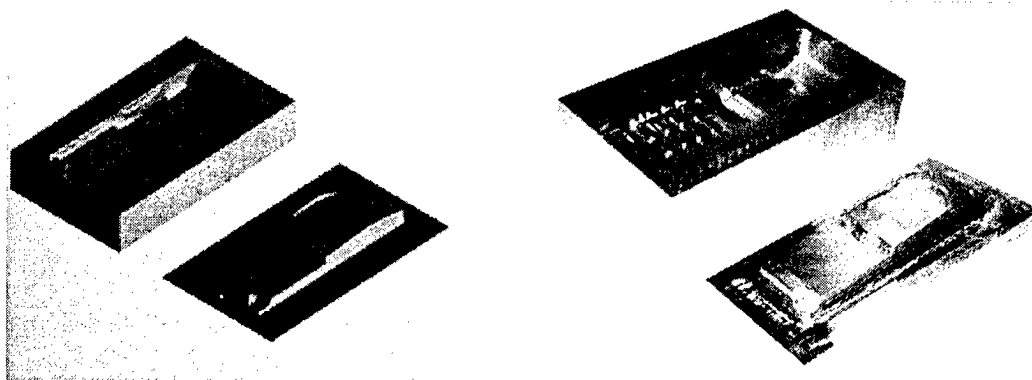


Fig. 4: CAD model and fabricated core and cavity inserts

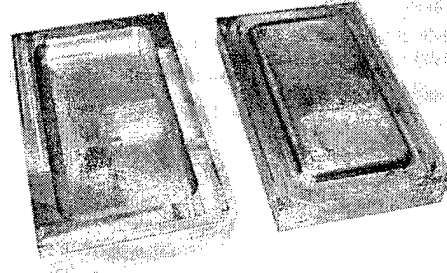
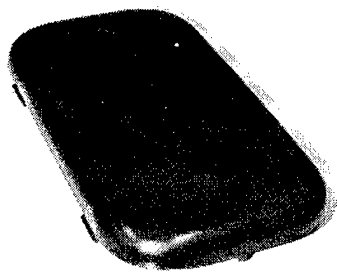


Fig. 5: Lamp cover as test part and its injection molds

The successful fabrication of injection mold inserts demonstrates the viability of the 3D Welding and Milling process. However, a further detailed experimental analysis regarding the accuracy and manufacturing time is required to verify its applicability for industrial usage.

The main advantage of SFF processes becomes evident when building parts with internal features. Among internal features, conformal cooling channel for injection molds is gaining an increasing importance for rapid tooling. The results so far indicate the positive effect of such conformal cooling channels on the lifetime of injection molds as well as on the quality of injected parts [5, 6]. Like 3D Printing and SLS processes, 3D Welding and Milling also enables building conformal cooling channels without using support structure when an appropriate value of offset for welding beads is selected. For the test purpose, a W-shaped conformal cooling channel is integrated in the mold insert, **Fig. 6**. The result shows the capability of 3D Welding and Milling to build the channels inside of the part. Due to the bead thickness, however, the limit of channel diameter is set around 20 mm.

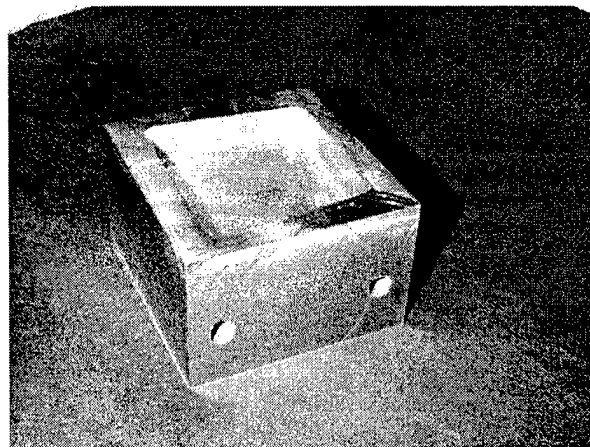
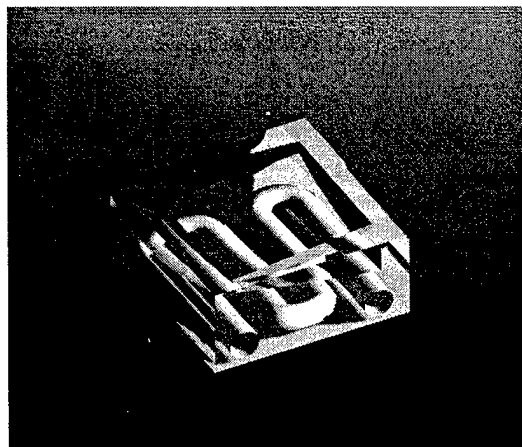


Fig. 6: Mold insert with conformal cooling channel

5. Thermal Management

The involvement of heat causes a thermal warpage of parts which is a common problem of additive processes [7]. To reduce the warpage, several possibilities can be taken into consideration. Besides the increase of thickness of the substrate plate, its preheating before the deposition is an effective method to reduce the warpage [8]. Moreover, preheating can be of benefit for a homogeneous microstructure. For these reasons, a heating plate is placed directly beneath the substrate plate to preheat it up to 200 °C.

The cooling rate after completing the deposition process exerts also an influence on the warpage. To reduce it, the part should be cooled down as slowly as possible. Therefore, the part is cooled down in the machine with the natural heat convection. When reaching the room temperature, the surface machining of the cooled part starts. In this machining operation, the total distortion of the part then completely corrected.

Besides the experimental investigation, a theoretical analysis of the deposition process is performed to minimize the thermal distortion. The analysis regarding the influence of different building directions on the warpage was performed in case of a single layer with a commercial FEM package ANSYS. The simulation indicates that the deposition with long beads causes more warpage than with short beads, as shown in **Fig. 7**. Consequently, when selecting building direction, the bead length should be taken into consideration.

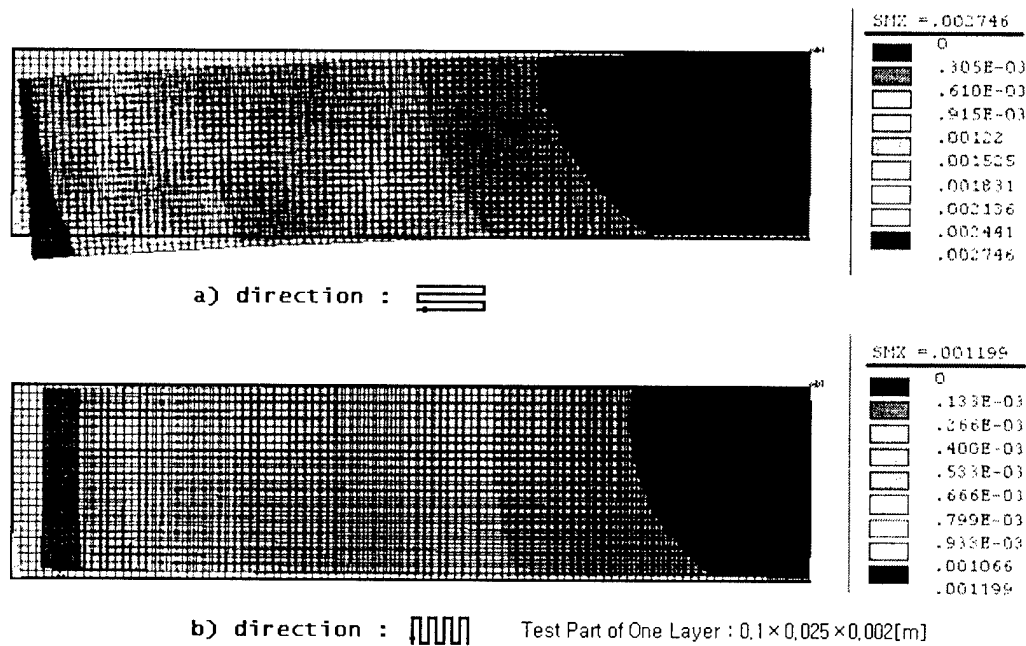


Fig. 7: Simulation result

6. Conclusions

According to the current state of the art, dimensional accuracy as well as surface quality of metallic parts and tools produced by SFF techniques are still far behind that of conventionally machined. To increase accuracy and surface roughness, a hybrid approach consisting of additive and subtractive technique called 3D Welding and Milling has been developed.

The multiple-welded tensile specimen fabricated by 3D Welding and Milling has a tensile strength of 60 kgf/mm² in the building direction which is comparable to the value of conventional mild steel. This value implies that the multiple-welded structure can be used as mold regarding the mechanical strength. The microstructure is nearly dense with a hardness value of 300 HV.

The successful fabrication of metallic parts, especially molds demonstrates that 3D Welding and Milling is an appropriate process to produce prototype molds. The combination of welding with milling operation not only increases both surface quality and accuracy, but it also gives a more manufacturing flexibility. Features like conformal cooling channels and multiple materials can be built.

A further process development should be focused on the increase of mechanical properties as well as effective thermal management to increase the quality of parts.

7. References

- [1] R. Merz, F.B. Prinz, K. Ramaswami, M. Terk, L. Weiss, "Shape Deposition Manufacturing", Proceedings of the Solid Freeform Fabrication Symposium, University of Texas at Austin, August 8-10, 1994
- [2] J. R. Fessler, R. Merz, A. H Nickel, F.B. Prinz, "Laser Deposition of Metals for Shape Deposition Manufacturing", Proceedings of the Solid Freeform Fabrication Symposium, University of Texas at Austin, August 1996, pp. 117-124
- [3] F. Klocke, H. Wirtz, W. Meiners, "Direct Manufacturing of Metal Prototypes and Prototype Tools", Proceedings of the Solid Freeform Fabrication Symposium, University of Texas at Austin, September 1996, pp. 141-148
- [4] F.B. Prinz, L.E. Weiss, C.H. Amon, J.L. Beuth, "Processing, Thermal and Mechanical Issues in Shape Deposition Manufacturing", Proceedings of the Solid Freeform Fabrication Symposium, University of Texas at Austin, September 1995, pp.118-129
- [5] E. Sachs, S. Allen, M. Cima, E. Wylonis, H. Guo, "Production of Injection Molding Tooling with Conformal Cooling Channels using the Three Dimensional Printing Process",

Proceedings of the Solid Freeform Fabrication Symposium, University of Texas at Austin, September 1995, pp.448-467

- [6] X. Xu, E. Sachs, S. Allen, M. Cima, "Designing Conformal Cooling Channels for Tooling", Proceedings of the Solid Freeform Fabrication Symposium, University of Texas at Austin, August 1998, pp. 131-146
- [7] N. W. Klingbeil, J. W. Zinn, J. L. Beuth, "Measurement of Residual Stresses in Parts Created by Shape Deposition Manufacturing", Proceedings of the Solid Freeform Fabrication Symposium, University of Texas at Austin, August 1997, pp. 125-132
- [8] R. K. Chin, J. L. Beuth, C. H. Amon, "Thermomechanical Modeling of Successive Material Deposition in Layered Manufacturing", Proceedings of the Solid Freeform Fabrication Symposium, University of Texas at Austin, August 1996, pp. 507-514

RAPID TOOLING BY INTEGRATING ELECTROFORMING AND SOLID FREEFORM FABRICATION TECHNIQUES

Bo Yang Ming C. Leu*

Department of Mechanical Engineering
New Jersey Institute of Technology
Newark, New Jersey 07102

Tel: 973-596-5668, Fax: 973-596-5601, E-mail: bxy0487@oak.njit.edu

Abstract: This paper describes a rapid tooling process that integrates solid freeform fabrication (SFF) with electroforming to produce metal tools including molds, dies, and electrical discharge machining (EDM) electrodes. Based on experimental data analysis, the geometry and material of the SFF part, the properties of the electroformed metal, and the process parameters are significant factors that cause inaccuracy in the manufactured tools. Thermomechanical modeling and numerical simulation is used to determine the geometry of the SFF part and the electroform thickness for minimizing the manufacturing time and cost while satisfying the tooling accuracy requirement.

Keywords: Solid freeform fabrication, Rapid tooling, Electroforming, Mold, EDM electrode, Finite element analysis.

1. INTRODUCTION

Solid freeform fabrication (SFF), or rapid prototyping (RP), is being increasingly used in industry for prototyping, tooling and manufacturing applications [1, 2]. Rapid tooling is the process of directly or indirectly employing RP technologies to fabricate castings, dies, molds and EDM electrodes. Currently used rapid hard tooling processes such as 3D KeltoolTM [3], 3-dimensional printing (3DP) [4] and RapidToolTM [5], first bind metal powders by various techniques to generate a green part. Afterwards the part is debinded, sintered, and infiltrated with copper or other metals to produce functional metal parts. The powder metallurgy approaches involve random noise shrinkage during the sintering process and thus the generated metal parts suffer dimensional uncertainty and they usually have rough surface finish.

Electroforming is the use of electrodeposition of metal onto a part that is subsequently separated from the deposit to produce a metal shell. This can be used to make molds and dies for replicating the part [6]. The metalized part, which has the required shape, dimensions, accuracy and roughness, is sunk into an electrolyte bath as the cathode and deposited a layer of metal, normally copper or nickel, for a specified thickness. The part is then separated from the metal shell. The shell is then backed with other materials to form a mold cavity or an EDM electrode. A nickel electroformed part can be used for a prototyping tool or even a production tool [7], and a

* Dr. Ming C. Leu is on leave at the National Science Foundation as the Program Director for Manufacturing Machines and Equipment.

copper electroformed part can be used as an EDM electrode [8]. Metals deposited by electroforming have distinct properties [9]. Dimensional tolerances can be very good, often up to 0.0025 mm, and surface finishes of 0.05 μm and better can be obtained quite readily if the master part is adequately smooth [10]. The emergence of rapid prototyping technology has brought about new opportunities for electroforming in rapid production tooling. Since electroforming can closely copy the geometry and surface quality of an RP part, the accuracy and surface finish of the produced tool is largely determined by the accuracy and surface finish of the RP part.

This paper first describes the tooling process and case studies on electroforming of SL parts to generate EDM electrodes and mold cavities. The investigation on the tooling generation demonstrates that the main sources of tooling inaccuracy are thermal deformations caused by burning out the SL part and by backfilling the electroformed metal shell with a molten metal. At the process of separating the metal shell from the SL part, the part is incinerated at about 560 °C. The thermal expansion of the SL part deforms the metal shell because the coefficient of thermal expansion of the SL part material is much larger than that of nickel or copper. In the backfilling process, the molten metal is cast into a metal box and solidified, which also generates thermal deformation. Only low melting alloy (melts below 135 °C) is used in the case studies so that the backfilling deformation is not serious.

A thermomechanical model is established to analyze the thermally induced stress during the burnout of the SL part. The model is implemented in ANSYS software to numerically simulate the thermal stress based on finite element method (FEM). The analysis demonstrates that appropriate geometry design of the RP part and appropriate electroform thickness not only reduce thermal stress thus improving tooling accuracy, but also minimize manufacturing time and cost. The presented study demonstrates that the integration of electroforming with solid freeform fabrication is a viable way for the making of metal dies, molds, and EDM electrodes.

2. TOOLING PROCESS AND CASE STUDIES

2.1 Tooling Process

The process for making EDM electrodes using SL parts and electroforming is illustrated in Fig.1. Compared with making EDM electrodes by direct electroplating of copper on positive SL parts [11], this method does not require uniform thickness of the plated copper. The negative (complementary) geometry of the EDM electrode is prototyped by stereolithography for use as the RP part. The part must be rigid enough to withstand the electroforming stress [12] induced during the metal layer deposition. Before electroforming of the SL part, metalization of the SL surface is needed to make the part electrically conductive. Several techniques for metalization of nonconductive materials are available [13]. Electroless plating, a process involving autocatalytic or chemical reduction of aqueous metal ions onto a base substrate, is used to metalize the SL part. The metalized SL parts are then electroplated with copper to a desired thickness. In the process of separating the SL part from the metal shell, prevention of the electroform deformation is extremely important. The RP part built with ceramic and other difficult-to-melt materials are

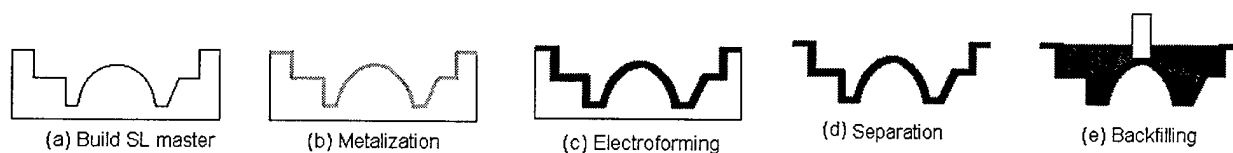


Figure 1. EDM tooling process

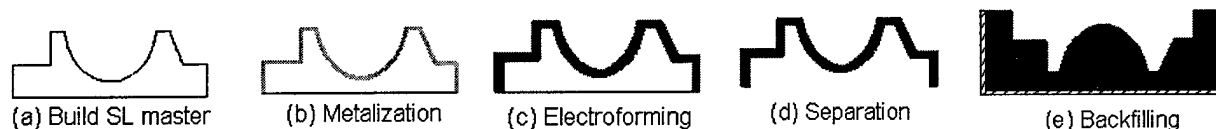


Figure 2. Mold tooling process.

preferred to be separated by mechanical extraction. Melting, burning out, or heat softening can be applied to wax and thermoplastic RP parts. SL resin is a thermosetting material, and burning out of the SL part is the preferred separation method. Complete incineration of the SL part is observed at the temperature of about 560 °C. During the burnout process, the heat results in expansion of the part. This may crack or deform the electroformed metal shell. The geometry of the RP part and the thickness of the electroformed metal shell needs to be optimized in order to minimize the manufacturing cost, while the stresses exerted on the metal shell due to the thermal expansion of the part do not crack the copper shell or generate unacceptable deformation. Because the EDM electrode does not contact the workpiece during the electrical discharge machining process, the strength of the electrode is not critical. A low melting alloy with good electrical and thermal conductivity is good for backfilling the shell to form an EDM electrode.

The rapid mold making process is very similar to the process for making EDM electrodes. This is illustrated in Fig.2. A layer of metal, which is thick enough to resist the deformation caused by the separation and backfilling, is electroformed upon an SL part metalized by nickel electroless plating. The deformation of the metal shell generated during the burnout process is largely affected by the electroforming thickness, material properties and the geometry of the part. Backfilling of the electroform is more critical in manufacturing a mold cavity compared with manufacturing an electrode due to the high strength required in the subsequent injection molding process. The harder the backfilled metal, the higher the strength of the mold cavity. However, a harder metal usually has a higher melting temperature. Casting with a high melting temperature metal tends to generate larger thermal stresses, which may cause larger deformation in the electroformed metal shell. To reduce the injection molding cycle time, conformal cooling lines may be put around the nickel shell before the backfilling process.

2.2 Case Studies

Two SL parts of the same geometry, as illustrated in Fig.3(a), are used to make EDM electrodes using the tooling process with the copper layer thickness of 2 mm and 4 mm. The cavity of the SL part is 12 mm deep. The SL cavities are polished to the surface finish of 1.24 μm . After polishing, key dimensions are measured three times and the average is recorded. After burning out the SL resin at the oven temperature of 560 °C, the corresponding dimensions are measured and compared with the data measured on the SL parts. It is found that the dimensional deviation of the electrode with 4 mm thick copper shell is smaller than that of the electrode with 2 mm thick copper shell. It means that the thinner the copper layer, the lower the dimensional accuracy of the electrode resulted from the burning process. The largest deviation is 0.24% for the 2 mm thick copper layer electrode, and 0.19% for the 4 mm thick one. The surface finish of the two finished EDM electrodes is measured, and the average surface roughness is about 1.26 μm for both electrodes. The copper shell is backed with a tin-lead alloy whose melting point is 103 °C. The finished 2 mm copper layer electrode is then used to machine a hard steel workpiece to a depth of 10 mm in 3 hours and 25 minutes.

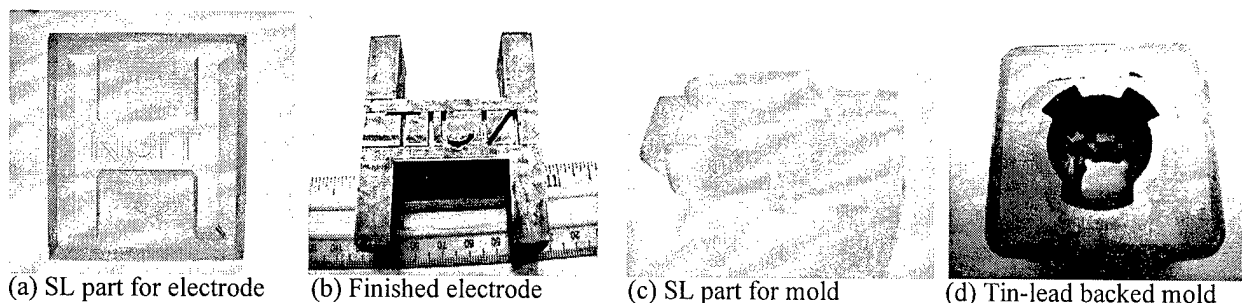


Figure 3: Electroformed electrode and Mold generated by the tooling process.

Two nickel electroformed mold cavities shown in Fig. 3(d) are made by the mold tooling process. Nickel is used in the electroforming because its mechanical properties are about the same as those of stainless steel and nickel is highly wear and corrosion resistant. After metalizing the parts with nickel to a thickness of about 0.005 mm by electroless plating, the parts are nickel-electroformed with sulfamate electrolyte to form nickel shells with the thicknesses of 2 mm and 4 mm. The electroformed SL parts are then put into an oven to burn out the resin at 560 °C. The dimensional deviation of the mold with 2 mm thick nickel is larger than that of the mold with 4 mm thick nickel. The largest deviation is 0.25%. The nickel electroforms are then backfilled with molten tin-lead alloy whose melting temperature is 138.5 °C. The surface finish of both mold cavities is measured about 1.27 μm , which is nearly the same as that of the SL parts.

2.3 Factors Affecting Tooling Accuracy

The factors that affect accuracy in the described tooling process include the accuracy of the RP part, deformation caused by electroforming stress [12], and thermal deformations generated during the separation and backfilling processes. With various techniques, electroforming can achieve deviation between the master part and the electroformed tool as small as 0.0025 mm [10]. Thermal deformations caused by burning out the part and by backfilling the electroformed shell with molten metal thus are important sources of inaccuracy. Low melting point alloys with good electrical and thermal conductivity can be used to backfill the shell to form an EDM electrode with small thermal deformation. An electroformed mold cavity backed with a high-strength metal can significantly improve the durability of the electroformed mold and increase the ability of the mold to resist deformation during the injection molding process. However, a high-strength metal always has a high melting point, which may generate large deformation in the mold cavity when it is solidifying.

3. MODELING AND ANALYSIS OF THE BURNOUT PROCESS

3.1 Thermomechanical Modeling of the Burnout Process

Thermal stresses induced during the burnout of an SL part are a multi-material, non-linear, transient thermal-mechanical coupling problem. Boley and Weiner [14] proved that the thermal solution is independent of any changes caused by thermally-induced stresses under the condition that the time history of displacement closely follows the change of temperature, and vice versa. Assume that the burnout process satisfies the condition because the thermal expansion closely follows the temperature variation, then the thermomechanical coupling problem can be simplified as an uncoupled, transient thermal stress problem. Under this assumption, the modeling of the thermal stress can be divided into two steps: thermal modeling and structural modeling.

Thermal modeling is used to compute the transient temperature field $T(x,y,z,t)$ during the burnout process. The governing heat conduction equation is

$$\alpha \nabla^2 T = \frac{\partial T}{\partial t} \quad (1)$$

where $\alpha = \frac{k}{c\rho}$, k , c , and ρ are heat conductivity, specific heat, and material density, respectively.

The two initial conditions are that the metal shell and the master are at the room temperature, T_r . Because the hot air inside the oven chamber is in a perfect thermal contact with the outer surface of the electroformed object, the thermal convection effect can be ignored during the burnout process. Thus the first boundary condition is:

$$T(p,t) = f(t) \quad (2)$$

where p is a point on the surface of the metal, and $f(t)$ represents the oven temperature.

Because the metal shell is in perfect contact with the RP part, the heat transfer at the boundary surfaces of the RP part and the metal shell is conduction dominated. So the temperatures at these surfaces are the same. In addition, the heat flux leaving metal shell through the contact surface equals to that entering the RP part. Thus for a point P on the contact surface of the metal and the RP part, the boundary conditions are:

$$T_m(P_b,t) = T_r(P_b,t) \quad (3)$$

$$k_m \frac{\partial T_m}{\partial n}(P_b,t) = k_r \frac{\partial T_r}{\partial n}(P_b,t) \quad (4)$$

where the subscripts m and r refer to the metal shell and the RP material, respectively, and n is the normal to the boundary surface at point P_b .

Structure modeling is used to calculate the thermally-induced stress exerted on the metal shell. The problem of thermoelasticity consists of determining the following:

6 stress components: σ_{xx} , σ_{yy} , σ_{zz} , σ_{xy} , σ_{yz} , σ_{zx} ,

6 strain components: ϵ_{xx} , ϵ_{yy} , ϵ_{zz} , ϵ_{xy} , ϵ_{yz} , ϵ_{zx} , and

3 displacement components: u , v , w

that need to satisfy the following fifteen equations:

$$\begin{aligned} 3 \text{ equilibrium equations: } & \left. \begin{aligned} \frac{\partial \sigma_{xx}}{\partial x} + \frac{\partial \sigma_{xy}}{\partial y} + \frac{\partial \sigma_{xz}}{\partial z} &= 0 \\ \frac{\partial \sigma_{xy}}{\partial x} + \frac{\partial \sigma_{yy}}{\partial y} + \frac{\partial \sigma_{yz}}{\partial z} &= 0 \\ \frac{\partial \sigma_{xz}}{\partial x} + \frac{\partial \sigma_{yz}}{\partial y} + \frac{\partial \sigma_{zz}}{\partial z} &= 0 \end{aligned} \right\} \quad (5) \end{aligned}$$

$$\begin{aligned} 6 \text{ stress-strain relations: } & \left. \begin{aligned} \epsilon_x &= \frac{1}{E} [\sigma_{xx} - \nu(\sigma_{yy} + \sigma_{zz})] + e \cdot \nabla T \\ \epsilon_y &= \frac{1}{E} [\sigma_{yy} - \nu(\sigma_{xx} + \sigma_{zz})] + e \cdot \nabla T \\ \epsilon_z &= \frac{1}{E} [\sigma_{zz} - \nu(\sigma_{yy} + \sigma_{xx})] + e \cdot \nabla T \\ \gamma_{xy} &= \frac{1}{2G} \sigma_{xy}; \gamma_{yz} = \frac{1}{2G} \sigma_{yz}; \gamma_{zx} = \frac{1}{2G} \sigma_{zx} \end{aligned} \right\} \quad (6) \end{aligned}$$

and 6 strain-displacement relations:

$$\left. \begin{aligned} \varepsilon_{xx} &= \frac{\partial u}{\partial x}; & \varepsilon_{yy} &= \frac{\partial v}{\partial y}; & \varepsilon_{zz} &= \frac{\partial w}{\partial z} \\ \varepsilon_{xy} &= \frac{1}{2} \gamma_{xy} = \frac{1}{2} \left(\frac{\partial v}{\partial x} + \frac{\partial u}{\partial y} \right) \\ \varepsilon_{yz} &= \frac{1}{2} \gamma_{yz} = \frac{1}{2} \left(\frac{\partial w}{\partial y} + \frac{\partial v}{\partial z} \right) \\ \varepsilon_{zx} &= \frac{1}{2} \gamma_{zx} = \frac{1}{2} \left(\frac{\partial u}{\partial z} + \frac{\partial w}{\partial x} \right) \end{aligned} \right\} \quad (7)$$

where e is the coefficient of thermal expansion, and the shear modulus G is related to Young's modulus E and Poisson's ratio ν by $G = \frac{E}{2(1+\nu)}$.

3.2 FEM Based Thermal Stress Computation

The above thermomechanical model is applied to an SL cylinder with the outer radius of 50 mm and length of 100 mm, which is nickel electroformed and then burned. The radius A of the inner hole of the cylinder and the electroform thickness t are variables. We assume that the oven is preheated to the burnout temperature (560 °C) and the temperature is constant during the burning

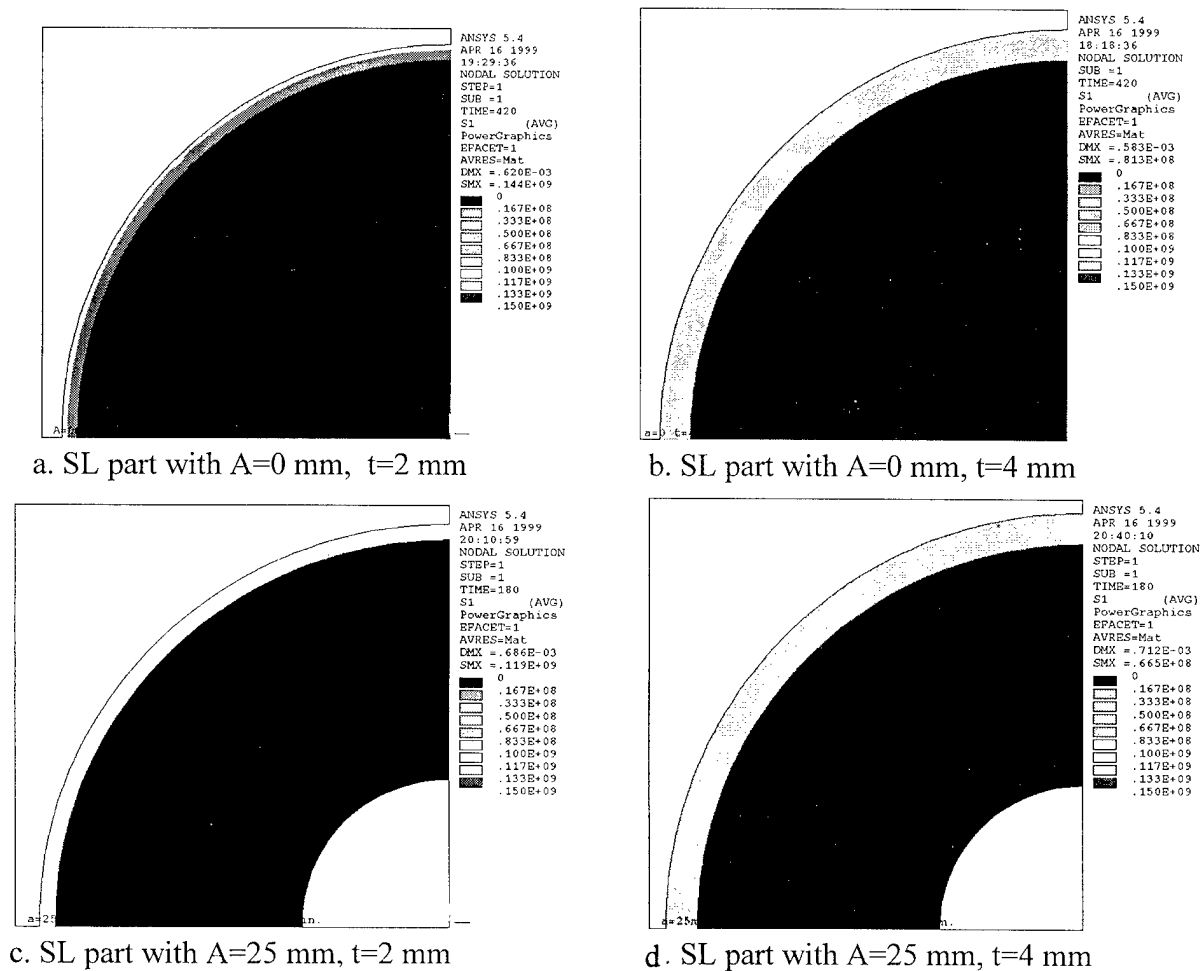


Figure 4. Simulation of thermal stresses with different SL parts and electroform thickness

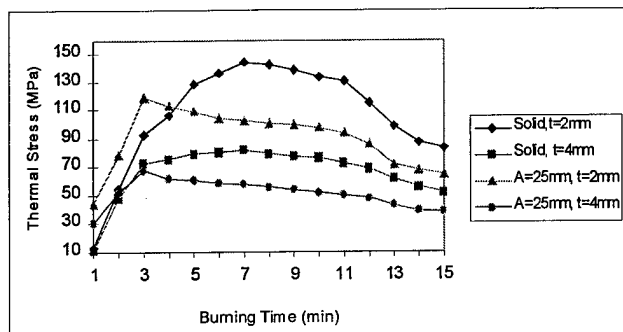


Figure 5. Maximum thermal stress vs. time during burnout process.

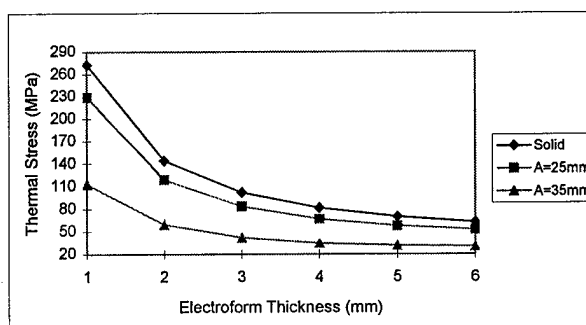


Figure 6. Maximum thermal stress vs. electroform thickness for burnout process.

process. To solve this problem, ANSYS 5.4, a finite element analysis software package, is used to simulate the thermal stress resulted from the burnout process. Fig. 4 shows the simulation results with four different sets of variables. For solid SL parts, when electroform thickness increases from 2 mm to 4 mm, the maximum thermal stress decreases from 144 MPa to 81.3 MPa (see Fig. 4(a) and 4(b)). If $A=25$ mm, compared with the solid SL parts the maximum thermal stress for 2 mm electroform thickness reduces from 144 MPa to 119 MPa (see Fig. 4(a) and 4(c)), and that for 4 mm electroform thickness reduces from 81.3 MPa to 66.5 MPa (see Fig. 4(b) and 4(d)). During the burnout process, the maximum thermal stress changes over time, as illustrated in Fig. 5. Fig. 6 illustrates that with the same SL part structure, the maximum thermal stress decreases when electroform thickness increases. The inner hole can always decrease the thermal stress: the larger the hole, the smaller the thermal stress. This demonstrates that thermal stress induced by the burnout process can be reduced when an RP part is built with appropriate design of its structure. The structure needs to be strong enough to resist the electroforming stress, which is determined by electroforming process parameters. In our case, if the electroforming stress exerted on the electroformed nickel shell is 10 MPa, the deformation caused by the electroforming stress can be calculated as is listed in Table 1. From the table, we can see that solid SL parts always have smaller electroforming deformations. When A increases, the electroforming deformation increases. Table 2 lists the build time and material cost for different SL parts. It shows by how much the inner hollow structure can save build time and material cost.

Table 1. Electroforming deformation (ED) for different sets of parameters A and t

	$t=1$ mm	$t=2$ mm	$T=3$ mm	$t=4$ mm	$t=5$ mm	$t=6$ mm
$A=0$ mm	0.0024	0.0046	0.0067	0.0078	0.0109	0.0128
$A=25$ mm	0.0043	0.0085	0.0142	0.0187	0.0231	0.0275
$A=35$ mm	0.0096	0.0194	0.0282	0.0372	0.0461	0.0547

Table 2. Comparison of build time and material cost for different SL parts

	Build Time (hour)	SL 5170 Material Cost
Solid	35.27	\$ 161.63
$A=25$ mm	26.46	\$ 121.25
$A=35$ mm	17.98	\$ 82.43

4. CONCLUSION

The method of solid freeform fabrication combined with electroforming for fabricating metal molds and EDM electrodes is presented. The case studies indicate that the described method is feasible for rapid tooling of molds and EDM electrodes. The electroforming thickness affects the mechanical property and dimensional accuracy of the mold. Thermal deformations caused by burning out the SL part and backfilling the electroformed metal shell with molten metal are identified as the major sources of inaccuracy. The thermomechanical modeling and FEM based numerical simulation of the stress induced during the burnout process is performed. The analysis demonstrates that the structure of the SFF part and the electroform thickness have significant effects on the fabrication time and cost and the tooling accuracy.

5. ACKNOWLEDGMENT

This work is partially supported by the New Jersey Commission on Science and Technology via the Multi-lifecycle Engineering Research Center at New Jersey Institute of Technology.

6. REFERENCES

1. Kruth, J. -P., Leu, M. C., Nakagawa, N., 1998, Progress in Additive Manufacturing and Rapid Prototyping, *Annals of the CIRP*, 47/2.
2. Leu, M.C. and Zhang, W., 1998, Research and Development of Rapid Prototyping and Tooling in the United States, *Proc. of First International Conference on Rapid Prototyping and Manufacturing*, Beijing, China.
3. Jacobs, P.F., 1997, Recent Advances in Rapid Tooling from Stereolithography, *Proc. of the Seventh International Conference on Rapid Prototyping*, San Francisco.
4. Sachs, E., Cima, M., Cornie, J., 1990, Three-Dimensional Printing: Rapid Tooling and Prototyping Directly from a CAD Model, *Annals of the CIRP*, 39/1:201-204.
5. Bourell, D.I., Crawford, R.H., Marcus, H.L., Beaman, J.J., Barlow, J.W., 1994, Selective Laser Sintering of Metals, *J. of Manufacturing Science and Engineering*, 68/2:519-527.
6. Spiro, P., 1968, Electroforming, Robert Draper Ltd.
7. Yang, B., Leu, Ming C., 1999, Integration of Rapid Prototyping and Electroforming for Tooling Application. *Annals of the CIRP*, 48/1.
8. Yang, B., Leu, Ming C., 2000, EDM Tooling by Electrodeposition of Rapid Prototyping Parts. *International Journal of Agile Manufacturing*, Vol. 1.
9. Safranek, William H., 1986, The Properties of Electrodeposited Metals and Alloys. Second edition, American Electroplaters and Surface Finishers Society, Orlando, Florida.
10. Degarmo, E.P., Black, J.T., Kohser, R.A., 1984, Materials and Processes in Manufacturing, Sixth edition, Macmillan Publishing Company, New York.
11. Leu, M.C., Yang B., Yao, W.L., 1998, A Feasibility Study of EDM Tooling Using Metalized Stereolithography Models. *Technical Papers of NAMRC, XXVI*, Atlanta.
12. Stein, B., 1996, A Practical Guide to Understanding, Measuring and Controlling Stress in Electroformed Metals, *Proc. of AESF Electroforming Symposium*, Las Vegas.
13. Duffy, J. I., 1980, Electroless and Other Non-Electrolytic Plating Techniques, Noyes Data Corporation, New Jersey.
14. Boley, Bruno A., Weiner, Jerome H., 1960, Theory of Thermal Stresses, John Wiley & Sons, New York.

Rapid Tooling for Injection Molding of Rubbers

J. Eschl, T. Blumenstock, P. Eyerer

Institute for Polymer Testing and Polymer Science

IKP - University of Stuttgart

Böblinger Straße 78 E

D - 70199 Stuttgart

<http://www.ikp.uni-stuttgart.de>

Abstract

Rapid tooling is known for molding of thermoplastics for years. Information about rapid tooling for rubber parts is quite rare. The different demands on tools for vulcanizing rubbers and some case studies will be shown. The emphasis is on cast resin tools, since this technique is cheap and can be used from everyone.

1 Introduction

In the past, several rapid tooling methods for injection molding of thermoplastics have been developed. However, there are no published examples concerning injection molding of elastomers. This paper illustrates the differences in the injection process, the demands on the tools and presents examples. These examples demonstrate the limitations and the needs for further development.

2 Different injection molding processes of thermoplastics and rubber - different demands on the tools

Overall, both processes are quite similar - molten material is injected with a screw into a cavity. Of course the particularities lead to different demands on the tools. Mainly the temperatures of the tools and the injected material differ.

Injection moulding of thermoplastics requires a high material temperature and a low mould temperature as the molten thermoplastic material will become solid if it cools. The production requires a transition from hot molten material to cold frozen material. Therefore the temperature of the mould is normally less than 80°C and the temperature of the injected material is between 200°C and 350°C. Rubbers vulcanise at high temperature (160°C – 200°C), thus the rubber is preheated to approx. 80°C or less to become soft enough to be injected into the hot tool. There, after a few seconds when the material warms up, vulcanisation starts. Depending on the material, the cycle time is about 100s. The part will be ejected at high temperature. Therefore the mould has a constant temperature of e.g. 180°C.

The rubber parts are of course very flexible so that the ejection forces are low. Thermoplastic parts have a reasonable stiffness, however due to shrinkage they can stick to the tool so high ejection forces are necessary. These forces often lead to a failure of the mold.

Tools for injection molding thermoplastics therefore need high strength at temperatures below 100 °C to withstand the clamping forces, (the forces during injection and ejection). Tools for producing rubber need to be stiff up to 200 °C. Since the tools are normally mounted at room temperature and then heated, the thermal expansion must also be considered.

3 Potential Process chains for manufacturing rubber parts

The constant tool temperature of 200 °C was the first criteria to reduce the number of process chains to be considered. The metal based process chains like the DMLS[®] from EOS, 3D-Keltool[®] or DTM's Rapid Steel are ideal. However, all of these materials contain copper which can be critical for the vulcanization with sulfur, thus coatings of the tools will be necessary and the compatibility with the rubber must be tested. These process chains are costly compared to others. The indirect ones are also time consuming, so that they may only be considered for very complex geometries. Cast resin tools, which have improved considerably during the last few years are well known from injection molding of thermoplastics. Here the advantages are the low investment costs, the tools can be made before drafting and tool design is finished. These tasks may be done directly on the model. Working with thermoplastics, the problems are the low strength, so the tools may break either due to the injection or ejection forces. This will be a less of a problem when using rubbers, but most of the cast resins soften above 160 °C and have a reasonable thermal expansion. This causes accuracy problems.

4 Making experience with case studies

The first tool should only show the feasibility of the process chains. So a part was chosen which can be molded in two mold halves with a simple parting surface. One mold half was manufactured in steel by conventional turning to reduce the costs. Figure 1 shows a modified damping ring with gate.

4.1 3D-Keltool

A model of the tool was built with stereolithography to be copied with the Keltool process (Figure 3). Therefore it was scaled with an oversize of 0,6 % as recommended by the supplier, the cavity and parting surface was finished to the correct dimensions. It was then sent to 3D-Systems where it is converted into metal within 10 days. This part showed exactly the same surface quality as the stereolithography pattern but was 0,2 % too small. The parting surface was slightly rounded, so it had to be planed. To avoid problems with the copper, a coating of chrome was applied by electroplating.

It was then no problem to mount the mould in the injection machine. The first shots showed the need for some venting holes at the pins of the part, it was then simple to mould several parts with standard injection parameters.

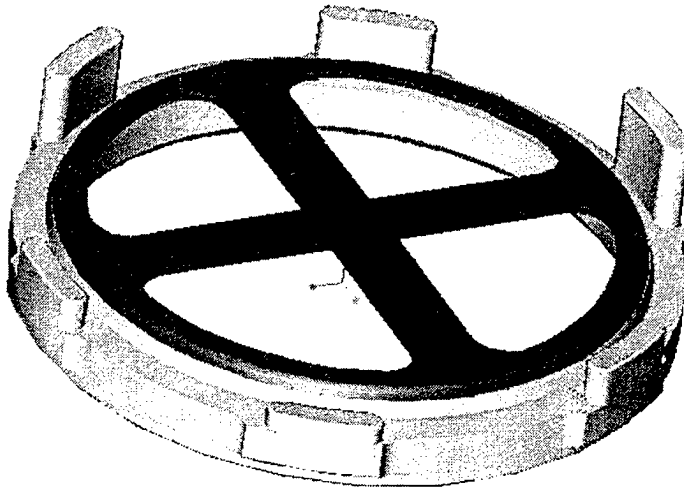


Figure 1: CAD-design of the test part with gate

4.2 Cast resin tool with Cubital's Solid Ground Curing SGC

Since the SGC has its advantages for big parts, the negative of the tool was designed in CAD and built. Cast resin was poured directly on the finished negative and pre-hardened to form the tool. The negative can be removed easily since it is mainly wax and the tool can be completely hardened. All these steps take about 5 days. As casting material, an epoxy resin from HEK was chosen, which is a standard material for casting tools for injection molding of thermoplastics. The tool was made as a insert in a mother mould. Since the resin has a reasonable thermal expansion ($\alpha = 3 \cdot 10^{-5} \text{ K}^{-1}$ at 50°C , $\alpha = 6 \cdot 10^{-5}$ at 190°C , a total of 0,4 % from 30 - 190°C), it was cut to a smaller diameter than the mother mold to allow enough room for expansion. It was then mounted on the injection molding machine and slowly heated to 180°C . During the molding process with different pressures, no problems occurred. However, some small deformation could be seen on the holes forming the pins of the part, this can be explained by the thermal expansion coupled with the softening of the material.

4.3 Cast resin tool with stereolithography model

This process chain starts directly with the part itself. It is built in the stereolithography machine (together with the gate), then it is accurately finished, also the stair stepping is removed. Here also some painting may be useful. Draft angles may be added by sanding, this is necessary to enable subsequent removal of the pattern from cast resin. Normally, the parting surface can be carved in wood or plastic material. In our case the other half of the tool already existed in steel. The part is then glued to the parting surface and coated with release agent. The first half of the tool can be casted with epoxy filled material. When this half is cured it serves together with the part to cast the second half (which was not necessary in our case). The injection molding took place as described above with out problems. It must be noted that the molded parts from this mould had excellent surface quality, the best of all the process chains tested.

Here two tools were tested from a commercial resin (HEK EP 250) and a highly filled mixture developed at IKP (Figure 3). This was done because most of the cast resins available for rapid tooling showed softening below 200°C in previous material tests. A measurement showing this behaviour is shown Figure 2.

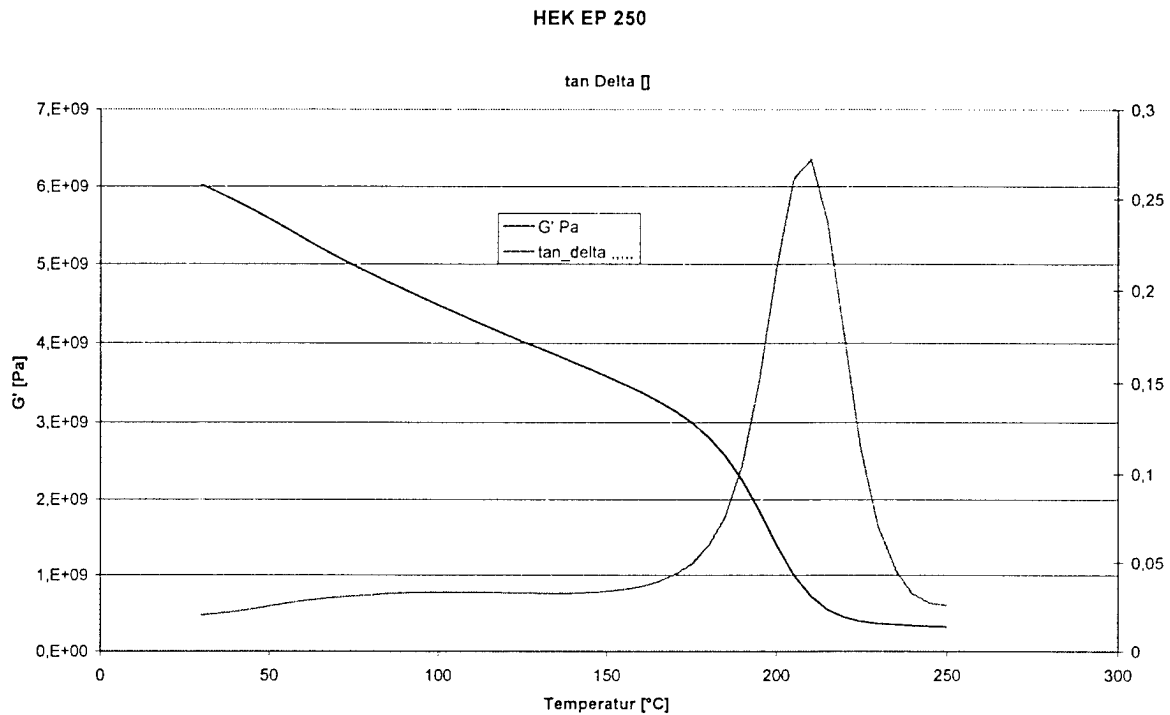


Figure 2: Thermo dynamic mechanical analysis of a cast resin

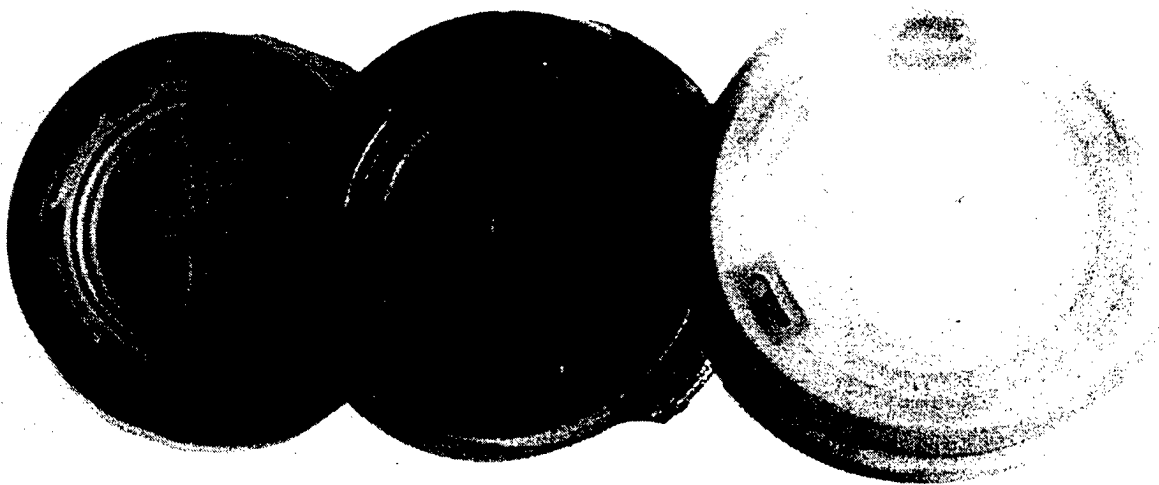


Figure 3: Tools made in Keltool, Cast resin, Stereolithography pattern

4.4 Tool made with metal spraying

The process chain for metal sprayed tools is similar to the cast resin process chain. The first step is the SLA master pattern which is mounted on a plate with the required parting surface. In the next step a low melting alloy has to be sprayed and the generated thin metal shell has to be backed with cast resin. The advantage of this technique compared to cast resin tools is the improved mould surface. The surface is less brittle than a cast resin surface and is generated within a short time. Of course the equipment for spraying metals is not available for everybody. It is also not possible to generate every shape, since the material is sprayed and for example holes cannot be reached.

4.5 Conclusion of case studies

With all of the mentioned process chains, it was possible to manufacture dozens of rubber parts. All tool materials were compatible with the used rubbers (FPM, ACM, NBR). Of course the metal tools appeared identical after the last shot to that at the beginning whereas some of the cast resin tools had small deformations. The accuracy of all tools is comparable and within the tolerances of usual rubber applications. To manufacture high precision parts, for example sealings which require to be accurate within some hundredths of a millimeter, these process chains are not suitable. With this simple part where the feasibility had to be shown, the tested process chains were more time and cost consuming than the conventional route (milling, eroding) so that the next comparison has to be made with a more complex geometry.

The cast resin, which was chosen carefully after mechanical tests at 200 °C, did not fulfill the demands completely. Other materials have to be found with improved thermal properties (thermal expansion, thermal conductivity) and most importantly, mechanical properties.

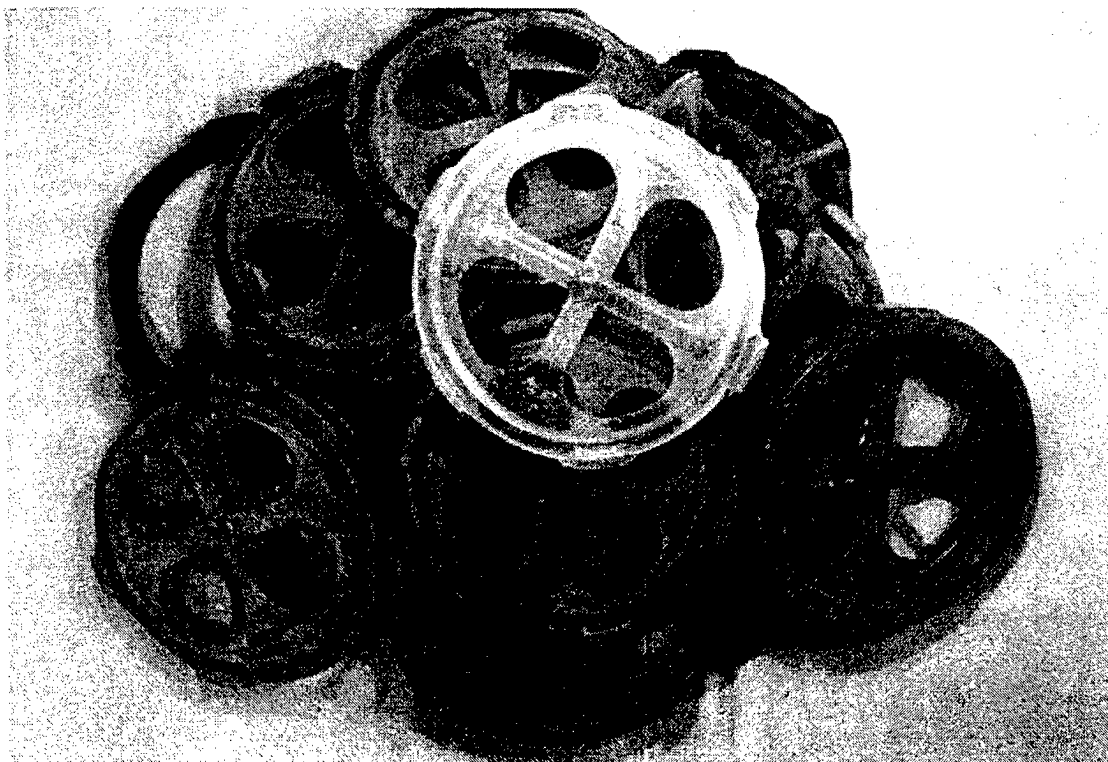


Figure 4: rubber parts in different materials from various tools, stereolithography part

5 Improved resins for casting tools

Since cast resin tools have several advantages, this process chain, mainly the material, is worthy of further improvement. A cast resin tool can be made in parallel to the tools design starting with the part. The parting line, drafting and the gate are designed manually by the tool maker. The molds also close properly. Finishing of the parting surfaces is not required. This step often takes a lot of time when using other tooling techniques.

The demands on cast resins for making tools can be defined as shown in Table 1.

Processing	Properties of cured material
<ul style="list-style-type: none">• Compatibility with stereolithography patterns (i.e. hardening below 70 °C)• Negligible shrinkage• Good surface quality• Good flow properties• Wetability (reinforcement)• Reaction not affected by humidity, fillers or reinforcement	<ul style="list-style-type: none">• Stiffness and strength at room and tool temperature (200 °C)• Cuttable with normal cutting tools• Low thermal expansion• High thermal conductivity• High density and heat capacity• Compatibility with rubbers (some materials disturb the vulcanization)

Table 1: Demands on Cast resins for tooling (rubbers)

These demands have to be considered either when selecting commercial resins or when searching for new cast resins or new filling materials. For example, most of the commercial tooling resins are filled with aluminum. However considering the thermal expansion, heat capacity, density or the thermal conductivity there are more suitable metals. On the one hand aluminum powder possesses a very good thermal conductivity, but on the other hand the thermal expansion is rather high. Since the tool temperature is high (200°C), it is important to use a cast resin with a low thermal expansion, therefore aluminum isn't a suitable filler. The IKP developed a cast resin tooling technique which allows use of reinforcement fibers on critical features and allows a fillerloading of about 5% in volume more than commercial cast resins. The combination of a high fillerloading and a suitable filler gives high stiffness and enables cast resin tooling even at 200 °C.

Figure 5 shows a rubber part together with metal inserts which are surrounded by rubber. It was manufactured in a tool with two mold halves and three slides made of new cast resin composition developed at the IKP.

6 Summary

The feasibility to produce rubber parts with rapid tooling techniques was shown. Of course all of the tested process chains show some problems to be improved. Cast resin tooling as a very affordable technique has a high potential to be improved in future.

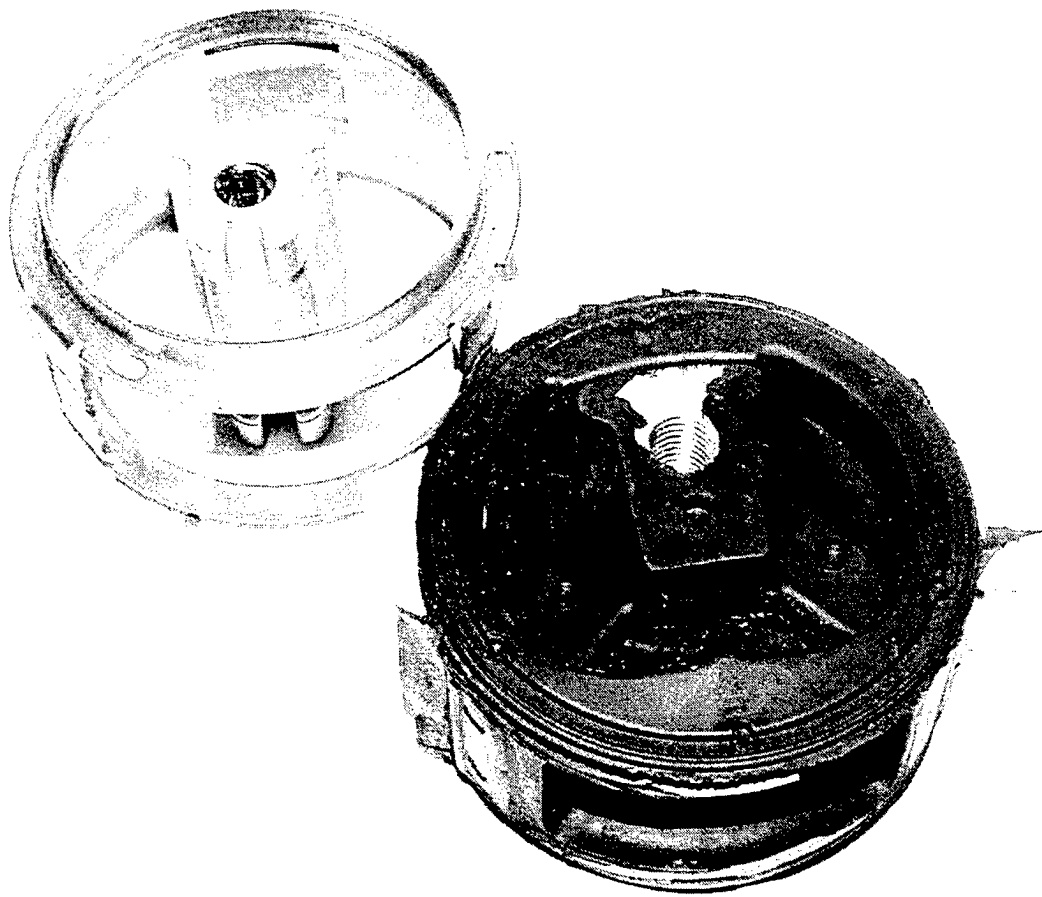


Figure 5: Rubber part vulcanized in a cast resin tool, inserts to be inmolded

Acknowledgement

Parts of the presented research were supported by the state of Baden-Wuerttemberg. The authors especially thank the project partners:

Bertrandt Fahrzeugtechnik GmbH
 Freudenberg Techn. Dienste KG
 Modellbau Satzke
 Glöckler Dichtsysteme – Günter Hemmrich GmbH
 KACO GmbH & Co
 Parker Hannifin GmbH
 Saar – Gummiwerke GmbH

Also many thanks to suppliers who provided tools for free:

3D-Systems
 Cubital

Investigation of Reinforced Ceramic Molds for Resin Patterns

Shirong He Hiroyuki Yoshiura Chiaki Mori
Oita Industrial Research Institute

Abstract

There are many methods to produce parts. Traditionally parts are fabricated via machining method for material removal. This technology has been enhanced with material addition technology which allows deposition of material layer by layer. However the principle for production has never been changed, the cost and time saving is constantly a goal for manufacturers. Using resin patterns as master pattern for precision casting is considered to be an effective method for the purpose of reducing cost and saving time. The appearance of inexpensive stereolithography system particularly created a possibility for local small and medium enterprises to develop the potential applications for RP units. In this report we focus on a process for which resin patterns formed with SL unit were used as master patterns. Numerical analysis and pattern removal test were utilized to investigate mold failures which were related to thermal expansion of resin within the mold, and the problems associated with the fracture mechanism of ceramic molds. As a result, it was clarified that: the fracture of ceramic molds was caused by the stress intensity state on the slope. To control thermal expansion, it was proven effective to reduce the thickness of resin patterns. In addition the efficiency of thick wall molds was limited and fiber reinforcement ceramic mold had the ability to resist the expansion force of resin patterns. By applying reinforcement fiber to ceramic molds, a production process that integrated CAD design, RP technology and investment casting proved promising.

1. Introduction

Since the stereolithography system was commercialized in the late 1980's, many manufacturing methods similar to this technology have been developed and a great number of researches were conducted to attempt to expand the potential applications of RP units.

Fabricators are not satisfied to create only a limited number of prototype parts, the intent to fabricate real parts using this technology is now a given requirement. For local small and medium enterprises, it especially is ideal to produce their products with low cost and short time. Local small and medium enterprises desire to have the technology, by which existing inexpensive stereolithography systems are harnessed to produce short run production of functional parts. We set our research theme as Mono Production of Complex Shape Part by a Stereolithography System. The goal of this research is to establish a process, which integrates CAD design, RP technology and investment casting.

There are many of similarities between this process and lost wax process. The difference is only that resin patterns are applied to the master patterns instead of wax patterns in the process. In this sense the process might be called lost resin process. Several local industrial research institutes in Japan currently have been conducting related research. Although the varieties of resin used for master patterns vary amongst researchers, there is a common problem, namely the fracture of the ceramic mold which results from thermal expansion of the resin patterns^[1]. The reason points to inability of a resin to change its solid phase to a solution while undergoing an application of heat during a burn out process^[2].

In this study, fracture mechanism of the ceramic mold was investigated by numerical analysis, and a composite mold was proposed as the means to protect the ceramic shell mold from fracture caused by thermal expansion of the resin pattern.

2. Details of the Process

The digital model of parts almost can be designed with all of the CAD software. However a design model has to be a shell structure in order to apply to the master pattern. There are several merits in shell

master patterns. Firstly it uses resin material less than a solid pattern, this contributes to the costs. Secondly the pattern with a relatively thin wall has the ability to reduce the action of thermal expansion, at this point it is expected that a thin wall structure will be effective to avoid the occurrence of cracks.

In spite of the merits, there are also some demerits besides, such as a large size data and deformation of master patterns. The large size data causes spending more processing time than a solid pattern, and deformation of master patterns affects the accuracy and precision of final parts. Moreover it requires skilled and experienced designers to design the shell patterns.

In aspect of mold building, the procedure is almost the same as normal investment casting process. Ceramic shell molds are built via coating slurry and stuccoing sand by 8 layers respectively. One thing different from the lost wax process appears during a pattern removal process. Since there is not any chemical or physical method to melt the resin, the master pattern just can be removed from the mold via burning out. Therefore thermal expansion of resin patterns is an unavoidable problem.

In table1 was shown the properties of resin and ceramic materials. The resin has a very large thermal expansion rate but its Young's modulus is much smaller than that of ceramics. Fortunately a smaller modulus of elasticity ordinarily can compensate the defectiveness of thermal expansion to some extent.

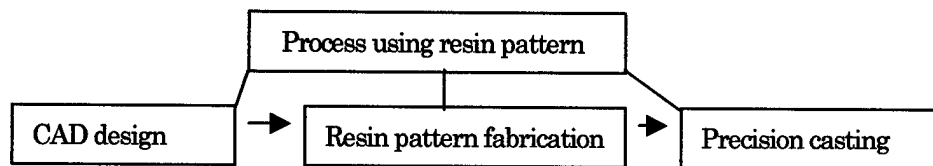


Fig.1 Brief flow of the process

Table 1 Material properties of resin and ceramics

	Young's modulus	Thermal expansion rate
Resin	270MPa	$130 \times 10^{-6}/^{\circ}\text{C}$
Ceramics	220000MPa	$9 \times 10^{-6}/^{\circ}\text{C}$

3. Fracture Mechanism of Ceramic Shell Mold

3.1 Analytical Model and Method

Numerical analysis (Boundary Element Method) was utilized to evaluate mechanical performance of the ceramic shell mold. The estimation terms included the thin wall effect of shell master patterns and the enhancement efficiency of thick wall molds.

For the analysis we established a localized analytical model, which was cut off from a typical quadrangle frame along symmetrical axes (shown in gif.2). Material coefficients used for this analysis were listed in table1. Considering there was no external load applied to the model and all the sections cut off from the entire frame body were along the symmetrical axes, The boundary conditions were:

- 1) Just the stress vertical to the boundary surface acts on the sections cut off from the quadrangle frame.
- 2) The upper surface of the resin pattern and lower surface of the ceramic mold are free.

3.2 Mechanism of Fracture

Some results from BEM analysis are shown in Fig.3. The stress proves a normal tensile state on the right section, where the failure occurs when the maximum principle stress reached the material strength. But the stress on the slope proves a peculiar distribution. This means that the stress at the corner is unlimited, and the fracture condition ought to be decided by comparing a stress intensity factor to the material toughness. Stress intensity factor is a parameter to describe the situation of the peculiar distribution stress. A crack occurs when the stress intensity factor reached the value of the material toughness, and finally causes the mold

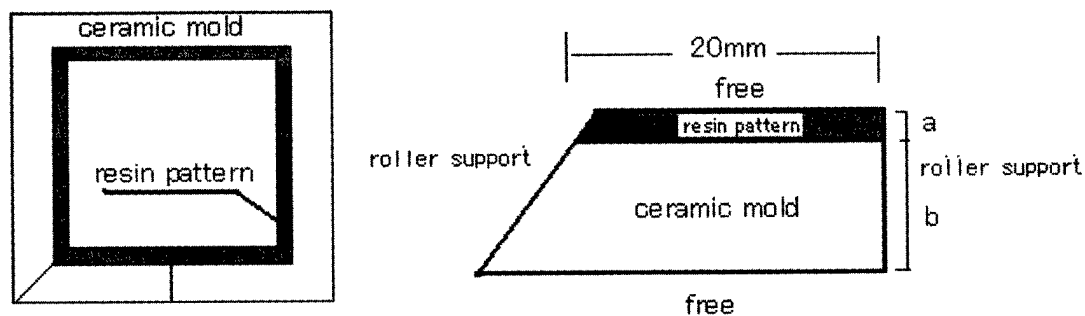


Fig2 Analytical model and boundary conditions

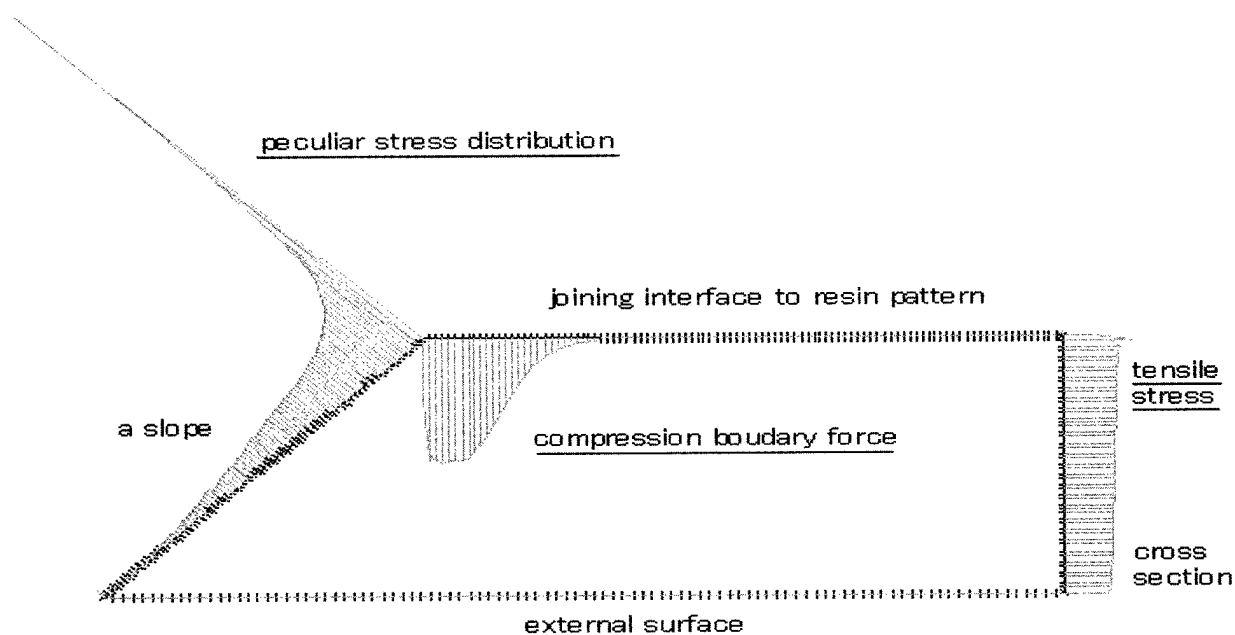


Fig.3 Stress situation on ceramic mold from analysis

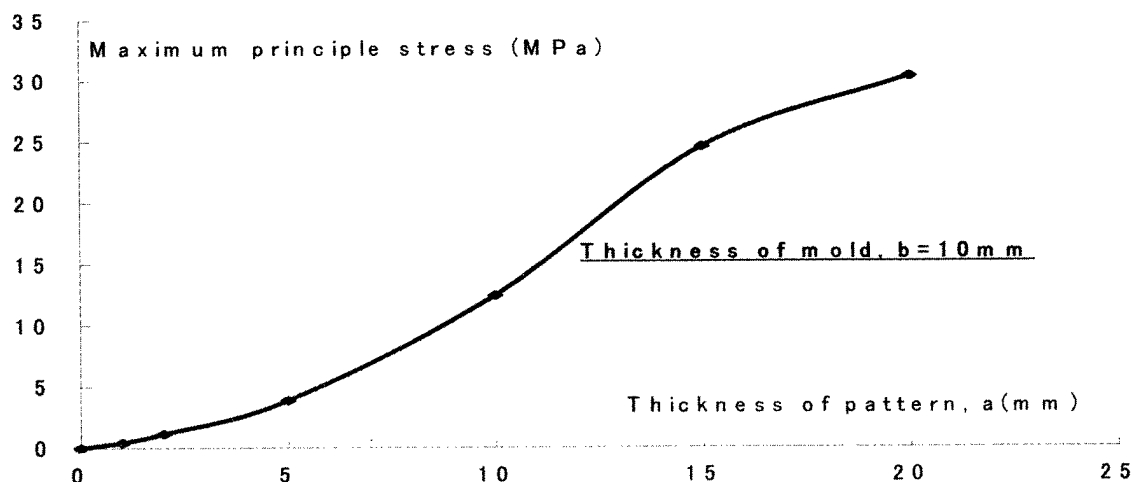


Fig.4 Relations of maximum principle stress to a

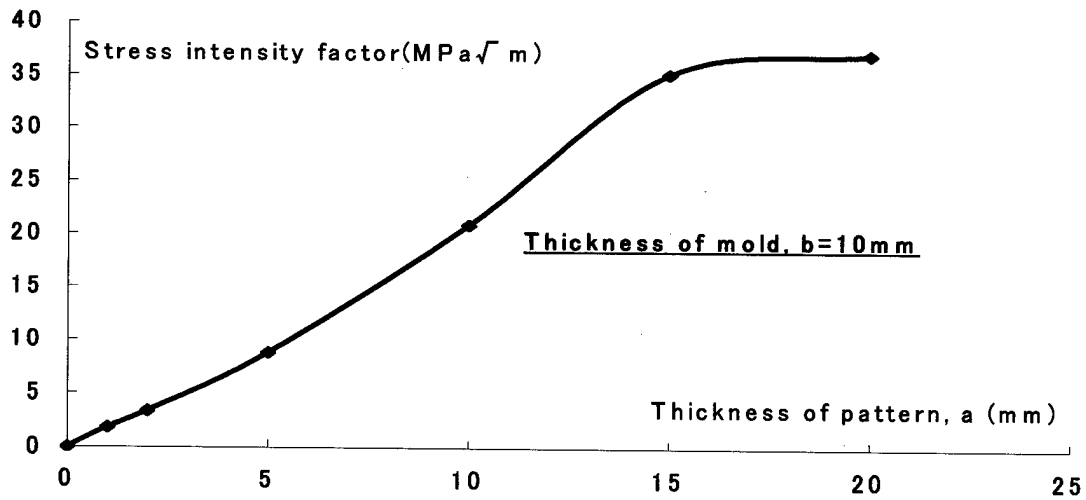


Fig.5 Relations of stress intensity factor to a

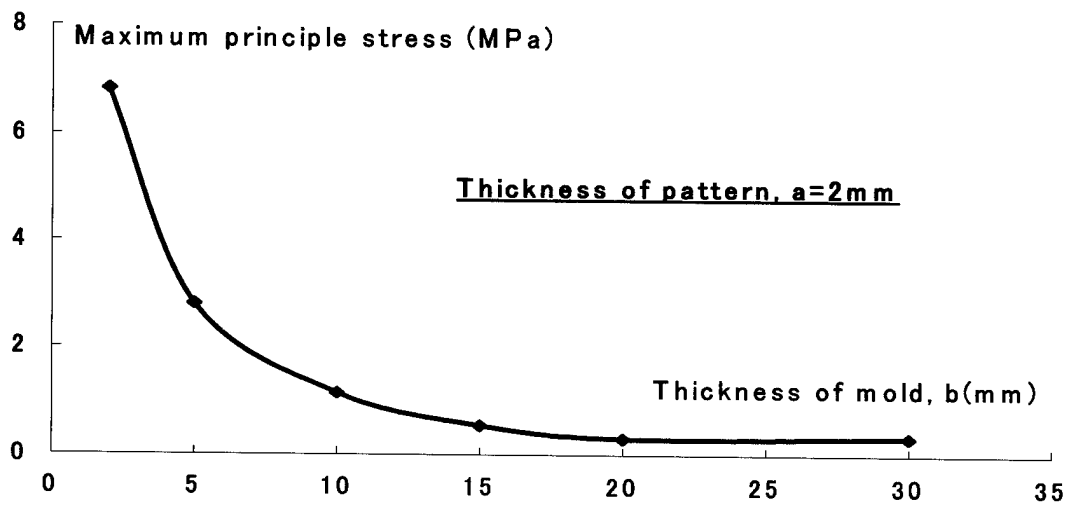


Fig.6 Relations of maximum principle stress to b

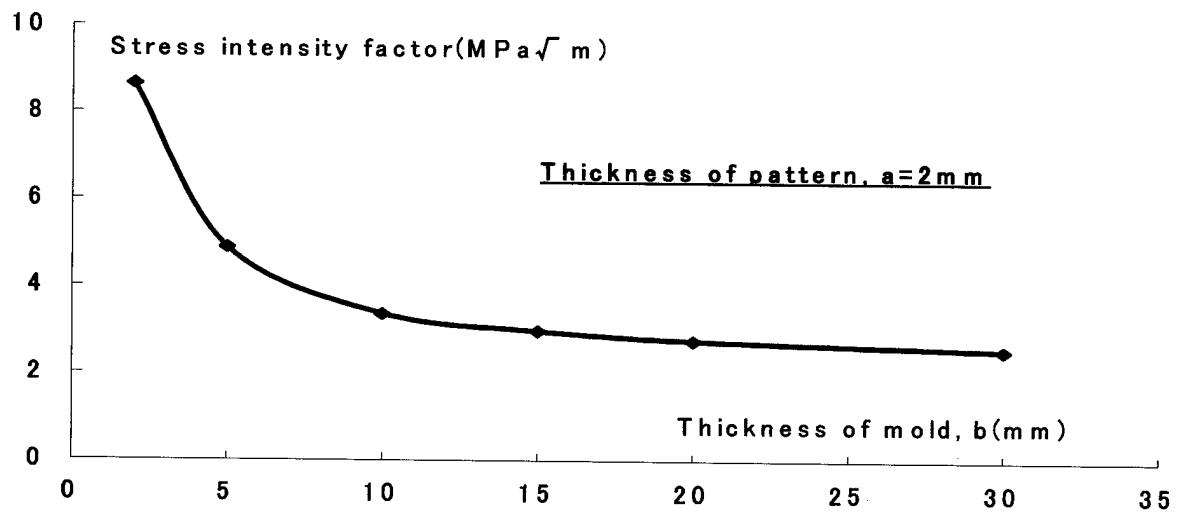


Fig.7 Relations of stress intensity factor to b

failure. Generally speaking the failure mode is dependent on a certain parameter of both mentioned above, either the maximum principle stress or the stress intensity factor, which reaches the critical value previously.

3.3 Effect of Shell Resin Pattern

As mentioned above even though a shell model has more complex geometries than a solid model in structure, the contributions to reducing the thermal expansion of the resin pattern can not be neglected. The effects of the shell pattern are clarified by BEM analysis, which was carried out under assuming the thickness of the mold is 10mm.

Fig4 shows the relations between thickness of the resin pattern and maximum principle stress on the cross section. The maximum principle stress increases along with an increasing thickness of the resin pattern. However when the thickness is thinner, the increment of the maximum principle stress against a constant increment of thickness will decrease. That is to say, the effect to control thermal expansion via reducing the thickness of master patterns is uneven for different thickness. There appear remarkable effects for thick wall patterns, but the effects will not be greatly expected for thin wall patterns.

Fig.5 correspondingly shows the relations between the thickness of resin patterns and stress intensity factor on the slope. The stress intensity factor vs. thickness curve can be regarded as a straight. The thinner the thickness, the smaller the stress intensity factor. This indicates that we have to reduce the thickness of resin pattern as much as possible to avoid cracking at the corner.

For example, if we assume that the maximum principle stress and the stress intensity factor are 1 MPa and $1 \text{ MPa}\sqrt{\text{m}}$ respectively, when the thickness of the resin pattern is 1mm, then when the thickness of the resin pattern become 5mm, the maximum principle stress and the stress intensity factor will reach 8.95 MPa and $4.82 \text{ MPa}\sqrt{\text{m}}$ respectively. In other words, if a mold that has the ability to keep without any failure behavior until the maximum thickness of resin pattern is 1mm, when using a resin pattern as a master pattern which has a thickness of 5 mm, the ceramic mold ought to have 8.95 times the strength and 4.82 times the toughness to prevent it from failure.

3.4 Reinforcement Effect of Thick-Wall Ceramic Mold

The ceramic shell mold used in foundries usually is a thin wall structure with a thickness of less than 10mm. It is easy to think of enhancing ceramic shell molds via increasing coating layers. But the efficiency by increasing the number of layers of the ceramic mold has not been clarified yet. Fig.6 shows the relations between the thickness of the ceramic shell mold and maximum principle stress on the cross section. Correspondingly Fig.7 shows the relations between the thickness of the ceramic shell mold and stress intensity factor on the slope. In this numerical analysis, we assume that the thickness of resin pattern is fixed to 2mm and the thickness of the mold is allowed to vary from 2mm to 30mm.

However the efficiency to reduce the maximum principal stress and stress intensity factor will decrease, when the thickness of the ceramic shell mold exceeds 10mm. Therefore the enhancement via increasing coating layers of the ceramic shell mold is limited. We can not obtain an ideal enhancement effect whilst the mold has a very large thickness.

4. Fiber Reinforcement Mold

4.1 Structure of Fiber Reinforcement Mold

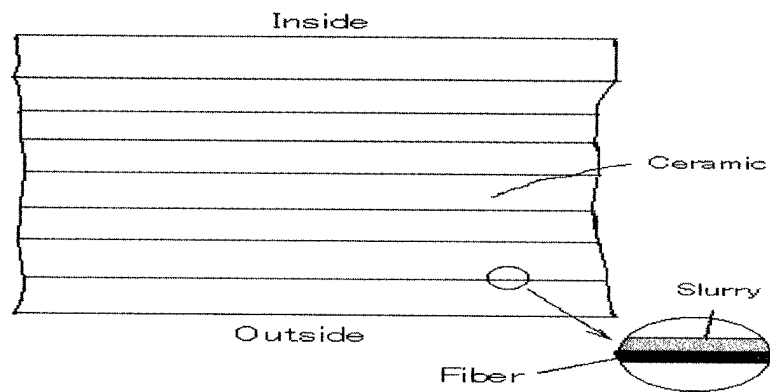
Reinforcement fibers used for the ceramic mold are short fibers such as glass fiber, carbon fiber and metal fiber with the length of less than 20mm. There are three ways shown below to apply the reinforcement fiber to the ceramic shell mold^[3].

- 1) Coat fibers as independent layers
- 2) Mix sand with fiber as stucco materials
- 3) Mix binder with fiber as a slurry

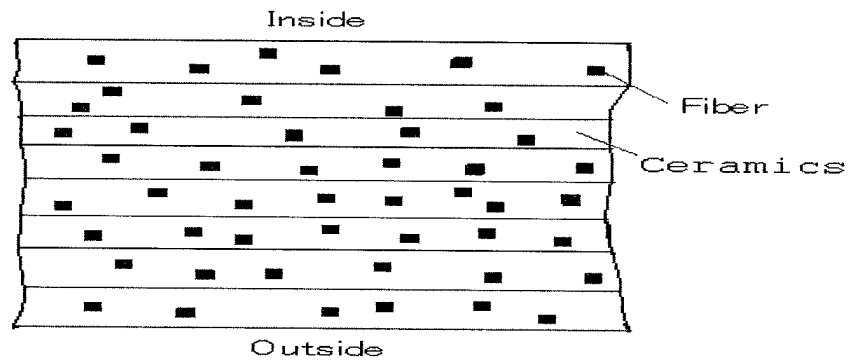
The structures of the fiber reinforcement molds are shown in Fig.8

4.2 Pattern Removal Test

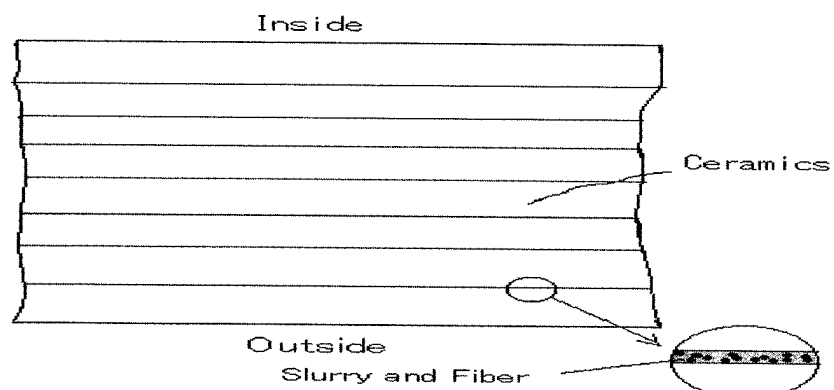
In order to evaluate mechanical performance of the fiber reinforced mold during removing the resin



(1) Coat the fiber as independent layers



(2) Mix sand with fiber



(3) Mix binder with fiber

Fig.8 Reinforcement methods

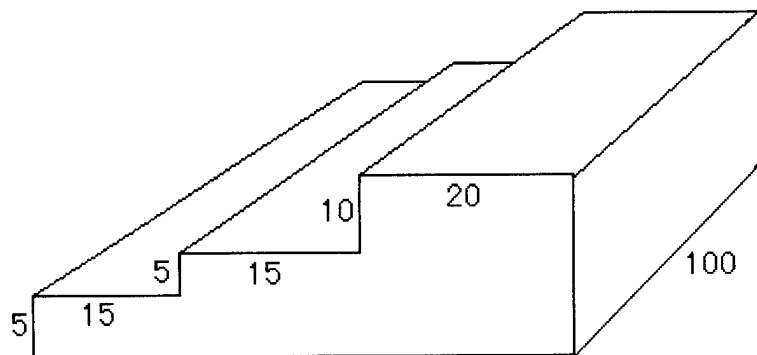


Fig.9 Stepped pattern

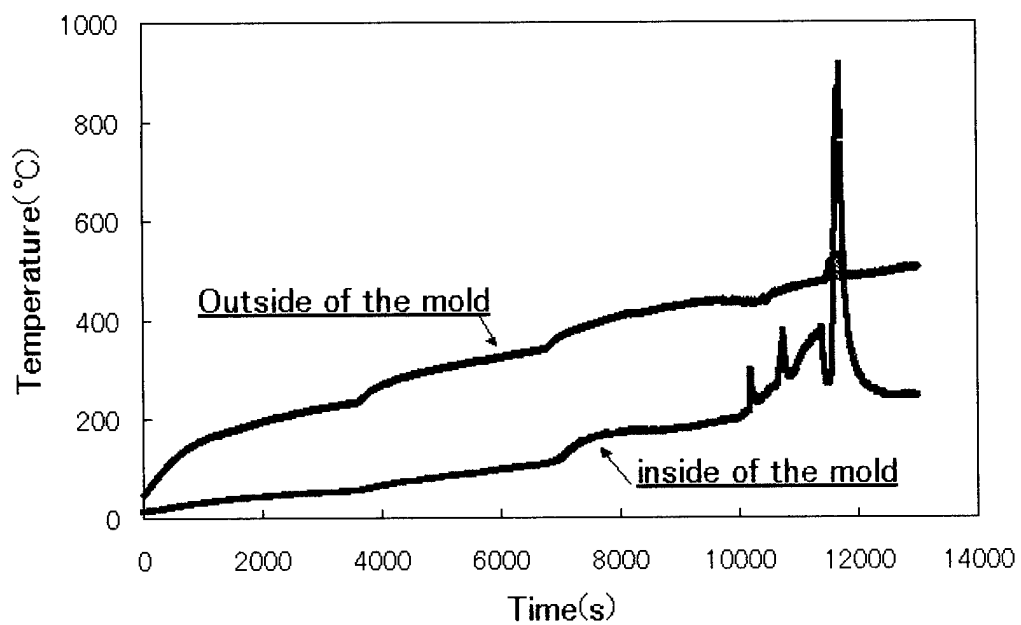


Fig.10 Temperature rising curves

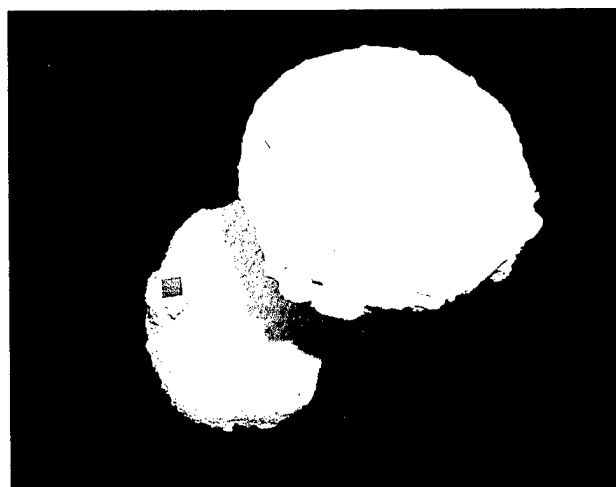
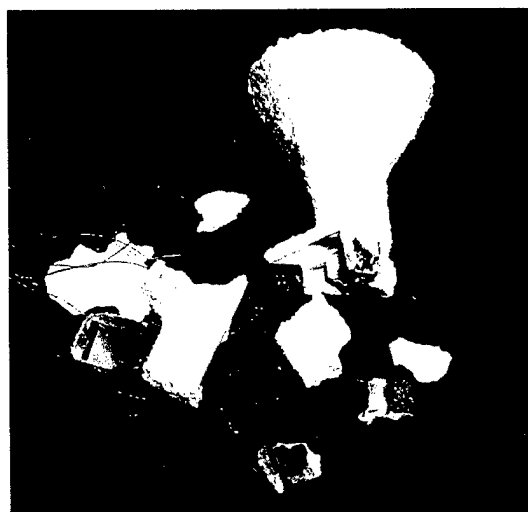


Fig.11 Situations of molds after test

patterns, a stepped model was used for CAD design, RP forming and mold fabrication. The shape and dimension of the master pattern is shown in Fig.9. The step pattern was firstly designed with Unigraphics and then the master pattern was formed with an RP unit. The specimen consists of the master pattern and a ceramic shell that was coated around the master pattern outside. The specimen was installed in the electric furnace prior to heating up.

The temperature rising curves are shown in Fig.10. Both curves represent the temperature of inside of the specimen and outside of that. The burning point of resin is about 530°C. Some peaks appear on the inside temperature curve that shows the resin pattern fired and then went out many times before pattern removal test had finished. Finally a large scale burning happened and continued for approximately 15 min. The behavior had occurred during the test was observed through a hole set on the door of the electric furnace.

4.3 Test Results

A normal mold was examined under the same test condition in order to compare to the reinforced mold. Fig11 shows the situations of the molds just after the resin removal test. Compared to the normal mold, which has fractured into some fragments, the reinforced mold keeps its state as perfect as it was before the test.

5. Conclusion

The failure of ceramic shell molds under the action of the expansion force of resin patterns is a serious problem in the pattern removal process. Several influencing factors such as shell patterns and thick wall molds, which affect the fracture occurrence conditions of molds, were analyzed numerically with BEM. The fiber reinforced ceramic molds were proposed as effective means to protect the structures from the expansion force of the resin patterns. The conclusions are as below:

1) The failure condition of the ceramic mold depends on a certain parameter between maximum principle stress and stress intensity factor, which reaches the critical value earlier. In most cases the cracks are mainly observed on the part near the corner, correspondingly it is considered that the fracture is caused by the stress intensity state on the slope at the corner.

2) To control thermal expansion via applying shell resin patterns to the master pattern, there is a remarkable effect when the thickness of resin pattern is thick, but when the thickness of resin pattern is thin the effect will decrease.

3) It is an efficient method for a thin mold to reduce maximum principal stress on the cross section and stress intensity factor on the slope via increasing coating layers, but the efficiency will be down, when the thickness of the ceramic shell mold exceeded 10mm. It is limited to strengthen the ceramic shell mold through increasing coating layers

4) Fiber reinforcement ceramic mold is an effective method to resist the expansion force of resin patterns. Compared to a normal mold, which has fractured into some fragments after the pattern removal test, the fiber reinforced molds prove having the ability to keep their states as perfect as they were before the test.

5) By using fiber reinforcement ceramic mold in the process that integrated CAD design, RP technology and investment casting, it is possible to establish a valuable application as a practical manufacturing process.

References

- [1] S. He , H. Yoshiura, and T. Mori," Investigation on Analytical Condition of Ceramics Shell Molds by Localized Model", OIRI Research Report,1999.4
- [2] S. He ,T. Mori and H. Yoshiura, "Fracture Mechanism of Ceramic Mold Using Resin Pattern",15th Rapid Prototyping Symposium,PP75-80,1998.11
- [3] S. He , H. Yoshiura, and T. Mori "Reinforced Ceramic Shell Mold" ,JIII Journal of Technical Disclosure, No.99-2282,1999.4

DIRECT MANUFACTURE OF SPATIALLY ENGINEERED COMPONENTS FOR AEROSPACE APPLICATIONS BY FUSED DEPOSITION OF CERAMICS

Charles Gasdaska, Vikram R. Jamalabad,
Daniel Dalfonzo, Thomas Paterson, Liang Xue, Lee Poandl

AlliedSignal Research & Technology
101 Columbia Road, Morristown, NJ 07962 – 1021, USA

ABSTRACT

The current progress of the AlliedSignal led team using the Fused Deposition of Ceramics (FDC) process is described. The program is focused on building and characterizing novel designs with spatially engineered multiple materials. This paper will describe the design, fabrication and properties of multi-material turbine engine components. The integration of process parameters, material properties, material modeling and stress analysis within the FDC manufacturing process will be highlighted using the example of a multi-material turbine blade. Improved build techniques to manufacture components not possible by regular techniques will also be demonstrated.

INTRODUCTION

We present here an overview of activities in Rapid Manufacturing (specifically, Fused Deposition of Advanced Materials) for the manufacture of high value components. Components manufactured by this process are intended to be functional and for insertion into components and systems. Issues relating to (a) feedstock and material development, (b) materials design, (c) novel component design, (d) toolpath and build procedures and (e) integrated design procedures. The program team members and their associated tasks are outlined in Table 1. The work presented here reflects the contributions of all the team members.

Descriptions of the Fused Deposition (FD) process are provided elsewhere [1, 3]. Figure 1 summarizes the process. The deposition is essentially 1-dimensional, and as such provides some unique capabilities to vary deposition within a layer. One goal of our program is to use this capability to demonstrate performance improvement through the use of multiple materials within a layer. For example, to produce compressive residual stresses. Also, the use of filament as the feedstock material and the extrusion process provide two other capabilities: production of unique material architectures in the filament which are retained after extrusion (e.g., fibrous monoliths); and enhancement of crystallographic texture by flow alignment of seed crystals in the filament. The concept of the fibrous monolith is sketched out in Figure 2.

To be used effectively, the capabilities described above require new design tools. Put another way, the ability to fabricate unusual material architectures is useless unless we have some design tools

to help us decide what we need to build. Consequently, another facet of our program involves materials and structural design. Materials design may be defined as both optimizing individual material properties and also as the arrangement of two or more materials to maximize some property such as strength, elasticity or thermal conductivity. Structural design then incorporates this information to design components with improved reliability and/or performance, using these material designs as input and varying parameters such as their shape and location in the component.

Program Team

Rutgers University Dr. Stephen Danforth Filament characterization, β -seeding	AlliedSignal Technology Program Management Charles Gasdaska AlliedSignal Technology Materials Development FDC Process Control	AlliedSignal Engines Milt Ortiz Structural Design Component Testing
Advanced Ceramics Research Dragan Popovich Filament Materials	AlliedSignal Ceramic Components John Pollinger Materials Fabrication	Dr. Anil Virkar Materials Design Dr. George Dvorak Materials Modeling

Table 1

Any design produced must be fabricated using FD, which requires modifications to standard toolpath software* to achieve optimum material properties. This work may be broadly characterized as changes in the toolpath required to ensure complete filling of the layer for all possible design elements. Finally, we will describe some of our preliminary efforts in design integration, which is the process of tying together all of the above ideas and incorporating them in a design procedure which includes process simulation, so that redesign and optimization can take place before the first "real" part is produced. Ultimately, this integration of design and manufacturing should lead to much faster design cycles. Our current FD process can produce a finished part in as little as two weeks (1-2 days for building, 9 days for binder burnout and two days for sintering). In the following, we will describe in more detail the work underway in our program that begins to tackle some of these issues.

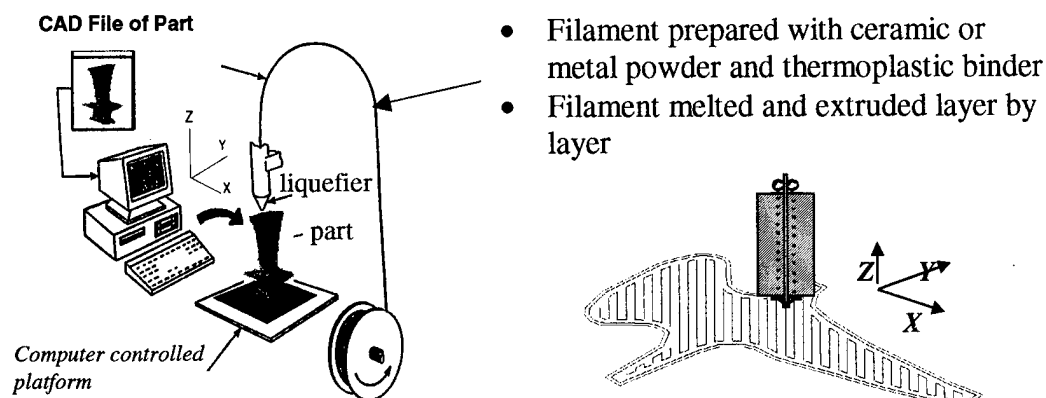


Figure 1: A schematic of the Stratasys FDM 1650 and a build layer.

* Initial work used manual modification of toolpaths output from the Stratasys QuickSlice® software.

FEEDSTOCK AND MATERIALS DEVELOPMENT

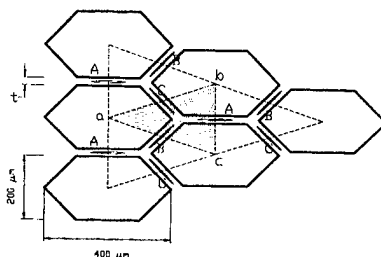
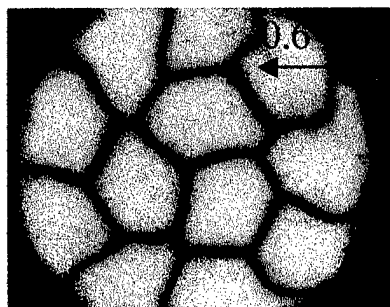


Figure 2. An example of the unique microstructures that can be produced by FD is illustrated by the FM microstructure above. Below is an idealized model used for predictive simulation as an aid in material and component design.

hexagonal β - Si_3N_4 crystal). This orientation can be used to advantage to change properties that are dependent on crystal orientation such as elastic constants and thermal conductivity. Preliminary work has shown that alignment does occur during filament fabrication, during FD and is enhanced after sintering. Rutgers University has been responsible for producing the β -seed crystals and we are currently scaling up the process to produce filament at ACR.

In order to utilize the multi-material capability of FD, materials that are compatible and co-sinterable must be developed. Since silicon nitride is the high temperature structural ceramic of choice for turbine engine components, our work has focused on developing compositions compatible with this material. We have been developing silicon nitride-based materials which contain dispersants to increase the co-efficient of thermal expansion (CTE) and which can be co-sintered with the baseline composition. With the proper arrangement of the two materials, compressive residual surface stresses can be developed on cool down from sintering. A number of promising compositions have been developed and an example of their application will be presented in the section on Component Design.

Development of a suitable solids-loaded filament was the primary focus of the work early in the program. This led to the successful development of silicon nitride (Si_3N_4) loaded filament. Parts manufactured from these filaments have been shown to have strength and properties comparable to conventionally processed material [2, 4]. More recently, we have concentrated on extending this work to include a variety of silicon nitride-based compositions, filaments with fibrous monolith microstructures and filaments containing β - Si_3N_4 seed crystals.

The work on β -seed crystals is designed to take advantage of the orientation of acicular crystals in the extrusion flow from the FD nozzle. The silicon nitride powders undergo a phase transition from α to β phase during sintering. The presence of the seed crystals will result in preferential growth of the β crystals during transformation, resulting in the development of crystallographic texture (the axis of the needle-like beta seeds corresponds to the c-axis of the

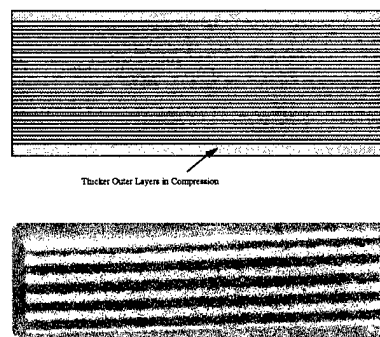


Figure 3: The modeling of a bimaterial ceramic component shown at top is manufactured and co-sintered (below).

Materials design work is being performed to understand the behavior of multiple material architecture. Most of the work to date has focussed on fibrous monolith and laminate/layered arrangements. The fibrous monolith microstructure has been modeled using finite element analysis and both residual stresses and crack propagation behavior have been modeled. The basic idea behind the fibrous monolith materials is to provide for crack deflection at cell boundary areas, thereby promoting graceful failure in an otherwise brittle material. The modeling work has identified properties required for the cell wall material in order to promote crack deflection. The concept of using FD to produce FM microstructures was verified early in the program using model materials consisting of carbon black and alumina [5]. We are now producing filament and building silicon nitride based FM materials. This material may be used to provide some damage tolerance in components susceptible to cracking from contact or impact stresses

By depositing alternate materials within a layer, complex laminate geometries with varying laminate thickness can be produced. One example of Anil Virkar's modeling work is illustrated in Figure 3. A multiple laminate is shown which produces a surface compressive stress and also a periodic stress in the interior. The advantage of this approach is that large compressive stresses can be produced with a lower risk of laminate interface failure and a higher resistance to internal crack propagation. A laminate design of this type is being evaluated for use in the blade attachment area of a silicon nitride turbine blade. Details appear in the following section. A part built with laminations is also depicted in Figure 3.

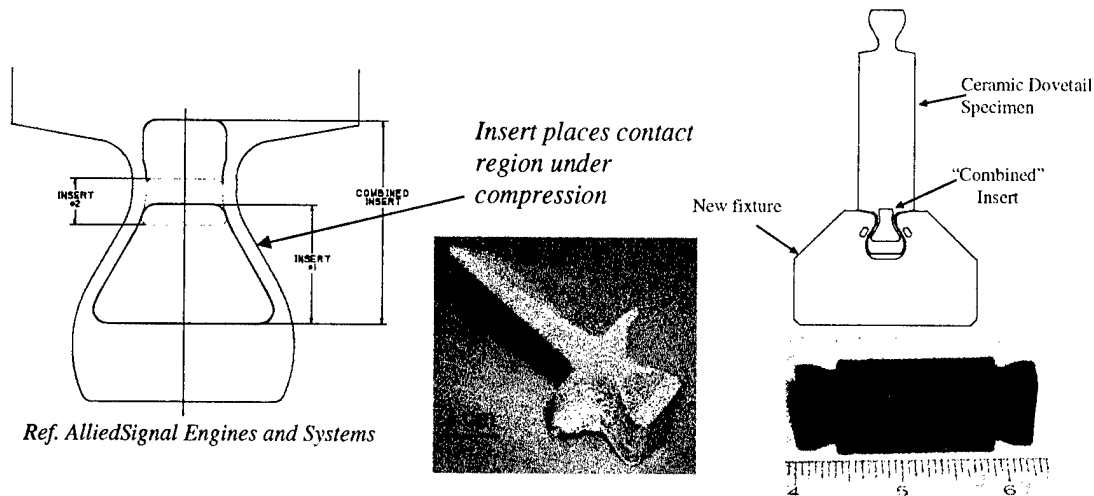


Figure 4: Bimaterial blades. At left is a series of overlaid designs of possible insert cross-sections for a blade dovetail. At center is a bisque-fired section of a bimaterial blade. At top right is the schematic of a test rig for the bimaterial dovetail with a sample specimen (single material) shown below.

NOVEL COMPONENT DESIGN

The goal of our program is to demonstrate the capabilities of FD to improve the performance of a silicon nitride turbine blade. With the compatible and cosinterable materials developed under this program, we have been using the multi-material capability of FD to introduce surface compressive stresses in the attachment area of a silicon nitride turbine blade. The blade is designed for insertion into a cooled metal disk. The compressive stresses improve the resistance to contact damage in the dovetail attachment area, where the ceramic contacts the metal disk[†].

[†] A proprietary compliant layer system is also being used to reduce the stresses in this area.

The Engines & Systems division of AlliedSignal has been developing the insert design, illustrated in Figure 4 (at left). The size and location of the insert has undergone a number of revisions, with the goal of getting the maximum reduction in stress possible. One of the later designs is shown in Figure 4. The insert is calculated to reduce the maximum stress in the attachment area by 25% and the overall stress by 40%. Future work will examine the use of a more complex material architecture for the insert, including the use of laminates instead of a solid insert.

The insert design concept will be verified using pull-test specimens with and without the insert. Samples will be tested to failure to verify the expected strength increase for the samples containing the insert. The sample configuration is also shown in Figure 4 (at right), along with an example of a sintered pull-test sample. Another part of the concept verification process is to demonstrate the capability of FD to produce parts that meet the turbine blade specifications. Our approach to this problem will be described in the section on integrated design procedures.

In addition to the turbine blade insert design, we have prepared a number of "concept" parts to highlight the capabilities of the FD process. One of the most promising capabilities is the production of parts with conformal cavities. For example, cooled ceramic turbine blades – difficult or impossible to fabricate conventionally – can be built using the FD process. Figure 5 shows a demonstration turbine blade built using FD. It contains a conformal cooling channel and trailing edge slots.

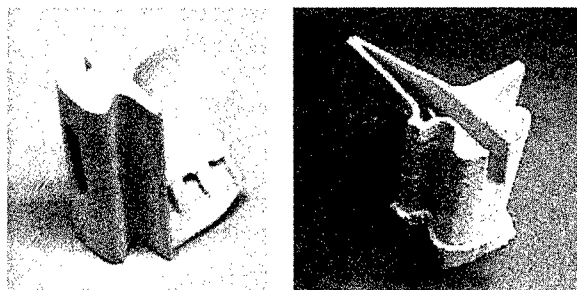


Figure 5: Conformally cooled Silicon Nitride blades, in bisque state. The blade to the right is sectioned to show the interior and has the support base intact.

TOOLPATH AND BUILD PROCEDURES

One of the limiting features of Fused Deposition of Ceramics is the formation of voids during slice filling. These voids can be caused by both procedural and systemic causes. Systemic loss of fill information is described in detail in [6] while procedural causes are addressed in [7]. It should be noted that surface finish of parts (primarily the stair-casing effect) is not attempted to be resolved in our studies. Appropriate flow control and deposition can minimize, but not eliminate these artifacts of the process[‡].

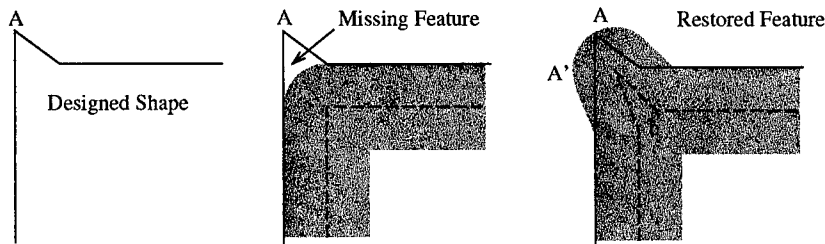


Figure 6: The corner of the component (at left) is not defined by the standard "minimum" distance offset procedure (center). The component built with a reformulated toolpath (at right) restores, to some extent, the original feature.

[‡] The blade we are building for this program will be surface finished in the so-called "bisque" state. Bisque sintering is a treatment that partially consolidates the component and increases part strength with little or no shrinkage. The material has the consistency of chalk and is easily machined. After machining, the component is sintered to full density.

The primary objective of this aspect of our program is to eliminate, or suppress, voids in the interior of the component. The secondary objective is to define features as required in the part design – including the disruption in connectivity that may be caused during toolpath generation. While the solution procedures and techniques are described in [6] and [7], highlights of the solutions will be given here.

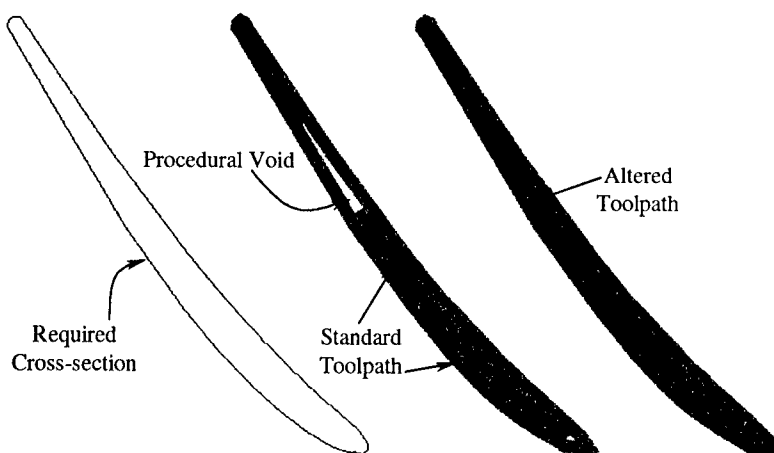


Figure 7: For the cross section defined to the left, standard internal offset procedures for internal filling leave a procedural void that will not be filled (top left end of the graphic at center). The altered toolpath for the graphic at right completely fills the void zone.

Voids are caused by improper toolpath generation – standard offsets from the perimeter of the 2-dimensional slice are inherently a *minimum* of the offset distance away from the perimeter. This implies that there are zones where the toolpath (perimeter or internal fill) is further away than the standard offset distance from the surface of the part. This leads to improper definition of a feature (Figure 7), incomplete fill (Figure 8) or persistent voids (Figure 9).

Techniques to remove these voids have been developed at AlliedSignal. The methodology to do this is to recreate contours while ensuring that the minimum distance from the surface of the component is the required offset distance. While this causes increased filling at some locations, the component does not have any procedural voids left in the virtually described slices. In the case of Figure 7, where the feature is too small for the road width required, the surface of the missing feature is used to recreate a similar feature – this “new” feature is not an exact copy of the original but is also not eliminated. Similar procedures are used to create the “dog-earing” of Figure 9 and the reformed filling of the narrow cross-section of Figure 8.

The algorithms are currently being incorporated into a toolpath generation software package that will be available in 2Q00. Development of design procedures to incorporate manufacturing changes in the component are under way. These include design decision issues relating to feature interactions (described in some detail in [7]). Flow control issues, relating to the controlled deposition of material along with incorporation of multi-material deposition are to be addressed as well. The package is expected to provide a toolpath that guarantees void free components with component features defined as per design requirements.

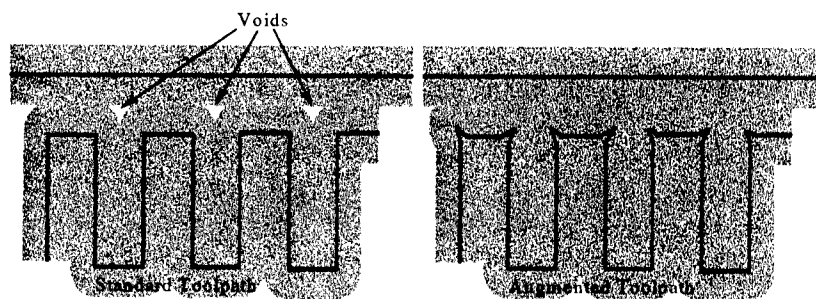


Figure 8: Sub-perimeter voids, caused by ill-defined corners (left). The solution is to relocate the corners such that predictable voids are removed (right).

INTEGRATED DESIGN PROCEDURES

Using SFF as part of this new manufacturing technology requires validation of its ability to manufacture parts with sufficient accuracy and reproducibility. We are using the design and fabrication of a silicon nitride turbine blade for this work. Our program calls for the fabrication of several blades by FD and the careful tracking of dimensional changes during the entire processing (including binder burn-out, bisque sintering, hand-finishing and sintering). A conventional slip-casting process and bisque machining of the same part (without an insert) is being used as a baseline for the purposes of comparison with a commercial process for functional quality parts. The FD part requires a minor amount of hand finishing to remove the stair-stepping texture of the as-built surface. In comparison, the bisque machining of each slip cast blade takes a few hours on a CNC machine. Moreover, the fixed costs and setup costs of the tooling/fixtures for CNC machining makes the individual cost of these components very high. Not only is SFF (in this case FD) able to produce parts difficult or impossible to build with conventional techniques (blades with inserts and/or conformal cavities), it provides them faster (3 weeks to the first part) and at a competitive cost (for "short runs").

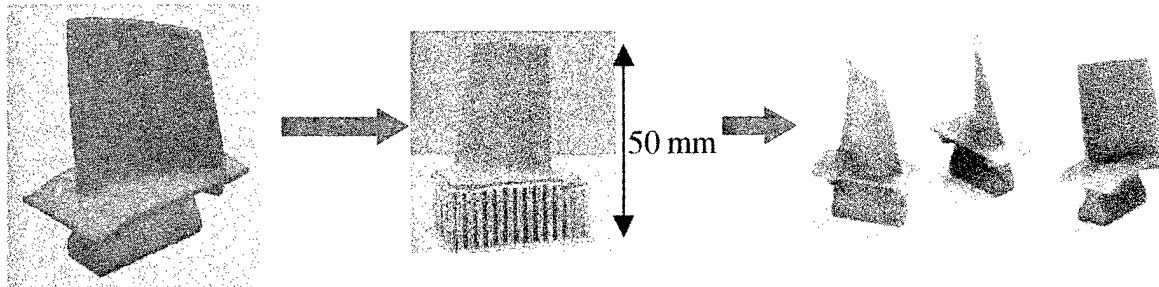


Figure 9: *From concept to creation: A blade, designed on the computer (left), is manufactured within 4 hours (center) and could be available for engine testing within 3 weeks (right).*

The first batch of monolithic turbine blades has been processed through sintering and is depicted in Figure 9. CMM measurements indicate that the green part needs to be redesigned to accommodate material removal during hand finishing and to compensate for some minor warpage. Assuming repeatability of these characteristics, it should be relatively easy to compensate for these or any other effects. We are now in the process of verifying this.

The FD process has many advantages and is worthwhile investigating and developing based solely on the advantages it brings in the ability to manufacture high value components. However, the true justification for this work lies in its integration with the new manufacturing paradigms looming on the horizon. Various referred to as agile, digital or rapid manufacturing, this new manufacturing model emphasizes speed, lower costs and customized design. The use of computer-aided design, engineering and manufacturing allows a virtual part to be "built" on a computer. Combined with computer modeling of an SFF process such as FD, design optimization can be performed much earlier in the design cycle, allowing for faster, better and cheaper components.

Our program encompasses every significant aspect of a manufacturing process – from materials development, to component design to manufacturing. The nature of the program demonstrates the tight coupling of each of these aspects with one another. The success of the program hinges on the effective integration of each of these segments. In effect, we believe that not only is this manufacturing technology uniquely positioned to exploit integrated design procedures, it is critical for its insertion into commercial activity.

SUMMARY AND CONCLUSIONS

The work of the DARPA-sponsored team on solid freeform fabrication of advanced ceramics has involved the interaction of materials design and development, structural design fabrication and component testing. Our work to date has demonstrated the ability of FD to produce unique microstructures such as fibrous monoliths and multi-material laminates using compatible and co-sinterable materials developed under this program. In addition, parts with complicated internal passages have been fabricated which would be difficult at best to manufacture using conventional techniques. We are integrating the FD process in the design cycle by using the multi-material capability to build a composite turbine blade with improved resistance to contact damage and will test and verify performance using a variety of test techniques.

ACKNOWLEDGEMENTS

This manuscript contains work performed as part of the "Solid Freeform Fabrication of Advanced Ceramics Phase II" project, funded by the Office of Naval Research and The Defense Advanced Research Projects Agency under Contract #N00014-97-C-0154. We appreciate the support and advice of Dr. Stephen Fishman, program monitor and Dr. William Coblenz and Mr. Kevin Lyons, program managers for the project. We would like to acknowledge the input and suggestions of the entire team and others, including: Milton Ortiz and Boris Mitlin (AlliedSignal Engines & Systems), Dr. Philip Whalen (AlliedSignal Inc.), Prof. Stephen Danforth, Dr. Sriram Rangarajan and Brian Harper (Rutgers University), Dr. John Pollinger and Doug Twait (AlliedSignal Ceramic Components), Prof. Anil Virkar (University of Utah) and Prof. George Dvorak (Rensselaer Polytechnic Institute).

REFERENCES

- [1] Agarwala, M. K., *et al.*, "Structural quality of parts processed by Fused Deposition", *Rapid Prototyping Journal*, Vol. 2, No. 4, 1996, pp. 4-19.
- [2] Clancy, R. B., *et al.*, "Fused Deposition of Ceramics: Progress towards a robust and controlled process for commercialization", *Proceedings of the Solid Freeform Fabrication Symposium*, Austin, TX, August 1997, pp. 185-94.
- [3] Comb, J. W., Priedeman, W. R. and Turley, P. W., "FDM technology process improvements", *Proceedings of the Solid Freeform Fabrication Symposium*, Austin, TX, August 1994, pp. 42-9.
- [4] Gasdaska, C. J., *et al.*, "Solid Freeform Fabrication of Silicon Nitride Ceramics", *Solid Freeform and Additive Fabrication*, Materials Research Society Symposium Proceedings, Vol. 542, 1999, pp.79-84
- [5] Gasdaska, C. J., *et al.*, "Functionally Optimized Ceramic Structures", *Proceedings of the Solid Freeform Fabrication Symposium*, Austin, TX, August 1998, pp. 705-712
- [6] Jamalabad, V. R. *et al.*, "Process improvements in Fused Deposition of Ceramics (FDC): Progress towards structurally sound components", *Proceedings of the 1996 ASME Design for Manufacture Conference*, Irvine, CA, August 1996, pp. 18-22.
- [7] Jamalabad, V. R. *et al.*, "Topology driven improvement of FDC build parameters", *Proceedings of the Solid Freeform Fabrication Symposium*, Austin, TX, August 1998, pp. 319-26.

PRODUCTION STRATEGIES FOR PRODUCTION-QUALITY PARTS FOR AEROSPACE APPLICATIONS

J. D. Cawley, J. E. Best, Z. Liu
Case Western Reserve University
10900 Euclid Avenue
Cleveland OH 44106

A. J. Eckel, B. D. Reed, D. S. Fox and R. Bhatt
NASA Glenn Research Center at Lewis Field
21000 Brookpark Road
Cleveland OH 44135

ABSTRACT

A combination of rapid prototyping processes (3D Systems' stereolithography and Sanders Prototyping's ModelMaker) are combined with gelcasting to produce high quality silicon nitride components that were performance tested under simulated use conditions. Two types of aerospace components were produced, a low-force rocket thruster and a simulated airfoil section. The rocket was tested in a test stand using varying mixtures of H_2 and O_2 , whereas the simulated airfoil was tested by subjecting it to a 0.3 Mach jet-fuel burner flame. Both parts performed successfully, demonstrating the usefulness of the rapid prototyping in efforts to effect materials substitution. In addition, the simulated airfoil was used to explore the possibility of applying thermal/environmental barrier coatings and providing for internal cooling of ceramic parts. It is concluded that this strategy for processing offers the ceramic engineer all the flexibility normally associated with investment casting of superalloys.

INTRODUCTION

Research on the production of fully-functional parts by rapid prototyping, or solid freeform fabrication, can be pursued via two complementary approaches; direct or indirect fabrication. The direct approach involves layer-wise construction in the material of choice. In contrast, indirect fabrication typically employs RP processes to produce a shaped cavity that allows a secondary operation, such as casting or injection molding, to produce the part. Depending on the constraints associated with a particular set of circumstances, either approach can be valid. The indirect approach can be advantageous if it is desired to ultimately transition to a more conventional manufacturing procedure once the prototyping phase is complete. Such was the case for the work reported herein.

The two components that were selected for evaluation are a low-force rocket thruster and a simulated-airfoil test specimen. These two parts are representative of anticipated aerospace applications for ceramics.

Rocket engines and gas turbine engines operate on fundamentally different principles. A rocket, in its conventional form, is an internal-combustion engine that needs no outside air to operate. It carries both fuel and oxidizer, which are burned together in a combustion chamber and produce hot gases that are discharged through a

nozzle. The resultant imbalance of forces in the chamber results in propulsion. In contrast, a gas turbine engine necessarily contains rotating machinery elements and relies on the ingestion of air to oxidize the fuel. Despite such differences, components for the two types of application have much in common from the point of view of material property requirements and complexity of design,

In particular, both types of propulsion systems have readily identifiable material challenges. Of particular interest with regards to engineering ceramic, is the thermal loads applied to dimensionally critical parts such as the injector nozzle for rocket engines and the first stage vanes and nozzles in a gas turbine engines. In both systems, the need for precise thermal management has severely limited the choices of materials. Typically, the solution is to employ materials that can be manufactured such that there are complex interior passages to allow active cooling of certain critical parts.

Currently, nickel-based superalloys dominate the high-temperature materials market for power-generation and aerospace engine applications. Such materials have a rich history and represent a triumph of metallurgical engineering; it is fair to say that the gas turbine engine would not be possible had superalloys not been developed. Efforts to improve the performance of modern gas turbine engines has imposed increasing service temperature demands on structural materials. In this context, it is important to recognize that "superalloys are utilized at a higher fraction of their actual melting point than any other class of broadly commercial material" [Sims, 1984]. Cleverly designed cooling systems have extended the range of service, but the margins for further improvement appear modest and attention has turned to materials substitution. In particular, covalently bonded ceramic materials, such as silicon carbide and silicon nitride, have received a great deal of attention. Ceramics offer improved refractoriness and have the additional benefit of lower density (of particular relevance to rotating components). Low fracture toughness and high processing costs have proven to be the major obstacle to their widespread application.

The issue of fracture toughness has been addressed using two different approaches, fiber-reinforcement of composites [Chiang et al., 1993; Evans, 1990] and the development of in-situ toughening based on microstructural design [Evans, 1990; Li and Yamanis, 1989; Khandelwal et al., 1995; Sajgalik et al., 1995]. In particular, the development of high-toughness silicon nitride has proven remarkably successful and it will be used as a reference point in this discussion as well as the baseline material in the proposed research project. Materials are available that are both tough and strong, and that maintain their desirable properties to high temperatures. There are a number of commercial sources of in-situ toughened silicon nitride with K_{IC} of around 7-8 MPa \sqrt{m} and four-point bending strength of 700-800 MPa. Two fundamental questions arise: Can an arbitrary desired geometry be readily obtained using a process?, and What is the cost associated with such a process? These two questions apply equally well to applications in rocket and gas turbine engines. The later will be discussed first.

The issue of high processing costs is important in several contexts. Firstly, the production of silicon nitride is a powder-based process. Typically, the storage of geometrical information (shaping) is carried out in a separate unit operation from that used to develop the microstructure (firing) with the powder processes used in the fabrication of ceramic components. Thus, tooling must be specifically designed to accommodate any dimensional changes that are encountered during subsequent

densification. Iterative redesign, or simple modification, of tooling can be prohibitively expensive. Post densification machining of ceramics also is expensive [Anon., 1993]. This is particularly true when high value-added ceramics are used. To a certain extent, green machining can be used to bring a piece into tolerance before firing [Teeter, 1966; Butler et al., 1990], but there is a fundamental limitation associated with all machining approaches; they are restricted to removal of material from the external surface (and boring of holes of simple geometry). This limitation is particularly severe for the opportunity discussed below.

Cooled metallic components for both rocket and turbine applications typically have internal passages through which bypass air is circulated. The geometries are usually complex; features are included to induce turbulence and to control the relative flux of cooling air to different parts of the blade or vane. The complex interior surface is almost always produced by a "coring" technology coupled to a sophisticated investment casting process; for most applications, it cannot be produced by machining [Clegg, 1991].

The use of (ceramic) cores in investment casting is a complex process. The most commonly used core system is based on silica. As-fabricated cores are porous vitreous silica of relatively coarse particle size. The core is used in combination with a shell (also typically silica-based). During investment the hot metal is shaped by both the shell (which defines the external surface) and the core (which defines the internal surface). The heat available from the metal during solidification causes the silica to devitrify, i.e., it crystallizes to form the polymorph cristobalite. During subsequent cooling, the displacive phase transformation which occurs at roughly 200 to 250°C causes the core to breakup and become a loose powder. Crushing is promoted by the thermal contraction of the metal. At room temperature, the core is removed by a combination of chemical etching and flushing. A few core systems are available that do not employ silica, but they are typically very difficult to remove. To summarize, a core has to be sufficiently strong to shape the persistent material and, when this process is complete, lose its strength completely.

Coring in a powder-based process is problematic because, in general, the persistent material cannot be used to convert the state of a core nor does the powder compact have sufficient strength to crush the core. Early efforts at replacing metallic components with ceramics assumed that the ceramic components would operate uncooled [e.g., Devendra, 1990]. In part, this was motivated by a desire to increase efficiency by reducing the parasitic use of cooling air, but a larger issue is simply the manufacture of such a component as there is no equivalent to a coring technology for powder based processing. (Furthermore, there has been concern that both the steady state and transient thermal stresses associated with the internally-cooled ceramic hardware would be unsustainable.)

The alternative to coring-casting is to machine a large number of small parts and use a complex assembly to produce the required functionality. Although widely used, particularly in rocketry applications, such systems are inherently far less reliable and much more costly than "monolithic" parts.

Thus, both the issues of manufacturability and the cost of manufacturing have become important issues in the potential application of engineering ceramics in gas turbines. The objective of this work was to evaluate the use of a combination of RP

processes to produce cores and molds that could be used to produce parts typical of the intended field of application.

DESCRIPTION OF COMPONENTS AND MATERIALS

The first component selected was a 25lbf rocket thruster designed by researchers at the NASA Glenn Research Center, which can be evaluated using an existing rocket test stand. Key geometrical features are: a 37° flare fitting used to attach the chamber to the injector body on the test stand; a cylindrical combustion chamber; and a converging-diverging throat section leading to a conical exit. The entire part is a body of revolution.

The second component was a simulated airfoil test sample that was equivalent to the specimens used by NASA engineers in their original work to develop thermal barrier coatings for superalloys. Original castings were reverse engineered to obtain the design. The specimen has a geometry that is intentionally simplified. The section to be exposed to the flame during testing is a teardrop shaped; the cross section has two semicircular ends of differing radius joined by flat side. The base of the specimen, used for mounting, is a right circular cylinder. The part is hollow and cooling air can be introduced during testing.

The components were produced from a particular silicon nitride alloy (GS-44, AlliedSignal Ceramic Components, Torrance CA) which was supplied as a spray dried powder. This material was calcined to remove the organic binder prior to use in gelcasting formulations. A plasma-sprayed mullite coating was applied to the surface of one of the simulated airfoils prior to testing.

PROCESS STRATEGY

The process used to create the ceramic parts was gelcasting [Young et al., 1991; Janney et al., 1997; Omatete et al., 1998]. The principal attributes of this process in the context of this work is the ability to do room temperature pressureless casting to form a green ceramic part. As such the process is compatible with the use of polymeric molds and cores. The cast slurry solidifies by gelation; the carrier fluid in the ceramic slurry is actually an unstable aqueous solution of a monomer that is catalyzed immediately prior to mold filling. The resultant wet gelled parts were dried and fired following standard ceramic processes [Reed, 1995].

Molds were produced using stereolithography using a 3D Systems 250/40 machine with Ciba Geigy 5170 acrylate/epoxy resin. The cores were produced on a Sanders Prototyping ModelMaker using ProtoBuild™. As ProtoBuild is soluble in room temperature alcohols, cores were removed by submersing the wet gelled parts in vat of ethanol.

RESULTS

The strategy to produce the rocket thruster was to design a six-part mold that included a pullable two-part core, a two-part split mold, a baseplate, and an core-mold alignment fixture, see Fig. 1. Using molds of this type, parts were cast from plaster-of-Paris (to ensure functionality of the system), aluminum oxide (to demonstrate technology with a relatively low cost engineering ceramic), and silicon nitride (to produce testable parts).

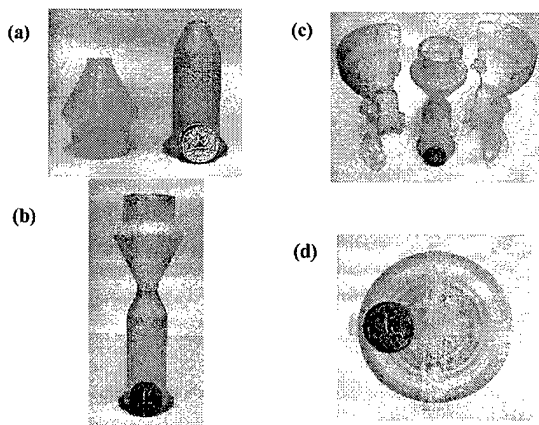


Fig. 1 Mold/core set to produce NASA rocket, produced in epoxy/acrylate by stereolithography.

Green and fired silicon nitride parts are shown in Fig. 2. Figure 3 shows the silicon nitride rocket thruster during testing at NASA Glenn. Significant features of the test are: i) standard mounting using a 37° flare fitting was demonstrated (no need to redesign particular to ceramic); ii) durability of the ceramic part was satisfactory (a series of firings of increasing duration, up to 5 mins., were carried out with no failure); significant thermal gradients are present in the part (estimated at up to 1000°C/mm in the throat). Clearly high quality parts are produced via this strategy.

The excitement regarding this strategy is in part the ability to produce useful parts and as importantly the ability to produce them rapidly; the total elapsed time between idea and ceramic part was 28 days (19 work days). This was for all steps from CAD to RP to ceramic processing. This creates a situation wherein it is possible to rapidly evaluate potential for performance, prior to committing to a systematic and exhaustive experimental plan to optimize component design.

A similar strategy was employed to produce the simulate-airfoil test specimen. A green part are presented in Fig. 4, specimens during testing are shown in Fig. 5, and post-test surface condition is documented in Fig 6. In this case, all parts exhibited adequate thermal shock resistance.

However, there was some corrosion of the leading edge of the uncoated specimen.

The specimen with the plasma sprayed coating showed no visible signs of degradation despite being subjected to burner for approximately one-half hour. The sequence of photos in Fig. 5 shows the effectiveness of internal cooling in a silicon nitride component. This is further documented in the measurements of surface temperature using pyrometric (both laser and two-color) of the surface temperature on the leading edge of the specimen under the flame, as presented in Fig. 7.

The first of these two specimens (the rocket thruster) clearly indicates a need for sophisticated thermal management. The second (the simulated-airfoil) demonstrates that the approaches, which have been so successfully exploited for metallic components, internal cooling and thermal barrier coatings, both can be effective for ceramic parts. The

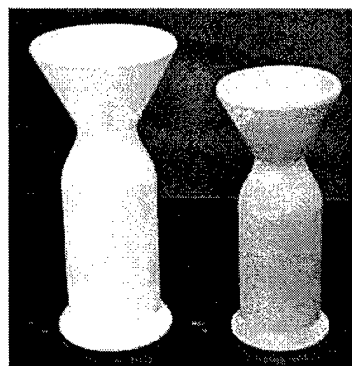


Fig. 2 Green (left) and fired (right) gelcast silicon nitride rocket thrusters.

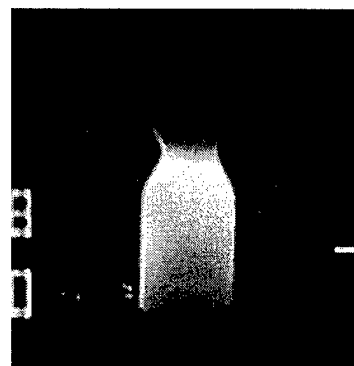


Fig. 3 Silicon nitride rocket thruster during testing in the H₂/O₂ test stand.

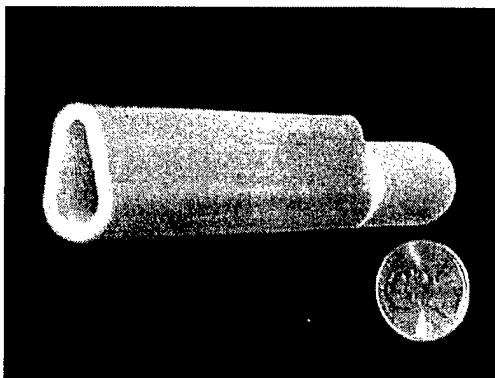


Fig. 4 Green gelcast simulated airfoil.

combination of these results motivated a series of experiments to evaluate the potential for producing more complex internal cooling passages using soluble cores.

Figure 8 shows the assembly of a ProtoBuild core in a epoxy/acrylate mold designed to produce a thin walled (40 mils, or 1 mm) hollow cylinder with thin (13 mil, of 600 μ m) cooling channels that run the length of the part. The fired part is shown in Fig. 9. This demonstrates the ability to produce precise and finely detailed internal features.

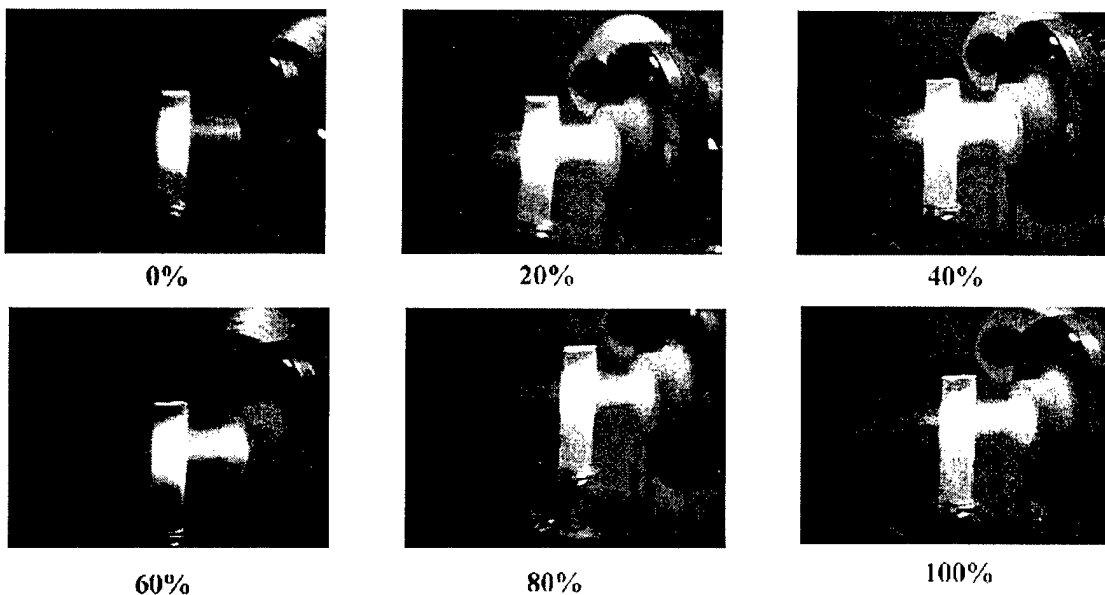


Fig. 5 Photographs of the uncoated silicon nitride simulated-airfoil test specimen in a Mach 0.3 jet fuel burner flame with differing percentages of 89.8 standard liters of internal cooling air flow. The effect of the cooling air can be seen in the reduction of the intensity of the brightness of the specimen.

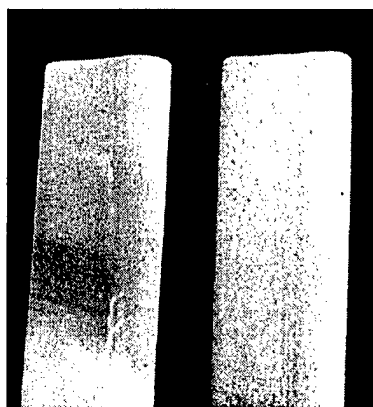


Fig. 6 Surfaces of uncoated and mullite-coated samples after testing.

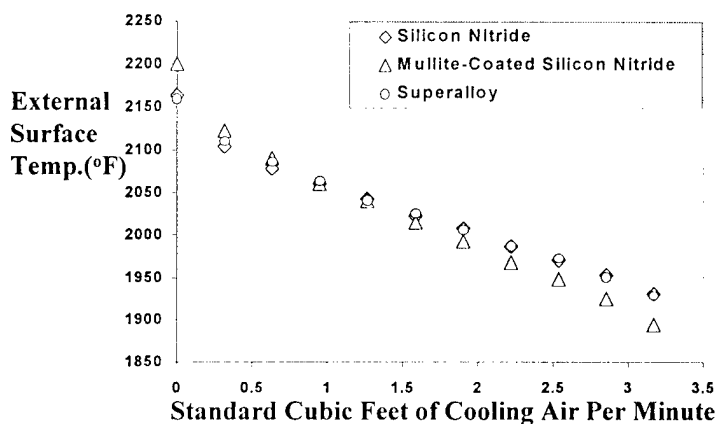
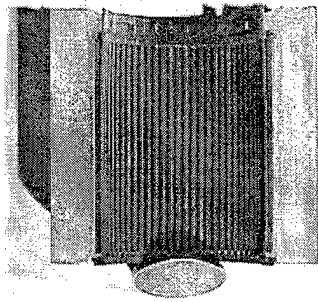
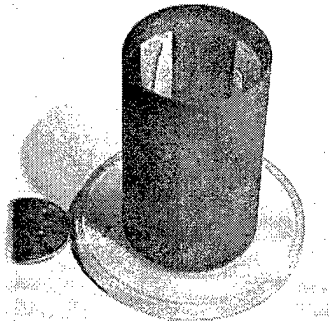


Fig. 7 Graphical depiction of the drop in surface temperature with increasing flow rate of internal cooling air for silicon nitride and superalloy specimens tested under similar conditions.

Actual Cylinder Mold System



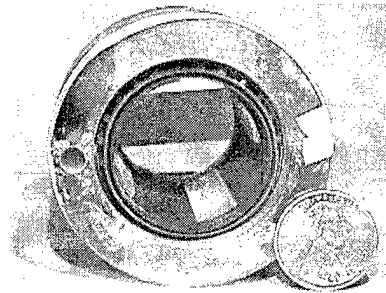
**Outer Gating with
Lining and Core Half**



Inner Gating with Lining



Half Assembled Mold



Full Assembled Mold

Fig. 8 Photographs showing the assembly of a core (dark contrast) and mold (light contrast) system used to make a thin walled hollow cylinder with closely-spaced narrow cooling channels that run its length. In order to facilitate removal from the mold, soluble liners were used to separate the part from the mold (a similar design was used to make the simulated-airfoil shown in Fig. 4).

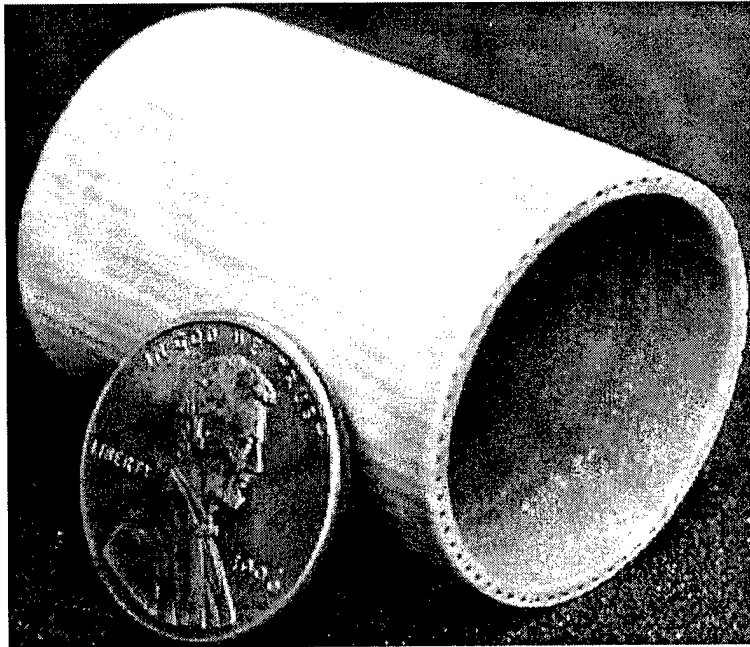


Fig. 9 Photograph of fired silicon nitride hollow cylinder with cooling channels.

SUMMARY

The results of the experiments suggest that all of the flexibility normalized associated with cast superalloy aerospace components, complex internal geometrical features produced by coring and ready application of surface coatings, are available to the ceramic engineer. Rapid prototyping has played a key role in allowing this demonstration in a rapid and cost effective manner. Finally, it is noted transitioning this approach to more conventional means is easy to envision, i.e., machined metal tooling of high durability and injection molded cores produced from the appropriate soluble organic.

ACKNOWLEDGEMENTS

The authors are grateful to AlliedSignal Ceramic Components, in particular, John Pollinger and Maxine Savitz, for providing us with the GS-44 silicon nitride powder. The plasma sprayed mullite coating on the airfoil test specimen was deposited by George Leissler of NASA Glenn. This work was supported by the NASA/CWRU Cooperative Agreement on Ceramic Processing (NAS3-404).

REFERENCES

- Anon., "Can We Get Serious About Ceramics? Before we can take advantage of these versatile materials, machining costs must be reduced," *Man. Eng.*, 111 [2] 54 (1993).
- Chiang, Y.-C., Wang, A. S. D., and Chou, T.-W., "On Matrix Cracking in Fiber Reinforced Ceramics," *J. Mech. Phys. Solids*, 41 [7] 1137 (1993).
- Clegg, A. J., *Precision Casting Processes*, Pergamon Press, Oxford, 1991.
- Devendra, K., and Syers, G., "Application of Engineering Ceramics in Gas Turbines," p. 93 in *Brit. Ceram. Proc. No. 46: Advanced Engineering with Ceramics*, The Institute of Ceramics (1990).
- Evans, A. G., "Perspective on the Development of High-Toughness Ceramics," *J. Am. Ceram. Soc.*, 73 [2] 187 (1990).
- Janney, M. A., Omatete, O. O., and Westmoreland, G., "Development of Low-Toxicity Gelcasting Systems," *J. Am. Ceram. Soc.*, 81 [3] 581 (1998).
- Li, C.-W., and Yamanis, J., "Super-Tough Silicon Nitride with R-Curve Behavior," *Ceram. Eng. Sci. Proc.*, 10 [7/8] 632 (1989).
- Omatete, O. O., Janney, M. A., and Nunn, S. D., "Gelcasting: From Laboratory Development Toward Industrial Production," *J. Eur. Ceram. Soc.*, 17 [2/3] (1997).
- Sajgalik, P., Dusza, J., and Hoffman, M. J., "Relationship Between Microstructure, Toughening Mechanisms, and Fracture Toughness of Reinforced Silicon Nitride Ceramics," *J. Am. Ceram. Soc.*, 78 [10] 2619 (1995).
- Sims, C. T., "A History of Superalloy Metallurgy for Superalloy Metallurgists," p. 399 in *Superalloys 1984*, edited by Gell, M., Kortovich, C. S., Bricknell, R. H., Kent, W. B., and Radavich, J. F., AIME, 1984.
- Teeter, A. R., "Binders for Machinable Ceramics," *Ceram. Age*, 82 [8] 30 (1966).
- Young, A. C., Omatete, O. O., and Janney, M. A., "Gelcasting of Alumina," *J. Am. Ceram. Soc.*, 74 [3] 612 (1991).

Stereolithography Patterns for Investment Casting: Prototyping to Production

Curtis Wahlgren and Suresh Jayanthi, DSM Somos, Two Penn's Way, Suite 401, New Castle, DE 19720

Introduction

Most people in the investment casting industry are aware of the use of rapid prototyping technology to make patterns that can be used in place of the traditional wax patterns for investment casting. Many foundries have begun to make use of various rapid prototyping techniques to broaden the range of options that they can offer to their customers. However there is still a reluctance on the part of many foundries to commit resources in order to understand and implement this 'new' technology.

Traditionally the primary users of investment casting parts made from stereolithography patterns have been the aerospace and medical industries. However, there is also a vast market for other industries that can benefit from stereolithography processes. Parts need to be made for the automotive industry, hand and power tools, oilrigs and recreational equipment to mention just a few.

In order to have a broader acceptance for stereolithography in investment casting there are two things that must happen. The first is that users must be made aware of the benefits of this. The second is that the preconception must be overcome that stereolithography patterns will just not work as well as wax patterns to produce cast parts of acceptable quality.

Our goals are:

- To convince those foundries that have not used stereolithography, or have had a brief but negative brush with it, that it makes good business sense to learn how to work with stereolithography patterns.
- To show those foundries that currently use stereolithography patterns regularly how they can expand their use of stereolithography in ways that will bring in revenue from new sources.
- To show that stereolithography patterns need not be restricted to casting *prototype* parts but can be extended to casting *production* parts as well.

The steps to accomplishing these goals are:

- Help people in the investment casting industry to become aware of the viability of stereolithography patterns and the benefits of using this technology.
- Establish reliable techniques for building stereolithography patterns that will withstand the stresses of shell preparation without physical deformation.
- Establish reliable procedures to remove the stereolithography patterns from the ceramic shell without shell deformation or fracture.
- Develop procedures that result in minimal residue left behind after burnout.

Implementation

There are many benefits to using stereolithography patterns in place of the traditional wax patterns in the investment casting process. There is no need for creating a tool to build the pattern. Instead, the pattern is built directly on a stereolithography machine using a CAD file that has been prepared to the exact specifications of the customer. This allows the foundry to use complicated patterns with fine detail and excellent accuracy, and in turn shortens the lead-time needed to turn out a set of parts. These patterns have a very smooth surface that is comparable to that achieved with wax patterns.

When using stereolithography patterns it is easy to modify the original design of the piece if examination of the final casting shows that a change is warranted. Design changes can be evaluated in a few days rather than waiting for weeks to see the result.

It is recognized that foundries have been using wax patterns for many years and understand how to work with them. As with any well-established process it is difficult to make a change. Our objective is to integrate the procedures for working with stereolithography patterns smoothly with existing methods.

Several factors must be considered when using stereolithography patterns. The pattern should be built by someone who is experienced with building parts of this type. A pattern that is properly built is essential to the success of the project. For a 3D Systems 'Quickcast™' part there must be no solid resin in the interior framework of the piece. The operator must also understand that certain geometries require special build orientations to produce a good part. For example solid, flat surfaces thicker than 20-30 thousandths of an inch should be avoided.

The designs for gating and rigging are different than those required for wax patterns. New processes are needed for removing the pattern once the shell is created. The material must be heated to a high temperature (about 1800°F) in order to vaporize all of the pattern. With a wax pattern, heating in an autoclave at a much lower temperature allows the wax to melt and run out. This is followed by high temperature firing to remove residual wax and to cure the shell.

For a stereolithography pattern made by using the Quickcast™ process, there is less thermal expansion of the material due to the internal structure of the part. Expansion of the wax pattern is one of the main reasons for shell failure during burnout. At the same time consideration must be made for the fact that the entire stereolithography pattern decomposes during burnout. There must be some provision for assuring that there is no internal pressure increase which can cause cracking of the shell.

The use of wax patterns is well characterized after many years of usage. On the other hand, few foundries have enough experience with stereolithography patterns to feel confident in working with them. Those that do work with these patterns sometimes find that different processes are necessary to work with different pattern materials and different geometries. Once they have invested the resources to develop a working process, a foundry is often reluctant to publicize its findings to the rest of the industry.

A knowledge gap must be bridged before production quality parts can be reliably created from stereolithography patterns. The means for building this bridge is already in place. This work will be done by the areas of expertise that already exist in the foundries. These are **1) Pattern Creation, 2) Shelling Process, 3) Burnout Process and 4) Casting Process**. Each has their own concerns that must be met.

Pattern Creation

The challenges here are to become expert at using the materials and processes available in order to create patterns that are accurate, resistant to changes in dimension (swelling and warping), and easy to remove from the shell. The stereolithography process has been shown to be accurate and a new generation of materials exists that are resistant to moisture absorption and warping. One of the primary tools that has enabled stereolithography to be used to prepare investment casting patterns is the Quickcast™ build style. The geometry of this build style is such that the part collapses in on itself during burnout. This prevents the pattern from expanding to such a degree that the shell is fractured.

The Quickcast™ style is not an easy one to become proficient with. There are many variables to control and it requires considerable experience to build good parts. There can also be problems with porosity of the part walls and with improper resin drainage. The part surface must be wiped carefully with solvent after it emerges from the resin vat. Immersing the part in solvent to clean it will damage the integrity of the internal structure. Any cells inside the part that are not free of resin will solidify and cause damage of the shell during burnout.

What are the material properties that are desirable in stereolithography patterns?

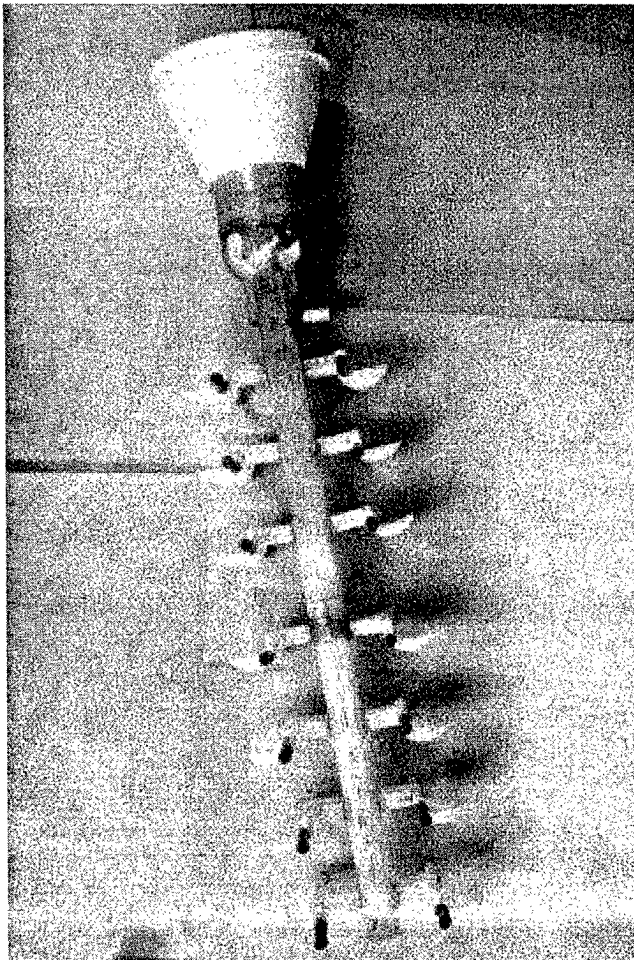
- They should have a low coefficient of thermal expansion.
- There should be little swelling of the part due to water absorption.
- The part must maintain its structural integrity during the casting process.
- There should be little or no ash residue left behind in the shell after pattern burnout.
- The presence of heavy metal contaminants must be eliminated.
- The pattern must have a smooth surface.
- The dimensions must be accurate over a period of a few days to several weeks.

There is a product on the market, Somos® 7100, that is one of the best resins for building parts with the Quickcast™ style. This material has been demonstrated to produce parts of exceptional quality (C.S. McDowell and S. Jayanthi, "Evaluation of Foundry Pattern Removal Performance of Several Epoxy-Based Photopolymers", Proceedings of the North American Stereolithography User Group Conference, February, 1997).

The physical properties of this material meet most of the current needs for stereolithography patterns. A better appreciation of the process will help to grow the market for stereolithography patterns. As stereolithography continues to make inroads into the investment casting market and as the demands upon the material increase, we

will endeavor to provide new materials and work with the foundries to develop new processes to accommodate these demands.

One of the goals of this study is to show that stereolithography patterns can be substituted for wax patterns when this would allow the project to be completed in a faster or more cost-effective manner. In addition, this process may allow the foundry to cast a part that would be difficult to produce using a wax pattern.



It is possible to build the casting tree with stereolithography instead of using the traditional wax tree (C.S. McDowell, M.C. Boomer, "Design of Stereolithography Trees for Use in the Investment Casting of Stereolithography Patterns"). This technique has the advantage of reducing the fracture of ceramic shells due to thermal expansion of the wax tree. Gates and runners can also be designed and built using stereolithography.

Pictured here is such a tree. The reader will note that the gates have also been built together with the tree using stereolithography. The pour cup is at the top and the sprue is the long tube leading from the cup to the various gates.

Some people question the ability of stereolithography patterns to take the place of wax patterns. They blame the material or the process when they try unsuccessfully to cast a stereolithography pattern using the

same process that has been used successfully for wax patterns.

It must be realized that the process must change since the material properties are very different. There is ample evidence to show that when a properly built pattern is used any part that can be cast from a wax pattern can be made using a stereolithography pattern. However the gating and rigging must also be done correctly and the proper shelling and burnout technique must be used

Shelling Process

The main problem introduced by the process of evacuation of the pattern is fracturing of the shell due to thermal expansion of the polymer or because of increased internal

pressure during burnout. According to previous experiments (K. Loose, Proceedings of Rapid Prototyping and Manufacturing, 1996, Dearborn, MI) the tensile stresses caused by thermal expansion are much greater than those caused by gas pressure. In addition, the Quickcast™ style is designed to limit the amount of expansion by the pattern during burnout. However it has been shown (C.S. McDowell and S. Jayanthi, see above) that the thermal expansion coefficient of the photopolymer material is an important factor in the shell preparation process.

Stereolithography can also be used as a secondary process to create wax patterns. Here the mold pattern (which is different from the investment casting pattern) is created by stereolithography. An investment casting pattern is made by injecting the wax material into the mold cavity and following the normal procedure for injection molding. This produces a pattern with all the advantages of one made directly by stereolithography. This brings a whole new set of requirements to the process that must be understood in order to make accurate and reliable tools.

Casting Process

Once the shell is prepared, there is very little difference in this part of the process from that used for shells made from wax patterns. If there are small channels within the part, the gating and rigging design will have to allow for these in order to insure complete filling of the pattern and a good casting.

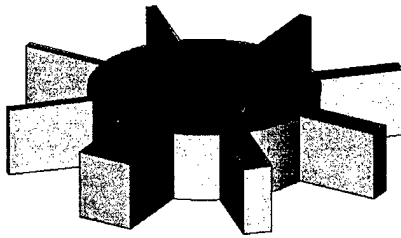
The main obstacle to moving from prototype parts to production casting is that end users must be assured of the reliability of the parts under stress conditions. The concern has been that the burnout process may not remove all traces of the pattern so that some residue remains inside the shell to interact with the metal during casting. This is particularly a concern when the resin contains small amounts of heavy metals. These metals will not evaporate during the burnout process and this can lead to the formation of zones that are susceptible to stress fracture. This cannot be tolerated in production parts.

Standards must be developed which will evaluate the reliability of the pattern removal process. If it can be shown that stereolithography patterns can be removed as reliably as wax patterns this will go a long way toward gaining acceptance in the investment casting industry. One solution would be to adapt current test methods that are used to evaluate parts cast from wax patterns.

It is particularly important to the aerospace industry that the cast parts are free from any failure zones if they are to be used as functional parts. The stresses on a turbine blade during use are much higher and failure is much more critical than for a bracket or a stethoscope head. Currently some production parts are made for aerospace using stereolithography patterns but this is for low stress applications. In the critical area of blade and vein work, all castings are still done with wax patterns.

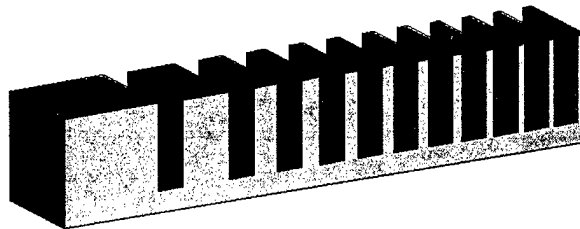
Evaluation of Test Parts

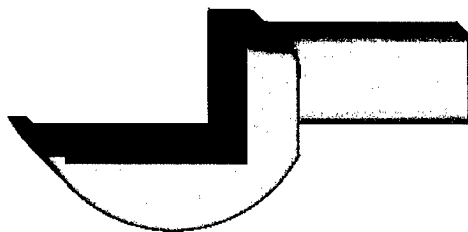
An essential component of comparing resin materials, build styles and casting processes is the design and evaluation of test parts. What is the thinnest cross-sectional area that will still allow the resin to drain from the part effectively? How thin can the part be and still maintain its structural integrity? What is the effect of different stresses on the part? How does the part hold up to points of high stress such as thin sharp edges? How do parts with a large z-height respond to the shelling process?



Several test parts have been designed to evaluate these properties. One is a disc with radiating arms of varying thickness. The objective of this piece is to see how thin a section can be before there is insufficient drainage of resin from the section. In addition, if the arm is too susceptible to bending there may be deformation from the desired geometry during the casting process.

Another piece looks like a rectangular comb with teeth of varying thickness. The objectives are similar to those for the piece described above but using angular rather than circular geometry.





This part has been designed to test the susceptibility of the shell to failure when there is a point of high stress on the piece. The thin, sharp front edge of the piece is an area where shell fracture during burnout is much more likely to occur than for right angles or rounded surfaces. With this geometry it is efficient to compare the effect of the casting, autoclaving and burnout process on the type of resin or to compare different processing methods with the same material.

A careful evaluation of the casting process and the resulting parts made with these test geometries is necessary to understand the performance of the stereolithography material and the build style used to prepare the pattern.

Future Work

There are three contributors to successful stereolithography-based investment casting. These are the materials, the processes and the end users. It is necessary that all these be working together if we are going to see a real expansion in the market. We at the Somos® group have the expertise in materials. It is up to us to evaluate how the material properties of stereolithography patterns impact the investment casting process.

We have seen a clear correlation between the Coefficient of Thermal Expansion of the pattern material and successful pattern removal. Further work needs to be done to expand on these findings. There needs to be a better understanding of the effects of heat deflection temperature and modulus of elasticity on the investment casting process. Through carefully planned experiments, we plan to examine more closely the relationship between physical properties, investment casting processes and the characteristics of the final cast part.

Going forward there will be further evaluations done with existing test part geometries. New part designs will also be used to evaluate materials and processes. Collaborations with various foundries will be undertaken with the goal of promoting the spread of stereolithography into the investment casting market. There will also be projects done with the cooperation of the American Foundrymen's Society and the Investment Casting Institute. We intend to publish our findings along with procedures on pattern preparation

and casting processes in order to make it easy for anyone to take advantage of the benefits of stereolithography for their investment casting business.

Acknowledgements

Special thanks are due to the members of the DSM Somos® team, and to some of our esteemed customers for their input into the material for this presentation.

Manufacturing High Resolution Parts with Stereolithography Method

Authors: Carsten Tille,
Technische Universität München – Feingerätebau
Boltzmannstraße 15
85747 Garching
Phone +49-89-289-15168
email tille@fgb.mw.tum.de
Ralf Deuke, Alphaform GmbH, Feldkirchen/Germany (rd@alphaform.de)
Rico Eidam, Siemens AG, Berlin/Germany (rico.eidam@blns.siemens.de)

1 Abstract

Due to the rapid development of micro techniques, there is a growing market need for appropriate RP methods in the micrometer range. Stereolithography in our experience has found to be the best approach for producing small and accurate parts. Our research project is focussed on the enhancement, development and test of RP systems based on stereolithography. An improved optical system gives us a today's part accuracy of 50 micrometers with the aim of 10 micrometers. A special focus is laid on optic and process. Prototypes produced by a stereolithography apparatus can be shown.

2 Introduction

International studies like the Wohlers Report 1998 [WOH98] show that the RP is a worldwide growing market. While RP in the beginning was mainly dominated by automotive and aircraft industries in the future we will see a change to precise parts for the consumer market, R&D and medical applications. Together with our partners, we found that there is a growing need for precise small and mid-sized prototypes that cannot be manufactured by conventional RP techniques. So, for example, the resolution and accuracy achieved by a conventional stereolithography apparatus like EOS' STEREOS Desktop, is in the range of 0.2 mm (0.008").

Our research project is aimed for improving the accuracy of the stereolithography method leading to application for micro techniques. Beside the new requirements for the hardware, we are on the way to an improved stereolithography process for this new field of application. The way to micro-RP can be obtained by two steps:

A visible progress is possible by upgrading conventional stereolithography apparatuses. Critical components are the laser, optical elements as well as the recoating system. The limit of structural resolution due to the design of those systems is in the range of an accuracy of 50..60 μm .

3 The unit: laser - scanner - optic

Curing of the photopolymer is usually realized by a focussed UV laser beam. The spot of the laser beam can be moved across the resin surface by a galvanometric scanner. This allows a selective curing of the UV-sensitive polymer. The cured area of the resin and hence the lateral resolution of the part is mainly determined by the diameter of the laser spot on the surface of the resin.

In a first step we want to increase the lateral resolution, i.e. by reducing the beam diameter in the build plane for a conventional stereolithography apparatus (e.g. for STEREOS Desktop) using the following demands:

- spot diameter 50 μm with
- build range 250 x250 mm.

3.1 Small spot for conventional stereolithography apparatus

Knowing the limitations of our project partner's stereolithography apparatuses, there are three components mainly effecting the lateral accuracy of a part:

- UV light source (laser),
- scanning system,
- focussing lenses.

The STEREOS Desktop stereolithography apparatus used for our tests showed a typical laser spot diameter of 250 μm . An analyses of the weak points of all optical components was done at a separate experimental setup.

3.1.1 Laser and Optic

The main cause for the large spot diameter is the beam quality of the HeCd laser. A typical value for the mode factor M^2 reported by the manufacturer is about 5. Therefore the focussing of the beam by a given focal length was limited to $d_s = 250 \mu\text{m}$. By simply replacing the UV light source by a HeCd laser with TEM_{00} beam quality ($M^2 = 1,05$) a first step is done. The spot diameter in the middle of the build area could be reduced to approx. $d_s = 70 \mu\text{m}$.

Due to the function principle of the scanning system an other error can be found at the focus plane: By deflecting the scanner mirrors towards the edge of the build plane the spot size will increase because of the short Raleigh range z_R of the focussed beam:

$$z_R := \frac{\pi \cdot w_s^2}{\lambda} \quad z_R = 5.754 \text{ mm}$$

z_R - Raleigh range, λ - wave length, w_s – ideal spot radius

One solution for this problem is the use of a flat-field lens, or even better, f-theta lens. This lens can focus a parallel laser beam on a flat image plane almost independent of the deflection of the scanner mirrors. In the case of an f-theta lens, the lens must satisfy the f-theta equation:

$$s = f' \cdot \Theta$$

s – image height, f' focal length, Θ - deflection angle,

to achieve a constant scanning speed of the laser spot across the scanning area with constant angular velocity of the mirrors.

First tests with a simple f-theta lens showed that a decrease in the spot diameter leads to a smaller build area, i.e. the spot diameter is in an acceptable tolerance range. To use the whole build area of the stereolithography apparatus (250 x 250 mm for the STEREOS Desktop) a new design of the beam expander and the f-theta lens was necessary.

The requirements for this optic can be described as:

- Beam diameter 50 μm
- Build area by $\pm 10^\circ$ scanner deflection 250 x 250 mm
- Acceptable tolerance of the beam diameter across the build area $\pm 5\%$
- Adjustable beam diameter 50 μm .. 150 μm .

Together with a given aperture diameter of the scanner and the focal distance of $f_{\text{f-theta}} = 500$ mm one can find the theoretical spot diameter $d_s = 2 \cdot w_0$ at the build plane:

$$w_0 := \frac{2 \cdot \lambda \cdot M^2 \cdot f}{\pi \cdot D} \quad 2 \cdot w_0 = 33 \mu\text{m}$$

D – maximum beam diameter at scanner (2/3 of aperture radius)

Figure 3-1 A shows the new beam expander and f-theta optic in the design phase.

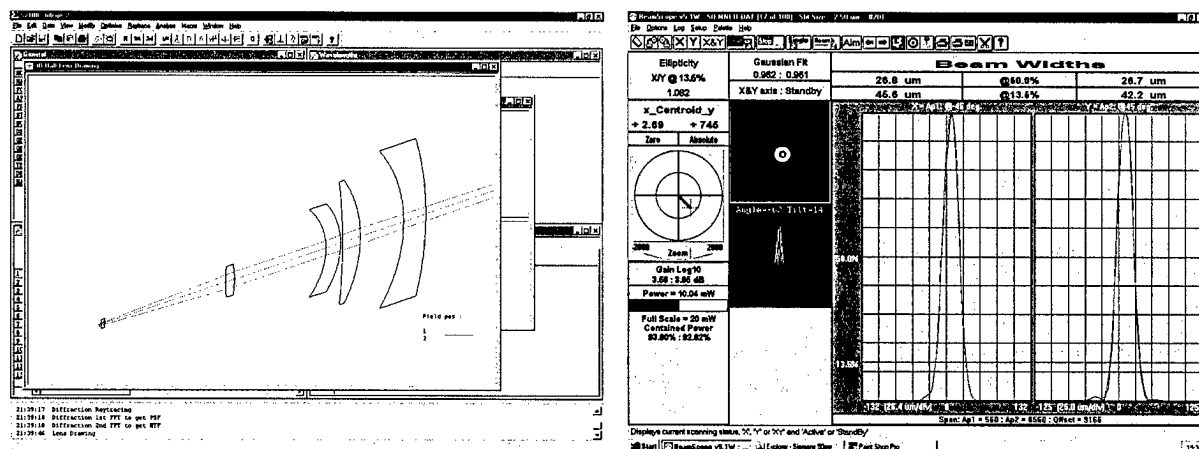


Fig. 3-1: A – Beam expander and f-theta lens of the 50- μm optic
B – Measured beam profile after installation of new components (Siemens)

The new optic was tested at TU München and installed in our partner's STEREO Desktop. The measurements showed that all specification could be met, Fig. 3-1 B. The beam diameter $d_s = 42 \mu\text{m} \pm 3 \mu\text{m}$ is relatively close to the diffraction limit across the whole build plane.

Fig. 3-2 displays the components at the experimental platform at TU München's laboratory.

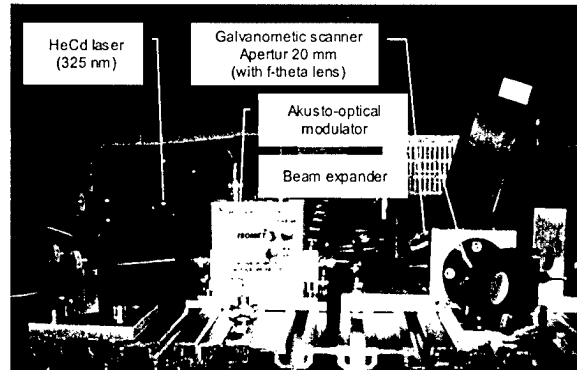


Fig. 3-2: Optical unit with 50- μm spot diameter (experimental setup)

3.1.2 Accuracy of the scanner unit

The third optical component responsible for the lateral part accuracy is the galvanometric scanner. The accuracy of the Scanlab SK1010 scan head used in STEREO Desktop was evaluated with a beam profiler that has a position resolution of less than $1 \mu\text{m}$. Long term position drift, position repeatability and short-term stability were measured. Fig. 3-3 shows the position of the laser spot for a short jump over a distance of $170 \mu\text{m}$. The enlargement shows the stability at a stop point.

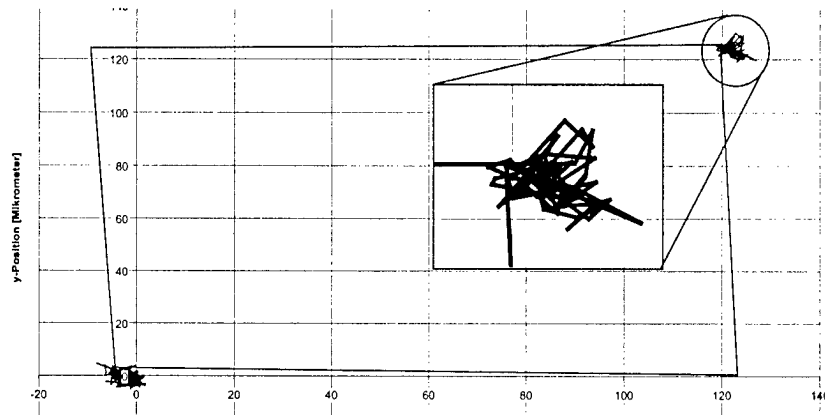


Fig. 3-3: Position repeatability of the laser spot

The positioning repeatability of the Scanlab SK1010 scanners could be determined to

- short-jump error $\pm 1..2 \mu\text{m}$ and
- long-jump error $\pm 2..5 \mu\text{m}$.

The standard deviation of the

- long-term position stability is $\pm 2 \mu\text{m}$ for $t = 30 \text{ min.}$

For the dynamic measurements of the spot position, we used a high-resolution UV sensitive photo plate. Limiting the maximum acceptable error to half of the beam width for SK1010 scan head a

- maximum scan speed of $<1000 \text{ mm/sec}$
is recommended.

As a conclusion, one can say that the minimal lateral part resolution for conventional stereolithography apparatuses like STEREOS Desktop is the range of $50 \mu\text{m}$.

3.2 High resolution optical unit

For higher resolution, great store is to set by the f-theta lens and scan head.

With our experimental setup, we are currently working on an optical system for a $10\text{-}\mu\text{m}$ spot diameter. The build area has a size of $100 \times 100 \text{ mm}$.

4 Exposure and part building

4.1 Limitations for part building

For the calculation of the process parameters, one must for the cure depth. As described before the scan speed is limited by the dynamic positioning accuracy of the scan mirrors. To illustrate the problem some basic calculations can show that there is a contradiction between the minimization of the laser spot diameter and the use of maximum laser power. We assume a desired cure depth of $C_d = 100 \mu\text{m}$ and the use of an optical unit with a $50\text{-}\mu\text{m}$ laser spot diameter.

Knowing from [JAC92] the cure depth C_d and the line with L_w are functions of laser power, scan speed and spot diameter:

Cure depth funktion:

$$C_d(P, vs, w_0) := D_p \cdot \ln \left(\sqrt{\frac{2}{\pi}} \cdot \frac{P}{vs \cdot w_0 \cdot E_c} \right)$$

Line width function:

$$L_w(P, vs, w_0) := 2 \cdot w_0 \cdot \sqrt{\frac{C_d(P, vs, w_0)}{2 \cdot D_p}}$$

P - laser power; vs - scan speed; w_0 - spot radius

Due to the optical unit (see section 3) the laser power and maximum scan speed is defined by

Max. laser power: $P_{\text{max}} := 30 \text{ mW}$

Max. Scan Speed: $vs_{\text{max}} := 1000 \frac{\text{mm}}{\text{sec}}$

This gives us the following values for:

Cure depth: $Cd(P_{max}, vs_max, w_0) = 316\mu m$ Line width: $Lw(P_{max}, vs_max, w_0) = 53\mu m$

It clearly can be seen that the cure depth is very large (over-curing). The solution for this dilemma is to reduce the laser power that passes into the resin. This can be done by an optical filter or an analog acousto-optical modulator. By reducing the laser power to

$P_{min} := 21.3\% \cdot P_{max}$ $P_{min} = 6.4\text{mW}$,

we now get the desired cure depth combined with a very thin line width:

Cure depth: $Cd(P_{min}, vs_max, w_0) = 100\mu m$ Line width: $Lw(P_{min}, vs_max, w_0) = 30\mu m$

Fig. 3-4 illustrates the relation between the maximum laser power and minimum spot size diameter for a given cure depth of $C_d = 100\mu m$.

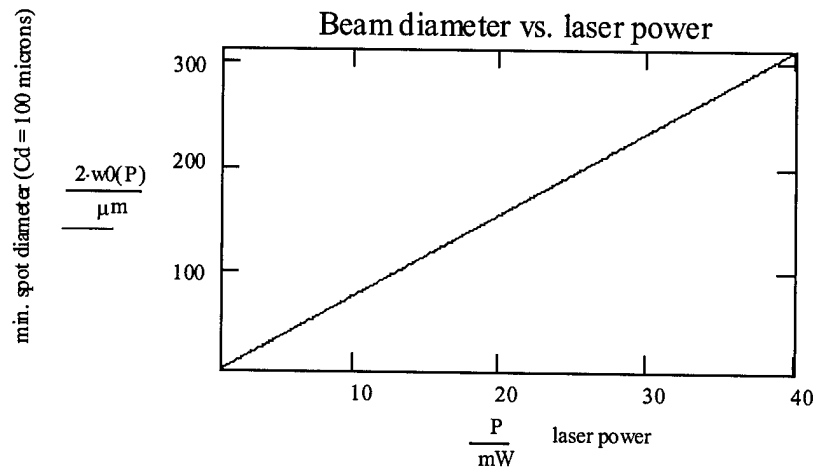


Fig. 3-4: Minimum beam diameter for curing 100- μm layer

Because of the reduction of the laser power one must take into account the extended build time for high resolution parts.

4.2 First applications

After successful optical tests, first structures were build with a STEREOS Desktop with enhanced resolution using a 42- μm spot diameter.

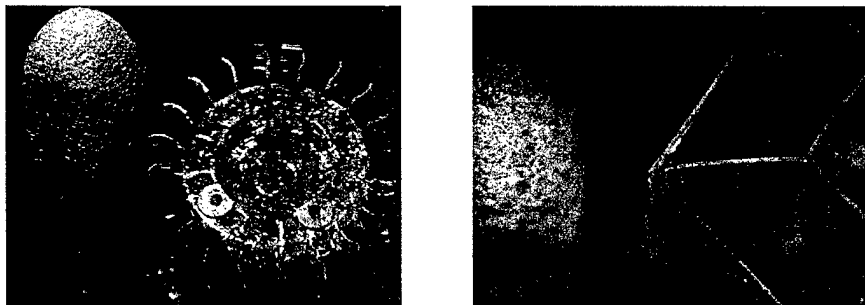


Fig. 4-1: A – turbine, B – honeycomb structure (wall thickness approx. 40 μm)

Following process parameters were chosen:

- laser power $P = 8 \text{ mW}$,
- scan speed $v_s = 1000 \text{ mm/sec}$ with,
- layer thickness $t_L = 100 \mu\text{m}$.
- material used for all parts SOMOS 7100 series.

After the building process a conventional cleaning procedure was performed. One must take special care of handling the small structures.

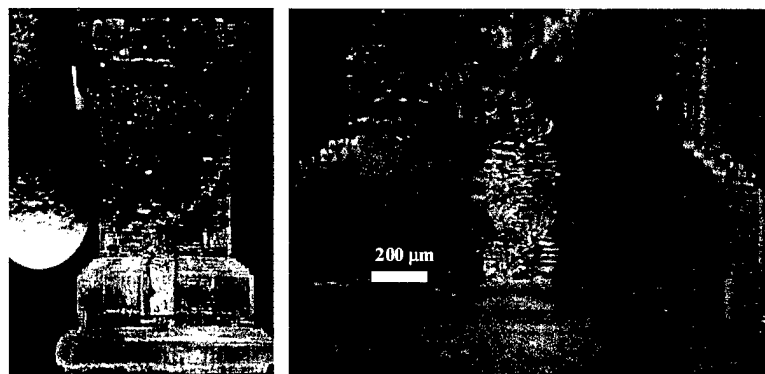


Fig. 4-2 A and B: Chess tower with inner spiral staircase, enlargement.

5 Conclusions

Knowing the limitations of today's stereolithography apparatuses one can considerably increase the lateral resolution of manufactured stereolithographic parts. For further reduction of the part's structural resolution to the range of less than 50 μm , the system design of the stereolithography apparatus must be reconsidered. For further progress in resolution a new recoating system and modifications of RP materials are necessary. Compared to other

approaches to micro RP this way combines a full build area with a relatively high structural resolution.

6 Acknowledgement

The author would like to give special thanks to all project partners and students who made this work possible. We also would like to appreciate for the financial support of BFS, München.

7 References

- [JAC92] Jacobs, P.F.: Fundamentals of Stereolithography. SME. Dearborn 1992
- [WOH98] Wohlers, T.T.: RP&Tooling 1998 Worldwide Progress Report.
- [DEU99] Deuke, R.: New Lasers for Stereolithography. uRapid99. London 1999.
- [MAR96] Marshall, G.F.: Optical scanning. M. Decker. New York.

APPLICATION OF SOLID FREEFORM FABRICATION TECHNOLOGY TO NASA EXPLORATION MISSIONS

Kevin Watson, *Exploration Office, NASA - Johnson Space Center, Houston, TX 77058*

Dan Petersen, *Manufacturing Integration and Technology Branch, NASA - Johnson Space Center, Houston, TX 77058*

Robert Crockett, *Milwaukee School of Engineering, 1025 North Broadway, Milwaukee, WI 53201*

Exploration Mission Concepts and Constraints

NASA has begun the process of planning for mankind's next steps in the human exploration of the solar system. Missions under consideration include a return to the Moon, visits to near-Earth asteroids, and the exploration of Mars. Although each possibility presents unique opportunities and challenges, a mission to Mars is believed to present the greatest challenges and to be the most defining case from the standpoint of required capabilities.

Current planning shows that the duration for a Mars mission will be on the order of 900 days (1). This total includes approximately 6 months for both the outbound and return transits and roughly 500 days on the surface of the planet. These figures are determined by the relative positions of the Earth and Mars that are necessary for trajectories requiring minimum expenditure of propulsive energy. Minimizing propulsion requirements significantly reduces the total required propellant mass and, thus, the total mass that must be launched from Earth and injected towards Mars.

One of the features of a mission to Mars which uniquely distinguishes it from spaceflight operations in Earth orbit is the inability to abort the mission and return quickly to Earth. In the case of Space Shuttle flights or International Space Station operations the crew can be back on the surface of the Earth in just a few hours if events demand. In the case of a Mars mission, however, astrodynamics and energy requirements dictate that, once on the way to Mars, the crew is committed to a journey of the full initially planned duration. A quick return to Earth is not possible.

Another feature of a Mars mission which uniquely distinguishes it from the operation of the International Space Station is that there will be no opportunity for resupply from Earth. Optimum opportunities to launch to Mars occur only at intervals of approximately every two years and the transit time is several months at best. Whereas hardware failures on spacecraft in low-Earth orbit can be managed by replacement of components sent from Earth, missions to Mars will have to be self-sufficient from the moment they leave Earth orbit (2). The lack of abort capabilities and the need for long-duration self-sufficiency demand that the crew have highly flexible and robust capabilities to maintain and repair all system hardware to enhance the probability of mission success. However, satisfying this need for robustness must not result in enormous quantities of spare parts which impose significant penalties in terms of mass and stowage volume.

Directions in Exploration Mission Supportability

Mission supportability includes all aspects of planning for, and implementation of, those processes, capabilities and facilities that are necessary to maintain vehicle systems in an operational status. By enhancing the robustness and flexibility of the support capabilities the probability of mission success can be significantly improved while minimizing impacts to total mission mass, stowage volume requirements, and cost.

One approach is to maximize commonality of hardware at all levels. Increased commonality reduces the number of unique spares that must be carried and increases the opportunities for exchange of hardware as the need arises. Since the probability of failure of all members of a common set containing "n" members is $P(f)^n$, where $P(f)$ is the probability of failure of each member, it can be seen that it should not be necessary to carry "n" spares since there should be a very low probability of all set members failing. On the other hand, if the members of the set are unique rather than common, it is much more likely that at least one spare must be carried for each member.

Another approach is to encourage repair at the lowest possible level. Typically, when a complex hardware assembly fails, the failure is attributable to a very limited number of small internal components rather than massive failure of the assembly at a gross level. If only the specific failed components are replaced, then the mass and volume of the required spares is significantly reduced. Traditionally, however, this approach would be truly effective only when component commonality is maximized as well. Otherwise, a massive number of small components would be required.

A third approach, which complements the others, is to provide the capability to manufacture replacement components *in situ* as required. A very significant advantage of this capability is that it reduces the need to carry specific, unique replacement components. Rather, replacements are generated as needed from feedstock material. Furthermore, *in situ* fabrication of replacement components reduces the chance that a required component will not be available and, also, reduces the chance that components are carried that will not be needed. The net effect is a major reduction in the mass and volume of spare components or assemblies and a significant improvement in mission robustness by reducing the risk of having the "wrong" set of spares. Options for *in situ* fabrication of non-electronic components include standard machining processes and solid freeform fabrication (SFF).

The Case for Solid Freeform Fabrication

It is certainly premature to select a single manufacturing methodology for *in situ* fabrication on space exploration missions; some general comments can be made, however, about the attractiveness of Solid Freeform Fabrication (additive manufacturing) relative to machining (subtractive manufacturing). One key consideration is the amount and form of feedstock materials. Assuming operations in reduced gravity, there is a need to keep the volume of materials in any melt processing to a minimum. This implies that raw materials used for subtractive manufacturing must be stored in "near net" shape (various sized billets / blocks /

sheets / rods). Although much mission hardware can be designed for remanufacture from a limited number of feedstock sizes, this will still impose a large raw material burden. Solid Freeform Fabrication systems universally have a more efficient packaging of feedstock materials.

Subtractive manufacturing by nature also produces a large amount of waste material relative to fully additive processes. This imposes additional requirements on the manufacturing facility such as containment of chips and lubricants in a reduced gravity environment. If the waste material is to be reclaimed and reused, additional material separation and melt processing steps are required. The need for tool changeouts, object fixturing, and manual or automated part positioning is also much greater in traditional machining.

Reducing the total mass and volume of an *in situ* manufacturing facility requires reducing the total number of machines; reducing the total human or robotic overhead requires reducing the total number of manufacturing / assembly steps. It is in this area that Solid Freeform Fabrication offers the most promise relative to more traditional techniques. One example would be a single FDM-type deposition system capable of building a thick-film circuit board, populating it by placing small components, and constructing the housing around it. In this case, a single machine has the capabilities of combining multiple functional materials (electrical conductors / insulators + structural materials), as well as performing assembly steps. This can potentially occur while the object is constructed in a single orientation with minimum human intervention.

Desirable Solid Freeform Fabrication Process Characteristics

Solid Freeform Fabrication processes must possess certain attributes to be attractive candidates for inclusion in the suite of space mission supportability capabilities. These desirable characteristics are described below.

Compatibility with multiple materials. A wide range of materials, both metallic and nonmetallic, are employed in spacecraft hardware. Although a single SFF process which could yield both metallic and nonmetallic components would be attractive, the continuing preponderance of metallic components indicates that, if a choice must be made, emphasis should be placed on processes which yield metallic components. However, since a variety of metallic alloys are utilized it is highly desirable that processes compatible with aluminum alloys, stainless steel, titanium alloys, and nickel alloys be employed.

Adequate properties in finished parts. It is critical that any part produced have mechanical properties that meet design requirements. In some cases, however, the properties required for a replacement part may be different than for an original part. This is because the original part may have to endure unique stress and environmental conditions during relatively brief mission phases. For example, an original part may have to endure severe thermal conditions or high static or dynamic loads during launch. If, after that mission phase, a replacement component is fabricated, it may no longer be faced with those conditions and, thus, not require the same mechanical properties. Extreme caution is mandatory in the application of this concept, however. All potential futures for a replacement part must be considered to ensure that the part will perform satisfactorily in potential off-nominal situations.

Capability to produce complex parts. Although many individual components in spacecraft hardware assemblies have quite simple configurations (e.g. washers, seals) many others are equally complex. Therefore, any SFF process that is employed must be capable of producing geometrically complex components.

Minimum number of processing steps. Attractive SFF processes will involve the fewest number of processing steps while retaining the capability of generating complex parts. This is important because increased numbers of processing steps imply greater time required to generate a part and more equipment to support the distinct steps.

Minimum crew interaction. Although crew involvement will be required for virtually all maintenance and repair operations, the primary purpose of the crew will be to explore. The introduction of processes which require additional crew time would be contrary to overall mission objectives. Thus, processes should require as little crew interaction as possible.

High production rate. Replacement part production should be accomplished in a "reasonable" period of time. Although the term "reasonable" is not readily definable, it can be said that replacement parts should be produced with sufficient speed to return an assembly to an operational condition prior to the occurrence of mission impacts and that the part production process should not become a bottleneck in maintenance and repair operations.

High yield - minimum wasted material. To gain maximum benefit from this technology, it is important that a very high percentage of the consumed feedstock material be incorporated into the final part. This requires the minimization of unconsolidated powder, overspray, or other loss of material. Also, the initial product should be near-net-shape so that material losses during final finishing are minimized.

Compatibility with reduced-gravity environments. Implementation of SFF processes in support of exploration missions will require performance in reduced-gravity environments. During transit phases, acceleration levels will be zero. While on the planetary surface, gravitational acceleration will be positive but less than the 1-g experienced on Earth. Acceleration effects could be manifested during both material deposition and, if a liquid phase is involved, solidification. These potential effects must be explored and processes developed which accommodate them.

Minimum final finishing. Initial production of near-net-shape parts results not only in higher yield, as discussed above, but also speeds the total production process, potentially requires less secondary processing equipment and consumes less power.

Minimum mass and volume of equipment. The equipment which is utilized in both initial production and secondary processing should be designed to minimize its mass and volume. This is important to maximize the overall benefit from the application of this technology.

Minimum power consumption. Spacecraft power is always at a premium. The power requirements for initial production and secondary processing should be such as to not impact operation of other spacecraft systems or to be a significant factor in power system sizing.

Minimized unrecoverable consumables. To the extent possible, unrecoverable consumables such as binders, inert gases and cutting fluids should be minimized. Unrecoverable consumables not only contribute to total system mass but also impart an additional load on filtration systems which are necessary to prevent contamination of the spacecraft environment.

Safety. Safety is a paramount characteristic. Any off-gassing or waste products must be controllable. Personnel must be protected from high temperature surfaces, sharp objects, inhalation of metal powders and fume, lasers, or other hazardous materials. All potential hazards must either be eliminated or controlled.

Limitations of the State-of-the-Art

Given the desirable process characteristics as presented above, it is instructive to review current SFF systems and the direction of their development. The research focus of Solid Freeform Fabrication technology for earthbound industrial use in many cases addresses the same needs of space-based manufacturing: materials development (especially metals), production rate, and surface finish. SFF systems that currently excel in these categories, however, may be unacceptable for use in a space-based manufacturing facility because of the unique requirements of the application. Compatibility with a reduced gravity environment, the mass/volume/consumables of the SFF equipment, and the safety issues associated with crewed spacecraft will ultimately drive the development of an *in situ* manufacturing system. In this discussion, we are considering only the direct manufacture of objects from SFF equipment. Using SFF to create patterns or tools for secondary operations (e.g. casting or injection molding) are unlikely to be practical solutions for one-of-a-kind manufacturing in a space-based facility.

In an abstract sense, Solid Freeform Fabrication systems can be categorized into *Stereolithography*, *Deposition*, and *Lamination* techniques. For purposes of this classification, stereolithography techniques include all methods that selectively solidify patterns within a supply bed of bulk material. This would include not only 3-D System's Stereolithography (SLA), but also systems such as Selective Laser Sintering (SLS) and Three-Dimensional Printing (3-DP). To meet the materials requirements of *in situ* manufacturing, stereolithography systems must use particles as the bulk feedstock material. This requires modification of standard SLA systems to use the photopolymer as a binder in ceramic (3) or metal (4) particulate slurries. In all of these particle-based systems, a greenbody is created on the machine in the desired geometry, and final properties are achieved through a second, higher-temperature sintering step.

The use of particles as feedstock allows for a wide range of materials to be produced using stereolithography techniques. Three-Dimensional Printing has historically focused on the creation of fully-dense structural ceramic objects (5). The Selective Laser Sintering system has recently been used to produce titanium objects through the addition of hot isostatic pressing (6). The significant amount of materials research in this area, combined with the fact that these systems have some of the highest throughput and accuracy, makes stereolithography systems attractive for *in situ* manufacturing. A primary consideration of these techniques for space applications is the placement and control of the feedstock material. The feedstock must be fully contained, yet allow energy (SLA, SLS) and/or material (SLS, 3DP) to reach the build surface. Possible methods of containment may include contact mask printing, or control of thin particulate layers by means of magnetic or electrostatic forces.

Deposition Systems (FDM, FDC, EFF, SDM, LENS, etc.) are well-suited to reduced gravity material handling. The majority of these processes achieve a liquid-to-solid transition by the rapid cooling of extruded beads from a small melt volume. Because the dimensions of these beads are below the capillary limit, gravity is not required for material flow and adhesion (7). Single deposition systems are compatible with multiple material types, including insulating and conducting polymers, metals such as steel (8), and ceramics (9). As the core of these systems is a simple x-y-z plotter, there is a good deal of commonality with robotic assembly systems, as

well as the direct manufacture of electronic thick film circuits (10). There are significant limitations to these systems, however, including materials, resolution, and throughput. Another key limitation is the need in most deposition systems to support overhangs. While this may at first seem counterintuitive for a reduced-gravity application, initial studies (7) show just how important a continuous substrate is for the correct placement of beads. Shape Deposition Manufacturing (SDM) and the Sandia LENS system are attractive for producing fully dense metals, but both systems have equipment mass, complexity, and potential safety problems which must be addressed for this application.

Lamination Systems, which stack-then-cut (LOM) or cut-then-stack (CAM-LEM) solid sheets of material, also offer ease of reduced-gravity feedstock handling. Composite objects can be directly manufactured, while metal and ceramic objects are possible by using particulate sheets combined with an additional sintering step (11). These systems have some severe geometry limitations, however, and share with deposition systems the need to support overhangs. An even more significant drawback is the amount of feedstock waste. Reprocessing of this waste, while generally not economically viable for earth-based systems, would be a key requirement for adapting lamination systems to space-based manufacturing.

It is not the purpose of this discussion to quantitatively rank SFF system capabilities against NASA needs. Indeed, the subtle differences in individual techniques, as well as the pace of development makes any ranking results dubious. As we have seen in industry, there is not a clear SFF "winner" – each system has found its niche. A space-based system will not have the luxury of multiple machines, however, so a combination of design compromises and system development will be required. Some of the challenges may be answered by combinations of Solid Freeform Fabrication processes, or combinations of SFF with machining (SDM is an example). Other possibilities include using SFF equipment to create thin shells in the correct geometry for filling with composite material (12) or using as a thin-walled mold for slurries of ceramic or metal particles.

Current NASA Activities in SFF

Since 1990 hundreds of parts have been fabricated at NASA's Johnson Space Center (JSC) in Houston for form, fit and functionality demonstrations; for wind tunnel tests; and to serve as casting masters, injection mold patterns, and working models. The use of SFF has proven beneficial in reducing design-to-manufacturing time for many assembled parts such as on-orbit crew tools and robotic arms joints. In addition, larger SFF parts have been assembled together for wind tunnel and fluid flow testing, including a three-foot model of the Space Station Crew Return Vehicle, and a two-foot diameter T-38 aircraft inlet duct, respectively.

At NASA's Marshall Space Flight Center (MSFC) in Huntsville, Alabama, eight different SFF technologies are employed to aid engineers in both the design and manufacturing of parts. Research efforts at MSFC have included support in development of direct ceramic and high-precision rapid prototyping (RP) capabilities, optimization of RP investment casting patterns, and transonic wind tunnel testing with RP models.

NASA is currently evaluating different technologies for further development and use to meet the goals for the Human Exploration and Development of Space. At JSC, activities and efforts for in-space manufacturing have focused on two principal areas: developing a roadmap and plan for rapid manufacturing of space flight hardware, and performing introductory tests of the fused deposition process in a reduced-gravity environment. The roadmap includes several milestones, from the development of basic systems requirements to the generation and investigation of potential material reclamation and recycling systems.

In June, engineers from both JSC and MSFC performed introductory tests of a deposition manufacturing experiment in a non-gravitational environment. A Stratasys Fused Deposition Modeling (FDM) 1600 rapid prototyping system was structurally secured into the NASA KC-135 research aircraft which provides brief periods of a reduced-gravity environment while flying parabolic trajectories. Once reprogrammed for approximately 20-second build cycles (approximate time of reduced gravity during each parabola), the FDM was used to fabricate 14 parts in 7 different configurations, including a tensile bar, vertical column, bridge with multiple piers, hourglass, cantilever beam, dome structure, and longer-span bridge with piers.

The purposes of the reduced-gravity tests were to:

1. Analyze the inter-layer bonding of an additive layered, fabricated component
2. Evaluate the dimensional stability of the specimens as compared against the same designs fabricated under normal gravitational conditions, and
3. Determine the overall operability of an extrusion-based manufacturing process without the assistance of gravity.

Although difficulties were experienced due to atmospheric humidity (with the ABS plastic material), and part stability during the 2-g pullouts, the tests still demonstrated the ability of a deposition process to fabricate parts in a non-gravitational environment. A complete summary of the tests and results are discussed elsewhere (7).

Planned Solid Freeform Fabrication Development Strategy to Support Exploration Needs

To support future human mission needs, NASA will work towards a better understanding of SFF process capabilities and limitations. The goal will be to find ways to enhance process control, surface finish, deposition rate, and part complexity capabilities. Emphasis will also be placed on reducing processing equipment size and power requirements. Furthermore, it will be necessary to gain insight into the influence of low-g and partial-g acceleration environments on process which may be sensitive to this factor.

Finally, NASA will develop an integrated supportability strategy to take advantage of opportunities presented by commonality, low-level repair, and SFF. This will have additional programmatic and design implication such as requirements for low-level failure modes and effects analyses, aggressive Repair Level Analyses, and deliverable 3-D models of all components which are candidates for SFF.

References

1. NASA, Johnson Space Center. NASA-SP 6107, "Human Exploration of Mars; The Reference Mission of the NASA Mars Exploration Study Team", 1997.
2. NASA, Johnson Space Center. DD-099-05 "Operations Concept Definition for the Human Exploration of Mars", 1999.
3. G. Brady, T. Chu, and J. Halloran, "Curing Behavior of Ceramic Resin for Stereolithography", in *1996 Solid Freeform Fabrication Symposium Proceedings*. Austin, TX: University of Texas at Austin (1996) 403-410.
4. W. Zimbeck and M. Pope, "Microstructures and Strengths of Metals and Ceramics made by Photopolymer-based Rapid Prototyping" in *1996 Solid Freeform Fabrication Symposium Proceedings*. Austin, TX: University of Texas at Austin (1996) 411-418.
5. S. Uhland *et al.*, "New Process and Materials Developments in 3-Dimensional Printing, 3DP", *Solid Freeform and Additive Fabrication, MRS Symposium Proceedings v.542*. Materials Research Society, Penn, 1999. p153-158.
6. S. Das, M. Wohler, J. Beaman, and D. Bourell, Processing of Titanium Net Shapes by SLS/HIP in *1998 Solid Freeform Fabrication Symposium Proceedings*. Austin, TX: University of Texas at Austin (1998) 469-477.
7. R. Crockett, D. Petersen, K. Cooper, "Fused Deposition Modeling in Microgravity", presented at this conference.
8. G. Wu *et al.*, "Feasibility of Fabricating Metal Parts from 17-4PH Stainless Steel Powder", in *1998 Solid Freeform Fabrication Symposium Proceedings*. Austin, TX: University of Texas at Austin (1998) 479-486.
9. S. Morissette, J. Lewis, J. Cesarano III, and D. Dimos, "Solid Freeform Fabrication Using Alumina-Poly(Vinyl Alcohol) Gel-Casting Suspensions", *Solid Freeform and Additive Fabrication, MRS Symposium Proceedings v.542*. Materials Research Society, Penn, 1999. p125-132.
10. B. King *et al.*, "Influence of Rheology on Deposition Behavior of Ceramic Pastes in Direct Fabrication Systems", in *1998 Solid Freeform Fabrication Symposium Proceedings*. Austin, TX: University of Texas at Austin (1998) 391-406.
11. J. Cawley, Z. Liu, J. Mou, and A. Heuer, "Materials Issues in Laminated Object Manufacturing of Powder-Based Systems", in *1998 Solid Freeform Fabrication Symposium Proceedings*. Austin, TX: University of Texas at Austin (1998) 503-510.
12. R. Crockett and V. Gervasi, "Gradient and Discrete Region Composites Produced by Solid Freeform Fabrication Techniques", *Solid Freeform and Additive Fabrication, MRS Symposium Proceedings v.542*. Materials Research Society, Penn, 1999. p25-30.

THREE – DIMENSIONAL PRINTING, 3DP™, OF ELECTRONIC CERAMIC COMPONENTS

S. Uhland*, R. Holman*, B. DeBear*, P. Saxton*, M. Cima* and E. Sachs*
Y. Enokido** and H. Tsuchiya**

* Massachusetts Institute of Technology, Cambridge, MA 02139

** TDK U.S.A. Corporation, Port Washington, NY 11050

Abstract

Products which incorporate ceramic components frequently demand properties and shapes that challenge contemporary forming techniques. The Three-Dimensional Printing, 3DP™, process has been modified to incorporate colloidal science for the fabrication of these fine ceramic parts. Dielectric components were built using a sequential layering process of a ceramic powder bed followed by ink jet printing of a binder. A well-dispersed slurry and optimized printing parameters are required to form a uniform powder bed with a high green density. Slurry-powder bed interactions affect the geometry of the component and produce structural and inter-layer defects ("differential slip casting"); the correct choice of binder system and slurry chemistry has, however, eliminated these defects. Removal of the printed components is an important processing step in 3DP™ since the part retrieval process plays a key role in the resulting shape and properties of the ceramic parts. Part retrieval is achieved through the redispersion of the powder bed. This technology has been used for the fabrication of dielectric radio frequency (RF) components with good dimensional tolerances. The dielectric characterization of RF filters was performed on dry-pressed and 3DP™ formed components in order to examine the effects of processing technique on performance.

Introduction

Dielectric ceramic components have made a large impact on the growth of the communications industry. The current technology has evolved to include pagers, automobile collision avoidance, global positioning systems and other frequency sensing devices. The growth was facilitated by the development of a unique class of ceramic dielectrics. These materials combine a high dielectric constant and low dielectric loss enabling new design possibilities. Conventional forming processes, such as die pressing, extrusion and tape casting are currently used to form such components. These processes restrict the geometry of the components to very simple shapes. Additional processing steps are required to meet the strict dimensional tolerances while machining is needed in order to produce components with more complex geometries. The macrostructure and microstructure of the components are non-uniform due to the nature of the forming processes. Density variations and stacking sequences lead to anisotropic physical properties that ultimately degrade the performance of the component. Thus, much of the past 15 years of ceramics processing research has been focused on the development of forming processes with excellent shape capabilities and improved reliability.

Our research has concentrated on combining modern ceramics processing with a solid freeform fabrication (SFF) method. The specific technique studied is 3-Dimensional Printing, 3DP™. This process is capable of producing complex-shaped ceramic, metal and polymer components directly from CAD files.¹ The 3DP™ process has been integrated with colloidal ceramic processing to produce parts using submicron powders.² There are four fundamental

aspects of the process that have been studied in detail. They are formation of the powder bed, the development of the binder system, liquid interaction between the slurry and binder systems and the redispersion of the unprinted powder bed. The physical properties of the printed parts are influenced by one or more of these principles.^{3,4,5,6} This paper discusses the physics and implications of forming ceramic components using the slurry-based 3DPTM process. RF components have been successfully fabricated using this process and their dielectric properties are briefly discussed.

Experimental Procedure

The Slurry-Based 3DPTM Process

Part generation began by jetting a well dispersed, 35 vol. % dielectric ceramic (MR2, TDK USA Corp.) slurry through a 127 μm orifice nozzle to form the powder bed, as illustrated in Figure 1a. The slurry was deposited by a single jet rastering over a porous substrate in the x and y directions, the “fast axis” and “slow axis”, respectively. The deposited slurry lines are stitched together forming the slurry layer, which solidified via slip casting. This wet layer was dried using a IR heat lamp upon the completion of the rastering process.

The binder, a polyacrylic acid (Acumer 1510, Rohm and Haas, Philadelphia, PA) and glycerol aqueous solution, was printed through an ink-jet nozzle (40 μm orifice) in a rastering procedure similar to the slurry jetting process. Binder droplets were selectively printed using a charge and deflection continuous jet printhead producing a 2-D image. The layer was heated to remove excess water. Sequential slurry and binder deposition processes were repeated to complete the part. Figure 1a illustrates the binder printing procedure.

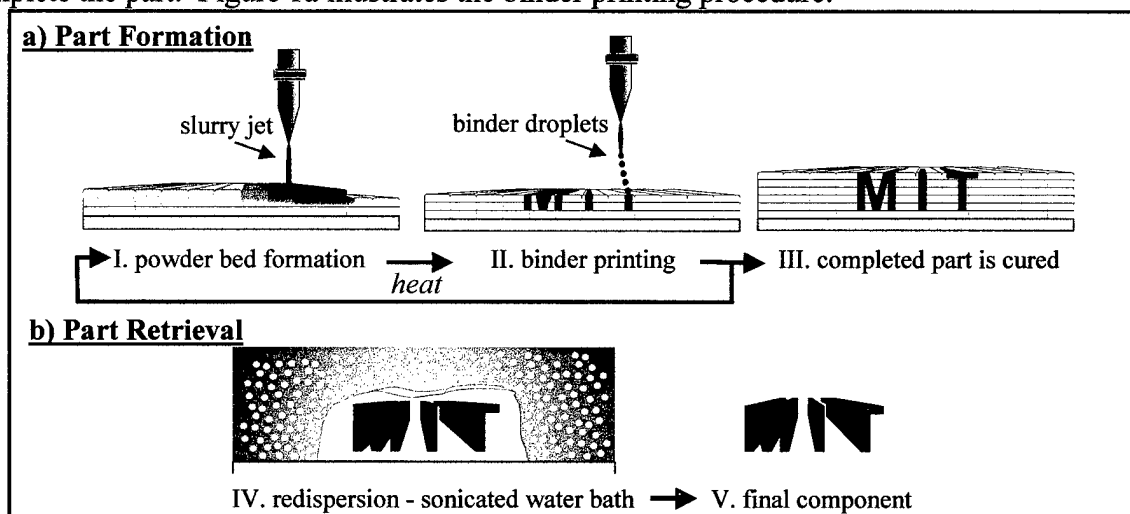


Figure 1: Slurry-Based 3DPTM a) Part Formation Process and b) Part Retrieval.

Imbedded parts were placed in an oven to thermally cross-link the binder. The binder was cured at 150°C for 45 min in an inert environment. The imbedded part and the powder bed matrix were placed into a sonicated water bath, as shown in Figure 1b. The unprinted powder bed spontaneously redispersed and the final components were recovered.

Results and Discussion

Powder Bed Microstructure and Formation Technique

The microstructure of the powder bed depends on the method used for its formation. The current technique used for powder bed formation is based on rastering a single slurry jet across a porous substrate. This process can produce a small population of relatively large pores (~5 to 10 μm). This results from slurry lines slip casting independently, creating valleys between adjacent slurry lines. The next layer of slurry will deposit a line directly over this valley, and a void will be produced if the slurry does not perfectly fill the valley between slurry lines.

Tape casting of powder bed layers was examined in an attempt to eliminate creation of voids. This method proved unsuccessful due to the formation of macro-scale bubbles (~1mm, see Figure 2). These were the result of entrapped air displaced from within the underlying pore structure by infiltrating liquid, which was forced up through the layer of slurry.

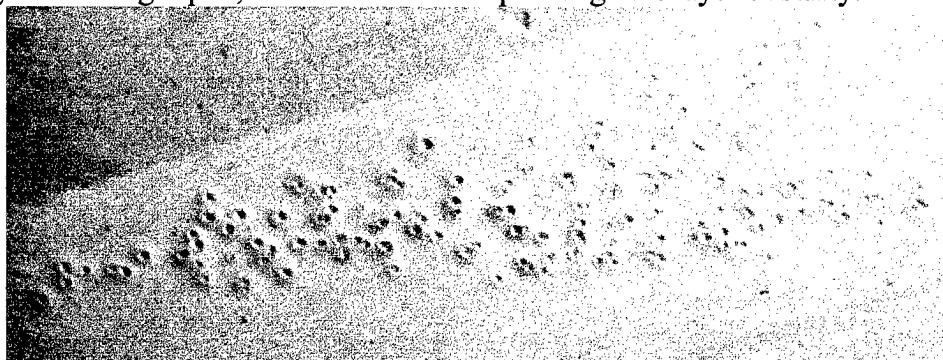


Figure 2: Tape Cast Powder Bed “Bubbling”.

A new approach to 3DPTM layer fabrication, termed line merging, is under development to rapidly deposit defect free slurry layers. This method is a compromise between the previous two methods. A jet of slurry is raster-scanned over the surface of the powder bed rapidly enough so that each new line of slurry is deposited before the previous line has slip cast fully ($t_{\text{cast}} < 300$ ms), but not fast enough to entrap air and produce bubbles (as in tape casting). Initial trials with Al_2O_3 powder beds have been completed, and the results look promising.

The Binder System

The binder system used in the slurry-based 3DPTM process must meet several requirements. One criterion for selection is based on its solubility characteristics. The binder is initially required to be a solution phase in order to infiltrate the fine pore structure of the 3DPTM powder bed, however the binder solubility requirements change drastically during the process. The imbedded 3DPTM parts are removed from the powder bed by redispersing the surrounding unprinted powder using a liquid medium. This demands that the binder be insoluble such that the printed components retain their geometries. Additional criteria emphasize the binder's intrinsic properties that determine the ink-jet printing performance of the binder as well as its powder bed interaction.

Four different binders have been investigated that include a styrene-acrylic copolymer, a cyanoacrylate, a urethane acrylate oligomer and a polyacrylic acid - glycerol system. The polyacrylic acid (Acumer 1510, Rohm and Hass, Philadelphia, PA) binder system has proven to be very effective with respect to the outlined criteria. A 2.4 vol.% solution ($\eta = 2.3$ cP and $\gamma = 71$ dynes/cm) was used for printing parts containing 1.0 vol.% binder. The binder was

crosslinked at 150°C yielding parts having excellent strength and chemical stability in order to survive the part retrieval process.

Differential Slip Casting

Binder-powder bed interaction plays an important role in controlling printing resolution, surface finish, and microstructure of the 3DP™ part. An important aspect of the binder-powder bed interaction is a differential casting effect of the slurry during the powder bed formation. The effect of the binder system on part formation in the slurry based 3DP™ process has been defined by Grau.⁶ The casting rates of the slurry were calculated from the model of Aksay and Schilling.⁷ The casting process is a colloidal filtration in which the solvent in the slurry is rapidly removed from the thin layer of slurry. The filtration rate is dependent upon the viscosity of the solvent in the slurry, pore fraction and pore size of the powder bed, and contact angle of the liquid on the solid. The rate of colloidal filtration is expected to differ locally for slurry-based 3DP™ powder beds since selected regions are printed with a polymeric binder solution. The regions in the powder bed that are printed with binder will have different pore structures and wetting behavior than regions that do not contain binder.

The casting rate of the slurry may be much lower over the binder-printed region than over the unprinted region when using an aqueous slurry solvent. The slurry casts quickly over the region that was not printed with binder while the slurry remains fluid over the region printed with binder. Slurry then migrates from the binder-printed region towards the surrounding unprinted powder bed. The differential casting kinetics can lead to major structural defects (illustrated schematically in Figure 3): a bump at the interface of the binder-printed region; increased surface roughness on the printed region; a non-uniform (i.e. curved) top surface; and a depression of the top surface below the level of the surrounding bed (adversely affecting height control).

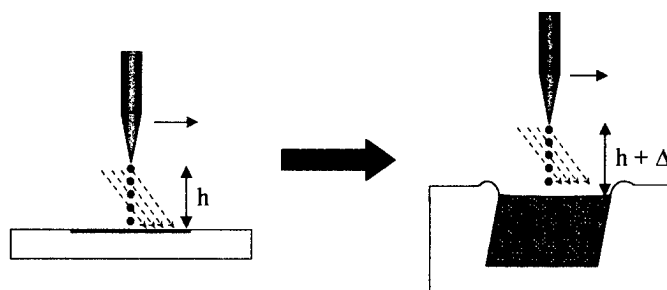


Figure 3: Schematic illustrating defect generation due to differential slip casting.

The effects are minimized by tailoring the wetting behavior of the solvent on the binder-printed region and by minimizing the volume of binder deposited. The curve in Figure 4a shows the ideal ratio of the cosines of the contact angles of the slurry solvent on the binder and on the ceramic powder that will give equal slip casting rates on the two regions. Figure 4b then shows the wetting properties of the binder as a function of alcohol content in the slurry solvent, with the ideal value for a given binder content by the horizontal line. Differential slip casting is minimized by choosing a slurry solvent composition on or near this line.

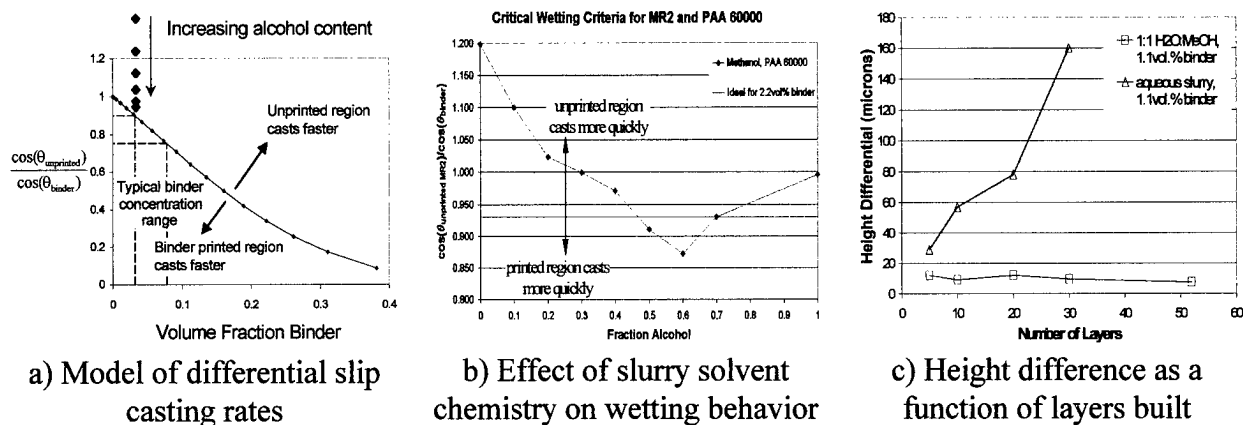


Figure 4: Minimizing differential casting through slurry chemistry modifications.

The effect on the height difference between the part and surrounding powder bed (Δ in Figure 3) is illustrated in Figure 4c for an aqueous slurry and for the optimized slurry chemistry containing alcohol. The optimized chemistry results in a very small height difference that does not increase as further layers are added. This has improved vertical dimensional control to within $\pm 10 \mu\text{m}$, and allows components of essentially any height to be manufactured.

Part Retrieval

An important characteristic of the slurry-based 3DPTM process is that the printed parts are imbedded within the powder bed matrix. The unprinted powder bed is cohesive due to the slip casting nature of the powder bed fabrication process. Retrieving the imbedded components from this brick-like structure is therefore a critical step.

Part retrieval is achieved by redispersing the unprinted ceramic powder that surrounds the binder-printed component(s) in an aqueous medium and is pictured in Figure 5.

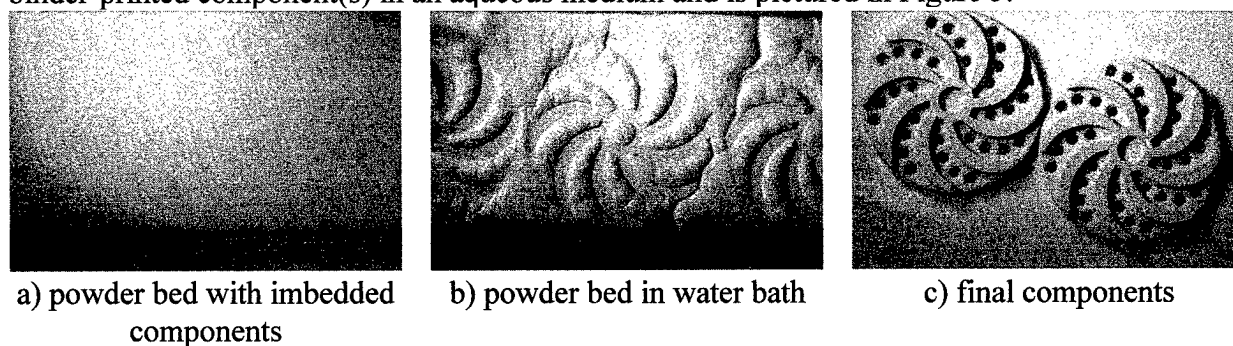


Figure 5: Slurry-Based 3DPTM Part Retrieval via Redispersion.

Successful redispersion depends upon the strength of the unprinted powder bed. Interaction forces of the ceramic particles control the strength of the powder bed. These interaction forces are controlled through the chemistry of the slurry used to form the powder bed matrix. A “redispersant”, low molecular weight polyethylene glycol (PEG 400, Carbowax, Union Carbide, Danbury, CT) is added to the slurry chemistry and remains in the pore structure of powder bed once it has been dried. PEG 400 offers two possible redispersion mechanisms. PEG forms soluble necks between adjacent ceramic particles. These bridges dissolve and break up the

network of particles allowing them to re-establish their electrostatic repulsive forces. A second mechanism results from water's "good solvent" characteristics with respect to PEG. The polymer chains swell and extend as they dissolve in the water entering the powder bed during the redispersion process. This acts as an additional force pushing the particles apart. The effect PEG has on the redispersion behavior of unprinted powder beds is dramatic. The redispersed mass was minimal for those samples without PEG (redispersed mass = 3 wt.%) while those containing 1 wt.% PEG (redispersed mass = 99.9 wt.%) dispersed to a fine powder.

A challenging aspect of slurry-based 3DP™ is designing the process such that redispersion is achieved after thermally curing the binder. The difficulty is a result of the degradation PEG in the presence of oxygen which is accelerated at elevated temperatures (>100°C). The degradation mechanism is complex and is caused by the existence of several possible modes by which the free radicals degrade to low molecular weight fragments⁸. Four approaches have been used to minimize the degradation. Two approaches were to minimize the binder curing time and the curing temperature itself, however, the time and temperature are fixed at a minimum of 150°C for 45 minutes to sufficiently cure the binder. The third was to eliminate the presence of oxygen during elevated temperature processing by curing in an inert argon atmosphere. The final method was to add an anti-oxidant, butylated hydroxy toluene (BHT), to the PEG that reduces the concentration of free radicals. The later two techniques proved very effective in reducing the degradation and ultimately restoring the redispersibility of the unprinted powder bed. Figure 6a demonstrates the effect of the curing atmosphere on the redispersed mass while Figures 6b and 6c illustrate the strong influence of curing temperature.

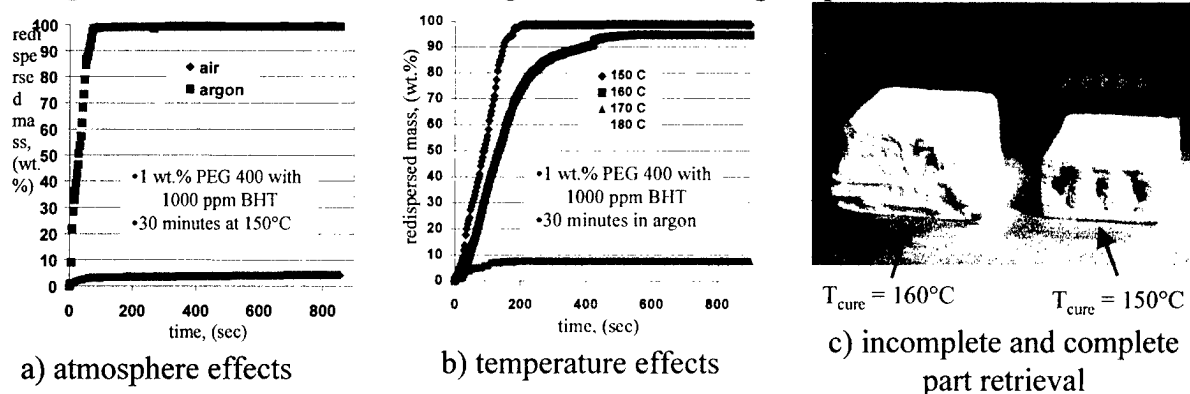


Figure 6: Curing Conditions and Their Effects on Redispersion.

Radio Filters and Their Properties

A dielectric ceramic slurry (35 vol.%, MR2, TDK USA Corp.) has been integrated into the 3DP™ process and RF components have been directly fabricated with dimensional accuracies as high as $\pm 20 \mu\text{m}$. These components represent the first functioning products manufactured using the slurry-based 3DP™ process. Fired and metallized 3DP™ RF filters are shown in Figures 7a and 7b.

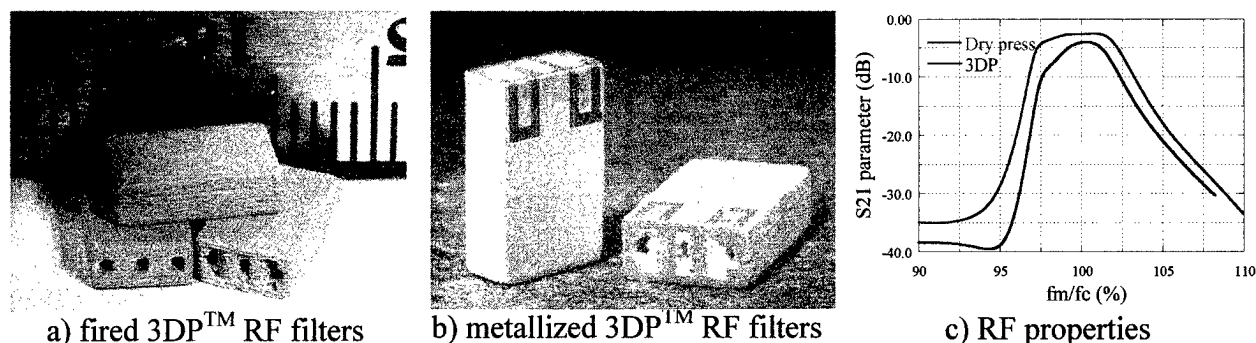


Figure 7: 3DP™ Manufactured RF Filters and Their Dielectric Properties.

The dielectric properties of these preliminary filters were very encouraging. Their properties were compared to those of similar dry-pressed filters as shown in Figure 7c. It is clear that the 3DP™ components functioned as filters having both accurate center frequencies with a respective transmission band, however, the dry-pressed proved to have less insertion loss and a wider transmission band. These differences in performance are in large part a result of the relatively high surface roughness of the 3DP™ filters with respect to the dry-pressed filters.

A significant fraction of this increase in surface roughness was the result of a limit in the resolution of the CAD software used to generate the 3DP file and has been eliminated. Figure 8 illustrates the improvement in the RF filter surfaces due to the software refinements.

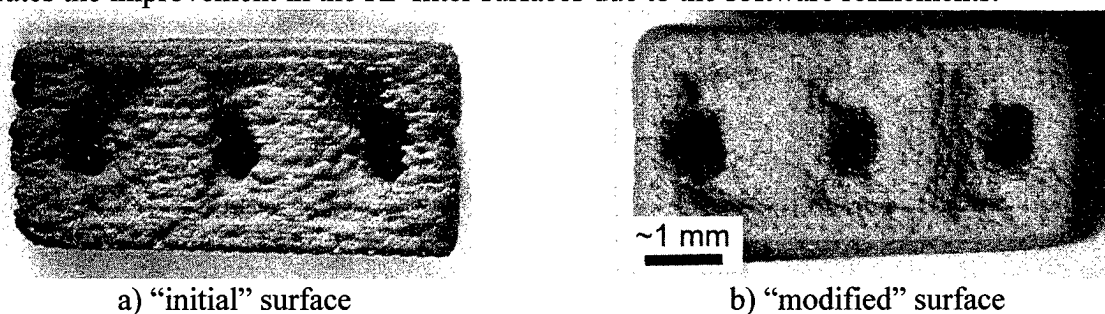


Figure 8: 3DP™ Software Improvements and the Effect on Surface Finish.

Other modes to achieve better dielectric properties are the basis of current research. One of these measures is the integration of a "Drop on Demand" printing technique which will provide higher accuracy in the placement of binder droplets during the printing process. A second step is focused on controlling the shape and size of the binder primitives that serve as the building block of the printed component. Finally, filters with highly complex geometries are being designed, which emphasizes the advantage of the 3DP™ process. These new geometries will reduce attenuation, and can not be formed using conventional fabrication techniques. Complex geometries have already been formed using the slurry-based process with current dielectric material (MR2) and are pictured in Figure 9. This provides a foundation for a wide range of complex shaped filters.

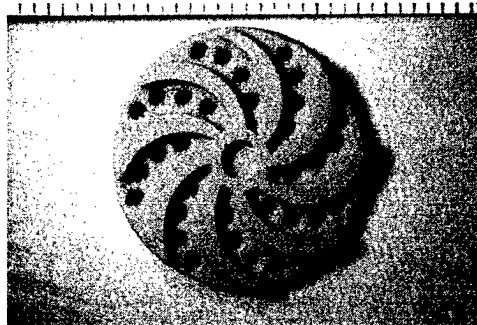


Figure 9: Shape Capability of the Slurry-Based 3DP™ Process. (scale in mm)

Conclusions

The 3DP™ process and colloidal processing techniques have been used to form dielectric ceramic components using a submicron powder. 3DP™ processing parameters and binder-slurry interactions have been optimized to minimize the generation of defects during the fabrication of the component. Imbedded components were successfully retrieved from a cohesive powder bed by adding PEG to the slurry formulation and closely controlling the binder curing conditions. RF filters have been successfully produced that represent the first functioning ceramic produced using this process. Future research is focused on the improvement of the filter properties by improving the surface finish and designing a geometry that will further reduce the attenuation of the filter.

Acknowledgements

The authors acknowledge TDK U.S.A. Corp., the CPRL staff and Jim Serdy and Dave Brancazio for their help and support.

References

- ¹ E. Sachs, M. Cima, J. Cornie, D. Brancazio, J. Bredt, A. Curodeau, T. Fan, S. Khanuja, A. Lauder, J. Lee, S. Michaels, *Annals of the CIRP*, 42, pp. 257-260, 1993.
- ² S. Uhland, R. Holman, M Cima, E Sachs and Y. Enokido, *Solid Freeform and Additive Fabrication - Proceedings of the Materials Research Society*, Vol. 542, pp. 153-158, 1999.
- ³ J. Grau, S. Uhland, J. Moon, M. Cima and E. M. Sachs, *Journal of the American Ceramic Society*, Vol. 82, No. 8, 1999.
- ⁴ P. Saxton, *M. S. Thesis, Massachusetts Institute of Technology*, June 1999.
- ⁵ B. DeBear, *M. S. Thesis, Massachusetts Institute of Technology*, June 1999.
- ⁶ J. Grau, *Private Communication*.
- ⁷ I. Aksay, C. Schilling, *Advances in Ceramics. Forming of Ceramics, Proceedings of the 85th Annual Meeting of the Amer. Ceram. Soc.*, 9, pp. 85-93 (1984).
- ⁸ F. Bailey, Jr., J. Koleske, *Academic Press*, New York, pp. 53-56, 1976.

Rapid Prototyping & Tooling In China

Yongnian Yan^{*}, Wanlong Wang^{**}, Renji Zhang^{*}, Lihua Lin^{*}

^{*} Department of Mechanical Engineering
Tsinghua University
Beijing 100084, P R China

^{**} Department of Mechanical Engineering
Northwestern University
Evanston, IL 60202, USA

Rapid prototyping & tooling (RP&T) is one of the most timely and cost effective tools for product design, evaluation, development and manufacturing. In the past several years, RP&T research and applications in China have achieved great progresses. In this paper, using the example of Tsinghua University RP Lab, we recall the development history, introduce the present status, discuss and identify the frontiers and questions encountered of RP&T research and applications in China.

1 Introduction

Rapid prototyping (RP) refers to the physical modeling of component or tooling geometry using layered manufacturing technologies. It is a fast growing area in the manufacturing processes. It deploys the computer-aided design (CAD), laser and computer numeric control technologies to quickly fabricate the polymer, wax, powder or paper-based prototypes from the solid CAD models. This process slices the 3D models into the 2D thin layers and then builds the prototype one layer at a time and stacks layer by layer until the part is finished. Thus it is also called as layered manufacturing or free form fabrication. Initially used for design tool, the use of RP technologies logically extends to rapid tooling such as molding, investment casting and sand casting [1].

Rapid tooling (RT), an emerging area in manufacturing technology, is regarded as one of the most important applications of RP technology. In the past several years, RT has been growing very fast and obtained tremendous success in the new product development, evaluation, tooling, and production manufacturing. These applications are widely used in the injection molding and metal casting industries.

To decrease the lead-time and cost of new product development and manufacturing thus to strengthen the competitive edges of industries, the academic fields have initiated the research on rapid prototyping and tooling at the beginning of nineties in China. At present, there are many educational institutes and companies have put tremendous efforts to educate the industry, to develop the RP&T equipment and processes, to transfer the technology from the research to the applications. After ten years' development, the RP&T research and application have obtained great progress. In this paper, we briefly introduce the overview of the present status,

development history, main achievements, applications and some special events to give the reader a briefly image of RP&T industry in China.

2 Overview of RP&T in China

Through 10 years' development, RP&T technologies have obtained great achievements in China. These include the equipment and process development, material research and development, proprietary software coding, rapid tooling process development and application, reverse engineering application and simulation, technology transfer and education, etc.

2.1 Machine Usage and Development

It is estimated that there are around 50 RP machines installed in China, including the machines developed in domestic and imported from overseas. These machines are distributed around universities and industries. The machines imported are mainly focusing on SLA, FDM, LOM and EOS. EOS has set up the first sales branch of the foreign RP&T companies in China in 1998.

In domestic, there are several universities and industrial companies developing the RP&T process and equipment. These developers include Tsinghua University (TU), Huazhong University of Science & Technology (HUST), Xi'an Jiaotong University (XJTU) and Beijing Longyuan Automated Fabrication System Co., LTD. The machines developed are shown in Table 1 [2].

Table 1 RP equipment or process developers in China

Company Name	Equipment or Process Developed
Tsinghua University	<ol style="list-style-type: none"> 1. Multi-functional RP Systems (M-RPMSI, M-RPMSII) 2. Slicing solid manufacturing (SSM500, SSM1600) 3. Melted Extrusion Manufacturing (MLM250) 4. Patternless Casting Modeling (PCM100)
Beijing Longyuan Automated Fabrication System Co., LTD	<ol style="list-style-type: none"> 1. AFS RP Machine (AFS-300) 2. AFS Rapid Measurement System 3. AFS Rapid Casting and Molding System
Xi'an Jiaotong University	<ol style="list-style-type: none"> 1. Laser Prototyping System (LPS-600, LPS-600A, LPS-350) 2. Compact Prototyping System (CPS-250) 3. Graphite Electrode Tool (GET-500A)
Huazhong University of Science & Technology	Huazhong RP (HRPIIA, HRPIII)
Nanjing University of Aeronautics & Astronautics	Developing an experimental equipment
Huabei Institute of Technology	Developing an experimental equipment

2.2 Academic and Professional Activities

In the past several years, RP&T community in China have sponsored and organized several important RP conferences and professional associations. In 1993, the first rapid prototyping research center -- Laser Rapid Forming Center of Tsinghua University in Beijing -- was set up.

Now there are at least 8 similar centers were established. In 1995, the first National Rapid Prototyping Conference of China was held in Tsinghua University. In 1997, the first RP association in China -- the Rapid Forming Technology Committee (RFTC), part of which is a third organization the Chinese Mechanical Engineering Society (CMES) -- was set up. The RFTC is also affiliated to the Chinese Electro-machining Association (CEMA). In 1998, there are several important events happened to Chinese RP&T community. First, the First International Conference on Rapid Prototyping Manufacturing has been held in Beijing. This is the first international event in RP&T area in China. In this meeting, 117 papers were received and more than 60 RP&T colleagues attending this meeting, including researchers, vendors, government officials, and service representatives [3]. Second, the Rapid Forming and Rapid Mold Manufacturing Conference was held in Xi'an. The third, the Rapid Forming Technology Committee has joined the Global Alliance of RP Associations, an organization dedicated to information sharing across international borders. As a part of this sharing, its participants from around the world explore and conduct activities that help convey the benefits of rapid prototyping and related technologies.

There are many educational and research institutes, and companies involving RP&T research and applications, such as Tsinghua University (TU), Xi'an Jiaotong University (XJU), Huazhong University of Science & Technology, Nanjing University of Aeronautics & Astronautics (NUAA), Beijing Long Yuan Automated Fabrication System Co., Ltd., National Huaqiao University (NHU), Shenzhen Productivity Center (SPC), North China Institute of Technology (NCIT), Nanjing University of Science & Technology (NUST), Dalian University of Science & Technology (DUST), Nantong Institute of Technology (NIT), Beijing Polytechnic University (BPU), Shanghai University (SU), Beijing University of Aeronautics & Astronautics (BUAA), Guangzhou China Weal Business Machinery Co. Ltd., Dongfeng Hanzhou Motor Corporation Heavy Machinery Plant, etc.

In the past several years, Chinese Natural Science Foundation (CNSF) has given the great support to the RP&T research and applications in China. There are many important projects and research teams receiving fund from this organization.

3 Research Areas

3.1 RP Process Study and Development

RP processes are widely investigated in China since the beginning of 1990s. The investigation covers the basic process, accuracy improvement, laser and control systems, post-processing, CAD data transfer interface, etc. The most studied processes are SLA, LOM, FDM, SLS and multi-functional RP systems.

Stereolithography Apparatus (SLA) process is investigated by several universities, such as TU, XJTU, HUST. In 1992, a SLA250 machine was installed in the Center of Laser Rapid Forming (CLRP), Tsinghua University. This is the first RP equipment in China. Now XJTU conducts a systematic study on the SLA. They have developed resin-based RP process -- Laser Prototyping System (LPS-600, LPS-600A, LPS-350) and Compact Prototyping System (CPS-250). This system uses the optical fibers to conduct the laser to polymerize the resin. According to their experiences, the most important problem is automatic stability of the liquid surface of the resin.

Laminated Object Manufacturing (LOM) process is studied widely in China. The CLRF in TU developed a sheet-paper based RP system --Slicing Solid Manufacturing. This system is mainly used for academic and experimental purposes. After several years' efforts, the CLRF has developed the largest work size RP machine (SSM-1600, 1600x800x700 mm³) and the first multi-functional RP system (M-RPMSI and M-RPMSII) which integrates the paper-sheet based and powder based RP processes. HUST has also developed a sheet-paper based RP system, which is incorporated with a Singaporean company for commercialization.

(3) Fused Deposition Modeling (FDM) process is mainly studied by the CLRF, TU. They developed another new RP method-Melted Extrusion Manufacturing, which is similar to FDM method, but has its own distinguish features. They are working on development of special nozzle design, filament fabrication of different materials, such as wax, nylon and ABS.

(4) Selective Laser Sintering (SLS) process is also studied in China. Beijing Long Yuan Automated Fabrication System Co., Ltd, a joint venture of China and US, has developed and commercialized a SLS-like RP system -- AFS300. They have sold several machines. A laboratory in NUAU puts their efforts to develop their own experimental system. This new machine has some different features, not only different with DTM, but also different from Long Yuan Co.'s AFS system.

(5) Multi-functional Rapid Prototyping Manufacturing System (M-RPMS) is studied and developed by the CLRF, TU for 6 years. It integrates the requirements of industrial applications and academic research and development. The development of this machine adheres to three basic principles: new concept, new design and new product.

- The New Concept is the new designing principle. It is the most important guarantee for the developing success of the production.
- The New Design is used for the new technology of software, process and equipment.
- The New Product is the M-RPMS-II machine. This laser rapid forming machine is intellectual property of Tsinghua University. Each function provided by this machine could match or exceed the quality of single-functional machines. Fig.1 shows the principle diagram of the M-RPMS-II machine [4]. The distinguished advantages of this machine are the low operating costs and the short operating time.

3.2 CAD Modeling & Data Transfer

The commercial CAD packages used in China are Pro/ENGINEER, AutoCAD, I-DEAS and SolidWorks, and the hardware/platform is PC and Workstation with Win95, UNIX and NT. Time taken to create a CAD model varies from several days to several months depending on the geometry complex and technical experiences of the computer operators. Models can be created from 3D CAD modeling, modified from the existing data, scanning or reverse engineering. Since the RP systems can only use the 3D solid models to build the part, it may be a time-consuming for model creation either from CAD packages or laser digitizing. Fig.2 shows a scheme of the data processing used in the CLRF, TU [5]. They have developed three versions of interface and data processing software for DOS, Windows95 and Windows NT respectively. The most recent

version is based on Windows NT. The software can display, edit, slice, fill cross-sectional area, add support, divide part in Z axis direction of the STL file.

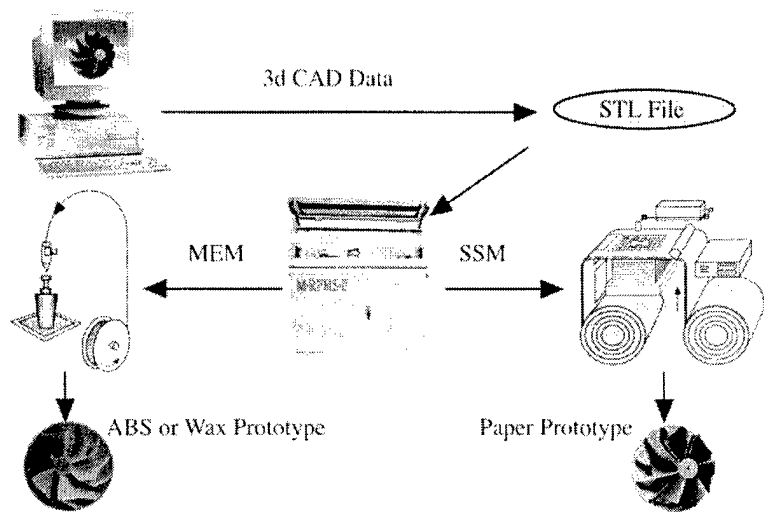


Fig 1. The principle diagram of M-RPMS-II machine

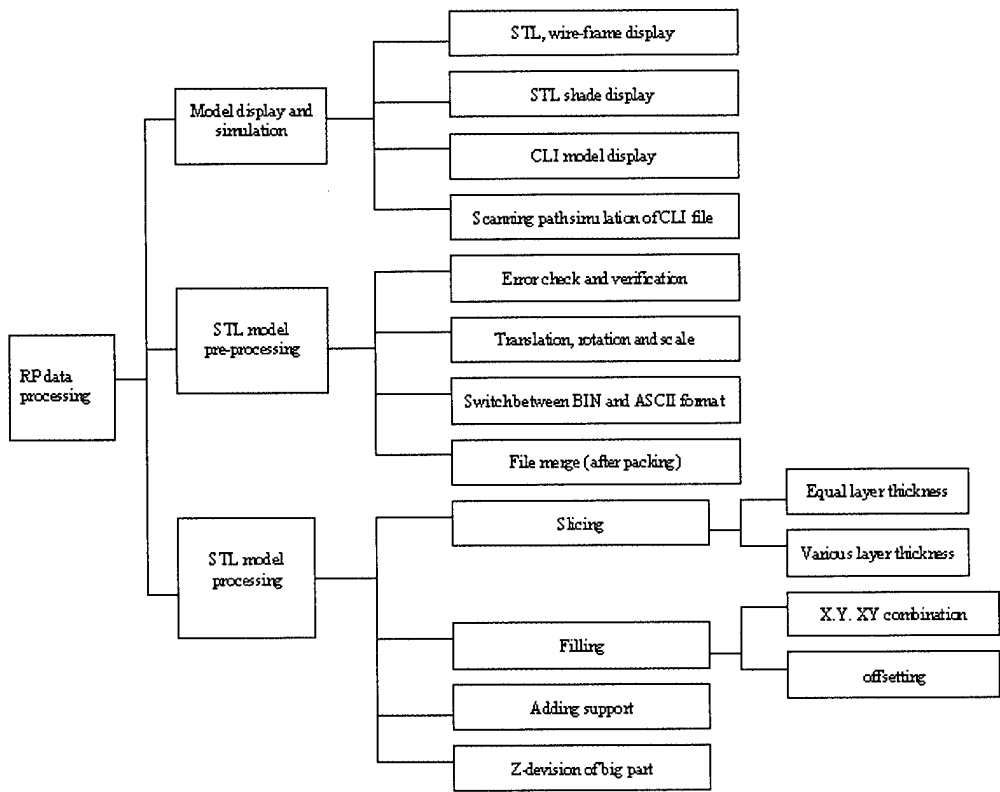


Fig 2 Data processing scheme of CLRF, Tsinghua University

3.3 Material Research

Material research is an important area for rapid prototyping technology. There are several research institutes in China dedicated in this area, such as Chemistry Department in Tsinghua University, Zhejiang University, Huazhong University of Science & Technology. The materials studied include the polymer, coated sheet-paper, binder materials, powder materials of ABS, wax and nylon, etc. The material properties studied cover the physical and chemical properties of RP materials, the mechanism of reaction, accuracy improvement, mechanical properties and improvement, distortion and warpage, etc.

3.4 Rapid Tooling and Manufacturing

Rapid tooling and manufacturing may be the most important application of rapid prototyping because the manufacturing capability may determine the future development of rapid prototyping industry. Because of the rapid building of physical models, RP prototypes provide a tremendous potential for rapid tooling and manufacturing. RP technologies are very limited if they can only be for design evaluation and functional testing. Through rapid tooling process, RP models can be easily used for injection molding and metal casting operations to manufacture the parts quickly, less costly and efficiently. Using CAD-solid modeling, part geometry can be expected to increase in design and manufacturing complexity. Designers and tool engineers can view the solid model prior to prototyping because of the properties of CAD-solid modeling. Molds and dies are normally required for effective mass production of plastic or metal products and components in manufacturing industry.

Because of the wide range of RP materials used such as wax, plastics, ceramics, cements, papers, and metallic powders covered with binders, RP prototypes can also be used as mold inserts or cores for injection molding and sand casting. One most frequent casting process using RP technology is investment casting. CLRF has developed the Ceramic Sheet Casting (CSC), a precise casting process. It has been used for automobile covered parts in the Changchun No 1 Automobile Factory. This process obtains SSM prototypes of positive and negative molds for an automobile covered part, then transfers to metal mold [6].

Another important rapid tooling process is called the Patternless Casting Molding (PCM). This innovative machine is focusing on making large or medium size casting mold. The material used in PCM is commonly used in resin sand casting so that the cost is relatively low. The process is still under development. The present disadvantage is that the surface finish is not very good due to the large size of sand, i.e. about 0.5mm in diameter, compared with powder used in DSPC and SLS, in which the particle size is smaller than 60 microns, and the experimental nozzle designed and fabricated by themselves [6].

4 The Center for Laser Rapid Forming

To introduce the RP&T in China, we cannot help but mention the Center for Laser Rapid Forming (CLRF) in Tsinghua University. The CLRF is the first research center dedicated to RP&T research, imports the first RP machine (SLA250), develops the first RP machine, and is the flag research institute of RP&T in China.

4.1 Basic Data

The CLRF was established in 1992 by Professor Yongnian Yan of Mechanical Engineering Department in Tsinghua University. The basic statistics is as below:

- People:
4 full professors, 2 Ph.D. advisors; 15 Ph.D. candidates, 10 odd master candidates, 3 post-doctorates, several visiting scholars; 18 Ph.D. and master students graduated from this lab.
- Facilities and hardware:
PMS-II, 1 M-220 (developed by CLRF), 1 PLCM-100 (Patternless casting molding), 2 SGI workstations, more than 30 PCs, 400 m² lab area and 400 m² workshop.
- Software:
3D solid CAD/CAM/CAE software packages; RP data processing software packages: Larc 97 and 98; Numeric control software based on PARK numeric control systems: Carc 97 & 98; and 3D object reconstruction software (non-sequential 3D points and CT image).

4.2 Divisions

There are 4 divisions in the CLRF: RP Reverse Engineering and Simulation, Data processing and RP CAD, Mechanical Design and Control System, Innovation for RP Technology and Materials.

4.2.1 RP Reverse Engineering and Simulation

CAD modeling for RP products can be based on the RP reverse engineering, metrical simulation and imitation for RP process. The research activities include:

- Reverse engineering with Computed Tomography (CT) and Magnetic Resonance Imaging (MRI);
- 3D Laser scanning measurement;
- Computer simulation for three kinds of RP processes (SSM, MEM and SL);
- Size precision simulation for process using MARC software for RP Metallic Moulds.

4.2.2 Data processing and RP CAD

Slicing file CLI can be finished and output through data processing according to the input from STL, DXF and / or STEP files. The research activities include:

- 3D Computer-Aided Design (CAD) model within Pro/Engineer;
- Data processing, diagnosis, and revision of STL software;
- Supporting structure software for different RP technologies;
- RP CAD software;
- Control software for SSM, MEM and M-RPMS of RP machines.

4.2.3 Mechanical Design and Control System

Design and manufacturing for mechanical system and control system of the laser rapid forming machines and devices. The research activities include:

- Multi-functional RPM testing platform;
- Slicing Solid Manufacturing (SSM) machine;
- Melted Extrusion Manufacturing (MEM) machine;
- Multifunctional RPM System (M-RPMS);
- Large scale SSM machine.

4.2.4 Innovation for RP Technology and Materials

New RP techniques and research and development for RP materials. The research activities include:

- StereoLithography (SL) technology;
- UV curable resin for SL;
- Slicing Solid Manufacturing (SSM) technology;
- Sticky paper for SSM;
- Melted Extrusion Manufacturing (MEM) technology;
- Waxy, nylon and ABS filaments for MEM;
- Selective Laser Sintering (SLS) technology;
- Powders (wax, polymers and metals) for SLS;
- Intelligent Design / Manufacturing System (IDMS) for metallic forming mold;
- Patternless Casting Molding (PCM) technology.

4.3 Research Activities

The main research activities in the CLRf are as below:

- Melted Extrusion Manufacturing (MEM) technology (process & equipment);
- Slicing Solid Manufacturing (SSM) technology (process & equipment);
- Integration of MEM and SSM process and equipment;
- RP process based on micro-drop technology;
- RP materials (coated paper, ABS wire, wax wire, high-strength, high-temperature & high-polymerization materials);
- Development of super-large size of RP equipment ($1.600 \times 800 \times 700 \text{ mm}^3$), two laser systems working concurrently;
- Patternless casting molding technology;
- No-baking ceramic casting process to produce metal parts from RP models.

5 Future Directions and Problems

It can be expected that the future development of RP&T in China will still heavily counted on the educational institutes. The industrial application may increase rapidly because of the intensified market competition and the unique advantages of RP&T technologies. From the research points of view, the following fields may be regarded as the future research directions:

rapid prototyping of the living materials such as human bones, automobile shape mold used for sheet metal extension and bending, and biotic shaping technology.

But there are also some problems existing in the RP&T development in the future. There are at least three problems perplexing the Chinese RP community. First, there is no sufficient funding. RP research, just like any other high-tech industry, needs a great deal of financial support to cover the high cost in academic and application research. Second, the Chinese industry needs time to fully realize the benefits RP&T can bring to their product design and manufacturing. This may somehow affect the development speed of RP&T in China. Third, there are not enough researchers to participate in this research field. Most graduated students move to overseas or change their career paths after graduation from universities.

6 Summary

This paper briefly introduces the present status, research activities, main research achievements and future research directions of RP&T technology in China. We first review the basic situations of RP&T in China including the RP equipment usage and development, and the academic research forces and professional activities. Then we discuss the main research areas and their achievements. To understand more detailed research activities, the CLRF in Tsinghua University is briefly introduced. Finally, the future research directions and difficulties encountered are also presented.

References

1. Wang, W. L., Conley, J. G., Stoll, H. W., "Rapid tooling error analysis for sand casting", *Transactions of the AFS (American Foundrymen's Society) 102nd Casting Congress*, Atlanta, GA, pp567-571, 1998
2. Institute of Mechanical Science of Ministry of Mechanics and Tsinghua University, "Studies on development trends, future applications, and strategies of rapid prototyping & manufacturing", Tsinghua University, December 1997
3. The Summary Report of the First International Conference on Rapid Prototyping Manufacturing, Beijing '98, Department of Mechanical Engineering, Tsinghua University, August 1998
4. Wang, W. L., Yan, Y. N., "Rapid Prototyping & Rapid Tooling in China", Rapid Prototyping & Manufacturing '99 Conference and Exposition, Rosemont, IL, April 20-22, 1999
5. The Rapid Forming Technology Committee of China home page: <http://www.geocities.com/CollegePark/Lab/8600/rftc.htm>
6. The Annual Summary Report of the CLRF and Yinfa Rapid Prototyping and Mold Making Corporation '1998. Department of Mechanical Engineering, Tsinghua University, March 1999

Rapid prototyping as an instructional and recruitment tool for attracting qualified high-school students to engineering as a career option

R. Umashankar, C. Choi and A. Ortega
University of Arizona, Tucson, AZ 85721

R. Vaidyanathan, G. Artz., T. Anderson and A. Mulligan
Advanced Ceramics Research, Inc., (ACR) Tucson, AZ 85706

During the summer of 1999, the College of Engineering at the University of Arizona (UA) offered a Summer Engineering Academy (SEA) to attract qualified high school students to consider engineering as a career option. On this program, UA and Advanced Ceramics Research, Inc. (ACR) teamed to make the students aware of the state of the art in manufacturing technology. This was done by providing an opportunity for the student teams to design and rapid prototype components for an electric car. Subsequently, these cars were tested in a specially designed wind tunnel and a special prize was awarded for the most aerodynamic design. Students were trained to use SolidWorks™ and Fused Deposition Modeling (FDM™) for Computer Aided Design (CAD) and rapid prototyping (RP), respectively. The design and model competition results were presented to the parents and faculty members of the College of Engineering. This innovative summer program offered high school students a glimpse of state of the art technology and helped to create excitement towards engineering as a career option.

I. Introduction

The recent explosive growth in computer power and connectivity is reshaping relationships among people and organizations, and transforming the processes of discovery, learning and communication [1]. Technologies such as computer-aided manufacturing hold much promise for educating and training a workforce for the new millennium. In the 21st century, American competitiveness and worker prosperity will be tied to the education and skill attainment of the workforce [2]. Future workers will need to update their knowledge and skills continuously. Dynamic partnerships and collaborations are essential to ensure that all Americans have affordable and convenient access to acquiring the knowledge necessary for the 21st century economy. The economic health of the Nation and the individual well being rest on the success of this team effort.

Investing in the education and training of the future American workforce will yield significant advantages for individual workers and employers alike, especially given the drive to create high-performance workplaces that emphasize worker autonomy and flexibility [2]. Workers with advanced or upgraded skills are one of the key investments for competitive business performance, which in turn are essential to raising the standard of living for all Americans [2]. The advantages of a highly trained and motivated workforce are clear. For example, one study found that establishments whose workforce had a 10 percent higher than average educational attainment level had an 8.6 percent higher than average productivity level [2]. Apart from productivity improvements, employees with a higher educational attainment level also are rewarded in a variety of ways, since employers recognize that a more skilled and educated workforce perform better.

The most obvious benefit to an employee with skills and education is higher wages. For example, in 1997, the average college graduate made 77 percent more than the typical high school graduate - \$40,478 compared to \$22,895 [2]. The economic payoff of a better-educated workforce is uniformly higher for both new and returning adult students. The unemployment rates are also lower for a better-educated workforce. A study of the unemployment levels and educational attainment between 1970 and 1997 found that higher educational attainment offers greater employment security [2].

As recently as the 1950s, 20 percent of the workforce was professional, 20 percent was skilled, and 60 percent was unskilled. In contrast, by 1997, while professionals continued to be 20 percent of the workforce, less than 20 percent are unskilled workers, while more than 60 percent are skilled workers [2 and references therein]. The US economy is projected to generate nearly 19 million new jobs in a ten-year period from 1996 to 2006, or 14 percent on average increase per year. Jobs requiring a bachelor's degree will increase 25 percent, nearly double the predicted national average [2]. Although these jobs vary in the type of industries, uniformly and increasingly, these new jobs will require a greater variety and portfolio of skills. These include basic, technical, organizational, and company-specific skills. Basic skills such as reading, writing, and computation are needed in jobs of all kinds. Technical skills would include baseline computer skills as well as computer-aided design and drafting for the manufacturing jobs of the future. As jobs of the future would require a greater degree of interaction between employees and customers, communication skills, analytical skills, problem solving, creative thinking, interpersonal skills, the ability to negotiate and influence, and self-management are necessary to be successful [2]. New technology, market changes, and competition drive companies to innovate, constantly upgrade products and services, and focus on continuous improvement of work processes. Therefore, in the future, employees must frequently acquire new knowledge and skills specifically relevant to the company's products and services, and their production processes or service delivery modes.

The reasons for this demand are many. Many products manufactured today incorporate advanced technologies such as digital circuits and advanced materials. Their manufacture relies on an array of automated technologies that control production and check quality. Materials delivery and product distribution also require understanding and applying sophisticated computerized information systems. Technology and knowledge are used increasingly to raise the value of services and products. The ability and availability of a modern workforce fully knowledgeable in such advanced technologies can help a business differentiate its service from that of its competitor and provide an edge in the marketplace. The primary market for such a workforce with the necessary technological background is from our children who are currently in secondary school (grades 9-12).

The importance of preparing and providing the necessary background for our children to face the workplace of the future can be understood from a recent report of the National Science Board, the governing body of the National Science Foundation [3]. In a previous report, the National Science Board (NSB) also urged "all stakeholders in our vast grass-roots system of K-12 education to develop a nation-wide consensus for a common core of knowledge and competency in mathematics and science" [4]. This report also states, "In the global context, a scientifically literate population is vital to the democratic process, a healthy economy, and our

quality of life" [4]. The future of the Nation is maintained through a continuous flow of talent into its science and engineering workforce – talent that consists of certain core skills and competencies derived from education and training shaped by the highest standards of quality [3]. The NSB believes that the Nation's economy would be best served by those people who are prepared for careers that produce the next generation of knowledge, products and processes in all sectors of the economy [3]. The two NSB reports [3, 4] specifically discuss setting content standards for improving math and science education. However, it could be argued that the issues raised by these two reports are equally relevant to the issue of motivating and enhancing student recruitment into engineering careers. Only students trained in the new technologies will be able to meet the challenges of the industries of the future.

An education system that has science, mathematics, engineering and technology education as its essential components is important to prepare our children for the future workplace. The NSB report goes on to say that, while US graduate education remains the envy of the world, the declining interest and participation of domestic students in science and engineering must be taken as a disturbing sign that K-12 mathematics and science education is failing to renew, expand and prepare our talent pool [3 and references therein]. The implication is that new innovative solutions must be found to prepare and motivate our youngsters to enter and be successful in the workforce of the future. These are perhaps best achieved through local strategies that promote academic achievement in mathematics and science with help from the federal level from agencies such as the Department of Education and the National Science Foundation [3].

The University of Arizona has been active in increasing the recruitment of qualified high school students into its engineering programs using its Summer Engineering Academy (SEA) and involvement in the Math, Engineering, and Science Achievement (MESA) program with the area schools. The Multi-cultural Engineering Program (MEP) at the College of Engineering, University of Arizona conducts the SEA for recruiting qualified high school students nationwide. This is used primarily as recruiting tool for the College of Engineering. In order to create excitement and interest in various engineering disciplines, the College recognized the need to adapt and tailor the SEA program to student interests and aptitudes. With the active support of the College of Engineering Administration, the Director of the MEP program decided to modify the SEA program based on student input and feedback. He visited several high schools in Arizona and met with students as well as high-school administrators and teachers. The student input suggested a need to radically change the SEA program content. For example, the Director asked the students, "How does a design idea become a reality"? The response from the students strongly suggested that the SEA program could include Computer-aided Design (CAD) and Rapid Prototyping (RP).

The university has several joint research programs with Advanced Ceramics Research Inc. (ACR), a local small business with expertise in rapid prototyping (RP) technology and advanced materials. The university requested ACR's assistance in developing a program to allow high school students to become familiar with engineering design, rapid prototyping and materials. The goal of this effort was to:

- Give high school students a look at the opportunities and experiences that engineering offers,
- Expose prospective engineers to a college campus and a manufacturing organization, and

- Create innovative cooperative partnerships between academic and industrial institutions.

II. Results of the Summer Engineering Academy (SEA) Program

The fundamental idea behind the SEA program was to show prospective engineers exactly how an idea becomes reality. In the current year program, two groups consisting of 35 freshmen and sophomores and 47 juniors and seniors participated. Among the juniors and seniors, there were 14 female students and 17 male students from under-represented groups. In this program, the students, separated into teams, were asked to design aerodynamic cars whose coefficient of drag would be determined in a wind tunnel. The students were taught the general concepts of materials science, aerodynamics, CAD, and rapid prototyping by selected faculty from the University of Arizona College of Engineering. Five undergraduate guidance counselors trained the students to use Solidworks™ to design the models. The students visualized and modeled aerodynamic cars and prepared .stl files of the cars using Solidworks™. Examples of model cars are shown in figures 1 and 2. The .stl files were emailed to ACR, who prepared the .sml files for building the parts using an in-house FDM 1600 machine. The students toured the ACR rapid prototyping facilities while the models were being built. They were excited by the fact that the models that they had conceptualized and designed were being built in their presence.

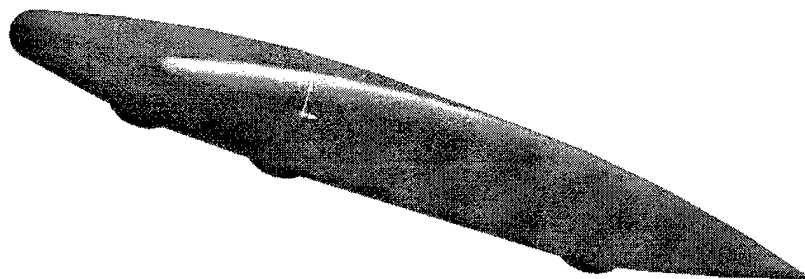


Figure 1. A solid model prepared by participants in the SEA program

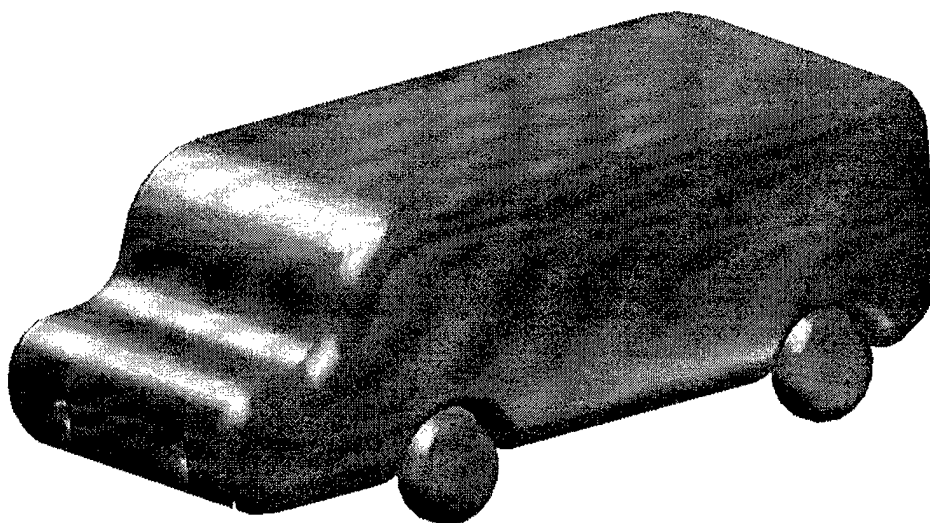


Figure 2. A solid model of a school bus/van prepared by participants in the SEA program

The prototype cars were then tested in a specially designed and built wind tunnel at the University of Arizona College of Engineering. The students obtained first-hand experience of the principles of aerodynamics by actually seeing their concept models tested in the wind tunnel. The wind tunnel is shown in figure 3. A close up image of a model in the wind tunnel is shown in figure 4. The wind tunnel data was analyzed and interpreted by the students. This provided them a feedback as to how their cars would perform if they were built to full scale. Additionally, program managers from the Department of Transportation presented concepts for a transportation system of the future.

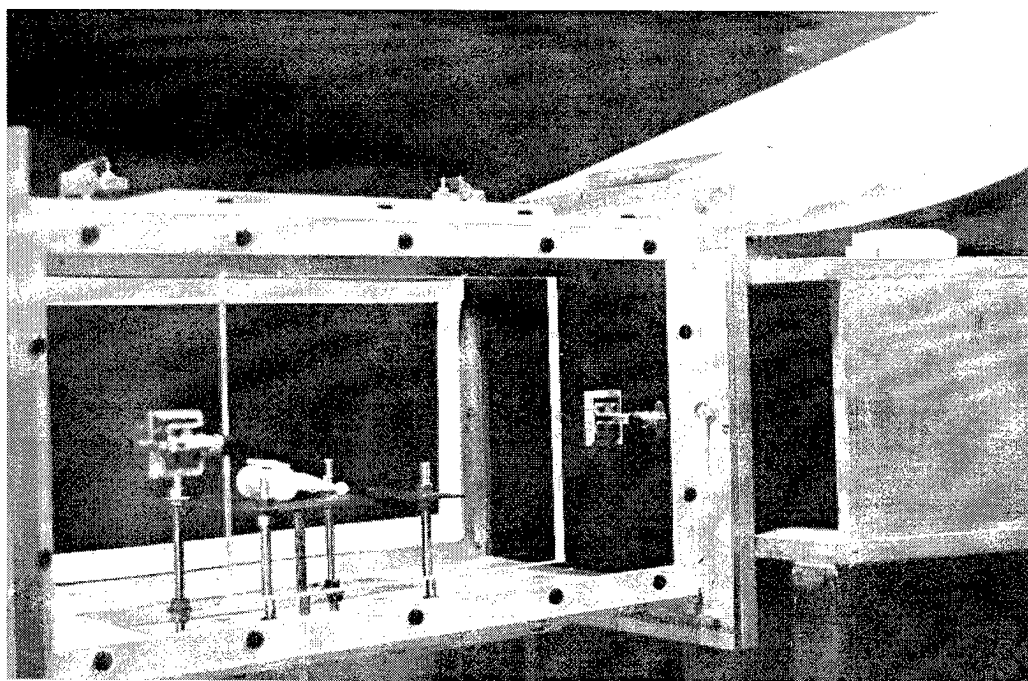


Figure 3. An image of a prototype car inside the wind tunnel

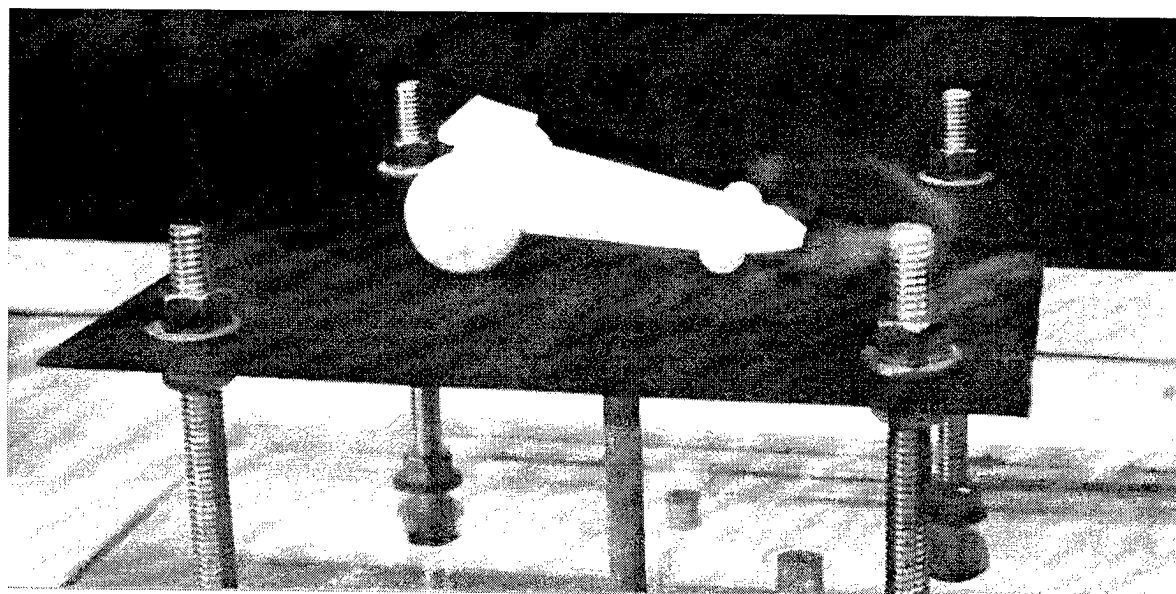


Figure 4. Close up view of the prototype car inside the wind tunnel

III. Discussion

The results from the SEA program were encouraging to both ACR and the University of Arizona. The response from the high school students and their parents were overwhelmingly positive and showed that this innovative educational experiment combining CAD and RP was successful in showing how exciting engineering careers of the future could be to potential engineers. The SEA program introduced high school students to many different engineering disciplines. All the students loved working with the CAD software, since it was user-friendly and intuitive. A large number of students expressed an interest in joining materials science and mechanical engineering disciplines. The program was so successful that the College of Engineering has already received many inquiries from the parents of high school students interested in attending the SEA program in 2000. Current and future program information is expected to be posted on the University of Arizona College of Engineering web-site by Fall '99. Future program information can also be obtained by contacting Cecilia Gaxiola, Engineering Bldg. Room 200, P. O. Box 210020, AZ 85721-0020, Tel: 520-621-4018.

Acknowledgments

The authors gratefully acknowledge the assistance of Ms. Susan Bowers of the University of Arizona College of Engineering and Mr. Joseph Walish of ACR in preparing the presentation and paper.

REFERENCES

1. "Knowledge and distributed intelligence," available at <http://www.ehr.nsf.gov/kdi/>
2. "21st century skills for 21st century jobs," a report of the US Department of Commerce, US Department of Education, US Department of Labor, National Institute of Literacy, and the Small Business Administration, available at <http://www.vpskillsummit.org>, (January 1999).
3. "Preparing our children: Math and Science Education in the National Interest," available at <http://www.nsf.gov/nsb/documents/1999/nsb9931/nsb9931.htm>.
4. National Science Board, Failing our children: Implications of the Third International Mathematics and Science Study, July 31, NSB-98-154, hereafter referred to as the "July Statement".

Tenth Solid Freeform Fabrication Symposium - 1999

Author/Attendee List

Mukesh Agarwala (401, 759)
University of Dayton
University of Dayton Research Institute
300 College Park
Dayton, OH 45469-0150
USA
Phone: (937) 229-3965
Fax: (937) 229-3433
Email: agarwala@udri.udayton.edu

Seokyoung Ahn
University of Texas
Department of Mechanical Engineering
Austin, TX 78712-1063
USA
Phone: (512) 471-5838
Fax:
Email: syahn@mail.utexas.edu

David Alexander
Pratt & Whitney
M/S 707-26
PO Box 109600
West Palm Beach, FL 33410-9600
USA
Phone: (561) 796-6149
Fax: (561) 796-7454
Email: alexnder@pwfl.com

Helene Ansquer (495)
University of Connecticut
IMS
97 North Eagleville Road
Storrs, CT 06269-3136
USA
Phone: (860) 486-4410
Fax: (860) 486-6745
Email: Helene@mail.ims.uconn.edu

Clint Atwood
Sandia Nat'l Labs--NM
Mechanical Engineering Department
Sandia National Laboratories
Albuquerque, NM 87185-0958
USA
Phone: (505) 844-0816
Fax: (505) 844-5589
Email: clatwoo@sandia.gov

Amit Bandyopadhyay (319, 361)
Washington State University
School of Mech. And Materials Engg.
PO Box 642920
Pullman, WA 99164-2920
USA
Phone: (509) 335-4862
Fax: (509) 335-4662
Email: amitband@mme.wsu.edu

Ludrick Barnard (719)
Technikon Free State
President Brandt Street 26
Bloemfontein, Free State 9301
South Africa
Phone: (+27) 51 507 3256
Fax: (+27) 51 507 3199
Email: lbarnard@eng.tofs.ac.za

Joe Beaman (199, 281, 297)
The University of Texas at Austin
Mechanical Engineering Department
MC C2200
Austin, TX 78712-1063
USA
Phone: (512) 471-3058
Fax:
Email: jbeaman@mail.utexas.edu

Anna Bellini
University of Illinois at Chicago
842 W. Taylor St.
Department of Mechanical Engineering
Chicago, IL 60607
USA
Phone: (312) 413-7408
Fax: (312) 413-0447
Email: abelli3@uic.edu

Barry Bender
Naval Research Lab
Code 6354
Washington, DC 20375
USA
Phone: (202) 404-1532
Fax:
Email: bender@anvil.nrl.navy.mil

Tenth Solid Freeform Fabrication Symposium - 1999

Author/Attendee List

Alain Bernard (39, 129)
CRAN
Faculte' des Sciences BP 239
Vandoeuvre Cedex, 54506
France
Phone: (+33) 3 83 91 27 29
Fax: (+33) 3 83 91 23 90
Email: alain.bernard@cran.u-nancy.fr

Jack Beuth (383)
Carnegie Mellon Univ.
Department of Mechanical Engineering
5000 Forbes Ave.
Pittsburgh, PA 15203-3890
USA
Phone: (412) 268-3873
Fax: (412) 268-3348
Email: beuth@andrew.cmu.edu

Jan Helge Bøhn (679)
Virginia Tech
Mechanical Engineering
Blacksburg, VA 24061-0238
USA
Phone: (540) 231-3276
Fax: (540) 231-9100
Email: bohn@vt.edu

Klas Boivie (563)
Woxencentrum
KTH The Royal Institute of Technology
Brinell Vagen 68
(Brinellvägen 68) Stockholm, 10044
Sweden
Phone: (+46) 8 790 6371
Fax: (+46) 8 21 08 51
Email: kbv@cadcam.kth.se

Rick Booth
DTM Corp.
1611 Headway Circle, Building 2
Austin, TX 78754
USA
Phone: (512) 425-2931
Fax: (512) 339-0634
Email: boothr@dtm-corp.com

Dave Bourell (281, 297)
The University of Texas at Austin
Mechanical Engineering Department
MC C2200
Austin, TX 78712-1063
USA
Phone: (512) 471-3170
Fax: (512) 471-7681
Email: dbourell@mail.utexas.edu

Craig Brice (369)
The Ohio State University
2041 College Road
Columbus, OH 43210
USA
Phone: (614) 292-6263
Fax: (614) 292-7523
Email: brice.12@osu.edu

John Brooks (375)
Sandia National Labs-CA
PO Box 969
MS 9430
Livermore, CA 94550
USA
Phone: (925) 294-2051
Fax: (925) 294-3410
Email: jabrook@sandia.gov

Ira Bryant
University of Oklahoma
Dept. of Aerospace and Mechanical
Engineering
865 Asp Ave., Room 212
Norman, OK 73019
USA
Phone: (405) 325-5011
Fax: (405) 325-1088
Email: ihbryant@ou.edu

Zbigniew Bzymek (147, 487)
University of Connecticut
191 Auditorium Road
U-139ME
Storrs, CT 06269
USA
Phone: (860) 486-2275
Fax: (860) 486-5088
Email: bzymek@uconnvm.uconn.edu

Tenth Solid Freeform Fabrication Symposium - 1999

Author/Attendee List

Neil Calder
British Aerospace
Samlesbury Aerodrome
Blackburn, Lancashire BB2 7LF
UK
Phone: (44) 1254 768087
Fax: (44) 1254 766176
Email: neil.calder@bae.co.uk

Paul Calvert (103, 327, 511)
University of Arizona
Tucson, AZ 85721
USA
Phone: (520) 322-2994
Fax: (520) 322-2993
Email: calvert@engr.arizona.edu

Jamie Canino (571)
Milwaukee School of Engg.
Rapid Prototyping Center
1025 N. Broadway
Milwaukee, WI 53202-3109
USA
Phone: (414) 277-4554
Fax: (414) 277-7470
Email: caninoj@msoe.edu

James Cawley (393, 833)
Case Western Reserve University
500 White Bldg.
10900 Euclid Avenue
Cleveland, OH 44106-7204
USA
Phone: (216) 368-6482
Fax: (216) 368-3209
Email: jxc41@po.cwru.edu

Joe Cesarano
Sandia National Labs--NM
1001 University Blvd. SE
Albuquerque, NM 87106
USA
Phone: (505) 272-7624
Fax: (505) 272-7663
Email: jcesara@sandia.gov

Chi Keung Chan (163)
University of Hong Kong
Pokfulam Road
Hong Kong,
China
Phone: (852) 28592642
Fax: (852) 28585415
Email: edwinchan@bigfoot.com

Yu-Chi Chang (111, 121)
Stanford University
Building 530 Room 226
Stanford, CA 94305-3030
USA
Phone: (650) 723-1301
Fax: (650) 723-5034
Email: michchang@leland.stanford.edu

Richard Chartoff (401)
University of Dayton
Rapid Prototype Development Lab
300 College Park
Dayton, OH 45469-0130
USA
Phone: (937) 229-2517
Fax: (937) 229-2503
Email: chartoff@udri.udayton.edu

Yih-Lin Cheng (687)
Stanford University
Building 530 Room 226
Stanford, CA 94305-3030
USA
Phone: (650) 723-1138
Fax: (650) 723-5034
Email: shelleyc@leland.stanford.edu

Uichung Cho (29)
The University of Texas at Austin
Mechanical Engineering Department
MC C2200
Austin, TX 78712-1063
USA
Phone: (512) 471-7347
Fax:
Email: uichung@mail.utexas.edu

Tenth Solid Freeform Fabrication Symposium - 1999

Author/Attendee List

Sangeun Choi (663)
Case Western Reserve University
Center for Automation and Intelligent
Systems Research
Glennan Bd. #210
Cleveland, OH 44106
USA
Phone: (216) 368-5118
Fax: (216) 368-8776
Email: scx@pris.eeap.cwru.edu

Michael Cima (411)
Massachusetts Institute of Technology
77 Mass Avenue, Bldg. 12-011
Cambridge, MA 02139
USA
Phone: (617) 253-6877
Fax: (617) 258-6936
Email: mjcima@mit.edu

William Coblenz
DARPA-DSO
3701 N. Fairfax Drive
Arlington, VA 22203-1714
USA
Phone: (703) 696-2288
Fax: (703) 696-3999
Email: wcoblenz@darpa.mil

Alexander Cooper (427)
Stanford University
Building 530 Room 128
Stanford, CA 94305-3030
USA
Phone: (650) 723-0565
Fax: (650) 723-5034
Email: agcooper@stanford.edu

Khershed Cooper
Naval Research Laboratory/ONR
Code 6324
4555 Overlook Ave., SW
Washington, DC 20375
USA
Phone: (202) 767-1278
Fax: (202) 767-2623
Email: khershed.cooper@nrl.navy.mil

James Crocker (479, 495)
Institute of Materials Science
University of Connecticut
97 N. Eagleville Road, U-136
Storrs, CT 06268
USA
Phone: (860) 486-4410
Fax: (860) 486-4745
Email: james.e.crocker@uconn.edu

Bob Crockett (671, 857)
Milwaukee School of Engg.
Rapid Prototyping Center
1025 N. Broadway
Milwaukee, WI 53202-3109
USA
Phone: (414) 277-7275
Fax: (414) 277-7470
Email: crockett@msoe.edu

Stephen Danforth (351, 519, 775)
Rutgers, The State University of New Jersey
607 Taylor Road, Rm. 133
Piscataway, NJ 08854-8065
USA
Phone: (732) 445-2211
Fax: (732) 445-6699
Email: danforth@rci.rutgers.edu

Suman Das (281)
The University of Texas at Austin
Mechanical Engineering Department
MC C2200
Austin, TX 78712-1063
USA
Phone: (512) 471-5838
Fax: (512) 471-8727
Email: das@lff.me.utexas.edu

Ma Di (77)
Nanyang Technological University
BioMedical Engineering Research Center
Nanyang Avenue
639798
Singapore
Phone: (65) 7906324
Fax: (65) 7912274
Email: p144846745@ntu.edu.sg

Tenth Solid Freeform Fabrication Symposium - 1999

Author/Attendee List

Philip Dickens
De Montfort University
The Gateway
Leicester, LE1 9BH
UK
Phone: (+44) 116-257 7689
Fax: (+44) 116-257 7025
Email: pdickens@dmu.ac.uk

Jianpeng Dong (111, 121)
Stanford University
Building 530 Room 226
Stanford, CA 94305
USA
Phone: (650) 723-1138
Fax: (650) 723-5034
Email: jdong@leland.stanford.edu

Ruth Dunham
Hawthorne & York International, Ltd.-VCM
2500 N. 24th Street, Suite 200
Phoenix, AZ 85008
USA
Phone: (602) 275-4633
Fax: (602) 273-6503
Email: ruth.dunham@bioengineering.org

Deba Dutta
University of Michigan
Mechanical Engineering Department
2250 G. G. Brown Labs
Ann Arbor, MI 48109
USA
Phone: (734) 936-3567
Fax: (734) 647-3170
Email: dutta@umich.edu

Indranath Dutta
Naval Postgraduate School
Department of Mechanical Engineering
700 Dyer Road
Monterey, CA 93943
USA
Phone: (831) 656-2851
Fax: (831) 656-2238
Email: idutta@nps.navy.mil

Chad Duty (59)
Georgia Tech
334465 Georgia Tech Station
Atlanta, GA 30332
USA
Phone: (404) 894-1836
Fax: (404) 894-9342
Email: gt4465a@prism.gatech.edu

Ingo Ederer (631)
TU Munich - Feingeraetebau
Boltzmannstrasse 15
Munich, 85747
Germany
Phone: (+49) 89 289 15 168
Fax: (+49) 89 289 15 192
Email: ingo@fgb.mw.tum.de

Mark Ensiz (529)
Sandia National Labs--NM
Mechanical Engineering Department
PO Box 5800 MS 0958
Albuquerque, NM 87185-0958
USA
Phone: (505) 844-6873
Fax: (505) 844-2894
Email: mtensz@sandia.gov

Johannes Eschl (453, 809)
IKP, University Stuttgart
Böblingerstr. 78 E
Stuttgart, 70199
Germany
Phone: (+49) 711 641 2306
Fax: (+49) 711-641-2264
Email: eschl@ikp2.uni-stuttgart.de

Georges Fadel (47, 187, 209)
Clemson University
Box 340921
Mechanical Engineering
Clemson, SC 29634
USA
Phone: (864) 656-5620
Fax: (864) 656-4435
Email: georges.fadel@ces.clemson.edu

Tenth Solid Freeform Fabrication Symposium - 1999

Author/Attendee List

Xu Fen (9)
National University of Singapore
Manufacturing Division, Dept. of MPE
Singapore, Singapore 119260
Singapore
Phone: (65) 8746491
Fax: (65) 779-1459
Email: engp5288@nus.edu.sg

Steffi Finke (639)
TNO Institute of Industrial Technology
P.O. Box 5073
Oostsingel 209
2611 RH Delft,
The Netherlands
Phone: (+31) 152608 762
Fax: (+31) 152608 8725
Email: s.finke@ind.tno.nl

Steven Fishman
Office of Naval Research
800 N. Quincy St.
Arlington, VA 22217
USA
Phone: (703) 696-0285
Fax: (703) 696-0934
Email: fishmas@onr.navy.mil

Brian Fuhrman (59)
Georgia Institute of Technology
327047 Georgia Tech Station
Atlanta, GA 30332
USA
Phone: (404) 894-1836
Fax: (404) 894-0957
Email: bf52@prism.gatech.edu

Charles Gasdaska (825)
Allied Signal, Inc.
101 Columbia Road
Morristown, NJ 07962
USA
Phone: (973) 455-4022
Fax: (973) 455-3008
Email: charles.gasdaska@alliedsignal.com

Erik Geiss (537)
University of Connecticut
Dept. of Material Science
97 North Eagleville Road
Storrs, CT 06269
USA
Phone: (860) 429-1552
Fax:
Email: geiss@main.phys.uconn.edu

Ian Gibson (85)
University of Hong Kong
Pokfulam Rd.
Hong Kong,
Phone: (852) 2859 7901
Fax: (852) 2858 5415
Email: igibson@hkucc.hku.hk

Mike Gou
Cryco Inc.
8107 Altoga Drive
Austin, TX 78724
USA
Phone: (512) 926-8931
Fax: (512) 929-8257
Email: mgou@cryco.com

Damien Gray
DTM Corp.
1611 Headway Circle, Building 2
Austin, TX 78754
USA
Phone: (512) 425-2871
Fax: (512) 339-0634
Email: grayd@dtm-corp.com

Michelle Griffith (375, 383, 529)
Sandia National Labs--NM
Mechanical Engineering Department
PO Box 5800 MS 0958
Albuquerque, NM 87185-0958
USA
Phone: (505) 284-2096
Fax: (505) 844-2894
Email: mlgriff@sandia.gov

Tenth Solid Freeform Fabrication Symposium - 1999

Author/Attendee List

Richard Hague
De Montfort University
Queens Building
The Gateway
Leicester, LEICS LE1 9BH
UK
Phone: (44) 116 257 7064
Fax: (44) 116 257 7025
Email: rhague@dmu.ac.uk

Russ Harris
De Montfort University
Rapid Manufacturing Group, Queens 1.30
The Gateway
Leicester, LEICS LE1 9BH
UK
Phone: (44) 116 2551551 x6649
Fax: (44) 116 2577052
Email: rharris@dmu.ac.uk

Shay Harrison (471)
University of Connecticut
97 North Eagleville Road
Storrs, CT 06264
USA
Phone: (860) 486-4410
Fax: (860) 486-4745
Email: slh95001@uconnvm.uconn.edu

Ashwin Hattiangadi (319)
Washington State University
710 S.E. Chinook Dr., Apt. #Q74
Pullman, WA 99163
USA
Phone: (509) 334-6822
Fax:
Email: ashwin@mme.wsu.edu

Giorgos Hatzilias
RPMI Georgia Tech
Manufacturing Research Center 336
813 Ferst Dr.
Atlanta, GA 30332-0560
USA
Phone: (404) 385-0894
Fax: (404) 894-0957
Email: giorgos.hatzilias@marc.gatech.edu

Carl Hauser (265, 273)
University of Leeds
School of Mechanical Engineering
Woodhouse Lane
Leeds, West Yorkshire LS2 9JT
England
Phone: (+44) 113 2332172
Fax: (+44) 113 2332150
Email: mench@leeds.ac.uk

Shirong He (817)
Oita Industrial Research Inst.
Takae-nisi, 1-4361-10
Oita, Oita 870-1117
Japan
Phone: (81) 97-596-7100
Fax: (81) 97-596-7110
Email: shirong@oita-ri.go.jp

Zongyan He (229, 461)
Drexel University
Department of Mechanical Engineering & Mechanics
3141 Chestnut Street
Philadelphia, PA 19104
USA
Phone: (215) 895-1235
Fax: (215) 895-1478
Email: hez@drexel.edu

Matt Hegler (543)
Institute for Micromanufacturing
Louisiana Tech University
911 Hergot Ave.
Ruston, LA 71272
USA
Phone: (318) 257-5100
Fax: (318) 257-5104
Email: maxwell@coes.latech.edu

Kurt Hertzog
Delphi Automotive
PO Box 20366
Rochester, NY 14602-0366
USA
Phone: (716) 359-6735
Fax: (716) 359-6015
Email: Kurt.T.Hertzog@DelphiAuto.com

Tenth Solid Freeform Fabrication Symposium - 1999

Author/Attendee List

Neil Hopkinson
De Montfort University
Queens Building
The Gateway
Leicester, LEICS LE1 9BH
UK
Phone: (+44) 116 2506454
Fax: (+44) 116 2577052
Email: nhopkins@dmu.ac.uk

Elaine Hunt
Clemson University
Box 340921
Department of Mechanical Engineering
Clemson, SC 29634
USA
Phone: (864) 656-0321
Fax: (864) 656-4435
Email: Elaine.Hunt@ces.clemson.edu

Tonya Huntley (727)
Defense Nuclear Facilities Safety Board
LANL
625 Indiana Ave., NW
Washington, DC 20004
USA
Phone: (505) 667-6827
Fax: (505) 661-4120
Email: tonyah@dnfsb.gov

Brad Jackson
The University of Texas at Austin
Mechanical Engineering Department
MC C2200
Austin, TX 78712-1063
USA
Phone:
Fax:
Email: brad.jackson@mail.utexas.edu

Kevin Jakubenas
Bechtel Bettis
PO Box 79
West Mifflin, PA 15122
USA
Phone: (412) 476-6749
Fax: (412) 476-5151
Email: jakubena@Bettis.gov

Vikram Jamalabad (825)
Allied Signal Research & Technology
101 Columbia Road
Morristown, NJ 07960-1021
USA
Phone: (973) 455-3668
Fax: (973) 455-5991
Email: Vikram.Jamalabad@AlliedSignal.com

Sundiata Jangha (219)
RPMI Georgia Tech
813 Ferst Drive
Atlanta, GA 30332-0406
USA
Phone: (404) 894-7687
Fax: (404) 894-0957
Email: gt0538b@prism.gatech.edu

Daniel Jean (59)
Georgia Tech
332544 Georgia Tech Station
Atlanta, GA 30332
USA
Phone: (404) 894-1836
Fax: (404) 894-0957
Email: gte815f@prism.gatech.edu

Haeseong Jee (171, 793)
Hong-Ik University
Department of Mechanical Engineering
72-1 Sang-Su, Mapo-Ku
Seoul, 121-791
Korea
Phone: (+822) 320-1685
Fax: (+822) 322-7003
Email: jacobjee@wow.hongik.ac.kr

Rui Jiang (19, 767)
Northwestern University
2145 Sheridan Road
Evanston, IL 60201
USA
Phone: (847) 467-3291
Fax: (847) 491-3915
Email: r-jiang@nwu.edu

Tenth Solid Freeform Fabrication Symposium - 1999

Author/Attendee List

Akiya Kamimura (583)
University of Tokyo
Design Engineering Lab, Dept. of Engg.
Synthesis
Hongo 7-3-1, Bunkyo-ku
Tokyo, 113-8656
Japan
Phone: (+81) 3-5841-6329
Fax: (+81) 3-3818-0835
Email: kamimura@design.t.u-tokyo.ac.jp

Takayuki Kamitani (503)
Osaka Sangyo University
Department of Information Systems
Engineering, Faculty of Engineering
3-1-1 Nakagaito
Daito, Osaka 574-8530
Japan
Phone: (+81) 720-75-3001
Fax: (+81) 720-70-1401
Email: kamitani@ise.osaka-sandai.ac.jp

Ron Kander (311)
Virginia Tech
Materials Science & Engineering Dept.
213 Holden Hall
Blacksburg, VA 24061
USA
Phone: (540) 231-3178
Fax: (540) 231-8919
Email: rkander@vt.edu

Sangkyun Kang (427)
Stanford University
Building 530 Room 128
Stanford, CA 94305-3030
USA
Phone: (650) 725-0107
Fax: (650) 723-5034
Email: kangsk@leland.stanford.edu

Nakis Karapatis (255)
Swiss Federal Institute of Technology
Dept. of Mechanical Engineering-ICAP
Lab for Production Management &
Processes
Lausanne, 1015
Switzerland
Phone: (+41) 21 693 3861
Fax: (+41) 21 693 3509
Email: nakis.karapatis@epfl.ch

Thomas Kenney
Parker Hannifin
14 Robbins Pond Rd.
Ayer, MA 01432
USA
Phone: (978) 784-1217
Fax: (978) 784-1400
Email: ytkenney@parker.com

Berok Khoshnevis (743)
University of Southern California
ISE Department
University Park
Los Angeles, CA 90089-0193
USA
Phone: (213) 740-4889
Fax: (213) 740-1120
Email: khoshnevi@usc.edu

Carey King
The University of Texas at Austin
Mechanical Engineering Department
MC C2200
Austin, TX 78712-1063
USA
Phone:
Fax:
Email: cking@ccwf.cc.utexas.edu

Don Klosterman (401, 759)
University of Dayton
Rapid Prototype Development Laboratory
300 College Park
Dayton, OH 45469-0131
USA
Phone: (937) 229-2794
Fax: (937) 229-2503
Email: klosterman@udri.udayton.edu

Radovan Kovacevic (735)
Southern Methodist University
3160 SMU Blvd.
Dallas, TX 75093
USA
Phone: (214) 768-4865
Fax: (214) 768-2116
Email: kovacevi@seas.smu.edu

Tenth Solid Freeform Fabrication Symposium - 1999

Author/Attendee List

Ashok Kumar (179, 647)
University of Florida at Gainesville
237 MEB
Gainesville, FL 32611
USA
Phone: (352) 392-0816
Fax: (352) 392-1071
Email: akumar@ufl.edu

Catherine Kuo
University of Illinois at Chicago
842 W. Taylor St.
Department of Mechanical Engineering
Chicago, IL 60607
USA
Phone: (312) 413-7408
Fax: (312) 413-0447
Email: ck1@imsa.edu

Kwok Tung Kwok (155)
University of Hong Kong
Rm. 824, Department of IMSE
Profulam Road
Hong Kong, China
China
Phone: (852) 2859-7967
Fax: (852) 2858-6535
Email: ktkwok@hkusua.hku.hk

John Lawton
DSM Somos
Two Penn's Way
Suite 401
New Castle, DE 19720
USA
Phone: (302) 328-5458
Fax: (302) 328-5693
Email:

Bruno Le Razer
University of Warwick
Rapid Prototyping & Tooling Centre
Gibbet Hill Road
Coventry, Warwickshire CV4 7AL
England
Phone: (+44) 1203 572 991
Fax: (+44) 1203 524 878
Email: b.le-razer@warwick.ac.uk

Ming Leu (591, 783, 801)
National Science Foundation
4201 Wilson Blvd., Room 550
Arlington, VA 22230
USA
Phone: (703) 306-1328 x 5279
Fax: (703) 306-0298
Email: mleu@nsf.gov

Feng Lin (77, 139)
Drexel University
PO Box 34479
Philadelphia, PA 19101
USA
Phone: (215) 895-6688
Fax: (215) 895-2094
Email: linf@drexel.edu

Zhiwei "Jennifer" Lin
The University of Texas at Austin
Mechanical Engineering Department
MC C2200
Austin, TX 78712-1063
USA
Phone:
Fax:
Email: linzhiwei@hotmail.com

Gayle Link (239, 727)
Stanford University
Building 530 Room 226
Stanford, CA 94305-3030
USA
Phone: (650) 723-1138
Fax: (650) 723-5034
Email: ramdeen@leland.stanford.edu

Qingbin Liu (435)
University of California at Irvine
Dept. of Mechanical and Aerospace
Engineering
Irvine, CA 92697-3975
USA
Phone: (949) 824-5607
Fax: (949) 824-8585
Email: qbliu@eng.uci.edu

Tenth Solid Freeform Fabrication Symposium - 1999

Author/Attendee List

Zhien Liu (393, 833)
Case Western Reserve University
Dept. of Material Science & Engineering
10900 Euclid Avenue
Cleveland, OH 44106
USA
Phone: (216) 368-4219
Fax: (216) 368-3209
Email: lxz@po.cwru.edu

John Lombardi (427)
Advanced Ceramics Research, Inc.
3292 E. Hemisphere Loop
Tucson, AZ 85706-5013
USA
Phone: (520) 573-6300
Fax: (520) 573-2057
Email: j.lombardi@acrtucson.com

Harris Marcus (147, 471, 479, 495, 537)
University of Connecticut
IMS U136
97 North Eagleville Road
Storrs, CT 06269-3136
USA
Phone: (860) 486-4623
Fax: (860) 486-4745
Email: hmarcus@mail.ims.uconn.edu

James Maxwell (543)
Institute for Micromanufacturing
Louisiana Tech University
911 Hergot Ave.
Ruston, LA 71272
USA
Phone: (318) 257-5100
Fax: (318) 257-5104
Email: maxwell@coes.latech.edu

Raymond Meilunas
Northrop Grumman
MS A01-26
Bethpage, NY 11714
USA
Phone: (516) 346-6247
Fax: (516) 346-3670
Email:

Wilhelm Meiners (655)
Fraunhofer Institute for Lasertechnology
Steinbachstrasse 15
Aachen, 52074
Germany
Phone: (+49) 241 8906 301
Fax: (+49) 241 8906 121
Email: meiners@ilt.fhg.de

Tamotsu Murakami (583, 711)
University of Tokyo
Dept. of Engineering Synthesis
Hongo 7-3-1, Bunkyo-ku
Tokyo, 113-8656
Japan
Phone: (+81) 3-5841-6327
Fax: (+81) 3-3818-0835
Email: murakami@mech.t.u-tokyo.ac.jp

Amit Muraleedharan
The University of Texas at Austin
Mechanical Engineering Department
MC C2200
Austin, TX 78712-1063
USA
Phone:
Fax:
Email: amitk@mail.utexas.edu

Alexander Nickel (239, 727)
Stanford University
Building 530 Room 226
Stanford, CA 94305-3030
USA
Phone: (650) 723-0565
Fax: (650) 723-5034
Email: anickel@leland.stanford.edu

Rafiq Noorani
Loyola Marymount University
7900 Loyola Blvd.
Los Angeles, CA 90045-8145
USA
Phone: (310) 338-2831
Fax: (310) 338-6029
Email: rnoorani@lmumail.lmu.edu

Tenth Solid Freeform Fabrication Symposium - 1999

Author/Attendee List

Jeffery Norrell (247)
The University of Texas at Austin
Mechanical Engineering Department
MC C2200
Austin, TX 78712-1063
USA
Phone:
Fax:
Email: norrell@mail.utexas.edu

Olli Nyrhila
Electrolux Rapid Development
Aholantie 17
Rusko, 21290
Finland
Phone: (+358) 2 4365611
Fax: (+358) 2 4399620
Email: olli.nyrhila@notes.electrolux.fi

Naotaka Ohgawara
ASPECT Inc.
CI Mansion Keio-inagi 1F
3105-1 Higashi-naganuma
Inagi City, Tokyo 206-0802
Japan
Phone: (81) 42-370-7900
Fax: (81) 42-370-7901
Email: ohgawara@aspect.rp.co.jp

Seok-Min Park (199, 297, 793)
The University of Texas at Austin
Mechanical Engineering Department
MC C2200
Austin, TX 78712-1063
Phone:
Fax:
Email: smpark@mail.utexas.edu

Jouni Partanen
3D Systems
26081 Avenue Hall
Valencia, CA 91355
USA
Phone: (661) 295-5600, x 2443
Fax: (661) 257-1200
Email: partanenj@3dsystems.com

Joseph Pegna (695)
Concordia University
1455 De Maisonneuve
Montreal, PQ H3G 1M8
Canada
Phone: (514) 848-4193
Fax: (514) 848-3175
Email: pegnej@alcon.concordia.ca

Daniel Petersen (671, 857)
NASA/Johnson Space Center-EM3
2101 NASA Road 1
Houston, TX 77058
USA
Phone: (281) 483-8387
Fax: (281) 244-1301
Email: daniel.d.petersen1@jsc.nasa.gov

Rolf Pfeifer (615, 623)
Institute for Polymer Testing and Polymer
Science
Böblingerstr. 78E
Stuttgart, Baden-Württemberg 70199
Germany
Phone: (49) 711 641 2269
Fax: (49) 711 641 2264
Email: pfeifer@ikp2.uni-stuttgart.de

Anna Pisapia
Hawthorne & York International, Ltd.-VCM
2500 N. 24th Street, Suite 200
Phoenix, AZ 85008
USA
Phone: (602) 275-4633
Fax: (602) 273-6503
Email: anna.pisapia@bioengineering.org

Christoph Pistor (95, 343)
University of Utah
505 Central Campus Drive
Salt Lake City, UT 84112
USA
Phone: (801) 519-9453
Fax:
Email: Christoph.Pistor@hotmail.com

Tenth Solid Freeform Fabrication Symposium - 1999

Author/Attendee List

Fritz Prinz (111, 121, 239, 427, 687, 727)
Stanford University
Building 530 Room 226
Stanford, CA 94305-3030
USA
Phone: (650) 723-0084
Fax: (650) 723-5034
Email: fbp@cdr.stanford.edu

Joe Puskar
Sandia National Labs--NM
PO Box 5800
MS 0367
Albuquerque, NM 87185-0367
USA
Phone: (505) 844-8491
Fax: (505) 845-9659
Email: jdpuska@sandia.gov

Dan Qiu (519)
Rutgers-The State University of New Jersey
Mechanical & Aerospace Engineering
118 Marvin Lane
Piscataway, NJ 08854
USA
Phone: (732) 445-5769
Fax:
Email: danqiu@caip.rutgers.edu

Sriram Rangarajan (351, 775)
Rutgers University
607 Taylor Rd.
Center for Ceramic Research
Piscataway, NJ 08854
USA
Phone: (732) 445-5616
Fax: (732) 445-6699
Email: rangs@rci.rutgers.edu

Ashlee Riddle
University of Illinois at Chicago
842 West Taylor Street
Department of Mechanical Engineering
Chicago, IL 60607
USA
Phone: (312) 413-7408
Fax: (312) 413-0447
Email: riddler@imsa.edu

Raed Rizq
University of Minnesota
125 Mechanical Engineering
111 Church St. SE
Minneapolis, MN 55455
USA
Phone: (612) 625-9844
Fax: (612) 626-6583
Email: rizo@me.umn.edu

David Rosen (67, 219)
Georgia Institute of Technology
School of Mechanical Engineering
813 Ferst Dr.
Atlanta, GA 30332-0405
USA
Phone: (404) 894-9668
Fax: (404) 894-9342
Email: david.rosen@me.gatech.edu

Emanuel Sachs (411, 865)
Massachusetts Institute of Technology
77 Mass Ave.
Cambridge, MA 02139
USA
Phone: (617) 253-5381
Fax:
Email: sachs@mit.edu

Srinivas Samavedam (1)
The University of Hong Kong
IMSE Dept. HKU
Hong Kong
Phone: (852) 2859 7967
Fax:
Email: srinivas@hkusua.hku.hk

Jeffrey Schultz (311)
Virginia Tech
Materials Science & Engineering Dept.
213 Holden Hall
Blacksburg, VA 24061
USA
Phone: (540) 231-3899
Fax: (540) 231-8919
Email: jeschult@vt.edu

Tenth Solid Freeform Fabrication Symposium - 1999

Author/Attendee List

Hermann Seitz (631)
FGB, TU Munich
Boltzmannstrasse 15
85747 Garching,
Germany
Phone: (49) 89 289-15166
Fax: (49) 89 289-15192
Email: seitz@fgb.mw.tum.de

Wolfgang Sigmund
University of Florida
Materials Science & Engineering, 225 Rhines
Hall
PO Box 116400
Gainesville, FL 32611-6400
USA
Phone: (352) 846-3343
Fax: (352) 392-7219
Email: wsigm@mse.ufl.edu

T. J. Sleboda
DTM Corp.
1611 Headway Circle, Building 2
Austin, TX 78754
USA
Phone: (512) 425-2936
Fax:
Email: tsleboda@dtm-corp.com

Geoff Smith-Moritz
Rapid Prototyping Report
CAD/CAM Publishing Inc.
1010 Turquoise St., Suite 320
San Diego, CA 92109
USA
Phone: (619) 488-0533
Fax: (619) 488-6052
Email: rpreport@cadcamnet.com

Yong-Ak Song (793)
Korea Institute of Science and Technology
KIST
PO Box 131 Cheongryang
Seoul
Republic of Korea
Phone: (+82) 2-958-5638
Fax: (+82) 2-958-5649
Email: yongak@kistmail.kist.re.kr

Jurgen Stampfl (427, 687)
Stanford University
Building 530 Room 226
Stanford, CA 94305-3030
USA
Phone: (650) 725-0107
Fax: (650) 723-5034
Email: jim@rpl.stanford.edu

Jeorgen Steinberger (303)
Daimler Chrysler
Wilhelm Runge Str. 11
PostFach 2360
89013 Ulm, D-89013
Germany
Phone: (49) 7315052911
Fax: (49) 7315054212
Email:
Juergen.Steinberger@DaimlerChrysler.com

Peter Stierlen (289)
Institute for Polymer Testing and Polymer
Science
Boeblingerstrasse 78E
Stuttgart, Baden-Wuerttemberg 70199
Germany
Phone: (+49) 711-641-2276
Fax: (+49) 711-641-2264
Email: stierlen@ikp2.uni-stuttgart.de

Brent Stucker
University of Rhode Island
Industrial & Manufacturing Engineering
2 East Alumni Avenue
Kingston, RI 02881
USA
Phone: (401) 874-5187
Fax: (401) 874-5540
Email: stucker@uri.edu

John Stuecker
Sandia National Labs--NM
1001 University SE
Albuquerque, NM 87106
USA
Phone: (505) 272-7663
Fax: (505) 272-7304
Email: jnstuec@sandia.gov

Tenth Solid Freeform Fabrication Symposium - 1999

Author/Attendee List

Wei-Nien Su
De Montfort University
Rapid Manufacturing Group, SERC 00.19
The Gateway
Leicester, LEICS LE1 9BH
UK
Phone: (+44) 116-2506466
Fax: (+44) 116-2577583
Email: wsu@dmu.ac.uk

Carlos Suchicital (311)
Virginia Tech
Materials Science & Engineering Dept.
213 Holden Hall
Blacksburg, VA 24061
USA
Phone: (540) 231-7043
Fax: (540) 231-8919
Email: ctas@vt.edu

Richard Sun (479, 495)
The University of Connecticut
IMS, U-136
97 North Eagleville Road
Storrs, CT 06268-3136
USA
Phone: (860) 486-4410
Fax: (860) 486-4745
Email: lis95001@uconnvm.uconn.edu

Wei Sun (139)
Drexel University
Dept. of Mechanical Engineering
32nd & Chestnut Street
Philadelphia, PA 19104
USA
Phone: (215) 895-5810
Fax: (215) 895-2094
Email: rpd@drexel.edu

Charles Taylor
Syneon
4380 26th Street
San Francisco, CA 94131-1810
USA
Phone: (415) 648-3443
Fax: (415) 642-1352
Email: cstaylor@syneon.com

Charles Thomas (599, 607, 751)
University of Utah
Department of Mechanical Engineering
Salt Lake City, UT 84112
USA
Phone: (801) 585-6939
Fax: (801) 585-9826
Email: cthomas@me.mech.utah.edu

Jim Thomas (335)
University of Notre Dame
Department of Aerospace and Mechanical
Engineering
374 Fitzpatrick Hall
Notre Dame, IN 46556-5637
USA
Phone: (219) 631-9371
Fax: (219) 631-8341
Email: thomas.66@nd.edu

Carsten Tille (849)
TU Munich - Feingeraetebau
Boltzmannstrafle 15
Garching, 85747
Germany
Phone: (+49) 89-289-15168
Fax: (+49) 89-289-15192
Email: tille@fgeb.mw.tum.de

Chris Urban (553)
Milwaukee School of Engg.
Rapid Prototyping Center
1025 N. Broadway
Milwaukee, WI 53202-3109
USA
Phone: (414) 277-4554
Fax: (414) 277-7470
Email: urbanc@msoe.edu

Ranji Vaidyanathan (103, 327, 883)
Advanced Ceramics Research, Inc.
3292 E. Hemisphere Loop
Tucson, AZ 85706-5013
USA
Phone: (520) 573-6300
Fax: (520) 573-2057
Email: r.vaidyanathan@acrtucson.com

Tenth Solid Freeform Fabrication Symposium - 1999

Author/Attendee List

Neal Vail
118 E. Mulberry
San Antonio, TX 78212
USA
Phone: (210) 734-8838
Fax:
Email: cnvail2@swbell.net

Hubert Vander Plas
Hewlett-Packard Laboratories
1501 Page Mill Road, MS 1L-6
Palo Alto, CA 94304-1126
USA
Phone: (650) 857-8722
Fax: (650) 236-9885
Email: hvp@ieee.org

Aditad Vasinonta (383)
Carnegie Mellon Univ.
Department of Mechanical Engineering
5000 Forbes Avenue
Pittsburgh, PA 15213-3890
USA
Phone: (412) 268-8870
Fax: (412) 268-3348
Email: aditad@andrew.cmu.edu

Lisa Veitch
IDA
1801 N. Beauregard St.
Alexandria, VA 22311
USA
Phone: (703) 578-2864
Fax: (703) 578-2877
Email: lveitch@ida.org

Natesan Venkataraman (351)
Rutgers - The State University of New Jersey
Department of Ceramic & Materials Engg.
607 Taylor Rd.
Piscataway, NJ 08855
USA
Phone: (732) 445-5570
Fax: (732) 445-3258
Email: vna@rci.rutgers.edu

Ralph Wachter
Office of Naval Research
800 N. Quincy St.
Arlington, VA 22217-5660
USA
Phone: (703) 696-4304
Fax:
Email: rw@ieee.org

Thomas Craig Wadham
DTM Corp.
1611 Headway Circle, Building 2
Austin, TX 78754
USA
Phone: (512) 425-2870
Fax: (512) 639-0634
Email: wadhamc@dtm-corp.com

Curtis Wahlgren (841)
DSM Somos
2 Penn's Way
Suite 401
New Castle, DE 19720
USA
Phone: (302) 328-5635
Fax: (302) 328-5693
Email: cwahlgren@dsmsomos.com

Hongyun Wang
The University of Texas at Austin
Mechanical Engineering Department
MC C2200
Austin, TX 78712-1063
USA
Phone:
Fax:
Email: Hongyun_Wang@mail.utexas.edu

Wanlong Wang (19, 767, 873)
Northwestern University
2145 Sheridan Road
Evanston, IL 60202
USA
Phone: (847) 467-3291
Fax: (847) 491-3915
Email: wwang@nwu.edu

Tenth Solid Freeform Fabrication Symposium - 1999

Author/Attendee List

Tobias Wasser (95)
University of Utah
MEB 2202
50 S. Central Campus Drive
Salt Lake City, UT 84112-9208
USA
Phone: (801) 581-8983
Fax: (801) 585-9826
Email: wasser@eng.utah.edu

Kevin Watson (857)
NASA
2101 NASA Road One
Mail Code: EX13
Houston, TX 77058
USA
Phone: (281) 483-0971
Fax: (281) 244-7478
Email: kwatson@ems.jsc.nasa.gov

Lee Weiss (427)
Carnegie Mellon University
Robotics Institute
217 Smith Hall
Pittsburgh, PA 15213
USA
Phone: (412) 268-7657
Fax: (412) 268-5570
Email: lew@cs.cmu.edu

Dawn White
Ford
PO Box 2053
MD 3135 SRL Bldg.
Dearborn, MI 48121-2053
USA
Phone: (313) 248-7469
Fax: (313) 390-0514
Email: dwhite15@ford.com

Kirk L. Williams (543)
Institute for Micromanufacturing
Louisiana Tech University, PO Box 10137
911 Hergot Ave.
Ruston, LA 71272
USA
Phone: (318) 257-5100
Fax: (318) 257-5104
Email: micro@bayou.com

Joe Wright
Lockheed Martin Missiles & Fire Control
PO Box 650003
M/S SK-03
Dallas, TX 75265-0003
USA
Phone: (972) 603-2507
Fax: (972) 603-0419
Email: joe.m.wright@lmco.com

Martin Wohler (281)
The University of Texas at Austin
Mechanical Engineering Department
MC C2200
Austin, TX 78712-1063
USA
Phone: (512) 471-2197
Fax: (512) 471-7681
Email: mwohler@mail.utexas.edu

Kris Wood (29, 247)
The University of Texas at Austin
Mechanical Engineering Department
MC C2200
Austin, TX 78712-1063
USA
Phone: (512) 471-0095
Fax:
Email: wood@mail.utexas.edu

Guohua Wu (775)
Rutgers - The State University of New Jersey
866 Johnson Apts.
Davidson Road
Piscataway, NJ 08854
USA
Phone: (732) 445-5769
Fax: (732) 445-3124
Email: gwu@caip.rutgers.edu

Yi Xu
NTT Data Cmet
Kamata Tsukimura Bldg. 7F
5-15-8, Kamata, Ohta-ku
Tokyo, 144-0052
Japan
Phone: (+81) 3-3739-6611
Fax: (+81) 3-3739-6680
Email: joe@nttd-cmet.co.jp

Tenth Solid Freeform Fabrication Symposium - 1999

Author/Attendee List

Bo Yang (801)
New Jersey Institute of Technology
52 Rutherford Place
Kearny, NJ 07032
USA
Phone: (201) 997-4631
Fax: (973) 596-8483
Email: bxy0487@oak.njit.edu

Wei Zhang (591)
New Jersey Institute of Technology
753 Kearny Ave., 2 Fl.
Kearny, NJ 07032
USA
Phone: (973) 642-4994
Fax: (973) 596-5601
Email: zhangwei@oak.njit.edu

Jack Zhou (229, 461)
Drexel University
Department of Mechanical Engineering &
Mechanics
3141 Chestnut Street
Philadelphia, PA 19104
USA
Phone: (215) 895-1480
Fax: (215) 895-1478
Email: zhoug@drexel.edu

Keyword Index

17-4PH metals	775	Colloid infiltrant	297
304 stainless steel	383, 537	Combustion synthesis	503
3-Axis machining	607	Composed density	487
3-axis milling	793	Composite tooling	553
3-D Honeycomb structures	319	Composites	401, 571
3-D model	503	Computational fluid dynamics	247
3DKeltool	809	Conformal cooling channel	793
3D-Printing	695	Conformal cooling	553, 571, 759
ABS plastic	335	Containment test	155
Accuracy study	711	Continuous layered manufacturing	679
Acrylate	453	Contour crafting	743
Adaptive slicing	67	Control parameters	1
Additive/subtractive material processing	687	Controlled porosity	319
Aerospace components	825, 833	Cooling	553
Alkenes	543	Curing	453
Alumina	623, 759	Curl	247
Aluminum alloys	435	Curved layer build style	401
Aluminum	655	Cylinder fabrication	435
Anisotropy	443	Data Exchange Standard	171
Arc welding	793	Database Management Systems (DBMS)	85
Archery bow	29	Decision-based Design	67, 219
Atmosphere	265	Deflection	727
Automated fabrication	679	Delamination	273
Automation	121, 679	Deposition patterns	239
Balling	265	Deposition	59
Binder burnout	327, 563	Design of experiments	103, 369
Bounding box	163	Diamond-like carbon	537
Buckling	351	Dielectric ceramics	865
Buddha	751	Diffusion-limited aggregation	229
CAD	121, 171	Digital mock-up	1
CAD/CAM	817	Direct laser deposition	369
CAM	121	Direct metal	265, 273
CAM-LEM	393, 663	Direct SFF	529
Canister	247	Direct-writing	543
Carbon	543	Downdraft	247
Case studies	809	Droplet-based net-form manufacturing	435
Cast resin	809	EDM electrode	801
Casting	687, 767	Ejection	219
Centrifugal rubber mold casting	719	Elastic model	239
Ceramic composites	361	Elastic-perfectly plastic model	239
Ceramic fabrication	103	Electric-Discharge-Machining	687
Ceramic mold	817	Electrochemical liquid deposition	229
Ceramic	393	Electroforming	801
Ceramics manufacturing	833	Electrophotography	647
Ceramics	319, 743	Electroplating	687
Chemical reaction heat	503	Empirical similarity method	29
Chemical	59	Engineering ceramics	427
China	873	Engineering Education	883
ChristalEyes™	147	Environmental performance	783
Christmas Tree Step	239	Epoxy resin	461
CLM	679	Epoxy	453
CMM	47	Extrusion Freeform Fabrication	103, 327
CNC Machining	121	Extrusion	351, 639
Coating	393		

Keyword Index

Fabrication	59	International space station	857
Fast Freeform Fabrication (FFF)	767	Internet	147
Fault-tolerant	155	Inventor	147
FDM	679	Investment casting	817, 841
FDMet	775	Iso-surface Extraction	77
Feedstock	775	Iterative method	163
FEM	453	K-12 Education	883
FGMs	571	Knowledge-based system	9, 39
Finite element analysis	801	Laminate theory	343
Finite element modeling	319, 351	Laminated Object Manufacturing (LOM)	401
Formative processes	743	Laminated Object Manufacturing	711, 759
Fractal geometry	229	Laminated Objects	663
Fractal growth modeling	229	Lamination	393
Fractal	95	Large scale prototyping	751
Fracture mechanics	817	Laser deposition	727
Freeform growth	543	Laser rapid forming	873
Freeform powder molding	647	Laser	59, 655
Freeform	59	Lattice	571
Functional parts	335, 711	Layer density	255
Functionally graded materials	695	Layer manufacturing	775
Functionally Gradient Materials	179, 199	Layered Manufacturing	139, 519,
Fused Deposition Modeling	95, 343,		591, 663, 695
	671, 679, 883	LCVD	59
Fused Deposition of Ceramics	351, 825	LENS	369, 375,
Fused deposition process	361		383
Fused-deposition	335	Lifecycle analysis	783
Gas precursors	537	Lin-Kernighan Algorithm	95
Genetic algorithms	209	Liquid-crystal resins	443
Geometric processing	111	Loading and unloading	679
GMA welding	735	LOM	393
Gradients	571	Lost mold/wax process	319
Growth	247	Lumped model	29
H13 tool steel	375	Machining	427
Hardness	727	Maitreya	751
Heat exchanger	571	Manufacturing	865
Heterogeneous components	179	Martensite	727
Heterogeneous solids	187, 199	Martensitic (400 series) Stainless Steels	727
High pressure laser chemical vapor deposition	543	Master pattern	767
Holes, fine	297	Material properties	453
Hot Isostatic Pressing	281, 759	Maximum strength	487
Hydrogels	511	Mechanical alloying	311
Ice Patterns	591	Mechanical properties	343
Inconel 625	281	Mechanical property	427
Infiltration	289, 461,	Mechatronics	695
	563	Medical images	599
Inhomogeneous object	77	Mesoscale prototyping	849
Injection molding	219, 461	Mesosopic	687
	607	Mesostructure	335
Injection molds	793	Metal parts	655
Inorganic material	503	Metal powder	229
In-situ fabrication	671, 857	Metallic prototypes	639
Inspection	129	Metallography	265
Integral Can	281	Micro fabrication	687
Interlayer bonding	639	Microgravity	671

Keyword Index

Microscale processing	297	Process maps	383
Microstructure modeling	461	Process modeling	103, 247, 825
Microturbine engine	427	Process parameters	273
Microwave resonators	865	Process planning	1, 67, 85, 111, 121
Minimum	163	Process selection	9, 19
Mixed mode convection	247	Processing	273
Modeling	179	Prototype test	29
Mold SDM	427	Prototyping	59
Mold	767, 801	Pulsed Laser	537
Molds	759	Radio frequency filters	865
Molten droplet deposition	435	Raman scattering	479
Molybdenum	411	Rapid Freeze Prototyping	591
Multi-jet 3DP	631	Rapid manufacturing	711
Multi-material	519, 695	Rapid Prototyping & Manufacturing	9
Multi-modal structures	695	Rapid Prototyping (RP)	85
Multiple material freeform fabrication	187, 199, 209, 825	Rapid prototyping process	39
Muscle-like actuators	511	Rapid Prototyping	1, 19, 47, 77, 139, 179, 273, 427, 461, 591, 647, 655, 663, 783, 873
Nearest neighbor heuristic	95	Rapid steel	563
Neck formation	411	Rapid tooling	19, 219, 461, 553, 623, 655, 783, 793, 801, 809, 873
Nickel	255	Rapid	59
Novel buildstyles	95	Real-time image processing	735
Nuclear Magnetic Resonance (NMR)	471	Refrigerative stereolithography	583
Numerical analysis	817	Re-normalization Group Method	229
Object-oriented design	9	Reverse engineering	47
Optimal design	179	Rheology	351, 639
Optimal laser path	487	Rotation operations	95
Optimization	1, 39, 129	RP	663, 817
Orientation	1	Rubber	809
Oxidation	265	Ruled edge layer prototyping	751
Part quality	247, 273	SALD virtual laboratory	147
Pattern	95	SALD	479
Phase transformation	727	SALDVI virtual laboratory	147
Phenolic resin	461	SALDVI	495
Plastic sheet	599	Sand casting	19
PMMA	303	Sand painting	695
Poly (ether ether ketone) (PEEK)	311	Sanders prototyping	833
Polyacrylamide polyacrylic acid	511	SandForm	759
Polycarbonate (PC)	311	Scale model testing	883
Polymer diffusion	335	Scanning process simulation	129
Polymer parts	401	Selective aggregation	695
Polymerization	453	Selective Area Laser Deposition	471
Polymers	461	Selective Laser Powder Remelting	655
Polystyrene molds	615	Selective Laser Sintering (SLS)	85, 311
Pore structure	361	Selective Laser Sintering	255, 265, 273, 281, 297, 303, 503, 563, 615, 655, 759
Portable	487	Semi-solid metal	639
Powder based freeform fabrication	647	SFF System	487
Powder sintering	461	SFF	171, 663
Precision manufacturing	849	Shape Deposition Manufacturing	111, 239
Precursor resin	289		
Preferences	67		
Print queue	679		
Process control	369		

Keyword Index

ShapeMaker 2000	599	TetraLattice	553
Shrinkage	453	Thermal expansion coefficients	343
Silica	759	Thermal expansion	443
Silicon Carbide	289, 471, 479, 537	Thermal manufacturing	247
Silicon nitride	327, 427, 615	Thermal stresses	239
Silicon processing	687	Thermoplastics	743
Silicon	289	Thick layer rapid manufacturing	607
Similarity	29	Thick layer rapid prototyping	599
Simulated annealing	95	Thin-walled structures	383
Simulated core-cavity	553	Three dimensional printing	411, 631, 865
Simulation	1, 453	Ti-6Al-4V	369
Sintering aids	327	Titanium	655
Sintering dynamics	303	Tool path generation	121
Skeletons, metal	411	Tool path selection	19
Slicing algorithm	155	Tooling	759
Slip casting	615	Toolpath Generation	519
SLPR	655	Toolpath	95
SLS	247, 695	Tortilla	247
Smart rendering	487	Transfer	571
Solid Freeform Fabrication	121, 139, 229, 591, 647, 663, 783, 801, 865	Transmission Electron Microscopy	471
Solid modeling	187, 199	Traveling salesman problem	95
Sorting	155	Trowels	743
Space exploration	857	Twin formation	471
Space filling curves	95	Vacuum casting	623
Space-based manufacturing	671, 857	Vapor	59
Spin casting	719	Virtual environment	1
Stainless steel	529	Virtual prototyping	1
State correlation	29	Virtual reality	147
Steel	655	Virtual rendering	147
STEP	171	Virtual tubejoining	147
Stereolithography	67, 219, 443, 453, 583, 833, 841, 849	Volume modeling	77
Stereoview	147	Vulcanization	809
STL format	155	Warping	273
STL	47, 77, 171	Wax	631
Stratasys	335	Weld penetration	735
Strength	335	Welding bead	793
Stress concentration	319	Wire feed process	529
Stress cracking	273	World Wide Web	147
Stress reduction	571	Zig-Zag conformal cooling	553
Structural ceramics	427	Zirconia	297
Structural optimization	209		
Supports	583		
Surface defects	239		
Surface tension	265		
Tape casting	393		
TEM	471		
Temperature induced forming	623		
Tessellation	47		
Tetra lattice	571		